1980 Laser Program Annual Report

Lawrence Livermore National Laboratory

DISCLAIMER

UCRL-50021-80
Distribution Category
UC-21, 22

UCRL--50021-80-Vol.1

DE83 002429

Volume 1

1980 Laser Program Annual Report

Scientific Editors: Lamar W. Coleman
William F. Krupke
Publication Editor: John R. Strack
MS date: June 1981

Lawrence Livermore National Laboratory
University of California • Livermore, California • 94550

Available from: National Technical Information Service • U.S. Department of Commerce
5285 Port Royal Road • Springfield, VA 22161 • $19.00 per copy • (Microfiche $3.50)

ACKNOWLEDGMENTS

Preparing a comprehensive technical report of this magnitude is a large effort that involves the work of many people. The overall content of this report is, of course, the result of the efforts of the entire staff of our Program. The names of authors and major contributors responsible for a particular piece of work appear at the end of the article describing that work. The authors had the added tasks of organizing and writing the material and patiently participating in the iterative editing, review, and proofreading processes necessary for final publication. The able and responsive assistance of the Section Editors in collecting and reviewing the article was an especially valuable contribution to this report.

The process of preparing and publishing this report required the talents and participation of many members of the LLNL Technical Information Department. We are indebted to all of them for their help and support in this task: Elsa Pressentin coordinated all aspects of production, keeping them under control and on schedule. Donald Cowden, William Fulmer, Wilma Leon, Betty Stuermer, and Sharon Watson planned, guided, and coordinated the artwork and layout. Wilma Leon, in particular, deserves special mention for the prodigious commitment of her time and talent, seeing the effort through from its inception to final printing. William Fulmer and Rick Wooten brought considerable imagination and creativity to designing the general format and in preparing divider pages, section introductions, and covers. The innovative photography that appears on the annual slip cover, volume covers, and divider pages is the result of the imaginative and painstaking work of Don Gonzalez, Jim Stouts, Ben Walker, Ted Johnson, and Ken Way, the quality of their effort was enhanced by continuing support from Ken Hall of the Photography Department. The tedious and exacting job of proofreading was capably done by Jill Silvers, Solveig Shearer, Yvernia Hatcher, Delores Mason, and Duncan Frissell. Composition of a difficult, demanding text was the work of Cathy Wood and Stacy Bookless; their cheerful willingness to undertake last-minute revisions and corrections was a mainstay of the effort. Lynn Davidian and Mike Genin coordinated the vending of the mathematics and tabular text, and Tom Smith handled the classification and patent releases. Elaine Price ensured that composition resources remained available despite setbacks in the schedule. Final type specification and review for format consistency were expertly handled by Margaret Sylvester. Mel Moura did his usual fine job of coordinating the printing and binding contracts and maintaining high standards of printing quality under an extremely tight schedule. Charles McCaleb provided constant editorial support and overview, while the excellent job of editing complex technical articles was accomplished by John Strack, Jerry Grow, Phil Anderson, June Canada, Wally Clements, Thomas Elkjer, Steve Greenberg, Tom Jones, Doug McNaughton, Pamela Simpson-Smith, and Lee Taylor. Richard Pond and Robert Budwine of the Classification Office went to great lengths to ensure that issues concerning the sensitivity of technical information were resolved quickly. Bert Weis of the Patent Office was responsible for the meticulous review and final clearance of this material for public use.

Olga Parker of the Laser Program Multimedia Group has devoted a great deal of her time to coordinating the preparation of the original versions for most of the illustrations used in this report. The Program clerical staff and administrative assistants sustained the responsibility for preparing the original manuscripts, in addition to their normal workloads. Their contributions are greatly appreciated. To these people, and all the others we have not mentioned by name, we offer our thanks for their hard work and for a job well done.

Suzanne Anderson, our assistant in preparing this report, merits our special thanks; her extremely capable and persistent dedication was an essential ingredient in every aspect of the generation and production of this report. It has been a pleasure once again to work with John Strack, our Publication Editor, throughout the production of this report. His enthusiasm, energy, and expert approach in balancing the design, editorial, and technical requirements have produced an outstanding publication.

L. W. Coleman
W. F. Krupke

FOREWORD

This report presents the unclassified activities and accomplishments of the Laser Program at the Lawrence Livermore National Laboratory for the calendar year 1980. The classified work of the Program in 1980 is being reported separately. The Laser Program at LLNL, comprised of both Laser Fusion and Laser Isotope Separation efforts, is supported by the United States Department of Energy.

Our purpose in preparing this report is to present our work in depth for the benefit of the inertial confinement fusion and isotope separation communities. Accordingly, concepts, theoretical analyses, computational results, design and configuration of experiments, data, and results are presented in detail to allow critical technical evaluation and to make it possible to reproduce or extend any of the work presented here. In 1980 we realized significant scientific and engineering accomplishments in all areas of our Program. In the fusion effort, a major highlight of the year has been the conversion of the Argus laser to a green/blue target irradiation facility and the experimental demonstration of dramatic improvements in critical laser–plasma coupling and drive parameters; in the isotope separation effort, a major highlight of the year has been the successful scaling of copper vapor laser devices to a level of 150 watts maximum extractable power per aperture, an attractive level for use in uranium enrichment plants.

This report is published in three volumes; the major sections correspond to the division of technical activity in the Program. Section 1 in Volume 1 provides a Program Overview, presenting highlights of the technical accomplishments of the elements of the Program, a summary of activities carried out under the Glass Laser Experiments Lead Laboratory Program, as well as discussions of Program resources and facilities. Section 2, also in the first volume, covers the work on solid state Nd:glass lasers, including systems operations, Nova and Novette system development, and supporting research and development activities.

Volume 2 contains five sections that cover the areas of target design, target fabrication, diagnostics, and fusion experiments. Section 3 reports on target design activities, plasma theory and simulation, code development, and atomic theory. Section 4 presents the accomplishments of the Target Fabrication Group, Section 5 contains the results of our diagnostics development, and Section 6 describes advances made in the management and analysis of experimental data. Finally, Section 7 in Volume 2 reports the results of laser target experiments conducted during the year.

Volume 3 is comprised of three sections, beginning with Section 8 on Advanced Lasers. Both theoretical and experimental research and development activities on advanced laser systems are presented here. Section 9 contains the results of studies in areas of energy and military applications, including those relating to electrical energy production by inertial confinement fusion systems. Finally, Section 10 presents results from selected activities in the Advanced Isotope Separation Program.

L. W. Coleman
W. F. Krupke

Contents

Volume 1

Volume 2

Volume 3

Section 1 Laser Program Overview

Laser Program Overview

Contents

Laser Program Overview

Introduction

The principal components of the Laser Program at the Lawrence Livermore National Laboratory (LLNL) are laser fusion and laser isotope separation. The goals of the Laser Fusion Program are to produce significant well-diagnosed thermonuclear implosions in the laboratory and to exploit this capability for military applications in the near term and for civilian power applications in the longer term. The military applications of laboratory implosions are two-fold: (1) to investigate and enhance our understanding of nuclear weapons physics in support of the weapons program, and (2) to simulate effects of nuclear explosions on military targets. A further, implicit feature of the program is to strengthen and broaden the intellectual resource base of the weapons program through the process of developing and applying inertial confinement fusion (ICF) technology. The longer-term objective of developing ICF technology for civilian power applications is one that offers a very high payoff, but one that also entails a considerably higher technical and economic risk.

Through the mid-1980s the Laser Fusion Program will focus on achieving ignition conditions in a thermonuclear plasma, a necessary milestone on the way to either application of ICF technology. In order to develop the basis of scientific understanding leading to the demonstration of ignition, we have constructed and operated a series of experimental facilities over the past eight years. Using Nd:glass lasers, a mature and flexible technology, we have been able to progress from Janus (40 J, 1973) to the construction of Nova. Experiments conducted on our facilities have resulted in progressively increasing fuel temperatures and densities. More importantly, these experiments have greatly increased our understanding of the interaction of intense laser light with targets and of the physics of laser-driven implosions. This, in turn, has enabled us to identify critical requirements for ICF targets and, consequently, has led to significant advances in both target design and target fabrication technology.

During 1980, we emphasized strengthening our understanding of the physics of laser fusion targets, both directly driven and radiation-driven, and improving our ability to diagnose the properties of relatively cold, dense plasmas. Operating the Argus facility at 0.53 and 0.35 μm, we have explored the wavelength scalings of absorption, stimulated scattering, and x-ray conversion processes and their impacts on target performance. Figure 1-1 summarizes the results of our

Fig. 1-1

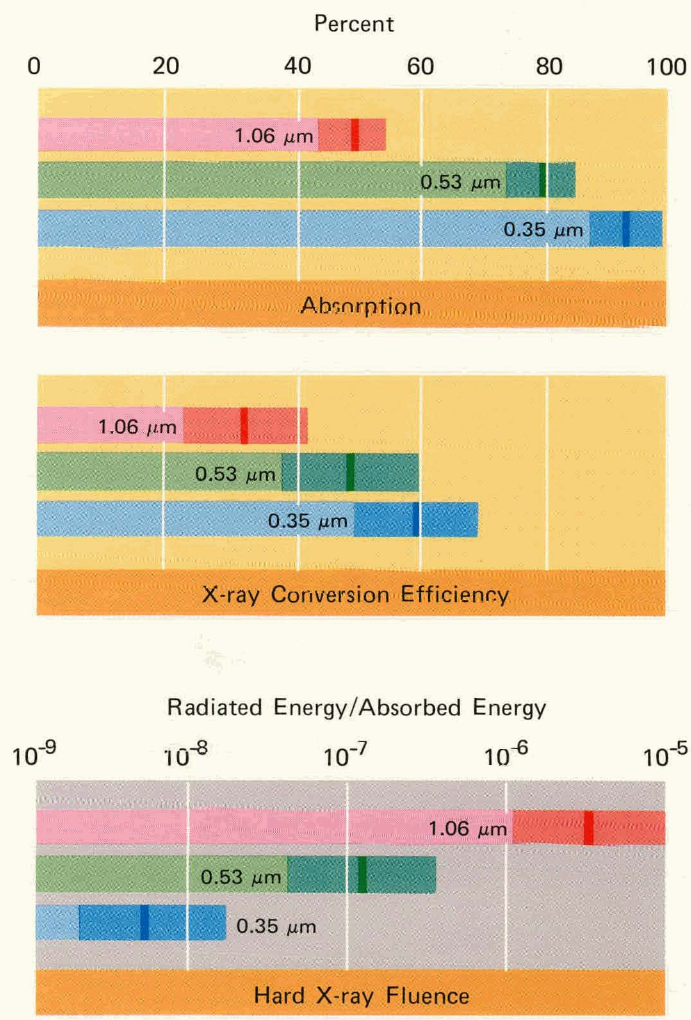

experimental measurements of absorption, soft x-ray conversion efficiency, and suprathermal x-ray production obtained with 1.06-, 0.53-, and 0.35-μm laser irradiation of Au disks at intensities of 3×10^{14} W/cm^2. The dark vertical bars surrounded by color blocks represent the measured values and their associated uncertainties. These initial experiments have verified the theoretical predictions of dramatically improved target coupling and reduced suprathermal electron production at short wavelengths. With Shiva, we extended our series of measurements of dense [>100× liquid density deuterium–tritium (D–T)] implosions, with improved confidence in the diagnostic results.

Our target fabrication effort is devoted to the development of various technologies required for both current targets and more complex targets required in the future. We have fabricated both radiation-driven and directly driven target types, are continuing to study both types, and will be able to test either type with Nova. We have made advances in several aspects of target technology, especially in the development of diagnostic targets, including bromine-seeded and copper-coated spheres. Our techniques for target characterization and metrology were further advanced for both transparent and opaque targets.

Through improved target theory, we have obtained a better definition of the relation between absorbed energy and target gain. We have developed theoretical models for the performance of hohlraum targets which are in good agreement with our experimental data. The critical task of designing the experiments to be conducted on the next generation of facilities (Nova and PBFA II) has been initiated. In 1980, we refined the design of heavy-ion driven targets and found significant improvement in their theoretical performance.

Fig. 1-2

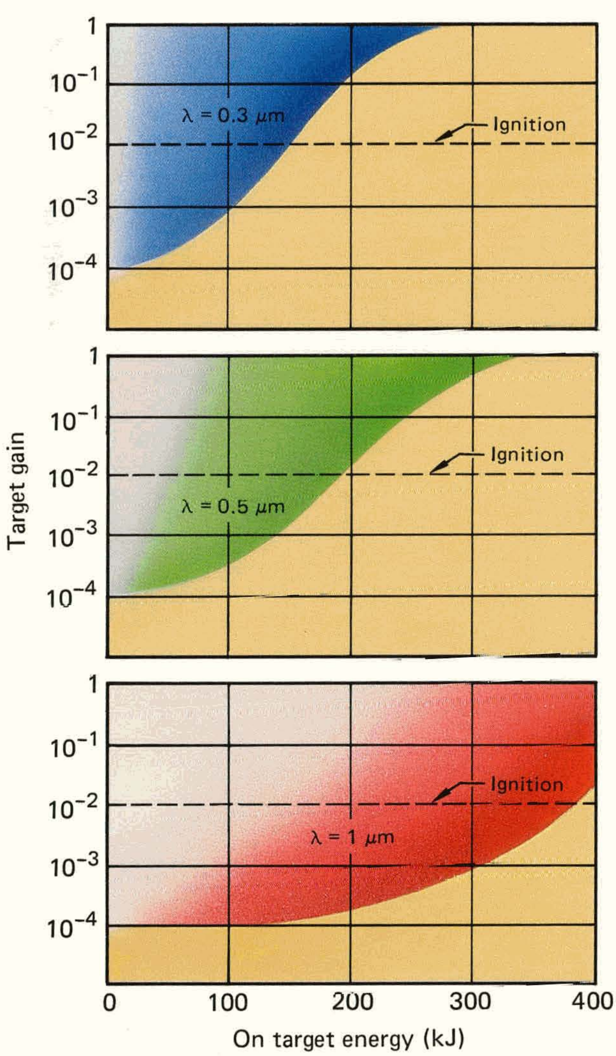

Supported by our improving understanding of and confidence in wavelength scalings, our current projections of attainable target gain as a function of on-target energy at 1, 0.5, and 0.3 μm are summarized in Fig. 1-2. The densest (most intense) color region shown for each wavelength denotes the best target performance that we confidently believe can be realized shortly after experiments begin with the requisite driver, provided that the necessary target fabrication and diagnostics capabilities have been developed. The continuously fading colors, progressing toward higher target gain and lower energy out to the theoretical limits (white), signify target performance that we believe is achievable but with continuously decreasing probability in the near term. Raising the probability of achieving increasingly efficient performance represented by the fading color in the figures requires correspondingly increasing expenditures of time, money, and effort.

We have completed the design of the twenty-beam Nova laser, which is capable of producing nominally 200 to 300 kJ of 1.05-μm light, or 130 to

200 kJ at 0.53 or 0.35 μm, in a 3-ns pulse. At present, we have received DOE approval for the completion of ten beams of Nova, and are awaiting final DOE review of our proposal to complete the full system with frequency flexibility. In order to obtain new data to increase our confidence in the design of Nova targets for ICF milestones and to gain experience in operating Nova hardware and subsystems, we will replace the present Argus system with two Nova beam lines which will provide 15 to 20 kJ of 1.05-μm radiation, and up to 10 to 14 kJ of 0.53-μm light in a 3-ns pulse. This system, Novette, will operate in late 1982 to early 1983. Shiva and Argus will be retired in 1981 to permit changeover to the Novette system.

In parallel with the development of our fusion target design and fabrication capabilities and with the target experiments program, we have pursued the investigation of alternative driver technologies, emphasizing those drivers which offer the promise of reduced cost and higher efficiency. During 1980, we were designated as lead role laboratory for short-wavelength laser development. We have formulated a national program plan involving industrial contractors and have coordinated the efforts at the three DOE Defense Program laboratories. Within the resource guidance provided by DOE, the plan provides for the construction of a 10-kJ system test bed and 100-kJ power amplifier module in the 1985–1986 timeframe, as a means of evaluating pulse-compressed excimer laser technology. Several other advanced laser concepts will also be evaluated at a lower level of effort.

For both military and civilian applications, it is essential that technology be developed in the context of its ultimate use. With respect to civilian power applications, in 1980 we have continued the conceptual development of the high-yield lithium-injection fusion-energy (HYLIFE) converter, performed cost analyses relative to fusion power plants using the HYLIFE converter, and introduced a new liquid metal reaction chamber concept which utilizes a liquid-metal/wick structure facilitating a higher pulse repetition rate than is feasible with the HYLIFE design. In the area of military applications we have conducted ultra-high pressure shock wave experiments to acquire equation of state data for aluminum and copper in the pressure regime 0.3 to 3 TPa. A more extensive review of our military applications activities can be found in our classified 1980 annual report.

In 1979, LLNL was designated as lead laboratory for target experiments using short-wavelength lasers. Three major support laboratories were identified (the University of Rochester Laboratory for Laser Energetics, KMS Fusion, Inc., and the Naval Research Laboratory) where glass laser facilities devoted to ICF research are in operation. As lead laboratory, we are responsible for providing technical direction to the support laboratories and for integrating their activities into the national program. During 1980, lead laboratory management was put into effect, and coordination of the support laboratory programs with the LLNL program was established. The lead laboratory program has fostered technical interchange among the laboratories and has progressed significantly toward its goal of more effective use of national resources in achieving the ICF Program's objectives.

The goal of the Laser Isotope Separation Program is to develop laser isotope separation technology for both military and civilian applications. The Atomic Vapor Laser Isotope Separation process (AVLIS), which we are developing for the production of enriched uranium fuel for light-water reactors, promises to be more efficient and less expensive and energy-consuming than the technologies currently available.

The Laser Isotope Separation program has been organized into four progressive stages: starting with technology evaluation, followed by technology demonstration, engineering demonstration, and economic demonstration. We are now nearing the end of the first stage. We demonstrated the scientific feasibility of the uranium atomic vapor process in 1974, and have subsequently developed the technology for the laser, vaporizer, and extractor systems. In 1980, we integrated the Venus copper vapor laser system into our process-simulation experiments, substantially increasing the volume of vapor illuminated. We also initiated the operation of the Mars process chamber, which will provide a significant increase in uranium vapor production for our scaling experiments.

Author: J. L. Emmett

Summary of Major Activities

In this report, we present our achievements and research accomplishments for calendar year 1980. These results represent the combined activities of more than 550 people, working with a total operating budget of $65.9 million for the year. In this overview, we present a summary of the major technical activities of the program, followed by highlights of the lead laboratory program and summaries of program resources and physical facilities.

Fusion Lasers

In 1980, we administratively combined the Solid State Laser and the Advanced Quantum Electronics Programs to form the Fusion Lasers Program. This action enables us to take advantage of the technical and program management experience we gained in developing and deploying large Nd:glass laser systems (Argus, Shiva, Nova) to benefit

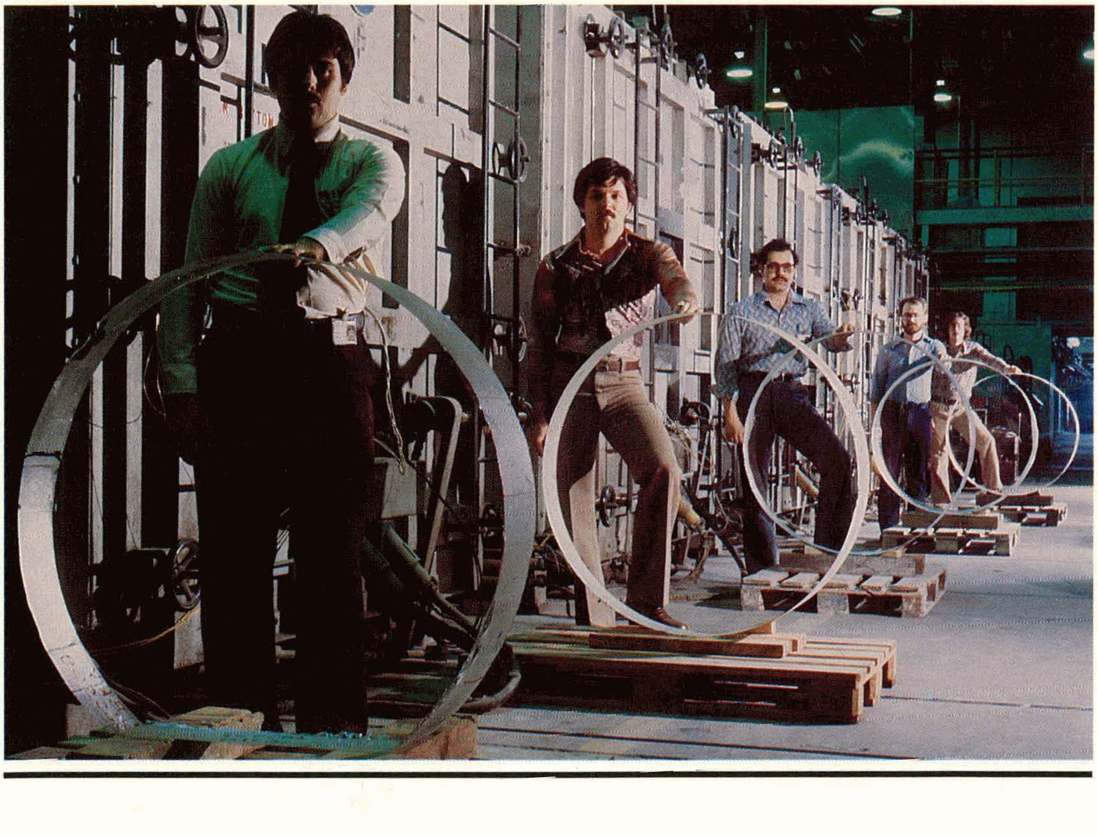

Fig. 1-3. The 1.2-m-diam BK-7 Nova mirror blanks.

our advanced laser systems development activities. The overall objective of the Fusion Lasers Program is—through our in-house technical efforts and through our Lead Role Laboratory assignment for advanced lasers—to provide the short-wavelength laser system facilities required for the National ICF Program.

Solid State Laser Program

The objective of the Solid State Laser Program is to design, construct, and operate the Nd:glass laser facilities required for inertial fusion research at LLNL. In 1980, we directed our efforts to the five technical areas discussed in Section 2, "Solid State Laser Systems and Technology":

- Nova.
- Shiva/Argus operations.
- Novette.
- Solid state laser R&D.
- Basic research.

Nova was originally designed to provide 200 to 300 kJ on target at 1.05 μm at a maximum power of 200 to 300 TW. The final design completed in 1980 indicates that the upper end of this performance range will be achieved. The Nova project proceeded well during 1980. The first phase of Nova, approved by DOE, involves the construction of both the laboratory building (to house ten 74-cm-diam beam lines) and the Nova office building. By the end of 1980, both structures were more than 50% complete. The Nova laser chain design using phosphate laser glass was frozen in 1980, and we have initiated procurement of all long-lead optical components except for the laser glass. Figure 1-3 shows a number of 1.2-m-diam BK-7 mirror blanks that will be used to turn the 74-cm-diam Nova laser beams onto the target.

During 1980, we operated the Shiva laser on a two-shift schedule, providing pulses with a maximum power of 20 TW and a maximum energy of 20 kJ. The operational flexibility of Shiva allowed us to conduct experiments with pulse widths from 100 ps to 35 ns. During the year, we obtained a great deal of scaling information on fusion targets.

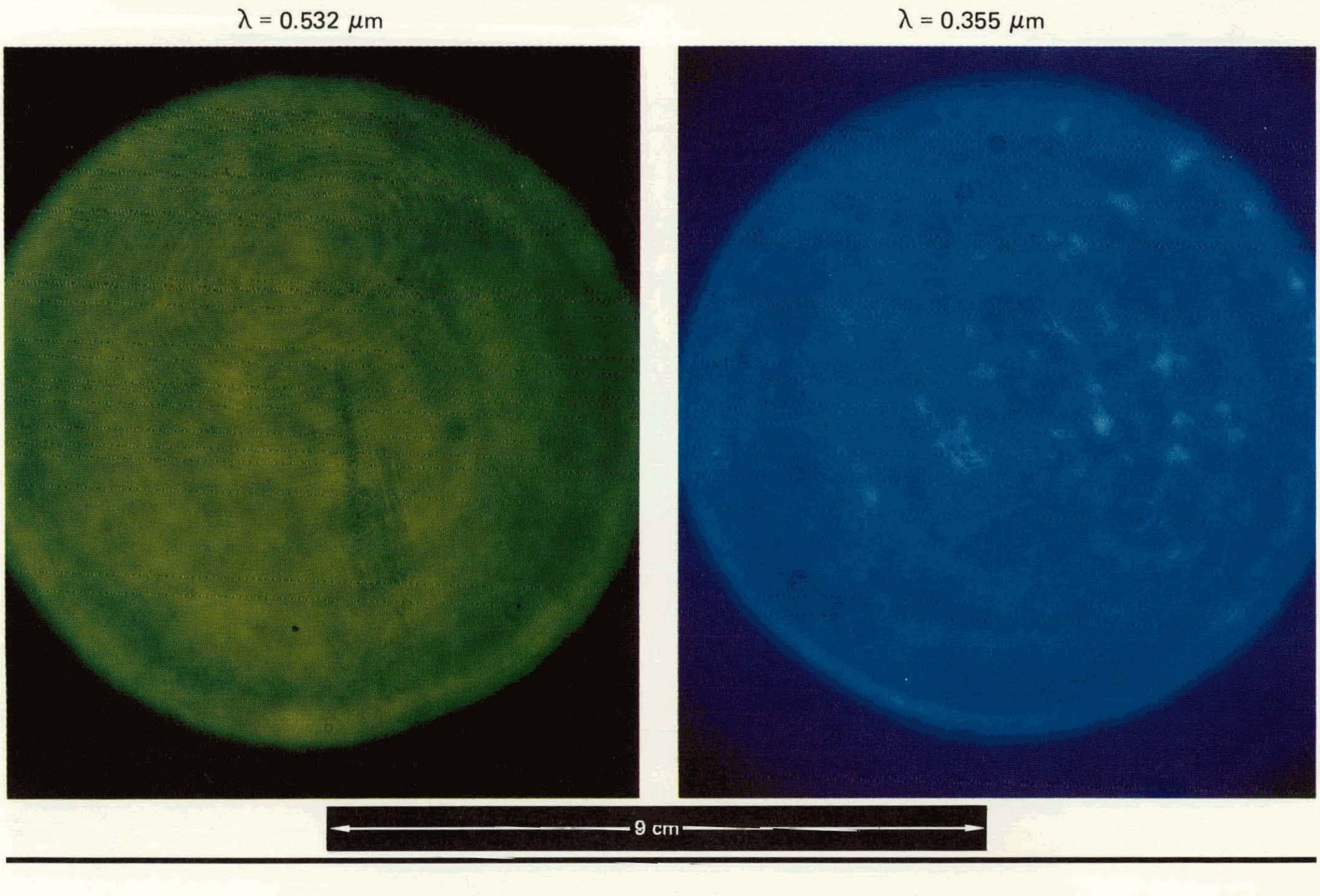

Fig. 1-4. Second- and third-harmonic output beams of the Argus laser.

Of particular note, we were able to drive a target to a D–T fuel density of 100 to 200 times liquid density.

We operated the Argus laser as a multi-wavelength irradiation facility in 1980. We demonstrated external conversion efficiencies of 75 and 55% to the second (2ω) and third (3ω) harmonics, respectively. With good beam quality as shown in Fig. 1-4, we operated the up-converted laser system at the 30-J level and acquired a complete set of absorption, x-ray conversion efficiency, and hot electron data for comparison with laser plasma coupling models and simulations.

In 1980, we designed the two-beam Novette laser system based on Nova laser hardware and incorporated 74-cm-diam harmonic conversion crystal arrays. The Novette laser system will provide up to 20 kJ of 1.05-μm light and up to 14 kJ of 0.53-μm light on target in a 3-ns pulse.

The Solid State R&D efforts focused on successfully prototyping the Nova plasma shutter and the Nova 46-cm-aperture amplifier (shown in Fig. 1-5), which uses split laser disks. Significant progress was also made on the development of large-area graded-index glass components for use in low-loss, high-damage-threshold spatial filter lenses. Technology development of harmonic crystal arrays and the design of an effective multi-color system configuration has also progressed significantly.

Advanced Lasers

The objectives of the advanced lasers effort are to identify, demonstrate and assess short-wavelength laser driver systems capable of being scaled to achieve the ICF milestones of high pellet gain (>50) and power production.

In 1980, our research and development activities (presented in Section 8, "Advanced Lasers") emphasized pulse-compressed rare-gas halide (RGH) laser systems as the baseline approach to meeting the program objectives. Using the RAPIER (Raman Amplifier Pumped by Intensified Excimer Radiation) RGH laser system test bed, we demonstrated the technical feasibility of the hybrid pulse-compression system architecture. A 20-fold temporal pulse compression was achieved by first compressing the 60-ns output pulse of the e-beam excited A-amplifier by a factor of 3 using the technique of angle-multiplexing, followed by a seven-fold compression using the technique of backward-wave Raman scattering. The latter was accomplished using methane gas as the Raman medium, contained in a grazing-incidence light-channel cell.

Toward the end of 1980, we developed a concept for a new pulse-compressor laser system architecture, the Raman Accumulator, in which the (KrF) excimer pump

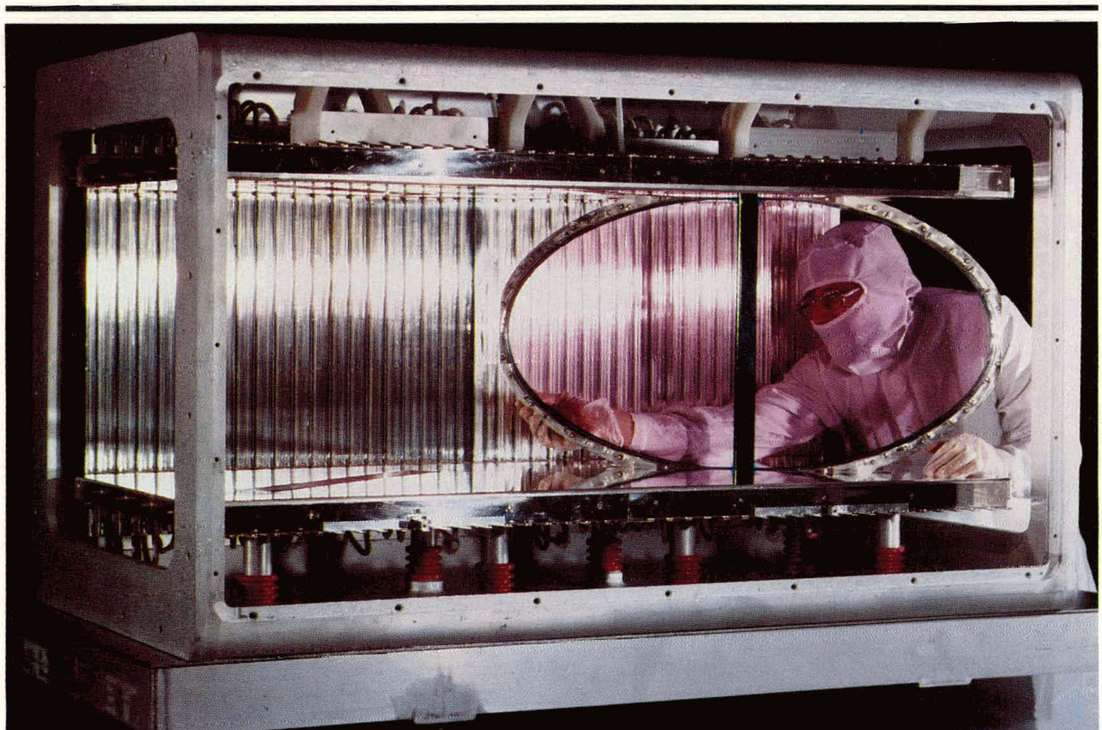

Fig. 1-5. A 46-cm-diam Nova output amplifier.

medium and the Raman converter medium are contained in coupled resonator cavities. Preliminary analyses of this regenerative type of laser system indicate that a very compact and cost-effective multimegajoule driver system can be configured. A conceptual layout of a megajoule accumulator system is shown in Fig. 1-6.

In addition to our primary efforts on RGH laser systems, we have continued to develop and evaluate two other advanced laser systems. The V:MgF_2 laser is representative of high-average-power solid state lasers. Crystal growth experiments carried out at the Lincoln Laboratory have shown that solid solutions of crystalline VF_2 and MgF_2 can be grown up to 10 wt% VF_2 without significant quenching of excitation energy. This VF_2 concentration level is well in excess of that required for efficient pumping of large V:MgF_2 fusion lasers. In addition, absolute spectral cross sections and the energy storage lifetime of the V:MgF_2 laser medium have been determined as a function of temperature.

We continued the analytic and computational investigation of the free-electron laser (FEL) as a fusion driver. We have continued to extend and refine our models of the optical beam interaction with the electron-beam/wiggler structure, with emphasis on propagation effects. We have also examined the feasibility of using a circular betatron as an electron-beam accelerator in a high-current FEL system and have identified the key technical issues requiring further evaluation.

Target Design

The design of targets to achieve the program goals requires the combined efforts of our plasma, code development, and design groups. As described in Section 3, "Target Design," these groups develop theories of beam-plasma interactions, implosions, and thermonuclear microexplosions, build requisite computer codes, and use these tools to design targets and simulate experiments.

In 1980, we succeeded in using the Shiva laser to implode D–T fuel to densities over 100 times liquid D–T density at a temperature of 0.5 keV in laser-driven hohlraum targets. Preshot theoretical predictions of the target performance are in excellent agreement with the measured results. Theoretical models have been developed which correctly predict hohlraum temperatures and suprathermal electron scaling.

Recent experimental confirmation of theoretical predictions of improvements in laser plasma coupling at short wavelengths represent a very significant development in ICF research. Theoretical scaling from the

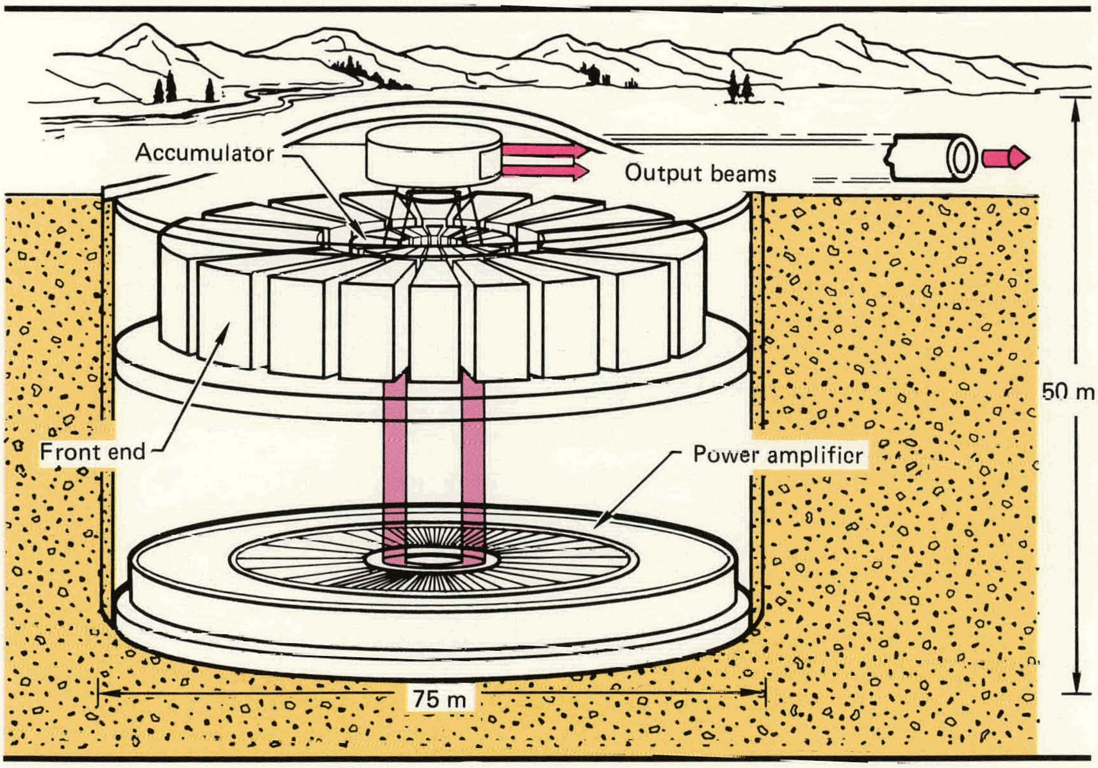

Fig. 1-6. Megajoule excimer accumulator system layout.

preliminary results of Shiva hohlraum experiments indicates that the suprathermal electron problem will be controlled in Nova and reactor targets by using 3ω light ($0.35\ \mu m$). We have pursued theoretical studies addressing plasma heating, electron generation, transport, and stimulated processes. Our theoretical predictions of the importance of Raman processes in targets with sufficiently long plasma scale lengths were confirmed. Further experiments with well-diagnosed plasma conditions in larger underdense plasmas are needed to solidify our theoretical analyses, which predict that the hot electrons are generated predominantly by the Raman and $2\omega_p$ processes.

The capabilities of LASNEX have been enhanced through introduction of new operational and code structure features. New modeling of atomic physics processes important in ICF have been pursued.

Our calculations continue to support the theoretical possibility of achieving ignition and scientific breakeven with a 10-kJ short-wavelength laser, provided that stringent symmetry, fluid stability, pulse shaping, and frequency shaping requirements can be met. However, these milestones will most likely be first achieved with 0.1- to 1-MJ drivers (Nova, PBFA II) because success at the 10-kJ level requires approaching ideal target performance limits, whereas there is reserve and margin for uncertainty at the 0.1- to 1.0-MJ level. The feasibility and scale of ignition–scientific breakeven are only weakly coupled to the feasibility and scale of the high-gain fusion microexplosions required for civilian and military applications. Nevertheless, we have developed a scenario of experiments that can be performed with 0.1- to 1-MJ drivers to demonstrate that sufficiently high gains can be achieved at the multimegajoule size and to confirm theoretical scaling.

We made significant advances in the design of charged-particle targets in 1980. We have produced a design for a heavy-ion reactor target whose theoretical performance matches that of a short-wavelength laser target design. We have also developed a design for a light-ion target that achieves ignition (in calculations) when driven by about 2 MJ of light ions.

For direct implosions, we are pursuing both single- and double-shell designs with low-density outer shells. The low-density feature makes the achievement of high gain possible without reliance on unproven methods of controlling fluid instabilities. These current designs do not yet achieve what we believe to be their ultimate performance potential, but we have several promising concepts for improved designs that provide higher gains with less driver energy. Our estimates of fusion-reactor driver requirements and our calculated gain curves remain the same as those presented last year.

Target Fabrication

Our primary target fabrication tasks are two fold: to develop the technologies needed to produce targets that meet future requirements and to provide the targets required for our current experimental program. Much of this work encompasses research and development of materials and techniques versatile enough to meet the needs imposed by a variety of target concepts and designs (described in Section 4, "Target Fabrication").

The major portion of our work is done in the areas of hollow sphere development and production, coatings and layers, cryogenics, characterization (micrometrology) and analysis of materials, and D–T fuel fill. In 1980, we made advances in all these areas.

Through the development of new equipment and procedures, we have been able to increase the diameters of the glass microspheres we produce to 1.7 mm. We have also begun to produce hollow metal spheres with our liquid droplet systems (as well as by blowing the metal spheres individually). We have developed techniques for filling spheres with special gases for diagnostic purposes. Bromine is a particularly interesting material for neutron activation and x-ray line emission measurements of compressed target fuel density. We have successfully put bromine as a tracer in D–T filled microspheres. The techniques for filling microspheres with D–T have been improved for better control and reliability, in addition to better control of contamination from foreign materials on the microspheres during fill.

Our work on coatings and layers this year has included continued development and use of the molecular beam levitation system for coating individual microspheres. Processes for batch coating microspheres are being developed and evaluated. We have continued to build our capabilities to produce uniform, smooth polymer- and metal-seeded organic coatings. Metallic coating techniques have been employed, for example, to uniformly coat copper onto microspheres as a diagnostic material for implosion experiments.

Stepped-joint hemispheres are assembled around an inner assembly to form the outer shell in two-shell targets, as shown in Fig. 1-7. We are able to produce and assemble these mating edge-stepped parts with the high quality required for targets.

Characterization and analysis of materials, parts, and complete targets are difficult but essential tasks. A variety of microanalytical and metrological techniques are brought to bear on these problems. We have developed an energy-selectable monoenergetic x-ray source that produces high-resolution microradiographs of optically opaque targets to 1-μm accuracy. We have continued developing automated surface-mapping capabilities that use both interferometry and electron backscattering. Microsectioning techniques developed for target spheres permit us to examine the inner structure of the target wall and corroborate our nondestructive measurements.

Our cryogenic work this year has centered on three areas: (1) experimenting with fill tubes and hydrogen isotope "powders" for forming thick fuel layers, (2) continued study of the layers formed by a fast refreeze technique, and (3) in designing and evaluating cryogenic target holding, positioning and shielding hardware.

We have done mathematical modeling to describe the process rates in an ICF target factory. An analysis of such systematics can help identify critical rate and process factors for further study and optimization.

Fusion Experiments, Diagnostics and Analysis

The Fusion Experiments program element has the responsibilities to plan and conduct our laser fusion experiments, to develop and implement the necessary diagnostic techniques and instrumentation, and to reduce and analyze the data from experiments. This work in 1980 is presented in detail in Sections 5, 6, and 7 of this report (i.e., "Diagnostics," "Management and Analysis of Experimental Data," and "Laser Fusion Experiments and Analysis," respectively).

We used the Argus Nd:glass laser to conduct a series of experiments to study the wavelength scaling of absorption, scattering, x-ray conversion efficiency, and hohlraum target performance. The output of the laser was converted to the second and third harmonic at 9-cm aperture; the experiments were conducted with $\gtrsim$30 J at either wavelength. The results support the predicted favorable theoretical scalings of increased absorption and x-ray conversion efficiency and reduced fraction of energy in suprathermal electrons at shorter wavelengths.

Our major target experiment efforts with Shiva centered on achieving and diagnosing compressed D–T fuel densities in excess of 100 times liquid density and understanding the conditions required to achieve this density to support the scaling to Nova targets. We have also conducted a series of experiments with Shiva to study a number of other physics issues and scalings important to hohlraum-driven targets and to directly irradiated targets. Targets irradiated for equation-of-state studies at Shiva have produced the highest pressure shock waves yet observed in the laboratory.

We have made substantial progress in the development, improvement, and implementation of our diagnostic instrumentation during the year. We have succeeded in absolutely calibrating our soft x-ray streak camera to provide absolute x-ray spectral measurements with 15-ps time resolution.

Fig. 1-7. Double-shell target.

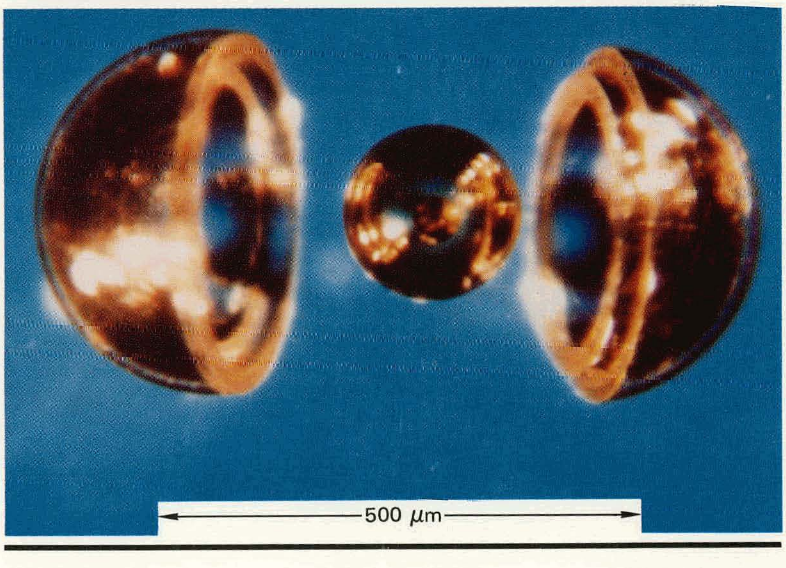

Spatial discrimination was added to the soft x-ray streak camera and to Dante in order to localize sources of x-ray emission, and new schemes using multilayer x-ray interference mirrors for improved energy discrimination were adopted. The 22× magnification Wolter x-ray microscope-streak camera system was completed at Shiva and used to obtain x-ray images with high spatial and temporal resolutions both from target self-emission and with x-ray backlighting (an example is presented in Fig. 1-8).

High-energy x-ray measurements have been extended to 200 keV with a unique new filter-fluorescer system, and an optical streak camera has been successfully used to simultaneously record the high-energy x rays and the laser pulse to obtain absolute, high-resolution timing. Advanced techniques for fabricating thick, high-resolution micro-structures for imaging suprathermal x rays have been developed. We are pursuing techniques for generating x-ray pulses suitable for x-ray probing diagnostics and have conducted analyses of the requirements on these sources for diagnosing various classes of targets via backlighting.

Experiments at Shiva with targets containing Br seed gas added to the fuel provided data on the retrieval fraction of the Br tracer. Neutron activation of the Br will allow a direct measurement of compressed fuel ρR. We were able to image x-ray line emission from the Br in these experiments to determine fuel density.

A new optical instrument for diagnosing Brillouin and Raman sidescattering has been designed and the data collection system constructed. We have prepared a detailed design for a 4ω UV probing–interferometry plasma density diagnostic system for the Novette facility.

Additional advances were made in the development of charge coupled devices for data recording in a number of diagnostic applications and new optically triggered switches for providing fast, high-voltage electrical pulses required by some of our instruments have been built and tested.

We purchased and installed a VAX 11/780 computer as part of our formalized Fusion Experiments data management and analysis effort. Currently installed in a temporary location, the computer system is up and running, and many of our analysis codes are now operating on it. We have also received approval for, and have designed, a permanent addition to our office building for the Fusion Experiments Analysis Facility. Upon completion of the building, the computer system will be moved to it and made operational to handle the reduction and analysis of our unclassified and classified target experiment data, which will be acquired directly from the laser facilities over a special data link.

We are rapidly developing the programming and computational tools, resources, and expertise to provide capabilities for "quick-look" data processing, fully automated analysis, interactive analysis, individual shot archival, shot summaries, and experimental series data bases.

Fig. 1-8. High-resolution spatially and time-resolved x-ray images with x-ray backlighting of laser-driven disk target.

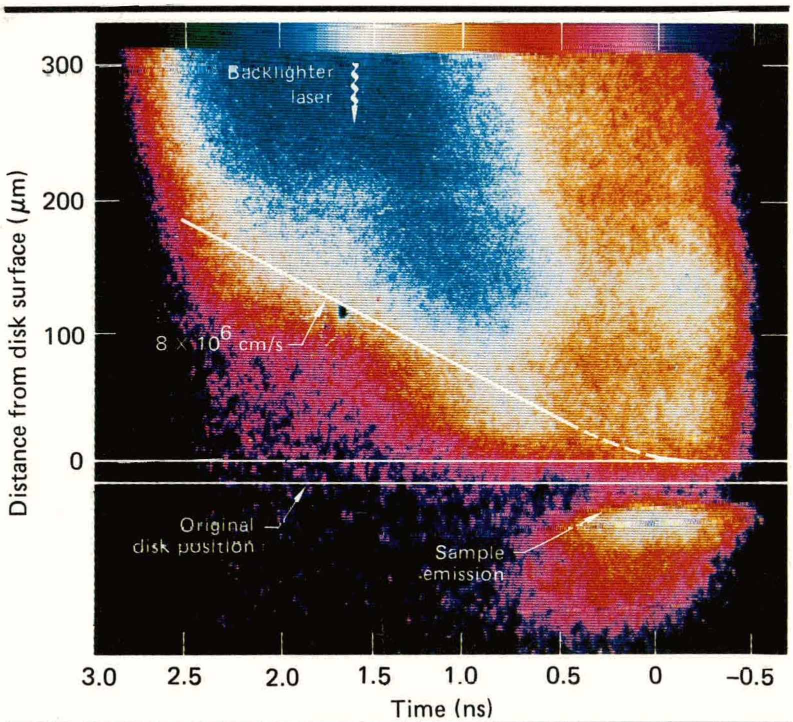

Energy and Military Applications

The objective of the Energy and Military Applications effort is to develop scenarios for the application of ICF technology to meet both military and civilian energy requirements. In our work, which is reported in Section 9, "Energy and Military Applications," we estimate the potential benefits and risks of each application, evaluate alternative development strategies, and create conceptual designs of test facilities and power plant reactors. For civilian energy production, we have been conducting a design study for a 1000-MW_e generating station. The design is based on the liquid-metal wall that converts the pulsed radiation output of the fusion pellet to heat without suffering excessive wall damage. This year we have examined many engineering aspects of liquid-metal systems, including the effects of corrosion, the effects of liquid-metal vapor on heavy-ion beam transmission, the technical requirements on liquid-metal pumps, and reactor safety issues.

In 1980, we proposed a new reaction chamber concept that utilizes a liquid-metal/wick structure which has the advantage of liquid-metal wall protection while permitting operation at higher pulse-repetition rate than is feasible with the HYLIFE design; it also can accommodate the use of either a laser or heavy-ion driver without requiring high liquid-metal flow rates.

In anticipation of the future deployment of ICF power plants, we performed some cost analyses of the HYLIFE converter and scoped the allowed costs of associated drivers, parametric in the cost of electricity. We also began the technical analysis to define a meaningful set of engineering objectives for an ICF reactor test facility.

Laser Isotope Separation

The purpose of the DOE Laser Isotope Separation (LIS) Program is to demonstrate a uranium isotope enrichment process that is both more energy efficient and less expensive than present technologies for producing fuel for light water reactors. In the LLNL Laser Isotope Separation Program, we are working toward this goal by developing an Atomic Vapor Laser Isotope Separation (AVLIS) process in which the U^{235} atoms in an atomic uranium vapor stream are selectively ionized using powerful tunable lasers. We then separate the ionized atoms from the vapor stream using electromagnetic forces.

In 1980, the AVLIS Program achieved significant technical progress in several areas (see Section 10, "Advanced Isotope Separation"). We combined the Regulis uranium separator with the improved SPP-II copper-vapor/dye laser system in order to conduct enrichment runs. We also integrated the Venus laser–power amplifier system into our process-simulation experiments, achieving a substantial increase in the volume of uranium vapor illuminated. The uranium vapor production rate will be increased 10-fold from earlier capabilities with the operation of the Mars vaporizer–chamber.

During 1980, we achieved a major advance in copper vapor laser (CVL) technology with the first successful operation of a large-bore (7.5-cm diam) longitudinal discharge device. When configured as an oscillator, we achieved a single-aperture output power in excess of 85 W at a pulse-repetition frequency of 5 kHz. We project a maximum extractable power of 135 W from the same devices configured as an amplifier.

We have continued to develop our economic model of the AVLIS process, including the results of recent technology advances. Our analyses continue to reinforce the position that AVLIS offers the advantage of both low capital and low power costs, relative to alternative enrichment technologies.

Lead Laboratory Program for 1.06-μm and Shorter-Wavelength Target Experiments

During the next few years there must be a strong theoretical, computational, and experimental effort to provide the basis of understanding for the design of Nova targets. In order to make optimal use of the available glass laser facilities in support of Program milestones, and to integrate the scientific talent resource at these facilities into the National Program, the Lead Laboratory for 1.06-μm and Shorter-Wavelength Target Experiments (Glass Laser Experiments) was established in November 1979. LLNL was designated as lead laboratory, and KMS Fusion, Inc. (KMSF), the Naval Research Laboratory (NRL), and the University of Rochester (U/R) Laboratory for Laser Energetics (LLE) were designated as major "support contractors," with funding continued over a period of several years. With the facilities at these four laboratories, the understanding of both target design and target physics can be advanced. The capabilities of the Nd:glass laser facilities at the support laboratories are summarized in Table 1-1.

The lead laboratory research activity at LLNL encompasses target experiments, target design, plasma physics theory, target fabrication, and technology development, as a part of a full-spectrum ICF program. The objective of the major support laboratory efforts is twofold: to complement the efforts at LLNL by pursuing promising alternative approaches and to supplement LLNL's efforts in areas of critical importance. Through lead laboratory management, LLNL provides technical direction to the support laboratories, to ensure that their activities are well integrated into the national program, and to ensure that the support laboratories are well-informed concerning both technical progress and strategic planning within the national program.

The Lead Laboratory Office is part of the LLNL Laser Program reporting to the Associate Director for Lasers. The Lead Laboratory Office does not have a permanent staff; instead, it draws on the resources of the LLNL Laser Program as required. In this way, a broad range of technical expertise is available as needed for proposal review, program evaluation, and technical consultation. All contracting activities within the lead laboratory program are carried out by the DOE Nevada Operations Office (NVO).

Resource allocations within the ICF program, including the funding levels for each of the support contractors, are determined by the Office of Inertial Fusion as part of the DOE budgeting process. Each contractor develops a work plan, in consultation with the lead laboratory, which then submits its recommendations regarding that work plan to NVO as a basis for contract negotiation. Program authority resides within DOE, while the lead laboratory provides technical direction and supplies technical information and guidance.

Technical direction is accomplished within the Glass Laser Experiments program by the process of technical interaction. Members of the technical staffs of the participating laboratories meet on a frequent and informal basis to discuss program plans and technical objectives.

Lead laboratory management provides for efficient use of the resources available in the program. The exchange of personnel and equipment is encouraged; joint experiments with LLNL personnel have been carried out at both KMSF and the University of Rochester. Work directed toward the goals of the National ICF Program can be proposed for the larger facilities (e.g., Nova) as they become available.

Because 1980 was the first full year of lead laboratory operation, it was necessary to establish and develop the entire set of operational administrative procedures and formal relationships. By the end of 1980, all three support laboratories were under contract, and a program of funded research activities in universities and industry (unsolicited proposals) had been structured.

Each support laboratory program has identified an area of concentration. At the University of Rochester, the emphasis is placed on experiments carried out at 0.35 μm, using the frequency-tripled output of the single-beam GDL laser. Omega, the 24-beam laser, can be configured to illuminate targets with a symmetric arrangement of 6, 12, or 24 beams. It will first be used for studies of multiple-beam, direct illumination at 1.05 μm. Off-line investigations of frequency-conversion technology, thin-film coating development, and laser damage also are included in the U/R program.

In addition to these activities, the U/R facilities are also available to outside users under the DOE-sponsored National Laser

Table 1-1. Nd:glass laser facilities at support laboratories.

Laboratory	Laser	No. of beams	Diameter (cm)	Total aperture (cm^2)	Power/energy at 1 μm (TW/kJ)	Comments
KMSF	Chroma I	2	14	308	1.9/0.9	Green operating
						Blue proposed
U/R, LLE	GDL	1	9	64	0.5/0.125	Blue operating
	Omega	24	9	1527	12/4	Blue proposed
NRL	Pharos	2	10.5	173	−/1	Long pulse (3 to 4 ns) combined beams

Users' Facility (NLUF). In 1980, several proposals for use of the NLUF were reviewed, and initial funding was granted to investigators. Experiments will be carried out in 1981 on the NLUF by several outside users, primarily in the area of diagnostic development.

The KMSF program emphasizes both target-fabrication technology and laser-plasma interaction physics. Each of the three target-fabrication activities in the national ICF program—Los Alamos, LLNL, and KMSF—has developed a range of fabrication techniques for fusion targets. During 1980, initial steps were taken to integrate these three activities into an optimized program in order to make the best use of the available resources. In addition to the development of target fabrication technologies, which complements the activities at LLNL and Los Alamos, in 1980 KMSF provided target-fabrication support to other laboratories in the program.

The experimental program at KMSF concentrates on two areas of investigation: physics of long-scale-length plasmas using long-focal-length, illumination optics, and uniform, direct illumination studies using the very fast "clamshell" optics to provide nearly uniform coverage of a sphere with two beams. Experiments are carried out at both the fundamental (1.05 μm) and the second harmonic (0.53 μm) of the KMSF laser.

At NRL, the ablative acceleration of thin foils is the principal subject of study. The objective is to evaluate target designs in which deleterious plasma physics effects are reduced by using a low driving intensity (10^{13} to 10^{14} W/cm^2). In this approach, hydrodynamic stability and implosion symmetry are the paramount issues. Both experimental and theoretical studies of foil acceleration are included in the NRL program.

In 1980, the support laboratories provided several notable contributions to the ICF program. At U/R, it was demonstrated that frequency tripling of Nd:glass output could be highly efficient (approaching 70% tripling efficiency in a fully optimized system). At KMSF, low-leakage microspheres were fabricated, and delivered to LLNL. In the experimental program, holographic-interferometry observations were made of the coronal density profile in high-Z spheres, and a high-density plasma jet was designed for studies of long-scale-length plasmas. At NRL, stable acceleration of foils up to a velocity of 10^7 cm/s was observed. Diagnostic development was initiated to determine if the foil was expanding or compressing during this acceleration. High absorption and high ablative efficiency were observed at the irradiation intensity levels employed.

In the funded research activity emphasis is placed on fundamental studies of target interaction physics, especially plasma physics effects arising in the laser-plasma interaction, reactor design studies, and novel laser concepts. In 1980, LLNL program funds were set aside to support this activity. In 1981, funds were earmarked in the ICF budget for that purpose.

Lead laboratory activities will continue in 1981. The basis of cooperative effort and integrated use of several facilities has been established. We anticipate that technical interactions and joint activities among the participants will continue to develop.

Program Resources

For fiscal year 1980, resources in the Laser Program totaled \$65.9 million in operating funds, \$4.9 million in equipment funds, and \$58.2 million for construction projects. The total number of internal program personnel—including the Nova line-item construction project—was 584. Figure 9-1 and Table 1-2 provide a graphical and tabular summary of the operating funds and personnel levels for both the Laser Fusion and Laser Isotope Separation Programs over the past 10 years.

Fig. 1-9. Ten-year history of laser program operating funds and personnel.

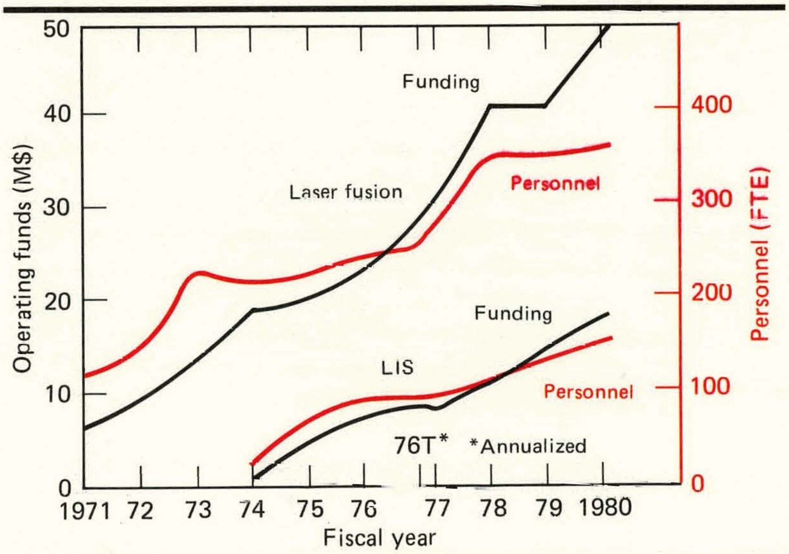

Table 1-2. Ten-year history of operating funds for Laser Fusion and Laser Isotope Separation Programs.

	Fiscal year										
	1971	1972	1973	1974	1975	1976	1976T[a]	1977	1978	1979	1980
Operating costs ($ million)											
Laser Fusion	6.5	9.5	13.5	18.4	19.9	22.2	7.0	30.8	40.4	40.6	48.0
Laser Isotope Separation	—	—	—	0.74	4.8	7.2	2.1	8.1	10.9	14.2	17.9
Personnel											
Laser Fusion	124	156	232	223	230	244	259	281	355	355	362
Laser Isotope Separation	—	—	—	23	70	90	92	94	116	131	151
Equipment ($ million)											
Laser Fusion	0.4	0.9	1.1	1.17	2.0	2.4	0.5	2.8	3.6	3.1	2.8
Laser Isotope Separation	—	—	—	0.13	0.7	1.5	0.3	2.4	1.9	2.2	2.1

[a]Transition quarter.

Table 1-3. FY 1980 Laser Fusion Program operating resources. ▼

Budget category	Personnel	Cost ($ thousand)
Nd:glass laser development	45	7 550
New laser development	30	3 990
Pellet design and fabrication	120	14 785
Target-interaction experiments	123	16 325
Diagnostics development	30	3 310
System studies and applications	11	1 750
Heavy-ion source development	3	315
Total	362	48 025

Budget category	Personnel	Cost ($ thousand)
Atomic-vapor process uranium isotope separation	124	13 600
Plutonium isotope separation	17	2 090
Deuterium laser isotope separation	2	200
Plutonium gas centrifuge	5	750
Advanced tritium recovery	2	160
Atomic-vapor process industrial participation	1	50
Total	151	16 850

Table 1-4. FY 1980 Laser Isotope Separation Program operating resources.

Laser Fusion Program

Operating funds of $48 million represented a 9% increase in buying power over FY 1979. This allowed the required emphasis on Nova prototyping and the experimental program, as shown in Table 1-3. The staff increased by only seven employees over the previous year, allowing us to expend additional resources in industry and the academic community. The Nova project was appropriated $56 million, bringing the total to $79 million of the authorized $195 million. Construction of the office and laboratory buildings continued, and orders were placed for some long-lead special-facility procurements.

The Fusion Target Development Facility was appropriated $1 million of the $7.6 million total project cost, allowing the detailed design of conventional and special facilities, and the bidding of a single contract to design and construct the facility.

Equipment funding was reduced for FY 1980, again emphasizing the need for increased funds in this area. The outlook for FY 1981, however, is positive and should help reverse this trend.

Laser Isotope Separation

In FY 1980, the operating budget for the Laser Isotope Separation Program was $17.85 million, the equipment budget was $2.1 million, and the general plant project budget was $1.15 million. The personnel numbers reflect all LLNL employees in direct support of the programs: scientific, technical, nontechnical, clerical, and craft. In addition to this in-house LLNL complement, we use non-LLNL contract personnel to support peak program loads. This effort averaged approximately 30 people for FY 1980. A breakout of the LIS Programs by FY 1980 budget category and personnel is given in Table 1-4.

Program Facilities

Introduction

The Laser Program continued to experience significant growth in 1980; we made important progress towards providing permanent housing for more of our people and experiments. We completed new office and laboratory buildings, made significant progress in the construction of the Nova Project, carried out modification and modernization of many existing facilities, and accomplished the successful initial planning and design for additional new facilities. New construction efforts centered on the Nova office building and laboratory addition, while the activation of the Mars facility for LIS was completed and some new temporary offices were obtained. A major effort involved the renovation of the 381 office building interior to repair earthquake damage and to upgrade its seismic response characteristics.

Table 1-5 summarizes the comparative space distribution for the program for 1979 and 1980. The current total of 367 151 ft^2 represents a 4.0% increase from 1979 and indicates the continuing expansion of office and laboratory space requirements.

Facilities Planning

Facilities planning has always been a major concern of our program. In order to properly site and coordinate the planned Laser Program facilities, we undertook a long-range planning effort. We retained the firm of Royston, Hanamoto, Alley and Abey (RHAA) to assist in this planning effort. Their previous work involved developing a master siting plan for the Laboratory.

The program's master planning effort was divided into two sections: A long-range plan, shown in Fig. 1-10, which would concentrate on program expansion through the year 2000, and a five-year plan, depicted in Fig. 1-11 which would concentrates on the near future. The long-range plan has been completed, and its major findings have been endorsed by both the program and

Facilities	1979	1980	% Change
Permanent office	50 930	50 930	0
Owned office trailers	68 247	74 007	8.4
Rental office trailers	7 456	11 329	51.9
Permanent laboratories	187 548	191 956	2.4
Technician support areas	38 929	38 929	0
Total	353 150	367 151	4.0

Table 1-5. Laser Program space distributions for 1979 and 1980 (areas in ft^2).

Laboratory management. Among the major findings and decisions are the following:

- We will make an effort to replace obsolete permanent and temporary facilities with new, modern laboratories.
- The growth of the program will extend eastward and will eventually occupy 115 of the Laboratory's 627 acres.
- Our current facilities construction plan has been modified to decrease the population density and will provide a more campus-like setting with appropriate pathways, trees, and landscaping.

We are proceeding with design and construction activity based on the five-year plan. We are primarily concerned with the completion of the major facilities indicated in Fig. 1-11 and the associated movement of people within the program.

Earthquake Damage. The January 24, 1980 earthquakes were considered by seismologists to be of moderate intensity; nonetheless, the temblors caused extensive interior damage to Building 381 and somewhat less damage to Building 391. Three earthquakes measuring 5.5, 5.2, and 4.8 on the Richter scale occurred between 11:00 and 11:03 a.m. Aftershocks continued for several days, with a second moderate quake of 5.6 occurring on January 26. In addition to the damage caused to the building interiors, many pieces of experimental apparatus were dislodged. The earthquakes moved the Shiva laser space frame, but it settled very close to its original position. The target-room space frame was displaced by about 1 in., and it subsequently had to be jacked back into position and reattached. There were no injuries.

We have upgraded our seismic safety requirements. Repair of Building 381 cost approximately \$325 000, with \$50 000 in repairs scheduled for 1981. We estimate that approximately \$450 000 was spent repairing the total facility damage left by the earthquakes. We are implementing a comprehensive disaster plan that will allow us to deal more effectively with a disaster. The upgraded office building now meets our latest construction standards, which are based upon the maximum credible earthquake that could occur at the Laboratory.

Nova (Buildings 391 and 481). Construction of the Nova project began in 1979 with the Building 391 laboratory addition commencing in May and the first work on the Building 481 offices starting in October. Work on both structures has continued to progress through 1980, on schedule, with an anticipated completion date of December 1981 for both facilities. An activation and migration plan for the new buildings is currently in the development stage. By the end of 1980, both structures were more than 50% complete, and all major design work had been finalized. Current cost estimates are \$22.1 million for the Building 391 laboratory addition and \$6.6 million for the Building 481 office building. The Nova Office Building will provide offices, conference rooms, and drafting areas for 200 people; the Nova Laboratory will increase the floor area of the existing Building 391 laboratory by 160%, adding 106 000 ft^2 to the original laboratory's 66 750 ft^2. Figure 1-12 shows how the new office building will appear and its relation to the present office building. Figure 1-13 is representative of the interior plan of the office building.

Fusion Target Development Facility (Building 298). Initial site preparation began in December 1980 for a major new facility for the Target Fabrication research. The 47 500-ft^2 Fusion Target Development Facility (FTDF) will cost approximately \$7.6

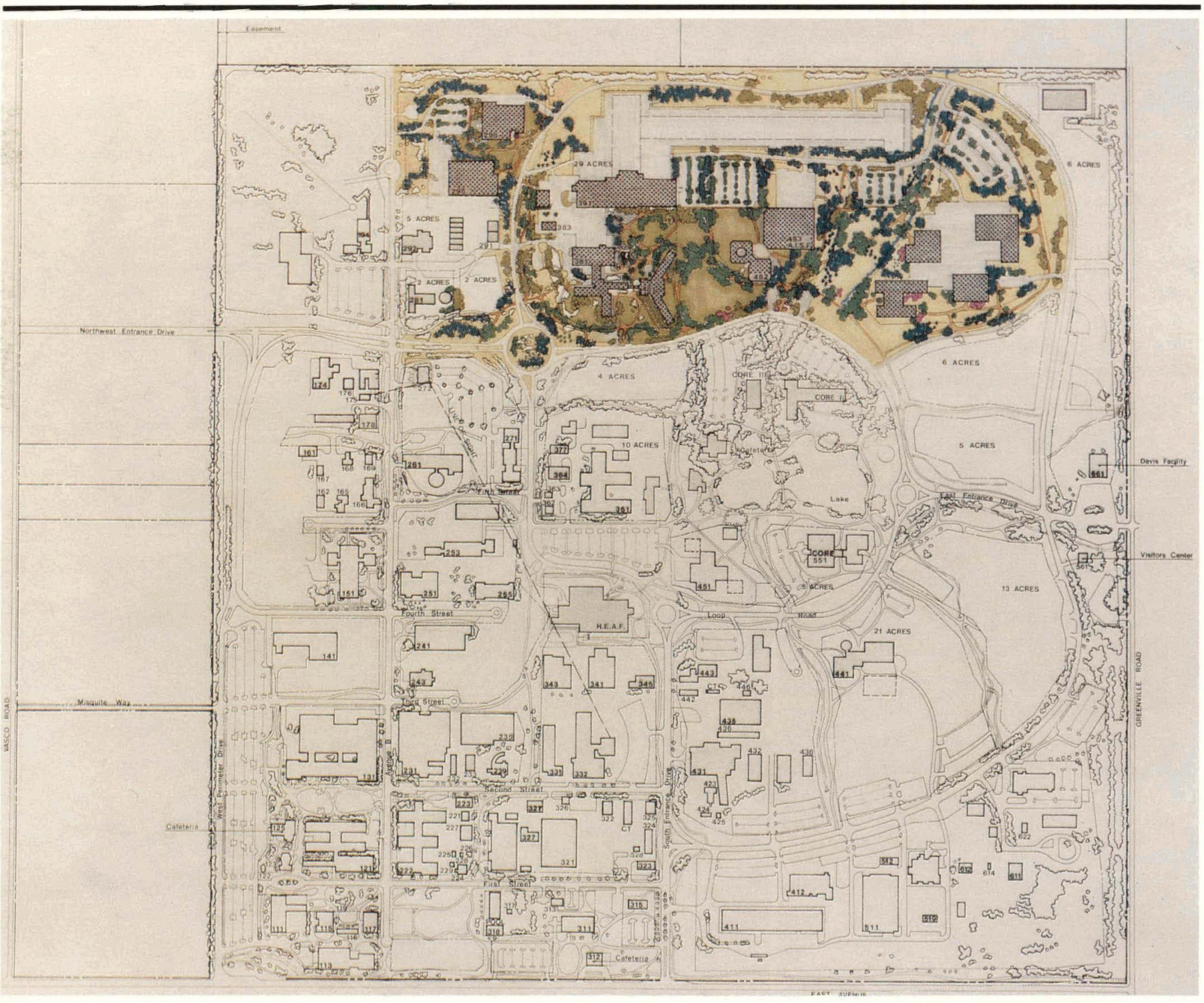

Fig. 1-10. Long-range facilities plan.

million and will provide a centralized target analysis, development, and fabrication facility for this laser fusion group. FTDF will represent a significant departure from construction techniques previously used at LLNL. In the "Design-Construct" approach being used for FTDF a single contractor is responsible for the architectural, engineering, and construction phases of the job and builds the facility using standardized

Fig. 1-11. Five-year facilities plan.

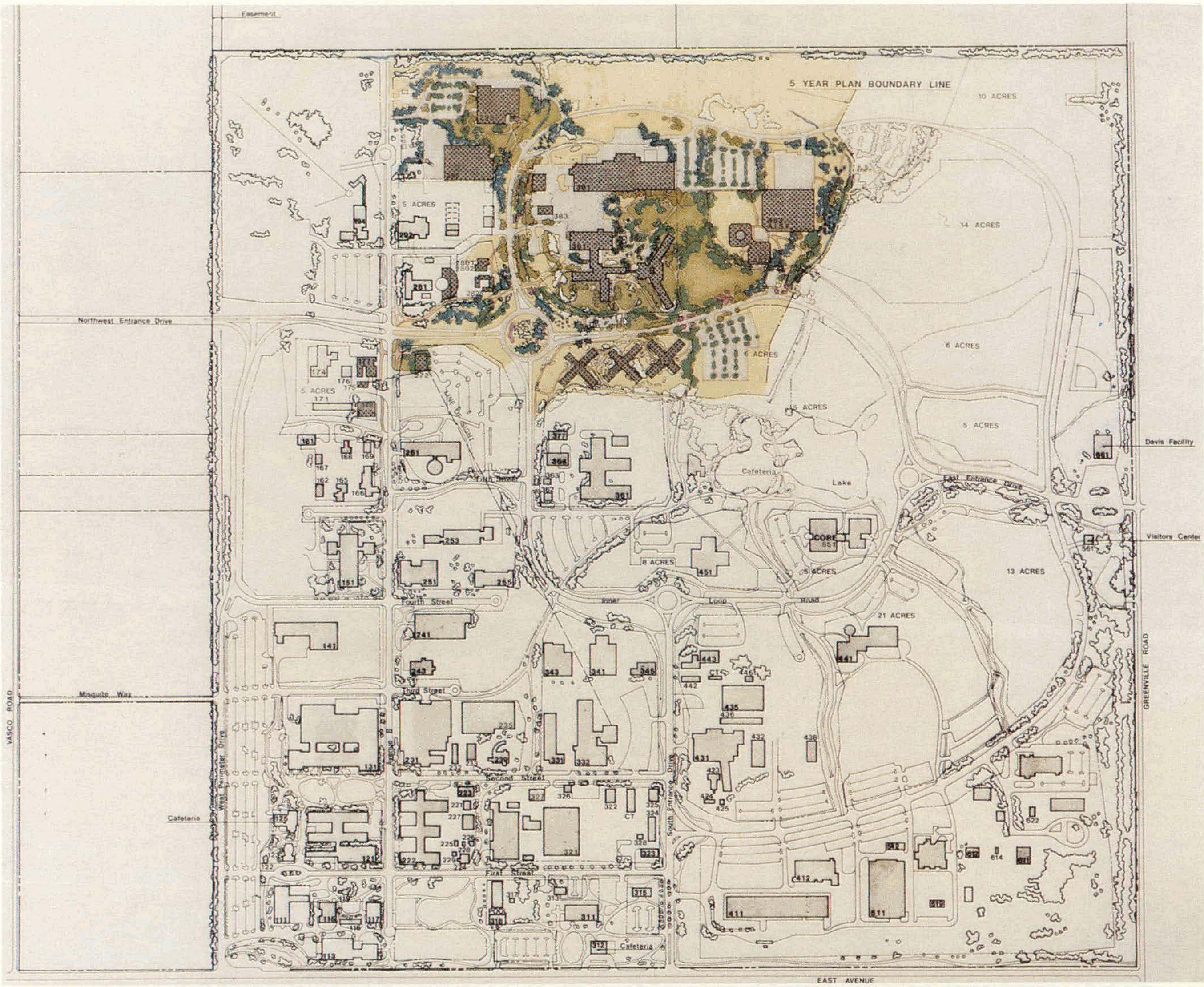

Fig. 1-12. Exterior view of Building 481, Nova office building.

methods of construction, such as tilt-up concrete wall panels and standard utility packages. This technique, increasingly more popular and successful with private commercial interests in technical fields, is resulting in lower costs per square foot than conventional techniques. As Figs. 1-14 and 1-15 show, the new building will be an attractive, functional laboratory.

Laser Program Machine Shop (Building 383). Design of a new facility, financed with general plant funds, got underway in

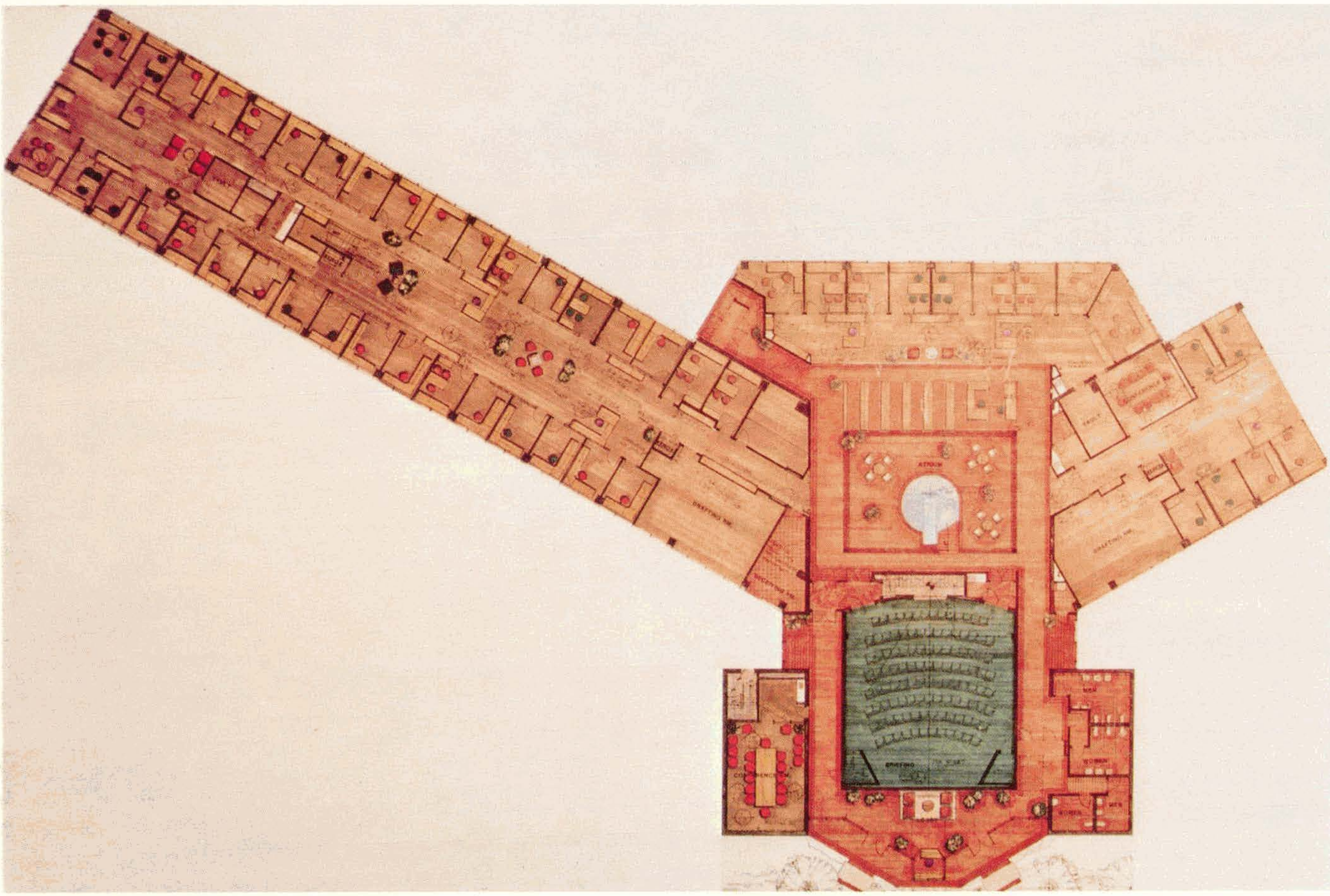

Fig. 1-13. Interior plan of Building 481.

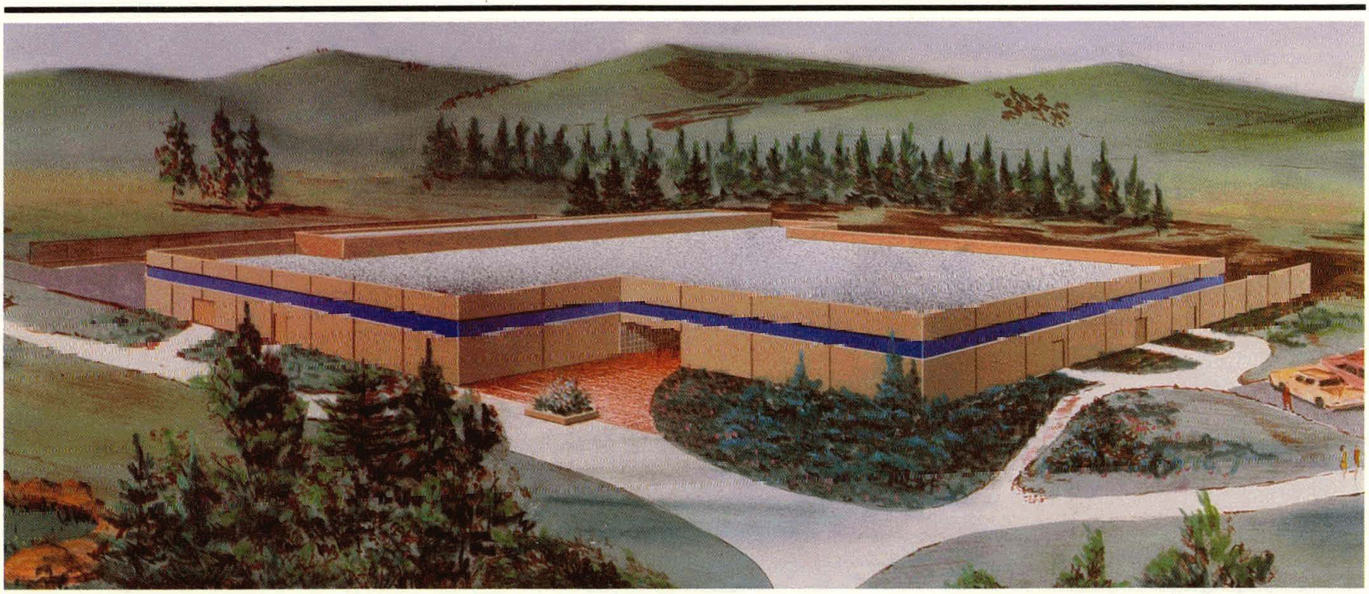

Fig. 1-14. Exterior view of Building 298, FTDF.

October 1980, with initial site preparation beginning in December. Planned as a 4500-ft^2 support facility, it will house a machine shop and provide an improved food-vending area to support second-shift workers. The facility will be located immediately southwest of the Nova Laboratory (Building 391). The preengineered building, designed to harmonize with the exteriors of the Nova Office Building and Laboratory, will improve working conditions for the machinists and will increase the available floor space of the present facility (now 2500 ft^2) by 80%. The current schedule is for personnel and machinery from the existing machine shop to move into Building 383 during the summer of 1981. This facility will provide important support for activation of the Novette and Nova laser systems.

Fusion Experiments Analysis Facility. A general plant funded project, estimated to cost $350 000, will result in an addition to the existing laser fusion office building, Building 381. The primary programmatic goals of this centralized facility will be to combine computer and analysis resources into one location close to the laser facilities and personnel to be served. The building will house a data-analysis system (a DEC VAX 11/780 computer), which is compatible with, and will be directly linked to, the data-acquisition and control computers in our laser facilities. The building site and exterior finish have been selected and detailed. Engineering design began in December. Construction will be completed early in calendar year 1982. Figure 1-16 is a rendition of the new Fusion Experiments Analysis Facility.

Nova Storage Tent. Initial design, procurement, and preparation efforts have been completed to erect a tent around the reactor dome of Building 281. The Nova Storage Tent will provide a low-cost (less than $10/ft^2), acceptable quality supplementary parts storage area for the Nova project. Our experience with constructing the Shiva laser underscored the need for adequate storage that can provide both

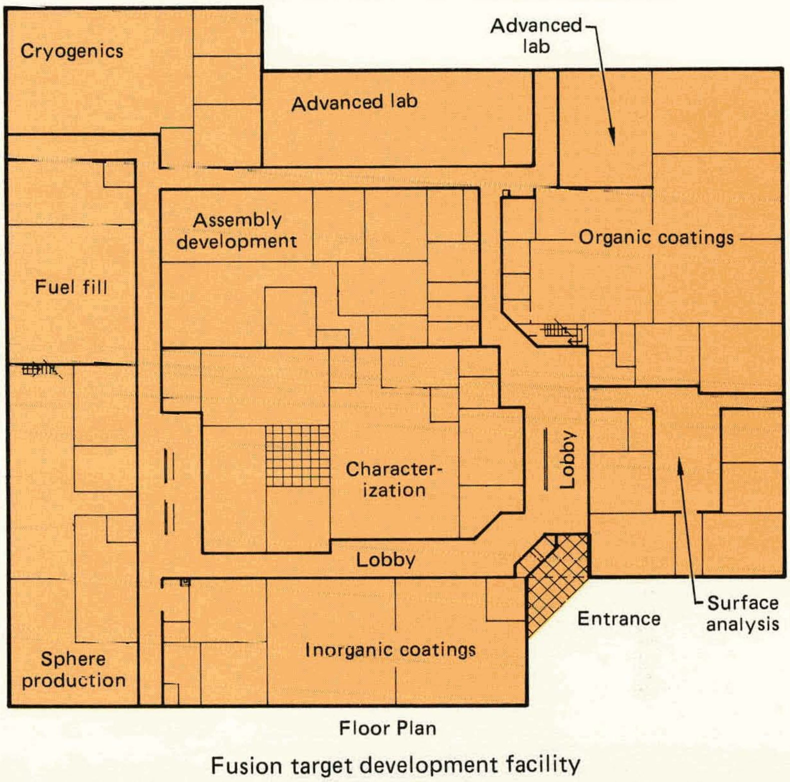

Fig. 1-15. Interior layout of Building 298, FTDF.

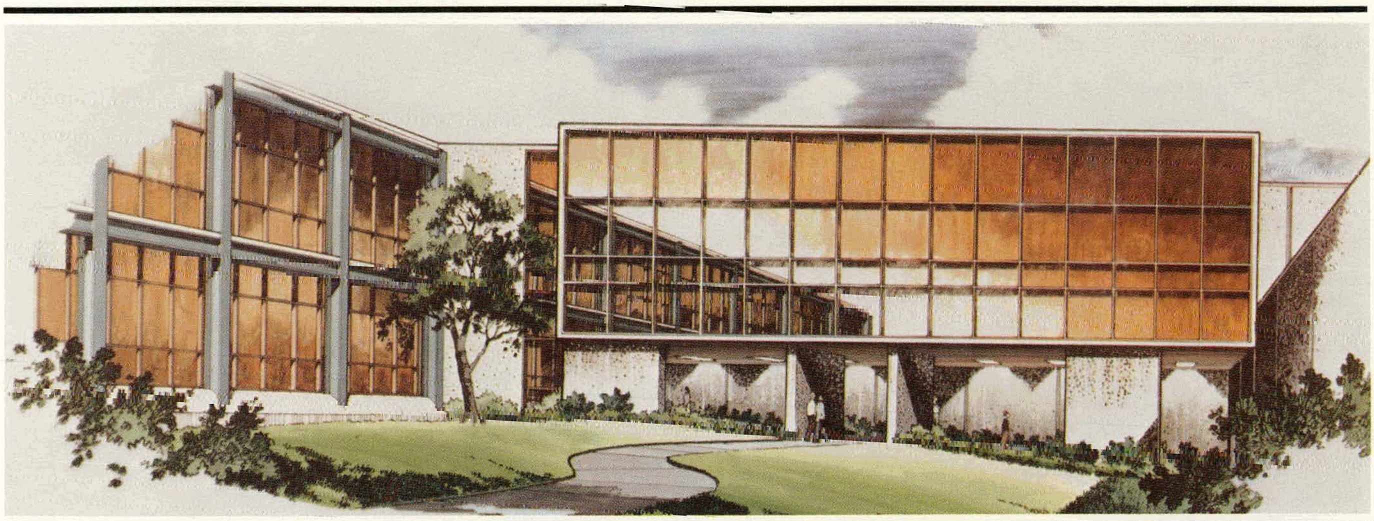

Fig. 1-16. Building site and exterior finish of Fusion Experiments Analysis Facility.

protection from the elements and improved physical control of the laser hardware. When completed, the tent will provide approximately 10 000 ft^2 of storage space, with the dome interior of Building 281 supplying another 5000 ft^2.

Laser Facilities/Hazards Control (Building T-2825). A new 5760-ft^2 portable building was obtained to provide office space for the Laser Facilities and Hazards Control teams and personnel waiting for clearances. The new offices were occupied in October 1980.

Laser Isotope Separation

Mars (Building 175). The construction of the Mars building, which began in September 1979, was completed in 1980. Beneficial occupancy of the structure was received during April and activation of the facility was concluded in time for a December 12 dedication. The 4400-ft^2 building, which was designed to house the Mars electron-beam experiment, was built as a General Plant Project for the Laser Isotope Separation program at a cost of $475 000.

Building 178. Scheduled for construction bidding at the beginning of 1981, Building 178, a new support facility providing general laboratory space will be located immediately south of Building 175. Space will be allocated as required to support the LIS program. This 8000-ft^2 building will cost an estimated $630 000 and will be cofunded from GP funds by Defense and Nuclear Energy Programs.

Laser Electro-Optical Facility (LEO). Planned as a General Plant project, the 7000-ft^2 Laser Isotope Separation Laser Electro-Optical facility (called LEO) will house the Neptune laser system. Neptune is a continuation of the copper vapor laser development currently underway in LIS. Final site selection has been made and Title II design was begun in 1980. With total estimate costs for the facility at $1.0 million, LEO is expected to be completed by late FY 1981.

Advanced Isotope Separation Facility. The planned new Advanced Isotope Separation Facility (AISF) will provide laboratories and offices to meet the expanded needs and objectives of the Laser Isotope Separation Program. The AISF will include 75 000 ft^2 of laboratories and 49 000 ft^2 of offices to house 175 people. Construction will begin in early FY 1982 and will be completed near the end of FY 1983, at a total cost of $25 million. The firms of Ried and Tarics Associates, and Syska and Hennessy are under DOE contract to provide the architectural and mechanical–electrical engineering. Figure 1-17 is a preliminary design that represents the presently conceived configuration of the building.

The AISF will be located east of the Nova complex, with the office building sharing an open green space with the Nova office building. The office building is a two-story

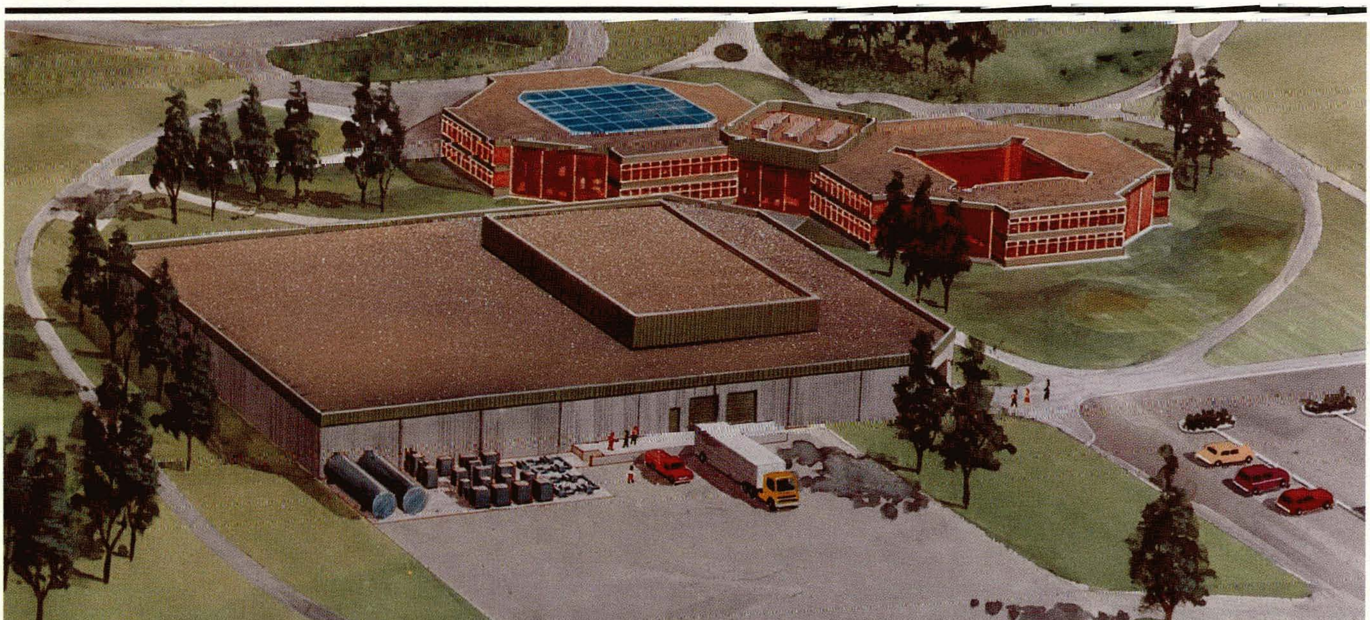

Fig. 1-17. Preliminary design of Advanced Isotope Separation Facility.

structure with a closed-circulation floor plan. The laboratory building will be located northeast of the office building and will house a wide variety of laser and separator component and system-development activities. The building will be modular, open, and capable of housing several major experiments in sequence or in parallel.

Additional facilities issues to be addressed include the following:

- Construction of the proposed Novette facility.
- Nova Phase I.
- Refurbishment study of the Building 381 office building.
- Continued seismic safety work throughout the program.

Long-Range Facilities Goals

The next few years will witness a major part of the Program's expansion and development. With the completion of the Nova project, FTDF, AISF, LEO, and Building 178, the program will be able to concentrate on long-range programmatic efforts. The overall objective of facilities planning remains the transition from temporary or obsolete facilities to permanent laboratories and office buildings that meet the operational needs of the program. Past experience with Building 381, the Laser Fusion Office Building, and Building 391 has proven that it is possible to create interesting, functional, and architecturally exceptional facilities that are both economical and practical.

Section 2 Solid State Laser Systems and Technology

Solid State Laser Systems and Technology

Contents

Solid State Laser Systems and Technology

Introduction

The Solid State Laser Program is an element of the Fusion Lasers Program (see "Summary of Major Activities" in Section 1) that has the objective of developing, constructing, and operating the Nd:glass laser facilities for inertial confinement fusion (ICF) research at LLNL. In pursuit of this objective, the Solid State Laser Program has been organized into five separate elements:

- Nova.
- Operations—Shiva/Argus.
- Novette.
- Solid State R&D.
- Basic Research.

These elements reflect the major ongoing projects and the research directions of the Solid State Laser Program.

Nova is designed at the 200- to 300-kJ energy level to achieve target ignition. Figure 2-1 is an artist's rendering showing how the Nova facility will look when completed. The Nova project is presently authorized for Phase I construction, which includes the buildings and the first 10 beams of the laser system. For the completion of the Nova project, we have planned to expand the system to 20 beams, with harmonic-conversion optics added to all 20. This configuration can provide experimental capability at frequencies of 1ω, 2ω, and 3ω in 1985 at the 150- to 300-kJ energy level.

During 1980, the Operations Group converted one 8-cm-diameter beam of the Argus laser to perform target-irradiation experiments at the second (2ω) and third (3ω) harmonics. We achieved external conversion efficiencies of 75% to 2ω and 55% to 3ω. We expect >70% conversion efficiency for the 3ω

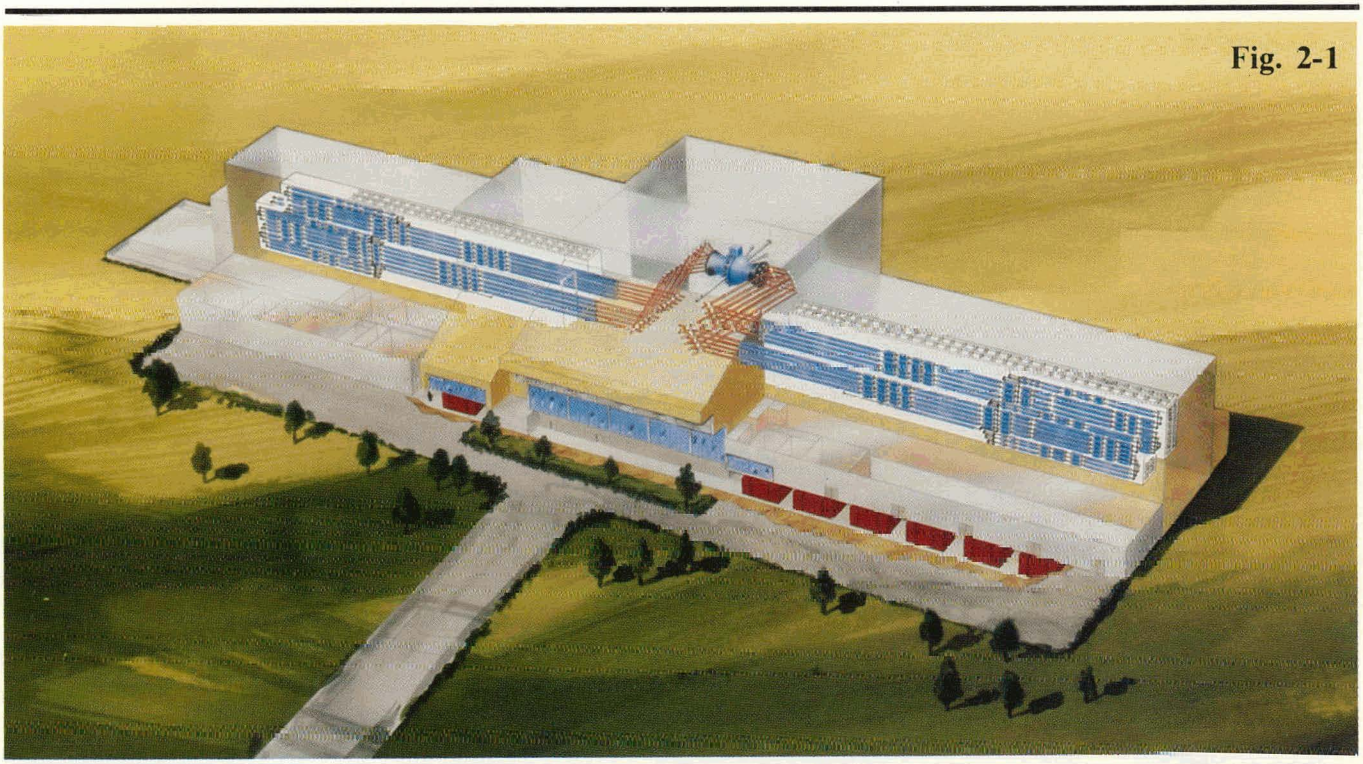

Fig. 2-1

harmonic as well by using antireflection coatings with high damage thresholds. This work, together with the technology development of harmonic crystal arrays described below, provides the basis for harmonic conversion of the 74-cm-diameter beams of the Novette (see below) and Nova lasers. Using the 2ω and 3ω Argus beams, the Operations Group conducted a series of target experiments that strongly support the theoretical predictions of higher target-absorption percentage ($\sim$90% at 3ω) and a significantly lower hot-electron production rate.

We operated Shiva throughout the year on a two-shift basis and obtained a great deal of scaling information pertinent to our classified target designs. Most importantly, we conducted many well-diagnosed compression experiments showing deuterium–tritium (D–T) fuel compression to >100 times its normal liquid density.

We have designed a laser system, called Novette, that uses two beams of the Nova design and 74-cm-diameter harmonic-conversion crystals to provide up to 20 kJ of 1ω radiation and up to 14 kJ of 2ω radiation on a target in a 3-ns pulse. A team that includes the staff of the Nova project and the Operations Group, is preparing to construct this laser in the Argus high-bay building. Novette can be ready for target experimentation in the fall of 1982.

The Solid State Research Group supports the Nova project by researching prototypes of the plasma shutter and the 46-cm-diameter amplifier, investigating new 1.0-μm coatings, and conducting research in other areas, such as that being done in conjunction with the University of Texas at Austin on the compensated pulsed alternator. A great deal of effort has been expended on harmonic-conversion technology, including potassium dihydrogen phosphate (KDP) crystal growth, multiwavelength coatings, and theoretical analyses.

Our basic research program, supported by the Office of Basic Energy Science, DOE, does research in areas of long-term interest to the project areas. Special successes in 1980 were achieved in the theoretical modeling of spectral lines in multicomponent glasses and in the measurement of absolute quantum efficiencies in Nd-doped materials using photoacoustics. Other areas of activity include the measurement of linear and nonlinear properties of optical materials at 1.06 μm and at the second, third, and fourth harmonics.

Author: J. F. Holzrichter

Operating Systems

Introduction

The Operations Group has the responsibility for maintaining, operating, and upgrading the Argus and Shiva laser systems. During 1980, this responsibility encompassed a wide spectrum of technical challenges, some of them literally earthshaking.

On January 24, 1980, an earthquake of magnitude 5.5 occurred within 20 km of the Laboratory site. Fortunately, only minor damage occurred to laser system components. Mounting bolts on the Shiva space frame were damaged, there was some flooding in capacitor banks due to broken pipes, and the Argus laser was incapacitated by falling ceiling tile and component shifting. Operations Group personnel, assisted by staff members and technicians from the Nova design team, set to work to repair the earthquake damage as soon as it was safe to do so. By February 20, both Argus and Shiva were restored to operation. Intensive and dedicated effort by LLNL and Bendix Field Engineering personnel, who together make up the Operations Group of the Fusion Lasers Program, resulted in the timely repair of both systems.

Throughout the remainder of 1980, our technical challenges involved extensive high-density target experiments on Shiva, the fielding and operation of many new target diagnostics, and a campaign on the Argus system to explore wavelength dependence of target performance and conversion efficiency. We operated the Shiva laser system at maximum powers of up to 20 TW, at maximum energies of 10 kJ, and at pulse widths of 100 ps to 35 ns. The reliability of the Shiva system as a target shooter allowed us to perform several series of experiments with widely differing requirements.

During 1980, we operated the Argus laser as a multiwavelength irradiation facility. During the first half of the year, we performed 2ω (0.53 μm) target experiments and harmonic-conversion studies. In September, we converted Argus to 3ω (0.35 μm) and used it to successfully complete experiments comparing 2ω and 3ω target performance. In addition, we performed several experimental series addressing questions of harmonic conversion that are vital to the design of the Nova and Novette laser systems.

In September, the Operations Group was asked to perform preliminary designs for a new laser system, Novette, to replace the Argus facility. A significant portion of the Operations Group staff was involved in this effort, which is reported in a series of articles later in this section.

Authors: W. E. Martin and J. T. Hunt

Shiva Operations

Operations Summary. During 1980, we continued to use the Shiva laser system for fusion experiments. We conducted several experimental series, including NPIRE, SHIVA FLY, PINLITE, ENTERPRISE, HEET, APOLLO, and a radiation chemistry series, and we also performed extensive tests and system shots to support the experimental series. Many of the experiments performed this year required development of new capabilities and system upgrades; these are covered in the following articles. Figure 2-2 shows the distribution during 1980 of the 181 target shots and the 44 shots for system characterization and system development. Target shots are those in which beams are aligned to a target in the target chamber and target diagnostic data are collected. Laser-system shots are those in which one or more arms of the laser are fired for beam characterization or propagation studies. Table 2-1 summarizes the target shots performed this year and the laser parameters used.

In late January of 1980, system operation was interrupted for a month by an earthquake. However, we quickly repaired the earthquake damage and reactivated the laser system; the first post-earthquake target shot was taken on February 20, and system performance was normal.

Most experiments in 1980 were conducted at pulse lengths between 100 ps and 1.0 ns. Typical maximum-output power and energy values were 20 TW and 10 kJ, respectively. This has become the more or less standard mode of operation, and the system performance is routinely very good. Figure 2-3 includes some typical performance data, as well as data obtained as a result of upgrading the system and expanding its performance. Note, for example, the high-energy points at 600 ps and the data at pulse widths beyond 1 ns.

System Performance. During March, we resumed target irradiation experiments, at 600-ps pulse duration, to study the effects of target-size scaling on the density achieved by x-ray driven targets. In this experiment

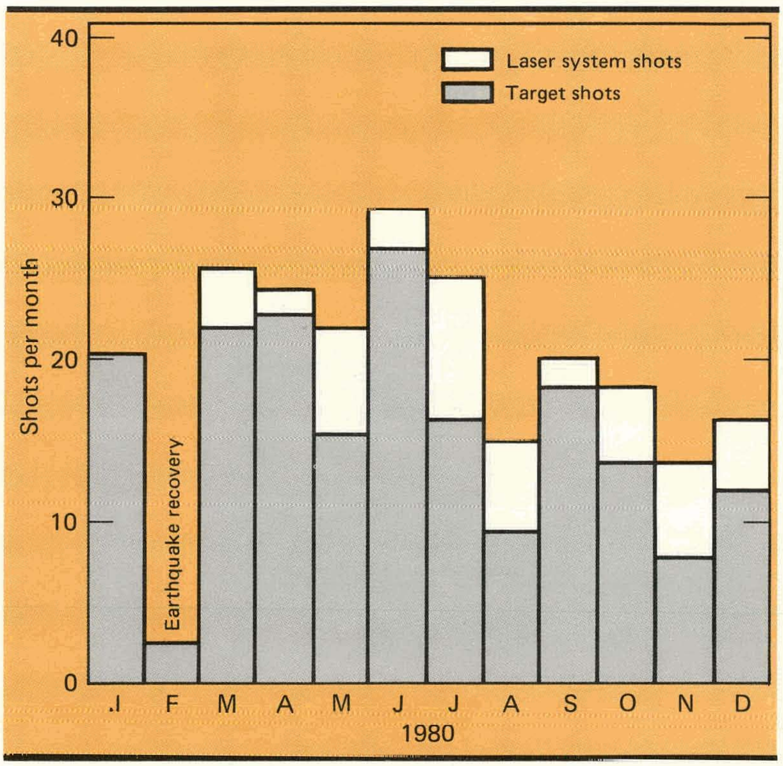

Fig. 2-2. Histogram showing the number of Shiva shots performed each month in 1980.

series, we successfully irradiated 34 targets with energies between 6 and 9 kJ. In March, we also added additional low-energy x-ray diagnostics and performed 15 more target-density experiments. In addition, to test the use of bromine as a neutron-activated seed gas for measuring the fuel density of imploded targets, we irradiated two ball targets filled with D–T and bromine.

We investigated system parasitics and measured system amplified spontaneous emission (ASE). No parasitics were detected from the lower 10 arms (with a sensitivity of about 1 W), but ASE was measured to be 107 μJ per arm; this included 35 μJ per arm of flashlamp light from the delta amplifiers. Furthermore, we determined that, for constant output energy, elimination of the preamplifier dye cell only increases system ASE by about 15%.

In June, we started a series of experiments to characterize our x-ray backlighter system. We completed 22 target shots at 100 ps and four shots at 600 ps.

During July, 27 full-system shots were conducted with Shiva in support of x-ray backlighting characterization experiments, density measurements with x-ray driven targets, and pinhole transmission measurements to ascertain system focus properties. These experiments were performed with 600-ps (FWHM) Gaussian pulses, with energies on the target from 1 to 8 kJ.

The pinhole transmission measurements were preceded by system calibration shots and target-chamber transmission measurements. To achieve a suitable transmission, defined as observing 97% of the incident energy exiting the opposing lens, we found it necessary to replace the target-chamber debris shields that protect the chamber optics. We then irradiated a 500-μm pinhole target; 90% of the incident energy passed through the pinhole.

In September, we conducted 20 system shots on Shiva. We completed the HEET target series and a radiochemistry series using targets containing bromine; these experiments were performed at 600 and 200 ps, respectively. We then modified the lengths of the upper arms in preparation for the upcoming x-ray backlighter series. This series, called ENTERPRISE, required us to reconfigure the system so that we could irradiate the target for 600 ps while simultaneously irradiating a backlighting

Table 2-1. 1980 Shiva shot summary.

Month	Experiment	Beams	Pulse width (FWHM)	Energy (kJ)	Power (TW)
January	Pulse-width dependence (scaling)	1-20	2 ns	2 to 8	1 to 4
February	Earthquake recovery				
March	Size dependence	1-20	600 ps	8	13.3
	Radiation chemistry (bromine tracer)	1-20	600 ps	8	13.3
April	CAIRN	1-20	600 ps	8	13.3
May	1/2 CAIRN	1-10	600 ps	4	6.7
	High-energy tests	17	600 ps	0.75	1.3
June	X-ray backlighter characterization	11-20	100 ps	0.2 to 0.8	2 to 8
July	X-ray backlighter characterization	11-20	600 ps	1 to 4	1.7 to 6.7
August	Density measurements	1-20	600 ps	8 to 9	13 to 15
	Equation of state	1-10	600 ps	7	11.7
September	Radiation chemistry (bromine tracer)	1-20	200 ps	3 to 4	15 to 20
	HEET	11-20	600 ps	2 to 3.5	3.3 to 5.8
October	ENTERPRISE	1-20	600 ps	4 to 8	6.7 to 13.3
November	PINLITE	11-20	35 ns	4	0.1
December	NPIRE	1-20	900 ps	8 to 9	8.9 to 10
	SHIVA FLY	1-20	900 ps	8	8.9

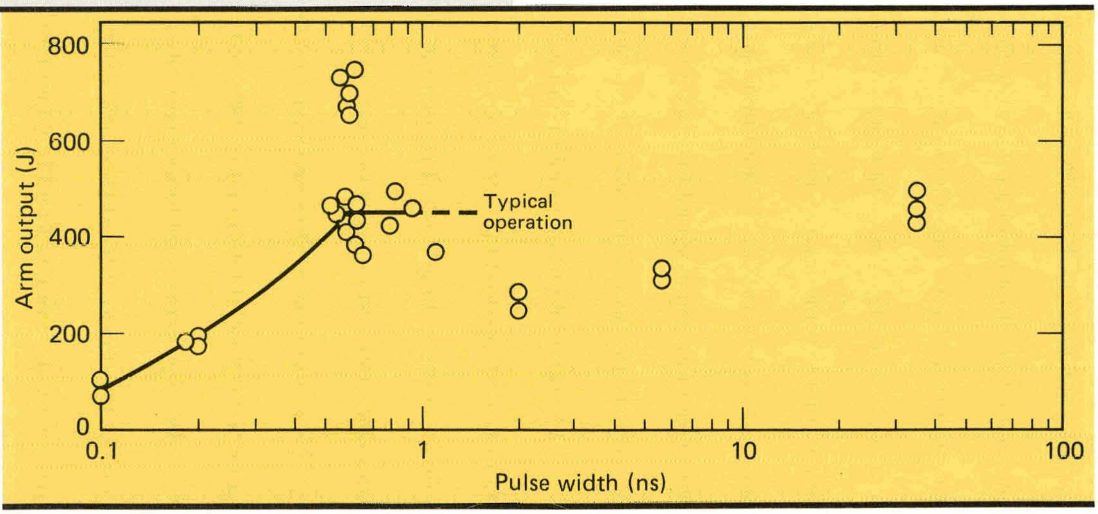

Fig. 2-3. Energy per Shiva arm vs pulse width for various experiments performed during 1980.

target for 2.8 ns. We accomplished this by delaying by an increasing amount each of the 10 beams used on the backlighting target. Figure 2-4 shows the resulting time profile of the backlighter pulse; this plot was generated using the pulse width measured by the input streak camera and the energies measured by the output calorimeters. For future backlighter experiments, we will use synchronized pulses from both a long-pulse and a short-pulse oscillator. The target will be irradiated with the bottom 10 arms, using an adjustable pulse width from 100 ps to 1.0 ns. The backlighter will be irradiated with the top 10 arms, using a second oscillator to provide a pulse width adjustable from 4 to 35 ns. This capability is being developed for operation in 1981, and we expect to achieve 400 to 500 J per arm at 5 ns.

One series of experiments, called PINLITE, has already required operation with 35-ns pulses (these data are included in Fig. 2-3). We performed calculations indicating that gain saturation would not be a problem, but there remained an uncertainty about pinhole closure. We started converting the system for operation at 35 ns at the end of October. This activity, which we completed near the middle of November, required integration of an additional long-pulse single-axial-mode oscillator and a switchout based on our standard oscillator system (see "Optical Pulse Generation" later in this section). The new oscillator required us to restage the front end, adding several new components. The output pulse of the oscillator is approximately 70 ns in duration; the switchout was adjusted to transmit a 4- to 35 ns slice from the center of this pulse. To provide proper drive to the front end of the Shiva beam-splitter system, we integrated and tested a YAG preamplifier, a Faraday rotator, and a fast Pockels cell.

After taking system characterization shots at 35 ns, we determined that pinhole closure could be avoided and no damage would occur if the system was fired at 500 J per arm with only the α-rod/β-rod spatial-filter pinhole in the beam. The only difficulty we encountered was that reflections from α-rod faces were strong enough to put noticeable fringes on about half the beams (near field); however, these fringes were not severe enough to affect quality of the focused beam.

System Upgrades and Improvements. Several new diagnostics were developed or brought on line during 1980. We developed a new low-energy detection system, Dante N, and added an optical pyrometer to the target chamber. We also installed a high-magnification (22×) x-ray microscope for use in the x-ray backlighting experiments. New Raman spectrometer diagnostics were integrated into the target chamber, and new laser diagnostics were installed, including a near-field photo diagnostic that has proved to be very useful. Using a streak camera coupled to a CCD camera, which provides a digitized pulse signal, we now acquire a record of the ouput laser pulse shape. Software improvements that were made during 1980 include control of the nitrogen cooling, rod cooling monitors, and digitized beam photos. During June, we improved the stability of the new operating code (RSX-11m-3.2) in the PDP computers.

The optical relay telescope that is now used between the preamplifier table and the arms of Shiva is depicted schematically in Fig. 2-5. It uses four lenses mounted on an evacuated tube; the lens pairs form two telephoto lenses with effective focal lengths f_1

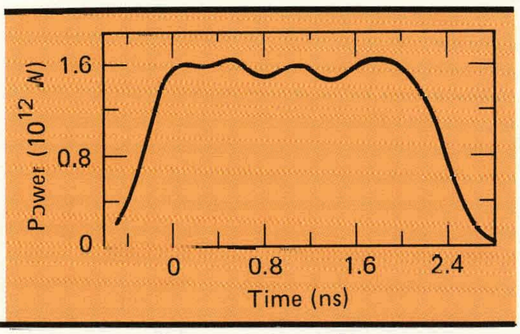

Fig. 2-4. Output pulse from Shiva upper arms used to irradiate the x-ray backlighter.

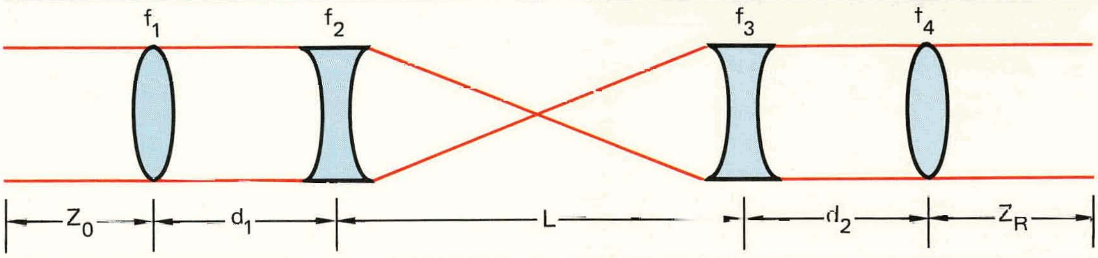

Fig. 2-5. Schematic of the Shiva penthouse optical relay.

and f_0. The relay distance of this combination is given by

$$Z_R = M\left(f_1 + f_0 - \frac{f_1 d_2}{f_3} - \frac{f_0 d_1}{f_2}\right) - M^2 Z_0 \quad , \qquad (1)$$

where Z_0 is the object distance and M is the magnification. This relay provides a much longer relay distance than is possible with a comparably sized two-lens relay. In addition, it can be used over a wide range of magnifications by merely adjusting d_1, d_2, and L.

Fig. 2-6. Near-field photograph of Shiva beam No. 17 at output energy of 700 J.

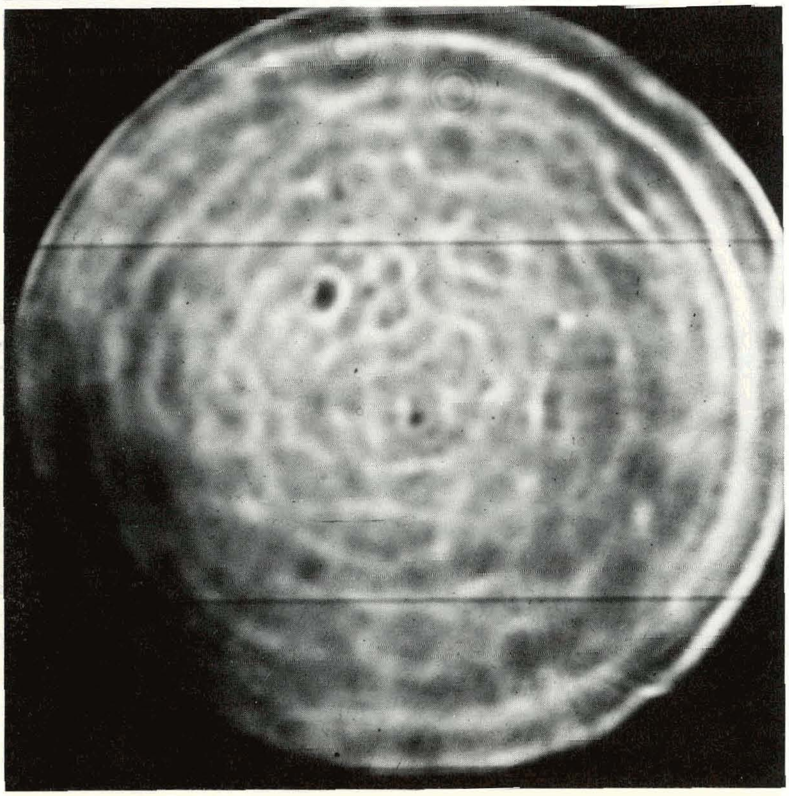

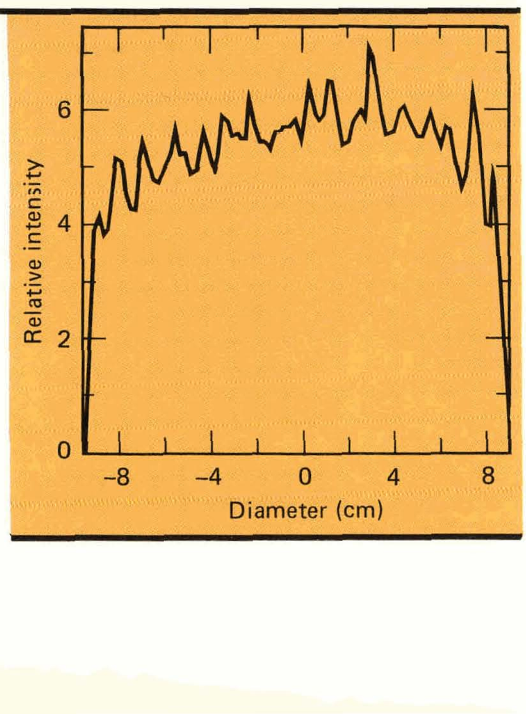

Fig. 2-7. Relative intensity plot along a diameter of the near-field photo shown in Fig. 2-6.

During May and June, to determine the requirements for achieving system operation at the 15-kJ level, we upgraded and tested one arm (No. 17) of Shiva to achieve 750 J of output energy. Preceding these tests, we replaced all damaged components in the arm and thoroughly cleaned the optics. Calculations indicated we needed more front-end drive than was currently possible without damaging the penthouse optics. We accomplished this by replacing the penthouse image relay, making the beam smaller, and increasing the input aperture transmission. Several test shots were taken; the data from these shots are included in Fig. 2-3 at approximately 600 ps.

The diagnostics for the high-energy shot consisted of calorimetry and near-field photography. We took near-field photos during full-power shots to determine beam quality and, at low power, to check for damage. Figure 2-6 shows a near-field photo taken at approximately 700 J. Figure 2-7 is a plot of relative intensity along a diameter scan of the photo. Little or no damage occurred during these tests. These beam diagnostics show no excessive beam breakup and indicate that the intensity modulation is only 1.6 to 1, at the worst. The highest average flux occurred at the input to the β-γ spatial filter, where the flux level reached about 6 J/cm^2. We have, therefore, shown that operation of Shiva at 15 kJ with pulses as long as 1.0 ns is both possible and practical.

Author: C. D. Swift

Major Contributers: D. R. Speck, R. R. Baltzer, R. L. Bolt, J. D. Wintemute, W. A. Jones, T. L. Weiland, and the Shiva Operations staff

Argus Operations

Operations Summary. During 1980, we concentrated our efforts to answer questions associated with frequency conversion of laser light and with target performance at short wavelengths. Our primary goal was to assess the practicality and desirability of equipping Nova with a short-wavelength capability. As part of our program designed to reach that goal, we continued the baseline series of second-harmonic (0.53-μm) target-interaction experiments discussed in last year's annual report.[1] These experiments were interrupted by the January 24th earthquake, but were resumed within a month. After completing the baseline shots, we followed with a complementary series of target shots at the third harmonic, 0.35 μm. In both of these experimental series, we used single-sided illumination, employing only the south arm of Argus.

Meanwhile, we dedicated the north arm of Argus to studies of the frequency-conversion process and beam propagation at short wavelengths. Our measurements of doubling and tripling efficiencies provided data on which to base the design of the harmonic-conversion equipment for Nova. The experience we gained from the third-harmonic tests led to an improved alignment procedure for the south-arm third-harmonic target experiments. Also, we found an intensity-dependent loss mechanism in the index-matching fluids normally used with KDP crystals. In further studies, we identified both the loss mechanism (transverse Raman scattering) and a specific new index-matching fluid that does not exhibit this loss.

We also used the Argus north arm to study the bulk-damage threshold of phosphate laser glass. Finally, at the end of the year, we performed a series of experiments to test a tandem-crystal frequency-conversion scheme[2,3] that holds the promise of broadening the range of laser output intensities for which efficient doubling occurs. This technique may also allow rapid conversion to a third-harmonic configuration with no extra crystal hardware.

In fielding all of these experiments, we operated Argus for eight months as a 0.53-μm target shooter during the day and as an infrared laser for frequency-conversion tests at night. After we converted the south arm to 0.35 μm, our target-shooter experimental schedule required double-shift operation. A third shift performed the remaining north-arm experimental work, operating on weekends for the last three months of the year.

System Improvements. In line with the primary character of Argus as a target shooter, we incorporated no major changes into the Argus system in 1980. We did, however, improve its operation by adding a new high-repetition-rate YAG preamplifier and modifying the preamplifier-stage layout. The inclusion of a new YAG preamplifier in the system has increased the permissible rate at which we can generate amplified oscillator pulses to one pulse per second. Our previous YAG preamplifier distorted the beam badly when it was operated faster than one pulse in 10 seconds. The faster pulse rate has greatly facilitated the alignment of various optical paths used for triggering diagnostic equipment, both in the laser and the target bay. At the same time, we simplified the optical-path layout on the center table, which reduced the number of optical components in the beam and improved the quality of the laser-beam profile.

Personnel safety considerations led us to add beam shields on the center table; these shields were designed to allow only purposeful access to the laser beam path. In the target bay, the optical components on the diagnostic tables are already protected by enclosures that perform this safety function, while also reducing air turbulence and dust deposition.

We modified the vacuum plumbing on the target chamber to include roughing lines to each of the diagnostic packages. This allowed us to operate with less risk of damage to diaphragms and targets from sudden pressure fluctuations. We also added straps to the disk amplifiers to prevent excessive motion during an earthquake; this corrects a problem noted after the earthquake in January of 1980.

Late in the year, we installed on the north arm a commercially available Q-switched YAG laser with harmonic-conversion options. This laser will be used for crystal alignment in the fourth-harmonic (0.27-μm) conversion-efficiency experiments scheduled for early 1981. The laser is also being evaluated as a target-alignment aid for Novette, where its selectable peak output (7 W at 1.06 μm, 2.25 W at 0.53 μm, 1.25 W at 0.35 μm, and 0.5 W at 0.27 μm) appears to meet our alignment requirements, as presently envisioned.

Finally, in preparation for the complete disassembly of Argus to make way for Novette in September 1981, we removed the neutron time-of-flight tube from the east end of the target bay. This improved the traffic flow in the area around the transmitted-beam diagnostic table.

Target Experiments at 0.53 μm. We finished the final "green" target experiments (so called because of the color of the laser light) in August. The experimental layout and alignment techniques are those reported last year.[1] We did, however, use two different 90-cm clear-aperture doubling crystals in completing these target shots: an 11.9-mm Type II KDP crystal with windows and index-matching liquid, and a "bare" 9.9-mm Type II KDP crystal. The crystal change was required because of damage to the index-matched crystal. We installed the second crystal without an index-matching housing because of an intensity-dependent loss mechanism in the index-matching fluid that we discovered during the north-arm conversion experiments. (See "Second-Harmonic Conversion Efficiency" and "Index-Matching Fluids for Large Apertures" later in this section.)

In the course of the 0.53-μm experiments, we damaged a number of dielectric coatings. From the rather limited data set, we estimate damage thresholds of 3.2 J/cm^2 for high-reflection mirror coatings and 1.6 J/cm^2 for dichroic beam-dump coatings, both with 700-ps pulses. We were, therefore, limited to energies on the target of 30 J or less and to a peak intensity at the target surface of less than 3×10^{15} W/cm^2.

We performed a total of 164 green target shots in 1980, each using some or all of the south-arm disk amplifiers. In addition, we used 1798 rod-amplifier shots to align the frequency-doubling crystal and to adjust the target-illumination optics. We also fired the amplifiers 399 times to set up, calibrate, align, and time various laser and target diagnostic equipment.

Target-Experiment Optics at 0.35 μm. In September, we removed all equipment associated with the 0.53-μm laser beam and installed optics for a 0.35-μm beam. We modified the optical layout considerably from the 0.53-μm beam path because of the more stringent alignment requirements for the tripling configuration and because of an increased respect for the fragility of presently available 0.35-μm coatings. We fired the first system shot generating 0.35-μm energy on September 25, and we fired the first target shot the next day.

The primary modifications we made to the 0.53-μm layout were the elimination of all coated reflectors after the KDP crystals and the addition of a Q-switched, mode-locked oscillator for crystal and target alignment purposes. We moved the 3.0× beam-reducing telescope to the output of the final spatial filter and added a third main-beam turning mirror to provide space for the new frequency-conversion crystals. The 1.06-μm laser alignment and diagnostic equipment, located behind the first of the three turning mirrors, was essentially unaffected by this change.

The doubler crystal was 11.9 mm thick, and the mixer was 9.9 mm thick; both were KDP crystals cut in a Type II orientation. As indicated in Fig. 2-8, the output 0.35-μm light was polarized 14° counterclockwise from the horizontal and parallel to the extraordinary axis of the mixer crystal. This polarization was selected to match our earlier 1.06-μm and 0.53-μm target-irradiation experiments. With this crystal configuration, the doubler ordinary axis must be parallel to the mixer extraordinary axis.

For the incoming 1.06-μm light, a polarization angle of 45° with respect to the

Fig. 2-8. Orientation of doubler and mixer crystals for 0.35-μm experiments.

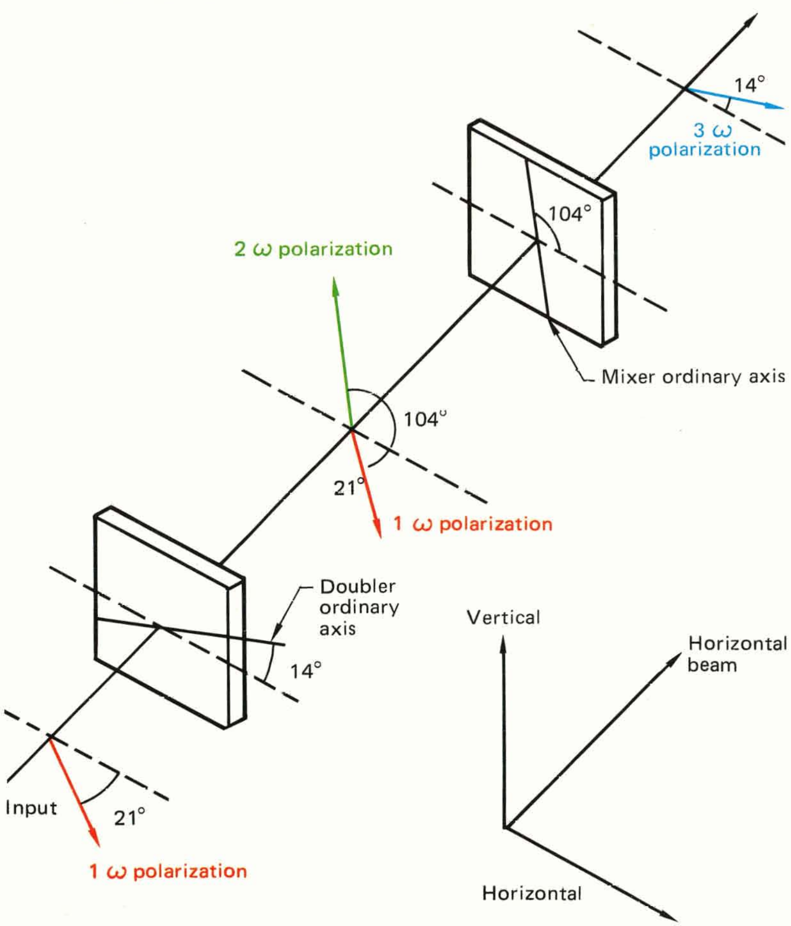

doubler-crystal ordinary axis maximizes 0.53-μm production.[4] At the experimental intensities (2.5 GW/cm^2), however, this angle would supply the mixer with more 0.53-μm light required for maximum conversion to 0.35 μm. We used a half-wave plate placed before the crystal to adjust the intensity ratio to the desired level, rotating the plane of polarization to an angle of 35° with respect to the crystal ordinary axis. This angle was selected to produce a 1.4:1 ratio of 0.53- to 1.06-μm beam energy, as required for maximum 0.35-μm production.

All optical components installed following the mixer crystal were fused-quartz (Suprasil) components, chosen for their low-loss UV transmission. The first element was a trichoic beam dump. The coating on this component was intended to be highly reflective at 1.06 and 0.53 μm, while being highly transmissive at 0.35 μm, to remove the residual 1.06- and 0.53-μm components from the laser beam. The quartz beam splitter, used for both the incident-beam diagnostic assembly (IBD) and the reflected-beam diagnostic assembly (RBD), was uncoated.

Operating Systems

The target bay beam diagnostics included

- A 1.06-μm IBD with a calorimeter, a near-field camera, a far-field multiple-image camera, an alignment TV, and a streak camera.
- A 0.35-μm IBD with a calorimeter, an equivalent-plane multiple-image camera, an alignment TV, and streak-camera fiducial optics.
- A 0.35-μm RBD with a calorimeter, an equivalent-plane multiple-image camera, an alignment TV, and a streak camera.
- A 0.35-μm TBD with a target-plane multiple-image camera, an alignment TV with backlighting optics, and an energy-transport streak camera.
- A mix-ratio monitor with separate calorimetry for 1.06- and 0.53-μm beams.
- A crystal-alignment package with a high-gain photomultiplier sensitive to 0.35-μm energy and a mode-locked oscillator for generating 0.35-μm energy.

A schematic showing the diagnostics and beam-path layout is given in Fig. 2-9.

We often positioned the f/2.2 target-illumination lens away from best focus to

Fig. 2-9. Schematic of diagnostics and beam-path layout for 0.35-μm experiments.

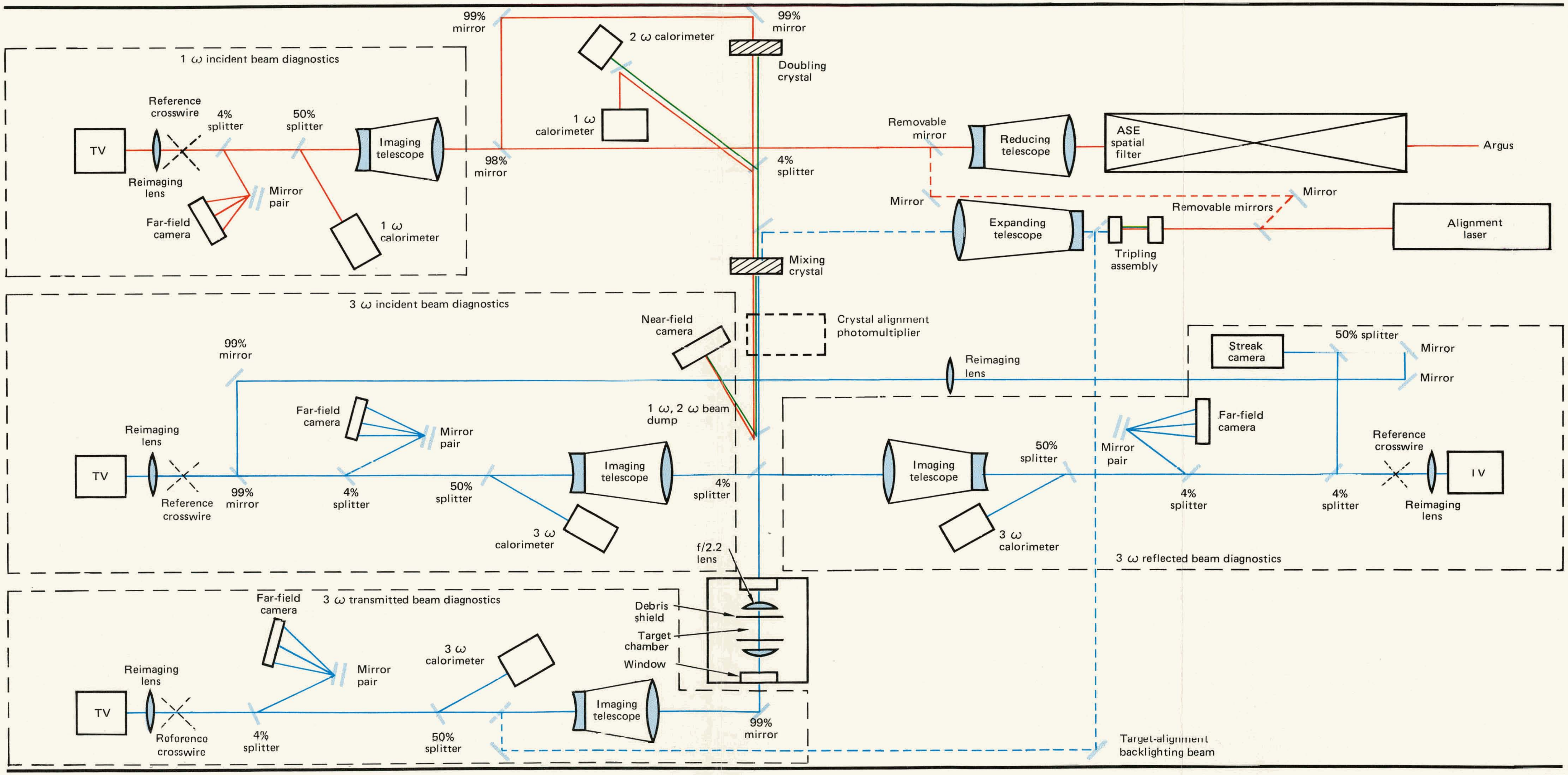

obtain the required intensity on the target surface. We adjusted the 0.35-μm RBD and IBD multiple-image cameras to record a plane equivalent to the target plane. Such adjustment was not required of the TBD camera, which was always focused at the desired point of laser-target interaction through a second f/2.2 lens.

We began the system alignment leading to each target shot by centering the target in the orthogonal fields of view of the target-alignment optics, which determine the location of the target within the chamber. Next, we adjusted the target-alignment oscillator to provide a 4-cm-diam 0.35-μm beam. Together with a diffusing wheel located before the target chamber, we used this beam to backlight the target for viewing on the TBD TV. The north target-chamber lens was adjusted to focus and center this image of the target. We then aligned the main beam line using the 1.06-μm cw alignment laser, and we adjusted the small-aperture 1.06-μm pulsed beam from the target-alignment oscillator to be collinear with the main beam line. The beam intensity ($>$0.3 MW/cm^2) from the target-alignment oscillator generated sufficient 0.53- and 0.35-μm energy in the main frequency-conversion crystals for alignment purposes. The 0.35-μm beam was detectable with an intensified viewer or UV-sensitive photomultiplier. A removable mirror directed this beam into a high-gain photomultiplier through UG-11 filters, so that only 0.35-μm light was detected. The angle of incidence for each of the KDP crystals was then adjusted for maximum signal.

We directly determined the spot size in the target plane by recording a preamplifier shot on the TBD multiple-image camera together with a time exposure of the backlighted target. Adjustments in spot size and location were made by moving the south lens. The incident-beam equivalent-plane camera could then be set by adjusting the 0.35-μm IBD telescope lens to a point previously calculated to be appropriate for the offset of the south lens from focus. The RBD multiple-image camera was focused by using the uncollimated 0.35-μm beam transmitted from the TBD side of the target chamber to backlight the target. A final TBD spot-size picture was then recorded.

Target diagnostics fielded for various experiments have included

- A Dante spectrometer, to measure x-ray yield in 10 bands from 200 to 700 eV.
- A filter fluorescer (FFLEX) and a 4-channel x-ray diode array, to measure x-ray yield in several bands from 5 to 70 keV.
- A 7-channel x-ray diode array, to measure x-ray yield in 7 bands from 4 to 29 keV.
- An x-ray streak camera, to time-resolve the low-energy x-ray yield in the range from 200 to 700 eV.
- Pin diodes, to measure (through interference filters) near-UV to infrared scattered light.
- A zone plate camera, to image the target with 2- to 20-keV x rays.
- An x-ray microscope, to image the target with 400-eV to 3-keV x rays.
- A box calorimeter, to enclose the target and measure scattered 0.35-μm energy.
- An energy-transport streak camera, to viewe the target from the TBD and measure shock transit time to the back of the target.
- A reflected-energy streak camera, to compare the arrival time and temporal shape of the 0.35-μm reflected beam to the 0.35-μm incident-beam pulse.

Target Experiments at 0.35 μm. During the year, we performed 115 target shots at 0.35 μm. In addition to full-system target shots, we used 1007 preamplifier shots for alignment and 218 shots for general laser testing and troubleshooting. There was a noticeable and continuous reduction in overall conversion efficiency due to exposure of the crystal surfaces to humidity.

The previously described experiments produced damage to the trichoic coatings on four different beam dumps; thresholds for significant visible damage were quite variable. The first dump was removed because it reflected only 80% of the 0.53-μm light. It exhibited some damage after a 0.35-μm shot at a fluence level of 1.1 J/cm^2 (1.5 GW/cm^2). The residual fluence on this shot was 0.2 J/cm^2 at 0.53 μm and 0.4 J/cm^2 at 1.06 μm. The dump was used for 50 shots, each with total fluences above 0.2 J/cm^2.

The replacement dump survived 7 shots before being extensively damaged. The largest fluence generated during these shots was 0.8 J/cm^2 (1.1 GW/cm^2) for 0.35 μm; 0.1 J/cm^2 for 0.53 μm; and 0.2 J/cm^2 for 1.06 μm.

The third dump displayed light damage after 22 shots at 0.35-μm with fluences up to 0.9 J/cm^2 (1.4 GW/cm^2). Extensive heavy damage was caused by a single shot with fluences of 1.0 J/cm^2 (1.4 GW/cm^2) at 0.35 μm, 0.3 J/cm^2 at 0.53 μm, and 0.3 J/cm^2 at 1.06 μm.

The fourth dump, still in use at the end of 1980, exhibited extensive light damage after 10 shots, each with a total fluence less than 1.3 J/cm^2.

On the average, the beam dumps were replaced after only 29 shots. In each case, the damage appeared on the trichroic coating. The 0.35-μm antireflection (AR) coating on the second surfaces was unaffected, as were the AR coatings on the target-chamber lenses and windows. (Several debris shields, which are also AR coated, have suffered damage to the coating facing the targets.) The problem with coated beam dumps led us to develop new filter glasses to provide the desired wavelength discrimination (see "Laser Glass" in this section).

North-Arm Physics Experiments. In March 1980, we activated the north arm of Argus as a test bed and used an 8-cm-diam beam for conversion-efficiency measurements on several KDP samples. Doubling and tripling efficiency tests were completed in July, and we then spent several weeks investigating the effect of the conversion process on beam quality. In addition, we checked the effect of a 2 × 2 crystal array on beam near-field and far-field profiles. After the crystal-array tests, the KDP crystals were moved to provide space for a series of high-energy 1.06-μm shots that were used to determine the damage threshold of several types of phosphate laser glass being considered for use in Nova. In another series of shots, we investigated the magnitude of intensity-dependent scattering processes in various candidate index-matching fluids.

In high-power conversion tests at 0.53 μm, we have observed an offset of the optimum angle of incidence from that determined by the lens-and-crosswire technique[4] used originally to align the KDP crystals. We performed a series of experiments in which we discovered an asymmetry in the shape of the fringes recorded by the lens-and-crosswire technique. This asymmetry explained the difference in alignment between that technique and the present alignment technique (see "Argus Frequency-Conversion Experiments" in this section).

Finally, we used the preamplifier stage of the north arm to provide energy for a series of 4-cm-aperture shots to test a tandem-crystal concept of frequency conversion; this concept may prove highly cost effective in the Nova laser. We will finish our studies on harmonic conversion in 1981 by measuring the quadrupling (fourth-harmonic) efficiency.

We modified the north arm of the Argus laser for measurements of harmonic-conversion efficiency, using a 3.0× telescope to reduce the beam diameter to 8 cm. Figure 2-10 shows how the various components were assembled on the north diagnostic table. Results of these experiments are discussed in "Argus Frequency-Conversion Experiments" in this section. The essential components include doubling and mixing crystals and the six calorimeters that measure doubler-input 1.06-μm energy, doubler-output 1.06- and 0.53-μm energies, and mixer-output 1.06-, 0.53-, and 0.35-μm energies.

Harmonic conversion efficiencies are quoted in terms of efficiencies "external" or "internal" to the nonlinear crystals. It is important to understand the difference. External harmonic conversion efficiency is defined in the case of doubling as the ratio of the converted (0.53-μm) output energy to the input fundamental (1.06-μm) energy. For frequency tripling, the external conversion efficiency is defined as the ratio of the output (0.35-μm) energy to the input (1.06-μm) energy. Internal conversion efficiencies are higher than external conversion efficiencies because of the Fresnel reflection losses suffered at the uncoated crystal interfaces. In our experiments, these losses amount to 8.5% for 0.53-μm energy and 28% for 0.35-μm energy (including the uncoated diagnostic beam splitter). Consequently, we can achieve a significant improvement in harmonic conversion efficiency, especially for tripling or quadrupling, by eliminating the Fresnel losses of the KDP crystals.

We have been able to achieve external conversion efficiencies of 77% to 0.53 μm and 55% to 0.35 μm using 1.06-μm pump intensities of 2.5 GW/cm^2 and above. These values correspond to internal conversion efficiencies of 83% at 0.53 μm and 69% at

0.35 μm. Maximum focusable energies in the bare-crystal configuration were 119 J at 0.53 μm and 43 J at 0.35 μm. In later south-arm shots, we were able to produce as much as 54 J of 0.35-μm light.

We investigated the discrepancy between the aligned angle of incidence determined by the negative lens technique and the aligned angle of incidence required for maximum conversion efficiency and determined by tuning the doubler crystal angle and measuring the resulting conversion efficiency curve. We recorded the $\sin^2 x/x^2$ fringes for a series of shots with energies between 0.2 and 350 J and then compared the fringe location to the reference crosswire shadow. The images of the 0.53-μm $\sin^2 x/x^2$ pattern in Fig. 2-11 result from exposing a 10-mm-thick KDP crystal to diverging 1.06-μm laser light at (a) 4 mJ/cm^2 and (b) 7 J/cm^2; note the variation of pattern spacing with fluence. We found that the angular separation of the minima decreased with increasing intensity, as expected, but that there was no shift of these minima with respect to the crosswire. Densitometer traces corrected for the film D/log E response curve, however, generally showed that the maxima were displaced by angles ranging from 0.15 to 0.2 mrad in a direction away from the crystal optical axis. Therefore, the lens-and-crosswire alignment procedure, which required centering the crosswire between the dark fringes, was inherently flawed.

Further tests with a small collimated, high-repetition-rate probe beam exhibited no asymmetry when the crystal was angle tuned. In addition, the 0.35-μm target-experiment crystals, aligned with a photomultiplier and a nearly collimated beam, have demonstrated conversion efficiencies equivalent to the maximum obtained with a similar crystal configuration on the north arm. Thus, we have concluded that the diverging-lens technique does not result in correct alignment of large-aperture crystals. This result is most likely due to the birefringent properties of the crystals.

During the course of our harmonic-conversion experiments on the Argus north arm, we monitored the homogeneities of the near-field beams at 1.06, 0.53, and 0.35 μm by taking hard-film photographs at planes lying near the doubling and mixing KDP crystals. Although the north arm is image relayed, the use of the 3× Galilean telescope to reduce the incident 1.06-μm beam diameter from 28 to 9.5 cm moves the final relay plane from the target chamber to a location near the mixer crystal. As a result, the beam profiles at the three frequencies were not strictly comparable, although the distances between film planes were not so large as to invalidate the comparisons. The optical homogeneities of the 0.53- and 0.35-μm beams were higher than the homogeneity of the parent 1.06-μm beam because the conversion efficiencies were obtained using the present KDP crystal thicknesses at a flux

Fig. 2-10. Schematic of components for frequency-conversion experiments.

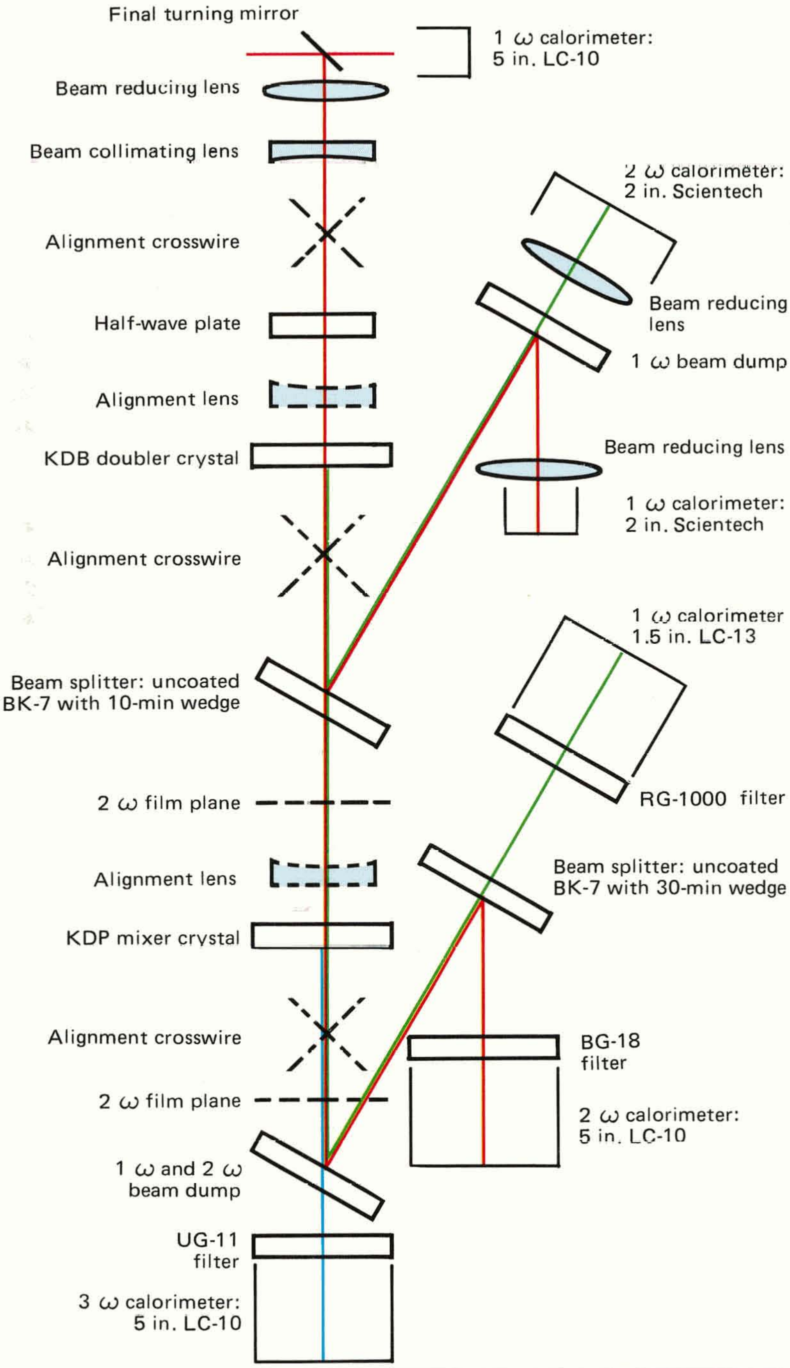

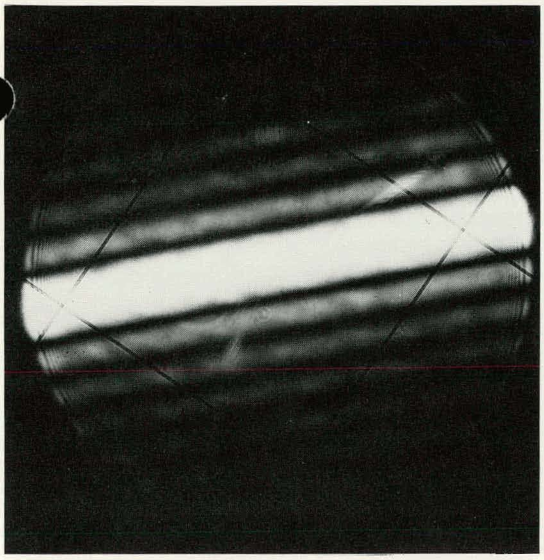

(a) Fluence = 4 mJ/cm^2

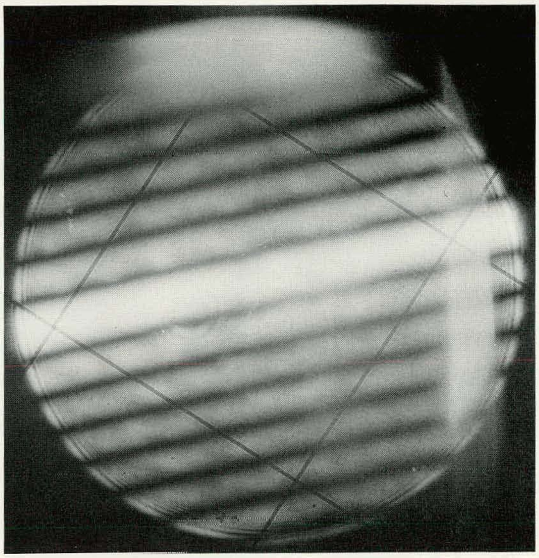

(b) Fluence = 7 J/cm^2

Fig. 2-11. Two photographs of the 0.53-μm fringe pattern, showing the variation of pattern-spacing with fluence.

near 3 GW/cm^2, where the conversion efficiencies peak. Beam hot spots were, therefore, less efficiently converted, and the beam was smoother. The results of these near-field measurements indicate that the 0.53- and 0.35-μm beams varied in intensity only by $\pm 20\%$ across 80% of the beam aperture.

As a consequence of the detailed beam analyses carried out in support of the near-field intensity distributions of the Argus beams at 1.06, 0.53, and 0.35 μm, we derived a new value for the Argus north-arm effective beam area. This parameter is important for determining the average beam fluence at the output of the laser chain.

Author: J. S. Hildum

Major Contributors: G. T. Hermes, G. J. Linford, and B. C. Johnson

Engineering Summary and Upgrades

One major effort during 1980 was reestablishing laser-system integrity after the January earthquake. Recovery efforts of this type show both the good and bad aspects of our overall system-design strategy.

Early in 1980, we began detailed planning for upgrading Argus to a 28-cm frequency-doubled configuration. Program requirements and target-performance considerations caused us to abandon this approach, however, and we proceeded directly with a plan to operate a pair of full Nova arms in the Argus bay (the design of the resulting laser, Novette, is discussed in "Novette Design Considerations" in this section). One practical effect of this decision is that Argus will be shutdown in the fall of 1981 and Shiva shutdown in early 1982. Therefore, in September 1980, the decision was made to stop upgrade modifications to Shiva and Argus and devote this manpower to the Novette design. Therefore, all long-term operating funded engineering activities, with the exception of Novette prototypes, and the Shiva x-ray backlighting modifications, were terminated in September 1980.

Between March (the end of the earthquake recovery) and September, additions and modifications to enhance our target-irradiation and laser capabilities were continued in the following order of priorities (highest priority listed first):

- Reduce identifiable hazards.
- Support new target experiments.
- Improve reliability.
- Improve turnaround.
- Reduce manpower requirements.

We fielded several new target diagnostics (see "Shiva Operations Summary" in this section), and we made a major modification to the system to eliminate a serious source of noise in our recording instruments (primarily in the R7912 oscilloscopes) caused by target x-ray emission. We also accomplished the major system goal of bringing target data into the control room.

For several years, target diagnostic data were collected locally in the target chamber area and brought manually to the control room for reduction. This was a time-consuming process that made it extremely difficult to obtain shot-readiness feedback from the instruments. We have now completed the software and installed the necessary links to enable direct data transfer to the control room. We have also initiated generation of software to enable us to detect instrument status prior to a shot. This one change reduced the target data-reduction time by 20 min. A detailed discussion of these changes appears in Section 5.

We made several modifications to our electronics systems this year. Within the power conditioning area, we enhanced system automatic-control features and expanded the high-bandwidth digital-control bus into the target space frame. The latter modification enables us to obtain high-resolution streak pictures from newly developed CCD cameras in near real time; before this upgrade, such pictures took us weeks to obtain. We use this system for x-ray streaks from target diagnostics and for optical streaks from laser diagnostics. During the year, we also developed our system-integration capabilities within the control system. We devoted our primary control-system efforts to developing an interlocked target-shot sequence that ensures that the operator is aware of all system elements that are not active and enabled prior to a target shot. These developments are discussed in detail below.

Our modifications of the mechanical systems were aimed at improving capacitor-bank safety, providing x-ray backlighting capability, improving beam relaying, improving laser-diagnostics capability at the beta Pockels cell, and reducing system operating costs for nitrogen gas. In addition, using Shiva, we supported the development of the Nova plasma shutter. All of these items are also discussed in detail below.

Author: P. R. Rupert

Earthquake Recovery. The January 24, 1980, earthquake struck 16 kilometres north of the Laboratory with a peak magnitude of 5.5 on the Richter scale. There were no personnel injuries and only minor component damage within the Shiva and Argus lasers. Building damage was also minor, but all of the Shiva target-space frame seismic anchor bolts sheared due to movement of the space frame. The laser-frame anchor bolts remained intact. Before resuming unlimited access to the Shiva target and laser bays, we resecured both space frames and realigned the Shiva target space frame. With the help of Rigging International, Inc., and Bigge Rigging, we completed these tasks by February 5. We then realigned the laser chains, cleaned up the remaining damage, and demonstrated full Shiva performance by firing a target shot on February 20. We repaired minor component damage on the Argus laser and high bay and restored the system to operation on February 19, less than a month after the earthquake.

This outstanding achievement is attributable to the soundness of the laser system design and to the intensive effort and dedication of all participating personnel. The following discussion provides more detail on our recovery activities and the lessons we learned in reactivating the laser systems.

After the earthquake, we made a plan and schedule for reactivating Shiva. We used this plan, which was revised several times as new information became available, to monitor progress and allocate resources during the reactivation phase. The final version of the plan is shown in Fig. 2-12 (pp. 2-16 and 2-17). This management tool greatly aided in focusing our resources on the appropriate areas.

The components attached to the Shiva frame stayed in alignment with respect to each other, but the target frame moved with respect to the laser frame. Before we performed any surveying or recovery work, the frames were first made safe so that people could work in the area. This required the fabrication of new seismic anchors that could fit outside of the damaged anchors. We secured the laser-bay space frame by February 2 and the target-bay space frame by February 4, and we designed the permanent replacement anchors for the laser space frame to allow safe subsequent realignment.

After we secured the frames, surveyors determined the location of both frames with respect to benchmarks outside Building 391 (which had not moved); their survey showed that the laser frame was within 1/16 in. of its previous position. The frame's primary seismic anchor was intact, but the bolts holding the frame bearings, which resist turning about the seismic anchor, were sheared in the quake. The bearings themselves, which are rollers between plates, were not damaged.

The target frame had moved 0.4 in. west and had rotated counterclockwise approximately 0.75 in., as measured at the f/14 spatial-filter entrance. All 20 of the target frame's concrete-buried, 0.75-in.-diam anchor bolts failed. Some of the radial bearing bolts also failed, and some of the roller bearings were damaged. The rollers are held in place by endless fiber belts, some of which had rotted; this allowed the rollers to fall out of place when the frame moved, and some of the bearings were crushed. With the help of Rigging International, we jacked up the 230 000-kg frame about 6 mm and removed, inspected, repaired, and reinstalled all bearings. We then lowered the frame onto these bearings, moved it to its realigned position and securely fastened it. Throughout this maneuver, the frame was under complete restraint in case of another earthquake. Both frames were in alignment to within original tolerances on February 5—only 12 days after the earthquake.

The laser space frame is designed as an optical bench, which means it is very stiff and fixed at a single point; from this point, the frame is allowed to expand in all directions. To prevent distortions of the structure due to thermal gradients, all other support points are on rollers. The fixed point is a seismic anchor with the primary functions of

- Making the system safe against personnel injury.
- Containing system damage, so that the facility is repairable under reasonable cost and schedule limitations.
- Resisting an earthquake acceleration in any direction equal to 25% of the acceleration of gravity.

This was our design standard, which used a reasonable safety factor to cover material and installation shortcomings. The new anchoring system is designed to withstand an acceleration of 0.5 g.

For optical stability, all laser components were mounted to the frame with very stiff supports. All bolted interfaces between these component supports and the frame were designed with bolts proportionally stronger than the floor bolts. None of these failed. If we had had the frames tied too rigidly to the floor, there is a chance that the large earthquake forces would have been transmitted through the frame, with subsequent structural damage and (possibly) falling components.

The anchor bolts that failed were tested in the LLNL testing laboratory and were found to have an ultimate tensile strength of 93 300 psi and an ultimate shear strength of 53 300 psi. The frame design performed as intended, and we have determined that the combined shear and torsion loads applied to the target frame bolts were in excess of 0.25 g. In retrospect, then, this system performed very well; the space frame design team, headed by C. A. Hurley, is to be congratulated.

There was minor damage to catwalks, and one end of the optical-trigger beam tube fell from its mounting; however, the earthquake caused no significant damage to any of the target-chamber or data-acquisition systems. Nevertheless, as part of the recovery effort, all of our R7912 instruments were cycled through our Tektronix maintenance trailer, which provided a head start on recovery. No instrument damage was found. We also checked the alignment of all of the experiments that have long lines of sight; we found no problems that could be traced to the earthquake, except with the neutron time-of-flight diagnostic. These checks provided an opportunity to correct alignment problems that had existed prior to the earthquake. Because actual earthquake damage was minimal, we also spent time adding new diagnostics, reconfiguring several experiments, and performing other target-chamber maintenance items.

Our computer system was undamaged and came back on line without incident. The only problem was several broken disks, which fell due to inappropriate storage.

We found somewhat greater problems in the power-conditioning area. There was water damage due to broken low-conductivity water lines and fire sprinkler lines, and movement of the capacitor bank broke some insulating sheets under the capacitors. Drying the bank and replacing the insulating sheets required a concentrated effort by a large number of technicians.

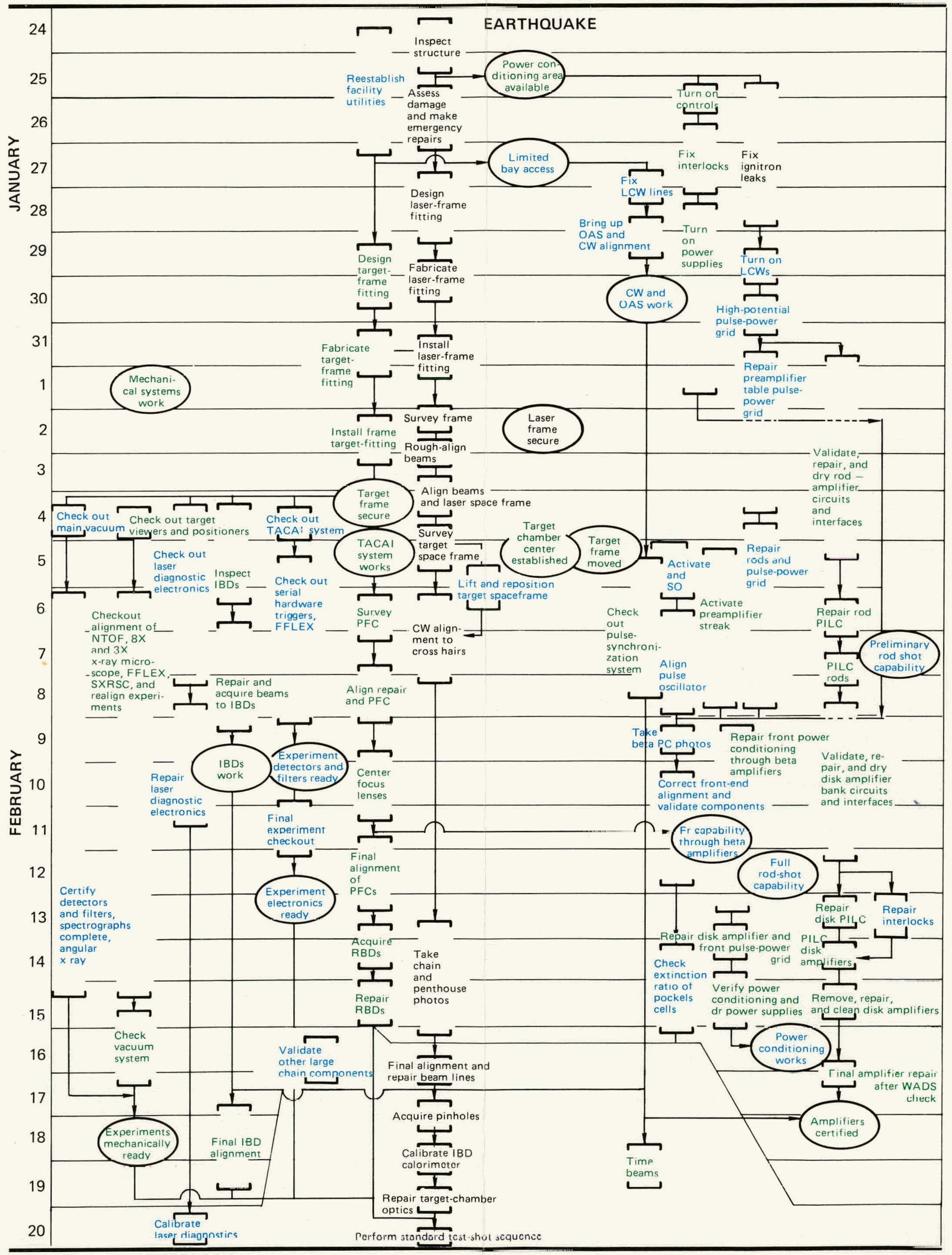

Fig. 2-12. Schedule for reactivating Shiva after the January 24, 1980, earthquake.

The speed of the work was limited by the amount of specialized capacitor-handling equipment that we have available; this equipment is adequate for normal operations, but was not intended to support such an intensive large-scale effort. As a result, the power conditioning repair was one of the pacing tasks in reactivating the facility. One of the design lessons we learned from this incident is to specify impact strength on our sheet insulating materials in the future.

After assessment of earthquake-induced damage to the Argus laser system, we found that

- Twenty-three of 56 optical tables were shifted off their grouted bases.
- There was substantial damage to the ceiling-mounted air-distribution and diffuser units, and there were water leaks in wall-mounted piping.
- Seven disk amplifiers had dropped off their mounting rollers.
- A majority of the magnetically mounted optical components had moved. Many of these had fallen to the optical-table surfaces and some, including the master oscillator and 4-cm rod amplifiers, had fallen 60 cm to the concrete floor.
- Two Faraday-rotator insulators were broken.

We were concerned first about the integrity of the ceiling, as tiles and fixtures continued to fall to the floor for some time following the earthquake. We removed loose tiles and fixtures and secured the remaining components before starting any recovery effort. After certifying the building safe for occupation, we restored electrical power and vacuum service and stopped the water leaks. We relocated and regrouted all shifted optical tables to within 6 mm of their original positions.

We installed restraining clamps on all disk amplifiers to prevent any movement off the roller supports, and we installed larger bases on magnetically mounted components to prevent the tip-over response observed during the earthquake. The few optical components that had broken were replaced from existing spares, so no time was lost obtaining new components. We found that the oscillator had only minor damage; we were able to restore it to preearthquake performance within one week. We then realigned the entire laser chain and fired the first system shot on February 19—only 26 days after the earthquake.

We noted an instability of the cw alignment beam during system realignment. We traced this problem to two sources: several optical tables had cracked grout, although they had not shifted position, and the extensive damage to the air-diffuser system had created very uneven flow patterns in the target bay. We regrouted the unstable tables and installed beam tubes to eliminate air turbulence near the laser beam. The diffuser system could not be repaired immediately, but use of the beam tubes allowed alignment to proceed on schedule.

We made some modifications to the facility to improve safety and decrease the damage potential of any future earthquakes. These changes included restraining large components and cabinets in the bays and adjacent areas and developing specifications for maximum allowable loadings on magnetic supports.

There was no major damage to the pulse-power system on Argus. The damage that did occur was confined to capacitor racks that had moved a few inches from their initial locations and to cables that had fallen out of their trays. Although the visible damage was slight, we performed a thorough cleanup and examination of the pulse-power system. Our major concern was the possibility that the pulse-power insulation system was breached, which could result in a serious shock accident or cause major damage to the control system. To ensure that the pulse-power system was safe we performed high-potential tests to a level of 20 kV dc on all pulse-power cable shields. The laser system was operational within a few days after successful completion of the high-potential test.

Events during and immediately after the earthquake pointed out a number of improvements that could be made both in the facility and in our emergency procedures.

We uncovered a need for immediately activated emergency lights to provide illumination during the period before the emergency generators come on line. As a result, we have installed battery-powered emergency lights in selected portions of the building, and we now forcefully emphasize the requirement for maintaining emergency exits unblocked. An escape ladder between the basement level of the target bay and the main floor in Shiva was inadequate for its intended use; we have installed a permanent, safer ladder.

To facilitate immediate electrical power shutdown, we have updated our building power drawings and the labeling of our power sources, and we have placed power-panel locator plans throughout the building. We have taken similar actions for city water, low-conductivity water, sprinkler systems, and natural gas; the main shutoff points for these systems have been identified in our Disaster Plan (see below). Personnel who would be likely to be called on to shut off these systems have been shown their location, and disaster drills are being conducted.

Substantial water damage from broken sprinklers resulted from sprinkler valves that were chained open. We are leaving these valves chained open, to prevent inadvertent shutdown, but we have procured bolt cutters and developed a procedure for prompt shutdown if necessary. We have instituted a procedure by which standby personnel can turn the system back on if required.

We have developed a Disaster Plan to deal with incidents in which emergency services cannot respond immediately and normal communications are lost. This will enable us to evacuate the building, deal with injuries and other problems, account for personnel, and secure the building. These procedures are not intended to replace normal emergency services, but to facilitate their effectiveness during a Laboratory-wide emergency. We are also continuing to upgrade our readiness with drills and modifications to take maximum advantage of the lessons learned during the earthquake recovery.

Authors: J. W. Herris, A. J. Levy, P. R. Rupert, C. A. Hurley, R. R. Baltzer, B. T. Merritt, and J. D. Williams

Major Contributors: J. T. Hunt, D. R. Speck, C. D. Swift, C. E. Thompson, and the LLNL solid-state technicians

Target Diagnostics. The responsibilities of the Target Diagnostics Group span the operation and maintenance of the electronics data-acquisition system and the target-chamber diagnostic systems. A description of these systems may be found in previous annual reports.[5–7]

By 1980, target diagnostics on Shiva had been developed into a mature subsystem. Our major system upgrade during the year consisted of new data-acquisition software that allowed us to operate from the control room using the PDP 11/34 computer. Table 2-2 summarizes the status of the data-acquisition system for target-diagnostic instruments as of the end of 1980 and compares it to the status at the end of 1979.

Because of the minimal effect of the earthquake on target diagnostics, we had time to correct a number of diagnostic alignments and related problems during the recovery period. Meanwhile, we continued work on the implementation of new diagnostics, and Nova construction crews cut two openings into the east wall of the target room to provide access for equipment and personnel.

Our activities in 1980 spanned more than a dozen target-shot series. On several series, we diagnosed targets to determine density and performance, and we also gathered information on Nova-style targets. A third group of experiments involved diagnostic development, such as x-ray backlighting and new density-measuring techniques.

Table 2-3 summarizes the full complement of Shiva target diagnostics that could be fielded for experiments as of the end of 1980. Implementation of the latest diagnostics increased our capability to measure x-radiation and spectrally shifted laser light from the target plasma. Complete diagnostic descriptions and results are presented in Sections 5, 6, and 7 of this report.

While operating existing diagnostics and implementing new diagnostics throughout the year, we also made a significant improvement in our electronic data-acquisition system and in other target systems.

Table 2-2. Summary of data-acquisition system for target-diagnostics instruments.

Component type	Total number on line 1979	1980
CAMAC crates	11	12
R7912 transient digitizers	28	30
7903 oscilloscopes	10	11
7844 oscilloscopes	4	4
7104 oscilloscopes	0	2
Thomson CSF oscilloscopes	0	2
Integrator channels	89	149
Calorimeter channels	62	70

Diagnostic	Detectors: Type	No.	Measurement	Activated
Neutron				
Yield	Scintillation/PM	3	Time resolved	Jan. 1978
Time of flight	Scintillation/PM	2	Time resolved	Jan. 1978
Yield	Cu activation	2	Counting	Apr. 1978
Yield	Pb activation	1	Counting	Oct. 1978
ρR	CR-39 track	4	Multichannel proton counting	Oct. 1978
Yield	Dioxane activation	1	Counting	Dec. 1978
ρR	Si activation	2	Counting	Jan. 1979
Yield	Ag activation	1	Counting	Mar. 1979
Interval	Fluor/microchannel plate	1	Time resolved	Mar. 1979
X ray				
3× microscope	Film	4	Spatially resolved, time integrated	Mar. 1978
Zone plate camera	Film	3	Spatially resolved, multispectral, time integrated	Apr. 1978
8× microscope	Film	4	Spatially resolved, time integrated	June 1978
2- to 5-keV spectrograph	Film	1	Spectrally resolved, time integrated	June 1978
High-energy streak camera	Film	2	Time resolved	Sep. 1978
Angular high-energy	Fluor/vacuum photodiode and PIN diode	16	Time resolved, time integrated	Nov. 1978
Pinhole camera	Film	1	Spatially resolved, time integrated	Dec. 1978
Dante S	XRD-31 diode	10	Spectrally resolved, time resolved	Jan. 1979
Filter fluorescer	Fluor/PM	19	Spectrally resolved, time integrated	Jan. 1979
Ar spectrograph	Film	1	Spatially resolved, time integrated	Mar. 1979
Si spectrograph	Film	1	Spatially resolved, time integrated	Mar. 1979
Dante M	XRD-31 diode	6	Spectrally resolved, time resolved	July 1979
Calorimeter	LC-29	1	Time integrated	Sep. 1979
Sub-keV spectrograph	Film	1	Spectrally resolved, time integrated	Sep. 1979
High-energy timing	Microchannel plate	1	Time resolved	Jan. 1980
Sub-keV streak camera	CCD array	1	Spectrally resolved, time resolved	Mar. 1980
Optical/x-ray streak camera	Film	1	Time resolved	Mar. 1980
Br spectrograph	Film	1	Spectrally resolved, time integrated	Mar. 1980
Dante N	XRD-31 diode	5	Spectrally resolved, time resolved	Apr. 1980

Table 2-3. Shiva target diagnostics **(continued on p. 2-19).**

New system software allowed us for the first time to operate the target acquisition, control, and instrumentation (TACAI) system from the control room using our PDP 11/34—a concept envisioned for this subsystem early in the Shiva design.[8] The original master-slave architecture of the system has been retained, with the PDP 11/34 now fulfilling the role of master. The PDP 11/34 is linked to the LSI-11 slave via two fiber-optic serial lines. During the year, we met our objectives in this project, which were to

- Reduce the manpower required in the support and operation of the original TACAI system.
- Improve operational reliability.
- Integrate this subsystem into the overall laser control system.

We wrote the software for the master in Fortran IV Plus, under RSX-11M, using a multiprogramming approach to facilitate system maintenance and expansion. The master program currently consists of nine tasks, each of which performs a distinct function (Fig. 2-13). Task-to-task communication and synchronization is performed via a shared region, and RSX-11-type messages are sent to and received from a central task that arbitrates between operational requests and handles the master-slave command and data transfers. This architecture makes it relatively easy both to add tasks and to link the operation of TACAI to the operation of other PDP 11/34 subsystems via DECNET. Currently, linkage is limited to the initiation, by power conditioning, of preshot system setup and verification of system readiness.

This diagnostics control system is significantly faster than our previous method and may be operated from either the control room or the target room. All data transfer directly to the PDP 11/34, eliminating the use of floppy disks either as a system device or as a data transfer media. We have implemented an identical system on Argus.

We also rewrote the indirect command files used to control quick-look data processing and file management; this minimizes operator confusion and the possibility of lost data after a shot. Parameter files define the type of processing and the file manipulation to be performed as a function of shot type and laser facility. On Shiva, shot data are automatically transferred to the PDP 11/70, using the

DECNET facility, and are subsequently deleted from the PDP 11/34.

To use the new software for processing shot data acquired by means of the LSI-11 TACAI version, we wrote a program to perform the required transfer and type conversion of shot data from floppy disks to a PDP 11/34 file. All of the new software may also be run on the PDP 11/70, thus providing a backup capability that previously did not exist.

We are currently adding preshot and background diagnostics to TACAI to improve operational reliability. These diagnostics will be part of the preshot initialization sequence and will be aimed at detecting hardware-state errors, out-of-tolerance conditions, and other operational problems that could result in the loss of shot data. The background diagnostics will detect problems that are still in the incipient stage and not likely to cause loss of data, such as degenerating fiber-optic links.

Other target-diagnostic upgrades that we accomplished in 1980 include activation of an eight-rack diagnostic station outside the target bay to implement the Dante S and M systems. This move eliminated target-generated noise from target data. Subsequent investigation into previously

	Detectors			
Diagnostic	Type	No.	Measurement	Activated
22× microscope/ streak camera	Film	1	Spatially resolved, spectrally resolved, time resolved	June 1980
Pinhole sub-keV streak camera	Film	1	Spatially resolved, spectrally resolved, time resolved	Nov. 1980
Angular high-energy	Film	1	Spatially resolved, time integrated	Nov. 1980
Au spectrograph	Film	1	Spectrally resolved, time integrated	Dec. 1980
Plasma/Ion				
Energy balance	LC-27 calorimeter	34	Time integrated	Jan. 1978
Zone plate camera	Cellulose nitrate	1	Spatially resolved, time integrated	May 1978
Energy balance	LC-38 and LC-39 calorimeters	3	Time integrated	May 1979
Light				
Energy balance	LC-21 calorimeter	30	Time integrated	Jan. 1978
Energy balance	PIN diode	38	Time integrated	Jan. 1978
Energy balance	Box calorimeter	24	Time integrated	Oct. 1979
Brillouin scattering	Spectrometer/ diode array	1	Spectrally resolved, time integrated	Nov. 1979
Pyrometer streak camera	Film	1	Spectrally resolved, time resolved	Apr. 1980
Raman spectrograph	Discrete InAs array	25	Spectrally resolved, time integrated	June 1980
Raman timing	Pyroelectric	1	Time resolved	July 1980

Table 2-3. (cont.)

Fig. 2-13. Software structure of the TACAI system. ▼

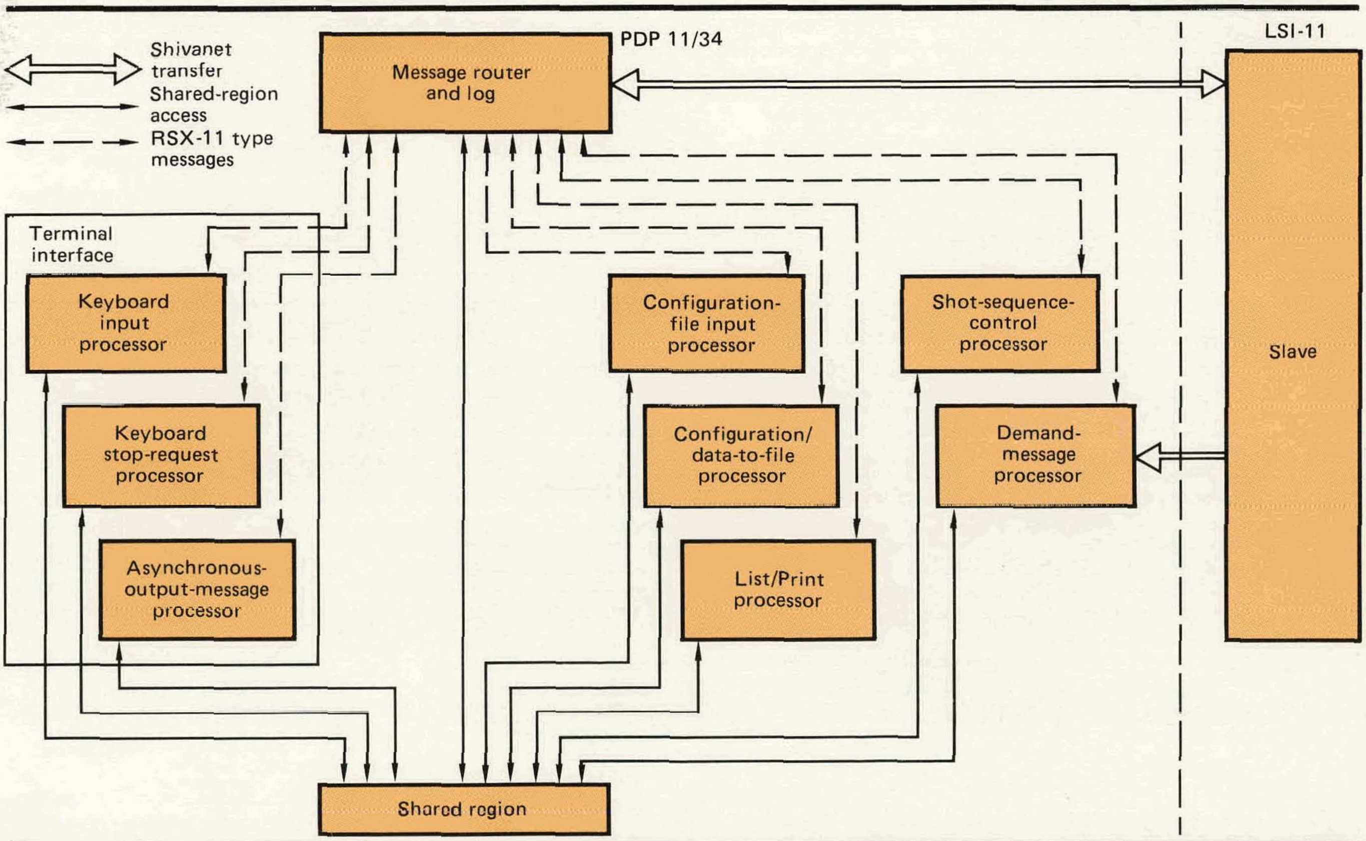

unnoticed baseline noise showed that it was being generated within the XRD-31 detectors.

For the first time, we incorporated CCD technology on Shiva in a direct digital readout of the sub-keV x-ray streak camera. Because of the large amount of data associated with this two-dimensional array, we interfaced this diagnostic into the power-conditioning system to take advantage of its higher digital bandwidth and ease of implementation.

To produce fiducial timing pulses for the x-ray delay and Raman timing diagnostics and for plasma shutter tests, we added three additional optical detectors to the diagnostics system. By comparing a fiducial pulse to the instrument trigger pulse, we determined our short-term trigger-system jitter to be less than 200 ps.

We recalibrated the energy balance module (EBM) calorimeter system, and then made a visual inspection of the system. This check, prompted by erratic behavior of the EBMs during the summer, revealed a substantial gold coating on the optical windows, which required careful off-line cleaning.

To provide pumping capability for the 22× x-ray microscope diagnostic, we expanded the auxiliary vacuum system by extending the 4-in.-diam manifold approximately 20 ft. We added air and N_2 lines for valve actuation and diagnostic backfilling, and we replaced the existing vacuum ball valve on the target inserter with a sliding-valve assembly. The new valve cured periodic sealing problems and is much easier to operate.

We removed our leak-detection spectrometer from its location on the target chamber and incorporated it into a bypass arrangement around the west turbomolecular-pump high-vacuum gate valve. This arrangement gives us the ability to obtain maximum instrument sensitivity and also provides a convenient technique for finding large vacuum leaks (up to several hundred mTorr) in the chamber.

The addition of new catwalks on the east side of the target frame enhanced our operational capability, both by providing a second means of access to the target inserter and by improving cross-chamber access (nonexistent at the target-chamber level due to diagnostic blockage). The addition of a small catwalk section at the target-chamber level opened the way for installation of the Dante H diagnostic, which will block access to the target inserter from the original stairs. We also added an emergency exit ladder from the basement to the mezzanine level.

Upgrades to the Argus target diagnostic system include

- Reactivating foreline cold traps and installing new hardware controls.
- Adding separate roughing lines to several diagnostics.
- Removal of all or part of two neutron-activation diagnostics.
- Modifying the N_2 fill lines.

During the earthquake recovery period, we improved the CAMAC serial highway by adding new fiber cables and transmitter-receiver modules, thus replacing a previously unmaintainable system of varying fiber cables and optical elements.

Authors: C. E. Thompson and D. J. Kroepfl

Major Contributors: M. D. Fiore, E. J. Powell, and T. L. Schwab

Optical Pulse Generation. Until September 1980, we continued to operate Shiva with the original oscillator. We then installed both a new actively mode-locked and Q-switched (AMQ) oscillator and a single-axial-mode Q-switched oscillator with expanded capabilities. The decision to install a new AMQ short-pulse oscillator on Shiva dates back several years. We found that the electronics on the original oscillator did not interface to the computer very well,[9] and we also experienced some electrical noise problems.[10] The new control electronics have been described in previous annual reports.[9,11] During 1980, these controls were completed and debugged. We reported on the development of the new oscillator hardware, for Argus, in 1979.[12] By deciding to use this hardware on Shiva also, we were able to make a quick switch to the new oscillator and minimize downtime.

The pulse width of the new AMQ oscillator can be adjusted from 100 ps to 1 ns, with the energy in a single pulse ranging from 200 to 300 μJ. However, the requirements on Shiva have gone towards pulses in the range of 3 to 5 ns for some experiments; for other experiments, pulses as long as 35 ns are needed. For this longer pulse range, we developed a single-axial-mode, long-pulse oscillator and decided to install it, with a pulse slicer, on Shiva. The characteristics of the long-pulse oscillator are described in "Oscillator Development" in this section.

X-ray backlighting experiments on Shiva will require the synchronization of the AMQ and long-pulse oscillators, so that one oscillator can be used for target irradiation and the other for x-ray backlighting. We also decided to use a single beam line to propagate both pulses from the oscillator table into the system. In this scheme, the pulses are stacked one behind the other on the oscillator table, spaced by about 40 ns. Both pulses are then injected into each arm of the system, and the two Pockels cells in each arm are timed to select the appropriate pulse in each arm.

The decisions to install the long-pulse oscillator on Shiva, to synchronize it with the AMQ oscillator, and to use a single beam line for backlighting experiments constrained the design layout of the new front end of Shiva. The design was further influenced by the ground rules for making changes on an operating system: we seek to minimize changes to the basic system and, thereby, minimize downtime as much as possible. The system layout with the two new oscillators is shown in Fig. 2-14.

Fig. 2-14. Schematic of the new oscillator system installed at Shiva.

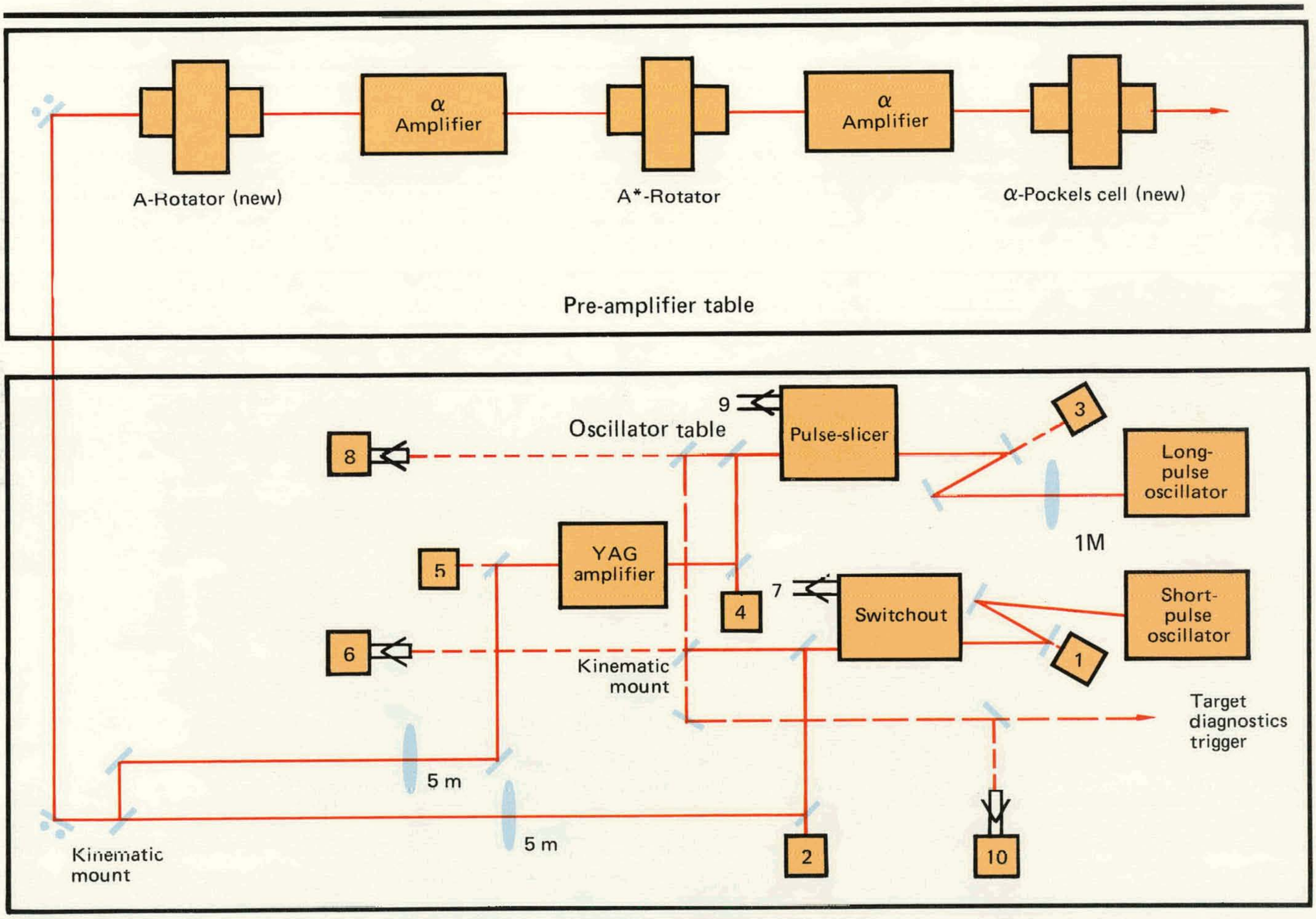

Diagnostics

1. Pulse train
2. Single short pulse
3. Long pulse
4. Sliced-out pulse
5. Amplified sliced-out pulse
6. Single short pulse } To digitizer 1 via fiber optic
7. Rejected pulse train } To digitizer 1 via fiber optic
8. Sliced-out pulse } To digitizer 2 via fiber optic
9. Rejected long pulse } To digitizer 2 via fiber optic
10. Pockels cell timing pulse (to digitizer 3 via fiber optic)

Figure 2-15 shows a photograph of the new oscillators on Shiva. The new arrangement differs in several ways from that of the old oscillator system.[13] The oscillators are pointing in the opposite direction relative to the earlier layout; this change in direction was influenced partly by the desire to have both the oscillators on the table and partly by the location of the instrument racks at the right-hand side of the table. We also had to match the beams from both oscillators into both the existing beam line for the system and the target-diagnostics trigger beamline. To do this, we have a 1-m lens following the long-pulse oscillator; this lens is positioned to make the effective beam size of the long-pulse oscillator the same as that of the short-pulse oscillator. Both oscillators are then matched into the system with a 5-m lens, as shown in Fig. 2-14.

Figure 2-14 also shows how we can select the beam from either oscillator to trigger the target diagnostics by using a removable kinematic mount. The beams from both oscillators are the same in the diagnostic-trigger beam line. The length of the beam path from the long-pulse oscillator into the system was also adjusted, so that the relative timing of the pulses in the main beam line and the target-diagnostics trigger beam line were the same. This means that we can select the diagnostics trigger from either oscillator without any further timing corrections at the target area. We use a second removable kinematic mount (Fig. 2-14) to select either or both oscillators for the system. With the mirror removed, the short-pulse oscillator goes into the system; with the mirror installed, the long-pulse oscillator is selected.

The output energy from the pulse slicer, which follows the long-pulse oscillator in the beam path, is in the range from 20 to 40 μJ/ns. In the range from 2 to 5 ns, the energy from this oscillator is considerably less than the AMQ oscillator. Thus the long-pulse oscillator beam line requires an additional YAG preamplifier, with gain of about 10, as shown in Fig. 2-14. This led to the requirement for additional isolation between the YAG preamplifier and the alpha amplifiers in the front end. An additional Faraday isolator was also installed on the preamplifier table, as shown.

We had initially installed a dye cell on the preamplifier table, following the alpha amplifiers, for ASE suppression. The dye cell worked well with short pulses (from 100 ps to 1 ns), but, with longer pulses, the pulse

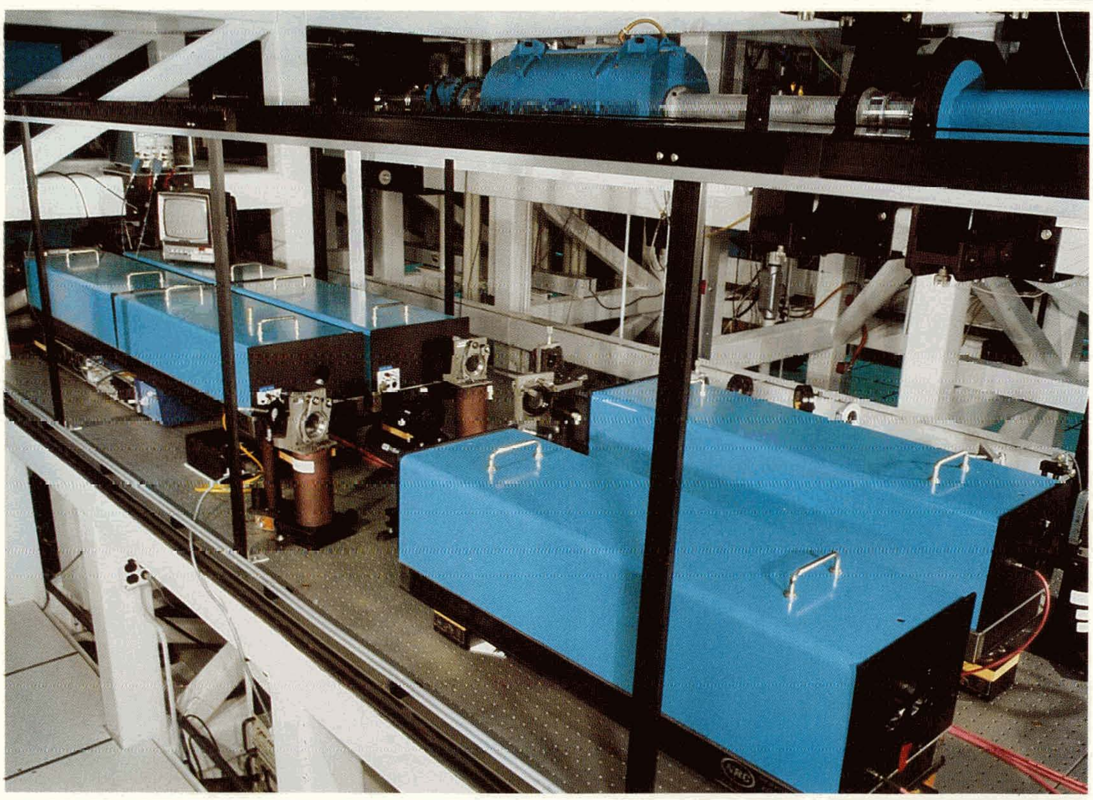

Fig. 2-15. The new oscillator installation at Shiva.

energies required to saturate the dye would be high enough to damage the dye cell. Therefore, we installed a fast Pockels cell at this location for isolation and ASE suppression. The development of the driver for this Pockels cell was described in the 1979 Annual Report,[14] and the description is continued in "Fast Pulse Development" in this section. The alpha Pockels cell for this setup is characterized in "Oscillator Development" in this section. The planar-triode driver and alpha Pockels-cell system has an optical rise time of about 2 ns, a jitter of less than 400 ps, and a transmission of 80%.

The new electronic controls for a single oscillator have been described in previous annual reports.[9,11] We used two sets of these controls for the installation of two new oscillators, and we made minor modifications to the controls to adapt them to the two synchronized oscillators. Figure 2-16 shows a schematic of the controls. An important improvement is that the high-frequency units of each oscillator's control have seven adjustable delay channels. The high-speed signals from the master oscillator are sent to various parts of the system on fiber-optic cables, as described in the 1979 Annual Report.[15] We can, therefore, send high-speed signals to locations in the laser bay and target area without electrical-noise interference.

Our installation strategy was aimed at minimizing downtime and other interferences with Shiva operations. We installed the new AMQ on the oscillator table in Shiva, next to the old oscillator; installed all the electronic controls and power conditioning for the new oscillator; debugged this system and interfaced it with the Shiva computer controls; fired the new oscillator with the old oscillator during front-end and system shots; and solved the electrical interference problems. We then temporarily injected the new oscillator into the system and did propagation shots through the front end, checked automatic alignment (OAS), timed the Pockels cells in the individual beams, and did propagation

Fig. 2-16. Electronic controls for the two synchronized oscillators.

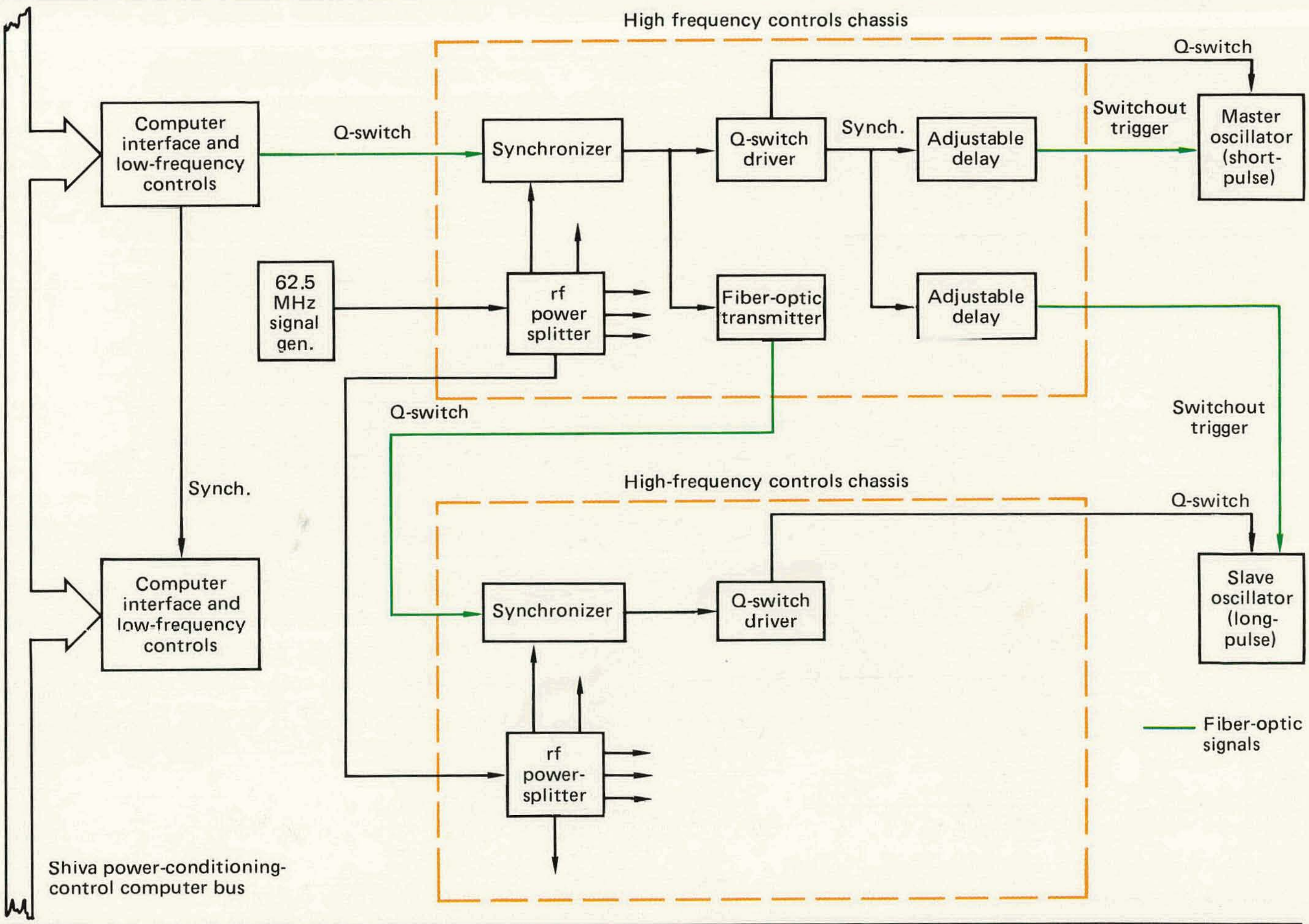

shots through each arm to determine beam quality and energy. All of this was done with minimal interference to the shot schedule of the old oscillator. When we were reasonably sure that there were no major problems with the new oscillator, we removed the old oscillator completely, brought the new oscillator on-line in its final position, and interfaced it completely with the system in less than a week. We then installed the long-pulse oscillator, the YAG amplifier, the Faraday isolator, and the alpha Pockels cell to complete the installation shown in Fig. 2-14.

System Integration of New Oscillators. There are three main interfaces of the new oscillators with the Shiva system:

- The optical interface, which is discussed above.
- The computer, or slow-timing interface, which is built into the control.
- The fast-timing interface, where the main improvements have been made.

A characteristic of the AMQ oscillator is that the timing of the optical pulse is known more than 1 μs in advance, with an accuracy of better than 1 ns. This allows us to set up accurate adjustable-delay generators at the oscillator to trigger devices that need accurate and fast timing signals relative to the optical pulse.

In the old oscillator system, we used the fast-timing properties of the oscillator to trigger only the pulse switchout system and the ASE Pockels cells.[10] With the new system, we expanded this to further include the front-end ASE Pockels cell, the prepulse detector system, the front-end streak camera, the pulse slicer for the long-pulse oscillator, and the transient digitizers used with the oscillator and Pockels cell diagnostics. In Fig. 2-17, we show how we arranged the delay channels to trigger these devices. The circled numbers indicate the fiber-optic outputs at the back of the high-frequency unit. Note that channel 1 is used to drive all the other channels; this allows us to move all the other delay channels together relative to the oscillator pulses.

The control electronics were designed such that each delay channel can be enabled separately. Table 2-4 shows the repetition rate for each delay channel for four modes of operation under control-room computer control: local mode, 1-pps mode, 10-pps mode, and the shot countdown mode. The 1-pps mode was used for automatic alignment and pulse-width measurements with the streak camera. Note that we never trigger the ASE Pockels cells in the arms and the streak camera faster than 1 pps and that we trigger the display transient digitizers at 10 pps all the time, even during the shot countdown sequence. We made the appropriate software changes to set up these various modes of operation.

Oscillator and Front-end Diagnostics. During 1980, we also improved our diagnostics on the oscillators and front end (see Fig. 2-14 for the location of all the diagnostics). We continued to display the prelase signal of the oscillator on a dedicated oscilloscope, as described for the first AMQ oscillator in the 1976 Annual Report.[16] We also improved the switchout systems by implementing a display that had been used successfully on Argus for some time. We take the rejected pulse train, from the first polarizer after the first Pockels cell in the switchout system, and combine it with the single pulse that is transmitted through the switchout with some delay. The display for this switchout system is shown in Fig. 2-18(a). From this display, we can see where the pulse is switched out of the pulse train, how much of the pulse is switched out, and how much is transmitted through the switchout. On Shiva, we have further improved this switchout diagnostic by using

Fig. 2-17. Allocation of the seven adjustable delay channels in the master high-frequency unit.

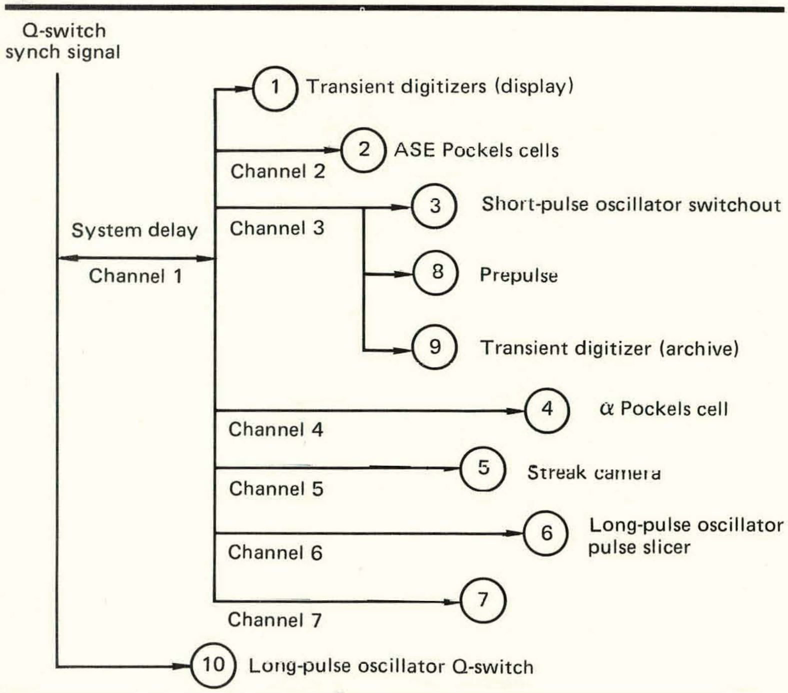

fiber-optic cables to take both the rejected train and a fraction of the switched-out train to a fast ITT F4000 planar diode. We adjusted the length of the fiber-optic cables to give the appropriate delay to the switched-out pulse, and we obtained the display shown in Fig. 2-18(a). With fiber-optic cables, we can also place the diode in a low-noise environment to get very clean displays.

We have found that fast-rise-time, high-voltage drive to the Pockels cells generates significant electrical noise and that we could not position a fast diode next to the switchout and obtain the clean displays shown in Fig. 2-18. Figures 2-18(b) and 2-18(c) show displays for the pulse-slicing system using 5- and 35-ns pulses, respectively, from the long-pulse oscillator. From these displays, we can see that the first stage of the pulse slicer is not opening completely, since the sliced-out section of the pulse does not completely go down to the baseline. We use these displays to monitor planar-triode performance and pulse-slicer alignment. The displays for both oscillators are combined and sent to the control room, where they are displayed as shown in Fig. 2-18(d). In this case, both oscillators are synchronized in preparation for x-ray backlighting experiments.

Oscillator Synchronization. To synchronize the AMQ and long-pulse oscillator, we first must arrange to have both lasers reach peak energy in their Q-switched pulses at the same time. We then slice a pulse from the long pulse synchronously with the short pulse from the AMQ oscillator.

In "Oscillator Development" in this section, we describe how we generate the electrical signals to open the Q-switches on

Table 2-4. Modes of operation of the adjustable delay channels.

		Trigger-enabled repetition rate (pps)			
			Computer mode		
System	Channel	Local mode	1-pps	10-pps	Shot
System delay	1	10	10	10	10
Digitizers (display)	1				
ASE Pockels cells	2	1	1	1	Shot
Short-pulse OSC switchout	3				
Prepulse	3	10	1	10	Shot
Digitizer (archive)	3				
α Pockels cell	4	10	1	10	Shot
Streak camera	5	1	1	1	Shot
Long-pulse OSC pulse slicer	6	10	1	10	Shot
Target area (plasma shutter)	7	10	1	10	Shot

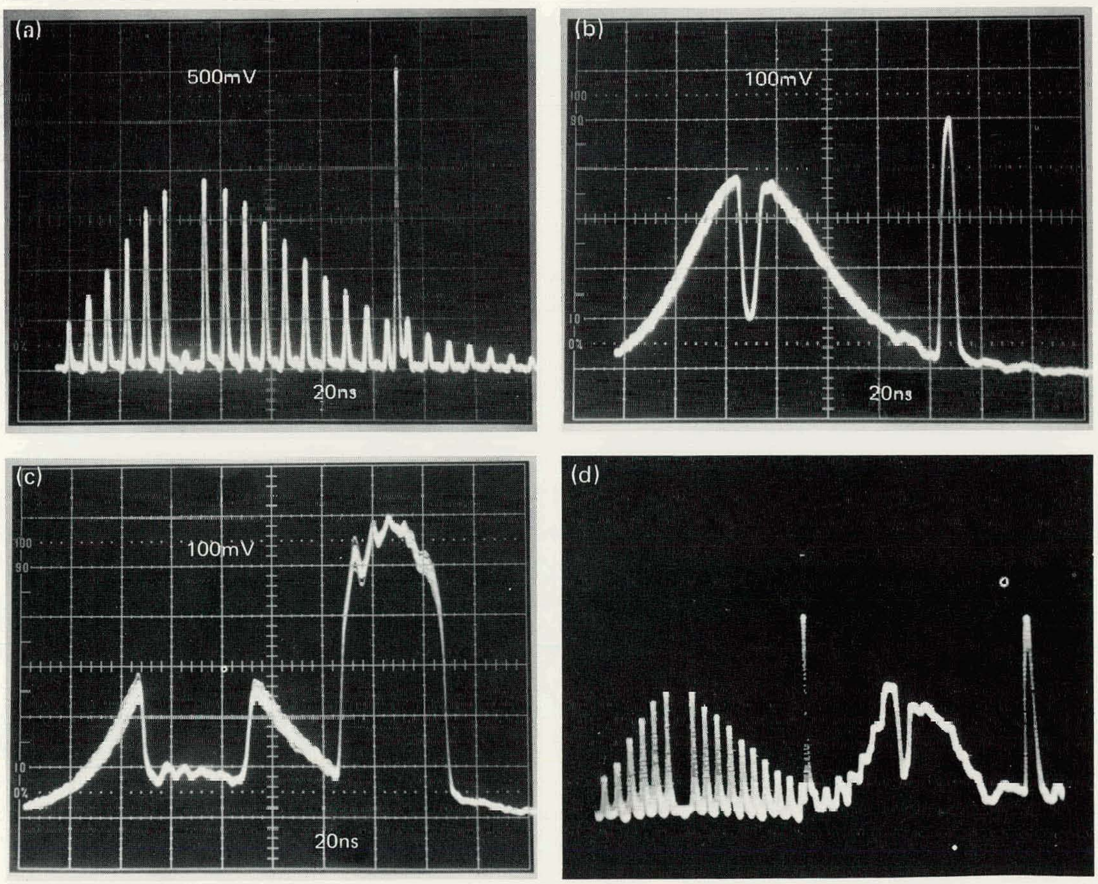

Fig. 2 18. Oscillator diagnostics displays for the single-pulse switchout system and the pulse slicer.

both oscillators. We use a delay generator in each high-frequency chassis to adjust the timing of the Q-switching of both oscillators. Generally, we find that the buildup time in the long-pulse oscillator is much faster (since it has a much shorter optical cavity) than in the AMQ oscillator, so we have to delay the Q-switch signal to the long pulse oscillator more. Since we use acoustic-optic Q-switches in both these oscillators, there is a convenient mechanical delay for the Q-switching of these oscillators. The velocity of the acoustic signal, as is travels from the transducer on the top of the Q-switch substrate towards the laser beam, is 5.95×10^5 cm/s. We have placed the Q-switch on a translation stage, as described for the Argus oscillator in the 1979 Annual Report.[12] Therefore, we can adjust the Q-switching time by moving the Q-switch up or down in the cavity relative to the laser beam. The acoustic-signal velocity of 5.95×10^5 cm/s means a delay of 4.3 ns per 0.001 inch of motion, and we can easily adjust the Q-switch delay in 1-ns increments with a simple translation stage. We routinely used this feature to adjust the Q-switch timing of the long-pulse oscillator relative to the short-pulse oscillator.

We use one of the adjustable delays from the master high-frequency chassis to trigger the pulse-slicer, which then cuts a pulse from the output of the long-pulse oscillator. This allows us to adjust the timing of the sliced-out pulse in 1-ns increments, relative to the short pulse from the AMQ oscillator. The jitter of the long pulse, which is entirely determined by the jitter in the adjustable delay channel and the fiber transmitter/receiver, is about ± 50 ps for a good delay channel, but can deteriorate to about ± 200 ps.

For the experiments planned on Shiva, a long pulse of about 5 ns is used to drive the backlighting target, and a streak camera is used to resolve the target dynamics that are initiated by a 100-ps to 1-ns pulse. For these purposes, the performance of the present synchronized oscillators is acceptable. For future systems, however, we will have to improve the synchronization. We will explore several methods, most of them based on using the short pulse from the AMQ oscillator to directly trigger the pulse slicer.

In practice, it is quite easy to adjust the relative timing of the two oscillators. The delay to the pulse slicer is adjusted until we obtain the correct relative timing between the pulses. We then adjust the Q-switch in the long-pulse oscillator until the pulse is sliced out of the center of the long pulse, as shown in Figs. 2-18(b) and 2-18(c). To obtain the desired relative timing of the pulses at the target area, we measure the timing at the target position and then determine the correct relative timing on the oscillator table. Once this is done, we can calibrate the relative timing at the point where the oscillators are combined. We then repeatedly obtain the correct timing at the target.

The new oscillator installation on Shiva is a major step forward in the development of the oscillator technology for large systems, and we will gain valuable experience for improving the front-end designs of Nova and Novette.

Author: D. J. Kuizenga

Major Contributors: L. W. Berkbigler, D. C. Downs, R. W. Carey, J. A. Oicles, D. R. Speck, B. C. Johnson, D. E. Waldbeser, and R. B. Wilcox

Electronic Systems. In 1980, we directed electronic system developments on Shiva mainly toward improving system safety and performance and toward providing support for new laser and diagnostic hardware.

In the constant effort to improve safety on Shiva, we have modified the large grounding hooks used to short out capacitors in the capacitor bank. These hooks were connected to building ground at points not readily visible to the personnel using the hooks. We found this to be unsatisfactory, so we connected the cables at visible points to a special copper ground bus that has been welded to the building ground. This modification provides increased personnel safety in a potentially dangerous area.

This year we also implemented a new safety feature to prevent capacitor-bank dump-switch failures from remaining undetected. Such an undetected failure is a potential fire and electrical hazard. We modified the dump-switch system so that, if the switch fails to operate in the system charge cycle, the shot sequence is aborted, and an error message identifying the power supply associated with the failure is displayed to the operator. Detection itself is accomplished by monitoring the charge rate of all the charging power supplies.

As discussed in "Shiva Operations Summary" in this section, we have extended the power-conditioning A-system and B-system buses into the target-bay space frame. This extension required the addition of another 60-kV optical isolator and a 50-V bus terminator. Initially, there was some concern that extending the bus up the target-bay space frame would introduce noise into sensitive target-diagnostics experiments. Experimentation and several months of operation have shown that this is not the case, however, as the diagnostic instruments continue to function properly.

The timing sequences generated by power conditioning have undergone some changes due to the installation of new laser oscillator electronics to support the new sychronized long-pulse and AMQ oscillators. (These oscillators and their timing sequences are discussed in the previous article.) It is now possible, for instance, to run the oscillator remotely at a 10-pps trigger rate during shot sequences. We did this to improve the stability and uniformity of the laser oscillator from shot to shot. Along with the new trigger rate, the new electronics give us the capability of storing (latching) the configuration of the oscillator at shot time. Two new timing sequences have also been defined and implemented for doing setup and troubleshooting of the laser oscillator system.

To improve the reliability of the power-conditioning system, we have acquired a Systron/Donner 3700 logic-board tester. We use this tester primarily for test and repair of computer input and output cards. It has reduced our card repair time for a typical input card from 30 to 10 min. We have also implemented an on-line test facility for PILC/WADS card sets[17] in the power-conditioning work area. This allows technicians to test cards for the PILC/WADS system on the power-conditioning bus without having to climb into the space frame.

To minimize system downtime, we are now maintaining a small supply of conditioned ignitron switches. We have designed and built a rack that has cool water flowing through the ignitron coolant jacket and heat lamps pointed at the top of the ignitron. This keeps all of the mercury condensed in a pool at the bottom of the ignitron and allows it to be used in the system immediately after installation.

The spark gaps of the Pockels-cell driver[18] became erratic during September and October. We solved the problem when we found that the method of reassembling the gaps is critical for ensuring proper seating of the top electrode. We subsequently revised our maintenance procedures and found that the spark gaps operated reliably throughout the rest of the year. We further increased the reliability of the spark gaps by installing two new high-voltage power supplies in late 1980, and we also implemented a new interlock system to interlock these power supplies with the equipment-rack doors. New adjustment worm-gear brackets were also fabricated from brass to replace the original plastic ones; this step resolved a problem we had with gear brackets breaking in the course of spark-gap calibration.

We also corrected another persistent problem in 1980. The ignitron trigger leads were originally designed to be held in place by the spring tension of the connectors. As the connectors aged, however, the trigger leads began to fall off, resulting in a set of amplifiers not firing. We prevented this from occurring again by adding specially made brackets that physically hold the trigger leads in place.

The computer systems on Shiva have had several additions and changes over the past year. Some changes in system configuration were made to accommodate both the new release of the DECNET communication network (from Digital Equipment Corporation) and the updated RSX-11M operating system. Various features of these software packages have helped us improve the operation of user programs and have facilitated our system integration effort (discussed below). We made some hardware changes in the PDP 11/70 to make it capable of backing up any of the PDP 11/34 systems in the event of a failure of these system processors. This eliminates a potential single-point failure that could stop operation of the full system. During the year, we also reworked the error-handling programs on the power-conditioning PDP 11/34 to make more efficient use of system resources. We have purchased two new magnetic storage disks for the control system. One is used for the power-conditioning computer to meet the additional data-storage requirements of the new CCD streak cameras. The other is a large mass-storage disk that is slated for use with the inventory control system being designed for the PDP 11/70.

We are designing this inventory control system to maintain all mechanical, electrical, and optical parts inventories for the entire Laser Program. To facilitate this development effort, we purchased a relational data-base management system (ORACLE) from Relational Software, Inc., and installed it on the PDP 11/70. We have also purchased a forms-management system (FMS-11) from Digital Equipment Corporation for collecting and transmitting data in an orderly fashion.

In the area of system integration, we have written a library of Fortran-callable routines with appropriate error processing for DECNET. This library provides a coherent programming interface to the network for intersystem communication. For example, power-conditioning and laser-diagnostics systems now routinely collaborate on preshot setup. If setup errors occur, the shot sequence is halted, and an error display is queued for the operator, indicating the offending hardware status. Figure 2-19 shows an error display indicating that all beam-diagnostic front-end processors (FEPs) are not in data acquisition mode. Each FEP is denoted by a colored letter within the blue space frame outline. These additions were largely possible through the use of the RSX-11M operating system, which we upgraded in late 1979.

By the end of the year, we had designed and partially implemented automatic shot-setup capabilities for power conditioning to prevent inadvertent operator error and to save time. We can now set up the entire control spectrum of the power-conditioning system automatically. In the automatic mode, all of the hardware-selection panels are disabled, and the system is driven totally from the programmable switch panel. The hardware panels do, however, reflect the current status of the system.

We have written a program that records beam images taken from the Quantex Video Digitizer and displays a color-enhanced image of the beam; this aids in evaluating beam quality. Figure 2-20 shows a color-enhanced image at an output aperture of 20 cm. A further software improvement concerns the operation of the beam-line wall shutters and system crosshairs. The travel time of the wall shutters is approximately

Fig. 2-19. Laser-diagnostics error display.

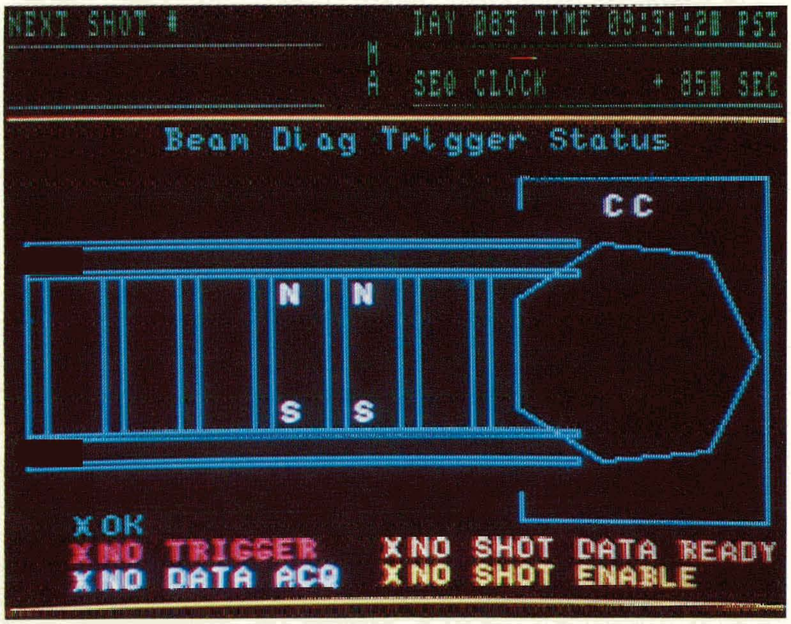

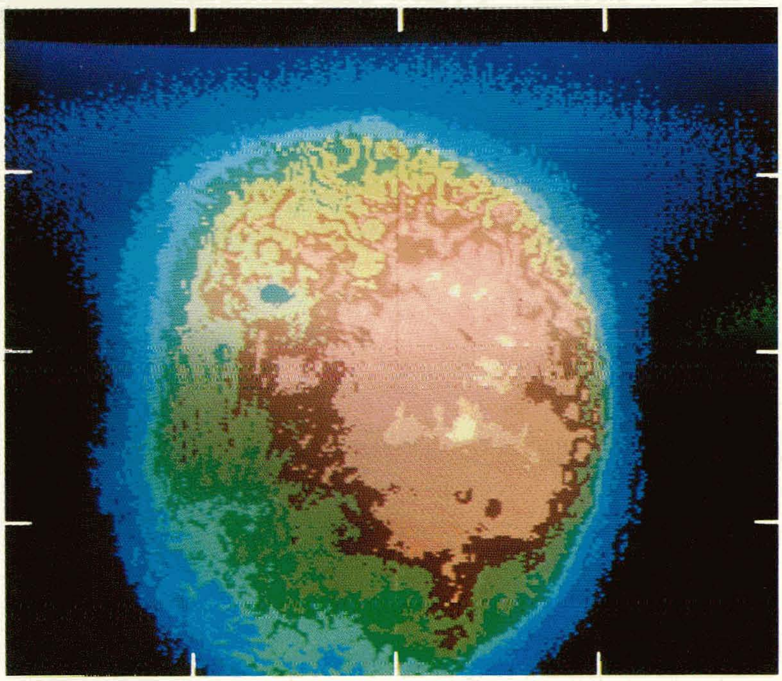

Fig. 2-20. Color-enhanced display of digitized beam image.

40 s. In the past, the shutters could only be opened one at a time; in 1980, we redesigned the software that drives the wall shutters to provide asynchronous operation. We installed water-flow and level switches in all of Shiva's 48 rod amplifiers, and we added automatic monitoring of the rod-water flow and levels. The time-intensive task of inspecting each individual rod on the space frame can now be done by looking at the display in the control room (Fig. 2-21).

We have added ladder-alignment crosshair control to the power-conditioning system.[19] The power-supply interlock routine discussed above checks the status of these crosshairs at the beginning of every shot sequence. If they are out of configuration, the operator receives an error display.

The Shiva capacitor banks have been carefully designed to guard against catastrophic failure. Nevertheless, in 1980, we recognized a failure mode that can result in a damaged amplifier. Two large disk amplifiers suffered massive internal damage as a result of this failure mode, which is precipitated by an arc, external or internal, from the bushing of a capacitor to its case. This is shown as a short across C_{bc1} in Fig. 2-22. The result of this failure is the same as triggering the ignitron: current starts to flow in the lamp circuits, and the flashlamps become ionized. The current rise in these circuits is limited by the inductors, but the total current, i_1, from circuits 2 through n, soon exceeds the value of fuse F1, breaking its element. At this point, since the ignitron is not turned on, i_1 becomes zero. While current is flowing in circuits 2 through n, the voltage across the inductors opposes the voltage on the capacitors, limiting the current. When the current through these inductors is interrupted, the voltage across them changes sign and rises to approximately 32 kV, at which point the protective spark gaps across the inductors ionize. At some point after the voltage across the inductors has reversed and is climbing to 32 kV, this voltage plus the voltage still on the capacitors is sufficient to ionize the ignitron switch by exceeding its breakdown voltage. At this point, the following conditions exist:

- The lamps are ionized in the amplifier with the circuit fault.
- The protective spark gaps across the inductors are ionized.
- The ignitron is ionized.

The result is that the energy left in capacitors 2 through n is discharged in the flashlamps of a single amplifier at a high rate because the inductors, which limit current (and therefore energy rate), are effectively short-circuited by the arcs across their spark gaps. Many of the fuses in circuits 2 through n also blow, but not until it is too late. Major damage to the flashlamps occurs either at the

Fig. 2-21. Display of rod-amplifier coolant level and flow status.

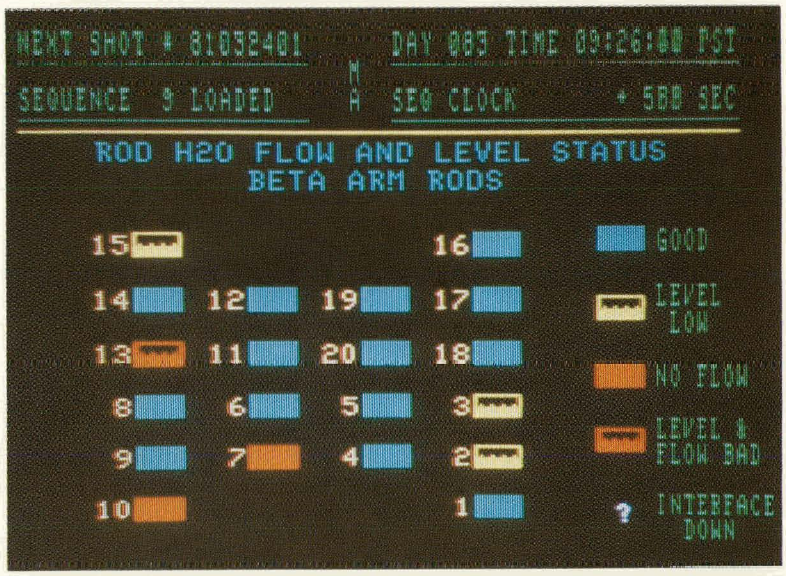

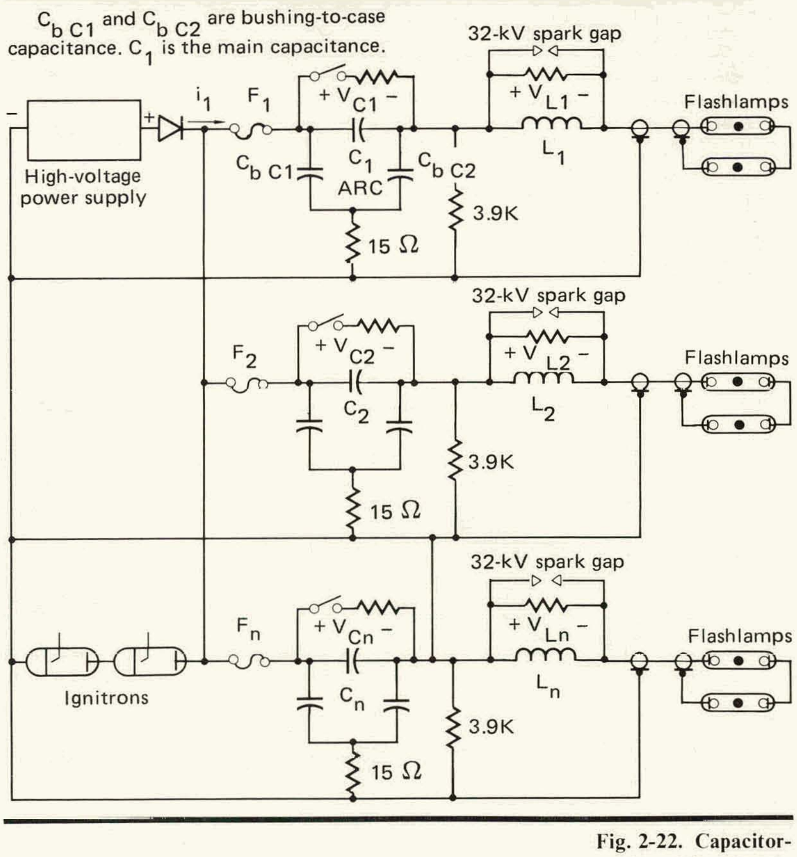

Fig. 2-22. Capacitor-bank and flashlamp circuit.

time of the fault or the next time the amplifier is fired. We have launched an effort to solve this problem and to prevent it in future systems.

Authors: R. W. Carey, D. J. Christie, and P. R. Rupert

Major Contributor: E. H. Padilla

Laser Diagnostics. During the past year, we made a number of upgrades in our Shiva laser diagnostics to improve our data collection, analysis, and reliability. Included among these upgrades was the implementation of a readout and analysis system for the input streak camera. This streak camera, equipped with a linear array made by Reticon Corporation, has previously been read out on an oscilloscope.[20] We have added a digitization interface so that the signal from each element of the 1024 × 1 array is serially read out at a 7-MHz clock rate. This voltage-vs-time signal, which is proportional to the intensity-vs-time of the laser pulse, is sampled, digitized, and stored in the memory of our control interface, residing in an LSI-11 FEP. A schematic of this system is shown in Fig. 2-23. We send the data from this FEP to the laser-diagnostics PDP 11/34, where a plot of the temporal pulse shape is produced and the (FWHM) pulse length is determined. We generate a graphics display (Fig. 2-24) at the laser-diagnostic operator console and, upon operator request, produce a hard copy.

Fig. 2-23. Schematic of output streak-camera data-acquisition system.

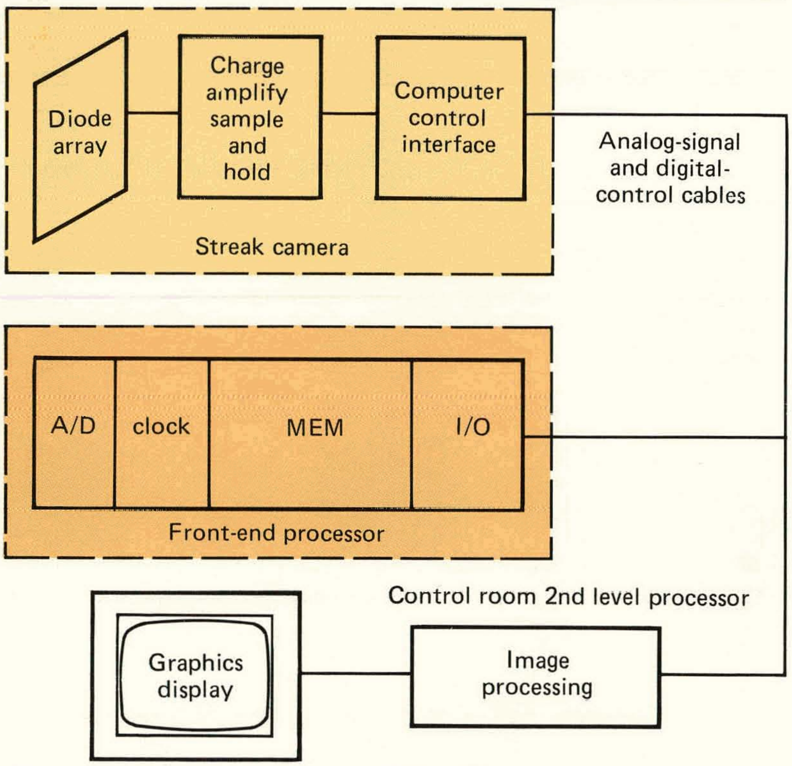

We have also developed an output streak-camera computer readout and analysis capability. We equipped the camera with a CCD-array readout system (see "CCD Applications in ICF Diagnostics," in Section 5), and we retrieve the data from the local memory of the CCD camera via its connection to the power-conditioning bus system. The interface to the camera memory is via an LSI-11 bus that is converted to CMOS level in a TTL-to-CMOS converter. The converted signal is interfaced to the power-conditioning bus through a power-conditioning bus-interface unit (BIU), which takes the CMOS signals to the 50-V level of the power-conditioning bus.[21] The control and data path is illustrated in Fig. 2-25.

The operator controls the streak-camera memory from the power-conditioning control console. From this console, we can display the contents of the CCD camera memory in real time by selecting its video output mode under computer control. We use this feature in initial timing and alignment of the camera by capturing and displaying a low-power pulse on a TV monitor near the streak camera. We can also write into the camera memory with the computer system. This allows us to read a line from the memory, construct a trace of intensity vs time, and then write the line back into the memory and display it on the TV monitor. This procedure facilitates alignment and establishes the correct intensity level to obtain a good signal-to-noise ratio within the saturation limits of the CCD.

During a system shot, we read the data via the power-conditioning bus and transfer it to the third-level PDP 11/70 machine, where it is stored on the system disk. The entire data file from the CCD array is then processed to yield the time-vs-intensity trace and FWHM. The color-enhanced data file from the CCD, and a reduced plot as it is displayed on Shiva, are shown in Fig. 2-26. Implementation of this readout and analysis system has reduced the time required for us to obtain data from several days to a few minutes.

During the year, we also added new diagnostics for the new Shiva oscillators (described in "Optical Pulse Generation" in this section).

To enhance our capability to observe damage in the beam line, we have designed a near-field photographic capability for the incident-beam diagnostics (IBD) package. We added this package to the IBD on beam No. 16. A beam splitter provides a photograph of a plane equivalent to the input lens of the target chamber. To obtain the image of this plane, we added a 4 × 5 film pack and beam splitter to the IBD. The splitter is in a converging beam; therefore, we had to design the splitter to compensate for the distortion it causes in the transmitted beam. Photodensitometer scans of the image provide data on the depth of spatial modulation in the beam at the plane of the target-chamber optics. Before we implemented this addition to the IBD, we could acquire the desired image only by blocking the input of the IBD with a film

Fig. 2-24. Sample graphics display of oscillator temporal pulse shape.

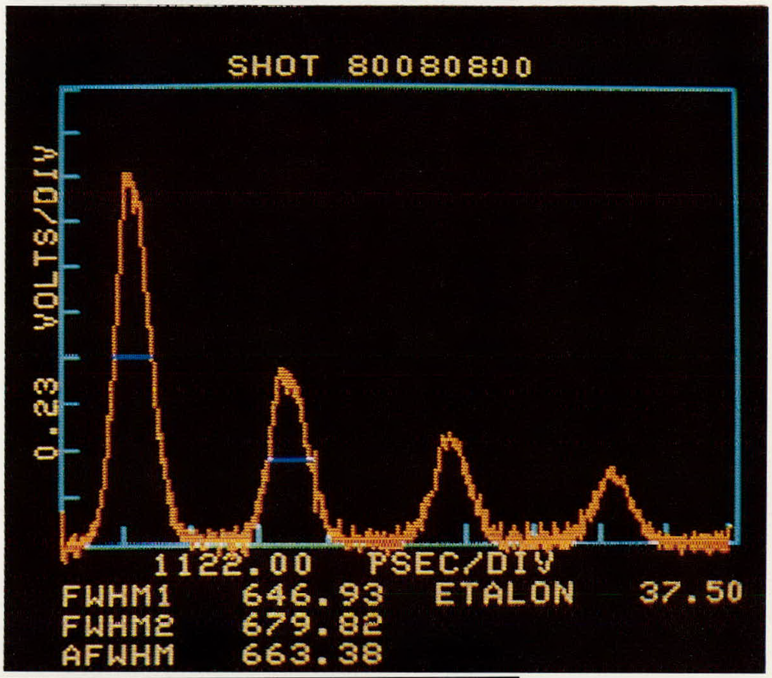

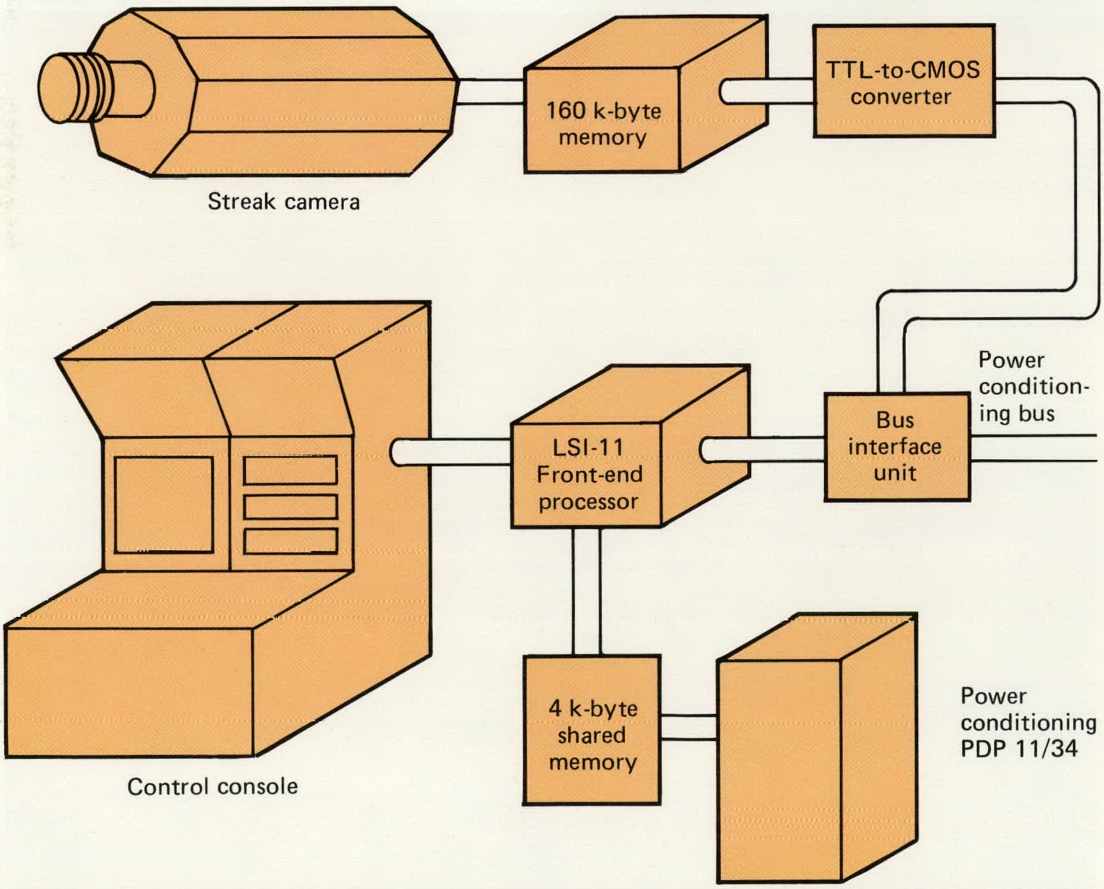

Fig. 2-25. Control and data path for data acquisition and analysis.

pack, thereby losing the incident-beam diagnostics.

Before we terminated our software efforts on laser diagnostics this year, we completed a software effort to write and centrally locate all laser-diagnostics software documentation. As part of this effort, we made some additions to the system and gave several seminars to familiarize other users and the technicians with the overall software architecture.

We completed implementation of a backup for the laser-diagnostics second-level processor; we can now back up this PDP 11/34, in the event of its failure, with the top-level PDP 11/70 (see the previous article). This is accomplished by executing an indirect command file that does the necessary software redirection and instructs the operator to make specific hardware patch-panel changes. These patches reroute the serial fiber-optic links of the FEPs from the PDP 11/34 to the PDP 11/70.

Authors: R. G. Ozarski and J. B. Richards

Major Contributors: D. A. Cloyne, D. M. Benzel, R. W. Carey, J. R. Hamilton, and R. E. Hugenberger

Mechanical Maintenance and Upgrades. The Operations Group planned to implement several mechanical upgrades and improvements on the Argus and Shiva laser systems during 1980. The January earthquake, and a late-summer decision to phase Shiva out of operation in 1981, caused us to rework these plans. We have continued work on those modifications of Argus and Shiva that are necessary for supporting the frequency-conversion work and the x-ray backlighting experiments.

The improvements and upgrades to the Shiva and Argus laser systems ranged from optical relays and alignment devices to

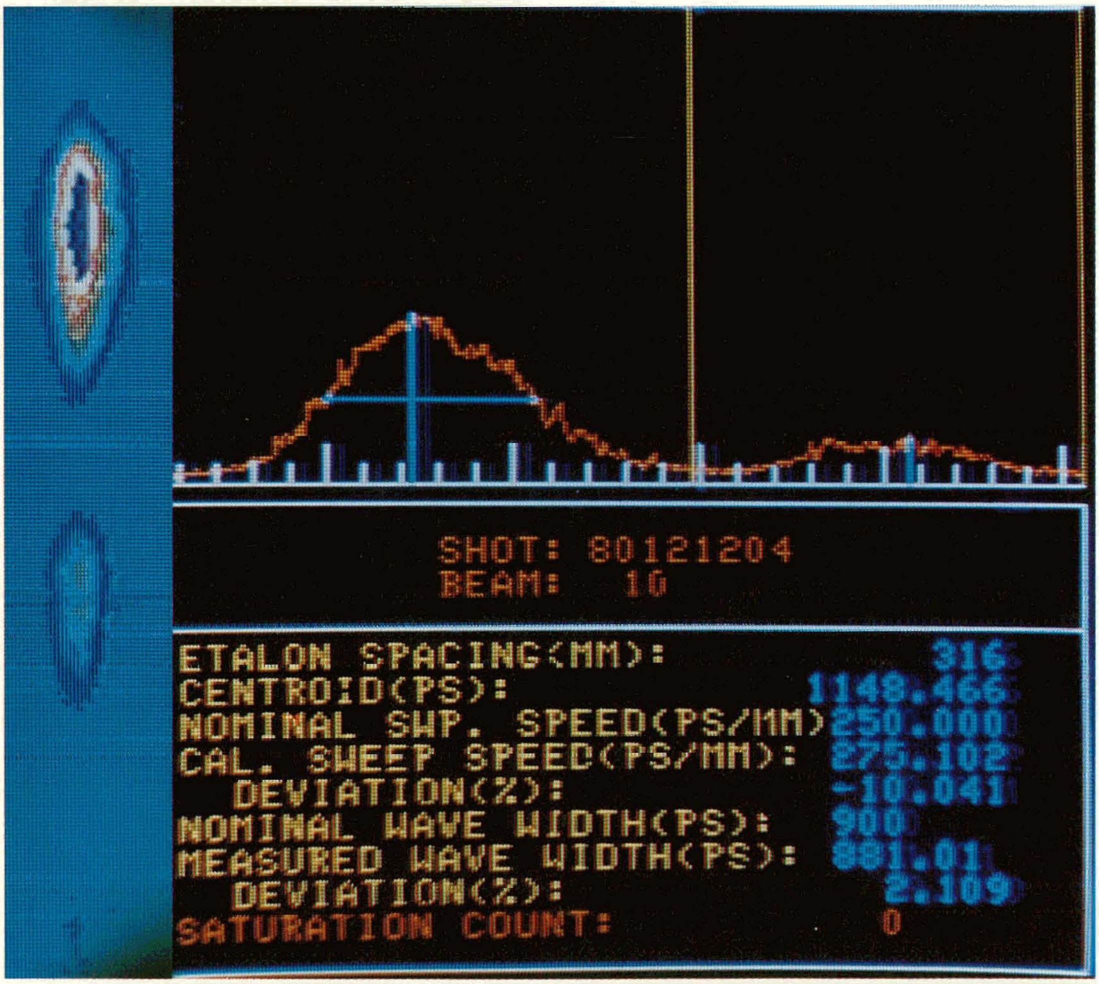

Fig. 2-26. Sample graphics display of raw and reduced streak-camera data.

routine maintenance improvements in the power-conditioning equipment. The latter work included refurbishing the capacitor grounding-hook cables and replacing 50 pneumatic cylinders (of the 564 cylinders in the system). In addition, a total of 1400 ft of air lines was replaced with a new non-degradable line, and a torque check was run on all fasteners.

We designed and fabricated an x-ray backlighting optical-relay system to provide time-delayed pulses for studying implosion dynamics. Some of this hardware was installed in 1980, and system tests are scheduled for early 1981. X-ray backlighting requires incorporating a time delay of from 25 to 60 ns in the upper 10 arms relative to the lower 10 arms. We accomplished this by inserting sets of turning mirrors in the laser beams, thus allowing the length of the beam path to be changed.

Figure 2-27 (next column) is a schematic of a typical delay path. The translation stage, with its mirror pair, is mounted on the space frame (east of the splitter turning mirrors) on precision ball bushings and round ways. An adjustable clamp and a micrometer provide fine positioning, over a 5-cm range, at any location within the total excursion of 92 cm. This fine-adjustment feature permits us to precisely time each of the four sets of mirror assemblies, relative to one another, without disturbing the laser timing optics. The translation-stage assembly can be mounted on any arm to provide a delay range of from 25 to 60 ns. Once the assembly is in position on the space frame, the overall stage excursion provides up to a 6-ns timing change. The 5-cm fine-positioning adjustment will then allow up to 300 ps of fine tuning.

Crosshairs for mirror alignment are manually installed (and removed) in front of the mirrors. Figure 2-28 (below left) shows the splitter-bench turning mirrors, and Fig. 2-29 shows the translation stage.

Fig. 2-27. Schematic diagram of a typical delay used for the x-ray backlighting system.

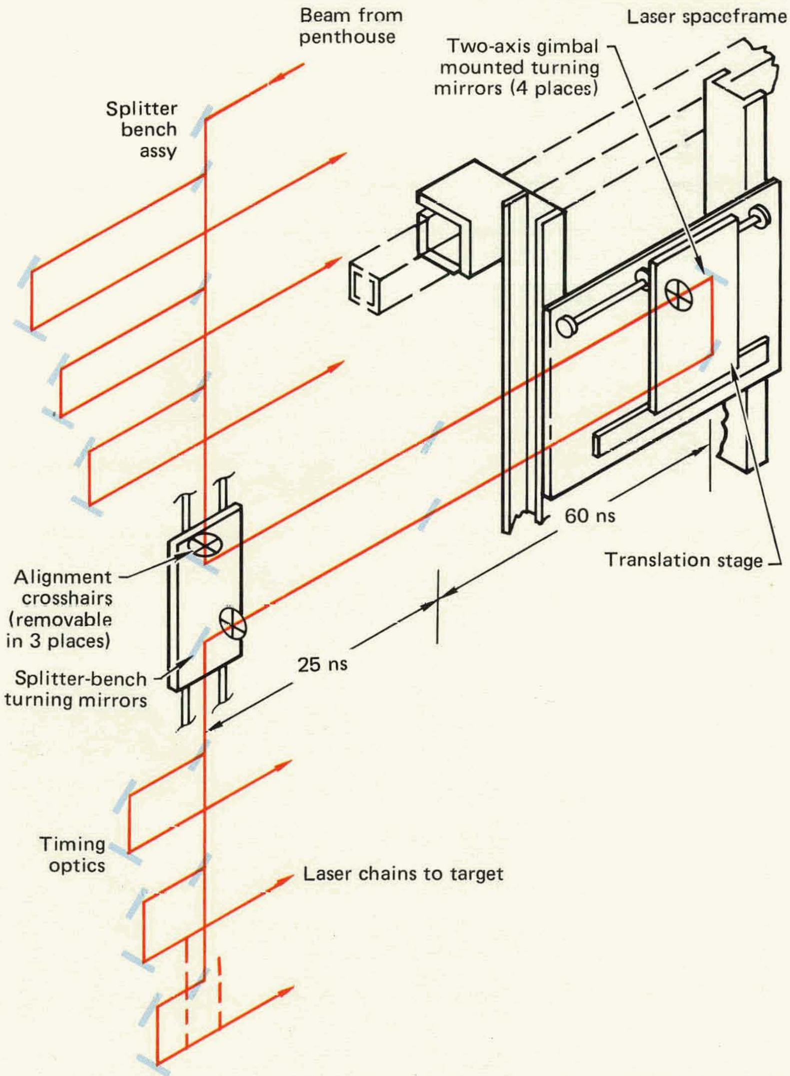

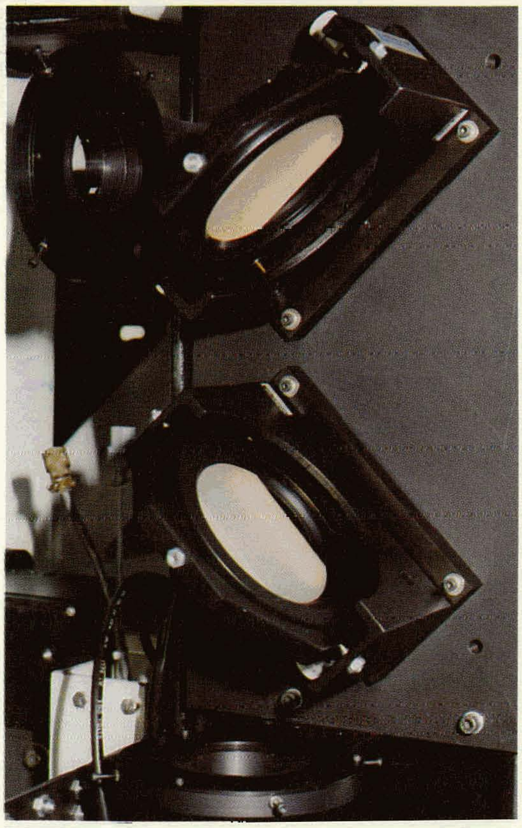

Fig. 2-28. Closeup view of the splitter-bench turning mirrors in the delay path, showing two removable crosshairs.

We also installed a beam-profile camera (Fig. 2-30) at the bottom of each splitter assembly. The photographs taken by this instrument are used to evaluate the quality of the beam and to verify its centering on the apodized apertures.

To improve system performance, we designed and installed a four-lens optical relay (see "Shiva Operations" in this section) in the "up-leg" between the preamplifier and the first turning mirror. We used a pair of lenses, mounted in identical cells, at both the input and output ends of a 340-cm-long

Fig. 2-29. Closeup view of the translation stage, showing the third removable crosshair (top left) and the two-axis turning mirrors.

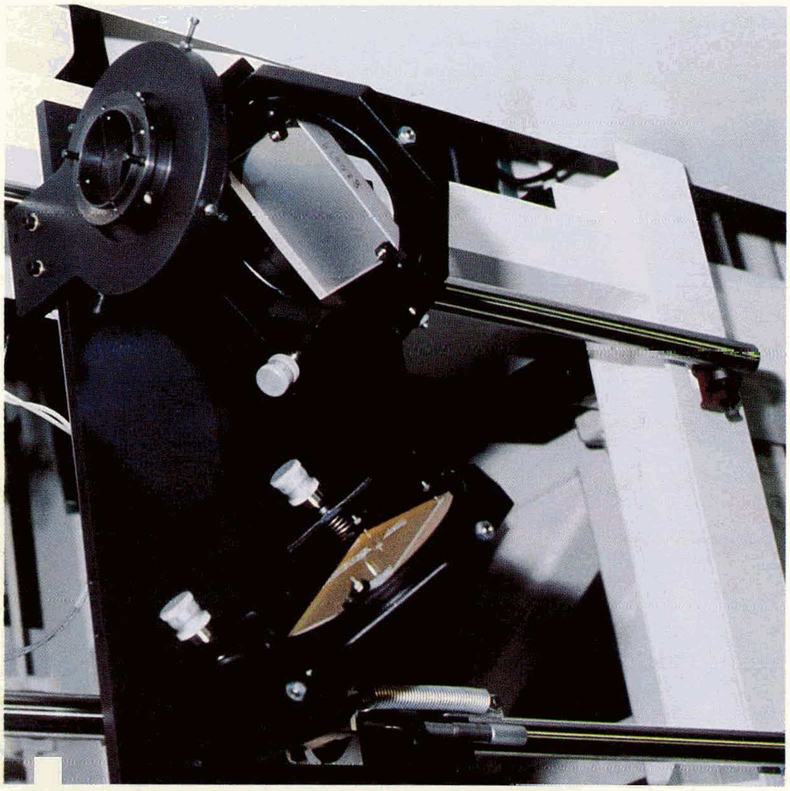

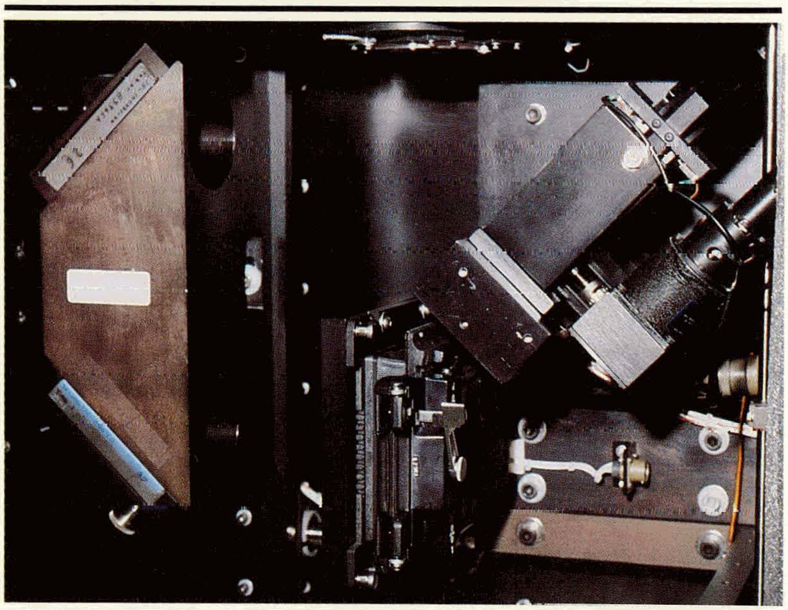

Fig. 2-30. Closeup view of the beam-profile camera assembly.

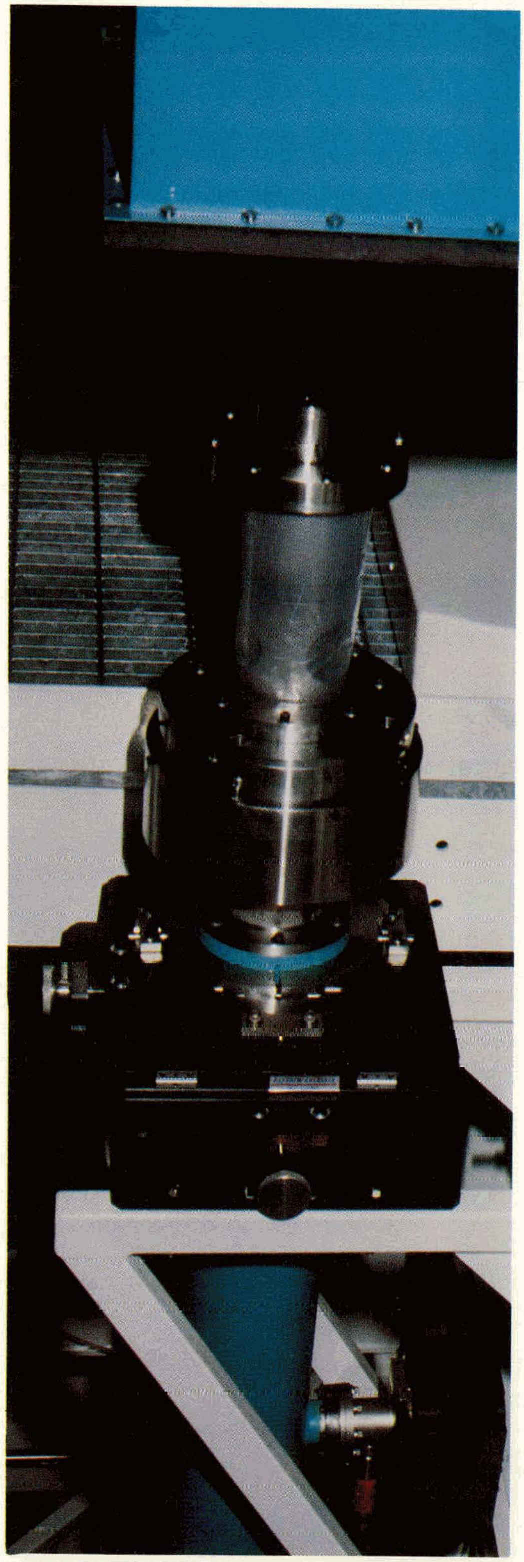

Fig. 2-31. Closeup view of the upper assembly of the optical relay.▶

vacuum tube to provide an optimum alignment for relaying the 21-mm-diam preamplifier beam to the arm inputs. The system magnification of 1.2 produces an output beam 25 mm in diameter. Flux loading was reduced, and the relaying distance was approximately double that of the original two-lens system. We used existing optics and spatial-filter hardware and suspended the relays from the laser space frame by specially designed kinematic mounts. These consist of a pair of gimbals on the relay vacuum tube that, in turn, are registered on a two-axis translation stage. Figure 2-31 shows the upper end of the optical relay and the hardware for attaching it to the space frame.

We installed beta Pockels-cell beam-splitters on all 20 Shiva arms. Our previous method of diagnosing beam energy at midchain positions was done with a polarizer assembly, in which the beam-splitting ratios fluctuated with humidity changes. The new splitter assembly in each arm is comprised of two beam splitters mounted at Brewster's angle; this assembly provides a stable signal for beam-energy measurements and a modulation-free near-field photograph.[22]

We improved the alignment stability of each arm of Shiva by reducing the beam diameter entering the 5-cm-diam beta rod amplifier. The apodizing aperture at the front end of each chain was changed from 9.5 to 8.5 mm. This decreased the beam diameter from 5 to 4.5 cm at the input to the 5-cm rod. This reduction at the front end required expansion of the beam at the midchain point. We accomplished this by modifying the spatial filter between beta disks with an extension and an output lens with a longer focal length.

We relocated the beta rod amplifier, beta Pockels cell, polarizer, and beam-splitter assembly (Fig. 2-32) on the chain to make room for the installation of a new calorimeter. We also modified the Shiva nitrogen flow system, reducing the annual usage of nitrogen by 30%; this has resulted in a significant saving (approximately $75 000) in operating costs. Each beam line in Shiva is flushed with nitrogen gas obtained from a large liquid-nitrogen tank and boiler located outside the building. This nitrogen is used to cool the active laser components after firing and to reduce the percentage of oxygen in the amplifier flashlamp assemblies during lamp firings. (When the concentration of oxygen in the system is less than 5%, photoionization cannot occur.) Initially, Shiva had two nitrogen flow rates: a standby total-system flow of 200 cfm, and a postshot cooling flow of 2000 cfm. To conserve nitrogen, we changed the continuous-flow standby rate to 40 cfm. However, at this flow rate, the concentration of oxygen in the laser components approaches 5%. Therefore, to reduce this level, we let nitrogen flow through the system at the old rate of 200 cfm for 10 min before a shot.

The modified nitrogen flow system comprises a high-flow valve (2000 cfm), a medium-flow valve (200 cfm), and a low-flow valve (40 cfm). We chose to install a remotely controlled valve in series with the original low-flow valve, as this was the most cost-effective modification to the valving and control system. The three nitrogen flow valves can be actuated either from the local control panel or from the control room via a computer interface to the power-conditioning system. The valves are monitored through microswitches on the

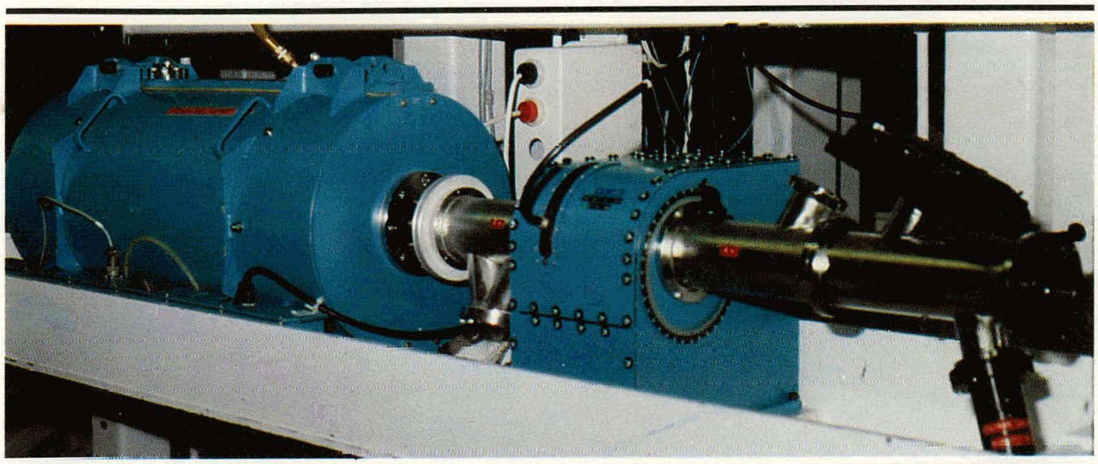

Fig. 2-32. View of (l to r) a beta rod amplifier; Pockels cell; polarizer; beam splitter, with its near-field camera and photodiode; and the newly created space for the add-on calorimeter.

valve cams. The computer interface provides us with system-configuration control; it also minimizes nitrogen usage by automatically timing the high flow rate and turning it off after a selected time. During a shot sequence, the valve actuations are also automatically controlled.

Authors: W. A. Jones and H. G. Patton

Major Contributors: T. O. Ross, D. Girotto, D. P. Milani, C. D. Sanner, J. D. Degough, J. F. Rommelfanger, D. E. Wentworth, and J. E. Lietzke

Shiva Component Maintenance Summary. The routine operation of high-energy laser systems causes damage to some optical components, and continuing inspection and replacement of glass surfaces is a part of operating the system. Maintaining high-quality, low-modulation laser beams requires that we replace optical components when damage to their surfaces or to the bulk glass reaches a predetermined size or density.

While it is too early to write a complete history of the life of Shiva laser components, we have determined that approximately 80% of the component failures we have experienced can be eliminated on future systems. Proper component design, clean operation, coatings performing to their design specifications, and the elimination of spurious reflections and foci are all important. Our experience indicates that component lifetime can be extended almost indefinitely by conservative system operation. While such conservative operation is not always compatible with the requirements of meaningful target experiments, we strike a balance between the desire for higher energy for experiments and the costs of replacing components.

For the purpose of failure analysis, laser components can be divided into three categories:

- The Shiva disk amplifiers are most sensitive to contaminants. The disks are irradiated by 1.06-μm laser light and about 20 J/cm^2 of wideband flashlamp light, both of which contribute to the melting and vaporization of particulates and to subsequent glass damage. The flashlamp pump light is capable of evaporating small contaminant particles in

Table 2-5. Firings of Shiva laser major components from January 1978 to October 1980. ▼

Component	No. in system	Average firings/ component	Average firings FY 80
Preamplifier rods	7	3154	1098
2.5-cm alpha rod amplifiers	20	2193	925
5-cm beta rod amplifiers	20	3020	910
10-cm disk amplifiers	60	434	144
15-cm disk amplifiers	20	350	140
20-cm disk amplifiers	20	301	140

Item	No. in Shiva	Reworked annually (%)	No. reworked in FY 80
Alpha rods	27	112	33
Beta rods	25	96	17
Beta disks	360	14	85
Gamma disks	80	26	25
Delta disks	60	31	15
Large turn mirrors	20	27	3
Final-turn mirrors	20	27	—
R/alpha polarizers	100	14	11
R/beta polarizers	100	14	6
Beta polarizers	80	11	7
Delta polarizers	40	37	13
Fold mirrors	63	24	3
Ladder splitters	21	21	5
Vacuum windows	20	70	14
Debris shields	20	268	13
Output SFLs[a]	40	30	30
Beta SFLs	80	18	—
Gamma SFLs	40	9	5
Delta SFLs	20	18	7
F/6 focus lens	40	27	9
80-mm triplet lenses	20	50	—

[a]SFL = spatial-filter lens.

Table 2-6. Summary of ▲ rework of Shiva optics.

Disk amplifiers
- Flashlamp explosions.
- Surface damage to the disks from contaminants.
- Low gain resulting from weak flashlamps or contaminated surfaces.

Passive laser elements
- Coating damage.
- Contamination on the surfaces.
- Optical damage to the bulk of the glass due to ghost foci or very high beam modulation (>30 J/cm^2).
- Mechanical damage from improper handling or installation.

Rod amplifiers
- Damage to the rod face coatings and bulk glass caused by beam modulation and ghost reflections.
- Flashlamp explosions.
- Low gain created by deterioration of the antireflection coatings on the rod faces.
- Water leaks caused by the failure of the O-ring sealing in the cooling channel between the rod barrel and the quartz shield.

Table 2-7. Failure modes for Shiva optical components. ▶

the amplifier, causing the laser disks to become pitted.[23]

- The coated optical elements, such as lenses, splitters, polarizers, and mirrors, are prone to optical damage and to contamination from dust, fingerprints, and other foreign matter.
- The rod amplifiers fail from laser damage, water-coolant seal leaks, and flashlamp explosions.

Table 2-5 shows the number of times we fired the major components of the Shiva laser from January 1978 to October of 1980, Table 2-6 summarizes the rework of Shiva optics, Table 2-7 summarizes the component failure modes for each category, and Table 2-8 summarizes the rework of Shiva laser components.

Two criteria are used to determine when to clean or replace dirty or damaged optics. One criterion is subjective. We periodically take and review near-field photographs, such as the one shown in Fig. 2-33. This photograph is taken at a point just before the beam enters the target chamber. The hard structure on the beam is due to damage sites; the approximate location of the damage can be judged by noting the focus of a site and inserting and removing spatial-filter pinholes. The photographs are analyzed subjectively, and components are cleaned or replaced on the basis of this analysis. The other criterion is related to laser performance; when the combined damage and contaminate level creates obscuration greater than 1% per arm, or 0.05% per surface, we replace the offending optic(s).

The average lifetime of components has exceeded our prediction. The leak in the rod-amplifier water seal[24] (listed in Table 2-5) is

Table 2-8. Summary of rework of Shiva laser components.

	Failure mode	Alpha rod amplifier	Beta rod amplifier	Beta disk amplifier I	Beta disk amplifier II	Beta disk amplifier III	Gamma amplifier	Delta amplifier
1977	L	5	1	—	—	—	—	—
	FF	—	—	—	—	—	—	—
	EF	1	3	—	—	—	—	—
	D	1	2	1	—	—	—	—
	L_oG	—	—	—	—	—	—	—
	uV	1	—	—	—	—	—	—
1978	L	15	11	—	—	—	—	—
	FF	4	4	—	—	—	1	—
	EF	—	—	3	—	—	—	1
	D	4	—	—	3	1	—	4
	L_oG	—	—	—	—	1	—	—
	uV	—	—	—	—	—	—	1
1979	L	12	18	—	—	—	—	—
	FF	1	1	8	1	4	2	1
	EF	1	—	1	1	—	1	—
	D	6	4	4	—	4	7	3
	L_oG	5	2	4	7	1	2	—
	uV	5	4	—	1	—	—	—
1980	L	7	6	—	—	—	—	—
	FF	1	2	—	—	—	3	3
	EF	2	—	—	—	—	1	2
	D	4	1	2	2	—	9	5
	L_oG	18	12	2	1	1	1	2
	uV	8	3	—	—	—	4	1

Note: L = Water leak;
FF = Flashlamp failure;
EF = Exploded flashlamp;
D = Laser damaged optic;
L_oG = Low gain; and
uV = Broken blast shield.

the only exception. We have tested several new seal designs, but adequate statistics are not yet available. We have verified that laser-system components, properly designed and operated, can provide output of 6 GW/cm^2 with acceptable failure rates. Some important factors in insuring this are

- The mechanical assemblies surrounding the glass must be designed for clean, simple assembly.
- All components exposed to flashlamp or laser light must not degrade under that radiation.
- Assemblies must be made and operated under clean-room (class 100) conditions.
- Beam modulations must be kept below the damage threshold for the coatings and bulk glass, and ghost reflections must be considered and blocked when necessary.

Authors: H. G. Patton and S. K. Guntrum

Major Contributors: J. W. Herris, J. F. Rommelfanger, D. P. Milani, and J. E. Lietzke

Fig. 2-33. Shiva beam near-field photograph used to subjectively assess optical-component damage.

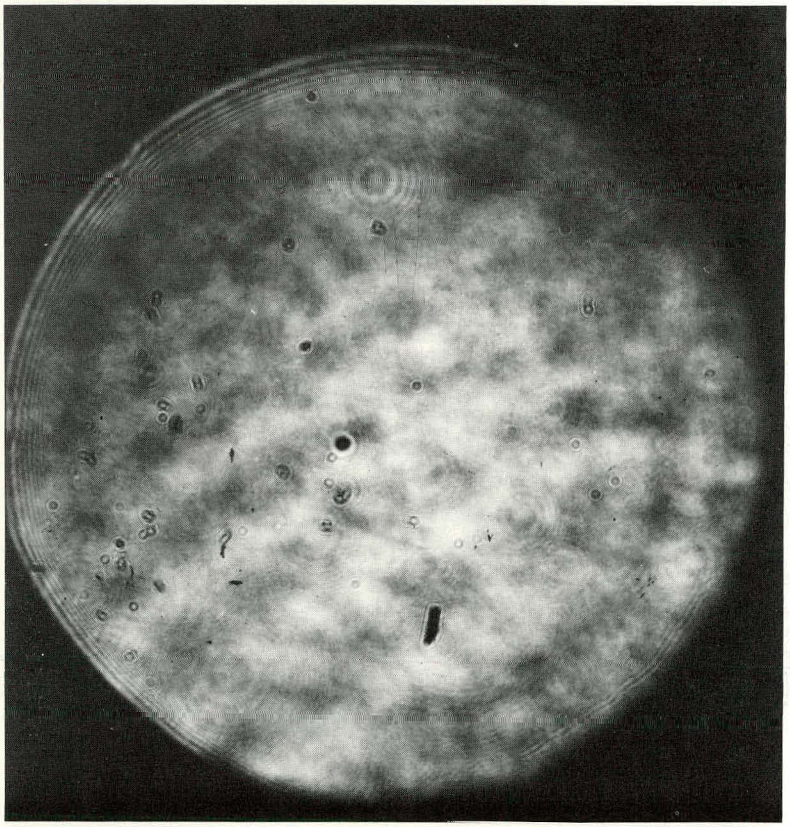

Target-irradiation wavelength	1.05 and 0.53 μm
Final amplifier aperture	46 cm
Final beam aperture	74 cm
Focusing optics	—
Initial activation	f/3.5 Nova target lenses
Later operation	f/1.5 reflecting system
Frequency-conversion crystals	74-cm clear aperture, 18 mm thick, one 5 × 5 monolithic array of 15- × 15-cm elements and one 3 × 3 monolithic array of 26- × 26-cm elements
Pulse length	100 ps to 5 ns
Energy per arm	10 to 15 kJ at 1.05 μm; 7 to 10 kJ at 0.53 μm
Design fluence	Same as Nova
Power conditioning	Same as Nova
Laser glass	Same as NOVA
Target shots start	Oct 1982

Table 2-9. Novette technical baseline and projected performance.

Novette

Introduction

Novette is a two-beam, two-wavelength target-irradiation facility whose projected performance at both 1.05 and 0.53 μm exceeds the 20-beam Shiva system. Table 2-9 lists Novette's technical baseline and projected performance. The system is readily upgradable to 0.35-μm target-irradiation capability by adding a second KDP crystal array to each of its two arms and changing the optical elements between the second crystal and the target. Multiple-wavelength operation and the large aperture of Novette will require an advanced target-focusing system; several options are under consideration, including an f/1.5 axicon system.

The concept of the Novette facility arose to satisfy several Laser Program priorities:

- First was the need to perform short-wavelength target experiments at power densities comparable to those of Shiva to obtain essential data on target performance vs wavelength scaling.
- Second was the desire to assist the Nova design effort by small-scale system testing and by prototyping new Nova hardware.
- Third was the necessity for freeing funds for work on other problems. The operating costs of a 10- to 20-kJ Novette facility will be substantially less than those of the Shiva facility.

The proposed facility will meet these needs while effectively using Laser Program resources and experience.

Author: J. T. Hunt

Novette Design Considerations

Staging. The Novette laser system consists of two phosphate-glass laser chains of the type that will eventually be fielded on Nova (Fig. 2-34). This chain consists of a driver section, which terminates at a 208-mm amplifier aperture, followed by clear-aperture output-amplifier stages 315 and 460 mm in diameter. Although the driver section contains primarily Shiva hardware, the amplifiers will be retrofitted with phosphate glass. The high energy needed to drive the larger Nova amplifiers requires that we add two 208-mm box amplifiers to the Shiva driver chain. The 315-mm-aperture and 460-mm-aperture output amplifiers are of box geometry also, each containing two disks; there will be four amplifiers (eight disks) in the 315-mm stage, and three amplifiers (six disks) in the 460-mm stage. Space is provided such that, should a future upgrade be desirable, one additional amplifier at each diameter can be added. Following the last amplifier stage, the beam will be expanded to 740 mm in diameter. Directing the output beam through the potassium dihydrogen phosphate (KDP) doubling crystals to Novette's target-focusing optics requires two mirrors in one arm and three mirrors in the other.

The actual Nova chains will require a single fold at the output of the spatial filter that expands the beam diameter from 208 to 315 mm. The length of the high bay in Building 381 requires that the Novette chain have an additional fold at the output of the 91.7- to 150-mm spatial filter. Both chains will be driven by a common oscillator/preamplifier section as in Shiva. Present plans are to terminate the oscillator/preamplifier with 50-mm-diam rods to provide a nominal output energy of 10 J. The master oscillators and the preamplifier stages will be housed in a side lab of the high bay in Building 381; the beam will be transported into the main laser bay from this side lab with a spatial-filter relay element.

The Novette chains will be spatially filtered and fully relayed. The object plane of the relay will be a hard aperture placed at the entrance to each chain, with successive image planes occurring near the input lens of each spatial-filter/relay element and beyond the first turning mirror in the target bay. Table 2-10 summarizes the spatial-filter/relay parameters for the Novette baseline chain. The pinhole diameters are chosen so that the beam intensity on the pinhole edges does not exceed 10^{11} W/cm^2

Fig. 2-34. Schematic of Novette optical system.

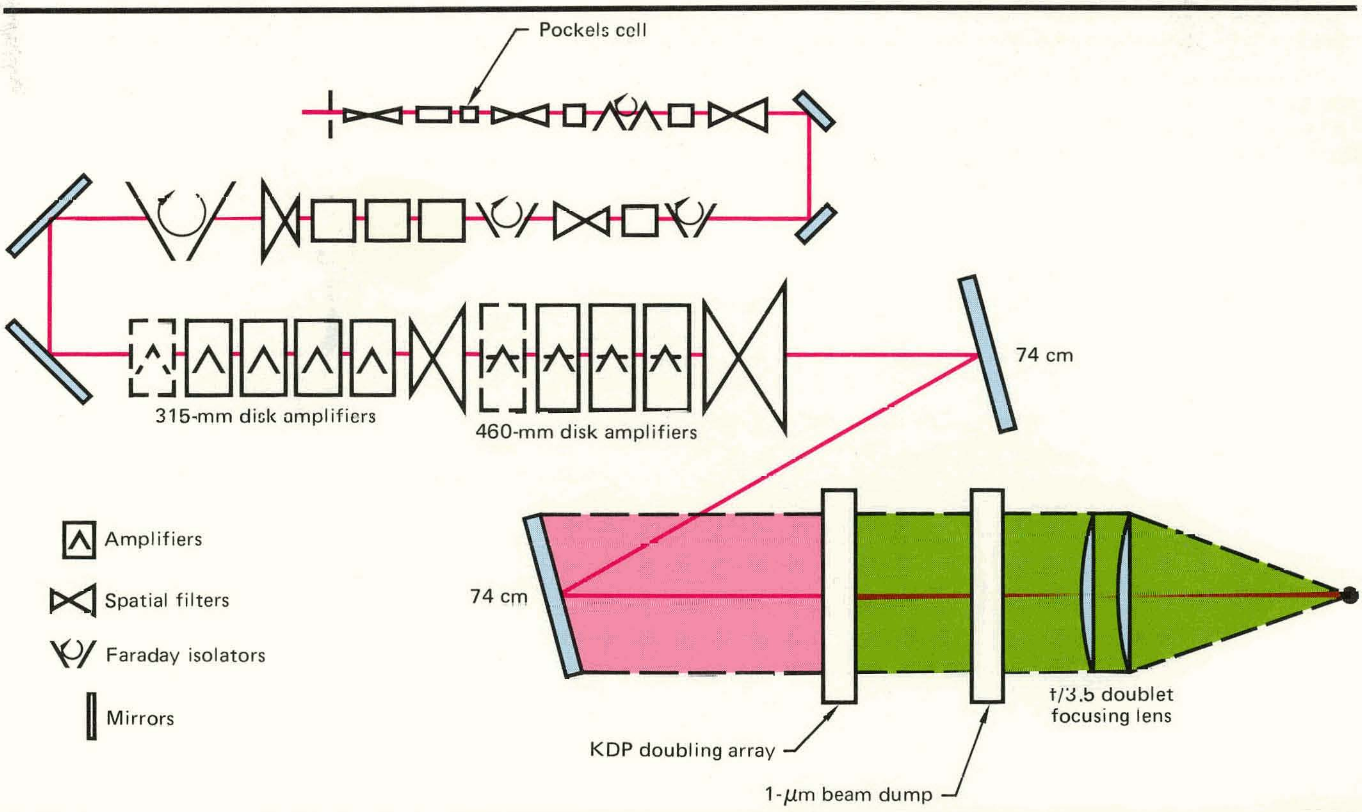

for a nominal performance energy of 10 TW per chain with a 1-ns pulse. Pulses shorter than 1 ns can create larger intensities, but will propagate through the pinhole before closure. For longer pulses, the chain B values decrease, thereby reducing the pinhole loading. The calculation of pinhole sizes depends upon the noise model used; in our calculation, we used a model that agrees well with the noise spectra observed for the Argus and Shiva lasers.

Glass Properties. The choice of phosphate glass for Nova was predicated upon the following considerations:

- Low nonlinear index of refraction.
- High gain.
- Saturation fluence parameters competitive with silicate glasses.
- Proven performance in laser systems.
- Reasonable cost.

Table 2-11 lists some important physical properties of this glass, along with properties of the ED-2 silicate glass used extensively in previous systems. Shown are lasing wavelength, λ; cross section for stimulated emission, σ_p; fluorescence lifetime, τ; line width, $\Delta\lambda$; linear index of refraction, n_0; nonlinear index of refraction, n_2; and saturation fluence, E_s. The saturation fluence shown in Table 2-11 corresponds to a value for which the output fluence from the test sample was 5 J/cm^2.

Recent experiments have shown that the saturation fluence is dependent upon the fluence level. Figure 2-35 illustrates this for LHG-8 glass. The saturation values shown in Table 2-11 are a valid comparison, since all test samples were pumped to approximately the same small-signal and net gains. We account for the variation of E_s with fluence in our system performance calculations. From our data, we conclude that the saturation properties of phosphate glasses are superior to the ED-2 type of silicate glasses over the range of fluences of interest for Nova.

The specifications for the bulk properties of production phosphate glass are

- Attenuation $\leqslant 0.0015$ cm^{-1}.
- Homogeneity = $\pm 1 \times 10^{-6}$.
- Damage fluence $\geqslant 35$ J/cm^2.

The quoted damage fluence is relative to the beam in air; actual fluence in a tilted disk is reduced by the index of refraction.

Amplifier Design. The new, more efficient box-amplifier design, described in last year's annual report,[25] has been adopted for use. Table 2-12 shows some important design characteristics of the 315- and 460-mm amplifiers.

Frequency Conversion. The 0.53-μm target-irradiating beam will be generated at a position between the last turning mirror and the target focusing optics by passing the 74-cm-diam beam through an array of KDP frequency-doubling crystals (Table 2-13). The Fresnel reflection losses from the crystals will be minimized by placing them between two windows with antireflection (AR) coatings, which are index-matched to the KDP crystal material with a fluid. The individual crystals of the array will be precision cut to the appropriate phase-matching angle by computer-controlled diamond-turning techniques. This accurate finishing of the crystals, together with their initial precision alignment in the array, will obviate the need for individual segment adjustments. After assembly, the array will perform as a single monolithic crystal. The

Table 2-10. Novette optical-chain spatial-filter/relay parameters.

Filter relay (mm)	f/No.	Pinhole diameter (mm)	Angular acceptance aperture (μrad)
460/740	20	2.3	250
315/460	16.5	1.25	240
208/315	20	1.0	240
150/208	20.8	0.8	257
91.7/150	10.6	0.3	308
37.5/91.7	22.9	0.64	745
27/37.5	72	1.9	873

Table 2-11. Properties of phosphate amplifier glass.

	Vendor	λ (μm)	σ_p (m^2)	τ (μs)	$\Delta\lambda$ (nm)	n_0	n_2 (10^{-13} esu)	E_s (1 ns)
Phosphate								
LHG-8	Hoya	1.053	4.0	400	25.9	1.52	1.1	4.5
Q-88	Kigre	1.054	4.0	400	26.3	1.53	1.1	3.6
LHG-750	Schott	1.053	4.0	400	25.5	1.515	1.1	—
Silicate								
ED-2	O.I.	1.064	2.7	359	34.4	1.56	1.41	4.5

crystal thickness has been chosen to optimize 2ω energy-conversion efficiency over the anticipated operating range of the system.

Fluence Limitations at 1.05 μm. Performance of Novette, as with our other glass-laser systems, is limited by the threat of beam-induced damage to optical components. In present systems, the greatest threat has been to AR coatings on the input lenses of spatial filters and on the target-focusing optics. To achieve higher performance with Novette, and eventually with Nova, we will increase the damage resistance of the spatial-filter input lenses by using uncoated optics.

To assess the threat of surface damage and to develop guidelines for Novette chain design, we adopted the following rules, generated by the Nova design team from available damage data:

- Bulk glass damage and damage to high-reflection (HR) coatings are presently not limiting performance.
- For 1-ns pulses, uncoated surfaces damage at a median fluence of 16 J/cm^2, with 70% of the surfaces tested damaging between 14 and 19 J/cm^2. At other pulse lengths (0.1 to 3 ns), uncoated surface damage appears to follow a $\sqrt{\tau}$ dependence.
- AR surfaces damage at 1 ns at a median fluence of 5 J/cm^2, with 80% of the surfaces tested damaging between 4 and 7 J/cm^2. In addition, their damage threshold appears to increase slightly between 1 and 3 ns and appears to scale as $\sqrt{\tau}$ for pulses shorter than 1 ns.
- There is a reasonable expectation that damage thresholds will increase. This expectation is based upon recent progress with graded-index AR surfaces, superpolished AR coatings, and laser polishing of uncoated surfaces.

With these guidelines, the Nova design team established three fluence groups (A, B, and C) for which to target the Nova 1.06-μm design. The A group is the median fluence values obtainable today, the B group represents the highest values obtainable from today's production coatings, and the C values represent an estimate of what may be possible in the future if certain advanced approaches can be brought to production. Our greatest short-term hope is for graded-index components suitable for damage-free laser operation at the B fluence levels.

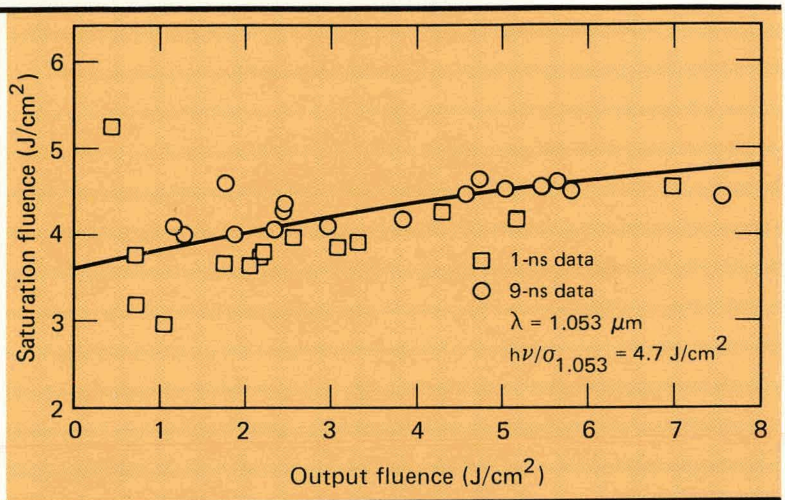

Fig. 2-35. Measured ▲ saturation fluence of LGH-8 phosphate glass.

Clear aperture	315 mm	460 mm
Thickness	43 mm	43 mm
Disks per module	2	2 (split)
Small-signal gain per module	1.78	1.93
Gain coefficient	5.6	6.2
Energy density	260 J/l	290 J/l
Glass volume per module	14 l	28 l
Bank energy per module	375 kJ	600 kJ
αD	3.5	3.2

◀Table 2-12. Phosphate-amplifier design characteristics.

Crystals	
Material	KDP (potassium dihydrogen phosphate)
Type of cut	Type II (θ_m = 59.23°)
Geometrical shape	Square parallelepiped
Array 1	
No. of crystals	25 + 5 spares
Length	150 (±0.01) mm
Width	150 (±0.01) mm
Thickness	18 (±0.01) mm
Array 2	
No. of crystals	9 + 3 spares
Length	260 (±0.01) mm
Width	260 (±0.01) mm
Thickness	18 (±0.01) mm
Finishing tolerance	±60 μrad from optimum phase-matching angle; ±0.5 mrad in other principal axis directions
Windows	
Material	BK-7
Clear-aperture diameter	800 mm
Thickness	40 mm
Antireflection coating	Exterior window surfaces will be finished with conventional AR coating (both 1.05 and 0.53 μm)
Index-matching fluid	
Material	Polychlorotrifluoroethylene (halocarbon oil No. 56)
Layer thickness	4 to 10 μm

Table 2-13. Specifications for the Novette frequency-doubling crystal array.

Fluence Limitations at 0.53 μm. The 74-cm-aperture optical train required to generate and transport the 0.53-μm beam to the target-focusing optics is shown in Fig. 2-34. Although the threat of damage to these optical elements is not inordinately high, it is still a matter of concern. Recent 1-ns measurements, for example, indicate that the 0.53- and 1.05-μm damage thresholds are comparable (Table 2-14). The assigned A and B fluence levels at 0.53 μm are given in Table 2-15.

Table 2-14. Laser-damage thresholds of production optical components for 1-ns pulses.

Surface type	Damage threshold (J/cm^2) 1.05 μm	0.53 μm
Thin film, AR	4 to 7	3 to 6
Thin film, HR	6 to 10	2 to 6
Beam dump (separate wavelengths)	—	2 to 8
Bare polished glass	14 to 18	18
Gradient index	10 to 14	11 to 13

Table 2-15. Fluence levels at 0.53 μm for Novette design.

	AR coated		HR coated		Uncoated	
	1 ns	3 ns	1 ns	3 ns	1 ns	3 ns
A fluence[a]	4.5	4.5	4.5	4.5	16	28
B fluence[a]	6	6	6	6	19	33

[a]Fluence levels in J/cm^2

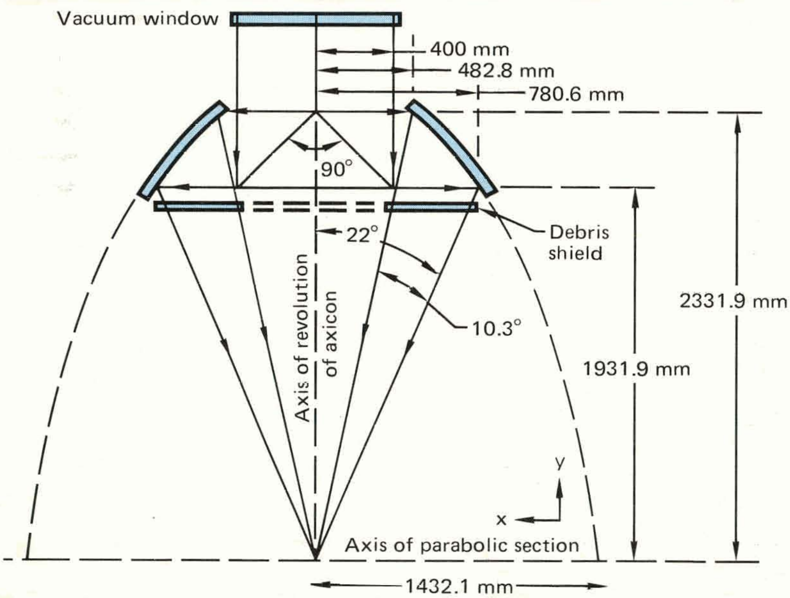

Fig. 2-36. Novette f/1.5, 800-mm all-reflecting axicon focusing optics.

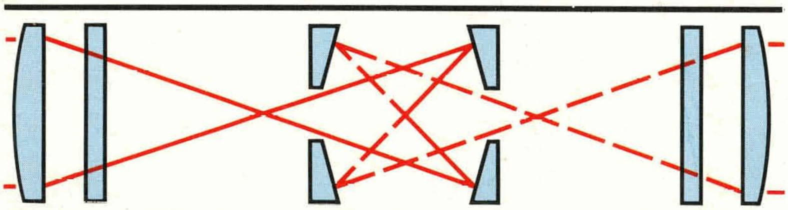

Fig. 2-37. Schematic of single-reflection f/1.5 clamshell.

Novette Target-Irradiation Geometry. The primary mission of Novette is to perform 0.53-μm target-irradiation experiments for direct comparison with those conducted at 1.06 μm on Shiva. Ultimately this will require a 74-cm focusing system with an f/No. of 1.5 or less. Unfortunately, conventional lenses of this speed limit laser performance due to intensification of flux on the exit surface of the lens. An advanced all-reflecting system cannot be fabricated in time for the proposed October 1982 target shot, however. For present purposes, we have chosen the Nova f/3.5 doublet focusing system. A decision regarding use of an all-reflecting system will be made later.

An all-reflecting focusing system, such as the axicon shown in Fig. 2-36, is viewed as the best candidate for the advanced system. In this figure, the cross section of the inner cone is a 45° isosceles triangle, and the cross section of the outer cone is a parabola given by $z = \pm y^2/2R$, where R = 2864.2. This type of all-reflecting system has the benefit of being free of chromatic aberration and avoids the absorption and nonlinear propagation effects inherent in transmitting optics. Another advantage of the axicon is the reduction in the damage threat that comes from reduced beam fluence and the higher damage thresholds of reflective coatings. Since present specifications require a focal accuracy of 20 μrad, and not the 0.4-μrad tolerance of a 0.53-μm diffraction-limited system, fabrication will be difficult; nevertheless, it is within the present state of the art.

Figure 2-37 shows an f/1.5 clamshell backup option that is less desirable, but this option meets the f/1.5 specification by using a combination of spherical clamshell mirrors and an f/3.5 doublet lens (or corrector plate). The axial glass thickness is 150 mm, the intensification on the vacuum window is less than 5%, and the clamshell mirrors are moderately sensitive to tilt (0.2 mrad FOV). In this scheme, protection of the mirror from target debris is a serious operating problem; also, a different refractive element would probably be required for each wavelength. This option is under consideration, however, because, compared to the axicon, it has a greatly reduced cost and less technical risk.

In summary, the baseline design uses Nova f/3.5 doublet lenses for initial activation. If practical, an all-reflecting system will be installed later; if not, the backup f/1.5 clamshell arrangement could be used to provide the required fast target focusing.

Authors: J. T. Hunt and D. R. Speck

Major Contributors: J. A. Glaze, W. F. Hagen, W. W. Simmons, and J. B. Trenholme

Novette Laser Performance

We have estimated the performance of the baseline Novette chain using the SNOBOL and MALAPROP computer codes. Table 2-16 summarizes the results of the SNOBOL calculations for the A and B fluence values described in the previous article. The calculations include the beam energy, the mean energy density, and the interstage B values. Figure 2-38 summarizes the results of MALAPROP calculations that estimated the peak energy density at the entrance and exit lenses of the spatial filters. These calculations indicate that beams entering the spatial filters will typically have a peak-to-average modulation of 2 to 1, which spatial filtering reduces to approximately 1.4 to 1.

For A fluences in the 3- to 5-ns regime, chain performance is limited by damage to AR-coated optics at either the exit lenses of the large-aperture spatial filters or at the focusing optics. Since both the peak and mean fluences steadily increase with increasing beam diameter, all other optical elements of the chain are well below their damage threshold. At 1 ns, beam modulation (induced by self-focusing) in the final stage of amplification shifts the damage threat to the uncoated entrance lens of the final spatial filter. At these conservative damage levels with A fluences, each beam can provide 8.0 TW during short-pulse ($\tau \leqslant 1$ ns) operation and 10.5 kJ during longer-pulse (3 to 5 ns) operation.

At B fluences, each beam can provide 9.4 TW during short-pulse operation and 13.5 kJ in the long-pulse regime. With long pulses ($\tau \geqslant 3$ ns) at B fluences, the chain is limited by gain saturation and energy storage as much as by damage threats. The amplification stages prior to the 460-mm stage must be driven into deep saturation to obtain the required drive for the 460-mm heads. In this regime, the exit lenses of the final two spatial filters and the target-focusing optics all experience about the same damage threat.

The large number of components subject to damage risk at B fluences for long pulse durations prompted us to investigate a more conservative chain staging. Table 2-17 compares the code calculations for a laser chain run at 3 ns with a fourth 460-mm amplifier added to the baseline. The performance with the additional amplifier is slightly degraded at 1 ns (down from 9.4 to 8.75 TW per beam); long-pulse performance improves, however, and the damage threat is substantially reduced.

We projected the frequency-doubled (0.53 μm) performance from the performance at 1.05 μm with the aid of two additional computer codes: ENERG-2ω and X-GAP. The code ENERG-2ω, which calculates energy-conversion efficiency, was used to optimize the KDP doubling-crystal thickness for the operating range of the system. These optimization calculations assumed that the overall beam divergence and crystal alignment errors did not exceed 100 μrad. Figure 2-39 shows the conversion efficiency of the optimum KDP crystal thickness (18 mm) for $0.75 \leqslant I_0 \leqslant 3.5$ GW/cm^2.

After establishing the conversion efficiency, we estimated the energy incident on the target by reducing the 0.53-μm beam energy that exits the crystal by the amount due to transmission losses from the beam dump (0.95), the diagnostic beam splitter (0.95), and the focusing optics (0.93). X-GAP and MALAPROP code calculations predicted the additional beam modulation caused by diffraction from the crystal interstices and its subsequent growth through the optical train from the crystal to the target-focusing optics.

Fig. 2-38. Maximum beam-energy densities of the Novette baseline chain at 1 ns for A damage fluence.

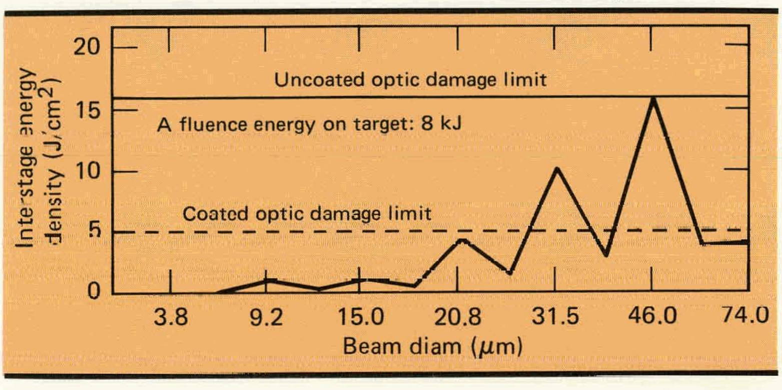

Initial saturation fluence = 3.8198 J/cm^2

1 ns

A fluence

Comp No.	Component description	Diam (cm)	Thick (cm)	No. and ang[a]	Refr index	Nonln index	S.S. gain	Sat gain	Energy (J)	B-Int added	B-Int total	Fluence J/cm^2
	PINHOLE		Delta-B[b]						0.1776			
1	S.F. output lens	3.75	0.5	1	1.507	1.24	0.99	0.99	0.1758	0[c]	0[c]	0.023
2	Wave plate	3.75	0	1	1	0	0.7	0.7	0.1231	0	0[c]	0.0227
3	ROD, 50 mm	3.75	40	1	1.523	1.05	20	17.69	2.178	0.0628	0.0634	0.2817
4	Pockels isol	3.75	11	1	1.5	1	0.87	0.87	1.895	0.0482	0.1117	0.2817
5	S.F. input lens	3.75	0.5	1	1.507	1.24	0.99	0.99	1.876	0[c]	0.1142	0.2451
6	PINHOLE		Delta-B[b]						1.876		0.1137	
7	S.F. output lens	9.17	1	1	1.507	1.24	0.99	0.99	1.857	0[c]	0.115	0.0406
8	DISK, 94 mm	9.17	2.4	−6	1.523	1.05	6.5	5.95	11.05	0.0213	0.1363	0.239
9	Faraday isol	9.17	4.3	1	1.67	2.1	0.88	0.88	9.722	0.0303	0.1666	0.239
10	DISK, 94 mm	9.17	2.4	−6	1.523	1.05	6.5	5.555	54.01	0.1076	0.2743	1.168
11	S.F. input lens	9.17	1.2	1	1.507	1.24	0.9199	0.9199	49.68	0.0277	0.3019	1.168
12	PINHOLE		Delta-B[b]						49.68		0.1878	
13	S.F. output lens	15	1.2	1	1.507	1.24	0.99	0.99	49.18	0[c]	0.3118	0.4016
14	Faraday isol	15	2.5	1	1.67	2.1	0.92	0.92	45.25	0.03	0.3418	0.3976
15	DISK, 150 mm	15	3	−4	1.523	1.05	3.6	3.178	143.8	0.1106	0.4524	1.162
16	S.F. input lens	15	1.4	1	1.507	1.24	0.9199	0.9199	132.3	0.0321	0.4845	1.162
17	PINHOLE		Delta-B[b]						132.3		0.1826	
18	S.F. output lens	20.8	1.9	1	1.507	1.24	0.99	0.99	131	0.0216	0.5061	0.5561
19	Faraday isol	20.8	2.9	1	1.67	2.1	0.89	0.89	116.6	0.0474	0.5535	0.5506
20	DISK, 208 mm [ ]	20.8	2.5	−3	1.523	1.05	2.2	2.028	236.3	0.0715	0.6251	0.9936
21	DISK, 208 mm	20.8	2.5	−3	1.523	1.05	2.2	1.949	460.5	0.1426	0.7677	1.936
22	DISK, 208 mm [ ]	20.8	2.5	−3	1.523	1.05	2.2	1.833	844.1	0.2713	1.039	3.549
23	S.F. input lens	20.8	1.8	1	1.507	1.24	0.9199	0.9199	766.5	0.1261	1.165	3.549
24	PINHOLE		Delta-B[b]						766.5		0.6806	
25	S.F. output lens	31.5	2.8	1	1.507	1.24	0.99	0.99	768.7	0.0816	1.247	1.423
26	Faraday isol	31.5	4.8	1	1.67	2.1	0.9	0.9	691.8	0.2019	1.449	1.409
27	DISK, 315 mm [ ]	31.5	4.3	−2	1.523	1.05	1.7	1.544	1068	0.1837	1.632	1.958
28	DISK, 315 mm [ ]	31.5	4.3	−2	1.523	1.05	1.7	1.502	1604	0.281	1.913	2.941
29	DISK, 315 mm [ ]	31.5	4.3	−2	1.523	1.05	1.7	1.453	2331	0.4181	2.331	4.273
30	DISK, 315 mm [ ]	31.5	4.3	−2	1.523	1.05	1.7	1.4	3264	0.6014	2.933	5.983
31	S.F. input lens	31.5	2.6	1	1.507	1.24	0.9199	0.9199	3002	0.3071	3.24	5.983
32	PINHOLE		Delta-B[b]				0.9999		3002		2.075	
33	S.F. output lens	46	3.7	1	1.507	1.24	0.99	0.99	2972	0.1955	3.435	2.581
34	Slit apodizer	46	3	1	1.507	1.24	0.99	0.99	2942	0.157	3.592	2.555
35	DISK, 460 mm [ ]	46	4.3	−2	1.523	1.05	1.85	1.569	4616	0.3741	3.966	3.968
36	DISK, 460 mm [ ]	46	4.3	−2	1.523	1.05	1.85	1.493	6890	0.5779	4.544	5.923
37	DISK, 460 mm [ ]	46	4.3	−2	1.523	1.05	1.85	1.417	9763	0.8488	5.393	8.392
38	S.F. input lens	46	3.7	1	1.507	1.24	0.9199	0.9199	8981	0.6131	6.006	8.392
39	PINHOLE		Delta-B[b]				0.9997		8979		2.766	
40	S.F. output lens	74	5.7	1	1.507	1.24	0.99	0.99	8889	0.3481	6.354	2.982
41	Focus optics	74	16.3	1	1.507	1.24	0.9	0.9	8000	0.9401	7.295	2.953

[a]Dash preceeding number denotes Brewster angle orientation.

[b]Delta B refers to B accumulated between pinholes.

[c]Denotes a B value of less than 0.01.

Table 2-16. Calculations of Novette baseline chain performance at 1, 3, and 5 ns for A and B fluence levels.

1 ns B fluence					3 ns A fluence					3 ns B fluence				
Sat gain	Energy (J)	B-Int added	B-Int total	Fluence (J/cm^2)	Sat gain	Energy (J)	B-Int added	B-Int total	Fluence (J/cm^2)	Sat gain	Energy (J)	B-Int added	B-Int total	Fluence (J/cm^2)
	0.3219					0.5472					6.36			
0.99	0.3186	0^c	0^c	0.0416	0.99	0.5417	0^c	0^c	0.0708	0.99	6.296	0^c	0^c	0.8226
0.7	0.223	0^c	0^c	0.0412	0.7	0.3792	0^c	0^c	0.0701	0.7	4.407	0	0^c	0.8144
17.21	3.838	0.1122	0.1134	0.4964	16.52	6.266	0.0623	0.063	0.8105	9.448	41.64	0.5414	0.5497	5.386
0.87	3.339	0.085	0.1984	0.4964	0.87	5.451	0.0463	0.1093	0.8105	0.87	36.23	0.3074	0.8571	5.386
0.99	3.306	0^c	0.2028	0.4319	0.99	5.397	0^c	0.1117	0.7051	0.99	35.87	0.016	0.8731	4.686
	3.306		0.202			5.397		0.1112			35.87		0.8676	
0.99	3.273	0^c	0.2043	0.0715	0.99	5.343	0^c	0.1125	0.1167	0.99	35.51	0^c	0.8784	0.7758
5.872	19.22	0.0372	0.2415	0.4157	5.764	30.79	0.0201	0.1325	0.6661	4.688	166.4	0.1208	0.9991	3.6
0.88	16.91	0.0528	0.2943	0.4157	0.88	27.1	0.0282	0.1607	0.6661	0.88	146.5	0.1524	1.151	3.6
5.261	88.96	0.1824	0.4767	1.924	4.92	133.3	0.0943	0.2551	2.884	3.196	468.1	0.4109	1.562	10.13
0.9199	81.83	0.0456	0.5223	1.924	0.9199	122.6	0.0228	0.2779	2.884	0.9199	430.6	0.08	1.642	10.13
	81.83		0.3194			122.6		0.1662			430.6		0.7693	
0.99	81.02	0.0163	0.5385	0.6615	0.99	121.4	0^c	0.286	0.9915	0.99	426.3	0.0285	1.671	3.481
0.92	74.53	0.0494	0.5879	0.6549	0.92	111.7	0.0247	0.3107	0.9815	0.92	392.2	0.0867	1.758	3.446
3.054	227.6	0.1788	0.7667	1.84	2.92	326.1	0.0875	0.3982	2.637	2.326	912.3	0.2775	2.035	7.375
0.9199	209.4	0.0509	0.8176	1.84	0.9199	300	0.0243	0.4225	2.637	0.9199	839.2	0.068	2.103	7.375
	209.4		0.2953			300		0.1446			839.2		0.4606	
0.99	207.3	0.0342	0.8518	0.8803	0.99	297	0.0164	0.4388	1.261	0.99	830.8	0.0458	2.149	3.528
0.89	184.5	0.075	0.9269	0.8715	0.89	264.3	0.0358	0.4747	1.249	0.89	739.4	0.1002	2.249	3.493
1.981	365.5	0.1121	1.039	1.537	1.932	510.7	0.053	0.5276	2.147	1.726	1 276	0.142	2.391	5.366
1.878	686.2	0.2173	1.256	2.885	1.811	925	0.0998	0.6275	3.889	1.584	2 022	0.2375	2.629	8.501
1.744	1 197	0.3969	1.653	5.032	1.67	1 545	0.1755	0.803	6.494	1.457	2 946	0.3639	2.992	12.39
0.9199	1 101	0.1788	1.832	5.032	0.9199	1 421	0.0769	0.8799	6.494	0.9199	2 710	0.1467	3.139	12.39
	1 101		1.014			1 421		0.4575			2 710		1.036	
0.99	1 090	0.1157	1.948	2.018	0.99	1 407	0.0498	0.9297	2.605	0.99	2 683	0.095	3.234	4.968
0.9	981	0.2863	2.234	1.998	0.9	1 266	0.1232	1.053	2.579	0.9	2 415	0.2349	3.469	4.918
1.511	1 482	0.2586	2.493	2.718	1.483	1 877	0.1106	1.163	3.441	1.395	3 368	0.2074	3.676	6.174
1.463	2 169	0.3871	2.88	3.976	1.432	2 687	0.1624	1.326	4.926	1.342	4 521	0.2863	3.963	8.287
1.411	3 060	0.5608	3.44	5.61	1.378	3 704	0.2301	1.556	6.79	1.293	5 848	0.38	4.343	10.72
1.358	4 155	0.783	4.223	7.617	1.327	4 914	0.3138	1.87	9.008	1.25	7 311	0.4855	4.828	13.4
0.9199	3 822	0.391	4.614	7.617	0.9199	4 520	0.1541	2.024	9.008	0.9199	6 725	0.2293	5.058	13.4
	3 821		2.782			4 520		1.144			6 725		1.918	
0.99	3 783	0.2489	4.863	3.285	0.99	4 475	0.0981	2.122	3.886	0.99	6 657	0.146	5.204	5.78
0.99	3 745	0.1998	5.063	3.252	0.99	4 430	0.0788	2.201	3.847	0.99	6 591	0.1172	5.321	5.723
1.529	5 728	0.4724	5.535	4.924	1.5	6 646	0.1852	2.386	5.713	1.426	9 396	0.2712	5.592	8.077
1.453	8 321	0.7113	6.247	7.153	1.424	9 465	0.2734	2.659	8.136	1.355	12 730	0.38	5.972	10.94
1.379	11 480	1.016	7.263	9.867	1.354	12 810	0.3826	3.042	11.01	1.294	16 470	0.5055	6.477	14.16
0.9199	10 560	0.7209	7.984	9.867	0.9199	11 780	0.2682	3.31	11.01	0.9199	15 150	0.3448	6.822	14.16
	10 550		3.369			11 780		1.286			15 150		1.765	
0.99	10 440	0.409	8.393	3.504	0.99	11 670	0.1523	3.462	3.914	0.99	15 000	0.1958	7.018	5.033
0.9	9 400	1.105	9.497	3.169	0.9	10 500	0.4113	3.874	3.875	0.9	13 500	0.5288	7.547	4.982

5 ns A fluence					5 ns B fluence				
Sat gain	Energy (J)	B-Int added	B-Int total	Fluence (J/cm^2)	Sat gain	Energy (J)	B-Int added	B-Int total	Fluence (J/cm^2)
	0.5472					6.353			
0.99	0.5417	0^c	0^c	0.0708	0.99	6.29	0^c	0^c	0.8217
0.7	0.3792	0^c	0^c	0.0701	0.7	4.403	0	0^c	0.8135
16.52	6.265	0.0374	0.0378	0.8104	9.452	41.61	0.3246	0.3295	5.383
0.87	5.451	0.0278	0.0656	0.8104	0.87	36.2	0.1843	0.5138	5.383
0.99	5.396	0^c	0.067	0.705	0.99	35.84	0^c	0.5234	4.683
	5.396		0.0667			35.84		0.5202	
0.99	5.342	0^c	0.0675	0.1167	0.99	35.48	0^c	0.5266	0.7753
5.764	30.79	0.012	0.0795	0.666	4.688	166.4	0.0724	0.599	3.598
0.88	27.1	0.0169	0.0964	0.666	0.88	146.4	0.0914	0.6904	3.598
4.92	133.3	0.0566	0.153	2.884	3.197	468	0.2464	0.9368	10.12
0.9199	122.6	0.0137	0.1667	2.884	0.9199	430.5	0.048	0.9848	10.12
	122.6		0.0997			430.5		0.4614	
0.99	121.4	0^c	0.1716	0.9914	0.99	426.2	0.0171	1.002	3.48
0.92	111.7	0.0148	0.1864	0.9815	0.92	392.1	0.052	1.054	3.445
2.92	326.1	0.0525	0.2389	2.636	2.326	912.1	0.1664	1.22	7.373
0.9199	300	0.0146	0.2535	2.636	0.9199	839	0.0408	1.261	7.373
	300		0.0868			839		0.2763	
0.99	297	0^c	0.2633	1.261	0.99	830.6	0.0274	1.289	3.527
0.89	264.3	0.0215	0.2848	1.249	0.89	739.3	0.0601	1.349	3.492
1.932	510.7	0.0318	0.3166	2.147	1.726	1 276	0.0852	1.434	5.365
1.811	925	0.0599	0.3765	3.889	1.584	2 022	0.1425	1.576	8.5
1.67	1 545	0.1053	0.4818	6.494	1.457	2 946	0.2183	1.795	12.38
0.9199	1 421	0.0462	0.5279	6.494	0.9199	2 710	0.088	1.883	12.38
	1 421		0.2745			2 710		0.6216	
0.99	1 407	0.0299	0.5578	2.605	0.99	2 683	0.057	1.94	4.967
0.9	1 266	0.0739	0.6317	2.579	0.9	2 414	0.1409	2.081	4.918
1.483	1 877	0.0664	0.6981	3.441	1.395	3 368	0.1245	2.205	6.173
1.432	2 687	0.0974	0.7955	4.926	1.342	4 520	0.1718	2.377	8.286
1.378	3 704	0.1381	0.9336	6.79	1.294	5 847	0.228	2.605	10.72
1.327	4 914	0.1883	1.122	9.008	1.25	7 310	0.2913	2.896	13.4
0.9199	4 520	0.0925	1.214	9.008	0.9199	6 724	0.1376	3.034	13.4
	4 520		0.6864			6 724		1.151	
0.99	4 475	0.0589	1.273	3.886	0.99	6 657	0.0876	3.121	5.78
0.99	4 430	0.0473	1.32	3.847	0.99	6 591	0.0703	3.192	5.722
1.5	6 646	0.1111	1.432	5.713	1.426	9 396	0.1627	3.354	8.077
1.424	9 465	0.164	1.596	8.136	1.355	12 730	0.228	3.582	10.94
1.354	12 810	0.2296	1.825	11.01	1.294	16 470	0.3033	3.886	14.16
0.9199	11 780	0.1609	1.986	11.01	0.9199	15 150	0.2069	4.092	14.16
	11 780		0.7717			15 150		1.059	
0.99	11 670	0.0914	2.077	3.914	0.99	15 000	0.1175	4.21	5.033
0.9	10 500	0.2468	2.324	3.875	0.9	13 500	0.3173	4.527	4.982

Initial saturation fluence = 3.8198 J/cm²								Additional 460-mm amplifier				
Comp No.	Component description	Diam (cm)	Thick (cm)	No. and ang[a]	Refr index	Nonln index	S.S. gain	Sat gain	Energy (J)	B-Int added	B-Int total	Fluence J/cm²
	PINHOLE		Delta-B[b]						0.9514		0[c]	
1	S.F. output lens	3.75	0.5	1	1.507	1.24	0.99	0.99	0.9419	0[c]	0[c]	0.1231
2	Wave plate	3.75	0	1	1	0	0.7	0.7	0.6593	0	0[c]	0.1218
3	ROD, 50 mm	3.75	40	1	1.523	1.05	20	15.48	10.2	0.1049	0.1061	1.32
4	Pockets isol	3.75	11	1	1.5	1	0.87	0.87	8.877	0.0753	0.1814	1.32
5	S.F. input lens	3.75	0.5	1	1.507	1.24	0.99	0.99	8.788	0[c]	0.1853	1.148
6	PINHOLE		Delta-B[b]						8.788		0.1845	
7	S.F. output lens	9.17	1	1	1.507	1.24	0.99	0.99	8.7	0[c]	0.1866	0.1901
8	DISK, 94 mm	9.17	2.4	−6	1.523	1.05	6.5	5.601	48.73	0.0322	0.2189	1.054
9	Faraday isol	9.17	4.3	1	1.67	2.1	0.88	0.88	42.88	0.0446	0.2635	1.054
10	DISK, 94 mm	9.17	2.4	−6	1.523	1.05	6.5	4.511	193.4	0.1432	0.4067	4.184
11	S.F. input lens	9.17	1.2	1	1.507	1.24	0.9199	0.9199	178	0.033	0.4397	4.184
12	PINHOLE		Delta-B[b]						177.9		0.2544	
13	S.F. output lens	15	1.2	1	1.507	1.24	0.99	0.99	176.2	0.0118	0.4515	1.439
14	Faraday isol	15	2.5	1	1.67	2.1	0.92	0.92	162.1	0.0358	0.4873	1.424
15	DISK, 150 mm	15	3	−4	1.523	1.05	3.6	2.769	448.8	0.124	0.6113	3.628
16	S.F. input lens	15	1.4	1	1.507	1.24	0.9199	0.9199	412.8	0.0334	0.6447	3.628
17	PINHOLE		Delta-B[b]						412.8		0.205	
18	S.F. output lens	20.8	1.9	1	1.507	1.24	0.99	0.99	408.7	0.0225	0.6672	1.736
19	Faraday isol	20.8	2.9	1	1.67	2.1	0.89	0.89	363.8	0.0493	0.7166	1.718
20	DISK, 208 mm [ ]	20.8	2.5	−3	1.523	1.05	2.2	1.879	683.3	0.0721	0.7886	2.873
21	DISK, 208 mm	20.8	2.5	−3	1.523	1.05	2.2	1.745	1 193	0.1318	0.9204	5.014
22	DISK, 208 mm [ ]	20.8	2.5	−3	1.523	1.05	2.2	1.603	1 911	0.2229	1.143	8.035
23	S.F. input lens	20.8	1.8	1	1.507	1.24	0.9199	0.9199	1 758	0.0952	1.239	8.035
24	PINHOLE		Delta-B[b]						1 758		0.5938	
25	S.F. output lens	31.5	2.8	1	1.507	1.24	0.99	0.99	1 741	0.0616	1.3	3.223
26	Faraday isol	31.5	4.8	1	1.67	2.1	0.9	0.9	1 567	0.1524	1.452	3.191
27	DISK, 315 mm [ ]	31.5	4.3	−2	1.523	1.05	1.7	1.456	2 281	0.1361	1.589	4.181
28	DISK, 315 mm [ ]	31.5	4.3	−2	1.523	1.05	1.7	1.403	3 201	0.1963	1.785	5.868
29	DISK, 315 mm [ ]	31.5	4.3	−2	1.523	1.05	1.7	1.351	4 323	0.2726	2.058	7.925
30	DISK, 315 mm [ ]	31.5	4.3	−2	1.523	1.05	1.7	1.301	5 624	0.3641	2.422	10.31
31	S.F. input lens	31.5	2.6	1	1.507	1.24	0.9199	0.9199	5 174	0.1764	2.598	10.31
32	PINHOLE		Delta-B[b]						5 174		1.359	
33	S.F. output lens	46	3.7	1	1.507	1.24	0.99	0.99	5 122	0.1123	2.71	4.447
34	Slit apodizer	46	3	1	1.507	1.24	0.99	0.99	5 071	0.0902	2.8	4.403
35	DISK, 460 mm [ ]	46	4.3	−2	1.523	1.05	1.85	1.476	7 482	0.2109	3.011	6.432
36	DISK, 460 mm [ ]	46	4.3	−2	1.523	1.05	1.85	1.401	10 480	0.3061	3.317	9.009
37	DISK, 460 mm [ ]	46	4.3	−2	1.523	1.05	1.85	1.333	13 970	0.4212	3.739	12.01
38	DISK, 460 mm [ ]	46	4.3	−2	1.523	1.05	1.85	1.275	17 810	0.5511	4.29	15.31
39	S.F. input lens	46	3.7	1	1.507	1.24	0.9199	0.9199	16 390	0.3729	4.663	15.31
40	PINHOLE		Delta-B[b]				0.9999		16 390		2.065	
41	S.F. output lens	74	5.7	1	1.507	1.24	0.99	0.99	16 220	0.2118	4.874	5.443
42	Focus optics	74	16.3	1	1.507	1.24	0.9	0.9	14 600	0.5719	5.446	5.388

[a]Dash preceding number denotes Brewster angle orientation. [b]Delta B refers to B accumulated between pinholes.

Table 2-17. Comparison of Novette Baseline and additional amplifier performance at 3 ns.

Figure 2-40 is a summary of our performance calculations and shows, for the baseline chain, operating envelopes of energy deliverable to a target vs pulse length. Curves are shown for both A and B fluences for 1.05 and 0.53-μm beams. The shaded regions denote the 100-μrad uncertainty in the frequency-doubled phase-matching condition. Each frequency-doubled beam can provide between 5 and 7.5 TW for short pulses and 6 to 10 kJ for a pulse duration of 1 to 3 ns. For pulses of 3 to 5 ns, the 1.05-μm beam intensity at the crystal is less than optimum, reducing the 0.53-μm beam energy to 6 to 8 kJ. Finally, Fig. 2-41 summarizes the system performance with an additional

Baseline B-fluence

Sat gain	Energy (J)	B-Int added	B-Int total	Fluence J/cm^2
	6.36		0[b]	
0.99	6.296	0[b]	0[b]	0.8226
0.7	4.407	0	0[b]	0.8144
9.448	41.64	0.5414	0.5497	5.386
0.87	36.23	0.3074	0.8571	5.386
0.99	35.87	0.016	0.8731	4.686
	35.87		0.8676	
0.99	35.51	0[b]	0.8784	0.7758
4.688	166.4	0.1208	0.9991	3.6
0.88	146.5	0.1521	1.151	3.6
3.196	468.1	0.4109	1.562	10.13
0.9199	430.6	0.08	1.642	10.13
	430.6		0.7693	
0.99	426.3	0.0285	1.671	3.481
0.92	392.2	0.0867	1.758	3.446
2.326	912.3	0.2775	2.035	7.375
0.9199	839.2	0.068	2.103	7.375
	839.2		0.4606	
0.99	830.8	0.0458	2.149	3.528
0.89	739.4	0.1002	2.249	3.493
1.726	1 276	0.142	2.391	5.366
1.584	2 022	0.2375	2.629	8.501
1.457	2 946	0.3639	2.992	12.39
0.9199	2 710	0.1467	3.139	12.39
	2 710		1.036	
0.99	2 683	0.095	3.234	4.968
0.9	2 415	0.2349	3.469	4.918
1.395	3 368	0.2074	3.676	6.174
1.342	4 521	0.2863	3.963	8.287
1.293	5 848	0.38	4.343	10.72
1.25	7 311	0.4855	4.828	13.4
0.9199	6 725	0.2293	5.058	13.4
	6 725		1.918	
0.99	6 657	0.146	5.204	5.78
0.99	6 591	0.1172	5.321	5.723
1.426	9 396	0.2712	5.592	8.077
1.355	12 730	0.38	5.972	10.94
1.294	16 470	0.5055	6.477	14.16
0.9199	15 150	0.3448	6.822	14.16
—	—	—	—	—
	15 150		1.765	
0.99	15 000	0.1958	7.018	5.033
0.9	13 500	0.5288	7.547	4.982

[c]Denotes a B value of less than 0.01.

460-mm amplifier. This staging produces higher 1.05-μm beam intensities at the crystal for pulse durations between 3 and 5 ns. The improved frequency-doubling conversion efficiency in this case would produce about 1 kJ more per arm of 0.53-μm light for pulse durations from 3 to 5 ns.

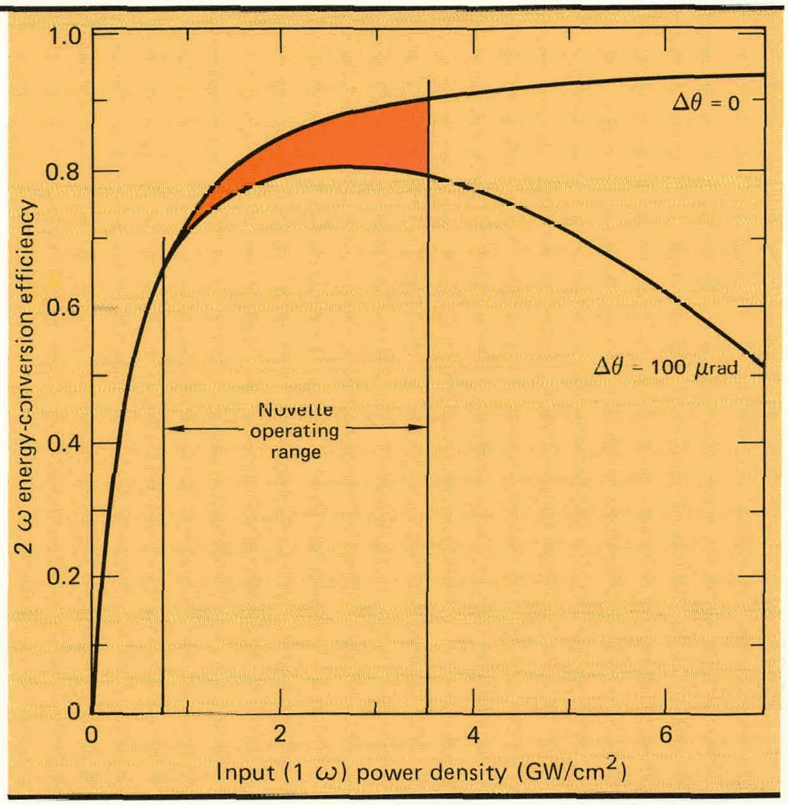

Fig. 2-39. Conversion▲ efficiency of optimum-thickness KDP crystal.

Fig. 2-40. Summary of Novette performance calculations.▼

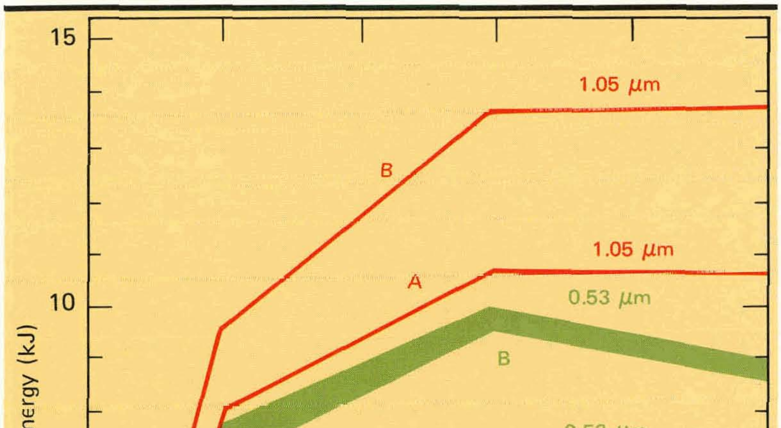

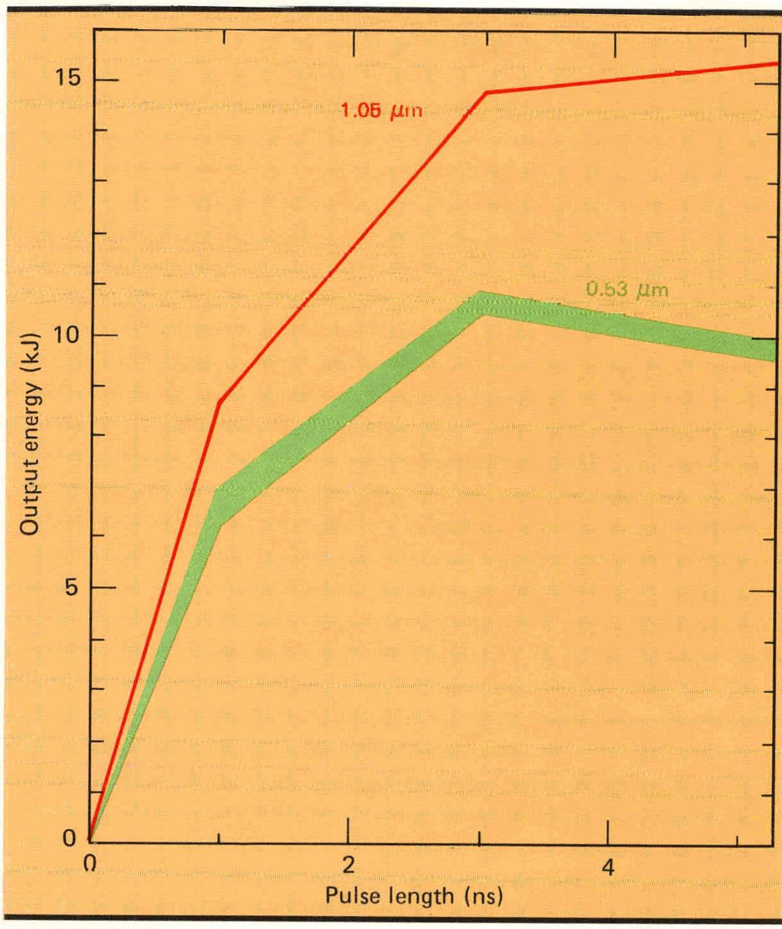

Fig. 2-41. Summary of Novette performance calculations with an additional amplifier.

In summary, a baseline design for the two-arm Novette system has been developed to provide target irradiation at fundamental and second-harmonic wavelengths. The initial system performance is predicated on operating at A fluence levels, with the capability of providing output commensurate with B fluences when appropriate large-aperture optics can be obtained. At A fluences and the fundamental wavelength, Novette can deliver to the target 10 to 15 TW of peak power for short pulses (1 ns) and 15 to 20 kJ of energy for longer pulses (3 to 5 ns). Second-harmonic power and energy on target are typically 80 to 85% of these levels. The maximum fluences associated with these performance projections are within A-fluence damage levels at the respective wavelengths, indicating that routine target irradiation at these powers and energies is possible with minimal damage risk to critical large-aperture optics.

Authors: J. T. Hunt and D. R. Speck

Major Contributors: J. A. Glaze, W. F. Hagen, W. W. Simmons, and J. B. Trenholme

Novette Master Oscillator Room

For Novette, as for Nova, we will have a separate master oscillator room (MOR)[26] that will be housed in the rooms adjacent to the laser bay. The requirements for the Novette MOR can be briefly summarized as follows:

- Target irradiation pulses in the range from 100 ps to 5 ns.
- X-ray backlighting pulses in the range from 20 ps to 5 ns.
- Ultraviolet probe pulses of ~20 ps.
- Target-diagnostics trigger beams of 10 and 100 μJ.
- High-repetition preamplifiers to generate enough energy for direct second-harmonic crystal alignment.
- A fully relayed beam from the oscillators to the input of each chain.
- A single beam line from the MOR to the high bay in Building 381, using time multiplexing for target irradiation, x-ray backlighting, and UV probing experiments.
- Sufficient energy from the MOR to give the following energy levels through the laser-arm input aperture: 2.2 J at 5 ns; 2.2 J at 3 ns; 0.35 J at 1 ns; and 0.04 J at 100 ps.
- Oscillators fully diagnosed and beam-energy levels measured after exiting each amplifier in the MOR.
- Fully automatic alignment of the MOR.

A layout of the Novette MOR that satisfies all these requirements (and more) is shown in Fig. 2-42. We use synchronized short-pulse (AMQ) and long-pulse (single-axial-mode Q-switched) oscillators to provide the pulses in the range from 100 ps to 5 ns. These are very similar to the new oscillators we installed on Shiva (described in "Optical Pulse Generation" in this section). For Novette, we will use Nd:YLF at 1.054 μm in the oscillators, both of which have been demonstrated with YLF; the YLF short-pulse oscillator is described in the 1978 Annual Report,[27] and a YLF long-pulse oscillator is described in "Oscillator Development" in this section.

To obtain the 20-ps pulses, we will use a regenerative pulse compressor[28,29] that will compress pulses from 100 to 20 ps. Thus, we need another short-pulse (AMQ) oscillator to drive the regenerator; this oscillator will be synchronized with the main AMQ oscillator.

We use a 0.25-in.-diam YLF amplifier after the long-pulse oscillator and then use four 10-mm-diam amplifiers (with gain = 10). The 10-mm diameter is a reasonable compromise, given the necessity for a high repetition rate and for energy sufficient for both aligning the SHG crystal and driving the 50-mm amplifiers in the laser bay. With this amplifier layout, and using a 7.2-mm-diam beam with a square spatial profile, we get about 70 mJ for 100-ps to 1-ns pulses and up to 300 mJ for 5-ns pulses. The development of these amplifiers is described in "Amplifier Development" in this section. We have found that Nd:YLF is the ideal material to use for these amplifiers because it is almost athermal at 1.05 μm, making possible an amplifier with repetition rates in the range of 1 to 10 ps. As an alternative to YLF, we are considering athermal glasses, such as Q-98 and Q-100, which would require a lower repetition rate.

We have laid out the MOR beam relaying and aperturing to get maximum output power with good beam quality through a 10-mm aperture. We amplify a Gaussian beam through the third of the five amplifiers and use a very tight spatial filter, with magnification M = 1, to give a very clean Gaussian beam. We then use a hard aperture to transmit only the center 15% of the Gaussian beam. A pinhole in the next spatial filter (with M = 5.2) minimizes diffraction rings in the following amplifiers and relays the beam to the next spatial filter going into the laser bay. This relaying scheme optimizes the output energy in the 10-mm beam at the cost of amplified spontaneous emission (ASE), which will be controlled by the tight pinhole in the M = 1 spatial filter and by the fast Pockels cells. The final Pockels cell in the system is used to rotate the polarization of the 20-ps pulse from the regenerator. This pulse is then separated from the main beam for UV probing with a polarizer in the laser bay.

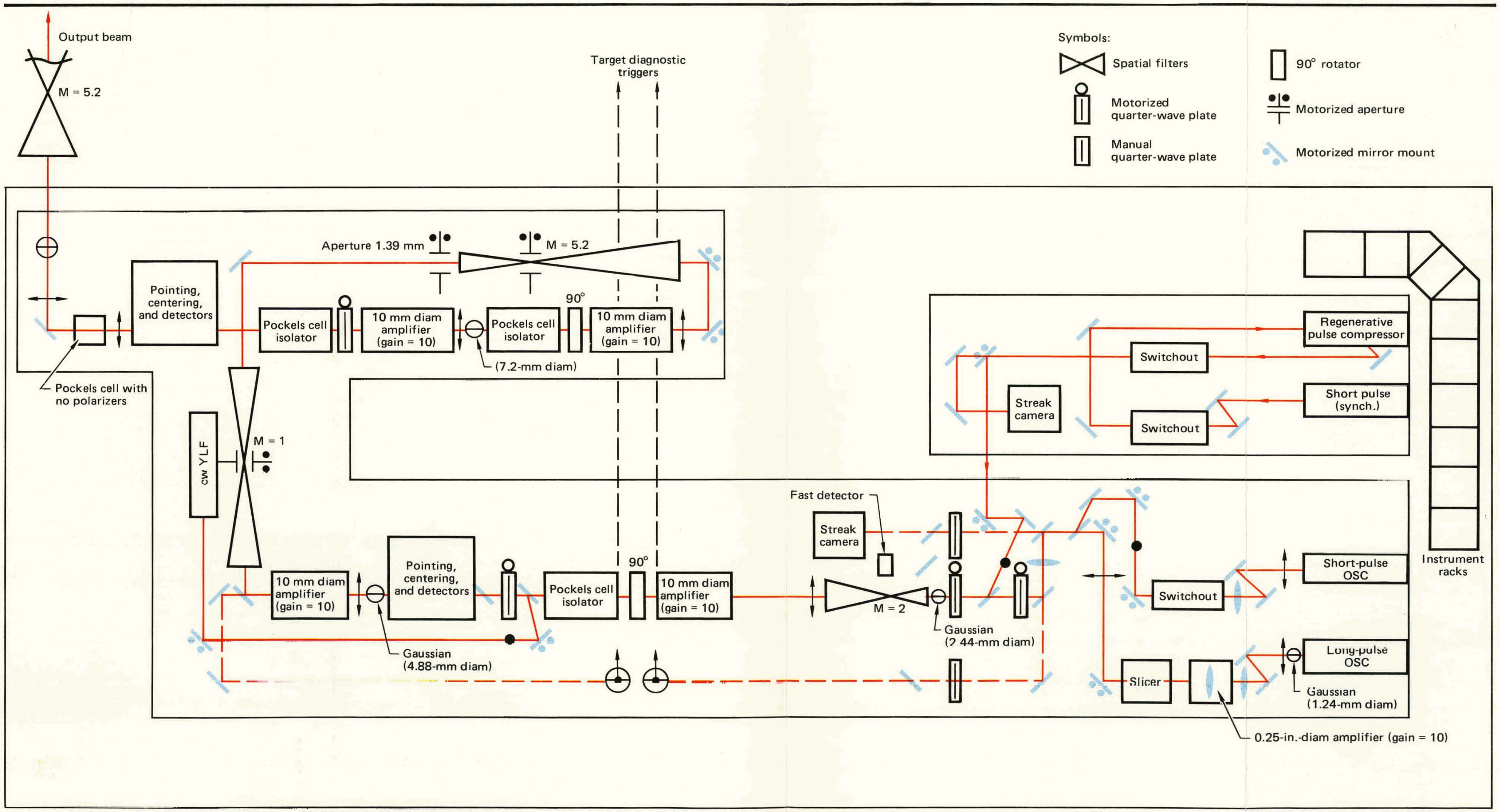

Fig. 2-42. Schematic of the Novette master oscillator room. (Not to scale.)

Oscillator diagnostics will be very similar to the diagnostics for the new Shiva oscillators; automatic alignment will be performed by the two sensors shown in Fig. 2-42.

Author: D. J. Kuizenga

Major Contributors: J. E. Murray, E. S. Bliss, D. R. Speck, and W. E. Martin

Novette Facility

Novette will occupy the high-bay laboratory and basement areas in Building 381 (areas now used for the Argus laser) along with some additional space in the adjacent laboratory area. The laser amplifier chains will reside in the west end of the high bay, and the output will be directed toward the target area in the east end of the high bay. To increase available space for the many components in the target area, we will elevate the target chamber above the beam lines, which will enter the chamber from the east and west. The master oscillator and its utilities will reside in the laboratory space adjacent to the southwest side of the high bay. The control room and the target-diagnostics data-acquisition room will remain in the spaces now used for those purposes on Argus. The Novette central computer (VAX) will be installed in the present Argus operations room, while the Novette operations room will be located in the laboratory room between the control room and the master oscillator room—a central location with easy access to the high bay, control room, and oscillator room. A plan for the first floor of the Novette facility is shown in Fig. 2-43.

Figure 2-44 shows the basement plan for Novette. The power-conditioning energy-storage banks and power supplies will

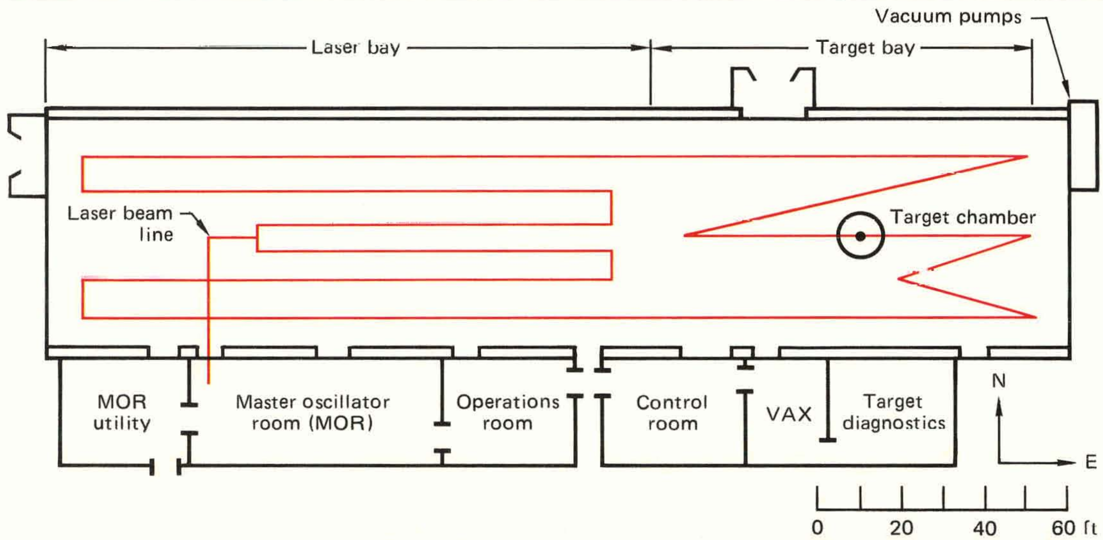

Fig. 2-43. First-floor plan for the Novette target-irradiation facility in Building 381.

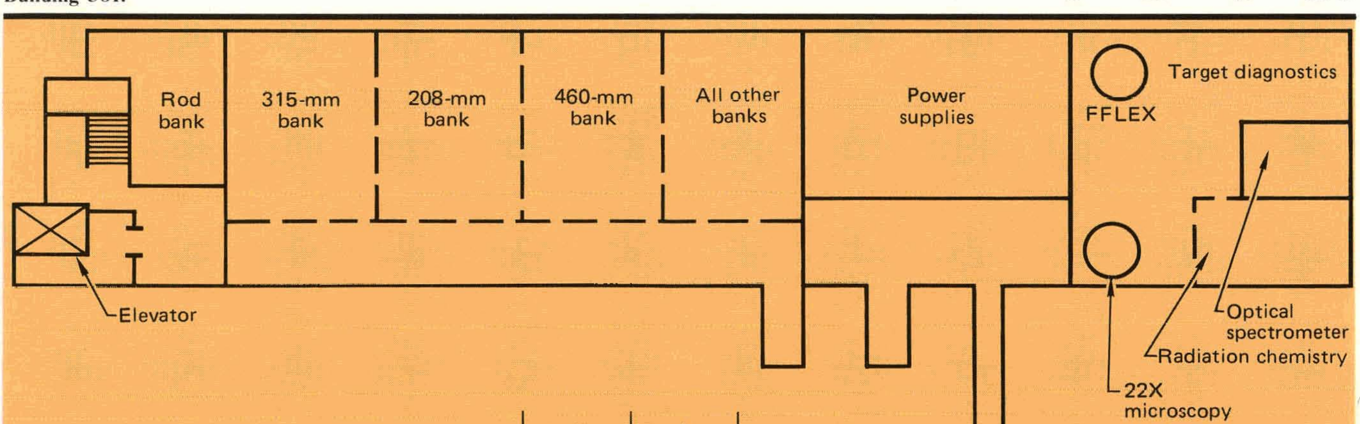

Fig. 2-44. Basement plan for Novette in Building 381.

occupy the west end of the basement, as they presently do for Argus. Target-diagnostic sensors and laboratories will reside in the east end of the basement directly under and to the east of the target chamber. Lines of sight to the target chamber will be provided through holes drilled in the concrete-slab floor of the high bay.

The 210-ft length of the Nova laser chains requires an additional fold to fit them and the target area into the 230-ft-long high bay of Building 381 (Fig. 2-44). The beam will exit the MOR at a height of 8 ft and will pass over the south section of the laser space frame to the center space frame. There, the beam will be amplified by 50-mm-diam rod amplifiers, split, and directed through the input aperture of each of the laser arms, as shown in Fig. 2-45. The laser beamlines will be 4.5 ft off the floor, supported on three space frames made of welded steel tubing and attached to the 3-ft-thick concrete floor of the high bay. The additional fold in the Nova chains will occur at the end of the center space frame element at the output of the 95 mm/145 mm spatial filter. To shorten the outer legs of the Nova configuration, containing the large-diameter output amplifiers, the 315-mm-diam Faraday rotators are relocated to the inside legs of the outer space frames. Figure 2-46 illustrates the configuration of the laser chains and space frame sections in the laser section of the high bay.

These output-amplifier legs and the beam paths for the laser diagnostics will still extend the entire length of the high bay. The frequency-conversion optics and target

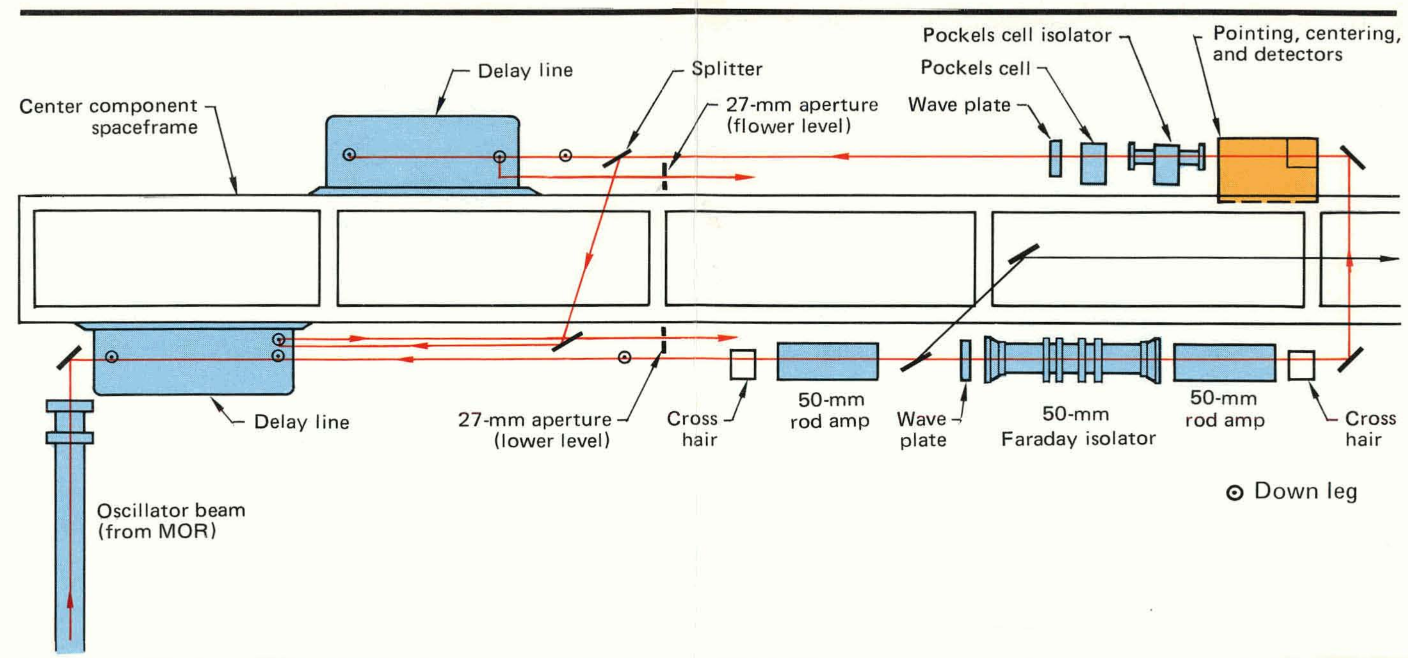

Fig. 2-45. Schematic ▲ plan of the initial rod-amplifier and beam-splitter assembly of Novette.

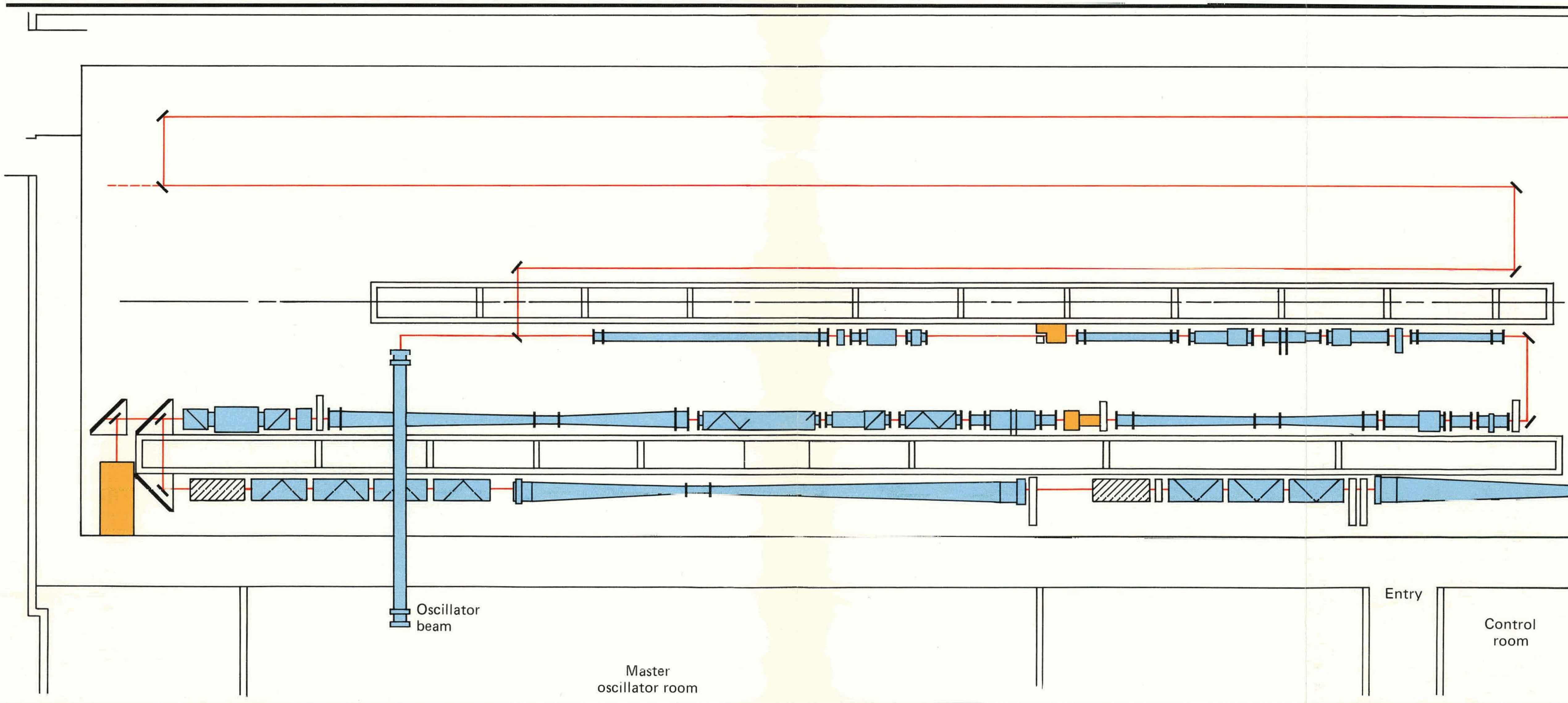

Fig. 2-46. Schematic plan of the Novette laser chain.

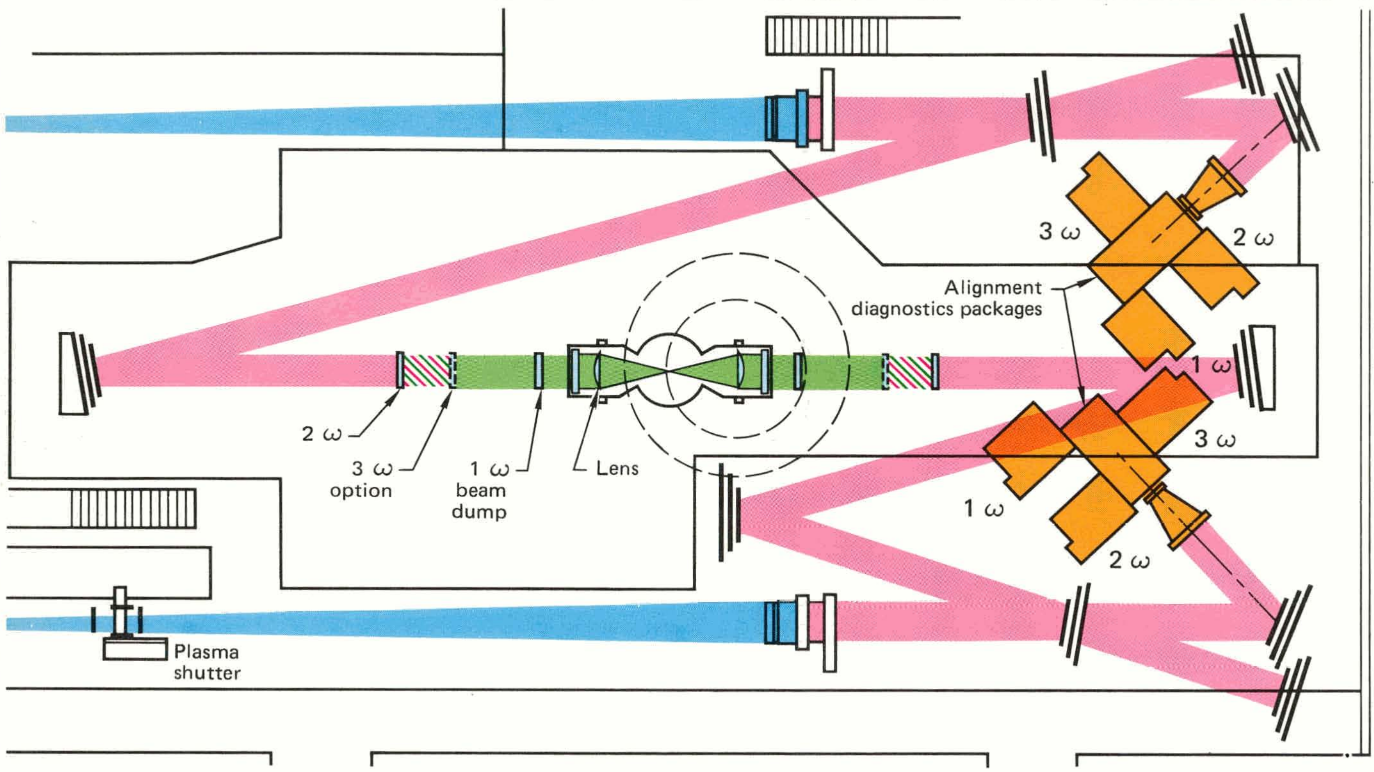

Fig. 2-47. Schematic ▲ plan of the north target area in the east end of the Building 381 high bay.

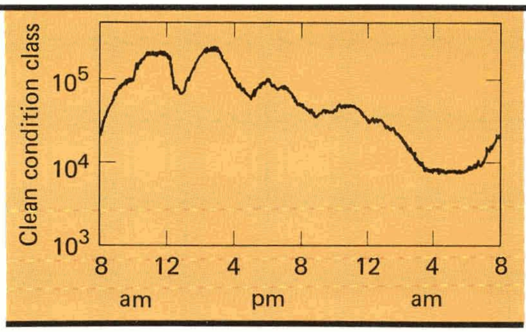

Fig. 2-48. Plot of a 24-hour particulate count taken in the center of the laser room 5 ft above the floor.

chamber will use the space in the center of the bay between the beam lines (Fig. 2-47). The laser-output spatial filters, the first turning mirrors, the beam-diagnostic mirrors, and the alignment/diagnostics packages will be at the same height as the laser chains (4.5 ft). To provide space for long target-diagnostic lines of sight and to prevent overcrowding of the target-area floor, the final turning mirrors and target chamber will be at a height of 12 ft. To simplify the wavelength conversion and the design of the thin-film coatings on the turning mirrors, the KDP crystals for frequency conversion will be located between the final turning mirrors and the target chamber.

Figure 2-47 illustrates the target-bay beam lines, showing both the crystal-array configuration used for frequency doubling and the required auxiliary optics. Adequate space is provided for adding a second crystal in each beam for frequency tripling. The target chamber and its auxiliary equipment will be taken from Shiva and modified to provide horizontal mounting and to accommodate the focusing optics for the two large-diameter Novette beams. The vacuum system for the chamber will be the basic Shiva system, with the forepumps located outside the high bay, as shown in Fig. 2-43. Catwalks will provide access to the upper-level beam-line components, the target chamber, and the target diagnostics mounted around the chamber waist.

The planned installation of Novette in the Building 381 high bay caused us to reevaluate the dust and particulate level in that room. The high bay has an area of 12 000 ft^2 and is 28 ft high. Currently, air is delivered to a plenum above the false ceiling, diffused into the bay through holes in the ceiling panels, and removed from the bay at floor level along the north and south walls. The circulated and makeup air is filtered with 95% filters, i.e., filters that remove 95% of particles 5 μm or larger.

Prior to the January 1980 earthquake, the room operated between class 100 000 and class 10 000 clean condition. After the earthquake, the structural integrity of the ceiling was restored, but the air distribution system was not. A particle count taken at the end of 1980 is shown in Fig. 2-48. Contaminant samples recently taken from the surfaces of the Argus laser components indicate that the contaminants are predominantly earth (clays), clothing fibers, and acoustic-tile particles (the walls and one-half of the ceiling are covered with conventional sound-absorbing tiles). The floor is covered with a carpet selected for its low shedding property; no carpet fibers were present in the contaminant samples.

We desire that the Novette laser operate in an environment significantly cleaner than class 10 000—approaching, if possible, class 1000, which appears to be the practical limit for upgrading this room within reasonable cost constraints. To achieve this clean condition, we will use high-efficiency particle air (HEPA) filters as the primary air filter, remove the ceiling acoustical tiles, improve entries into the bay, seal the wall tiles, and significantly clean up the bay surfaces. The HEPA filter modules will be located at strategic points along the laser; they will lower the contaminant level of the laser-bay air and provide localized class 1000 clean conditions at the critical laser components. This solution provides the clean environment necessary for the laser, easy working access to components, and low initial and operational costs.

Authors: D. R. Speck and H. G. Patton

Major Contributors; C. E. Thompson, P. R. Rupert, C. A. Hurley, J. R. Braucht, and S. J. Brajkovich

Nova

Introduction

The Nova project will provide the next logical increase in laser energy over the currently operating 10-kJ Shiva system and will be the primary laser inertial-confinement-fusion (ICF) experimental facility in the mid-1980s. The energy levels and proposed wavelength flexibility will allow us to improve our understanding of ICF physics absorption mechanisms and implosion processes and to define target physics for advanced laser drivers under development. The primary programmatic objective is to demonstrate the ignition of thermonuclear burn as a step toward demonstrating the feasibility of ICF fusion.

The full Nova laser will consist of 20 beams capable of concentrating 200 to 300 kJ of energy (in 3 ns) and 200 to 300 TW of power (in 100 ps) on experimental targets by the mid-1980s.

The first phase of the Nova project involves construction of a 5 500-m^2 (59 000 ft^2) office building, a 10 700-m^2 (115 000 ft^2) laboratory building and installation of a 10-beam Nd:glass laser system adjacent to the existing Shiva facility (see Fig. 2-49). During Phase II, an additional 10 Nova beams will be installed in the Shiva building. The full Nova complement of 20 beams will be brought to an integrated target chamber in two opposed clusters of 10 beams each. Other target configurations are possible if required.

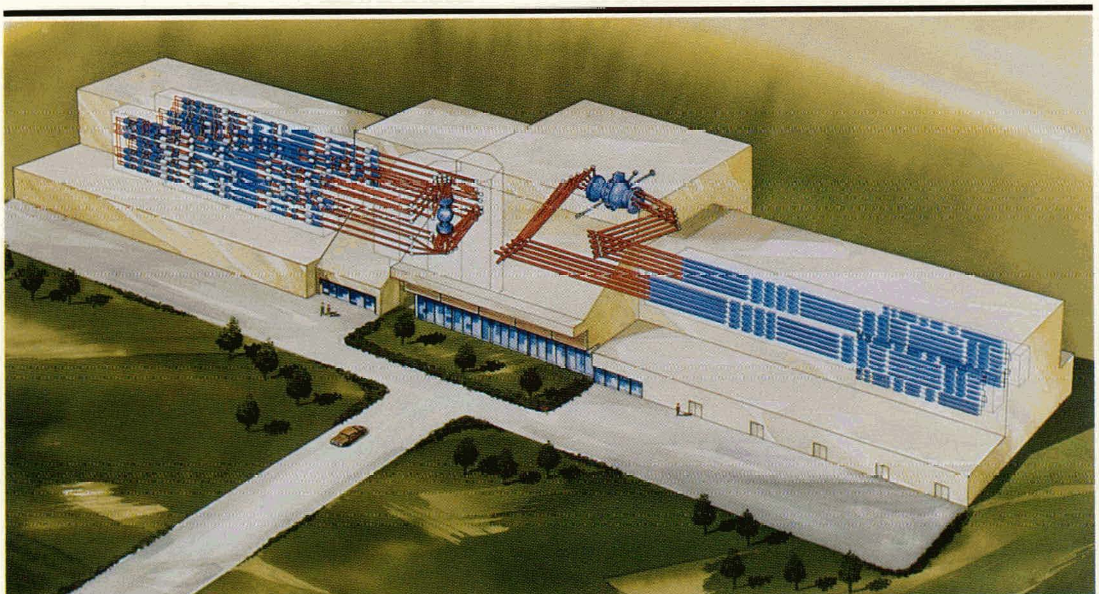

Fig. 2-49. Artist's concept of 10-beam Nova I laser system (right) installed adjacent to the Shiva laser system (left).

Although Nova was authorized by Congress at $195M, we learned in January 1980 that the Presidential Budget request for FY81 did not contain any funding for the Nova Project. Since our Phase I plan, authorized by DOE in FY80, was based on an appropriation of $43M, we were forced to prepare for significant changes in our procurement activities. We were hopeful that Congress would decide to continue to fund the Nova Project through FY81, but we were not sure of the revised funding level until midyear. Therefore, we developed a cost plan that would allow the project to survive without a FY81 appropriation and that would minimize the cost and schedule impact.

This zero-budget plan entailed completing the design and construction of the two buildings as originally planned, completing the laser design at a slightly lower rate, completing all awarded laser contracts, and retaining project staff until FY82. This plan would enable us to use FY81 funds if they were authorized by Congress. Fortunately, by midyear the House Appropriations Committee had recommended that Nova receive $25M in FY81, and this, in fact, occurred. However, as a result of the funding uncertainty and the lower funding level, Phase I completion is now scheduled for the third quarter of FY83 at a cost of $140M.

The past year was an intensive design and construction period for the conventional construction portion of the project. We awarded the remaining $17.5M in construction contracts for both the laboratory building and the office building. The laboratory building has progressed to a fully enclosed structure that is, at present, 66% complete. The office building went from concrete footings to the steel and concrete frame structure shown in Fig. 2-50.

By proceeding with completion of the buildings as rapidly as possible, we ensured that the conventional construction items (which are frequently subject to problems of weather, high inflation, labor disputes, etc.) would not delay completion of the project. We expect both buildings to be complete at the end of 1981.

In spite of the funding uncertainty, considerable progress was made on the laser design and procurement of long-lead components. The baseline chain, described more fully in "Laser System Design and Performance" (see next article), was solidified and accepted for controlled-change documentation. We initiated procurement of all the optical components except for the laser glass, which was under intensive development by three vendors. The preproduction development of fluorophosphate laser glass was not successful within the required time frame. Therefore, we made the decision to switch to a phosphate laser glass and have now initiated preproduction efforts with two suppliers.

While phosphate glass possesses a higher nonlinear refractive index than fluorophosphate glass, it is significantly less expensive and has been manufactured in the large sizes and to the high optical quality specifications required for Nova. These features make it the material of choice. Further discussion of glass manufacturability and figures of merit are contained in "Nova Optical Components" later in this section.

Laser Engineering progress in 1980 further encompassed

- Solidification of subsystem and component criteria through a formalized design review process (see "Project Management Systems").
- Establishment of engineering development and test facilities for central controls and for pulse-power-conditioning subsystems ("Controls" and "Power Conditioning," respectively).
- Prototype Nova component/subsystem testing in each facility ("Power Conditioning" and "Controls," respectively).

Finally, prototype test and evaluation continues, aimed at:

- Achievement of higher-fluence damage thresholds on production component surfaces (see "Damage Studies").
- Demonstration of a working, system-compatible plasma shutter for chain protection against target back reflections (see "Plasma Shutter").
- Evaluation of YLF and a thermal glass (Kiger Q-100) for high-repetition-rate preamplifier and alignment applications on Nova (see "Oscillator Development").

The remaining laser subsystems are in various stages of final design and limited procurement activities, as described in subsequent portions of this section.

A total of $12.5M of laser contracts was awarded this year. We completed development of our management system for cost and schedule (see "Project Management Systems").

The project scope is now under review by DOE to determine whether Phase II will be completed concurrently with Phase I and whether 2ω and 3ω frequency conversion is to be added to the system for higher target performance. The cost and schedule for the full project with frequency-conversion enhancement depends on the timing of the DOE decision and by projected funding rates at that time.

In addition to laser performance, the system criteria are

- That the system fit comfortably and snugly within the planned laboratory building now under construction. Figure 2-51 shows an artist's concept of the Nova laser system overlaid with the Shiva and Nova laboratory building. This requirement is met, as shown in subsequent portions of this section.
- That the primary target-irradiation geometry consist of two opposed, open-cone beam clusters, each converging on the target location.

Figure 2-184 (see "Target System" later in this section) is an artist's concept of the Nova target chamber. The west beams are equally spaced in angle on the surface of a cone whose vertex is at the target. These beams are opposed by the east beams so that east and west beams radiate through a coordinate system centered at the target. The space frame allows the cone angle to be varied from 80 to 100°, if required, for various experimental target designs (such variation would entail significant "down" time of the laser system itself while components were being moved). The initial choice of cone angle is 100°, and this choice represents the Nova baseline configuration.

Figure 2-183 (see "Target System" later in this section) also shows some of the ancillary target-event diagnostic systems. This configuration will allow for a full complement of experimental and diagnostic instruments. The insert line drawing illustrates design criteria for the overlap of Nova beams at a representative target. In the (common) focal plane, the beam-overlap spot is not expected to exceed 150 μm in diameter, including allowances for alignment, positioning, and verification tolerances. This criterion applies for a

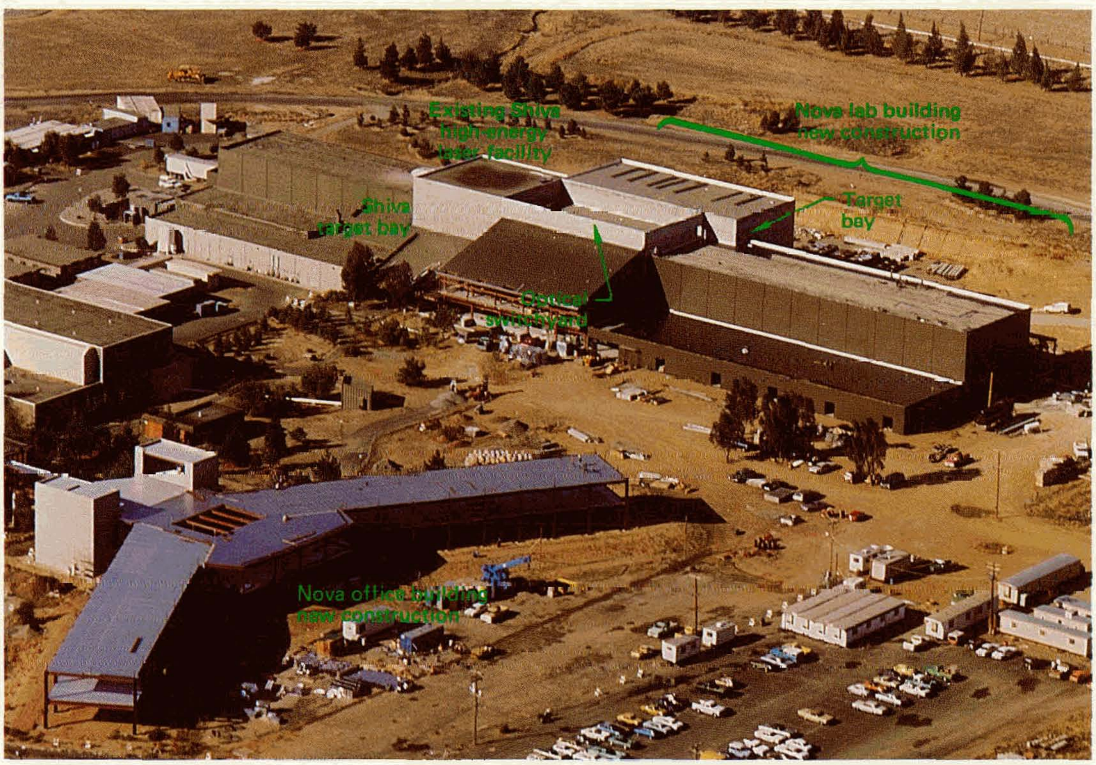

Fig. 2-50. Aerial photograph of Nova construction site, showing status as of November 17, 1980.

baseline focal length of 2.25 m (f/3 target-focusing optics). Further target-system descriptions will be presented in "Target Systems."

- That the Nova laser system be designed with the flexibility required to incorporate future modifications as they become feasible and desirable. Two such modifications are discussed next.

In recent experiments on the Argus laser system, we have demonstrated that, by using the nonlinear optical properties of potassium dihydrogen phosphate (KDP) crystals, we can double or triple the frequency of the basic 1.05-μm wavelength from high-power Nd:glass lasers with efficiencies exceeding 70%. Since shorter wavelengths are much more favorable for ICF laser-target physics, we have proposed to implement this option in the Nova facility. (This enhancement of the Nova facility is presently under review by DOE and will be determined shortly.) If approved, we would be able to focus approximately 200 kJ of green (0.53 μm) or blue (0.35 μm) light onto laser fusion targets.

The energy from Nova, particularly if it is at the shorter wavelengths, should be capable of producing the extremes of temperature and pressure required to ignite a small pellet of thermonuclear fuel. That is, it should create conditions such that the 3.5-MeV alpha particles released by the D–T reaction in the central core of the compressed fuel are trapped in the compressed fuel and used to further heat the fuel.

Also, space has been allocated within the Nova baseline chain layout (Fig. 2-54 of "Baseline Chain Layout") to add additional amplifiers in both the penultimate 31.5-cm amplifier stage and the final 46-cm amplifier stage. It is possible that advanced Nova targets will require higher energy pulses of longer duration than those presently contemplated. Additionally, future experiments on Nova call for temporally shaped pulses which, in turn, will also require amplifiers with reserves of both power and energy capability. In either situation, the additional amplifiers will be required.

Space also exists in the laser bay for additional (but smaller) amplifier chains, as adjuncts for extended target diagnostics.

Summary. The first phase of the Nova Project is well under way. The buildings are more than 50% complete, the laser is in the final detail-design phase, and many long-lead laser components have been ordered. Our laser calculations indicate the system will perform at the upper end of the predicted performance range. We are preparing to incorporate frequency doubling and tripling into the laser system. Subject to DOE approval, we will proceed with Phase II and add frequency conversion.

Authors: R. O. Godwin and W. W. Simmons

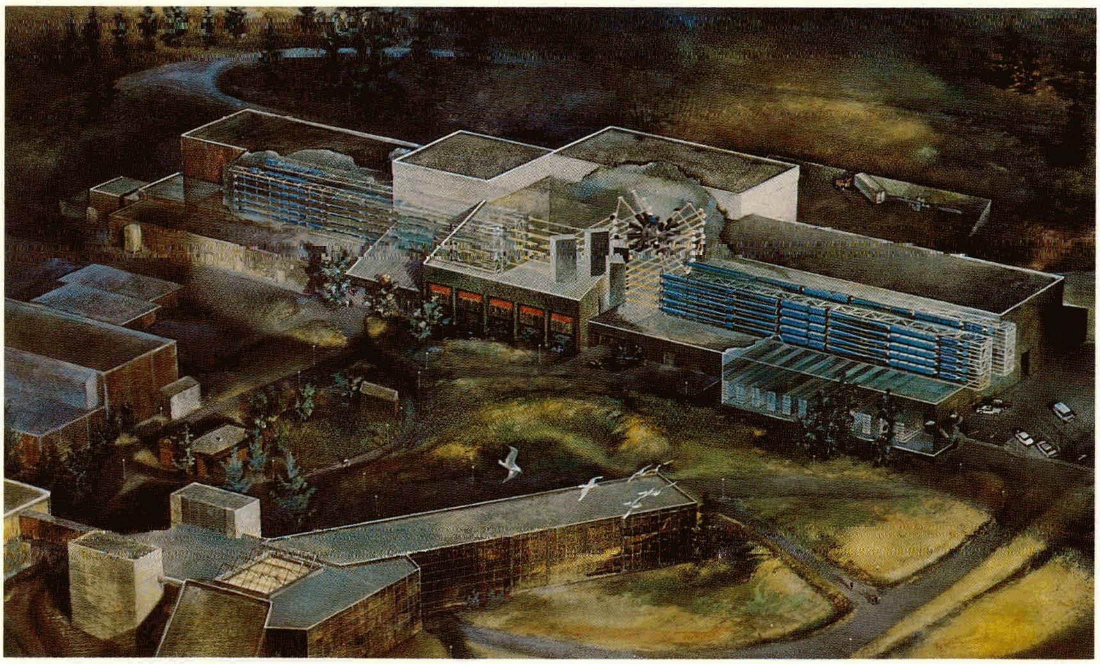

Fig. 2-51. Artist's concept of 20-beam Nova laser system overlaid with Shiva/Nova laboratory building.

Nova Laser System Design and Performance

Design Considerations. We have designed the Nova laser system with master-oscillator-power-amplifier (MOPA) architecture. As shown in Fig. 2-52, a laser pulse of controlled temporal shape is generated by the oscillator, preamplified, and split into 20 beams (10 beams in Phase I). After traversing an adjustable optical-delay path (used to synchronize the arrival of the various beams at the target), the pulse enters the amplifier chain. This chain consists of (1) a rod amplifier and several disk amplifiers to increase the pulse power and energy, (2) spatial filters to maintain the spatial smoothness of the beam profile while expanding its diameter, (3) Faraday and Pockels isolators to prevent the entire laser from breaking spontaneously into oscillations that could drain its stored energy and damage the target prematurely, and (4) a plasma shutter, located at the focus of the last spatial filter to protect the laser chain from target back reflection.

The beam is collimated between spatial filters in the laser chain. Thus, each of the components in a particular section has the same diameter. In the 4.0-cm-diam section, the amplifier is a single glass rod, and the isolator is an electro-optic (Pockels) cell crystal placed between crossed polarizers. This cell operates as a fast (10 ns) optical gate, preventing interchain oscillations and, at the same time, reducing to tolerable levels unwanted amplified spontaneous emission (i.e., radiation due to passage of spontaneous decay photons through the chain, which can strike and damage the target before the laser pulse arrives). In all larger-diameter sections, the amplifiers consist of face-pumped disks set at Brewster's angle to the passing beam. In Table 2-18, we summarize the energy-storage and gain characteristics of the various Nova amplifiers when phosphate glass is employed. Polarization-rotating Faraday isolators assure interchain isolation. We will realize substantial savings by reusing most Shiva laser components up to 21 cm in diameter in Nova.

We have optimally designed our spatial filters to provide entrance-lens-to-entrance-lens imaging. Thus, smooth beam intensity (through the cross-sectional area) is projected along the chain, and energy extraction by the laser pulse is maximized. The beam has a fill factor of more than 70%

Table 2-18. Parameters of Nova phosphate disks amplifiers.

Clear aperture (mm)	94	150	208	315	460
Disk thickness (mm)	24	30	25	43	43
Disks/module	6	4	3	2	2 (split)
Small-signal gain/module	7.4	4.2	2.3	1.78	1.93
Specific gain (cm^{-1})	0.113	0.100	0.093	0.056	0.062
Stored energy density (J/l)	530	470	440	260	290
Glass volume/module (l)	2.26	4.5	5.3	14	28
Bank energy/module (kJ)	144	216	200 (288 (Shiva)	375	600
αD	2.2	3.0	3.8	3.5	3.2

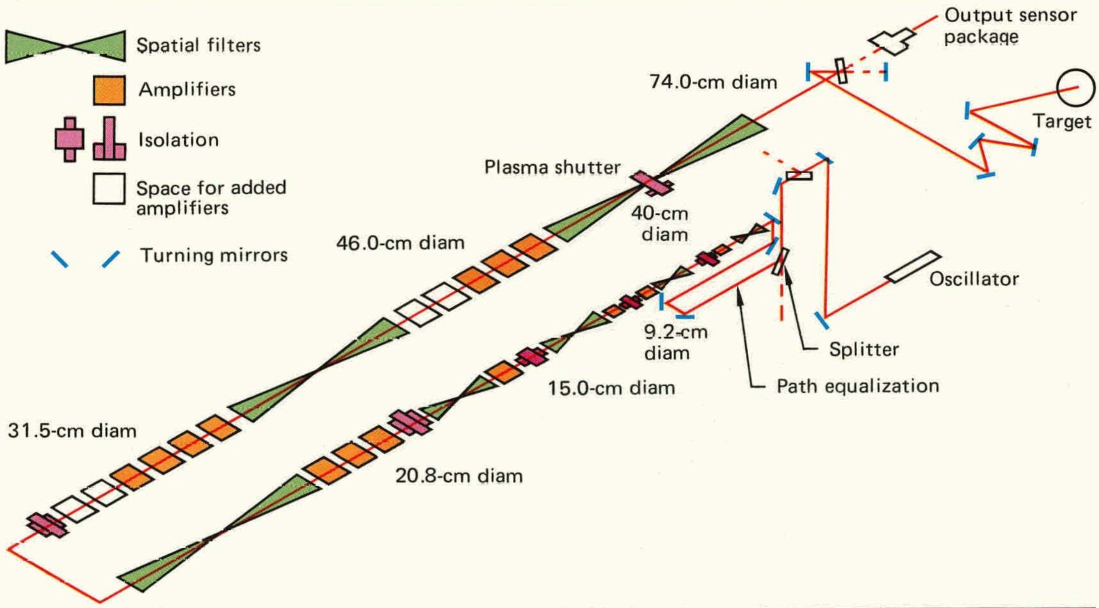

Fig. 2-52. Schematic diagram of major Nova optical components.

(defined as the ratio of the beam energy to the energy in a flat beam of the same maximum intensity). Pinholes (located at the spatial-filter focal planes) are large enough to avoid self-closure (due to the ablation of material forming the pinhole edge) during the passage of the pulse.

When the pulse exits from the final beam-expanding spatial filter, it has been amplified to an energy level of 10 to 15 kJ, and its diameter is 74 cm. Turning mirrors direct the beam to the target chamber, where focusing lenses concentrate it on the target. The first of the turning mirrors is partially transparent, allowing approximately 2% of the pulse to enter the output-sensor package. This unit senses and reports on the alignment status, energy and power, spatial quality, and other characteristics of the beam. The plasma shutter, located at the focal position of the final spatial filter, protects the laser by preventing light reflected from the target from reaching the laser amplifiers. In the absence of this protection, such light would travel back down the chain (being amplified in the process) and might destroy some of the optical components.

Table 2-19. Surface-damage thresholds for AR-coated and uncoated optical surfaces.▼

	Damage threshold, J/cm^2		
"A" fluence (median of conventional surfaces) (ns)	0.1	1.0	3.0
Coated surfaces	1.6	5	5.5
Bare polished surfaces	5.1	16	28
"B" fluence (upper 30% of conventionally manufactured surfaces) (ns)	0.1	1.0	3.0
Coated surfaces	2.5	8	8.5
Bare polished surfaces	6	19	33
Graded index surfaces	—	12	—

Characteristics	Silicates	Phosphates	Fluorophosphates
n^2/n_2 (disk amps) (relative)	1.0	1.4	2.3
σ (typ.) ($\times$ 10^{20} cm^2)	2.7	4.0	2.5
E_s (J/cm^2)	4-5	3.8-4.5	4.6-5.5
	Nova specifications		
Attenuation (cm^{-1})	0.0015		
Homogeneity	$\pm 1 \times 10^{-6}$		
Damage fluence (J/cm^2)	35		
Small scattering-site density	5×10^{-5} cm^2/cm^2 of equivalent surface. No sites larger than 0.5 mm.		

Table 2-20. Relative▲ material properties for phosphate, fluorophosphate, and silicate glasses.

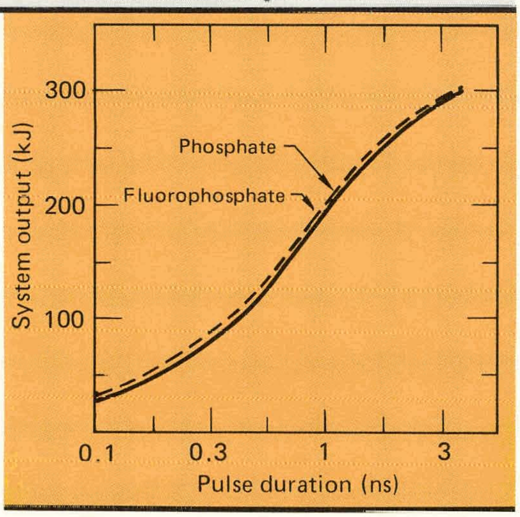

Fig. 2-53. Twenty-beam optimized Nova system output, as a function of pulse duration, for phosphate and fluorophosphate glass amplifiers.

Damage-to-Optics Considerations. In each section, the beam is amplified to near the lens-damage threshold for maximum energy output at a specified pulse duration. This "isofluence" design maximizes the energy output per unit cost while keeping the chain, as a whole, below the component-damage limit. The fluence (energy per unit area) at which optical components suffer damage has been the subject of intense investigation and improvement. On the basis of extensive measurements, we have established numerical damage thresholds for components representative of current surface-preparation technology (Table 2-19). It is apparent that uncoated surfaces will tolerate higher fluences than will antireflection-coated (AR-coated) surfaces. Thus, spatial-filter input lenses, which are subject to the highest fluence, are left uncoated in the Nova design. However, to allow for the possibility that graded-index technology can achieve damage thresholds comparable with bare surfaces, we have specified use of phase-separated glass for the spatial-filter entrance lens material.

Glass Properties. Table 2-20 illustrates relative material properties of significance for phosphate, fluorophosphate, and silicate glasses. Phosphate-based glass features very high intrinsic gain due to its high cross section σ, as well as sufficient energy-storage capacity (proportional to the saturation fluence E) for the realization of Nova laser performance goals. Further, it has proven to be manufacturable in large sizes to Nova specifications of optical quality and damage resistance. Fluorophosphate glass has a lower, more-desirable nonlinear refractive index (proportional to n_2). For that reason, it is capable of performance somewhat superior to that of phosphate. Optimal chain design minimizes this performance advantage. Comparative performance of the baseline chain, using phosphate or fluorophosphate, amounts to a 5 to 10% advantage for fluorophosphate, as shown in

Fig. 2-53. Fluorophosphate has not proven to be manufacturable to Nova specifications in large pieces. We have, therefore, selected phosphate as the Nova laser amplifier material.

Baseline-Chain Layout. The layout of one Nova baseline chain is shown in Fig. 2-54. In general architecture, it resembles the chain layout presented in the 1979 Laser Program Annual Report.[30] The significant changes are twofold: all disk amplifiers now feature phosphate glass; in addition, the final thickness of the amplifier disk has been increased (from 38 to 43 mm). This change gives increased energy performance at longer pulse durations for a slight penalty (~5%) for pulses shorter than 1 ns.

We have taken ghost foci into account in laying out the baseline chain (Fig. 2-54; also see "Nova Optical Components"), locating components near spatial-filter lenses to avoid the occurrence of such foci within any glass material. Also, the uncoated entrance lenses of the high-power filters are of meniscus design to help minimize the effect of these foci.

Baseline Performance (Figs. 2-55 to 2-57). Full-system simulations using our comprehensive modeling code (MALAPROP) have resulted in the performance profiles shown in Fig. 2-57. These figures plot peak and mean beam fluence as a function of distance along the chain for several pulse durations spanning the range of interest to Nova design. Locations of the spatial-filter lenses are indicated by "bowties" at the top of the figure. On-target energy for the indicated pulse duration is inset. "B"-fluence thresholds (Table 2-19) for coated and uncoated lenses are shown as dashed lines. Average beam fluences are represented by dots. In each case, the calculations were done at that performance level representing the onset of damage.

At the shortest pulse durations, we observed a striking growth of the peak-to-average ratio throughout the beam-transport space between the final spatial filter and the target-focusing optics. This is a manifestation of self-focusing attributed to the nonlinear index of the glass in the laser chain and of the nitrogen in the 50-m air path through which the beam is passing.

As the pulse duration increases, beam intensity decreases and this nonlinear effect

Fig. 2-54. Optical schematic of one Nova amplifier chain.

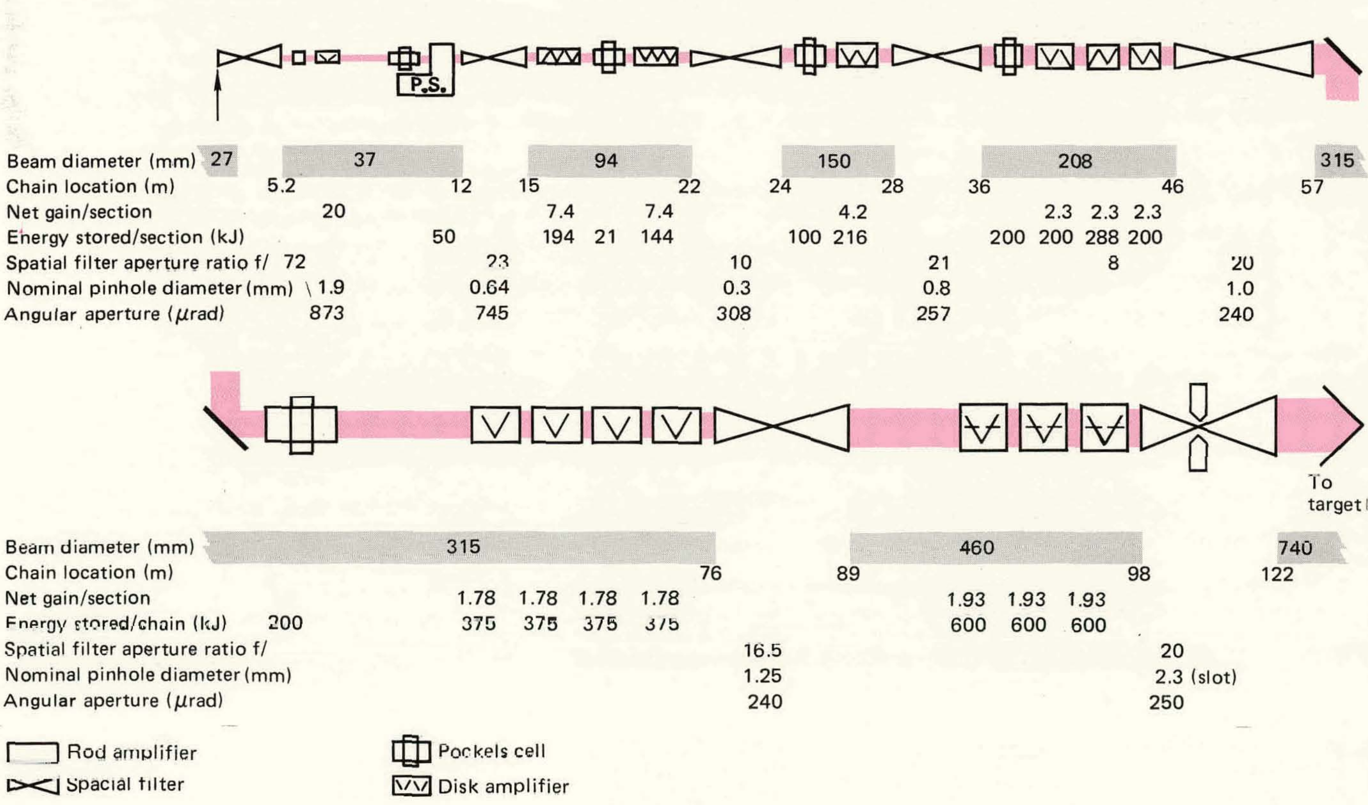

dies away. In fact, the most-threatened component becomes the (uncoated) final spatial-filter entrance lens for a 1-ns pulse. At the longest (3 ns) pulse duration, the chain is running under "isofluence" conditions. The beam extracts 50% of the stored energy in the final 46-cm amplifier.

Fig. 2-55. Performance limits over the temporal design range of Nova (0.1 to 3 ns).

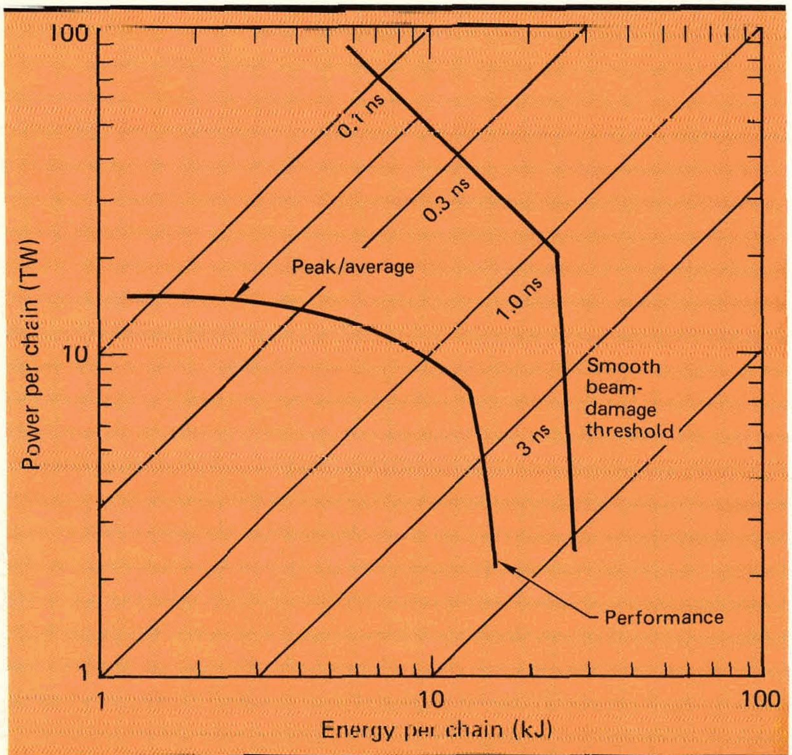

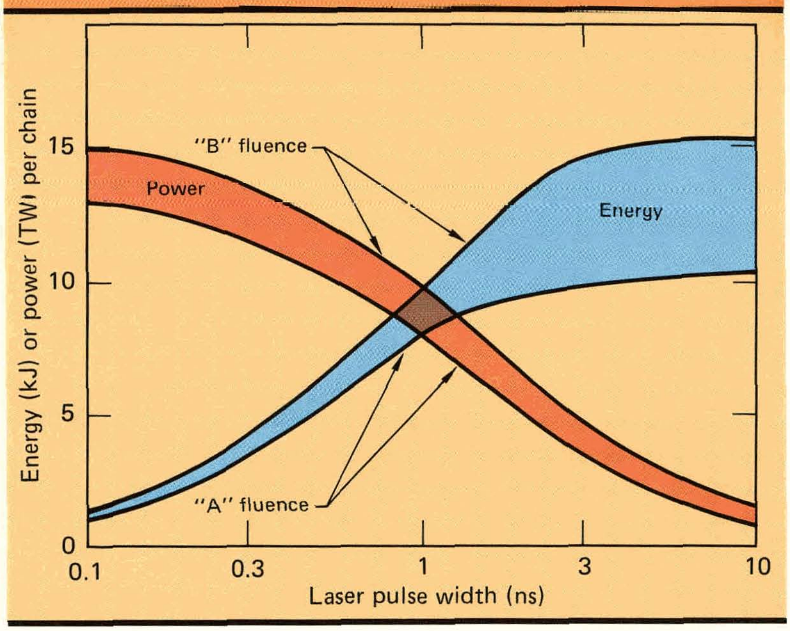

Fig. 2-56. Energy and power per Nova chain as function of pulse duration for "A" and "B" fluence limits.

When damage fluence levels become higher, we can add additional amplifiers in the final stages to reach higher energy outputs.

These baseline-chain performance estimates are summarized in Fig. 2-55, which illustrates the "safe" performance region for one Nova chain. If the beam were perfectly smooth spatially, and if it filled 70% of the available amplifier aperture, the laser could be operated at points indicated along the upper curve. However, small component imperfections introduce modulation on the beam. Thus the laser can only be operated without beam damage to components at or below the performance curve, which is determined by dividing the upper curve by the peak/average ratio. The range of

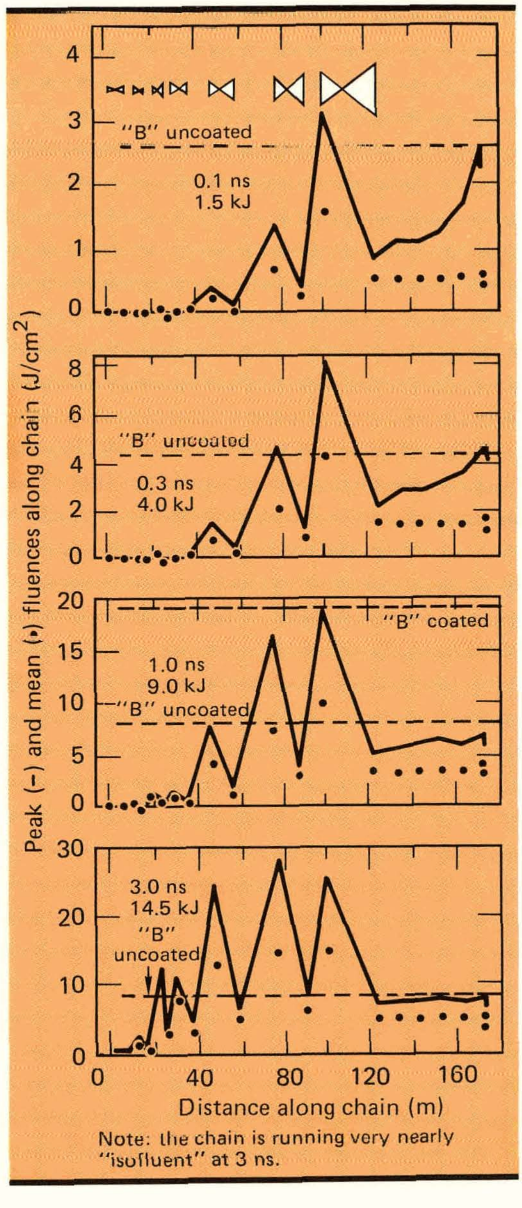

Fig. 2-57. Performance profiles of one Nova chain for four pulse durations. ▶

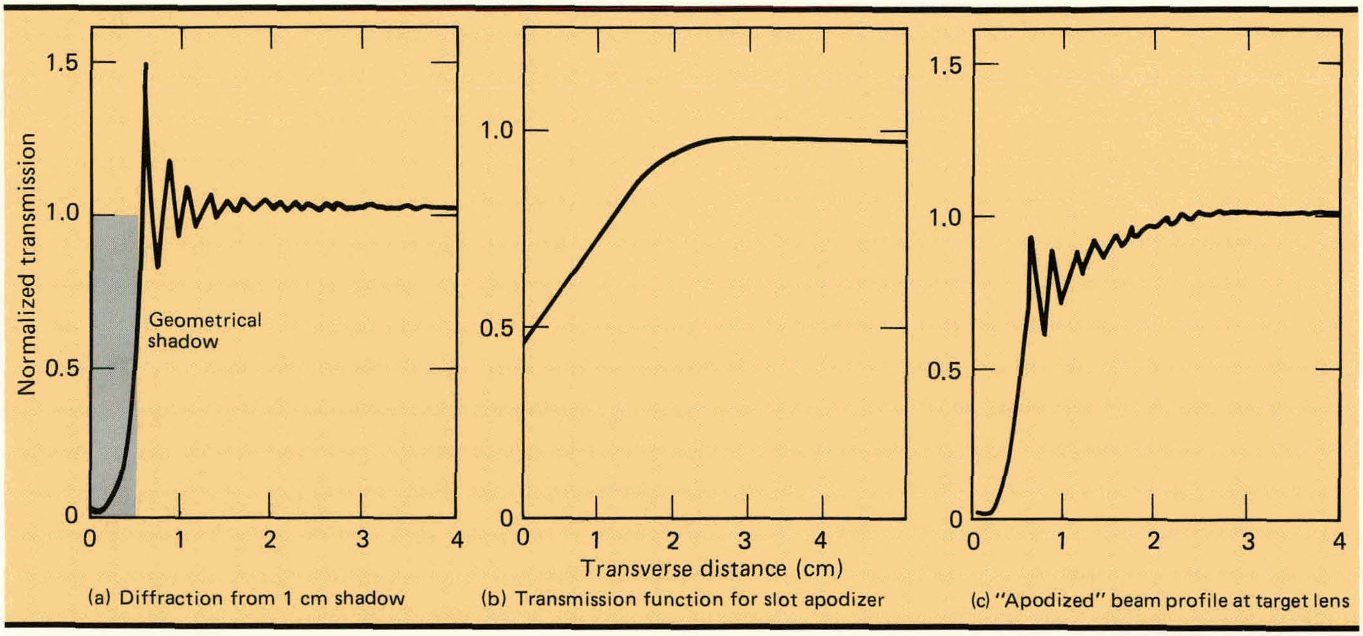

Fig. 2-58. Straight-edge diffraction ripple is reduced by apodization.

performance expected between "A" and "B" fluence limits is shown in Fig. 2-56.

Apodization. We have employed disks split along their minor axes in the 46-cm amplifiers to realize greater energy storage and gain from these units. Consequently, when a split beam is propagated through a spatial filter and over a 50-m distance to the target-focusing optics, the edges of the split evolve through diffraction to produce a significant peak fluence at the target optics.[30] When the edge of the shadow is modified through apodization, this ripple growth is reduced to tolerable limits. The principle involved is shown in Fig. 2-58. Diffraction from a hard-edged slot in the beam produces modulation and a high peak–average ratio [Fig. 2-58(a)]. When the beam is passed through an absorbing element of transmission characteristic [Fig. 2-58(b)], the output beam [Fig. 2-58(c)] exhibits reduced modulation, and the peak–average ratio at the geometrical slot shadow is reduced to a "safe" level. We have incorporated such an apodizing element into the baseline chain (as shown in Fig. 2-52), and prototype apodizing plates to prove the concept are on order. We have further found that overall system performance is unaffected by replacement of the (round) pinhole in the final spatial filter by a one-dimensional slit. These changes have been incorporated in the baseline performance calculations summarized above.

Author: W. W. Simmons

Master Oscillator/Preamplifier. The master-oscillator room (MOR) for Nova will be a complete independent laser subsystem capable of delivering pulse energies to the damage limit of its 5-cm output amplifiers. In addition to initial pulse formation, the MOR will provide all the gain variation, temporal and spatial shaping, and prepulse discrimination for the entire Nova system. It will be located beneath the optical switchyard and will be isolated electrically from the rest of the laser system. To minimize the threat of damage to its optics from airborne particles, it will be a Class 10 000 clean room (less than 10^4 particles larger than 0.5 μm per cubic foot of air). The control system for the MOR will be totally separable from the main control room to allow setup and maintenance to proceed independently from the rest of the laser.

The changes made last year in the MOR design increased its total gain and the amount of high-shot-rate energy available for alignment tasks. Also, we established a grounding strategy within the MOR to isolate the oscillator controls and fast-timing generators from electrical transients at shot time.

Figure 2-59 shows our current MOR layout. The major changes made are the additional gain-10, 1-cm clear aperture, high-shot-rate preamplifier and an optional beam path on the north table that has the effect of bypassing the apodizer. These changes increase the high-shot-rate pulse energy available at the MOR output from

0.30 to 30 mJ at 100-ps pulsewidths. With Nd:YLF preamplifiers, the corresponding shot rate could be as high as 10 Hz (see "Thermal Lensing in Nd:YLF"). The additional preamplifier also allows the MOR output fluence (without the bypass) to reach damage levels over the full range of pulse widths available. Should additional drive be required, we are providing space in the splitter array (see "Beam Splitter Array") for an additional 5-cm rod amplifier and isolator.

The following aspects of last year's layout have been retained:

- Completely relayed beam lines from the output of either oscillator to the input of the splitter array.
- Two alignment systems for automatic alignment of either pulsed oscillator or the cw alignment laser to the preamplifier beam line and of the preamplifier beam line itself to the laser.
- Rotatable waveplates followed by polarizers for all gain adjustment, allowing the amplifiers to be operated at a fixed gain.
- An alternate injection point for the alignment laser to provide a backup for the alignment lasers located in the laser bays.
- Room for the future addition of an oscillator, a regenerative compressor, and an identical preamplifier chain to provide a diagnostic-pulse capability. These components are shown dashed in Fig. 2-59.
- Location of as much gain as possible ahead of the apodizer to minimize ASE at the target.
- Expansion space on the central table for temporal pulse shaping.

We designed the MOR grounding scheme shown in Fig. 2-60 to minimize noise problems from the Pockels cell drivers and the rod amplifiers. The MOR contains a single point ground to which all grounds in the room converge. This ground point is connected to local building ground and the outside world through a ground-fault monitor similar to those presently used on Shiva. Any current flow in that monitored leg (other than that from capacitance to

Fig. 2-59. Layout of Nova master-oscillator room, with optional beam line to effectively bypass apodizer, and additional high-shot-rate amplifier.

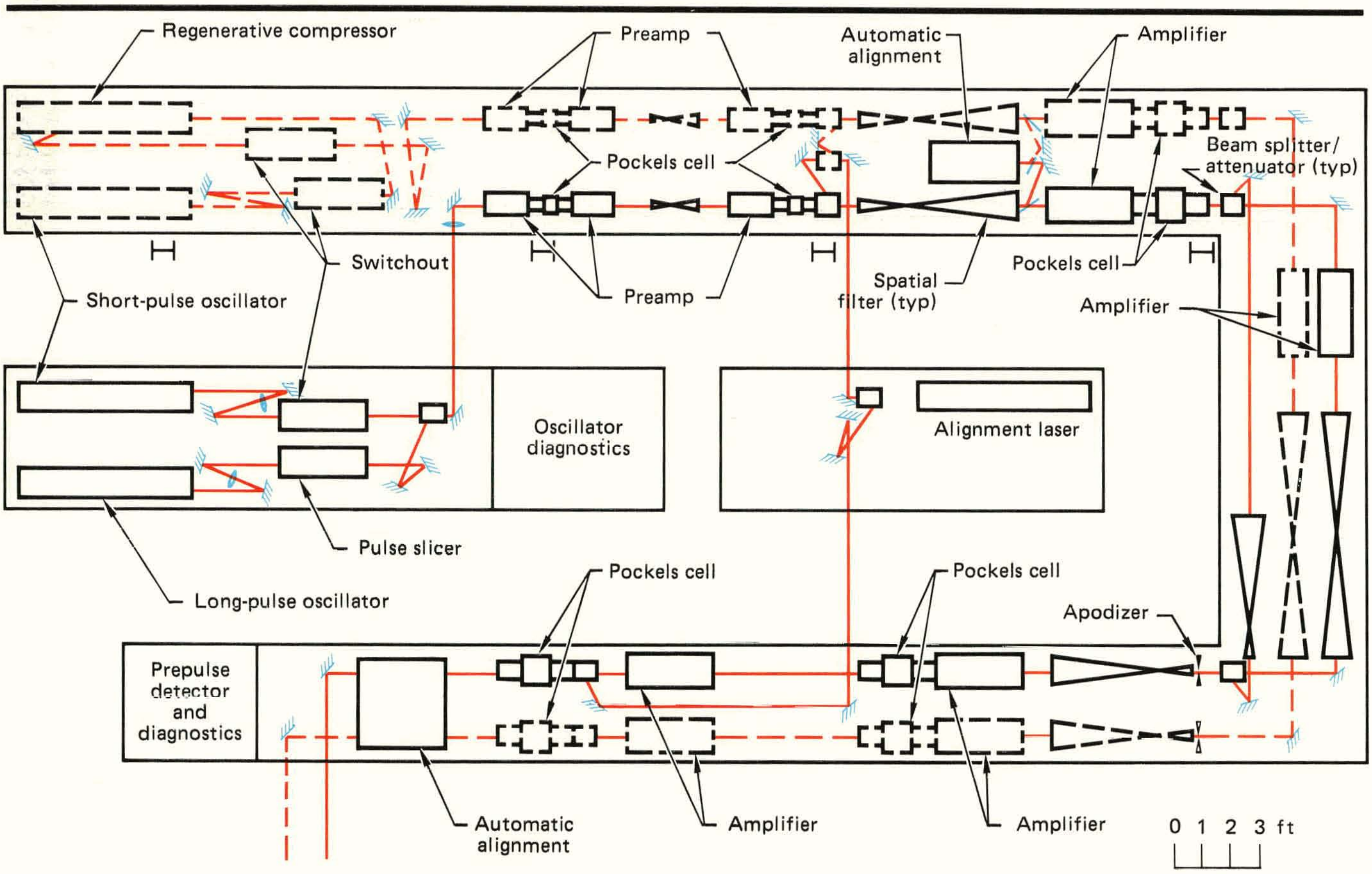

isolation transformer shields) is indicative of undesirable electrical connection to the outside world.

This scheme is made effective by the use of extensive fiber optics to electrically isolate control and monitor signals and by the employment of isolation transformers to separate ac mains grounds. To ensure the star grounding system shown, we provided multiple isolation transformers to eliminate a separate ground net made up of mains ground wires.

Further discussion of oscillator controls and fast timing is contained in "Oscillator Control and Pulse-Distribution System." Development of the planar triode Pockels cell drivers to be used in the Nova MOR is discussed in "Fast Pulse Development."

Authors: J. E. Murray and J. A. Oicles

Major Contributor: D. J. Kuizenga

Beam-Splitter Array. Our design for the Nova beam-splitter array includes beam transport from the MOR to the chain inputs, the optics necessary to divide the MOR output 20 times, space for additional amplifiers after the first four splits, separate cw alignment lasers for the east and west laser bays, and sufficient automatic alignment hardware to keep the entire array aligned. Figure 2-61 shows the beam paths from the MOR to each of the 20 chains.

Fig. 2-60. Grounding scheme for Nova master-oscillator room.

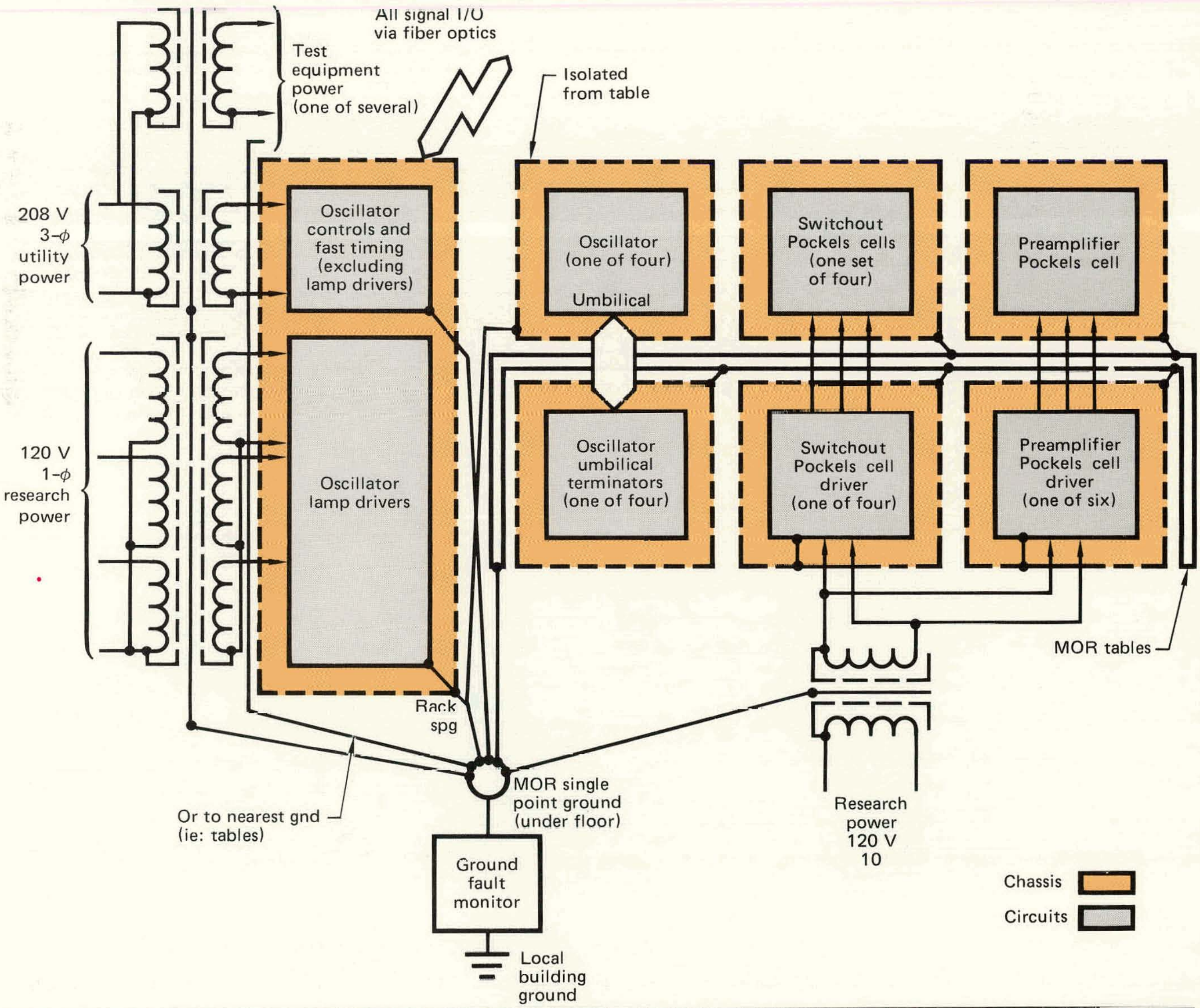

A major change from Shiva is our use of adjustable splitters rather than fixed, partially reflecting optics. A rotatable $\lambda/2$ waveplate ahead of a thin-film polarizer allows the split ratio at the polarizer to be adjusted without sacrificing pulse energy. For example, all the high-shot-rate MOR output energy can be directed to a single chain to maximize the pulse energy available for alignment of its harmonic arrays. Additionally, the adjustable splitters allow gain variations of the individual chains to be accommodated without wasting drive energy. The reflection–transmission ratio at each splitter will be computer controlled so that updates of the settings for target shots can be made automatically, based on the conditions and yields of any previous shot.

Author: J. E. Murray

Major Contributors: E. S. Bliss and G. S. Bradley

Nova Laser Chain—Components

Each laser chain is a series of amplifier stages, with a maximum amplifier aperture of 46 cm. Spatial filters between the amplifier stages provide for filtering, relaying, and beam expanding. Faraday rotators, Pockels cells, and plasma shutters protect the optical surfaces from back reflections and subsequent damage. The following paragraphs describe the engineering features of the components that make up each laser chain.

Disk Amplifiers. Amplifier design was described in detail in the 1979 Laser Annual Report.[31] This design was based on research and development that led to the 34-cm prototype box amplifier and to the first engineering layout for the three sizes of box amplifiers. Since that report was written, we have completed the mechanical design for two sizes of box amplifiers, namely 20.8 and 31.5 cm. We also have a complete design for a 5-cm rod amplifier. A prototype 46-cm

Fig. 2-61. Layout of Nova beam-splitter array, showing beamline from MOR through optical switchyard and into east and west laser bays. Space frames and beam-transport components for 20 laser chains are not shown.

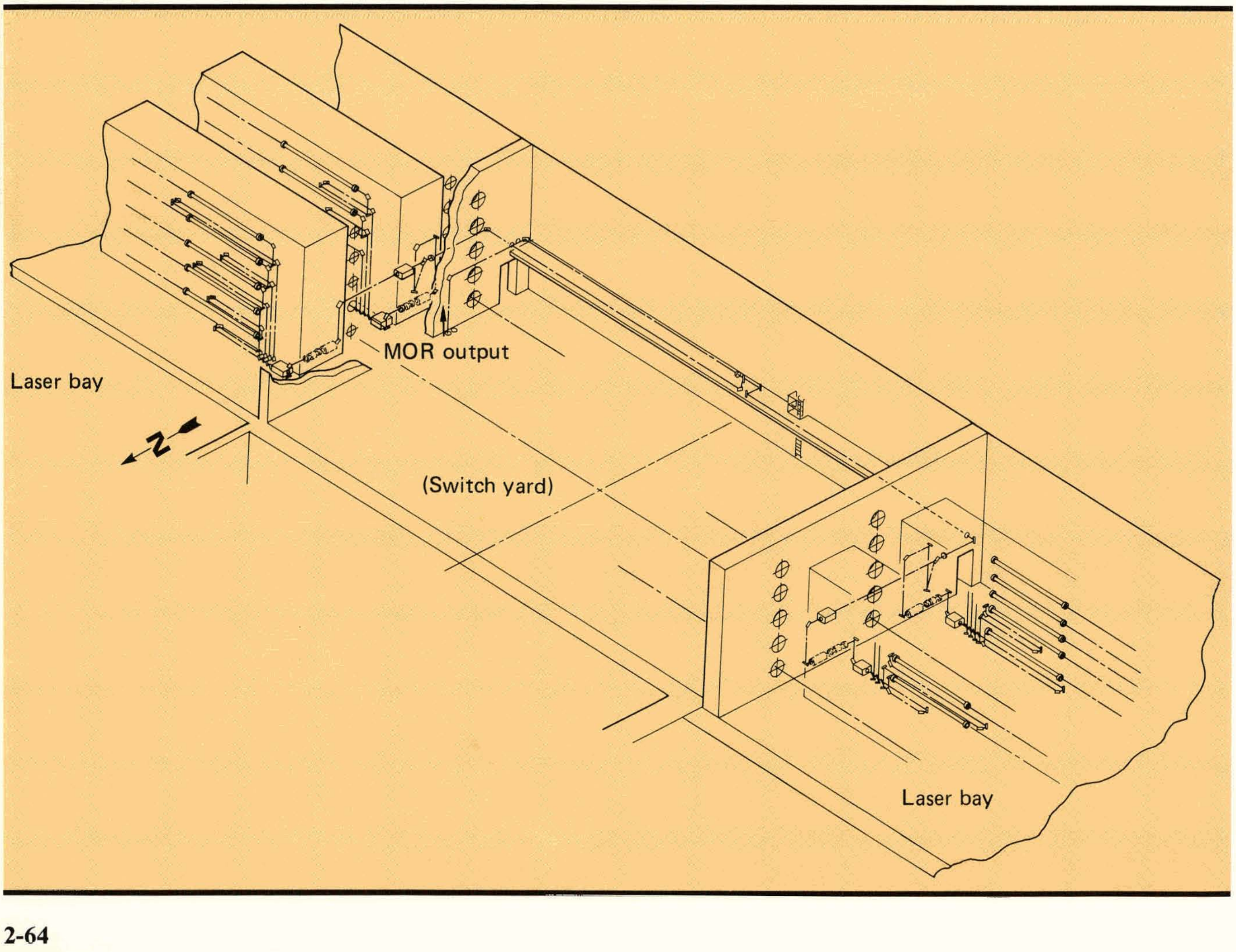

amplifier has been built and is being tested. Figure 2-62 is a photograph of this prototype hardware being assembled.

We have used information from the prototype tests in the final design of the 46-cm amplifier. Figure 2-63 shows a cut-away rendering of the assembly.

This design incorporates the latest innovations in amplifier technology. We use a rectangular or box pumping arrangement in which the flashlamp light passes through the laser disks before striking other flashlamps; each large laser disk is split in half to reduce amplified spontaneous emission; and the disks are spring-mounted in electroformed elliptical holders and held vertically in kinematic mounts. The pump cavity is designed for maximum reflectivity

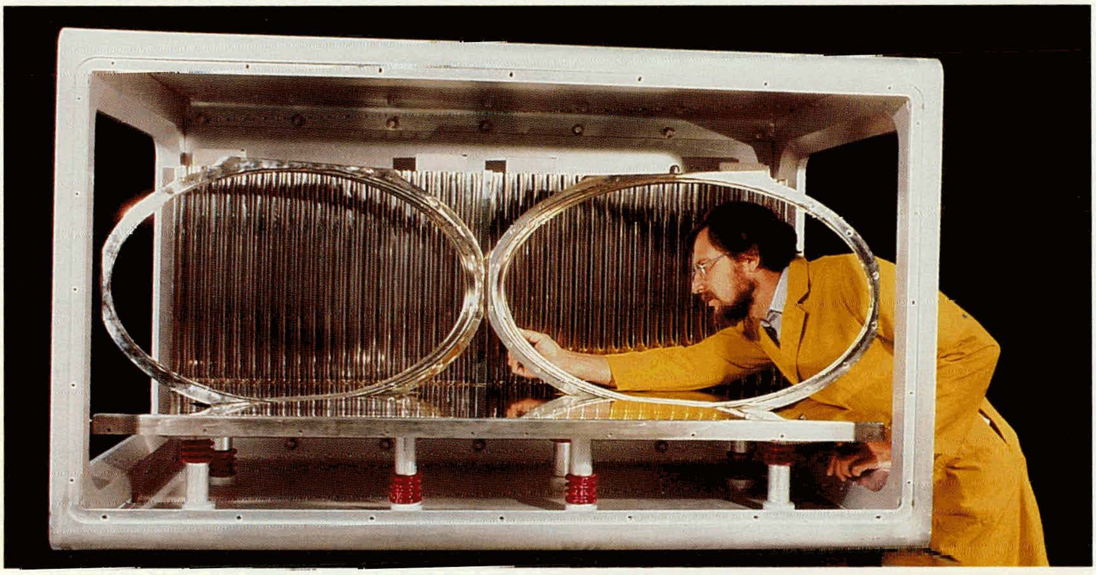

Fig. 2-62. Prototype 46-cm box amplifier being assembled.

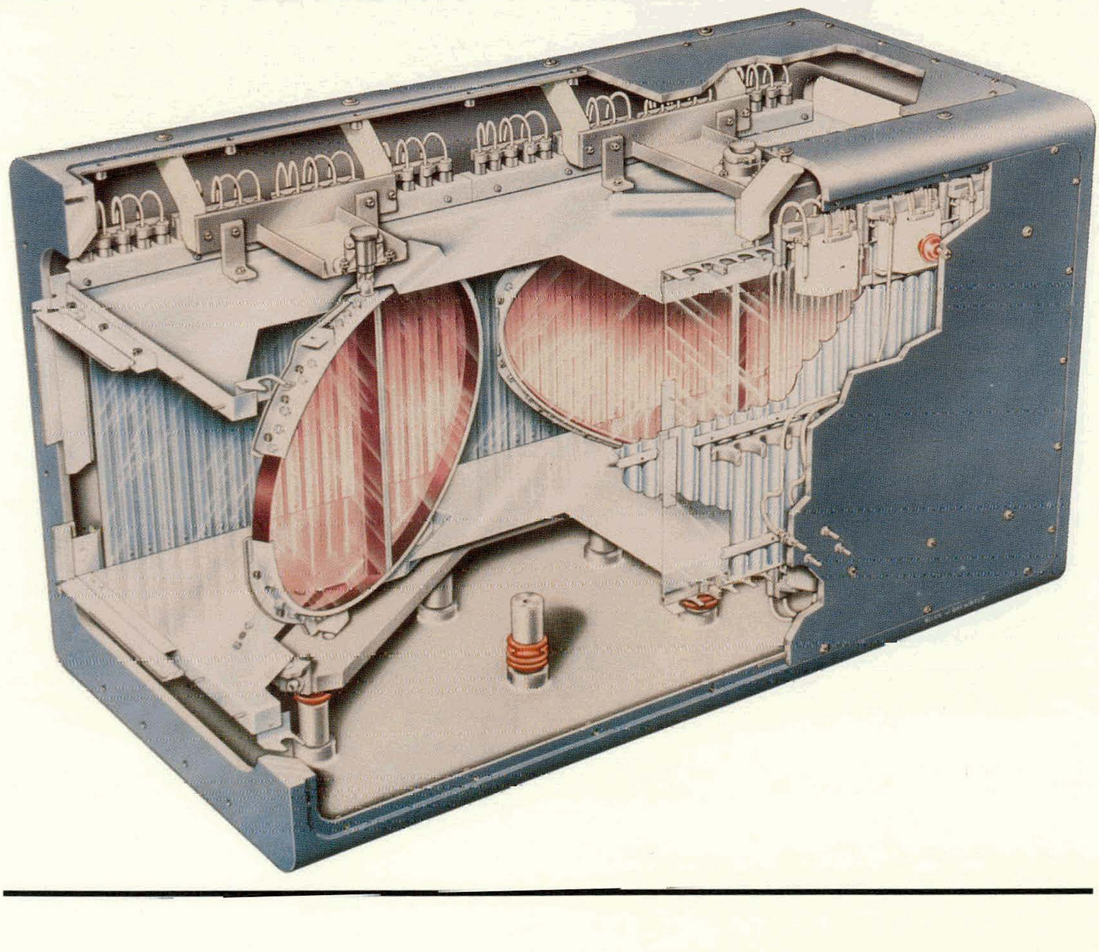

Fig. 2-63. Artist's drawing of 46-cm box amplifier with large split disks.

of the pump light and is kept small for maximum pumping efficiency.

To reduce costs, we have designed and built the prototype disk holders and reflectors using an electroforming process of nickel followed by silver-plating, which eliminates approximately 50% of the machining normally required. Since this was a learning process, we made several attempts before producing parts with acceptable quality. These parts are shown in Fig. 2-62. The crenulated lamp reflector is in the background; the flat reflector with a recessed hole is at the bottom; and the elliptical disk holders are captured by the top reflector. Quality control of the silver-plating is critical to successful operation of the pump cavity.

Fig. 2-64. End view of 20.8- and 31.5-cm disk amplifiers.

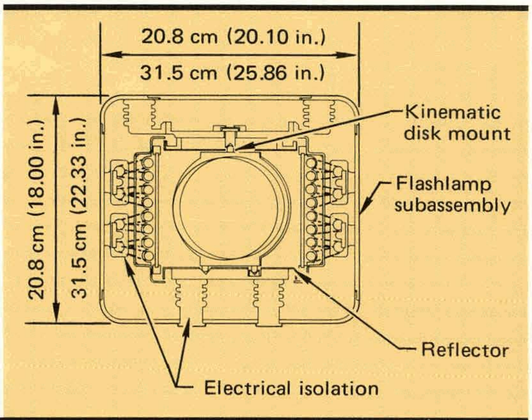

Fig. 2-65. Cross section of 5-cm rod amplifier.▼

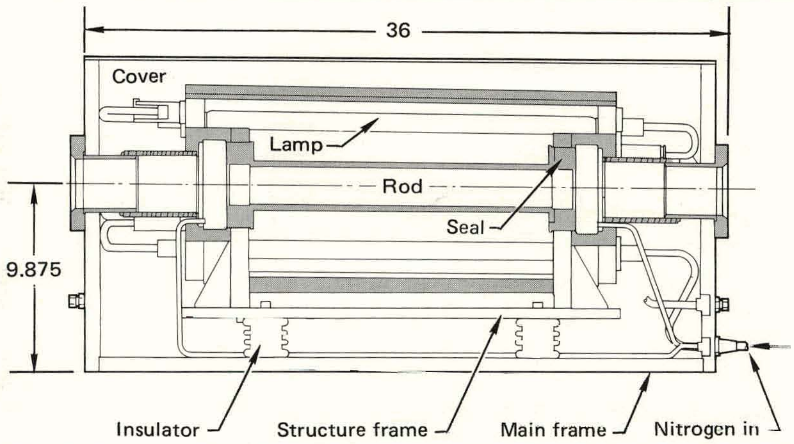

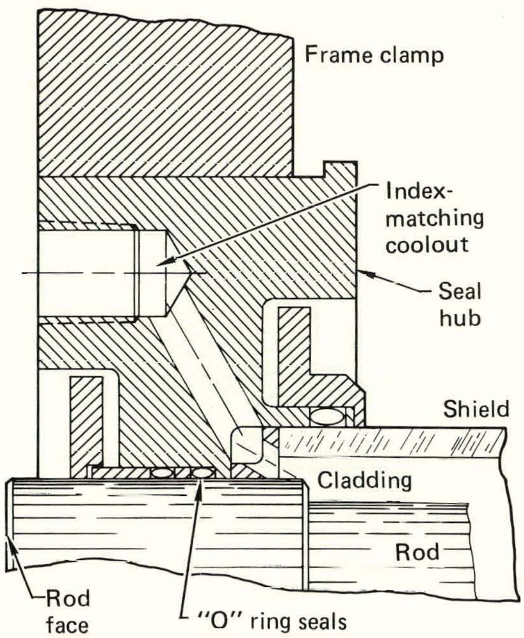

Fig. 2-66. Detail of rod-amplifier O-ring seals.

We designed the 20.8- and 31.5-cm amplifiers with features similar to those of the 46-cm amplifier, except that the lamp orientation is longitudinal. A discussion of the advantages of transverse lamp geometry in the 46-cm amplifier is given in the 1979 Laser Program Annual Report.[31] Figure 2-64 shows an end view of the 20.8- and 31.5-cm amplifiers. This box design allows us to build the world's largest disk amplifiers both simply and economically.

Figure 2-65 is a cross section through the center of a new 5-cm rod-amplifier design. In this design, we addressed issues related to existing Shiva rod amplifiers—the main issue being dependable operational lifetime. The critical areas for redesign were O-ring seal failure, structural integrity, excessive size, and difficult mounting.

The new O-ring seal design was accomplished by allowing enough room to properly configure the seal. In addition, we added absorbing cladding to the outside diameter of the rod ends to absorb the parasitic modes of 1-μm light that reduce laser gain and to shield the O-rings. Detail of the seal design is shown in Fig. 2-66. As in the disk amplifiers, a stiff structural frame cradles, supports, and clamps the rods at the seal locations. This frame is supported and isolated from the main-housing frame by sturdy standoff insulators. A dielectric hood covers the entire assembly. We use dielectric retractable tubing to couple the rod assembly to the main-frame end plates, which forms an enclosed beam path. All power leads and coolant lines are located at the frame end plates. Six lamps in series, mounted in half shells, swing from a bottom pivot to clear the rod assembly for replacement, inspection, and cleaning.

Authors: C. A. Hurley, F. A. Frick, G. G. Lee, and M. G. Demos

Spatial Filters. Seven spatial filters (vacuum tubes sealed at both ends with lenses), located between the amplifier stages in each laser chain, control beam propagation by filtering, relaying, and expanding the beam. Sizes and general features of the spatial filters were discussed in the 1979 Laser Program Annual Report.[32]

Figure 2-67 shows the relative sizes of the four largest spatial filters; because of their length and weight, we will fix them to the space frame. All laser chain components are mounted on cradles that accommodate rolling the components away from the space frame for crane access. Only the lens adjusters and the spatial filters will be moved in this manner, however they will not be cradle-mounted. Instead, they will be hung on the tube flange, and a portable cradle will be swung into place for removing each lens positioner. Center spools will also be removable. Attached to each spool is the vacuum system and the pinhole manipulator. This motor-driven manipulator can locate the pinhole in the x- and y-directions under vacuum-loaded conditions. Adjustment in the z-direction is used only on smaller spatial filters where the beam waist has a short axial length. The center section of the laser—and largest—spatial filter in each chain will accommodate the plasma shutter as the last isolation stage.

Vacuum enclosures are rolled and welded stainless steel tubes, tapered to follow the beam contour and to minimize pump volume. They are welded in ten-foot

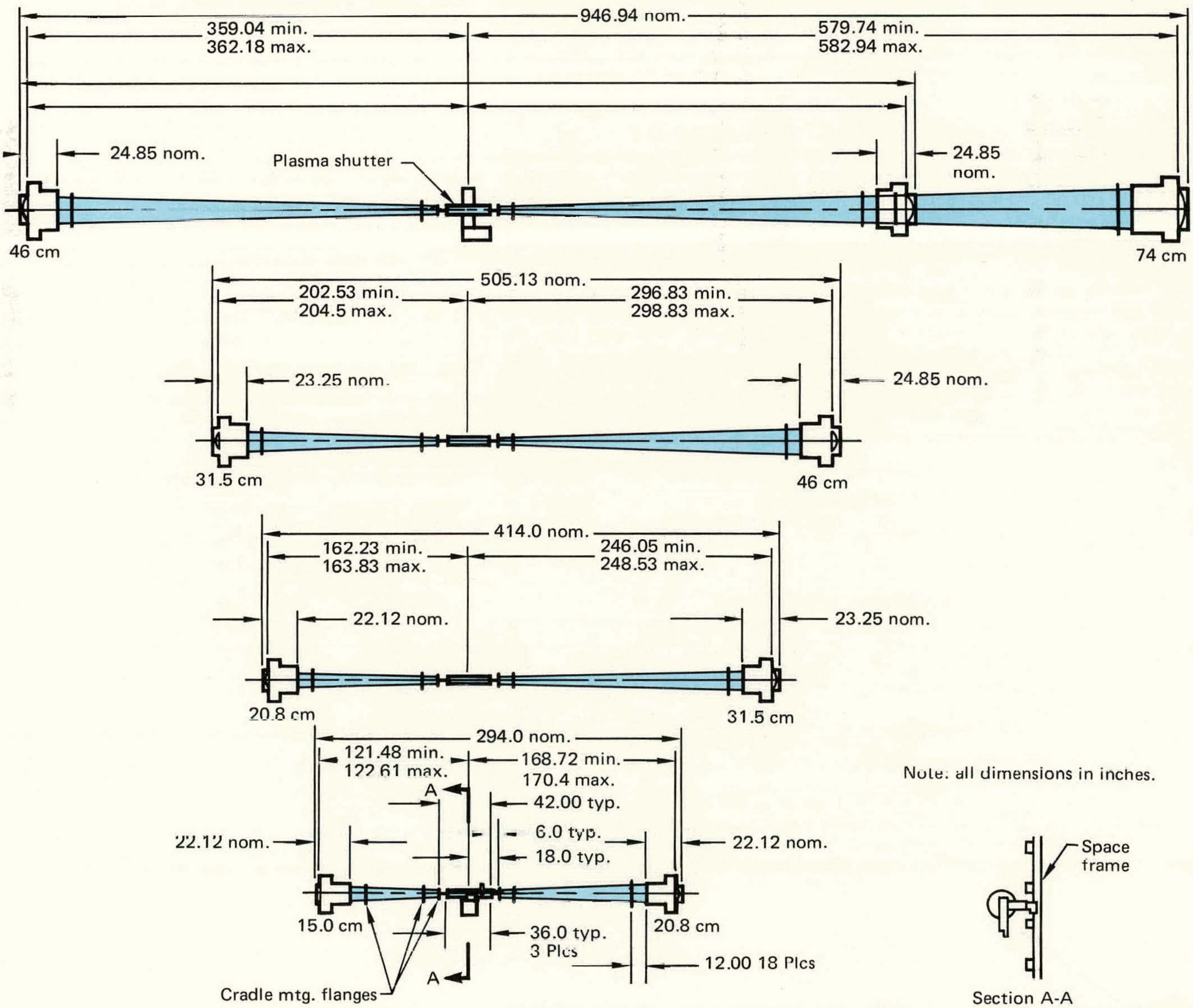

Fig. 2-67. Parameter drawing array of the four larger spatial filters.

increments and have hard gasket seals at the center spool and "O"-ring seals at the lens positioners. Vacuum in these four filters will be maintained with 1000-litre/s cryo pumps. The remaining units will be pumped with ion vacuum-pumping systems.

The spatial-filter lenses will be brought on the beam axis with lens adjusters capable of moving each lens in the x, y, and z directions under full vacuum, and the vacuum integrity of the system will be maintained through the stainless steel bellows shown in Fig. 2-68. To increase production quantities and reduce unit costs, common parts and subassemblies will be used on all filter units.

Fig. 2-68. Engineering drawing of adjustable holder for typical spatial-filter lens, showing jack screws, bellows, and gear reducer.

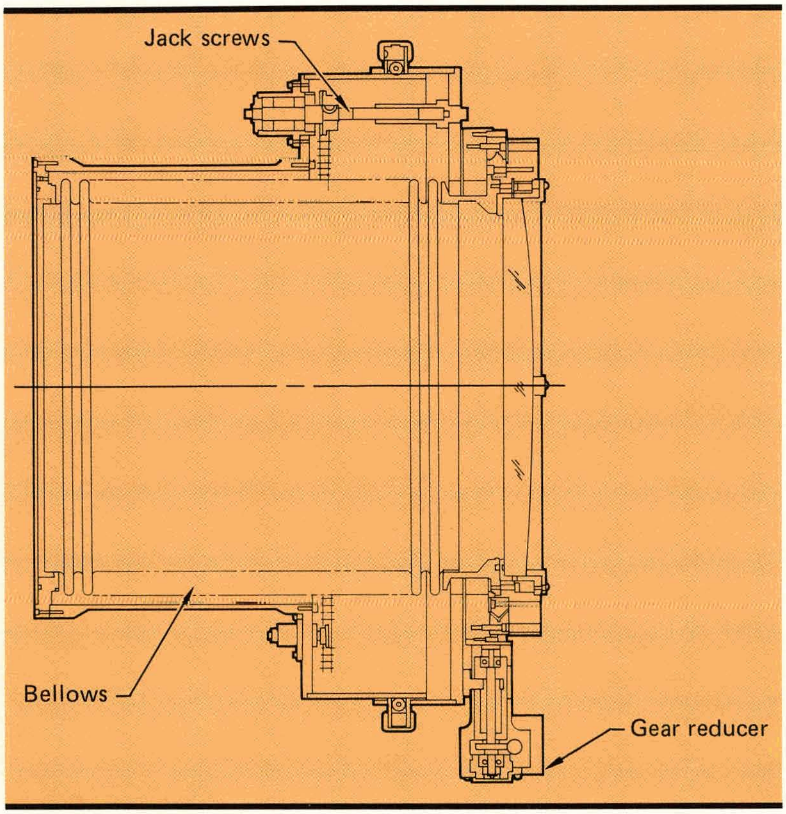

Fig. 2-69. Lens holder, showing x–y adjustment mechanism. ▶

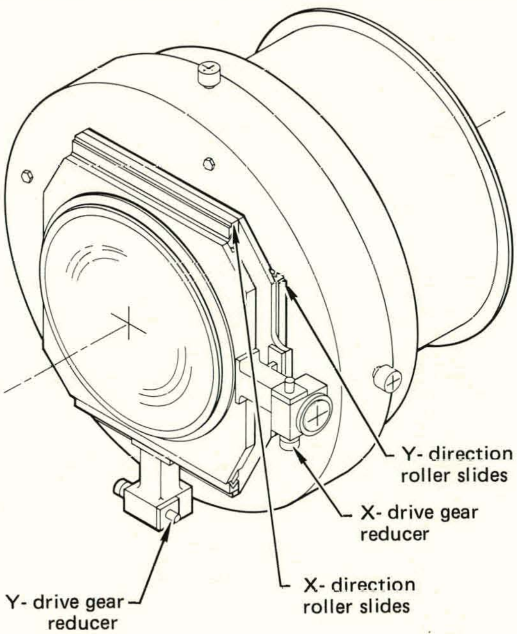

We have made calculations to determine stress and deflection of various parts of the spatial filter system. Forces are gravitational and vacuum loads. In addition to closed-form calculations, detailed finite-element computer analysis were made on critical components in the system. Sap IX analysis were performed on the lenses to determine stress and deflection, and to study the stress birefringent effects on laser beam propagation. Large plates act as lens supports. These plates take the full vacuum load and transfer it to the main body through a system of roller bearings and slides.

This roller-bearing slide system will be driven through gear reducers to translate the spatial-filter lenses in the x–y plane (see Figs. 2-68 and 2-69). SAP IV analyses show the maximum deflection of the lens plate on the 46-cm lens adjuster is 5.145 μm (0.00021 in.) along the roller slides and 73.9 μm (0.0029 in.) between the slides (Fig. 2-70).[33] This plate is made of aluminum alloy. It measures 40 × 40 × 3.5 in. thick and has a 34-in. hole through its center. It is the main structural support for the lens and must fold the lens system to reasonable deflections.

The gear reducers on the 46- to 74-cm spatial filter will be driven with stepping motors to automatically position the input and output lenses. Jack screws (Fig. 2-68) will be used to manually drive all other lenses, together with the x–y slide system, in the z direction.

Authors: C. A. Hurley, C. B. McFann, Jr., B. Gim, and J. R. Braucht

Faraday Rotator Isolators. A Faraday rotator isolator is an electro-optic device used in the Nova laser system to protect beam optics from back reflections and oscillations between the amplifier stages. It consists of an FR-5 terbium-doped rotator disk, a solenoid coil that surrounds the rotator, and polarizer end plates (at each end of the coil) twisted about the optic axis by a relative 45° (see Fig. 2-71). When the coil is activated, it induces a magnetic field through the disk, which causes the polarization of a beam passing through the disk to be rotated in proportion to the strength of the field. This rotation, in conjunction with the appropriate relative orientation of the polarizer plates, allows for a 45° rotation and unattenuated transmission of the beam in one direction and a 45° rotation and deflection of a back-reflected beam. The deflected back beam is absorbed with a glass plate.

The Nova Phase I laser system requires 42 Faraday rotators: two 5-cm aperture rotators and ten each of the 9.4-, 15-, 20.8-, and 31.5-cm clear-aperture rotators. We will take the 5- and 20.8-cm rotators directly from the Shiva laser system. The 9.4-cm clear-aperture rotators, which are also Shiva hardware, are being modified to allow for insertion of a passive 45° crystalline-quartz rotator that will be used for alignment purposes. The design parameters for the new 15- and 31.5-cm clear-aperture isolation units are presented in Table 2-21.

We designed the 15- and 31.5-cm Faraday rotators for Nova by scaling mechanical design parameters from the 20.8-cm Shiva Faraday rotator.[34] Although this design has already been discussed in detail,[34] portions are again discussed to explain deviations.

Coil mounting and cooling are the same as on the 20.8-cm rotator. Fringing fields exterior to the magnet are kept to a minimum by surrounding the magnet with a cylindrically symmetric aluminum conducting shield whose length is approximately twice its diameter. Because of its proximity to the magnetic field, however, this shield carries an energy penalty. To keep this penalty to a minimum and still have a workable design, we used shield-to-coil diameter ratios of approximately 2 for the 15-cm rotator and 1.6 for the 31.5-cm rotator.

All components near the coil are made of either plastic or glass to avoid distortion of the magnetic field. The polarizer plates require a very accurately machined mount that is difficult to obtain with plastic;

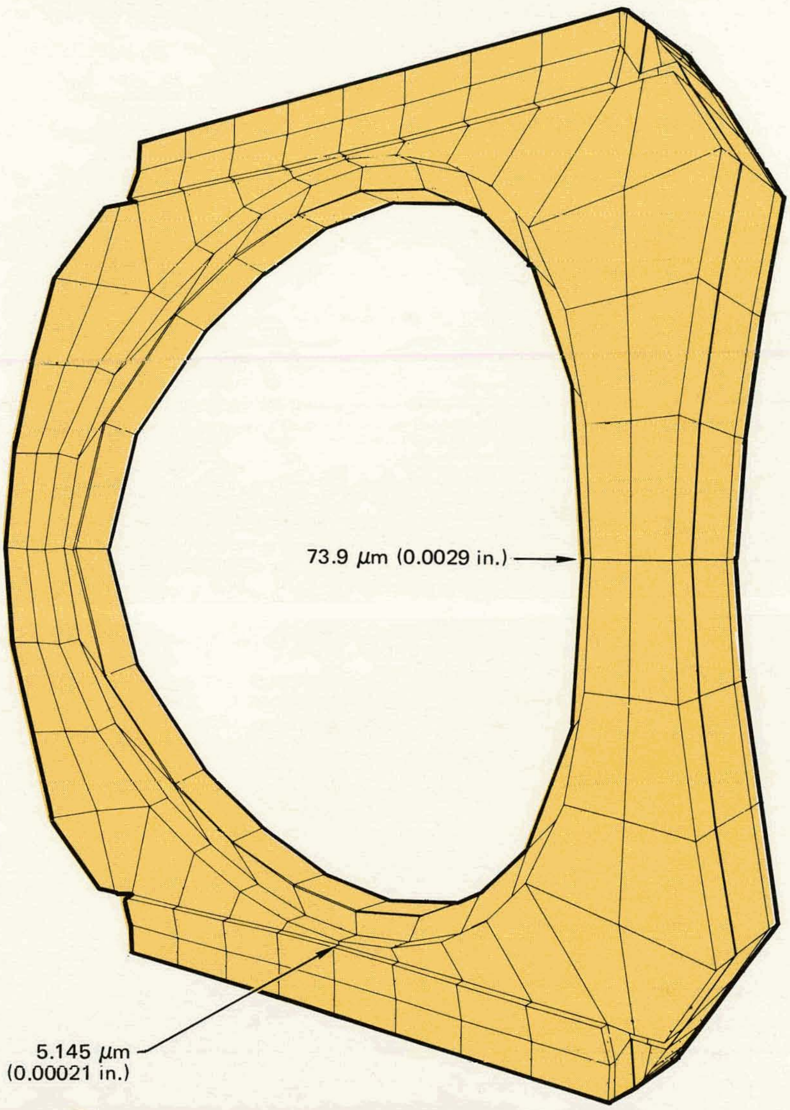

Fig. 2-70. Computer-generated graphic of lens-holder plate with distortion.

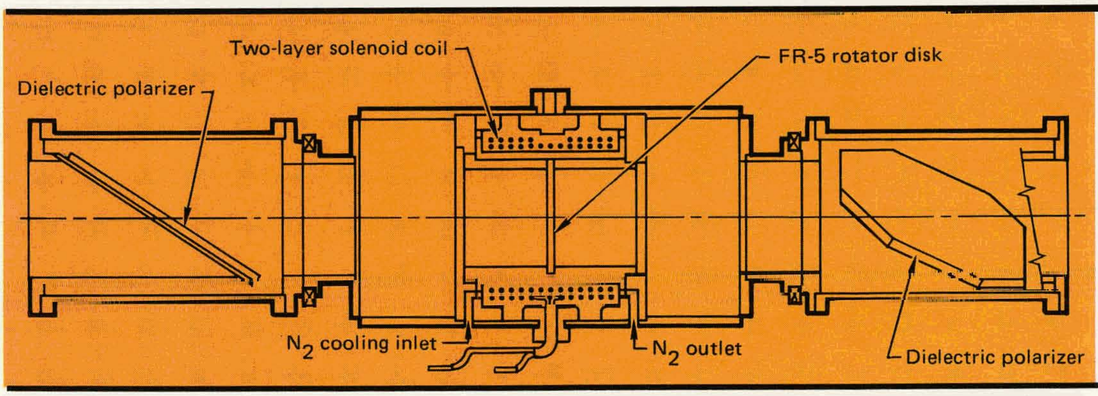

Fig. 2-71. Cross section of 31.5-cm Faraday rotator.

therefore, to minimize field distortion, we mount them on aluminum supports at a distance from the coil where the field is less than 0.04 T.

The 15-cm rotator is used to prevent oscillation between the 9.4- and 15-cm amplifiers and does not require polarizer plates on both sides of the coil. However, the rotator does require that there be no offset of the beam. We meet this requirement by using two polarizer plates on only one side of the coil (see Fig. 2-72). The centerline of the plate closest to the coil is mounted 60-cm from the coil to minimize magnetic-field interference. The 31.5-cm unit, in contrast, does require polarizers on each side of the coil. Because of its mounting location on the laser chain, however, beam offset can be compensated for easily, and one polarizer plate on each end—mounted 82 cm from the coil—provides sufficient isolation.

Author: A. Martos

Table 2-21. Nova design parameters for two clear-aperture Faraday rotators.

Parameter	Clear Aperture 15-cm	Clear Aperture 31.5-cm
Forward transmission	0.93	0.93
Minimum rejection, dB	−36	−18
Length of rotator-polarizer, m	1.90	3.26
No. of polarizer plates	2 at entrance	1 + 1
Polarizer plate thickness, cm	1.0	2.0
Beam offset	no	yes
Beam diameter, cm	15	31.5
Clear aperture, cm	15.6	32.1
Glass diameter, cm	16.6	33.1
Glass thickness, cm	1.0	1.97
Coil diameter, cm		
inner layer	22.1	38.8
outer layer	24.1	40.8
Coil length, cm	21.2	36.7
Turns for 2 layers	77	140
Wire gage	No. 6	No. 6
Shield inside diameter, cm	40.0	62.2
Shield length, cm	110	157
Inductance, H	676	4050
Resistance, mΩ	71.1	226
Magnetic energy stored at 45° rotation, kJ	59.8	79.3
Peak coil current, kA	13.3	6.3
Peak center field, T	3.87	1.96
Time to peak rotation, ms	0.83	2.83
Rotation homogeneity, dB	−32.5	−32.5
Capacitance, μF	416	812
Volts to change, kV	19	16
Capacitor energy storage, kJ	74	104

Nitrogen Cooling System. We performed a sequence of engineering analyses to optimize convective cooling of the Nova laser-chain components and to determine the size of the required nitrogen supply system. In particular, we evaluated the thermal responses of the large Nova disk amplifiers to alternative nitrogen cooling schemes.

Our first analysis addressed radiant-energy exchange inside a box amplifier during convective cooling of the laser disks. We determined the radiant-energy exchange rates analytically and found those at the disk surfaces to be comparable in magnitude to the convective exchange rates. This result was corroborated in an independent experimental study, where the severity of optical distortions in convectively cooled laser disks correlated directly with the temperature of the warm lamp cavities adjacent to the disks. Consequently, radiant-energy exchange was considered in all subsequent analyses.

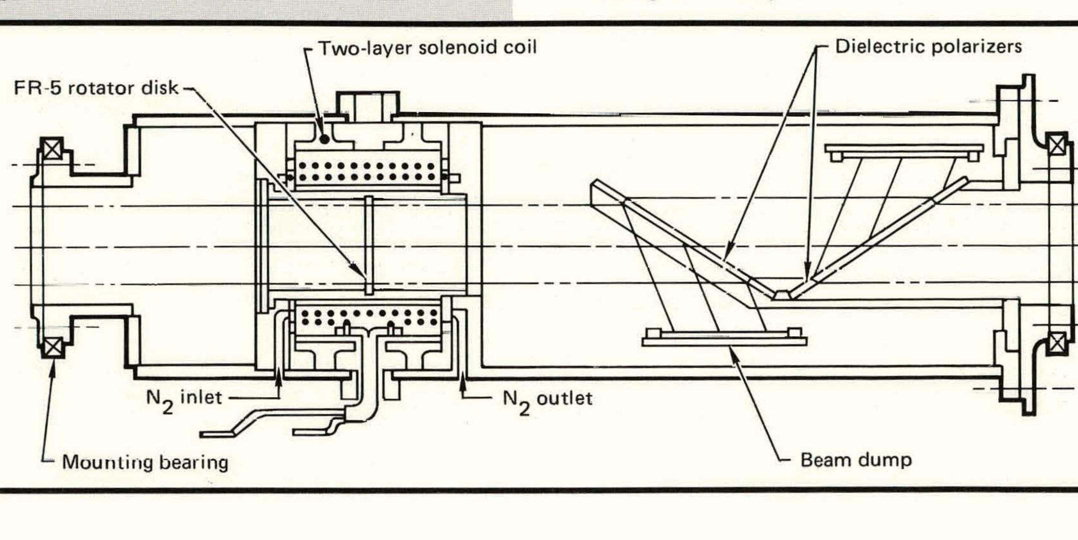

Fig. 2-72. Cross section of 15-cm Faraday rotator.

In the second analysis, we addressed the detailed thermal response of a convectively cooled laser disk to establish the relative importance of internal conduction vs convection and radiant-energy exchange in producing optical distortions. Using a disk conduction model with an explicit analytical solution, we evaluated thermal responses for a range of representative amplifier conditions. The results obtained suggest thermally induced optical distortions result from nonuniform convection at the disk surface and not from internal heat conduction within the disk. Further, we demonstrated that this effect may be amplified enough by radiant energy from the surrounding lamp cavity to preclude beam alignment. On the basis of these findings, we have adopted the independent introduction of nitrogen into the lamp cavities and the disk cavity for the design of the Nova disk amplifiers.

In a third analysis, we addressed the thermal response of a chain of box amplifiers for a range of nitrogen flow rates in the disk and lamp cavities. By design, all disk cavities in the chain must be cooled in series; however, we considered both parallel and series cooling of the lamp cavities in this analysis. Cooling periods were evaluated using coupled heat-transfer models for the lamp cavities and the disk cavity. Since series cooling of the lamp minimizes the cooling period for a given total nitrogen supply rate, the lamp cavities in a chain of Nova box amplifiers will be cooled in series and the nitrogen flow rate will be maintained at the limit set by noise and vibration considerations.

Using the results of these analyses and the known cooling performance of the Shiva components in the chain, we calculated cooling periods for an entire Nova laser chain. With the nitrogen velocity in the lamp cavities set below a limiting value of 25 fps, the remaining nitrogen was apportioned to the disk cavities such that the same cooling period applied to all laser disks. Figure 2-73 presents the resulting correlation of cooling period with nitrogen supply rate. The Nova nitrogen supply system will be sized on the basis of this correlation and the anticipated test schedule.

Author: H. Julien (Kaiser Engineers Inc.)

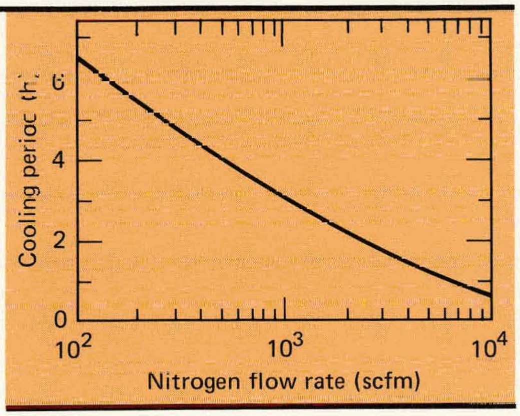

Fig. 2-73. Calculated cooling performance of single Nova laser chain showing cooling period vs nitrogen flow rate.

Beam Transport: Mirror Assemblies

The output beams of the Nova laser have a clear aperture of 74 cm. A total of 69 turning mirrors is used in the Phase I ten-beam system from the first beam aperture to the target. Twenty of these mirrors have a clear aperture of 31.5 cm, and 49 have a clear aperture of 74 cm. Ten each of the 31.5- and 74-cm-aperture mirrors are 98% reflecting (the transmitted 2% is used for beam diagnostics). All of the 31.5-cm-aperture mirrors are the same size and weight; because of different angles of incidence, the 74-cm mirrors come in four sizes. Table 2-22 lists the physical properties of these mirrors and their orientations on the space frame.

To hold the mirrors we explored several conventional mirror-mount designs, including those used on the Shiva laser system.[35] (Shiva mirror mounts are too small for Nova.) The mount design chosen for all Nova mirrors consists of an x–y adjustable mounting plate to which a bezel (that holds the mirror) is attached through three supports (see Fig. 2-74). Four different sized mounts, one of which uses two different bezel sizes, are required to accommodate the five mirror sizes.

The three supports that hold the bezel to the mounting plate are attached to the bezel at three points 120° from each other. These supports are connected via a conventional rod end (spherical joint) at the bezel and hinges at the other end. All moving mount components are preloaded to prevent unwanted free movement of the mirror. One support is of fixed length, and the other two

Table 2-22. Mirror sizes and orientation.

Nova

Item and location		Control aperture (cm) ϕ	Diam (cm) D	Thickness (cm) t	Weight kg (lb)	Angle of incidence Θmin/Θmax (deg)	Tilt angle from vertical, βmin/βmax (deg)	No. required. for 10-beam laser
1 Amp. chain	98% fold	31.5	60.4	7.0	50.3 111	All 45.0	0	10
2 Amp. chain	100% fold	31.5	60.4	7.0	50.3 111	All 45.0	0	10
3 Switchyard	98% turn	74.0	94.0	10.0	174 383	All 22.5	0	10
4 Target area	100% turn (size A)	74.0	109.0	16.0	375 825	27.3/39.6	0/69.7	11
5 Switchyard and target area	100% turn (size B)	74.0	94.0	12.0	209 460	12.5/26.8	0/53.8	18
6 Switchyard	100% RBD mir	74.0	82.0	12.0	159 350	0	0	10
					Total number of mirrors			69

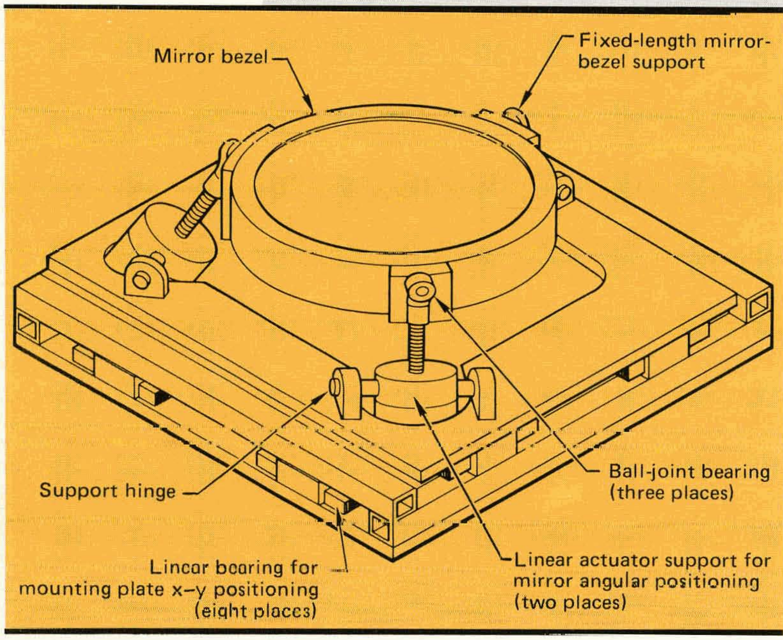

Fig. 2-74. Nova turning mirror mount.

are adjustable to give the mirror angular adjustment about two mutually perpendicular axes. The adjustment is stepper-motor driven through a combination worm-gear and ball-screw linear actuator. A worm-gear reduction of 100 to 1 and a lead of 0.25 in. on the ball screw provides overall resolution of 0.50 μrad/step through a total range in excess of 79 mrad.

The mirror is supported in a high-strength steel bezel (as on the Shiva first turning mirrors)[35] that has an open back to reduce weight and allow transmission of the beam on the transmitting mirrors.

We achieved a mounting-plate x–y adjustment of ±4 cm by using two plates attached, through linear bearings, to a box frame between them. The mirror mounts to one plate, and the other plate mounts to the space frame. Adjustments are made through ball screws.

We supplied clearance in the transmitting-mirror mounting plates to allow the beam to pass. For weight reduction, we also made large cutouts in the nontransmitting mirrors. A SAP IV[36] finite-element stress analysis has been completed to determine plate thicknesses and cutout patterns that provide the least deflections under the worst loading conditions.

Authors: C. A. Hurley and A. Martos

Nova Optical Components

Laser Glass. We made a major decision this year to switch the Nova laser glass from fluorophosphate to phosphate glass. This switch results in a 5 to 10% performance reduction over the full temporal range of the Nova design (see "Laser System Design and Performance" for the Nova performance analysis).

Before making the switch, we had to consider the relative technical and cost risks between fluorophosphate and phosphate laser glass. Although fluorophosphate glass had proved difficult to melt in striae-free, high-homogeneity quality, the glass companies working on the program (Hoya Corp., Schott Optical Glass, Inc., and

Owens–Illinois, Inc.) had made outstanding progress in learning how to melt massive pieces of homogeneous fluorophosphate laser glass (up to 8 liters in volume). In addition, they had developed a high-performance monolithic edge cladding for the large disks.

One significant technical problem remained intractable, however: the relatively low bulk-damage thresholds in the fluorophosphate disks, that seemed to be caused by microscopic platinum particles distributed throughout the glass.[37] Although considerable progress had been made in reducing the damage-site density from 10 cm^{-3} to approximately 10 cm^{-3}, we still needed another factor of 100 improvement. Otherwise we would be faced with the high operational cost risk of having to replace laser glass frequently. While the glass companies remained optimistic about solving the problems, the rate of improvement in damage resistance slowed to such an extent that we believed further improvements would require a new technical approach. After assessing the risk and time factors associated with further development, we decided they were unacceptable when compared with the projected performance.

The other driving consideration was cost. The glass companies and LLNL estimated that fluorophosphate glass would be very expensive (approximately twice the price of phosphate glass) because of melting difficulties (which indicated low production levels) and the cost of the raw materials (particularly high-purity AlF_3).

Although these problems and concern over the schedule were responsible for our decision to use phosphate laser glass in Nova, the fluorophosphate program, nevertheless, demonstrated that large high-quality melts of this type of glass are possible.[38] Fluorophosphate glass remains of long-range interest because of its low nonlinear index and potential use in the ultraviolet spectral region; consequently, Hoya and Schott are continuing development at a low level. Other segments of the US optics community have also benefitted from the program, finding this glass very useful in the color correction of high-acuity optical systems. Because of the program, Schott now makes fluorophosphate glass in the US at lower cost and in much larger sizes than previously available.

Phosphate laser glass has a recent and limited history of use in lasers for fusion research (the Omega laser at Rochester, the 14-cm laser at KMS Fusion, and Gekko XII at Osaka University, Japan), but none of these lasers requires the massive size or damage resistance needed for Nova. Therefore, we have carried out extensive characterization and damage tests at LLNL to assure the suitability of the glass. In 1980, the glass vendors began a prototype program to make the largest Nova phosphate laser disks. Phosphate disk sizes are presented in Table 2-23.

Damage resistance is illustrated in Fig. 2-75, where the damage-site density in phosphate and fluorophosphate glass is compared to the Nova requirements. Clearly, phosphate damage levels do not represent a significant risk.

In addition to the high-quality optical requirements, we specify that the phosphate glass for Nova have seven other characteristics:

1. Stimulated emission cross section of 4×10^{-20} cm^2.
2. Refractive index of 1.52 ± 0.005 at 1053 nm.

Table 2-23. Nova phosphate disks.

	Elliptical-contour			
Aperture, cm	Major axis, cm	Minor axis, cm	Thickness, cm	Volume, l
9.2	20.2	10.8	2.4	0.4
15.0	30.9	16.4	3.0	1.2
20.8	41.8	22.3	2.5	1.8
31.5	62.9	34.2	4.3	7.3
46.0[a]	44.7[a]	49.2	4.3	7.4

[a]The disk is split, making the major axis a semi-major axis.

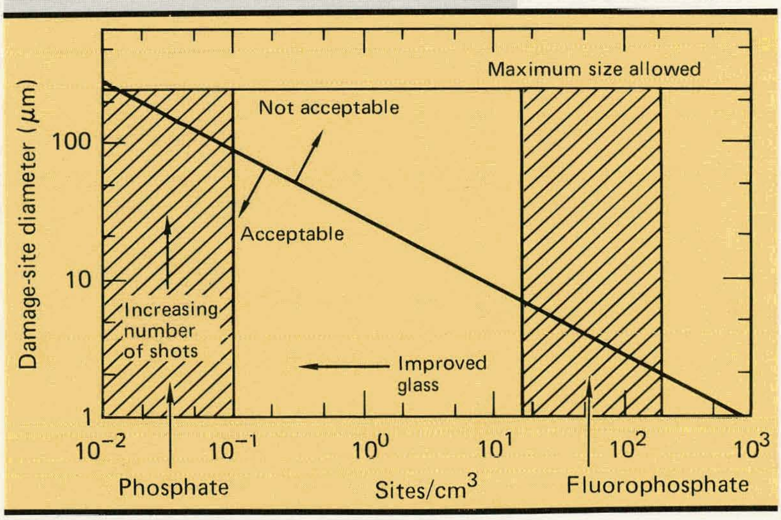

Fig. 2-75. Allowable damage-site density as function of site diameter for Nova laser glass.

3. Nonlinear refractive index of 1.2 $\pm 10^{-13}$ esu.
4. Fluorescence-peak wavelength of 1053 $\pm$ 0.5 nm.
5. Nd^{3+} fluorescence lifetime $\geqslant 350\ \mu s$ in the disks and $\geqslant 370\ \mu s$ in the rods.
6. Absorption coefficient of $\leqslant 0.05\ cm^{-1}$ at 400 nm.
7. No solarization when pumped by Ce-doped quartz flashlamps.

The first four items ensure that the glasses from different manufacturers will be optically equivalent. The fifth item is very important because laser amplifier gain is directly proportional to fluorescent lifetime. This lifetime is shortened considerably if the glass contains significant amounts of water, which can be a problem in phosphate glass. Item 6 refers to the background absorption, due to ionic platinum, in the visible region. If this absorption is high, the pump light will be significantly attenuated. We have found that phosphates are resistant to solarization when the pump light is properly filtered (see "Laser Glass, Solarization").

The disk edge cladding on the 31.5- and 46-cm disks will be of the poured-type, with frit-type cladding optional on the smaller disks (see "Laser Glass, Edge Cladding"). For the first time we will also try a cladding on the barrel of the laser rods. This cladding will extend 30 mm inward from each end of the 5-cm diam, 480-mm-long rod to protect the O-ring seal in the amplifier and to help suppress parasitic laser oscillation modes. We will test prototype clad rods before committing to production.

To have the capacity needed to produce the large volume of precision glass required for Nova and other programs requiring a state-of-the-art glass-melting capability, both Hoya Corporation and Schott Optical Glass, Inc., have been expanding their facilities. Schott has substantially enlarged its plant in Duryea, Pa. (a new area set aside for ongoing work on laser fusion programs is illustrated in Fig. 2-76). And Hoya Corporation, which previously manufactured glass for the high-technology US market in Japan, has purchased a building in Fremont, Calif. (Fig. 2-77), where it expects to be ready to pour glass in January 1982.

We expect Hoya and Schott, both of whom will do production in the US, to be the major vendors for Nova laser glass. Kigre,

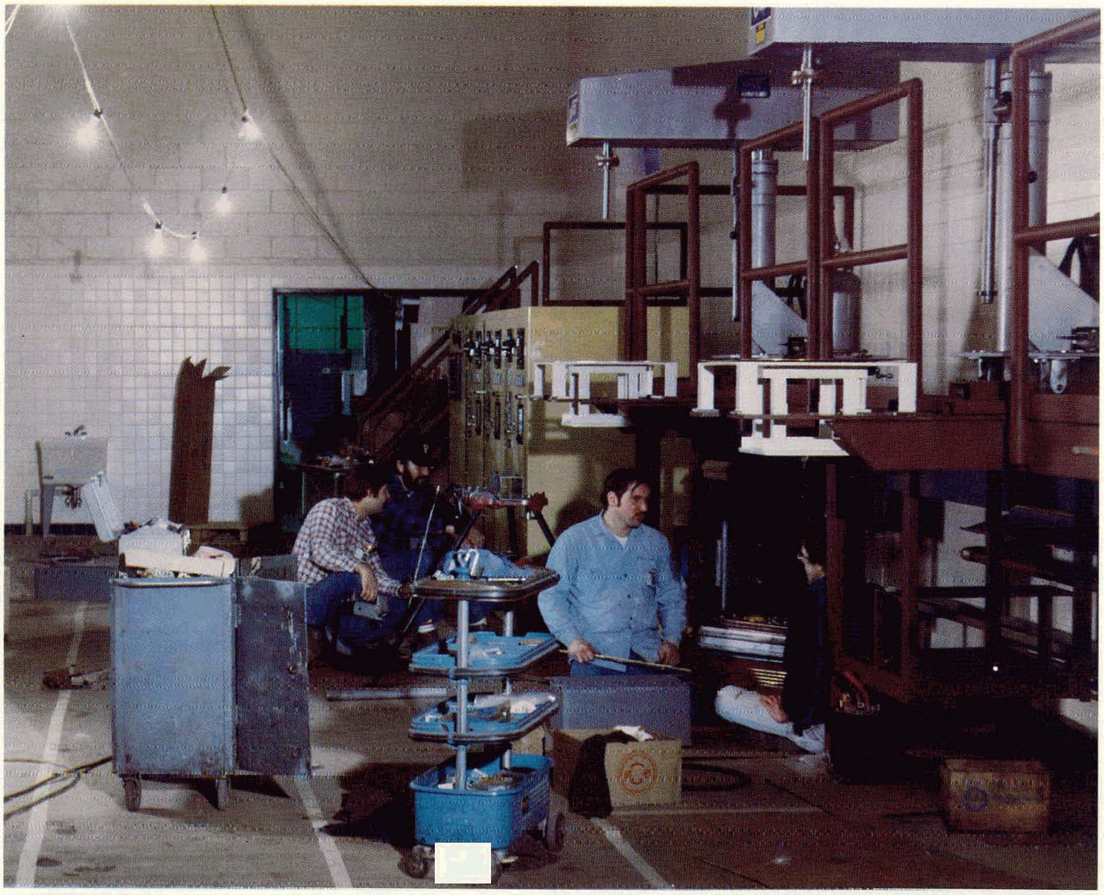

Fig. 2-76. Preparation of new melting and annealing area at Schott Optical Glass, Duryea, Pa.

Inc., Toledo, Ohio, is also a potential vendor for 20.8-cm-aperture and smaller laser disks.

We regret that Owens–Illinois, Inc., a supplier of laser glass for Shiva, a participant in the fluorophosphate program, and an early developer of phosphate glass, decided to leave the laser-glass business in 1980.

Schott Optical Glass, Inc., is manufacturing BK-7 substrate glass, in blanks ranging from 10 cm to over 1 m in diameter, which will also be used in the Nova project. There are two basic quality specifications for this glass: one for the transmitting optics, where the index homogeneity is high precision ($\Delta n \leqslant \pm 1 \times 10^{-6}$), and one for the reflecting optics which, while they must be free from excessive stress and bubbles, do not have a tight index specification. The largest high-precision blank is the "leaky" (2% transmission) mirror for the diagnostics, which is 94 cm in diameter and 10 cm thick—a volume of about 70 liters. A total volume of about 800 liters of substrate glass goes into the 1053-nm-wavelength, 10-beam, Nova Phase I laser. By the end of 1980 Schott had poured essentially all of this glass and had proceeded through about 40% of the fine annealing and final dimensioning. Figure 2-78 shows some rough-cut BK-7 blanks (about 1.2 m diam) at the Schott plant in Duryea, Pa.

In 1980, as part of our development of components with improved antireflection damage thresholds, we obtained four 46-cm-aperture, phase-separated glass blanks from Hoya Corporation. Three of these prototype blanks have been sent to Perkin–Elmer Corporation for fabrication into 46-cm-aperture input spatial-filter lenses for Nova. These blanks, which are 53 cm in diameter and 4.5 cm thick, contain about 10 liters of substrate glass and meet the stringent

Fig. 2-77. Hoya Optics, U.S.A., Inc., Fremont, Calif.

Note: row of annealing ovens is seen to the left.

Fig. 2-78. Several Nova turn-mirror blanks at Schott Optical Glass.

optical-quality requirements for Nova. Figure 2-79 shows part of a set of interferograms, taken by Hoya with a 30-cm aperture interferometer to provide a composite analysis of one of the blanks, to demonstrate $\Delta n \leqslant \pm 1 \times 10^{-6}$. Hoya is offering this material under the designation ARG-2.

After the surfaces of the blanks are ground and polished to the accuracy required for lenses or windows, they are acid-leached to provide a broadband, high-damage (10 to 12 J/cm^2 for 1 ns with 1060-nm light) antireflection coating (specular reflection $\sim$1/4%). Before 1980, leaching was done on small samples of about 5 cm diam. In 1980, we turned our attention to the problem of obtaining uniform leaching over large optical surfaces. With large optical surfaces the requirement is to maintain high optical quality (fractional wavelength path difference) along with uniform reflectivity and high damage resistance.

In the etching of phase-separated glass a weak chemical solution preferentially attacks a silica-poor phase more vigorously than it does a silica-rich one, resulting in a fine spongelike structure on the surface. Figure 2-80 shows a 160× SEM photomicrograph of a typical etched, phase-separated surface. To maintain the surface figure over large surfaces, extreme uniformity is required during the etching process. Our earliest results from submerged etching systems showed a sensitivity to eddies and flow perturbations. Since this sensitivity has persisted and since large systems are much more prone to flow variations, efforts to develop an acceptable submerged system will probably be abandoned.

We have recently begun pursuing spray systems[39] and are concentrating on a fine-spray or mist process to renew active materials and remove spent products. Parts are rotated slowly while being sprayed, and attempts are being made to slow down the process to improve uniformity and permit better averaging. We are trying two procedures at present: one involving jets broken into a spray by impingement on a secondary surface, the other involving a similar system that produces additional breakup with a fine plastic screen.

The present cycle consists of

1. Thermal soak.
2. Solvent degrease.

Fig. 2-79. Hoya Corporation interferograms (λ = 633 nm), showing optical homogeneity of 46-cm phase-separated lens blank of ARG-2 from several points in the aperture.

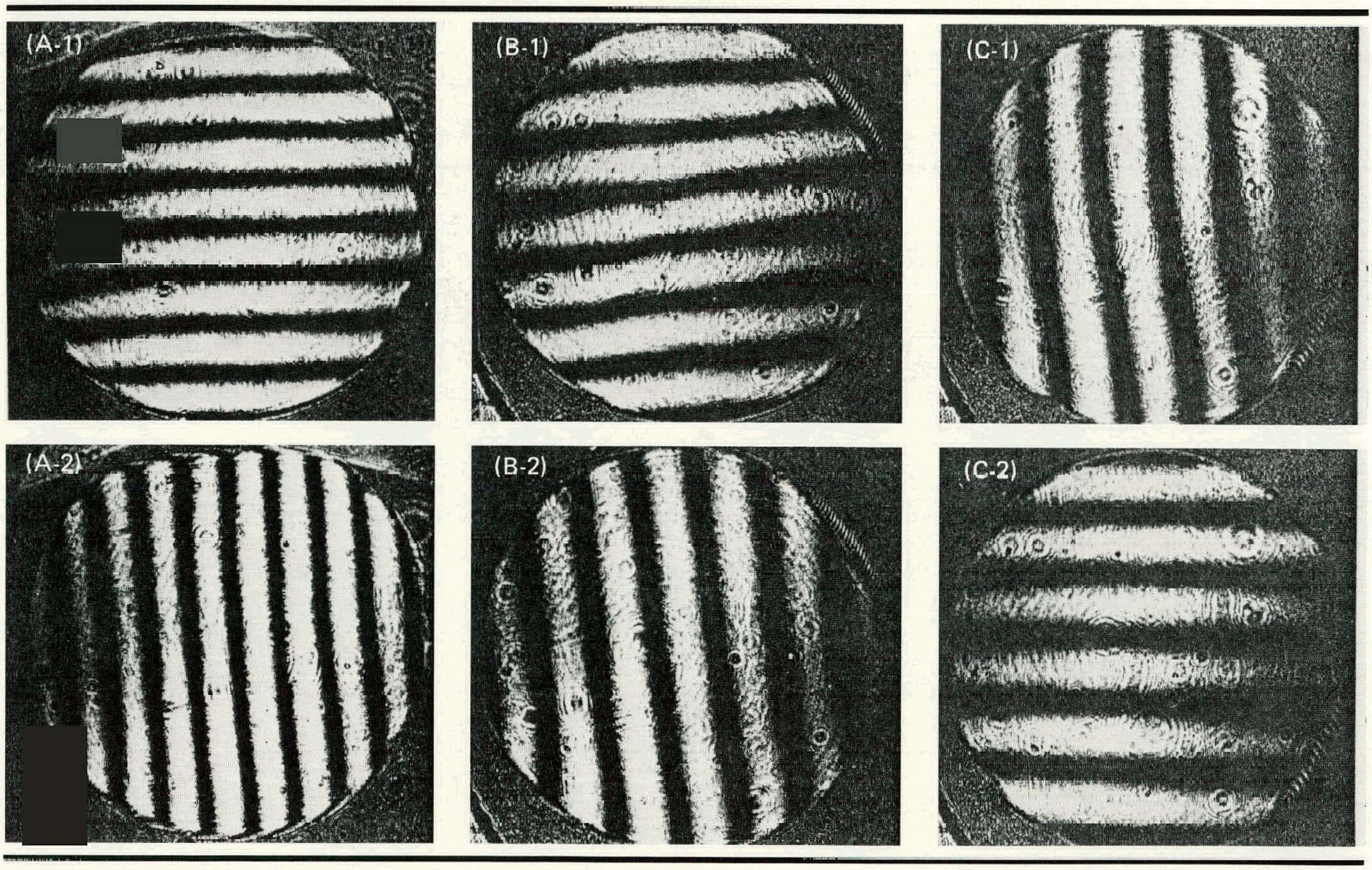

3. Etch.
4. Water rinse.
5. Vapor dry.

Our efforts so far have been concerned with unformity and with understanding the cycle rather than with reflectivities. However, we have achieved reflectivities on the order of 0.1% at 1.06 μm.

The two interferograms in Fig. 2-81 are of an ARG-2 phase-separated glass disk (15 cm diam) etched early in the program and demonstrate the need to develop a uniform leaching process. Considerable progress in understanding removal rates has been made since this work was done by using 5-cm-diam samples.

The phase-separated ARG-2 material may also be used uncoated, as might ordinary glass. The general damage characteristics of the material are apparently about the same as those for similar nonphase-separated glass. Recent damage tests at 1064 nm for 1 ns on bare unleached surfaces of ARG-2 yielded about 16 J/cm^2, comparable to BK-7 glass. Using the ARG-2 Nova input spatial-filter lenses without leaching remains an option, depending on the ultimate results of leaching development and the fluence requirements.

As a possible alternative to the phase separated glass, Schott Optical has done considerable work on extending previously known techniques for leaching nonphase-separated borosilicate crown glasses to produce the antireflection effect. Our tests on small samples have yielded damage results very similar to those obtained with the leached phase-separated material. The antireflection effect is not broadband, however, but must be adjusted for minimum reflectivity at a single wavelength.

A promising application for the leaching of nonphase-separated glass is on the output

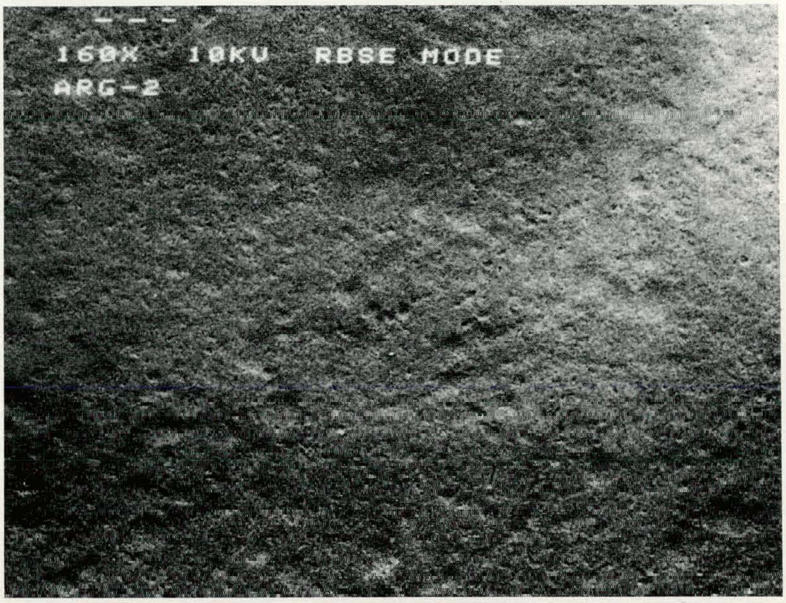

Fig. 2-80. SEM photomicrograph of leached ARG-2 surface (courtesy of International Scientific Instruments, Inc., Santa Clara, Calif.).

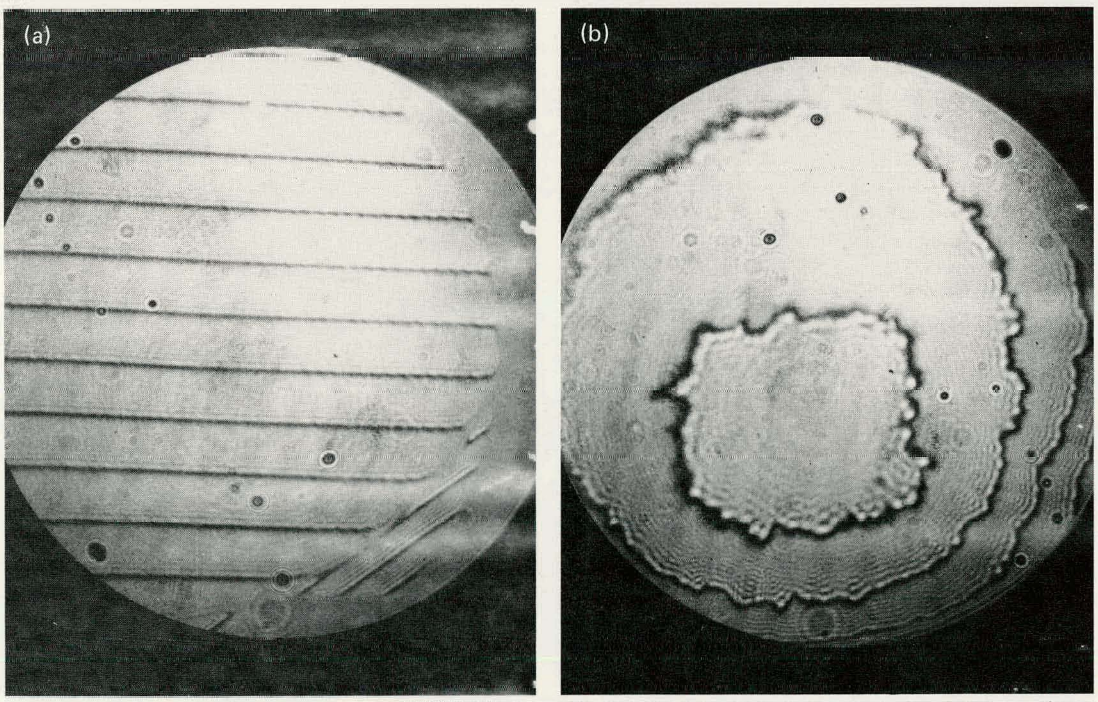

Fig. 2-81. Interferogram (λ = 633 nm) of 15-cm phase-separated glass disk of ARG-2 (a) before and (b) after acid leaching by immersion.

spatial-filter lenses currently being manufactured from BK-7 glass. If the process proves effective, it could allow the laser to operate at higher fluences than would be permitted by the standard antireflection coatings currently in the baseline design.

Hoya Corporation is manufacturing the 31.5-cm-stage FR-5 Faraday rotator glass for Nova. These large disks are 70% terbium oxide by weight and represent a substantial achievement in glass formulation and melting. About 33 cm in diameter by 2 cm thick (1.7 liters), they have a very tight specification for homogeneity ($\leqslant \pm 2 \times 10^{-6}$), striae (none), inclusions ($\leqslant 0.04$ $cm^2/100\ cm^3$) and stress birefringence ($\leqslant 4$ nm/cm). Five disks demonstrating conformance with these specifications were delivered in 1980.

Flat-Optics Facilities and Production. During 1980 Eastman–Kodak Co. and Zygo Corp., the two principal flat-optics finishers for Nova, each constructed large, precision flat-lapping machines for use in their facilities. These unique machines, designed, built, and installed specifically for the Nova project, will be operational in early 1981. The basic technology for the machines is similar, but they differ considerably in detail because of the technical preference of the manufacturers, who have each designed the machine they believe will give the best performance (see Table 2-24). In general, they will be used to finish identical parts. The salient characteristics and advantages of this type of machine for precision flat polishing

Table 2-24. Specific characteristics of precision lapping machines.

	Eastman–Kodak	Zygo
Table		
Material	Granite	Granite
Diameter, m (in.)	4.06 (160)	3.66 (144)
Thickness, m (in.)	0.76 (30)	0.61 (24)
Weight, kg (tons)	27 000 (30)	18 000 (20)
Conditioning Tool		
Material	Fused silica (Kodak-owned blank)	Granite with Pyrex pads
Diameter, m (in.)	2.08 (82)	2.03 (80)
Thickness, m (in.)	0.33 (13)	0.30 (12)
Weight, kg (tons)	2500 (2.8)	2700 (3)
Table-drive motor, hp	20	10
Maximum table speed, rpm	1	2
Table mount	3.05-m-diam (120-in.-diam) ball-bearing system leveled by hydraulic jacks	47-point hydrostatic bearing system
Table accuracy (change during rotation), m	0.25 to 0.50 over full surface	0.08 to 0.13 over 1-m-diam surface

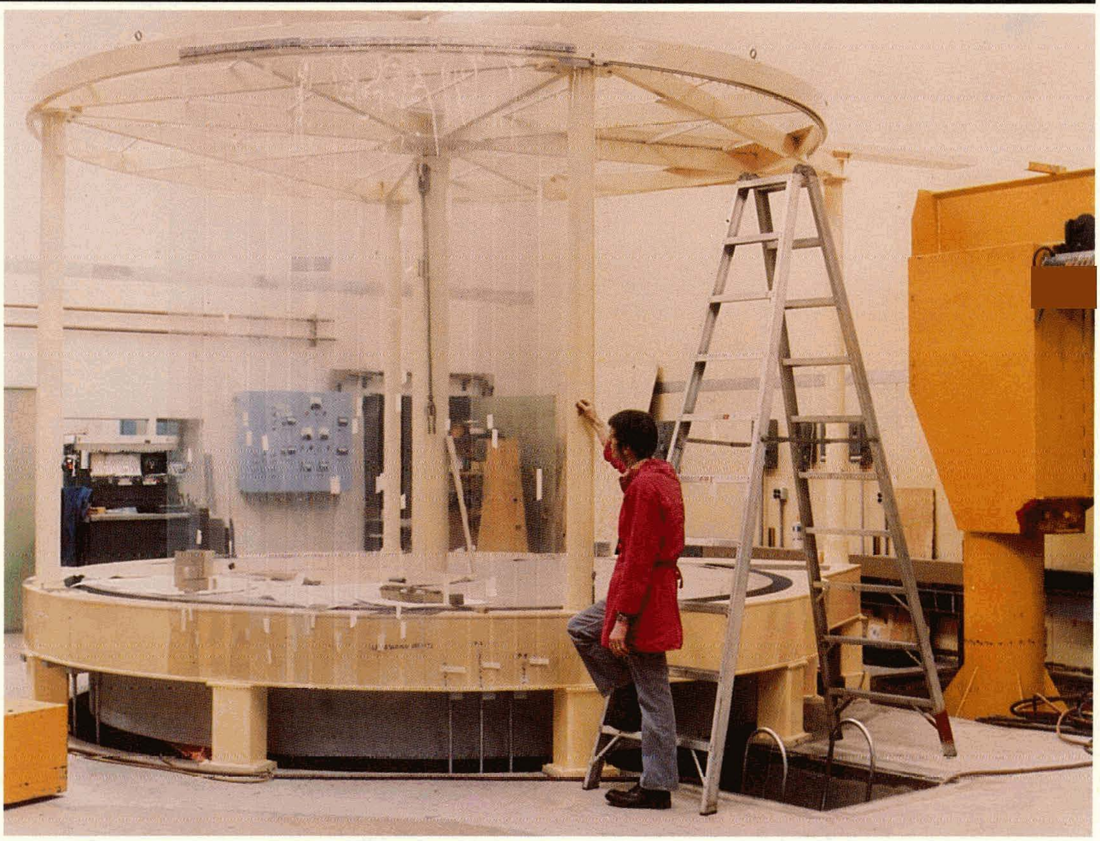

Fig. 2-82. Precision flat lapping machine (4 m) being constructed at Eastman Kodak Co., Rochester, N.Y. Granite table weighs 27 000 kg (30 tons).

has been described previously in the literature.[40,41] Fundamental requirements included: a lapping table at least three times the major dimension of the part to be polished; a table stiff enough to support a pitch lap accurately to a fraction of a wavelength; a conditioning flat for continuous adjustment of the pitch surface contour; and close thermal control of the pitch and the surrounding environment.

The Kodak machine shown in Fig. 2-82 makes extensive use of computer-controlled systems, including local air and slurry temperature controls within ±0.025°F, and work-station rotation controls to maintain constant work rate. The number of stations can be adjusted up to six, depending on the size of the parts to be finished.

The Zygo machine (Fig. 2-83) has a data logger that monitors about 60 parameters, such as temperature, pressure, and lap shape. Many of the monitored parameters can be controlled automatically.

Each company is also constructing an 80-cm-aperture Fizeau interferometer that operates at 633 nm for testing the optics to be fabricated on the machines. These instruments will be close to the machines and in a similar thermal environment.

Lens Design, Facilities, and Production. The lenses for Nova fall into two categories, depending on manufacturing technology: (1) long-focal-length, high-f/number spatial-filter lenses that use thin blanks and require little or no asphering and (2) short-focal-length "fast"-focus and diagnostics lenses that require significant aspherics.

Each Nova chain has a series of 14 spatial-filter lenses, to be mounted in seven spatial-filter assemblies, with optical characteristics as indicated in Table 2-25. Starting with the third assembly, the input lenses are meniscus-shaped so that the first back-reflected ghost is nearly collimated. All other lenses are shaped for optimum coma correction.

The Nova spatial-filter assemblies have been designed to minimize the number and intensity of potentially damaging ghost foci, which are produced by single or multiple-surface reflections in the spatial-filter lenses (Fig. 2-84). The Shiva design minimized this

Table 2-25. Optical characteristics of spatial-filter assemblies.

Assembly	Nominal-stage aperture, mm: Input	Nominal-stage aperture, mm: Output	Magnification	f/No.	Length, m
1	27.0	37.5	1.389	80.3	5.18
2	37.5	91.7	2.445	22.9	2.96
3	91.7	150	1.636	10.6	2.57
4	150	208	1.387	20.8	7.43
5	208	315	1.514	20.0	10.46
6	315	460	1.460	16.5	12.79
7	460	740	1.609	20.0	24.00

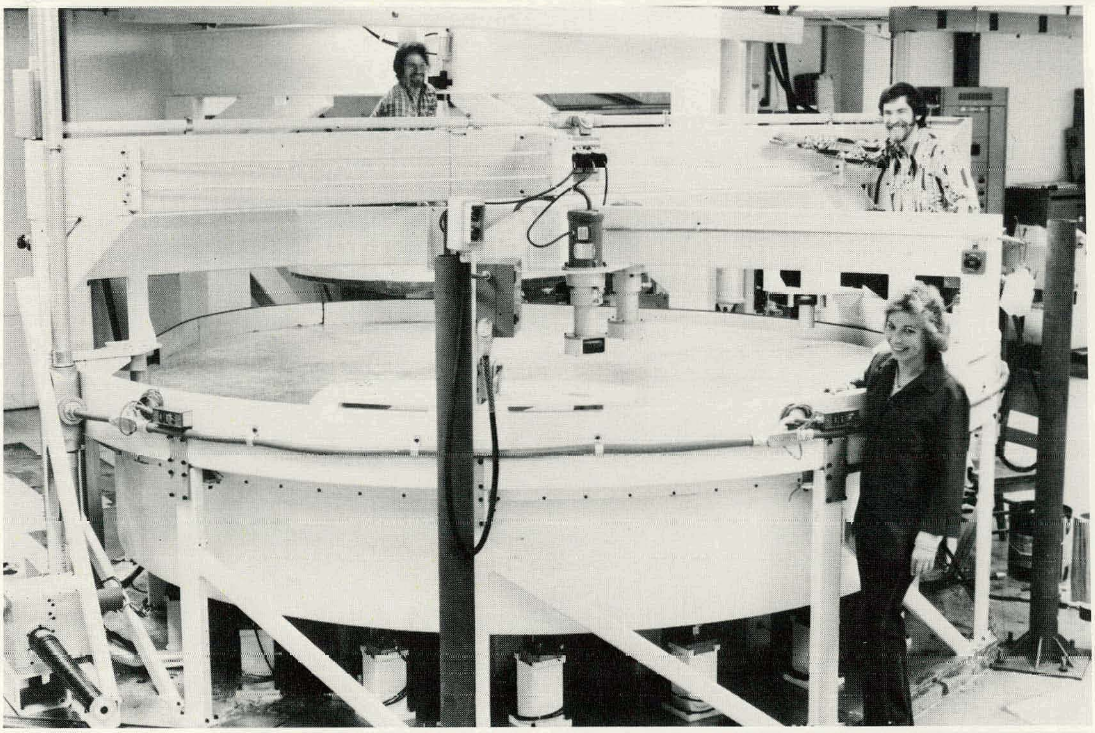

Fig. 2-83. Zygo Corp. 3.7-m, precision flat lapping machine, Middlefield, Conn.

problem by requiring the use of AR multilayer optical coatings with reflectivities of less than 0.1% per surface. However, Nova will operate with fluence densities at the input spatial-filter lenses that will exceed the damage threshold of these AR coatings by 50% or more.

Currently, there are two approaches to obtaining input lenses with high damage thresholds. The lenses can be uncoated, in which case they will have surface reflectivities of 4% per surface. The second approach is leaching, which will produce reflectivities in the range of 0.2 to 0.5% per surface.

Since either approach would increase the risk of ghost-focus damage, the Nova optical-train design incorporates two complementary design features. First, the region around the pinhole manipulator will be baffled so no light can travel backward or forward through the spatial filter unless it passes through the pinhole. This will prevent ghost images from being relayed through the laser chain. (The pinhole manipulators in Shiva effectively provide this blocking function at the smaller filters; however, the 31- and 46-cm Nova filters would be poorly baffled by the manipulator alone.) Second, the optical design of the spatial-filter input lenses has been changed to a shape or "bending" that will move the worst ghost focus to a safe location. The single-reflection ghost from the second surface of the input lenses will be slightly divergent so that this ghost will focus slightly upstream from the previous spatial-filter pinhole and, therefore, be blocked.

Fig. 2-84. Illustration of sources of "ghost" images in Nova spatial-filter assemblies.

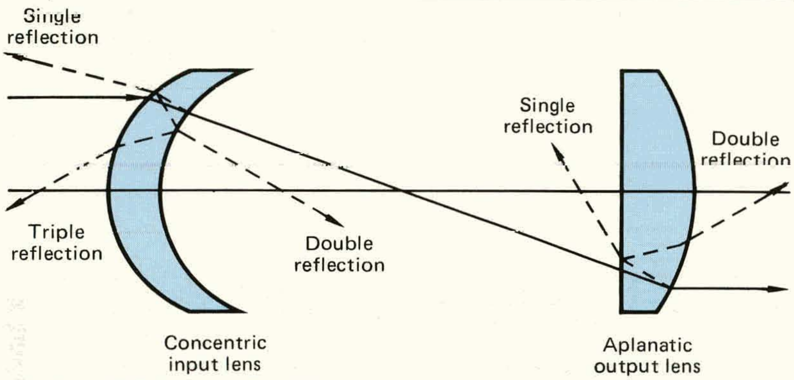

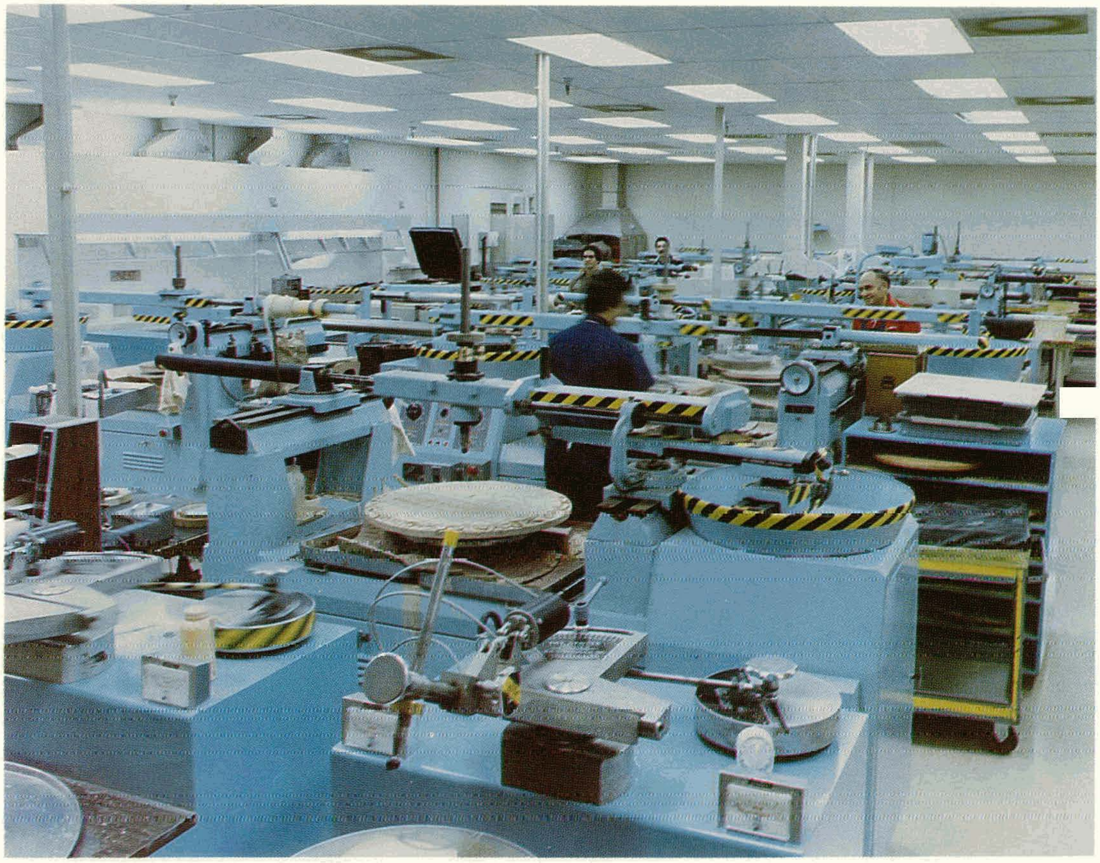

Note: machines in foreground will be used for aspherizing after spherical surfaces have been completed on machines in background.

Fig. 2-85. Part of Perkin Elmer Corp. facility, Wilton, Conn., being used for manufacturing Nova spatial-filter lenses.

Table 2-25 provides the aperture, magnification, and length of the Nova spatial-filter assemblies.

Perkin–Elmer Corp., Norwalk, Conn., is manufacturing all the 9.17- through 46-cm-aperture spatial-filter lenses. During 1980 they progressed well into the fabrication of the output lenses and the tooling for the input lenses. To accomplish their task, they have set up a special integrated manufacturing and test facility, part of which is shown in Fig. 2-85. Figure 2-86 shows a fine-ground 46-cm output lens being blocked on a polishing machine.

Tinsley Laboratories, Inc., Berkeley, Calif., is manufacturing the 74-cm-aperture spatial-filter lenses. Several are in the manufacturing cycle, and the first is nearing completion. Figure 2-87 shows the testing of a 74-cm-aperture lens at Tinsley.

Focus and diagnostics lenses are "steep" aspherics and require special facilities for fabrication. Tinsley Laboratories is manufacturing the focus lenses, for which the aspheric surface has a deviation of about 0.3 mm from the best fit sphere. Manufacturing of these lenses was temporarily put on hold in 1981 pending a final design decision on the exact focal length and material, but Tinsley has continued on schedule with the design and fabrication of a proprietary (Tinsley funded) six-degrees-of-freedom, computerized aspheric figuring machine. The six "axes" are x, y, z, lap position, lap stroke, and part rotation speed. Figure 2-88 shows this machine during construction. When used in conjunction with Tinsley's high-accuracy, surface-contour-measuring equipment,[42] this machine will perform an iterative computer-controlled convergence to the desired aspheric shape.

Eastman–Kodak Co. has the contract for the manufacture of the 80-cm-diam, f/2, single-element diagnostic lenses, which have aspheric surfaces with about 1.1-mm deviation from the best-fit sphere. They tooled for the production of these lenses during 1980 and will begin manufacture early in 1981. Their tooling also includes a proprietary (Kodak-funded) precision aspheric generator.

Coating Facilities and Technology. During late 1979 and early 1980, respectively, Optical Coating Laboratory, Inc. (OCLI) and Spectra Physics were funded to construct large optical coating chambers to handle the production coating of Nova optics. These chambers were to include

- A stainless-steel vacuum vessel.
- Vacuum pumps, plumbing, valves, and gauges.
- Rotation equipment for multiple substrates.
- Substrate heaters.
- Electron beam and resistance-heated vapor sources.
- A thin-film monitoring system.

Fig. 2-86. Nova spatial-filter output lens (46 cm) blocked for polishing at Perkin–Elmer Corp.

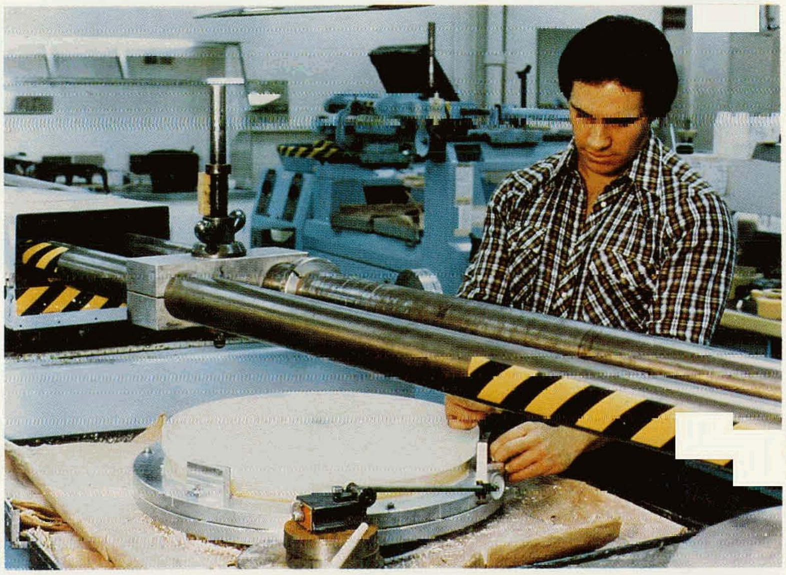

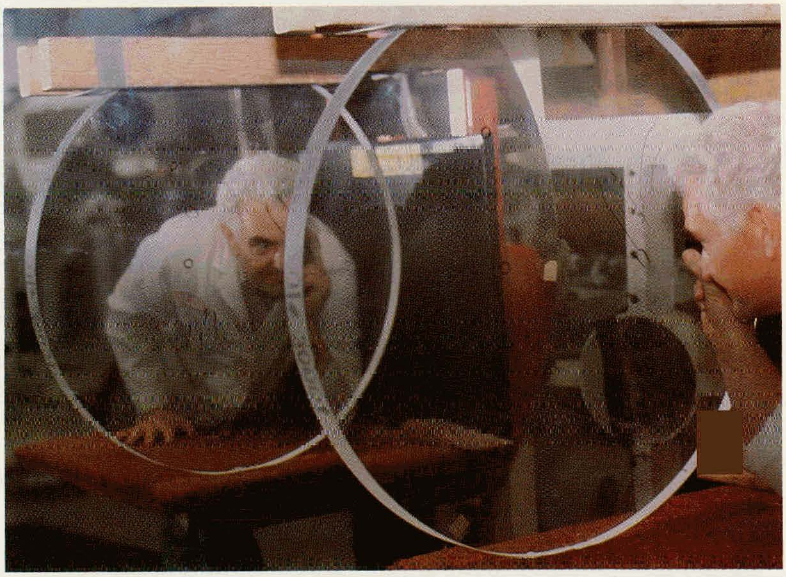

Fig. 2-87. Nova f/2 spatial-filter output lens (74 cm aperture/80 cm overall diam) being inspected at Tinsley Laboratories, Berkeley, Calif.

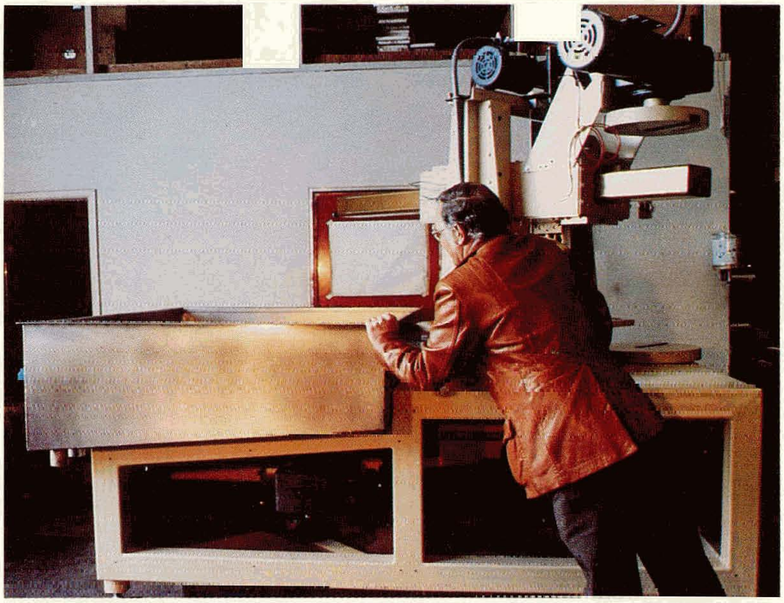

Fig. 2-88. Six-axis, ▲ computer-controlled optical figuring machine (80 cm capacity) in construction at Tinsley Laboratories.

Fig. 2-89. Shell and doors of 3-m Nova coating tank being readied for assembly by OCLI. ▼

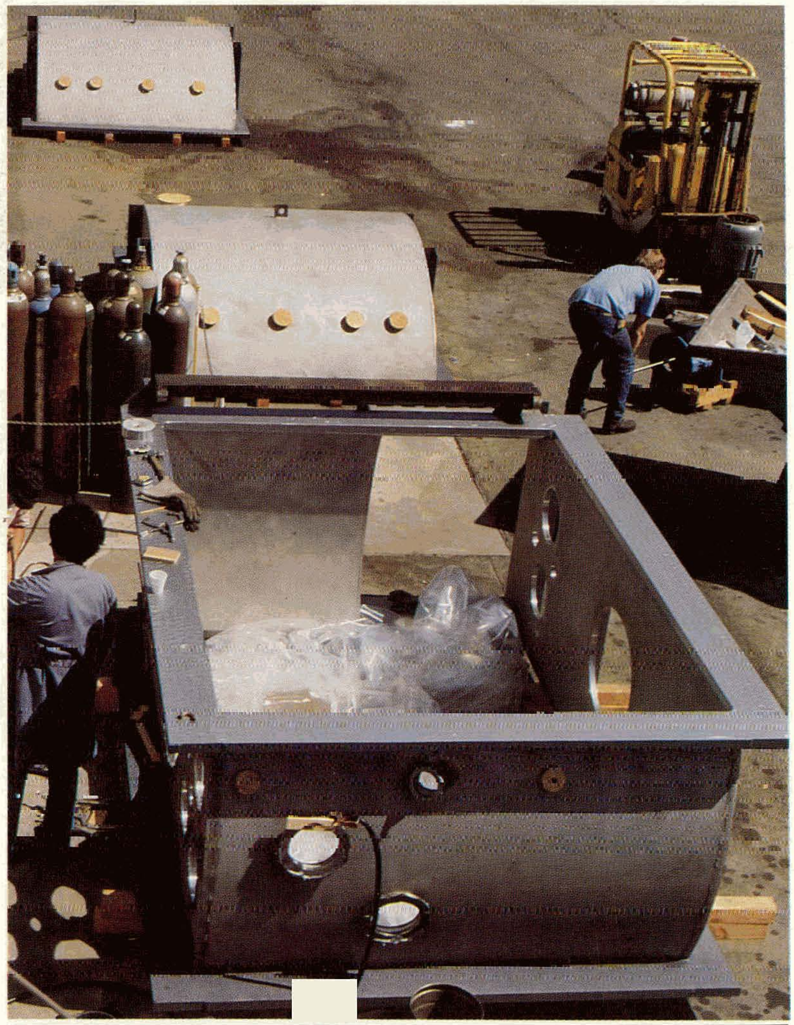

OCLI has completed construction and check-out of chamber 1018 (their designation for the LLNL unit) and will conclude the final qualification tests in the first quarter of 1981. To date, the chamber has met or exceeded its design goals. It is similar to an existing but somewhat smaller unit (100 in. diam) used for the coating of Space Shuttle windows and, more recently, for Shiva polarizers and mirrors.

The new chamber (1018) is a domed vertical cylinder of 3 m (120 in.) diam with two opposing doors positioned at 2.75-m (110-in.) chords. One door opens into a clean room and the other into a maintenance area to minimize contamination of clean staging areas during system maintenance.

Figure 2-89 shows the shell and doors of the 3-m-diam Nova coating tank being readied for assembly by OCLI. The assembled chamber, complete with internal fixturing, is shown during check out in Fig. 2-90. The figure also shows radiant quartz heaters being tested in the chamber base. The aluminum foil lining the walls is for ease of cleaning. Four substrate positions plus the propeller vapor-distribution mask are visible in the upper portion of the chamber.

In addition to this chamber construction, OCLI is engaged in two studies that will also be completed near the end of the first quarter of 1981. The first study is a detailed review of deposition parameters affecting polarizer production yield; the second is an upgrade of the Luron^R cleaning procedure to accommodate massive optics of up to 109 cm diam.

Spectra Physics chamber A2 (their designation for the LLNL chamber) is scheduled for operation in the third quarter of 1981. Different in design from the 1018, chamber A2 is a domed vertical cylinder of 2.4 m (96 in.) diam that is split on the diameter, with an added 46-cm (18-in.) flat section between halves. One half is used as the door (Fig. 2-91). The separation of the two halves of the chamber shell during fabrication can be seen in Fig. 2-92.

Spectra Physics suggested that cryopumps be used to obtain chamber vacuum in an effort to further reduce chamber contamination, and LLNL funded a study to investigate their usefulness. A total of 32 witness pieces were coated with AR and high-reflection films, using a standard diffusion pump, a diffusion pump plus a

Meissner trap (liquid-nitrogen trap), and a cryopump.

Subsequent damage testing of the witness pieces on the LLNL comparative damage tester (CDT) at 1.064 μm, 1 ns supported the decision to used cryopumps, as shown in Figs. 2-93 and 2-94.

In interpreting these figures, the following explanation applies. A test sample measured on the CDT will damage below, between, or

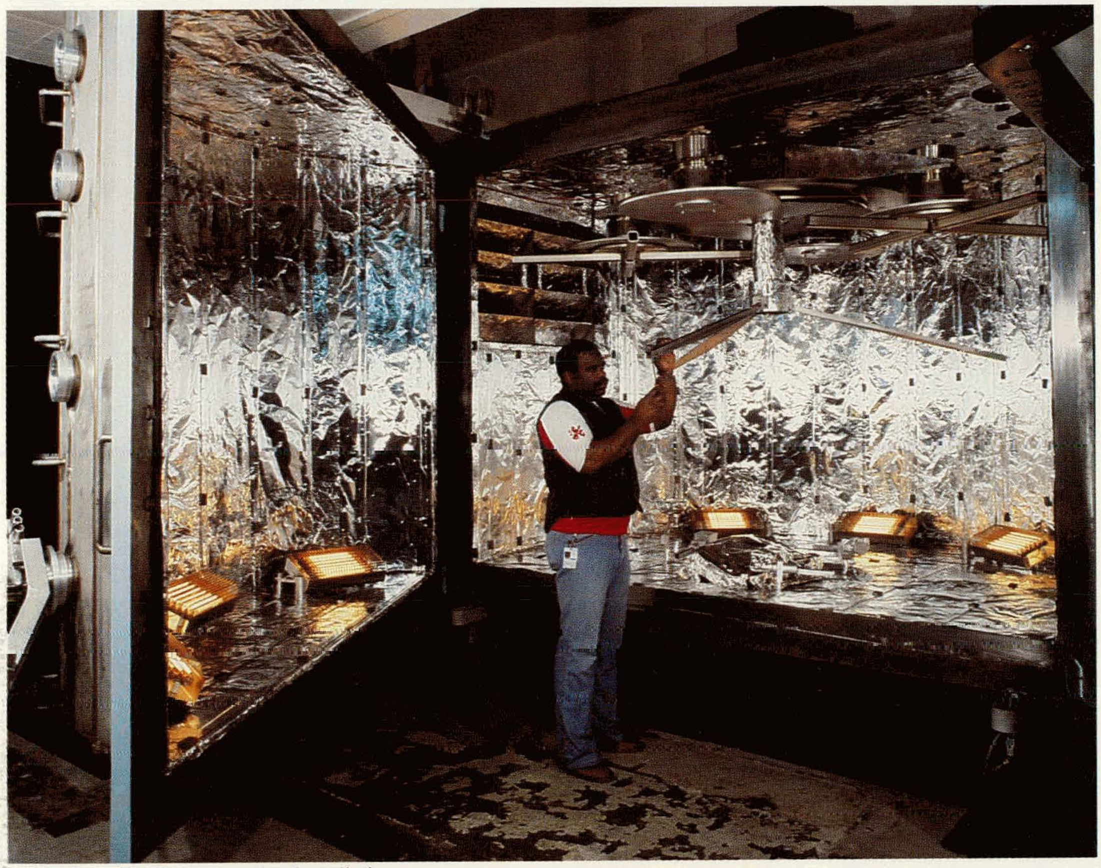

Fig. 2-90. Three-metre Nova coating chamber after assembly at OCLI.

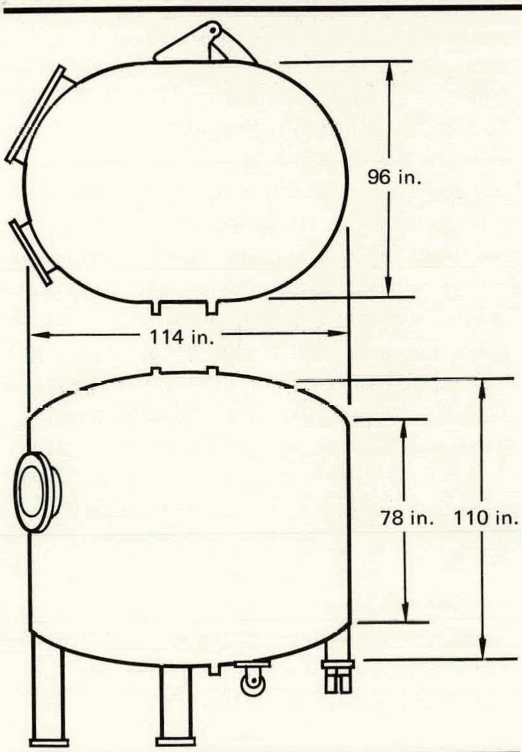

◀ Fig. 2-91. Sketch of 2.4-m Nova coating tank designed by Spectra Physics, Mountain View, Calif.

Fig. 2-92. Shell of 2.4-m Nova coating chamber being fabricated for Spectra Physics by March Metalfab, Inc., Hayward, Calif. ▼

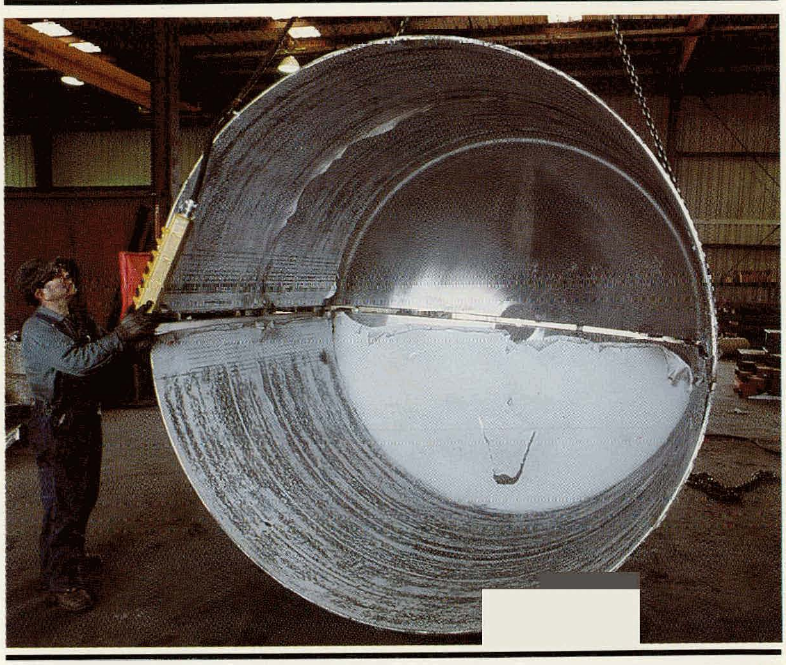

above the two reference standards. For example, part No. 22 of Fig. 2-93 represents damage occurring between 5.6 and 6.9 J/cm^2. The arrowheads point to these reference standard values. The dot represents the subjective feeling of the operator about the real location of the damage threshold. Another condition is shown in Fig. 2-94, where part No. 19 has a threshold value below 2.1 J/cm^2, the lower of the references used in this measurement. Finally, absolute threshold measurements are reported as a data point with an error bar, as for part No. 34.

Fig. 2-93. Damage threshold of high-reflection coatings vs vacuum-pumping conditions.

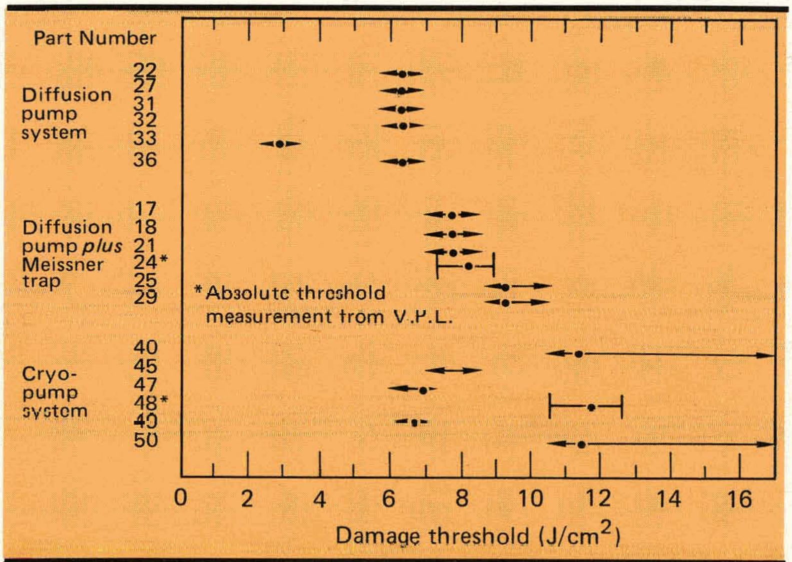

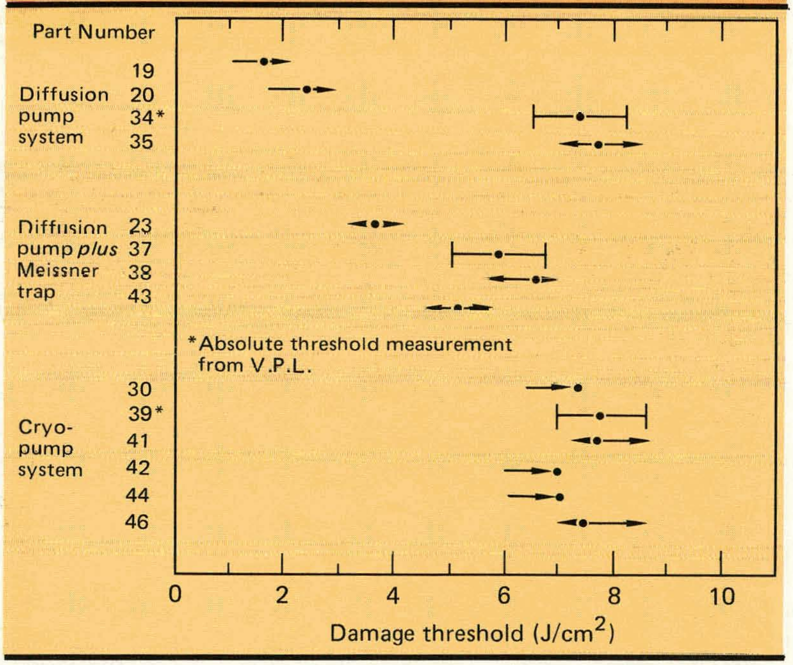

Fig. 2-94. Damage threshold of antireflection coatings vs vacuum-pumping conditions.

In September 1980, Spectra Physics submitted a final report with the following conclusion: "Replacing a diffusion pump with a cryopump eliminates substrate and film contamination due to diffusion-pump oil, and significantly lowers the residual gas load due to hydrocarbon impurities. Spectra Physics will use cryopumps on the 96 in. coater."[43]

Optical Test Instrumentation. Zygo Corp. is manufacturing an 80-cm-aperture interferometer to be used principally for optical subassembly testing for such 74-cm-stage Nova optical components as the turn mirrors, windows, focus lenses, etc. The system will have an accuracy of $\lambda/10$ at 633 nm and $\lambda/17$ at 1064 nm in the empty optical cavity. However, the accuracy of the test results may be improved by a factor of 2 by using calibration grids and a computerized data-reduction system.[44] Included as part of the interferometer is a vibration-isolation air-suspension system.

As indicated previously, the interferometer is being built to operate at wave lengths of both 633 and 1064 nm. It has been designed so that, with minimum modification, it may be extended to operate at both 530 and 350 nm. Operation at 530 nm requires the addition of a laser and some small optical and mechanical components. For 350 nm, the Zerodur transmission flat will also have to be changed. A schematic of the system is shown in Fig. 2-95.

In 1980 Zygo completed the optical and mechanical design for the instrument and ordered all long-lead items. The glass blanks for the transmission flat, the reference flat, and the collimating lens have been received by Zygo and are currently being ground and polished in the Zygo optical shop. The mechanical cells for these components are being manufactured under subcontract and will be delivered to Zygo early in 1981. A modular approach to the design has permitted the use of many standard Zygo components for the smaller parts, which are available "off the shelf." A Zygo Zapp automatic interferogram reduction system is also included. Delivery is expected by July 1981.

A 46-cm-aperture Fizeau interferometer has also been purchased from Zygo Corp. and will be used in the clean room to test laser amplifier assemblies. A very simple method has been found to modify this instrument so it can also be used as a polariscope.

In 1980 we fabricated and put into use an oil-immersion assembly for homogeneity testing of large optical blanks prior to precision finishing. This is especially important during the development and prototype stages when new materials are being developed. The oil-immersion assembly has a clear aperture of 68 cm, which is large enough to test the largest Nova laser disks.

Incorporated in the system is a unique pumping system for the index-matching oil so that the oil layer can be very thin and the windows can be atmospherically supported during the test. The assembly is composed of a closed housing that has both a fixed and a movable window of precision-polished BK-7. The blank is suspended within the housing and is immersed in oil; as oil is pumped out of the housing, atmospheric pressure brings the windows and the blank together. Then excess oil is removed, leaving the windows and the blank separated by surface-tension-supported thin films. After use, the windows can be easily separated when the housing is refilled with oil.

A variety of index-matching oil is available, depending on the index of the glass to be tested. The test most frequently performed with the device is interferometry. However, it can also be used for striae, inclusions, and stress birefringence with the optic under test having ground surfaces. Figure 2-96 shows an inspection of a polished fluorophosphate laser glass disk

Fig. 2-95. Schematic of 80-cm-aperture Nova interferometer being manufactured by Zygo Corp., Middlefield, Conn.

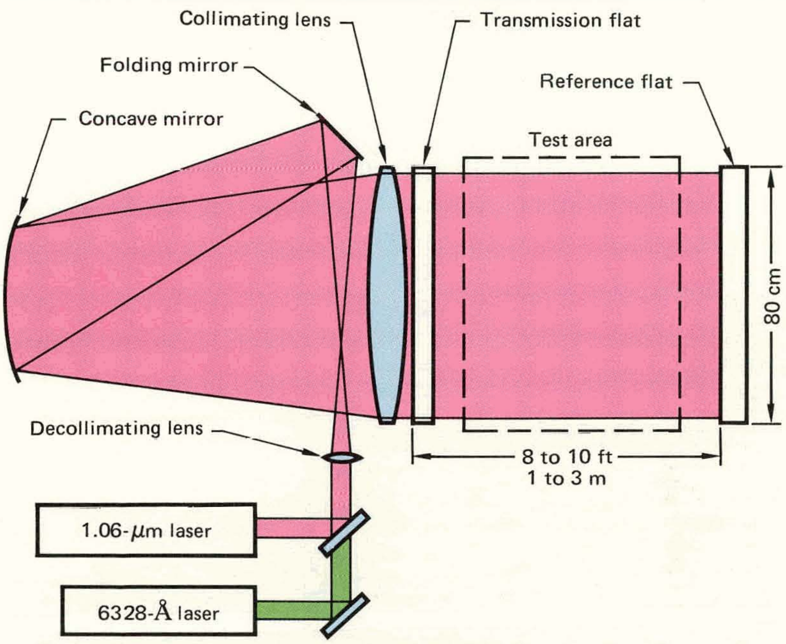

Note: an additional laser and auxiliary optics may be added for 532- and 355-nm wavelength interferometry.

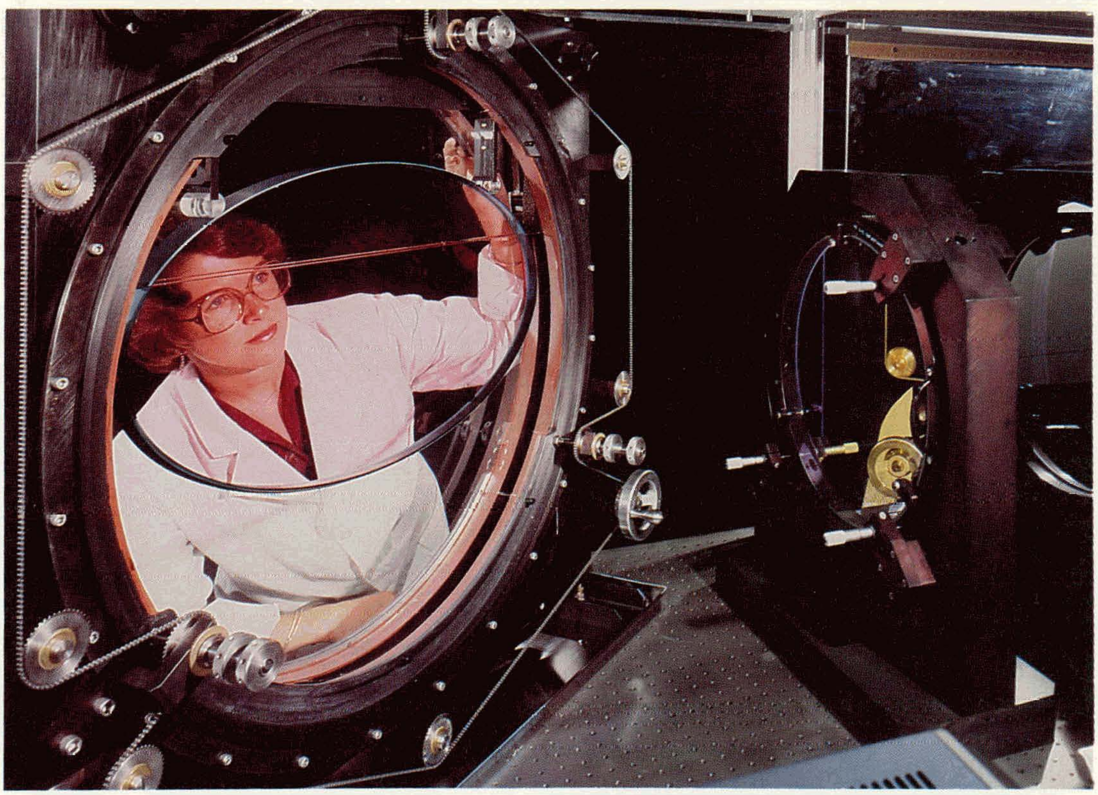

Fig. 2-96. Partially filled 68-cm-aperture, LLNL oil-immersion assembly with fluorophosphate laser disk

in the assembly, with the oil only partially filling the cavity.

Nova optics require that dielectric coatings be used to control the reflectance and transmittance of the optical surfaces. To assure coating quality, coatings will be scanned with an instrument called the OTR (overall transmittance and reflectance photometer). Figure 2-97 shows the schematic layout of the system.

Two identical units are being manufactured, one for use at OCLI during Nova production and one for general use on Nova at LLNL's discretion. The instrument design and manufacture is a joint effort between OCLI and LLNL, with OCLI being responsible primarily for the opto-mechanical structure and LLNL for the detector and electronics.

The OTR photometer, shown isometrically in Fig. 2-98, consists of

- A computer-driven x–y scanner for 109-cm optics.
- A 1064-nm optical head.
- Provision for a 528- to 351-nm optical head.
- A digital electronics system.

The electronics (Fig. 2-99) consist primarily of digital systems (i.e., LSI-11 computer, hardcopy unit, video display, floppy disks, detectors, and amplifiers).

The x–y scanner is 2.7 m wide, 2.7 m high, and 4.5 m long. The scanner can hold optics weighing up to 1200 lb. Plano–plano optics

Fig. 2-97. Schematic of overall transmittance and reflectance photometer (OTR).

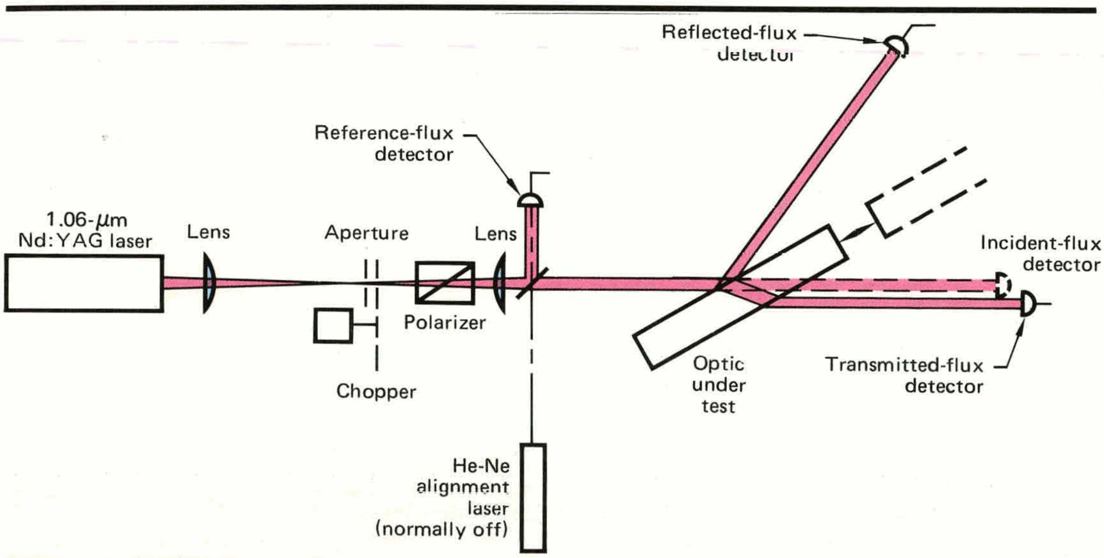

Fig. 2-98. Isometric of Nova OTR photometer being manufactured by OCLI.

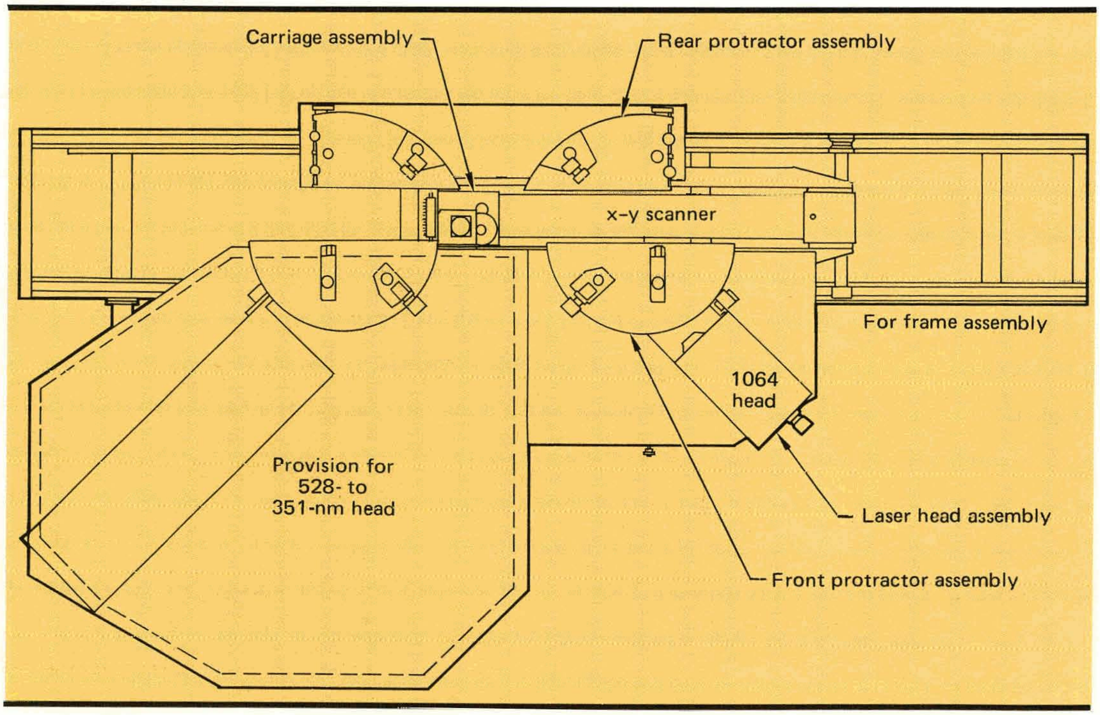

will be scanned continuously as reflectance and transmittance data are taken "on the fly." The system is also capable of performing "point-by-point" measurements on steeply curved surfaces (such as the surface of fast lenses).

The optical head contains both a 1064-nm Nd:YAG laser and a helium–neon alignment laser that is combined with the primary beam in such a way that both beams are collinear. The primary laser beam is spatially filtered and polarized either S, P, or 45° with a Glan Thompson prism. The optical head is mounted on a large horizontal protractor that is used to set the angle of incidence in the range 0 to 65° in a horizontal plane.

A mechanical wheel chops the laser output so the ambient light level can be determined and subtracted out (thus the instrument can be used in a lighted room as long as the ambient light is relatively constant). Because the amplitude of the laser varies over time, a beam splitter extracts a portion of the beam for reference. The transmittance of the optic under test is determined by the ratio of the transmitted signal divided by the reference signal after the ambient level is subtracted from each signal. Reflectance is determined in a similar manner by measuring the reflected signal instead of the transmitted signal.

The instrument achieves its high accuracy and repeatability by using a minimum of carefully designed analog circuits, digitizing the signals as soon as possible, and using the high arithmetic precision of the system's LSI 11/23 computer. The computer subtracts the ambient levels, finds the transmittance ratio, normalizes and averages data, and does other signal-processing functions.

The computer prompts an operator through the setup and measurement cycle. It controls data acquisition by programming the x–y-scan motor controllers and the sample control module. The sample control module is also synchronized with the chopper and the X-axis motor controller and is programmed to take data each specified number of millimetres on the test optic. The computer also checks for out-of-tolerance data, presents the data in tabular and graphical formats, and archives the data onto a floppy disk for later comparison or analysis.

We chose photoconductive silicon photodiodes (EG&G YAG 100) as the detectors because of their high linearity and their high sensitivity at 1064 nm. The temperature of the photodiodes is very carefully controlled, and the units are specially packaged—each with a small thermoelectric cooler and a thermistor in a TO-8-sized can (0.6 in. diam). A special diffuser lens in front of each detector eliminates photodiode spatial nonlinearities.

We developed a damage-site camera to record the onset of bulk laser damage in materials. The camera images and magnifies the damage track, using forward-scattered laser light. Using this camera, we can detect the presence of very small ($<10\ \mu m$) damage sites with densities as low as $10/cm^3$.

Bulk damage sites in glass and KDP crystals are thought to arise, respectively, from metallic particles from the glass-melting process and from misoriented crystals in the crystal lattice that have probably nucleated on impurities. Discrete damage sites result when energy fluences in the range 2 to 20 J/cm^2 (1 ns at 1064 nm) pass through test samples. When an intense visible laser beam, such as a 5-mW helium–neon (He–Ne) laser (632.8 nm), is transmitted along the same light path, the forward-scattered light from these discrete damage sites makes the sites visible to a trained unaided eye and, especially, to an

Fig. 2-99. Simplified electronics block diagram of Nova OTR photometer.

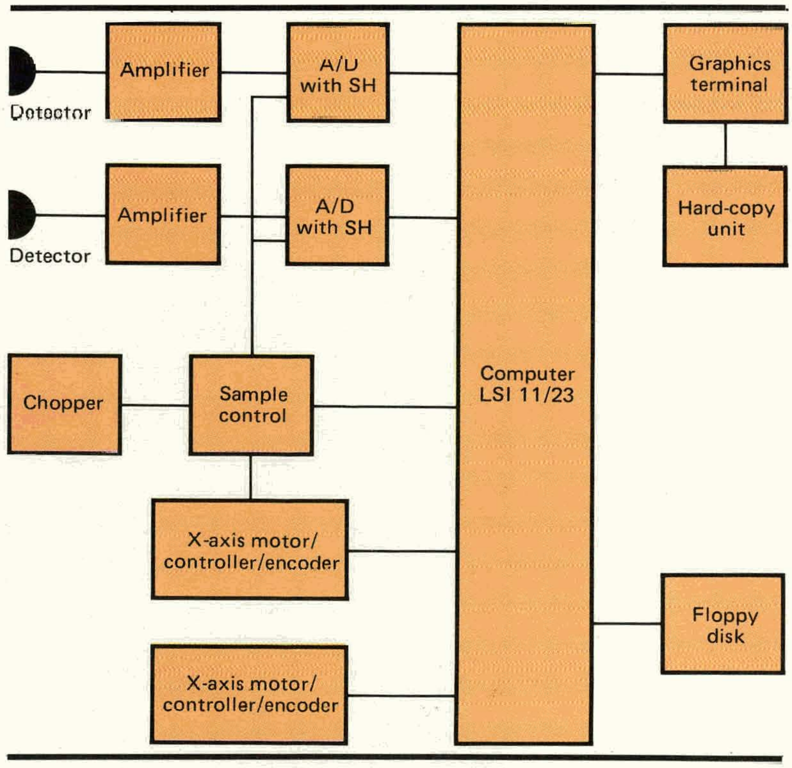

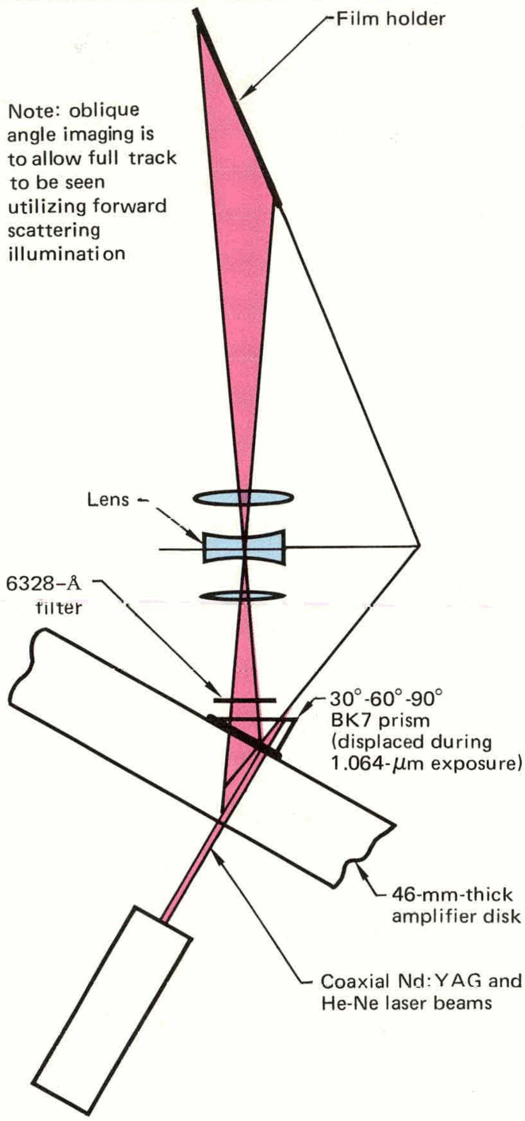

Fig. 2-100. Optical layout of damage-site camera.

optically aided eye. If the forward-scattered light from these sites is imaged, the ensemble of damage sites can be viewed or recorded on film.

In Fig. 2-100 we show the optical layout of the damage-site camera, which is being used to record bulk damage sites in a 46-mm-thick amplifier disk. The He–Ne laser is placed on one side of the amplifier disk and co-aligned with the Nd:YAG laser beam (which travels in the same direction as the He–Ne laser beam). On the opposite side of the optics, facing the two laser sources, is the damage-site camera. The camera consists of a prism, a 632.8-nm band-pass filter (used only if room lights are a problem), a camera lens, and a film holder. These parts are housed in a light-tight camera housing. The 30-60-90° prism is adjacent to the test optic and prism. This prism is removed during the firing of the 1064-nm pulsed laser.

The optical axis of the optical system is tilted away (30°) from the axis of the illuminating He–Ne laser beam to exclude the laser beam from the entrance aperture of the system and to enable one to view the entire extent of a bulk damage track through the optic under test. The column of damage sites, which is more or less normal to the flat faces of the optic, must be imaged onto the film plane such that all damage sites are in good focus at one time.

This imaging is done according to the Scheimpflug condition,[37,38] in which the image plane intersects the line formed by the

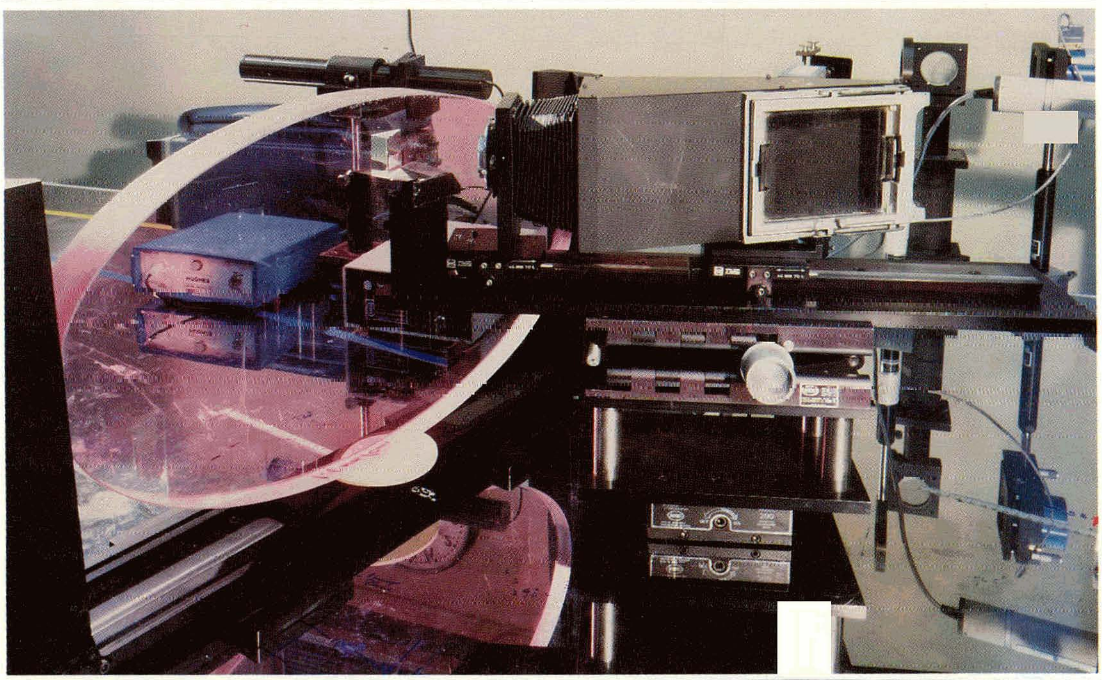

Fig. 2-101. Damage-site camera set up to record bulk damage in 31.5-cm Nova laser disk.

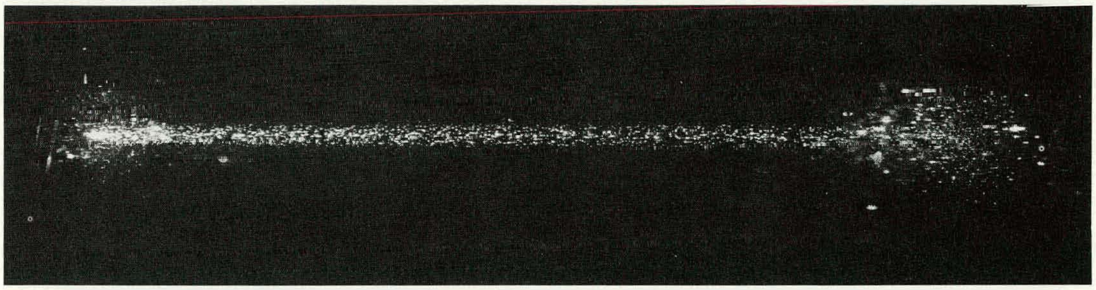

Fig. 2-102. Damage track in fluorophosphate glass, produced by 1064-nm-wavelength 15 J/cm², 1-ns laser pulse.

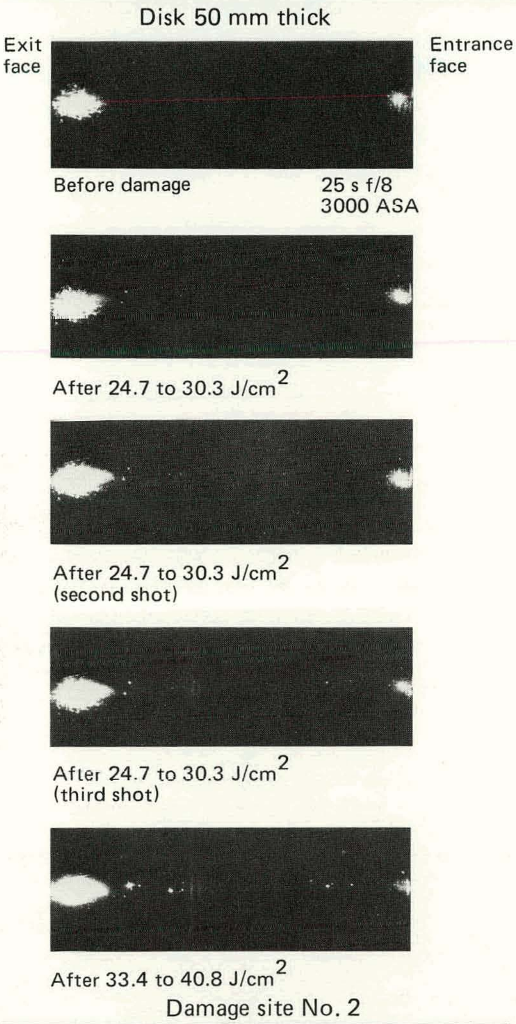

◀ Fig. 2-103. Fluorophosphate glass, showing increasing damage volumes with multiple shots.

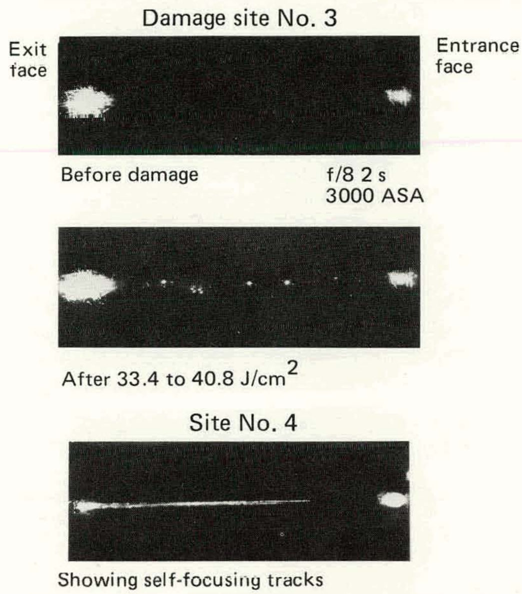

Fig. 2-104. Fluorophosphate glass, showing difference between discrete damage sites and self focusing tracks.

object plane and lens principal plane. Meeting this condition produces a sharp focus between the column of damage sites and the film plane in the damage-site camera. The magnification of the camera is approximately 2×.

Figure 2-101 shows the camera being used to record the damage test results on a 315-mm, fluorophosphate-glass laser disk.

Figure 2-102 is a picture, taken with the camera, of a severe damage track in fluorophosphate glass. This track was generated by 15 J/cm^2 of 1064-nm, 1-ns laser light, and the damaging laser beam was 1 mm in diameter. The large bright spots at the ends of the track result from surface scattering of the He–Ne beam.

We illustrate the growth of damage sites with multiple shots in Fig. 2-103. The increased scattering intensity as more shots are taken indicates larger damaged volumes. Some of the sites in the final frame in Fig. 2-102 are 0.5 to 1 mm in diameter. When the laser fluence is even higher, self-focusing tracks appear, as seen in Fig. 2-104.

A discussion of laser damage in fluorophosphate can be found in "Fluorophosphate Laser Development." For information on laser damage in KDP crystals see "Bulk Damage in KDP."

Authors: E. P. Wallerstein, S. E. Stokowski, G. R. Wirtenson, and N. L. Thomas

Major Contributors: T. M. Quick, J. Bob Brown, N. J. Brown, L. G. Seppala, and J. B. Willis

Frequency Conversion

In anticipation of a formal DOE decision to implement a frequency-conversion subsystem for Nova, we have performed most of the necessary conceptual design and optimization work. This work includes the design of

- A KDP crystal array for large-aperture beams.
- A baseline layout and geometry for the crystal array.
- A "tandem" crystal approach for the generation of either 2 or 3ω light, with high efficiency and great flexibility.

The results of this design work are described in the following sections.

KDP Crystal Arrays. In spite of a limited single crystal size, an array of small-aperture crystals can achieve harmonic generation over a large aperture (74 cm diam). We have employed this concept in the Nova design, using the Type II phase-matching cut in potassium dihydrogen phosphate (KDP), as illustrated in Fig. 2-105. In addition to providing multiwavelength flexibility, the Type II cut gives a higher conversion efficiency for the same beam intensity and crystal length, has a wider acceptance angle, and yields larger crystals than the Type I cut. While these might seem to be subtle advantages at first, they become significant when we consider the massive amount of KDP that will be required. The full Nova (20 beam) frequency-conversion system requires 40 identical crystal arrays, containing a total of about 300 crystal plates, each 27 × 27 × 1.2 cm in size. When we began to seriously consider a frequency-conversion subsystem for Nova, the volume of single-crystal KDP needed for 2 and 3ω exceeded the production capability of the US by approximately a factor of 5. In addition, the largest Type II KDP crystals then available were approximately a factor of 2 smaller in aperture than what we needed. However, the crystal growers have made rapid progress toward our goals. Their crystals are currently within a factor of 2 of our volumetric requirement and within more than 90% of our clear-aperture requirement. We feel confident that the necessary large-aperture crystals will be available in time to meet the Nova activation schedule.

At present, the optical-damage threshold of production KDP is marginally acceptable for Nova. We are working closely with the vendors to identify the contaminants that find their way into this material. The vendors

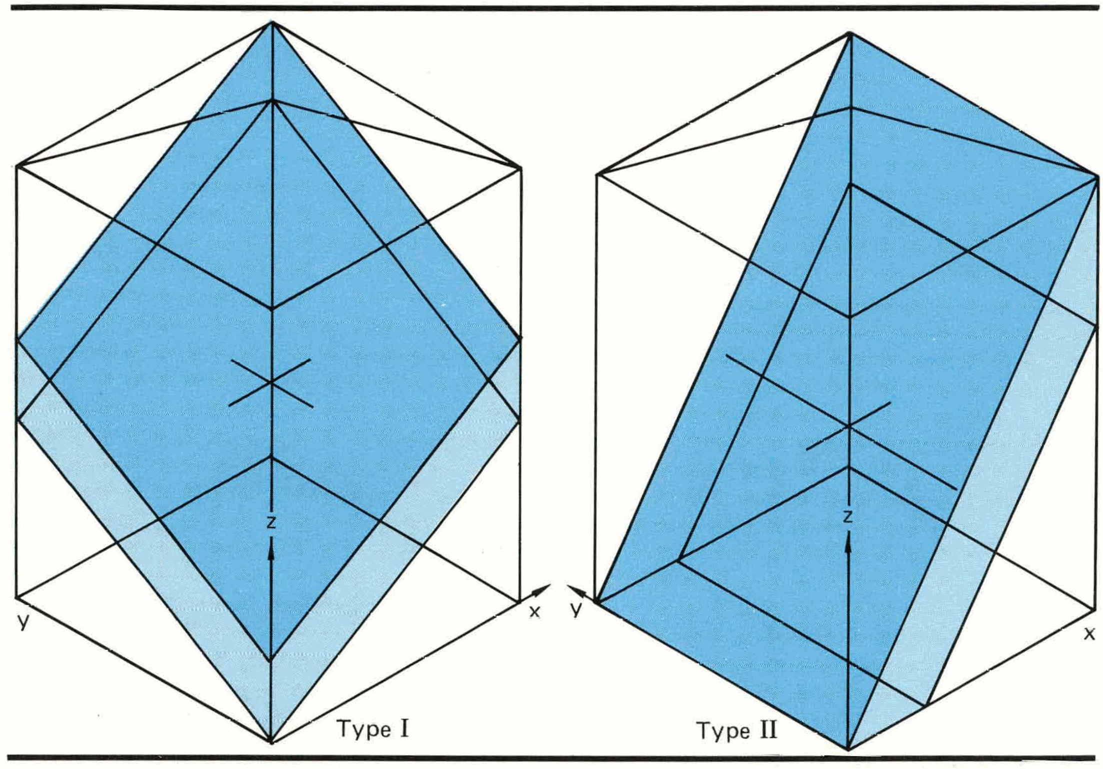

Fig. 2-105. Phase-matching cuts in potassium dihydrogen phosphate (KDP) crystals.

are also implementing some of our LLNL clean-room techniques in their KDP production. A detailed description of this work is given in "Bulk Damage in KDP."

The effects of 14-MeV neutrons on KDP have also been investigated. It appears that the KDP crystal arrays will easily withstand the intense neutron fluence in the vicinity of the Nova target chamber. This work is summarized in "Radiological Analysis."

We are currently analyzing the problem of accurately supporting the KDP crystal segments in a large-aperture array. The 74-cm-diam aperture, combined with the projected single crystal size limit of 27 × 27 cm, has driven us to abandon the 2 × 2 element edge-accessible concept in favor of the 3 × 3 element crystal-array design, shown in Fig. 2-106. Individually adjustable crystals in this latter design would significantly increase the complexity of these arrays. Therefore, we are developing a precision crystal-machining technique for constructing a monolithic assembly, as discussed in "Precision Orientation Apparatus." In this design, the crystal segments are supported between antireflection-coated windows. An index-matching fluid is used between the KDP and window surfaces, as shown in Fig. 2-106, to reduce Fresnel losses. The proper fluid has yet to be chosen, although two attractive candidates have been identified (see "Index-Matching Fluids for Large Apertures"). With precisely machined crystals, the whole array can be treated as a monolith with the necessary tuning adjustments.

Baseline. Our objective in this design is to convert the infrared (1.053 μm) light to visible (0.527 μm) or ultraviolet (0.351 μm) light, at some point after the last disk amplifier, in each of the 20 Nova amplifier chains. Four key issues are to be addressed for implementing this harmonic generation concept on Nova:

- Multiwavelength target-irradiation flexibility.
- Beam propagation without optical damage.
- Laser/crystal/target alignment and diagnostics, at the harmonic wavelengths.
- Crystal-array simplicity.

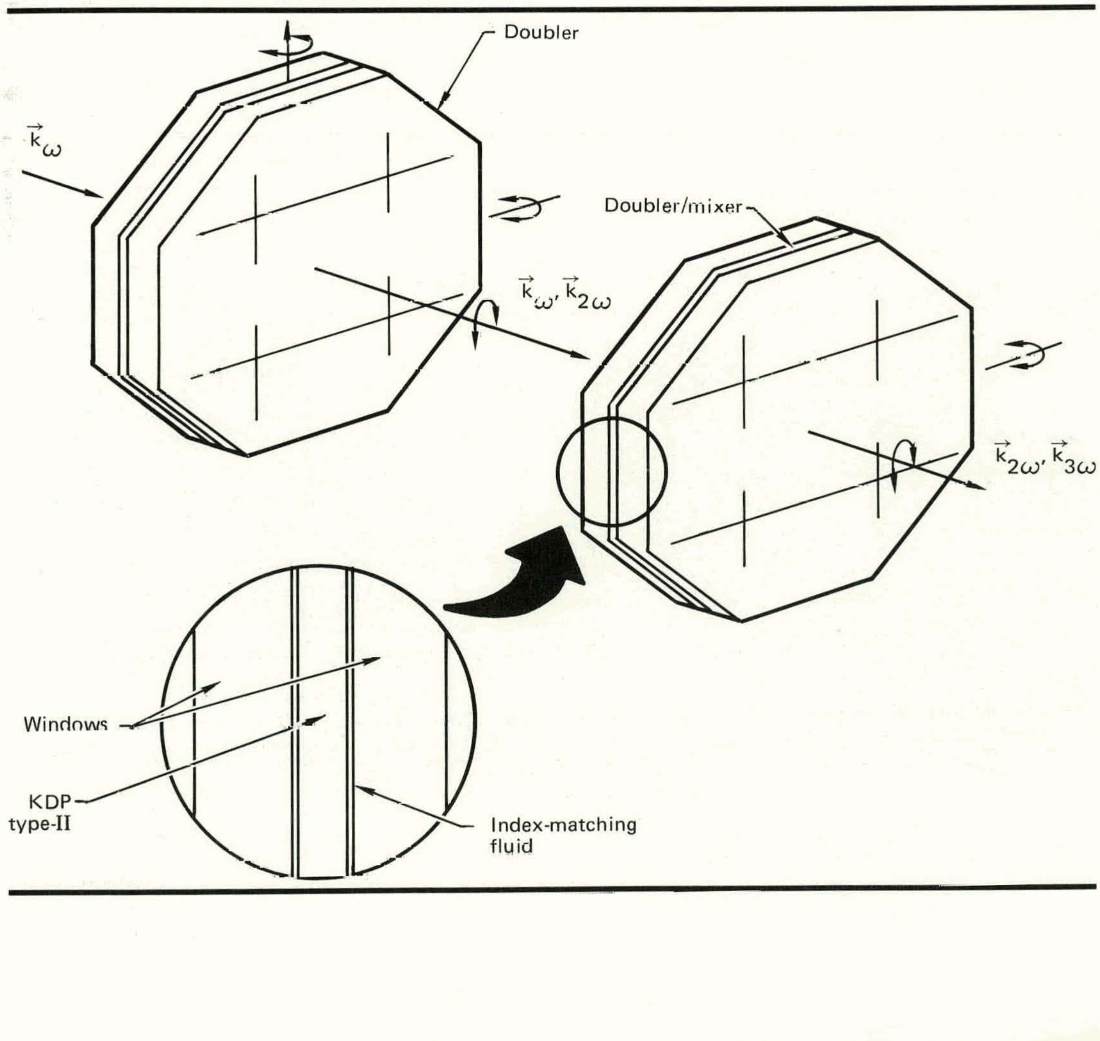

Fig. 2-106. Proposed Nova large-aperture KDP crystal arrays.

These issues form constraints for optimizing system performance.

Our task is to choose both a location and a crystal-array design that maximizes on-target performance per dollar, at the harmonic wavelength, while meeting our target-irradiation requirements and the above constraints.

The five possible locations for the crystal arrays in the Nova amplifier chain are shown in Fig. 2-107. The number of optical elements that must transmit, reflect, or focus more than one wavelength increases as the crystals are moved back toward the laser chain (away from the target focusing lens). Designing and constructing large-aperture optics to operate at more than one wavelength (or to be replaced when changing wavelengths) is extremely expensive and, therefore, unattractive. As a consequence, we must minimize the number of components that need to be changed and require that all optical elements operate with full performance at only one wavelength. Option (a), in Fig. 2-107, comes closest to meeting these requirements. In this option, the focus lens must operate at all three wavelengths, and it is the most difficult configuration to diagnose. However, we have identified two attractive focusing systems that require only a single wavelength-dependent component (beam dump) and can facilitate the incident harmonic-energy diagnostic. Their major drawback is that the target equivalent-plane photograph might be compromised. The baseline design for the Nova frequency-conversion system is illustrated in Fig. 2-108.

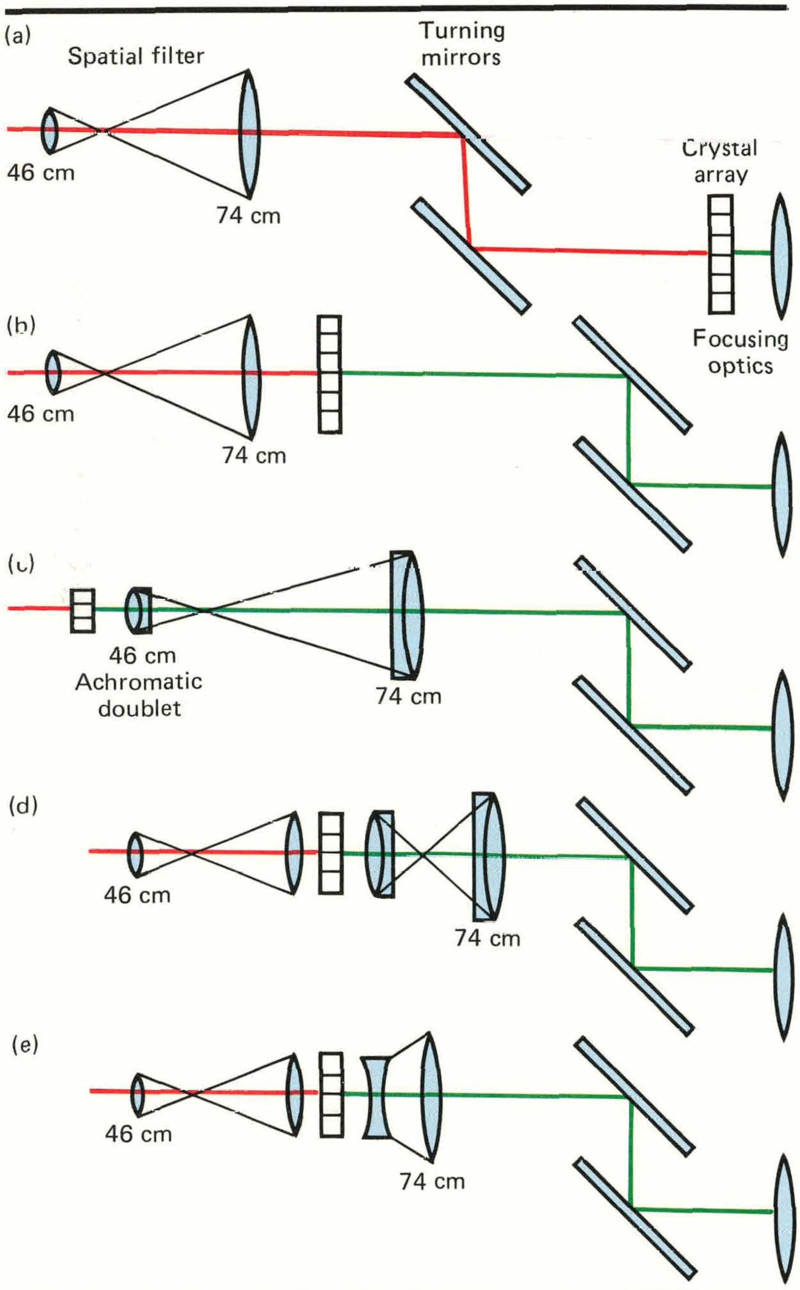

Fig. 2-107. KDP crystal-array location options.

After passing through the last spatial filter, the infrared beam (1ω) is imaged onto the focus lens by a system of mirrors having a high reflectance at 1ω. These mirrors are also used to transport a diagnostic reflection (at the 2 and 3ω harmonic wavelengths) back to the modular alignment/diagnostic sensor, located behind the first turning mirror. The reflected beam intensity (less than 4% of the harmonic intensity), while overly energetic for diagnostic purposes, is well below the mirror-damage threshold. Although this places an additional reflectivity requirement on the mirror coatings, high damage resistance and high reflectivity are not required. The details of this design are discussed in "Expansion of Output Alignment/Diagnostics Subsystems for Multiwavelength Operation."

The optical elements in the two focusing systems being analyzed are shown in Fig. 2-109. Both rely on phase-separated or leached, broad-band antireflection surfaces on substrates with high transmittance at all three wavelengths (such as BK-10, fused silica, or fluorophosphate glasses). The combination of short wavelength and spatial modulation from the gap between the crystal segments places a severe limit on the amount of glass used at this location. As a guideline, we have chosen an upper bound of $\Delta B \leqslant 3$ rad to limit the growth of small-scale modulation (damage threat) and defocusing

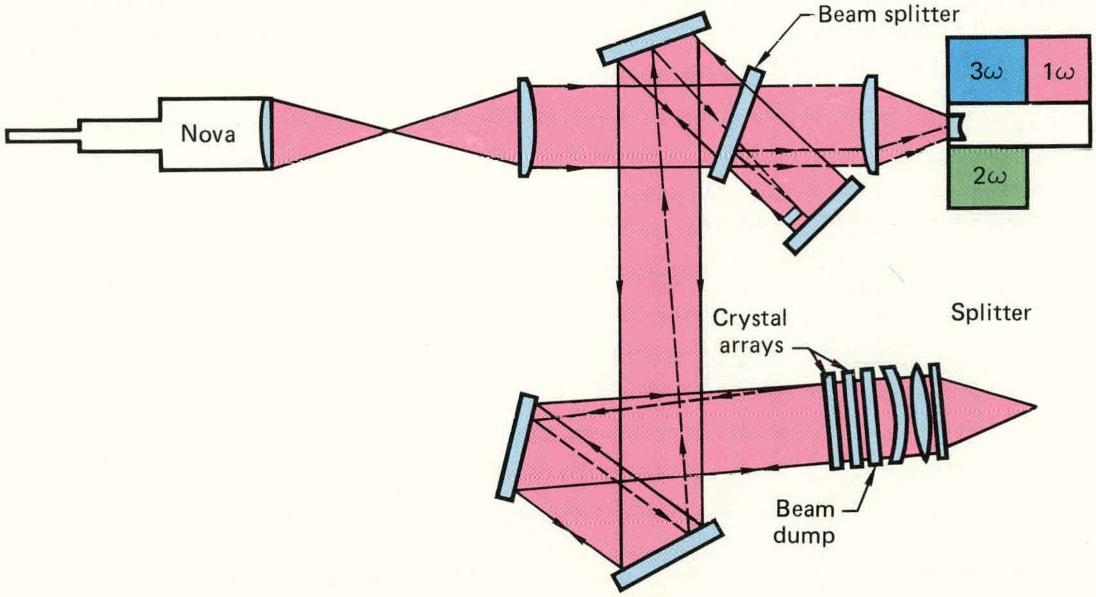

Fig. 2-108. Nova frequency-conversion baseline optical path.

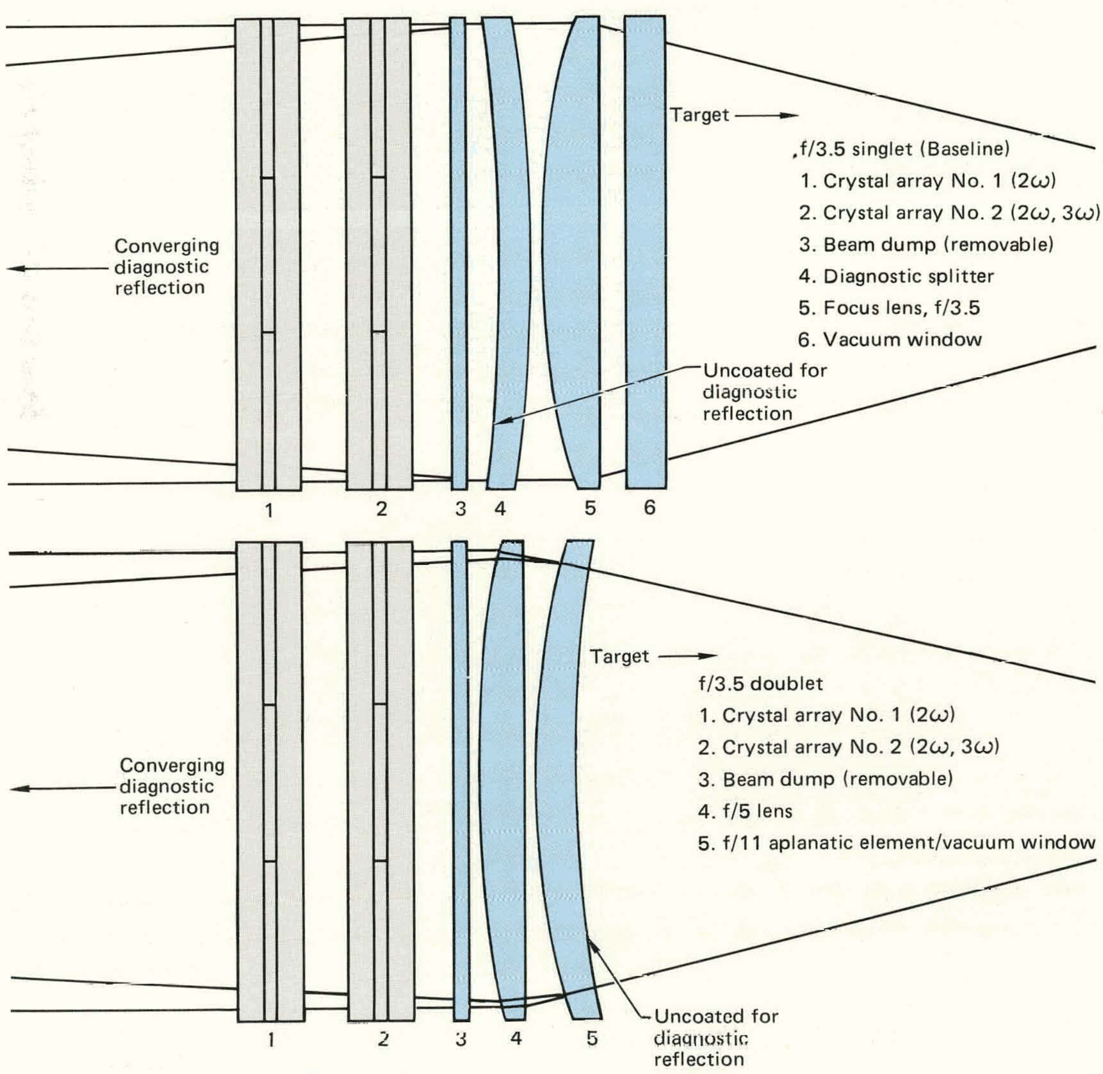

Fig. 2-109. Nova frequency-conversion optics, including frequency-conversion crystal arrays.

in the target plane. A detailed analysis of the propagation is under way.

Tandem Crystal Arrays. We have developed a system that, by employing two identical crystal arrays, can produce the second and third harmonics over a wide range of input intensities. Conventional approaches to this problem would require using three different crystal assemblies, significantly increasing the cost and reducing the number of interchangeable parts. As illustrated in Fig. 2-110, two major concepts have been brought together in this design:

- The second harmonic is generated by using two Type II, 1.2-cm-thick KDP crystal arrays operating in tandem.[45] This permits operation with effective crystal lengths of either 1.2 or 2.4 cm, as shown in Fig. 2-111. In the past, the tandem approach has been used on low-power lasers, both to increase the effective crystal length and to compensate for beam walk off and

Fig. 2-110. Tandem second-harmonic generation (SHG) and cascade third-harmonic generation (THG), using Type II KDP crystals.

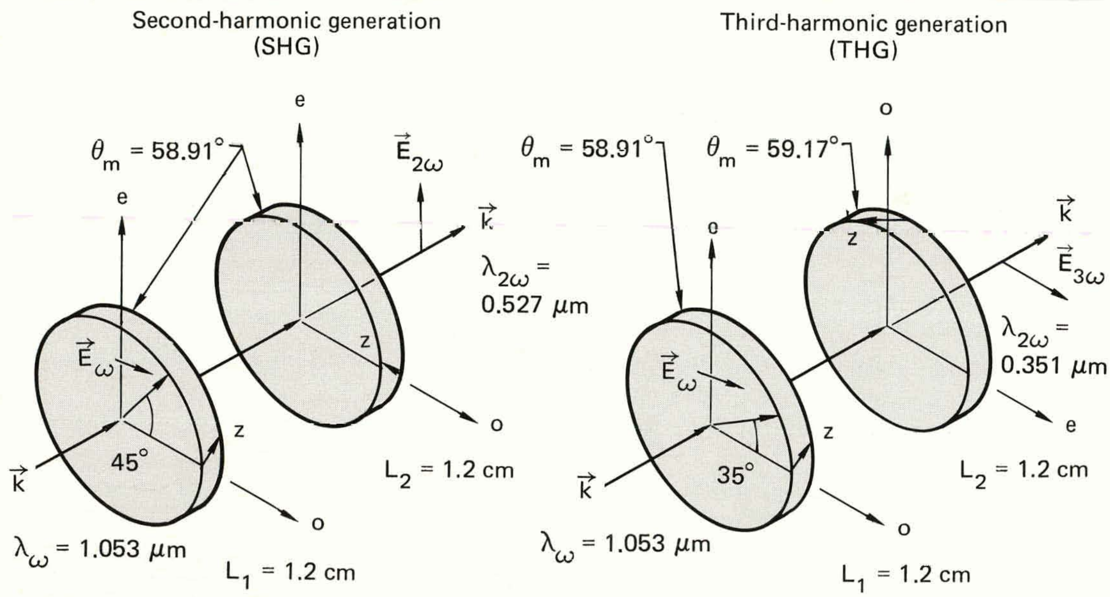

Fig. 2-111. Graph of second-harmonic conversion efficiency vs fundamental intensity for flat and Gaussian temporal input profiles.

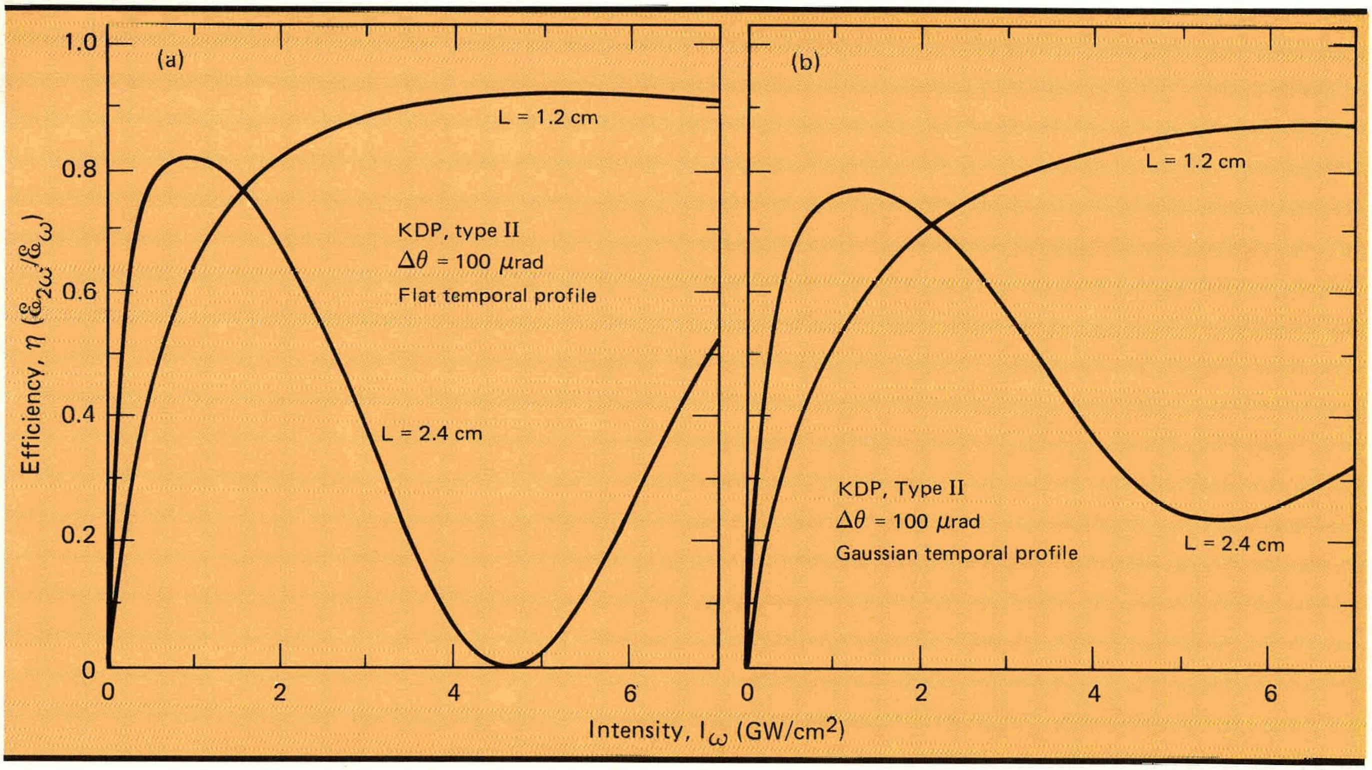

misalignment.[46,47] Efficient conversion is achieved over a wide range of input intensities.

- Third-harmonic generation is achieved by using (as shown in Fig. 2-112) the Type II/Type II polarization-mismatch scheme,[48] simply by rotating the two crystals in a plane perpendicular to the beam direction, and tuning the second crystal to the mixer phase-matching angle ($\Delta\theta \approx 4.4$ mrad). Efficient conversion is achieved over a somewhat smaller input-intensity range than that achieved with second-harmonic generation. Our design works best at the low-intensity end of the pulse-width range—from 2 to 5 ns.

Each of the array gimbals will provide a two-axis tilt for phase-matching alignment and rotation about the beam direction, as illustrated in Fig. 2-113. We must also control the relative phase of the 1ω and 2ω waves entering the second array (for tandem second-harmonic generation only). This is achieved by employing the dispersion of air to compensate for the dispersion in the windows and the index-matching fluid. This relative phase control can also be achieved by tilting one or both arrays about the insensitive (ordinary) axis, thereby changing the optical path through the windows and fluid.

The complete assembly, as presently envisioned, is located just upstream of the focus-lens drive, as shown in Fig. 2-113. We are considering ways to incorporate the frequency-conversion system into the focus-lens drive assembly to further simplify the mounting hardware requirements and shorten the propagation distance.

A detailed propagation and ghost-focus analysis is now being prepared. Performance is most sensitive to the component's location, damage threshold, and nonlinear index. At present, many of these parameters can only be estimated. Even so, by using

Fig. 2-112. Graph of third-harmonic conversion efficiency vs fundamental intensity for flat and Gaussian temporal input profiles.

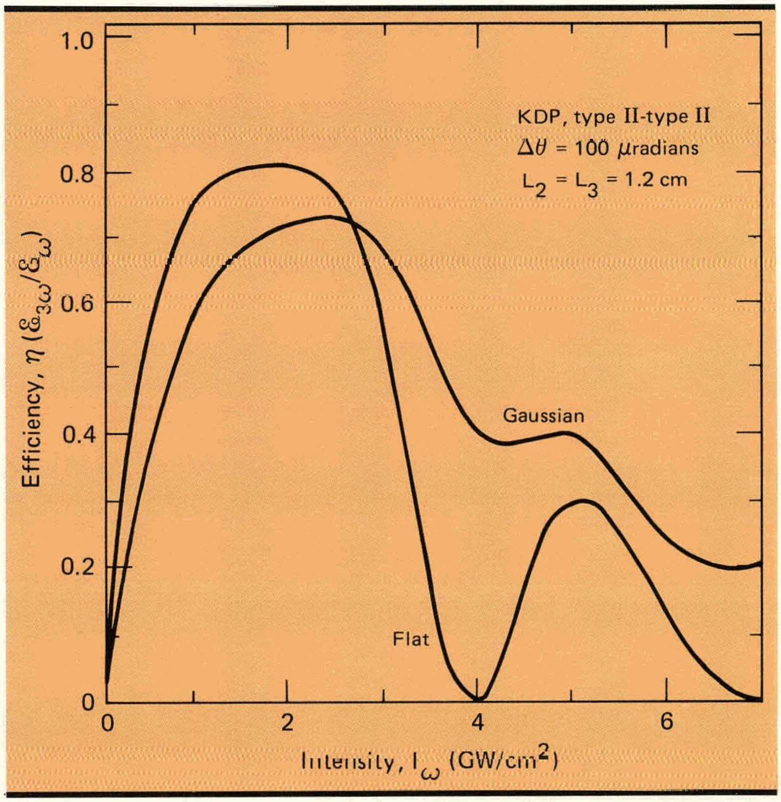

Fig. 2-113. Exploded and partially cutaway view of the harmonic generator assembly (left), and a schematic drawing showing the location of the assembly on the target chamber (right).

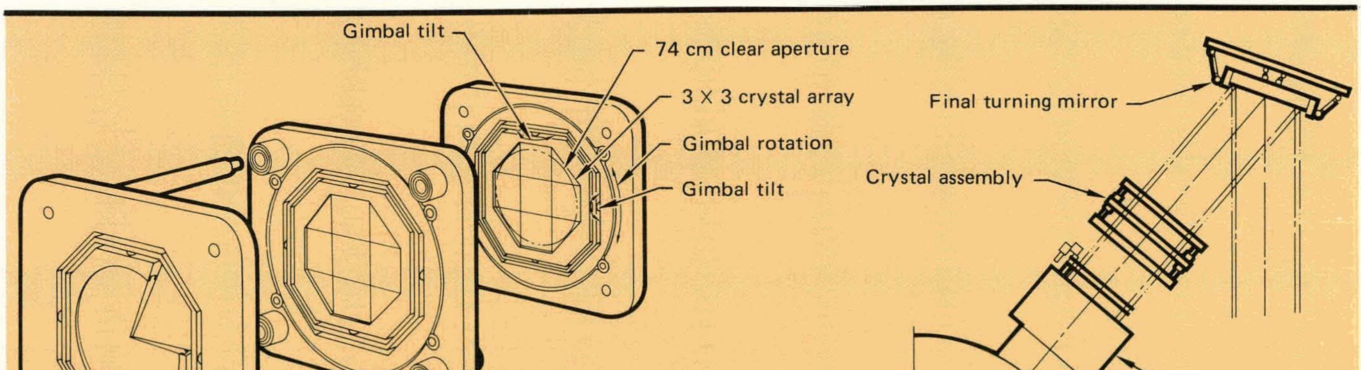

Fig. 2-114. Calculated curves for expected Nova performance at the second and third harmonics.

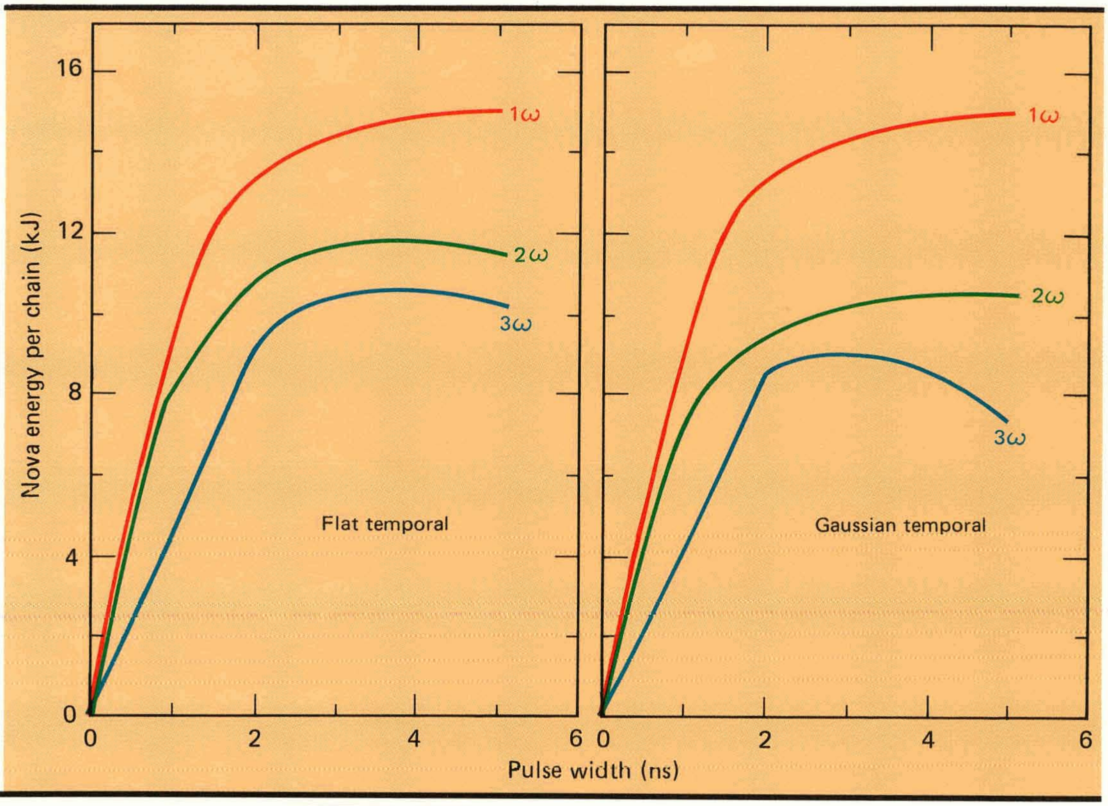

Fig. 2-115. Plan, end, and elevation views of the full Nova system.

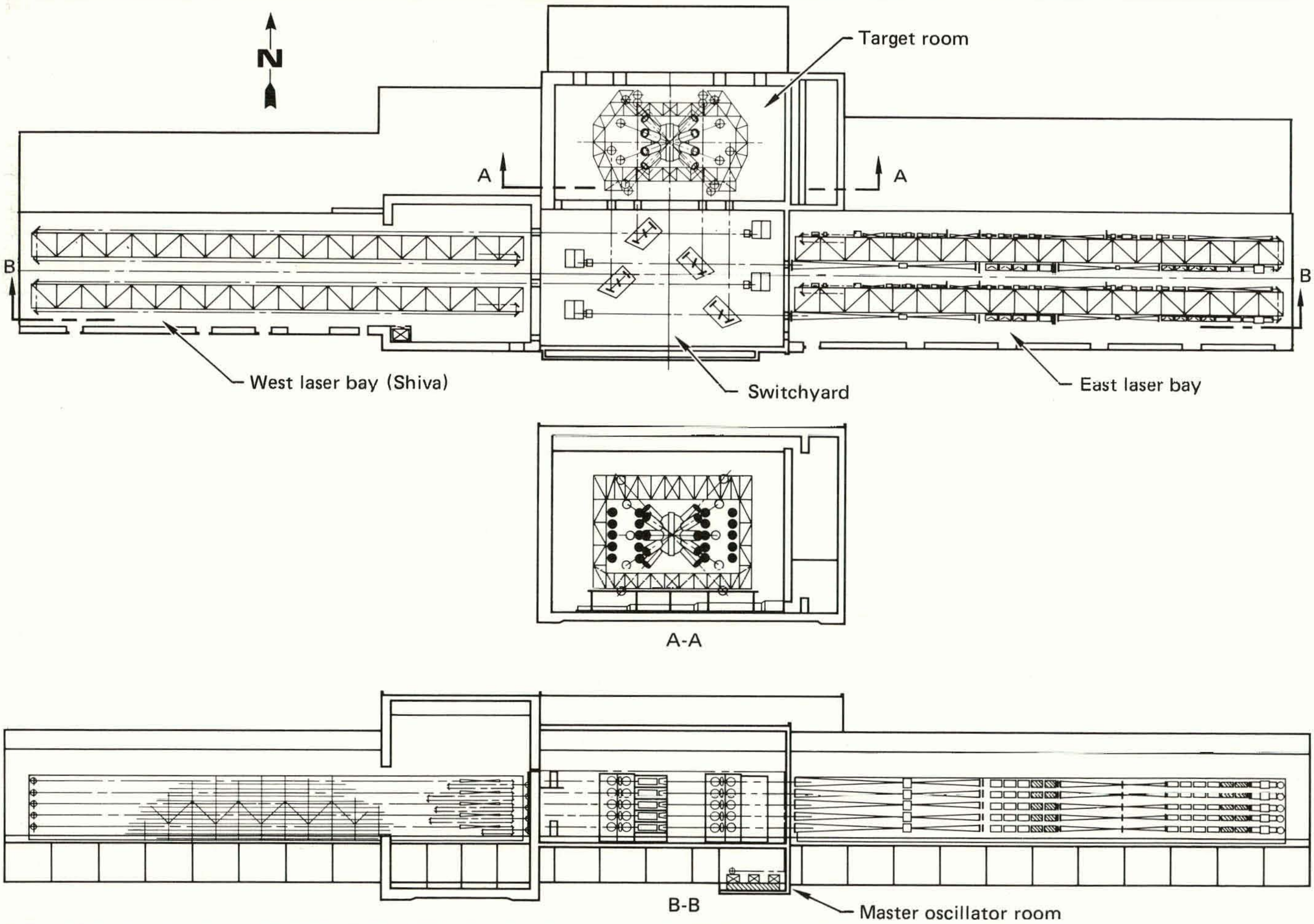

these estimates, we have calculated the expected Nova performance at 2 and 3ω. The results, summarized in Fig. 2-114, are for both flat temporal/flat spatial and Gaussian temporal/flat spatial input profiles. It should be noted that the 3ω performance is significantly influenced by the temporal shape, reflecting the narrower input intensity range for high conversion efficiency.

The advantage of driving the crystals with a flat temporal profile can be seen clearly in Fig. 2-114. This advantage is consistent with our target pulse-shaping requirements.

The frequency-conversion system we are designing will give Nova the ability to operate at the fundamental, second, and third harmonics and will combine this ability with the flexibility of changing wavelengths easily. The technical risks of such a large-scale undertaking are being reduced and the target-performance payoffs are great. With the addition of this frequency-conversion subsystem, the Nova laser will have the capability for high-energy, multiwavelength target irradiation by the mid-1980s.

Author: M. A. Summers

Major Contributors: E. S. Bliss, E. M.Booth, A. Budgor, D. Eimerl, B. C. Johnson, R. G. Ozarski, W. L. Smith, S. E. Stokowski, E. P. Wallerstein, and W. E. Warren

Space Frames

Introduction. Space frames serve as stable supports for optical components, as discussed in the 1979 Laser Program Annual Report,[49] which describes the state of space frame design at that time. Since then, we have been making design changes in the switchyard and target areas to allow convenient conversion to Nova Phase II. This requires that the switchyard and target areas be designed for compatibility with a system having 10 beams coming from the east wing and 10 beams from the west wing, as shown in Fig. 2-115.

The switchyard mirror stations can be moved to accommodate Phase I irradiation (10 beams from the east laser only), as shown in Figs. 2-116 and 2-117. To point 10 beams at the target, this scheme uses a total of 39 mirrors in the switchyard and target room. The mirrors shown at left in Fig. 2-116 are in the switchyard, and those to the right, around the target chamber, are in the target room. The final leg of each beamline in the target room will lie as a ray on the side of a

Fig. 2-116. Mirror geometry for the 10-beam Nova Phase I.

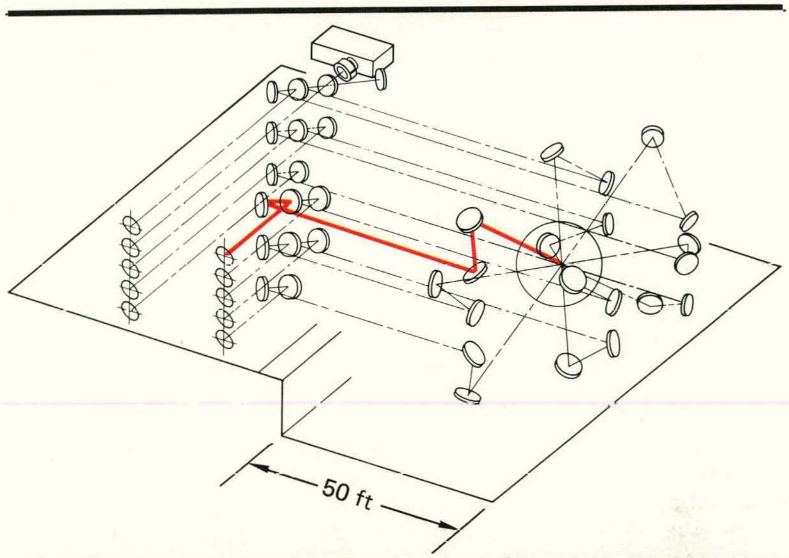

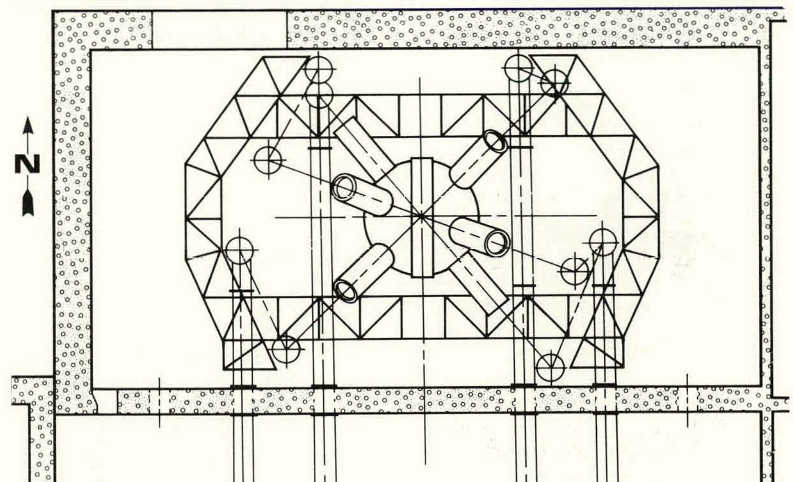

Fig. 2-117. Plan view of the Nova switchyard and target room for the 10-beam Nova Phase I.

cone having a nominal included angle of 100°. There will be two opposing cones with their common horizontal axis oriented east and west; beamlines will be opposed for alignment purposes.

As shown in Fig. 2-118, we are designing the laser-bay space frame as two separate frames that are independently tied to the floor at their midpoints with a seismic anchor and allowed to thermally expand outward from these points. The frames are structurally designed to have open interiors for maintenance and utility access.

Figure 2-119 is a plan view of the target room and switchyard, showing the arrangement to be used with 20 beams. (The 10-beam geometry is shown in the 1979 Laser Program Annual Report.[49]) We are redesigning these frames so they will be compatible with both Phases I and II of Nova. Figure 2-120 is an elevation view of the same area. The location of mirrors on the periphery of the 100° cone is also shown here.

Another space frame is located in the master oscillator room, in the basement. This frame, like the others, is constructed of square cross-sectioned beams. It is table height and is tied together structurally below the raised floor level. A set of table "islands" will stand above the raised floor. They will support hardware on surfaces that are a sandwich construction of plate steel and a commercial honeycomb table top, which is the final working surface.

Analysis. We evaluated three space frame structural designs for Nova during 1980. These evaluations involved computer analyses based on dynamic loading conditions. (The switchyard frame will be analyzed in 1981.)

We performed a modal analysis for each design to establish the fundamental and higher harmonic frequencies of structural vibration and mode shapes. Using the analytic modal results for comparison, we did evaluations to determine the influence of frame-member sizes and locations, as well as variations in support and anchor restraint conditions, on the lowest mode frequency.

Once we decided that a frame design was satisfactory, as determined by modal analysis, we evaluated the response of the structure by performing a dynamic analysis. Actual ground-vibration data, obtained at the Nova site, were used in this analysis. We also evaluated the design for the frame-structure supports and anchors. This evaluation was based on static and dynamic loading conditions during normal operation, as well as for a specific seismic loading condition.

Laser Frame. The laser-bay structural design consists of a frame that is 192 ft long, 27.5 ft high, and 10 ft wide, with beam members made of 6-in.-square tubing.

To give the frame longitudinal stability, we provided diagonal bracing at midheight along the length of both sides. For lateral stability, we also provided diagonal bracing at the tower structures, which are located at

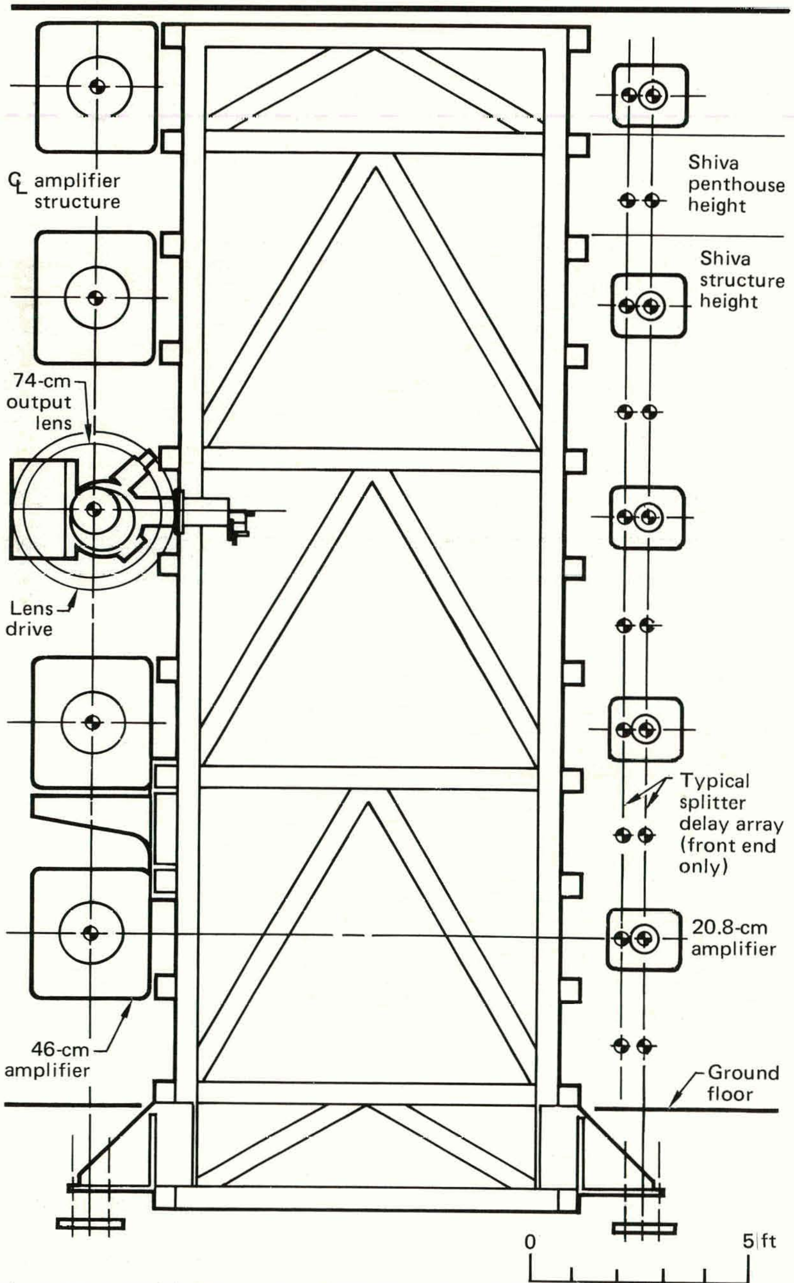

Fig. 2-118. Elevation cross-sectional view of the laser frame, showing the 20.8- and 46-cm amplifier arrangement.

20-ft intervals along the length of the frame. Additional in-plane diagonal bracing is provided at three levels along the length of the frame.

Support members are used, at 20-ft intervals, on both sides of the frame. The supports provided at these points allow the frame to thermally expand and contract lengthwise [Fig. 2-121(a)].

We used the SAP IV computer model[50] for the dynamic analysis of the frame. It included 1352 modal points, 2081 beam members, and 115 plate members. The results of this modal analysis showed the three lowest frequencies to be

- 6.90 Hz.
- 7.02 Hz.
- 7.26 Hz.

The lowest frequency, 6.90 Hz, corresponds to a "sliding" of the frame in a direction along its length [Fig. 2-121(b)].

The second frequency, 7.02 Hz, corresponds to a lateral "rocking" of the frame, with the largest lateral displacement near the middle of the frame. The mode shape is a single curve of the frame, from end to end [Fig. 2-121(c)].

The third frequency, 7.26 Hz, corresponds to a lateral "rocking," in opposite directions, of the *ends* of the frame. This mode shape is a twist of the frame [Fig. 2-121(d)].

Next, we obtained deformations of the frame by using the actual, measured forcing function data. The frame displacements, as related to spatial filter locations on the frame, are shown in Fig. 2-122. With a maximum translation of $\pm 3.415\ \mu m$ and a

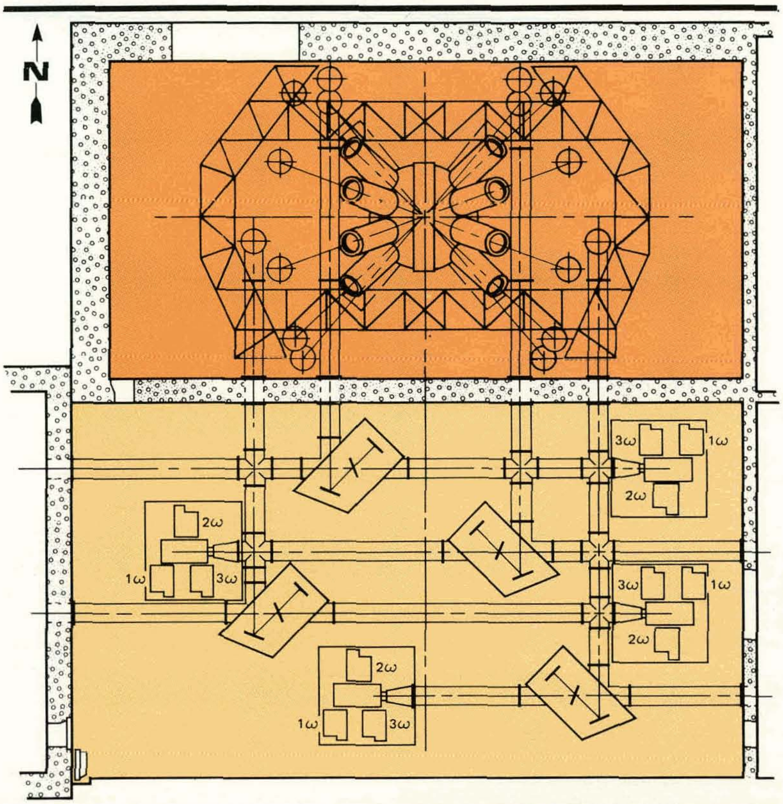

Fig. 2-119. Plan view of the full 20-beam Nova switchyard and target room.

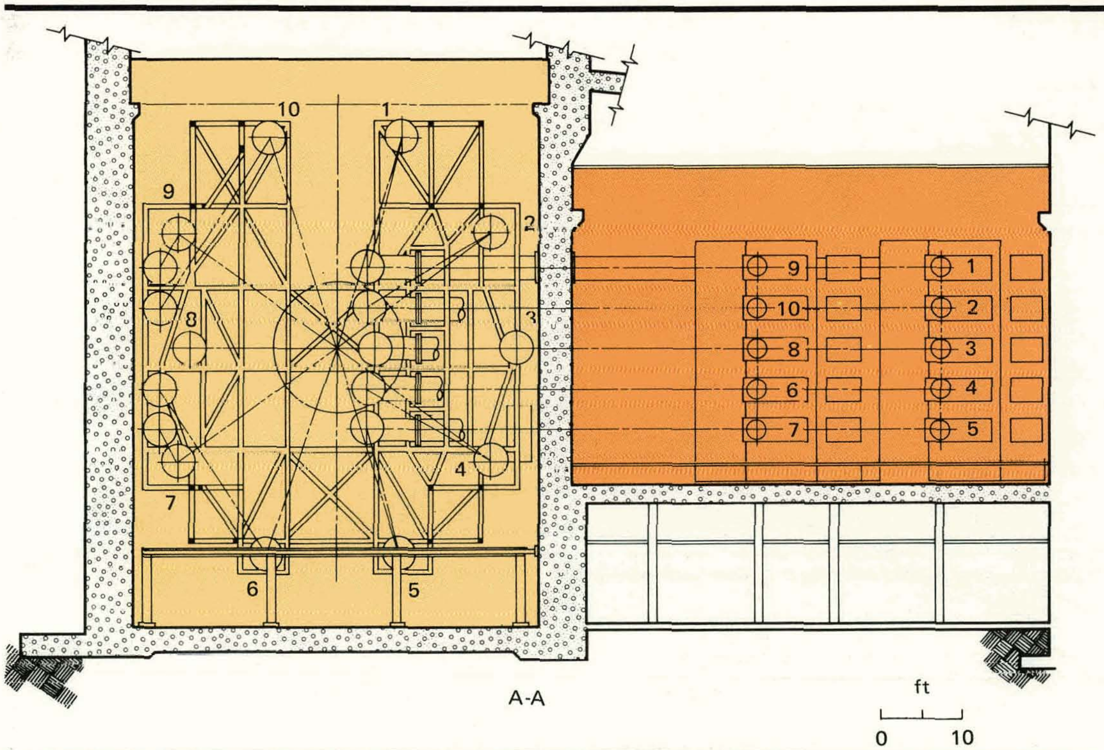

Fig. 2-120. Elevation view of the Nova switchyard and target room.

maximum rotation of $\pm 0.972\ \mu$rad, the deformations were within acceptable limits.

Our analysis of equipment servicing requirements indicates that a passageway, going through the frame to connect the three aisleways, is needed to allow access to both sides of the structure. As shown in Fig. 2-121(a), the passageway will be located near the midlength of the frame.

Two seismic anchors will be provided on one side of the frame, one at each side of the passageway opening.

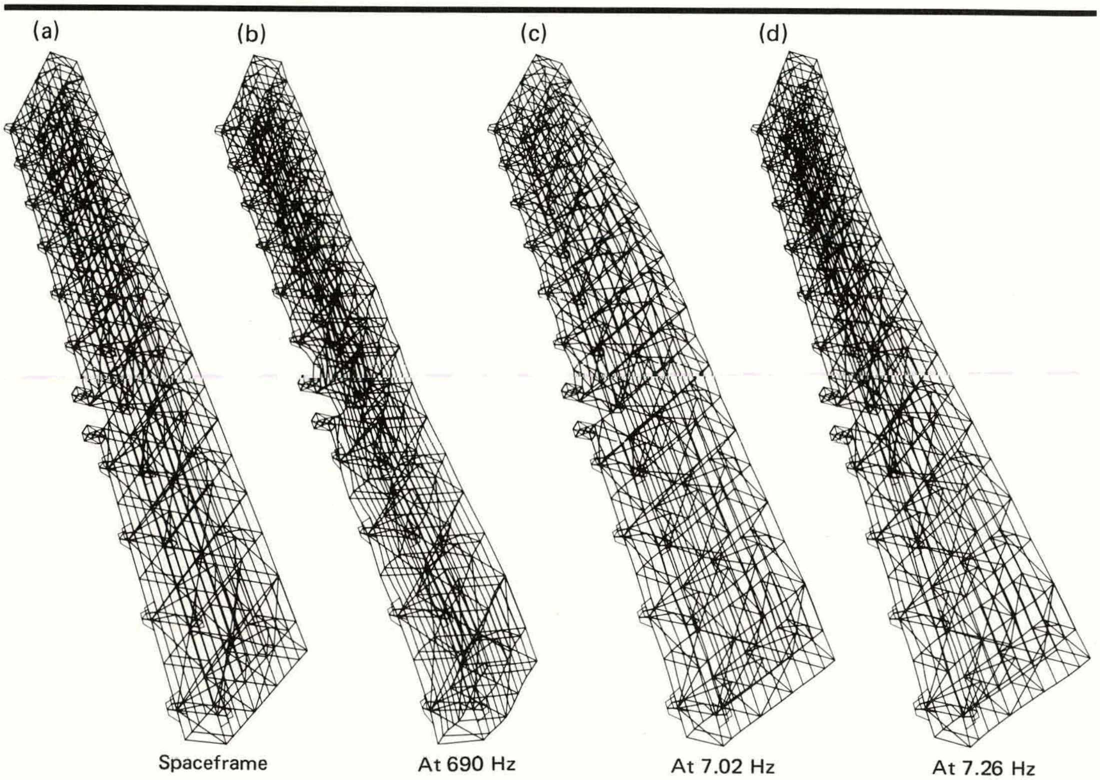

Fig. 2-121. Computer-generated drawing of one side of the laser space frame, showing its motion at various frequencies.

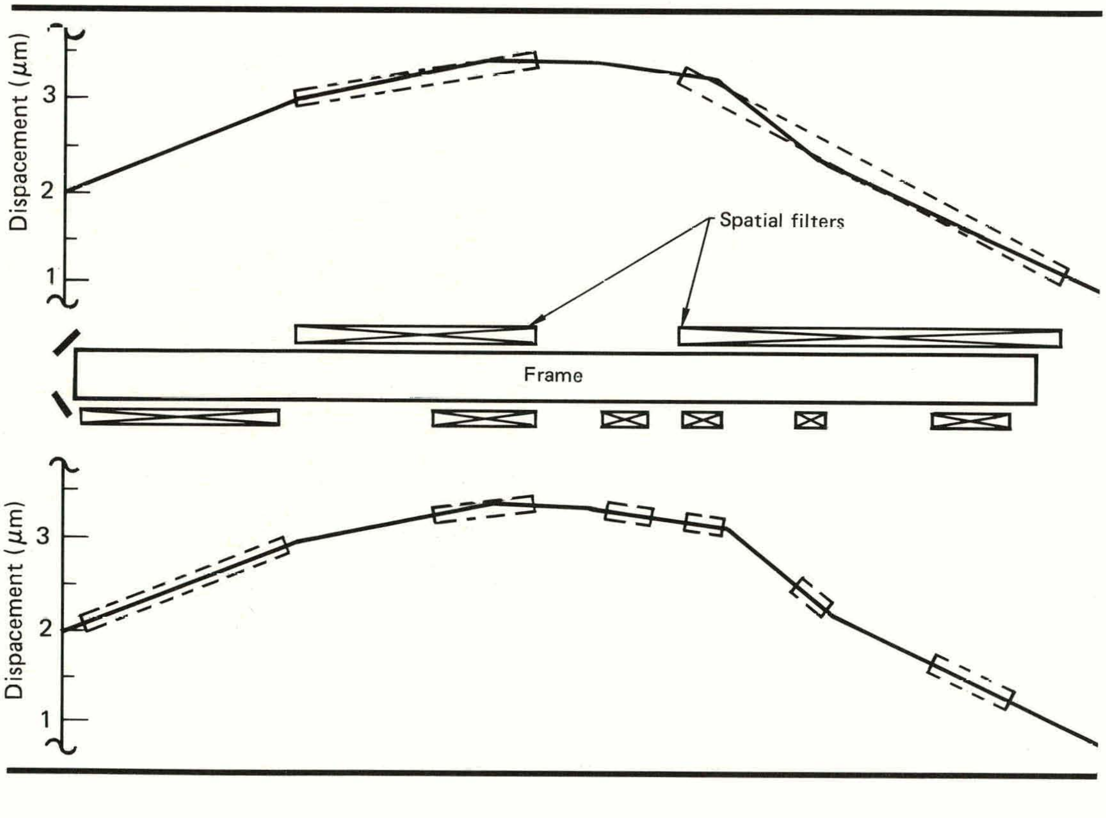

Fig. 2-122. Graph of the peak root-mean-square displacements of spatial filters on the space frame.

For ease of fabrication, all diagonal bracing will be made of 4-in.-square tubing.

Target Frame. The structural design for the target chamber and mirror support (target-frame structure) is shown in Fig. 2-123. It includes a tower to transfer structural loads directly from the target chamber to the foundation, and a rectangular box frame to support mirrors at various locations. The mirror-support structure rests on a beam-grid structure that is secured to the building's walls for lateral support and vertically supported by diagonally braced columns. The mirror-support structure is not connected directly to the beam-grid structure, however, but is supported by rollers located between the structures. This permits vertical loadings to be transferred to the beam-grid structure and allows for thermal expansion.

Normal expansion of the mirror-support structure is controlled by securing it to the target-chamber support tower at the beam-grid elevation.

Additional lateral stability for the target chamber is provided by a truss system that connects the top of this tower to the mirror-support structure.

The SAP IV computer model used for the dynamic analysis of the structure included 546 modal points and 1430 beam members. The results of this modal analysis showed the three lowest frequencies to be

- 3.16 Hz.
- 3.99 Hz.
- 4.81 Hz.

The lowest frequency, 3.16 Hz, corresponds to a lateral displacement of two opposing sides in the upper part of the mirror-support structure.

The second frequency, 3.99 Hz, corresponds to a lateral displacement, in opposite directions, of two sides of the mirror-support structure. This corresponds to a "twist" of the structure.

The third frequency, 4.81 Hz, corresponds to a lateral displacement of two opposing sides in the upper part of the mirror-support structure. These sides are perpendicular to the sides displaced at the lowest frequency.

Using actual, measured forcing function data, we found that the deformations were within acceptable limits, with a maximum translation of $\pm 2.816\ \mu$m and a maximum rotation of $\pm 0.361\ \mu$rad.

Master Oscillator Support. We based the structural design for the master-oscillator table frame on tubes, with 4- and 6-in.-square cross sections, which support the table-top plates and equipment loads.

To accommodate thermal expansion, the table is supported by rollers at numerous points. The rollers permit motion only along the length of the table. An anchor is provided near the middle of the table.

The SAP IV computer model used for the dynamic analysis of the frame structure included 551 modal points and 978 beam members. The results of this modal analysis showed the lowest three frequencies to be

- 19.4 Hz.
- 24.8 Hz.
- 30.3 Hz.

The lowest frequency, 19.4 Hz, corresponds to a "sliding" motion along the length of the table.

The second frequency, 24.8 Hz, corresponds to a lateral "rocking" of the table.

The third frequency, 30.3 Hz, corresponds to an upward "humping" of the frame between supports.

We determined that the deformations were within acceptable limits, with a maximum

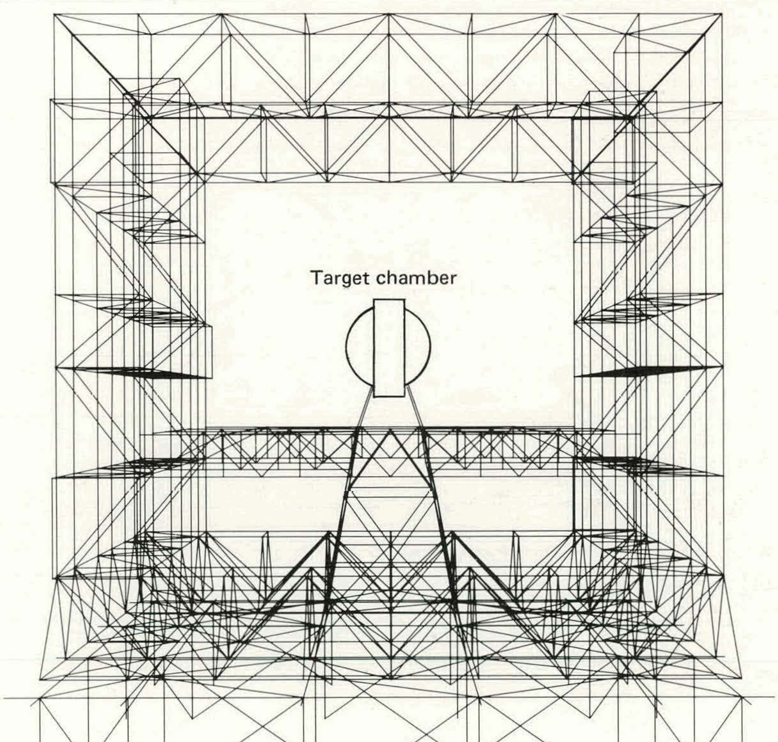

Fig. 2-123. Computer-generated drawing of the space frame structure for the target chamber and mirrors.

translation of ±0.239 μm, and a maximum rotation of ±0.147 μrad.

Authors: C. A. Hurley, D. Miller, G. Bradley, A. Silverman, and I. Stowers

Component-Assembly Facilities

The 3670-ft^2 clean room in Building 391 is adjoined by two smaller rooms, each 400 ft^2 in area. Figure 2-124 is a plan view of this Class 100 or better facility, which has a vertical air flow with an air velocity of about 30 m/min. The high-efficiency particulate-air filters mounted overhead are not shown in the figure. At left are two high-pressure freon spray booths; the smaller booth is used to clean the rod and disk amplifiers, and the larger booth is used for the box amplifiers. Also identified are the assembly stations, flashlamp test station, polarizer–interferometer station, transport carts, and other equipment used in cleaning or assembling the amplifiers and their components.

The clean room will be used primarily to clean and assemble all of the opto-mechanical components associated with Nova's 5-cm-aperture rods, as well as the beta, gamma, and delta disk amplifiers and the 20.8-, 30.5-, and 46-cm box amplifiers. A total of 305 Nova amplifiers will be processed in this facility initially; then it will be used for continuous operational maintenance.

As necessary, we are modifying the clean room and are designing new fixtures to transport, clean, and assemble the larger Nova box amplifiers.

We have designed carts to readily transport the box amplifiers to the various cleaning, assembly, and checkout stations.

The large, high-pressure freon spray booth has been designed with an internal rail system for transferring the box amplifiers from the transport carts into the booth. Here the housing and other amplifier components will be sprayed clean, removing all particulate contamination. In seconds, the liquid freon spray (at 1000 psi) will typically remove about 99.9% of particles 5 μm or larger. The booth protects the operator from the spray and confines the vapor for efficient recovery and recycling.

Fig. 2-124. The Class 100 clean room facility in Building 391.

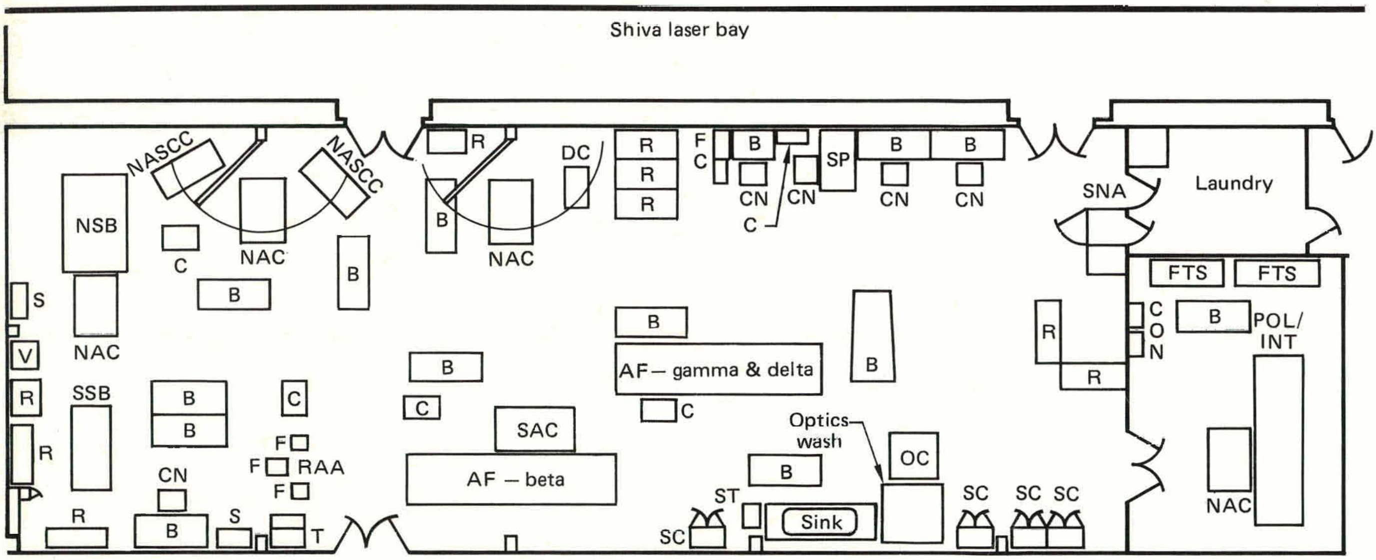

AF – Assembly fixture
B – Bench
C – Cart
CH – Chair
CON – Control unit
D – Desk
DC – Disk Cart
F – Fixture
FC – File cabinet
FTS – Flashlamp test station
NAC – Nova amplifier cart
NASCC – Nova amplifier side cover cart
NSB – Nova spray booth
OC – Optics cart
POL/INT – Polarizer/interferometer unit
R – Rack
RAA – Rod amplifier assembly
S – Sealer (plastic)
SAC – Shiva amplifier cart
SC – Storage cabinet
SHA – Shower
SSB – Shiva spray booth
ST – Still
T – Tools
V – Vacuum

Two assembly stations for the Nova amplifiers will be added to the clean room. These stations, which are specifically designed for the large-aperture box amplifiers, will be placed at the rear wall. The stations are designed to allow all components going into the box amplifier, such as the flashlamp subassembly and disk-holder assembly, to be put together while on the transport carts. Before the amplifiers leave the clean room for final installation onto the space frame, they will be transferred to the polarizer–interferometer station where they will be checked and any optical distortions of the amplifier disks will be measured. This station is located in the former "W" room, which has been added to the Building 391 clean-room facility.

Authors: F. Frick, C. Hurley, and C. McKee

Power Conditioning

Introduction. During 1980, Nova power-conditioning personnel primarily developed hardware and tested preproduction subsystems in preparation for the purchase of large quantities of material. Through these activities, we achieved significant cost savings and performance improvements.

Most of this power-conditioning work was done in Building 611, which serves as an electronics laboratory and flashlamp test facility. The building layout, showing the areas where this work took place, appears in Fig. 2-125.

We ordered the first megavolt-ampere (MVA) Nova power supply. Built during 1980, it arrived at year's end and will be tested during 1981. (We will also order

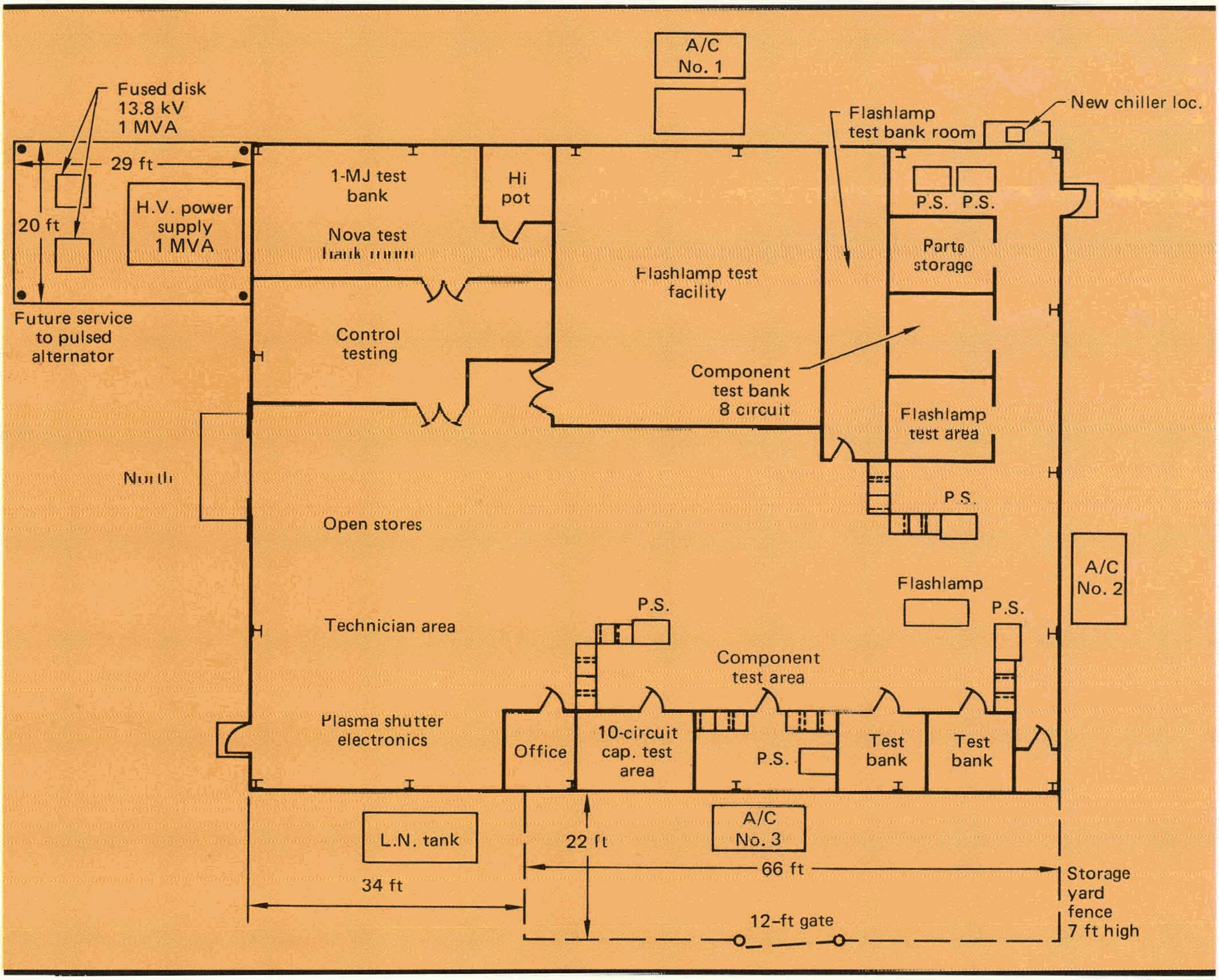

Fig. 2-125. Layout and activity diagram for Building 611, the power-conditioning electronics laboratory.

followup units in 1981.) This power supply has 15 times the capacity of the Shiva supplies but costs only four times as much, achieving a useful economy of scale.

Batches of capacitors were obtained from each of three high-density capacitor vendors: Aerovox, General Electric, and Maxwell. We tested these units to obtain a statistical basis for understanding the construction performance of the large Nova bank, as well as to develop projections for its performance. Our tests showed adequate performance and qualified vendors.

Fig. 2-126. Nova 1-MJ test capacitor bank.

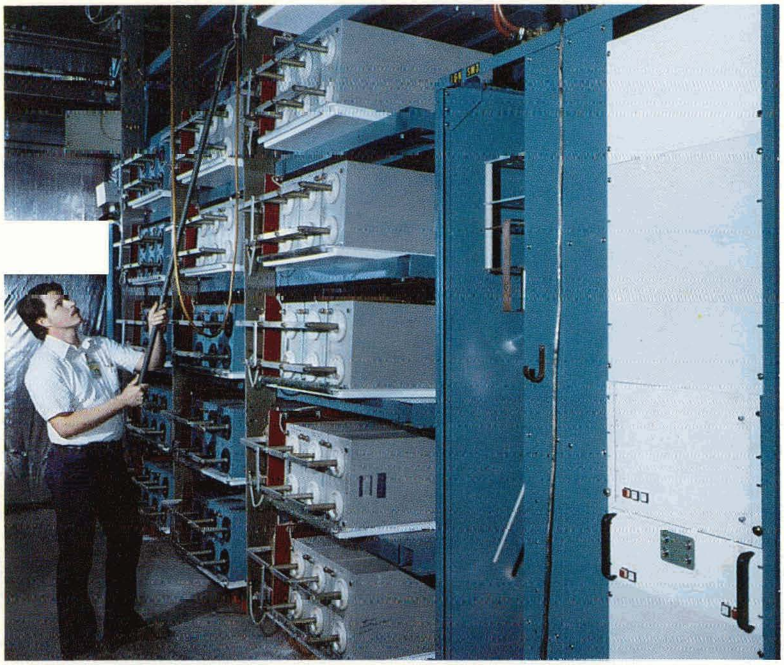

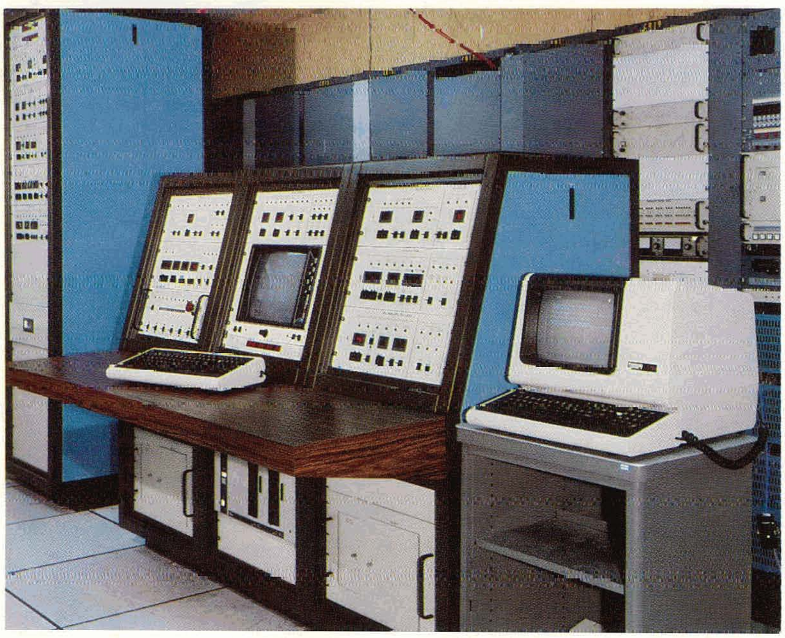

Fig. 2-127. Nova power-conditioning control-panel prototype for the 1-MJ capacitor bank.

Various components and subsystems in the capacitor bank itself were improved. Resistors for high-power dissipation were found with 5 to 10 times the energy-absorption capacity of the units previously used. We evaluated these new resistors at the component level and installed them in the 1-MJ Nova system test bank, shown in Fig. 2-126. For cost-effectiveness and reliability, we also made many improvements in the ignitron switch.

We refined the layout of the Nova capacitor bank in detail so that its installation can proceed efficiently and on schedule. A total floor space of 13 300 ft^2 is needed for the 60-MJ Nova Phase I bank, as compared with the 10 000 ft^2 used for Shiva's 25-MJ bank. Many cost-saving ideas have been incorporated into the construction details.

So that more than one quartz vendor might qualify for Nova procurements, we drew up a new flashlamp specification. To assure reliable system performance, we thoroughly tested those aspects of the flashlamps that were changed from prior versions; we also tested the flashlamps under Nova operating conditions.

We defined much of the hardware for the control area and built and tested hardware prototypes. Power-conditioning controls were carefully designed to fit into the hierarchical structure of the central control system. The power-conditioning system communicates with the higher-level VAX computer and the operator console via a four-port memory. The computer system controls all the pulse-power hardware, provides shot timing and synchronization, collects and displays system status, and collects and archives pertinent data. The system is designed to operate, and has been tested, in a high-electrical-noise environment. The hardware developed during 1980 includes the Nova fibre-optic bus, control panels, lamp-circuit diagnostics (LCD), and the computer-to-power-supply, capacitor-bank, and interlock interfaces, as well as the optically coupled high-voltage monitors. Figure 2-127 is a photograph of the prototype power-conditioning control-system console for the 1-MJ Nova test bank.

During much of 1980, we have been engaged in detailed design work for the oscillator control and pulse-distribution system. At the time of this writing, the schematics are nearing completion, and hardware fabrication and testing of the first units are scheduled for 1981. These activities are discussed in detail in the rest of this section.

Author: K. Whitham

Nova Power Supply. During 1980, by competitive bid, we procured the prototype Nova power supply[51] from Aydin Energy Systems, Palo Alto, Calif.

The Nova power supply is a large voltage doubler, capable of charging a 12-MJ capacitor bank to 22 kV in approximately 30 s. This power supply uses a vacuum contactor, that opens when the bank reaches the proper voltage, as its control element. To limit the inrush current, the power supply uses a resistor step-start. We have taken great care in designing the transient voltage-suppression networks on the primary and secondary of the transformer.

We will use seven power-supply units in Nova Phase I, which will be staged as shown in Table 2-26. These large supplies will be connected to utility power via 13.8-kV fused disconnects.

In this procurement, performance responsibility is shared between LLNL and the vendor. The LLNL specification[52] details the components required and how these components are to be assembled. The vendor takes responsibility for the hardware that is provided, and LLNL is responsible for system performance.

The procurement cycle began with a competitive bid among six companies. We awarded the contract to Aydin Energy Systems on the combined basis of cost and technical evaluation. Seven power supplies were ordered for Nova Phase I. Once the prototype is accepted, according to the specification,[52] the other six units will be manufactured and delivered.

We have also developed an instrumentation package to monitor the voltage and current of the prototype dc power supply. This package was designed and built at LLNL and delivered to Aydin for incorporation into the prototype power supply. It contains two redundant voltage sensors, isolated with fiber optics, and a current monitor. The monitor, a transductor, is also electrically isolated.

The first phase of the procurement cycle was completed with delivery of the prototype power supply (Figs. 2-128 and 2-129) on

Table 2-26. Power-supply staging for Nova Phase I.

Component	Energy, mj	No. of power supplies	No. of switches
94-mm disk }	5.04	1	20
150-mm disk }	—	—	—
208-mm disk	6.88	1	20
315-mm box	15	2	40
460-mm box	18	2	30
Spare	—	1	—
Total		7	110
100-kVA supplies[a]			
50-mm rod	0.600	1	2
94-mm FR[b]	0.210	1	1
150-mm FR	0.800	1	2
208-mm FR	2.0	2	4
315-mm FR	2.0	2	4
LCD[c]	0.07	1	7
Spare	—	1	—
Total		9	20

[a]Reused from Shiva.
[b]Faraday rotator.
[c]LCD = Lamp and circuit diagnostics.

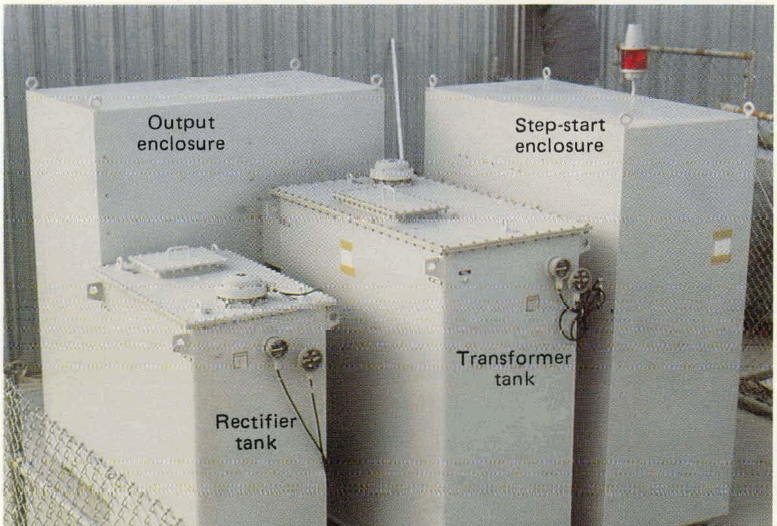

Fig. 2-128. Prototype Nova power supply manufactured by Aydin.

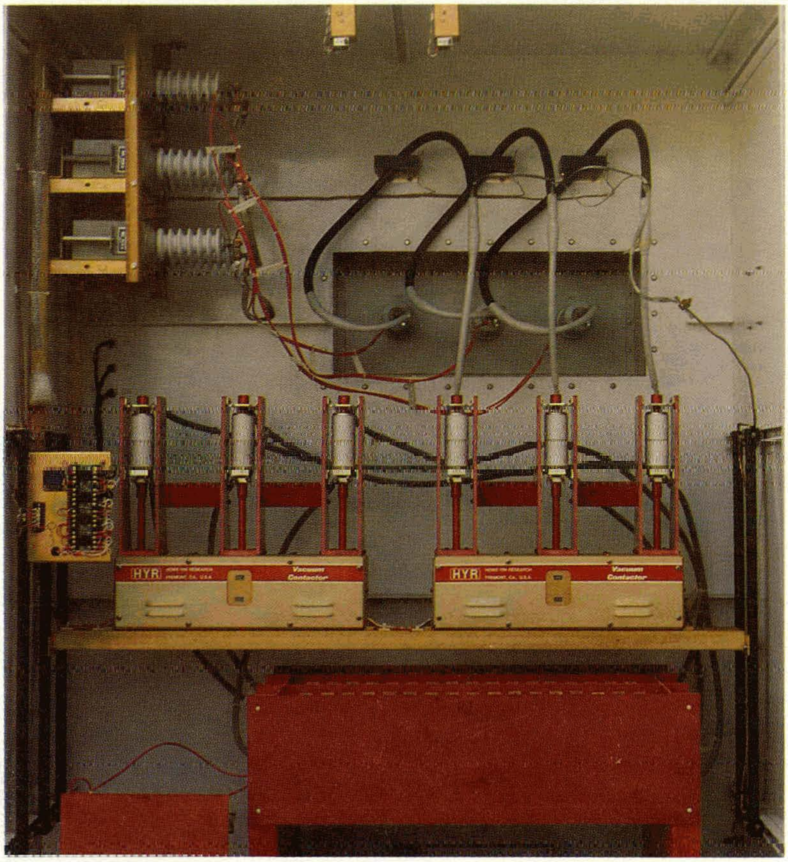

Fig. 2-129. Detailed interior view of step-start enclosure in prototype power supply.

December 30, 1980. Acceptance testing of the power supply will begin in early 1981.

Author: B. Merritt

Major Contributor: L. Berkbigler

Capacitor Development. During 1980, we tested capacitors extensively. This testing had a twofold purpose:

- To determine whether high-energy-density capacitors could deliver the needed shot life for the Nova bank.
- To obtain reliable comparisons of the effectiveness of different capacitor construction methods, called "builds" in the industry.

Although we had previously tested only small samples of capacitor builds, our results indicated that the use of high-energy-density capacitors was feasible. From these limited data, we generated a preferred Weibull plot.[53] In 1980 we were able to place the performance of these capacitors on a firm statistical basis. Testing was started in February 1980 and will continue into early 1981.

The 12.5-kJ/22-kV high-energy-density capacitors have two basic builds: (1) a paper/polypropylene/dioxophthalate build and (2) a paper/castor-oil build. Capacitor manufacturers are free to choose the build they prefer to supply. Our testing allows us to determine the builds that will meet Nova capacitor-bank requirements.

To make a meaningful comparison between builds, we have to test a relatively large sample of capacitors for a large number of shots. We have chosen to test 35 capacitors of each build. The three-part testing consists of (1) nonoscillatory discharges, (2) high-reversal discharges, and (3) high voltage life.

Nonoscillatory discharges, which imitate a typical flashlamp discharge, have the following characteristics:

- Charge voltage: 24 kV.
- Discharge peak current: 5 kA.
- Charge time: 12.5 s.
- Hold time: 2.5 s.
- Discharge voltage reversal: 10% max.

In these tests 30 of the 35 capacitors are run to 20 000 discharges, or until failure occurs. The five remaining capacitors are run to 100 000 discharges, or until three of the five fail.

High-reversal discharges are designed to reveal flaws in workmanship or design. Two capacitors, which have run 20 000 shots in the first test, are tested for 1500 discharges (or to failure) under the following conditions:

- Charge voltage: 22 kV.
- Discharge peak current: 60 kA.
- Charge time: 22.5 s.
- Hold time: 2.5 s.
- Discharge voltage reversal: 85%.

The test for high-voltage life provides evidence of adequate capacitor lifetime. In this test two capacitors, which have run 20 000 shots in the first test, are charged to 24 kV and held at that voltage for 1000 h, or until failure.

The ranking of capacitor builds is based on successful completion of the high-reversal and high-voltage-life tests, as well as on the number of shots between failures, as projected over the life of a Nova-sized bank.

If capacitor failure results from fatigue, caused by repeated stressing of the dielectric system, a Weibull distribution function can be used to analyze the data. The form of the function is as follows[54]:

$$F(N) = 1 - \exp\left[-(N - N_o)/(N_a - N_o)\right]^b \quad , \qquad (2)$$

where F equals the fraction of capacitors that have failed, N is the shot life, N_o is the minimum life expectancy, N_a is the characteristic life, and "b" equals the Weibull slope.

Equation (2) can be converted into a straight-line relationship, as either

$$\ln\left(\ln\{1/[1 - F(N)]\}\right) = -b \ln(N_a - N_o) + b \ln(N - N_o) \quad , \qquad (3)$$

or

$$\log\left(\log\{1/[1 - F(N)]\}\right) = -b \log(N_a - N_o) - 0.3622 + b \log(N - N_o) \quad \cdot \qquad (4)$$

Eq. (4) becomes

$$\log\left(\log\{1/[1 - F(N)]\}\right) = a + b \log(N - N_o) \quad , \qquad (5)$$

where "a" is a constant. Thus, for a given N_o, a least-squares analysis yields an "a" and a "b" for the best straight-line approximation.

The value of N_o is specifically chosen to minimize the sum of the squares of the deviation of the experimental points from the best straight line. From a physical standpoint $N_o \geqslant 0$; for capacitor test data, N_o usually equals zero.

Given an ordered set of failures, at shot life values of $N_1 \leqslant N_2 \leqslant \ldots N_i \leqslant \ldots N_k$, out of a sample size m, the data are analyzed as follows. For large values of m, where m > 20

$$F(N_i) = i/Z \quad , \qquad (6)$$

where Z = m + 1, and i equals the *i*th failure.

If units are removed from the test before they fail, and before the test is over, the method of analysis suggested by Nyman[55] is used.

$$F(N_{k>i}) = (i/Z) + \left[(k - i)/Z'\right] \quad , \qquad (7)$$

where

$$Z' = Z/\left[1 + j/(\ell + 1)\right] \quad \cdot \qquad (8)$$

In Eqs. (7) and (8) i equals the number of failures before any units are removed from the test, j equals the nonfailed units removed from the test, k equals the *k*th failure after the nonfailed units are removed from the test (k > i), and ℓ = m – i – j, or the number of units left in the test.

Now that we are able to calculate F(N), we can make a Weibull plot. A sample plot is illustrated in Fig. 2-130, with the symmetrical 90% confidence bands shown. The plot is for the values b = 1.3, N_o = 0, and N_a = 200 000 (Ref. 56).

The slope of the straight line in the plot is the Weibull parameter "b". The characteristic life, N_a, can be read from the graph by observing the value for the life that corresponds to F(N) = 1 – exp(–1) = +0.632. Having obtained this straight line, we can further analyze the data.

This plot yields a graphic example of why as many capacitors as possible should be tested for qualification. For example, at the N_{10} level (10% failed), the 50% confidence-level life is 35 000 shots. In a 4000-capacitor (50 MJ) Nova I, this 10% would represent 400 failed capacitors. Therefore, we could expect an average of 35 000/400, or 87.5 shots between failures (at the 50% confidence level) during the entire 35 000 shots.

It is apparent from Fig. 2-130 that we could not be 90% sure of this failure-rate number, within a factor of 8, if only two capacitors were tested. Thus, we could only be 90% sure of achieving at least 87.5/8, or

Fig. 2-130. A Weibull plot, such as this, allows us to predict anticipated failure rates for a given shot life.

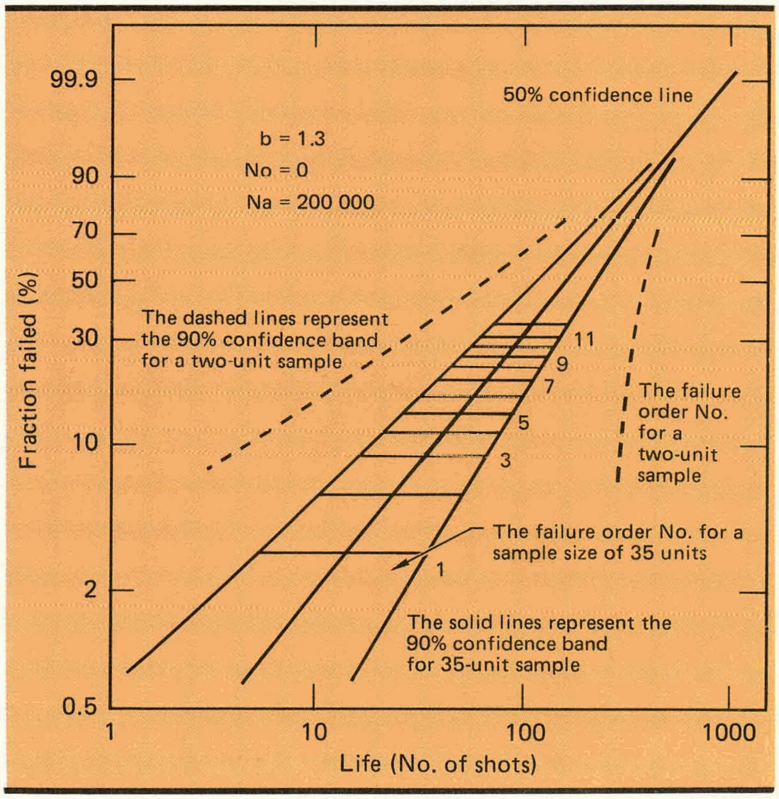

11 shots between capacitor failures, for the first 400 failures (4375 shots).

However, if 35 units from each vendor were tested, the 90% confidence band, at the N_{10} level, would shrink to 1.95 (at b = 1.3). Therefore, for the plot of Fig. 2-130, we could be 90% certain of achieving at least 35 000/1.95, or 17 950 shots of the N_{10} (400 failed) level on Nova I; that is, 17 950/400, or 45 shots between failures. Thus, by increasing the number of samples tested (from 2 units to 35), we gain, at the 90% confidence level, a factor of 4 in our ability to predict the average life expectancy (from 11 to 45 shots between breakdowns).

The Weibull plot can also allow us to establish a figure of merit for capacitor vendors. For example, suppose we wish to be 90% sure of achieving 100 shots between failures on a 4000-unit system at the N_{10} level. This would represent 400 failures (at 100 shots between failures), or 40 000 shots on the minimum 90% confidence band at 10% failed. If 35 units were tested, the 50% confidence-level lifetime at 10% failed would be 1.95 × 40 000, or 78 000 shots.

Now, suppose that vendor X's qualification test data yielded the results shown in Fig. 2-130. Thus, on the basis of three failures in 35 samples, b equals 1.3, N_o equals 0, and N_a equals 200 000. We would then find that the 50%-confidence N_{10} level falls at 35 000 shots. However, since 35 000 shots is a factor of 35/78ths of the capacitor lifetime desired, the operating voltage should be lowered to $(35/78)^{1/8}$, or 0.905, of V_{TEST}. With a test voltage of 24 kV, this would give an operational voltage of 24 times 0.905, or 21.7 kV.

If X's capacitors had a capacitance of 52 μF each and were priced (in quantity) at \$600 each, the energy stored in each capacitor would be $(21.7)^2 \times 52/2$, or 12 250 J, and the cost would be 600 × 100/12 250, or roughly 4.9 cents per joule.

If the capacitors of other vendors were priced in a similar manner, a rational purchasing method—based on their value to the Nova program—would exist. Note that if only two capacitors were tested, the rationale for this method could not exist because the data would be too widely scattered to be of value.

Another, similar method of vendor ranking can now be explained. This second method is also based on the predicted average number of shots between failures, but in a slightly different way. The method is as follows. First, the fraction failed for 10 000 shots (scaled to 12.5 kJ) is found. Next, the total number of projected failures is calculated. Then, once the estimated cost per failure is derived, the capacitor-bank costs (for installation and repairs) are calculated. The effective cost per capacitor equals the capital investment plus repair costs, divided by the capacitance that has been purchased for the capacitor bank.

Vendor X's ranking would be found as follows. Since X's capacitors each have a capacity of 52 μF, the rated voltage, V_R, for 12.5-kJ operation is

$$V_R = \left[2(125 \times 10^3)/52 \times 10^6\right]^{1/2} \tag{9}$$
$$= 21.9 \text{ kV}$$

Suppose, as before, that the test data graphed in Fig. 2-130 were obtained at 24 kV. The scaling of 10 000 shots to the 12.5 kJ level, or 21.9 kV, becomes

$$N = (10\,000)\,(21.9/24.0)^8$$
$$= 4806$$

The fraction failed at this shot life is

$$F(4806) = 1 - \exp\left[-(4806/200\,000)\right]^{1.3}$$
$$= 0.0078, \text{ or } 0.78\%$$

For a bank containing 4000 capacitors, the total number of failures is calculated as being 31. If the cost per failure is approximately \$10 000 because of down time, damage, and the possible loss of an experimental shot, then the total cost of the capacitor bank becomes 4000 capacitors at \$600 each plus 31 failures at \$10 000 each, or \$2.710 million. Since this figure represents the cost for a 50-MJ capacitor bank, the cost per joule is 5.42 cents. If the cost per failure were \$5000, the cost per joule under the same conditions would be reduced to 5.11 cents.

In summary, we feel we have developed a meaningful and fair method for comparing the different capacitor builds. The capacitor testing completed to date has told us that the 12.5-kJ capacitor is a viable choice for Nova; it has also told us how well each manufacturer can build these capacitors.

Author: B. Merritt

Major Contributors: B. Carder, R. Burch, and C. Trapp

Bank-Component Development and Nova Layout. During 1980, we made significant improvements to the capacitor-bank components. Two components that underwent major changes were the ignitron switch rack and the pulse-forming network (PFN) board. The functional relationships of these components are shown in Fig. 2-131.

The ignitron switch rack houses a pair of size "D" ignitrons and associated hardware. The ignitrons are mounted in a coaxial structure to which cables are attached. The anodes are heated, and the cathodes are water-cooled. Pulse transformers couple electrically isolated triggers to the ignitors of the ignitrons, and diagnostics monitor the performance of the switch and circuit.

We made four major changes to the switch rack. First, we modified the structure that attaches the cables to the ignitron switch assembly. The cables are now attached directly to the top, as shown in Fig. 2-132. When this new setup is compared to the Shiva ignitrons, with their side attachments, the improvement in accessibility is evident.

The second major change, also visible in Fig. 2-132, is in the placement of current bugs used in the lamp-circuit diagnostic (LCD) system (see "Control System"). These sensors were formerly located in junction boxes in the laser bay. By placing the current bugs at the ignitron switch, we can provide an adequate voltage standoff without installing a costly insulation system. When compared to the original location, the new placement also offers improved access.

Third, we have installed sensors to monitor the switch voltage and current, as well as the current to each ignitor. These monitors are described in more detail in "Control System."

Fourth, we have replaced the pair of 500-W anode-seal heat lamps—used with each of Shiva's ignitrons—with a low-cost, efficient resistor heater. These lamps were a major contributor to the air conditioning load of the laser building. For Nova, we are using resistors mounted in copper blocks, which are clamped to the anode of each ignitron, as shown in Fig. 2-133. The resistors consume only 26 W of electricity while heating the anode to 55°C. The heater is electrically isolated to 50 kV dc by a 110- to 6.3-V isolation transformer.

The pulse-forming network consists of a high-voltage fuse, a ceramic charge resistor,

Fig. 2-131. Schematic diagram of typical power-conditioning circuit.

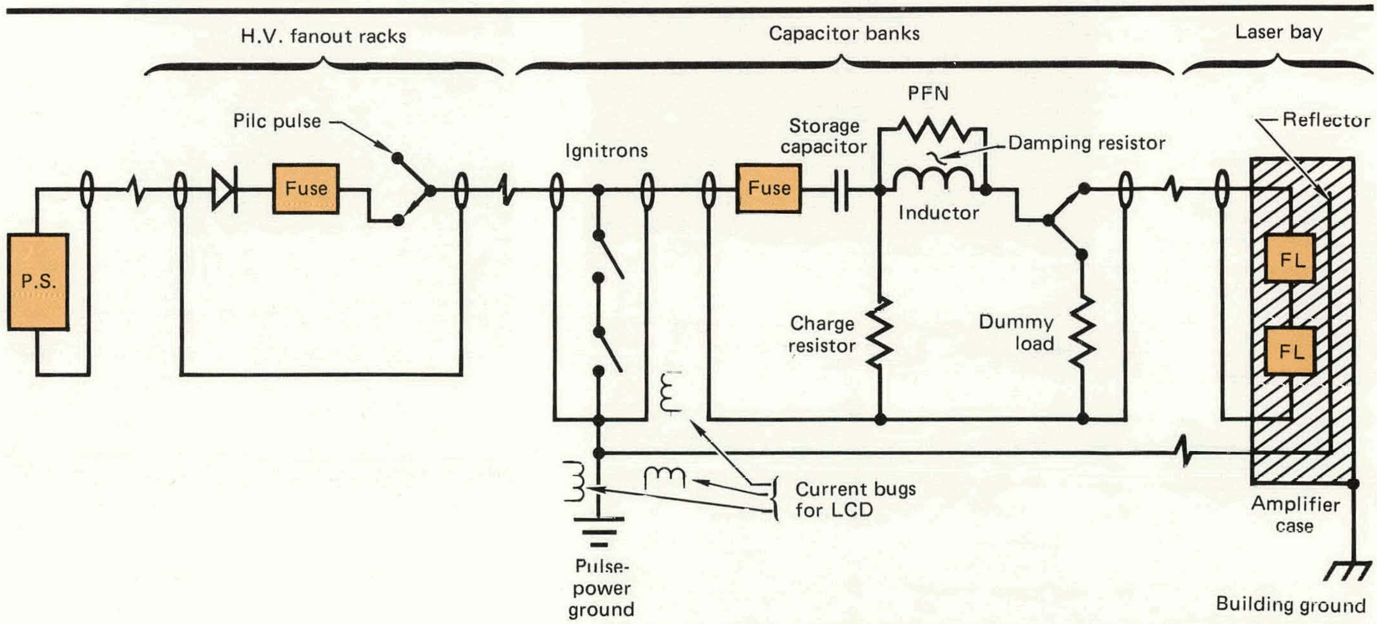

Fig. 2-132. Ignitron switch, showing cable terminations at top and placement of current bug.

a ceramic dummy-load resistor, and a pulse-shaping inductor that has a bar switch for switching between the dummy load and the flashlamp load. The dummy-load resistor approximates twice the flashlamp impedance. This fact, which will be used during testing and debugging of the pulse-power system, will allow the monitoring system to show switch position, dummy load, or flashlamps.

During 1980, we made a considerable effort to improve the resistors used for the PFN. In particular, we tested resistors extensively for use as dummy loads and dumps. The dummy load is an alternate load for the energy-storage modules. The dumps are used in the crowbar system to discharge the capacitor bank. Samples of these resistors are shown in Fig. 2-134.

The requirements for the dummy load are an impedance of about 8 Ω, an ability to withstand energies of 50 kJ, and a voltage rating of 22 kV. We found three ceramic resistors that met these requirements: two disk-type resistors and one tubular resistor, all of which are capable of absorbing 200 kJ in a single pulse. The resistors have been tested at 50 kJ per pulse at a 5-min repetition rate. The disk-type ceramic resistors have achieved thousands of shots before failure, while the tubular type has only been able to achieve a few hundred shots. However, the tubular resistor has just been developed, and

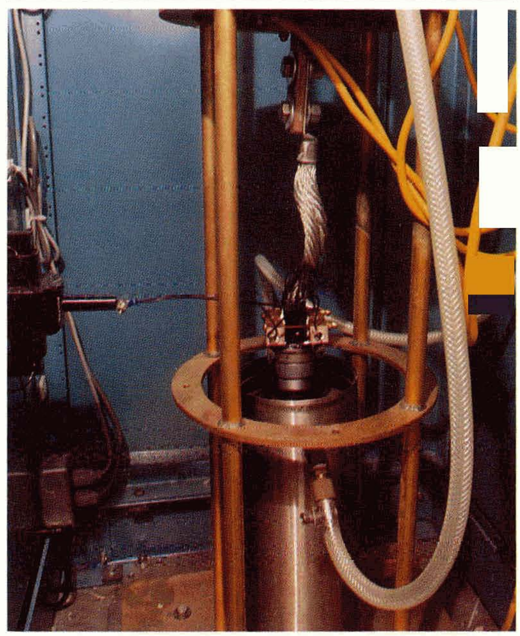

Fig. 2-133. Resistor ▲ heater, shown attached to ignitron anode seal.

Fig. 2-134. Resistors tested for the PFN: ceramic-disk dump, dummy load with cooling fins, ceramic-disk dummy load (back, left to right), and tubular resistor (foreground).▼

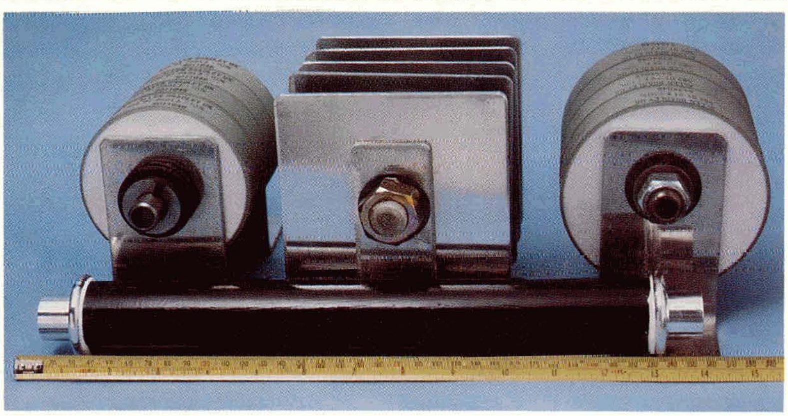

we anticipate that it will improve as the manufacturing process is refined; it should also cost significantly less than the disk-type resistors.

The requirements for the dump resistor are an impedance of 1000 to 2000 Ω, the ability to withstand energies of 200 kJ in a single pulse, and a voltage rating of 22 kV. We have tested two types of resistors for this application: a ceramic disk and a tubular ceramic, both of which are capable of absorbing 200 kJ in a single pulse. Repetitive testing on both types of resistors will begin early in 1981.

The capacitor-bank layout for the Nova system consists of 15 rows of capacitor racks, covering 13 287 ft^2, with 50.5 MJ of storage capacitors and 50 diode stacks for the Faraday rotator units. The staging of this bank is given in Table 2-27.

The capacitor modules, as seen in Fig. 2-135, will be made up of two- (25 kJ), three- (37.5 kJ), and four-can (50 kJ) units, as required for each flashlamp circuit. The capacitors will be isolated from the rack by a vacuum-formed tray made from 1/4-in.-thick ABS sheet plastic.

The capacitor-bank dump system consists of approximately 260 pneumatically operated seven-circuit units, with a 1000-Ω ceramic resistor in each circuit. This type of resistor can absorb energies of up to 500 kJ without damage.

The cable trays for the high-voltage cable will be fabricated from 3/16-in.-thick ABS sheet plastic. These trays will be 10 in. wide by 3 in. high.

Authors: B. Merritt and R. Holloway

Major Contributors: R. Burch and C. Trapp

	Number		Lamps			Circuits		Bank	Total
Component	Per arm	Total	Size (in.)	Per circuit	Total No.	per compo- nent	Total circuits	energy/ circuit (kJ)	bank energy (kJ)
Rods									
MOR	4	16	19	6	96	1	16	42[a]	672[b]
Splitter	2	—	—	—	—	—	—	—	—
Arm	1	—	—	—	—	—	—	—	—
9.4-cm disk	2	20	44	2	320	8	160	18	2 880[b]
9.4-cm FR	—	—	—	—	—	—	—	—	—
MOR	2	12	—	—	—	1	12	21	252[b]
Arm	1	—	—	—	—	—	—	—	—
15-cm disk	1	10	44	2	240	12	120	18	2 160[b]
15-cm FR	1	10	—	2	—	4	40	25	1 000[c]
20.8-cm disk	1	10	44	2	320	16	160	18	2 880[b]
20.8-cm disk	2	20	44	2	320	8	160	25	4 000[c]
20.8-cm FR	1	10	—	—	—	5	50	40	2 000[d]
31.5-cm disk	4	40	44	2	800	10	400	37.5	15 000[c]
31.5 FR	1	10	—	—	8	4	40	42	1 680[b]
46-cm disk	3	30	19	5	2400	16	480	37.5	18 000[c]
			Total		4496	Total	1638	Total	50 524
			44		2000	Rotator	142	Shiva[b]	10 524
			19		2496	Lamp	1496	Nova[c]	38 000
								Shiva[d]	2 000

[a]Operated at 22 kV. [b]Shiva components at 3 kJ.
[c]Nova components at 12.5 kJ. [d]Shiva components at 5 kJ.

▲ Table 2-27. Power-supply staging for Nova.

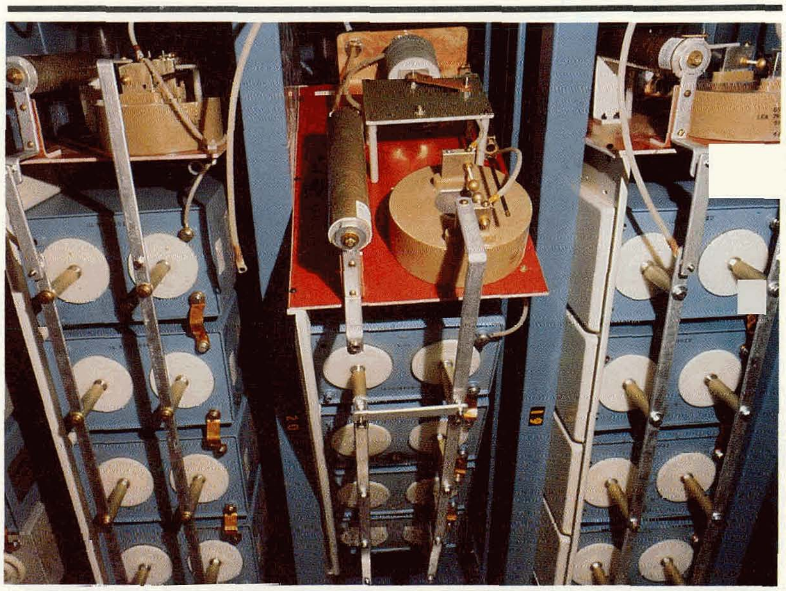

Fig. 2-135. Nova four-can capacitor modules, with middle module positioned for better view.

Flashlamps. During 1980, we released a new specification (LES 22292) that details the flashlamp requirements for Nova. The two principal changes from the previous specification are

- That the flashlamps used on Nova will be operating at a higher energy loading.
- That tolerances on scatches, bubbles, and other minor imperfections in the quartz tubing have been relaxed because there is no evidence that the presence of surface scratches increases the failure rate.

Developing this new specification took a great deal of background effort. The changes in our requirements were based on extensive discussions with lamp and quartz vendors and on the results of a significant testing program.

Previously, only one quartz manufacturer could meet the specification. As a result of extensive testing at LLNL and EG&G, we now consider a second quartz manufacturer to be equally acceptable. Having a second source for quartz could well result in lower flashlamp costs for Nova.

Testing included running 30 lamps (that met the new specifications) for 10 000 shots without failure and running 5 lamps at 60% of their explosion limit for 110 shots, again without failure. In addition, we optically inspected the quartz before and after testing.

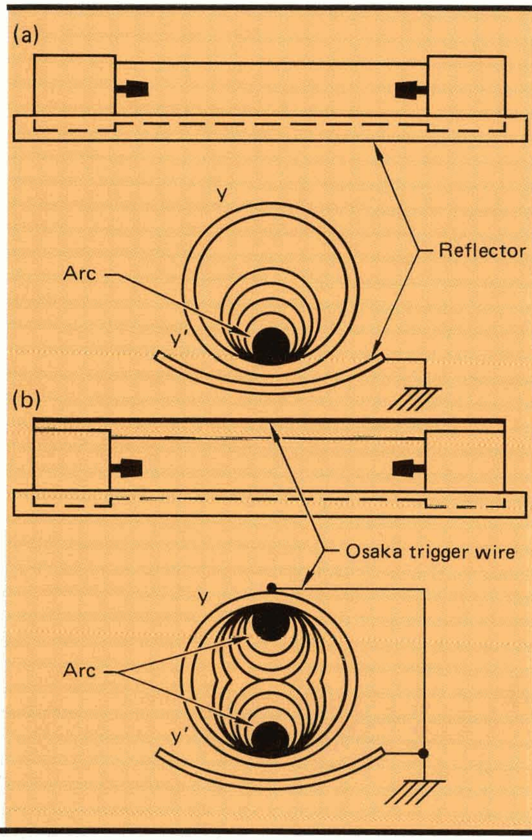

Fig. 2-136. An external trigger wire (b) causes a more-symmetrical plasma arc in the flashlamp than would be formed without the trigger wire (a).

To determine new specifications with regard to scratches, we scratched four 112-cm arc-length flashlamps extensively (with No. 120 sandpaper), both in the radial and longitudinal directions. These lamps exploded at the same energy levels as unscratched lamps. We operated eight 112-cm arc-length flashlamps successfully for 10 000 shots at Nova energies (18.5 kJ per lamp), at approximately Nova pulsewidths (3τ = 0.955 ms).

We also began testing a new flashlamp, with a 47.4-cm arc length and a 2.0-cm bore, that will be used in the 46-cm box amplifier and in the 5.0-cm rods for Nova. This test will ultimately be run for 10 000 shots on a five-lamp circuit operating at 50 kJ. The circuit, energy, and pulsewidth are identical to those we expect to use in Nova. By the end of 1980, about 5000 shots of this test had been completed.

As part of the testing program for the new 47.4-cm arc-length flashlamp, we are experimenting with a flashlamp triggering method invented by K. Yoshida.[57] His triggering method is shown in Fig. 2-136. Essentially, the use of the additional wire

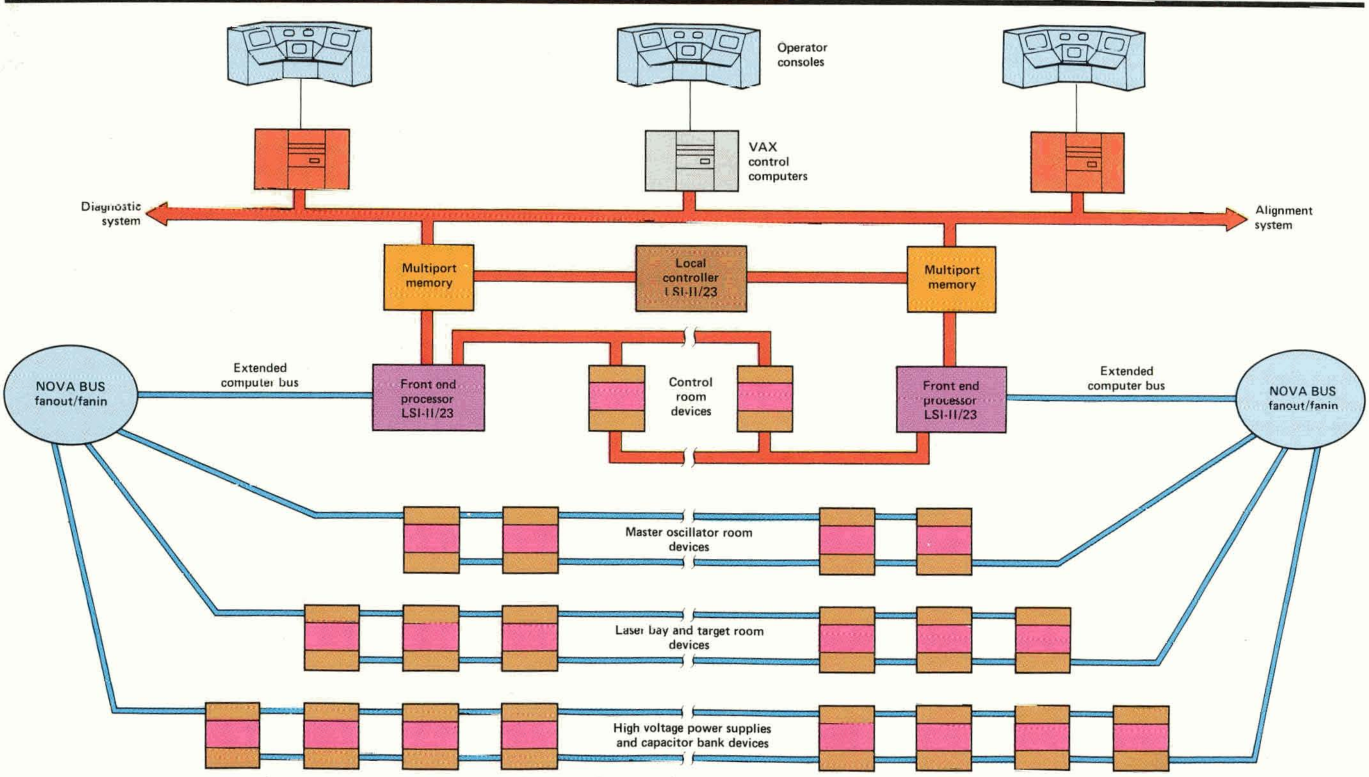

Fig. 2-137. Block diagram of control-system architecture.

causes a more uniform electric discharge, which lowers the compressive stress in the quartz, thereby increasing lamp life. Qualitatively, we have seen an improvement in the quartz, but we do not have enough data, as yet, to quantify the improvement. Testing in this area is continuing.

Author: B. Merritt

Major Contributors: C. Trapp and R. Burch

Control System. The power-conditioning control system for Nova is illustrated in Fig. 2-137 (p. 114). Digital Equipment Corporation VAX-11/780 computers monitor and control the pulse-power system via redundant LSI-11/23 front-end processors (FEP). Each processor bus is serialized and is extended throughout the laser facility by a fiber-optic network. An extended bus system is being used because the software that controls the bus is simplified and the efficiency of the bus for handling data (data bandwidth) is maximized.

To transmit the many bus signals over a fiber-optic cable, the computer-bus address bits, data bits, and control bits must be sent as a serial bit stream. This serial bus, called Novabus, is distributed throughout the laser facility and is converted back into a parallel format when it returns to the FEP. Novabus is designed to operate at 10 megabits/s and to interface with each laser-system device that is controlled, monitored, or synchronized. We incorporated operational requirements for redundant bus operation and system synchronization into the Novabus design.

As outlined in the 1978 Laser Program Annual Report,[58] we are dividing control-system development into four phases:

- Phase A—develop and integrate a fiber-optic bus.
- Phase B—upgrade existing control-system interfaces.
- Phase C—develop and integrate new device interfaces.
- Phase D—develop and integrate the control-room segments of the control system.

During 1980, we completed Phase B and half of Phase C. The work accomplished toward this end is summarized, by major groupings, in the remainder of this section.

Novabus—We developed an effective fan-out/fan-in device that interconnects the control-room computers with the laser-system devices. Figure 2-138 shows the engineering prototype, along with interface boards for the computer and remote devices.

Control Panels—We are designing a set of control panels that will be used to activate and maintain the power-conditioning system. Figure 2-139 shows one of the seven panels, along with the logic boards that interface the panels to the control-system computers. Each panel is associated with specific devices in the laser system. These panels augment the primary control consoles and give maintenance personnel the diagnostic tools to isolate failed or degrading components. The panels in the control room and those in the Master Oscillator Room operate as a compatible set.

VAX Software—During the past year we began designing and implementing high-level control programs, using touch-panels overlaid on raster-scan displays. An example of such a control menu is shown in Fig. 2-140. This control menu allows an operator to control the power-conditioning system from a very high level. The operator can initialize the power-conditioning hardware by selecting any of a number of common system configurations. Then the operator can modify the selected system configuration, on the component level, for the particular application. The sequencer, which automatically fires the laser, is also

Fig. 2-138. Fan-out/fan-in device for distributing the fiber-optic Novabus throughout the laser facility.

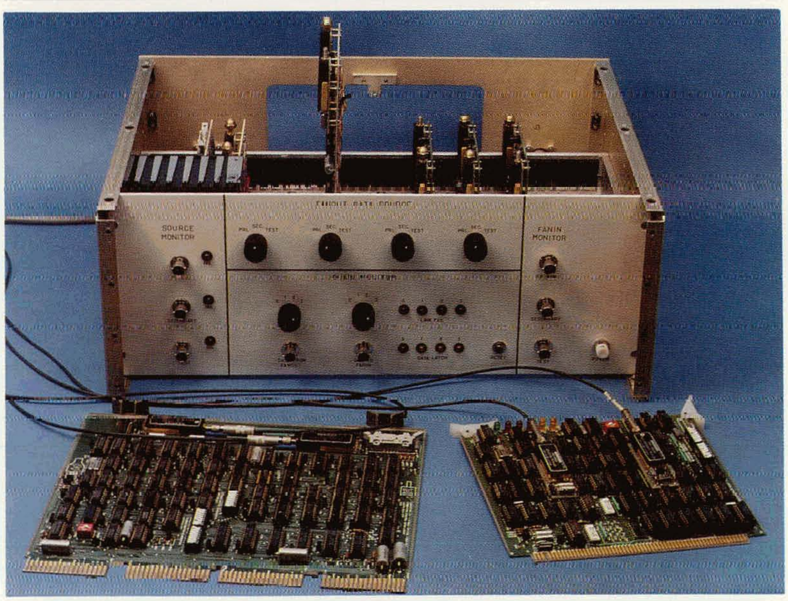

controllable from this menu. Any lower, more-detailed control level is available from other control menus that are also reachable from this menu.

FEP Software—Control-system software development is progressing rapidly and is keeping up with new hardware development and installation. The coding for power supplies, ignitrons, and all Novabus components is complete. The sequencer routines are nearly finished, enabling the sequencing of 30 presently-defined time-ordered channels. Although all the maintenance panels are operational, some are awaiting additional hardware development. An event recorder—to be used for displaying logged event information—is now being written; it will communicate with the two front-end processors, via a multiported memory. The control system can run independently on one of the two front-end-processors (as shown in Fig. 2-137), or simultaneously on both. Any of the 16 Novabus device chains may be allocated to either front-end processor, providing flexible load-sharing control and recovery from all single- and many double-point failures. The control-system software presently occupies 26k words of memory, in addition to the 16k-word multiported memory. Approximately 95% of the software is written in Praxis ("Configuration and Data Management"); the remaining 5% is in Macro-11.

Lamp-Circuit Diagnostics—The LCD system is the primary diagnostic tool for

Fig. 2-139. Sample control panel and logic boards used for testing the ignitron switches.

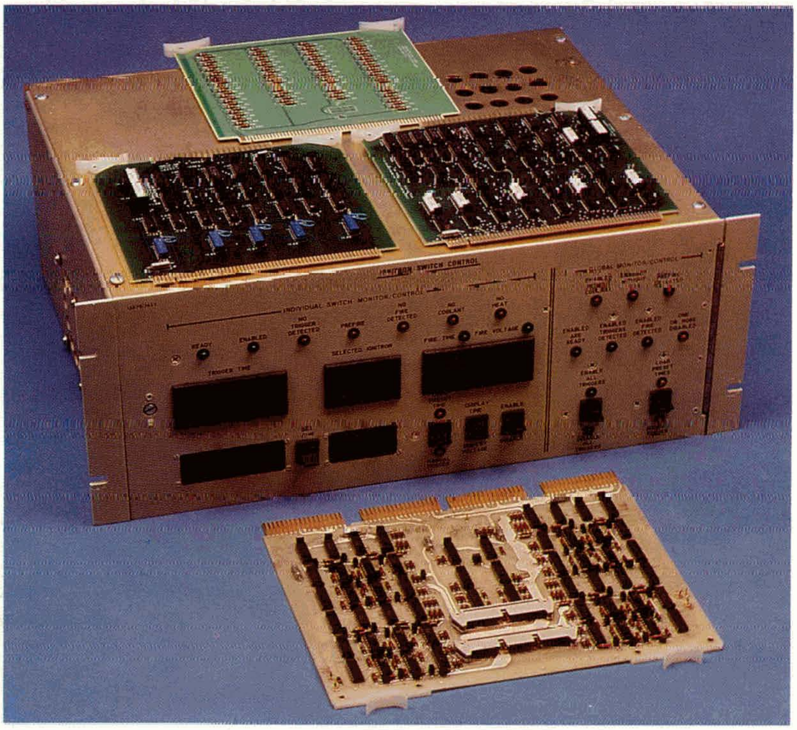

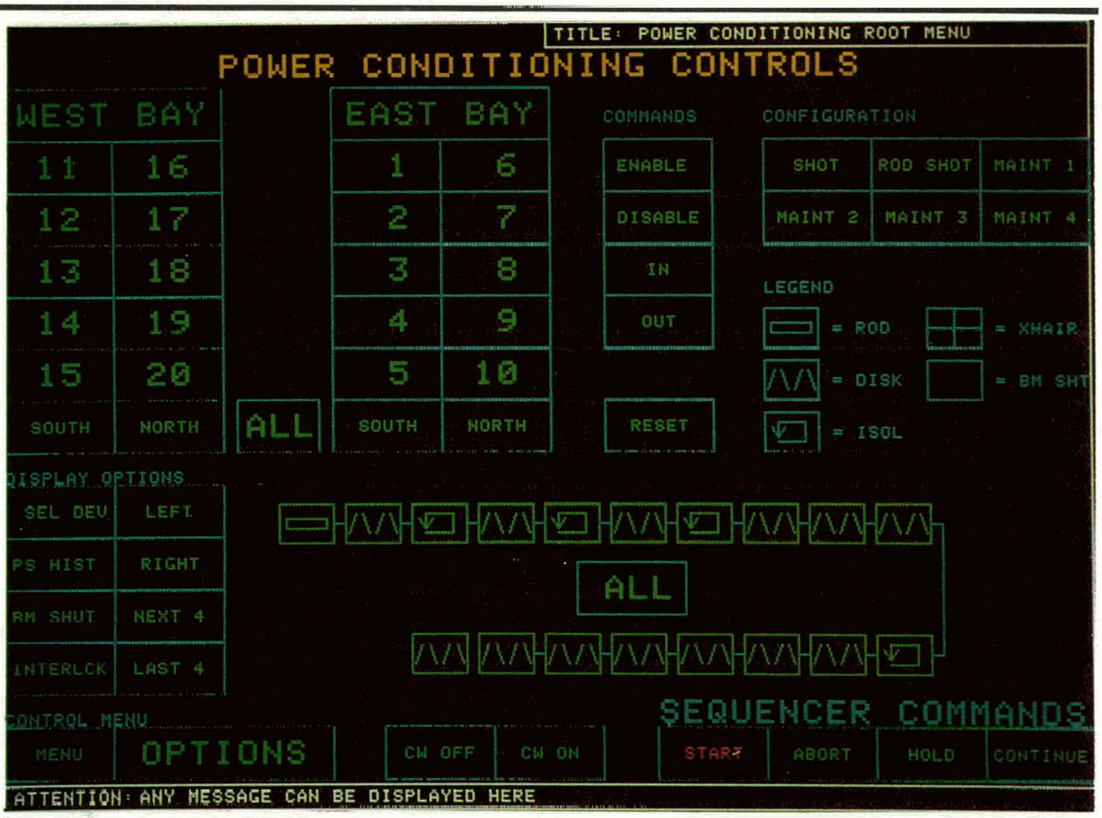

Fig. 2-140. Touch-panel display used to control and monitor the status of the laser system.

power-conditioning flashlamp circuits. It automates many troubleshooting tasks and can rapidly determine the operational readiness of the lamp circuits. The LCD system records flashlamp and ground currents during full-energy laser shots, as well as during the lower-energy PILC tests. After the event, control-room computers read the currents, compare them to expected values, and alert operators to discrepancies. (Figure 2-141 is a photograph of the two chassis in the LCD package, and Fig. 2-142 shows the PC cards for the prototype.) We are completing the initial debugging; further tests will be done by installing and operating the system on the power-conditioning prototype bank in Building 611. Since the chassis will be mounted in a rack next to the ignitron switches, we have placed special emphasis on designing and testing for noise immunity. Tests to characterize the noise immunity of this critical electronics package are continuing.

Power-Supply Interface—Figure 2-143 shows the prototypes for the megavolt-ampere (MVA) power-supply interfaces. The top one was produced at Aydin Energy Systems, the bottom one at LLNL. These chassis permit the power-conditioning control system to provide a reference voltage to the power supply, to monitor the voltage to which it charges, to initiate and terminate charging, and to monitor diagnostic signals

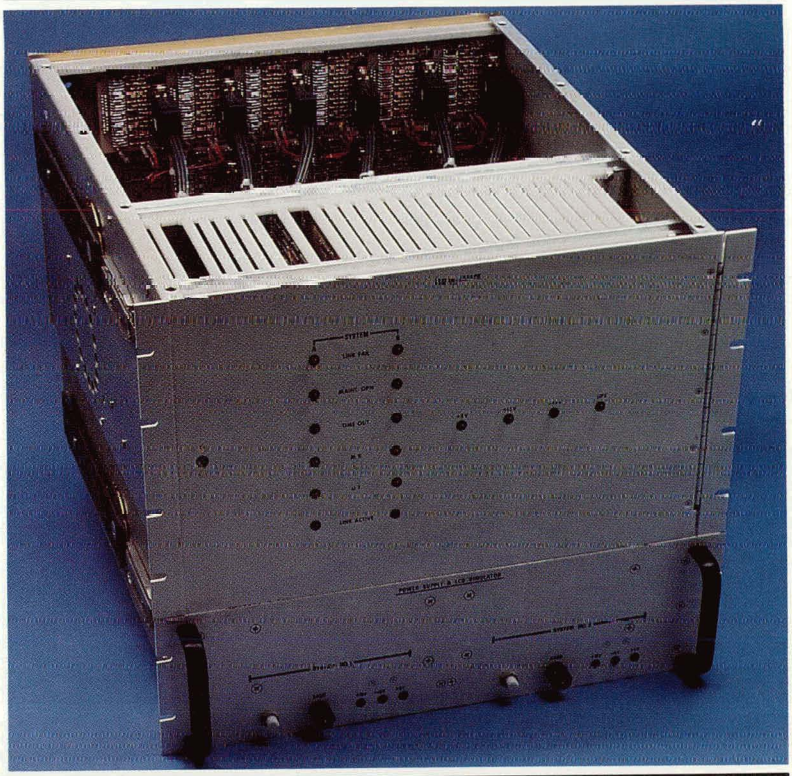

Fig. 2-141. Chassis used for flashlamp-circuit diagnostic testing.

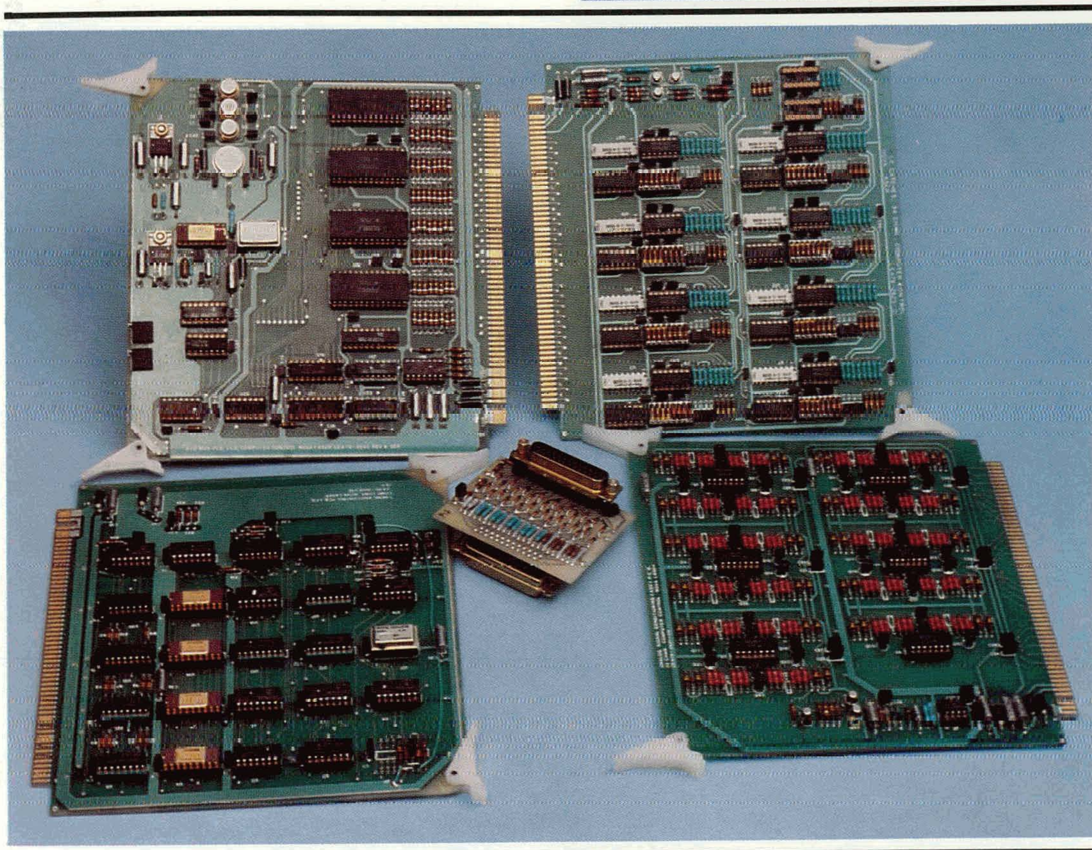

Fig. 2-142. Printed circuit cards used in the flashlamp-current monitor.

from the power supply. The MVA supply does not regulate; it simply stops charging when the output voltage reaches the reference voltage. If the output voltage were to approach a destructive level because of a failure, redundant feedback loops would allow the system to stop charging. The design of the 100-kVA power-supply interface is already being modified for Nova, but the prototype has not been constructed yet.

Fig. 2-143. Control-system interface chassis used in MVA power supplies.

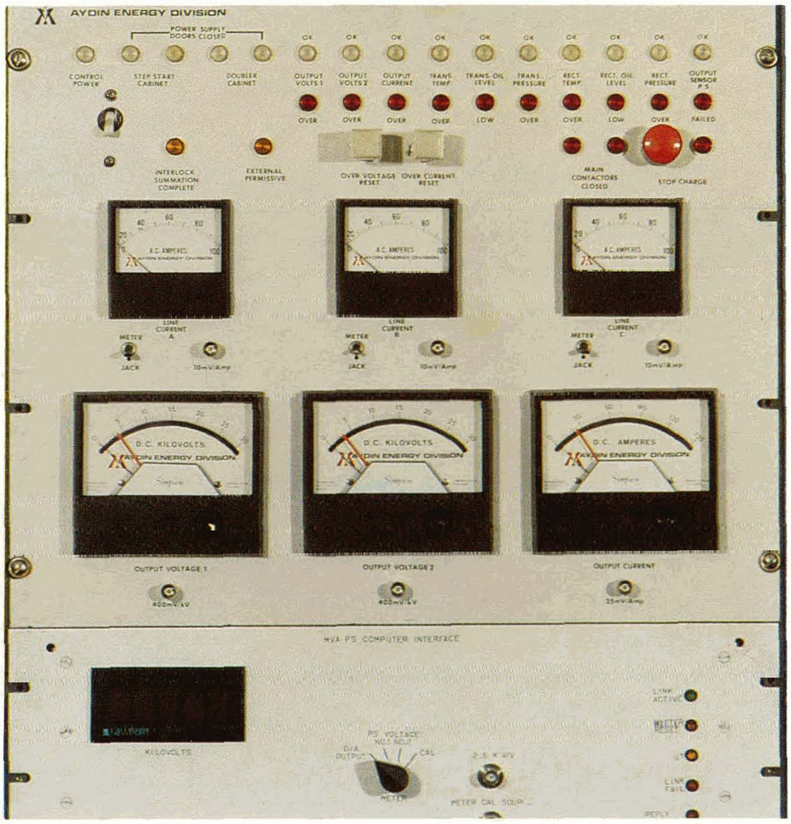

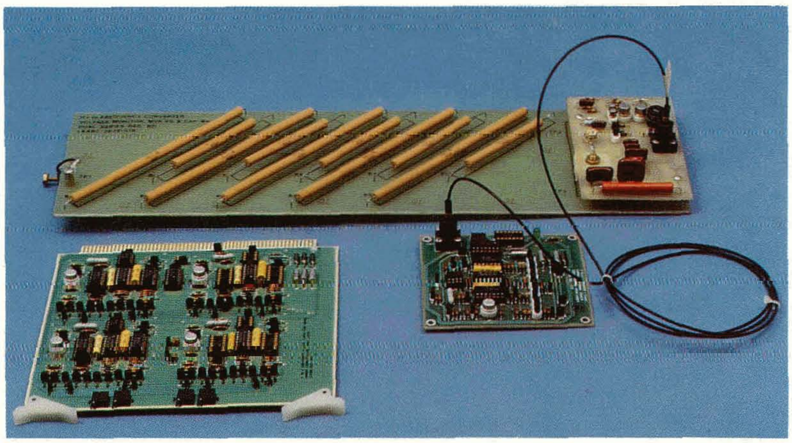

Fig. 2-144. High-voltage monitor implemented with fiber optics.

Capacitor-Bank Interface—The primary function of the capacitor-bank interface is to allow the power-conditioning control computers to fire the ignitrons with precisely timed trigger signals. It also monitors voltage across the ignitrons, detects prefires, and monitors the capacitor-dump switch positions. The prototype, which was designed and constructed in 1980, is currently part of the power-conditioning capacitor-bank prototype controls in Building 611. Since the interface chassis is located very close to the ignitrons, special precautions are being taken to design and test for noise immunity. For example, all inputs and outputs are either optical or are heavily filtered at the chassis boundary. In addition, the timers that generate the ignitron trigger signals have special circuits to help prevent false triggering or resetting. Figure 2-144 shows the components for an optically isolated high-voltage monitor that was developed in 1980 and incorporated into the interface. This unit allows measurement of the ignitron voltage, with no electrical connection between the interface and monitored voltage.

Interlocks Interface—The interlocks interface provides "hard-wired" logic for the safety interlock system and allows the control-room computers to monitor the condition of all interlock signals. The paramount design considerations in the system are reliability and flexibility. Reliability is enhanced by using voted, triply-redundant logic for failure-prone inputs, by buffering the interface inputs enough to prevent damage at 120 V ac, and by using high-level logic for noise immunity. Flexibility is assured by using a patch panel, thereby allowing changes and additions to be made to the interlock logic.

Figure 2-145 (opposite) is a photograph of the breadboard interface currently being tested. It will be installed in the power-conditioning prototype bank-control system for testing in early 1981.

Authors: L. Berkbigler and D. Gritton

Major Contributors: G. Dallum, A. DeGroot, W. Edmonson, R. Holloway, H. Lane, J. Oicles, J. Smart, W. Sokoloski, and R. Stan

Oscillator-Control and Pulse-Distribution System. The Nova oscillator-control and pulse-distribution system controls up to four Nova oscillators and generates the fast-timing signals (with subnanosecond jitter) necessary to synchronize the operation of various Nova components, such as the ASE Pockels cells, the plasma shutters, and the streak cameras used in target diagnostics.

To generate system requirements for Nova, we drew on our experience with the oscillator controls of the Argus and Shiva systems. We originally implemented the Shiva oscillator control system to run one oscillator, later expanding it to operate two. When it became apparent that an increased demand for synchronization channels with nanosecond accuracy, together with our plans to implement up to four oscillators on Nova, would require an expanded capability from the new controls, we integrated both the control and synchronization functions into a single modular system, with the system timing dependent only on the single radio-frequency (rf) signal used to mode-lock the short-pulse oscillators.

Figure 2-146 is a block diagram of Nova's overall oscillator-control and pulse-distribution system; it reflects the following design requirements:

- An order-of-magnitude increase in the number of available fast delay channels with 1 ns resolution and accuracy.
- A modular approach, to accommodate four Nova oscillators.
- A control interface with Novabus.
- An increased noise immunity in rf handling functions.
- A greater emphasis on operator/interface compatibility.

The key pulse-distribution element of the system is an array of 128 fast-timing delay channels, each of which is implemented as shown in Fig. 2-147. As the simplified timing diagram in Fig. 2-148 illustrates, all delay generators are triggered simultaneously by a master-start pulse that originates in the power-conditioning computer (PCC). One of these delay generators can be used to make the oscillator switchout time occur after the master start. The other delay generators may then be programmed to provide triggers, which can occur at any time up to about 1 μs before switchout. To date, approximately 40 of the 128 available channels have been allotted for synchronizing various Nova devices, and it is likely that additional channels will be allotted for this purpose. As with previous designs, each delay channel consists of a programmable counter synchronized to a 62-MHz reference oscillator, followed by a programmable delay line used for 1-ns fine-resolution adjustment. However, the programming of these counters and delay lines is no longer done with local thumbwheel switches for each delay channel. While this approach was adequate for the seven delay channels per chassis on the Shiva controls, the 128 channels of Nova demand a more sophisticated programming method.

A data-handler hardware block, as shown in Fig. 2-146, is needed to interface the delay channels to the power-conditioning computer and the local mode controller. The data handler will store all programmable delay information locally, service all delay channels during the data handler's normal cyclic refresh operation, and write-protect desired channels to prevent inadvertent reprogramming. Access to the data handler is available to the power-conditioning computer via the Novabus interface and to a local controller. Since both may have access to the data handler on a timeshared basis,

Fig. 2-145. Prototype chassis containing logic cards for the safety interlock system.

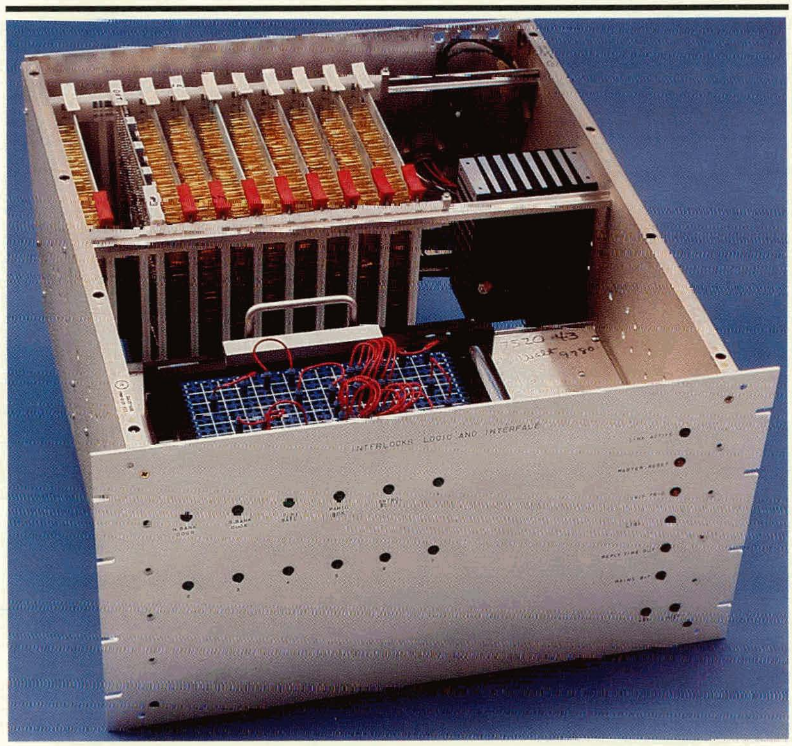

Fig. 2-146. Block diagram for Nova oscillator-control and pulse-distribution system.

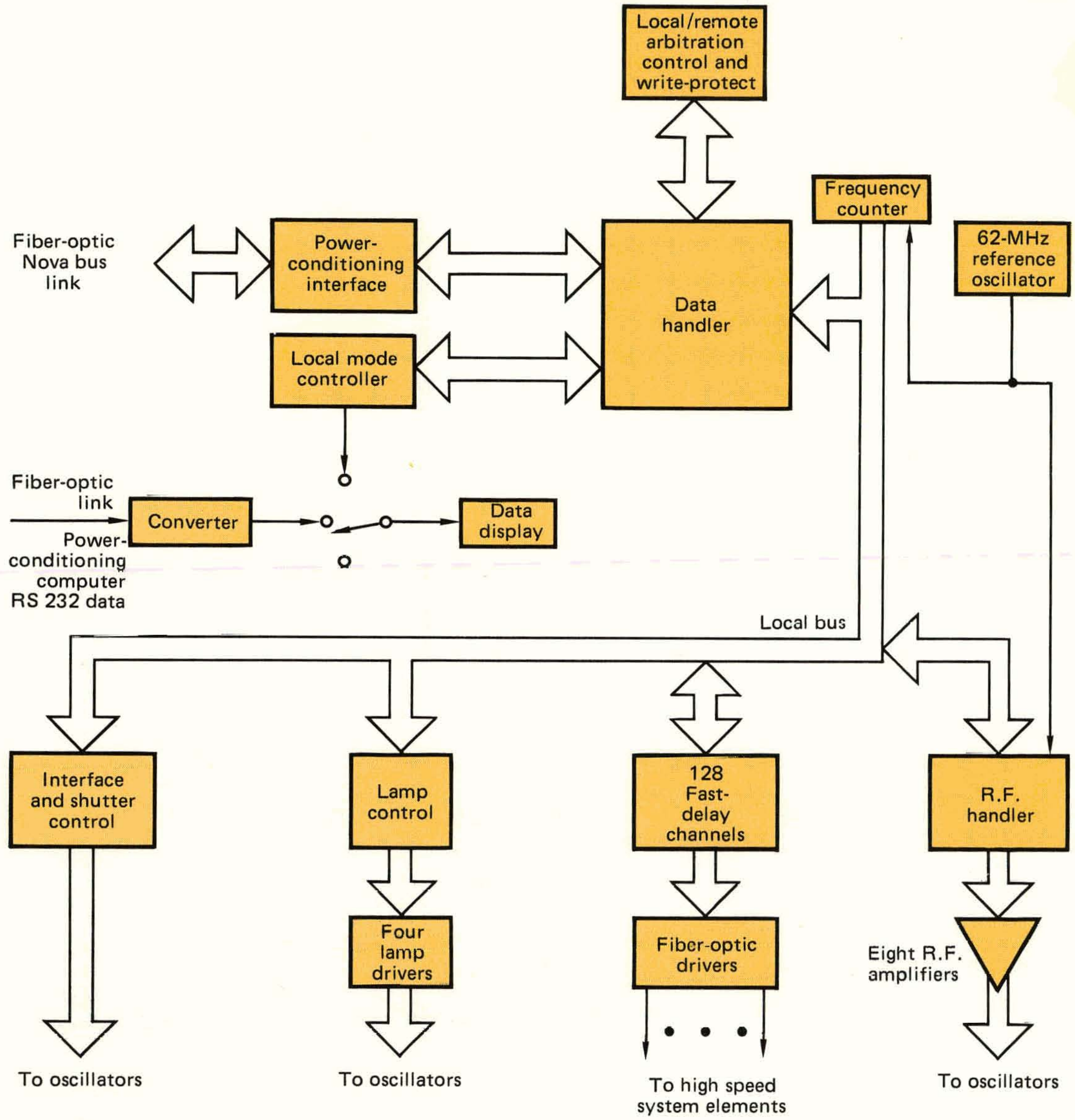

Fig. 2-147. Block diagram for a single fast-delay channel.

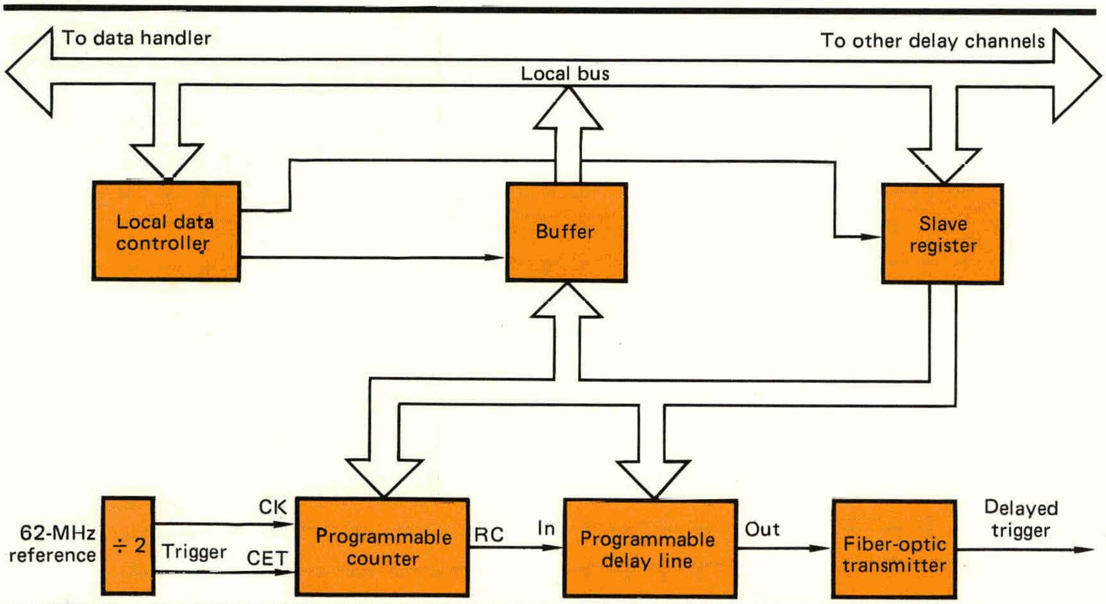

logic has been included to give priority access to the computer, thus avoiding the necessity for special timing logic in the computer software.

The data-handler hardware depends on a 256 × 8 electrically alterable read-only memory (EAROM) that is used to service all 128 delay channels. The appropriate programming words are first loaded into this memory (instead of into the delay channels directly) via the power-conditioning computer, or from a local keyboard. As shown in Fig. 2-147, a slave register at each delay channel receives the latest programming information during the data handler's normal cyclic refresh operation. Each slave register locally programs the high-speed counter and delay line that form a single fast-delay channel. A refresh rate of several hundred times per second ensures that this operation does not impact adversely on the timing of the power-conditioning software, which interrogates the oscillator controls 10 times/s. The power-conditioning computer system also examines the contents of each slave register periodically over the same bus structure. The computer then compares these data with the expected data and flags any errors. Finally, to protect the delay memory from being changed inadvertently, a hardware write-protect function is manually set to selectively lock out blocks of delay memory (and, consequently, the corresponding delay channels) from being accidentally reprogrammed.

We are also revising the methods used to display information associated with each oscillator and timing channel. Simpler systems have used light-emitting-diode (LED) indicators and digital readouts. To address the complexity of the Nova system, we are implementing a dedicated black-and-white video display. This display will normally be controlled from the power-conditioning VAX computer, but will also be capable of stand-alone operation.

The remainder of the overall system is dedicated to the various oscillator-control functions, such as lamp and interlock/shutter control, and is very similar to the approach taken with Argus and Shiva.

Nova operators will be able to do complex local setup operations with off-line oscillators while the on-line units support Nova system operations. Because the video display is software-generated, it can be formatted as necessary to facilitate the setup.

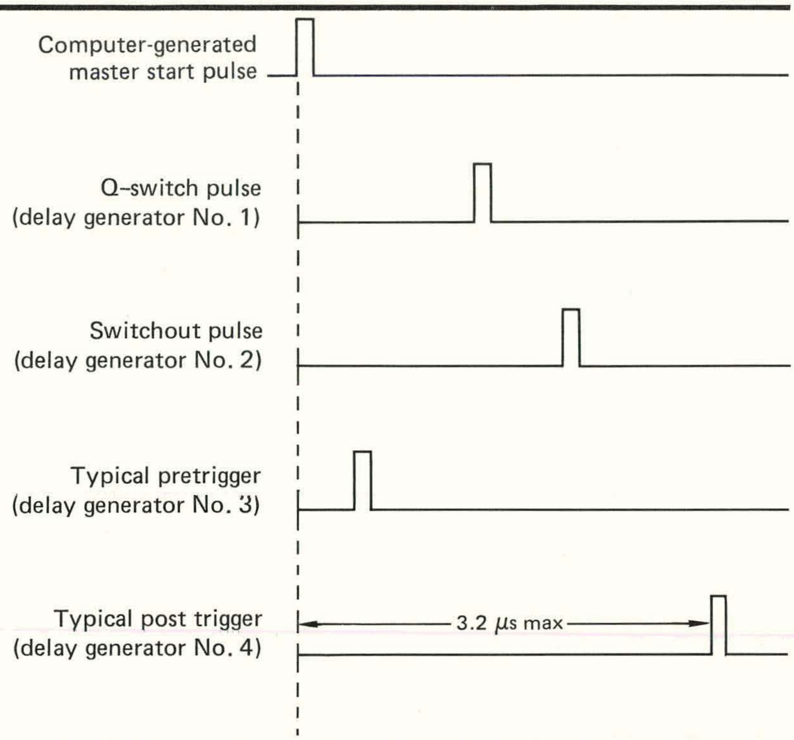

Fig. 2-148. This simplified diagram illustrates the relative temporal sequence of delay-generator timing pulses.

Use of the modular-system approach will make it easier to accommodate expansion to meet new requirements.

Authors: J. Oicles and J. Morton

Nova Alignment/Laser Diagnostics

Requirement and Design Guidelines. The function of the Nova alignment and diagnostic system is to contribute to the optimized irradiation of each target by

- Directing the beam from the oscillator to the target without vignetting at component apertures.
- Precisely positioning pinholes in all of the spatial filters.
- Positioning output beams accurately onto a variety of targets.
- Adjusting beam-path lengths to obtain the simultaneous arrival of all pulses at the target.
- Timing the Pockels cell and Faraday rotator gates for maximum isolation.
- Monitoring the temporal, spatial, and energy evolutions of the laser pulse from the oscillator, along each amplifier chain, and, finally, to the target.
- Acquiring and processing diagnostic data in a short time (compared to the laser

turnaround time) so that data can be used as a basis for adjusting laser parameters before the next shot.

To assure consistency in component design, we have adopted guidelines dealing with hardware organization, manual and motor-driven adjustments, data acquisition, and calibration techniques. These guidelines are listed in Table 2-28.

Table 2-28. Design guidelines for the alignment and diagnostic systems.

Hardware organization

- Tasks are to be divided into groups, each being performed by independent subsystems.
- All components are to be interfaced to the central control system.
- Alignment and diagnostic functions are to be performed by shared sensor packages.
- Modular construction is to be used for components.
- Key components should be compatible with expansion of the laser to 20 beams and with system output at one-half and one-third of the fundamental wavelength.

Adjustments

- All manual adjustments are to be lockable.
- All motor-driven adjustments will have limit switches for periodic indexing checks. Key motors will also be tracked by optical encoders.
- Portable motor drivers will be built for use during component tests and installation.

Data forms

- Alignment data are to be obtained and presented in a video format.
- The same video data are to be presented to the operators and the alignment computer.
- The alignment systems are to be synchronized to the pulsed oscillator for potential shot-time data collection.
- Sensors will contain internal signal-level adjustments to maintain operation within the dynamic range of the detectors.

Calibration

- Film calibration data are to be recorded on all photographs.
- Sweep-speed calibration data are to be recorded on every shot.
- Provisions are to be made for calibrating the diodes and calorimeters, both on-line and off-line.
- Software routines to measure alignment-loop scale factors and cross-coupling matrices will be written.
- Self-testing capabilities are to be included when possible.

Table 2-29. Operating modes for the master oscillator room (MOR) and beam-splitter array.

Mode No.	Description
1	Actively mode-locked and Q-switched (AMQ) oscillator, with all beams balanced at the chain input.
2	AMQ oscillator, with distribution to chains as specified by operator.
3–4	Q-switched oscillator, with same balance options as above.
5–6	MOR cw oscillator through preamps, with same balance options as above.
7–12	Each of the above, but with the beam reduced in diameter to pass through the MOR limiting aperture without loss.
13–14	MOR cw oscillator directly into the beam-splitter array, with balance options 1 and 2.
15–16	Beam-splitter-array cw oscillator, with balance options 1 and 2.
17	Pulse-arrival synchronization oscillator, with beams balanced at the chain input.[a]
28	Pulse-arrival synchronization oscillator, with all output going to only one chain.

[a]Pulse synchronization will be accomplished with the system currently in use on Shiva.[59]

Master Oscillator Room and Splitter-Array Alignment/Diagnostics Subsystems. The master oscillator room (MOR) contains a cw alignment laser, pulsed oscillators, and preamplifiers. The pulse-arrival synchronization system is also located here. As illustrated in Fig. 2-149, beams from the various sources follow a variety of paths into the splitter array, where they are divided among the individual amplifier chains of the main laser. A second cw alignment laser is located in the splitter-array area. A combination of insertable shutters, rotatable half-waveplates, and polarizers determines which oscillator is selected, down which path it propagates, and what fraction of its energy is directed into each chain.

The correct selection of individual shutters and waveplates is initiated automatically by the control system when the operator chooses from a menu of operating modes, such as those listed in Table 2-29. In any of these modes, the selected oscillator is aligned with respect to all subsequent alignment sensors, ensuring that light from any of the several sources follows the same path through the amplifier chains. Each alignment sensor in the MOR and splitter array provides data for one or more alignment loops. The associated motorized gimbals and other components are identified by color in Fig. 2-149. For example, the selection of a pulsed oscillator and the pointing (P) and centering (C) of its output on the MOR beamline is accomplished by the first alignment sensor and the red components preceding it. Letter codes show the functions performed at each sensor location. The alignment sensors are of the same design as the chain input sensor described last year.[60] Since each control loop is affected (to some degree) by the loops that precede it, dead bands and specific control sequences are employed to prevent hunting.

A 90° quartz rotator is part of every Pockels cell assembly so that alignment beams can be transmitted when the Pockels cell is not fired. In addition, 90° quartz rotators are installed in the beamlines at several locations as part of the beam-switching system, but they are not shown in the figure.

Additional half-waveplate/polarizer combinations in the MOR are used as variable attenuators. They allow the MOR output energy to be adjusted without changing the voltage at which the preamplifiers are fired. Control-system software can use data from the laser diagnostics, the power-conditioning system, and the alignment system to perform automatic closed-loop energy balance, drive-level adjustment, and alignment simultaneously. The potential for task coordination of this sort is implicit in control-system organization, as described in "Nova Control-System Development."

Diagnostic measurements in the MOR and splitter-array subsystems, are made at the locations shown in Fig. 2-149. As in all parts of Nova, energy is measured with either a photodiode or an absorbing glass

Fig. 2-149. Schematic of master oscillator room (MOR), showing beams following various paths into the splitter array, where they are divided among the amplifier chains of the main laser.

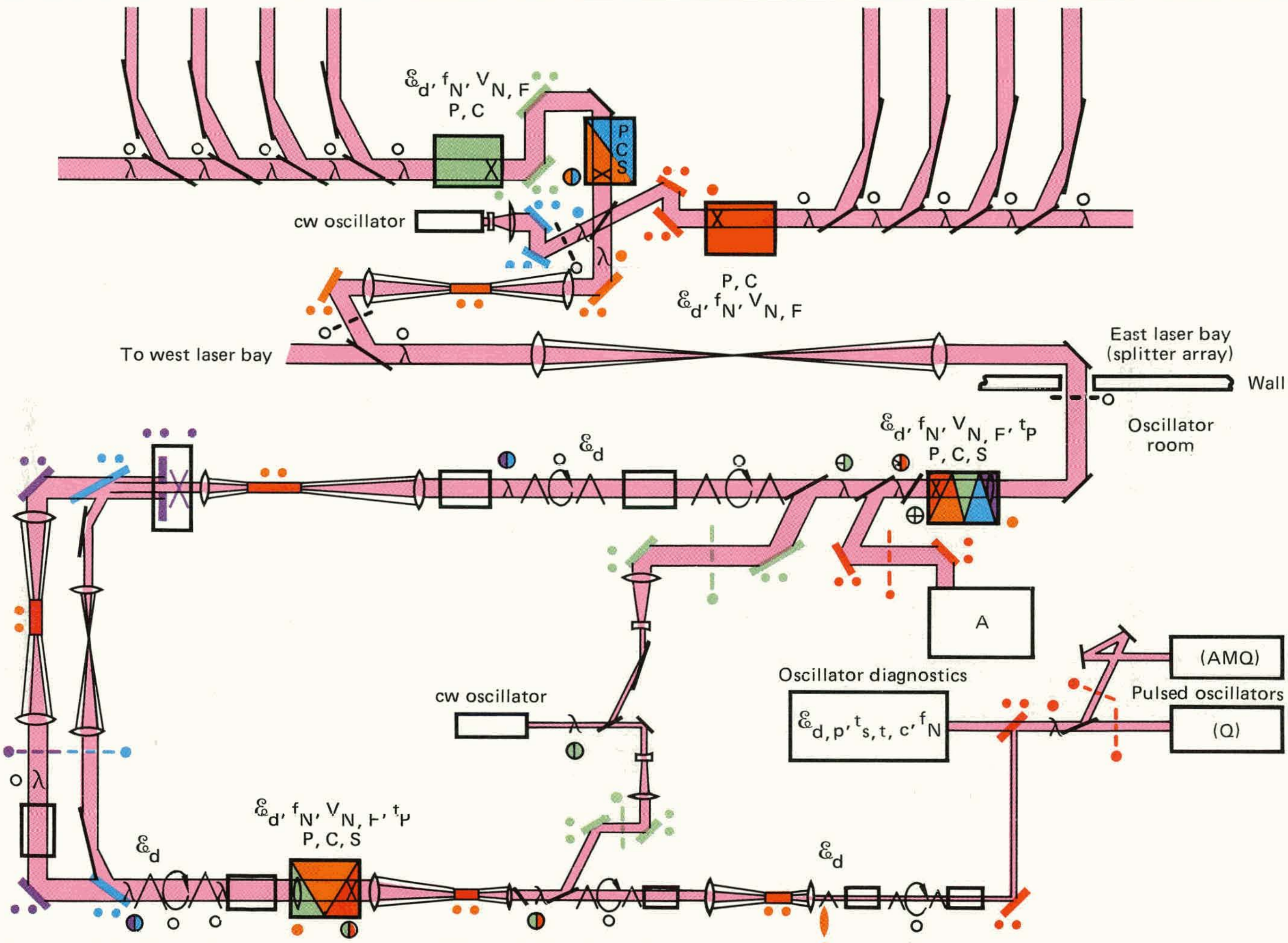

Alignment functions of sensors

P = Pointing
C = Centering
S = Spatial-filter pinhole alignment
F = Focusing
A = Pulse-arrival synchronization

Diagnostic functions of sensors

& = Energy measurement
d, by a photodiode
c, by a calorimeter
p, for prepulse detection

f = Photographic film
V = Video (CCD or vidicon) camera
N, near-field image
F, far-field image
T, target-plane image

t = Temporal measurement
s, by a streak camera
t, of the oscillator pulse train
c, of the oscillator prelaze for cavity alignment
P, for Pockels cell timing

Components

= Rod amplifier
= Disk amplifier(s) with total number of disks as shown
= Crosshair
= Pockels cell
= Faraday rotator
= Polarizer pair
= Polarizer, beam splitter, or mirror
λ = Half-wave plate
= Shutter
o = Motor-driven component
= Motor-driven component used in two alignment loops

calorimeter, depending on the expected signal level.

As described in "Master Oscillator/Preamps," additional oscillators and a second main beam path may be installed in the MOR. The alignment and diagnostic functions of this second beamline would be similar to those of the first beamline.

Amplifier Chain and Output Alignment/Diagnostics Subsystems. The alignment loops and various sensor functions in the amplifier chain and laser output sections are identified in Fig. 2-150. The chain input sensor described last year[60] provides a pointing and centering reference after the single rod amplifier. The faces of the rod are wedged slightly to avoid etalon effects for long pulses, so the beam is steered by its passage through the rod. Placing the alignment sensor after the rod, instead of ahead of it, allows rods to be replaced without permitting associated alignment changes to propagate down the whole chain. The sensor location allows the control loop to adjust the beam path ahead of the rod and thus compensate for changes caused by a slightly different rod wedge or rod rotation. The aperture of the spatial filter ahead of the rod is large enough to accept these changes, which are implemented by motions of the two gimbals and input aperture ahead of the spatial filter.

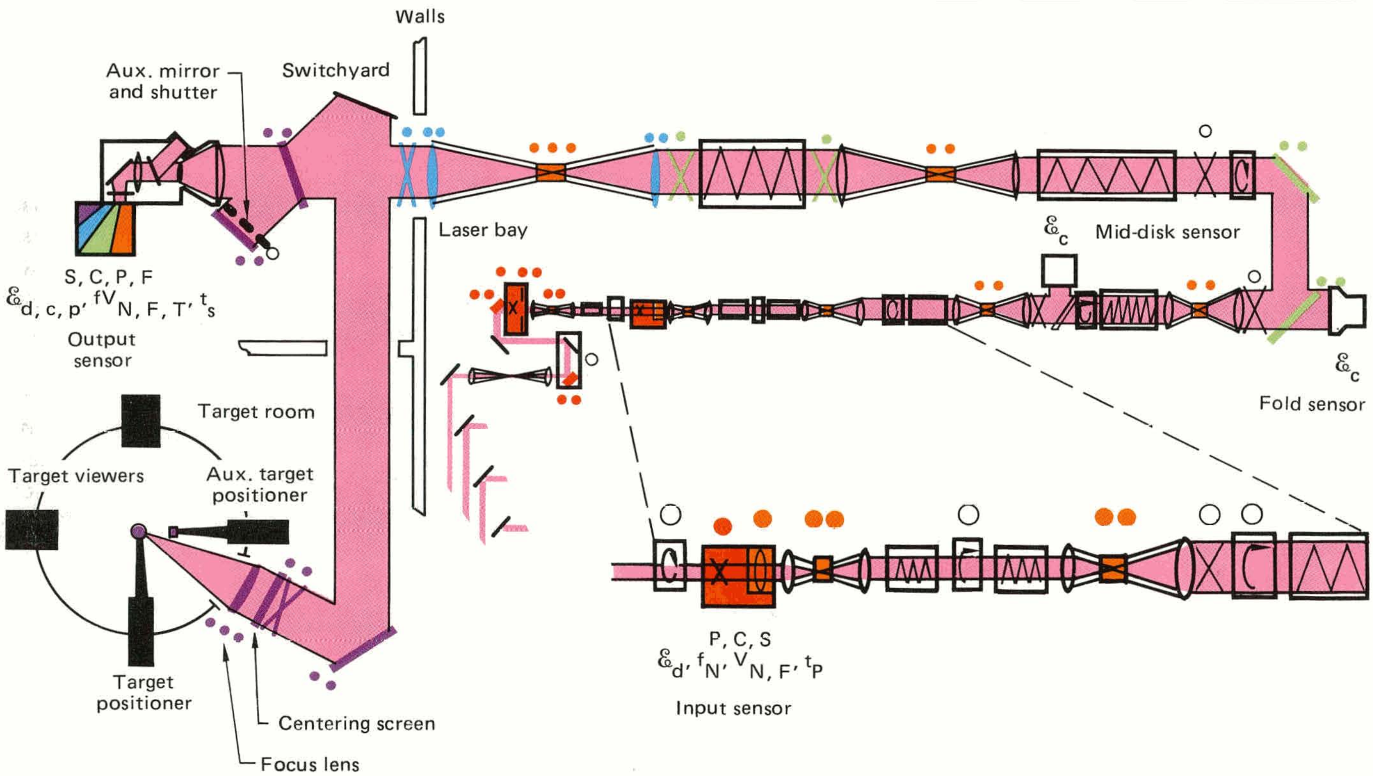

Fig. 2-150. Schematic of alignment loops and sensor functions in the amplifier chain and output sections of the laser.

Alignment functions of sensors

- P = Pointing
- C = Centering
- S = Spatial-filter pinhole alignment
- F = Focusing
- A = Pulse-arrival synchronization

Diagnostic functions of sensors

- $\mathcal{E}$ = Energy measurement
  - d, by a photodiode
  - c, by a calorimeter
  - p, for prepulse detection
- f = Photographic film
- V = Video (CCD or vidicon) camera
  - N, near-field image
  - F, far-field image
  - T, target-plane image
- t = Temporal measurement
  - s, by a streak camera
  - t, of the oscillator pulse train
  - c, of the oscillator prelaze for cavity alignment
  - P, for Pockels cell timing

Components

- ▭ = Rod amplifier
- ⋀⋀⋀ = Disk amplifier(s) with total number of disks as shown
- X = Crosshair
- = Pockels cell
- = Faraday rotator
- ⋀ = Polarizer pair
- / = Polarizer, beam splitter, or mirror
- λ = Half-wave plate
- — — — = Shutter
- o = Motor-driven component

The insertable crosshair at the input aperture is referenced to the center of the aperture. It moves with the aperture and provides a beam-center indicator that propagates through the entire chain when the spatial-filter pinholes are removed. However, the other nine insertable crosshairs, which follow it in the beam path, are permanently referenced to the space frame. They define the nominal propagation path through the system, all the way to the focus lens on the target chamber. The first of the permanent reference crosshairs is actually part of the input sensor and provides the reference for closed-loop input centering.

The ability to image the beam in any of the chain crosshair planes is provided by the output sensor (described in detail shortly), which faces back into the amplifier chain through the partially transmitting, first output turning mirror. The two motorized gimbals at the midchain fold are used to maintain closed-loop alignment with respect to the crosshairs on either side of the largest disk-amplifier section. The motorized lenses on the output spatial filter provide the capability to do a closed-loop output alignment to the final chain crosshair (centering) and the output sensor (pointing). The remaining amplifier-chain crosshairs are not used in any automatic alignment loops; however, the beam positions at these locations are monitored for departure from nominal alignment.

The output sensor also provides (far field) imaging capability for aligning spatial-filter pinholes. The same backlighting and video processing techniques in use on Shiva apply to Nova pinhole alignment.

The first and last output turning mirrors are used to center the beam on the focus lens in its "home" (center of travel) position and to point the beam at a target centered in the target chamber. The output sensor receives light from the direction of the target chamber by using an auxiliary mirror near the sensor, as described in last year's report[63] and shown in Fig. 2-150. To provide data for centering the beam on the focus-lens crosshair, light propagating toward the target is reflected back after passing the crosshair. The silhouette of the crosshair against the beam profile is then imaged by the output sensor. The reflector is an insertable flat mirror, and mechanisms for accurately positioning it and the crosshair are described in "Target Systems."

Because fusion targets are of various shapes and sizes, they do not lend themselves to beam alignment by a standardized procedure. Thus, both the closed-loop pointing and focusing of the beam are done with a surrogate target. For example, a reflecting spherical surrogate might be used, in which case all beams are automatically pointed to the sphere's center and brought to a focus one-half radius away from it by procedures described previously[64,65] and used on Shiva for several years.[62]

A spherical surrogate is always used during operation of the pulse-arrival synchronization system[59] because a strong collimated back reflection is needed to return a signal to the synchronization sensor in the splitter array, as shown in Fig. 2-149. Adjustments in pulse-arrival time are then made with motorized translation stages located just ahead of the two gimbals at the input of each chain.

A CCD array can be used as the surrogate target[66] for pointing and focusing. This permits automatic positioning of the beams, in any specified pattern, in the plane of the array. If offsets from the "aligned-to-surrogate" position are desired, they are obtained by motions of the focus lenses away from their home positions. This is a particularly simple step because the focused beams follow the motions of the focusing lenses with a scale factor of unity.

As with any surrogate-target alignment approach, the exchange of surrogate and real targets must be done with great accuracy. The viewers and target positioners for accomplishing this are discussed in "Target Systems." Verification of each beam's final position with respect to a transparent target or surrogate can be obtained by viewing the beam in the target plane, using the output sensor on the opposing beam.[65]

As emphasized in the design guidelines in Table 2-28, alignment and diagnostic functions are to be performed by shared sensors when possible. Various diagnostic measurements are made in the chain and output sections of the system. The sensor locations and functions are identified in Fig. 2-150. In many cases, the same sensors perform both alignment and diagnostic functions. The auxiliary mirror behind the first turning mirror directs light reflected from the target into the output sensor.[63] The 200-ns (approximately) delay between the incident and target-reflected light is used to discriminate between them for calorimetry measurements, as described in "Output Sensor Design."

Expansion of Output Alignment/ Diagnostics Subsystems for Multiwavelength Operation. The output alignment and diagnostics system has been designed to accommodate expansion of the laser to frequency doubled and tripled operation. This has necessitated the inclusion of provisions for aligning the frequency-conversion crystals to the 1.05-μm beam, aligning the frequency-converted beams onto the target, and diagnosing the 2 or 3ω light incident on and reflected from the target. The additional components required for multiwavelength operation are shown in Fig. 2-151. The output sensor design for a multiple wavelength system is discussed in "Output Sensor Design."

To align the KDP crystal(s) to the 1.05-μm beam, a highly sensitive photodiode (or photomultiplier) with 1.05-μm rejection filters is placed in the target chamber, and the pulsed oscillator and YLF (yttrium lithium fluoride) amplifiers in the MOR are pulsed at a repetition rate that is consistent with thermal distortion constraints (expected to be on the order of 1 Hz). For 2ω operation, the KDP is oriented to maximize the green light generated by the low-level pulses. For 3ω operation, the crystals are first aligned for a maximum output of 2ω light (as above). Then the mixer is tilted open-loop to the slightly different angle required for frequency tripling. Experiments have begun on Argus to demonstrate these procedures.

Positioning of these frequency-converted beams on a target will probably require the use of a local light source whose diameter, alignment, and state of collimation are matched to those of the main beam. This results because only a small amount of 2ω light can be generated by driving the 74-cm-diam KDP crystals with just the high-repetition-rate part of the main laser. The signal is expected to be marginal, either for detection by a CCD in the target position or for alignment by detecting the light reflected back to the output sensor from a spherical surrogate. The amount of 3ω light generated with low-level 1ω input pulses is even less.

Local 2 or 3ω beams (74 cm diam) can be introduced into each beamline without using additional large-aperture mirrors and lenses. This is done by injecting a small beam

Fig. 2-151. Output alignment components for 2ω and 3ω.

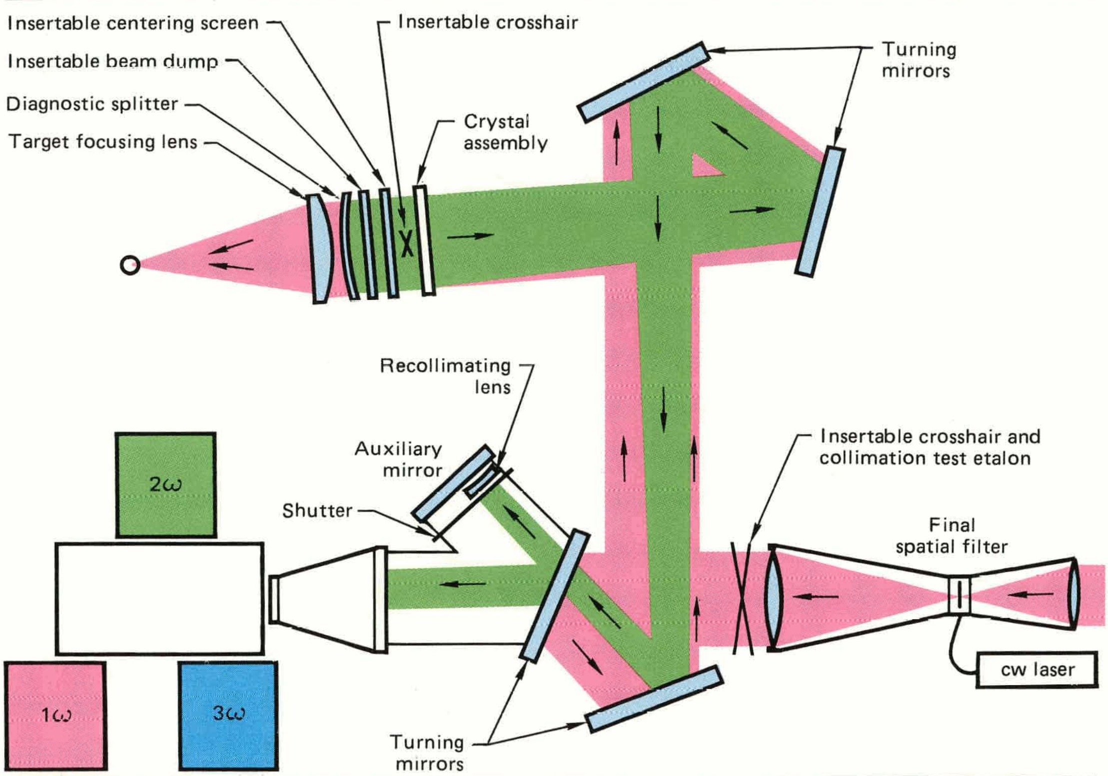

at the input of the final spatial filter with insertable mirrors from a local 1-, 2-, or 3-ω oscillator source. The 2 and 3ω source is expanded to the full 74-cm beam diameter by remotely inserting an additional small lens inside the spatial filter. The combination of this lens and the output lens of the spatial filter produces a full-aperture collimated beam. Separate lenses and manipulators are used to accommodate the change in focal length between 2 and 3ω. The output sensor is used to ensure that the local cw beams are properly collimated, centered, and propagating parallel to the 1ω chain output. The small diameter 1ω beam provides the necessary intensity for crystal alignment.

Once a cw or high-repetition-rate pulsed beam is available at the appropriate harmonic wavelength, the output centering, pointing, and focusing tasks are performed in the same manner as for 1ω, but with the use of harmonic wavelength versions of the output sensor and CCD surrogate. For 1 and 2ω, spot checks of the various steps in aligning to the target can be made either by using low-level pulses propagating through the whole system and "frame-grabbing" an appropriate frame from the video network or by saving data from selected CCD cameras in local digital memories. However, the amount of 1ω light required to generate even a low-level 3ω signal makes such checks impractical for the blue light.

The output sensor performs diagnostic measurements of the incident light on the target and the light reflected from it for all three wavelengths. However, since the 2 and 3ω light originates in the frequency conversion crystals, which are nearer to the target chamber than is the sensor, the sampling of incident 2 or 3ω light cannot be done in the same way as it is for the 1ω beam. For diagnostics of 2 or 3ω light, a splitter is used, in either the frequency-conversion or focus-lens assembly, to reflect a slowly converging 2 or 3ω beam back toward the output sensor, as shown in Fig. 2-151. This splitter is tilted slightly so that, on reaching the first output turning mirror, the converging diagnostic reflection is at the edge of the aperture and subtends only about 5% of the beam area. The fraction of the diagnostic beam that is transmitted by the mirror does a double pass through a negative lens in front of the auxiliary mirror and is recollimated as it heads back toward the output sensor.

The diagnostic splitter is so close to the target that the 2 or 3ω incident light and the reflected signals from the target arrive at the sensor within about 15 ns of each other, which is too close for temporal discrimination by the gated photodiode calorimeters described in "Component Development." Therefore, the target-reflected light and recollimated diagnostic beam must enter the sensor with enough of an angular difference to be completely separated spatially in the far field. This is accomplished by incorporating a wedge in the recollimating lens so that it also repoints the incident diagnostics beam by the appropriate angle. Because of its offset and reduced diameter, it has an insignificant effect on the full-aperture signals that also traverse the same path for other alignment and diagnostics functions.

Component Development. The chain input sensor previously described[60] has been tested in the form of a table-top breadboard, using prototype versions of the CCD camera,[67] the filter wheel mechanism, and the insertable crosshair assembly. The optical performance of the sensor and the resolution of the CCD array camera meet the design requirements for cw operation. Our plans currently call for using virtually identical packages in the master oscillator and splitter-array subsystems. We identified potential improvements for each of the prototype devices, and these are currently being implemented. Tests of the full sensor have not yet been conducted with a pulsed input beam.

The development of the photodiode charge amplifier, a key component for every low-level pulsed-energy measurement in the system, has been a major focus of effort during 1980. A prototype package is now being tested in the severe electromagnetic interference (EMI) environment of Shiva to simulate conditions in Nova.

Every photodiode calorimeter is connected by a short cable to one of the photodiode charge amplifiers, each of which consists of a gated charge amplifier, an analog-to-digital converter, and a control/communications section. The gated amplifier section is illustrated schematically in Fig. 2-152. Varying the feedback and compensation in the operational amplifier, under computer control, enables the amplifier to operate over a wide dynamic range of input energies with programmable gain control. This minimizes the need to mechanically change filters in front of the diode to accommodate changes in laser energy.

One reason for gating the amplifier is that many photodiodes in the system are exposed to flashlamp light pulses up to a millisecond in duration, as well as to laser pulses of a few nanoseconds duration. If the diode output were integrated over the full duration of a flashlamp pulse, the flashlamp light would dominate the measurement. Therefore, the photodiode is shorted through a low impedance most of the time the flashlamps are on. During this time, the input to the charge amplifier is isolated from the photodiode by a high impedance, and the feedback capacitor of the charge amplifier is shorted. Just before the arrival of the laser pulse, the input of the charge amplifier is connected to the photodiode and the feedback capacitor and photodiode shorts are opened. The photodiode signal is integrated briefly; then the amplifier is returned to its original state. The gating is accomplished with FETs, which transfer some spurious charge when they switch. This unwanted charge is cancelled out with a charge-compensation gate that injects an equal charge of the opposite polarity.

The gating circuitry can operate with rise times as short as 10 ns, and the gate width can be as narrow as 30 ns. In addition, the extinction ratio is sufficient to short out pulses that exceed the saturation level of the amplifier by 100 times. Therefore, it is possible to use the gated amplifier to discriminate between two closely spaced laser pulses even if they are of significantly different energies, as well as between flashlamp light and a single laser pulse. In either case, the integrated signal is sampled and held until a 12-bit analog-to-digital converter digitizes and latches the data for transfer to the appropriate front-end processor (FEP). The FEPs are key components in the data-acquisition system described previously[68] and are part of the system-wide control network.

The sequencing of gating events and data transmission to the FEP is performed by the control/communications section of the amplifier unit. A logic-state machine, programmed into two 1024 × 8 read-only memories (ROMs), controls all aspects of the amplifier operation. This ROM-coded state machine performs all required conditional logic in a small physical space, compared to conventional TTL logic. Moreover, the machine lends itself to the incorporation of self-test functions and is easily modified to accommodate new requirements by reprogramming the ROMs. All communications of data and commands between the amplifier package and the FEP are done over a 125-kbaud serial link, using a universal asynchronous receiver/transmitter (UART).

At the FEP end of the communications link, an interface with the FEP supplies control commands and receives data and status information from the amplifiers. This

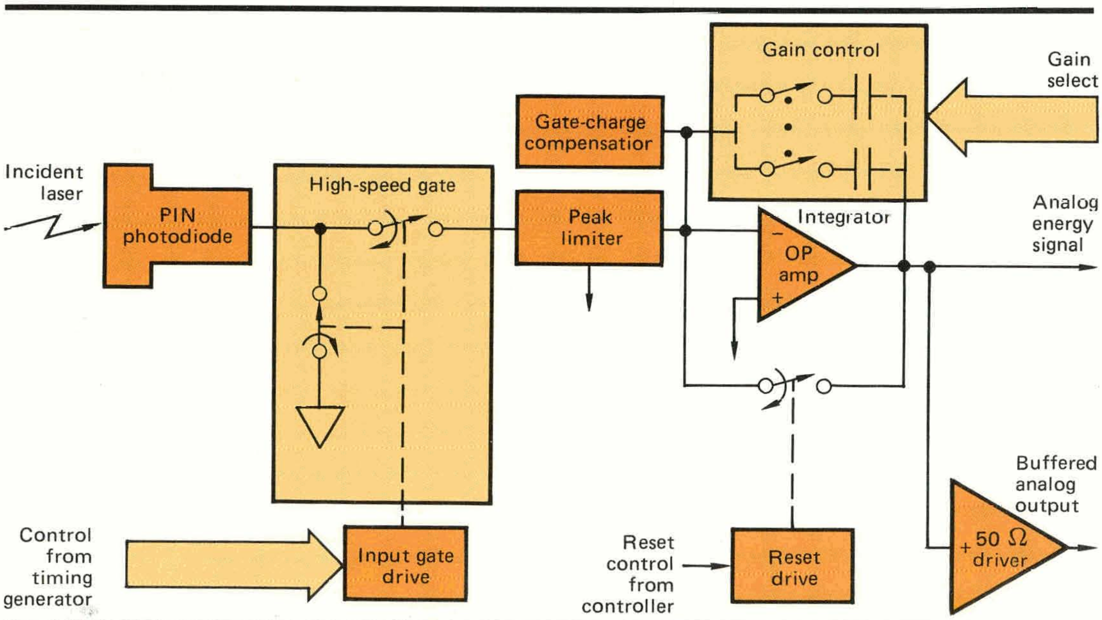

Fig. 2-152. Schematic of gated amplifier.

interface, which uses one multiplexed input/output port to serve 20 amplifiers, has two primary modes of operation: a single-transfer mode and a direct-memory-access (DMA) mode. In the single-transfer mode, one charge amplifier is selected. Commands and data are then exchanged with it by read and write cycles of the processor. In the DMA mode, the interface is given the number of amplifiers to which a control word is to be sent (or from which data are to be read), the channel number of the first amplifier, and the address in the memory where the commands reside (or where received data are to be placed). Then the interface, without processor intervention, sequentially performs the transaction with each amplifier. For example, after a shot all amplifiers have data ready to send to the processor. In the DMA mode, the data from each amplifier are read and placed in memory without requiring a separate processor request for each amplifier. This increases the speed with which data can be collected and simplifies the software required for the process.

The charge amplifier and the controls, communications links, and interfaces associated with it have successfully completed preliminary tests.

Output Sensor Design. We have designed the output sensor to make independent measurements at three wavelengths. To discriminate between incident laser light and light reflected from the target, it uses a combination of angular and temporal separation techniques. As shown in Fig. 2-153(a), the wavelengths are separated from each other in a central beam-splitter box. A separate alignment and diagnostics module is attached to the central box for each of the three wavelengths. Each module provides the capabilities listed in Table 2-30.

A common input telescope comprised of lenses L1 and L2, as shown in Fig. 2-153(b), is used for all the operating wavelengths. This telescope reduces the beam diameter as much as possible, without exceeding coating-damage limitations under pulsed-shot conditions. Because of dispersion in L1 and L2, each wavelength accumulates a different set of aberrations that must be individually corrected later in the optical train. Beam splitter B9 reflects 3ω light and transmits 1 and 2ω light. Beam splitter B10, in turn, reflects 2ω light and transmits 1ω light. Then, the three L3 and L4 lens pairs (one pair per wavelength) compensate for accumulated aberrations, recollimate the beam, and further reduce the beam diameter for each

Fig. 2-153. Perspective (a) and geometry (b) of output sensor, showing beam-splitter components.

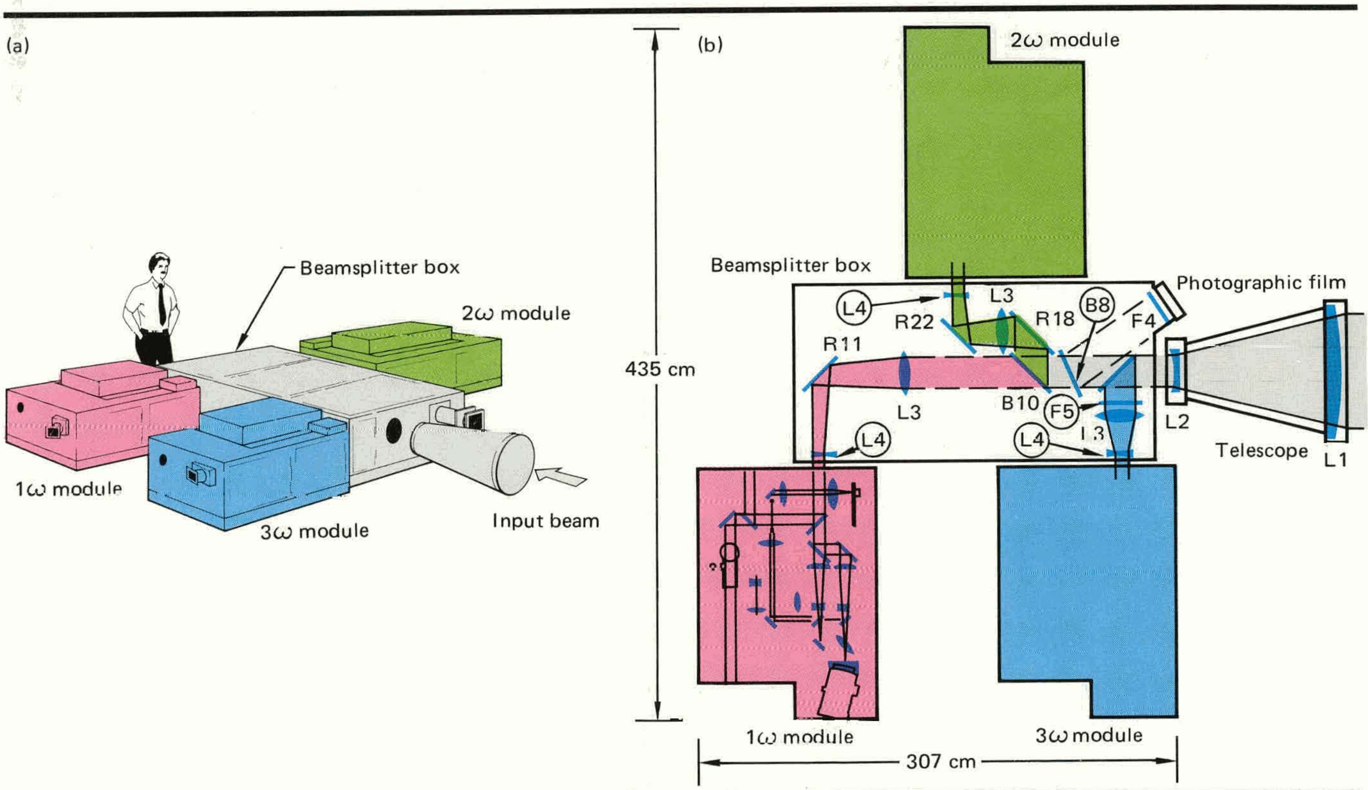

wavelength. However, during pulsed operation, this second reduction in beam diameter must be preceded by a reduction in energy to avoid optical damage. Accordingly, filter F5 is inserted to absorb a portion of the 3ω light, and beam splitter B8 is inserted to reflect a portion of the 1 and 2ω light. Filter F4 subsequently transmits only enough 1ω light to produce a near-field photograph of a plane approximately equivalent to the plane of the target-chamber focus lens.

The alignment and diagnostics module, depicted in Fig. 2-154, contains the additional optics required for 1ω. The 2 and 3ω modules are of nearly identical design and differ only in details related to discrimination between incident and target-reflected signals. At the time of a pulsed shot, reflector R1 is out of the beam, and beam splitter B2 reflects part of the beam toward the calorimetry section by way of R13 and B14. Reflector R12 is normally out of the beam during pulsed operation since the external interferometer is basically a cw instrument.

Light transmitted by B14 will be used to drive a streak camera or a prepulse monitor through interfaces that have not yet been designed. However, fiber-optic cables will carry light from all 10 output sensors to two shared streak cameras, one for incident light and one for target-reflected signals. One

Table 2-30. Output sensor capabilities. (Except where noted, the capabilities are the same for all wavelengths.)

Calorimetry measurements

- Total energy entering target-chamber focusing lens.
- Energy reaching target plane within a specific diameter (four choices of diameter), i.e., focusable energy.
- Energy reflected from target back through target-chamber focusing lens.

Near-field imaging

- Standard TV format for three fields of view (20, 45, and 100 cm) with 425-m total focus range (300 m for 2 and 3ω).
- Photograph of beam in plane approximately equivalent to focusing lens plane (1ω only).

Far-field or target-plane imaging

- Standard TV format for four 1ω fields of view (0.20, 0.45, 1.00, and 5.00 mrad) with 30-mm total focus range relative to focus of f/3 target-chamber focusing lens.
- Standard TV format for three 2 and 3ω fields of view (0.11, 0.25, and 1.25 mrad).
- Multiple exposure-level photographs of target plane taken with reflected light and of equivalent plane using incident light.

Miscellaneous

- Operates in preshot alignment mode with as little as 10 μW cw power to the sensor, and in a shot-diagnostic mode with up to 700 J.
- Auxiliary outputs for streak-camera, prepulse-monitor, or interferometer modules.
- All operating mode changes and adjustments are stepper-motor driven.

Fig. 2-154. Schematic of 1ω module. ▼

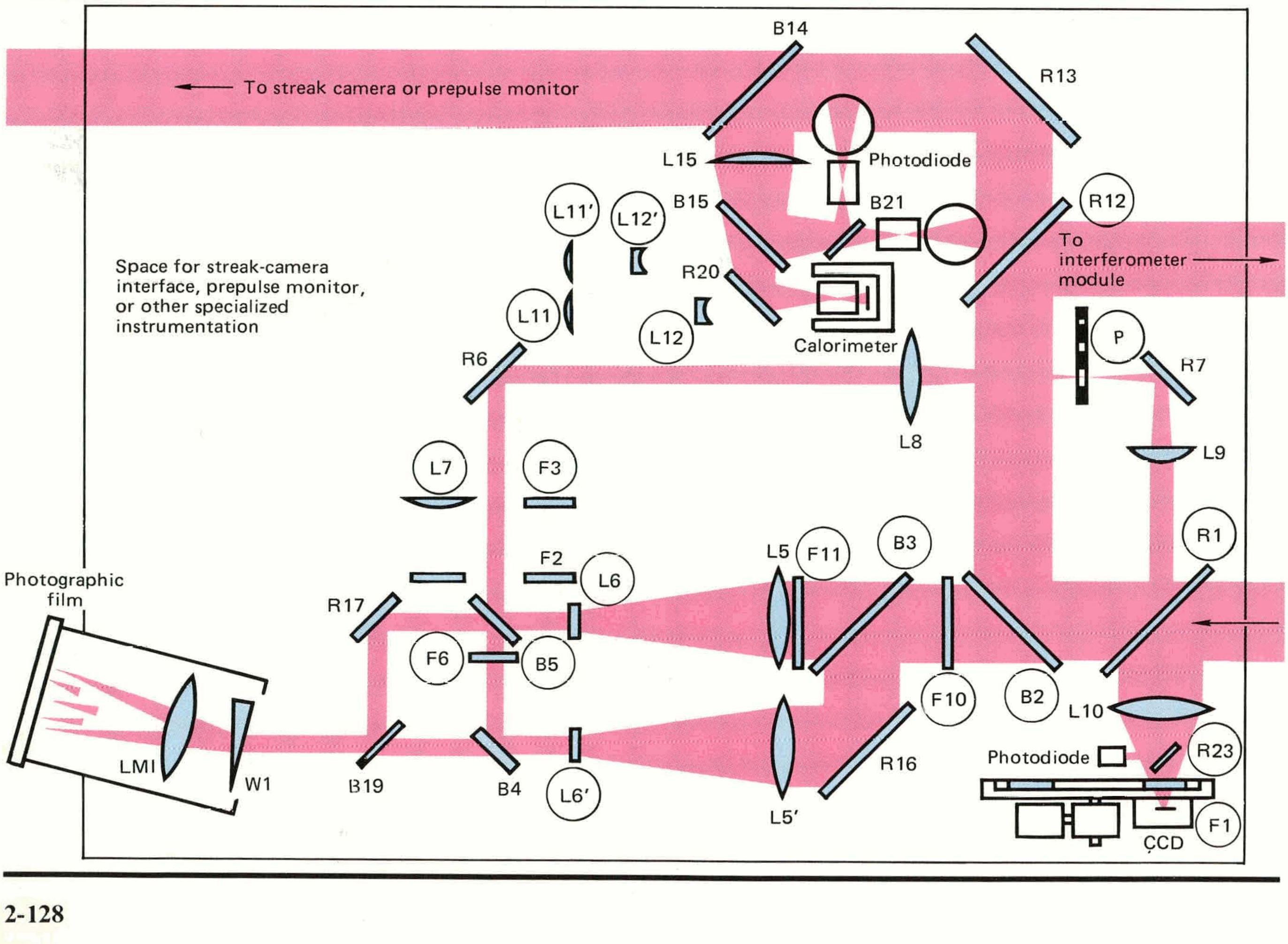

incident pulse will be routed through a long optical delay to generate an incident fiducial on the reflected light data.

The signal is split three ways within the calorimetry section, shown in more detail in Fig. 2-155. The combined incident laser light/target-reflected light is sampled by two fast photodiodes housed in integrating spheres and by an absorbing calorimeter. For 1ω light, the signals from the diodes are gated to distinguish between incident and reflected light. During the arrival of the incident pulse, one photodiode is shorted by the gating circuit of its charge amplifier while charge from the other diode is collected. Approximately 100 ns later the gating of the detectors is reversed. When the reflected pulse arrives, it is integrated by the amplifier and detector that were originally shorted, and the detector that collected the incident signal now rejects the later-arriving reflected signal.

The outputs of these two amplifiers—representing the incident and reflected beam energy—are then digitized, and the amplifiers are reset. Meanwhile, the absorbing glass calorimeter measures the sum of the incident and return energy, which provides a self-consistency check.

For various target sizes and focus conditions, there is a large variation in the far-field image size and in the corresponding optical intensity in the focal plane of lens L15 (see Fig. 2-154). These variations could cause unreliable operation of the photodiodes and calorimeter. To prevent such difficulties, the photodiodes are mounted in integrating spheres located beyond the focal plane. Light reaches the photodiodes by diffuse reflection from the internal surface of the spheres. Because of this, the photodiodes are always uniformly illuminated and therefore insensitive to changes in beam focus and to changes in the transverse position of the beam as well. The effects of variations in beam size on the calorimeter are minimized by imaging the input aperture of the sensor package onto the calorimeter. Since all three calorimetry beams pass through a focus on the way to their respective detectors, a small vacuum cell is placed in each focal region so that sufficient energy can be transmitted without creating an air arc at the focus.

For 2 and 3ω, the small diameter of the incident diagnostics beam (compared to that of the sensor aperture) allows it to enter the sensor at a significant angle (Fig. 2-151). As a result, the incident beam and target-reflected light in the 2 and 3ω modules are spatially separated at the input windows of the vacuum cells. Carefully positioned masks block incident light from one diode and target light from the other. Since the calorimeter again measures both, the same set of three energy measurements is obtained.

As noted in "Amplifier Chain and Output Alignment/Diagnostics Subsystems," the output sensor is used to provide near-field images of beams and backlighted crosshairs in the amplifier chain, as well as in the centering-screen plane near the target chamber. In this mode of operation, collimated light entering the sensor emerges from L4 in the splitter box and enters the 1ω module (Fig. 2-154) still collimated, but with a smaller beam diameter. As the beam continues through B2 and B3, its diameter is further reduced by L5 and L6, which are also spaced to maintain the beam's collimation.

At this point, virtual images of all the near-field planes of interest have been compressed into a space about 20 cm long between L5 and L6. For near-field imaging, L7 is inserted in the beam reflected from B5. It is mounted on a longitudinal translation stage with a range of more than 20 cm so that it can be positioned one focal length from any near-field image plane. Next, the beam passes through focus and expands until it reaches L8. As the beam converges past L8, a real near-field image appears in the focal plane of L8 (the pinholes at P are out of the beam in this mode of operation and

Fig. 2-155. Gating signals for incident and reflected discrimination.

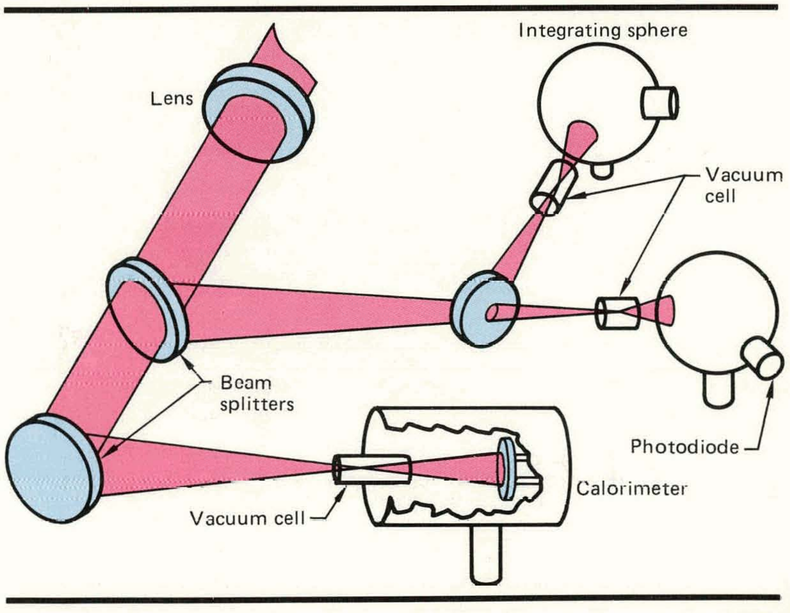

therefore do not vignette the image). Since this plane is one focal length from L9 and the CCD imager is at the focus of L10, the image is relayed to the CCD. To adjust the signal level, filters (F1) with a range of transmission values are positioned (by a filter wheel) in front of the CCD.

Several modes of far-field imaging are implemented in the sensor design. For the lowest magnification, far-field viewing mode (the largest acceptance angle), light entering the module is immediately directed through L10 to the CCD by reflector R1. This field of view is not used at shot time because the insertion of R1 prevents light from reaching the calorimeters and the multiple-image camera. However, a short path is required for a wide field of view. This results from the marked increase in the clear aperture that becomes necessary with increasing propagation distance when the source of the light entering the sensor is very far inside the focal plane of the target-chamber focus lens, when diffuse reflections from a large target are being observed, or when an opposing beam with a transverse offset in the target chamber is being viewed. In this viewing mode, focusing is done by moving L4 away from its nominal position in the beam-splitter box [see Fig. 2-153(b)].

The higher magnification fields of view for far-field and target-plane imaging use a longer light path. Lens L4 is returned to its nominal position; so, for collimated light entering the sensor (as from a point source at the focal plane of the target-chamber lens), the beam will remain collimated after passing through L4. With R1 removed from the beam, part of the light passes through B2 and B3 into lenses L5 and L6. These lenses add 4× to the imaging magnification but maintain beam collimation. Light reaches lens LMI by way of B5, R17, B19, and wedge W1. It reaches lens L8 by way of B5 and R6 (with L7 out of the beam). Since the source appears to be at infinity with respect to lenses LMI and L8, it is imaged at the focus of each lens.

In the case of lens LMI, a row of images with successively lower exposure is recorded on film because wedge W1 has partially reflecting coatings on both surfaces to generate a series of partial internal reflections. One of the pinholes at P is located at the focal point of L8, and an image of the source within the selected pinhole is relayed to the CCD. Lenses L11 and L12 (two pairs) further increase the available magnification by 2.2× or 5× depending on which pair is inserted. At shot time, with reflector R23 in the beam, the light is deflected into a diode calorimeter for a measurement of focusable energy. Filters F2 and F3 control the signal level in calibrated steps so that air breakdown does not occur in the focused light cone following L8.

The target plane frequently does not coincide with the focus of the target-chamber lens. Also, it is often desirable to image the target plane in an opposing beam without moving the near-side target-chamber lens. Under these circumstances, the object plane of interest is generally not at infinity as viewed from the sensor. The focusing adjustments needed to compensate for these object-plane offsets are provided by translations of L6 along the beam axis. So, with respect to LMI and L8 (which follow L6 in the light path), the object plane is always at infinity. A key feature of this design is the incorporation of the focus adjustment ahead of the point in the beam at which the light follows separate paths to the CCD and multiple-image camera. This ensures that the operator can always preview the image that will be photographed.

The apparently redundant path followed by light reflected from B3 to R16 and through L5′ and L6′ is necessary because the focus adjustment for imaging the target plane on the film with light reflected from the target is different from the adjustment for imaging the equivalent plane in the incident beam using light directly from the laser. Although light from both sources enters the sensor, the target-reflected light will have been deflected a few milliradians out of the plane of Fig. 2-153(b) by the auxiliary mirror identified in Fig. 2-150. Some light from each source passes through B3, but L6 is adjusted to properly focus only the incident-beam equivalent plane on the film. The light from the target also reaches the film, but it is out of focus and offset because of the angular difference.

The largest angular difference that can be introduced is set by practical limitations on the field of view of the sensor optics. For 1ω irradiation of large targets, or for a significant defocus of the beam in the target plane, this will result in some overlap of incident and reflected images. However, even for the largest targets, no more than half of each image will be in the overlap region, and meaningful data analysis can still be performed. As noted, a larger angular difference is possible for 2 and 3ω: for these wavelengths full separation is achievable.

Light is also reflected from B3, and L6′ is adjusted to properly focus the reflected target image on the film. The incident beam light that follows this path is out of focus and offset on the film. The net result of this dual-focus arrangement is that two pairs of slightly separated beams reach the film. Separation of the pairs is provided by appropriate angular adjustment of R17 and B19.

All routinely adjusted components in the output sensor are driven by stepper motors. Circled labels are used in Figs. 2-153(b) and 2-154 to distinguish these components from those having fixed adjustments. For example, beam splitter B2 in Fig. 2-154 is actually three different beam splitters mounted on a vertical translation stage. These splitters have different transmissions and reflectivities so that, for low-signal alignment tasks, all the light can be transmitted for CCD viewing or reflected for streak-camera alignment. At shot time the signal is split. A few of the motor-driven adjustments are used for changing the field of view and for making focus adjustments, as described earlier. The rest, like B2, are required to meet the dynamic range requirements placed on the sensor by the 10-μW signal level of the cw alignment beams and the 700 J that might be transmitted to the sensor at shot time.

Authors: E. S. Bliss, R. G. Ozarski, and D. W. Myers

Major Contributors: R. D. Boyd, R. E. Hugenberger, J. Parker, and L. G. Seppala

Controls

Nova Control-System Development. During 1980 we focused attention on major hardware and software products previously identified as being common throughout the Nova control system, as shown in Fig. 2-156

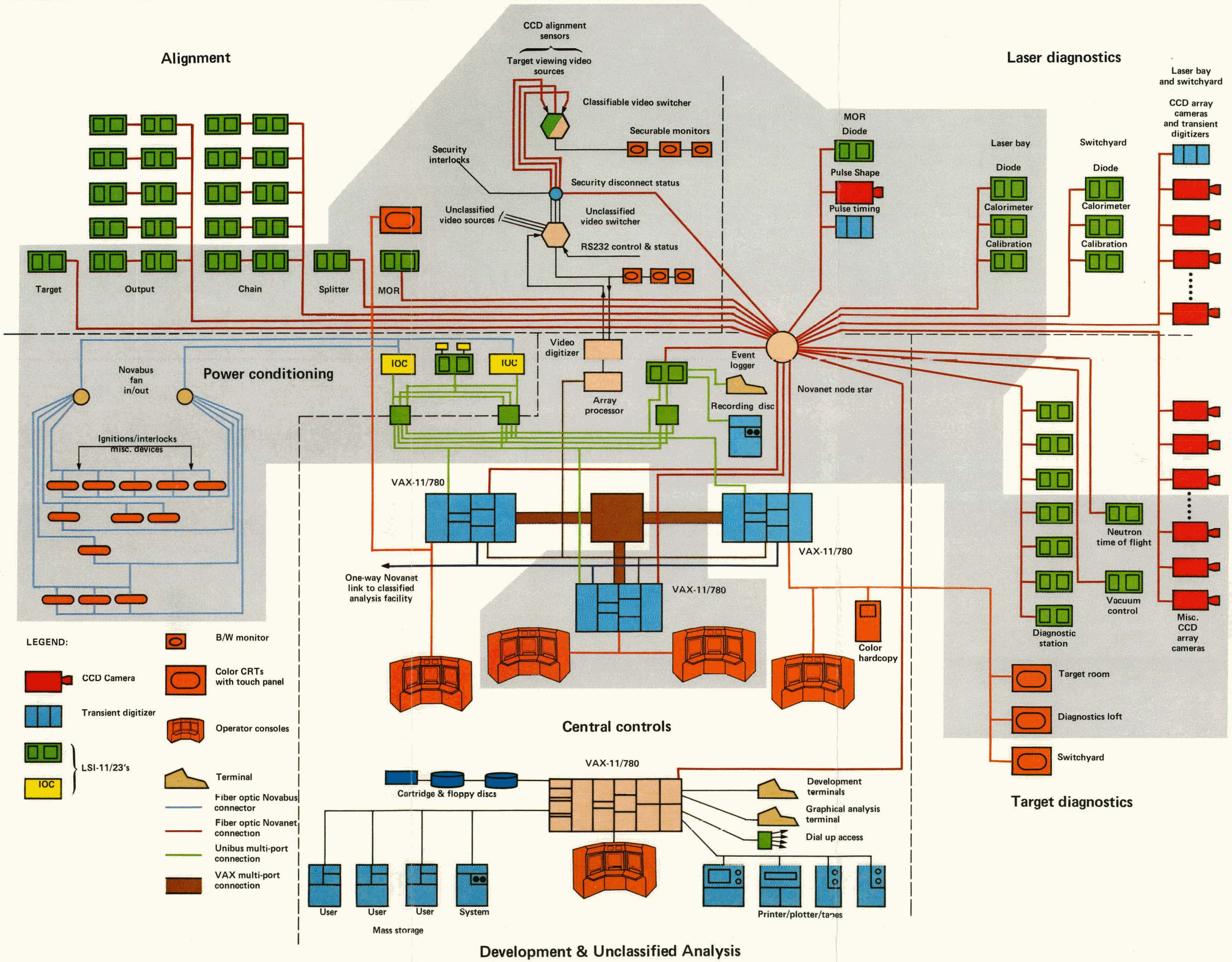

Fig. 2-156. Nova control-system architecture, showing portion to be duplicated for Novette (blue).

and discussed in the 1979 Laser Program Annual Report.[69] Each of these prototypes will require further effort during the coming year.

Our development of the Nova control system is by an evolutionary process.[69] Beginning with a strong base in the proven features of the Shiva control system, we have made constant progress toward higher levels of performance and lower overall cost. From our Shiva experience we have applied

- Computer controls for flexibility.
- Distributed controls performing localized functions.
- Organization in four major subsystems: alignment, power conditioning, laser diagnostics, and target diagnostics.
- Operational control from a central location.

Increasingly more powerful technology has become available for our use, particularly in computers, fiber optics, and interfacing hardware. This technology has had a strong influence on the evolution of the control system.

The need for less overall manpower has led us to eliminate (within technical and organizational constraints) the multiple development of similar hardware and software products by various groups. Instead, we have joined forces to develop these products during the year before they are needed for the major subsystems. To the extent that this goal is accomplished, we can transfer the developmental staff, allowing them to follow through on subsystem applications.

Other factors have encouraged us to follow a controls-development strategy that yields substantial capability on an early schedule. For example, a strong operational need exists for early use of a centralized control system to support the high-level diagnostic and reporting activities that will be necessary and useful during laser installation and checkout.

We have developed prototype equipment for new control-system requirements, notably in image analysis (for alignment and diagnostics) and higher-speed communications. To reduce ongoing maintenance and development efforts on Nova to levels below those experienced in our Shiva operations, we have planned a strongly integrated system that allows us, from the earliest phases of operation, to tightly coordinate the four major subsystems.

The section delineated in light gray in Fig. 2-156 indicates the subset of Nova control-system hardware architecture we plan to use to provide control capability for the Novette laser system.[70] The flexibility of the architecture is confirmed by our ability to easily adapt it to this new application without modifying the basic subsystem hardware and software "building blocks."

The 16 products identified as common requirements for Nova controls are listed, under four major categories, in Fig. 2-157:

- High-performance communications.
- Uniform data management.
- Special products.
- Operator interface.

Six of the 16 common hardware and software products were designed and prototyped during 1980: Novalink, configuration management, raw data base,

Fig. 2-157. Product-development areas for Nova control system.

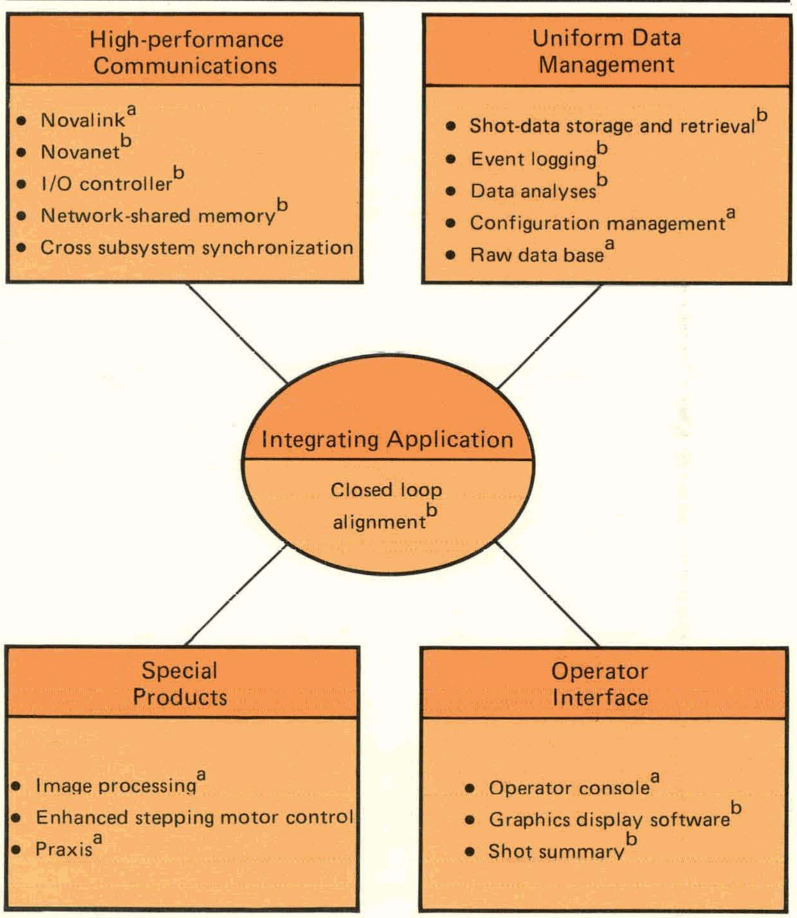

[a]Prototyped during 1980

[b]Feasibility demonstrated in 1980

image processing, Praxis, and operator console. Eight others were developed enough to prove their feasibility (e.g., Novanet, I/O controller, network-shared memory, etc.).

Each prototyped product represents a major advance in approach and implementation in a particular problem area of control-system technology. In such cases, where many individual high-technology products are being developed in parallel, the feasibility of each design, as well as its compatibility with other designs, must be constantly tested and proven. Accordingly, we decided to develop an integrated application that would include all the prototype designs. The closed-loop alignment of a spatial-filter pinhole on a small test laser system was chosen, as shown in Fig. 2-158. From a controls perspective, this system simulates one beam of the larger Nova system.

The system was successfully demonstrated November 29, 1980. The demonstration included hardware and software products ranging from the programmable operator console to the final alignment of a spatial-filter pinhole.

Authors: F. W. Holloway, G. J. Suski, and J. M. Duffy

Novanet. Novanet, the high-speed fiber-optic serial communications system that will interconnect the various distributed computers and devices in the Nova laser control system, was developed and successfully prototyped during 1980. No other communications network available today even approaches Novanet's computer-to-computer and computer-to-device communication capabilities and speed.

Our experience from implementing the Shiva laser control system has shown us that interprocessor communication is a critical constraining factor with respect to system

Fig. 2-158. Functional block diagram for Nova central-controls demonstration.

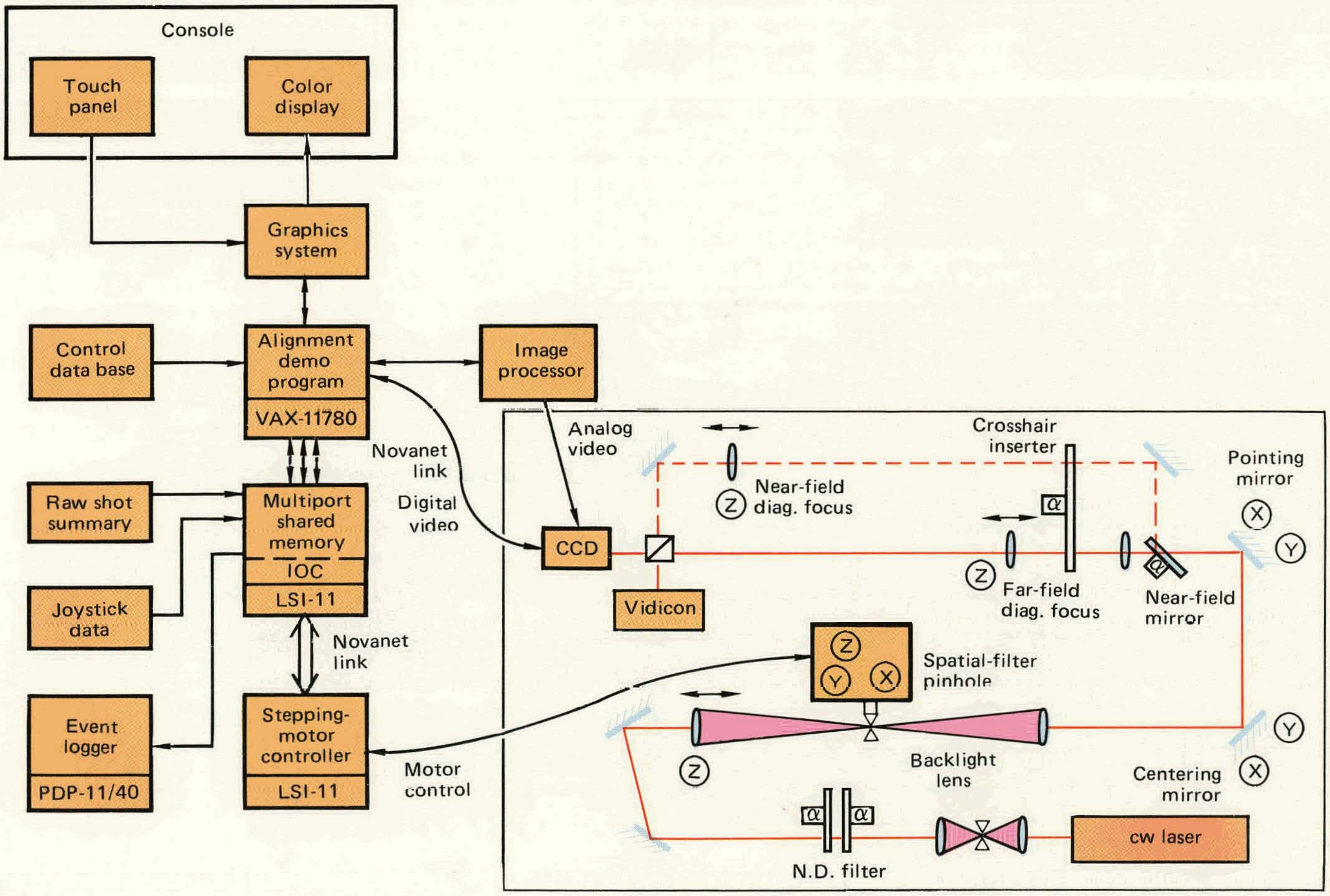

integration, operating speed, and computer-system overhead. In addition, Nova control-system communications must handle the large amount of data that will be transferred on Nova because of heavy reliance on charge-coupled-device (CCD) array cameras for alignment, beam characterization, and target diagnostic functions.

Novalink, the hardware portion of Novanet, provides 10^7 bits/s of asynchronous transfers between multiple nodes on a common fiber-optic bus.[71] We have minimized computer system overhead by using direct-memory-access (DMA) data transfers, combined with hardware error detection and acknowledgment, in each 50-bit packet. We have kept the minimum length of the message small to allow efficient transfer to non-DMA devices, such as the operator switch panels.

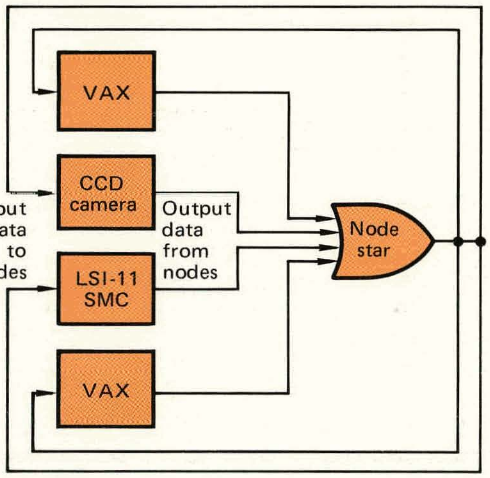

Fig. 2-159. A node star provides the logical equivalent of a bus structure by sending messages from each node in the system to every other node; all connection paths are through fiber optics.

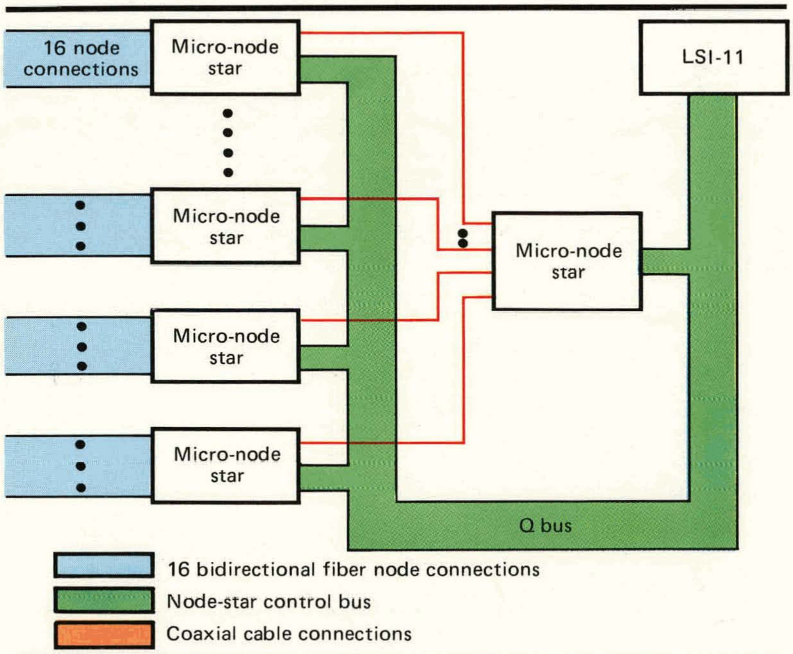

Fig. 2-160. A node star of any required size can be implemented by using several identical micro-node stars, each controlled through an interface to an LSI-11.▼

Various hardware-packaging schemes provide interfacing to DEC VAX-11/780 and PDP-11 minicomputers and to LSI-11 microcomputer-based control and data-acquisition systems.

The architecture of Novanet employs the logical equivalent of a bus structure by using a physical "star" connection point to which each node in the system is connected, as shown in Fig. 2-159. This "node star" allows any processor to communicate directly with any other device or processor. The effective transfer rate is 25 μs per 16-bit word, which meets our original design specification.[72,73]

We have designed and built a prototype node star and finalized the design and control specifications for the operational version. The node star is comprised of several identical stand-alone modules ("micro-node stars"), each controlled through an interface to an LSI-11. Each micro-node star can handle 16 fiber-optic nodes. Modular packaging will allow us to implement a node star of any required size (Fig. 2-160), thus meeting the requirement for flexibility and expandability in the control system.

Besides its principal function of logically implementing a fiber-optic "bus," the node star has added functions that will ease maintenance and improve its performance in the overall Novanet system. It can isolate defective nodes to prevent interference with the rest of the network. It can also be segmented, as shown in Fig. 2-161, into separate networks, thereby isolating large data-block transfers. This keeps them from interfering with shorter device-control transfers.

We decided to implement the lowest level protocol (the most primitive and most often used) as a part of the communications hardware, thereby taking much of the communications load away from the microcomputers and placing it in the communications interfaces. Giving the communications primitives burden to the Novalink hardware allows the microcomputer to be used more efficiently for its original task.

Therefore, we implemented the protocol in microprogrammed state machines at every node connection to the network. A state machine is a device that steps through multiple conditions, based on input stimuli. Each condition, or state, produces a unique set of output signals based on the input. Microprogramming the state machine means putting the instructions that control the state machine into a memory. Then, to modify the function of a network node, we merely reprogram the memory of the state machine, without having to redesign the circuit.

We used Advanced Micro Devices (AMD) microprogrammed controllers (AMD 2910) and bipolar fusible-link PROMs in the state machines. Two of these state machines are on each node interface. Their high-speed operation (100- and 200-ns cycle times) allows them to handle the incoming and outgoing data stream at 10^7 bits/s.

System requirements include the ability to address remote devices (nonprocessors) on the network—a very unusual feature in communications networks. Most devices we plan to use are interfaced with asynchronous buses (Q-bus, UNIBUS, or Shiva TTL bus). Therefore, to implement the normal asynchronous handshake signals, a serial handshake is required for each 16-bit word. That is, for every action signal received, an acknowledgment (a handshake) is sent back to the original sending device. This handshake reply (R), along with seven other message types, is contained within the packet preamble, as illustrated in Fig. 2-162. The necessity of the handshake reduces the effective data rate by a factor of 2; it also requires that message packets be checked for errors, adding further overhead to the single-word transfer. Nevertheless, when the communications network operates in a closed-loop control system, the advantages of using a handshake to support standard buses outweigh the disadvantages of the added overhead.

In Novanet, one node, called the "master," performs the function of keeping the network bus active. At any instant, only one node is the network "master" and all other nodes are "slaves." The bus master has three ways of maintaining bus activity:

- Actual data transfers to or from nodes.
- Master-only polls (MOP).
- Master-slave interrupt polls (MSIP).

The microprogrammed controller on the master device automatically performs either master-only polls or master–slave interrupt polls on completion of a DMA data transfer. This polling allows other nodes to either gain mastership of the communications bus or to service interrupts. The normal slave response is a simple REPLY (Fig. 2-162) if an interrupt or a service of mastership is not required. Since a typical installation will have only a fraction of the 256 possible nodes implemented, microprogrammed timeouts are performed on nodes that are not responding.

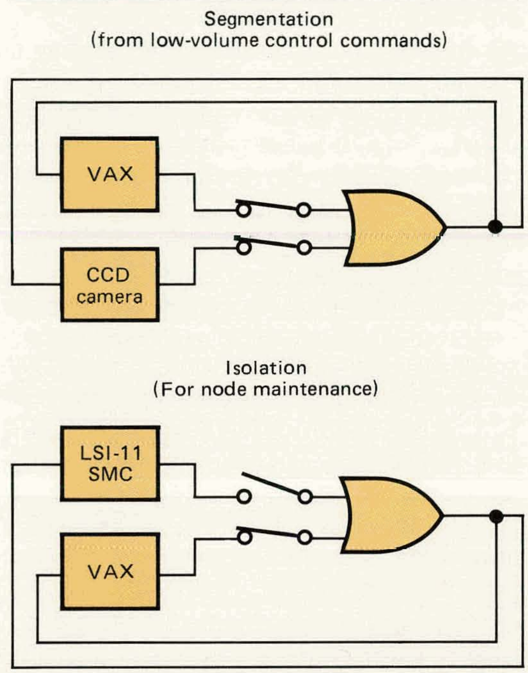

Fig. 2-161. Each micro node star can be segmented into separate networks and can disconnect improperly performing nodes.

Fig. 2-162. Details of Novalink serial "packet."▼

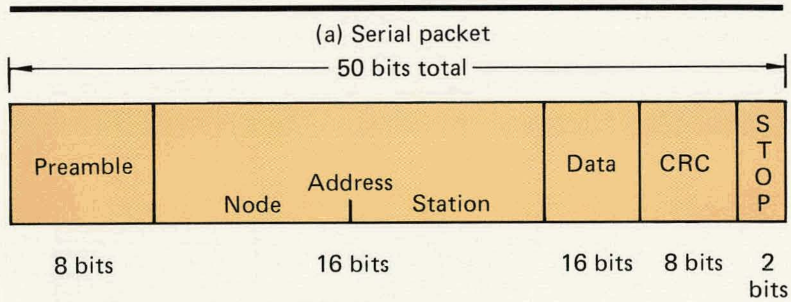

(b) Preamble message types

Request		
	Read request	RRQ
	Write request	WRQ
Replies		
	Reply	R
	Slave-interrupt reply	SIR
	I'm master reply	IMR
	Error reply	ER
Bus control		
	Master-slave interrupt poll	MSIP
	Master-only poll	MOP

The user need not be concerned with this level of protocol. The driver software in the host machine merely sets up a DMA transfer, and the link hardware interrupts on a completed block transfer to the addressed slave. The hardware implements the lowest level protocol requirements with micro-programmed state machines, relieving the host processor of these duties. In fact, in the short time between two sequential block transfers, a node might possibly lose its master status. For example, the node processor might take several milliseconds to set up the second transfer. In the interim, a second node could request and be granted bus mastership, initiate and complete a data transfer, and then begin its own master polling sequence. The original node would then regain its master status, and initiate and complete its second transfer.

This entire sequence is transparent to the user program, with the possible exception of several milliseconds of delay, which is the maximum polling latency time.

We also implemented interrupts on Novanet. (An interrupt is the temporary stop of a logical sequence of events to do something else, followed by a return to the mainstream of events.) However, because of network overhead, the interrupt service time can be quite long compared to an interrupt of hardware that is connected directly to a processor. The slave-interrupt reply (SIR) is sent to the current communications bus master, which can choose to service or ignore the interrupting node, depending on predefined switch settings on the line-controller board.

This allows the interrupts to be partitioned into eight separate or overlapping "service areas." A master can respond to all eight service areas if desired. If the current master is set to ignore a particular interrupt, the interrupt is not cleared; instead it is sent to the next master when that master polls the interrupting slave node. Consequently, once a master node enables a slave-node interrupt, it must occasionally request mastership of the communications bus in order to service the interrupt.

The hardware for Novalink consists of three types of node interfaces and a device that implements the node star. The node star is not a true network node, but may be controlled by one of the node processors to allow automatic fault isolation. The three node interfaces are:

- Master–slave controller (MSC).
- Multiple device interface (MDI).
- Q-bus device interface (QBDI).

The MSC interface consists of two quad-size DEC printed circuit boards interfaced to the Q-bus (the LSI-11 backplane bus), as illustrated by the block diagram in

Fig. 2-163. Master–slave-controller (MSC) interface portion of Novalink.

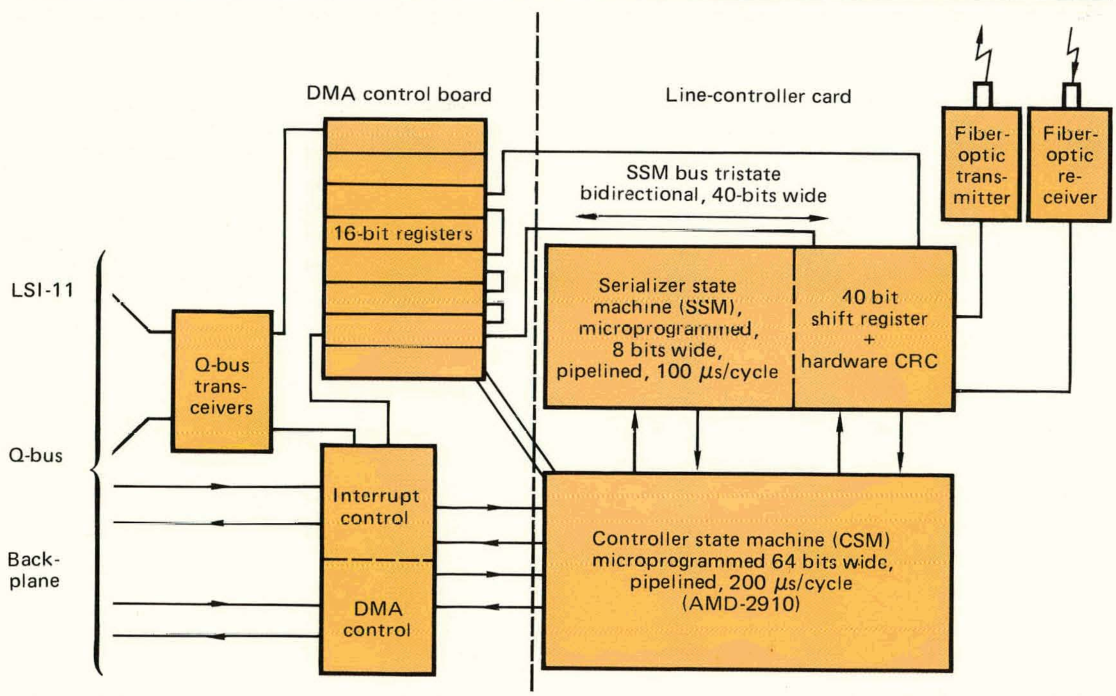

Fig. 2-163. The circuit boards are connected by ribbon cable that runs between two 50-pin edge-connectors on the boards.

The DMA control board provides the Q-bus interface with seven 16-bit registers, bus DMA and interrupt control logic, and the node address-recognition logic. The design includes an 18-bit Q-bus address register (BAR) for compatibility with the LSI-11/23. It also allows a DMA buffer to cross the 32k-word memory-range boundary imposed by the instruction-set architecture of an LSI-11. The card is also compatible with the multilevel interrupt structure of the LSI-11/23. To allow Novanet connections for UNIBUS machines (such as the PDP-11 and VAX), we are using a commercial UNIBUS-to-Q-bus converter.

The line-controller board implements the fiber-optic serial interface to the Novanet. On the board are two microprogrammed state machines, one controlling the serial line at 10 Mbits/s (100 ns/bit) and the other handling the protocol and operating at a 200-ns rate. The first state machine—the serializer state machine (SSM)—and a 40-bit shift register comprise the universal asynchronous receiver transmitter (UART), as shown by Fig. 2-163. (We readily admit that our UART is not "universal." We use the term only because most communications engineers will identify the correct functional use from the acronym.)

The SSM consists of an address counter, a PROM, and a pipeline register to pre-fetch the next instruction while the present one is being executed. Its byte-wide output is sufficient to control all the functions of the 40-bit-long shift register and the cyclic-redundancy-check (CRC) circuitry. The SSM executes two linear programs—one each for the receive and transmit cycles. Since a full-duplex device is not required, the UART is a half-duplex device. The UART includes hardware CRC circuitry and appends eight check bits plus two stop bits onto the shift-register output. When in the receive mode, the UART computes an independent check sum and compares it to the appended check sum to detect transmission errors.

The controller state machine (CSM) is 64 bits wide and uses the Advanced Micro Devices AMD 2910 microprogrammed controller. The AMD 2910 executes a set of 16 instructions that include a variety of conditional branches, as well as a five-deep microprogram stack for subroutine nesting. It also includes an internal loop counter for programmed timer functions. The 64-bit by 512-deep PROM set contains the code for controlling both the UART and the DMA and interrupt control functions on the adjacent board. Also included are several microdiagnostic programs that aid in board fault location. These diagnostic programs are accessible by attaching wire-wrap jumpers to the board.

The line-controller card also includes a general-purpose 16-bit input/output port that remains operational even if the LSI-11 is halted. This port will typically be used to initiate a bootstrap sequence to load the LSI-11 from another network-connected computer. The bootstrap program sets up an initial DMA "read" from the optical line. If a certain sequence is followed, the LSI-11 accepts the next data stream and deposits it in memory. Once in memory, this data stream is executed as if it were a program.

Multiple-device-interface (MDI) logic provides us with the ability to interface to a number of different devices and buses, as shown in Fig. 2-164. MDI is our primary node interface for the CCD TV cameras that will be used extensively in the Nova alignment and diagnostics systems. In addition to the CCD camera interface, MDI provides a 16-bit parallel input/output port with the same functions and pin connections as the DEC 16-bit I/O card, the DRV-11. The MDI includes full interrupt support for both the CCD camera and the 16-bit I/O port.

The MDI consists of a three-card set based on the 122-pin Augat-size cards (7 by 7-1/4 in.). The microprogrammed UART used by the MDI is identical in design to those used in the MSC cards. The MDI also uses a microprogrammed controller (AMD 2910) to implement the network protocol and to control its Q-bus, as shown in Fig. 2-164. The MDI Q-bus is electrically equivalent to, but mechanically different from, the DEC Q-bus. However, the MDI Q-bus is directly compatible with the CCD camera. Therefore, it can be installed directly in the CCD camera memory box, effectively making the camera a fully functional network node.

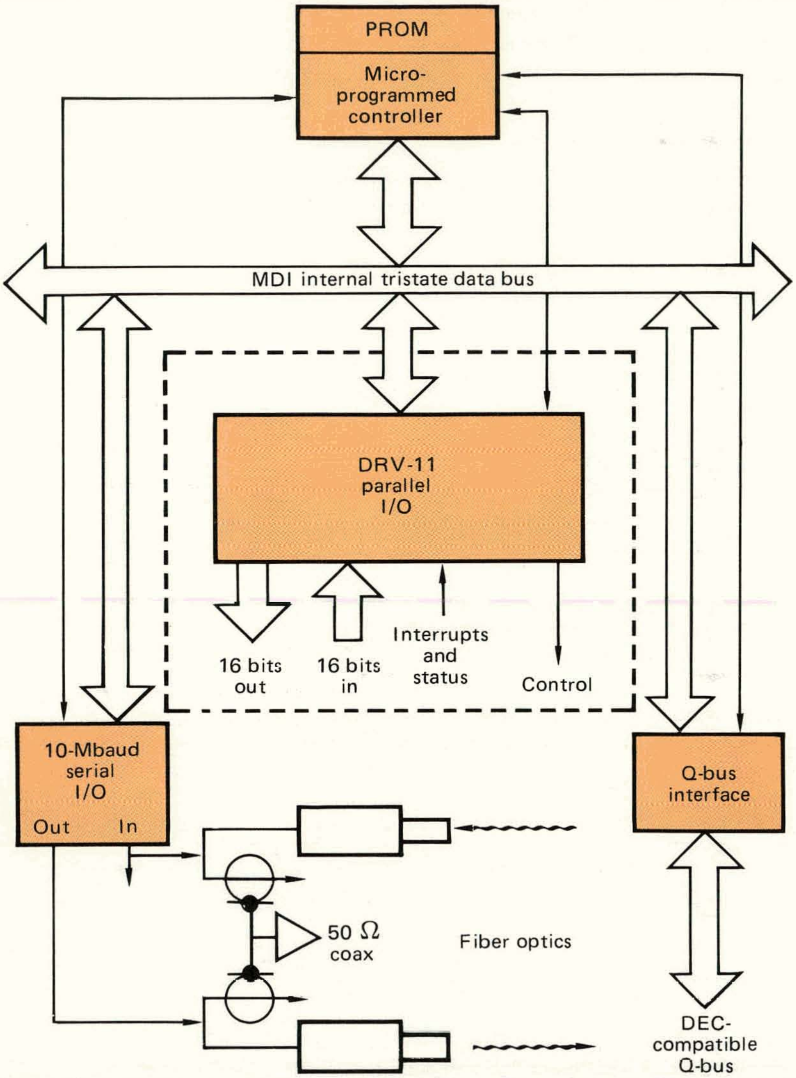

Fig. 2-164. Multidevice ▲ interface (MDI) logic provides the ability to interface with a number of different devices and buses.

The Q-bus device interface is a DEC quad-size (11-1/2 by 8-1/2 in.) card that is functionally identical to the MDI, without the 16-bit I/O port. It generates a mechanically and electrically compatible DEC Q-bus, allowing the user to connect any Q-bus-compatible device to Novalink. This card takes the place of the LSI-11 microcomputer in a quad-size backplane and generates Q-bus signals based on the network commands. It includes a fiber-optic transmitter and receiver and wire coaxial-cable network connectors, as do all Novalink node interfaces.

A network analyzer has been designed and built to aid in debugging the network hardware and software. This device displays the network activity on a CRT, as illustrated in Fig. 2-165. It has display qualifiers (trigger control) to allow presentation of selected events out of the 10-megabit/s data stream. A commercial digital logic analyzer (Biomation 1650 D) and a Tektronix 604 display allow an operator to analyze a snapshot of 16 bits by 500 words of real-time network activity.

Authors: J. Severyn, P. VanArsdall, S. Ruddock, and W. Schaefer

Major Contributor: R. Demaret

Novanet Software. Novanet is the data-communications network that forms the backbone of the central control system for the Nova laser fusion project. Virtually all modern data-communications systems are implemented as hardware/software hybrids

Fig. 2-165. Block diagram of network-analyzer functions. ▼

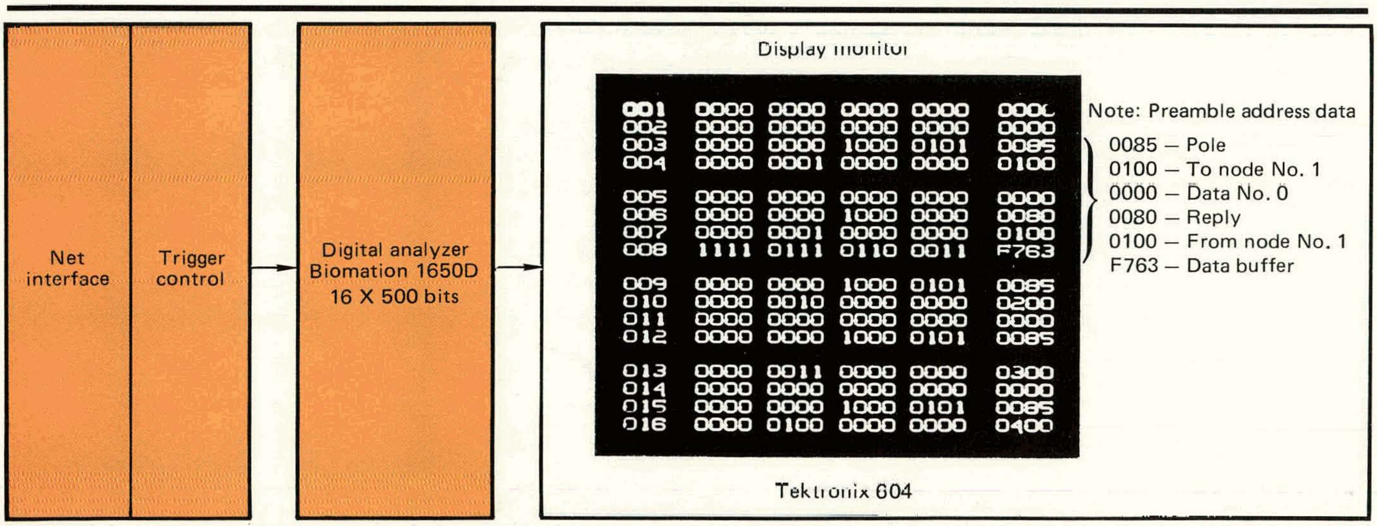

to maximize their performance and flexibility. To see how this may be done, let us first examine the software for Novanet to understand its function and how the hardware/software dividing line was chosen for this network.

While the hardware of a communications system is sending electrical or light pulses between circuit boards, the details of the system should be transparent to its users, who should think of network activity in terms of the transfer of files and other structures between processes. The function of the software in any communications system is to use the hardware's pulses to transmit the user's structures in a rapid and reliable manner. To accomplish this task in a manageable and maintainable way, we have separated the software into functional layers. Each node in the system has identical layers, and we think of each layer as communicating with its equivalent layer via a protocol, as shown in Fig. 2-166. Of course, what actually happens is that each layer in a node communicates through its interface to the layer below it until the hardware layer is reached. At this point, the message has been converted to a string of pulses that the hardware sends. In the remote node, the pulse string is received and the message is passed up through the layers until it reaches its destination.

Each software layer effects its own protocol; hence, the software layers impose an analogous layering of protocols. Each protocol layer typically encapsulates the data in its own header and trailer, which is additional information added to the data, as shown in Fig. 2-167. Thus, at a given layer, whatever is handed to it from above is treated like data, encapsulated in a header and trailer that are meaningful to the equivalent layer in the remote node, and the whole package becomes data for the next lower layer.

With this explanation in mind, let's look at the layers of protocol and the message encapsulation developed and prototyped for the Novanet system during 1980. Figure 2-168 is a block diagram of the protocol layers in a processor node in this network.

Now let's examine each protocol layer in some detail. Until now, we have described the layers as though all of them were implemented in software. However, this is not necessarily the case. Often, in the interest of performance, the lower level(s) of protocol will be implemented by hardware. In Novanet, the hardware implements the lowest level of the protocol, including direct-to-memory transfers to and from the processors' memory. The choice of which

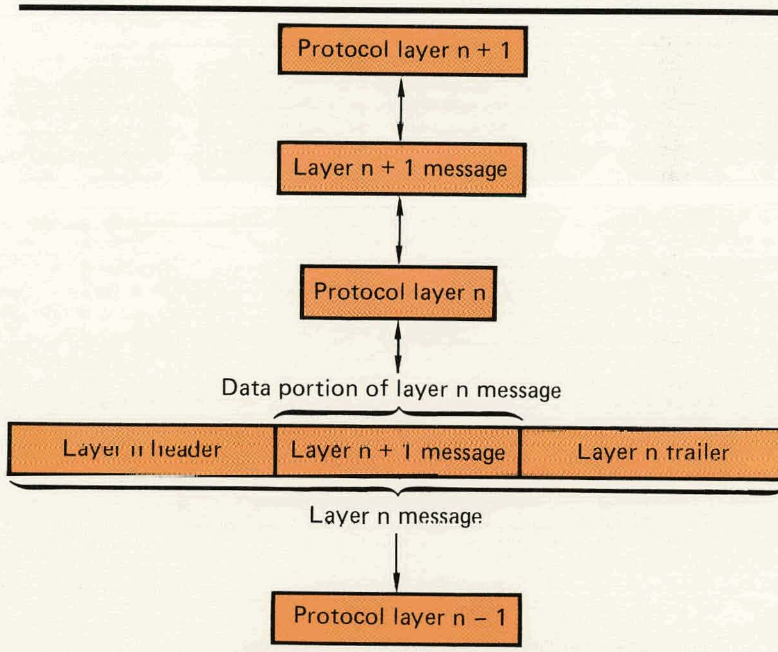

Fig. 2-167. Each layer of network protocol encapsulates the data needed for its functions onto the header and trailer of the message it receives.

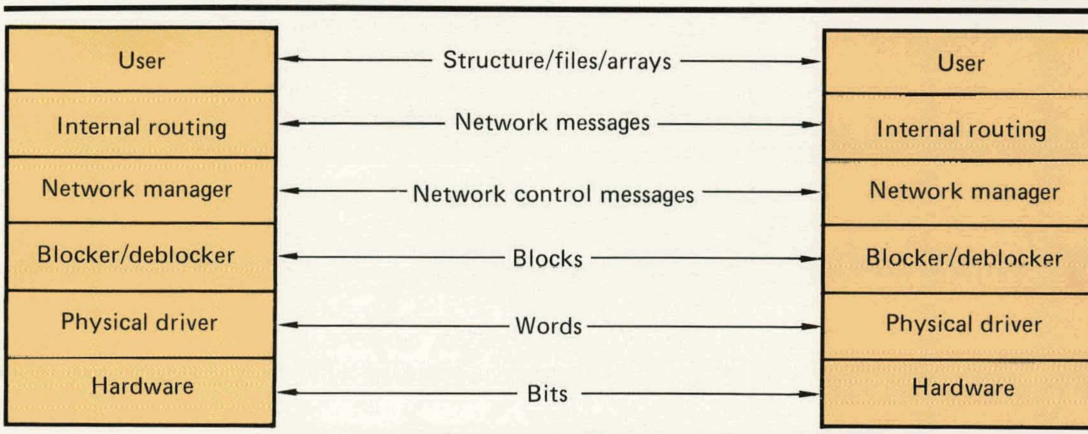

Fig. 2-166. A protocol layer facilitates communication between two control-system users in terms of structures, files, or arrays, by communicating to the layer below it, until the hardware layer transmits "bits" of information.

protocols should be implemented in hardware and which should be relegated to the software is affected mostly by performance, flexibility, and cost constraints.

The hardware layer (described in detail elsewhere in this section) consists of the fiber-optic transmitters and receivers, the associated control hardware, and a state machine that implements the lowest level of the protocol. The hardware's interface to the physical driver is through its control registers and the direct-memory-access (DMA) hardware.

The physical-driver layer is the lowest of the software layers and is part of the operating system of the node in which it resides. The physical driver is responsible for synchronizing software requests for hardware action with the state of the hardware. At appropriate times, the hardware registers are accessed to start a new transfer or to obtain the status of the hardware. The hardware layer can also detect some errors. When an error is detected, the physical driver communicates this to the error-handling layer(s) of software.

Fig. 2-168. Novanet protocol layers and typical uses.

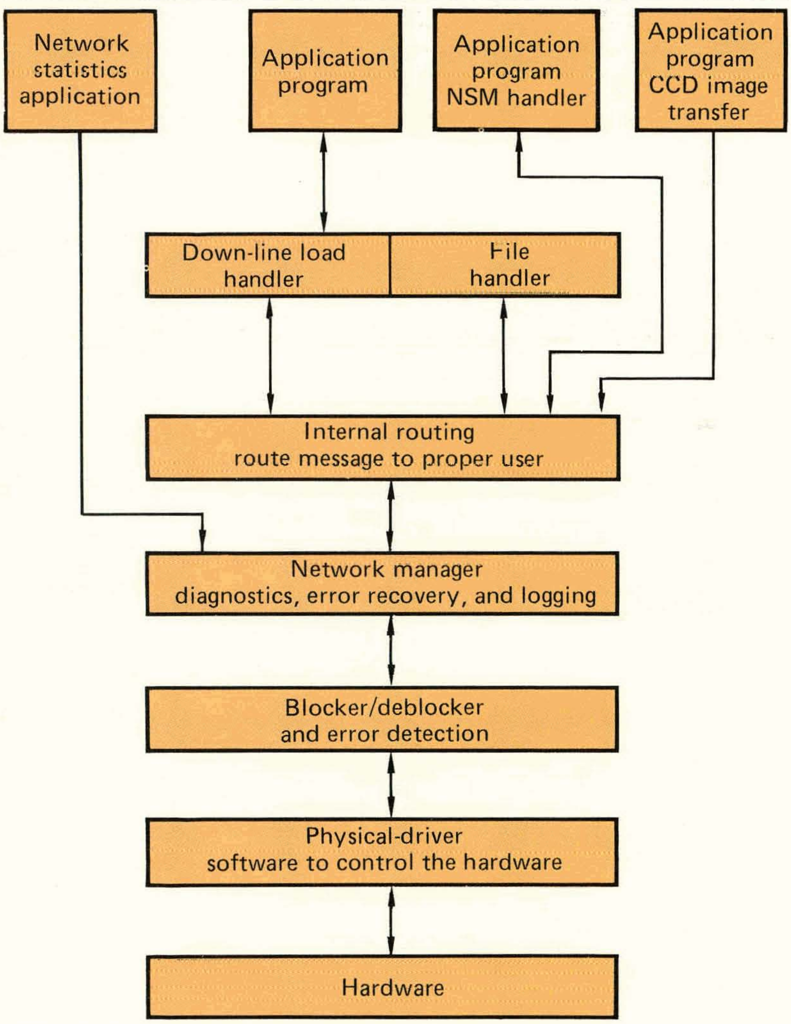

The blocker/deblocker layer is the next higher software layer. It is convenient to have a maximum-size block that the network will send as a single DMA transfer. This ensures that the nodes will always be able to receive messages in pieces without having to allocate very large buffers for the task. During transmission, a long message is broken down into blocks that the physical driver can send. When the blocks are received, they are reassembled (deblocked) into the message. In addition to blocking and deblocking messages, this layer performs error recovery at the block level. If the hardware detects an error during block transmission or reception, the physical driver passes this fact to the blocker/deblocker layer, which will either retransmit or ask for a retransmission of the block. If the error cannot be corrected by retransmission, it is reported to the network-management layer. When a node is not actively transmitting, the blocker/deblocker ensures that it is in a state to receive messages from other nodes.

The network-management layer is above the blocker/deblocker and manages the network from the node's point of view. Its tasks include keeping track of nodes on this particular node's segment, sending segment-change requests to the node-star manager, running diagnostics on other nodes on the segment, logging network errors and other network-significant events, and sending the local error log to the network controller when it is requested. The network-management layer also decides what to do about errors that the lower layers pass to it. In general, if the blocker/deblocker is unable to transmit a message correctly, the network-management layer logs this fact, together with all known information about the type of error, and requests that the router inform the user that the message could not be transferred. This is the only sensible course of action because only the user knows the importance of the lost message relative to the current operating environment.

The highest layer in what is usually considered network software is the internal routing layer, which routes messages to their destination process in the node. This layer is trivial if only one process is running in the node. If two or more processes in the same node wish to communicate, however, this layer handles the complete transaction.

This completes the network software layers as they are usually envisioned. However, some special services are provided for the Nova controls system that to the users' programs look like network software and to the network software appear as users' programs. They include file-transfer routines, routines to allow one node to down-line-load another node, and network-shared-memory (NSM) services. The file-transfer routines allow data and program files to be moved from one node to another, as from a development system to the nodes in which they will be used. The down-line-load capability allows a remote processor, such as an LSI-11 stepper-motor controller (SMC), to be loaded with its control software and to have the execution started from another node. This capability can also be used to automatically reload and restart a node that has failed.

The Novalink hardware takes care of normal DMA transfer operations. If an error or other exception is detected in the transfer, however, the hardware interrupts the processor and lets the software determine how the exception should be handled. Thus, for performance reasons, the software determines and sets the transfer parameters in the hardware, but the hardware does the transfer without software intervention unless an exception is found. This allows the transfer rate to be maximized without increasing the loading on the CPU. The errors and exceptions are handled more easily in the software and, since our fiber-optics data links are inherently low noise, the added work has a minimal effect on the processor's load.

The prototype Novanet hardware and software, with its capability for high-speed fiber-optic communications between all computers and devices on a network, was shown to be appropriate for general Nova application by its successful performance in recent demonstrations.

Author: J. Hill

Network-Shared Memory: the Control-System Programmer's View of Novanet. As a communications-network service utility, we have developed a common software package for program-to-program communications. This package, called network-shared memory (NSM), is a method by which programs in the same computer (or in different computers) can share tables of control and status information.

In designing the NSM package, we wanted to provide a uniform interface for each program that would be independent of the computer system in which it resides. To efficiently generate control-system programs, we had to minimize the effort required to use the communications network and ensure that we could easily add new tables, users, and computers. We also had to make sure that the execution time and programming-space overhead of the package were minimized so as not to exclude it from use in critical applications.

Our experience with network applications on Shiva provided goals and suggestions to add to the above criteria. First, the user interface to the Shivanet package required that the user know a great deal about network hierachy and operation in order to write control-system programs. Therefore, the programs on Shiva more often reflected communications strategy rather than the laser control functions to be performed. Second, we found that systems that used shared memory between programs and computers were conceptually easier for control-system engineers to program and maintain. However, there was one disadvantage to using shared memory: it was often difficult to prevent one program from inadvertently modifying the data while another program was using it. Therefore, with all the above criteria in mind, we designed the NSM system and implemented a prototype package.

The NSM system treats the network as a large collection of data tables that can be accessed by any program on any computer in the control system. Called "regions," these named tables are the basic addressable elements of shared data. In general, a region is implemented as a Praxis data structure that contains the control or status information for a single control-system entity or for a simple collection of like entities. Regions have been used in our prototype demonstration system to reflect the current position of spatial-filter pinholes, as well as to communicate the name of an image for display on the graphics system.

An example of the region concept, as used in the central-controls demonstration, is given in Fig. 2-169. Operator commands are placed in one region of the graphics system. When this region is updated, the automatic pinhole-alignment program wakes from its hibernated state to process these commands. Should control of a particular spatial-filter pinhole be required, the alignment program uses the NSM routines to open the region that corresponds to that pinhole, to enter the command, and to close the region. Waiting for that update is a mapping program that, in turn, updates the command region for the appropriate stepping-motor controller, which then moves the motors accordingly. Status information is transferred in the same manner, but in the opposite direction, and is displayed on the color display.

The person who implements each of the above programs need only be concerned with the use and specification of each region, as if it were memory residing in his or her own program. The actual hardware configuration of the system is shown in Fig. 2-169. That the programs reside in different computers or that the data are, in some cases, transferred over the network hardware does not affect the applications program. The actual shared memory (multiport) increases system performance but is not a necessity since the NSM simulates its presence.

The collection of regions relating to a particular application is called an "environment" and contains shared or local copies of the region data, as well as those tables required by the NSM to manage region activity. Regions are defined by the control system engineer during an interactive session with the configuration control-data-base "Librarian" utility. Then another utility generates the Praxis data structures required by the environment.

After the user calls in the NSM package to manipulate the environment-management tables, the programmers can map necessary regions into their data space, gain exclusive

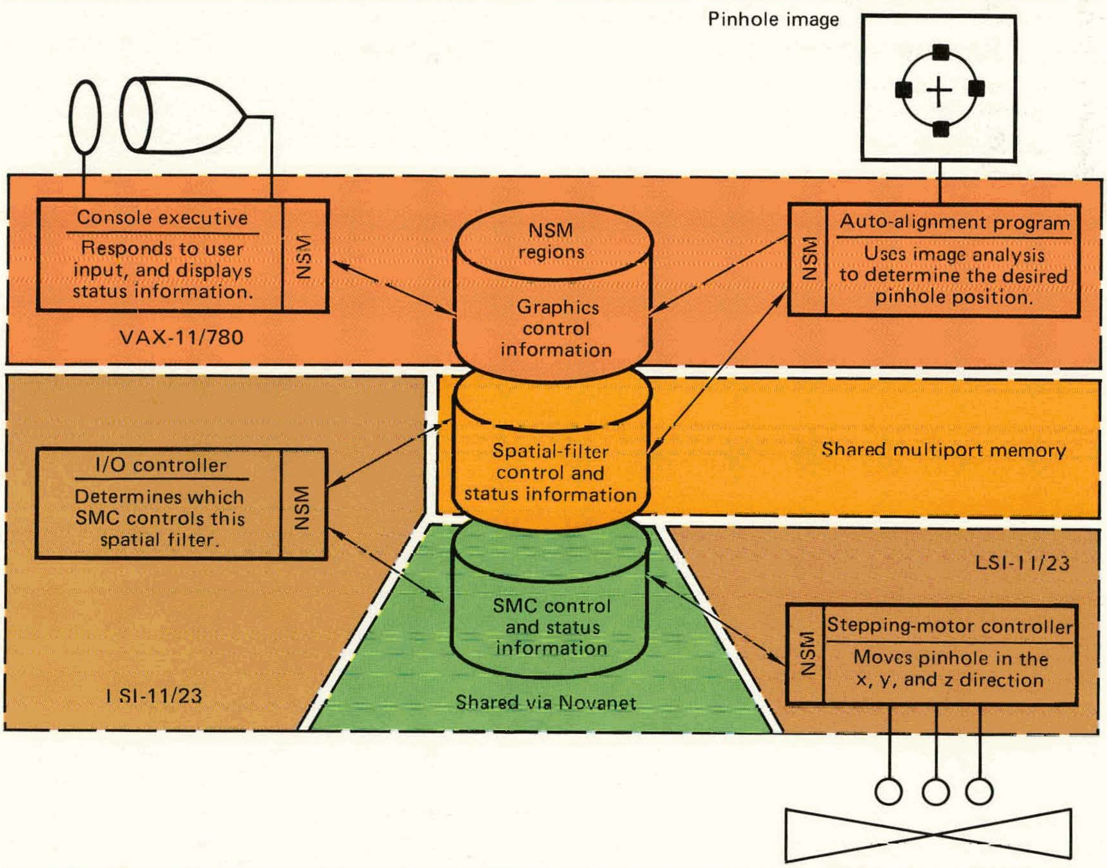

Fig. 2-169. The network-shared memory system (NSM) shares tables of control and status information (regions) between programs resident on several computers.

access to a given region, and then manipulate the data within the region.

On each computer is a system-level program, called the "server," that manages system environments. The server is responsible for transferring region updates to other nodes and for activating programs in hibernation. (The interaction of regions, environments, user calls, and the server is shown in Fig. 2-170.)

Our project plan calls for the NSM to support regions shared between programs that will be residing in the following processors:

- Digital Equipment VAX-11/780.
- Digital Equipment LSI-11/23.

They will be connected via any of the following peripherals:

- Novalink high-speed, fiber-optic DMA serial link.
- MA-780 VAX to VAX multiported memory.
- MPM-11 UNIBUS multiported memory.

The current implementation status for the total package is shown in Table 2-31.

Since the system will be implemented on at least two computers, the NSM was designed to use the same source code for all but the lowest level machine-dependent routines, thereby saving much implementation effort and ensuring that changes to one package will be immediately carried over to the other. The Praxis programming language, described in "Praxis," was instrumental in that effort. These savings would not have been possible with any other available programming language. The ability to produce transportable code was one of the main goals of the language project.

Author: J. Duffy

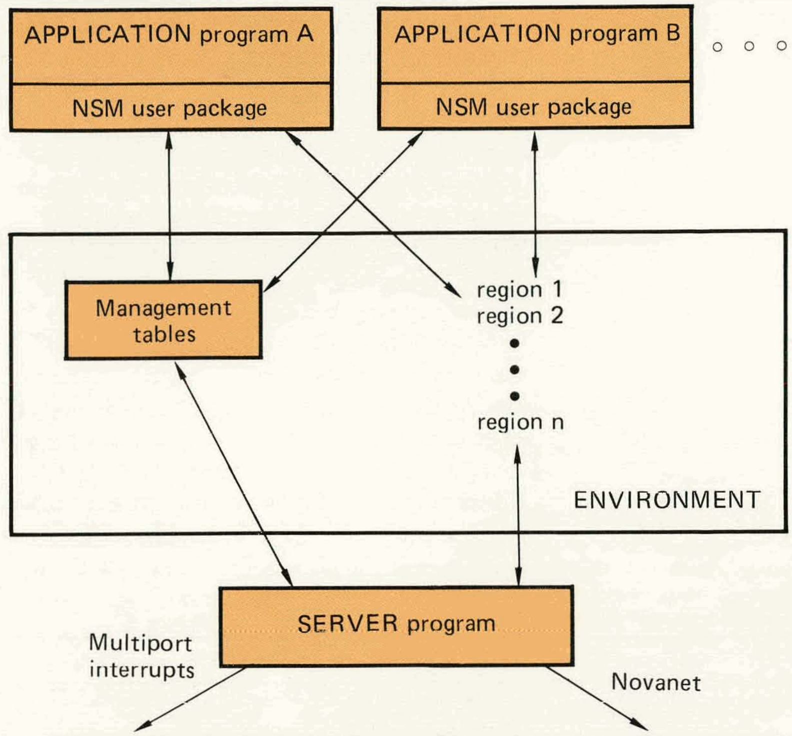

▲ **Fig. 2-170. The NSM user package provides a clean interface between the application programs and region data.**

NSM system component	VAX-11/780	LSI-11/23
User package	Yes	Yes
Server-system program	Yes	Yes
Region-generation utilities	Yes	Yes
Regions in local memory	Yes	Yes
Regions in UNIBUS-shared memory	Yes	Yes
Regions in VAX-shared memory	No	No
Regions shared over Novanet	No	Yes

Table 2-31. Implementation status of NSM packages.

Central Operator's Consoles. Four identical computer-driven operator consoles, each containing three high-resolution color-graphic displays, will be located in the Nova central control room to provide efficient user/machine interaction with the entire Nova facility. We can use these displays to program hundreds of different control panels that, if hardwired, would fill a very large room. The necessity for any hardwired control panels, which are labor-intensive and quickly outdated, has been minimized.

Improved user/machine interaction was a key influence on the design of the custom-manufactured console. A completed prototype unit is shown in Fig. 2-171.

In designing the desk area, we paid careful attention to leg room and the shape of the console so that operator strain, visual parallax, and glare would be minimized. The cabinet has an overall height of 62 in. at the top front, which permits a standing person to look over the top of the console and view related operations in the control room. The console, itself, is bent around the operator by 30° on each wing to improve viewing for both the operator and observers.

Each console contains three 19-in., high-resolution color monitors, mounted at eye level in each of three adjacent sections. Each of these CRTs (Ramtek model RM 9400) is a raster scan device—640 by 512 pixels—capable of doing vector and text drawing, as well as of performing such coordinate transformations as pan, zoom, translation, and rotation. Figures and text can be drawn with up to 16 colors selected from a total of 256 possibilities. These actions are accomplished, within the Ramtek, with on-board microcomputers. The center color monitor is overlaid by a transparent touch-input device that is configured as an x–y potentiometer. Whenever the screen is touched, this device supplies numeric screen coordinates to the display system, allowing the operator to select items from displayed menus of options. Mounted above the center display are two 9-in. black-and-white TV monitors (Conrac) that can be used to view the output from any TV camera or CCD array sensor in the facility. This allows for visual checks of the automatic alignment system, as well as for information feedback to an operator performing remote manual-control operations. A joystick is available for remote manual operations.

Authors: P. J. VanArsdall and F. W. Holloway

Nova Operator-Interaction Graphics. The Nova operator-interaction graphics system is designed to use color displays and other devices within the central-operator consoles to present the status of the laser system and to accept operator commands. A prototype version of this graphics system has been demonstrated as an operator interface to a simple alignment problem. It provided displays such as those shown in Figs. 2-172 and 2-173.

This system has met several major design objectives, including:

- Removing much of the clutter usually associated with each user maintaining pictorial representations within his or her own application programs.
- Taking much of the overhead of executing graphics instructions from the VAX computers and offloading it on microcomputers specifically designed for the job.
- Enforcing the use of identically structured modular calls for graphics by all the programmers of the Nova control system.

To accomplish these objectives, the operator-interaction graphics software is divided into two major phases, as shown in Fig. 2-174. In phase one, the details of

Fig. 2-171. Control-system engineer testing graphics software on prototype Nova central-operator console.

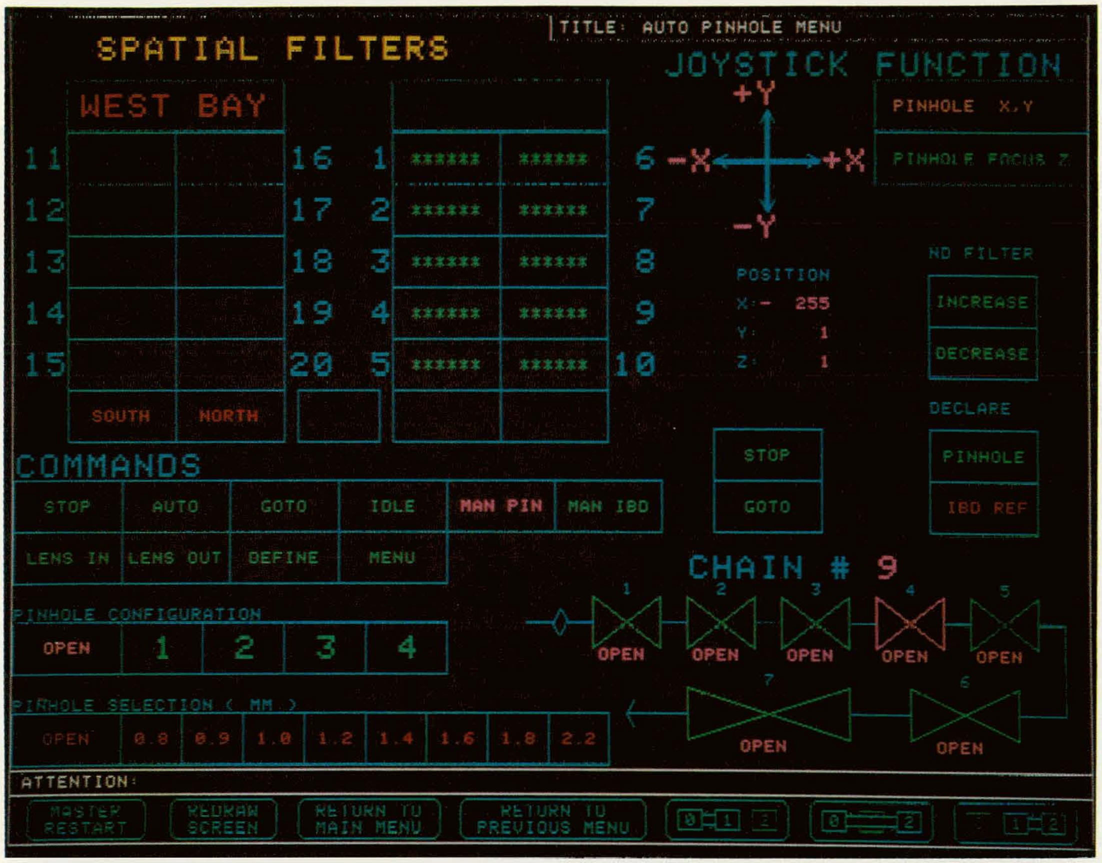

Fig. 2-172. The prototype central-operator console displays the command menu for aligning spatial filters; when touched, selected points will implement control functions.

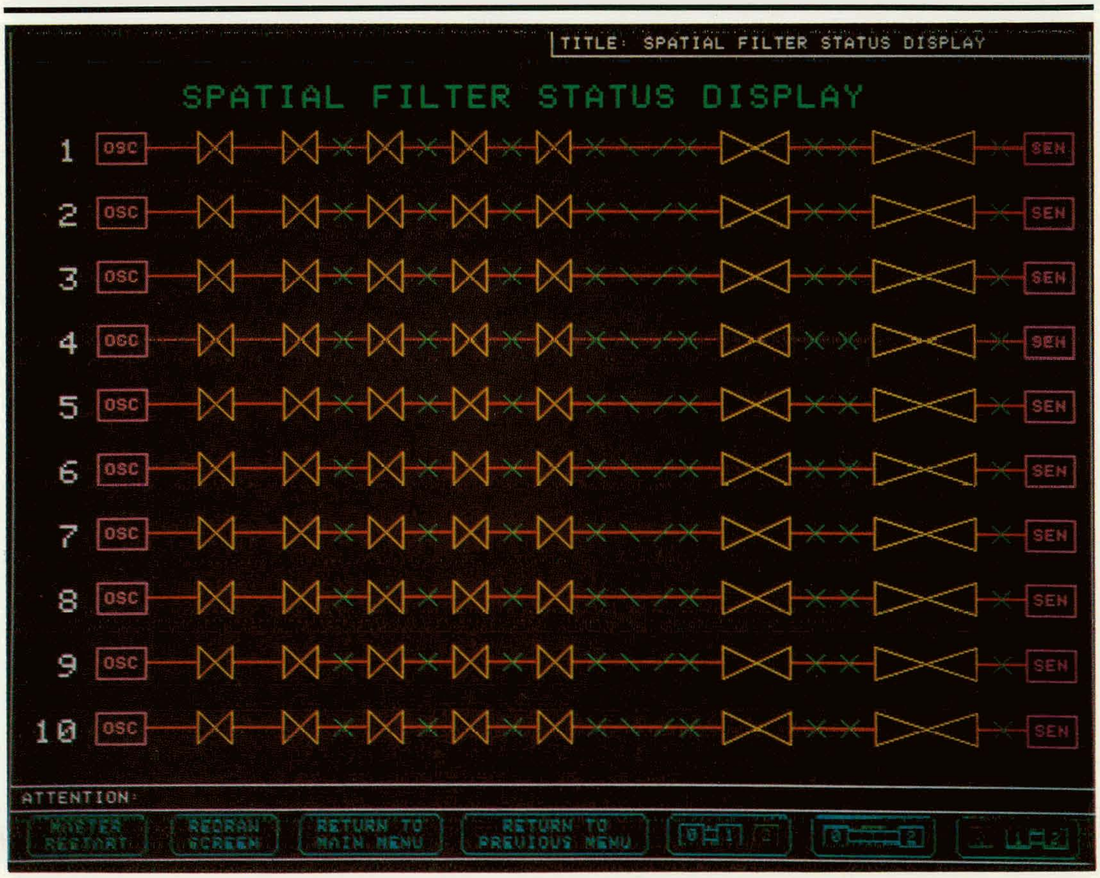

Fig. 2-173. This side display will accompany a set of control menus, similar to that illustrated by Fig. 2-172, to show the operator the complete status of all spatial-filter alignment functions.

picture definitions are entered into picture and subpicture libraries before there is a need to display the pictures on the control system. These pictures are called frames. When display becomes necessary, phase two is entered, and the user's control programs submit graphics commands to a single graphics executive program. This executive program controls each display on an operator console and, to provide feedback to the user's control program, interprets input from the touch panel by matching touch coordinates with subpicture definitions.

To enter picture definitions into the picture and subpicture libraries, a Praxis program is written and executed. This program first accesses a library of predefined routines to make up the user's own lists of picture instructions. Then it inserts these lists into a list called a frame list. The calls to insert subpictures into the frame list contain arguments that allow users to associate certain instances of lines and text with a label and to decide whether these instances will be touch-selectable.

During operations, the graphics executive program accesses these libraries and stores the definitions in VAX virtual memory for rapid access. Then the user's control program can easily request that its frame be displayed and change various labeled instances of lines and text to reflect either a new status from the control system or input from an operator's touch panel.

Touch-panel inputs are received by the graphics executive, which searches its lists of instances of lines and text defined within the frame. When it finds a match, it supplies the user program with the label and index. While searching for a match, the graphics executive marks the place on the screen where the operator has touched it with a blinking cursor, thus providing immediate feedback. The graphics executive reserves areas at the top and bottom of the screen for special use, such as for displaying time-of-day text, control of the side screens, and system messages. Two other features have been implemented in the graphics executive. To reconstruct events, all requests for frames and touch inputs are presently recorded by the Nova event logger, described in "Event Logger." Also, a programmable voice synthesizer attached to each console can be used to issue verbal warnings when significant events take place in the system.

We have gained a substantial advantage by designing the graphics executive so it "knows" all the frame and subpicture representations. In the future, this advantage will enable us to implement special features that would otherwise be impossible. For example, if the graphics executive could hierarchically step through sets of command menus, it would free the user's control programs from having to hold the information needed to accomplish this function. This implies that a user's programs could be inserted anywhere in the flow of logical control without having to modify other users' programs with information as to what precedes or follows. We are also exploring the option of having the graphics executive post all system-status updates on

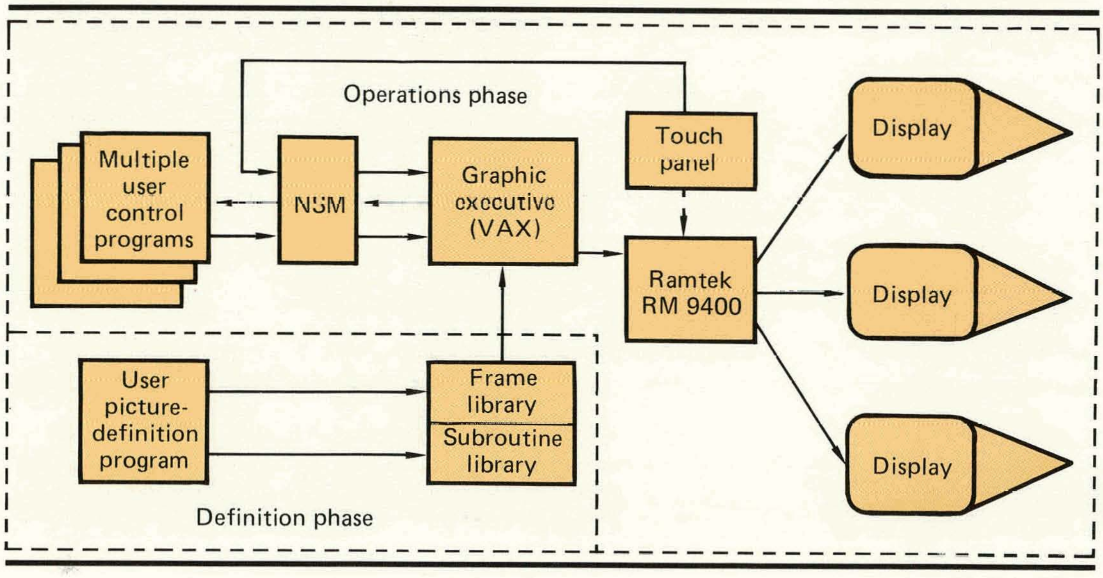

Fig. 2-174. Block diagram of operator-interaction system, showing major hardware and software components and the information flow paths among them.

the relevant frames so as to remove this tedious process from the user packages. Another important feature we plan to implement is a graphics editor. A laser operator or experimentor could then use the CRT and touch panel interactively to design frames. This would allow a specialist, with no knowledge of how to program the computer, to make additions to the graphics library.

Author: J. Wilkerson

Major Contributor: J. Krammen

Nova Image Processing. Our decision to use video sensors on the Nova laser system made the use of digital image processing a requirement for closed-loop alignment. This concept, proven feasible in the Shiva automatic pinhole-alignment system, is a major advance in closed-loop alignment technology and a significant advance in the state of the art. Automatic alignment through closed-loop image processing is capable of

- Quicker laser alignment than is possible manually.
- An accuracy comparable to that obtained by hand.
- More-consistent alignment results.
- Allowing specialized analyses to be done in special cases.

The closed-loop video-analysis system on Nova consists of a Quantex image-acquisition and storage device (comprised of a video digitizer and image buffer), a high-speed array processor (AP), and a central VAX-11/780 computer, as shown in Fig. 2-175.

Once we selected this architecture, we designed hardware and software interfaces to allow images in the Quantex memory to be communicated to the array processor and, from there, to be efficiently stored on the system disk. Then we developed the software to annotate images, to write partial images into Quantex memory, and to interface all Fortran and AP-assembly language routines to Praxis (the system-implementation language for Nova). Finally, we set up an optical bench to test the video-analysis algorithms as they were developed.

The central computer that controls the image-analysis process for the Nova laser system will also be handling other tasks, such as Novanet communications, console graphics, and alignment-applications software. For this reason, we chose image-processing-hardware architecture to minimize the computational load on the VAX computer. The array processor and Quantex video digitizer are capable of doing a considerable amount of processing without having to interact with the main computer.

In a typical video operation, a CCD camera-generated image is "grabbed" by the video digitizer, either through a command

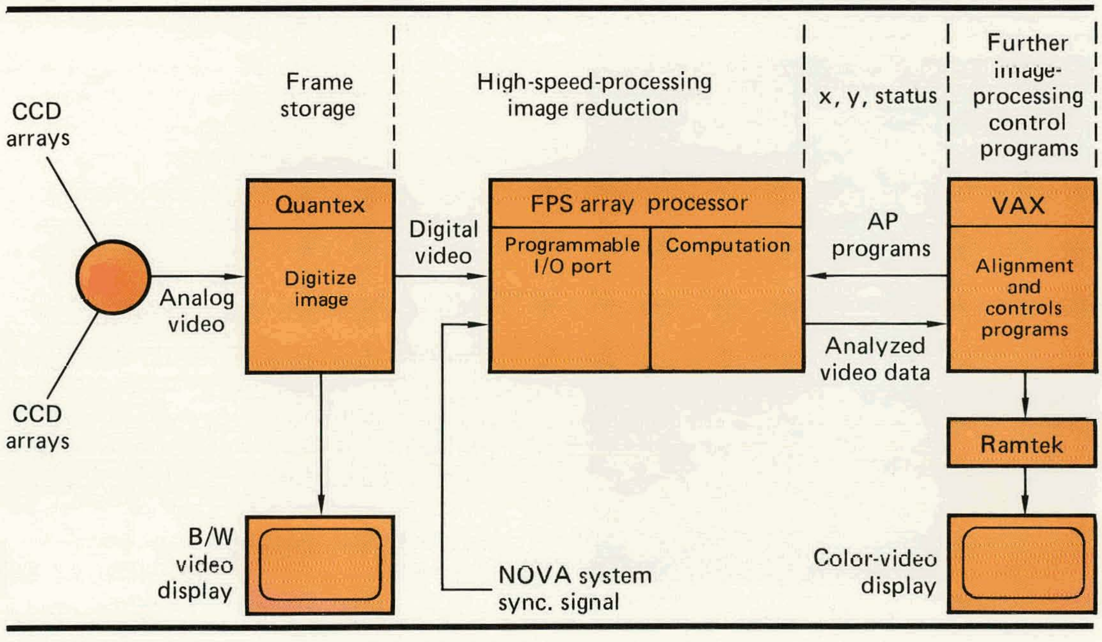

Fig. 2-175. Architecture of the Nova video-analysis system.

from the central computer or by a system-synchronization signal (in the pulsed-alignment operating mode). The central computer then instructs the AP to read and analyze the image, which in turn provides the applications program in the VAX with parameters describing the characteristics of the image being examined (such as the center point of a pinhole).

Up to 200 components of the Nova laser will have to be aligned before each system shot, constraining the alignment operation for each alignment task to a very short time. We also want to make image processing adaptable to changes that would normally affect its reliability. Therefore, we have developed the following criteria for image processing:

- Less than one second per alignment task.
- Insensitivity to variations in image "quality" due to background intensity and noise, the intensity of the pinhole image vs that of the background, intensity variations across the pinhole, and images that are partially off the screen.
- Simple to interface to the controls software.
- A high degree of flexibility.

One of the first capabilities we developed for the system was the ability to display, on the operator-console color screens, color-enhanced versions of black-and-white images. Such an image is shown in Fig. 2-176. This ability was needed to visually analyze intensity variations within images, to aid in developing the image-analysis algorithms, and to provide a long-term capability for doing beam diagnoses in Nova.

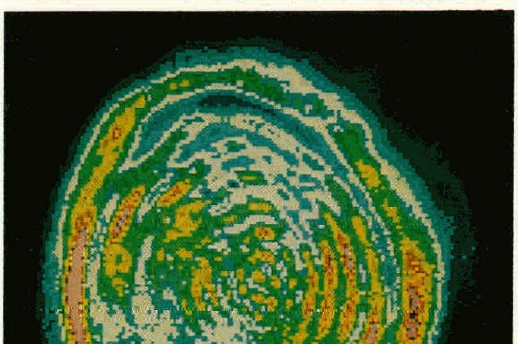

Fig. 2-176. Color-enhanced version of black-and-white pinhole image.

Our major image-processing activity in the past year has been the development of a pinhole image-analysis software package that can meet the above criteria. We were able to take advantage of the high speed and greater capability of the Nova image-processing hardware to achieve significant advances in reliability and image fault tolerance over the current Shiva automatic pinhole-alignment system.[74] As illustrated in Fig. 2-177, the current algorithm utilizes a four-step procedure:

- First, a threshold operation is performed to convert all points either to zero intensity (typically background) or to a single high-intensity value. Conversion depends on whether the original intensity of the point was below or above a threshold value. To determine a useful threshold level, an intensity distribution (histogram) of the image is performed in the AP. A low-intensity peak corresponds to the dim background, while a peak at a higher intensity is due to the bright pinhole. This distribution is then scanned by the AP, and a threshold intensity that lies between the two distribution peaks is chosen. This thresholding simplifies the further steps, but must be modified should uneven illumination exist on the CCD camera. In such rare instances, the AP calculates the gradient of the pinhole image before thresholding is done.
- Second, a median filter operation is performed in which each point is assigned a value that is the median of all point intensities in a surrounding square. The square ranges in size from 3 × 3 to 7 × 7 pixels, depending on the noise level of the image. This operation eliminates noise components from the image, as shown in the upper left quadrant of Fig. 2-177.
- Third, a two-dimensional gradient, performed on the image by the AP, assigns intensities in the resulting image according to the magnitude of the intensity differences of surrounding pixels in the original image (see Figs. 2-178 and 2-179). Note in Fig. 2-178 that the largest pixel values in the resulting image are at the edge locations of the original image. The result is an image in which the edges of the

pinhole are intensified, as shown in the upper right quadrant of Fig. 2-177.

- Finally, a center point is determined, based on the center of the four points at the extremities of the delineated pinhole images (lower left in Fig. 2-177). A circularity check is also performed to allow correct center-point determination when part of the pinhole is obstructed or off the image "screen."

This algorithm is superior to the successful Shiva automatic alignment system for pinhole and focused-spot analyses. In particular,

- It requires less than one second of analysis time while (to ensure greater reliability) it performs 100 times the number of computations performed on Shiva.
- It meets the design goal of being insensitive to image quality and successfully handles images that are partially off the screen.

To further aid in devising more sophisticated image-processing techniques, we developed a prototype interactive image-processing system that allows the user to perform various detection and filtering techniques on an image and to store and retrieve useful results. A menu is displayed that shows the functions currently implemented and the critical parameters that must be input for each selected function. The user is prompted to supply any missing parameters. Also, any sequence of functions that the user might need repeatedly can be placed in a file and can then be executed with a single instruction, as required.

When fully developed, this system is expected to accelerate the development of other image-analysis techniques. These

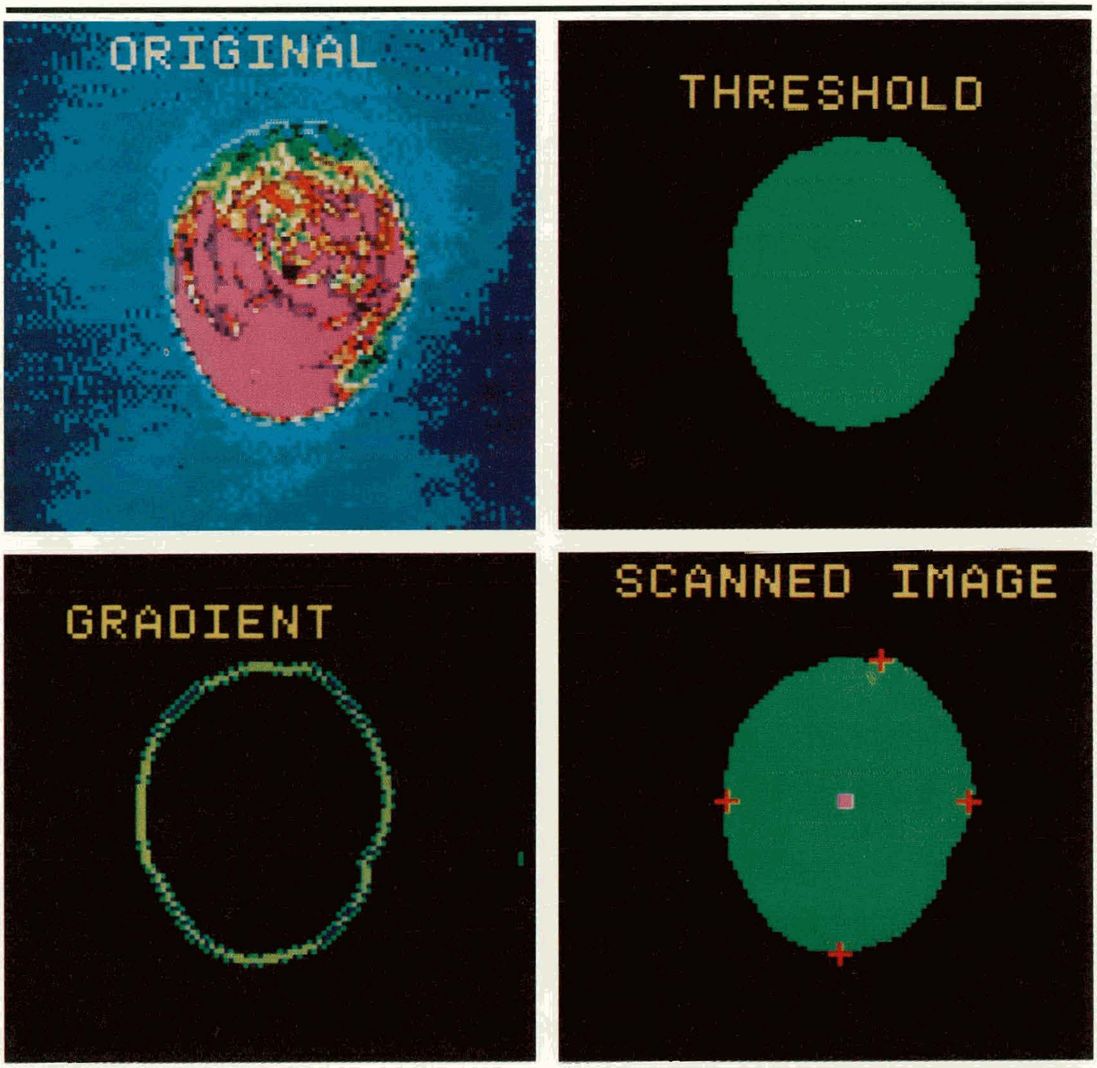

Fig. 2-177. Four-step Nova video-analysis process.

techniques will be important since, in the alignment process for the entire laser system, we will be required to process many different classes of images, such as those used in crosshair-based centering. Changes and improvements will also be necessary when the analysis methods are tested on the real system. The flexibility built into both the video-analysis and interactive image-processing systems will aid in future work on the Nova alignment system.

Authors: C. Humphreys and G. J. Suski

Event Logger. An event logger, composed of an independent processor and associated storage units, is a fundamental part of the Nova central-control-system architecture. In a large control system such as Nova, it is necessary to monitor, record, and verify (in real time) large numbers of significant system-wide events or operations in the chronological order in which they occur.

The design criteria for the event logger stemmed from experience with the Shiva system. They include the ability to provide a continual series of snapshots of laser system status (similar to what is done by an airline flight recorder) during both normal and abnormal operations.

Fig. 2-178. Sample pinhole image areas and convolution gradient matrix used for pinhole image analysis.

What the computer "sees".

0	0	0	0	0	0	0
0	0	0	0	0	0	0
0	0	0	0	0	0	0
0	100	100	100	100	0	0
0	100	100	100	100	100	0
0	100	100	100	100	100	100
100	100	100	100	100	100	100

Typical intensities, I (k, ℓ), in a thresholded image.

1	1	1
0	0	0
−1	−1	−1

Horizontal edge kernel, H (i, j).

−1	0	1
−1	0	1
−1	0	1

Vertical edge kernel, V (i, j).

0	0	0	0	0	0	0
0	0	0	0	0	0	0
0	200	300	300	200	100	0
0	200	300	300	300	200	0
0	300	0	0	100	200	100
0	200	0	0	0	100	100
0	100	0	0	0	0	0
0	0	0	0	0	0	0

Intensities, R (k, ℓ), in an edge-enhanced image.

Acquire and threshold the original image

Apply each of the kernels to the original image, taking the maximum magnitude at each point (k, ℓ)

Yielding

$I(k, \ell)$

$$R_H(k, \ell) = \left| \sum_{i=0}^{2} \sum_{j=0}^{2} I(k+i, \ell+j)\, H(i, j) \right|$$

$$R_V(k, \ell) = \left| \sum_{i=0}^{2} \sum_{j=0}^{2} I(k+i, \ell+j)\, V(i, j) \right|$$

$$R(k, \ell) = \max\,[R_H(k, \ell), R_V(k, \ell)]$$

Fig. 2-179. Example of gradient calculation in Nova image analysis.

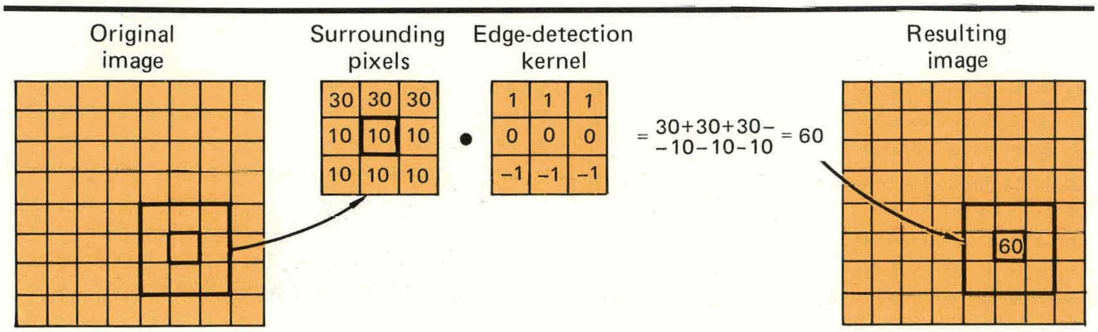

Each major control subsystem (alignment, laser diagnostics, power conditioning, and target diagnostics) will use the event logger to retain records of events and to provide displays of event sequences for operator review. Each record will be date- and time-stamped and identified as to its source. By this method, a comprehensive permanent record of the systems' status and its nominal operating parameters will be maintained. It will also be possible to correlate the data with the performance of specific laser system components.

The Nova event logger is designed to meet the following criteria:

- It must provide operations personnel with an immediately readable English text description of what is (and is not!) occurring on the laser system so they can quickly gain a clear and concise understanding of current conditions without having to translate large quantities of numerical data listings.
- For reliability and to avoid interference with laser system operations, it must be implemented independently from the remainder of the computer system and yet allow events to be recorded from any location within the remainder of the control system.
- It must present a low overhead interface to the remainder of the control system so as not to burden users with voluminous details of event logging; it must also be efficient enough internally to reasonably satisfy the combined logging-rate requirements of all users.
- To ease maintenance and troubleshooting of the laser system and control-system hardware and software, it must be human engineered and highly user-interactive so that operators can quickly and efficiently recall the last day's or week's events.
- Its interface and synchronization characteristics must be compatible with all of the control subsystems.

The functional operations of the Nova event-logger hardware and software are shown schematically in Fig. 2-180. As shown, the entire event-logging and

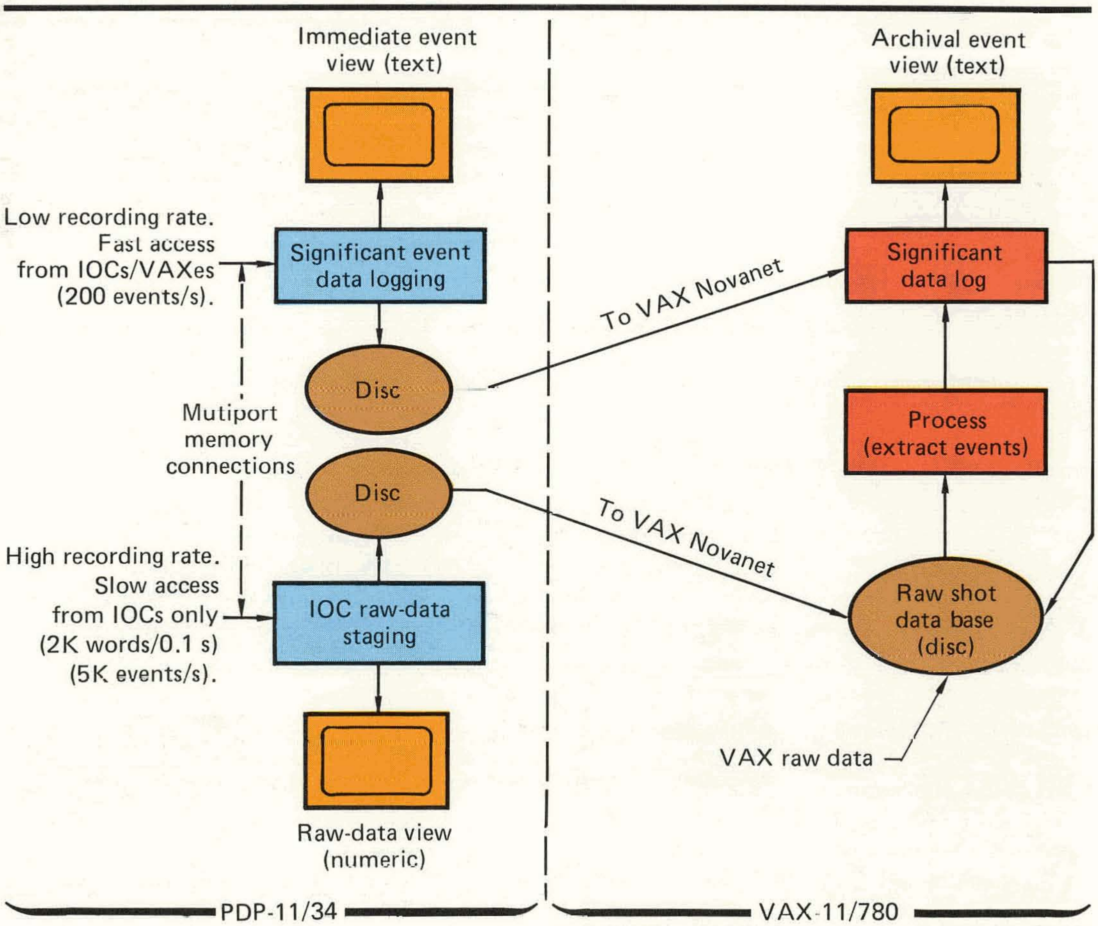

Fig. 2-180. Block diagram of Nova event-logging system, showing system structure and data flow.

processing function is a cooperative effort between the VAX computer and a stand-alone computer. The stand-alone portion consists of the computer, a high-speed disk-storage unit for event archiving, CRT terminals for event display and operator interaction, multiport memory connections, and a Novanet link for communication with the control-system computers. The Novanet link will permit general file transfers, thereby allowing event data and shot data to be consolidated into a single data base. This concept again evolved from operational experience with Shiva.

The event logger provides two types of data logging. The first type is English text descriptions and records that can be recorded at rates of 20 to 200 words per second. Real-time access is provided by displaying the data on event-logger displays. This logging method will be used to record such parameters as alignment data, system configuration before a target shot, interlock integrity, and diagnostic voltages.

A second type of data logging is provided for packed binary or specially formatted data that can be stored at a speed of 20 000 sixteen-bit words per second but cannot be reviewed on the display screen in real time. After each shot the data will be retrieved, unpacked, formatted into English, and displayed to the operators. Extremely detailed data, typically numerical data showing the condition of power supplies and equipment, are recorded in this manner. Correlation of these data with real-time events and target shot data can still be accomplished, but not until after a shot sequence is concluded.

Any of the system data sources may, at any time, invoke either of the two logging modes to fulfill their specific requirements during maintenance, setup, or target shots. Users can choose whether to store an event temporarily, permanently, or not at all by dynamically setting a parameter associated with each event. This option provides a diagnostic capability that allows a user to test a specific subsystem without storing unneeded data. Additional options allow users to manually or automatically override previously set-up conditions in order to store events that, while not normally stored, might be needed occasionally.

Each Nova subsystem has a specific set of coded identifiers so that the interactive historical traceback feature can be invoked only for that specific subsystem. This allows fast sorting of system parameters for a specific data shot. For example, we should be able to quickly analyze whether a particular laser arm was correctly aligned or if a specific power supply produced full power for that shot.

We have completed prototype development and testing of the event-logging system and, using the development VAX-11/780 and a PDP-11/40 salvaged from Argus, have demonstrated it. As indicated in Fig. 2-180, all subsystems communicate through the VAX and its multiport memory to the event-logger CPU. During 1981 we will implement a fully functioning event logger on an upgraded processor (PDP-11/34) salvaged from Shiva.

Author: R. J. Calliger

Major Contributors: E. Jaeger, J. Severyn, and J. Wilkerson

Configuration and Data Management. If low overhead maintenance and continued development are to be achieved in a large, flexible, continually expanding and changing control system such as Nova's, an accurate record of the system's configurations, data, and programs must be maintained. In Nova, we have developed prototype software tools to handle this requirement in several areas, including configuration and data management.

In the first of these areas, configuration management, we have developed a librarian package that allows us to maintain a precise record of the current configuration of the more than 1000 devices, computers, and data-acquisition elements in the Nova laser system. Since, at any given time, several engineers, scientists, and technicians can be involved in changing this configuration, one easily accessible source for this information (both from a software and user point of view) must be provided.

Figure 2-181 illustrates the functional organization of the data-base librarian. This librarian is currently being used to maintain a single version of configuration-related data in the following categories:

- Physical devices—description and location.
- Data structure—used in common by many system programs.

- Network communications—tables used to communicate between distributed system programs.
- Operator display information—used to graphically describe operator control displays and the instructions needed to display and update system devices according to their status.

In a typical use, a configuration change (like the addition of a stepping-motor-controlled mirror) is entered into the control-system configuration data base, using English language commands to the librarian. The librarian then automatically updates other records of information affected by this change, such as a set membership record containing the location of all motors in the system. A system-regeneration procedure, currently in the design stage, will then be executed to propagate these changes to the component system tables and programs that actually implement the control system and its functions. The most important features of the configuration-management update process are the use of an English-language input system (as shown in Tables 2-32 and 2-33), and the automatic propagation of changes throughout the control system. These features will help people who lack an expert background in computers to maintain and continue development of the Nova laser; they will also help developers coordinate and document system changes.

Table 2-32. Sample of input to control data-base librarian.

Input	Comments
CREATE A REGION	Flag words describing record type.
THE REGION NAME IS "JOY-CONTROL"	Name used to store the record region.
THE REGION DESCRIPTION IS "RAMTEK-CONSOLE-JOYSTICK-CONTROL-REGION"	Brief description of region purpose.
THE ENVIRONMENT NAME IS "AL"	Network-shared-memory (NSM) environment.
THE CLASS IS "GENERAL-CLASS"	Type of region.
THE ACCESS NAME IS "JOY-CONTROL"	Name of region in Praxis program.
THE STRUCTURE TYPE IS "JOY-STICK-CONTROL-TYPE"	Name of Praxis structure to map on region.

Fig. 2-181. Block diagram of Nova central-control data base.▼

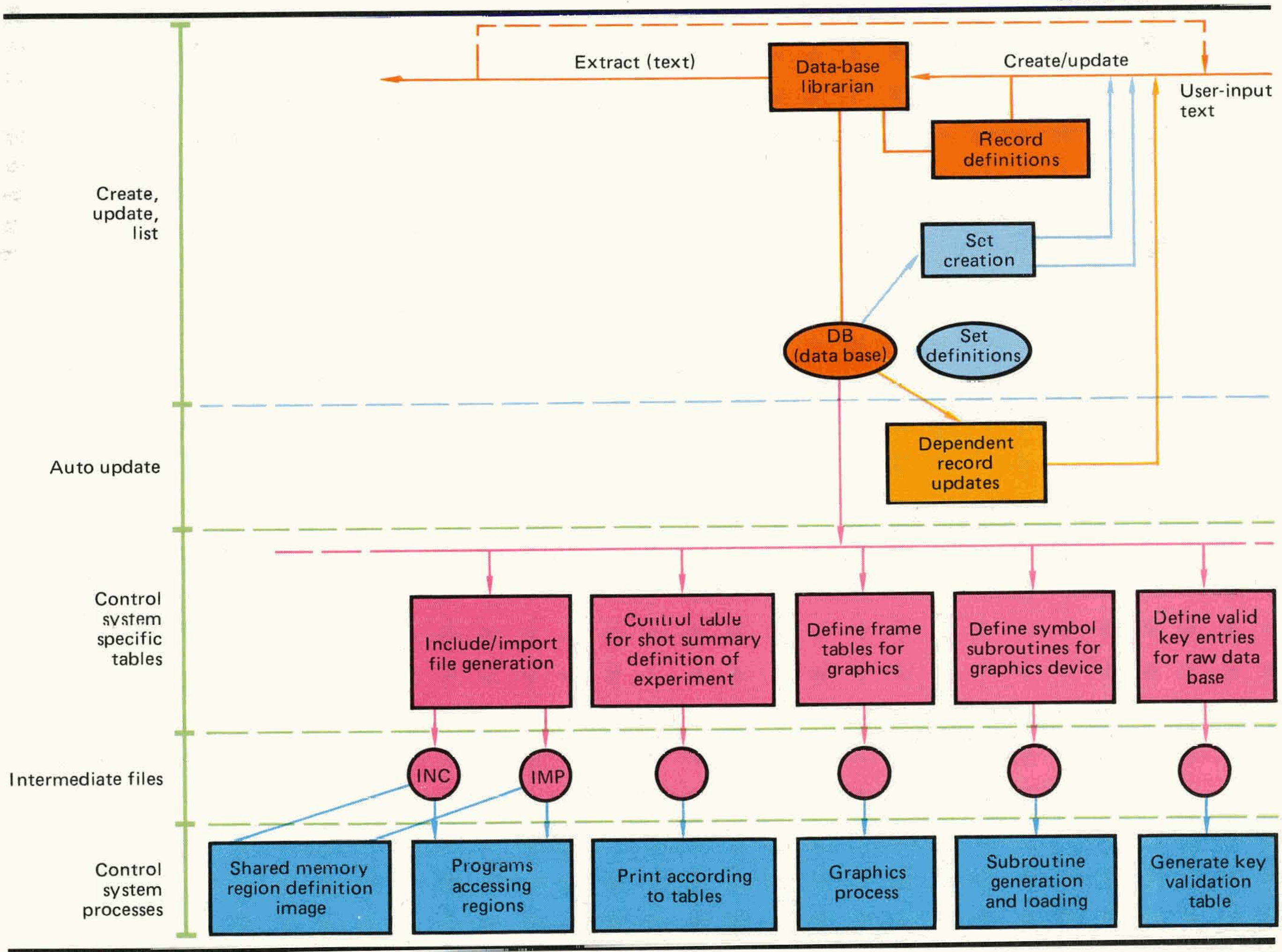

In addition to storing the system configuration in an easily accessible form, we must also store the raw data for each shot. The challenge in this case is to store the large volumes of data in such a way that they remain documented and easily accessible for a long time. This long-term capability would be required, for example, when data have to be correlated over a six-month series of target experiments. In addition, a uniform method of storing raw data in the various control subsystems will ease the process of combining data, as in analyzing the output of an amplifier (laser diagnostics) vs the number of times it has been fired (power conditioning).

To achieve a system that resolves such problems while keeping the required low overhead for high-volume data recording, we implemented a prototype of the raw-data-base management system. When fully operational, this system (Fig. 2-182) will identify all recorded data by three keys (names) that are, together, unique. These keys must be entered into the system before data are stored by a program. This "predefinition" process for the keys also includes providing a description of the corresponding data.

While the keys allow us to identify the data with an English-language description, we must still identify the data format in terms usable by the accessing programs. To accomplish this goal, we also store program data structures that define the organization of the information recorded in the raw data base. By keeping this "roadmap" to the information in the same data base as the data, we are immunized against the loss of data due to the location and format changes that are expected to occur as Nova evolves.

Authors: D. McGuigan and G. J. Suski

Table 2-33. Eight record types currently implemented in control data-base librarian.

Record type	Comments
DEVICE	Used to describe physical devices.
ENUMERATION	Used to describe a Praxis feature.
ENVIRONMENT-TYPE	Used to describe an NSM environment.
PARAMETER	Used to describe a Praxis feature.
PICTURE	Used to describe a Graphics subroutine.
REGION	Used to describe an NSM region.
SET	Used to describe record types.
TYPE	Used to describe a Praxis feature.

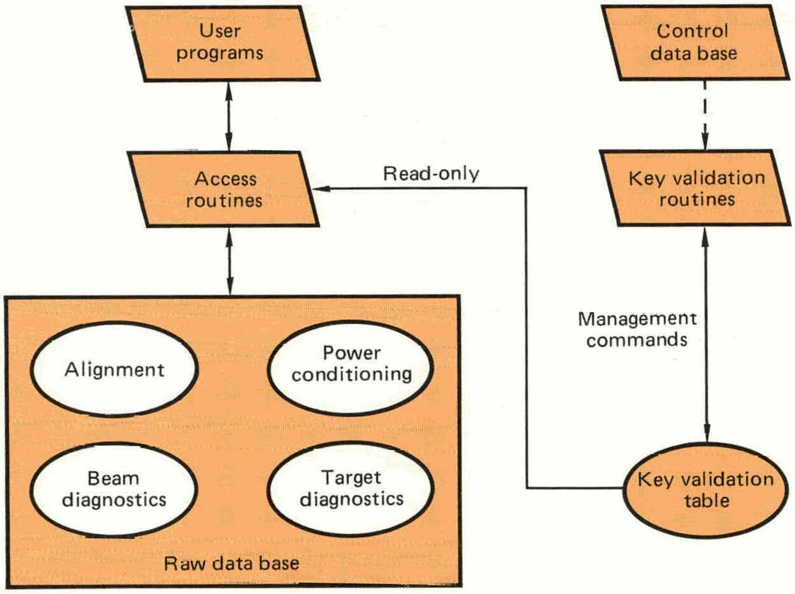

Fig. 2-182. Block diagram of the architecture of the raw-data-base system.

Praxis. Praxis is a modern high-level computer language for efficient programming in control and systems applications. It is being developed for use as the standard language on the Nova control system.

The development of Praxis began with an initial study by Bolt Beranek and Newman, Inc. (BBN), funded by the Defense Communications Agency (DCA), to determine the requirements for a communications programming language.

In January 1979, LLNL funded BBN to augment the DCA design and to implement a Praxis compiler for Digital Equipment Corporation's PDP-11 computer. With the clarification of the Nova controls design and schedule, BBN's work was expanded to include development of a VAX (native-mode) compiler, documentation, additional language design, and a high-level input/output package.

In March 1980, the preliminary PDP-11 compiler successfully passed two critical milestones. The first was passed when the compiler, which is written in Praxis, compiled itself successfully on the PDP-11 systems, proving that the bulk of the compiler was correctly implemented.

The second milestone was passed with the implementation of a Nova controls application of the language, for a ROM-based LSI-11 processor. A 2000-line assembly-language stepper-motor-control program was recoded in Praxis, compiled, and burned into read-only memory (ROM). This demonstrated that the language was indeed powerful enough to replace detailed assembly-language sequences and that the compiler correctly implemented the controls-oriented features.

In December 1980, we took final delivery from BBN of the completed Praxis compilers, support software, and documentation. These products were three Praxis compilers:

- A VAX/VMS version that generates VAX code.
- A VAX/VMS version that generates PDP-11 code.
- A PDP-11/RSX-11M version that generates PDP-11 code.

and related documentation:

- An RMS input/output package.
- A 300-page reference manual.[75]
- An input/output manual.
- A compiler internal-structure document that describes, in detail, the various parts of the compiler and how it operates.

In addition, we completed two in-house documents:

- A 28-page *Introduction to Praxis.*[76]
- A 300-page document, *Programming in Praxis.*[77]

We have, with a remarkable degree of success and acceptance, been using Praxis for control-systems programming since the summer of 1980. More than 70 000 lines of operational Praxis code have been written, of which one-third is controls-related.

We have standardized on Praxis for all controls-programming tasks on Nova and Novette.

Praxis is a high-order language designed for the efficient programming of control and systems applications. It is a comprehensive, strongly typed, block-structured language in the tradition of Pascal, with much of the power of the forthcoming Ada language. It supports the development of systems composed of separately compiled modules, user-defined data types, exception handling, detailed control mechanisms, and encapsulated data and routines. Direct access to machine facilities, efficient bit manipulation, and interlocked critical regions are provided within the language.

Since the control-system environment differs in important ways from application to application, and from machine to machine, Praxis has features to handle these differences. High-level facilities that mask machine dependencies and foster machine independence (portability) usually prevent the use of the exact programming capability needed for real-time, control-applications programming. However, Praxis is a high-level language that has controlled access to machine dependencies.

The examples used in the following paragraphs illustrate some of the features and characteristics of Praxis. Our intent is to give the reader an impression of the "flavor" of the language without describing all of it in detail. The reader is invited to read the other documentation[75–77] for a more complete exposition.

Praxis is a strongly typed language. The programmer is given a collection of predefined types and can construct new types. Every variable, constant, parameter, and expression has a type. All types can be deduced at compile time, and the compiler requires that each value be used in a way that is consistent with the rules associated with its type. For example, it is a compile-time error to attempt to pass an integer parameter to a routine that requires a real number parameter.

The Praxis language includes many block-structured statements. A block is a method of packaging statements and declarations so that their scope is clearly specified and controlled. Each block-structured statement is delimited by an XXX/endXXX pair, where XXX represents the particular statement name. For instance:

<u>for</u> . . . . <u>endfor</u>
<u>if</u> . . . . <u>endif</u>
<u>procedure</u> . . . . . <u>endprocedure</u>
<u>select</u> . . . . <u>endselect</u>

This block structuring also enforces a particular programming style that is more readable and maintainable than that of unstructured programming. To differentiate between reserved words in the language and user-defined names, we will <u>underline</u> reserved words such as <u>if</u> and <u>otherwise</u>.

A simple example in Praxis is the matrix multiplication of two N by N matrices, named SpecA and SpecB, and storing of the result in Spectrum:

```
for I := 1 to N do
  for J := 1 to N do
    Spectrum [I,J] := 0
    for K := 1 to N do
      Spectrum [I,J] := Spectrum [I,J]
          + SpecA [I,K]* SpecB [K,J]
    endfor
  endfor
endfor
```

This example only makes sense within the scope of the declarations for the variables used. In Praxis programs, all variables must be declared before use. Thus, the above code would be preceded by a series of statements, such as:

```
declare
  N = 32
  SpecA : array [1..N,1..N] of integer
  SpecB : array [1..N,1..N] of integer
  Spectrum : array [1..N,1..N] of integer
enddeclare
```

Note that the loop indices (I, J, and K in this example) are declared by the "for" statement. This declaration block could be written more concisely in various forms. For example, one method would be to use a user-defined type for the array declarations, thereby ensuring that the three arrays are all of the same type and that they would remain so through subsequent software maintenance. Thus, the declarations could take the form:

```
declare
  N = 32
  matrix is array [1..N,1..N] of integer
  SpecA : matrix
  SpecB : matrix
  Spectrum : matrix
enddeclare
```

In this block, three forms of declaration have been used. "N" is declared as a constant, "matrix" is declared as a user-defined data type, and "Spectrum" is declared as a variable of type "matrix."

A more-detailed control-programming application follows. In it, a hardware input/output device on a PDP-11 computer is read directly, in a multiprocess environment. In this example, the resource (an I/O device) is protected by an interlock variable in a critical region. Another process with a similar code, using the same resource, will not be able to preempt the critical-region code sequence.

```
Declare
  status : location (8!176420) volatile
           logical
  datum : location (8!176422) volatile
          char
  padlock : static interlock
  temporary : char
enddeclare
Region padlock do
  Repeat //null loop
  Until (status and 8#200) <> 8#0
  temporary :=datum
endregion
```

The attribute "volatile" on the status and datum variables informs the compiler that these variables must be referenced directly each time they are mentioned in the program, and that no optimizations are to be performed on them. The volatile attribute of a variable allows the variables to be used as I/O registers, as has just been illustrated, and to be used in shared memory.

The location attribute informs the compiler to place the variable in the physical address specified by the octal (8!) integer constant in the parentheses. The variable is static and always resides at that location. The attribute places the static interlock at a fixed location determined by the compiler.

The "logical" predefined data type can be thought of as a bit-string data type on which independent operations on each bit can be performed. In the "until" clause, each bit in the status variable is tested with the corresponding bit in the octal (8#) logical constant, and the result is compared to a logical zero.

An application of type conversion is shown in the function "Upper," which converts any occurrence of a lower-case letter to an upper-case letter:

```
function Upper (inchar:char)
  returns outchar:char
  if inchar <=$a
    or inchar >=$z do
    outchar := inchar
    return
  endif
    outchar := char (integer (inchar) -
8!40)
endfunction {Upper}
```

The previous function example used the return statement for explicit exit from a routine (i.e., procedure or function). This statement is one of several such statements that eliminates the need for a GOTO in the language. The lack of the GOTO statement is an important feature in the language. The following example uses two other control flow statements, together with block labeling, to program an application that normally requires a GOTO statement. This section of code will, for each of a series of motors, slew the motor until it is beyond the minimum position. It is finished processing when all of the motors are serviced, or when any one of the motors goes beyond a maximum allowed position.

```
primary :
  For index := 0 to number_of_motors do
    Position : = Motor_position [index]
    While Motor [index] = on do
      if position > min_position do
        loop primary
      orif position > max_position do
        break primary
      otherwise
        Slew_motor(index)
      endif
    endwhile
    endfor {primary}
```

The "loop" statement causes iteration to occur in the "for...endfor" loop; that is, it acts like a GOTO the for, which causes the iteration count of the loop to be incremented, the test for completion to be performed, and the "for...endfor" block to be executed if the iterations have not been completed. The "break" statement, on the other hand, is a block exit statement. In the above case, it exits three levels of blocks: the "if...endif," "while...endwhile," and "for...endfor," and execution continues after the "endfor." Labels can only appear on blocks (at the beginning and end) and are only used with the break, loop, and retry (in critical regions) statements.

The language has several predefined data types:

- Discrete types
  - integer – signed
  - cardinal – unsigned integer
  - char – ASCII character
  - boolean – true/false
  - enumeration – programmer-specified values
- Control types
  - interlock – locked/unlocked
  - logical – bit string
  - pointer – pointer to a typed object
- Floating types
  - real – floating point
  - long real – double precision real
- Aggregate types
  - array – array of any type, access by index
  - structure – various type components, access by name
  - set – set of discrete types
- Routine types
  - procedure – typed procedure variables
  - function – typed function variables
- Other types
  - general – union of all types (used as formal parameter)

User-defined data types can then be characterized in terms of the predefined types or other user-defined types.

Praxis programs are built from separately compilable modules of the form:

```
module complex_number_package
  export
    complex,
    real_part,
    imaginary_part,
    complex_sum.
declare
  complex is hidden structure
    r : real
    i : real
  endstructure
enddeclare
function real_part (c : complex)
    returns x : real
  x := c.r
endfunction
function imaginary_part (c : complex)
    returns y : real
  y := c.i
endfunction
function complex_sum (c1,c2 : complex)
    returns sum : complex
  sum.r := c1.r + c2.r
  sum.i := c1.i + c2.i
endfunction
endmodule {complex_number_package}
```

The declarations of "complex," "real_part," "imaginary_part," and "complex_sum" are made available, at compile-time, by the "export" to other separately compiled modules that "import" the declarations. Note that types, as well as data and routines, can be imported and exported.

In summary, the Praxis language is particularly designed for control and system implementation needs. Complex language features, such as generic procedures, overloading of operators, and parallel processes, have been intentionally left out. We felt that these concepts were either not understood enough to be incorporated at this time, or that they need not be part of the language. Thus, Praxis has been kept well within the bounds of the state of the art of language design.

In conclusion, Praxis is an extremely powerful, modern programming language that is well suited to the task of controlling the Nova and Novette lasers.

Author: J. R. Greenwood

Major Contributors: F. W. Holloway, J. M. Duffy, A. Evans Jr. (BBN), C. R. Morgan (BBN), M. C. Zarnstorff (University of Wisconsin, Madison), W. I. Nowicki (Stanford University), and E. Killian (BBN)

Target Systems

This section includes descriptions of the target chamber, beam-focusing lenses and positioners, the target support and alignment structure, target diagnostics, and control of the radiation environment.

Target Room. We will locate the target chamber in a concrete-shielded room north of the laser bay and optical switchyard, as shown in Fig. 2-183. Laser beams will be routed to the target chamber by a series of turning mirrors mounted on a steel space frame, as already described in the "Mechanical Subsystem" section.

During Phase-I operation, we will irradiate the target with two 5-beam open cones, one each on the east and west ends of the target chamber. The included angle of the cone centerlines is 100°. (The flexibility exists for changing this angle to 70° by relocating the final turning mirrors and replacing the hemispherical heads of the chamber.)

In Phase II, we will add 10 more beams in the west laser bay and reroute the existing beams so there will be no crossover between the east and west systems. Figure 2-184 shows the Phase-II target chamber.

Target Chamber. As described in the 1979 Laser Program Annual Report,[78] the target chamber will be supported 10 m above the floor, in the center of the target room. The main body of the chamber will have a 1-m-wide central ring, with an inner radius of 2.13 m, to provide structural support for the target positioner, target-alignment optics, high-vacuum system, and target-diagnostics instruments.

We have designed two removable hemispherical heads, to be attached to the center ring, with ports for the laser beams, x-ray-effects experiments, and target diagnostics.

Phase-I requirements call for an experiment yielding 1×10^{17} neutrons from a 100-kJ, 1-ns laser pulse. The neutron, x-ray, and debris fluences generated by this neutron yield are not high enough to require local shielding or protection of the chamber by a first-wall absorber. Thus, the minimum radius of a hemisphere is dictated by mechanical considerations, primarily mounting of the focusing lenses. The baseline lens for Phase I has a focal ratio of f/3.5, with a 740-mm clear aperture, but we are making provision for a future change to a lens with a focal ratio of about f/1.6. Because these faster lenses will, of necessity, have to be inside the target chamber, the ports in the hemispheres must be large enough to admit the full laser beam plus some mechanical hardware. For Phase I, these considerations dictate a 1.65-m minimum chamber radius. Since neutron activation is not a large problem, the structural material can be stainless steel, which is more familiar to most vacuum-vessel fabricators than aluminum.

We are designing the target chamber for Phase II for laser energies of up to 300 kJ and for yields of up to 5×10^{18} n, with as much as 3.2 MJ of cold x rays and 4.0 MJ of target debris. As described in the 1977 Laser Program Annual Report,[79] these conditions will require:

- A first wall for absorbing x rays and debris.

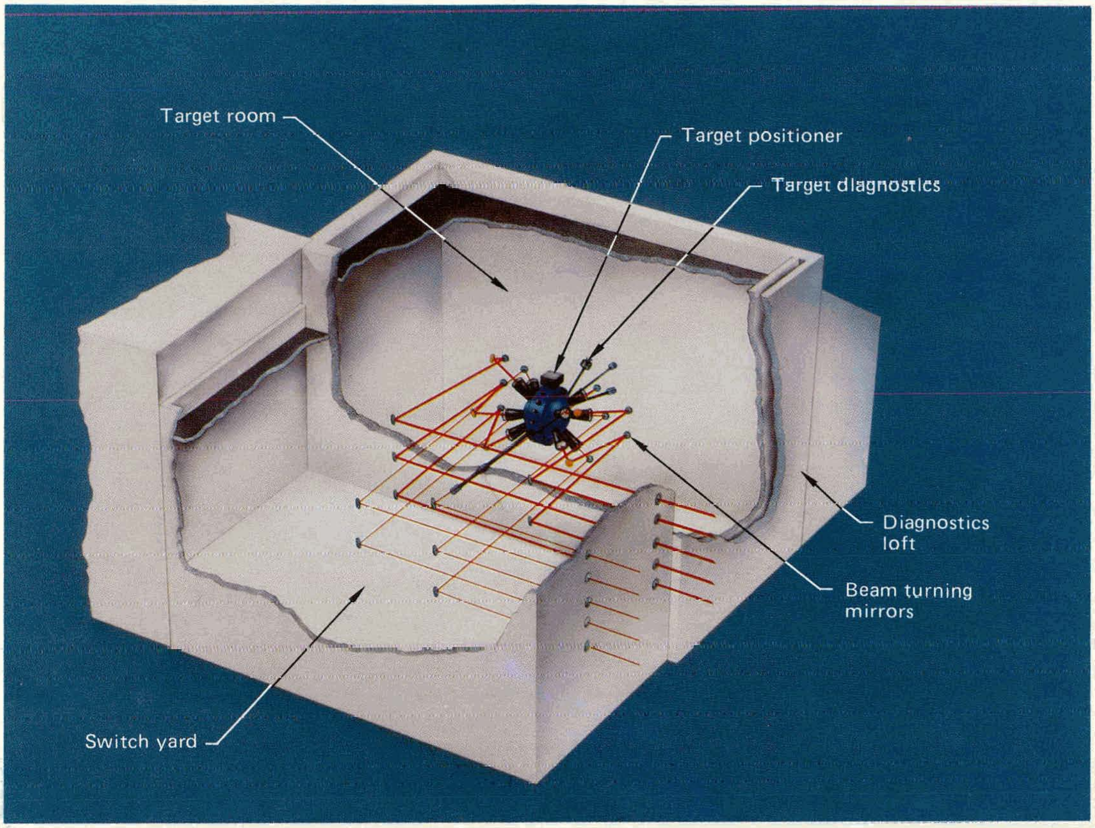

Fig. 2-183. Nova target room and switchyard arrangement.

Fig. 2-184. Nova target chamber, showing Phase II-arrangement with 20 laser beams on 100° cone.▼

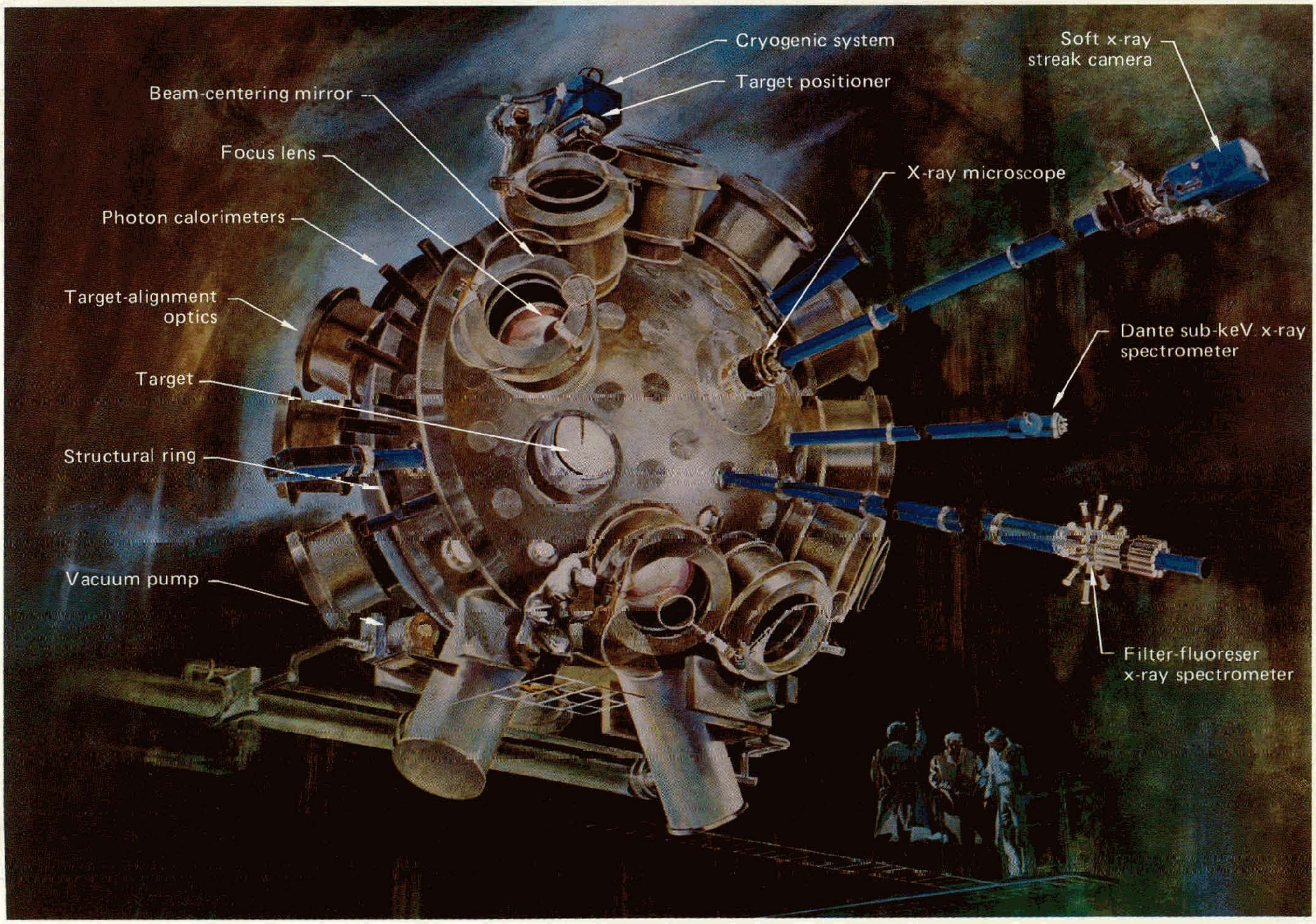

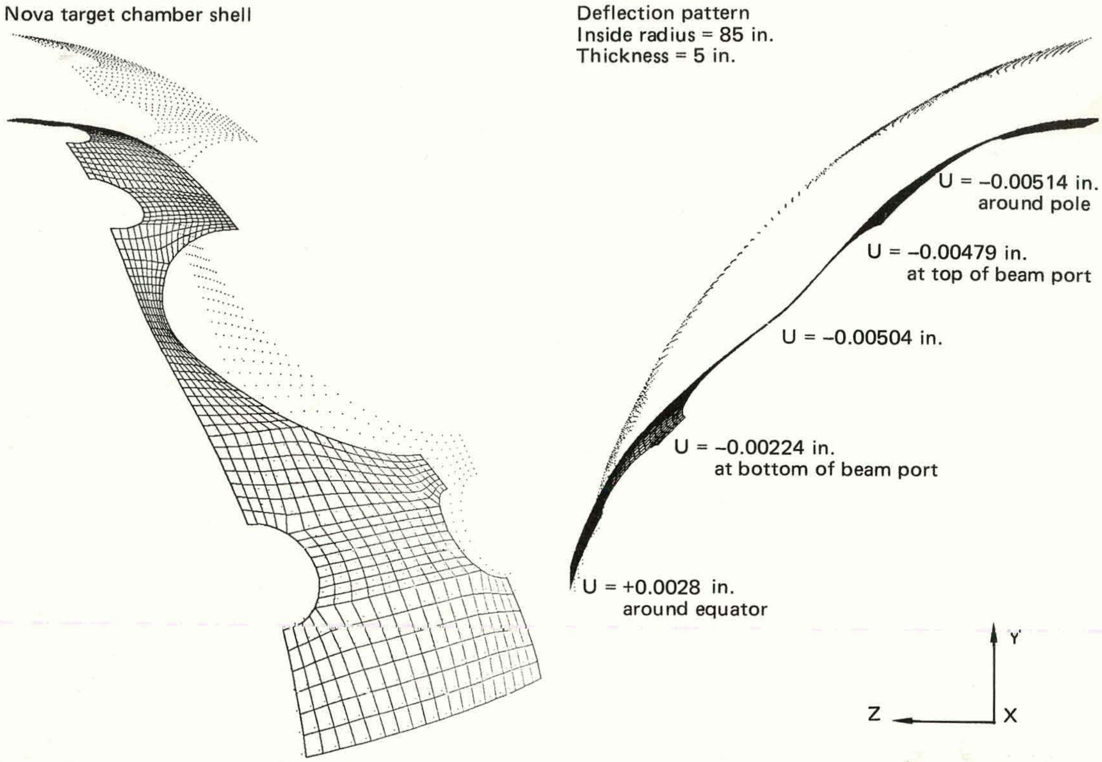

Fig. 2-185. Computer printout of predicted deflections in an element of the Nova target chamber, using SAP IV finite-element code.

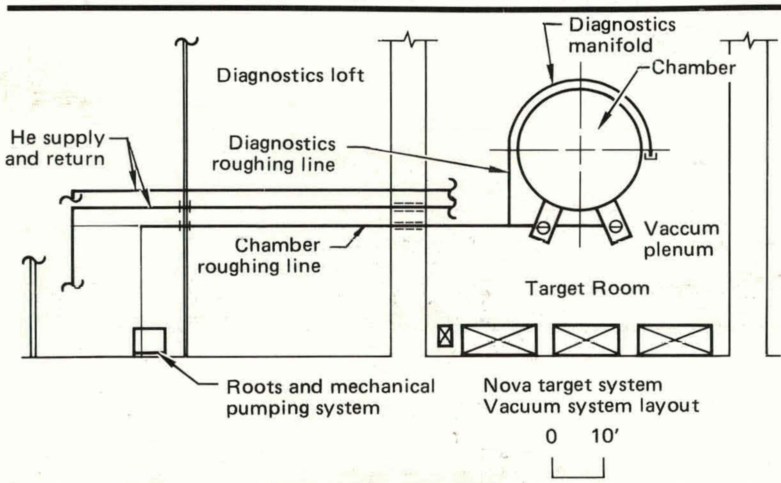

Fig. 2-186. Nova vacuum-system layout.

- An aluminum vessel to allow neutron-activated materials to decay rapidly to an acceptable level.
- A water shield around the chamber to limit activation of the steel space frame and concrete building.

To accommodate 10 lenses per side (instead of five) and to reduce x-ray fluence on the first wall, the radius of the Phase-II chamber must be at least 2.3 m.

In 1980 we conducted finite-element stress and deflection analyses, using the SAP IV code. The model chamber had a radius of 2.1 m and a thickness of 7.5 cm, which resulted in a maximum vacuum-load differential deflection of 230 μm around the beam ports, as shown in Fig. 2-185. While the accompanying stresses were extremely low, this deflection was deemed to be too high for stable lens and diagnostic support. The radius of the model chamber was changed to 2.3 m to increase the distance between beam ports, and its wall thickness was increased to 12.5 cm to produce a scaled differential deflection of less than 50 μm, which will provide adequate stability to support the lens positioners and diagnostic sensors with no loss of alignment during pumpdown.

Vacuum System. The vacuum system will use mechanical pumps and Roots blowers for rough pumping and turbomolecular and cryogenic pumps for high-vacuum pumping. We will attain a pressure of 10^{-5} Torr in 30 min and, ultimately, reach a base pressure of 10^{-7} Torr. An overall layout of the vacuum system is shown in Fig. 2-186.

In 1980 we developed the basic design for a central vacuum-system control architecture. Our experience on Shiva has led us to a central controls concept that will

- Increase system reliability and flexibility by grouping interacting controls together, allowing an operator to determine the effect of a single action on the entire system.

- Reduce the necessity of communicating over a large geographical area (three widely spaced rooms) to ensure the integrity of the vacuum system's many subsystems.
- Efficiently control all target-diagnostic vacuum elements, thus avoiding inadvertent valve openings.
- Enhance personnel safety conditions.
- Increase the useful lifetime of equipment.

Design Criteria. In general, we are developing the centralized vacuum-system controls to be hardware- and software compatible with the overall Nova-laser control system. The major design goals are as follows:

- A control system that is easy to learn and operate and that can be quickly changed or modified.
- Software-intensive control, with modular programming, that is easy to change or to which new commands and hardware can easily be added for different experiments.
- Centralized control, with a minimum number of specialized hardware panels. Otherwise, as experiments change, we will have to build a new panel for each set of diagnostics.
- Easy field expansion, to meet the changing requirements for new or modified target diagnostics that will be added or removed, for different types of target shots.
- Incorporation of control fail-safes, interlocks, and redundancy, including provisions for sensor failures and ambiguous readings.
- Complete system-state indication and error-history logging before, during, and after each shot.

Implementation. The structure of the vacuum control system[80] is shown as a block diagram in Fig. 2-187. Because the architecture of the overall Nova control system[81] has been discussed elsewhere, only a segment of it (a single VAX 11/780 and its control console) is illustrated. The vacuum controls can be operated from any one of the central-control-console/VAX combinations. Local control is also provided in each geographically distinct area of the Nova laboratory building to allow control during maintenance. Backup auxiliary controls are provided to ensure safety and system integrity during failures of the main control systems. Using the base-line design shown in Fig. 2-187, we have developed a design for the vacuum controls on the basis of the following criteria:

- Modular hardware and software will be used as far as is practical.
- All vacuum-pressure gauges and controllers will be standardized.
- All control and status functions will be performed via a color-interactive (touch panel) graphics-display console. Through a series of menus, sub-menus, and graphic

Fig. 2-187. Block diagram of portion of Nova centralized vacuum-system architecture; sensors and state inputs are at upper left, and all controlled devices are at right.

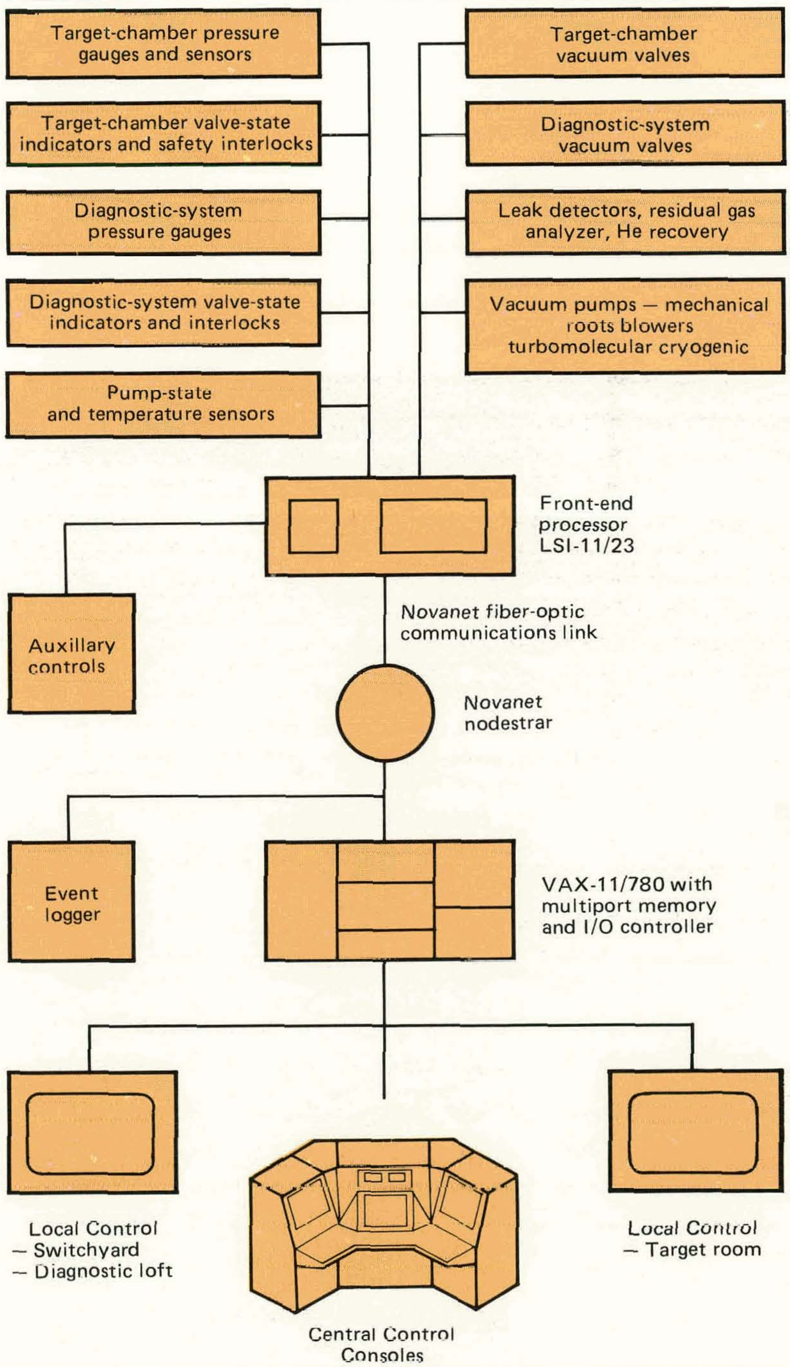

schematics developed in software, a series of "soft" control panels will be implemented. Touch points, located on the graphics display, will coincide with control and command functions.

- The entry of new or changed commands and control functions will also be performed via the graphics-display console, eliminating the need for major software reprogramming for functional changes.
- This will also eliminate the need for specialized control panels for each diagnostic subsystem.
- All programming will be done in the new Praxis language[82], a strongly typed and modular language.
- For safety, and to extend the lifetime of some of the more-delicate diagnostics, we are implementing a positive system-state indication feature. A separate switch for each controlled item (such as a vacuum valve) will be provided to indicate the absolute state of the equipment (valve open or closed).
- Additional safeguards include personnel interlocks to the target chamber to prevent the operation of any potentially hazardous equipment during entry. In the event of power failure or extended interruption of service, all equipment will be automatically put into a safe condition.

We completed the preliminary system specifications during the final quarter of 1980. The final hardware and software design should be completed in the first quarter of 1981.

Beam Focusing. Our baseline design was modified slightly in 1980 to use 800-mm-diam f/3.5 lenses with 74-cm clear apertures. Each lens will be supported by a three-axis manipulator, with all components outside the vacuum chamber, as shown in Fig. 2-188(a). The vacuum window is in the converging beam between the lens and the target. Because of this, its laser light fluence will be higher than that of the lens. At f/3.5 the increase is about 14%, which is tolerable. Should we wish to increase the speed of the lens to the f/2 range, however, as will be the case with Novette, the loading on the window will become unacceptably high. Therefore, we have looked at alternative ways of placing the lens inside the vacuum. To avoid contamination of the vacuum chamber and to enhance servicing and reliability, all electrical and mechanical components should still remain in the air. The preferred configuration, shown in Fig. 2-188(b), will be implemented for the Novette laser.

In the event that a future upgrade includes frequency conversion to 2 or 3ω, we must consider that the damage resistance of glass and its nonlinear refractive index will, respectively, decrease and increase drastically with the increased fluence. These conditions dictate that

- We have an absolute minimum of increased fluence, since there is glass in the converging beam.
- We minimize the amount of glass in the beam path, after the frequency-conversion crystals.

Both conditions can be met by combining functions, i.e., by letting the lens also serve as the vacuum barrier. This arrangement requires that we seal the lens to the chamber with a flexible bellows and that the lens positioner be capable of moving the lens precisely under the 6000-kg force of the external air pressure. Initial studies show that we can accomplish this task, as shown in Fig. 2-188(c). The price is higher cost, larger size, and greater complexity. This option can also incorporate frequency-conversion crystals as an integrated unit, should this be desirable, and can be fitted to the chamber as the 2 and 3ω conversions come on line.

Target Support. To support targets in the chamber, we will use a remotely controlled positioner, with four degrees of freedom, that will put them within 5 μm of the desired location. Controls for the target positioner will be integrated into the Novalink control system. Provision will also be made for handling cryogenic targets (and maintaining them in the frozen state) throughout installation, alignment, and exposure.

Target Alignment. We have a four-step plan for aligning the laser beams to the target:

- First, a surrogate target is placed in the geometric center of the chamber. Since all target diagnostic sensors are aligned precisely to that point, the location must not vary from shot to shot.
- Second, all beams are focused to this center position by means of lens positioners, which are guided by images

reflected from a spherical surrogate target into the output sensors or by images recorded directly on a CCD array used as a surrogate target.

- Third, the focal points are repositioned to various locations defined by the specific target to be irradiated. Each lens can be individually positioned to any spot within a 2-cm-diam sphere.
- Fourth, the surrogate is replaced by the actual target. Its position must be identical to that of the surrogate—within 5 μm of true center, as verified by a reliable optical instrument.

The center of the target chamber will be established by the intersection of three optical lines of sight, as defined by three optical telemicroscopes—called target alignment and verification instruments (TAVI). Basic criteria for the TAVIs were established in 1980. These instruments will be installed on very rigid mounts and aligned to a common center. They must then retain that alignment under long-term conditions of vacuum or atmospheric pressure, thermal shock from high-yield targets, and accidental impacts during normal operations.

Fig. 2-188. Nova laser beam-focusing options.

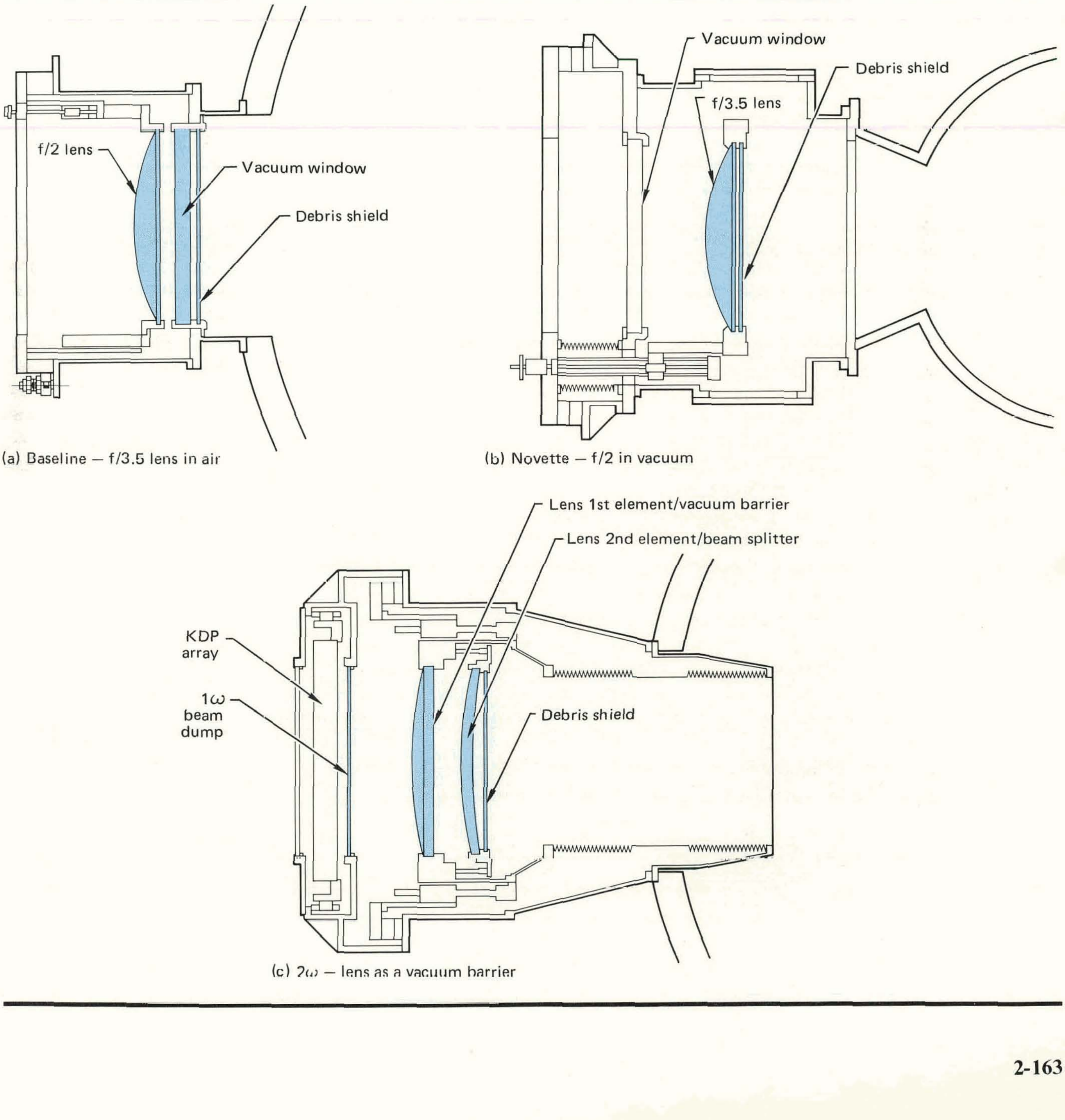

The TAVIs must have a field of view that will adequately cover all foreseeable targets and surrogates, as well adequate resolution for positioning them to within 5 μm of the true center. We will use a CCD camera with an active area of 7.5 by 9.8 mm and a resolution of about 60 m, so we will need variable magnification for viewing targets. Magnifications of 1/4, 1, 4, and 16 will be available through a turret-mounted lens system.

Our concept for meeting the Nova requirements has evolved by extending Shiva designs in light of our operating experience. The resulting concept of integrated TAVIs, as installed on the target chamber, can be seen in Fig. 2-184. The schematic diagram in Fig. 2-189 shows a cross-sectional view of the main subunits in a single TAVI—an optical transfer, an image-viewing stage, and a control assembly.

The optical transfer requires maximum stability, which is accomplished by building the relay structure as a single unit and by mounting it ruggedly, coupled closely to the target chamber. It is completely within the vacuum and is isolated from the housing, which also provides protection from unauthorized adjustment and accidental impact during operations. To add rigidity to the housing and to conserve space in the experimental area, the optical path is folded. The method used to accomplish this also yields an annular beam, which eliminates on-axis reflection highlights.

The optical transfer will form a full-size image of the target on a reticle, all within the vacuum. The image will be viewed through a vacuum window by the image-viewing stage.

In response to electrical commands, the image viewing stage will move in three axes—within a 25-mm-diam by 25-mm-long volume—to measure target image features at the various magnifications. The CCD camera will move with the turret, thereby maintaining alignment and focus at all positions in the image volume. Small variations in magnification with axial distance (and other distortions) will be compensated for by the microprocessor control system, which will service all command and status-reporting functions.

Target illumination will be provided by a small He–Ne laser, which will use beam splitters and the imaging optics to provide both front and back illumination. Beam intensity will be made continuously variable by means of rotating polarization plates. For back illumination, the annular beam will pass the target and be reflected by an annular mirror on the far side of the target chamber. The return beam, being directed precisely toward the TAVI objective, will be efficiently collected. The diameter and location of the front illumination beam will be controlled to illuminate only that portion of the target being imaged at the time.

A new feature of the Nova TAVI is the incorporation of interferometry to provide precise location in three axes. When a reflecting sphere is used as a surrogate target, the transfer unit can be operated as a spherical-wave interferometer. A spherical wave is introduced into the transfer unit by a

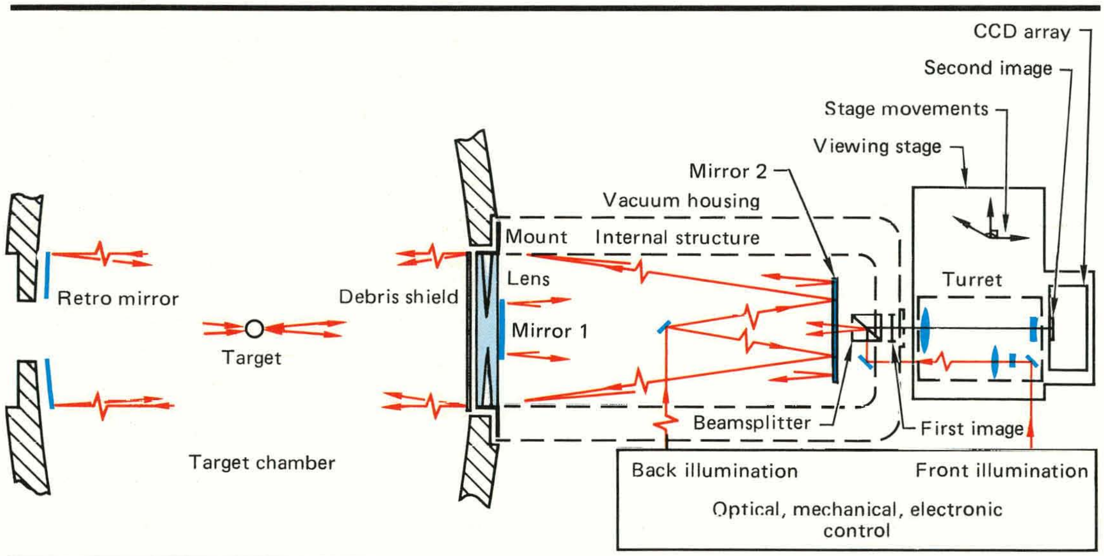

Fig. 2-189. Arrangement of Nova target-alignment and verification instrument (TAVI).

beam splitter located near the first image plane or reticle position. Fringes formed at the reticle by the reflected beam will be concentric when the sphere is axially aligned, and will become more widely spaced as the proper axial distance is approached. This concept will be experimentally verified in 1981.

Target Diagnostics. We have provided ports in the central ring and the hemispherical heads for an array of target diagnostics instruments. Instruments sensitive to neutron or gamma pulses will be located in the diagnostics loft, behind the concrete shielding wall, and will be connected to the target chamber by vacuum line-of-sight pipes. They include instruments with synthetic plastic fluors and photomultiplier tubes or fast electronic circuits (such as the filter-fluorescer detector and the high-speed streak cameras). Intrinsically hard instruments, such as the calorimeters and Dante fast x-ray detectors, can be mounted on shorter pipes, within the target room.

All ports will be precisely located in spherical coordinates.[83] In most cases, they will have a standard 8-in. i.d. to allow diagnostics to be interchanged between locations or even between different facilities, such as to Novette. Each instrument package will have a valve in the line-of-sight pipe to isolate it from the target chamber. Control of these valves will be integrated into the Novalink system. This will allow any component to be evacuated separately and help avoid vacuum accidents.

Target Diagnostics Data Acquisition and Control. Nova target diagnostics will provide target data-acquisition and control functions, as outlined in previous annual reports[84–86] for Argus and Shiva. CAMAC and LSI-11 interfaces will be used on most computer-controlled data-acquisition units. Our basic philosophy is to use standard acquisition and digitizing hardware from Shiva and Argus and to add hardware and software to integrate the target diagnostics into Nova's central controls. We will be supporting IEEE-488 Bus interfaces on Nova since many newer instruments use this standard computer interface.

Nova's target diagnostics differ in two major respects from those of Shiva and Argus. First, we are replacing our old Shiva CAMAC serial-highway link to the control room (at a 9600-bit/s rate) with Novalink interfaces.[87] This will be more compatible with other Nova systems; it will also provide 10^7 bits/s of data communications directly to the other processors (in particular, to the control-room VAX processors). Thus, the Nova system will allow more-rapid data acquisition and better real-time control.

The second major difference will be the extensive use of the Praxis language in the data-acquisition and control software. Our previous data-acquisition systems were written in various computer languages. These languages did not provide features conducive to modular programming with strong module bounds-checking. We believe that Praxis will enhance our program reliability while providing structured software interfaces for implementation of the target diagnostics.

The Nova target-diagnostics system will be operated primarily from the control-room consoles, using Ramtek touch-activated, color-graphics screens. The system will be experiment-oriented and menu-driven. The operator will first select an experiment type and then the diagnostics to be included in the experiment. Additions or deletions can then be made in the mix of acquisition modules for each diagnostic. An operator will be able to build an acquisition configuration from scratch or to use a file that describes a previous shot configuration.

Remote-control panels will also be placed in the diagnostics loft and in the switchyard near the target diagnostics, allowing operational checkouts to be performed locally. These remote panels will be interfaced to the control room, allowing the control-room computers to maintain the updated status of the entire system. Nova target diagnostics will rely heavily on the hardware and software tools developed by Nova central controls.

Radiological Analysis. To develop effective radiation protection,[88–90] we have examined neutron and photon dosimetry to determine the effects of pulsed radiation on instruments, shielding, dose contours, kerma factors for silicon and tissue, radiation flux densities along beam penetrations, and residual radioactivity in several materials that will be exposed to neutron radiation. In 1980 we examined the effects of radiation on

KDP crystals, as well as the effects of radiation leakage into the switchyard and laser bay through the 42-in.-diam holes.

Effects of Nova-Level Neutron Fluences on the Linear Optical Transmission Properties of KDP Crystals.[91] In three separate experiments at the LLNL Rotating Target Neutron Source facility (RTNS-II), we bombarded a 4.3 × 2.1 × 2.1-cm KDP sample with ten trillion 14.7-MeV n/s.

The total integrated fluence on the sample (from the three exposures) was 1.75×10^{15} n/cm^2. The transmission results, before the first and after the last exposure, are plotted in Fig. 2-190. We attribute the slight increase in transmission to surface scattering losses caused by "fogging" before the initial measurement. The only effect of the neutron exposure appears to be a slight decrease in transmission at about 360 nm. This will permit Nova II to operate at full performance (500 shots at 10^{19} n each) with no degradation in linear transmission.

Fig. 2-190. Linear optical transmission of KDP sample before and after exposure to 1.75×10^{15} n/cm^2.

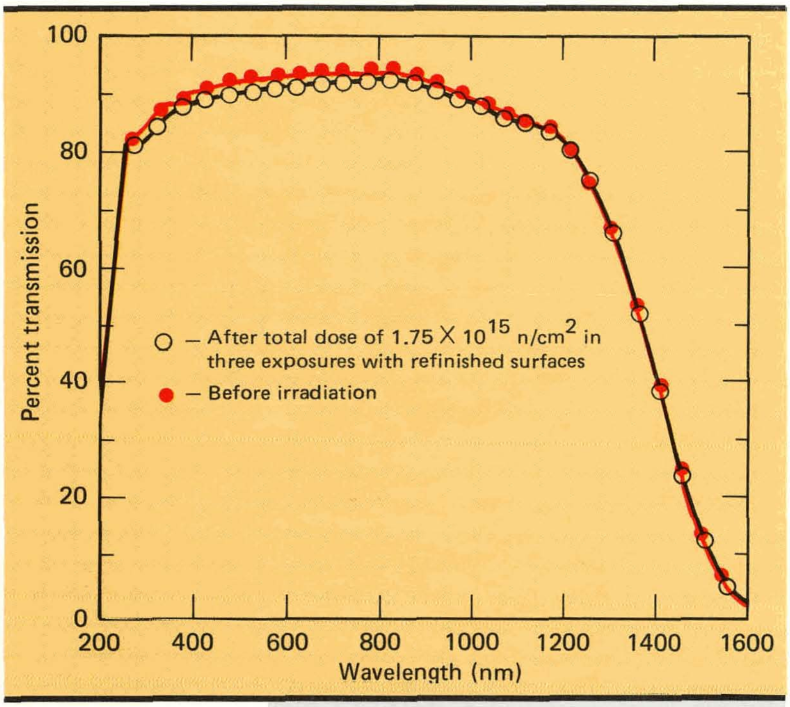

Neutron Energy Deposition and Residual Radioactivity Analysis. The energy imparted to the crystal during its bombardment with 14.7-MeV neutrons came from the recoiling nuclei, charged particles, secondary (de-excitation and radiative neutron capture) gamma radiation, and particle emission from the residual nuclei. The important neutron-induced reactions in KDP crystals are shown in Table 2-34. Our neutron-gamma transport and induced radioactivity calculations show that the particle emission from the residual nuclei contributed only about 1% of the total energy imparted to the crystal.

Table 2-35 is a summary of the energy imparted to the crystal. The RTNS-II fluence on the crystal is given for each exposure run. The Nova-equivalent pulse yield is calculated, assuming that the KDP crystal is exposed to the RTNS-II-equivalent fluence at a distance of 300 cm from the center of the Nova target. In 1981 we will evaluate the potential effects of the gamma radiation that will be produced in materials near the KDP plates.

Table 2-34. Important ▶ neutron-induced reactions in KDP crystals; excitation gammas are not shown.

Nuclear reaction	Half-life of product
^{2}H(n,γ)^{3}H	1.23×10^{1} yr
^{31}P(n,2n)^{30}P	2.50 m
^{31}P(n,γ)^{32}P	$1.43 \times 10_{1}$ d
^{31}P(n,p)^{31}Si	2.62 h
^{31}P(n,α)^{28}Al	2.31 m
^{39}K(n,2n)^{38}K	7.7 m
^{39}K(n,p)^{39}Ar	2.69×10^{2} yr
^{39}K(n,α)^{36}Cl	3.10×10^{5} yr
^{41}K(n,2n)^{40}K	1.26×10^{9} yr
^{41}K(n,γ)^{42}K	1.24×10^{1} h
^{41}K(n,p)^{41}Ar	1.83 h
^{41}K(n,α)^{38}Cl	3.73×10^{1} m
^{16}O(n,p)^{16}N	7.13 s
^{17}O(n,α)^{14}C	5.73×10^{3} yr

Table 2-35. Energy deposition in KDP sample during and after its bombardment with 14.7-MeV neutrons from the D–T reaction at RTNS II.

			Dose, rads[a]			
					Residual nuclei[b]	
Exposure No.	RTNS-II fluence (n/cm^2)	Nova-equivalent pulse (n)	Charged particles	Induced gammas	During irradiation	After irradiation
1	7×10^{11}	8×10^{17}	1.5×10^{3}	7×10^{1}	3×10^{1}	0.57
2	4.5×10^{14}	5×10^{20}	9.36×10^{5}	4.5×10^{4}	1×10^{4}	4.0×10^{2}
3	1.3×10^{15}	1.5×10^{21}	2.70×10^{6}	1.3×10^{5}	3×10^{4}	1.1×10^{3}
Total	1.75×10^{15}	2×10^{21}	3.64×10^{6}	1.75×10^{5}	4×10^{4}	1.5×10^{3}
	$\sum = 3.9 \times 10^{6}$ rads					

[a]Rad = 100 ergs/g of KDP.

[b]The induced radioactivity for a Nova pulse comes after the pulse.

After exposure to D–T neutrons, these materials will normally require a cooldown time before they can be handled safely. The external radiation levels from a KDP plate, exposed to 4.5×10^{14} n/cm^2, are shown in Fig. 2-191. A fluence of this magnitude, at 300 cm from the center of the target chamber, corresponds to a Nova shot with a yield of 5.7×10^{19} n. The isotopes produced in the crystal are almost exclusively beta emitters. Aluminum or glass that is one-half inch thick will reduce the external radiation levels by a factor of 300. Thus, maintenance operations on components near the KDP plates will not be affected by the induced activity in the crystals.

Radiation Leakage Through the 42-in.-Diameter Holes. Maximum neutron radiation will occur in areas that are on a line of sight with the target chamber. There are a number of 42-in.-diam beam penetrations through the north and east walls of the switchyard room, as illustrated in Fig. 2-192. The penetrations that result in maximum radiation in the laser bay are numbers 3 and 8, which are coplanar with the target. We made neutron-transport calculations to estimate the radiation levels at various locations inside and near these penetrations. The results (normalized to a 10^{17} neutron shot) are shown in Table 2-36. Our analysis of the other penetrations, including the diagnostic holes, will be completed in the near future.

Authors: F. Rienecker, Jr., M. S. Singh, J. R. Severyn, and R. J. Calliger

Major Contributors: M. A. Summers, R. A. Dickinson, E. A. Ries, J. F. Kane, C. B. McFann, R. K. Reed, C. E. Thompson, and J. Nemeth

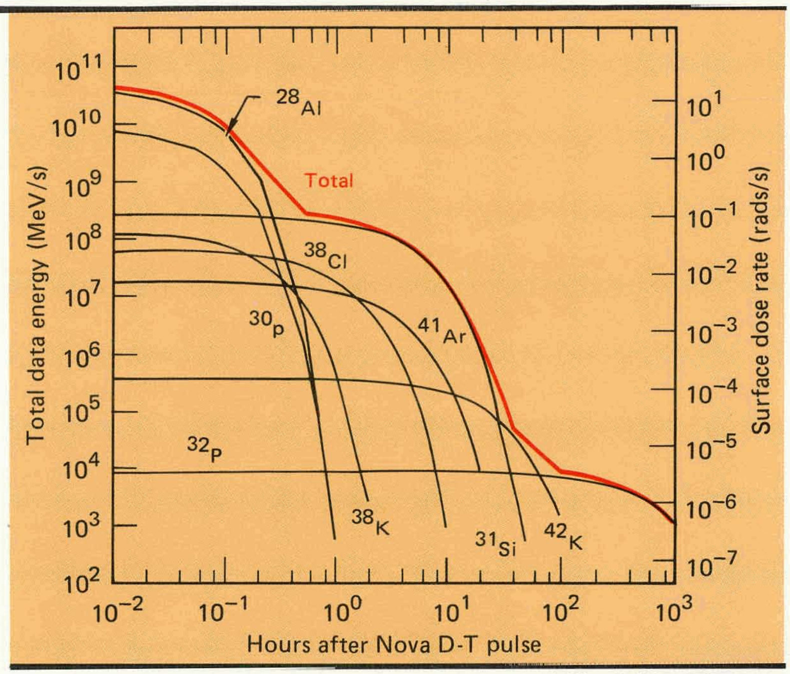

▲ **Fig. 2-191. Calculated residual energy and dose decay after a Nova shot yielding 5.7×10^{19} n.**

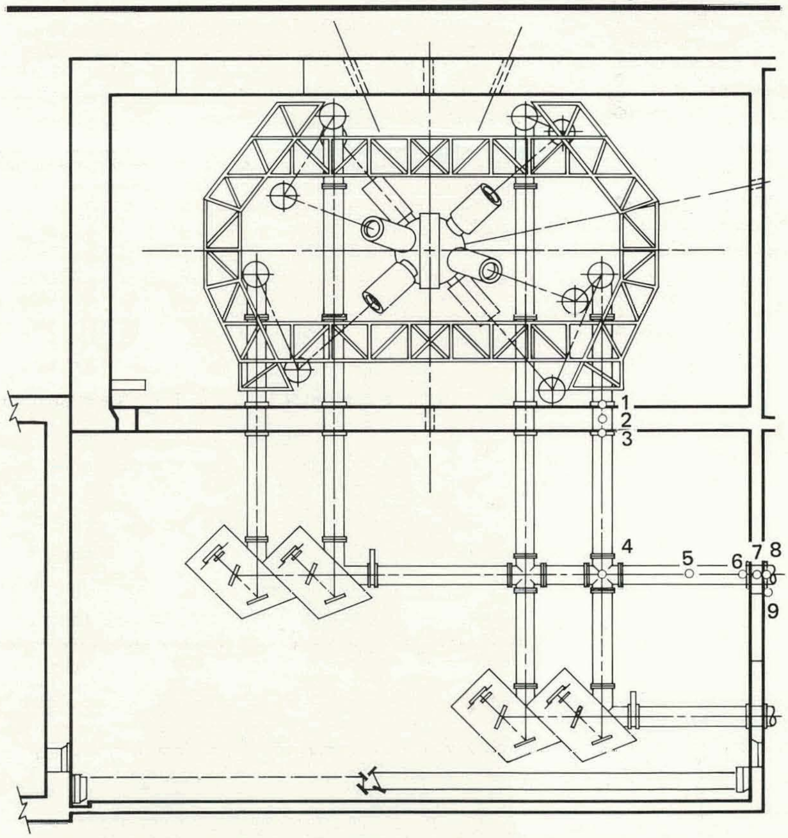

Fig. 2-192. Locations of estimated neutron radiation doses.

Location	Coordinates x	y	z	Dose (rem)
1	762	0	823	2.8×10^{2}
2	823	0	823	1.1×10^{2}
3	884	0	823	1.7×10^{1}
4	1590	0	823	9.2×10^{-2}
5	1590	0	1128	8.7×10^{-2}
6	1590	0	1524	2.3
7	1590	0	1555	2.5
8	1590	0	1585	1.1
9	1643	0	1585	6.4×10^{-1}

◀ **Table 2-36. Neutron-radiation doses inside the Nova facility from leakage through 42 in. diam penetrations 3 and 8, normalized to 10^{17} neutron shots. Locations of estimated doses are shown in Fig. 2-192.**

Conventional Facilities

The Nova conventional facilities are comprised of a laboratory building to house the laser, target chamber, and diagnostics facilities, of an office building to house 200 scientists and programmers, and of site facilities that provide functional services to both buildings.

The design for both buildings was completed during 1980, and the pace of construction increased for work started in 1979. (Previous annual reports describe the design philosophies and functional aspects of the laboratory building.[92,93]) Albert C. Martin and Associates of Los Angeles, Calif. continues as architect–engineer for facility design, and Kaiser Engineers of Oakland, Calif. continues to provide construction-management services for construction contracts let by the San Francisco Operations Office of the DOE. Construction of both buildings continues in a fast-track design/build mode.

Figure 2-193 shows a recent overall view of Nova construction progress through December 1980. Building 391, Increment II, is in the background, and the office building is in the center foreground. (Note the second-floor bridge at left that connects the new and old office buildings.)

Laboratory Building (Building 391, Increment II). We completed the design for the laboratory building and awarded the remaining building-construction contracts. These contracts, which comprised about half of the construction-dollar commitments, included

- Interior building finish.
- Building mechanical.
- Building electrical.
- Fire protection.
- Roofing systems.

All contracts were formally advertised and competitively bid in fixed-price, lump-sum

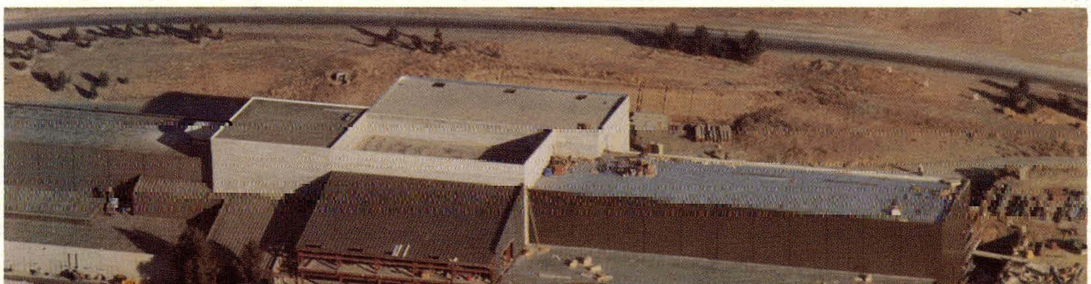

Fig. 2-193. Overall view of Nova construction site, looking to the northwest.

dollar amounts. In most cases, we found the bidding climate favorable, resulting in substantial competition and fair prices. Table 2-37 lists the laboratory-building contractors and current contract values.

Construction continued at a good pace throughout the year with minimal weather delays, and physical completion increased from 16% at the start of the year to 64% at year's end. The structural concrete and steel work were completed, along with the underground mechanical utilities. With the application of metal siding and roofing, including built-up roofing, the building was substantially closed in. This allowed the contractors to proceed with normal interior work, such as rough electrical work, plumbing, piping, fire protection, ductwork, masonry, and stud walls. Application of a plaster skim coat was started to seal the concrete-walled areas that have been designated as clean rooms. Most mechanical-equipment items—pumps, chillers, fans, air handlers, and cooling coils—were delivered on site. All four bridge cranes were installed, but final testing and checkout remain to be accomplished. Work proceeded on each of the eight different-sized shielding doors, with all shielding door frames placed and concrete backfill completed for some of the frames. The tracks for the rolling shielding door into the target room were completed. (This unique door will provide the 6-ft shielding thickness required for the 20-by-20-ft target-room access opening. It has two major moving parts, contains 155 cubic yards of concrete, and weighs 642 000 lb.)

Figure 2-194 illustrates the overall progress on Building 391, while Figs. 2-195 and 2-196 indicate the progress in some of the principal building areas. The existing

Table 2-37. Laboratory-building contractors and current contract values (as of December 1980).

Contract No.	Contract title	Contractor	Contract amount ($K)
1	Earthwork	Ford Construction Co.	401
2	Structural Steel and Metal Decking	Riverside Steel Construction Co.	1080
3	(Not used)		
4	Structural Concrete and Backfill	Peter Kiewit Co.	3767
5	Bridge Cranes	Sierra Crane & Hoist	408
6	Shielding Doors	Overley Mfg. Co.	974
7	Underground Mechanical Utilities	Pacific Mechanical Co.	610
8	Underground Electrical Utilities	Del Monte Electric Co.	1071
9	Building Mechanical	Scott Co. of Calif.	6412
10	Metal Siding and Metal Roofing	Peterson Construction Co.	547
11	Miscellaneous Metals	Pan American Steel Co.	177
12	Building Finish and Painting	C. Overaa Co.	1521
13	Building Electrical	Ferrero Electric Co.	1558
14	Access Flooring	J. L. Whittaker Co.	266
15	Built-Up Roofing	Enterprise Roofing Co.	160
16	Laser Beam & Diagnostic Hole Drilling	Penhall Co.	311
17	Fire Protection	Grinnell Fire Protection Systems Co.	341

Fig. 2-194. Nova laboratory Building 391, Increment II, showing progress to December 1980; the existing Shiva building at left is dwarfed by the Nova lab.

Shiva building is at far left in Fig. 2-194, while the installed bridge cranes are visible in the laser bay shown in Fig. 2-195. Note the laser-beam tube openings in the far wall of the laser bay and the ventilation openings penetrating the concrete-block wall at top and bottom right. In Fig. 2-196, the shielding-door locations appear at the first-floor and gallery levels, while the right wall shows the 42-in.-diam laser-beam tube openings to the Nova target room. Additional details of the laboratory building are available in other documentation.[93]

At year's end, we developed construction-contract documents for drilling laser-beam and diagnostic holes. The unique aspects of this work include precise alignment for radial drilling of 18-in.-diam diagnostic holes through 6-ft-thick concrete walls from the laser target location. Proposals for drilling these holes are due early in 1981.

Our contract construction work is now projected for completion at the end of November 1981, which is consistent with Laser Program (Special Facility) planning projections. Our current baseline budget for the laboratory building (developed in October 1980) is $23.8 million, including all engineering, construction, construction management, activation, and standard equipment.

Office Building (Building 481). This year we completed final design of the office building. The plan for the final space arrangement is shown in Figs. 2-197 and 2-198. The renderings for the building exterior are available from a separate source.[93] We also awarded five building-construction contracts in 1980 (Table 2-38), with each contract formally advertised, bid, and awarded as a fixed-price, lump-sum contract.

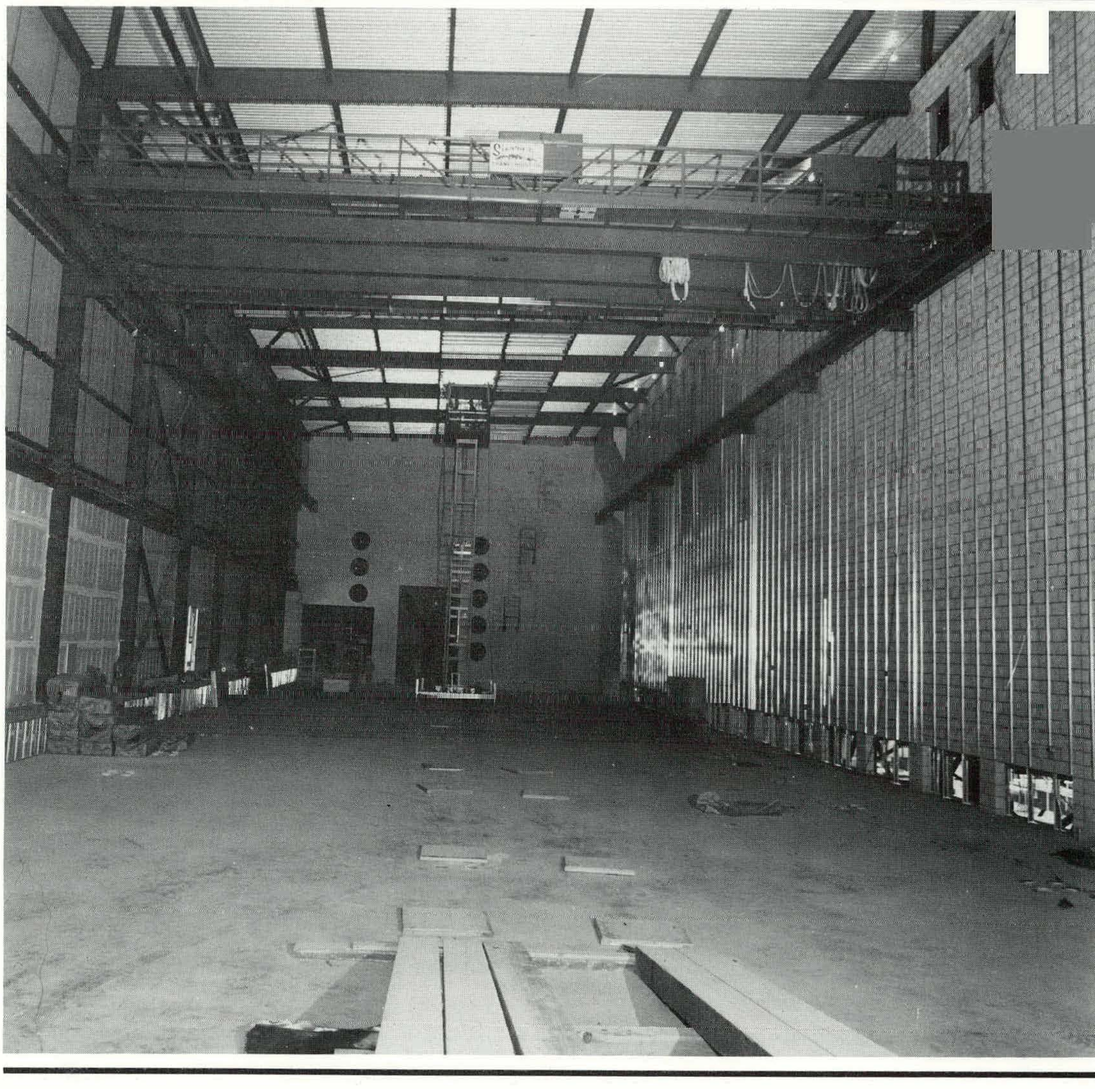

Fig. 2-195. View of the laser bay, looking toward the optical switchyard.

We continued to develop site-work requirements like pathways, parking, roadways, and site drainage to meet established budget limits. This contract package will be finished in 1981.

We also continued to evaluate furnishing needs. The furnishings will be ordered in 1981, allowing sufficient time for delivery prior to building occupancy.

In 1979 only isolated concrete footings were poured on the building pad. This past year we completed the structural concrete work, which consisted of the two towers and shear walls in the central core of the

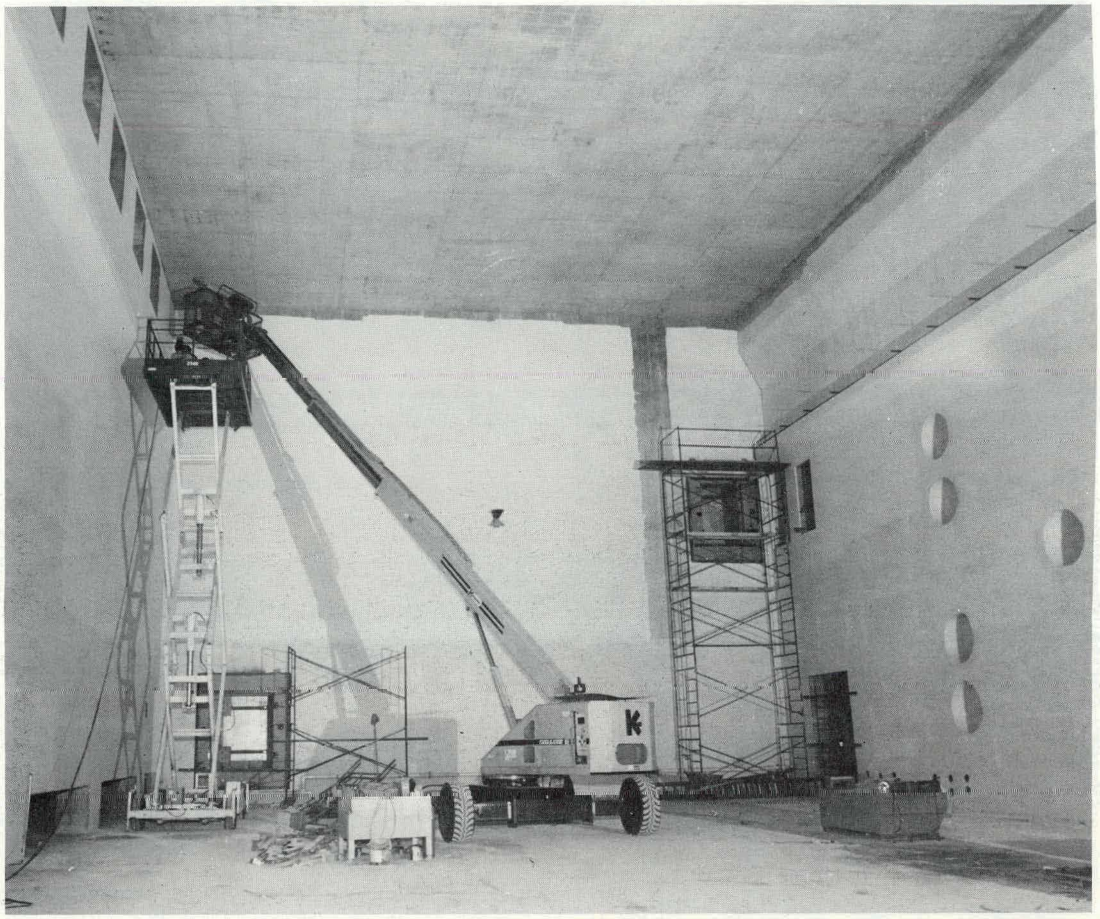

Fig. 2-196. Optical switchyard, showing ventilation openings at top and bottom of left wall.

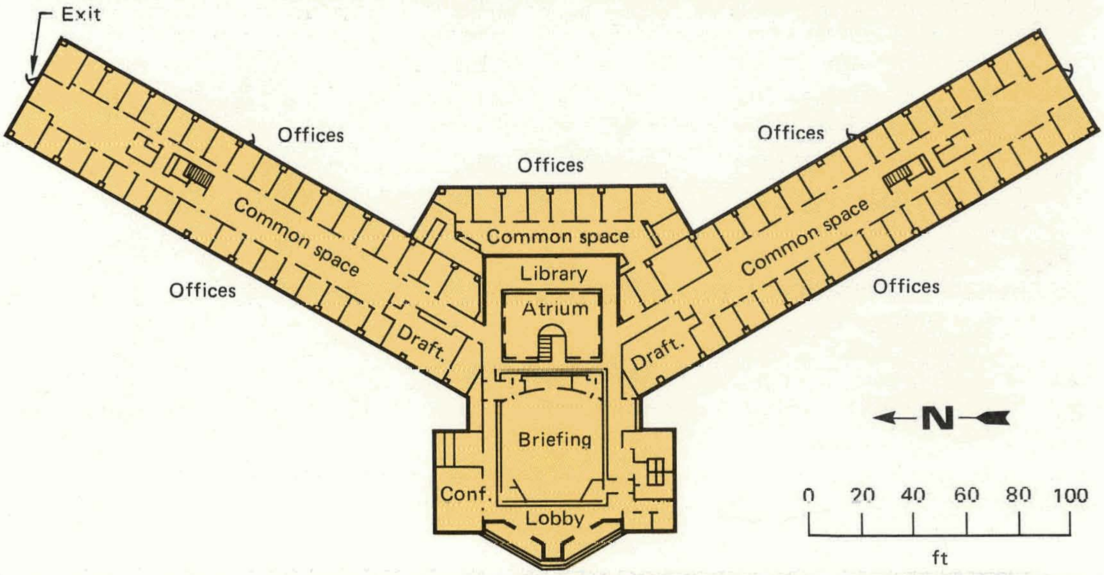

Fig. 2-197. Ground-floor layout of Nova office building.

Fig. 2-198. Second-floor layout of Nova office building.

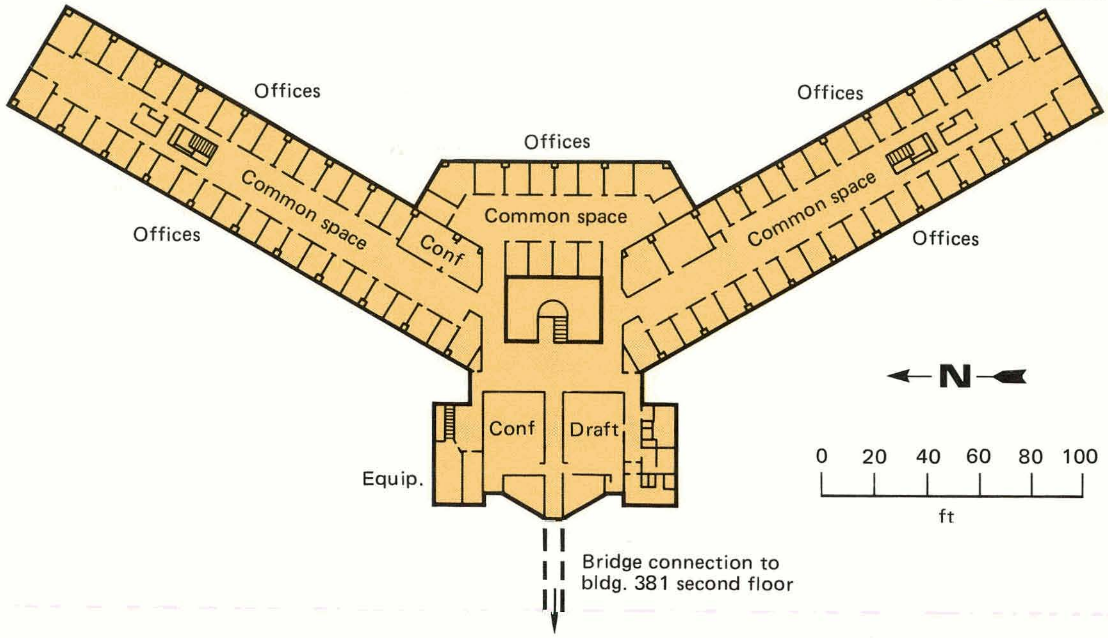

Table 2-38. Office-building contracts awarded in 1980 and current contract values (as of December 1980).

Contract No.	Contract title	Contractor	Contract amount ($K)
0-1	Structural Concrete	California Engineering Contractors	280
0-2	Structural Steel	Adams & Smith, Inc.	743
0-3	Building Electrical	Del Monte Electric Co.	774
0-4	Building Finish	J&K Builders, Inc.	3442
0-5	Building Mechanical	Lawson Mechanical Co.	1246

building. We also completed the structural steel work for the building frame so that follow-on contractors could start work. By year's end, we were preparing to pour the second-floor concrete decks. In the meantime, underground mechanical utilities had been substantially completed, and the installation of ventilation ducts, interior plumbing, and piping was started. Physical completion at the end of the year was 28%. Figure 2-193 shows the extent of construction completed on the office building near the end of the year. At this stage, the structural frame, metal floor, and roof decks are complete. (The concrete towers at center left will house mechanical equipment in the upper level.)

We expect to complete construction by the end of 1981 and to occupy the building in December. Our baseline budget for the office building (updated in October 1980) is $8.6 million and includes all engineering, construction, design and inspection, construction management, activation, and standard equipment.

Authors: C. P. Benedix and R. J. Foley

Project Management Systems

The Nova financial-planning and tracking system is in place and functioning smoothly and efficiently. We are supplementing this system with a schedule-control system, which will be especially useful during the assembly and activation phases of the project. This scheduling system emphasizes planning and control through time (rather than cost) variances. The complementary nature of the two systems provides an integrated and complete set of project management tools. We describe our progress with these bimodal systems in the articles that follow. We also describe the evolution of our integrated quality and safety assurance plan in terms of its implementation and effectiveness to date. The work-breakdown structure (WBS) for Nova is shown in Fig. 2-199. The financial-planning and tracking system, scheduling system, and quality-assurance system all use this structure.

Financial-Planning and Tracking System. The Nova financial planning and tracking system has three objectives:

- To ensure the development of accurate and optimum baseline plans showing time-phased costs by means of computerized procedures that allow for rapid and accurate revision of baseline cost schedules.
- To provide performance-measurement tracking reports that highlight deviations from planned dollar amounts and from planned times of expenditure for both commitments and costs by means of an integrated and uniform set of graphic tracking reports for all levels of the WBS. A schematic of the Nova financial processing system, showing the financial-planning and tracking phases, is given in Fig. 2-200.
- To provide a project accounting system based on the WBS that is consistent with the LLNL accounting system and that satisfies the requirements of the project office, LLNL, and DOE.

All manual and computer-processing procedures necessary to achieve the system objectives were in place by the end of 1979. We used these procedures during 1980 and found them to be very effective in maintaining a sound financial basis for the project and for providing good visibility about the project's financial status. At the end of October 1980 we established a new baseline plan based on markups of the previous baseline. The new baseline was established because FY81 funding was provided at $25 million, rather than the $43 million under which the old baseline was predicated. Also, the $25 million was made available in the fourth quarter of the fiscal year. In the interim, we had to plan on the basis of $0 million for FY81. The replanning procedures of the Nova planning and tracking system allowed us to establish and implement the new baseline in a timely manner.

We prepare the following key financial reports monthly:

- Performance-measurement graphs.
- Financial status report.
- Procurement tracking report.

The performance-measurement graphs are prepared at levels 0, 1, 2, and 3 for special facilities (laser) construction. For conventional facilities (buildings) construction, we also prepare performance-measurement graphs at level 4, showing financial

Fig. 2-199. Nova work-breakdown structure (WBS), shown down to level 3.

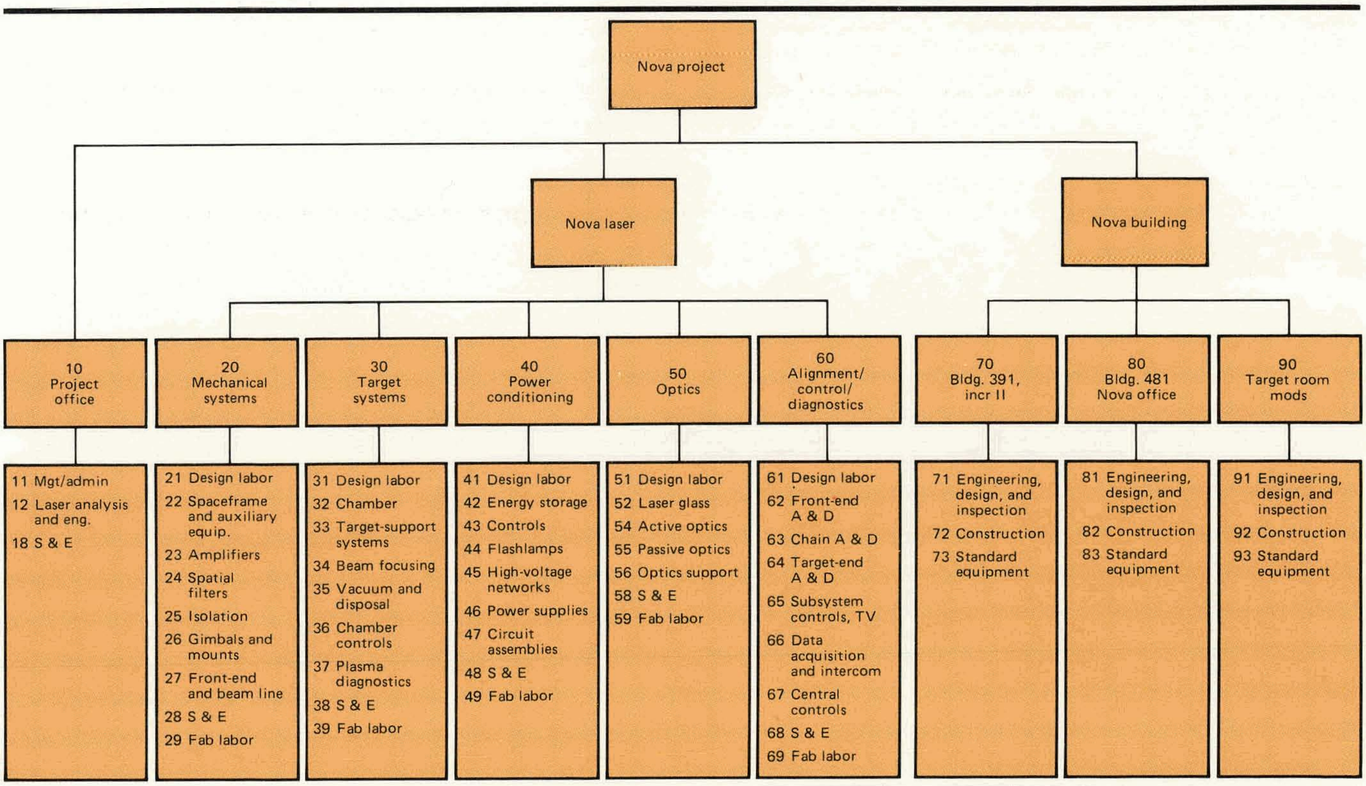

Fig. 2-200. Schematic of Nova financial processing system, showing financial-planning and tracking phases.

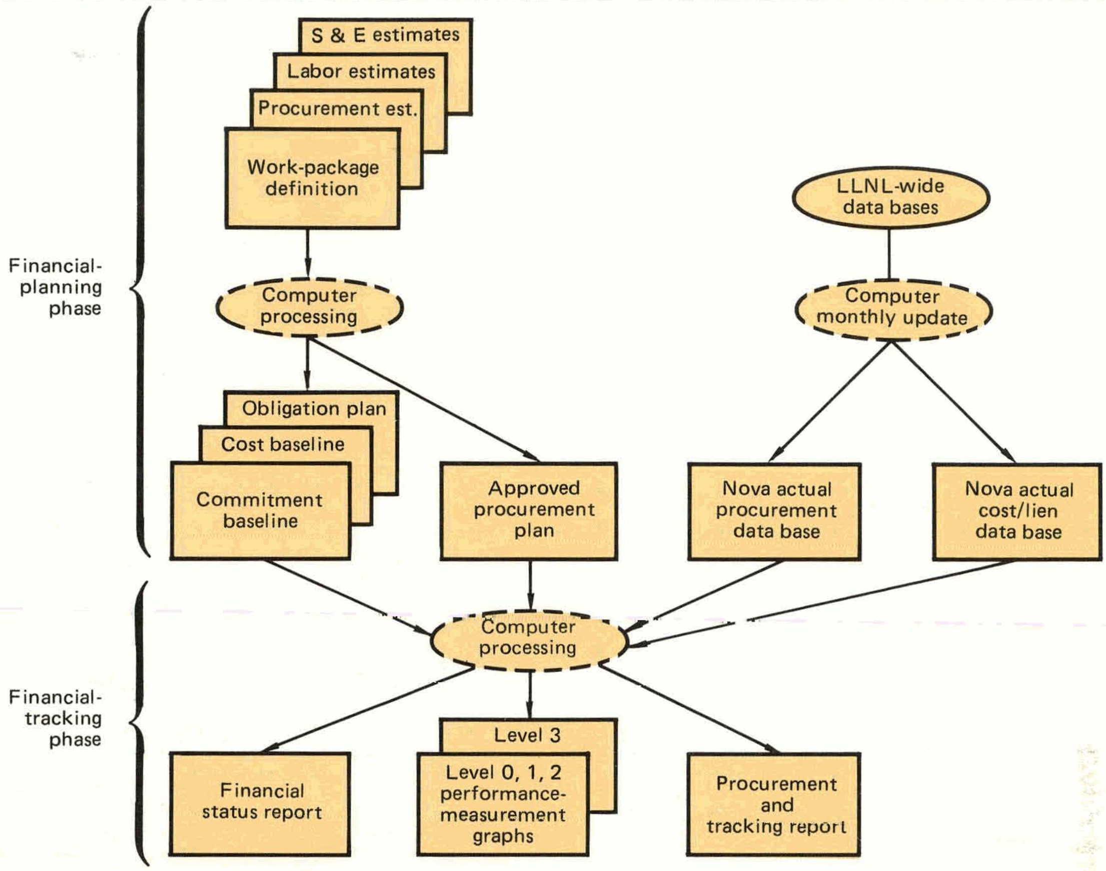

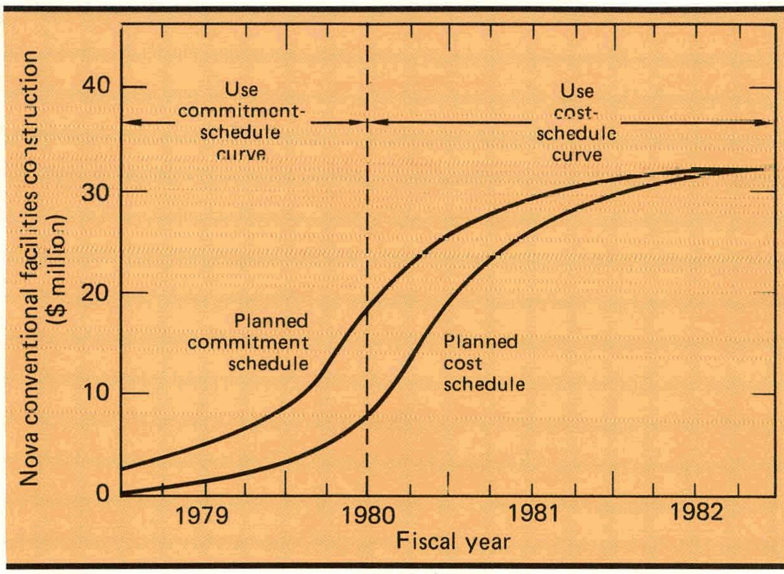

Fig. 2-201. Cost and commitment schedules for conventional construction.

performance for each major construction contract. During 1979, in financial deviations due to schedule for both special and conventional construction could be evaluated from an inspection of the commitment performance curves. Both level-1 WBS tasks were in the same design and procurement award phase in FY79. During 1980, however, the conventional construction task entered the delivery and construction phase while special-facilities construction remained in the design and procurement award phase. Figure 2-201 shows superimposed cost and commitment schedules for conventional construction, indicating the period for which each curve would be appropriate to measure financial deviation due to schedule. Figure 2-202 shows the same information for special-facilities construction.

The following figures illustrate the monthly performance-measurement graphs that we supply to DOE:

Figure	Report
2-203	November 1980 Total Project Commitments
2-204	November 1980 Special Construction Commitments
2-205	November 1980 Conventional Construction Costs

Figure 2-203 is the summary commitment variance financial report for the project for November 1980, as measured against the new October 31, 1980, baseline. Figures 2-204 and 2-205 are the summary schedule variance financial reports we prepare separately for special-facilities and conventional construction. An example of the financial status report is given in Fig. 2-206, and an example of the procurement planning and tracking report is given in Fig. 2-207.

The Nova financial-planning and tracking system is consistent with the LLNL accounting system and is designed within the framework of the Nova WBS, shown in the previous section. A single prime account, 7520, was established for Nova, and subaccounts were assigned as shown on the WBS; for example, subaccount 32 is used for level-3 costs associated with the target chamber. For procurements, Nova extends the LLNL accounting system to levels 4 and 5 by assigning a Nova control number to all purchase orders. A table of purchase orders vs Nova control numbers is then used to identify each monthly purchase-order charge at level 5 of the WBS. Procurement baselines are established at levels 4 and 5, and procurements are tracked at level 5 by noting deviations from estimated amounts and times of procurement.

The system incorporates both a financial-planning and tracking phase. The financial-planning phase occurs each time new cost baselines are prepared, which is done whenever

- A significant change in the technical scope of the project is authorized.
- A significant change occurs in the funding schedule.
- An allocation of contingency funds is authorized.

The financial-tracking phase involves monthly updates of commitments, costs, and

Fig. 2-202. Cost and commitment schedules for special-facilities construction.

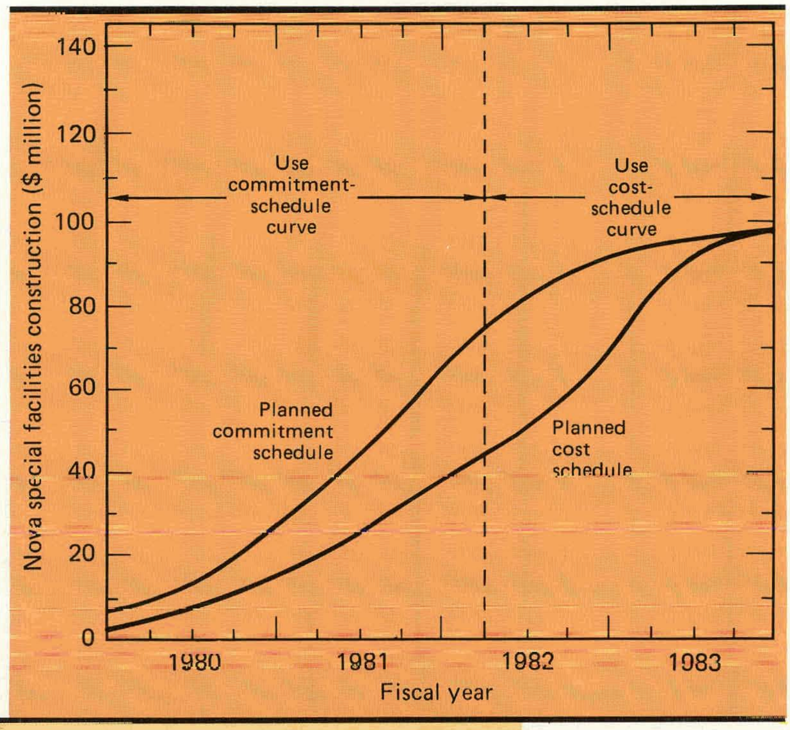

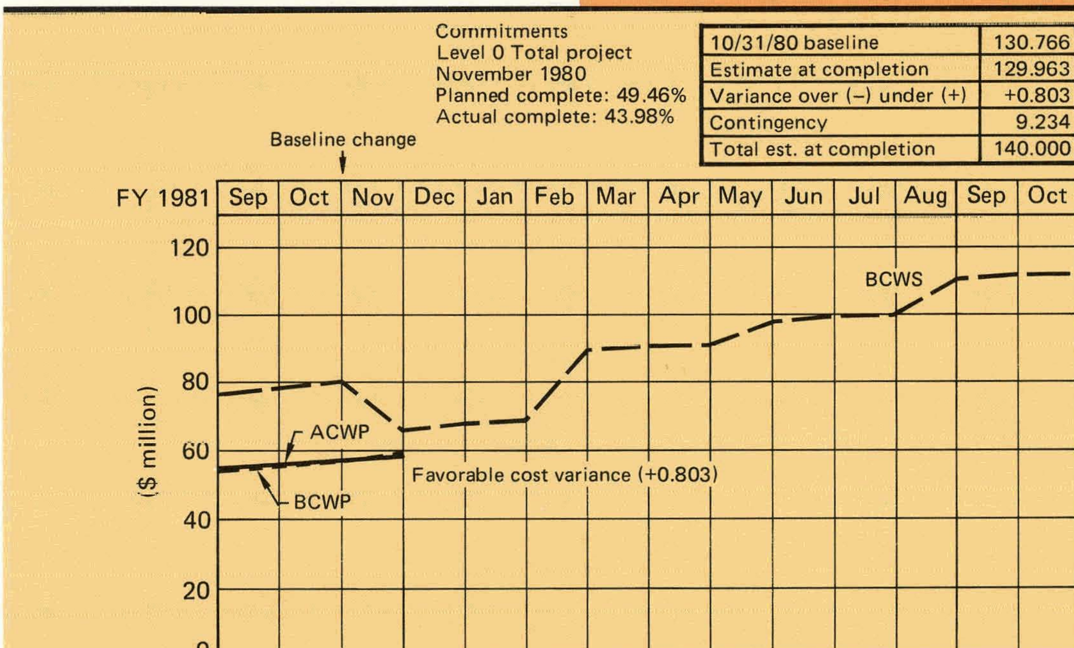

10/31/80 baseline	130.766
Estimate at completion	129.963
Variance over (–) under (+)	+0.803
Contingency	9.234
Total est. at completion	140.000

FY 1981	Sep	Oct	Nov	Dec	Jan	Feb	Mar	Apr	May	Jun	Jul	Aug	Sep	Oct
Schedule variance	–22.878	–23.730	–6.430											
BCWS	78.229	80.257	65.758	67.944	68.620	89.473	90.963	91.429	98.437	99.653	100.43	111.28	112.39	112.98
BCWP	55.351	56.527	59.328											
ACWP	56.373	57.479	58.525											
Cost variance	–1.022	–0.952	+0.803											

Fig. 2-203. Scheduled commitment of funds at level 0 (total project) for FY81.

obligations against the baseline plans. Performance-measurement graphs are prepared down to level 3, and detailed cost and variance reports are prepared down to level 5 for procurements.

Two interesting operational features of the Nova planning and tracking system should be noted. First, all input, output, and update of the project's financial data bases is done locally in the project area, using HP 2645A computer terminals linked to the LLNL Octopus network. Data-base update is done directly with the split-screen, data-revision feature of TRIX, with verification

Commitments
Level 1 special construction
November 1980
Planned complete: 35.61%
Actual complete: 28.14%
Baseline change

10/30/80 baseline	98.432
Estimate at completion	98.435
Variance over (−) under (+)	−0.003

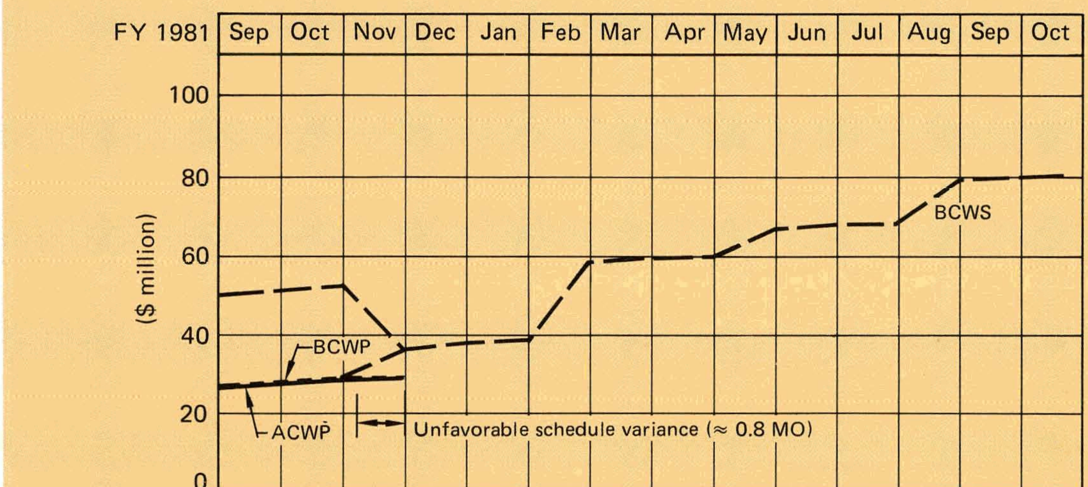

	Sep	Oct	Nov	Dec	Jan	Feb	Mar	Apr	May	Jun	Jul	Aug	Sep	Oct
Schedule variance	−23.652	−23.181	−6.619											
BCWS	51.707	52.373	36.139	38.022	38.449	58.632	59.669	60.087	67.043	68.214	68.712	79.462	80.486	80.989
BCWP	28.055	29.192	29.520											
ACWP	27.801	28.866	29.523											
Cost variance	+0.254	+0.326	−0.003											

Fig. 2-204. Scheduled commitment of funds at level 1 (special-facilities construction) for FY81.

Costs
Level 1 conventional construction
November 1980
Planned complete: 46.35%
Actual complete: 46.45%
Baseline change

10/30/80 baseline	32.334
Estimate at completion	31.528
Variance over (−) under (+)	+0.806

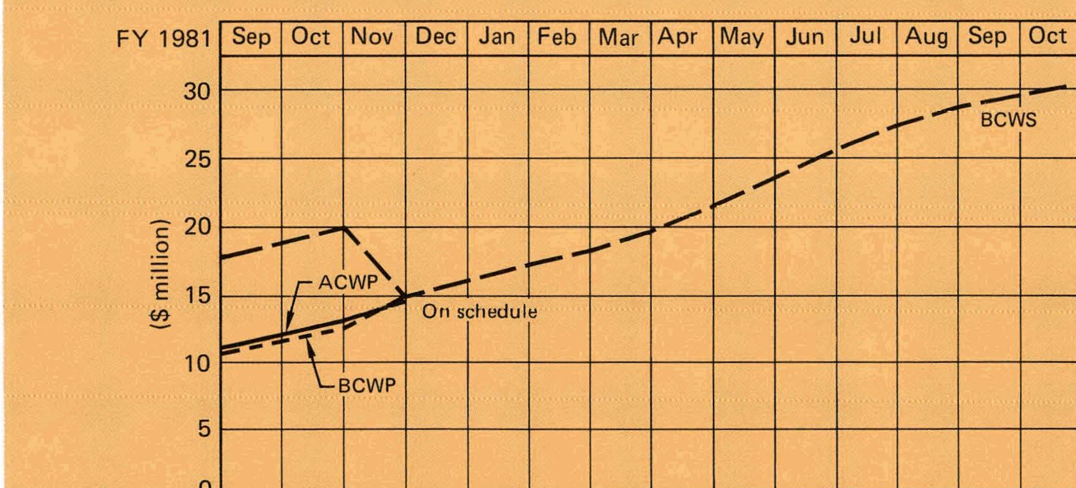

	Sep	Oct	Nov	Dec	Jan	Feb	Mar	Apr	May	Jun	Jul	Aug	Sep	Oct
Schedule variance	−7.322	−7.408	+0.033											
BCWS	18.967	20.014	14.987	16.052	17.269	18.293	19.767	21.589	23.654	25.690	27.604	28.946	29.889	30.567
BCWP	11.645	12.606	15.020											
ACWP	12.098	13.083	14.618											
Cost variance	−0.453	−0.477	+0.402											

Fig. 2-205. Scheduled costing of funds at level 1 (conventional construction) for FY81.

by bottom-line audit. The graphic financial reports are generated via the LLNL Octopus high-speed printer. We designed our financial data-processing system in this distributed fashion to ensure that the system remains user-oriented and responds to the dynamic financial processing needs of the project. Second, a special file of actual project costs and liens is maintained in a form consistent with the WBS organization of the project. This file is updated monthly, using the transactions of the LLNL detail ledger file. We made provision at the local project level to allow zero-sum data-base cost adjustments within the project WBS structure. This distributed cost-accounting approach allows us to compare actual costs against planned costs at the purchase-order level of our WBS. It also provides for treatment of diverse labor and procurement costs within the WBS framework.

The planning phase has formal procedures to ensure that baseline cost estimates are accurate. Standard forms for collecting cost and schedule estimates were designed to interface with computer programs that analyze the data.

Each time replanning occurs, computer codes are used to price the revised labor and procurement estimates. All planned expenditures are priced at the time of expected commitment of funds, using appropriate inflation-related escalation factors.

Fig. 2-206. First page of Nova financial-status report, shown for the Optics section of the WBS.

NOVA PLANNING & TRACKING — F I N A N C I A L S T A T U S R E P O R T — LAWRENCE LIVERMORE LABORATORY
DETAIL REPORT DPS JOB 72503 COSTS THROUGH NOV 80 H = K$ X 100 M = K$ X 1000 11:02:26 R 12/22/80 PAGE 21

INPUT FILES USED - - COST1215 PICB1212 S80WBS1FH PROC3SD RATE1218

WORK BREAKDOWN				PLANNED/ACTUAL K$ COSTS				K$ COST/DELIVERY SCHEDULE										
		SCHED VAR	BASE/LATEST	PLAN	/PEND/	OBG	COST	PRI	XXXX	SEP	OCT	NOV	DEC	JAN	FEB	LP81	FY82	AFT
5	OPTICS		27302/ 27306	13643	570	5446	6629	‹XXXXXXXXXXXXXXXXXXXXXX										
5	SUM OF LABOR	12	2820/ 2817	1626			1191	1030		48	57	56	53	52	52	393	725	363
51	LABOR - DESIGN	19	1773/ 1770	848			922	812		34	39	37	31	30	30	214	375	187
50	LABOR - FAB	-7	1047/ 1047	778			269	218		14	18	19	22	22	22	179	350	176
58	S+E	18	314/ 314	157		8	149	108		18	10	14	6	6	6	42	74	41
5	SUM OF PROCUREMENTS		24168/ 24176	11860	570	5438	5290											
5FL	INC FUTURE LIENS		/ 1588		15881													

WORK BREAKDOWN					PLANNED/ACTUAL K$ COSTS				K$ COST/DELIVERY SCHEDULE										
ID	REQ. #	P.O. #			PLAN	/PEND/	OBG	COST	PRI	XXXX	SEP	OCT	NOV	DEC	JAN	FEB	LP81	FY82	AFT
52	LASER GLASS			9562/ 9652	7959	9	410	1283											
5200L	INC FUTURE LIENS			/		I													
5201			10-20 DISK GLASS		953												O	D	D
5202			31&46 DISK GLASS		6290												O	D	D
5203			LASER ROD GLASS		180												O	DD	
5204A			LASER ROD FIN		19								O				D	D	
5204B			LASER ROD FIN TOOL		6								O				D	D	
5206			LASER DISK TOOL		200								O			DD			
5207			PHOS. PROTO. 46 CM		246								O			DD			
5230A	629833	4115209	PROTO GL SCHOTT				105		427										
5340B	629833	4115219	PROTO GL HOGA				65		465										

Fig. 2-207. Sample page of Nova procurement-planning and tracking report.▼

1 NOVA PLANNING AND TRACKING — NOVA PROCUREMENT PLANNING AND TRACKING REPORT — LAWRENCE LIVERMORE LABORATORY
REPORT 3DT S80WBS1FH PROC3SDU OPTICS 12/12/80 DPS JOB 72503 PAGE 27

LEVEL: 3 WBS NAME: ACTIVE OPTICS NUMBER: 54 PROJECT ENGINEER: PERRY WALLERSTEIN

NOVA	ITEM	QUANTITY	PLAN $K	LATEST EST $K	MINR COMM	COMM VAR	COST VAR	S C	IC	REQN MOYR	FY80 1234	FY81 1234	FY82 1234	FY83 1234	FY84 1234	FY85 1234	FY86 1234	PROC CODE
5401A	FR5 MATL	12	594	593		1	1	A		979M	O · D - · · · · D						–	S
5410A	15 CM ROT	10	90	90		1	1		980	1280M		R O · D · · · D					–	A
5410B	15 CM POLAR	24	151	151		0	0		980	1280M		R O · D · · · D					–	A
5410Z	FAB-COAT. SPARES	0	70	70		0	0		980	1280M		R OD · · · D					–	A
5420	MOR FE	0	40	40		0	0		980	1280M		R O · D · D					–	A
5420A	YLF CRYS & RODS	0	37	36		1	0	A		980M		R O · D · D					–	A
	TOTALS FOR SUB-SYSTEM		982	980		2	1											

After each estimating and pricing cycle, the Nova project manager conducts budget-review sessions with the lead engineers to determine where budget adjustments are needed to enhance laser performance, to stay within budget, and to prepare for effective operation of the completed facility. The automated procedures include generation of a time-phased obligation plan that is consistent with the schedule of expected funding and probable contingency expenditures. Time-phased performance-measurement baselines are generated automatically from the budget plan for both financial commitments and costs.

To measure performance during the tracking phase, the Nova financial-planning and tracking system displays (both numerically and graphically) deviations from the baseline values. The level-2 and level-3 graphs are distributed monthly to each of the lead engineers responsible for a level-2 cost center. Each lead engineer also receives financial status reports and a detailed listing of costs charged that month.

Schedule Control. Two distinct characteristics of the Nova project have influenced our schedule-control strategy. First, like most large facility projects, Nova evolves through design, procurement, assembly, and activation phases before becoming an operational experimental facility. Second, it is a procurement-intensive project: 70% of its funds go to suppliers and subcontractors working under numerous lump-sum, fixed-price contracts. These two characteristics caused us to develop a bimodal scheduling system. During the design and procurement phases, we use the financial-planning and tracking system to track and control both cost and schedule. During the assembly and activation phases we will use the financial system for cost control, and the schedule-information system for schedule monitoring and control. This bimodal system uses network-based critical-path methods[94] that, in turn, depend on "events" and an "assembly-breakdown structure" (ABS) as the basis for tracking, controlling, and reporting on the schedule. (Events are here construed as intermediate milestones; they and the ABS will be defined more fully below.)

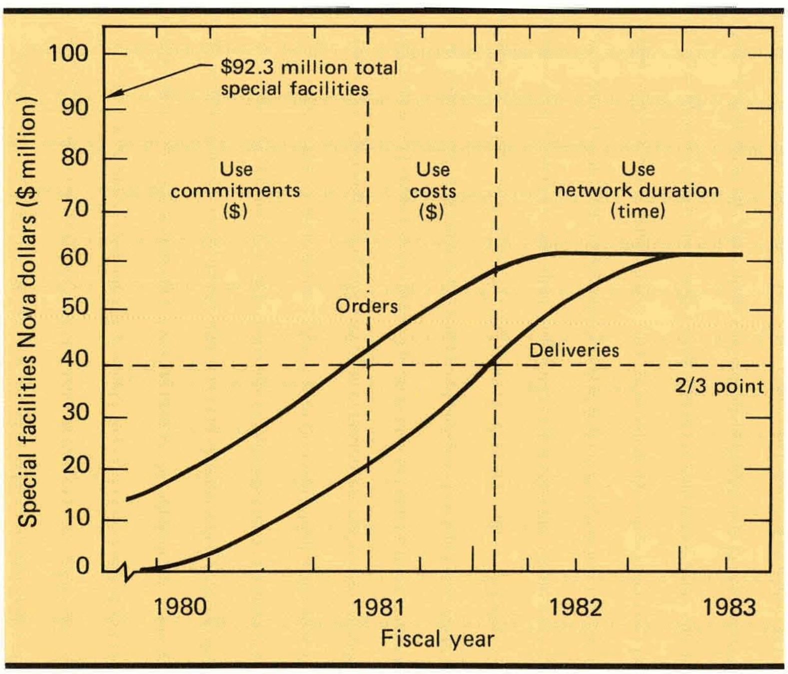

Fig. 2-208. Different schedule-performance parameters apply as Nova evolves.

The transition from the financial system to the network approach is shown graphically in Fig. 2-208. Finance-based schedule control has diminishing accuracy for time beyond the point where cumulative costs reach about two-thirds of the total project budget because of the flattening of the S-shaped curve.

During design and procurement, we use the Nova financial-planning and tracking system to measure schedule performance. Schedule performance in the design phase is measured by tracking committed dollars against financial baseline estimates. Although labor-intensive, the design phase is trackable in procurement terms because each design effort ends with the release of a purchase order. During the procurement phase we track actual costs against financial baseline estimates.

Component assembly and system activation are also labor-intensive; however, no schedule-performance parameter comparable to cumulative committed dollars exists for these phases of the project. Therefore, we will use projected schedule variance as the schedule-performance parameter for the assembly and activation phases. (System activation includes component installation, system test/checkout, and system-performance testing for Nova subsystems and assemblies.)

The Nova schedule-control process during assembly and activation is shown in Fig. 2-209. Our schedule-control objectives are

- To develop accurate, optimum, and realistic work plans to assemble and activate the laser system.
- To provide computerized methods for rapid evaluation of schedule performance and the revision of work plans.
- To provide performance reports that highlight schedule variances and their importance to or impact on project completion.
- To provide a basis for revising work plans.

We will use the Nova schedule-information system to provide the framework for identifying critical issues as feedback for Nova schedule control. These critical issues, along with schedule goals, form the basis of planning. The prime Nova schedule goal is to provide an operating Nova Phase I system by July 1, 1983. The work plan produced by the planning process is a detailed time plan for component assembly and system activation. We input this work plan and actual dates for past events into the schedule-information system. The schedule-information system computes schedule-performance parameters that, when reviewed by project management, complete the Nova schedule-control loop. Figure 2-209 describes these activities functionally.

Planning. Assembly and activation planning focuses on events representing the interfaces among the Nova cost centers or activation teams and the completion of activation tasks.

We define events in terms of the result achieved when the event occurs. This result is either a condition or a physical thing produced, i.e., an assembled spatial filter, a fully operational (diagnosed or performance tested) amplifier, building-beneficial occupancy, etc. We rely heavily on the project engineers to manage component-assembly activities within their respective cost centers. This means that time responsibility for work leading to these events rests with the project engineers.

We prepare a work plan for activities that go beyond the responsibility of any one cost center. We collect data that define events and tie them together in time (schedule logic). Doing this involves getting interfacing cost centers/activation teams to agree (make agreements) on these data, the most important of which are data specifying availability and need. We call these agreements "handshakes." It is essential that a handshake specify the terms of the event. For example, the laser space frame is needed by a certain date because alignment and diagnostic hardware installation must begin at that time. The configuration (state of completion) of the space frame at the event is negotiated between the affected project engineers.

Performance Measurement and Reporting. To integrate time responsibility for events at the assembly, we use the event definitions and an assembly-breakdown structure (Fig. 2-210). The ABS ties events to assemblies and provides an effective means for summarizing schedule status and performance information. For example, the event marking the final chain-performance test is tied to the level-2, ABS-element

Fig. 2-209. Schedule Information System provides feedback of Nova schedule control.

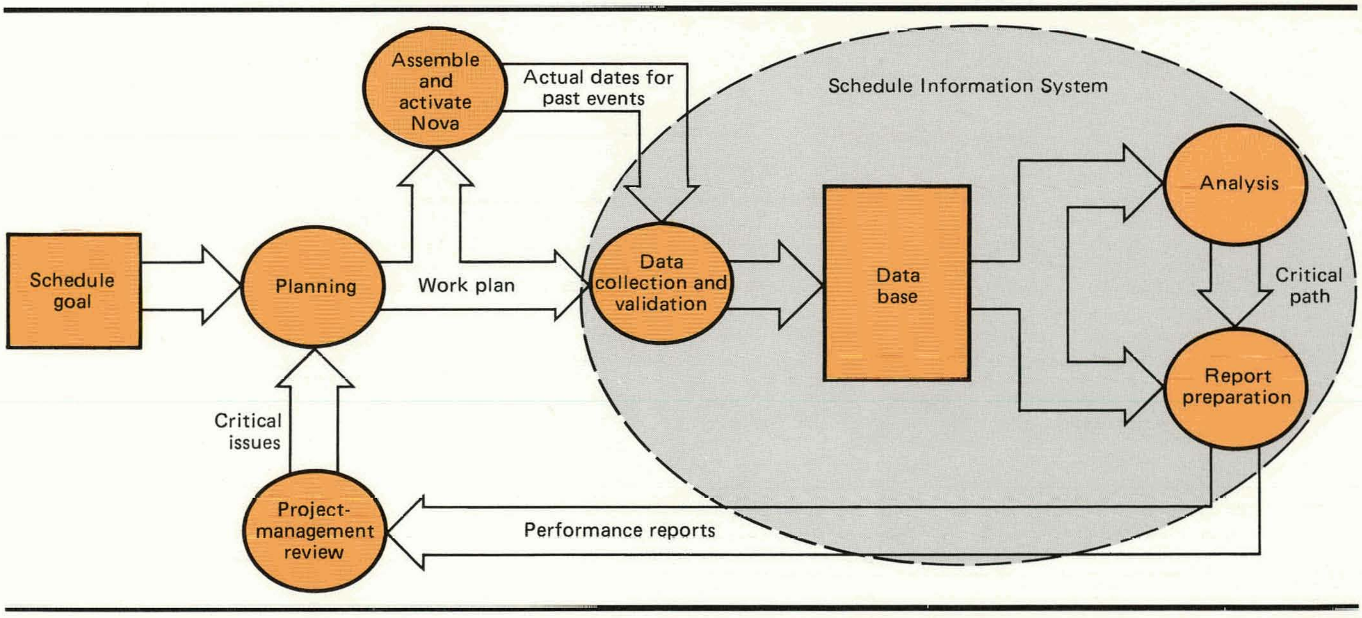

amplifier assemblies (ABS 1.5 in Fig. 2-210). This performance-test event marks the availability of all Nova amplifier assemblies. The ABS makes it possible to review the plan at any desired level of detail.

We will use the schedule-information system to generate performance-measurement information during assembly and activation. The prime function of this system is to provide the basis (input) for

Fig. 2-210. Assembly-breakdown structure (ABS) for Nova Phase I.

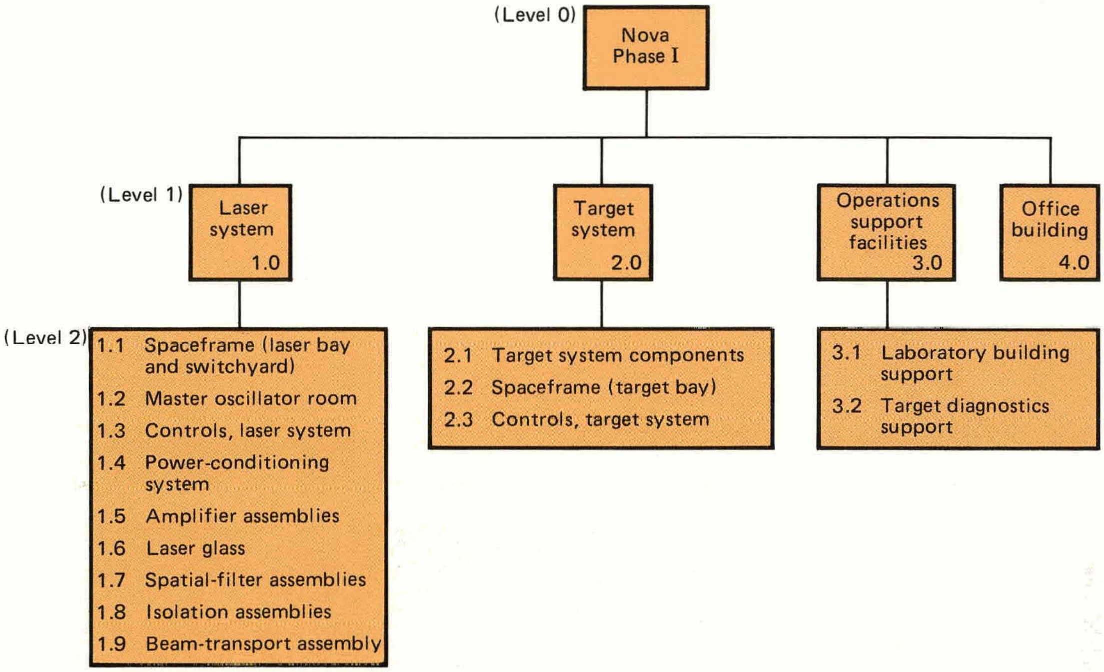

Fig. 2-211. Nova schedule and status summary, by phase. ▼

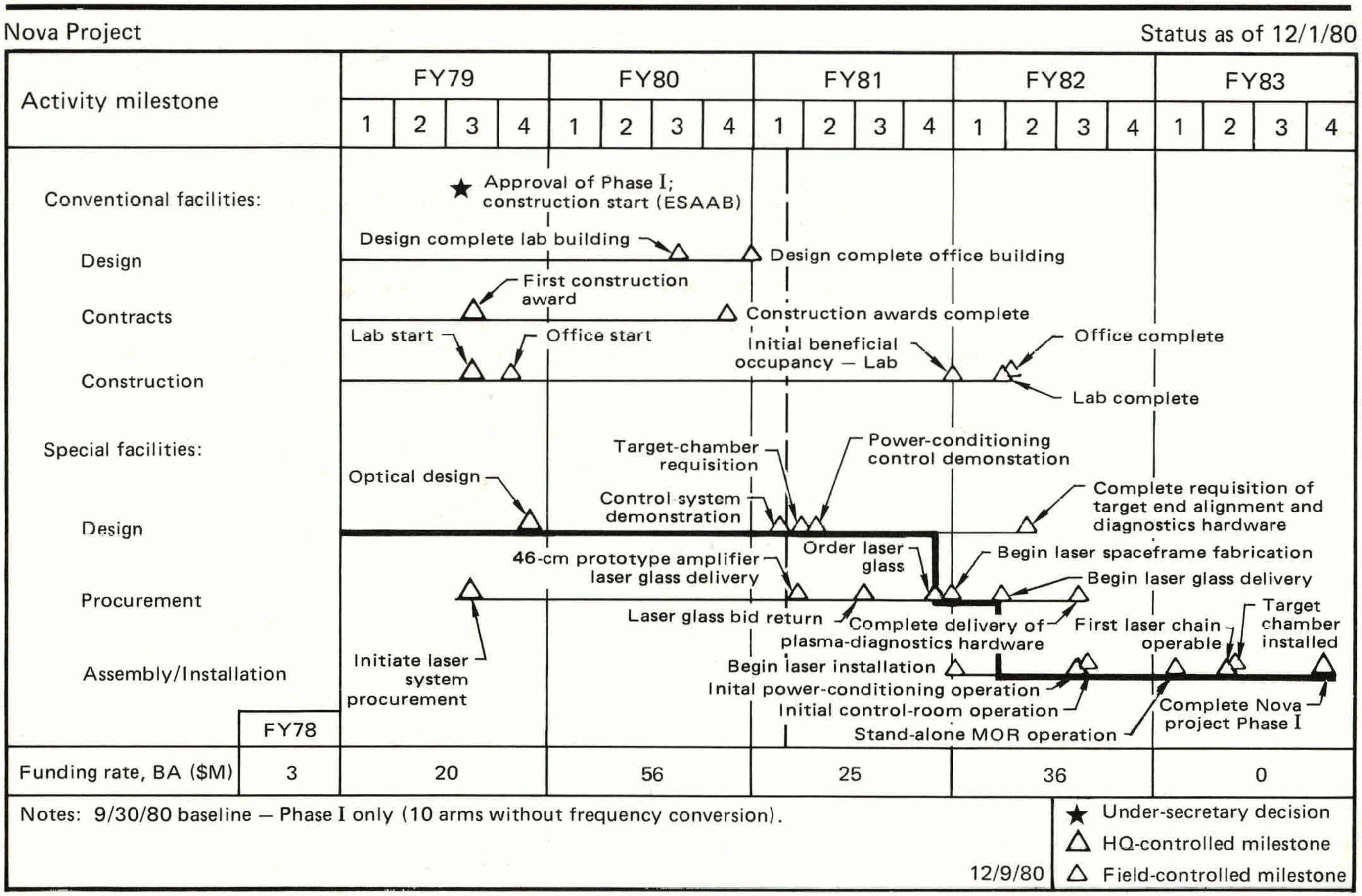

identifying critical schedule issues. This issue identification, the project-management-review bubble in Fig. 2-209, is judgmental in nature and requires an assessment of how each issue impacts on subsystem and/or Nova availability dates. The system identifies potentially delayed interface events and evaluates time variances for subsystems/assemblies.

We designed the schedule-information system to synthesize a network model of the project from the handshake data in the work plan. The system uses actual times for past events to find the network's critical path(s), thus identifying all potentially delayed events. We then evaluate time variances for events by comparing projected completion times with dates from the work plan.

We provide performance reports throughout the Nova project to summarize the project schedule and status (by phase) of the project. The Nova project schedule and status report, shown in Fig. 2-211, summarizes the total project schedule and status in bar-chart (Gantt) form. This chart is prepared in accordance with the DOE "Project Management System."[95] Major event milestones from the Energy System Acquisition Project Plan (ESAPP) are shown; both planned and actual completion are indicated for each milestone. Actual milestone completion is shown by solid triangles/stars. Project phases are displayed as separate bars, broken down by conventional and special facilities.

Assembly/activation phase reporting will display time variances from the network analysis. A typical report is shown in Fig. 2-212. Schedule-performance information is displayed for the laser subsystems (ABS level 2).

Implementation. We plan to begin using the schedule-information system in 1981. The following activities are planned:

Fig. 2-212. Nova schedule and status summary, by assembly.

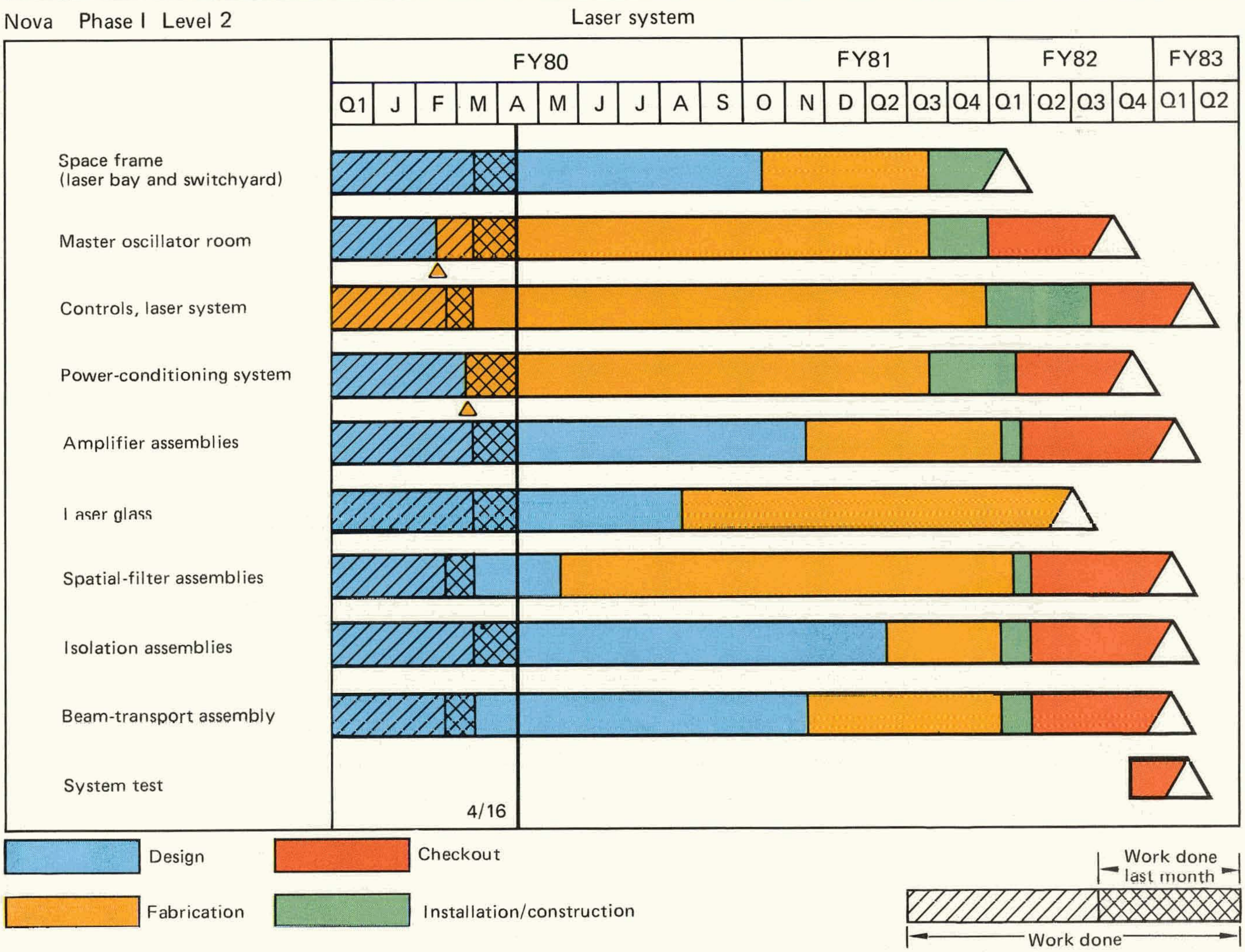

- An investigation of computer-graphics approaches to schedule bar-chart preparation.
- Development of a work plan for network-based schedule control during Nova system activation. Nova Phase-I system activation is currently scheduled to begin in FY82.

Quality and Safety Assurance System. We have now had a full year's experience with the integrated Nova system for quality assurance and safety. Unlike most assurance programs, our approach avoids the redundancies of separate quality and safety programs by encompassing all controls and assurance techniques in a master assurance plan supported by subordinate plans that focus on the key technical areas of the Nova project. Another distinction between our system and systems used by the aerospace or nuclear industry is that we assign responsibility for implementing the program to the people who are performing the work. That is, we do not rely on separate, independent organizations to perform quality assurance and safety functions. Checks and balances are built directly into the plan. They are implemented by the responsible engineer and project engineer at lower levels of the work-breakdown structure (WBS), and by the project manager, system project engineer, and project engineer at the top levels of the WBS.

During the year the Nova project special-facilities designs have evolved from early conceptual designs through final detail designs, and many have been competitively bid and awarded to industry. Conventional facility construction of the laboratory and office buildings was 64 and 28% complete, respectively, at the end of the year. Since the Nova assurance program is geared to the several phases of the project, the primary assurance-system accomplishments have been associated with implementing design controls for the special facilities and verification of construction controls via audit for the conventional facilities. In addition, we conducted an internal LLNL

Table 2-39. Master hazards list for special and conventional Nova facilities.

- Electrical shock
- Laser light exposure
- Radiation exposure
  - Neutrons, gamma rays, x rays (at shot time)
  - Secondaries (following a shot)
  - Tritium (preparation for a shot)
- Chemical contamination (PCB, Hg, others)
- Falling objects and falls
- Oxygen deficiency
- Explosions
- Fire
- Earthquake

Fig. 2-213. Sample preliminary hazards analysis (PHA) being prepared as part of the Nova design-review process.

SYSTEM: NOVA — RESPONSIBLE ENGINEER: MERRITT/HOLLOWAY — DATE: 5/5/80
PROJECT ENGINEER: WHITHAM — REVISION:
SUBSYSTEM: ENERGY STORAGE — SYSTEM PROJECT ENGINEER: SIMMONS — SHEET: 1 OF 1

1		2						3	
COMPONENT		HAZARD						CORRECTIVE ACTION	
NO.	DESCRIPTION	MODE	EFFECT	CLASS* 1	CLASS* 2	CLASS* 3	P**	RECOMMENDED	TAKEN
1	BANK, POWER-SUPPLY FANOUTS ETC.	OPERATING	ELECTROCUTION			X	L	[INTERLOCKS] [TRAINED PERSONNEL] [KEY ACCESS TO AREA AND TO PANELS OR DOORS] [GROUND HOOKS]	[INTERLOCKS] [ALL TECHS AND ENGINEERS HAVE TAKEN SAFETY COURSES AND CPR]
2	CAPACITOR, POWER-SUPPLY RESISTORS CABLES ETC.	FAILURE	FIRE, EXPLOSION, SHRAPNEL			3	L	[BARRIERS WITH KEY [FIRE ALARMS] [AUTOMATIC SHUTDOWN] [OPERATIONAL INTERLOCKS TO PREVENT FAILURE MODE] [SPRINKLERS] REVIEW OF MATERIALS	INTERLOCKS KEY ACCESS FIRE ALARMS SPRINKLERS

*HAZARD CLASS: 1-MINOR, 2-MODERATE, 3-MAJOR **P = PROBABILITY: L = LOW, M = MEDIUM, H = HIGH audit of our master assurance-program plan and participated in an audit conducted by the DOE.

Design Controls. The principal control technique that we used during the design phase of Nova is the design review. Design reviews are conducted for the system project engineer and are attended by a broad cross section of laser program, Nova project, and technical support personnel. The purpose of each review is to verify that the design being reviewed is capable of meeting Nova performance criteria, manufacturable, and safe and that it will interface properly into the system. The responsible engineer (or project engineer) presents the design to the attendees. Review summaries are prepared, and action items are assigned. The reviews are concluded by an authorization to proceed to the next logical step—first layout, detail design, or procurement, or by a request to resolve the open-action items and, possibly, to repeat all or part of the review.

One of the mandatory agenda items at each design review is presentation of a preliminary hazard analysis (PHA) for the design. The PHA uses the master hazards list (Table 2-39) as a starting point or checklist to identify the specific hazards associated with the design. Then the PHA is used to develop the potential failure modes that could lead to the hazards and the effects of the hazards if they do occur. An assessment of the severity and probability of occurrence is made, and appropriate corrective action measures are recommended. The criteria, in order of precedence for dealing with hazards, are

- To design for minimum risk.
- To incorporate safety devices in the design.
- To use warning devices capable of detecting the hazard and signaling its existence.
- To follow administrative procedures.

A sample of the PHA for the Nova energy-storage subsystem is shown in Fig. 2-213. Note that the PHA is closed out only after the recommended corrective action has been taken. PHAs have been prepared for every design reviewed during the year; Table 2-40 lists the reviews conducted during 1980. We have found the design-review process to be a very effective assurance tool, enhancing our confidence that the Nova designs are adequate, complete, and will safely satisfy Nova system requirements.

Assurance-System Audits. We conducted two internal assurance-system audits and participated in an audit conducted by DOE–SAN. Our assurance system requires that we periodically conduct independent audits. The audit process provides us with an important management tool to determine how well we are complying with the requirements of our assurance plans and whether the requirements are effective for ensuring the success of the project.

Table 2-40. Nova design reviews conducted during 1980.

Subject	Date	Conductor
Laser diagnostics	1/17	R. Ozarski
Plasma shutter	1/22	I. Stowers
Console displays	1/24	G. Suski
Input-beam sensors	1/30	E. Bliss
COL/Praxis language	2/04	J. Greenwood
Flashlamp circuit diagnostics	2/15	D. Gritton
Pockels-cell-driver subsystems	2/21	J. Oicles
2ω plans	3/04	M. Summers
Novabus	3/05	D. Gritton
Novalink	3/06	J. Severyn
MOR layout	3/14	J. Murray
Oscillator controls	3/14	J. Oicles
KDP procurement	3/25	S. Stokowski
Central controls	3/27	G. Suski
Output-sensor package	3/28	E. Bliss
Chain splits	4/04	A. Budgor/J. Glaze
Rod amplifiers	4/08	W. Martin
Space frame (support frame)	4/09	C. Hurley
CCDs	4/10	E. Bliss/J. Cheng
Target chamber	4/11	F. Rienecker
Fizeau interferometer	4/11	N. Thomas
Spatial filters	4/23	C. McFann
N_2-cooling of amp heads	5/06	H. Julien
Electrical layout—Nova bank review	5/09	B. Merritt/R. Holloway
Safety-interlock system	5/13	D. Gritton
Lamp-circuit diagnostics system	5/15	L. Berkbigler
20.8- and 31.5-cm amplifiers	5/27	C. Hurley
2ω baseline	6/05	M. Summers
Plasma shutter	7/24	I. Stowers/J. Oicles/ L. Bradley
2ω/3ω	9/05	M. Summers
Rod amplifier	9/09	S. Yarema/C. Hurley
Turning- and diagnostic-mirror gimbals	9/11	C. Hurley/A. Martos
Target chamber	9/16	F. Rienecker
20.8- and 31.5-cm disk amplifiers	11/06	C. Hurley/F. Frick
Clean room and assembly fixtures reconditioning and procedures	11/13	C. Hurley/F. Frick
Rod-amplifier engineering	11/14	C. Hurley/F. Frick
Nova/Novette output sensor	11/20	E. Bliss and/or Aerojet
TV distribution system	11/21	P. VanArsdall
15.0- and 31.5-cm rotators	11/26	B. Merritt
Nova/Novette KDP crystal mount (mechanical components)	12/02	J. Williams
Novette MOR	12/05	D. Kuizenga

Our audits were conducted by teams representing various disciplines within the Laboratory, including members from our Hazards Control Department and Quality Assurance office. The audit teams used detailed checklists to question key personnel responsible for implementing the assurance system. The teams presented their findings and recommendations to the Nova staff and prepared audit reports. We are now implementing their recommendations.

A summary of the audits conducted, their dates, and the key findings are shown in Table 2-41. The recommendations are included in the audit reports. While the table only shows areas in which deficiencies were found, it is important to remember that most of the findings were positive and tell us that the Nova team is doing an effective job ensuring a safe and successful laser fusion experimental facility.

Status of Assurance Planning. At the end of 1979 we had released only the master plan and convention-facilities subordinate plan. During 1980 we released the mechanical/target-systems and power-conditioning subordinate plans. A first draft of the alignment/control/diagnostics subordinate plan was also prepared. In 1981 we will complete and release the subordinate plans for alignment/control/diagnostics and for optical components. As a result of the recommendations from the various audits, we will make appropriate revisions to the plans that are already in effect. Internal audits of the mechanical/target-systems and power-conditioning subordinate plans are also scheduled for 1981.

Authors: F. Holcomb, L. C. Lewis, and A. J. Levy

Research and Development

Introduction

We are conducting a research and development program on solid-state materials and laser components to support Nova and other glass laser systems at LLNL, and advanced lasers as well. In this discussion, we present an overview of the progress on the various research projects conducted during 1980. These projects are discussed in greater depth in succeeding articles.

We have extended the analysis of target-irradiation geometries intended to provide uniform illumination of Nova type spherical targets while retaining compatibility with

Table 2-41. Summary of assurance-system audits conducted during 1980.

Audited area	Type of audit	Date	Deficient areas
1. Conventional Facilities Subordinate Assurance Plan	Internal LLNL	July	• Document and configuration control. • Continuity of assignments of responsibility during design and construction. • Nonconformance and corrective-action reporting and resolution. • Assurance records access and retrievability.
2. Master Assurance Program Plan	Internal LLNL	October	• Nova assurance plans are more "formal" than necessary. • Understanding of safety responsibilities for support facilities. • Formal hazards analyses are not as complete as designs. • Understanding intent of "controlled" documents and which documents fit in this category. • Interface criteria, their completeness, circulation, and use.
3. Master Assurance Program Plan	DOE-SAN	November	• Consistent with 1 and 2 above.

two-sided irradiation schemes. The MALAPROP computer propagation code was used to model the performances of Novette and Nova. We have also investigated the effects of pulse propagation on the temporal shape of the laser pulse used in our systems.

We analyzed the cost and performance of iodine lasers for comparison with the current Nd:glass laser designs and found that the advantages depend on laser pulse width. The two lasers have comparable performance for pulse widths of 1 to 2 ns; however, iodine is best for short pulses, while Nd:glass is better for long pulses. We developed a model of flashlamp output with short-pulse excitation that included the effects associated with arc growth. The model displays improved simulation of electrical characteristics for short pulse durations, but underestimates absorption losses for low-pressure lamps. We have also analyzed the upgrades for Nova to yield 10-ns pulses of megajoule magnitude. However, pulse limits must be observed because Nova system design and performance were found to be susceptible to laser-induced damage. In addition, a dual-ion model was designed to simulate the effects of gain saturation, since this is a parameter of significant interest.

For several years we have pursued the development of fluorophosphate glass for Nova applications. The primary advantage of this glass is its low, nonlinear index of refraction, which reduces the degree of self-focusing. This development culminated in successful production of 46-cm-aperture Nd-doped glass disks with the homogeneity required for Nova. However, heating of submicrometre-diameter platinum inclusions caused internal laser damage in the fluorophosphate glass and limited the glass operating fluence to impractically low levels. Though the glass vendors, Hoya and Schott, have made steady progress in reducing the density of platinum inclusions, we are not confident that the problem can be solved without affecting the Novette and Nova schedules. Therefore, we have decided to use Nd-doped phosphate glass in lieu of Nd-doped fluorophosphate glass, since the former has a significantly lower density of platinum inclusions (approximately 0.1 cm^{-3} in phosphate and 100 cm^{-3} in fluorophosphate) and smaller damage sites at comparable fluences. Though the nonlinear refractive index coefficient of phosphate glass is two times larger than that of fluorophosphate glass, the trade-off does not appear unreasonable, since it will result in only a slight reduction of laser performance for short pulse widths.

We have determined the specifications for edge cladding of phosphate glass disks, and the glass companies who supply the disks do not anticipate difficulties in meeting the requirements. Finally, we have investigated the possibility of solarization of phosphate glass under expected operating conditions. In this program, we have experimentally demonstrated that the use of cerium-doped quartz flashlamps has not resulted in any detectable solarization.

To predict laser performance we must rely on our knowledge of gain saturation in the laser amplifiers. Earlier, we performed a comprehensive study of gain saturation in Nd-doped fluorophosphate glass, and, following our decision to use phosphate glass for Novette and Nova, we extended the study to include phosphate-glass compositions. The completed measurements on two of these glasses are included in this report.

Laser-induced damage to optical elements, particularly those with thin film coatings, is an important factor in the performance and reliability of laser systems. Earlier studies of tantala–silica antireflection (AR) coatings deposited at various temperatures, rates, and background oxygen pressures indicated that coatings deposited at lower temperatures had a higher threshold to laser damage. We extended these studies during 1980 to include the effects of baking the coatings, and we found that baking generally reduced the volume-averaged absorption of coatings. This was particularly true for the coatings that initially had the greatest absorption. We also found that baking produced a large reduction in net stress and, in some cases, caused a change from tension to compression. However, damage thresholds were not generally changed by baking and did not exhibit a strong correlation with average absorption or stress. Substrate materials and optical polishes have also been studied to determine their influence on the damage threshold. In this study, tantala–silica AR coatings were deposited on fused silica and BK-7 glass substrates polished by conventional fresh-feed and bowl-feed techniques. The films or surfaces polished by the bowl-feed process exhibited the highest damage thresholds. In a study similar to the tantala–silica experiments just described, we examined the influence of deposition parameters for titania–silica AR coatings and, again, the lower-temperature coatings appeared to produce an increase in coating damage thresholds. The dependence of coating thresholds on pulse width was determined using pulses of 1.06-μm wavelength with 1- to 20-ns durations. We found that the threshold generally increased slowly for pulse widths from 1 to 5 ns and increased rapidly for longer pulse widths. The formation of graded-index AR surfaces by acid-etching phase-separated glass is an important development that was made during the past two years; these surfaces have exhibited damage thresholds that are two to three times greater than conventional thin-film coatings. Our efforts in this area have resulted in the commercial development of phase-separated glass for use in Nova.

Intrinsic scattering losses increase rapidly for light of decreasing wavelength and limit the application to visible or longer wavelengths for our present glass. We have decided to explore the applicability of this technique to the UV wavelengths associated with fusion experiments. This decision has caused us to begin development of film materials that produce graded-index surfaces. To facilitate development of this and other optical materials for shorter-wavelength applications, we performed damage measurements with second- and third-harmonic wavelength pulses (0.53 and 0.35 μm, respectively) of Nd:glass lasers and with the krypton–fluoride (KrF) laser (0.25 μm). In the case of potassium dihydrogen phosphate (KDP), which is the harmonic-generation material we intend to use on Novette and Nova, we found internal inclusion damage occurring at fluence levels below our minimum specification. After studying the nature and source of inclusions, we met with the crystal vendors to determine the parameters for modified growth conditions that are expected to improve the damage threshold of the crystals. Damage thresholds were found to be generally low for KrF laser coatings, although some coatings exhibited substantially higher thresholds.

During 1980, we completed fabrication and assembly of, and began testing, the 20.8- and 46-cm rectangular disk amplifiers. These amplifiers will be used on Nova and Novette because they are more efficient than their cylindrical counterparts. For Nova, we have also designed a new phosphate-glass rod amplifier that has greater gain and uniformity of radial-gain profile than the amplifier it replaces in Shiva. In studies on the cooling of disk amplifiers, we monitored the internal temperature of the disks with thermocouples and measured optical distortion by observing temperature distributions with a pyroelectric vidicon. We found an initial 2 to 3°C temperature rise in the disks after flashlamp discharge that was followed by a steady increase in temperature from radiative heating that, in turn, was caused primarily by the flashlamp reflector. Our observations indicated that a substantial reduction in cooling time could be achieved through changes in the flow of the coolant gas.

The actively mode-locked Q-switched (AMQ) oscillator on Shiva was replaced by a similar oscillator with improved electronics and computer controls. The new oscillator is a stable single-mode Q-switched oscillator with longer pulses whose single-mode performance is maintained by a feedback control circuit. To provide variable-duration pulses, we developed and installed a fast-pulse circuit based on planar triodes to drive the Pockels cell for switching a portion of the longer pulses to the amplifier chains. The fast-pulse circuit modification has provided us with pulse lengths as short as 2.2 ns. During 1980, a major effort was devoted to planning for oscillators and other front-end components required for Novette.

The harmonic generation of pulses at the full 74-cm output aperture has provided a major new technical challenge for Novette and Nova. Because this aperture is considerably larger than currently available KDP crystals, we have decided to use smaller crystals configured in arrays. To produce the arrays, we began a series of projects to address the issues of growing, fabricating, and assembling KDP crystals into arrays with the required alignment accuracy. We had previously demonstrated second-harmonic generation in 2 × 2 crystal arrays, where each crystal is independently aligned to the laser beam. However, a 3 × 3 array must be used for Novette and Nova to keep the size of individual crystals reasonably small and to avoid cumbersome alignments of individual crystals. Since crystal alignment is a significant factor, the larger crystal arrays will have fixed relative orientations and will be aligned as a single element. The key to success for this concept is the ability to fabricate crystals with identical orientation of the optic axis relative to the surface normal. We have conducted recent studies at LLNL on the suitability of single-point diamond turning for fabricating optical surfaces on dielectric materials. We found that diamond-turned surfaces have optical quality and damage thresholds that are comparable to conventionally polished surfaces. Because diamond turning offers the additional advantage of accurate control of crystal orientation, we have assumed development responsibility for the technique, which we have recently demonstrated is capable of controlling alignment within the tolerance required to achieve a 99% uniformity of conversion efficiency over the entire array. To assure an adequate supply of KDP crystals, LLNL is supporting vendor studies into methods of increasing the crystal size and growth rate. We have also developed techniques to align crystals and to determine beam quality and conversion efficiency. In addition, we have addressed the issues of beam propagation through the segmented array, choice of index-matching fluid, and techniques to filter unwanted light wavelengths.

At LLNL, we use capacitors to store the electrical energy supplying the flashlamps in our laser systems. However, this is an inefficient energy source for the flashlamps, since the capacitors provide relatively low-density storage, occupy considerable space, and have a limited repetition-rate capability. Therefore, we have supported development for the compensated pulsed alternator (compulsator) at the University of Texas in Austin. The compulsator stores rotational kinetic energy at high density for delivery in short pulses at the current and voltage required for laser flashlamp excitation. Our goals in this program are to

- Evaluate performance capabilities.
- Identify engineering problems.
- Develop computer models for optimizing performance in various applications.

The existing prototype compulsator was damaged by electrical arcing and was subsequently repaired. While the compulsator was undergoing repairs, an active rotary flux compressor was developed, and this unit has provided us with a data capability for testing computer models of the compulsator. During later testing, we discovered a source of reduced flux compression and low peak-power output in the compulsator. Since then, corrective measures have been proposed, and the compulsator is expected to achieve its design goals.

We have continued development of the plasma shutter during 1980. When this device is perfected, it will prevent damage to laser components from light reflected by the target. The shutter is designed to propel a high-density plasma across the beam path; the plasma is created by passing a high current through a wire, causing explosive evaporation and ionization of the wire. Two prototype shutter modules have been completed and tested. One of the modules had diagnostic equipment to determine plasma parameters and to study reliability and lifetime of the high-voltage electronics, while the second module was used to evaluate the control system, to study electromagnetic interference, and to test the wire-changing mechanism. We subsequently implemented design improvements that both eliminated an internal arcing problem and increased the velocity of the plasma front. The second module has been installed on an arm of Shiva for a full system test.

Author: W. H. Lowdermilk

Theory and Design Analysis

MALAPROP Code. During 1980, we continued to use the MALAPROP computer propagation code[96] for the modeling of Nova amplifier chains. To facilitate our modeling, we made five significant modifications to the computer program system; two modifications affected analysis of slotted-beam diffraction, one modification provided intensity distribution data, and two modifications improved automated analysis for proposed Nova baseline systems.

In October, we focused our attention on the diffraction effects of the slotted beam[97] generated in the final amplifying stage of Nova. We added the capability to MALAPROP for using an open-ended slit in the far field because a round pinhole at the focus prevented the near-field slot from reimaging. The slit width and the angle to the X-axis are input parameters that allow the user to select a width and an alignment determined by plasma-forming criteria. For width selection, we calculate the mean and maximum intensities in far-field bands that are analogous to far-field rings used in the pinhole selection process.

We were also concerned with near-field apodizing. To facilitate modeling a manufacturable apodizer, we added a new edge function to the existing linear masking function. Each mask has three regions that consist of a center section of width C and two adjacent edge regions of width W. For the new edge function, let Tc be the transmission in the center, α a constant dependent on the absorption parameter, and L the depth so that

$$Tc = e^{\alpha L} \quad .$$

In the edge regions, we set the transmission, T, as a function of distance, x, from the center section $0 < x < W$, to the following continuous function between Tc and 1:

$$T(x) = e^{-L\left[1-\left(\frac{x}{W}\right)^{\beta}\right]}$$

where β is generally set to 2. If the center width is zero, this function provides a two-branch discrete function. Our MALAPROP results indicate that apodization offers a performance improvement of approximately 10% for Nova.[98] In Fig. 2-214, we show a profile where the side growth from the apodized center slot is significantly less than the peaks due to single-point obscurations.

The statistical calculations that are performed with MALAPROP characterize the beam, but complete plots are necessary to assure inclusion of peak values when random noise is considered. However, this process is costly in large grids and often provides confusing data, so we have continued to rely on statistical calculations for determining the maximum beam intensity. Though we expected this method to give us criteria for differentiations of otherwise similar performance numbers, the calculations failed to provide any measure of the total area above a given threshold. To deal with this problem, we added a function to MALAPROP to count the number of grid points having intensities higher than those in a set of predetermined intensity values. As might be expected when using small areas of noise obscuration,[99] the peak intensities tend to be isolated.

Many of the Nova system analyses[100] are similar, requiring only changes to a small subset of input parameters and a similar summarization of the MALAPROP results. We automated the majority of our MALAPROP production by expanding the capabilities of the MATHSY[101] auxiliary program GAINN (now called FIND) by adding pinhole and slit-size selection to MALAPROP and by using the COSMOS production system on the Cray computer system. Given the pulse width and the desired output energy for a specific system residing in its library, FIND can determine all the global saturated gains necessary to run the standard damage analysis. FIND also reads the statistical data from the MALAPROP output and uses these data to plot the peak and mean fluence values throughout the system and to write the summary table. During 1980, we modified MALAPROP to select a pinhole or slit width using the criteria that previously had been manually applied. Pinholes are selected as the larger of an input minimum or the smallest size for which the mean pinhole

Fig. 2-214. Nova beam modelled by MALAPROP at final filter entrance (apodized center slot reduces side growth before and after filtering).

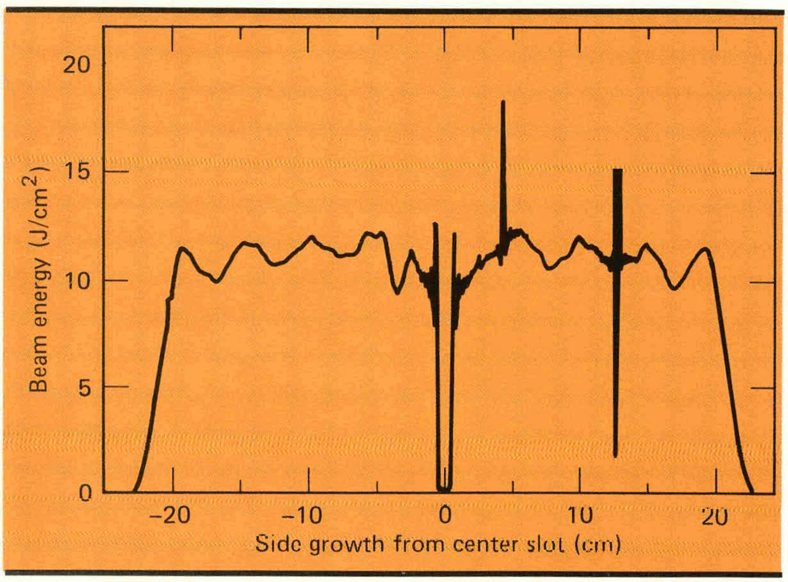

loading is less than an input level. (We currently use 100 GW/cm^2.) Because the slit mean loading is dependent on the far-field dimensions (entire bands are averaged), we also require that either the maximum load on the slit be less than the input limit or the width be increased by 300 μm/ns to prevent closure of the pinhole.

These minor changes in the MALAPROP system have enhanced its ability to process routine system modifications for the design of Nova.

Authors: W. E. Warren and W. W. Simmons

Major Contributors: D. Eimerl, W. F. Hagen, J. T. Hunt, G. G. Peterson, and J. B. Trenholme

Nova Target Illumination Studies

Nova 100° Beam Cone Illumination. The Nova Phase I baseline spherical illumination option[102] has two opposed bundles of five beams each. For optimum illumination, the centerlines for each bundle lie in a cone whose full angle is 105.8°, and the beams are spaced at 72° intervals around the cone circumference (Fig. 2-215). Several considerations involving laser flexibility and target performance led to a decision to decrease the centerline cone angle to approximately 100°. We therefore determined the performance of the target illumination with the reduced centerline cone angle.

The use of a smaller cone requires larger spots on the target sphere. Previously, the spots all subtended 110° (full angle), as seen from the target center. Larger spots increase the angle at which rays near the spot edge strike the target; more laser energy is reflected than absorbed. We anticipated having to accept a large energy loss as a result of the large increase in spot size. To our surprise, increasing the spot size from 110 to 114° resulted in a uniformity of the 100° beam cone that was better than that of the 105.8° beam cone. Enlarging the spot size increased the angle of the spot-edge rays by only 2° out of 35°, resulting in only a small energy loss.

The optimal beam profile for 114° angle spots on a 100° cone (Fig. 2-216) is almost the same as the previously calculated profile of the 110° angle spots for the 105.8° cone.[102] The minimum intensity is 76.4% of the maximum intensity for the former choice of beam shape and position. As shown in Figs. 2-217 and 2-218, the contours of constant intensity on the target sphere are somewhat different in the new profile, but are just as acceptable as those in the former profile shown in Ref. 102.

Laser Effectiveness for Uniform Spherical Illumination. When a multibeam laser system is used to uniformly illuminate a spherical target, each beam must produce a precise pattern of absorbed energy at a specific location on the target. The precise pattern can be found by varying the beam shape to maximize the overall uniformity of illumination.[103,104] The absorbed-energy pattern is

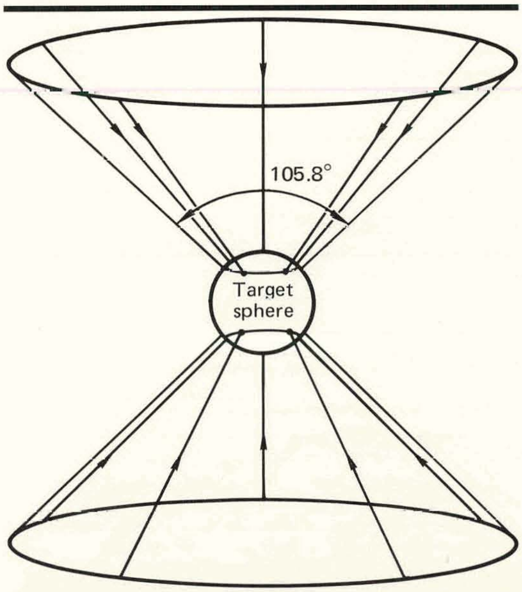

Fig. 2-215. Beam centerlines striking target sphere.

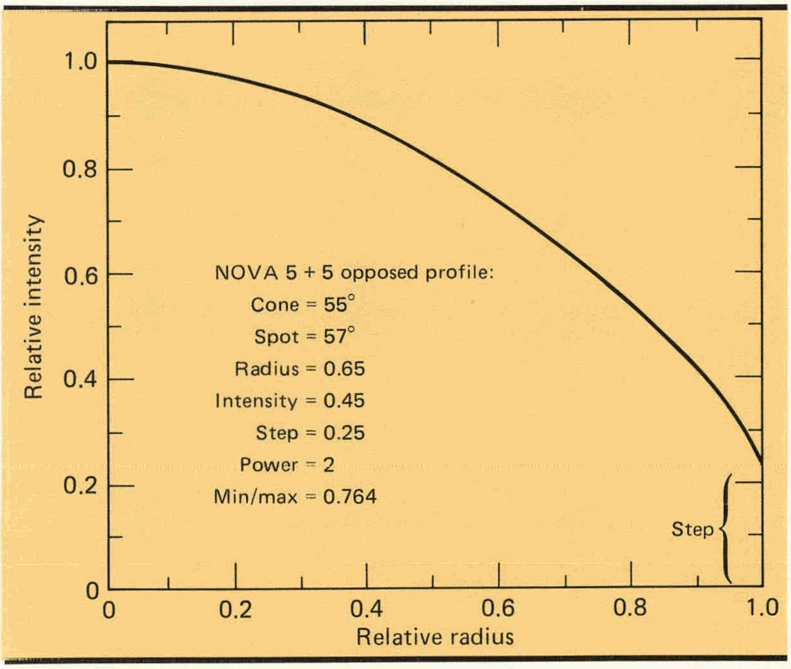

Fig. 2-216. Absorbed energy profile yielding 0.764 min/max.

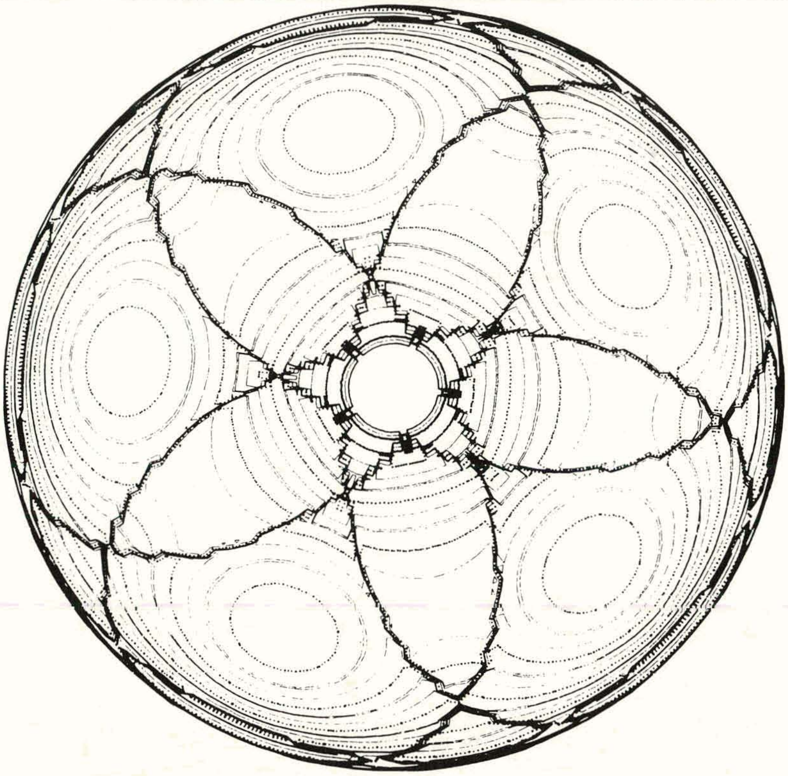

Fig. 2-217. North polar ▲ view of absorbed energy contours on a Nova target sphere.

Fig. 2-218. Equatorial view of absorbed energy contours on a Nova target sphere.▼

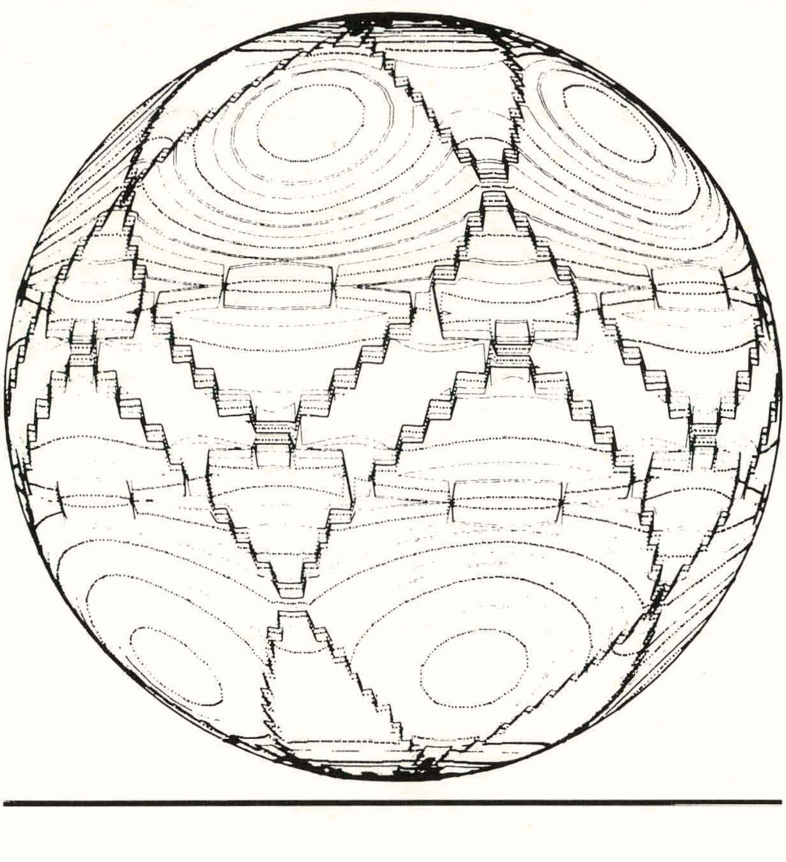

related to the intensity profile in the laser beam by the radius-to-angle transformation of the lens, the offset from the target center to the vertex of the converging beam cone, and the dependence of absorption fraction on the incident-ray angle. When all these factors have been taken into account, we have determined the laser-beam profile. Generally, the laser profile will not be uniform; thus, the laser cannot be used to full capacity unless we take corrective action, such as changes to the principal surface of the lens or the use of corrector plates (this problem is discussed later). We undertook to analyze the problem to determine if we could provide specific guidance for the design of the Nova Phase I focus-optics system.

Figure 2-219 illustrates the transformation from a known profile on a target sphere to a laser-beam profile. We used ray optics in this application, since the target is assumed to be sufficiently large that diffraction effects are small. For convenience, all lengths are measured in units of the target sphere radius. A ring on the spot profile has its intensity defined in terms of the angle, ϕ, from the center of the spot to the edge of the ring, as seen from the center of the sphere. If the focal point of the lens is at distance Q behind the sphere center, then the beam cone angle, ψ, corresponding to the spot angle, ϕ, is given by

$$\psi = \tan\left(\frac{\sin\phi}{\cos\phi + Q}\right) \quad . \tag{10}$$

The ray height, h, at the lens depends on the shape of the principal surface of the lens. If the lens is aplanatic (as with most laser focus lenses), then the principal surface is spherical, and the height is given by

$$h = f \sin\psi \quad , \tag{11}$$

where f is the focal length of the lens. For an aplanatic lens, the diameter, D, of the clear aperture is

$$D = 2f \sin\psi_m \quad , \tag{12}$$

where ψ_m is the angle of the marginal ray, so the f-number, F, is

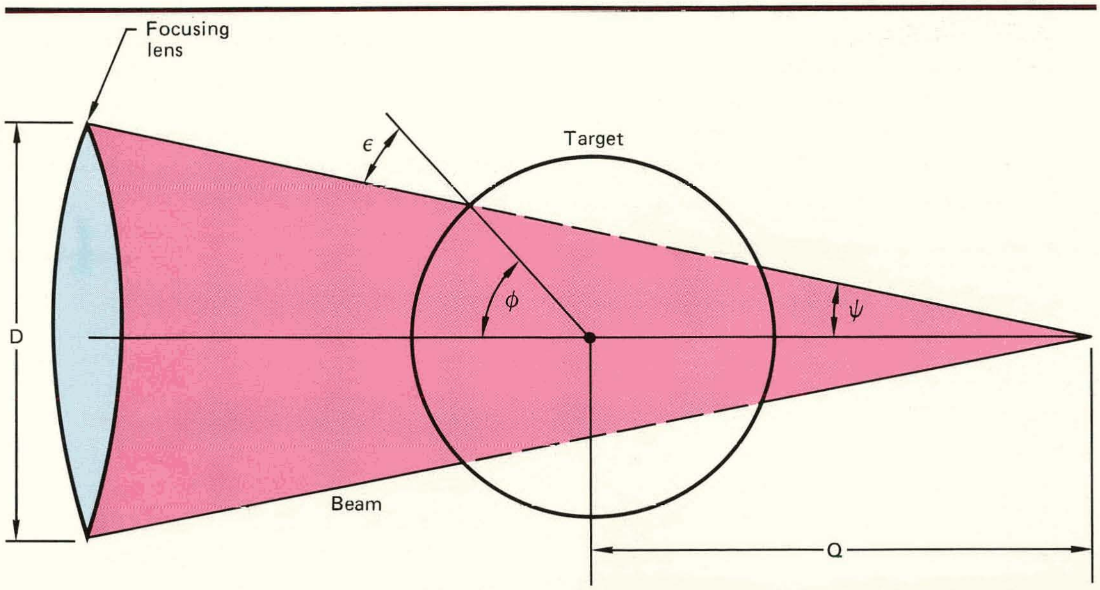

Fig. 2-219. Geometry of a laser beam hitting a target.

$$F = \frac{f}{D} = \frac{1}{2 \sin \psi_m} . \tag{13}$$

This means that Q is given by

$$Q = \frac{\sin \phi_m}{\tan \psi_m} - \cos \phi_m$$
$$= \sqrt{4F^2 - 1} \sin \phi_m - \cos \phi_m , \tag{14}$$

where ϕ_m is the marginal angle of the spot on the target, as seen from the target center. Hence, we find

$$h = \frac{f \sin \phi}{\sqrt{(\cos \phi + Q)^2 + \sin^2 \phi}} . \tag{15}$$

The angle ϵ between the incoming ray and the sphere normal is given by

$$\epsilon = \phi - \psi . \tag{16}$$

The intensity of the beam, B, is related to the intensity on the sphere, I, by

$$\frac{I}{B} = \frac{2\pi h \, dh}{2\pi \sin \phi \, d\phi} = \frac{f \sin \psi \, dh}{\sin \phi \, d\phi}$$
$$= \frac{f^2 \cos \epsilon \cos \psi \sin^2 \psi}{\sin^2 \phi} \tag{17}$$

The relationships between the absorbed-energy fraction and the incident-ray angle to the normal are the only remaining bits of information needed to determine the beam intensity as a function of beam radial position. In Fig. 2-220 we have combined a plot of experimental data[105] with two smooth curves. The lower curve is

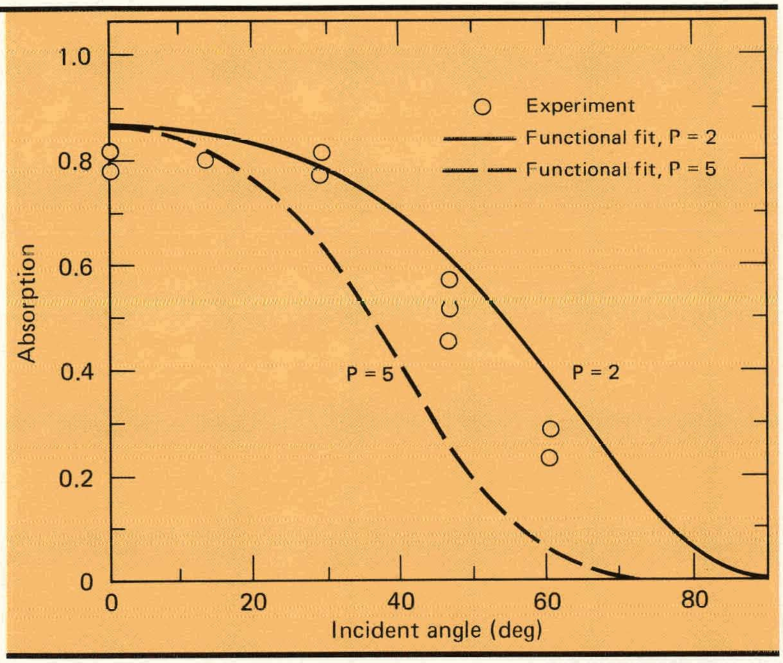

Fig. 2-220. Absorption of 1-μm laser light as a function of incident angle on a plane surface.

$$g = 1 - e^{-(2\cos^5 \epsilon)} , \tag{18}$$

and corresponds to inverse bremsstrahlung absorption in an atmosphere comparable to that above the actual target. The upper curve, suggested by the functional form of Eq. (18), is

$$g = 1 - e^{-(2\cos^P \epsilon)} , \tag{19}$$

where P = 2. The actual absorption lies between the two curves, at about P = 3.

To determine the laser-beam intensity, we performed the following steps and plotted the results:

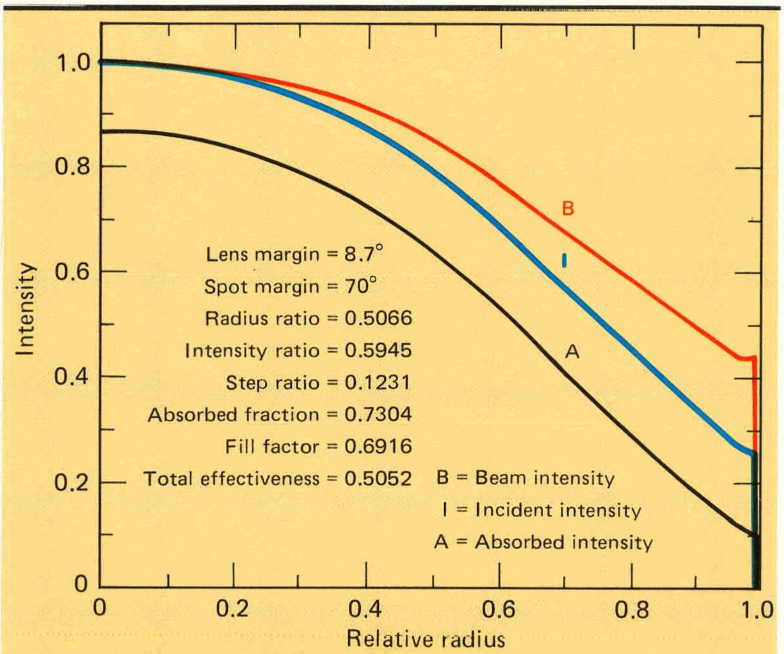

Fig. 2-221. Beam intensity out of laser, intensity on target sphere, and absorbed amount for 8.7° focus lens producing a 70° spot on a target sphere. Reflected-fraction function was R = exp(−2 cos²ϵ). ▲

Fig. 2-222. Beam intensity out of laser, intensity on target sphere, and absorbed amount for 3.5° focus lens producing a 70° spot on a target sphere. Reflected-fraction function was R = exp(−2 cos²ϵ). ▼

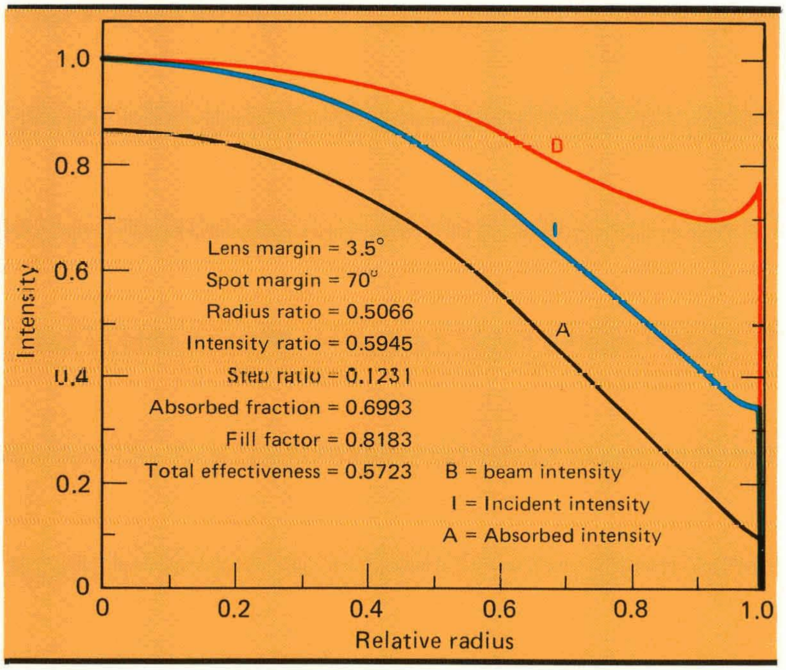

- Found absorbed intensity, A, from the known spot profile.
- Calculated ϵ and ψ from ϕ.
- Found incident intensity (I = A/g).
- Found beam intensity, B.
- Found beam coordinate, h.

A typical plot of this information is shown in Fig. 2-221. Curves are plotted for beam intensity, incident intensity, and absorbed intensity. Information is also shown on the plot for the lens-margin angle, ψ_m, and the spot-margin angle, ϕ_m, as well as the shape parameters for the spot. The absorbed fraction is defined as

$$a = \frac{\int_0^H A\, h\, dh}{\int_0^H I\, h\, dh} ,$$

where H is the beam radius. The fill factor is

$$e = \frac{\int_0^H B\, h\, dh}{\pi H^2\, B_m} ,$$

where B_m is the maximum beam intensity. The total laser effectiveness is the product of the absorbed fraction (effectiveness of target use of the delivered energy) and the fill factor (effectiveness of aperture use by the laser beam). In Fig. 2-222 we see the effect of changing from an f/3.3 focusing lens to an f/8.2 lens. Note that the higher f-number degrades absorption while improving the fill factor and, thus, the total effectiveness of spherical illumination.

We have calculated cases for spots corresponding to the Nova Phase I 10-beam geometry (5 + 5) and a 12-beam dodecahedral geometry that requires much smaller spots for the same uniformity. The results are summarized in Fig. 2-223 for P = 2 (10-beam geometry), P = 5 (10-beam geometry), and P = 2 and 5 (12-beam geometry). Note that both geometries are equivalent for f/2 or faster lenses, but the 5 + 5 geometry is more sensitive to absorption falloff at high angles and drops rapidly with slow lenses if P = 5. However, our calculations indicate that, for absorption corresponding to experimental data, the 5 + 5 geometry has good performance for f-numbers equal to or larger than f/4.

In all cases the total effectiveness is approximately 0.5, while the absorption and fill factors are about 0.7. Target design can be improved to increase laser absorption. Laser design can also increase the effectiveness; the key is an increase of the fill factor. This may be realized by transforming a near-uniform laser beam into a specific nonuniform profile at the target either by changing the lens principal surface or by using corrector plates (nonfocal systems). We realize that these changes may not be required in an experimental system, such as Nova, where we often change the beam profiles. However, if a uniform-spherical-illumination reactor system could be built, these changes would yield considerable benefits.

Author: J. B. Trenholme

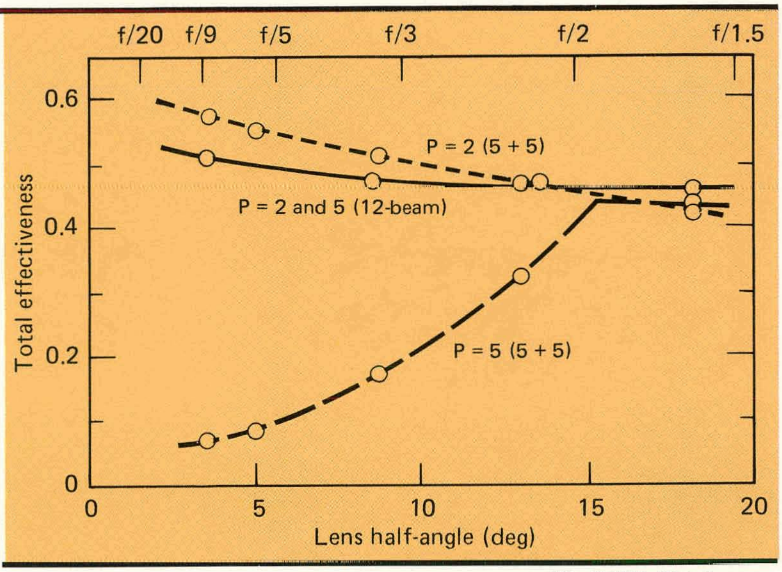

Fig. 2-223. Total effectiveness of the Nova Phase I 5 + 5 beam geometry and a 12-beam dodecahedral geometry for the two absorption curves shown in Fig. 2-220.

Modeling Saturation. To correctly model the performance of saturating glass-laser chains, we needed a fast, accurate gain model for saturating glass amplifiers in the lumped-element code, SNOBAL. As our basis for this model, we decided to use the available LLNL saturation data: input fluence, output fluence, and small signal gain. An equivalent saturation fluence, ϕ , can be derived from these data if we assume the Frantz–Nodvik saturation equation

$$\phi_2 = \phi_e \ln\left[1 + G(e^{\phi_1/\phi_e} - 1)\right] \quad , \tag{20}$$

where ϕ_1 is the input fluence, ϕ_2 is the output fluence, and G is the small signal gain. We then adjust ϕ_e until the equation is satisfied. Since this equation is functionally transcendental, we started with an approximation designed to fit the high and low fluence limits,

$$\phi_e = (\phi_2 - \phi_1)\left[\frac{1}{\ln G} + \frac{\phi_2^2}{2G\phi_1\,(G\phi_1 - \phi_2)}\right] \quad , \tag{21}$$

and we then used Newton iterations (four were enough for six-digit accuracy) to refine the value. These iterations took the form

$$A = e^{\phi_1/\phi_e} \ ,$$

$$B = 1 + G(A - 1) \ ,$$

$$C = \ln B \ ,$$

$$\phi_e = \phi_e - \frac{\phi_e C - \phi_2}{\left(C - \dfrac{G\phi_1 A}{\phi_e B}\right)} \quad . \tag{22}$$

To fit actual data, we accounted for fixed loss in the rods by splitting them into equal parts applied at the rod ends. For higher losses, we used a more complicated method in which the rod was split into low-gain pieces, for each of which losses were applied at the ends and Frantz–Nodvik saturation was used for the gain.

Unfortunately, because essentially all the experimental data have a gain of 9 ± 1, there are insufficient experimental data available to obtain ϕ_e as a function of input fluence and gain. Therefore, we had to extrapolate the data to both lower and higher gains. We chose the two-ion model, in which the many actual ions of different cross sections in the glass are fit by two groups. One group had low cross section, σ_{LO}, and one had high cross section, σ_{HI}. By this method, we obtained a good fit for the E-309 fluorophosphate data with the following parameters:

- Wavelength = 1.053 μm.
- Average cross section = 2.6×10^{-20} cm^2.
- Fraction with σ_{LO} = 0.97.
- Value of $\sigma_{LO} = 2.23 \times 10^{-20}$ cm^2.
- Fraction with σ_{HI} = 0.03.
- Value of $\sigma_{HI} = 14.56 \times 10^{-20}$ cm^2.

The values assigned to these parameters are not unique since offsetting changes in the low-cross-section fraction and value over a moderate range will lead to other equally satisfactory fits. The above values are in the middle of the best-fit band.

The two-ion model was used to extend the saturation data to other gains. There is some danger in this procedure, since no supporting data exist. However, we determined the equivalent saturation fluence of two-ion amplifiers of gains ranging from 1.2 to 100, for input fluences that gave outputs from 1 to 10 J cm^{-2} (the experimental range). From numerical calculations we arrived at analytic expressions of simple form that fit the equivalent saturation fluences well. The formulas for these expressions are

$$K_1 = 0.22 + \frac{0.32}{G + 0.7} \quad ,$$

$$K_2 = \frac{\left(1 + 0.11\,G - \dfrac{5}{G + 6}\right)}{K_1} \quad ,$$

$$\phi_e = \phi_0 \left[0.6 + K_1 \left(1 - e^{\frac{-\phi_1 K_2}{\phi_0}} \right) \right] \quad , \qquad (23)$$

where K_1 and K_2 are constants and ϕ_0 is the no-blockage saturation fluence of an ion with the average cross section

$$\phi_0 = \frac{h\nu}{\sigma} \quad . \qquad (24)$$

Figure 2-224 shows the fit for this expression. Solid lines in this figure are a two-ion-model fit to the experimental data at a gain of approximately 9. Dotted lines are the analytic expression shown above.

To adapt our formula to a variety of glasses, we modified the above expressions by introducing the following knobs:

- The initial saturation ratio, R.
- The saturation tilt factor, T.

As R is varied, the very-low-fluence value of ϕ_e changes, as given by

$$\phi_e = \frac{h\nu R}{\sigma} \quad , \qquad (25)$$

when $\phi_2 \ll \phi_e$.

The factor T changes the amount that ϕ_e varies with fluence. When T is zero, ϕ_e does not increase with input fluence. When T is unity, ϕ_e varies in the same manner as E-309 glass. Therefore, the saturation is found by performing the following steps:

- Determine R and T for the glass used by fitting the experimental saturation data. For each amplifier, ϕ_1 and G will be known.
- Calculate.

$$K_1 = 0.22 + \frac{0.32}{G + 0.7} \quad ,$$

$$K_2 = \frac{\left(1 + 0.11\,G - \dfrac{5}{G + 6}\right)}{K_1} \quad ,$$

$$\phi_e = \phi_0 \left[R + TK_1 \left(1 - e^{\frac{-\phi_1 K_2 T}{\phi_0}} \right) \right] \quad . \qquad (26)$$

- Apply the Frantz–Nodvik equation, using ϕ_e.

Saturation determined by this method agrees with experimental results. It should also give good agreement with actual amplifier energy gains, although we need saturation data at a variety of small signal gains to be sure. SNOBAL runs quickly with this method, with the same accuracy we expect with full use of the two-ion model.

Author: J. B. Trenholme

Nova Pulse-Shape Generation. Nova will provide enough energy to drive targets to high density. High density means high compression, which requires shaped pulses;

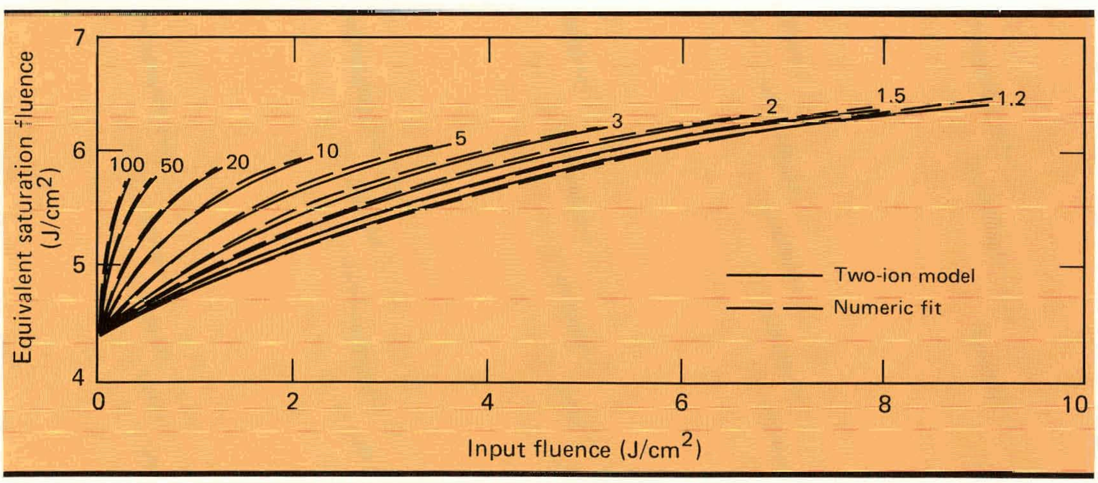

Fig. 2-224. Equivalent saturation fluence of E-309 fluorophosphate glass as a function of input fluence.

therefore, the laser system must be designed to produce shaped pulses. We developed methods of calculating the input pulse needed to produce the desired output from Nova (or any similar laser chain). Such calculations are now routine in our laser-chain design process.

The two pulse shapes[106] depicted in Fig. 2-225 are representative of those required for Nova experiments. Both pulses have flattened peaks and rapid decay. The pulse shown in Fig. 2-225(a) has an initial part consisting of a short, square section followed by a zero-power gap and a rectangular final phase. The other pulse shown in Fig. 2-225(b) has a long, flat lower-power initial phase followed by a smooth rise to the final peak. Both pulses produce essentially the same results at the target.

At first, it seems difficult to calculate the input shape needed to produce such output pulses. We noted, however, the lack of lower-level drain and other temporal effects in the saturation behavior of the phosphate and fluorophosphate glasses in the Nova chain. This meant that the chain output fluence was a function solely of the input fluence—i.e., after a specific fluence had passed through the chain, the gain was reduced by saturation to a known value. This reduction is independent of the temporal shape of the fluence. The next packet of photons was then amplified by an amount determined only by the preceding fluence, not by its temporal shape. As a result, a table of output fluence as a function of input fluence could be read "backwards" to derive input as a function of output. This process was performed by

- Integrating the output-power pulse shape with time to obtain its fluence.
- Reading the input-to-output fluence table to obtain input fluence.
- Differentiating to get the desired input-power shape.

We had trouble, of course, where nonlinear optical effects caused power-dependent shape distortions, but, even in this case, we had a good starting point from which to calculate our input pulse shape.

The input-to-output fluence table is produced (only once for each chain) by running an appropriate saturated-gain propagation code (we used the two-ion code GAINN) for a variety of input fluences and recording the input and output fluences for each run.

The table we used for the Nova phosphate–fluorophosphate baseline is shown in graphical form in Fig. 2-226. It is monotonic and has the characteristic heavily saturated curvature of a high-efficiency chain design. The all-phosphate Nova chain has a similar, but less linear, transfer characteristic. Results for the chain with phosphate drive and fluorophosphate in the 315- and 460-mm amplifiers are shown in Fig. 2-226.

Figure 2-225(a) shows the two-rectangle pulse shape, as desired at the output of the chain. In Fig. 2-227(a) the fluence of this

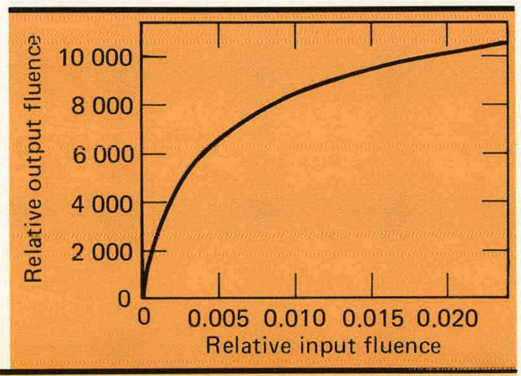

Fig. 2-226. Input-to-output fluence transfer characteristics of the Nova chain.

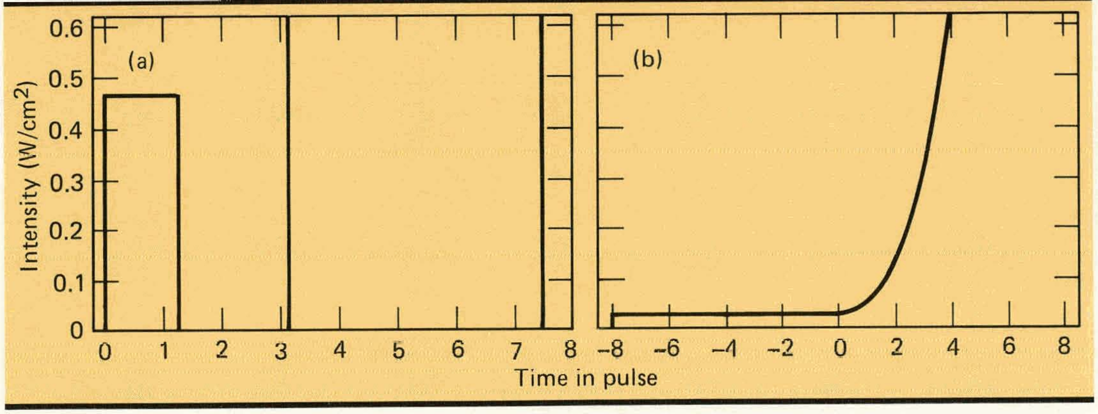

Fig. 2-225. (a) Two-rectangle laser pulse shape, as supplied by the target-design group. (b) The smoothly rising pulse shape. The target performance is roughly the same with this pulse as it is with the two-rectangle pulse.

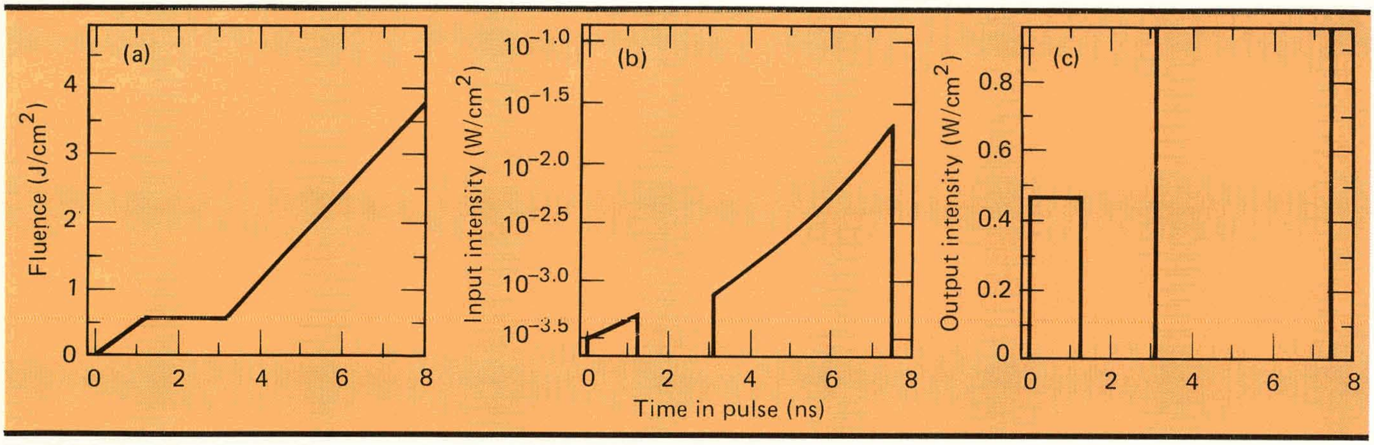

Fig. 2-227. (a) Desired output fluence as a function of time—the integral of Fig. 2-225(a). (b) Input intensity vs time required to produce Fig. 2-225(a) at the output of Nova. (c) The pulse of (b), after propagation through the Nova chain using the two-ion model in GAINN, is very close to the desired output shown in Fig. 2-225(a).

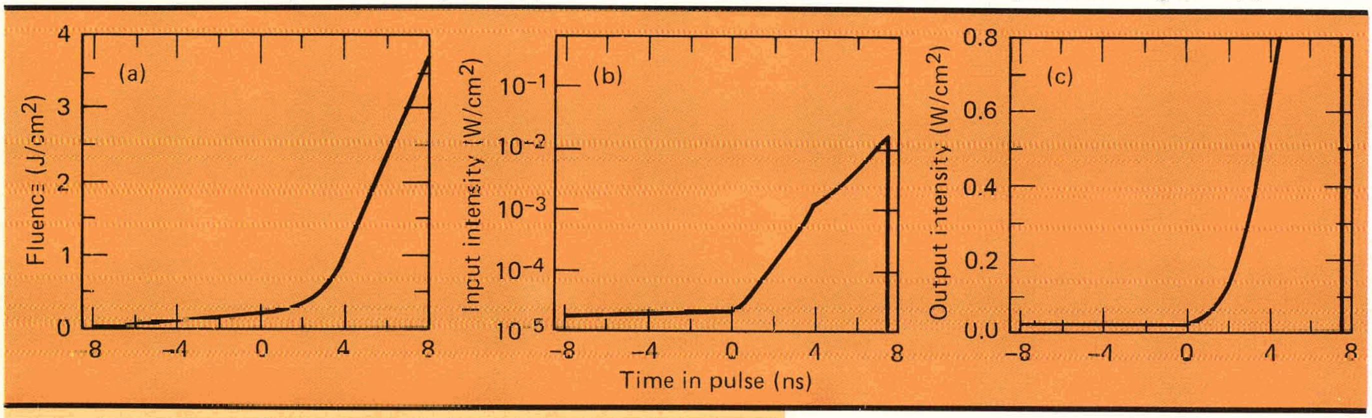

Fig. 2-228. (a) Desired output fluence as a function of time—the integral of Fig. 2-225(b). (b) Input intensity vs time required to produce Fig. 2-225(b) at the output of Nova. (c) The pulse of (b), after propagation through the Nova chain using the two-ion model in GAINN, is very close to the desired output shown in Fig. 2-225(b).

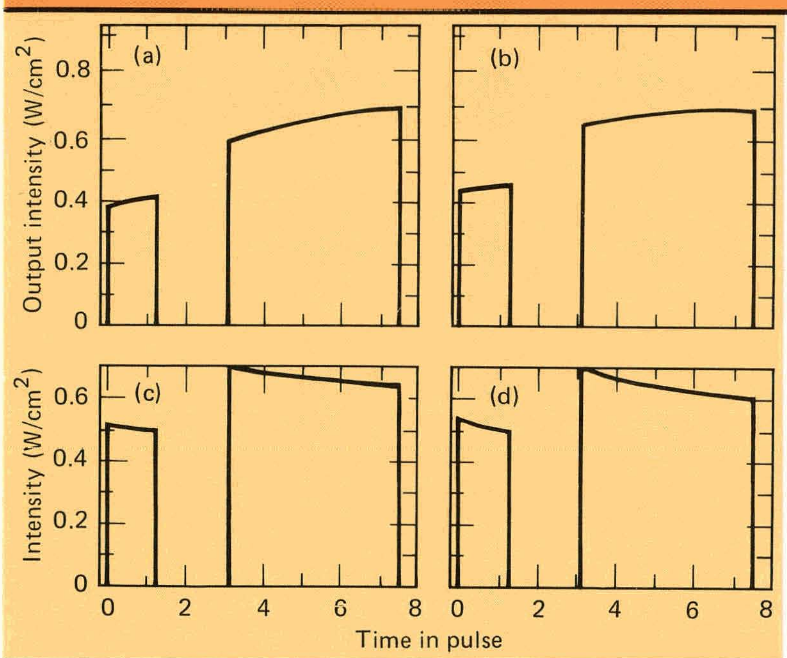

Fig. 2-229. The result of propagating the pulse in Fig. 2-225(a) through Nova at (a) 80%, (b) 90%, (c) 110%, and (d) 120% of the nominal energy of the pulse.

pulse as a function of time is graphed. The fluence is transformed by the function in Fig. 2-226 to produce an input fluence that is differentiated to give the required input intensity shown in Fig. 2-227(b). Figure 2-227(c) shows the results of running the calculated input pulse forward through the chain using GAINN; it is clear that the desired output is quite closely reproduced.

Figures 2-228(a) through (c) show the same sequence of steps as do Figs. 2-227(a) through (c) except that a smoothly-rising pulse instead of the two-rectangle pulse is propagated. Note that the 25:1 dynamic range of the output pulse requires a 1000:1 dynamic range in the input pulse.

We need to know how sensitive such factors as the output shape and energy are to the input parameters. Figure 2-229(a) shows the output resulting from the pulse of Fig. 2-225(a) with 80% of its correct amplitude; Fig. 2-229(b) is at 90%, Fig. 2-229(c) is at 110%, and Fig. 2-229(d) is at 120%. There are overall energy differences, shape distortions, and changes in the relative sizes of the two rectangles. The impact of these modifications on the performance of the target has not yet been evaluated. Figures 2-230(a) through (d) show the smoothly-rising pulse output for the same 80, 90, 110, and 120% sequence of input energies shown in Fig. 2-229.

Figure 2-231 shows the result of changing just the height of the first rectangle in Fig. 2-225(a) by plus or minus 10%; Fig. 2-232 shows the effect of varying a 1-ns block of the main rectangle by plus or minus 10%. To the first order, the changes are mirrored in direct proportion at the output, with some distortion of later portions of the pulse due to differences in saturation.

In summary, saturation in the Nova laser at a 3-ns pulse duration requires a preshaped input pulse of larger dynamic range than the desired output pulse. Input energy changes and shape errors are propagated with less effect. An input pulse produced with better than 1000:1 dynamic range and (perhaps) 5% amplitude stability will be required to maintain adequate control over the output pulse shape and to allow high compressions.

Authors: W. E. Warren and J. B. Trenholme

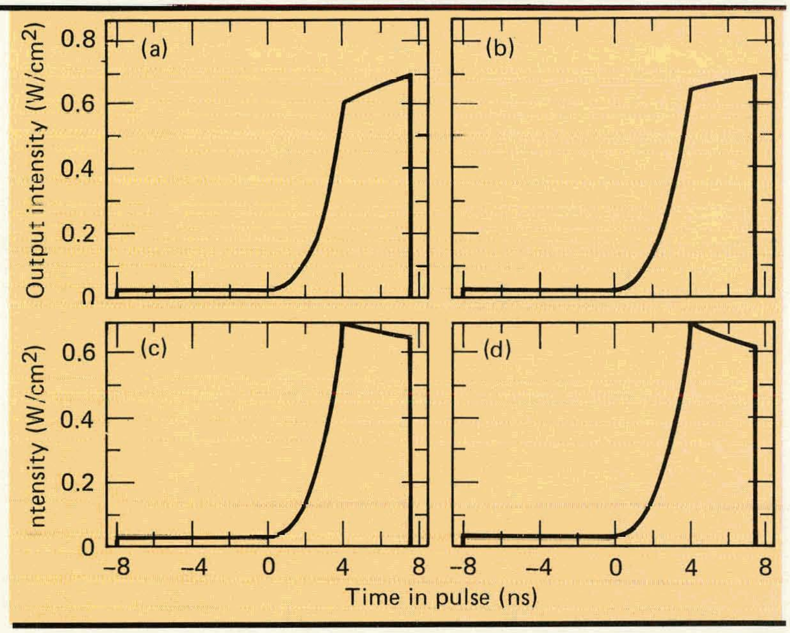

Fig. 2-230. The result of ▲ propagating the pulse in Fig. 2-225(b) through Nova at (a) 80%, (b) 90%, (c) 110%, and (d) 120% of the nominal energy of the pulse.

Fig. 2-231. The result of propagating the pulse in Fig. 2-225(a) through Nova with the first rectangle at (a) 90% and (b) 110% of its nominal ▼energy.

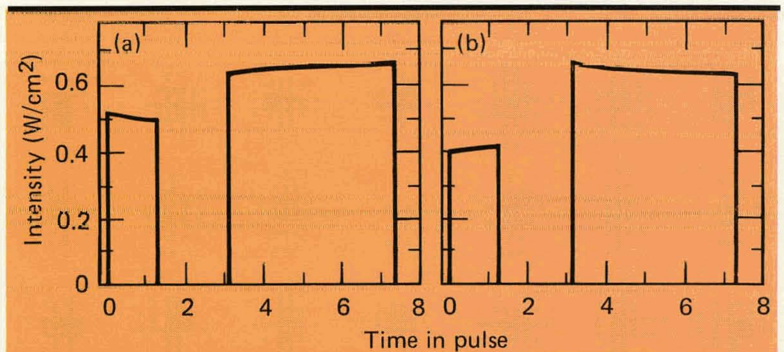

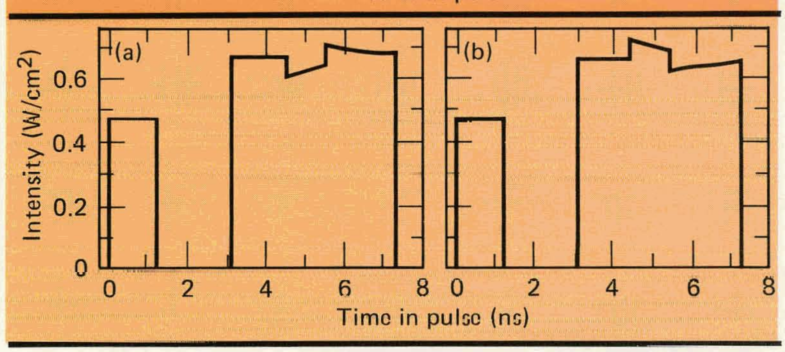

Fig. 2-232. The result of propagating the pulse in Fig. 2-225(a) through Nova with a 1-ns portion of the second rectangle at (a) 90% and (b) 110% of its nominal energy.

Evaluation of the Iodine Laser. The capabilities of the flashlamp-pumped iodine laser were evaluated and compared with Nd:glass for fusion-laser applications while the author was on sabbatical to the Max Planck Institute in Garching, Federal Republic of Germany. In particular, the Asterix III iodine laser at the Institute was investigated in detail.

Performance simulations and cost estimates similar to those developed for the designs of Shiva and Nova were employed for this comparison. The general conclusion was that the iodine laser is superior for pulse durations up to a few nanoseconds, where nonlinear effects limit the performance of Nd:glass; however, Nd:glass is superior for longer-duration laser pulses because it has better energy-storage capability.

We developed detailed models to simulate absorption, emission, saturation, and energy storage of the iodine laser. Significant modifications of the flashlamp model were necessary to obtain agreement with the experimental results.

The atomic-iodine photodissociation laser has only a single absorption line in the ultraviolet (277 nm). The absorption cross-section, σ_A, for perfluoroisopropyl iodide ($i\text{-}C_3F_7I$) can be approximated by

$$\sigma_A = 6.7 \times 10^{-19}\ \mathrm{cm}^2 \times \frac{e^{-\left(\frac{\lambda - 277\ \mathrm{nm}}{29\ \mathrm{nm}}\right)^2}}{\left[1 + \left(\frac{\lambda - 277\ \mathrm{nm}}{58\ \mathrm{nm}}\right)^2\right]} , \quad (27)$$

where λ is the wavelength. An integration of the iodine absorption with the flashlamp emission spectrum yields (for typical conditions) a total absorption efficiency of

$$\epsilon_A \simeq 0.82 - 0.41 \left[e^{-5.4\times 10^{-19}\ \mathrm{cm}^2 (n_I \ell)} + e^{-1\times 10^{-19} \mathrm{cm}^2 (n_I \ell)}\right] \quad (28)$$

for blackbody radiation in the wavelength interval from 220 to 340 nm, where n_I is the iodine density and ℓ is the path length in the absorber. This simplified dual-absorber model is valid for blackbody temperatures from 10 000 to 20 000 K. For high pump intensities and low iodine concentrations, the effective absorption is somewhat lower due to bleaching, as discussed in detail by Witte.[107] This correction was not included in our analysis.

The emission of the iodine laser is centered at a wavelength $\lambda_L = 1.315\ \mu\mathrm{m}$, with the emission spectra consisting of a hyperfine structure with six lines that can be overlapped by pressure broadening, as shown in Fig. 2-233. The effective emission cross section for the F3 → 4 transition can be approximated by

$$\sigma_{34} = \frac{7}{12}\sigma + \frac{5}{12}\Delta\sigma \quad , \quad (29)$$

where

$$\sigma \approx 3.5 \times 10^{-18}\ \mathrm{cm}^2\ \mathrm{GHz} \left\{ \frac{0.64}{\Delta\nu} + \frac{0.36}{\left[1 + \left(\frac{9.3\ \mathrm{GHz}}{\Delta\nu}\right)^2\right]\Delta\nu} \right\} \quad (30)$$

and

$$\Delta\sigma \approx \frac{3.5 \times 10^{-18}\ \mathrm{cm}^2\ \mathrm{GHz}}{\left[1 + \left(\frac{26.6\ \mathrm{GHz}}{\Delta\nu}\right)^2\right]\Delta\nu} \quad . \quad (31)$$

The line width, $\Delta\nu$ (FWHM), is determined by pressure broadening and a Doppler width of about 0.25 GHz. The pressure-broadening coefficients used in this analysis are 15 GHz/bar for i-C_3F_7I, 3.7 GHz/bar for argon, and 5 GHz/bar for sulfurhexafluoride (SF_6). The experimental results for various iodine lasers are in close agreement with the above two-line approximation, as shown in Fig. 2-234.

The effective saturation fluence, ϕ_{34}, for single-line extraction of the dominating F3 → 4 transition depends on the partial overlap of the six hyperfine emission lines and has a range of

$$\frac{14}{31}\frac{h\nu}{\sigma_{34}} \le \phi_{34} \le \frac{2}{3}\frac{h\nu}{\sigma_{34}} \quad (32)$$

for total line separation and for complete overlap, at low pressure and high pressure, respectively, corresponding to a maximum energy extraction ranging from 45 to 67%.

This complex saturation behavior can be approximated by defining two saturation fluences and sequentially applying the Frantz–Nodvik equation for the upper F3 and F2 sublevels. The effective saturation fluences of the two upper lines are determined by

Fig. 2-233. Iodine emission spectra for line widths of 0.25, 2, and 20 GHz, corresponding to argon pressures of 0, 0.5, and 5 bar.

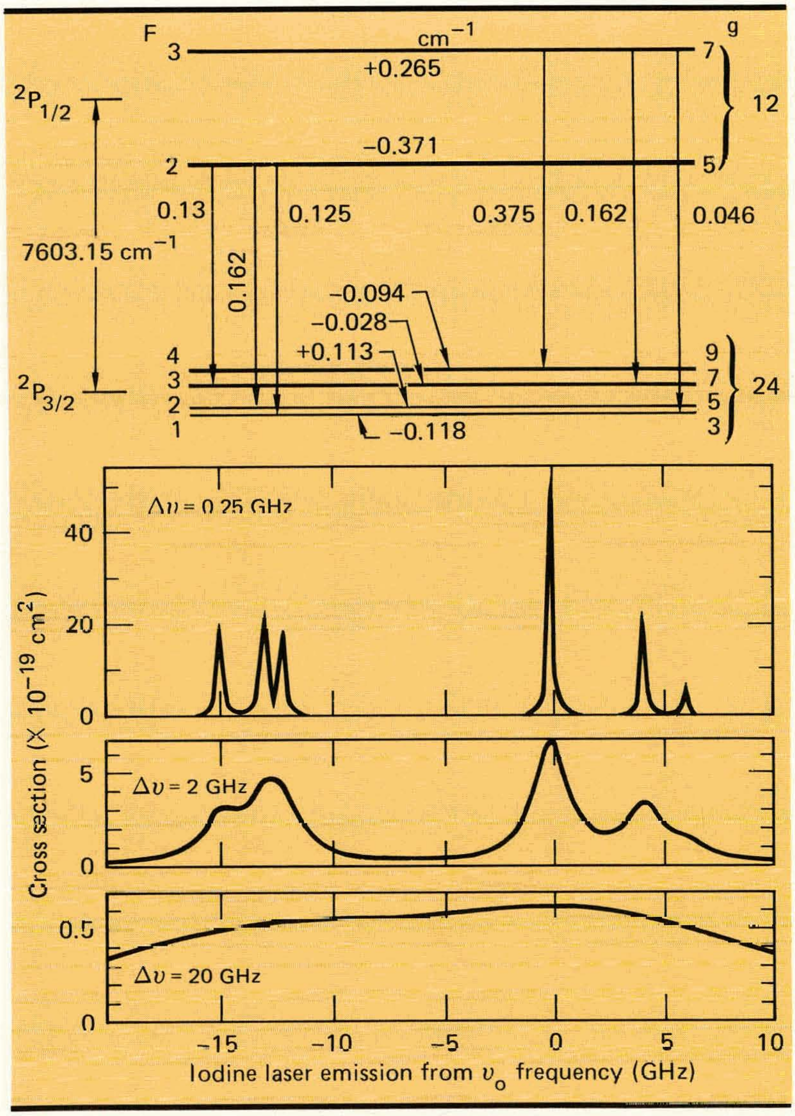

$$\phi = \frac{h\nu}{\left[1 + \left(\frac{7}{24 - \Delta g}\right)\right]^{\sigma}} ,$$

and

$$\phi_\Delta = \frac{h\nu}{\left(1 + \frac{5}{\Delta g}\right)^{\Delta\sigma}} , \qquad (33)$$

where

$$\Delta g \approx 10 \left[1 - e^{-\left(\frac{\Delta G}{\sigma} + \phi_i \frac{\Delta\sigma}{h\nu}\right)}\right] \qquad (34)$$

and ϕ_i is the laser input fluence. We have compared this calculation with the measured output energy from the iodine laser amplifier (V2) in Fig. 2-235.

The stored energy, E_s, of an amplifier can be determined by measuring the output energy of the amplifier as an oscillator with various output reflectances, R. From these measurements, the internal transmission, T, of the laser cavity can be deduced, as can the stimulated emission cross section. The output energy, E_o, for a pulsed iodine oscillator can be approximated by

$$E_0 \approx 0.97 \frac{\ln R}{\ln(RT^2)} (E_S - E_T) , \qquad (35)$$

where the threshold energy, E_T, is given by

$$E_T = \frac{h\nu}{\sigma_{34}} A \ln\left(\frac{1}{T\sqrt{R}}\right) , \qquad (36)$$

with A being the cross-sectional area of the laser beam. The factor 0.97 takes into account the effects of quenching, deactivation, and recombination processes for i–C_3F_7I. In Fig. 2-236 we show an example of the measured output energies from the V2 amplifier for various SF_6 pressures. We obtained the best fit to the data with a stored energy of 25.5 J, a cavity transmission of 95%, and an energy loss of 5%/bar. We believe that the loss in output energy may be caused by shockwaves reducing the effective clear aperture with increasing foreign-gas pressure.

The preceding models allow us to perform rough estimates of the various efficiency terms for the iodine laser. To obtain uniform gain distributions, we normally use a pressure-diameter product of about 0.3 bar/cm, which corresponds to an absorption efficiency of 63% for blackbody radiation within the 220- to 340-nm band. At 11 000 to 18 000 K, approximately 30%

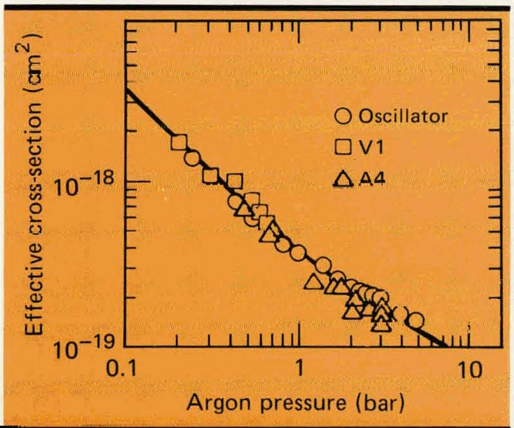

Fig. 2-234. Measured and calculated emission cross sections of the dominating F3 → 4 transition for various argon pressures.

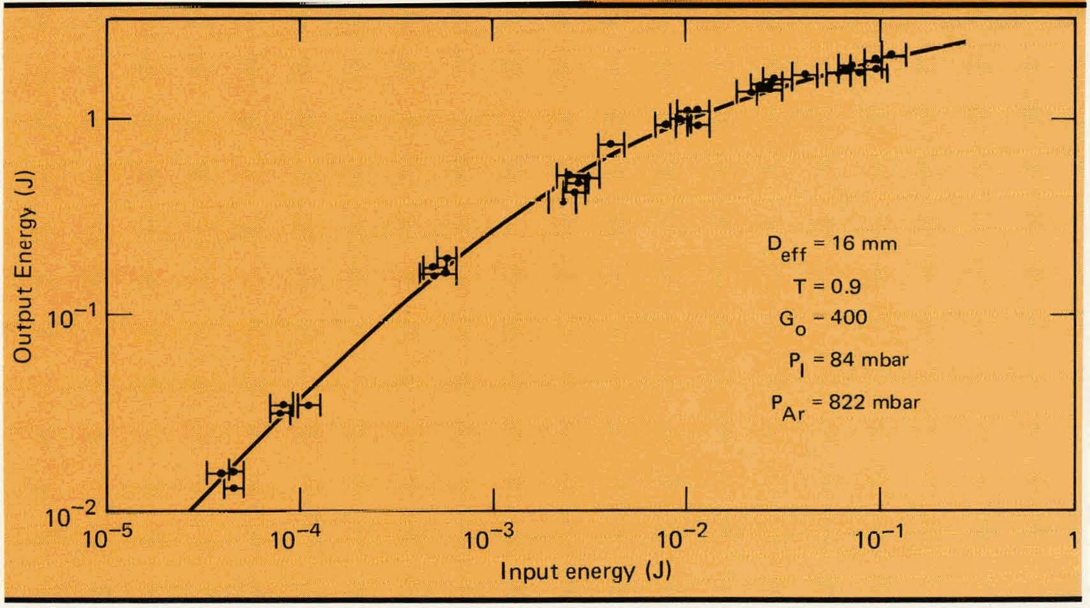

Fig. 2-235. Measured and calculated saturation characteristics of the V2 amplifier.

of the blackbody emission is within this band. The quantum efficiency from the absorbed photon to the emitted photon is 21%, and the quantum efficiency for excited-state iodine (I*) production is about 90%. This leads to an inversion efficiency of blackbody radiation of approximately 3 to 3.6%.

For flashlamps operating in the millisecond regime, overall lamp efficiencies of 70 to 80% have been measured. The flashlamp emission for short-pulse operation is shifted toward the ultraviolet and is partially absorbed in the flashlamp envelope. An overall lamp efficiency of about 60% is consistent with some short-pulse data and yields a maximum energy-storage efficiency of approximately 2%. However, we know that there are other losses that reduce this efficiency; e.g., shockwaves caused by the evaporation of condensed materials reduce the effective clear aperture to about 80% of its maximum. The coupling of flashlamp light into the laser medium is mainly dependent on the design of the pump cavity and reflectors. An overall efficiency of 1.4% was reported for a cylindrical laser cavity with a single central flashlamp; this yields a coupling efficiency greater than 70%. For

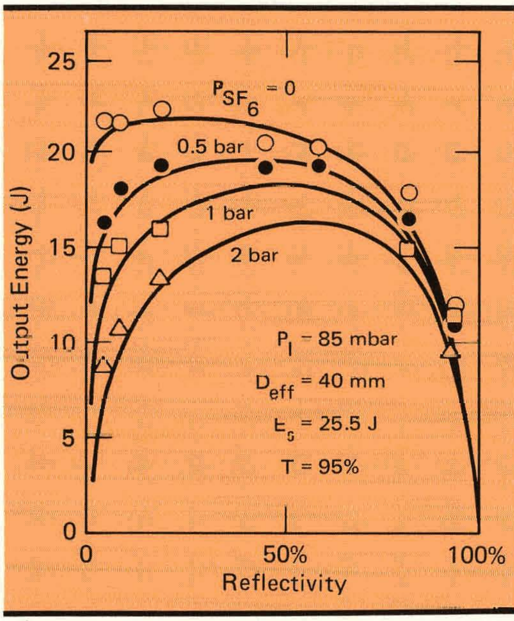

Fig. 2-236. Oscillator performance of the V2 amplifier for various output reflectors and SF_6 pressures.

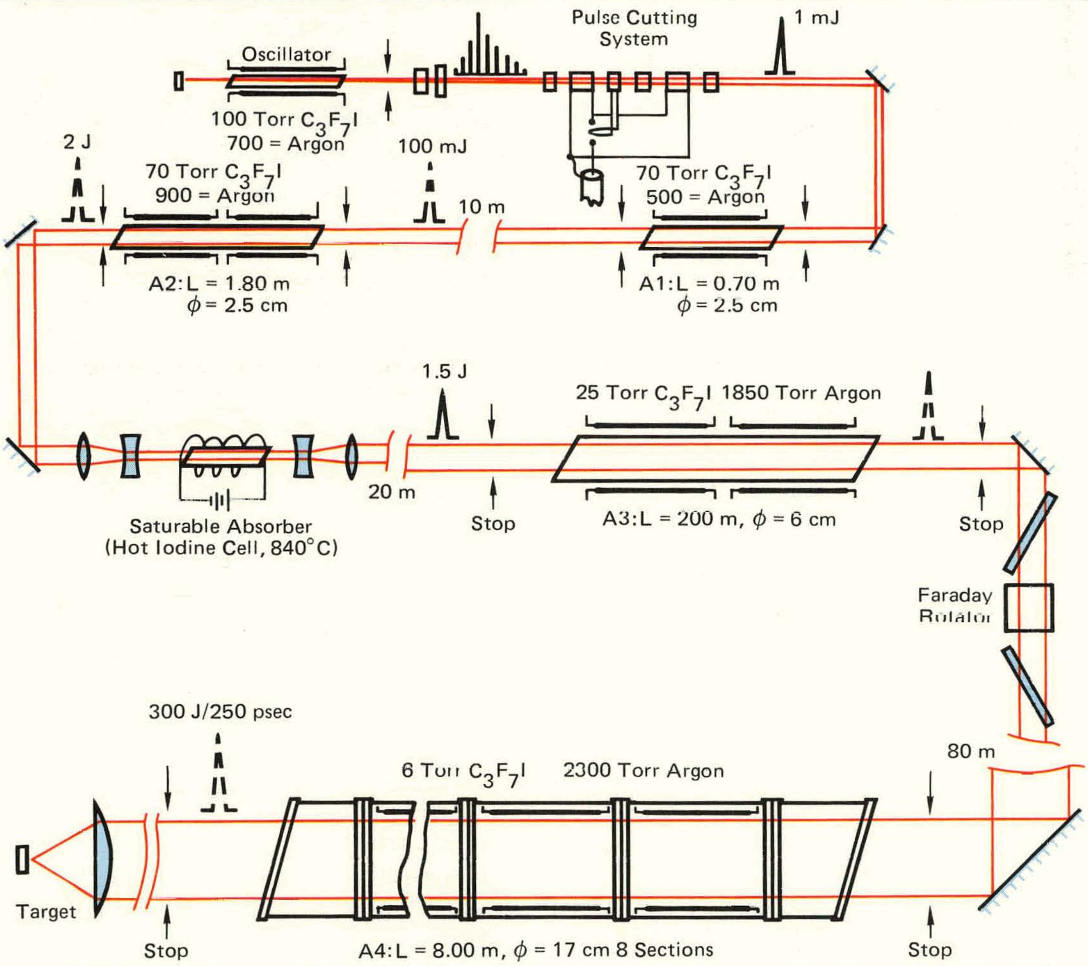

Fig. 2-237. Schematic layout of the Asterix III iodine laser.

pump cavities where the flashlamps surround the laser medium, we have measured energy-storage efficiencies of 0.5 to 0.8%, which correspond to coupling efficiences of 30 to 50%.

During amplifier operation the laser pulse is transmitted before the pumping process is completed so that the area losses caused by shockwaves will be reduced. This compromise reduces the pump-energy utilization to about 85%, while the extraction efficiency is limited to between 45 and 67% for low- and high-pressure amplifiers, respectively. With the Asterix III laser, about 30% of the stored energy is extracted because there is insufficient drive energy for the final amplifier; the transmission losses in the laser chain cause an additional efficiency reduction that leads to an approximate overall efficiency of 0.1%.

With significant improvements of the pump cavities, and with optimization of the laser-system design, an overall efficiency of 0.5% should be feasible for flashlamp-pumped iodine lasers. By comparison, we know that the overall efficiencies of Nd:glass lasers are 0.05% for Argus, 0.07% for Shiva, 0.25% for Nova, and 0.5% for Super Nova. However, these Nd:glass lasers were designed for high performance-to-cost ratios and not for maximum efficiency; significant improvements to the efficiency of these lasers could be obtained at increased cost.

To compare iodine and Nd:glass laser systems, it is essential to obtain similar types of cost estimates and to consider the differences in the various stages of development. For example, the Asterix III laser[108] (schematically shown in Fig. 2-237) is currently at a stage of development comparable to Cyclops.[109] The specifications for Asterix III are summarized in Table 2-42.

To optimize a laser system we must have a reasonable cost scale for the individual components. With the data available on the Asterix III amplifiers (Table 2-42), we performed rough scaling of the mechanical hardware and the gas-circulation system with the active volume, V, of the laser. These were applied in the form

$$C_{ME} \approx 8K\$ \sqrt{V[l]} \quad , \tag{37}$$

where C_{ME} is the mechanical-engineering cost. The per-window cost for optics, C_0, was scaled with the clear aperture, D, by

$$C_0 \approx \frac{6\$}{cm^2} D^2 \quad . \tag{38}$$

The cost for flashlamps and energy storage for the Asterix III amplifiers is very high in comparison to LLNL costs. The reason for the higher costs is attributed to the short pump-pulse durations required for iodine and to the relatively small size of the energy-storage bank. For a better comparison, we assumed a doubling of the energy-storage expenditure, and we scaled the cost for electrical engineering, C_{EE}, by

$$C_{EE} \approx 1K\$(N_L) + 0.32 \frac{\$}{J} E_B \quad , \tag{39}$$

where N_L is the number of lamps and E_B is the bank energy. We also applied the cost scaling developed for Shiva to all other components, such as isolators, focusing optics, and spatial filters.

We modified the lumped-element code, SPACE,[110] for the iodine laser and normalized it to the performance of the Asterix III laser shown in Fig. 2-237. There

Table 2-42. Iodine amplifiers for Asterix III laser.

Amplifier parameter	Unit	Type amplifier A1	A2	A3	A4
Active aperture (D_A)	cm	1.5	1.6	5.5	15.5
Active length (L_G)	cm	76.0	180.0	200.0	800.0
Lamp circle diameter (D_L)	cm	4.5	5.0	11.0	22.3
Clear aperture (D)	cm	2.5	2.5	7.5	17.0
Active volume (V)	litre	0.4	0.9	8.8	181.0
No. of flashlamps (N_L)	—	4	4	16	64
No. of circuits (N_C)	—	1	1	8	32
Arc length (L_A)	cm	65.0	79.0	92.0	92.0
Bore diameter (d)	cm	0.8	0.8	1.8	1.8
Capacitance (C)	μF	3.3	5.5	11.3	11.3
Maximum voltage (U)	kV	40.0	40.0	40.0	40.0
Xe fill pressure (P_{xe})	Torr	30.0	30.0	30.0	30.0
C_3F_7I pressure (P_I)	Torr	70.0	70.0	25.0	9.0
Ar pressure (P_A)	Torr	400.0	1000.0	2000.0	2300.0
Nominal input energy (E_B)	kJ	3.0	5.0	72.0	288.0
Nominal energy storage (E_s)	J	10–15	15–20	350.0	1400.0
Gain uniformity	—	1:30	1:30	1:30	1:10
Cost (FY76):					
Mechanical engineering	k$	1.1	1.2	15.0	65.0
Gas circulation	k$	2.6	4.0	14.0	35.0
Windows	k$	0.1	0.1	0.6	3.0
Flashlamps	k$	0.2	0.2	4.0	26.0
Energy storage	k$	5.6	6.8	55.0	190.0
Total cost	k$	9.6	12.3	88.6	319.0

(a) Performance of improved Asterix III laser.

No.	ID	Beam (mm)	No. of components	Thick (mm)	Pressure: Iod (mbar)	Pressure: Argon (mbar)	Bank (kJ)	Gain: Small signal	Gain: Saturated	Energy (J)	Inc. B value	Tot B value	Flux (J/cm²)	Cost (k$)
1	Amplifier 1	10	1	10	80	750	3	300.00	165.27	0.17	0.01	0.01	0.21	.10
2	Pockels cell	13	1	50	0	0	0	0.90	0.90	0.15	0.03	0.04	0.12	13
3	Amplifier 2	16	2	10	80	1900	5	300.00	20.63	3.07	0.08	0.12	1.53	13
4	Absorber	12	4	5	0	0	0	0.90	0.81	2.50	0.26	0.38	2.71	2
5	Turning mirror	60	3	0	0	0	0	0.97	0.97	2.42	0.00	0.38	0.09	3
6	Amplifier 3	60	2	20	33	5000	72	250.00	28.71	69.55	0.27	0.65	2.46	63
7	Beam splitter	60	1	20	0	0	0	0.98	0.98	68.16	0.21	0.86	2.46	2
8	Polarizer	60	1	30	0	0	0	0.97	0.97	66.11	0.30	1.16	2.41	3
9	Faraday rotator	60	1	20	0	0	10	0.98	0.98	64.79	0.25	1.41	2.34	15
10	Polarizer	60	1	30	0	0	0	0.97	0.97	62.85	0.29	1.70	2.29	3
11	Turning mirror	155	4	0	0	0	0	0.96	0.96	60.33	0.00	1.70	0.33	13
12	Amplifier 4	155	2	35	13	3750	288	200.00	8.57	517.11	0.55	2.24	2.74	267
13	Focusing optics	155	2	25	0	0	0	0.92	0.92	475.74	0.70	2.94	2.74	30
									0.93	443.87	2.94			
	Totals of interest						378		443.67	443.87		2.94		438

Z-value = 1.013 kJ/M$

Cost: ME = 186; EE = 213; Optics = 40

Input energy (J)	1.00000E-03
Pulse duration (ns)	0.3
Laser wavelength (μm)	1.315
Refractive index	1.503
Nonlinear index (E-13 esu)	1.2
Large scale noise (%)	0.2
Small scale noise (%)	0.02
Scatter loss per surface (%)	0.3
Absorption loss (%/M)	1.0

(b) Cost analysis of improved Asterix III laser.

No.	ID	Clear aperture MM	No. of components	Length (cm)	Cost (k$)	ME (k$)	Optic (k$)	EE (k$)	Stored joule	Efficiency (%)
1	Amplifier 1	25	1	76	10	4.9	0.1	5.0	12	0.39
2	Pockels cell	25	1	0	13	3.7	4.3	5.0	0	0.00
3	Amplifier 2	25	2	180	13	7.5	0.1	5.6	20	0.39
4	Absorber	48	4	0	2	1.0	1.0	0.0	0	0.00
5	Turning mirror	75	3	0	3	2.7	0.7	0.0	0	0.00
6	Amplifier 3	75	2	200	63	23.8	0.7	39.0	286	0.40
7	Beam splitter	100	1	0	2	1.2	0.4	0.0	0	0.00
8	Polarizer	100	1	0	3	1.4	2.0	0.0	0	0.00
9	Faraday rotator	100	1	0	15	6.7	6.0	2.0	0	0.00
10	Polarizer	100	1	0	3	1.4	2.0	0.0	0	0.00
11	Turning mirror	170	4	0	13	8.2	4.6	0.0	0	0.00
12	Amplifier 4	170	2	800	267	107.8	3.5	156.2	1171	0.41
13	Focusing optics	170	2	0	30	15.3	14.5	0.0	0	0.00
	Totals of interest				438	186	40	213		

Volume of laser medium = 192 liters

Number of flashlamps = 88

Table 2-43. Performance and cost of improved Asterix III laser.

are several hardware improvements that could easily be implemented to make Asterix III comparable with Argus. The performance and cost of an improved version of Asterix III are shown in Table 2-43 and Fig. 2-238. We have also shown in Fig. 2-238 the performance-to-cost ratio for Argus, at various pulse durations and identical fluence limitations (5 J/cm at 1 ns), scaled with the square root of the pulse duration; the relative performance of Shiva is shown in dashed lines. Note that Shiva was designed as a short-pulse laser and, thus, provides an approximate 40% improvement over Argus for 150-ps (or shorter) pulse durations.

The uncertainty band of ±15% primarily reflects the uncertainty in the relative cost of the Asterix III laser when compared to Argus. Moderate variations in the fluence limitations would affect the performance of both lasers in a similar fashion, though the relative comparison of the two systems would not be significantly changed.

In our analysis, we have considered only the cost of the laser hardware in FY76 dollars. The costs for target chambers, support structures, and facilities were assumed to be similar and were not included in this analysis. Hardware-development and system-development costs were also excluded from the analysis. From this analysis, we can conclude that both lasers are equivalent in the 1- to 2-ns regime. For short pulses, the iodine laser would provide an improvement two to three times better than Argus, while, for long pulses, Nd:glass lasers are superior. A detailed discussion on this subject is contained in Ref. 111. The support given to this analysis by the Projektgruppe für Laserforschung at the Institut für Plasma Physik in Garching is greatly appreciated.

Author: W. F. Hagen

Major Contributors: G. Brederlow, M. Nippus, G. J. Linford, and K. J. Witte

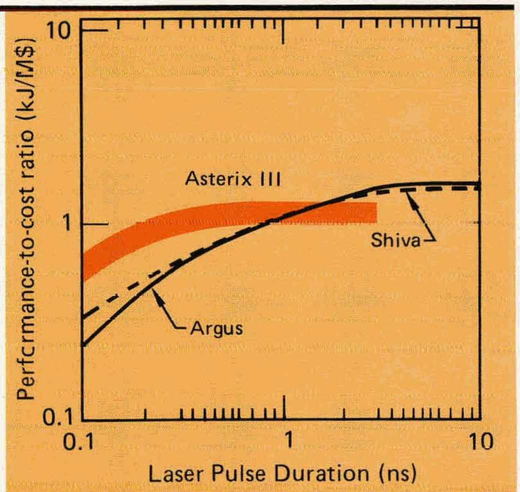

Fig. 2-238. Comparison of iodine and Nd:glass lasers for various pulse durations.

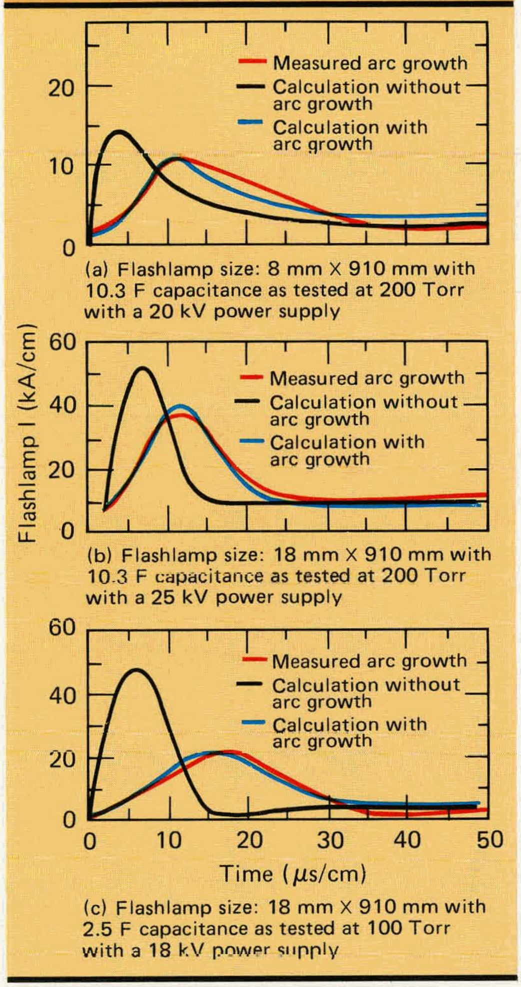

Fig. 2-239. Comparison of measured and calculated flashlamp currents, with arc growth and without arc growth.

Short-Pulse Flashlamp Model. During evaluation of the iodine laser, it became apparent to us that the present flashlamp model[112] required significant modifications for short pump-pulse durations (a few microseconds). There are large discrepancies between the experimental data taken by Linford[113] and the simulation models shown by the examples in Fig. 2-239.

In this short-pulse regime, the effect of arc growth cannot be ignored, especially for small lamps with high xenon pressures and low input energies. For example, we have observed that the arc expands at a rate of about 100 m/s for flashlamp pumping of Nd:glass lasers and requires 100 μs or more to fill the bore of the flashlamp. Because arc growth, at this rate, corresponds to a large fraction of the current rise time, inclusion of arc growth is essential for the accurate modeling of flashlamps.

Expansion velocities of from 40 to 3000 m/s have been experimentally observed for flashlamp arcs; these velocities are both well below and considerably above the speed of sound in xenon (180 m/s) at room temperature. The expansion velocity depends generally on the energy deposited into the conducting channel and on the type and density of the flashlamp gas.

In Fig. 2-240, we show an example for various input energies to a standard LLNL lamp. In this case, the average arc-growth velocities range from 40 to 120 m/s for input energies of 1 to 10 kJ. Our evaluation of the short-pulse lamps used by the Projektgruppe für Laserforschung in Garching, Federal Republic of Germany, results in average growth velocities of 1000 to 2000 m/s for typical input energies of about 3 kJ. We correlate these data with the initial specific-power growth rate, as shown in Fig. 2-241. By integrating the energy deposited into the arc, we can derive a more accurate, but slower, method for estimating the arc growth. The expansion of an unbounded arc channel can be correlated with the shock waves created during an explosive release of energy.[114-118] We modified this approach for confined arcs, including ionization and radiation losses, to match the flashlamp data.

Since typical flashlamp plasmas are close to local thermal equilibrium, we can approximate the degree of ionization by

Fig. 2-240. Determination of the effective arc diameter from the voltage and current characteristics of the flashlamps.

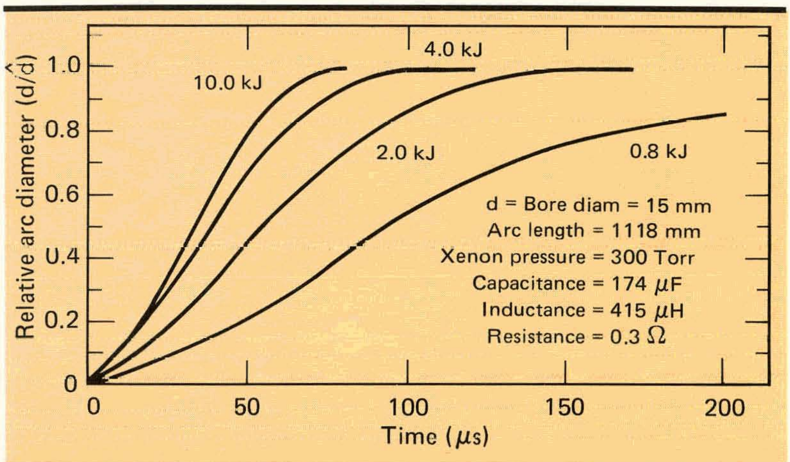

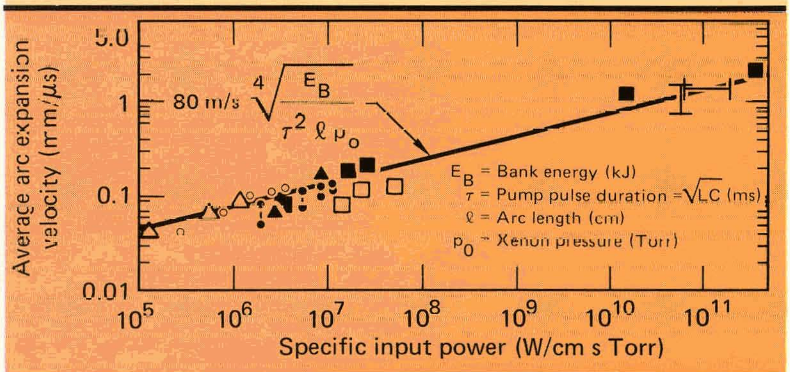

Fig. 2-241. Measured arc-growth velocities for various flashlamps and conditions. ▲

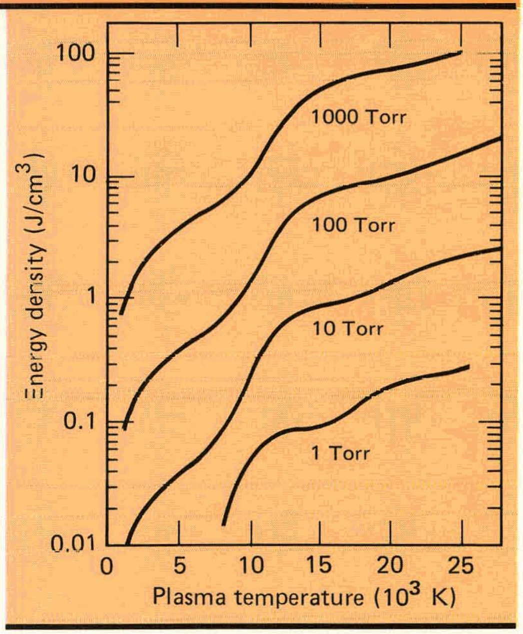

Fig. 2-242. Thermal- and ionization-energy densities of xenon plasmas for various pressures and temperatures.

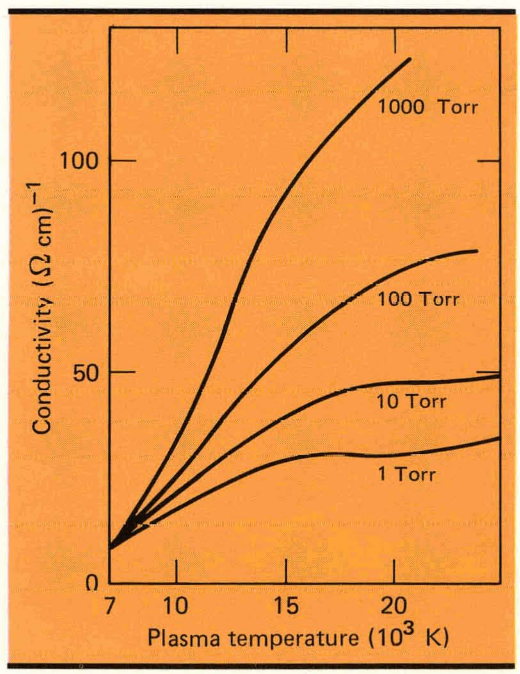

Fig. 2-243. Conductivities of xenon plasmas for various pressures and temperatures.

using the Saha equation. The plasma temperatures are sufficiently high that we must consider double and even triple ionization. From the degree of ionization, we can determine the thermal- and ionization-energy densities of the plasma, as shown in Fig. 2-242.

Under typical operating conditions, the total density of electrical input energy to a flashlamp is in the 1- to 100-J/cm^3 range, while the thermal and ionization energies of the arc become a large fraction for high xenon pressure and essentially increase the flashlamp "inertia." For short-pulse lamps, a xenon pressure of about 30 Torr is most effective because the input energy is limited to less than 10 J/cm^3. A higher pressure would reduce the response time and temperature of the plasma, leading to a reduced radiation efficiency in the UV pump band of iodine; a lower pressure would lead to higher temperatures, multiple stages of ionization, and a reduced emissivity of the plasma. In short, it is possible to adjust the temporal response of the flashlamp and the plasma temperature by changing the xenon pressure.

The calculated conductivities for xenon plasmas at various temperatures and pressures are shown in Fig. 2-243. The experimentally measured conductivity of the plasma compares well with the results of our calculations, obtained from the balance of the electrical and radiation energy.

The total radiant power emitted from the flashlamp consists of both continuum and line radiation. For transparent flashlamp plasmas, we must take emissivity and self-absorption into account. These effects require spectral and spatial integration over the plasma volume.

For plasmas in thermal equilibrium, we can approximate the effective absorption coefficient from the dispersion properties of the plasma. Our calculated absorption coefficients are of the same magnitude as the experimental data[119,120] shown in Figs. 2-244 and 2-245. We attribute the enhanced absorption observed at 0.9 μm to the strong lines of xenon at these wavelengths, while the increased transmission losses at ultraviolet wavelengths may be caused by absorption by the heated quartz walls.

Our work is still incomplete. Our lack of understanding of the absorption and reemission of flashlamp light is one of the weak links in our modeling of pump cavities. It is important to know where the absorbed energy goes. All indications so far are that most of it is lost.

Our model does provide a much better simulation of the electrical characteristics of

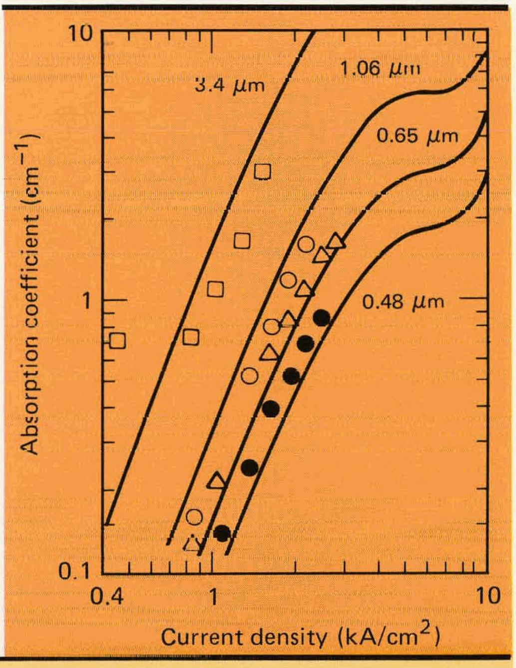

Fig. 2-244. Measured and calculated absorption coefficients for standard LLNL lamps at various wavelengths and current densities.

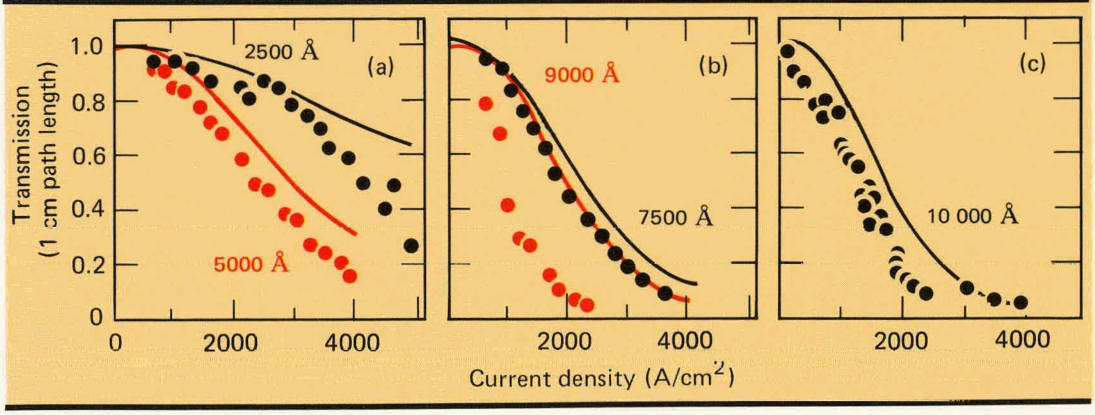

Fig. 2-245. Measured and calculated transmissions through 1 cm of xenon plasma as a function of current density at wavelengths of (a) 2500 Å and 5000 Å, (b) 7500 Å and 9000 Å, and (c) 10 000 Å.

flashlamps, especially for short pulse durations. The calculated absorption is of the correct magnitude (300 Torr), but, for low-pressure lamps, much higher transmission losses are observed than had been estimated. A more detailed description of this model is contained in a separate report.[121]

Author: W. F. Hagen

Super Nova. Lasers with output energies in the megajoule range and with pulse durations of 10 to 20 ns are required to investigate the performance of high-gain targets. It is possible that frequency-converted Nd:glass lasers can provide short-wavelength radiation at the megajoule level to improve target absorption and reduce preheating for inertial-fusion research.

An upgrade of Nova to a megajoule-class laser (Super Nova) may provide a capability for demonstrating high-gain microexplosions and the feasibility of the inertial-confinement fusion (ICF) approach for generating usable power with thermonuclear fusion. This upgrade requires neither new technologies nor new materials; it is essentially an extension of the Nova laser with a larger booster stage. The longer laser-pulse durations will allow operation of the laser at higher fluences because the damage limit to high-quality optical components generally increases as the pulse durations increase. Since the nonlinear effects become less important for long pulses, we can select low-cost laser glasses with high energy-storage capability. An example of such an upgrade option is discussed in detail.

The design of long-pulse lasers is dominated by the fluence limitation of the various optical components used in the system. The weakest links in an amplifier chain are the antireflection (AR) coatings. To avoid this limitation, we have used uncoated lenses on the input side of the spatial filters. However, the associated reflection losses do also reduce the effective energy extraction. Graded-index surfaces have damage limits lying between AR coatings and bare surfaces.

The trade-offs are best illustrated by plotting the ratio of extracted energy to cost as a function of the output fluence for amplifier stages with and without AR-coated spatial-filter lenses. In Fig. 2-246 we show an example of this comparison for a 74-cm amplifier stage of a typical silicate laser glass. The curves in the figure are envelopes for various numbers of disks per stage. For low fluence levels, few disks provide the best extraction-to-cost ratio, while for high fluence levels, many disks are required for optimal extraction. The details of this evaluation are shown in Fig. 2-247 for various numbers of disks per stage. There exists an optimal extraction and output fluence for every stage. Higher fluences actually reduce the extracted energy because of transmission losses and nonlinear effects.

In the example shown in Fig. 2-246, an average fluence limit at 10 ns of 30 J/cm^2 on bare surfaces provides the same extraction-to cost ratio as an AR coating with an average fluence limit of about 20 J/cm^2. At present, it is difficult to obtain AR coatings with damage thresholds sufficiently high to transmit high average fluences at 10-ns pulses (considering that the peak fluences are expected to be about 50% higher). In this case, the bare surfaces provide the better design option; however, graded-index materials appear to have sufficiently high damage thresholds to compete effectively with the bare-surface approach.

An evaluation of effective energy extraction depends to a large degree on the saturation characteristics of the laser material. From the experimental data

Fig. 2-246. Comparison of the performance-to-cost ratio of optimal 74-cm output stages with and without AR-coated spatial-filter lenses.

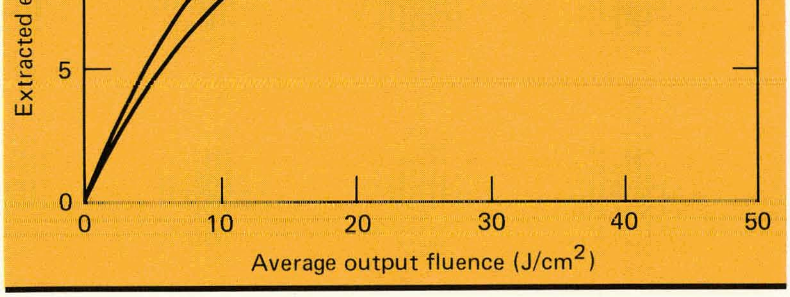

available, the effective saturation fluence increases with the laser fluence in the amplifier. This can be explained with site-to-site variations in the stimulated emission cross section. A dual-ion model is sufficiently accurate to simulate the experimental saturation data reported by Martin and Milam[122] by applying a single correction factor, k, to the calculated Judd–Ofelt cross section for each glass.

The best match to all the data was obtained with a degeneracy ratio of zero, a cross-section ratio of 20:3, and a gain coefficient ratio of 5:12 for the two ion species. The results of this evaluation for various laser materials is summarized in Table 2-44. The value σ_λ is the calculated Judd–Ofelt cross section at the wavelength of the measurement. The ratio $k = \sigma_0/\sigma_\lambda$, which shows the deviation of the cross section determined by saturation measurements and spectroscopy, was normalized to ED-2 silicate laser glass. The correction factor, σ_G/σ_λ, from gain measurements is also tabulated. There is a similar trend for σ_0 and σ_G, but the magnitudes are different.

The 30% deviation of k from unity for LHG-8 phosphate glass and LG-56 silicate glass has a large impact on system design and performance. For accurate simulations of various laser glasses, it is necessary to measure the gain and saturation for each glass in addition to obtaining spectroscopic data.

The sensitivity of the saturation characteristics on the evaluation of effective energy extraction is shown in Fig. 2-248, where an average saturation fluence of 5 J/cm^2 was applied instead of the dual-ion saturation model. In this case, an output fluence greater than 25 J/cm^2 would cause a reduction in the extracted energy-to-cost ratio due to transmission losses. In contrast, the dual-ion saturation model applied in Figs. 2-246 and 2-247 shows an increase in the effective energy extraction of up to 40 J/cm^2.

We evaluated a Nova upgrade to a nominal 1.5-MJ, 20-beam laser, applying Nova costs and the latest damage and saturation data. For this analysis, we used an average fluence limitation of 30 and 12.5 J/cm^2 for bare and AR-coated optics, respectively. Damage levels of up to 25 J/cm^2 at 10 ns have been measured on some research AR and high-reflective (HR) coatings. If production coatings, after aging, come close to such performance, we could tolerate a peak-to-average ratio of about two

Fig. 2-247. Extracted energy-to-cost ratio for 74-cm output stages with various numbers of disks.

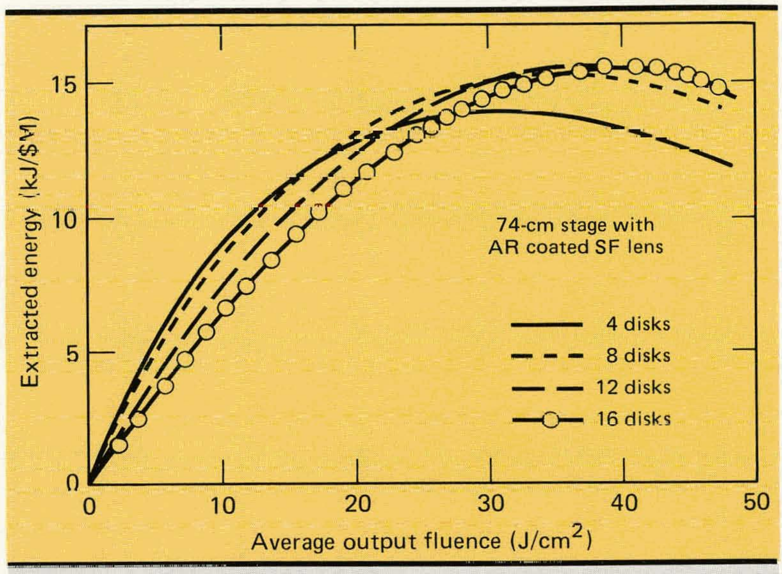

Glass	G_0	T(%)	λ	σ_λ	σ_0	σ_0/σ_λ	σ_G/σ_λ[a]
ED-2	6.3	96.2	1.0645	2.61	2.61	1.00	1.00
LSG-91H	4.1	88.5	1.0645	2.32	2.5	1.08	–
OI-H9	3.83	92.5	1.0645	1.44	1.7	1.18	–
LG-56	4.4	92.4	1.0645	0.90	1.2	1.33	–
Q-88	5.5	–	1.0645	2.82	2.4	0.85	–
YAG	6.36	97.0	1.0645	27–88	27	0.31–1.0	–
Q-88	12	99.0	1.053	3.9	3.5	0.90	0.93
LHG 8	8.5	98.6	1.053	4.0	2.8	0.70	0.93
LHG 10	7.5	98.0	1.053	2.55	2.4	0.94	0.84
E-309	9.6	89.5	1.053	2.44	2.2	0.90	0.92
LG-810	6.5	94.5	1.053	2.54	2.4	0.94	0.88
LG-802	5.9	86.3	1.053	3.26	3.2	0.98	–

[a] W. E. Martin and S. M. Yarema, Lawrence Livermore National Laboratory, Livermore Calif., Memo 79-206 (1979).

▲ Table 2-44. Dual-ion saturation results.

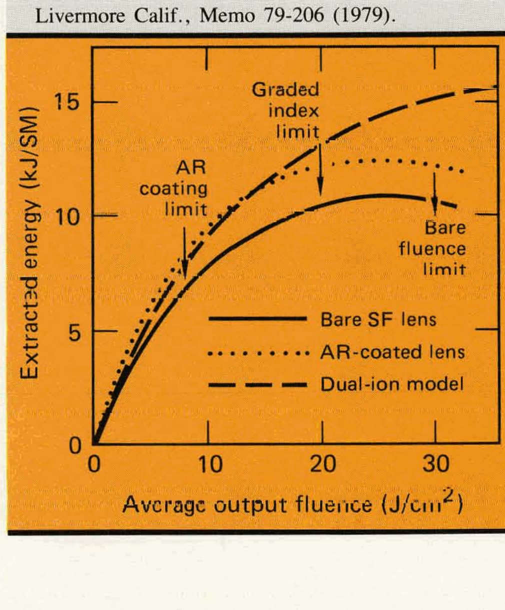

Fig. 2-248. Performance simulation of 74-cm output stages with a fixed saturation fluence of 5 J/cm^2.

for the 1.1-m focusing optics used in this analysis.

Preliminary (coarse-grid) MALAPROP simulations of Nova indicate peak-to-average values below a value of two for the cases where the influence of the long air path to the focusing lens is ignored. There are still significant uncertainties about what the real peak-to-average values will be.

We selected LG-650 laser glass as an example of a well-characterized, low-cost material with a low cross section. A low cross section reduces ASE, isolation requirements, temporal pulse distortion, and the need to segment the disks. However, the emission cross section for LG-650 (1.05×10^{-20} cm^2) is somewhat on the low side. The large melt of LG-660 glass made by the

Table 2-45. Saturated performance and cost estimates for Super Nova laser with LG-650 laser glass.

No.	ID	Diam (cm)	No. of components	Thick. (cm)	Index	N2 (esu)	Bank (kJ)	Gain: Small signal	Gain: Saturated	Energy (J)	Inc. B value	Flux (J/cm^2)	Cost (k$)
1	SF15	9.4	1	0.8	1.507	1.24	0	0.99	0.99	267	0.01	4.9	13
2	Disk	9.4	6	1.6	1.512	1.30	120	2.45	1.93	516	0.11	9.3	47
3	Pol	9.4	2	0.8	1.507	1.24	0	0.94	0.94	485	0.02	9.3	7
4	FR	9.4	1	0.8	1.670	2.10	20	0.98	0.98	476	0.02	8.7	12
5	Pol	9.4	2	0.8	1.507	1.24	0	0.94	0.94	447	0.02	8.6	7
6	Disk	9.4	6	1.6	1.512	1.30	120	2.45	1.81	807	0.18	14.5	47
7	Disk	9.4	6	1.6	1.512	1.30	120	2.45	1.65	1 332	0.31	24.0	47
8	SF15	9.4	1	0.8	1.451	0.95	0	0.93	0.93	1 239	0.03	24.0	12
									1.00	1 238	0.70		
9	SF15	15.0	1	1.1	1.507	1.24	0	0.99	0.99	1 226	0.02	8.8	17
10	Pol	15.0	2	1.1	1.507	1.24	0	0.94	0.94	1 152	0.03	8.7	13
11	FR	15.0	1	1.1	1.670	2.10	50	0.98	0.98	1 129	0.03	8.1	22
12	Pol	15.0	2	1.1	1.507	1.24	0	0.94	0.94	1 061	0.03	8.0	13
13	Disk	15.0	4	2.0	1.512	1.30	180	1.92	1.56	1 653	0.13	11.7	63
14	Disk	15.0	4	2.0	1.512	1.30	180	1.92	1.49	2 458	0.20	17.4	63
15	Disk	15.0	4	2.0	1.512	1.30	180	1.92	1.42	3 488	0.28	24.7	63
16	SF15	15.0	1	1.1	1.451	0.95	0	0.93	0.93	3 244	0.04	24.7	17
									1.00	3 241	0.75		
17	SF15	20.8	1	1.5	1.507	1.24	0	0.99	0.99	3 208	0.04	11.9	22
18	Pol	20.8	1	1.5	1.507	1.24	0	0.96	0.96	3 080	0.03	11.8	11
19	FR	20.8	1	1.5	1.670	2.10	80	0.98	0.98	3 018	0.05	11.3	39
20	Pol	20.8	1	1.5	1.507	1.24	0	0.96	0.96	2 898	0.03	11.1	11
21	Disk	20.8	3	2.4	1.512	1.30	240	1.65	1.37	3 974	0.15	14.6	82
22	Disk	20.8	3	2.4	1.512	1.30	240	1.65	1.33	5 299	0.21	19.5	82
23	Disk	20.8	3	2.4	1.512	1.30	240	1.65	1.30	6 877	0.27	25.3	82
24	SF15	20.8	1	1.5	1.451	0.95	0	0.93	0.93	6 396	0.06	25.3	22
									1.00	6 389	0.84		
25	SF15	31.5	1	2.3	1.507	1.24	0	0.99	0.99	6 325	0.05	10.2	32
26	TM	31.5	2	0.0	1.507	1.24	0	0.98	0.98	6 198	0.00	10.1	25
27	Pol	31.5	1	1.5	1.507	1.24	0	0.96	0.96	5 951	0.02	9.9	21
28	FR	31.5	1	1.5	1.670	2.10	300	0.98	0.98	5 832	0.04	9.5	98
29	Pol	31.5	1	1.5	1.507	1.24	0	0.96	0.96	5 598	0.02	9.4	21
30	Disk	31.5	2	3.0	1.512	1.30	320	1.37	1.23	6 892	0.10	11.1	90
31	Disk	31.5	2	3.0	1.512	1.30	320	1.37	1.22	8 391	0.12	13.5	90
32	Disk	31.5	2	3.0	1.512	1.30	320	1.37	1.20	10 104	0.15	16.2	90
33	Disk	31.5	2	3.0	1.512	1.30	320	1.37	1.19	12 035	0.18	19.3	90
34	Disk	31.5	2	3.0	1.512	1.30	320	1.37	1.18	14 183	0.21	22.7	90
35	Disk	31.5	2	3.0	1.512	1.30	320	1.37	1.17	16 541	0.25	26.5	90
36	SF20	31.5	1	2.3	1.451	0.95	0	0.93	0.93	15 383	0.10	26.5	35
									1.00	15 346	1.26		

Schott Optical Company has a cross section of about $1.9 \times 10^{-20}\,cm^2$ and may be a better choice, but we lack saturation data for this glass.

The chain layout shown in Table 2-45 is based on the full Nova chain with six 31.5-cm amplifiers and five 46-cm amplifiers. We added a 74-cm booster stage, one β amplifier, and two γ amplifiers. This amplifier chain has an isofluence capability of about 82 kJ at a hardware cost of about \$5.9 million. This laser could be housed by extending the present Nova building northward, as indicated in Fig. 2-249.

A detailed cost comparison of Super Nova, relative to the Nova Phase I procurement plan, is shown in Tables 2-46 and 2-47 in FY80 dollars. The Δ Super Nova columns in these tables show the additional cost for the Super Nova upgrade option assuming that the Nova Project has been completed and all amplifiers and frequency converters are installed. The Super Nova columns in the tables correspond to a stand-alone project.

From these rough cost estimates, the additional FY80 cost for the Super Nova upgrade is about \$250 million for the 1.06-μm system and about \$303 million for a complete 3ω system, leading to a total project cost for Nova and Super Nova of approximately \$533 million. By comparison,

Table 2-45 (cont).

								Gain					
No.	ID	Diam (cm)	No. of components	Thick. (cm)	Index	N2 (esu)	Bank (kJ)	Small signal	Saturated	Energy (J)	Inc. B value	Flux (J/cm ^{2})	Cost (k\$)
37	SF20	46.0	1	3.4	1.507	1.24	0	0.99	0.99	15 192	0.08	11.5	48
38	Disk	46.0	2	3.0	1.512	1.30	720	1.42	1.25	18 915	0.13	14.2	178
39	Disk	46.0	2	3.0	1.512	1.30	720	1.42	1.23	23 228	0.16	17.5	178
40	Disk	46.0	2	3.0	1.512	1.30	720	1.42	1.21	28 139	0.20	21.2	178
41	Disk	46.0	2	3.0	1.512	1.30	720	1.42	1.20	33 641	0.24	25.3	178
42	Disk	46.0	2	3.0	1.512	1.30	720	1.42	1.18	39 707	0.28	29.9	178
43	SF20	46.0	1	3.4	1.451	0.95	0	0.93	0.93	36 928	0.16	29.9	62
									1.00	36 839	1.24		
44	SF20	74.0	1	5.0	1.507	1.24	0	0.99	0.99	36 471	0.11	10.7	91
45	Disk	74.0	2	3.0	1.512	1.30	900	1.32	1.19	43 373	0.12	12.6	277
46	Disk	74.0	2	3.0	1.512	1.30	900	1.32	1.18	51 147	0.14	14.9	277
47	Disk	74.0	2	3.0	1.512	1.30	900	1.32	1.17	59 810	0.16	17.4	277
48	Disk	74.0	2	3.0	1.512	1.30	900	1.32	1.16	69 361	0.19	20.2	277
49	Disk	74.0	2	3.0	1.512	1.30	900	1.32	1.15	79 789	0.22	23.2	277
50	Disk	74.0	2	3.0	1.512	1.30	900	1.32	1.14	91 062	0.25	26.5	277
51	Disk	74.0	2	3.0	1.512	1.30	900	1.32	1.13	103 136	0.29	30.0	277
52	SF20	74.0	1	5.0	1.451	0.95	0	0.93	0.93	95 916	0.24	30.0	154
									0.99	95 322	1.72		
53	FO	110.0	1	33.0	1.057	1.24	0	0.86	0.86	82 358	1.13	12.5	1101
									1.00	82 202	1.13		
	Totals of interest						13 890		304.45	82 202	7.64		5867

Z-value = 14.011 kJ/M\$

Cost: ME = 1472; EE = 2139; Optics = 2256

Input energy	270 J
Pulse duration	10 ns
Laser wavelength	1.057 μm
Cost of laser glass	\$1/cc
Emission cross section	$1.05 \times 10^{20}\,cm^2$
SAT/JO cross-section ratio	1
Large-small-scale noise	0.2−0.02%
Scatter/absorption loss	0.3−0.2%/cm
Fill factor	0.8

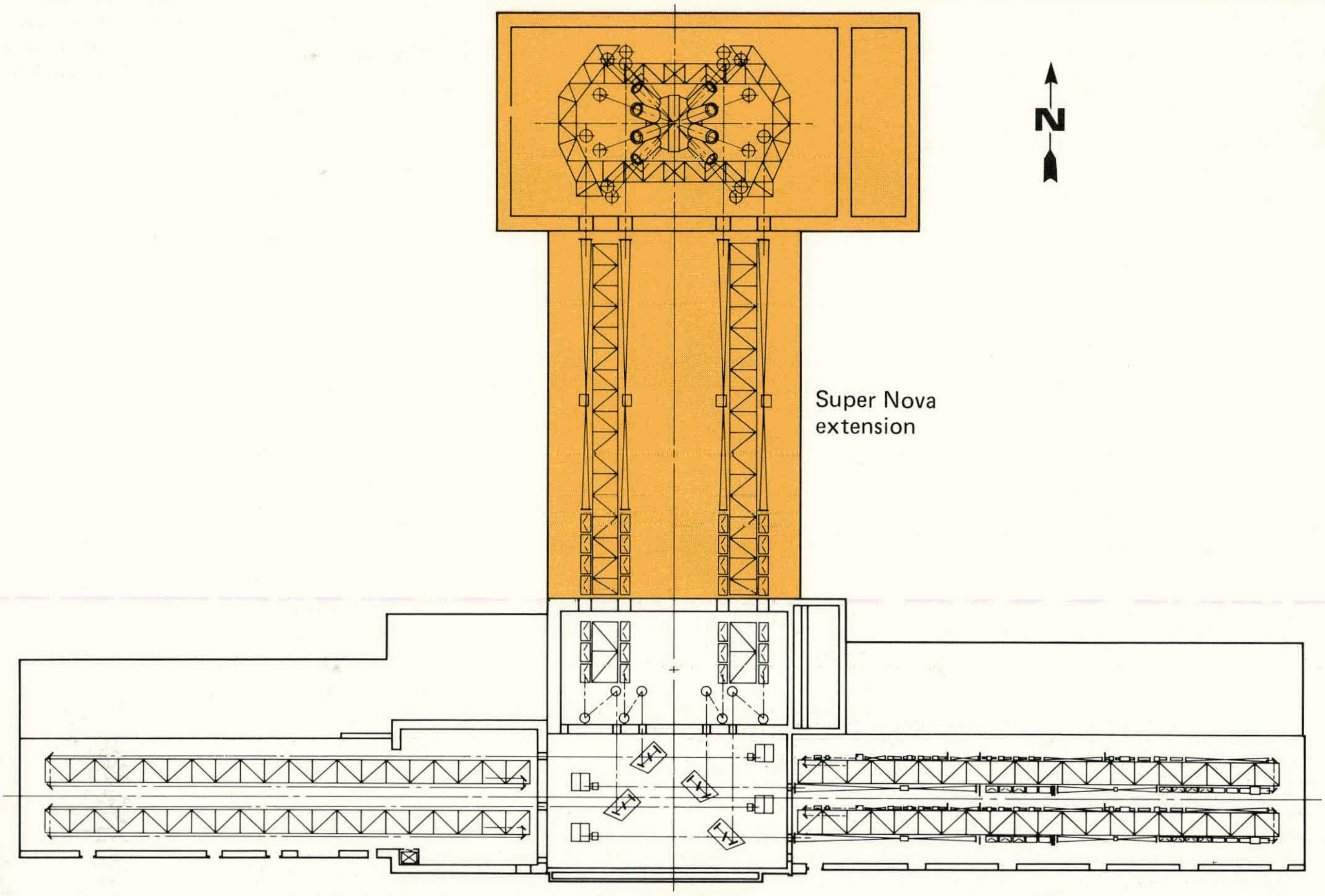

Fig. 2-249. Schematic ▲ layout of the Super Nova extension to the existing Nova laser.

Table 2-46. Cost comparison of Super Nova to Nova laser hardware in FY80 dollars.

		Nova 10 beams	Δ Super Nova 20 beams	Super Nova 20 beams
ME Amplifier chains		7.7	14.0	29.4
Spares	10%	0.8	1.4	3.0
Space frame and aux		4.9	~6.0	~10.0
Front end + misc		2.6	2.6	~3.6
Salvage		−1.6	0	0
Procurements		14.4	24.0	46.0
S&E	6%	0.9	1.4	2.8
Fab labor	17%	2.4	4.1	7.8
Design labor		4.6	~5.5	~7.4
Total ME		22.3	35.0	64.0
EE Amplifier chains		8.1	20.6	42.8
Spares	10%	0.8	2.1	4.3
Prototypes + test facility		2.2	~3.0	~4.0
Plasma shutter + misc	19%	1.5	3.8	7.9
Salvage		−0.9	0	0
Procurements		11.7	29.5	59.0
S&E	14%	1.7	4.1	8.3
Fab labor	12%	1.4	3.5	7.1
Design labor		5.3	5.9	7.6
Total EE		20.1	43.0	82.0
Optics				
Amplifier chain		13.3	39.5	45.1
Spares	20%	2.7	7.9	9.0
Prototypes		2.8	~2.0	~3.0
Tooling		3.7	~5.0	~7.0
Optics support + front end + misc		1.5	~3.6	~4.9
Salvage		−0.6	0	0
Procurements		23.4	58.0	69.0
S&E	1%	0.3	0.6	0.7
Fab labor	2%	0.6	1.2	1.4
Design labor		1.4	~2.2	~2.9
Total optics		25.7	62.0	74.0

a stand-alone project is estimated to cost \$455 million. In contemplating future megajoule-class laser facilities, it is clear that we are not constrained to utilize current Nova-type laser technologies and unit costs. We are currently examining design and

			Nova 10 beams	Nova 20 beams	Δ Super Nova 20 beams	Super Nova 20 beams
ME			22.3		35.0	64.0
EE			20.1		43.0	82.0
Optics			25.7		62.0	74.0
			68.1		140.0	220.0
Target:	Procurement		6.6		15.0	20.0
	Salvage		−1.0		0	0
	Labor		3.2		~4.4	~5.8
	S&E	11%	0.6		1.6	2.2
			9.4		21.0	28.0
Align.:	Procurement		7.4		16.0	20.0
	Salvage		−1.2		0	0
	Labor		4.6		7.7	8.4
	S&E	8%	0.5		1.3	1.6
			11.3		~25.0	~30.0
Project office:	Labor		2.9		4.2	5.0
	S&E	19%	0.6		0.8	1.0
			3.5		~5.0	~6.0
Laser	Total		92.3		191.0	284.0
buildings	laser office		22.0		~30.0	~50.0
			6.7		0	6.7
Contingency		13%	16.0		29.0	44.3
Complete 1.06-μm system			137.0	195	250.0	385.0
2ω	Optics	D^2	6.6	13	24	30
	ME	D^1	1.9	3	5	6
	Align.	D^0	2.0	4	1	4
			10.5	20	30	40
$2 + 3\,\omega \approx 1.8 \times 2\omega$			~19	~35	~53	~70
Complete 3ω system			156	230	303	455

Table 2-47. Cost comparison of Super Nova to Nova total laser system in FY80 dollars.

technology innovations that can lead to significantly lower unit energy costs at the megajoule energy level than those provided here as a reference case, based on fully developed technology.

Author: W. F. Hagen

Laser Glass

Fluorophosphate Glass Development. In 1980, the Hoya Corporation and Schott Optical Glass, Inc., made a major effort to eliminate the damage-causing platinum inclusions that were plaguing us in fluorophosphate glass.[123] They also attempted to prevent the Pt remaining in the glass melt from being reduced to its damage-causing metallic form. Co-doping the glass with Ce^{3+} appeared to help lower the density of Pt particles, but the density could not be reduced below 20/cm^3. We discuss here why this level of damage sites eliminates fluorophosphate glass from further consideration as the Nova laser glass.

Damage sites in laser glass scatter laser light, which, in turn, produces spatial modulations on the beam profile. The resultant local maxima in laser flux can damage optical components located further down the laser chain. In addition, large light-scattering centers (>0.1-mm diam) create long-wave spatial modulations that pass through our spatial filters; thus, less energy can be focused on the fusion target.

Because both damage sites and bubbles are scattering centers, we apply the same maximum scattering specification to both: i.e., that the fractional beam area obscured by damage sites, bubbles, and surface defects be less than 10^{-4}. Our bubble specification permits 3×10^{-5} fractional obscuration. If we apply the same limit to damage sites, we find the maximum allowable site density as a function of site size. This result is plotted in Fig. 2-250, where we see that many small scattering sites, but very few large ones, can be tolerated. In generating this graph, we have assumed a delta-function distribution in site diameters; i.e., all sites have the same diameter.

We find that exposure of the damage sites to multiple laser shots increases the damaged volume; e.g., four shots at 10 to 12 J/cm^2 (a typical Nova flux) increased the damage site diameter to 140 μm. Thus, we need a very low density of damage sites. At these low densities, an adequate testing procedure becomes a problem.

The difficulties in damage testing high-quality laser glass were apparent in fluorophosphate-glass tests conducted by both Hoya and LLNL. On the same glass sample, Hoya measured a damage threshold of 25.9 J/cm^2 for 3-ns laser pulses, while LLNL measured a threshold of 7.1 ± 1.3 J/cm^2. We attribute this discrepancy to differences in the beam sizes of the two test lasers; the Hoya beam diameter is 0.5 mm, and our beam diameter is 2.5 mm. Thus, we tested ~25 times the volume of laser glass that Hoya did. When we reduced our beam size to 0.5 mm, we also failed to damage the glass with four laser shots at 20 to 30 J/cm^2.

These results are a consequence of the small number of damage sites within the damaging laser-beam diameter; thus, the probability of detecting damage may be very low. To illustrate, let us assume that damage sites are randomly distributed within the laser glass volume. Then, the probability, p, of finding n sites on any given laser shot will follow the Poisson distribution,

$$P_D = e^{-\rho V} (\rho V)^n/n! \qquad (40)$$

where ρ is the average damage site density and V is the volume exposed to the laser flux. If $\rho = 100/\text{cm}^3$ and $V = 4 \times 10^{-3}$ cm^3, which is equal to a 0.5-mm-diam laser beam passing through a 2-cm thick piece of laser glass, there is a 67% chance that no damage sites will be seen. However, if the beam is 2.5 mm in diameter, then at least one damage site will be generated >99.99% of the time.

To at least partially solve the problem of observing low densities of damage sites when small-diameter laser beams are used, we could make several shots in different volumes to increase the total volume tested. However, we need damage-site densities as low as 1 site/12 cm^3 if the site diameter reaches 100 μm. To have a 99% probability of finding at least one damage site with that site density, we must test a volume of 55 cm^3. If the glass is 4.6 cm thick, we need a 4-cm beam diameter to cover the volume in a single-shot test, so that we must use a large-aperture laser, such as Argus, to test damage-resistant glass. However, the damage-site density of fluorophosphate glass was never reduced to a level sufficiently low to require testing on Argus. On the other hand, we did have to test phosphate glass on Argus because of the excellent resistance of this glass to laser damage.

Author: S. E. Stokowski

Fig. 2-250. Allowable damage-site density as a function of site diameter.

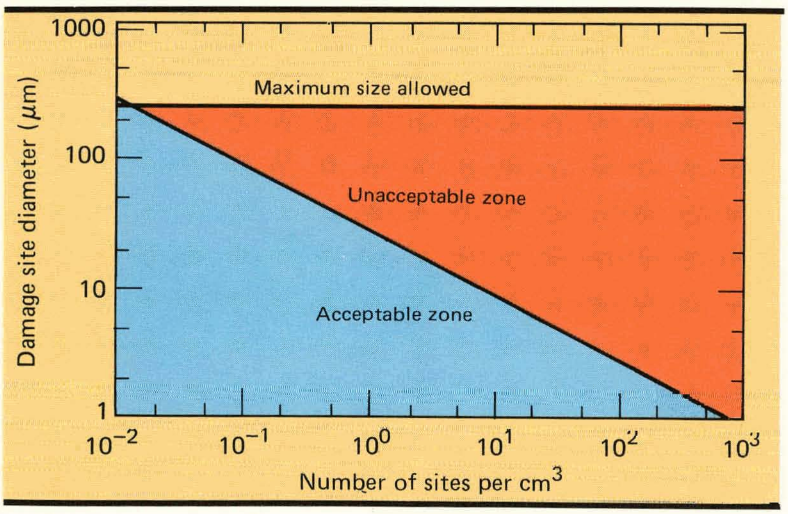

Phosphate Glasses. As progress slowed in our program to improve the damage resistance of fluorophosphate glass, we began to concentrate more on the development of phosphate laser glass. At the beginning of 1980, the existing commercial phosphate glasses were LHG-8 (Hoya Corp.), Q-88 (Kigre, Inc.), and EV-2 (Owens–Illinois, Inc.). In 1979, we reported on new phosphate glasses with stimulated emission cross sections 25% lower than the above commercial glasses.[124] Of particular interest to us are Hoya's P101 and Kigre's Q-94 glasses. In addition, Schott introduced a commercial phosphate laser glass, LG-750, that has properties similar to LHG-8 and Q-88, and Kigre developed an athermal glass, Q-98.

The measured spectroscopic properties and the thermal properties of these phosphate laser glasses are listed in Tables 2-48 and 2-49, respectively. In addition, the glass companies have supplied us with either 25.4- or 40-mm rod samples of the above glasses for gain-saturation measurements, which are now in progress.

Phosphate laser glass is significantly more resistant to laser damage than fluorophosphate glass. For instance, using 1.06-μm, 1-ns laser pulses in 2.5-mm-diam beams, we could not damage phosphate glass unless the fluence was above 20 J/cm^2. To determine the maximum damage-site density in phosphate glass for fluences below 20 J/cm^2, we had to perform damage measurements with the Argus laser facility so that we could test a much larger glass volume. We programmed Argus to provide 220 to 250 J per shot, and we decreased the beam aperture from 94 to 45 mm to obtain 12 to 13 J/cm^2. The samples were positioned at normal incidence to the beam; thus, the equivalent fluence for Brewster-angle incidence was 18 to 20 J/cm^2. A film plate placed at a position optically equivalent to the glass-sample location recorded the beam profile.

We tested three phosphate samples: an LHG-8 plate that was 27 × 27 × 3 cm, an LG-750 plate that was 15 × 15 × 2.5 cm, and a Q-88 A-disk that was 4.8 × 8.4 × 1.5 cm. Before the tests, we located all bubbles and scattering inclusions in each sample. We then exposed the LHG-8 and LG-750 to two shots each in different volumes and the Q-88 to one shot. After each shot, we visually inspected the exposed volume and located damage sites. Under 100× magnification, we observed that glass fracture had occurred at these sites. The results of these experiments are presented in Table 2-50.

Although we find that phosphate laser glass is not completely free of damaging inclusions, the damage-site density is so low as not to be of concern. By comparison, fluorophosphate glass generally contains 100 damaging inclusions per cm^3. In addition to having larger inclusion densities, fluorophosphate glass has larger damaged volumes at a given fluence level than does phosphate glass. Therefore, considering

Table 2-48. Spectroscopic properties of commercial phosphate glasses.

Commercial glass type	Company	n_D	$\sigma(10^{-20}\ cm^2)$	$\Delta\lambda_{eff(nm)}$	l_p(nm)	$\tau_0(\mu s)$
LHG-8	Hoya	1.531	4.0	25.9	1053.0	380
Q-88	Kigre	1.545	4.0	26.3	1054.0	380
Q-98	Kigre	1.555	4.3	25.5	1053.5	—
LG-750	Schott	1.525	4.0	25.5	1053.5	385
P101	Hoya	1.518	3.0	29.0	1053.0	400
Q-94	Kigre	1.540	3.7	26.2	1053.0	—

Note: The spectroscopic properties include:
n_D = Refractive index at 589 nm.
σ = $^4F_{3/2} \rightarrow {}^4I_{11/2}$ transition cross section of Nd^{3+}.
$\Delta\lambda_{eff}$ = Effective line width.
λ_p = Fluorescence peak wavelength.
τ_0 = Fluorescence decay time for Nd^{3+} concentrations < 0.1%.

Table 2-49. Thermal properties of commercial phosphate glasses.▼

Commercial glass type	Company	ρ (g/cm^3)	C_p (Jg^{-1} °C^{-1})	K (Jhr^{-1}cm^{-1} °C^{-1})	κ (cm^{2}hr^{-1})	ds/dT (10^{-6} °C^{-1})	α (10^{-7} °C^{-1})	ΔB (nm cm kg^{-1})
LHG-8	Hoya	2.820	0.75	18.8	8.9	0.6	102	1.9
Q-88	Kigre	2.679	0.88	26.5	11.2	3.2	95	2.1
Q-98	Kigre	3.099	—	—	—	—	—	—
LG-750	Schott	2.81	—	—	—	—	0.8	105
P101	Hoya	2.63	—	—	—	—	—	—
Q-94	Kigre	2.693	—	—	—	—	—	—

Note: The thermal properties include:
ρ = Density.
C_p = Heat capacity at 25°C.
K = Heat conductivity at 25°C.
κ = Thermal diffusivity.
ds/dT = Change in optical path length with temperature.
α = Thermal expansion (−20 to 50°C).
ΔB = Stress-optic coefficient.

Commercial glass type	Shot No.	Flux (J/cm^2)	No. of damage sites	Site density (cm^{-3})	Approx. size (μm)
LG-750	2	13.0	2	0.060	25
LG-750	3	11.4	5	0.125	5
LHG-8	4	11.6	1	0.020	—
LHG-8	5	13.0	1	0.020	—
Q-88	6	12.4	2	0.080	—

Table 2-50. Laser damage-test results on phosphate laser glasses with 1.06-μm, 700-ps pulse-duration laser pulses from Argus.

susceptibility to laser damage, we find that the phosphate laser glass is far superior to the fluorophosphate glass.

Author: S. E. Stokowski

Edge Cladding. The edge cladding on a laser disk ultimately absorbs most of the energy stored in the disk. During the pump pulse, the edge-cladding temperature rises significantly, and the resultant thermal stresses produced in the cladding and laser glass can lead to fracture. When we tested 34-cm fluorophosphate disks in an amplifier, two disks with a frit-type cladding and three disks with a poured-type cladding fractured at the cladding-laser glass interface. Another fluorophosphate disk with a poured-type cladding, which has a lower absorption coefficient, survived our tests. Because of the generally unfavorable results of these tests, we were encouraged to analyze and revise our specifications for edge cladding on disks. We designed the disk edge cladding within the following constraints:

- The cladding reflectivity at 1.05 μm must be less than the inverse of the largest possible transverse gain in the disk.
- The cladding thickness should be less than 3% of the minor axis of the disk.
- The thermal shock that occurs during pumping of the amplifier should not fracture the cladding.

We have three adjustable parameters to work with:

- Cladding bulk absorptivity.
- Cladding thickness.
- Cladding outer-surface finish.

The design constraints limit our choice of parameters. For instance, a high cladding absorption coefficient lowers the reflectivity but increases the thermal stress at the interface between the cladding glass and the laser glass. On the other hand, if we increase the cladding thickness to lower its reflectivity, the increased disk size will lower the pump flux and necessitate a larger amplifier at higher cost.

In our analysis, we have included experimental data and theoretical estimates of phosphate amplifier performance, calculated thermal stresses, and expected cladding properties. The characteristics of the Nova phosphate amplifiers are given in Table 2-51. The gains shown in the table were calculated from GAINPK (a glass pumping code) and are normalized to experimental data from silicate and phosphate amplifiers. The values listed in the last three columns are important to our

Table 2-51. Nova phosphate-amplifier characteristics.

Clear aperture (cm)	Thickness (cm)	Major axis (cm)	Minor axis (cm)	Glass volume (litre)	No. of disks	Path length (cm)	Maximum expected gain	Average gain coefficient α (m^{-1})
9.2	2.4	19.6	10.2	0.376	6	17.2	7.4	11.3
15.0	3.0	30.3	15.8	1.13	4	14.4	4.2	10.0
20.8	2.5	41.2	21.7	1.76	3	9.0	2.3	9.3
31.5	4.3	61.7	33.0	6.88	2	10.3	1.78	5.6
46.0	4.3	45.14	48.0	7.09	2	10.3	1.93	6.2

Clear aperture (cm)	Gain coefficient ratio: face-to-average	Maximum αd	Energy stored per disk (kJ)	Cladding interface area (cm^{-2})	Average cladding flux (J/cm^2)	Maximum edge reflectivity for parasitic suppression: Bulk	Maximum edge reflectivity for parasitic suppression: Surface[a]
9.2	2.00	2.21	0.199	115	1.7	0.035	0.28
15.0	2.27	3.03	0.530	223	2.4	0.01	0.024
20.8	2.05	3.83	0.768	252	3.0	0.003	0.0092
31.5	2.82	3.46	1.81	656	2.8	0.0052	0.0014
46.0	2.82	3.23	2.06	465	2.9	0.0074	0.0026

[a]4.3% reflection at the air/cladding interface is not included in this number.

choice of an edge cladding. Note that the 20.8-cm amplifier has about the same average energy flux on its cladding as the two largest amplifiers, a consequence of the higher gain in the 20.8-cm disks. We calculated the maximum allowable edge reflectivity by requiring it to be less than the inverse of the gain along the longest path in the disk. To meet the criteria for cladding reflectivity, the glass manufacturers must conform to the following:

- Match the refractive index of the cladding and laser glasses.
- Use Cu^{2+} as a 1.05-μm absorbing ion in the cladding glass.
- Roughen the air/cladding interface to suppress specular reflections.
- Minimize the bubble content of the cladding glass, particularly at the interface with the laser glass.

The glass manufacturers can match the refractive indices of the two glasses to within 0.01, thus, the reflectance due to this source will be 10^{-5}, which we can neglect. The cladding absorptivity, which is determined by the Cu^{2+} concentration, must meet the following criteria. Referring to Fig. 2-251, we can see that, for bulk modes,

$$R'_c e^{-2\alpha_c d/\sin\theta} < e^{-\bar{\alpha}_G L/\sin\theta} \quad , \tag{41}$$

where R_c is the air/cladding interface reflectivity, α_c is the cladding absorption coefficient, d is the cladding thickness, θ is the incidence angle, $\bar{\alpha}_G$ is the average gain coefficient, and L is the longest path in the disk. For surface modes,

$$R_c e^{-2\alpha_c d} < e^{-\bar{\alpha}_s L} \quad , \tag{42}$$

where α_s is the surface gain coefficient. If the cladding surface is polished, then $R_c = 1$ for $41.1° < \theta < 48.9°$ and $R'_c = 4.26\%$. Thus, α_c must fulfill the conditions

$$2\alpha_c d > \bar{\alpha}_G L \tag{43}$$

and

$$2\alpha_c d > \alpha_s L - 3.16 \quad \cdot \tag{44}$$

If the cladding surface has a ground surface, the specular reflectivity is considerably reduced and, therefore, the cladding absorption coefficient can be lowered. We specify a fine grind on the cladding surface, which is usually obtained with a 30-μm grit size. Except at high incidence angles (>80°), the specular reflectivity of a finely ground cladding surface is between 10^{-1} and 10^{-3}. Taking $R_c = 10^{-1}$ and $R'_c = 4 \times 10^{-4}$, we list α_cd for this case in Table 2-52. As a result, the highest absorption coefficient required is 1.6 cm^{-1} for a 6-mm-thick cladding on the 31.5-cm disk. Therefore, a ground surface is very helpful in suppressing parasitic oscillations, but it will not significantly reduce the overall amplified spontaneous emission (ASE) loss because the scattered light is still fed back into the disk. Thus, we do want to keep the cladding attenuation larger than the above minimum, so we chose 4 cm^{-1}, a factor of 2 higher.

Bubbles on the cladding-laser glass interface or in the cladding glass are particularly detrimental to the prevention of unwanted parasitic oscillations. The effects of voids within the cladding glass are reduced by the cladding absorptivity; however, the bubbles on the interface are 100% reflective at some incidence angles, and parasitic oscillations due to these interface bubbles will certainly occur. Our only solution is to minimize the total area of these bubbles. Fortunately, the glass manufacturers claim that the phosphate-glass

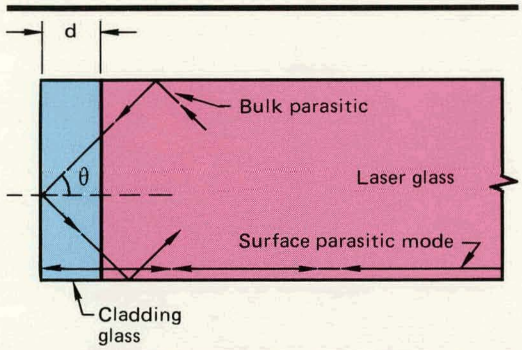

Fig. 2-251. Cross-sectional view of laser disk.

Table 2-52. Edge-cladding absorption coefficient (α_{cd}) required to supress surface parasitic modes.

Clear aperture (cm)	Case 1 Polished cladding: Parasitic modes: Bulk	Case 1 Polished cladding: Parasitic modes: Surface	Case 2 Ground cladding surface $R_c = 10^{-2}$: Parasitic modes: Bulk	Case 2 Ground cladding surface $R_c = 10^{-2}$: Parasitic modes: Surface
9.2	1.1	0.7	—	—
15.0	1.5	1.9	—	—
20.8	1.9	2.4	—	0.1
31.5	1.8	3.3	—	1.0
46.0	1.6	3.0	—	0.7

cladding provides a very clean interface with the laser glass.

Considering both the interface bubbles and the requirements on total edge cladding reflectivity listed in Table 2-51, we feel that the specular reflectivity of the cladding measured at 45° (at the major axis ends) should be less than 0.1% for the 20.8-, 31.5-, and 46-cm disks. The lower $\alpha_G D$ in the 9.2- and 15-cm disks allows us to set a less-stringent reflectivity value of 0.3%. In addition to the specular reflectivity, the nonspecular component can add to the overall ASE loss in the disks. Thus, we require that the amount scattered into 0.3 sr centered at 45° be less than 0.1% for the 20.8-, 31.5-, and 46-cm disks and less than 0.3% for the two smaller disks.

Fig 2-252. Calculated maximum tensile stress in an edge cladding, assuming a fluence loading of 0.04 J/mm².

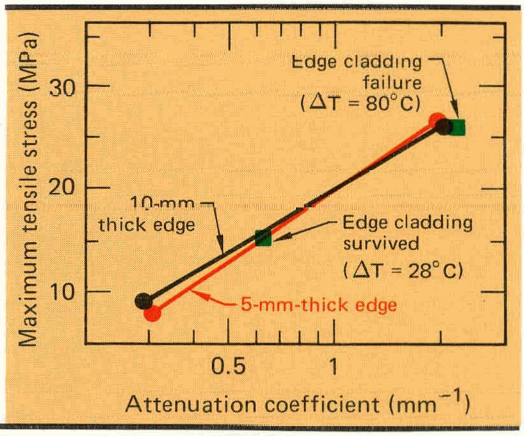

Fig. 2-253. Radial stress component plotted vertically on a cross-sectional view of a disk with a 5-mm edge-cladding thickness and an 80°C temperature rise.▼

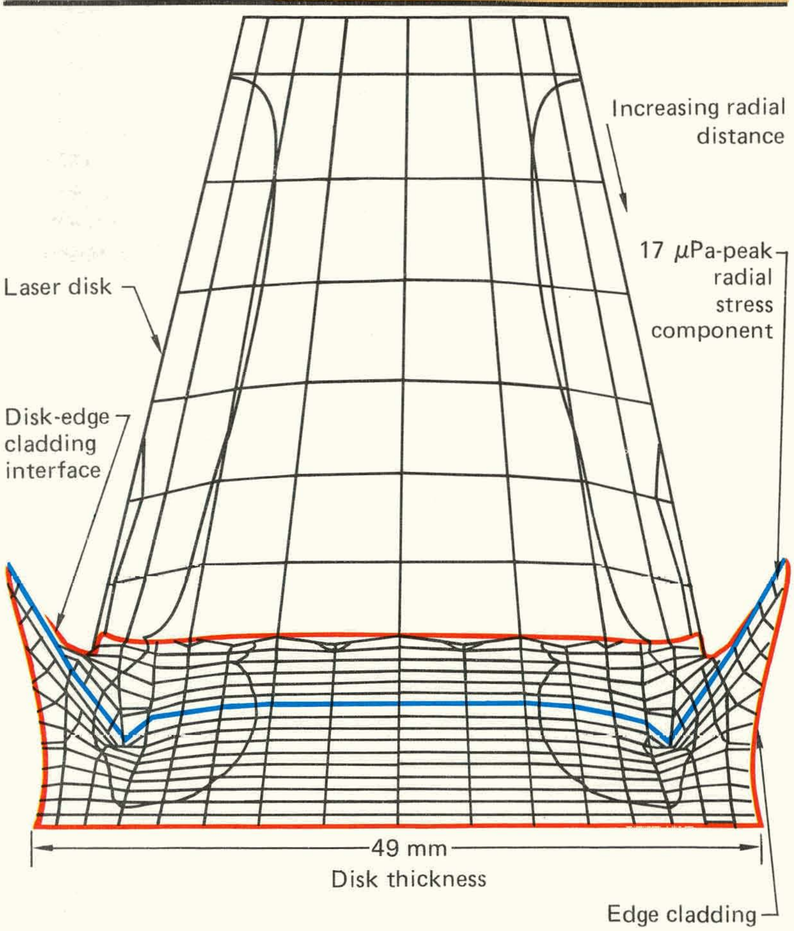

We addressed the problem of cladding survivability by undertaking a thermal stress analysis. We derived a simple analysis for the peak temperature rise in the coating caused by a square-wave heat-pulse input and by the thermal diffusion occurring during the 600-μs pump pulse. The assumed fluence on the edge cladding is 0.04 J/mm^2. For a 315-mm fluorophosphate disk with attenuation coefficients of 2 and 0.3/mm, the maximum temperature rise is 85 and 13.5°C, respectively. Using this calculated temperature profile and a finite element code (SAP4), we found that the calculated maximum tensile stresses are 31.4 μPa (4564 psi) and 8.8 μPa (1278 psi) for an edge thickness of 5 mm.

Two known data points are from disks tested in a 34-cm amplifier. A 5-mm-thick edge cladding with a 2.1/mm attenuation coefficient failed, whereas a 3.9-mm-thick cladding with a 0.63/mm attenuation coefficient survived. The estimated temperature rises of the disks were 88 and 28°C, respectively. These data points are plotted in Fig. 2-252, where we show the maximum stress vs attenuation coefficient. This figure also shows the results of our attempt to lower the stress by increasing the edge-cladding thickness. Two significant results shown in Fig. 2-252 are that edge-cladding thickness has little effect on maximum stress and that maximum stress for fracture is between 14.6 μPa (2100 psi) and 31.4 μPa (4560 psi) (or between 28 and 88°C temperature rise).

Figure 2-253 is a plot of the radial stress component of a disk with a 5-mm edge cladding and an 80°C temperature rise at the interface. The high stresses are concentrated at the disk faces, implying that fractures would start on the faces of the disks. However, Van Frechette of Alfred University examined the fractured cladding on the damaged fluorophosphate disks and concluded that fracture initiated at the cladding-laser glass interface. Thus, we assume that the bonding of the two glasses was probably very weak. We believe that additional evidence for this hypothesis

Table 2-53. Edge-cladding specifications for Nova laser disks.

Clear aperture (mm)	Cladding thickness (mm)	Maximum specular R(%) at 45°	Maximum scattered light into 0.3 sr at 45° (%)	Approximate cladding attenuation coefficient at 1.05 μm (mm^{-1})
92[a]	3.0 ± 1.0	0.3	0.3	0.4
150[a]	3.0 ± 1.0	0.3	0.3	0.4
208[a]	3.5 ± 0.5	0.1	0.1	0.4
315	6 ± 1.0	0.1	0.1	0.4
460 semi-ellipse	6.0 ± 1.0	0.1	0.1	0.4
straight edge	3.0 ± 0.5	—	—	—

[a]Frit-type cladding, which must meet reflectivity specification, is allowed.

comes from the observation of a haze at the interface created by a high density of very small bubbles. These bubbles are probably generated during manufacture by a reaction at the laser glass surface, which is likely a hydrolized layer. We suspect that the bubbles reduce the interface strength.

Because we are using phosphate glass in Nova, rather than fluorophosphate glass, we must estimate how a phosphate cladding will compare with a fluorophosphate (FP) cladding. To arrive at this estimate, we take the following factors into account:

- Izumitani of Hoya states that phosphate and FP glass have about the same mechanical strength.
- The quality of cladding-laser glass interfaces in phosphate-glass test pieces is much better than those in FP glass.
- Monolithic claddings on 14-cm Q-88 phosphate disks have been successfully used at KMS Fusion.
- Phosphate frit claddings on 20-cm LHG-7 disks at Osaka University have survived many shots with a fluorescence loading of 3 J/cm^2 on the edge cladding.

We conclude, therefore, that, if we keep the cladding attenuation coefficient below 6 cm^{-1}, phosphate cladding glass should survive in the Nova amplifiers. Table 2-53 presents a summary of our edge cladding specifications for the Nova disks.

Authors: S. E. Stokowski, S. M. Yarema, and I. F. Stowers

Solarization. Solarization is defined as a change in the optical absorption of a glass resulting from its exposure to light, usually ultraviolet or blue. The light-induced background absorption in solarized laser glass reduces laser pump efficiency because the glass absorbs light intended for the Nd^{3+} active ions. Solarization results from light-created color centers or from valence changes in impurity ions. Glass solarization can be avoided by preventing exposure to UV light or by stabilizing the impurity oxidation states. An example of the first technique is the use of Ce^{3+} in the flashlamp envelopes, or in the glass, to absorb UV light. Ions such as Sb^{3+}, Mo^{6+}, Nb^{5+}, and Ti^{4+} are used in laser glasses to stabilize the oxidation potential and thereby prevent long-term solarization. Unprotected silicate glasses are solarized by as few as 100 flashes from Ce-doped lamps; thus, Ce^{3+} is added to silicate as an antisolarant.

In 1977, researchers at the Laboratory for Laser Energetics (LLE) at the University of Rochester tested phosphate laser glasses for solarization by subjecting them to ~200 flashes from clear fused-quartz lamps. The LLE researchers did not see any change in the glass transmission, although they later found, after 1000 to 2000 shots, that the gain of their Omega and Zeta rod amplifiers was decreasing with the number of firings. They discovered that part of the gain reduction was caused by solarization of the phosphate laser glass. Because their amplifiers use clear fused-quartz flashlamps, the laser glass is exposed to UV light with wavelengths as short as 310 nm, which apparently causes solarization.

We decided to test both fluorophosphate and phosphate laser glasses for resistance to solarization in a 2000-shot test using an amplifier equipped with Ce-doped quartz flashlamps, which do not transmit wavelengths shorter than 360 nm. In 1978 we tested fluorophosphate glasses LG-812 and

E-309 in a 100-shot exposure and saw no change in the background absorption.

There are two approaches to the testing of laser glasses for solarization. One approach, which is the one we used, uses an actual amplifier in an operational test. The second approach employs a xenon arc lamp to expose a glass to low-power UV light over a long period of time. These two approaches will not be equivalent if the physical process causing solarization depends nonlinearly on UV power.

For our tests, we used 15-mm-thick, 48 × 84 mm elliptical disks of LHG-8, Q-88, and EV-4 phosphate glasses and LHG-10, LG-812, and E-309 fluorophosphate glasses of the same dimensions. We cut and polished the major axis ends to provide a 78.5-mm path for measuring transmission. We exposed all six disks simultaneously to flashes from Ce-doped quartz lamps. Before the test began, and after 250, 500, 1000, and 2000 shots, we measured the absorption spectra with a spectrophotometer and the continuous wave (cw) laser transmission at 441.6, 632.8, and 1064.2 nm.

After 2000 shots, the measured changes in transmission of all the glasses were less than 2%, which is equivalent to an absorption coefficient of 0.0025 cm^{-1}. For comparison, we calculated that a 0.1% reduction in pump efficiency would result from an absorption coefficient of 0.0025 cm^{-1} for wavelengths shorter than 600 nm. Thus, solarization of laser glasses will not be a problem in our amplifiers.

Our absorption measurements uncovered one interesting difference between phosphate and fluorophosphate glasses. Phosphate glasses have considerably more background absorption than fluorophosphate glasses in the blue and near-UV regions. This additional absorption can be seen in Fig. 2-254, where we compare the spectra of LHG-8 phosphate and LG-812 fluorophosphate glasses. The background absorption coefficient of LHG-8 is about 0.03 cm^{-1} in the 400- to 500-nm region. The source of this absorption is unknown, but the absorption does vary from sample to sample.

Author: S. E. Stokowski

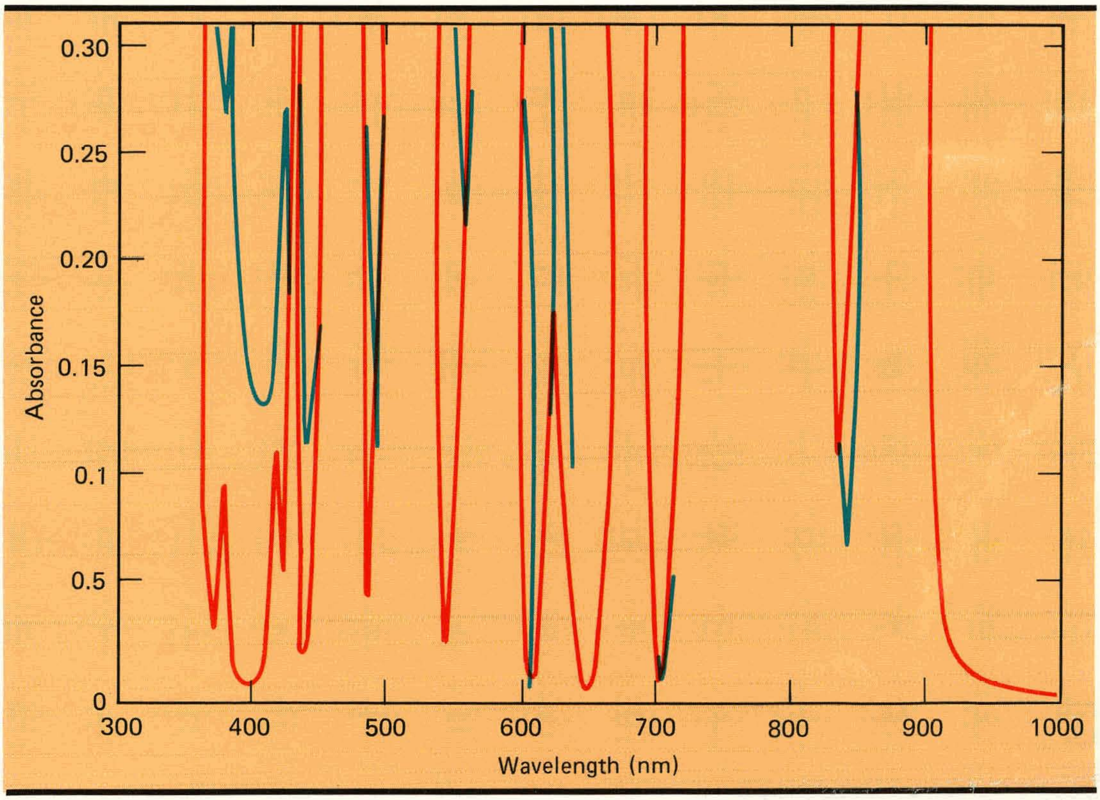

Fig. 2-254. Optical density of Nd:doped fluorophosphate (red line) and phosphate (green line) laser glasses. The samples are 78.5 mm long.

Gain-Saturation Properties of Laser Materials

Previous measurements of saturation fluence in silicate, fluorophosphate, and phosphate laser glasses were summarized in the 1979 Annual Report.[125] A more detailed report of this work is also available.[126]

In the latter part of 1980, we began measurements of the saturation fluence in seven Nd-doped phosphate glasses. For these measurements, we used a well-characterized 1053-nm pulse that was amplified by the test amplifier; the experimental configuration is shown in Fig. 2-255. For each pulse, we used calorimeters C1 and C2 to measure the input fluence, E_{in}, and output fluence, E_{out}, and we used diodes D1 and D2 to measure small-signal gain, G_o. We also measured the passive transmission of the rod. The parameters measured for each shot were used in the Frantz–Nodvik equation[127] to compute a value of saturation fluence, E_s. The experiment was iterated to provide us with values of E_s for 1.4- and 20-ns pulse durations at each desired fluence level, E_{out}. The rebuilt Cyclops laser (described in "Cyclops Design and Performance" in this section) was used as the source of the 1053-nm input pulses.

We have completed the measurements for two materials, LHG-8 and P101 phosphate glasses, produced by the Hoya Corporation. Plots of output fluence as a function of input fluence for these materials are shown in Figs. 2-256 and 2-257. To determine the fluence, we measured the energy transmitted through the 5-mm apertures centered on diagnostic beams at the input and output of the test amplifier (see Fig. 2-255), then we computed the fluence as an average over the area of the aperture and adjusted the fluence data to account for the increased beam size in the Brewster-cut amplifier rods. In the air outside the rod, beam fluences were greater than our plotted values by a factor approximately equal to the refractive index of the glass. The output fluence data were not adjusted to account for the passive transmission of the rod, since this transmission is treated by the Frantz–Nodvik computations. The ratio E_{out}/E_{in} computed from such data gives us the absolute gain of the amplifier, including passive loss, as a function of fluence in the rod.

We used the 1064-nm beam, which was produced by a continuous wave (cw) YAG laser, as a gain probe. The 1064-nm beam was passed through the center of the test amplifier at an angle of 2° relative to the saturating beam. For each material, it was necessary to measure the gain ratios at both the 1053- and 1064-nm wavelengths. To measure small-signal gain, G_o, at 1053 nm, we used the quasi-cw prelase beam from the

Fig. 2-255. Gain-saturation experiment with 1053-nm pulses.

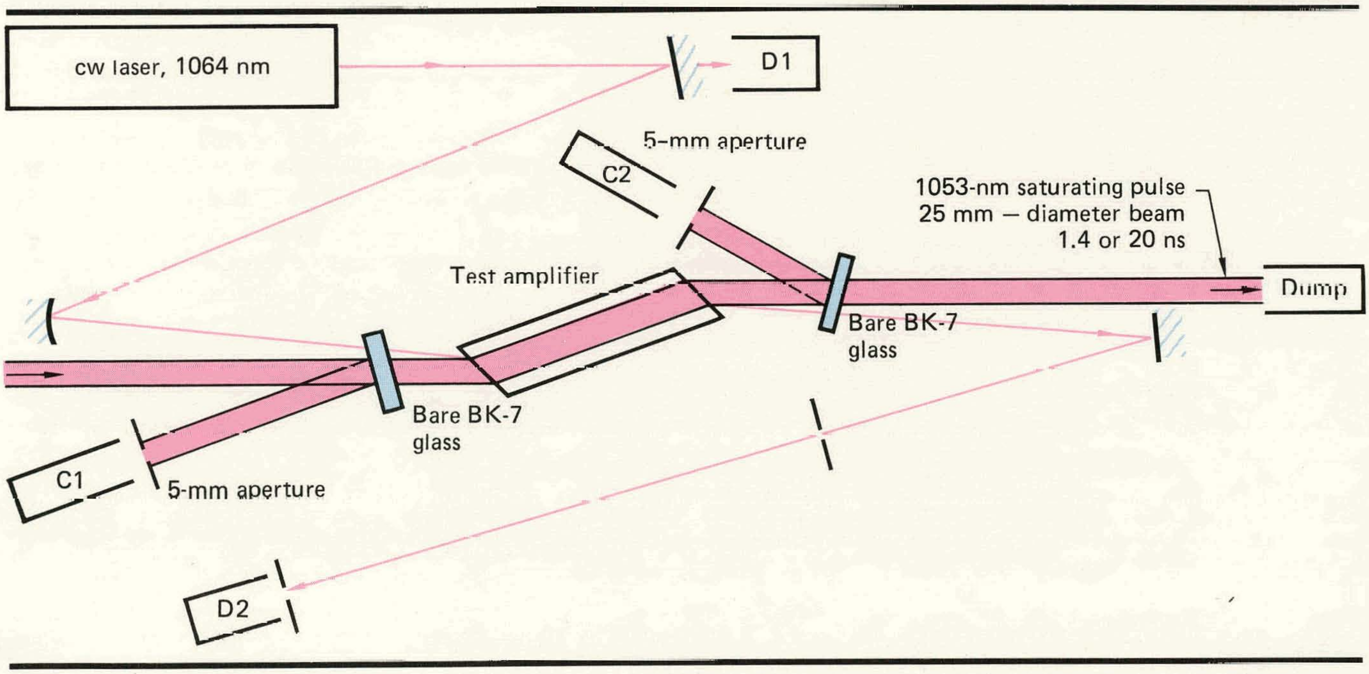

Nd:YLF Cyclops oscillator and shaped the beam to occupy the central 5-mm-diam volume of the amplifier, which was the volume used in calorimetric gain measurements. The gain-ratio data are shown in Table 2-54. The measurement precision was such that all of our measurements of the gain ratio were within 1% of the average, with a mean error of 0.5%. After we established the gain ratio, the 1064-nm gain probe was used to monitor the stability of the gain of the test amplifier.

With calorimetry, we obtained a measure of small-signal gain that was compared with the gain, G_0, measured by using the prelase beam. This is illustrated in Figs. 2-258 and 2-259, where we plot ratios (designated saturated gains) as a function of output fluence. We computed the gains in these figures by calculating the ratio of output calorimeter signal to input calorimeter signal for each firing. We then divided that ratio by the corresponding ratio for calorimeter signals, which were measured when the amplifier was not pumped, to determine the saturated amplifier gain. When we calculate amplifier gains with this method, the gains are independent of both the absolute calorimeter calibrations and the passive transmission of the amplifier rod. (This independence from detector calibration also applies to the measurements of G_0 performed by observing amplification of the prelase beam.) We used curve fits to predict the saturated gains at $E_{out} = 0$, and we directly compared the gains obtained from that extrapolation with G_0. During the tests on the glasses, we extrapolated gains of G = 7.64 for LHG-8 and G = 6.22 for P101. The corresponding values of G_0 measured with the 1053-nm oscillator prelase beam (at input fluences less than 5×10^{-4} J/cm^2) were G_0 = 7.76 for LHG-8 and G_0 = 6.27 for P101. A consistent feature of all recent saturation measurements[126] has been the small offset between the gain measured with a very weak cw probe and the calorimeter gain measurement. The offset is small for phosphate glasses, particularly for the P101 rod.

In Figs. 2-260 and 2-261, we show E_s as a function of output fluence for LHG-8 and P101. The values of E_s were computed from the Frantz–Nodvik equation, which was modified to include effects of passive loss. For some of the LHG-8 data, we used the value of G_0 measured with the 1064-nm gain probe and computed a value of E_s for each shot. For the remainder of the LHG-8 data, we used the mean value of G_0, since we did not have a calculated value for G_0. During these latter measurements, we attempted to

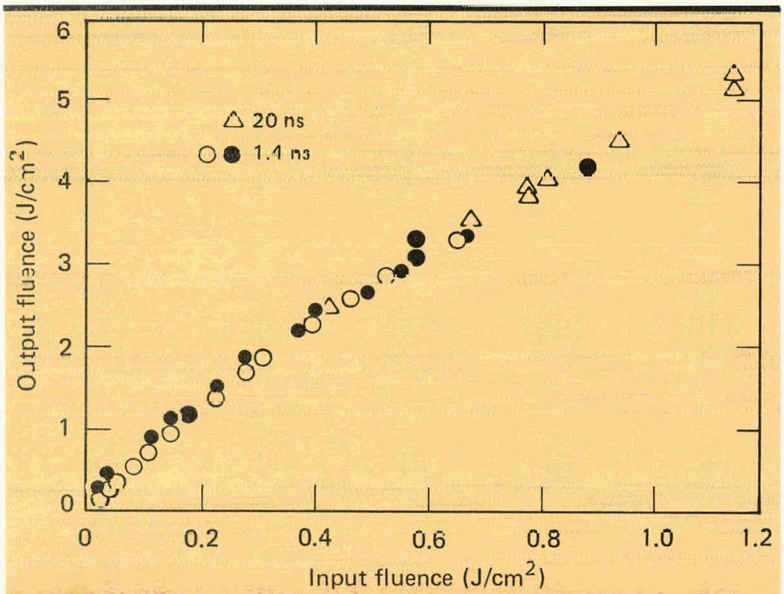

Fig. 2-256. Output fluence as a function of input fluence for an LHG-8 rod amplifier with passive transmission of 97.4%.

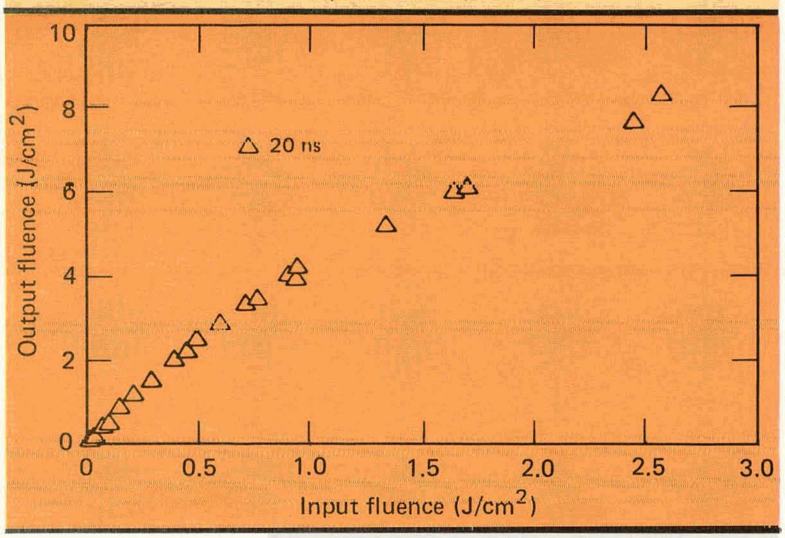

Fig. 2-257. Output fluence as a function of input fluence, measured with 20-ns pulses, for a P101 phosphate glass amplifier with a passive transmission of 96.3%.▲

Shot	Gain, 1053 nm	Gain, 1064 nm	Gain ratio
82	7.74	3.75	2.064
84	7.79	3.75	2.077
85	7.76	3.75	2.069
86	7.77	3.77	2.061
108	7.81	3.73	2.092
109	7.78	3.74	2.083
110	7.65	3.66	2.090
111	7.70	3.71	2.075
112	7.77	3.74	2.078
113	7.85	3.74	2.099
Average values	7.76	3.73	2.079 ± 0.012

Table 2-54. Comparison of small-signal gains of an LHG-8 amplifier measured at 1053 and 1064 nm.

obtain a cw probe at 1052 nm (near the Nd:YLF wavelength of 1053 nm) by using a cw YAG laser with an internal etalon. However, the output of this laser was unstable, and we discontinued its use.

For the P101 material tests, we computed all values of E_s with values of E_{in}, E_{out}, and G_0 that were measured in single firings. We attached error bars to representative data in Figs. 2-260 and 2-261 to indicate the

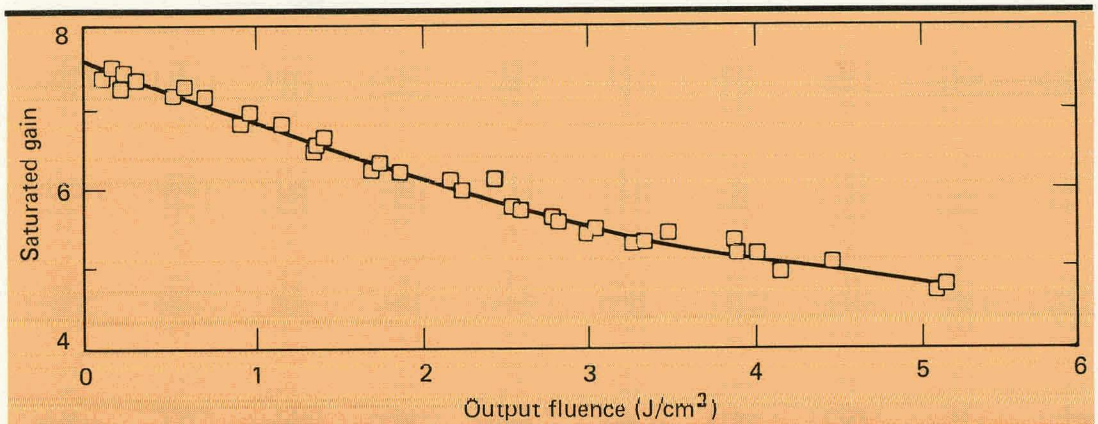

Fig. 2-258. Saturated calorimetric gain of the LHG-8 amplifier, where the curve is a spline fit to the data and predicts relative gain = 7.64 at E_{in} = 0.

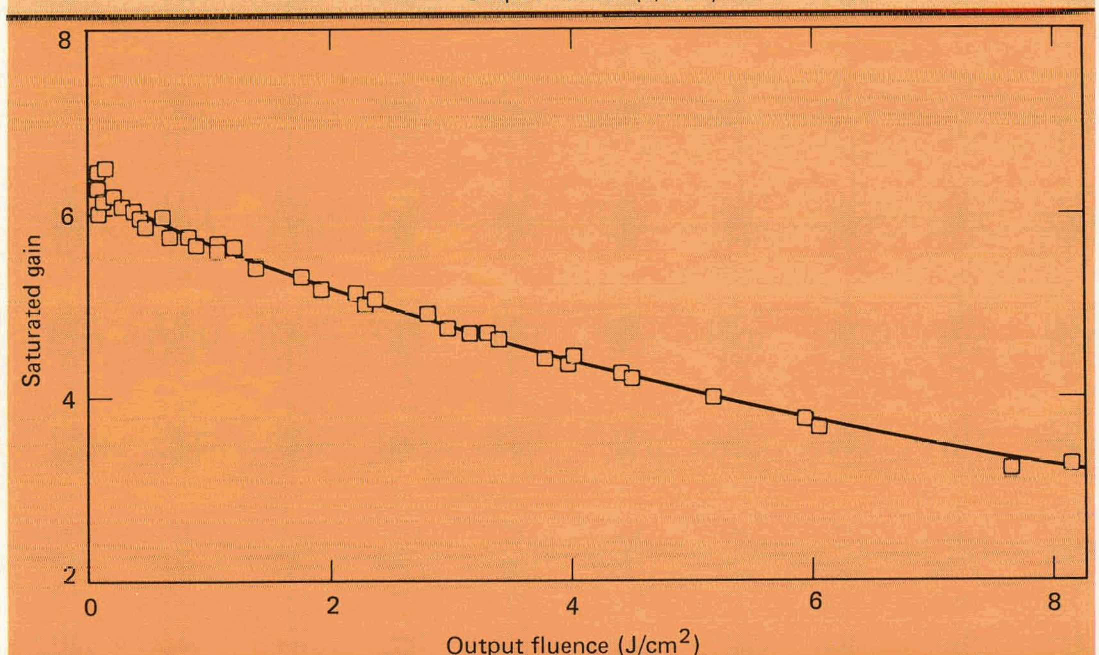

Fig. 2-259. Saturated calorimetric gain of the P101 amplifier, where the curve is a spline fit to the data and predicts relative gain = 6.22 at E_{in} = 0.

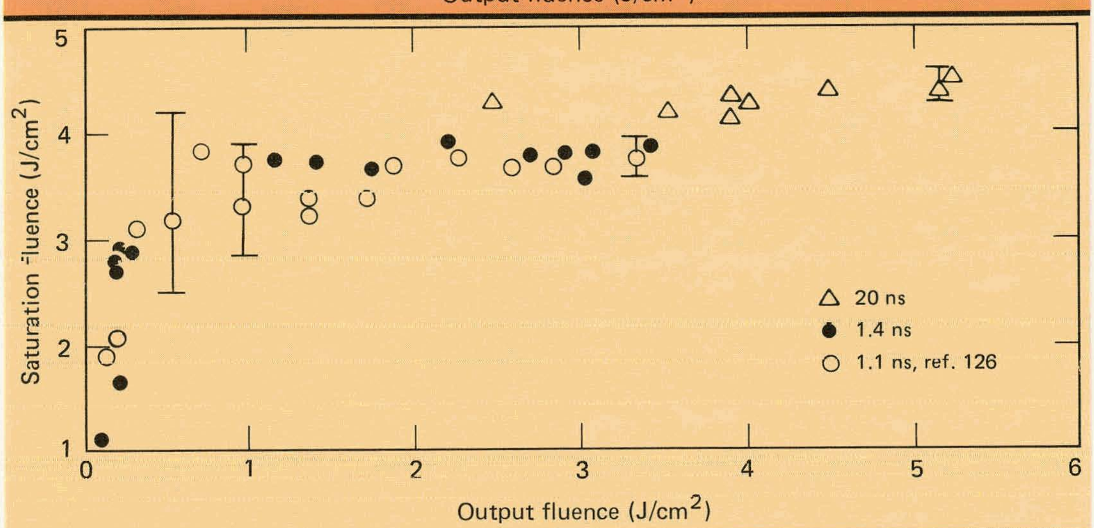

Fig. 2-260. Saturation fluence as a function of output fluence for an LHG-8 amplifier, with all values computed for transmission = 97.4%.

variations in computed values of E_s associated with a ±2% uncertainty factor in G_o. (The value of ±2% was chosen to represent the composite error for computations involving three parameters, E_{in}, E_{out}, and G_o, with each having an uncertainty of ±1%.) Note in Fig. 2-260 that we have included the values of saturation fluence for LHG-8 that were measured[125] in previous experiments. For LHG-8 we found that E_s increased slowly with increasing E_{out} and that the errors in computed values of E_s were large for small E_{out}. The small values of E_s computed for E_{out} were less than 0.5 J/cm^2 and mirror the 2% offset found between the G_o measurements performed with the prelase beam and with the calorimeter. These data are in close agreement with our earlier measurements for LHG-8.[125] In the case of P101, all values of E_s that we measured when E_{out} was greater than 1 J/cm^2 were well represented by the average value E_s = 5.3 J/cm^2. For both LHG-8 and P101, values of E_s measured with 20-ns pulses are slightly greater than those measured with 1.4-ns pulses.

Authors: D. Milam and S. M. Yarema

Major Contributors: D. B. Clifton, G. E. Murphy, S. E. Peluso, Jr., S. E. Stokowski, and J. B. Wood

Damage Studies

Electron-Beam-Deposited AR Films. In the 1979 Annual Report,[128] we described the results of a matrix study of deposition parameters for four-layer Ta_2O_5/SiO_2 antireflection (AR) films with halfwave SiO_2 undercoats produced by electron beams. The films were deposited at three substrate temperatures (175, 250, and 325°C), at three partial pressures of oxygen (0.5 × 10^{-4}, 1.0 × 10^{-4}, and 2.0 × 10^{-4} Torr), and at two deposition rates (1.5 and 5.0 Å/s). These depositions yielded a set of 18 films, and this set was duplicated in subsequent coating runs to provide us with a total of 36 samples. For each film, Optical Coating Laboratories, Inc. (OCLI), measured net stress and linear absorption, and we measured laser damage thresholds. The results indicated a possible advantage in deposition at 175°C and a lack of correlation between damage thresholds and either net stress or linear absorption.

In 1980, we continued this study by baking a set of the films for 4 h at 200°C. This postpreparation treatment is frequently used on Ta_2O_5 films. After the baking, OCLI remeasured net stress and absorption in most of the films, and we remeasured the 1-ns damage thresholds.

Table 2-55 shows the data derived from these tests. The results from baking were mixed—some damage thresholds increased,

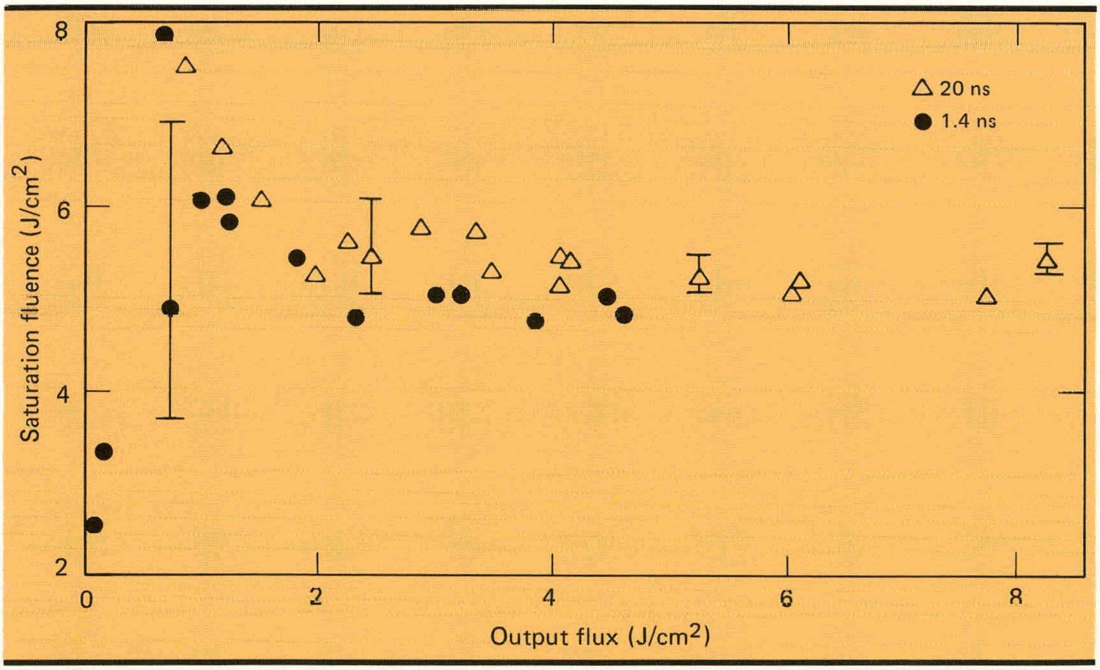

Fig. 2-261. Saturation fluence as a function of output fluence for a P101 phosphate amplifier with passive transmission = 96.3%.

while others decreased. One AR film sample in the baked set, tested with a 1-ns pulse from a 1064-nm laser, exhibited a damage threshold of 20 J/cm^2. This is the highest threshold that we have observed to date.

Figure 2-262 shows the thresholds for the films, measured before and after baking (at 200°C), as a function of absorption. Note that, for 14 of the 16 samples measured, film absorption was greatly reduced. However, there remains no general correlation between film absorption and threshold damage and no general increase in the average threshold, associated with baking, although the extreme thresholds were improved.

In the past, we observed that some of the production components that had failed to meet damage specifications had become acceptable after postpreparation baking. We assume the improvement to be from a reduction in very large film absorption.

As part of our investigation, we looked at the film surfaces under a microscope and discovered that some of the films were more textured than they had been before baking; however, we were unable to determine whether this was caused by contamination during the baking or by some other alteration to the film material.

In Fig. 2-263, we show the thresholds for films as a function of net stress, with measurements made before and after baking at 200°C. The baking produced a dramatic change in stress: unbaked films have a large compressive stress; baked films have a tensile stress. From the data in this figure, we conclude that there is no correlation between net stress and short-pulse 1064-nm laser damage thresholds. This leaves an alteration of local stress in the individual film layers

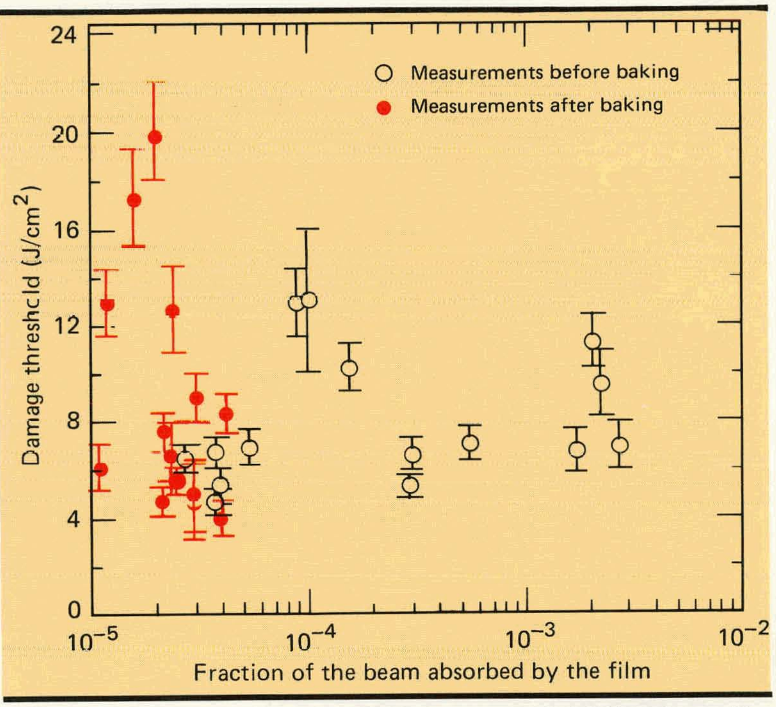

▲ **Fig. 2-262. Damage thresholds (1064-nm laser with 1-ns pulse duration) as a function of calorimeter-measured linear absorption for four-layer Ta_2O_5/SiO_2 AR films with halfwave SiO_2 undercoats.**

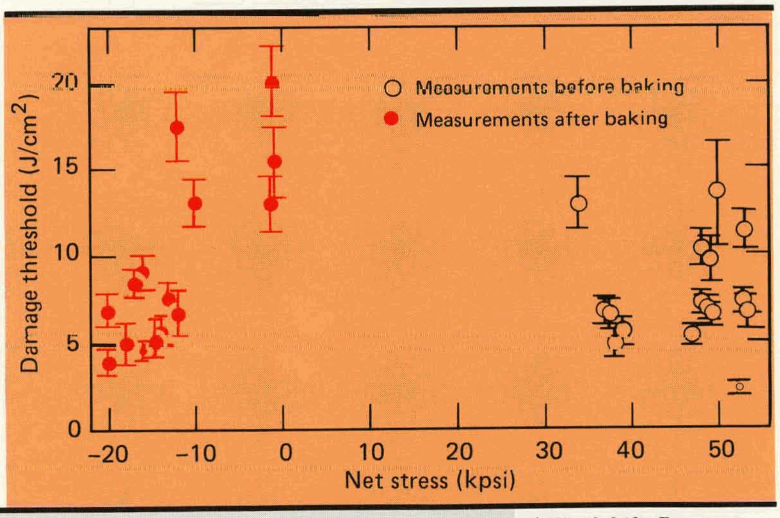

▲ **Fig. 2-263. Damage thresholds (1064-nm laser with 1-ns pulse duration) as a function of net film stress for four-layer Ta_2O_5/SiO_2 AR films with halfwave SiO_2 undercoats.**

Table 2-55. Damage thresholds (1064 nm laser with 1-ns pulse duration) for four-layer $Ti_2O_5 \cdot SiO_2$ AR films with halfwave SiO_2 undercoats fabricated by electron-beam deposition.

		Substrate temperature of 175°C		Substrate temperature of 250°C		Substrate temperature of 325°C	
Deposition rate (Å/s)	Oxygen partial pressure (Torr)	Sample	Threshold (J/cm^2)	Sample	Threshold (J/cm^2)	Sample	Threshold (J/cm^2)
1.5	0.5×10^{-4}	1	13.0 ± 3.0	7	7.1 ± 0.7	13	6.6 ± 0.7
		1B	17.4 ± 2.0	7B	4.7 ± 0.5	13B	6.8 ± 1.2
1.5	1.0×10^{-4}	2	18.7 ± 1.9	8	6.9 ± 0.7	14	4.7 ± 0.5
		2B	15.2 ± 2.0	8B	7.6 ± 0.8	14B	5.0 ± 0.8
1.5	2.0×10^{-4}	3	12.9 ± 1.4	9	6.7 ± 0.7	15	—
		3B	20.1 ± 2.0	9B	12.7 ± 1.8	15B	—
5.0	0.5×10^{-4}	4	7.1 ± 0.8	10	2.2 ± 0.3	16	—
		4B	8.4 ± 0.8	10B	6.5 ± 1.1	16B	—
5.0	1.0×10^{-4}	5	6.7 ± 1.0	11	5.3 ± 0.5	17	5.4 ± 0.7
		5B	9.0 ± 1.0	11B	3.0 ± 0.7	17B	5.6 ± 0.6
5.0	2.0×10^{-4}	6	11.3 ± 1.1	12	9.5 ± 1.4	18	6.5 ± 0.6
		6B	13.0 ± 1.3	12B	4.9 ± 1.2	18B	6.1 ± 0.8

B = Thresholds measured after baking.

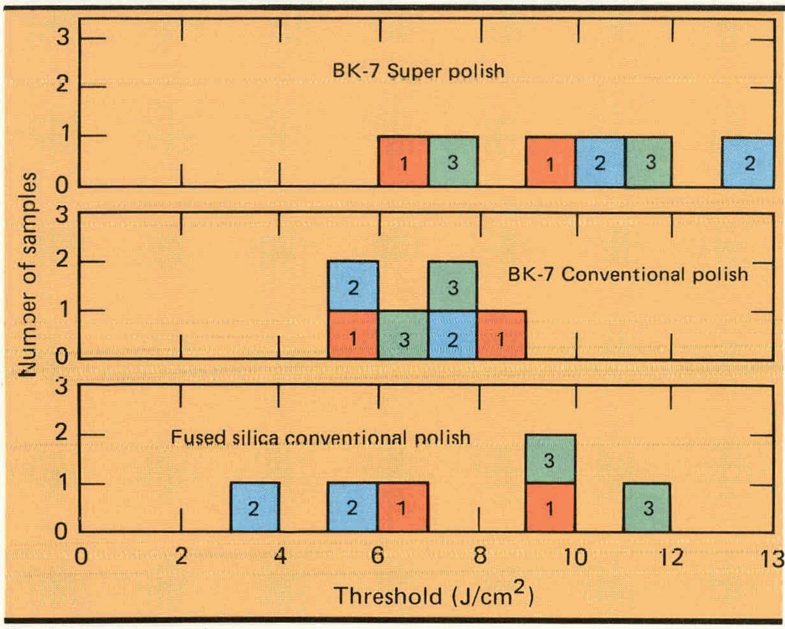

Fig. 2-264. Damage▲ thresholds (1064-nm laser with 1-ns pulse duration) for four-layer Ta_2O_5/SiO_2 AR films with halfwave SiO_2 undercoats deposited at T = 175°C, rate = 1.5 μ/s, and O_2 pressures = 1.0 × 10^{-2} Torr on three types of substrates.

Fig. 2-265. Damage thresholds of Ta_2O_5/SiO_2 AR films as a function of pulse duration of 1064-nm laser.▼

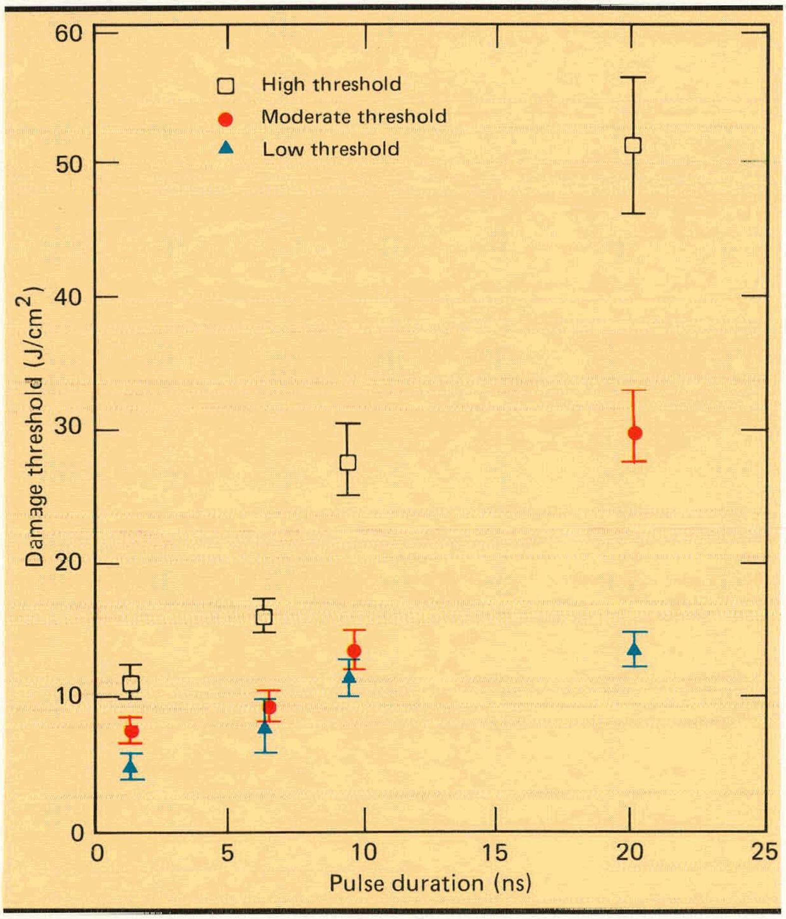

as the only possible way for macroscopic stress to influence threshold levels. Since net stress in the several layers of an AR film is the sum of stresses with different signs, zero net stress does not imply zero local stress. Therefore, local stress changes could possibly influence threshold damage level.

Our matrix study was helpful in determining the role of absorption, stress, and deposition temperature. However, the study suffered from two problems. First, only two coating runs were made under each set of coating conditions, which weakened statistical support for choosing an optimum matrix point. Second, the films were deposited on superpolished fused silica, which was viewed as the substrate least likely to mask the effects of changes in deposition parameters; however, neither the superpolishing process nor the silica material is likely to be routinely used to fabricate actual components for large 1064-nm lasers.

To test the influence of substrates, we collaborated with OCLI to make three additional coating runs under apparently optimum conditions (T = 175°C, rate = 1.5 Å/s, and O_2 = 1 × 10^{-4} Torr). In this test, Ta_2O_5/SiO_2 AR films were deposited on three types of substrates: superpolished BK-7, conventionally polished BK-7, and conventionally polished fused silica. The damage thresholds for 18 films from the three runs are shown in Fig. 2-264, where each datum in the histogram is numbered to indicate the coating run in which the corresponding film was produced. The thresholds of films on superpolished surfaces average higher than the thresholds of films on conventionally polished surfaces. Indeed, the thresholds of films deposited in this test under supposedly optimized conditions on *conventionally polished* BK-7 are approximately equal to the thresholds of films that we have deposited on such substrates under many different nonoptimum coating conditions. The data also illustrate variations that we usually observe when we attempt to produce identical films.

We have performed an additional matrix study with four-layer TiO_2/SiO_2 AR films with halfwave SiO_2 undercoats. In this study the films were deposited at four temperatures (175, 225, 275, and 325°C), two deposition rates (1.5 and 5 Å/s), and three oxygen partial pressures (0.7 × 10^{-4}, 1.2 × 10^{-4}, and 2.0 × 10^{-4} Torr). For this test, OCLI deposited the films on superpolished BK-7 glass. The films were exposed to 1-ns pulses from a 1064-nm laser, and the damage thresholds resulting from this test are shown in Table 2-56. As we saw previously with the Ta_2O_5/SiO_2 matrix, the probability of obtaining a good film was greatest at the lower temperatures. At the highest deposition temperature, 325°C, varying the oxygen pressure or deposition rate did not result in a high-threshold film.

Finally, we extended our data base by measuring the pulse-duration dependence of thresholds of three Ta_2O_5/SiO_2 AR films and three TiO_2/SiO_2 AR films. From among films that we had previously tested with 1-ns pulses, we selected films that had low, moderate, and high thresholds, and we then tested these six films with 6-, 9-, and 20-ns pulses. In Figs. 2-265 and 2-266 we show the data derived from these tests. Note that each curve has a similar shape and that the threshold increases slowly during the interval between 1 and 5 ns and then increases somewhat more rapidly for the longer pulse durations.

From our tests, we have learned the deposition parameters that will provide AR films with good damage resistance if the films are deposited on superpolished surfaces of either BK-7 or fused SiO_2; however, these depositions are not generally successful when the substrates are conventionally polished. We are currently evaluating the variations of conventional polishing and cleaning processes of the substrates so that we can determine how they affect film thresholds.

Authors: D. Milam, F. Rainer, and J. E. Swain

Major Contributors: G. E. Murphy and S. E. Peluso

Industrial Contributors: C. K. Carniglia, T. H. Allen, and T. A. Tuttle (Optical Coating Laboratories, Inc.)

Fig. 2-266. Damage thresholds of TiO_2/SiO_2 AR films as a function of pulse duration of 1064-nm laser.

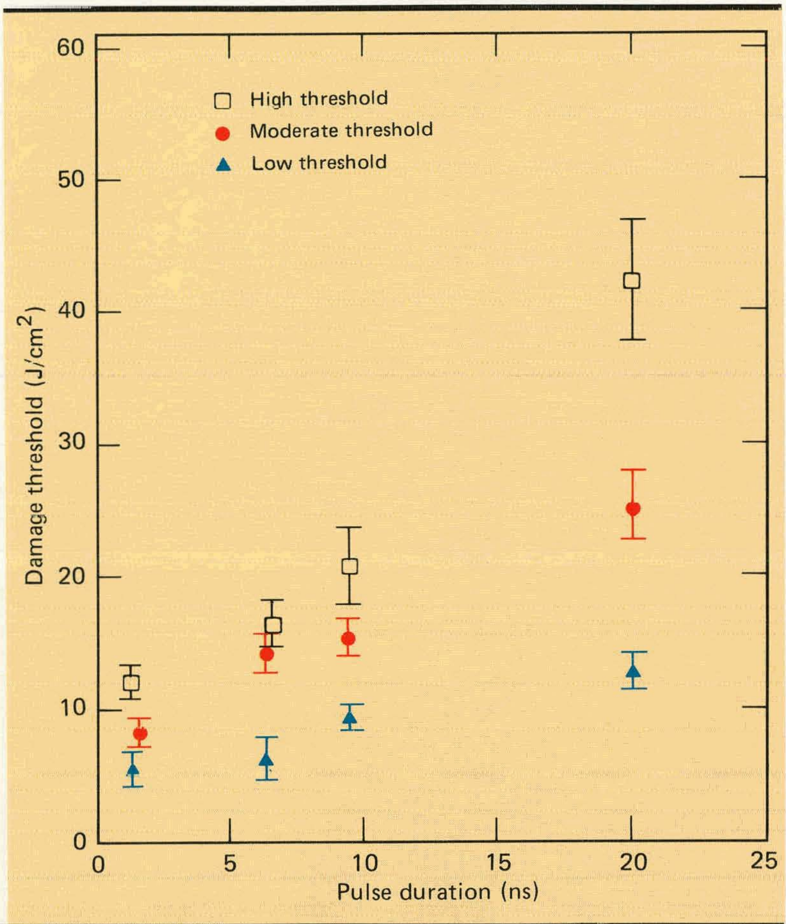

Deposition rate (Å/s)	Oxygen partial pressure (Torr)	Substrate temperature of (175°C) Sample	Threshold (J/cm^2)	Substrate temperature of (225°C) Sample	Threshold (J/cm^2)	Substrate temperature of (275°C) Sample	Threshold (J/cm^2)	Substrate temperature of (325°C) Sample	Threshold (J/cm^2)
1.5	0.7×10^{-4}	1	8.8 ± 0.7	7	6.1 ± 1.0	13	3.6 ± 0.4	19	4.0 ± 0.9
		1R	12.0 ± 1.2	7R	8.1 ± 0.8	13R	<2.5	19R	3.7 ± 0.8
1.5	1.2×10^{-4}	2	8.7 ± 0.9	8	13.7 ± 1.4	14	4.8 ± 0.8	20	4.3 ± 0.9
		2R	6.2 ± 1.2	8R	11.2 ± 1.2	14R	3.2 ± 0.6	20R	3.9 ± 0.8
1.5	2.0×10^{-4}	3	5.5 ± 0.9	9	8.0 ± 0.8	15	9.8 ± 1.0	21	3.9 ± 0.6
		3R	9.2 ± 0.8	9R	9.9 ± 1.0	15R	12.5 ± 1.3	21R	3.0 ± 0.8
5.0	0.7×10^{-4}	4	3.4 ± 1.1	10	3.7 ± 0.4	16	2.1 ± 0.6	22	4.0 ± 0.6
		4R	9.0 ± 1.3	10R	4.2 ± 0.7	16R	<2.0	22R	3.3 ± 0.8
5.0	1.2×10^{-4}	5	8.3 ± 0.8	11	10.2 ± 1.0	17	<1.3	23	3.8 ± 0.4
		5R	5.4 ± 0.9	11R	9.3 ± 1.0	17R	<1.4	23R	4.1 ± 0.7
5.0	2.0×10^{-4}	6	10.7 ± 1.1	12	7.2 ± 0.7	18	4.5 ± 0.6	24	4.2 ± 0.5
		6R	5.8 ± 1.1	12R	9.0 ± 0.9	18R	2.1 ± 0.8	24R	3.7 ± 0.8

R = Films made in repeat runs.

Table 2-56. Damage thresholds (1064 nm laser with 1-ns pulse duration) for four-layer $TiO_2 \cdot SiO_2$ AR films with halfwave SiO_2 undercoats deposited on superpolished BK-7.

Graded-Index Surfaces. We previously described damage studies made on graded-index surfaces that were formed by leaching polished surfaces of phase-separated silicate glasses.[129,130] When tested with 1-ns pulses of 1064-nm laser light, the surfaces produced by this process routinely yield damage thresholds of 10 to 12 J/cm^2 and have reflectivities that can be less than 0.5%. Our damage studies on these surfaces have mainly ceased, and our primary effort is now concentrated on producing optical components from the materials that have been developed. This latter program is described in "Nova Optical Components" in this section.

We are now investigating some of the few remaining questions pertaining to the use of graded-index surfaces with 1064-nm lasers. There is some indication that higher thresholds on these materials can be obtained by irradiating the surface at sequentially greater fluences beginning at a subthreshold level. This suggests that a passive treatment, such as pulsed irradiation by flashlamps or irradiation by a CO_2 laser, might raise damage thresholds. However, the sequential irradiation may alter surface reflectivity by collapsing the microscopic pore structure from which the films derive their AR properties; these pores are very small and difficult to observe by scanning electron microscopy (SEM). Replicas that would be suitable for investigation by transmission electron microscopy (TEM) tend to lock to the graded surface, and we have not yet been successful in obtaining high-resolution photographs of irradiated areas. Investigation of these areas will continue.

The new work with graded surfaces has dealt primarily with the application of graded-index films to materials, such as fused silica, that do not exhibit phase separation and with the investigation of phase-separable bulk materials that may be suitable for use at 355 nm. (Our existing materials are usable at 532 nm.)

We are studying the following three procedures for the production of graded-index films:

- After the phase-separable materials (silicate glasses) have been applied to other surfaces in liquid form, a baking operation removes volatiles, leaving a film that can be etched in the same manner as bulk material. Thin layers of existing materials may be usable at 355 nm.
- A microporous film, whose mass density yields an index of refraction suitable for use as a single-layer AR, can be produced by depositing, in liquid or vapor form, a film containing one or more components that can be removed by etching or leaching to leave a skeletal structure. Such skeletal structures can, in principle, be relatively pure silica or alumina and, therefore, usable at both 248 and 355 nm.
- A thin slab of bulk graded-index material can be thermally bonded to other glasses.

All three processes have been investigated, and the first two methods show promise as viable procedures for the production of graded-index films. We have produced a few films with good spatial uniformity and with 1064-nm damage thresholds comparable to the thresholds for graded-index surfaces on bulk material. The reflectivities of these films are sometimes less than 1%, but they still exhibit large sample-to-sample variation.

Authors: H. Lowdermilk and D. Milam

Major Contributors: T. M. Quick, J. E. Swain, and F. Rainer

Industrial Contributors: S. Mukherjee (liquid graded-index films, Battelle Laboratories, Columbus) and T. H. Hahs (liquid films, Owens–Illinois, Inc.)

Bulk Damage in KDP. We first noticed internal laser damage to KDP crystals during a routine measurement of surface-damage thresholds. In the two samples that we checked at that time, one of the samples was damaged when it was exposed to the 6 J/cm^2 fluence of a 1064-nm laser with 1-ns pulse duration, but the other sample revealed no damage when exposed to fluences up to 15 J/cm^2. To determine the range of damage, we initiated a survey of KDP materials from different sources. In our tests of about 20 samples, we were able to internally damage all KDP samples with laser fluences of 4 to 8 J/cm^2, except for those samples grown by

Lasermetrics, Inc; the Lasermetrics samples showed damage in the range of 11 to 15 J/cm^2. This bulk damage is not unique to KDP; we have previously damaged KD_2PO_4 (KD*P), RbH_2PO_4, RbD_2PO_4, and $(NH_4)H_2PO_4$ crystals at fluences of ~8 J/cm^2. Thus, the bulk-damage problem is common to many KDP isomorphs.

In our high-power laser systems, KDP crystals must withstand, without damage, laser fluences of >10 J/cm^2 at 1-ns pulse durations; thus, the KDP crystal growers must be able to improve the damage resistance of their KDP if we are to use this material. To solve the KDP damage problem, we are collaborating closely with three KDP suppliers: Cleveland Crystal, Inc., Interactive Radiation, Inc. (Inrad), and Lasermetrics, Inc. These suppliers have agreed to provide us with KDP samples that are grown according to our specifications so that we can perform tests on the damage resistance of the KDP material.

We are proceeding with two concurrent programs: one that identifies the inclusion damage at low fluence levels, and another that determines the growth conditions affecting KDP damage resistance. In 1980 we investigated the characteristics of internal damage in KDP using

- Optical and scanning electron microscopy.
- Experiments on the dependence of damage-site density on fluence.
- Experiments on pulse-length dependence of damage.
- Experiments on variation of damage resistance within a crystal boule.

The growth conditions we studied to determine their effect on damage threshold were

- Impurity concentration.
- Filter pore size for the KDP solution.
- Growth rate.
- Growth-tank size.

Our investigations of the damaged volumes by optical microscopy have revealed small (10- to 20-μm) regions where the KDP has melted and decomposed. We show a typical damage site in Fig. 2-267. (In transmitted light, the central opaque spot is approximately spherical and is surrounded by a volume where the refractive index has changed. This change is probably caused by stresses or a composition change.) We believe that damage is caused when an inclusion (as yet unknown) absorbs laser energy and locally heats the KDP to above its melting temperature (253°C).

With the optical microscope, we cannot see inclusions before damage, except for large (>30 μm) liquid-filled bubbles. We fractured various crystals to examine their surfaces with an SEM to determine if the sample had inclusions. This technique seems useful, since fracture appears to preferentially extend through the highly stressed region around an inclusion. In Fig. 2-268 we show an interesting feature on the fractured surfaces where we found potassium and phosphorus after conducting an elemental x-ray analysis. We believe that this inclusion may be a misoriented KDP microcrystal (as

Fig. 2-267. Damage in KDP produced by a 21-J/cm^2, 1064-nm, 1-ns laser pulse.

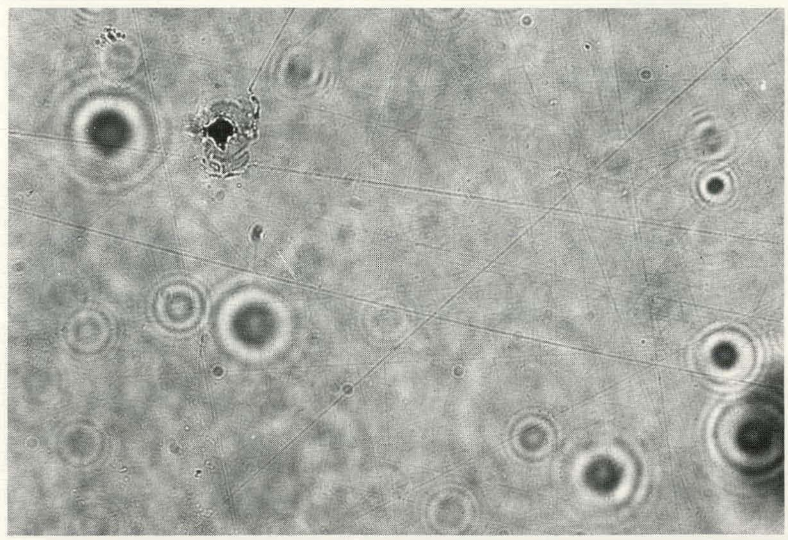

Fig. 2-268. Micrograph of a feature on a fractured surface of KDP.

suggested by Wood in his study of KDP damage[131]). We will continue our attempts to identify the damaging inclusion by using more-sensitive optical microscopy with image enhancement and by using micro-Raman techniques.

In some crystals exposed to >20 J/cm^2, we found 10^7/cm^3 damage sites; however, the initial damage was first observed with the two or three scattering sites that appeared in the 1-mm-diam He–Ne beam that we use for damage inspection. This number is equivalent to a density of 200 sites/cm^3. We find that, as the fluence increases, the density of damage sites increases, indicating the existence of a distribution of inclusions with different damage thresholds.

We checked the variation in damage threshold for samples taken from different parts of a boule and found no disparities.

Fig. 2-269. Bulk-damage threshold in KDP crystals as a function of pulse duration.

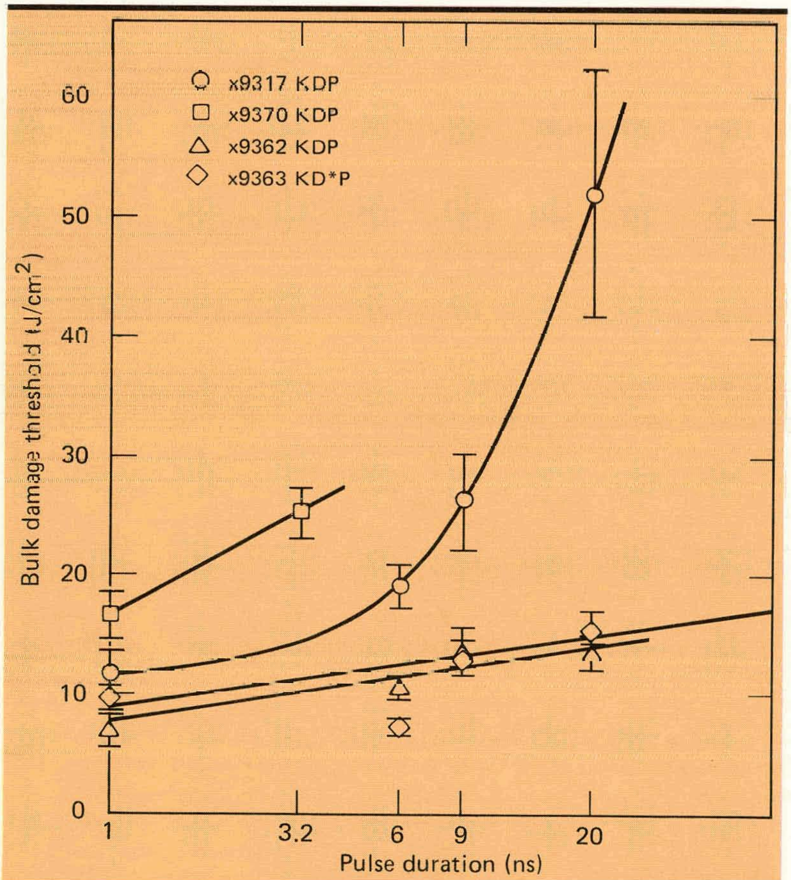

Table 2-57. Typical impurity concentration ranges in KDP crystals.

Element	Concentration	Element	Concentration
Na	1 to 3 ppm	Mg	1 to 2 ppm
Al	2 to 30	Si	10 to 20
Ca	4 to 15	Cr	1
Fe	1 to 7	Rb	1 to 3
Cs	3 to 10	Mo	1 to 10 ppm

From this, we concluded that, if inclusions reside in the growth solution, they will not be depleted during the growth run.

Most of our damage-resistance testing of KDP crystal samples was performed with a 1-ns laser pulse. However, since we can operate our fusion research lasers with different pulse widths, we decided to measure the damage threshold fluence with pulse widths between 1 and 20 ns. Our results are summarized in Fig. 2-269. The best damage-resistant KDP material had a stronger dependence on pulse width than the inferior material, and we speculate that this is caused by thermal diffusion from inclusions of different sizes in the two types of KDP. If the inclusions are smaller in the high-resistance KDP, more laser energy is required to heat them sufficiently to cause damage.

While we were attempting to identify the damaging inclusion, we studied the effects of different growth conditions on damage threshold values. We found no KDP damage site density or threshold dependence on either the growth rate or the concentration of impurities such as Fe^{3+}, Cl^-, V^{3+}, Cr^{3+}, Zr^{4+}, and $SO_4^{=}$. Our analyses of impurities in a typical KDP crystal are listed in Table 2-57, where we show the presence of some transition metals in quantities of 1 to 10 ppm. We regard these as high impurity levels because impurity concentrations $\ll 1$ ppm are needed to produce 10^7 to 10^8 inclusions per cm^3, providing that the inclusion size is ~ 0.25 μm. Therefore, to measure all possible impurity-generated inclusions, we need a technique capable of detecting concentrations to 10 ppb.

If damage-causing inclusions are resulting from microscopic particles or crystals in the growth solution, we may be able to resolve the problem by filtering the solution through microscopic pore filters. Under present conditions, the KDP growers filter the solution once when they load it into the growth tank. We measured damage thresholds of KDP samples grown in solutions where the solution had been passed through filters with pore sizes ranging from 0.05 to 1.2 μm. In these samples, we observed no difference in the damage thresholds; however, we found low thresholds in other samples that had been grown in unfiltered solutions. Thus, we conclude that either the damage-causing particulate is smaller than 0.05 μm or the particulate is present in the growth tank before loading.

After reviewing the preceding results, we agreed with the crystal suppliers that continuous filtering of the KDP solution is necessary to eliminate particulates during a growth run. The suppliers are now complying with this requirement. We intend to perform laser-damage experiments on the new crystals early in 1981, and we believe that the bulk-damage threshold of KDP will significantly increase if the crystal suppliers continue to improve their handling and filtering procedures.

Authors: S. E. Stokowski and J. E. Swain

Major Contributors: D. Milam, T. M. Quick, A. W. Casey, R. L. Landingham, A. R. Ulrich, and F. Rainer

Industrial Contributors: Interactive Radiation, Inc.—W. Runderman (KDP Crystal Growth); Cleveland Crystals, Inc.—L. Shiozawa and J. Luken (KDP Crystal Growth); Lasermetrics, Inc.—W. Osborne (KDP Crystal Growth)

Damage Thresholds at 532, 355, and 248 nm. Because of increased interest in wavelengths below 1064 nm, we have established the following new damage-test facilities:

- A KrF facility for testing with 20-ns, 248-nm pulses.
- A facility attached to the ILS laser for testing at 532- and 355-nm wavelengths using harmonics of the 1-ns, 1064-nm pulses from that laser.
- A modification of the comparative test laser to allow testing with 532-nm, 1-ns pulses.

We describe below these new facilities and the initial experiments performed at short wavelengths.

We built a KrF laser and damage-experiment facility in Building 162. The laser, fabricated by the Advanced Laser Group, has an oscillator excited by electric discharge; this oscillator provides input to a discharge-pumped, injection-locked amplifier. The laser-pulse duration is about 20 ns, but the waveform is complex, as shown in Fig. 2-270. The pulse energy is about 1 J. The output beam is linearly polarized and has a 15- × 40-mm rectangular cross section. Arcing in the amplifier cavity causes the the beam to be spatially nonuniform, so, for damage experiments, we use an aperture to select a more uniform central zone, 12 mm in diameter, from the beam.

The KrF damage experiment is shown in Fig. 2-271. The beam is focused by a lens with a 5-m focal length to produce a spot 1 to 2 mm in diameter at the damage sample. Diagnostic beams for beam photography and calorimetry are derived from reflections off a fused silica window. We use 1-Z photographic plates to record beam profiles; the low sensitivity of the plate emulsion eases the problem of shielding the plate from accidental exposure to room lights. Beam profiles are determined by densitometry of multiple-image photographs.[132] Pulse energy is measured by a Scientech single-port absorbing-glass calorimeter, which we calibrated with a less-sensitive calorimeter built at LLNL.

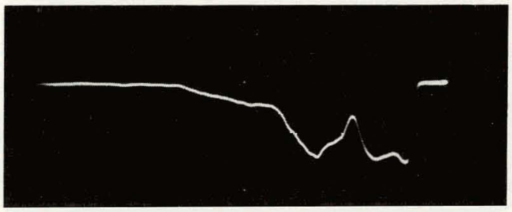

Fig. 2-270. Waveform of KrF laser used for damage measurements; FWHM is 20 ns.

Fig. 2-271. KrF damage experiment ▼

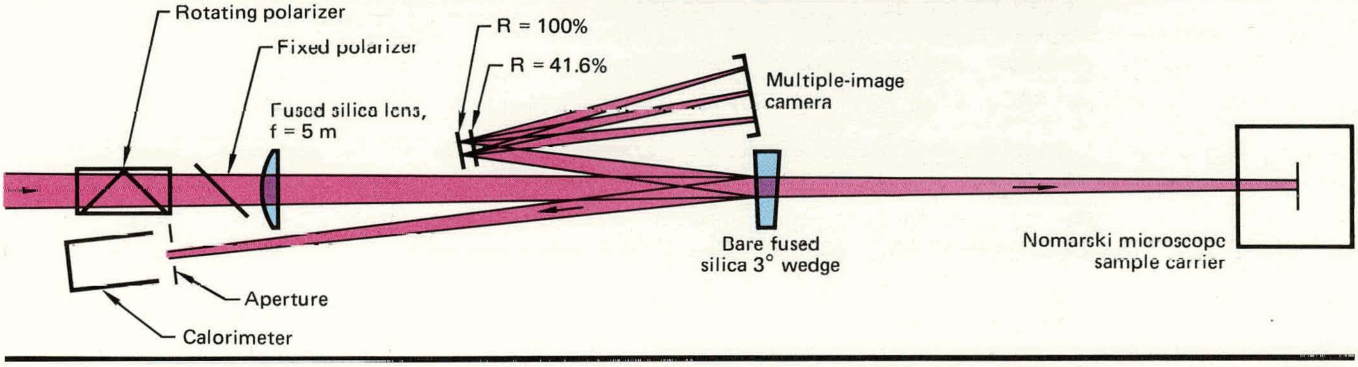

At the sample, the beam has an approximately top-hat profile, which is the nearfield pattern from the 12-mm aperture in the input beam, but exhibits modulation as large as 50% of the peak amplitude. However, the spatial structure of the modulation is large enough to be accurately analyzed with photography. The modulated beam shape is relatively constant from shot to shot, so that fluence at the sample can be controlled by using a rotating polarizer to regulate the input pulse energy.

The damage samples are mounted on a rotating stage attached to a Nomarski microscope, and the focal site is photographed before and after irradiation. Damage is defined as permanent alteration of the surface that is visible by this microscopic examination.

In the initial KrF damage experiments, we surveyed the thresholds of coatings available from several vendors. The results of these tests are shown in Fig. 2-272. The thresholds are generally quite low, but are encouraging in one respect: several thresholds exceed our initial goal of 5 J/cm^2.

It is interesting that thresholds of randomly selected antireflection films exceeded those of highly reflective films; a similar result was obtained in tests at 266 nm.[133] If this observation is found to be generally true, it is a significant reversal of our observations in damage tests with a 1064-nm laser. At 1064 nm, antireflection films have thresholds less than those of high-reflection films; we believe that the substrate–film interface of films designed for 1064-nm laser pulses is more prone to damage than the film material itself. The present KrF data suggest that interfaces are not the limiting problem in damage to UV films and that threshold improvements can be obtained by variations of film materials and deposition parameters without addressing the fabrication and cleaning of substrate materials.

We plan now to begin a systematic evaluation of thin-film components that will help us to select materials for further development, to determine whether glasses that transmit at 248 nm can be developed as an alternative for fused silica, and to study porous or graded-index films.

We have used the ILS laser to measure laser damage thresholds at 532 and 355 nm with the intent of studying the use of vidicon beam profilers,[134] which were prepared for use at these wavelengths, and of surveying thresholds of commercially available components. We obtained laser pulses at 532 nm by frequency doubling 1-ns, 1064-nm pulses from the ILS laser in a KDP crystal. The resultant 532-nm pulses were about 0.7 ns in duration. Pulses at 355 nm, obtained by tripling the 1064-nm pulses, were 0.5 to 0.6 ns in duration. Beams of the desired frequency were separated from the other beams by a prism.

The laser-damage experiment used for 532- and 355-nm pulses was like that used for KrF (see Fig. 2-271) except that one diagnostic beam was further divided to provide an input to the vidicon profiler and the input pulse energy was controlled by varying gain in the ILS amplifiers. The beam profiles were recorded by the profiler and analyzed by an on-line computer.[134] As a cross check, the beam profiles were also recorded on 1-Z photographic plates and reduced by densitometry. Pulse energy was measured with a calorimeter designed at LLNL.

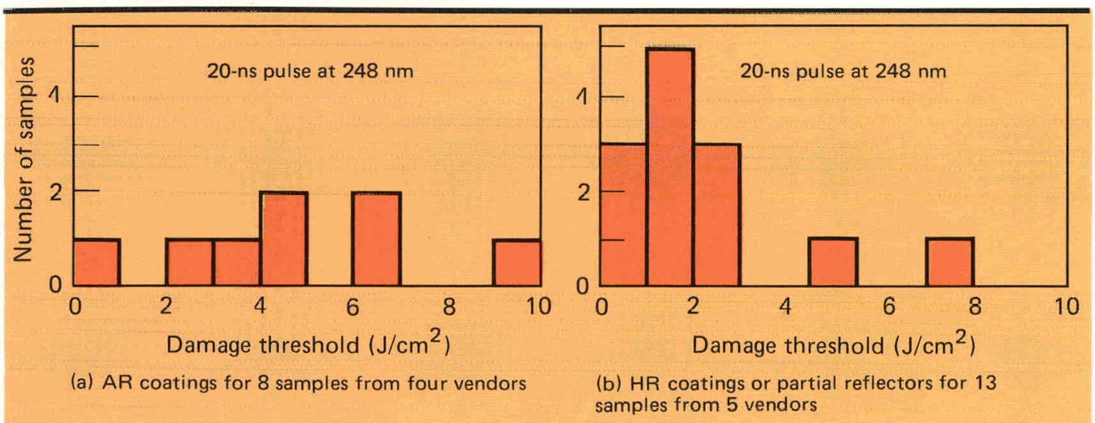

Fig. 2-272. Damage thresholds of commercially available optical thin films exposed to 248 nm, 20-ns laser pulses.

A plot comparing 532-nm fluence levels determined by film and by vidicon recording is shown in Fig. 2-273. There is no systematic difference, but the scatter is large. For reference, the agreement between the two recording techniques is routinely within 10% in our highly developed 1064-nm experiment.[135] We attribute the scatter in fluence levels measured at 532 nm to the presence of spatial modulation on the beam caused by inhomogeneity in the KDP crystals. A similar result was obtained in our analysis of thresholds for 355-nm pulses. We believe, therefore, that vidicons prepared for use at 355 and 532 nm are functioning properly.

In Table 2-58 we summarize the thresholds of commercially available coatings measured with 532- and 355-nm pulses. Thin films, listed as reflectors, partial reflectors, or antireflectors, were designed for use at the test wavelength. Dichroic films tested at 532 nm were reflective at 532 nm and transmissive at 1064 nm; those tested at 355 nm were reflective at both 1064 and 532 nm and were transmissive at 355 nm. We tested bare polished surfaces of BK-7 and fused silica at 532 nm and found them free of bulk damage at the stated threshold fluence levels. We also tested BK-7 and fused silica at 355 nm; the fused silica was free of bulk damage at stated surface thresholds, but the BK-7 suffered detectable color-center damage in single shots with fluences exceeding 3 J/cm^2. We have, therefore, deleted BK-7 surface-damage data from Table 2-58. The graded-index surfaces tested at 532 and 355 nm were etched surfaces of phase-separable materials developed for use at 1064 nm. Bulk damage in this glass occurred at 8 J/cm^2 at 355 nm, but was not observed in 532-nm tests.

In general, bare-surface damage thresholds at 532 nm were comparable to or greater than the 1-ns, 1064-nm bare-surface threshold average of 16 J/cm^2. This is encouraging because of its favorable implications for systems running at 2ω (532 nm). Film thresholds at 532 nm were lower than could be anticipated, probably due to use of TiO_2. Even at 355 nm, the threshold of silica was in reasonable agreement with 1064-nm results, which range from 7 to 10 J/cm^2. We observed no systematic difference between AR and HR thresholds at either 532 or 355 nm. Table 2-58 also provides a summary of 248-nm KrF data.

We have upgraded the comparative-damage test laser to operate with 532-nm pulses. This laser facility is used to perform all quality control measurements and is now being used to perform damage measurements on films deposited in large commercial evaporators. We added an amplifier to increase the output from 2 to 5 J at 1064-nm, and we installed a Type I CD*A temperature-tuned doubling crystal. A diagram of the laser is shown in Fig. 2-274. The 532-nm beam is separated from the residual 1064-nm beam by two dichroic mirrors that transmit at 1064 nm.

Fig. 2-273. Comparison of fluences in 532-nm beams computed with a vidicon profiler and from photographic plates.

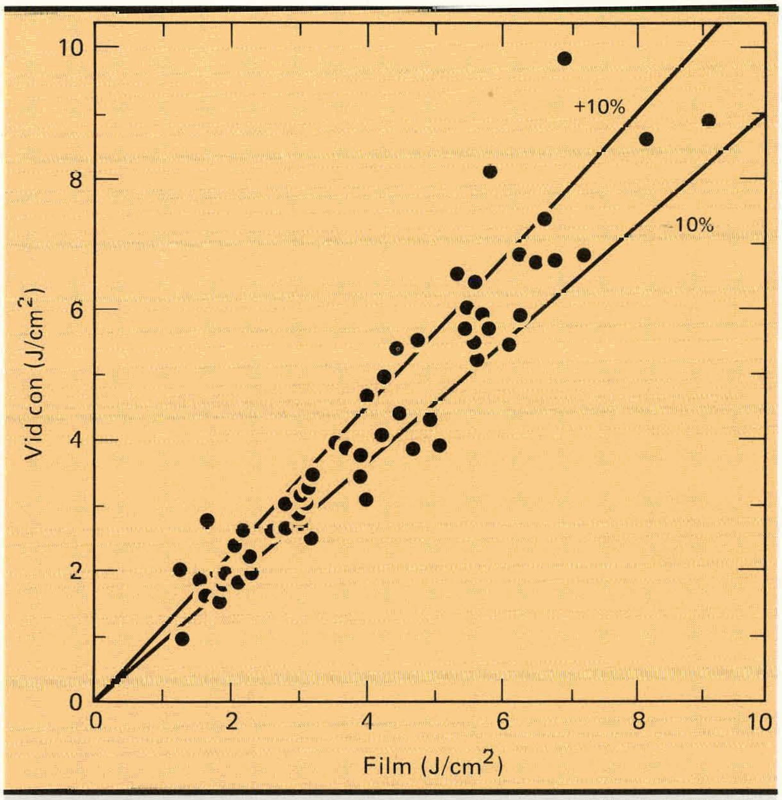

Surface type	Damage thresholds[a] (J/cm^2) 532 nm, 700 ps	355 nm, 600 ps	248 nm, 20 ns
High reflector	2.1 to 5.4 (3.9)	1.1 to 3.0 (2.3)	0.3 to 8.1 (1.8)
Partial reflector	3.0 to 3.4 (3.2)	—	1.9 to 4.7 (2.9)
Antireflector	1.3 to 6.2 (3.9)	0.4 to 2.7 (1.2)	0.7 to 9.4 (4.6)
Dichroic reflector	2.2 to 7.7 (5.0)	0.9 to 2.9 (1.8)	1.6
Bare polished	17.3 to 23.5 (19.4)	10.2 to 11.9 (11.6)	—
Gradient index	11.8 to 13.2 (12.5)	10.1	—

[a]Average threshold values are shown in parentheses.

Table 2-58. Damage thresholds measured with 532-, 355-, and 248-nm laser pulses.

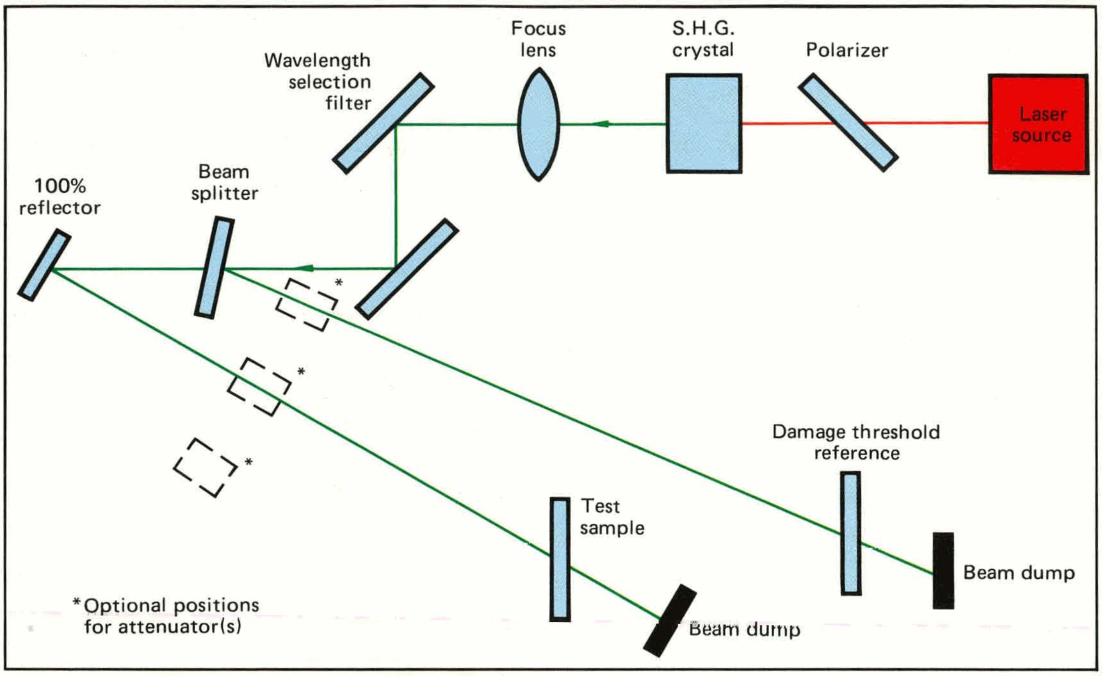

Fig. 2-274. Comparative-damage-test laser modified to operate at 532 nm.

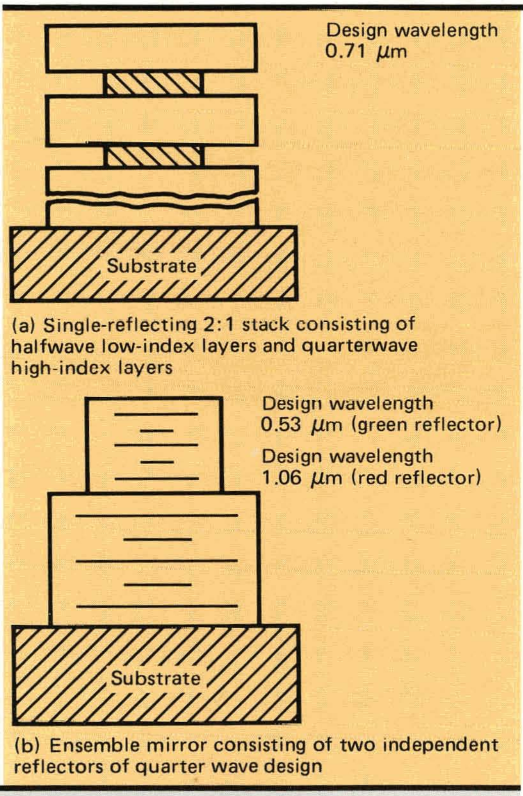

Fig. 2-275. Bichromatic mirror designs: (a) reflective 2:1 stack; (b) ensemble mirror.

Table 2-59. Damage thresholds for biochromatic films exposed to 1064- and 532-nm laser pulses.▼

	Damage thresholds[a] (J/cm^2)	
Coating type	1064 nm, 1.4 ns	532 nm, 1 ns
Antireflection, narrowband	4.0 to 6.5 (5.5)	2.4 to 3.5 (2.5)
Antireflection, broadband	4.0 to 6.5 (5.5)	2.4 to 3.5 (2.5)
Partially transmitting, 2:1 stack	6.5 to 9.0 (7.5)	2.5 to 5.0 (3.5)
Partially transmitting, ensemble	7.0 to 11.0 (8.5)	2.5 to 5.0 (3.5)
Maximum reflector, 2:1 stack	7.0 to 13.0 (11.0)	2.0 to 5.0 (3.0)
Maximum reflector, ensemble	6.5 to 9.0 (7.0)	3.5 to 7.0 (5.0)

[a]Average threshold values are shown in parentheses.

Thresholds are measured relative to the threshold of standard samples measured in the absolute 532-nm experiment.

For standard samples we use AR films on BK-7 glass. Both sides of the substrate are coated, and the thresholds of the two films generally are different. With this reference for the comparison experiment, we can determine the test-sample threshold to be in one of three ranges: less than either threshold of the reference; intermediate to the two reference thresholds; or greater than either reference threshold. Further, the relative fluence of the beams in the test and reference channels can be varied, thereby varying the absolute fluence at which these ranges lie.

We frequently test samples in both the absolute damage facility and the comparative laser. To date, the agreement has been excellent.

Our major experimental effort, supported by comparison laser damage measurements, was a study of bichromatic films designed to operate at 1064 and 532 nm. In this experiment, we tested AR films that reflected less than 0.25% of normally incident radiation at both wavelengths. The AR films consisted of five to seven layers of TiO_2 and SiO_2 deposited on BK-7 glass. Reflectors of two designs, an ensemble stack and a 2:1 stack, were successfully used to produce reflectors that transmitted, at either wavelength, 2% to 3% of p-polarized beams incident at 22.5° from the mirror normal. The mirror designs are shown in Fig. 2-275.

The ensemble design consists of two independent reflectors of quarter-wave design and is fabricated by placing a complete mirror for one wavelength over a mirror designed for the other wavelength. The 2:1 design consists of a single stack of half-wave low-index layers and quarter-wave high-index layers; the low-index layers are optically twice as thick as the high-index layers. These two designs were also used to produce mirrors with a reflectivity greater than 99.5% for either 532- or 1064-nm randomly polarized beams incident at 30° from the normal.

Laser-damage thresholds for the bichromatic coatings measured in the comparison experiment are shown in Table 2-59. Thresholds at 1064 nm are comparable to the thresholds observed in monochromatic 1064-nm films. Thresholds at 532 nm are approximately equal to the 532-nm thresholds shown in Table 2-58, but are lower than expected. There is no indication that one film design offers an advantage over the other.

Authors: F. Rainer, T. F. Deaton, and D. Wirtenson

Major Contributors: M. C. Staggs and J. B. Willis

Industrial Contributor: E. Enemark (bichromatic films, Optical Coating Laboratories, Inc.)

Epoxy Membranes. In 1980 we continued the development of epoxy membranes to replace BK-7 windows as debris shields. The membranes are made by pressing epoxy between optical flats to thicknesses ranging from 0.025 to 0.05 mm. Membranes with a 20-cm aperture have exhibited wavefront distortion as small as $\lambda/6$ at 632 nm, as shown by the interferograms in Fig. 2-276. In 1980, Acton Research Corporation produced membranes with a 30-cm clear aperture, but further work is needed to reduce wavefront distortion in 30-cm membranes. A free-standing 30 cm membrane and mounting frame are shown in Fig. 2-277.

We measured laser-induced damage thresholds for bare epoxy membranes with the comparative-damage test facility using 1064-nm, 1.4-ns pulses. Thresholds for permanent damage ranged from 7 to 20 J/cm^2 and were usually in the range from 10.3 to 17 J/cm^2. Two membranes were also tested at 532 nm, using the second harmonic of the 1064-nm, 1.4-ns pulses. Thresholds for the 532-nm pulses were 4.6 ± 0.5 and 5.0 ± 1.0 J/cm^2.

We successfully used an epoxy membrane in the Shiva laser in place of a BK-7 shield

Fig. 2-276. Transmissive wavefront distortion ($\lambda/6$ at 632 nm) for a 20-cm-aperture epoxy membrane.

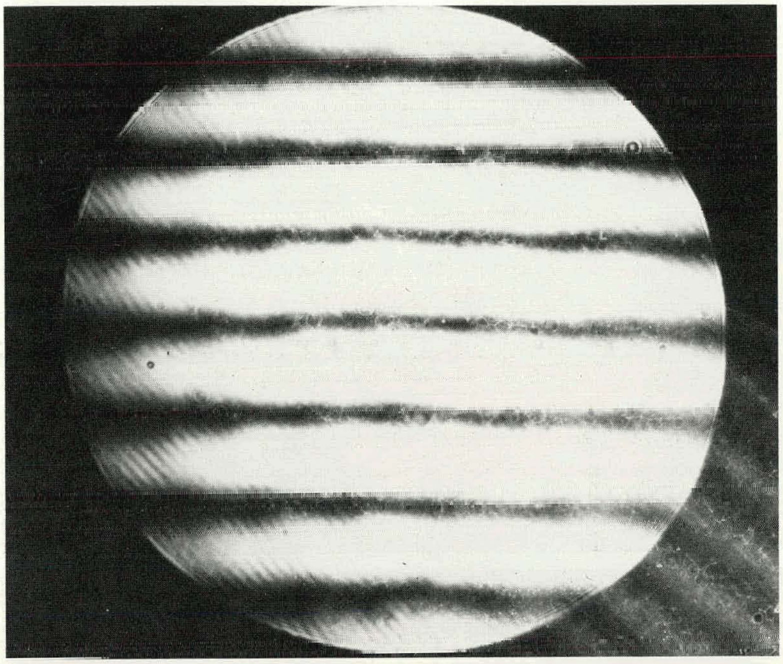

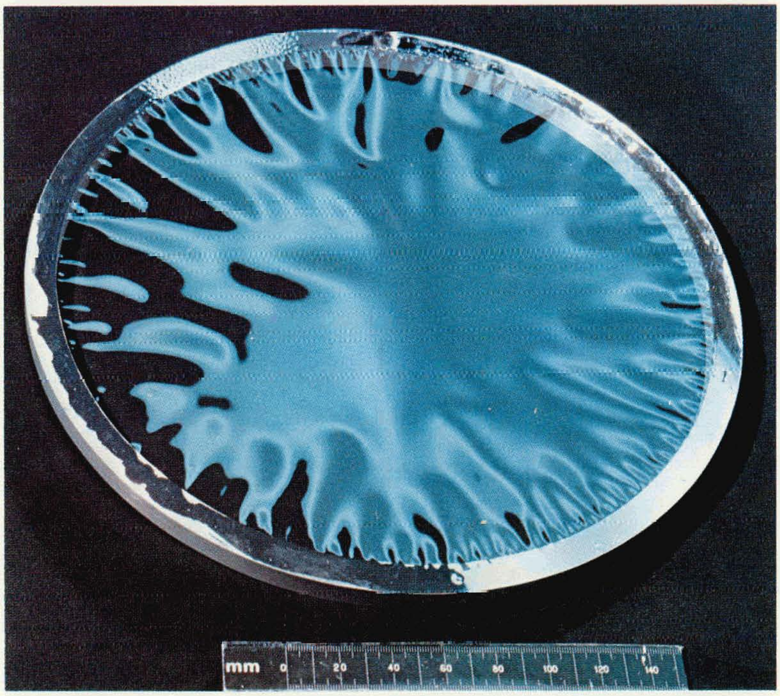

Fig. 2-277. Free-standing epoxy membrane with a 30-cm aperture.

during three high-energy shots. The membrane was then moved closer to the target, to a position where the average fluence was 4 J/cm^2, and the membrane remained unbroken through nine shots.

Author: G. R. Wirtenson

Major Contributor: J. B. Willis

Industrial Contributor: B. Flint (epoxy membranes, Acton Research Corporation)

Amplifier Development

Introduction. In 1980, we constructed two prototype laser amplifiers: a rectangular-design, 20.8-cm Nova disk amplifier that we tested with LSG-91H silicate glass, and a 46-cm transversely pumped rectangular design with split disks. The latter amplifier is currently employed in reliability tests pending arrival of its prototype disks. (A detailed description of the 46-cm amplifier is given in "Amplifiers" earlier in this section.) We also tested several fluorophosphate prototype disks with 34- and 31.5-cm apertures, designed a new rod amplifier for Nova, performed detailed temperature measurements on a 20-cm Argus disk amplifier, used a Shiva-design 1-cm rod preamplifier to test Nd:YLF rods for use at 10 pps on the front end of Nova, and continued to perform additional development efforts on multipass amplifiers.

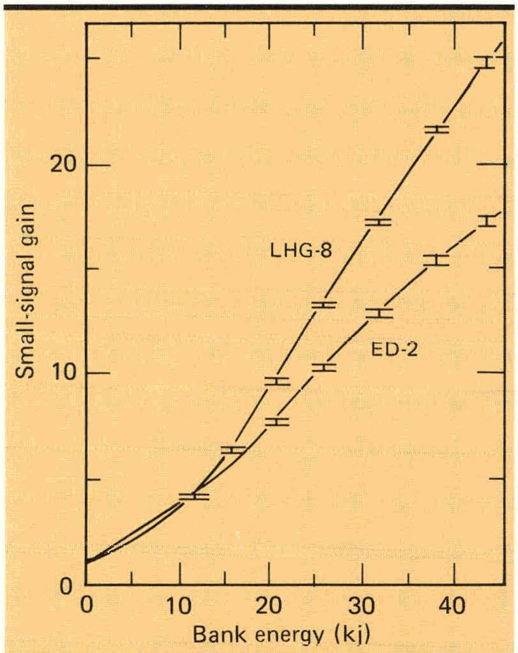

Fig. 2-278. Gain vs energy curves for the beta rod amplifier with ED-2 and LHG-8 rods.

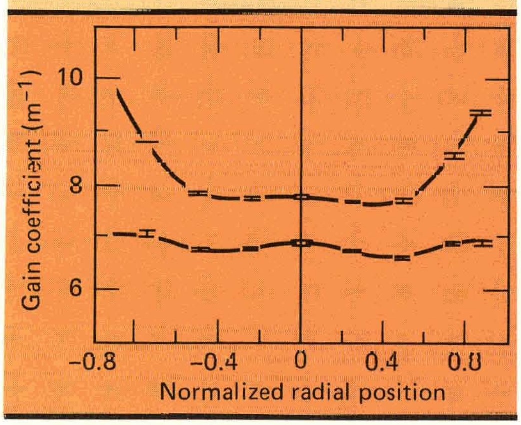

Fig. 2-279. Gain vs position curves for the beta rod amplifier with ED-2 and LHG-8 rods.

Nova Rod-Amplifier Design. We originally planned to fit Shiva beta rod amplifiers with phosphate glass for use in Nova. However, during the past year, we had the opportunity to test a beta rod amplifier with LHG-8 phosphate glass, and the results were disappointing in two respects. First, the centerline gain for the beta rod amplifier was lower than we had predicted, and, second, only about half the expected increase in performance was realized. Figure 2-278 compares the performance of the beta amplifier with silicate and phosphate rods. The gain profile (Fig. 2-279) also changed due to the different absorption characteristics of the two glasses.

Since this performance is marginal for Nova, we designed a new amplifier that also incorporates a number of desired mechanical improvements (described in "Amplifiers" earlier in this section), including better sealing, alignment stability, serviceability, and a different method of electrical isolation. To increase the gain, we lengthened the rod from 40 to 48 cm and increased the pump energy from 38 to 50 kJ. These changes will allow us to use the same lamp design that is used in the 46-cm disk amplifier.

Changes made to achieve a flat gain profile include a reduction of the rod doping to 4×10^{19} cm^{-3} and greater focusing of the pump light. The beta rod amplifier already had a highly focusing reflector design, which will be retained. The shield-glass diameter will be reduced, however, and either water or a water-alcohol mixture will be used for cooling. This thin low-index layer of glass acts as a lens to help pump the center of the rod more effectively.

The original beta amplifier used a shield glass containing an index-matched coolant to prevent parasitic reflections at the surface of the rod; samarium ions in the coolant absorbed the parasitic light at 1.06-μm. However, we do not plan to use this design on the Nova amplifier for two reasons: first, we lack a suitable absorber at 1.05 μm; and second, the hydrated $ZnCl_2$ index-matching fluid is corrosive and difficult to maintain. Thus, the gain improvement of ~10% in this amplifier does not justify its use.

A summary of the Nova and Shiva 5-cm amplifier specifications is shown in Table 2-60.

Prototype Testing. During 1980, several 34- and 31.5-cm fluorophosphate disks were tested in our 34-cm and transversely pumped Datum III prototypes, respectively. For the prototype tests we used ten 25-kJ circuits and 20 lamps, each with a 1.5-cm bore diameter and a 112-cm arc length, for the 34-cm prototype, and we used eight 25-kJ circuits with forty-eight 1.5- × 37-cm lamps for the Datum III. We tested a pair of frit-clad LHG-10 disks from the Hoya Corp., and we show in Fig. 2-280 a comparison of the gain vs input energy for the disks tested in each of the prototypes. The efficiencies of the two prototypes are nearly identical; both designs reach Nova gain levels with less than the budgeted pump energy. The gain profile of the transversely pumped Datum III amplifier is flat to within 10% across the aperture, with the major axis showing more variation (Fig. 2-281). The asymmetry shown in the figure is caused by end effects that can be cancelled by pairing the amplifiers.

We have also tested samples of fluorophosphate glass with monolithic edge claddings from Hoya, Schott, and Owens–Illinois. The 34-cm disks from Owens–Illinois and Schott performed well with respect to gain, but had severe edge-coating damage from excessive Cu-doping of the cladding glasses. This problem and its solutions are discussed in "Edge Cladding" earlier in this section.

We used the gain data obtained from these large fluorophosphate disks as input to computer models of phosphate-glass amplifier performance. The computer code GAINPK defines a cavity efficiency,

$$NJ = \frac{A\left(1 - \frac{-J}{350}\right)}{J^B} , \qquad (45)$$

and fits the experimental data to obtain the parameters A (cavity transfer slope efficiency) and B (power coefficient of current). Parameter A is a measure of the effectiveness of converting lamp output energy to stored energy in the glass at low currents, and parameter B accounts for the observed reduction in efficiency at higher

Table 2-60. Specifications for Nova and Shiva 5-cm amplifier designs.

Material or design factor	Nova rod-amplifier specifications	Shiva beta-rod-amplifier specifications
Glass	Phosphate	Silicate
Nd:doping	4×10^{19} cm^{-3}	6×10^{19} cm^{-3}
Length/diam.	48 cm/5 cm	40 cm/5 cm
No. of lamps	6	6
Arc length/bore	48 cm/1.9 cm	37 cm/1.5 cm
PFN (C/L)	208 μF/450 μH	158 μF/450 μH
$3\sqrt{LC}$	920 μs	800 μs
Bank energy	50.4 kJ	38.2 kJ
Gain	28	15

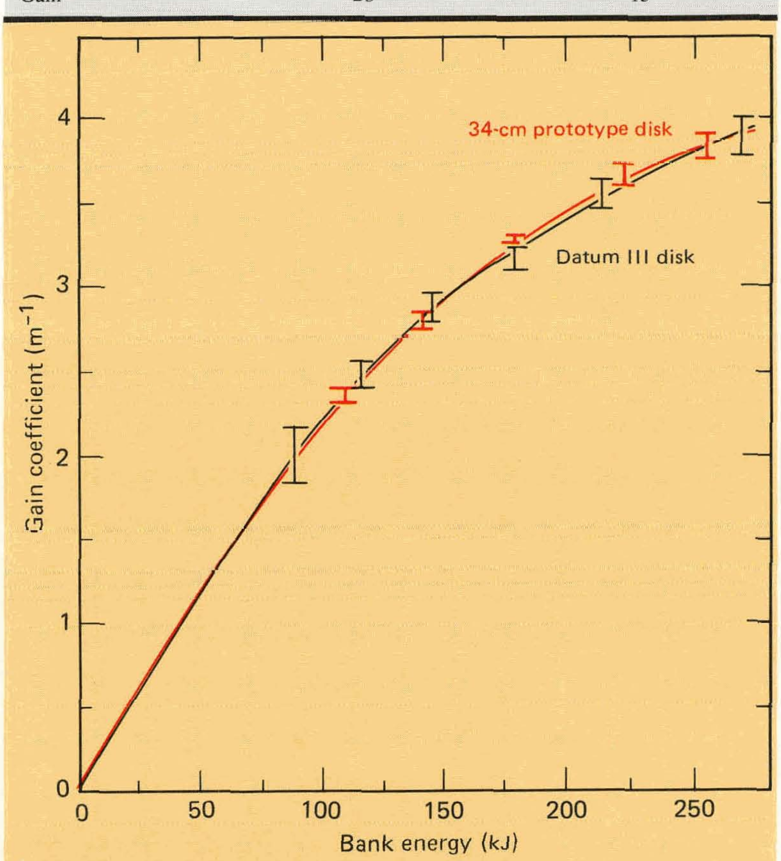

Fig. 2-280. Gain vs ▲ energy curves for LHG-10 frit-clad disks in 34-cm and transverse Datum III prototype.

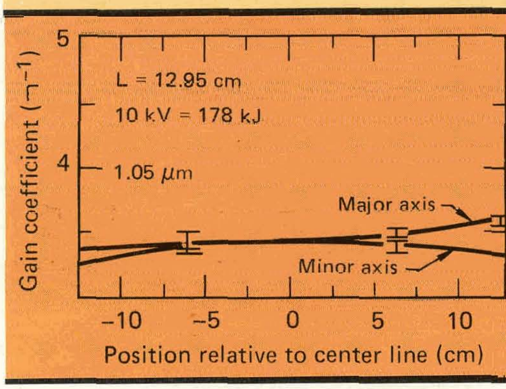

Fig. 2-281. Gain-profile curves for LHG-10 in Datum III prototype (transverse configuration).

current densities due to flashlamp self-absorption. The relative values of A and B for various sizes of Shiva amplifiers were obtained in this way and were used to simulate all of the Nova disk amplifiers using LHG-8 glass. Table 2-61 lists the input data and performance predictions for the Nova amplifiers, and Table 2-62 lists the glass parameters that we used in the simulations.

Prototype 20.8-cm Disk Amplifier. The Nova 20.8-cm disk amplifier is the smallest of the three rectangular amplifier designs; it has two flat arrays of eight lamps each and pumps three disks. This amplifier is essentially an upgrade of the Shiva delta amplifier. Previous modeling predictions led to a design that has the same level of performance as Shiva with only half the number of flashlamps and bank circuits. We built a prototype of this amplifier to test the expected increase in efficiency. Figure 2-282 shows the construction of a prototype that is a scaled-down version of a previous research disk amplifier (RDA).

Nova prototype disks were not available in 1980, so we tested the amplifier with 3.2-cm-thick silicate delta disks. The performance of the Nova design (measured without a shield glass) is compared with earlier Shiva delta measurements in Table 2-63. The centerline gain vs bank voltage is essentially identical; since both measurements were made with the same bank circuits, we indeed achieved the expected factor of two increase in efficiency. The curve in Fig. 2-283 shows the variation of gain coefficient vs pump energy for three ED-2 Shiva delta disks tested in the 20.8-cm Nova prototype amplifier. In this test, we used eight 25-kJ circuits and three disks of different thicknesses. Later, we were able to test the amplifier with a shield glass installed and found the small-signal gain reduced by 6%. Using all of these data as input to GAINPK, we extrapolated to the Nova performance using 2.5-cm-thick LHG-8

Table 2-61. Nova amplifier simulation using LHG-8 glass.

Type of amplifier	A	B	Gain	Bank energy (kJ)[a]
β	0.71	1.29	7.0	165
γ	0.90	1.29	4.4	250
δ	0.79	1.16	2.4	330
20.8-cm	1.20	1.16	2.1	165
31.5-cm	1.30	0.90	1.8	250
46 (37 kJ/ckt)	1.30	0.90	2.1	500
46 (50 kJ/ckt)	1.25	0.90	2.1	590

[a]20% explosion energy

Table 2-62. Glass parameters used to simulate Nova disk amplifiers.

LHG-8 glass parameters	Specification
Doping	$2 \times 10^{20}/cm^3$
Effective cross section	$3.92 \times 10^{-20}/cm^2$
Refractive index	1.523
Total branching ratio	0.4
Lifetime	311 μs

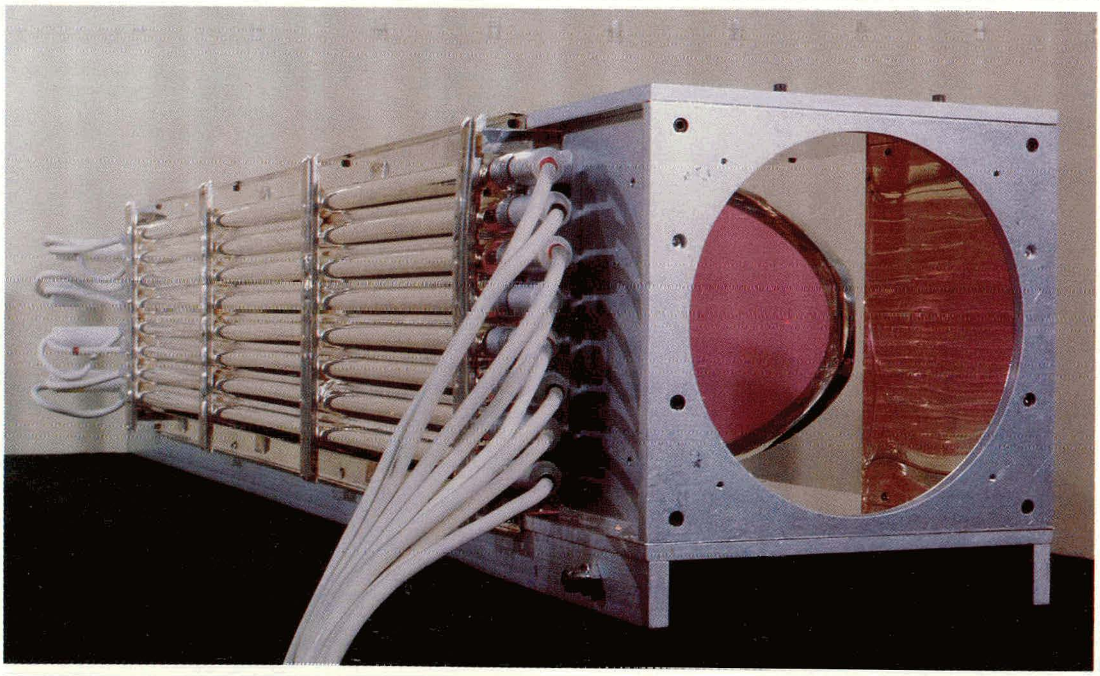

Fig. 2-282. 20.8-cm prototype.

phosphate disks. The expected gain at 22 kV is 2.1, which is comfortably above the required gain of 1.9.

We also measured the gain across the major and minor axes of the 20.8-cm amplifier and found the uniformity to be within 6%, as shown in Fig. 2-284. In this test, we again used eight 25-kJ circuits with three Shiva delta disks of different thicknesses. The curve is somewhat flatter than the earlier Shiva design, and its curvature is reversed; this unexpected characteristic is welcome because both amplifier designs will be used in the same chain, resulting in an extremely uniform combined-gain profile.

Thermal Lensing in Nd:YLF. Several alignment tasks on Novette and Nova (e.g., alignment of the target and of harmonic-generation arrays) would be most easily accomplished with a low energy pulse from the laser-amplifier front end propagated through the laser chain. The alternative, auxiliary lasers injected near the laser output and aligned to the main beams, is mechanically complex, expensive, and less accurate, making the front-end option very attractive.

The pulse energy available and the shot rate of the front-end amplifiers determine the usefulness of this alignment option. Alignment tasks require a relatively large number of shots, implying a high shot rate for reasonable alignment times. Operator-assisted tasks, such as target alignment, require a shot rate of 1 Hz or greater. The pulse energy required depends on the specific alignment task and varies from tens of microjoules for target alignment at 1053 nm to several joules for target alignment at the third harmonic.

There is a trade-off between shot rate and pulse energy from the front-end amplifiers. The maximum useful shot rate of a rod amplifier is determined by either thermal lensing or thermal birefringence. Extracting waste heat from the edge of the rod creates a radial temperature gradient that causes both the lensing and the stress-induced birefringence. Since these thermal effects increase with the power per unit length to the amplifier,[136] an increase in shot rate requires a decrease in the pumping energy per shot, leading to a decrease in gain.

The known optical and thermal properties[137] of Nd:YLF make this material a very promising candidate for a high-shot-rate amplifier. The material has a natural birefringence (0.022) large enough to completely overwhelm any thermally induced birefringence,[138] it has a large (6W/m-°C) thermal conductivity, and its negative dn/dT subtracts from other thermal-lensing contributions.[136] Nd:YLF also has a laser transition at 1053 nm that matches well to the peak of the phosphate-glass gain curve.

Table 2-63. Performance comparisons between Shiva delta and Nova 20.8-cm amplifier designs.

Bank voltage[a] (kv)	Centerline small-signal gain: Shiva delta disks	Centerline small-signal gain: Nova 20.8-cm disks
14	1.60	1.66
16	1.78	1.78
18	1.89	1.88
20	1.97	1.97
22	2.06	2.04

[a]Shiva design—16 circuits and 32 lamps.
Nova design—8 circuits and 16 lamps.

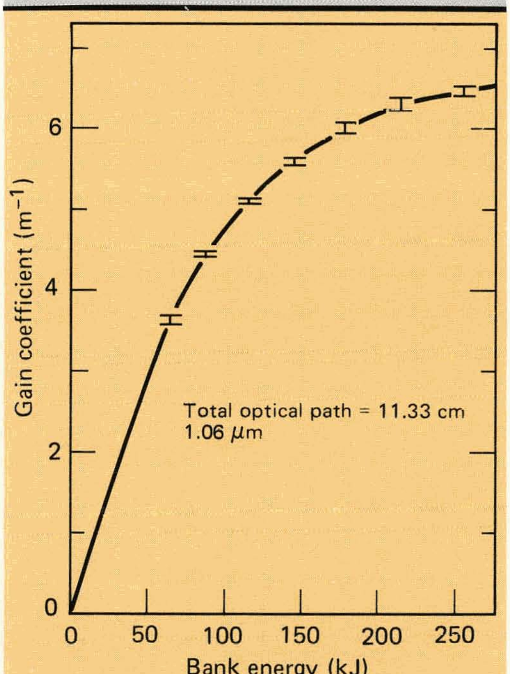

Fig. 2-283. Gain vs energy curve for 20.8-cm amplifier with LSG-91H disks.

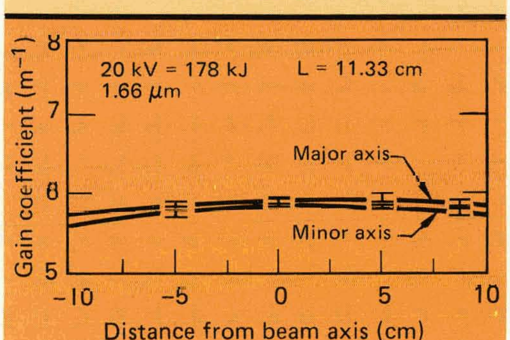

Fig. 2-284. Gain-profile curves for 20.8-cm amplifier with LSG-91H disks.

To assess Nd:YLF as a high-shot-rate preamplifier, we measured the small-signal gain and thermal lensing for a 1-cm-diam by 7.5-cm-long Nd:YLF rod. We determined the gain indirectly by running the amplifier in a laser resonator and finding the oscillation threshold as a function of mirror reflectivities. At threshold, the required pump energy, E, depends on single-pass amplifier gain, G, and mirror reflectivities, R_1 and R_2, as

$$E = \frac{1}{\sigma\kappa} \ln G = \frac{1}{\sigma\kappa}\left(\frac{1}{2} \ln R_1 R_2 + \ln T\right) \quad , \qquad (46)$$

Fig. 2-285. Single-pass gain vs pumping energy for 1-cm diametger Nd:YAG and Nd:YLF rods mounted in the same amplifier.

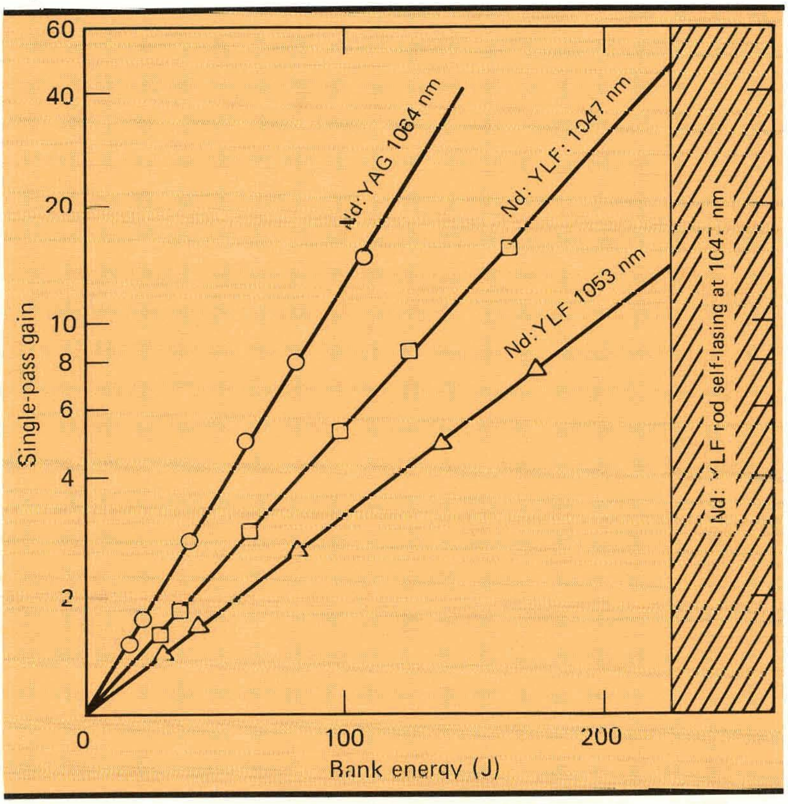

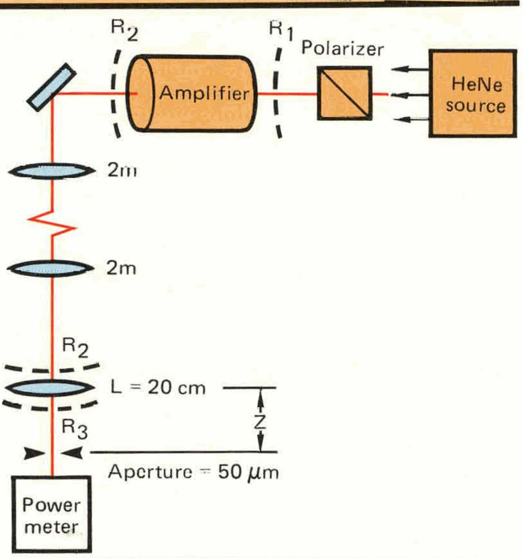

Fig. 2-286. Experimental setup for measuring thermal lensing.

where T is the transmission of cavity components, σ is the cross section, and κ represents all factors affecting pumping efficiency. Plotting E vs 0.5 ln R_1R_2 yields T, allowing G to be calculated. In Fig. 2-285 we show amplifier gain as a function of pumping energy for the 1047- and 1053-nm lines of Nd:YLF and, for comparison, the 1064-nm line of a Nd:YAG rod in the same amplifier. The two lines in Nd:YLF lase at different polarizations, allowing an intracavity polarizer to select one or the other.

In Nd:YLF, self-lasing in the rod on the higher-gain line at 1047 nm limits the maximum achievable gain at 1053 nm. The self-lasing threshold at 224 J for the data of Fig. 2-285 implies a maximum gain of approximately 13 at 1053 nm. The tested rod had flat, uncoated surfaces. AR coatings or Brewster's-angle faces would somewhat improve the maximum 1053-nm gain by increasing the self-lasing threshold at 1047 nm.

Figure 2-285 provides a measure of the ratio of the two cross sections in Nd:YLF. Both originate from the Stark split $^4F_{3/2}$ level and are thermally coupled at room temperature, giving a population ratio of n(1047)/n(1053) = 0.75. With this, and the slopes of the gain data in Fig. 2-285,

$$\sigma(1047\ \mathrm{YLF})/\sigma(1053\ \mathrm{YLF}) = 1.95 \pm 0.08 \quad . \qquad (47)$$

Had the gain ratio been as large as the literature value (Ref. 137), 3.44 ± 1.43, the maximum gain at 1053 nm would have been 4.3.

A comparison of Nd:YLF with Nd:YAG depends on pumping differences as well as cross sections. Nd:YAG has a substantially higher refractive index (1.82 vs 1.46) and a shorter fluorescence decay time (240 vs 480 μs). The pulse-forming network was changed from 120 μF and 302 μH for Nd:YLF to 60 μF and 302 μH for Nd:YAG. In both cases, we used the same pump head and lamps (two lamps, 5 × 76 mm, with 450 Torr of Xe). The following ratios obtained from Fig. 2-285 are useful in estimating the performance of Nd:YLF rods when they are substituted for Nd:YAG rods:

$$\frac{K\sigma\ (1064\ \mathrm{YAG})}{K\sigma\ (1047\ \mathrm{YLF})} = 1.54 \pm 0.07 \qquad (48)$$

and

$$\frac{K\sigma\ (1064\,\mathrm{YAG})}{K\sigma\ (1053\,\mathrm{YLF})} = 2.22 \pm 0.09 \quad . \tag{49}$$

Figure 2-286 shows our test arrangement for measuring thermal lensing. A diverging HeNe beam is polarized and passed through the 1-cm amplifier. Two 2-m lenses relay the plane of the rod output to a short-focal-length lens, L, which focuses it through a 50-μm aperture. Induced lensing and other distortion in the amplifier give a change in focal position and a reduction in peak transmission through the aperture. By plotting power transmitted through the aperture vs distance from the lens, L, with and without thermal input to the amplifier, we detected small changes in lensing and beam quality.

The sensitivity of this method depends only on the focal length of lens, L. The focal distance, Z, from L is given by

$$Z = R_3 / \left[1 + (\lambda R_3/\pi\omega^2)^2\right] \tag{50}$$

for wavefront curvature R_3 after L and beam radius, ω, at the lens. Using $1/R_3 = 1/R_2 - 1/f$, where $R > 0$ implies divergence, gives Z in terms of R_2:

$$Z = \frac{f}{1 - f/R_2 + \dfrac{(\lambda f/\pi\omega^2)^2}{1 - f/R_2}} \quad . \tag{51}$$

For these measurements, $f = 200$ mm, $\omega = 3$ mm, and $R_2 > 6$ m, so that

$$(\lambda f/\pi\omega^2)^2 = 2 \cdot 10^{-5} << f/R_2 = 0.033 << 1 \quad , \tag{52}$$

simplifying the result to

$$Z \simeq f/(1 - f/R_2) \quad \cdot \tag{53}$$

Changes in Z due to changes in R_2 are given by

$$\Delta Z = Z - Z' \simeq -f^2 (1/R_2 - 1/R_2') \quad \cdot \tag{54}$$

With no thermal lensing, $R_2 = R_1$; with thermal lensing, $1/R_2' = 1/R_1 - 1/f_{th}$. Therefore,

$$\Delta Z \simeq -f^2/f_{th} \quad \cdot \tag{55}$$

Figures 2-287 and 2-288 show data for 1-cm-diam by 7.5-cm-long Nd:YLF and Nd:YAG rods pumped in the same two-lamp pump cavity. In each of the three cases, the rods were pumped at 227 J/pulse, 3 pps, with 20 W of simmer for a total input power of 700 W. Power-off data were taken before and after the power-on data and were averaged. The aperture was centered transversely at each Z position for maximum transmitted power, and all data points are averages of at least two runs. For each case, the transmission data were normalized to the peak transmission with no power to the amplifier.

These data indicate a much smaller thermal effect in Nd:YLF than in Nd:YAG. The polarization for 1053 nm in Nd:YLF exhibited no measurable thermal effect at 700 W input, and the polarization for 1047 nm showed a slightly negative thermal lensing. Table 2-64 gives the thermal focal lengths.

We have no convincing explanation for the increase in peak transmission of the 1047-nm polarization when the Nd:YLF rod was pumped. One possibility stems from the poor optical quality of the Nd:YLF rod that we tested. Interferograms showed more than

Fig. 2-287. Thermal-lensing data for oppositely polarized lasing transitions in Nd:YLF at 700-W average power input to the amplifier.

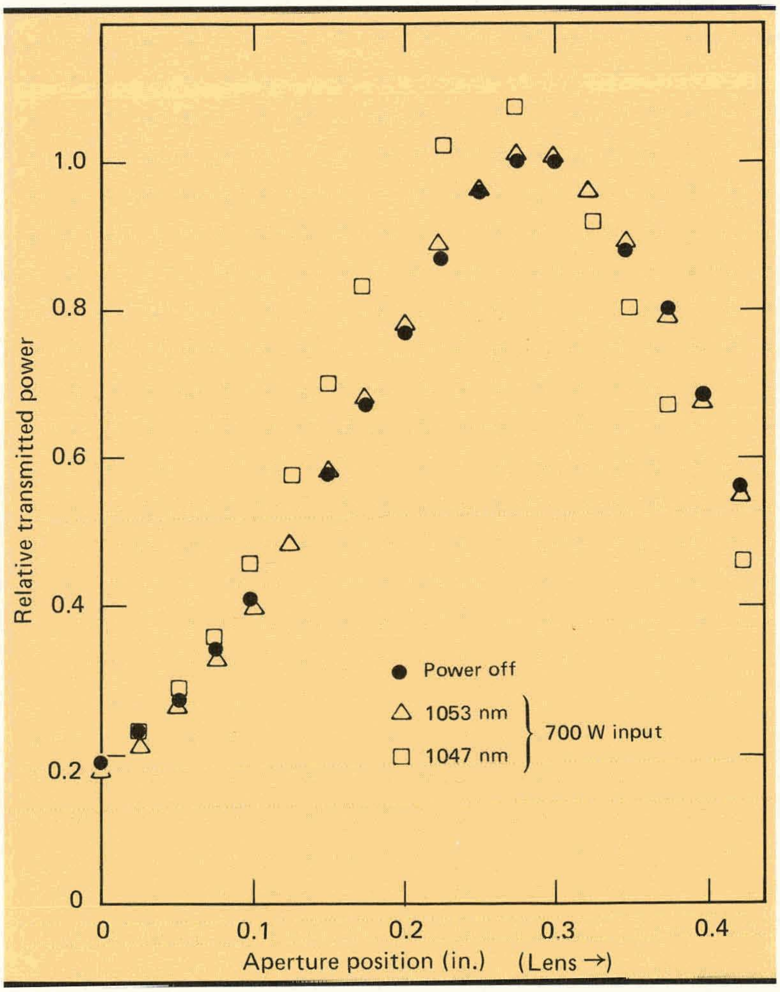

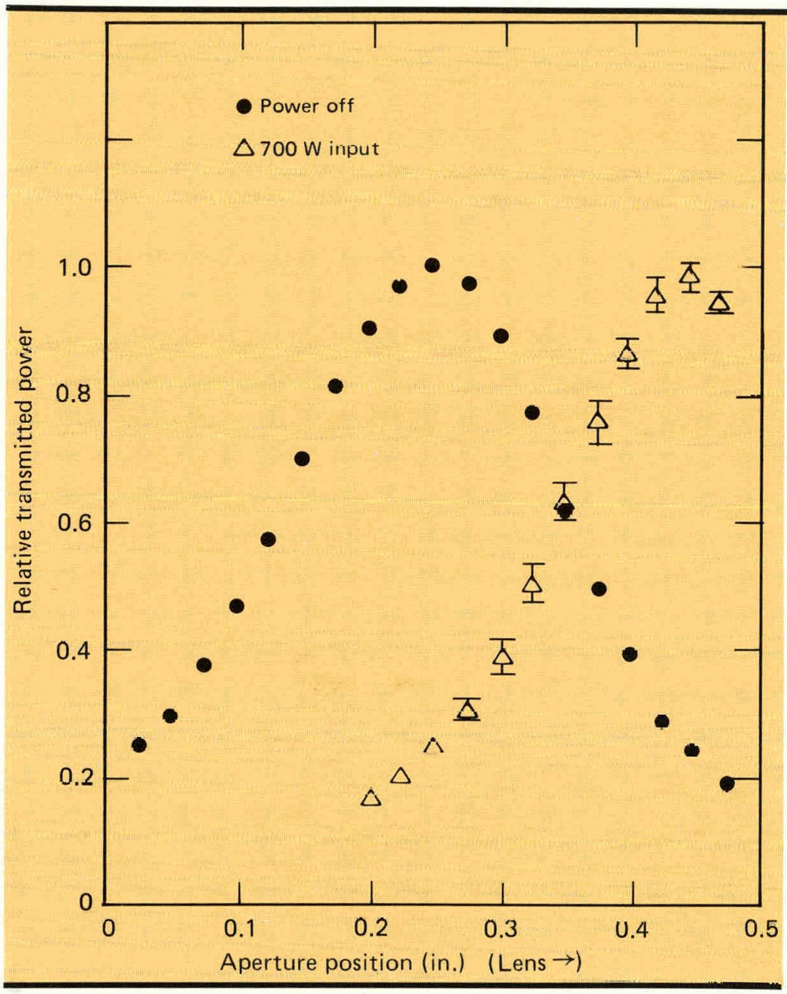

Fig. 2-288. Thermal lensing data for Nd:YAG at 700-W average power input to the amplifier.

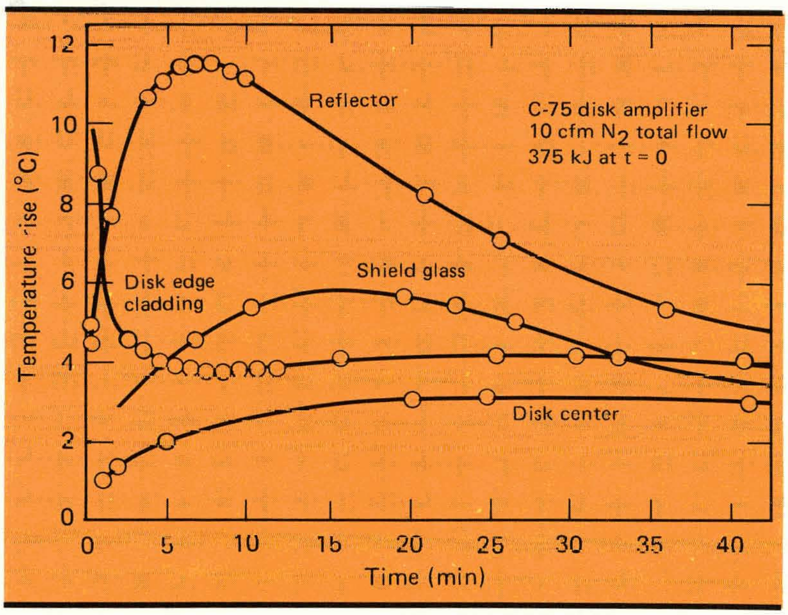

Fig. 2-289. Temperature vs time curves for several points in the Argus C-75 disk amplifier after firing.

one wave of distortion at 633 nm, and the maximum He–Ne power transmitted through the aperture with no power input to the rod was 75 to 80%, as compared to an expected 99% if the rod had been distortion free. A decrease in peak transmission would have implied additional distortion as well as lensing from the thermal input. Therefore, the increase in transmission might have been the result of cancellation of the static distortion due to the thermal effect.

We believe that Nd:YLF is an ideal choice for front-end amplifiers for Novette and Nova. A 1-cm clear-aperture amplifier could be operated at a gain of 10 and at 10 Hz with an estimated thermal lensing greater than 50 m. Further, a 3-cm-diam rod could be used, if it were available, to provide nine times as much energy at a gain of 10 and a shot rate of 1 Hz.

Amplifier-Cooling Experiments. The interval between shots on large glass-laser systems is limited by the cooling rate of the large disk amplifiers. Nonuniform temperature distribution in the disks leads to wedge and lens distortions that misalign the laser chain, and a relaxation time of 1-1/2 h is typically required before another shot can take place. We have looked at the heating and relaxation cycle of an Argus 20-cm disk amplifier in detail to understand how we might increase the shot rate of Nova, if this is desired (present shot rates are usually limited by target fabrication and shot-data reduction times).

Three major diagnostic techniques were used to monitor the temperature evolution of the amplifier. The first technique was direct thermocouple measurement of temperature at selected points in the amplifier. Figure 2-289 illustrates the temperature variation at several points vs time; note that the reflector temperature rise of 12°C is three times or more that of any other component. The initial temperature rise of the disk is only 2 to 3°C.

In the second technique, we monitored the optical distortion in the disk with real-time holographic interferometry. Figure 2-290 shows the arrangement of optical compo-

Table 2-64. Thermal focal lengths for Nd:YLF and Nd:YAG materials. ▶

Material	Wavelength (nm)	Thermal focal length, f_{th} (m)
Nd:YLF	1053	>150
Nd:YLF	1047	−63 ± 20
Nd:YLF	1064	+8.3 ± 0.4

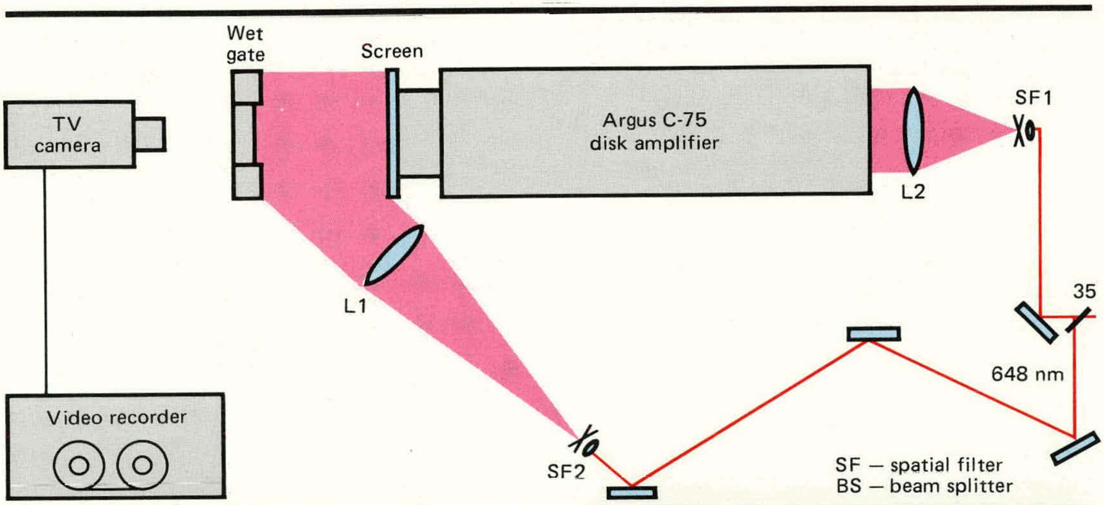

Fig. 2-290. Schematic of holographic interferometry setup for disk-distortion recording from the Argus C-75 disk amplifier.

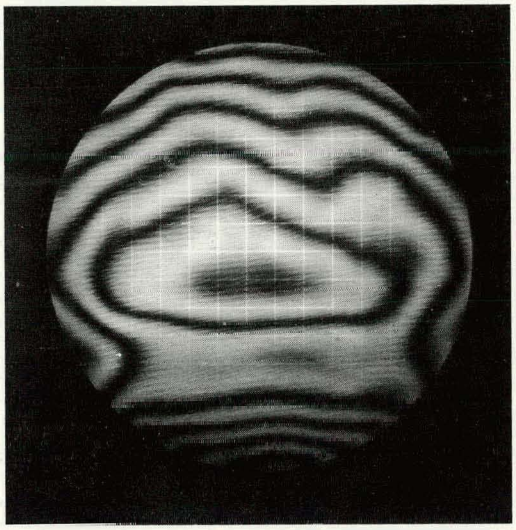

Fig. 2-291. Photograph of typical fringe field observed by holographic interferometry.

nents that we used to videotape fringes generated by temperature changes in the amplifier after firing relative to a preshot exposure. The photograph in Fig. 2-291 is an example of a fringe pattern observed approximately 10 min after the amplifier was fired; videotapes of these fringes provide a continuous record of disk distortion vs time.

In the third technique, we viewed the interior of the amplifier with a pyroelectric vidicon. Small temperature differences between components inside the amplifier were easily identified by this technique, and we were able to correlate these observations with the thermocouple data to show how the disk is heated. There is an initial rise of 2 to 3°C after the pump pulse that is followed by a steady rise in disk temperature due to radiation heating by hotter amplifier components. The hottest component is the flashlamp reflector; this reflector transfers its heat to the shield glass, which prevents the infrared radiation from reaching the disk until its own temperature rises. During this time, we have the opportunity to cool these two components and limit the maximum temperature rise of the disk. We changed the nitrogen flow pattern and rates in this amplifier and observed an immediate improvement. When the nitrogen flow is concentrated in the flashlamp cavity, the optical distortion remaining after an hour, was reduced to 0.25 wave at 1064 nm. Under normal flow conditions, 2.5 waves of wedge were observed after an hour.

We also used these diagnostics to study the effectiveness of a heat sink at the edge of the disk. The disks were potted into a specially fabricated disk holder with a high-thermal-conductivity silicone material. The result was a reduction in the initial spherical distortion near the disk edge, with a resultant reduction in peak distortion. However, the rate of recovery at later times did not change: the number of fringes remaining after an hour was approximately the same as for a standard disk holder without the heat sink but with an improved nitrogen flow. The effectiveness of the heat sink with thick monolithic claddings is yet to be determined.

Passive Switch for a Multipass Amplifier. In the Laser Program Annual Report for 1979,[139] we described analyses and experiments on an off-angle multipass amplifier geometry. The off-angle aspect allowed spatial discrimination against prepulses, eliminating the requirement for a fast temporal switch. The particular geometry that was studied minimized vignetting to allow maximum utilization of the amplifier's clear aperture, and the geometry was potentially scalable to any aperture because it did not require the switch.

The major disadvantage of the device was the poor extraction efficiency obtained from the amplifier; the maximum output obtainable with everything optimized was about one-half a saturation fluence. The low efficiency resulted from the need to extract the amplified pulse through one of the multipass mirrors. The output mirror reflectivity, when optimized for output energy, was in the 30 to 40% range, giving a high multipass loss and the low extraction efficiency.

This major limitation to the geometry could be eliminated by a switch that would act as a cavity dumper, extracting the amplified pulse after a specified number of passes. This switch would not need to discriminate against prepulses because of the off-angle nature of the geometry; consequently, an extraction efficiency as low as 70% would be very attractive for the switch.

In 1980, we realized that an angular-sensitive device could serve as a passive switch for off-angle geometries. Such devices are passive because they use the angular difference between passes to "switch" the beam and do not need to be altered in time. For example, harmonic generation in angle-phase-matched crystals has a very narrow acceptance angle and could be used to couple energy out of an off-angle geometry.

Figure 2-292 illustrates the basic idea with a four-pass off-angle geometry of the type described in the 1979 Annual Report.[139] Use of the small mirror at the input near the beam focus places a lower limit on the saturated gain of the multipass amplifier to avoid mirror damage. The passive switch is a Type I KDP second-harmonic generator (SHG) aligned for peak conversion on the fourth pass. The angle between passes (typically 2 mrad) would prevent significant conversion on the first three passes because of the narrow SHG acceptance angle (± 0.56 mrad-cm for Type I KDP). The intensity-squared dependence of SHG provides further discrimination because the pulse intensity is smaller on previous passes. On the fourth pass, 80% of the beam can be converted to the second harmonic (see "Argus Frequency Conversion Experiments" later in this section). A dichroic mirror, similar to those being designed for 1053-nm beam dumps (see "Wavelength Separation Filters" later in this section), would transmit ~95% of the second harmonic while acting as a maximum reflector at the fundamental wavelength of the multipass.

There are at least two additional examples of angle-sensitive devices that might be used as passive cavity dumpers. One example is a Fabry–Perot interferometer, which has a series of narrow angular transmission bands separated by reflection bands that are broader by a multiplicative factor equal to its finesse. A finesse 10 Fabry–Perot would be a good candidate except for the 10-times-higher fields between the mirrors, which greatly reduce its damage threshold. A second example is thin-film polarizers (TFP), which exhibit relatively narrow reflectivity vs angle characteristics. Current production TFPs change from 10 to 90% reflecting in approximately 3°, not fast enough for these off-angle geometrics, but interesting enough to warrant further investigation.

A second new aspect shown in Fig. 2-292 is the introduction of the input pulse at a small-diameter mirror near the plane between the lenses. This is possible only if the saturated gain of the multipass is large enough to keep the fluence on the small mirror below damage level when the drive

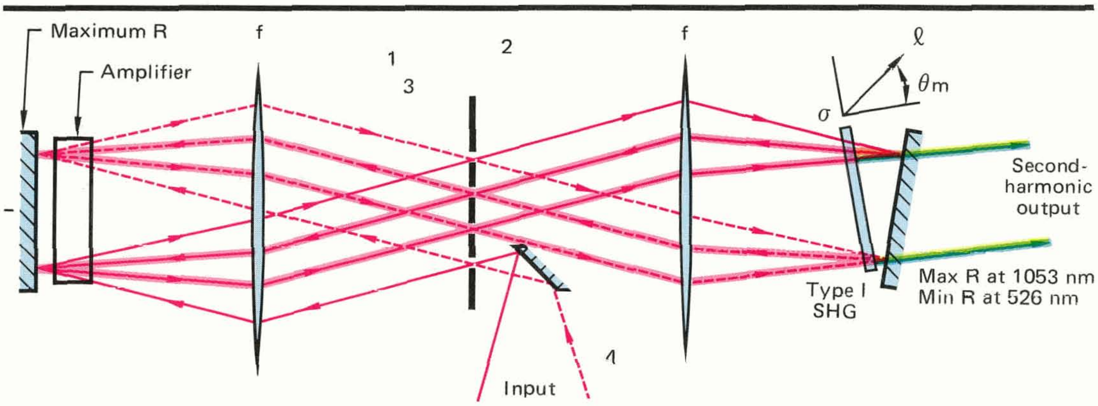

Fig. 2-292. A four-pass off-angle multipass amplifier using Type I SHG as a passive switch to extract a second-harmonic output pulse.

energies are sufficient for maximum output from the multipass. The maximum area of the small mirror for no interference with succeeding passes depends on the separation between pinholes, which, in turn, depends on the angular separation of adjacent pinholes, α, and the effective f-number of the lenses, $f^{\#}$. The following constraint results on the net saturated gain, G_{sat}, of the multipass amplifier:

$$G_{sat} \geq \frac{1}{\sqrt{2}}\left(\frac{1}{\alpha f^{\#}}\right) \quad . \qquad (56)$$

Substituting typical values, α = 2.0 mrad and $f^{\#}$ = 20, gives $G_{sat} \geq 440$, independent of the beam diameter.

We numerically analyzed the performance of the switched multipass using the same iterative relations used in 1979. However, the switch allowed the mirrors to act as high reflectors to maximize energy extraction, eliminating the need for optimization. Figure 2-293 shows the calculated performance for an amplifier with a gain of 7 and a single-pass cold-cavity transmission of 0.8; net saturated gain after 1 through 9 passes is plotted vertically against output pulse fluence. For three passes or less, there is no maximum output fluence, and the output increases monotonically with input as for a single-pass amplifier. For more than three passes, the output maximizes at 1.2 J_{sat}, after which more input decreases the output.

Figure 2-293 shows that the maximum output fluence is independent of the number of passes for more than three passes. The net saturated gain increases rapidly with the number of passes, but self-lasing eventually limits the gain that can be achieved, as we discussed last year in connection with the transmission-coupled multipass. We reported that carefully constructed beam dumps allow a multipass gain as high as 30 000 before self-lasing occurs. This limits the number of passes to six or less for the G = 7, T = 0.8 case shown in Fig. 2-293. Nevertheless, the maximum net saturated gain at an output of 1.2 J_{sat} would still be 3000, which is enough to allow the input to be injected as shown in Fig. 2-292.

Figure 2-294 shows the variation in output fluence with single-pass amplifier gain, G, and single-pass transmission, T, of the multipass components. Substantially higher outputs are achievable with higher G or T, but the small-signal gain is always limited by self-lasing. Because the geometry shown in Fig. 2-292 allows only even numbers of passes, a small increase in either G or T might require dropping the number of passes from six to four to prevent self-lasing, with a resultant substantial drop in saturated gain. Only for relatively large increases in G or T

Fig. 2-293. Net saturated gain of a multipass amplifier with maximum reflecting mirrors, shown as a function of output fluence for an amplifier with a gain of 7, for a single-pass *transmission* of 0.8, and for from 1 to 9 passes.

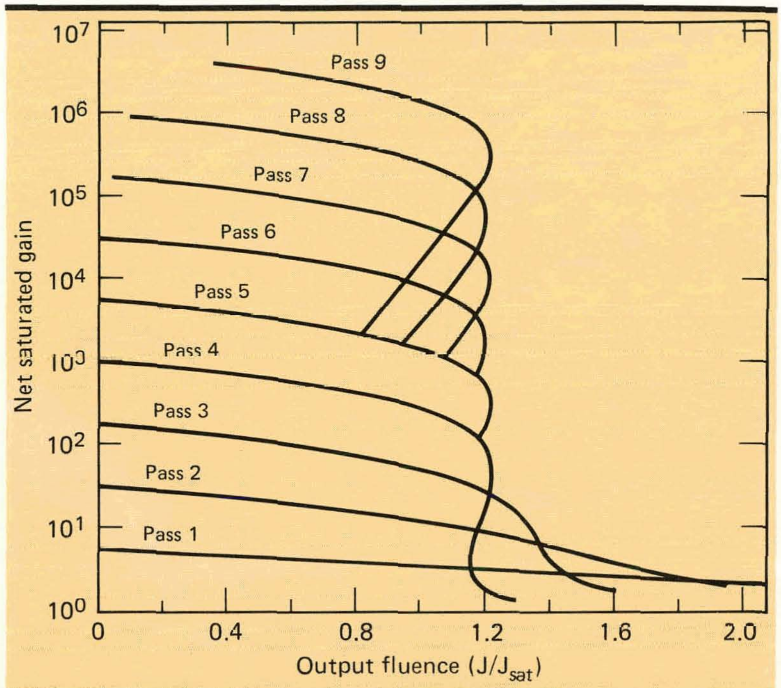

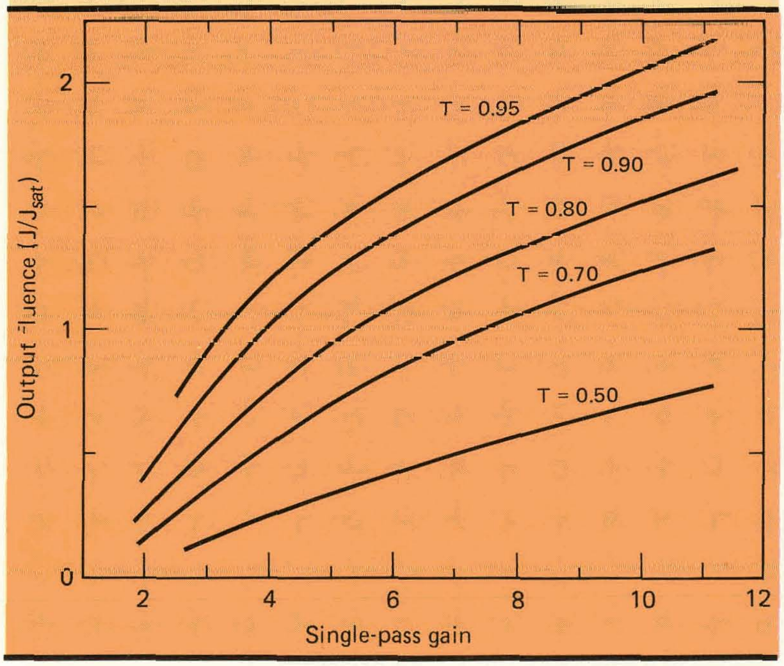

Fig. 2-294. Maximum output fluence vs single-pass amplifier gain for several values of single-pass transmission, T.

would saturated gain increase with output fluence.

The switch-coupled multipass is very much more attractive than the transmission-coupled device that was described last year. The switch-coupled multipass can deliver more than twice the output fluence, its gain is up by more than 10, and its amplified spontaneous emission (ASE) and aberration characteristics are much better. Its ASE will be similar to a linear chain with the same small-signal gain because the injected pulse and the ASE of the multipass now see exactly the same small-signal gain. The aberration problem improves because fewer passes are required to reach maximum output.

The major conceptual limitation for the switch-coupled multipass is a passive switch that couples out the fundamental rather than only the second harmonic, allowing additional amplification. Still remaining are the practical problems of aberration accumulation and beam dumps for absorbing multikilojoule pulses near a focus. These problems require experimentally demonstrated solutions.

Summary. Tests of large fluorophosphate disks indicate that high-quality disks can be manufactured with effective edge claddings. Monolithic (cast) claddings, in particular, promise to survive high fluorescent energy loading.

The 20.8-cm Nova prototype disk amplifier has demonstrated a doubling in pump efficiency over the Shiva delta design. Gain uniformity in both the 20.8-cm amplifier and the 34-cm transversely pumped Datum III prototype is better than in the Shiva designs. Based on measurements to date, projections of LHG-8 performance in Nova amplifiers are comfortably above the minimum Nova requirements.

A study of thermally induced optical distortions in disk amplifiers shows that radiative heating of the disk by other components is significant following the pump pulse. However, increased cooling applied to the flashlamp reflector and shield glass can substantially reduce the time between laser shots.

The use of phosphate glass in Nova rod amplifiers has led us to use a new design rather than the Shiva beta rod amplifier. To maintain a flat gain profile with LHG-8, we have changed the pump cavity-geometry and have reduced the rod doping. The rod has been lengthened and the pump energy increased for greater gain. Mechanical changes have also been made to improve reliability and alignment stability.

Our lensing measurements show that Nd:YLF exhibits a much weaker thermal-lensing effect than Nd:YAG. Consequently, we feel that the 1-cm-aperture amplifier is a good choice for the front end of Novette and Nova. It will operate with a gain of 10 at 10 Hz with a thermally induced lens weaker than 50 m.

The concept of a passive switch was introduced for coupling energy out of an off-angle multipass amplifier. This type of switch, based on the angular difference between passes, would greatly improve the performance of the off-angle multipass geometry.

Authors: S. M. Yarema and J. E. Murray

Major Contributors: D. B. Clifton, D. C. Downs, W. E. Martin, W. E. Warren, and B. Woods

Oscillator Development

Introduction. During the past few years, we have developed a stable and reliable actively mode-locked and Q-switched (AMQ) oscillator for Argus and Shiva. The characteristics and principles of operation of this device have been described in several publications.[140–144] In 1979, we described the hardware and improvements made to this oscillator for the Argus laser system.[144]

During 1980, we continued our efforts to improve the Shiva oscillator and continued our work for the new Novette and Nova laser systems. For Shiva, we accomplished the following:

- Completed installation for a new AMQ oscillator, including electronic controls.[145] This oscillator was designed to be fully compatible with the Shiva computer controls.
- Added a long-pulse oscillator to the system to provide pulses in the range of 2 to 35 ns (see "Engineering Summary and Upgrades" earlier in this section).
- Devised a method to stabilize the pulses produced by the long-pulse oscillator.

- Completed a research effort to determine the characteristics of the Pockels cells needed in the new Shiva front end.

During the year, to satisfy the need for a long-pulse oscillator at 1053 nm for the new Cyclops laser, we assembled and installed a Nd:YLF long-pulse oscillator on the system. The characteristics of this device are described below.

Near the end of 1980, we demonstrated the cw Nd:YLF alignment laser at 1053 nm required for the Nova and Novette systems. Initial test results show that more than 1 W of TEM_{00} power can be obtained from this device at 1053 nm. We intend to complete the characterization of this laser in 1981.

Long-Pulse Oscillator Development. Our requirements for complicated pulse shapes will increase as the Laser Fusion Program develops. To meet this need, we intend to develop a switch with the capability of shaping pulse lengths from a longer pulse. Since we have chosen to use a single-axial-mode Q-switched oscillator for this system, we must also ensure that the pulse provided by the oscillator is very stable. The AMQ-YAG oscillator can generate pulses in the range of 100 ps to 1 ns. However, we have planned fusion experiments that require 1- to 5-ns pulses and have also completed recent experiments with 35-ns pulses on Shiva. Since the AMQ-YAG oscillator pulse lengths are not within the desired range, we have chosen the single-axial-mode Q-switched oscillator method to provide the desired pulse lengths. This method entails the generation of a long, smooth pulse with a typical pulse length ranging between fifty and several hundred nanoseconds. This pulse passes through a Pockels cell switch that removes (slices) a portion of the long pulse to provide a pulse of the desired length.

A common problem with single-axial-mode Q-switched oscillators is that single-axial-mode operation cannot be obtained all the time. On some shots, the laser output is strongly modulated by the simultaneous oscillation of two or more axial modes. To achieve single-axial-mode operation, an etalon is usually put in the oscillator cavity to reduce the bandwidth. The device can be further improved by stretching the Q-switch buildup time to improve the discrimination of unwanted axial modes. A well-designed single axial mode typically will run stably for only a few minutes, producing a modulated shot only about once per 100 shots. Since this is marginally acceptable for laser fusion experiments, we have investigated a method to improve the reliability.

Our original single-axial-mode Q-switched device, shown schematically in Fig. 2-295, was much like an earlier laser developed for laser-damage and saturation measurements. To narrow the laser bandwidth, we use a two-plate resonant output coupler with quartz plates of different thicknesses (8 and 9 mm) at 6-mm spacing. This arrangement usually has a reflection peak near the center of the Nd:YAG line. Another thin etalon (2 mm thick), spaced about 8 cm from the resonant reflector, acts as a bandpass filter to provide the very narrow bandwidth required. The narrow bandpass can be adjusted relative to the bandpass of the two-plate stack by moving the thin etalon a fraction of a wavelength. The complete etalon device was housed in an Invar tube for stability. We

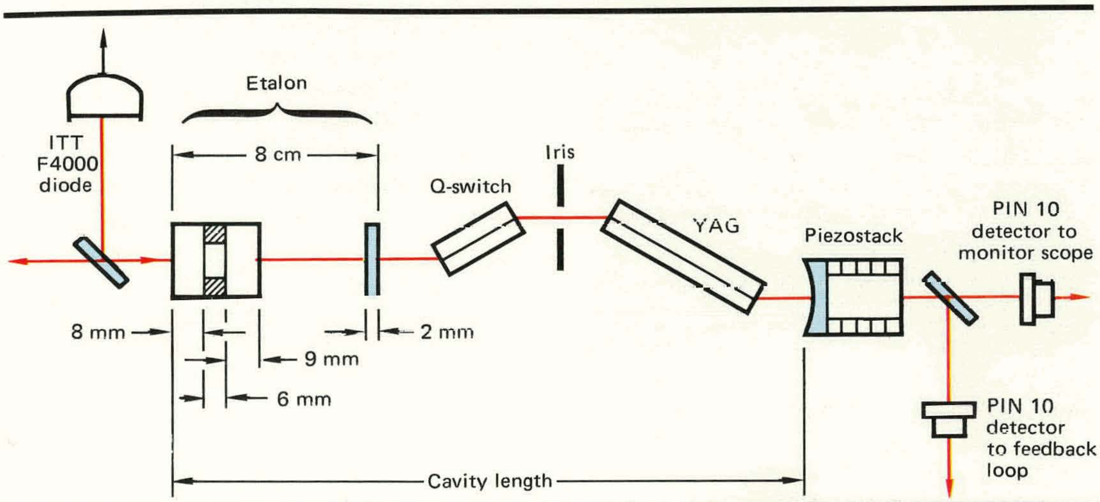

Fig. 2-295. Schematic of the single-axial-mode Nd:YAG laser showing details of the etalon design, laser components, and diagnostics. The etalon consist of uncoated quartz plates.

have further improved the single-axial-mode selection in this laser by allowing the oscillator to prelase for approximately 3 ms. (This is a technique previously developed for the AMQ oscillator to improve mode locking.[141]) When we employ this technique, the flashlamps are turned on at a constant level for about 4 ms, and the Q-switch loss is then adjusted so that the laser is slightly above threshold to permit the laser to oscillate for approximately 3 ms. During this time, the various axial modes can compete in an almost cw manner, and the single axial mode with only slightly lower losses than all the others will dominate. We have experimentally observed this effect when the loss in the Q-switch is set for a good prelase level. At this point, we get single-axial-mode operation on almost every shot, but a small increase in loss that eliminates the prelase and causes the Q-switch to operate normally will produce highly modulated Q-switch pulses. This transition is very sharp and quite spectacular to observe. We also shortened the cavity as much as possible to get maximum axial-mode spacing. Since we assembled this oscillator from components identical to those in the AMQ oscillator, the length of the short cavity was limited to about 45 cm. We also performed experiments with a long (102 cm) cavity similar to the regular AMQ oscillator cavity.

The output of the Q-switched oscillator is observed with a Tektronix 7104 oscilloscope interfaced to the oscillator with an ITT F4000 biplanar diode detector. In Fig. 2-296(a), we show a typical unmodulated single-axial-mode pulse, and a similar pulse with modulation (multimoding) is shown in Fig. 2-296(b). This multimoding, although sometimes an occasional event, is easily observed. However, if the laser and etalon are correctly aligned and a good prelase level is selected, the multimoding does not occur as a random event, but, rather, as an intermittent burst of multimode shots. We found that we could control continuous multimode operation by changing the cavity length with the piezostack on the rear mirror or by changing the distance between the thin (2-mm) etalon and the two-plate resonant stack. These experiments confirmed our conviction that the relative position between the narrow passband of the etalon and the position of the axial modes in the cavity determine laser behavior. We have also observed that multimoding occurs for only a very narrow range of rear-window adjustments. With the laser just free-running, we observed multimoding for about 1% of the shots. Thus, to stabilize the laser, we need signal feedback from the laser to set the cavity length.

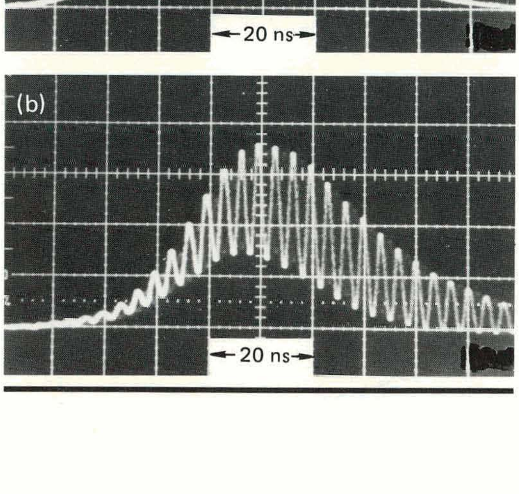

Fig. 2-296. Output pulses from single-axial-mode laser. The smooth pulse indicates single-axial-mode operation, and axial mode beats can easily be observed, as shown in the modulated pulse.

We can obtain further information on the mechanism controlling axial-mode selection by carefully observing the oscillator prelase signals. In Fig. 2-297, we show the effect on a series of prelase signals when the cavity length is decreased by a small fraction of $\lambda/2$ with the piezostack on the rear mirror. This signal is obtained using a PIN 10 silicon diode connected to an oscilloscope to observe the light leakage through the rear mirror. The signal obtained is negative going, and is displayed in this way on the oscilloscope. The laser is Q-switched at the end of the prelase, but the Q-switched pulse is so large that it can only be seen as a section of the trace missing at the end of the prelase signal.

Figure 2-297(a) shows a prelase signal for stable, single-mode operation with the relaxation oscillations smoothly dampened and a relatively flat prelase pulse. (This signal is similar to that of a good mode-locked oscillator.[143]) Of all the prelase signals shown, multimoding is observed only in Fig. 2-297(c), where we see a perturbation on the prelase just before the laser Q-switched. This perturbation is caused by a second axial mode rising above threshold. Prior to the oscillator Q-switching, both axial modes are present in the oscillator and both are Q-switched to produce a modulated pulse. As we continue shortening the cavity from the pulse shown in Fig. 2-297(c) to that shown in Fig. 2-297(d), we see that the perturbation shifts toward the start of the prelase pulse and that modulation is eliminated from the output pulse. In this case, the second axial mode has had enough time to completely suppress the axial mode that started at the beginning of the prelase. The most interesting multimode dynamics occur for the conditions displayed in Fig. 2-297(c). By making small adjustments in cavity length, we control the timing of the second-axial-mode oscillations and, hence, the relative amplitudes of the two modes. We can easily observe the resultant change in modulation depth on the Q-switched pulse.

Another clearly observable characteristic of the set of prelase signals shown in Fig. 2-297 is the change in slope of the prelase for various cavity lengths. To explain these changes and the previously described mode dynamics, we must consider that, as the Nd:YAG crystal is pumped during the prelase, the crystal heats up and expands. This causes an effective change in cavity length that affects the laser oscillation wavelength during prelase. Since this change is quite slow, the laser frequency will slowly scan during the prelase without producing sudden perturbations of the laser output. We should note here that subsequent cooling of the rod produces a temperature profile that results in thermal focusing. Since we always observe a positive thermal focal length, we know we have an effective Nd:YAG crystal length increase and, hence, an increase in wavelength during the prelase period.

In Fig. 2-298, we consider two positions of the axial modes in the cavity relative to the etalon transmission peak. The solid vertical lines in the figure represent the modes at the start of the prelase, and the arrows show the direction of scan. In Fig. 2-298(a), we show one axial mode close to the peak of the etalon at the start of the prelase. During prelase, this mode scans past the etalon peak and is unaffected by small changes in cavity loss; thus, the observed prelase signal does not experience the large changes shown in Fig. 2-297(a). In Fig. 2-298(a), we see that modes 2 and 3 experience more loss than mode 1 and do not oscillate because the long quasi-cw prelase period effectively keeps these modes below threshold. Now consider

Fig. 2-297. Sequence of prelase signals from single-axial-mode Nd:YAG laser. Perturbations show start of second axial mode, and slope changes indicate scanning of axial mode relative to the etalon transmission peak. The sequence repeats for cavity length changes of 0.53 μm or half a wavelength.

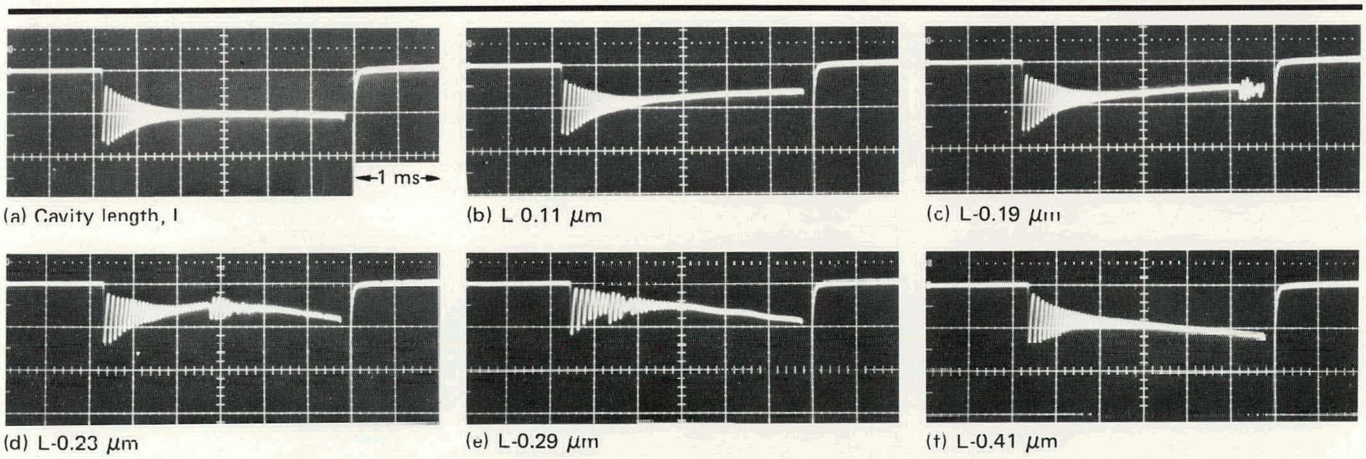

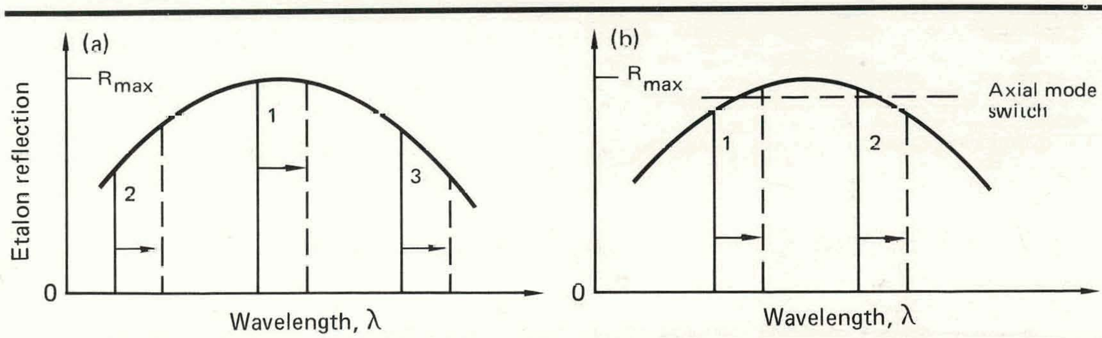

Fig. 2-298. Scanning of the axial modes relative to the etalon transmission peak. Solid lines show the modes at the start of the prelase, and the arrow shows the scan direction: (a) the best conditions for single-axial-mode operations and (b) typical axial mode competition.

the conditions shown in Fig. 2-298(b). Mode 2 is slightly closer to the etalon peak than mode 1, and hence starts oscillating at the start of the prelase period. During the prelase, however, this mode scans away from the etalon peak. Sometime during the prelase, as indicated in this figure, mode 1 has less loss than mode 2 and starts to oscillate. This second oscillation causes a perturbation on the output that we clearly observe experimentally. We should also note that the first mode to start oscillating scans away from the etalon, hence sees increasing loss; the output power goes down. The second mode sees decreasing losses as it comes on; the output power goes up. This is the pattern observed in Fig. 2-297(d). We can clearly see the slope changes described above, before and after the axial mode switch.

This slope change of the prelase is an important indication of the axial-mode locations relative to the etalon peak. Earlier, in Fig. 2-297(a), we showed an example of an ideal prelase signal. Using this signal as a reference, we should be able to detect small slope changes with a feedback loop and correct the cavity length to stabilize the laser.

The simplest scheme is to sample the start and end of the prelase, then compare signals and use the difference to drive a piezostack in a closed feedback loop. Figure 2-299 is a schematic of this feedback scheme. The output of the diode is first fed to a lowpass filter to smooth the relaxation oscillations at the start of the prelase. The signal is then coupled to an amplifier with a variable gain (10 to 1000, bias adjusted) and passed to two sample-and-hold circuits. These circuits sample the pulse at the start of the prelase, one circuit holding after about 50 μs, while the second holds after about 3 ms. Since the amplitude of the entire prelase can vary, this method samples the slope, but is insensitive to amplitude changes of the prelase from shot to shot. At an oscillator repetition rate of 10 pps, the sample-and-hold circuits hold the signals for approximately 100 ms before feeding the difference signal to the piezostack through another variable gain amplifier, lowpass filter, and output amplifier. This lowpass filter at the output has a 1-s time constant to average several oscillator pulses in the feedback loop. The output amplifier levels are set low enough to prevent system oscillations.

Fig. 2-299. Schematic diagram of a simple axial-mode stabilization feedback loop. Typical signal to the input of the sample and hold circuits is shown, as well as the timing signals for these circuits.

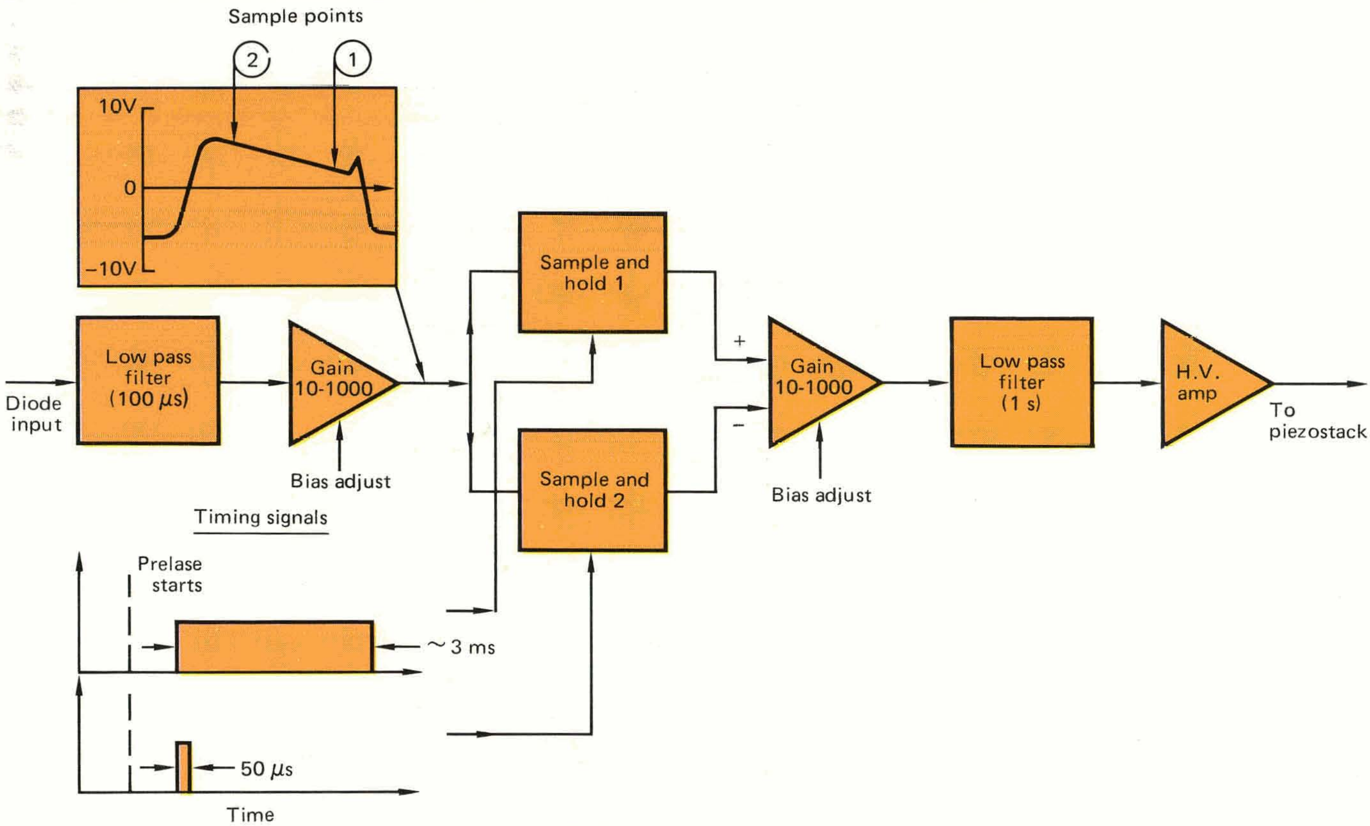

This simple feedback circuit works remarkably well and sustains continual oscillator operation in a single axial mode. Unless component failure occurs or some other operating parameter changes, this method for stabilizing the oscillator should prevent multimoding. We can demonstrate this by opening the feedback loop and allowing the laser to drift. When the loop is then closed, the laser goes to the condition shown in Fig. 2-297(a) within a fraction of a second. Note that the prelase signals in Figs. 2-297(a) and 2-297(d) can have the same level at the start and end of prelase, but a small change in the cavity length produces opposite-polarity error signals. Therefore, if the feedback loop is set up to stabilize the condition in Fig. 2-297(a), the condition in Fig. 2-297(d) is unstable and the feedback loop will unconditionally stabilize the laser for single-axial-mode operation. Our success with this loop in the single-axial-mode oscillator allowed its installation on the Shiva laser system in 1980.

We also examined the single-axial-mode behavior of this laser with a 102-cm cavity. The single-axial-mode selection by the etalon in this cavity worked very well, and we were able to obtain statistics for its multimoding events that were nearly identical to those obtained with the short cavity. This indicated that, with mode spacing at less than one-half that of the short cavity, there was still enough etalon discrimination to provide good mode selection. The appearance of a spurious mode was still completely dominated by the scanning of the laser during the prelase. However, we found that the slope change during the prelase was not sufficient to operate the stabilization feedback loop, since it was a much smaller change than the slope change for the short cavity. The frequency shift is proportionally less for the longer cavity with the same effective length change of the Nd:YAG crystal, therefore producing a much smaller slope change in the prelase. From these observations, we conclude that, for the feedback stabilization to function correctly, the design of the etalon is determined by the requirements for the feedback loop. This etalon will then provide good single-axial-mode selection. We will attempt to design such an etalon for a long cavity. Then a single oscillator can operate as a mode-locked laser when the modulator is turned on and as a single-axial-mode laser when the etalon is inserted. We believe that development of this etalon will have considerable advantages and flexibility for the oscillators installed on future laser systems.

We measured some other important characteristics of the single axial mode laser, such as the energy in the Q-switched pulse as a function of the pump power into the Nd:YAG crystal. We measured the average power with the laser running at 10 pps (with a Scientech power meter) for the laser prelasing and Q-switching, and then only prelasing. This allowed us to correct for the prelase energy, which is quite significant, particularly close to threshold. Figure 2-300 shows the results of our measurements with the short and long cavities. We produced more energy with the long cavity, since the mode volume in the crystal is larger. Our measurements of Q-switched pulse width were performed as a function of lamp current from recordings similar to those shown in Fig. 2-296(a). The results of these measurements are shown in Fig. 2-301. As expected, we obtained much longer pulse widths with the long cavity. If we calculate the peak power from the data in Figs. 2-300 and 2-301, assuming the Q-switched pulse is Gaussian, we get the results shown in Fig. 2-302 and see that both cavities produce approximately the same power. Since the peak power determines the amount of energy in the pulses sliced from the center of the Q-switched pulse, we conclude that sliced-pulse energy is minimally dependent on

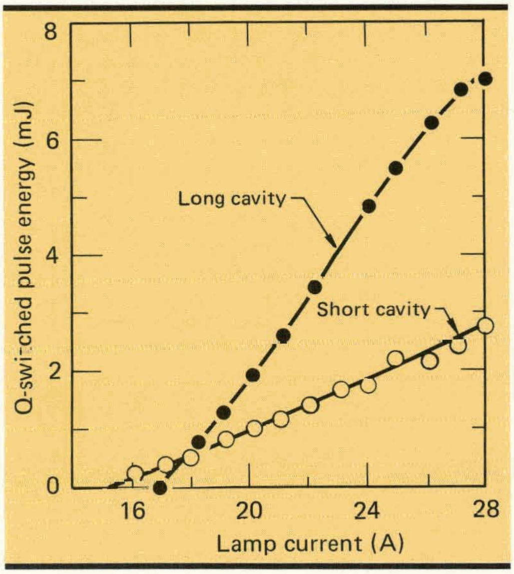

Fig. 2-300. Pulse energy from a Q-switched single-axial-mode Nd:YAG laser as a function of lamp current. The short cavity is as short as our components would allow, ~45 cm, and the long cavity is about 102 cm long, about the same as the regular AMQ oscillators in use.

cavity length. However, we can get greater energy in the sliced-out pulse by modifying the short cavity to improve the fill of the rod.

Another important characteristic of this laser is jitter in the buildup time. This time is measured from the opening of the Q-switch to the pulse peak. When we slice a short pulse from the Q-switched pulse, we open the pulse slicer after a fixed delay that commences when the oscillator is Q-switched. This method is similar to that employed for single-pulse selection in the AMQ oscillator and permits synchronization of the sliced-out pulse with the Shiva system and an AMQ oscillator.[142] (Installation of the new AMQ and single-axial-mode laser on Shiva is discussed in detail in "Shiva Operations" earlier in this section.) Amplitude jitter is introduced on the sliced-out pulse if the position where we slice a section from the long pulse is varied by jitter during the oscillator buildup time. We can see this laser pulse jitter if we trigger the 7109 oscilloscope trace when the laser is Q-switched. We used a Hewlett–Packard 5370A Time Interval Counter to study the nature of this jitter by measuring the mean delay, minimum and maximum delays, and standard deviation for 1000 pulses (≥50-ps accuracy).

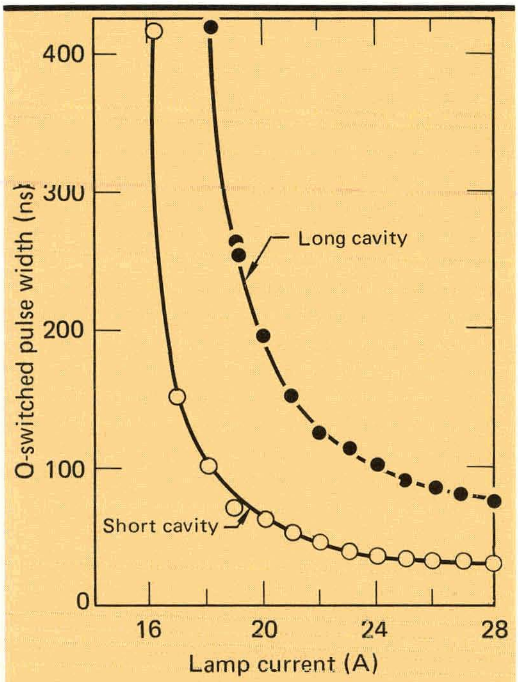

Fig. 2-301. Pulse width from a Q-switched single-axial-mode Nd:YAG laser as a function of lamp current.

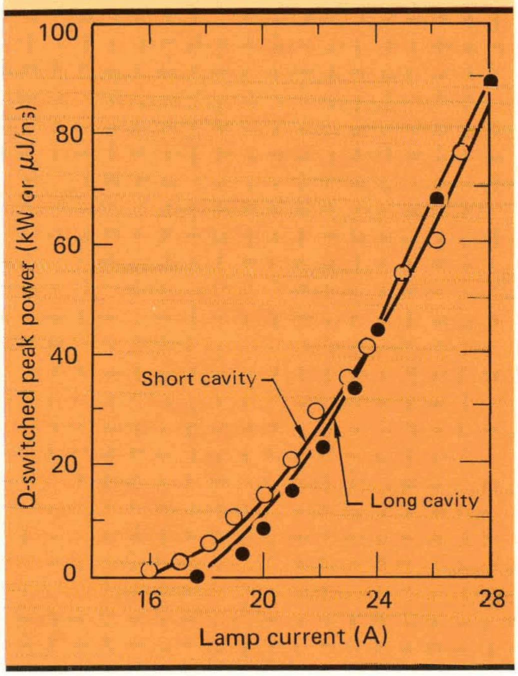

Fig. 2-302. Peak power from a Q-switched single-axial-mode Nd:YAG laser for the short and long cavity.

In Fig. 2-303, we plot the maximum jitter from the mean delay as a percentage of the pulse width given in Fig. 2-301. Our measurements showed that the actual jitters for the long and short cavities are approximately the same, but, since the pulses from the long-cavity oscillator are much longer, we show a lower percentage of long-cavity jitter in Fig. 2-303. (The maximum jitter for 1000 pulses is about 3.3 times the standard deviation of these jitter measurements.) This clearly shows the advantage of the long cavity in reducing jitter amplitude instabilities. In the new Shiva installation, we ensure that the lamp current for the short-cavity oscillator is restricted to less than 22 A to provide acceptable stability in this setup. With the long cavity, we can significantly increase the pump power and peak output power for the same amplitude stability.

We took considerable precautions to stabilize this laser and minimize the buildup jitter. The laser pump power was stable to better than 1%, the prelase fluctuations were less than 10%, and the Q-switch loss was stable to less than 1%, and the Q-switch was opened at the same phase of the rf drive to ensure identical opening of the Q-switch every time. We were unable to attribute the remaining laser jitter to any of these effects. Therefore, additional research may be needed to reduce buildup jitter in future systems. Part of this investigation will be conducted when we characterize the new Nd:YLF lasers for Nova and Novette.

During 1980, we also developed a 1053-ns single-axial-mode Nd:YLF laser oscillator for Cyclops (see "Cyclops Design and

Performance" later in this section). This laser system was designed for saturation measurements and component testing. The laser design was very similar to the short-cavity Nd:YAG laser just described. However, the two-stack quartz etalon design provided too much output coupling for Nd:YLF, producing a threshold above 25 A because of lower crystal gain. We finally got good performance from Nd:YLF by using a three-stack Ekalon reflector from Laser Optics, Inc., with an effective reflectivity of 87%. We also used another 2-mm quartz etalon spaced 8 cm from the Ekalon stack previously described for the Nd:YAG laser. We did not use a feedback stabilization circuit on the laser because the Nd:YLF showed no slope change in prelase. We had expected this because previous measurements had shown only minute thermal lensing in Nd:YLF. Hence, we experienced negligible effective change in the length of the Nd:YLF with a temperature rise. If we wish to include feedback stabilization in the Nova and Novette oscillators, we must scan the rear mirror with a piezostack during the prelase period. We plan to work on the details of this modification during development of the Nova and Novette YLF oscillators.

We also measured the characteristics of this Nd:YLF laser, and the results are shown in Fig. 2-304. This laser was not well optimized, but we obtained longer pulse widths and peak power levels about half those from Nd:YAG. This was expected because of the lower Nd:YLF gain; however, we cannot directly compare Nd:YLF results in Fig. 2-304 with the Nd:YAG data, since we used different pump cavities for each laser (crystal diameters were 5 mm for Nd:YAG and 4 mm for Nd:YLF).

In 1980, we learned much about the single-axial-mode oscillator. We can now proceed with the development of the etalon for the feedback-stabilized Nd:YLF-oscillator for single-axial-mode operation in a long cavity. When we complete this task, we can proceed to combine the function of the mode-locked oscillator and the single-axial-mode oscillator into a single laser for increased utility and flexibility in the Nova and Novette systems.

Fast Pockels Cell Switch Characterization. In the 1979 Annual Report,[146] we described a new driver for the various Pockels cells needed for the new Shiva oscillator installation and for the front end in the Nova and Novette systems. During 1980, we continued the development of the Pockels cell (see "Fast Pulse Development" in this report). When we had the single-axial-mode (long-pulse) oscillator operating in the laboratory, we characterized the pulse-slicing system and the 25-mm-diam alpha Pockels cell. This Pockels cell will be used in the Shiva preamplifier table for ASE suppression.

There are three types of Pockels cells on the Shiva front end that require a fast driver.

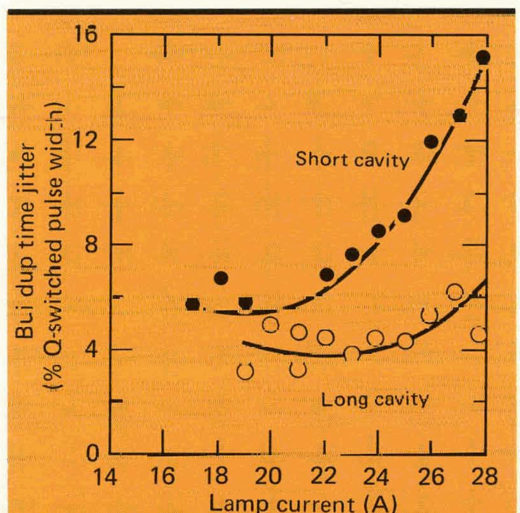

Fig. 2-303. Q-switch buildup time jitter measurements for single-axial-mode Nd:YAG laser. The maximum jitter given here for 1000 pulses, is about 3.3 times the standard deviation of these jitter measurements.

Fig. 2-304. Characteristics of the Nd:YLF single axial mode oscillator developed for Cyclops.▼

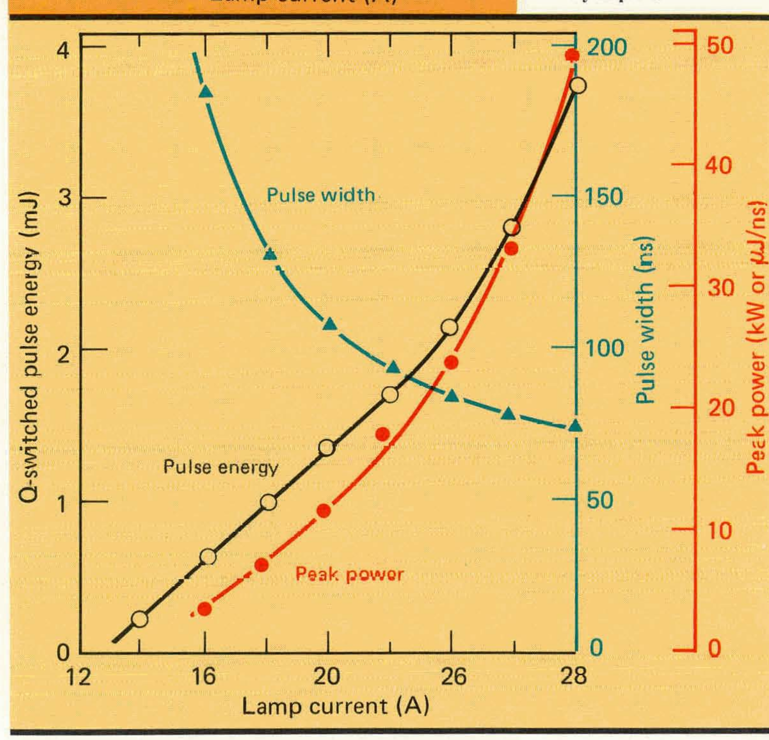

The first is a dual-crystal KD*P type produced by Lasermetrics, modified for 95-Ω impedance, with a 10-mm diameter and a half-wave voltage of 3.7 kV. This cell type is used for single-pulse selection from the AMQ oscillator. The second cell type is identical, except for 50-Ω impedance; the third cell type is an alpha cell with a 25-mm diameter, 50-Ω impedance, and a half-wave voltage of approximately 8 kV.

The Pockels cell driver that we developed can drive all three devices with the six planar triodes (Varian/Eimac Y690) in its output stage. All triodes are driven by the same pulse-generating source. (This device is described in the 1979 Annual Report[146]; a description of the most recent progress is contained in "Fast Pulse Development" in this report.) Two planar triodes are connected in parallel to provide drive to each 95-Ω Pockels cell, allowing us to drive three of these cells in the single-pulse switchout system for the AMQ oscillator. For the 50-Ω Pockels cell, we use three planar triodes in parallel to obtain enough current for its 50-Ω load. This allows us to drive two cells in the pulse slicer for Shiva's long-pulse oscillator. To drive the alpha type, we connect the six planar triodes in parallel and obtain about 8 kV with its 50-Ω load. We have also used this arrangement to drive a 5-cm-diam beta Pockels cell. In the laboratory, we have measured the optical switching time and transmission of the two-stage pulse slicer and the 25-mm-diam alpha Pockels cell with the long-pulse oscillator.

Figure 2-305 is a schematic of the two-stage pulse slicer. The Pockels cells in this system are dual-crystal KD*P devices (Lasermetrics 1072) with a half-wave voltage of about 3.7 kV, a capacitance of 14 pF, and a 50-Ω line. The fastest rise time we can expect from these cells is about 0.7 ns. We used an ITT F4000 biplanar diode to measure the output pulses from the pulse slicer. Figure 2-306 shows a typical range of short pulses. The shortest pulse shown in Fig. 2-306(a)—about 2.2 ns—is obtained without an avalanche transistor charge line in the pulse generator for the Pockels cell driver. The longer pulses in Figs. 2-306(b) and 2-306(c) are 6.2- and 35-ns long. From the 6.2-ns pulse, we measure an optical rise time of approximately 1.8 ns and fall time of 2.6 ns. The curved peak on the long pulse in Fig. 2-306(c) reflects the shape of the Q-switched pulse. We have clearly not reached the RC time constant of the Pockels cell and cable, and further improvements to the driver should allow us to slice out shorter pulses from the oscillator.

We further characterized the transmission of the pulse slicer. We first measured the transmission for the sliced-out pulse by placing the detection diode at the input of the slicer and then moving it to the output. We measured 64% transmission, typical for a two-stage switchout system. We find that most of the pulse-slicer transmission losses result from component loss. To show this, we placed the fast diode at the output of the slicer and recorded the transmission with

Fig. 2-305. Schematic of the two-stage pulse slicer.

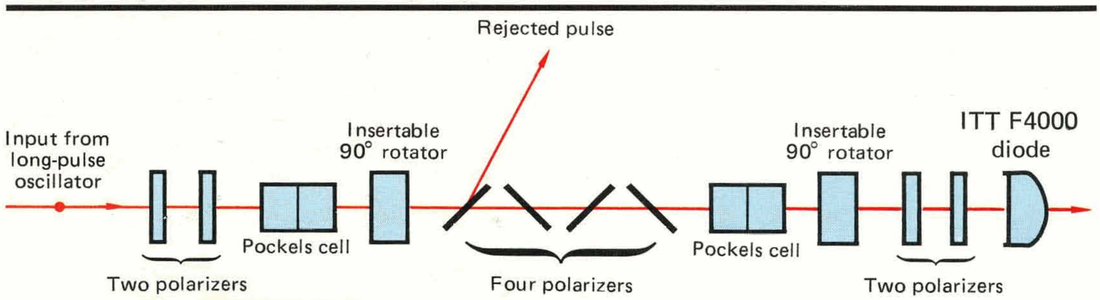

Fig. 2-306. Typical range of optical pulses obtained from the pulse slicer. The curved top of the long pulse in (c) reflects the shape of the Q-switched pulse.▼

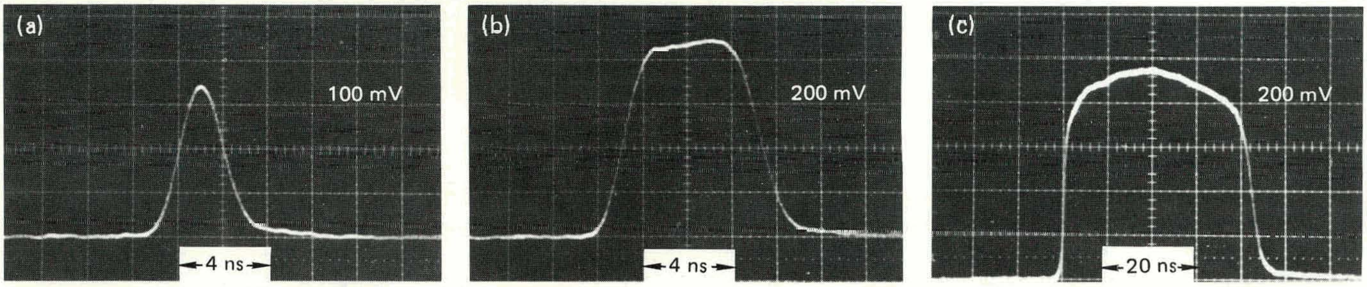

the driver off and with the 90° rotators inserted for each section. This opened each section so that the entire long pulse was transmitted. We then removed the rotators and turned the driver on to produce the 35-ns pulse, shown as trace 2 in Fig. 2-307(a). This pulse closely tracks the Q-switch pulse shape and shows that the driver output is not reduced during a 35-ns pulse. However, we observed that the sliced-out pulse is larger than the transmitted long pulse; we attribute this to the losses produced by uncoated 90° rotators. If we correct for the Fresnel losses, we find that the Pockels cell opens almost 100%. We were also able to increase the driver output, overdrive the Pockels cell, and observe the decrease in transmission. For shorter sliced-out pulses, we use this method to optimize the rise and fall times of the pulse slicer. In Fig. 2-307(b), we show the transmission of the pulse slicer with the driver on and the 90° rotators inserted. Under these conditions, there is no output while the driver is turned on, again indicating that we are effectively applying a half-wave voltage to the Pockels cells.

To optimize the rise and fall times of the two-stage slicer, we have to carefully set the relative timing of the two Pockels cells. We carefully cut cables to compensate for the delay between the two Pockels cells. We found a very accurate method to measure the relative timing of the two Pockels cells, as shown in Fig. 2-308. We turn the driver on, and slice out a pulse in the first stage of the pulse slicer, as shown by trace 1 in Fig. 2-308(a). We put a 90° rotator in the second stage to block the pulse sliced from the first section. Two short pulses are transmitted during the switching transition at the start and end of the pulse, as shown in Fig. 2-308(b). When the height of these two pulses is the same, as shown in Fig. 2-308(c), the relative timing of the Pockels cells is perfect.

We also measured other characteristics of the oscillator and pulse-slicer system. In Fig. 2-309, we show the range of pulse energies for typical 6.2- and 35-ns pulses. These data agree with the peak power measured for the oscillator and pulse-slicer transmission illustrated in Fig. 2-305. The shape of the 6.2-ns pulse is independent of the oscillator output, while the shape of the 35-ns pulse reflects the shape of the Q-switched pulse. Figure 2-310 shows some of these typical pulse shapes. In Fig. 2-310(a), the laser is close to threshold with a lamp current of 16 A, and we obtain a flat topped pulse with very low energy. At larger lamp currents, as shown in Figs. 2-310(b) and 2-310(c), we obtain pulses with round tops, reflecting the shape of the Q-switched pulse. On Shiva, we typically run the oscillator at 22 A, as a

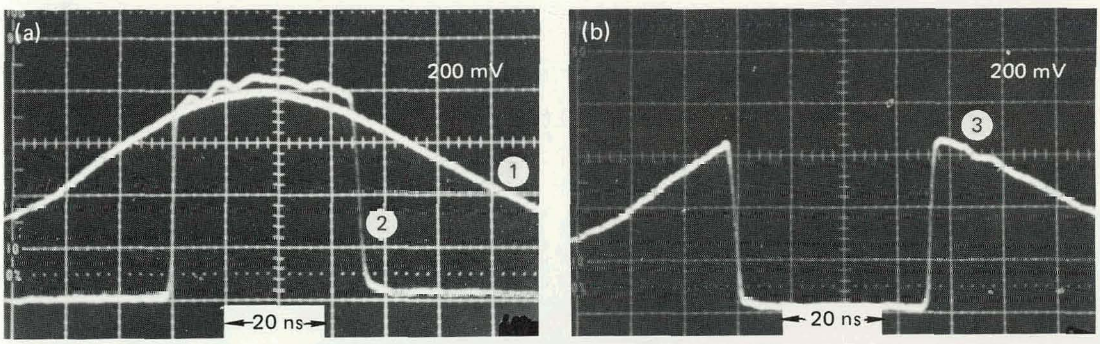

Fig. 2-307. Characterization of pulse slicer for 35-ns pulse. Trace (1) is the output with both rotators in and driver off, (2) shows normal output with rotators out and driver on, and (3) shows the output with driver on and rotators in. ◀

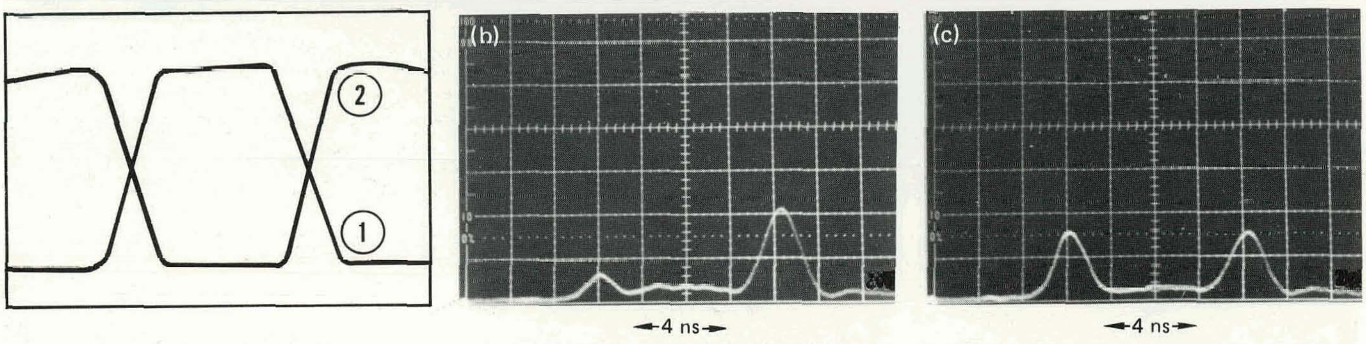

Fig. 2-308. Timing of the two Pockels cells in the pulse slicer; (a) shows the transmission curves of the two stages, with no rotator in stage 1, and a 90° rotator in stage 2. The output of the slicer in (c) shows perfect timing of the two Pockels cells. ▼

compromise between pulse energy and pulse shape.

We characterized the alpha Pockels cell with the six planar triodes in parallel in the driver output stage so that we could provide a half-wave voltage to drive the cell and open the switch completely. The results are shown in Fig. 2-311 (p. 2-257). We first recorded the transmission of the system by setting the output polarizer parallel to the input polarizer and turning the driver off (see trace 1). Then we recorded a sliced-out pulse by crossing the polarizers 90° and turning the driver on. The traces shown in the figure nearly overlap, indicating good transmission in the alpha Pockels cell system. The 2-ns rise time for trace 2 is just about equal to the RC time constant of the Pockels cell and cable combination, while the 5-ns fall time is determined by the driver. When we measured the input and sliced-output pulse from the device, we found that its overall transmission varied between 80 and 86%, depending on the area of the Pockels cell used. The performance of this alpha Pockels cell system is a considerable improvement of the state-of-the-art, and we can now effectively use it for interstage isolation and ASE suppression in the Nova and Novette systems. We also performed preliminary testing on a beta Pockels cell (5-cm diameter) and measured about 80% transmission, with performance similar to the alpha Pockels cell.

In all the above tests, we operated the Pockels cells at a 10-pps repetition rate; thermal problems, breakdown, or other difficulties were not observed. The timing jitter in these devices at this repetition rate is completely dominated by the jitter in the signal from the oscillator controls. We have not detected significant jitter in the planar triode driver, and we feel that the high repetition rate and very low jitter indicate a considerable improvement over spark-gap devices. We are now learning more about the long term stability and reliability of the devices installed on Shiva.

Author: D. J. Kuizenga

Major Contributors: D. C. Downs, J. A. Oicles, W. E. Martin, and R. Wilcox

Fig. 2-309. Energy in typical sliced-out pulses as a function of the pump power to the long-pulse oscillator.

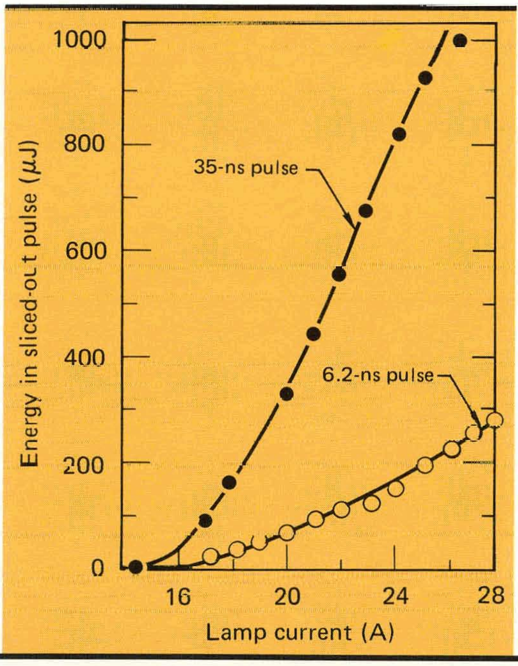

Fig. 2-310. Shape of the 35-ns pulses from the pulse slicer for various pulses from the long pulse oscillator. The shape of the sliced out pulses reflect the shape of the pulses from the oscillator.▼

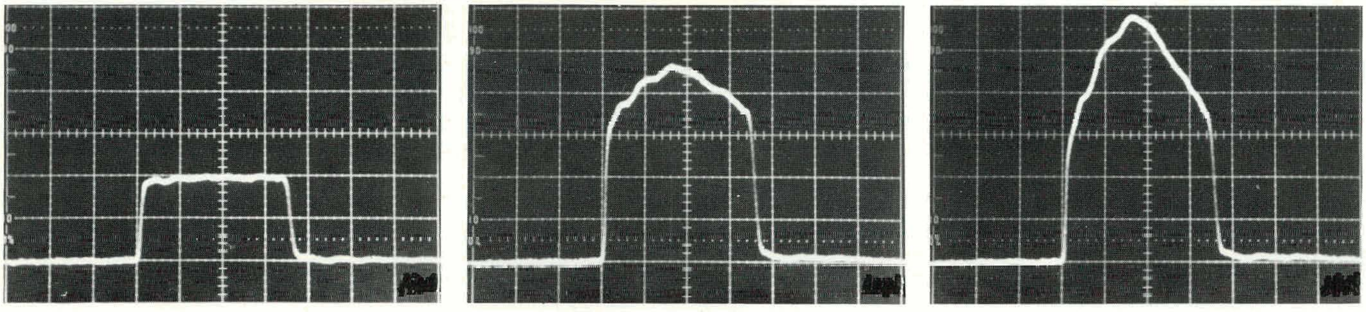

(a) Lamp current 16 A

(b) Lamp current 21 A

(c) Lamp current 25 A

Large-Aperture Harmonic Generation

Introduction. During 1980, harmonic generation evolved into a fully supported area of research and development in the Laser Program. Our major activities have been to

- Field a variety of harmonic-generation experiments on the Argus laser and support the harmonic-wavelength target efforts on Argus.
- Develop a broad understanding and useful numerical models of harmonic-generation physics.
- Develop the technology of large-aperture crystal arrays for efficient and dependable harmonic-generation on the Nova and Novette fusion lasers.
- Begin a materials development program to improve KDP and to obtain special glasses for the optical engineering of harmonic designs.

To familiarize our staff with the features of harmonic generation, a 150-page document, "Harmonic Generation for Fusion Laser Systems,"[147] was prepared in 1980. This document summarizes the basic physics of harmonic generation, the plans for implementing harmonic generation on the Argus and Nova lasers, and the wavelength dependence of laser fusion target physics.

Author: W. L. Smith

Theory

Introduction. The major objectives of our analysis of harmonic generation have been twofold: to understand the technique through the reduction of experimental data, and to provide guidance in the choice of design parameters for the conversion subsystems of large lasers. These objectives have been met through analysis and code development. We devised codes to address (a) the conversion process in KDP crystals (both configurations), (b) the effects on conversion subsystem performance of the diffraction patterns originating in the gap between array segments, and (c) the use of tandem crystals to generate both the second and the third harmonic. We looked at other options for frequency conversion using KDP crystals, such as alternates to the tandem arrangement, and identified some areas where further small-scale research is needed. Described here are the essential features of this effort.

Conversion Analysis. Harmonic generation is a well-known phenomenon, and our analysis followed the standard treatments.

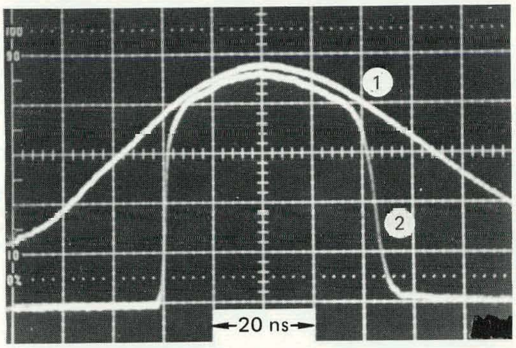

Fig. 2-311. Characterization of the alpha-Pockels cell for 35-ns pulse. Trace (1) is the output with the driver off and both input and output polarizers aligned parallel. Trace (2) is the output for normal operation with the driver on and the polarizers at 90° to each other.

We dealt with propagation using a local plane wave approximation and a slowly varying amplitude approximation. In those cases where diffraction is important inside the crystal, we used a paraxial approximation and fast Fourier transforms to propagate the waves. Each wave is characterized by its own individual absorption coefficient. This leads to the following set of equations:

$$D_1E_1 = -id(k_1/k_3)\, E_2^*E_3 \exp(i\Delta kz) \quad , \qquad (57)$$

$$D_2E_2 = -id(k_2/k_3)\, E_1^*E_3 \exp(i\Delta kz) \quad , \qquad (58)$$

and

$$D_3E_3 = +idE_1^*E_2 \exp(-i\Delta kz) \quad , \qquad (59)$$

where the operators D_j are

$$Dj = d/dz - (\gamma_j/2) - \nabla_\perp^2/2ik_i \quad . \qquad (60)$$

Here, d is the coupling constant through which waves 1 and 2 generate wave 3, γ_j are the intensity absorption coefficients, and k_j are the wave vectors. The two main parameters in this model are the coupling constant d and the phase mismatch Δk. The latter is related to the angle detuning by another parameter, $\beta = d\,(\Delta k)/d\theta$. Typical values for these parameters are

$$d = 1.48 \times 10^{-6}\ V^{-1} \qquad (61)$$

and

$$\beta_2 = -2544\ cm^{-1}/rad \quad . \qquad (62)$$

The absorption parameters for type 2 SHG are

$$\gamma_1 = 0.058\ cm^{-1} \quad , \qquad (63)$$

$$\gamma_2 = 0.020\ cm^{-1} \quad , \qquad (64)$$

and

$$\gamma_3 = 0.0\ \mathrm{cm}^{-1} \tag{65}$$

Using these equations and parameter values, we developed two sets of codes. The first set—conversion codes—integrated the equations numerically, omitting the diffraction term in the differential operator. The second set—diffraction codes—included the diffraction term, using fast Fourier transform techniques in just one transverse spatial dimension.

The predictions of the conversion codes were checked against analytic results and used to assist in the reduction of high-intensity data taken on Argus (see Fig. 2-312). The agreement with experiment was excellent with discrepancies lying in the 1% range, comparable with the experimental error in energy balance. This comparison leads to the values given above for d and β. An interesting effect was seen in these experiments; the crystal behaved as if its length were shorter than its mechanical length, as regards both detuning and conversion efficiency:

$$\ell/\ell_0 = 1 - K\ell_0^2 \tag{66}$$

The constant K is about 0.14 cm^{-2} for the crystals tested. This effect was attributed to crystal inhomogeneities. We plan a more thorough theoretical investigation of this crystal foreshortening in the coming year.

For third-harmonic generation (THG), the output of the second-harmonic codes is

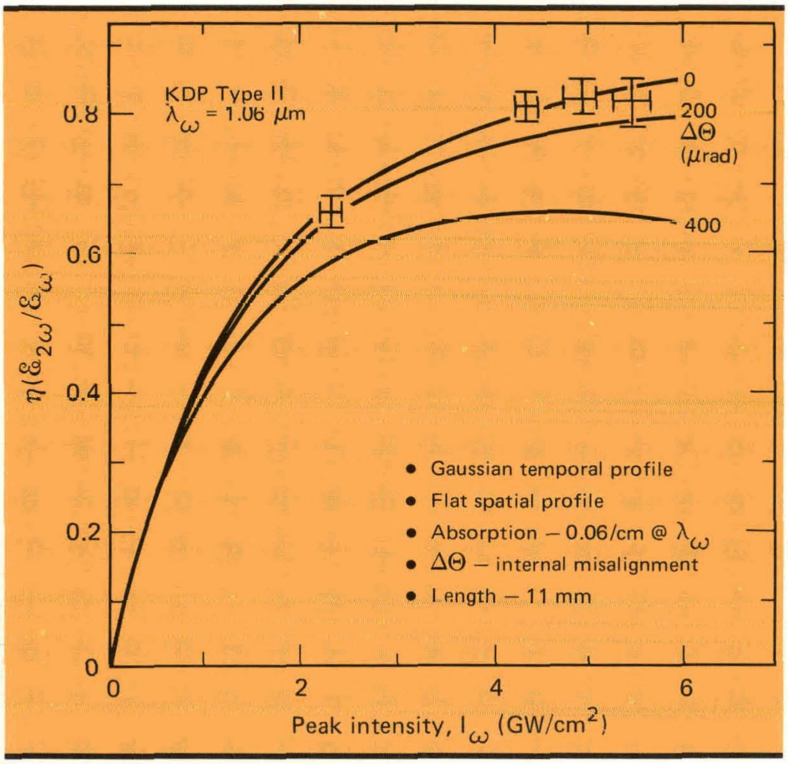

Fig. 2-312. Comparison of code predictions with Argus data.

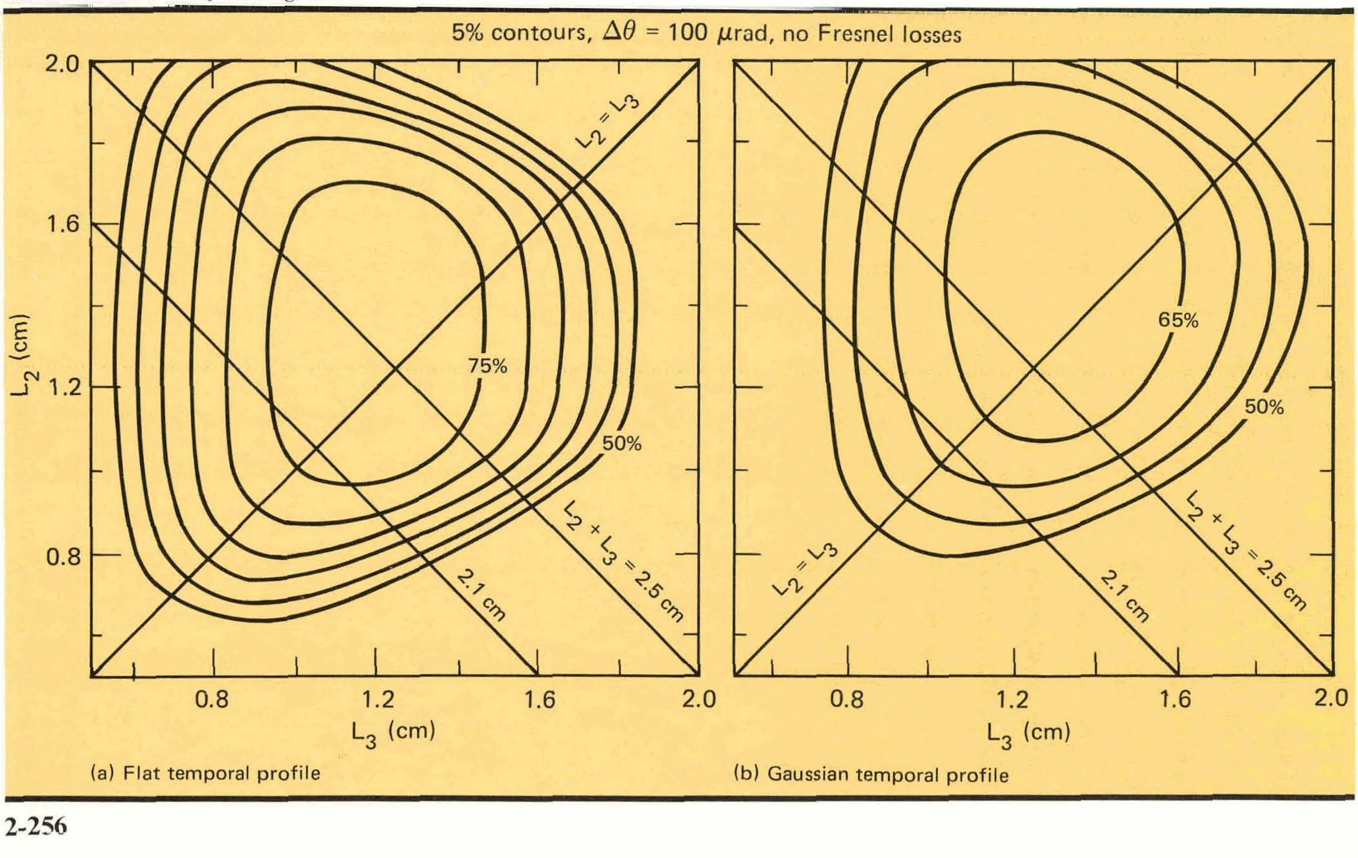

Fig. 2-313. Nova/Novette THG contour plots of constant 3ω efficiency as a function of the two crystal lengths.▼

fed into a third-harmonic code which is like the second-harmonic codes except that the detuning parameter is somewhat larger:

$$\beta_3 = -5700 \text{ cm}^{-1}/\text{rad} \quad . \tag{67}$$

Thus, we are able to predict the behavior of THG as a function of the crystal lengths at typical Nova/Novette intensities (see Fig. 2-313).

Diffraction From Intercrystalline Gap. The small gap between the segments of a crystal array causes a null in the generated beam, which diffracts and interferes with the direct beam. The resulting ripples have a broad spectrum of spatial frequencies and grow because of self-focusing in the elements of the harmonic-conversion subsystem between the crystal assembly and the target. A cursory examination of the self-focusing of these diffraction ripples showed us that this effect could cause substantial optical damage to the target focusing lens. We therefore needed a code to model the propagation of these ripples down to the target.

Existing codes such as MALAPROP had insufficient resolution to model the effect accurately; indeed, the required resolution in a two-dimensional propagation code is beyond the memory capabilities of existing computers. Consequently, we developed a one-dimensional code that is capable of modeling the crystal conversion, including diffraction effects in the crystal, and that also models the propagation of the resulting harmonic wave through the conversion subsystem right to the target. This code, capable of 15 μm resolution, has been used extensively to study propagation effects in the conversion subsystem. Its main limitations are speed and its restriction to one dimension. Typically one run at an appropriate resolution takes about 4 min on a Cray-1 computer. Figure 2-314 shows the near-field pattern of the 0.53-μm beam after emerging from the crystal and propagating 20 cm. The rapid spatial variation introduced by the crystal gap self-focuses in the system's downstream elements.

The key design parameter of the propagation studies is the ratio of peak intensity to mean intensity of the beam over a transverse plane. Figure 2-315 plots this ratio for a typical run in which a perfectly uniform 1.05-μm beam impinges on 1.8 cm of KDP crystal and the resulting 0.53-μm beam propagates subsequently through 1.5 cm of glass, 0.40 cm of air, 8 cm of glass, 40 cm of air, and finally 12.8 cm of glass. The gap between crystal segments is 4 mm and the input intensity 2.8 GW/cm^2. These are typical Novette values. The code was extensively used in designing the frequency-conversion subsystem on Nova and Novette.

Tandem Crystals. Lasers for fusion experiments operate over a range of pulse lengths and intensities. However, harmonic generation is sensitive to the intensity and the beam quality of the primary beam. At long pulse lengths the intensity on the crystal arrays is low enough that very thick

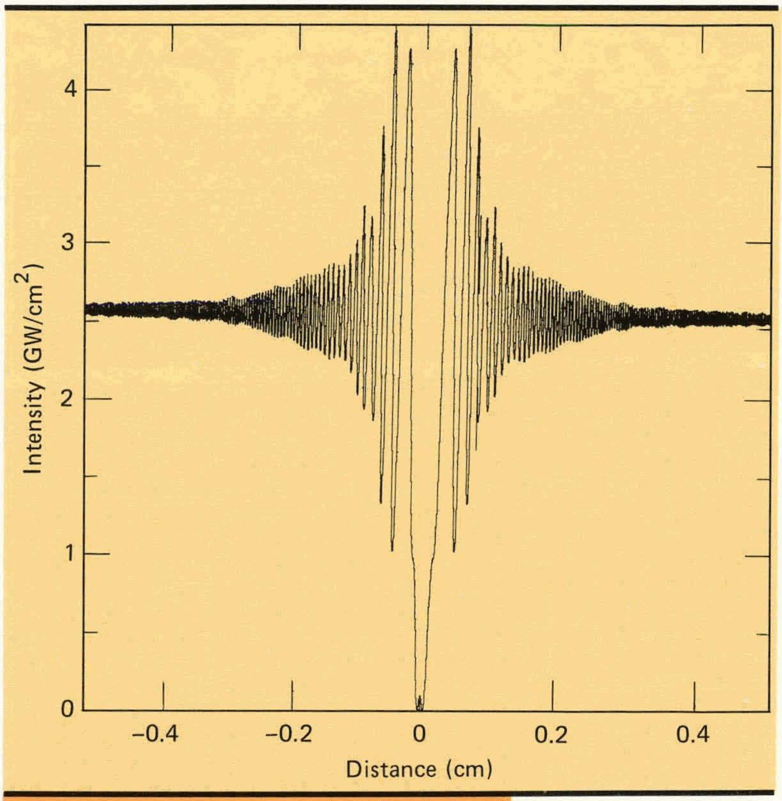

Fig. 2-314. Near-field pattern of diffraction ripples from crystal gap.

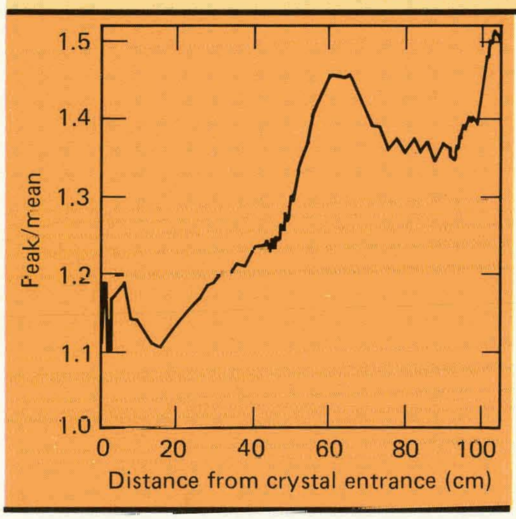

Fig. 2-315. Peak-to-mean growth in Novette configuration.

($\lesssim$2.5 cm) crystals are needed; such crystals have narrow angle-detuning curves and require both high quality primary beams and rigid mechanical tolerances on the array assemblies. Thinner crystals may be used at short pulse lengths, thus avoiding these problems. To resolve these and other concerns (see article on "Argus Frequency Conversion Experiments"), we introduced the concept of tandem crystals. In this arrangement two thin crystals (~1.2 cm) are used in place of one thick one (~2.4 cm). This has attractive features over the single crystal design, including:

- Less motion of crystal assemblies as pulse length changes and consequently greater system simplicity.
- Less stringent requirements on beam quality at long pulse lengths.
- Greater compatibility between the requirements for 2 and 3ω generation.

We analyzed the tandem crystal arrangement using the conversion codes and evaluated the system performance. This work is described in the article on "Argus Frequency Conversion Experiments." However, most properties of this arrangement can be seen from the low-conversion-efficiency regime. Consider a primary beam going through a pane of crystals. The second harmonic output is

$$E_2 = E_0\left[\frac{e^{ix_1}-1}{ix_1} + Re^{i(\phi+x_1)}\,\frac{e^{ix_2}-1}{ix_2}\right] \quad , \tag{68}$$

where E_0 sets the scale of the field and the detunings (ℓ = length, d = coupling constant) are

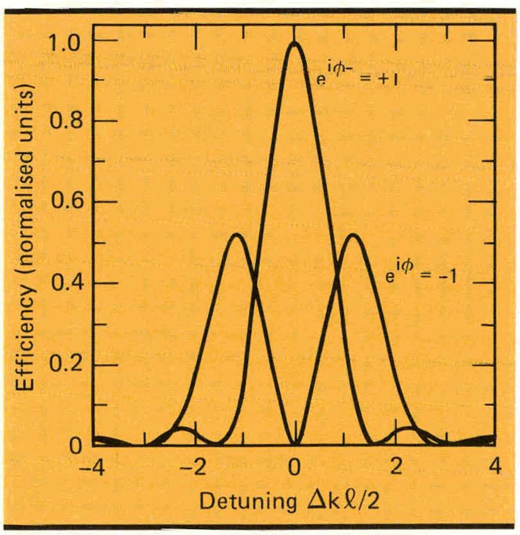

Fig. 2-316. Tandem-crystal detuning curves.

$$x_1 = \Delta k_1 \ell_1 \quad , \tag{69}$$

$$x_2 = \Delta k_2 \ell_2 \quad , \tag{70}$$

and

$$R = d_2\ell_2/d_2\ell_1 \quad . \tag{71}$$

The parameter ϕ is the phase difference accumulated between the crystals due to dispersion in the air. If the crystals have equal length, then R = 1 and one can distinguish two cases:

(a) The crystals are oriented so that $\Delta k_i = +\Delta k_2$. Then,

$$E_2 = E_0\left(\frac{e^{ix_1}-1}{ix_1}\right)\left[1 + e^{i(\phi+x_1)}\right] \tag{72}$$

If $e^{i\phi} = +1$, the detuning curve is that appropriate to a crystal at twice the length. If $e^{i\phi} = -1$, then it has a zero at $x_1 = 0$. Thus, the two waves generated in the two crystals interface destructively to provide a double-humped detuning curve (see Fig. 2-316).

(b) The crystals are oriented so that $\Delta k_1 = -\Delta k_2$. Then,

$$E_2 = E_0\left(\frac{e^{ix_1}-1}{ix_1}\right)\left(1 + e^{i\phi}\right) \quad . \tag{73}$$

If $e^{i\phi} = +1$, the detuning curve has a width appropriate to a crystal of length ℓ_1 but a conversion efficiency appropriate to a crystal of length $2\ell_1$. If $e^{i\phi} = -1$, the generated wave vanishes.

Clearly the case (b) orientation with $e^{i\phi} = +1$ is the interesting case for tandem crystals. The detuning curve remains wide enough to encompass all local directions present in the primary beam, but the conversion takes advantage of both the crystals. Using the conversion codes, we have also demonstrated this conclusion in the high-conversion-efficiency regime. Thus, tandem crystals give us the flexibility to efficiently handle a range of pulse lengths.

Author: D. Eimerl

Major Contributors: E. M. Booth, M. A. Summers, and W. E. Warren

Argus Frequency-Conversion Experiments. We completed a series of frequency-conversion experiments on the Argus laser to establish the feasibility of obtaining efficient energy conversion to the second (532 nm) and third (354 nm) harmonic wavelengths using a large (8-cm) flat spatial-profile beam. These experiments permitted validation of our computer code models and provided us with valuable guidance for selecting optimum crystal configurations for wavelength conversion of the Novette and Nova laser systems. Our energy-conversion efficiencies to 532 nm were in excess of 70%, and 355-nm conversion of greater than 50% was achieved. We measured near- and far-field beam-intensity distributions at both harmonic frequencies and found them comparable with those of typical 1064-nm beams.

Some anomalously low conversion efficiencies obtained in early stages of the experiments were caused by a large intensity-dependent loss occurring in the index-matching fluid layers between the KDP crystals and the AR-coated windows (see "Index-Matching Fluids for Large Apertures," in this section). This discovery caused us to use bare crystals in the subsequent experiments reported here. Dry nitrogen protected them from exposure to laboratory humidity.

In Table 2-65, we list the highest energy-conversion efficiency obtained with each KDP-doubling crystal. Bare-crystal values in Table 2-65 are those measured directly in the experiments; the AR-coating values refer to projected performance with no Fresnel losses. Table 2-66 lists the highest tripling efficiency for each crystal pair. The bare-crystal efficiencies are those actually measured. They include the losses due to reflection of the crystal surfaces and, in Table 2-66, the diagnostic beam splitter between the crystals. For each of two crystals, 22.9-mm Type I and 11.9-mm Type II, we found a maximum in the conversion efficiency as a function of 1064-nm input intensity. The conversion efficiency of the other three doublers was still increasing at the highest input intensities we applied. The tripling efficiencies listed are the largest measured for each configuration.

Second-Harmonic Conversion Efficiency. We tested five doubling crystals: 10 mm, 13.4 mm, and 22.9 mm Type I; 9.9 mm and 11.9 mm Type II KDP. The 10-mm Type I crystal was tested extensively with and without index-matching fluid (Cargille 5610). Below an incident intensity of 2 GW/cm^2 the conversion efficiencies were identical (see "Index-Matching Fluids for Large Apertures" later in this section), but, at higher intensities, we found that the bare-crystal efficiency continued to increase. The index-matched crystal conversion peaked at 44% and then decreased. From energy balance measurements we determined that the reduction in conversion efficiency was due to 532 nm energy missing from the crystal output. We noted a similar degradation of performance in an 11.9-mm Type II crystal matched with FC 104 fluid. Data taken at similar intensities with the small (2-mm) II S laser beam did not exhibit this behavior, suggesting an aperture-dependent loss mechanism. Stimulated scattering processes have been identified as the cause (see "Index-Matching Fluids for Large Apertures").

After confirming the presence of the loss in the index-matching fluid, we redesigned the crystal holders to eliminate the windows and fluid. All subsequent measurements used bare crystals. We summarize the bare-crystal

Table 2-65. Energy-conversion efficiency to the second harmonic.

2ω conversion efficiency				
			Maximum conversion efficiency	
KDP crystal type	Fluence (GW/cm^2)	Thickness (mm)	Bare crystal (%)	AR coatings (%)
II	5.71	11.9	73.6	79.5
I	2.71	22.9	71.1	76.8
I	6.39	10	57.6	62.2
I	2.78	13.4	51.8	55.9

3ω conversion efficiency					
				Maximum overall conversion efficiency	
KDP crystal types	Fluence (GW/cm^2)	Thickness (mm)		Bare crystal (%)	AR[a] coatings (%)
II-II	2.60	11.9	9.9	55	70
I-II	2.45	13.4	11.9	54	69
I-II	2.50	22.9	11.9	50	63

[a]Diagnosing the two-stage 3ω process required an uncoated beam splitter between the second- and third-harmonic crystals. Hence, there are six uncoated surfaces that, together, produce a Fresnel loss of approximately 22%. The Fresnel loss is restored to obtain the performance in this column.

Table 2-66. Energy-conversion efficiency to the third harmonic.

Fig. 2-317. Second-harmonic energy-conversion efficiency vs input intensity.

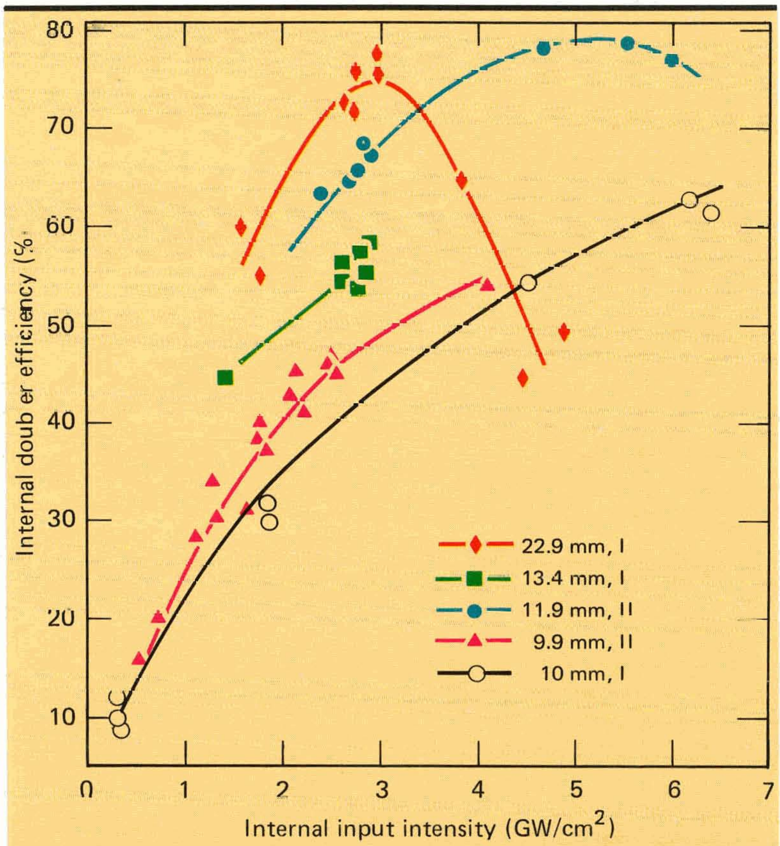

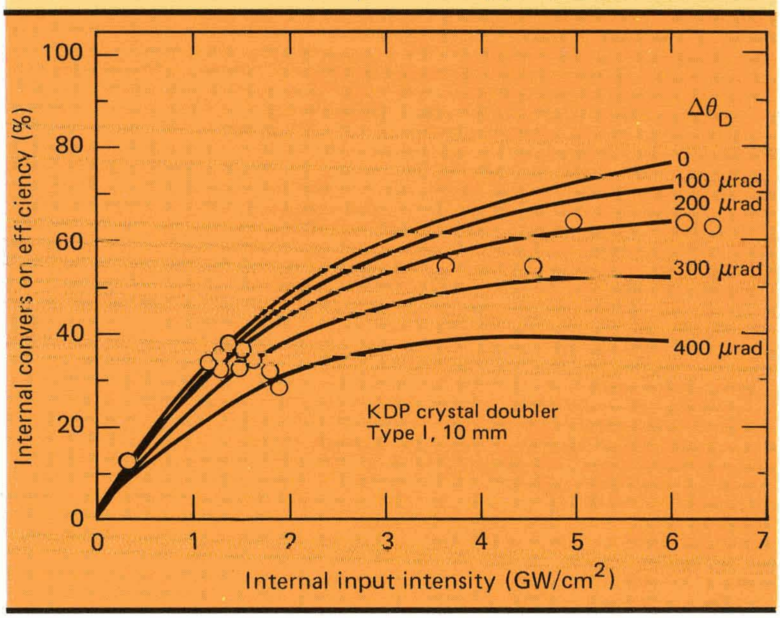

Fig. 2-318. Second-harmonic energy-conversion efficiency vs input intensity compared with plane-wave theory for 10-mm-thick Type I crystal.

conversion-efficiency variation with intensity for the five crystals in Fig. 2-317.

In Figs. 2-318 through 2-321, we plot the experimental conversion efficiency as a function of intensity for the different crystal types and compare it with plane-wave calculations. The listed angles and efficiencies are internal to the crystal. The data suggest an equivalent angular-phase mismatch, or crystal misalignment, of about 0.20 mrad. We obtain good agreement with theory if we assume this nonzero angular phase mismatch even for the crystal's optimum alignment position. (Theoretical curves are labeled with internal mismatch angles; externally measured angles, the ordinate used in the graphs for the tuning curve data, are 1.5 times larger.) One possible source for mismatch is beam divergence. However, the irreducible divergence of our input beam is limited to 0.10 mrad by the final spatial filter in the laser. Since we have used intensities too low to induce nonlinear-index effects in the laser, the intrinsic beam divergence should be even lower. Yet when we compare data with theory, we find average external mismatch angles near 0.20 mrad. We have not identified the source of this minimal mismatch.

We also measured the variation of doubling efficiency with angle of incidence for 10-mm- and 22.9-mm-thick index-matched crystals with the small-diameter ILS beam. When the 22.9-mm Type-I crystal was installed in Argus, we repeated the tuning-curve test, finding that the variation of conversion efficiency with angle in this large-aperture bare crystal configuration agreed with the small-beam data generated at ILS. The tuning-curve data are summarized in Fig. 2-322.

In early Argus harmonic work in 1980, we used the negative-lens technique[148] to orient the crystal for maximum conversion efficiency. Later, however, we found that the setting determined by this method differed from the one required for maximum conversion by angles of 0.05 to 0.25 mrad for the doublers and 0.20 mrad for the 9.9-mm Type-II mixer crystal. This offset is shown in Fig. 2-322 for the doubler crystals. The article "Intensity-Dependent Angular Offset Experiments" describes our further examination of this alignment technique.

Third-Harmonic Conversion Efficiency. Our tripling experiments were performed with three bare crystal configurations: 22.9-mm Type I/11.9-mm Type II; 13.4-mm Type I/11.9-mm Type II; and 11.9-mm

Type II/9.9-mm Type II. In general, satisfactorily-large tripling efficiencies were measured at high intensity, but our range of incident intensities was insufficient to provide a thorough check of theoretical predictions. The zero abscissa setting was determined by centering negative-lens-generated low-power alignment fringes onto a reference crosswire. The high intensity turning curves are offset by 50 to 200 mrad relative to this setting.

We adjusted the mix ratio—532 energy/1064 energy incident on the third-harmonic crystal—to the desired 1.4 in the Type I–Type II configurations by angle-tuning the doubler crystal. We found that while the conversion efficiency of a Type I crystal tuned to its peak may be fairly stable, tuning to some point off the best-phase match angle can result in significant conversion efficiency variation from alignment errors and mechanical instabilities. In addition, we found the width of the tuning curve to be a function of the incident intensity (see article on "Intensity-Dependent Angular Offset Experiments"). The net result is that variations in the laser output can strongly affect the net conversion efficiency. We reduced these problems in the Type II–Type II configuration by using polarization tuning. In this procedure we tuned the doubler to the phase-match angle; we then adjusted the angle between laser polarization and the plane determined by the crystal optic axis and the propagation direction to control the 532-nm energy produced.

We also found that the third-harmonic experimental data suggest nonzero mismatch angles. Unfortunately, conversion-efficiency dependence on laser intensity varies in a manner too complex for us to determine the effective mismatch angle from our limited range of intensity measurements.

For our recent 355-nm target shot series on the Argus south arm (see article on "Target Experiments—532 nm"), we selected a polarization-tuned, 11.9-mm Type II/9.9-mm Type II crystal configuration. This arrangement produced a maximum tripling efficiency of 55%, duplicating the performance on the previous north arm measurements (see Table 2-65). The extensive data obtained during the course of the target irradiation series confirmed that good tripling efficiencies are achievable over a several-month period under typical operating conditions.

The results of the experiments reported in this section demonstrate that it is possible to achieve high conversion efficiencies from both second- and third-harmonic wavelengths using large (8-cm) beams on the Argus laser. Reasonable agreement has been obtained between experimental results and theory. Routine operation of the Argus

Fig. 2-319. Second-harmonic energy-conversion efficiency vs input intensity compared with plane-wave theory for 13.4-mm-thick Type I crystal.

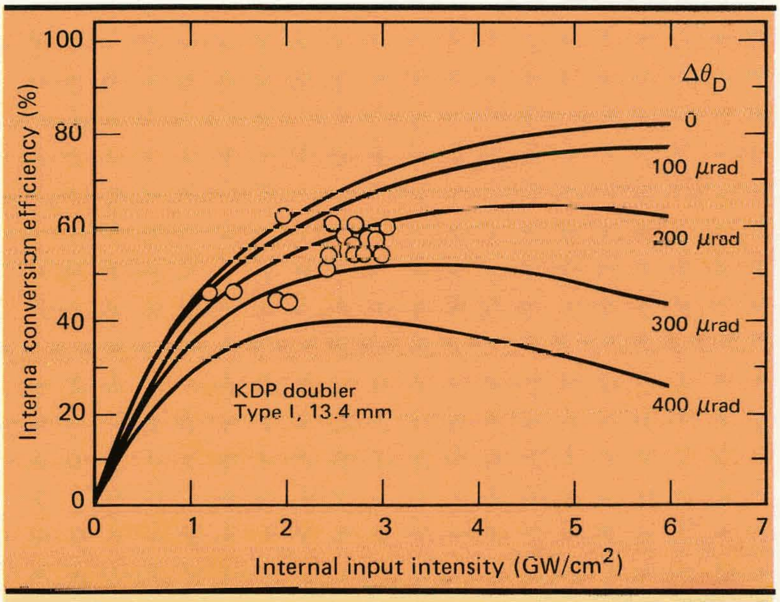

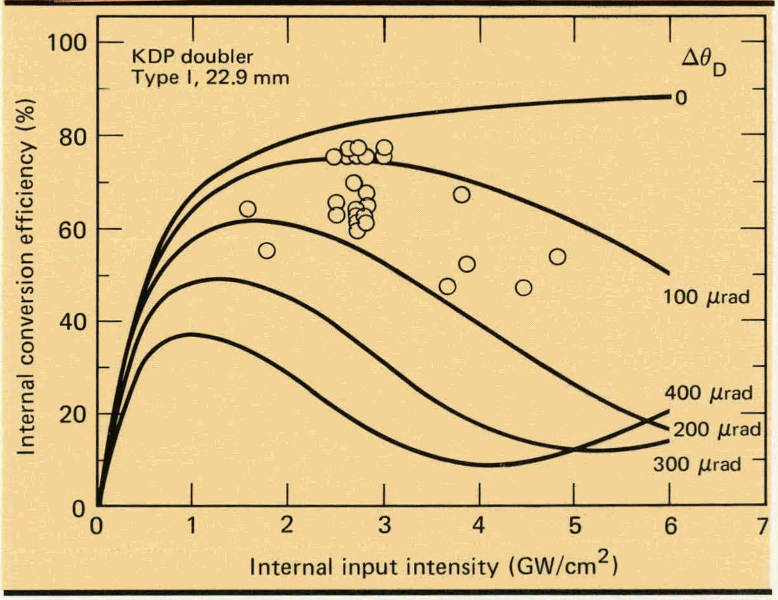

Fig. 2-320. Second-harmonic energy-conversion efficiency vs input intensity compared with plane-wave theory for 22.9-mm-thick Type I crystal.

system for target-irradiation experiments at shorter wavelengths is largely attributable to the experience and understanding gained during the frequency-conversion experiments described above.

Authors: J. S. Hildum and B. C. Johnson

Major Contributors: G. J. Linford and W. L. Smith

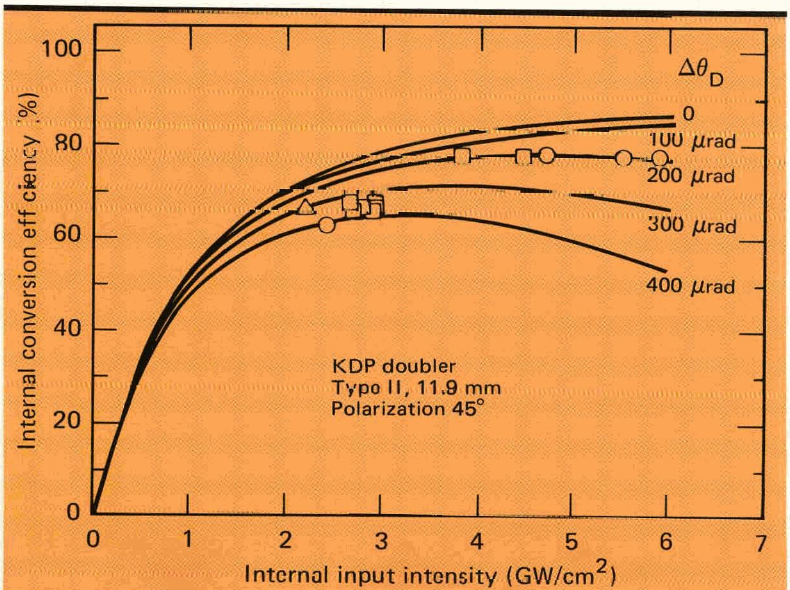

Fig. 2-321. Second-harmonic energy-conversion efficiency vs input intensity compared with plane-wave theory for 11.9-mm-thick Type II crystal.

Intensity-Dependent Angular Offset Experiments. At the beginning of our research with large aperture (10-cm) doubling and mixing crystals, we performed angular crystal alignment using a negative lens (of focal length f) placed in the 1064-nm beam incident on the doubling crystals.[149] As shown in Fig. 2-323, this created a virtual source at a distance –f behind the negative lens. When we directed a 1064-nm beam of moderate intensity (~50 MW/cm^2) onto the negative lens, we could see the directions for phase-matching as a series of bright green bands on a screen behind the crystal.

We adjusted the doubling crystal in angle until the main lobe of the characteristic $\sin^2 x/x^2$ (sinc^2) phase-matched band pattern was precisely bisected by the fiducial crosshair. However, when we measured the high intensity (up to 10 GW/cm^2) doubling efficiency as a function of angular alignment of the crystal, we found that the maximum harmonic conversion efficiency occurred at a position systematically offset from the peak of the tuning curve by several hundred microradians. We investigated this offset by conducting further experiments over a range of incident 1064-nm intensities (0.001 to 10

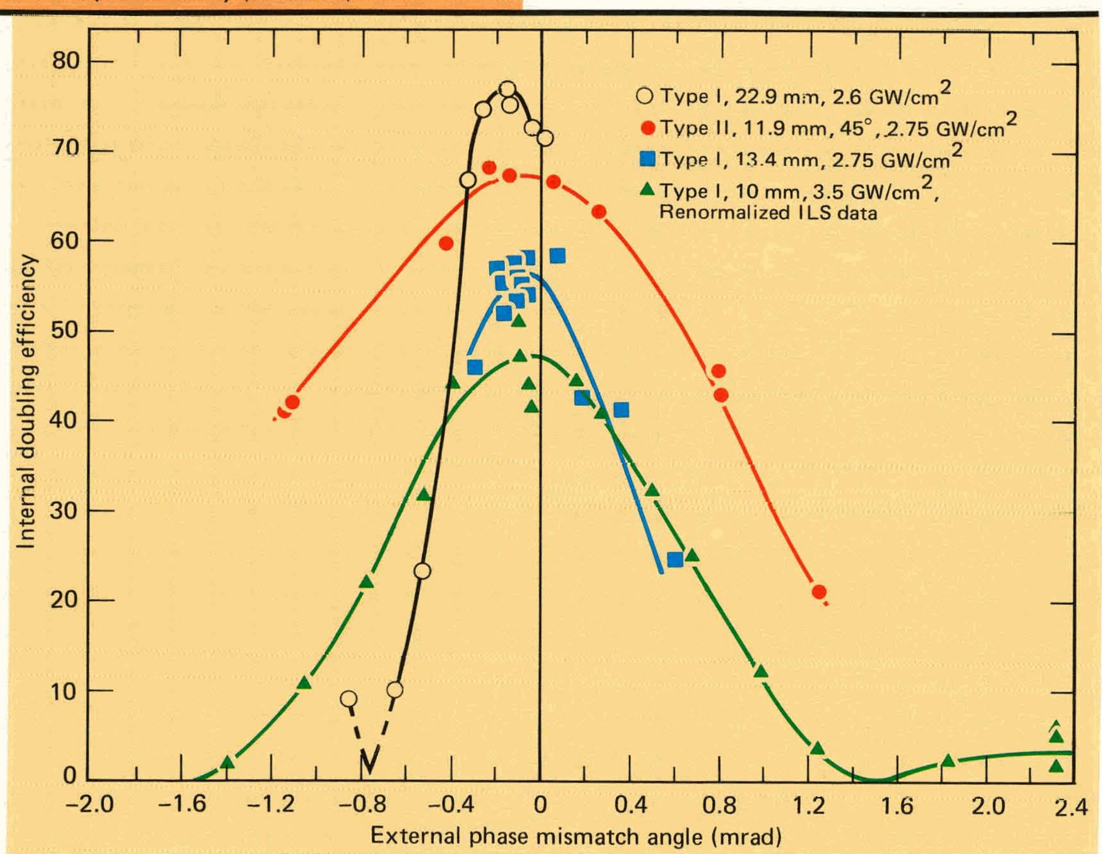

Fig. 2-322. Second-harmonic energy-conversion efficiency vs angle.

GW/cm^2) using the apparatus shown in Fig. 2-323. We photographed the characteristic sinc^2 phase-matched pattern using Royal-X-Pan (RXP) film.

During our first experiment, we varied the input intensity to the 10-cm Type I KDP crystal from 0.004 to slightly over 10 GW/cm^2. Figure 2-324 shows a plot of intensity vs angle of the $(\sin^2 x/x)^2$ phase-matched pattern (PMP) alignment fringes obtained in this experiment. As shown here, the anisotropy of the PMP central peak corresponds to an angular skewness of 0.15 to 0.2 mrad.

We then made harmonic conversion measurements for the same crystal using a small-probe 1064-nm Nd:YAG laser and a stepping-motor-driven mirror to vary the angle of incidence over an appropriate range to generate the full sinc^2 phase-matched band pattern. The results of this experiment (shown in Fig. 2-325) indicated that the central PMP sinc^2 intensity distribution is apparently completely symmetrical.

We conclude that the apparent crystal offset phenomenon was not the result of an intensity-induced angular shift but was instead an artifact of the "negative lens" alignment method.[149]

The green 532-nm sinc^2 intensity distributions on the RXP film exhibited minima whose spacing we observed to narrow with intensity for incident 1064-nm intensities higher than one GW/cm^2. Figure 2-326 shows the relative agreement between the observed narrowing and the theoretical calculations of the effect.

The essential results of our measurements are as follows:

- No intensity-dependent shift of the negative lens-generated PMP peak was observed.

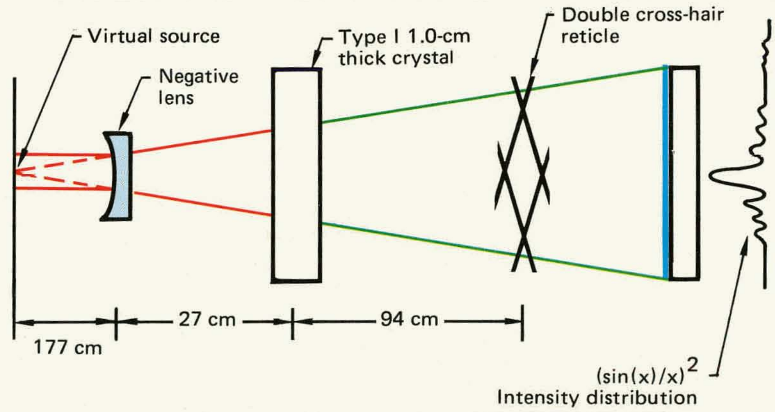

▲ **Fig. 2-323. Crystal offset experiment.**

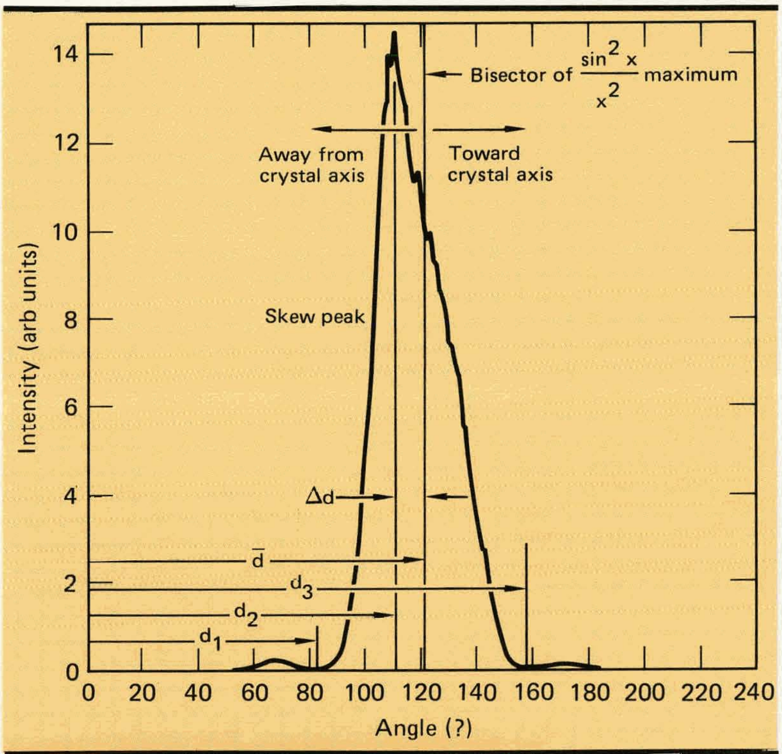

▲ **Fig. 2-324. Negative-lens PMP fringe angular- intensity distribution.**

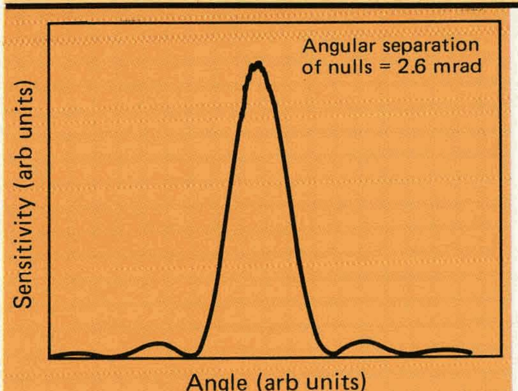

Fig. 2-325. Scanning-mirror PMP fringe angular-intensity distribution.

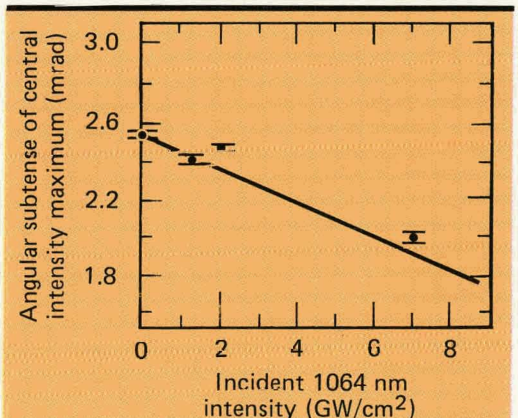

◀ **Fig. 2-326. Variation of PMP minima with incident 1064-nm intensity.**

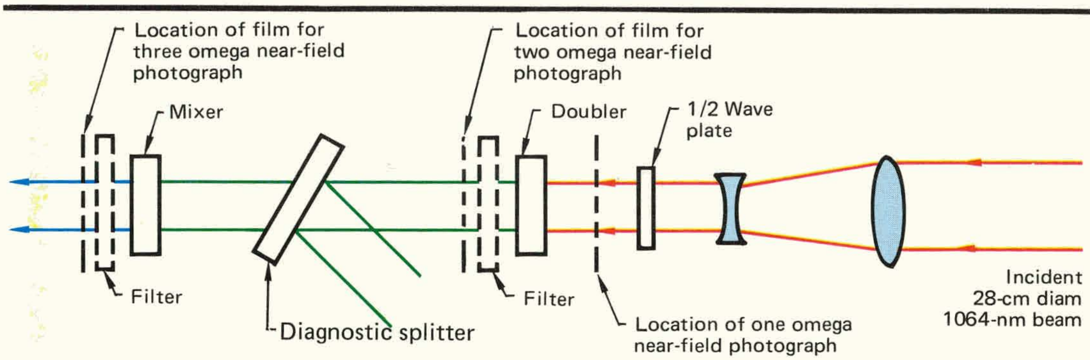

Fig. 2-327. Schematic of apparatus for taking near-field photographs of harmonically converted laser beams.

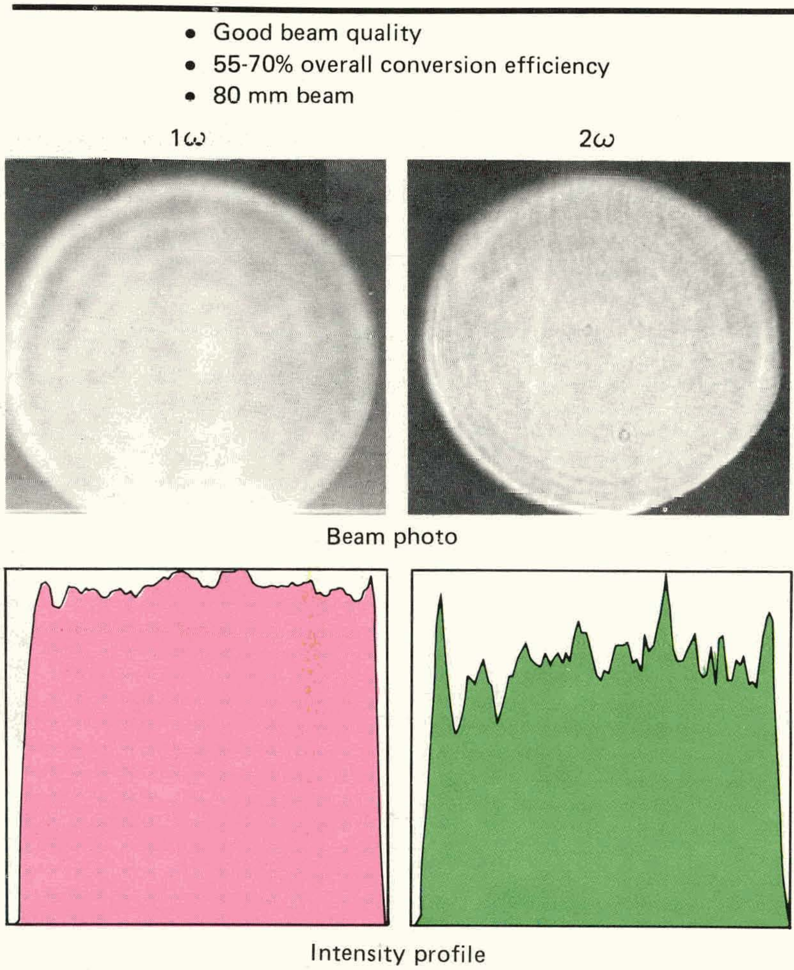

Fig. 2-328. Near-field photographs and intensity scans of 1064-nm fundamental and 65% green external-conversion-efficiency beams.

- The negative-lens-generated PMP appears to be asymmetric with its central intensity peak offset from the midpoint of the first two sinc^2 nulls.
- The direction of the peak offset is consistent for all shots and corresponds to a direction *away* from the crystal optic axis.
- The magnitude of the peak offset ranged from 70 to 280 μrad, with perhaps a slight tendency to decrease at high intensities.
- A low-intensity angular scan of the same crystal taken without using a negative lens showed a *symmetrical* PMP.
- The full width between minima of the negative-lens-generated PMP decreased with increasing intensity, in good agreement with plane wave theory.

As a consequence of these measurements, we no longer rely on the negative lens technique for accurate alignment of large-aperture harmonic conversion crystals.

Author: G. J. Linford

Major Contributors: B. C. Johnson, E. M. Booth, K. D. Snyder, W. L. Smith, and C. Vercimak

Beam Spatial Quality. Since optical components including fusion targets are damaged by laser pulses with excessive intensity modulation, it is important to measure the near-field intensity distributions of the fundamental and harmonically-converted laser beams. During the course of the harmonic conversion experiments on the Argus north arm, we photographed the near-field beams at 1064-, 532-, and 355-nm wavelengths. Figure 2-327 shows the experimental arrangement. After obtaining a near-field beam exposure, we calibrated the Royal-X-Pan (RXP) film response by exposing a separate multiple-image photograph at the same wavelength on the ILS laser using sheets of film from the same box. Both films were then developed by identical processes. We scanned and digitized the near-field picture and multiple-image photographic densities. We generated a density vs log exposure (or D log E) curve for the RXP film and converted the optical density data to energy data using computer graphic routines.

The resulting energy profiles, together with the near-field photographs for the fundamental and harmonic pulses, are shown in Fig. 2-328. This 532-nm green

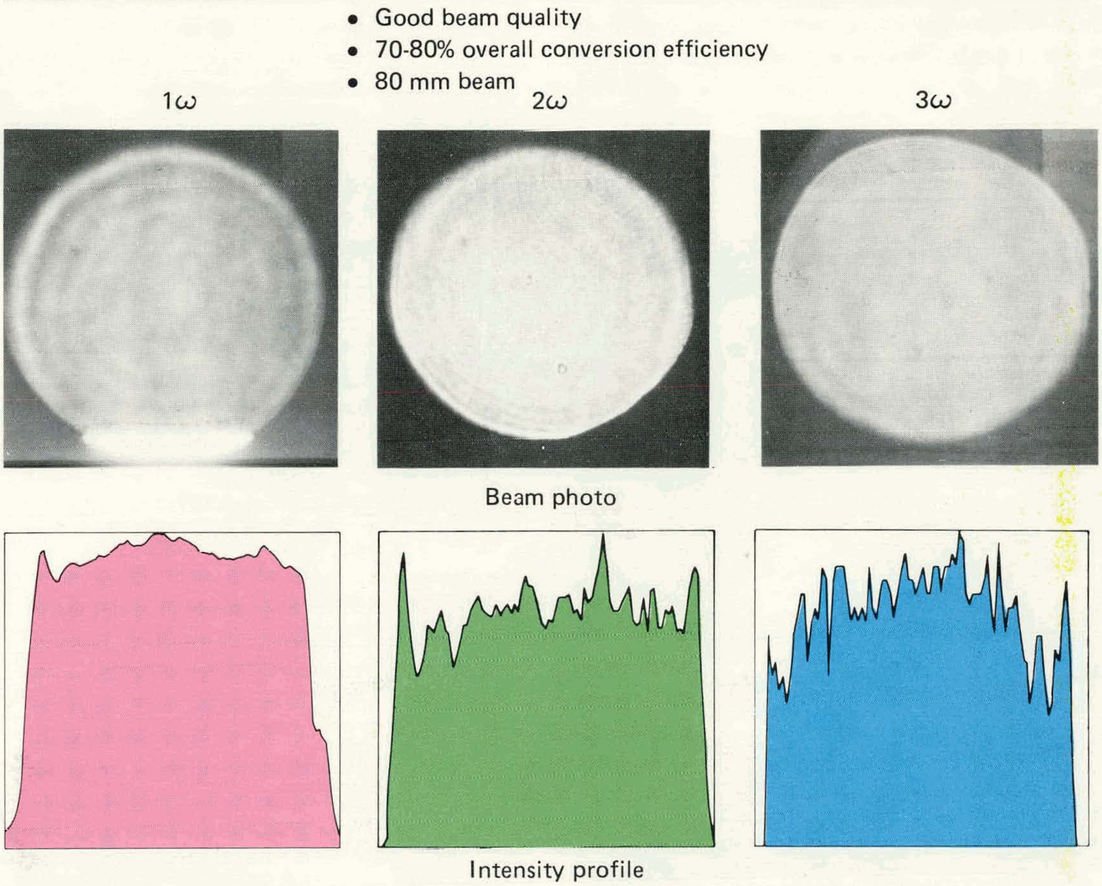

Fig. 2-329. Near-field photographs and intensity scans of 1064-nm fundamental, 532-nm doubled, and 355-nm tripled laser beams.

beam was generated at a 65% external-conversion efficiency. The intensity modulation in each beam is approximately 25%.

In Fig. 2-329, we show the results of near-field beam analysis for our tripling experiments. This figure displays the actual 1064-, 532-, and 355-nm beam near-field photos accompanied by computer-reduced intensity profiles. In this case we reduced the 532-nm conversion efficiency slightly since, for optimum 355-nm conversion, it is necessary to mix a 2:1 intensity ratio of 532- and 1064-nm beams. Once again the 25% beam modulation at 532 nm is similar to that at 1064 nm.

The results of these near-field measurements indicate that the 532- and 355-nm beams vary in intensity by 30% across 80% of the beam aperture. (See Table 2-67 for a summary of these data.) In general, the harmonically converted beam modulations depend on the details of the harmonic-crystal conversion process and the input beam characteristics. It should be noted that since we took the 1064-, 532-, and 355-nm near-field photos at increasing distances from the output lens, there is no precise 1:1 correspondence of the pertinent diffraction conditions or structures in the photographs.

Table 2-67. Observed beam modulation on harmonically converted Argus north arm.

Wavelength (nm)	Displacement from output lens (cm)	X-scan av fluctuation (%)
355	250	36
532 (high efficiency)	50	26
532 (for mixer)	50	14
1064	10	26

Author: G. J. Linford

Major Contributors: B. J. Demartini and W. L. Smith

10-cm Crystal-Array Prototype. In 1980, we completed testing of the 10-cm 2 × 2 crystal-array prototype that was built in 1979.[150] Figure 2-330 shows this device, and Fig. 2-331 shows its mechanical design. This is our second array prototype and the last to employ individually held and externally orientable crystal segments. Future arrays will use precision-fabricated segments oriented for phase-matching, as described in the articles under "Fabrication of KDP Array Segments" that follow.

The tests described here are the first of a crystal array on a fusion laser. We used the Argus laser reduced to 8-cm clear aperture. Our objectives were to test the array alignment stability and conversion efficiency, and to photograph the harmonic spatial profile in the near and far fields.

Fig. 2-330. Crystal array prototype of four KDP segments in 2 × 2 geometry.

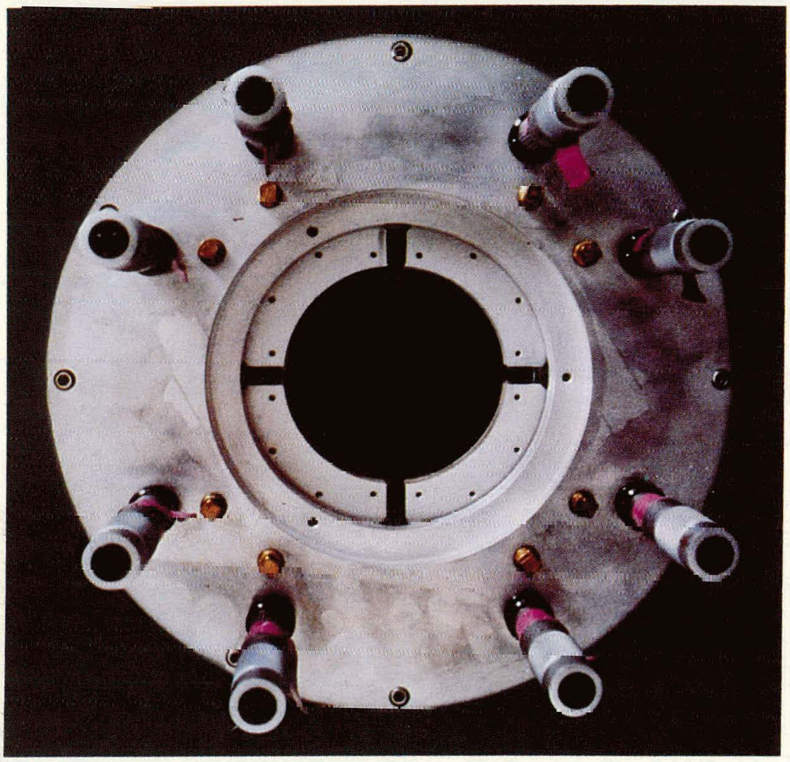

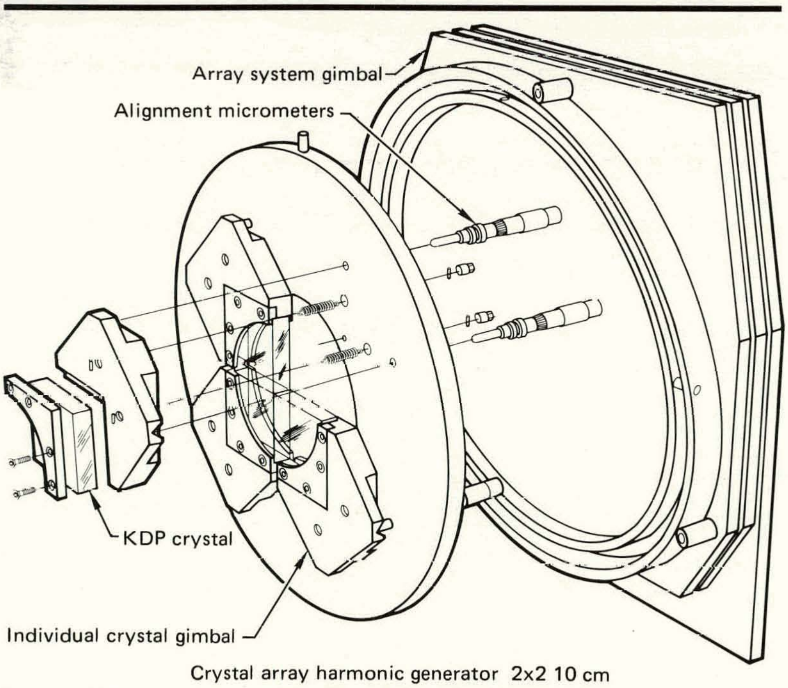

Fig. 2-331. Assembly view of 2 × 2 harmonic array prototype.

The KDP crystals were Type II, 13 mm thick, chosen to allow direct comparison with a monolithic crystal in use on Argus. The four array segments were mutually aligned for phase-matching on the smaller ILS laser using an expanded mode-locked pulse train and a photodetector. The adjusting micrometers for the individual segments were then fixed in place. All further day-to-day alignment of the external array would move it as a whole using the micrometers on the array mount.

The array was then transferred to Argus and aligned, using the negative-lens technique,[150] in the same manner as a monolithic doubler. The first series of tests was run, as initially planned, with the array filled with index-matching fluid. Next, because of difficulties encountered with these fluids (see "Index-Matching Fluids for Large Apertures"), the array was drained, reassembled, and retested with the KDP crystals bare. The data presented here are for the bare array.

For the near-field beam photography, 1.064-μm, highly-collimated pulses nominally of 80 J were fired into the array and converted with 50 to 60% efficiency to the second-harmonic wavelength. We recorded the harmonic profiles on Plus-X film at a distance of 3 m beyond the array. A multiple-image exposure on film from the same batch was made on the ILS laser, at the same wavelength and pulse duration, and developed with the Argus film. The D log E curve obtained from this multiple exposure was used to analyze the Argus data in the established manner.[151]

Figure 2-332 shows the near-field profile of a 37-J harmonic pulse generated with 50.7% external conversion efficiency at 2.6-GW/cm^2 input intensity. The photograph in Fig. 2-332(a) shows the diffraction stripes resulting from the 0.5-mm-wide gap between the segments. Figure 2-332(b) shows the energy profile of this pulse smoothed by averaging the energy within 0.9-mm by 0.9-mm pixels. Figure 2-332(c) shows a cut through the profile at the position indicated by the arrow in Fig. 2-332(a). The resolution of this cut—0.1 by 0.1 mm—shows the high-frequency modulation present on the profile. The diffraction stripes from the intercrystal gaps are of approximately the same order as the modulation from other sources in the laser.

The intermediate- and far-field distributions of the harmonic pulse are shown in Figs. 2-333(a) and 2-333(b). The intermediate photograph was taken at a distance of 0.7 m before the focus, and the far-field photograph at the focus of an 8.2-m

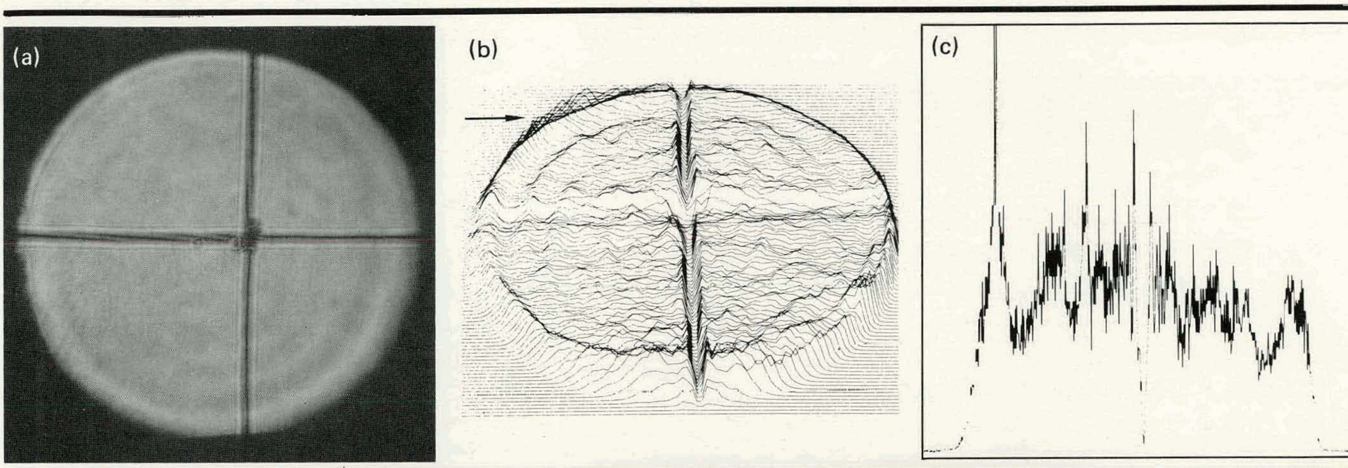

▲ Fig. 2-332. (a) Near-field photograph of harmonic pulse generated with 2 × 2 crystal array. Diameter of this pulse is 8 cm. Diffraction stripes result from 0.5-mm intercrystal gap; (b) energy profile of harmonic pulse smoothed to resolution-element size 0.9 by 0.9 mm; (c) higher resolution cut (0.1 by 0.1 mm) through harmonic profile at location shown by arrow in (b).

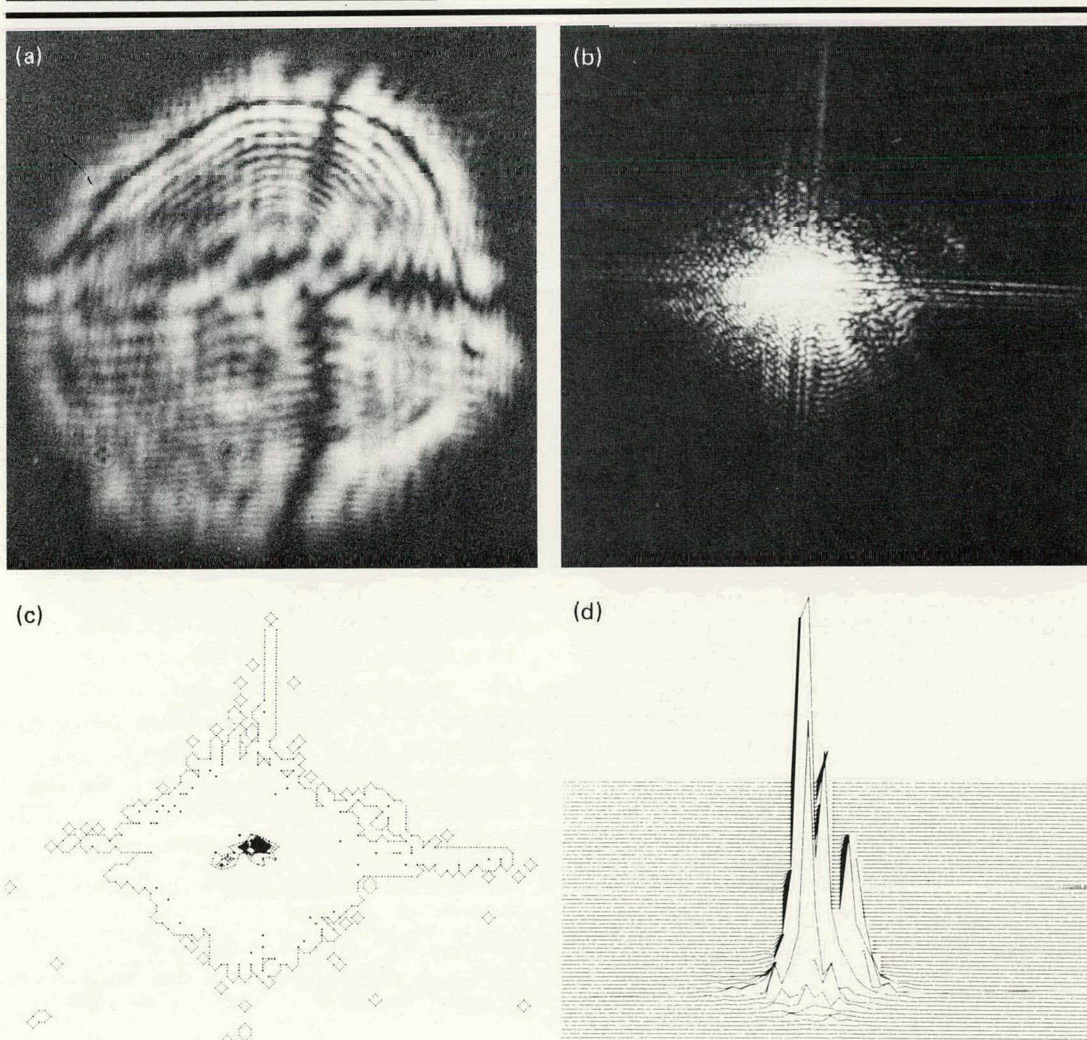

Fig. 2-333. (a) Intermediate-field profile of harmonic pulse generated in 2 × 2 crystal array; (b) far-field energy profile of harmonic pulse from 2 × 2 array. Photograph taken at focus of 8.2-m lens; (c) iso-energy view of far-field profile; (d) isometric view of energy distribution of far-field profile.

lens. Figures 2-333(c) and 2-333(d) show iso-energy and isometric views of the far-field distribution.

Regarding alignment stability and conversion efficiency, the 2 × 2 array performed essentially the same as a single-crystal doubler. In a four-shot test of phase-match angle sensitivity at 2 GW/cm^2 input intensity, the efficiency decreased by 10% of its maximum value at rotations of 60-μrad internal angle. The maximum external conversion efficiency obtained with the bare array was 62.7% at an input intensity of 3.2 GW/cm^2. Restoring the reflection losses increases this figure to 67.5% internal conversion efficiency.

Author: W. L. Smith

Major Contributors: T. F. Deaton, F. A. Frick, B. C. Johnson, G. J. Linford, F. T. Marchi, G. G. Peterson, and J. B. Willis

Fabrication of KDP Array Segments

Introduction. Harmonic conversion of Nova and Novette requires the development of new array technology for orienting and finishing KDP crystals. Schedules do not allow sufficient time to grow KDP boules large enough for single crystals with 74-cm clear aperture; thus, a need for arrays is created. Elements in arrays as large as 3 × 3 could be individually aligned, but the mounting hardware would be very complex and expensive. To avoid mechanical complexity, as well as to extend sizes beyond 3 × 3 arrays, we are developing the required technology for monolithic arrays without alignment controls on individual segments.

Monolithic KDP arrays for harmonic generation require a precision orientation capability and a new finishing technique for the individual array segments. To achieve single-crystal performance, each segment in the assembled array must contribute at full conversion efficiency for a single orientation of the total array. We have demonstrated an alignment instrument for determining the optimum phase matching direction for a KDP segment. We have also demonstrated a finishing technique for KDP that can easily make orientation corrections to individual segments. This finishing technique, diamond turning, uses very stable machine tools with diamond cutters to obtain optical-quality surface finishes and very small machining tolerances.

The array assembly will sandwich the segments between much thicker windows for mechanical strength, and index-matching fluid will be used between segments. We are considering the possibilities of optically contacting the KDP segments to each other or to one of the windows, cementing the segments to one window with a high-viscosity index-matching fluid, or floating the segments freely between the windows in low-viscosity index-matching fluid.

We are constructing a prototype array to evaluate our finishing, orientation, and assembly procedures and to test mechanical aspects of the array assembly. The prototype will be a 3 × 3 array, with each segment measuring 5 × 5 × 1.8 cm. It will have a 15-cm clear aperture, and will be suitable for high-power tests on Argus. The alignment instrument for this prototype will be separate from the diamond-turning machine. KDP segments for the prototype and for Novette will be finished by the LLNL Metrology Group on an existing diamond-turning machine. Although this arrangement increases the number of handling steps for each segment, it takes advantage of an operational diamond-turning facility without perturbing it for incorporation of alignment capability. Additionally, this arrangement allows separate and parallel optimization of both the alignment instrument and the diamond turning of KDP. A disadvantage is the possible introduction of transfer errors between the facilities, but these errors have been minimized by using identical mounting chucks and orientation stages.

Figure 2-334 shows a flow diagram, from receipt to array assembly, for finishing the prototype array segments. The segments initially go to the diamond-turning facility for surface finishing to obtain a flat optical

Fig. 2-334. Flow diagram for finishing the prototype array segments.

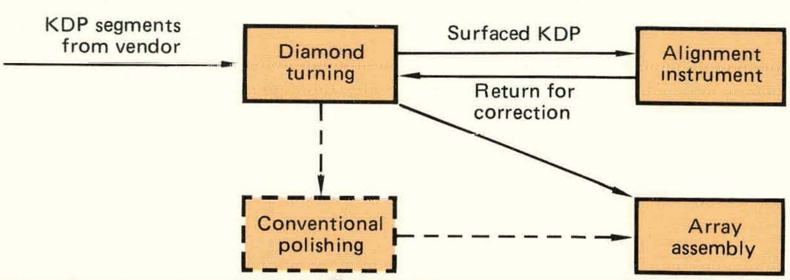

surface for an orientation reference; they are then transferred to the alignment instrument for orientation and go back to the diamond-turning facility for correction. This sequence must be repeated at least once to confirm the final orientation of each segment. The final diamond-turning operations reduce the thickness of each segment and trim its edges to the required dimensions. Finally, the segments are transferred to a clean room for assembly into the array. In the event that the tooling marks from diamond turning cause diffraction or propagation problems, the segments will receive a final polishing using conventional techniques, but we consider this very unlikely.

For the Novette arrays, we will use the alignment instrument and diamond-turning facility as developed for this prototype array. However, the number of segments required for Nova, ~400, necessitates combining the alignment instrument with the diamond turning machine to cut down on the number of steps required for finishing each segment.

The following two articles describe the alignment instrument being developed for the prototype and Novette arrays and the procedures for diamond turning of KDP.

Author: J. E. Murray

Major Contributors: P. C. Baker, F. T. Marchi, W. L. Smith, and M. A. Summers

Precision Orientation Apparatus. Monolithic arrays require precision orientation of the individual array segments. The segments must each be oriented with respect to their crystalline axes so that their phase-matching directions are parallel in the assembled array. For convenience, we orient the phase-matching direction parallel to the surface normal in each segment. Figure 2-335 shows the three independent angles that affect harmonic conversion efficiency. The angle θ between the beam direction and the crystalline z-axis solely determines phase matching. Any departure from the optimum direction introduces a $\Delta\theta$ that causes phase mismatch and reduces conversion efficiency. The angle $\Delta\alpha$ between the segment edge and the intersection of the crystalline x–y plane represents a misalignment of the ordinary and extraordinary axes and causes an error in polarization direction for the segment. The angle of rotation of the x and y axes away from the optimum for harmonic generation is labeled $\Delta\phi$. Both $\Delta\alpha$ and $\Delta\phi$ affect the magnitude of the effective nonlinear coefficient.[152]

We established the tolerance for these angles from the desired conversion efficiency of the total array. Requiring that each segment in the assembled array convert at $\geqslant 99\%$ of its maximum high-power second-harmonic (SH) conversion efficiency gives the following tolerances:

$$\Delta\Theta \leqslant \pm 60\ \mu\text{rad-cm}$$

$$\Delta\alpha \leqslant \pm 50\ \text{mr}$$

$$\Delta\phi \leqslant \pm 50\ \text{mr} \tag{74}$$

Since the angle sensitivity for phase matching increases in proportion to crystal length, the $\Delta\theta$ tolerance (here normalized to 1 cm) decreases with crystal length. Of these tolerances, only $\Delta\theta$ requires orientation during finishing because the $\Delta\alpha$ and $\Delta\phi$ tolerances are satisfied in the rough-cut segments from the KDP vendors.

The alignment instrument uses small-signal second-harmonic generation (SHG) to determine $\Delta\theta$. We obtain a complete angle-tuning characteristic for each KDP segment with a low-power laser, as indicated in

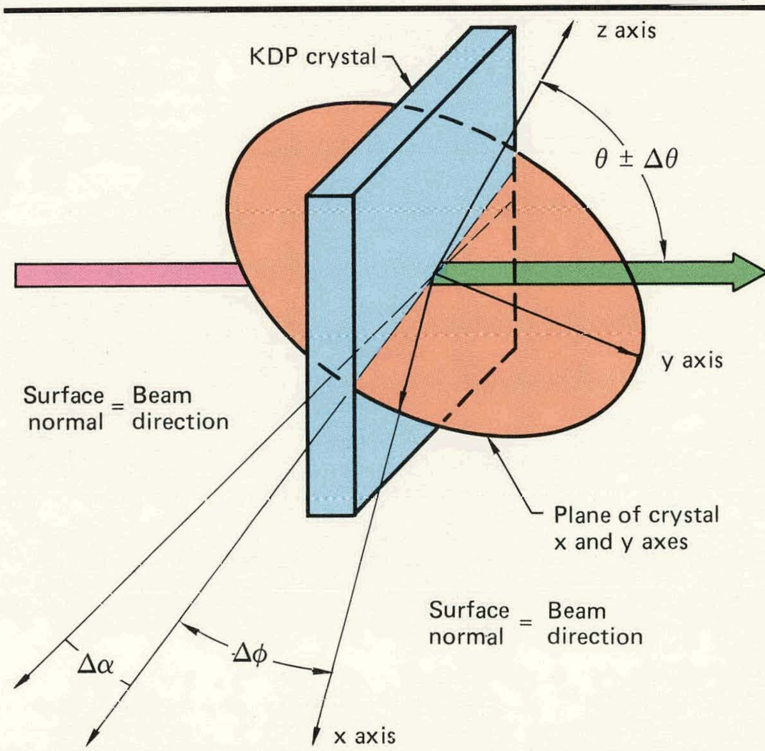

Fig. 2-335. The three independent angles that uniquely define the crystalline axes with respect to the array segment and determine the second-harmonic conversion efficiency.

Fig. 2-336. From these data, a microcomputer calculates the optimum direction relative to the surface normal. So that neither the temperature of the KDP nor the laser wavelength contribute to the tolerance on $\Delta\theta$, they must be held to $\Delta T \leqslant \pm 0.1°C$ and $\Delta\lambda \leqslant \pm 1.25\ cm^{-1}$ for a 1-cm crystal.[153] Consequently, all the segments for a given array must be oriented at the same absolute temperature and wavelength to these tolerances. Additionally, the assembled array must be operated at this same temperature and wavelength to maintain the phase-matching direction parallel to the surface normal of the array.

We satisfy $\Delta\lambda$ by using a Nd:YLF laser in the alignment instrument. Its gain line width is sufficiently narrow, $12.5\ cm^{-1}$ FWHM,[154] to ensure the $\Delta\lambda$ tolerance. Further, this is the same laser type that will be used for the Novette and Nova pulsed oscillators, so that compensation for wavelength differences between orientation and operation will not be necessary.

The temperature-controlled enclosure shown in Fig. 2-337 houses the KDP segments during orientation and ensures that the temperature tolerance is satisfied. The enclosure uses air as the working fluid, with enough dry N_2 added to keep the humidity below 40%. A liquid chiller holds the radiator a few degrees below the desired temperature, and the electrical heater adds the required power to bring the air to that temperature. A temperature probe located just downstream from the radiator controls the power applied to the heater. The fan mixes the air and circulates it every few seconds. Both the liquid cooler and the closed-loop controller for the heater are commercial units. A prototype enclosure of this type held the temperature to $20.00 \pm 0.02°C$ for several days against an ambient temperature variation of $\pm 1°C$. Further, the control system returned the internal temperature to within 0.1° of 20.0°C in less than a minute after the enclosure was opened and filled with room-temperature air, which was several degrees above 20°C.

The tolerance on $\Delta\theta$ requires finding the peak of the angle-tuning curve to within ±2.7% of its FWHM. Consequently, the alignment instrument requires that the tuning-curve data have a relatively high signal-to-noise ratio. A cw-pumped, repetitively Q-switched Nd:YLF laser will provide plenty of average second harmonic (SH) power for easy detection, but its pulse-to-pulse variation of ±5% will cause ±10% noise on the SH signal. Consequently, the alignment instrument requires a normalizing signal to provide a ratio for the SH signal

Fig. 2-336. Schematic of the alignment instrument that locates the optimum phase-matching direction using small-signal second-harmonic generation.

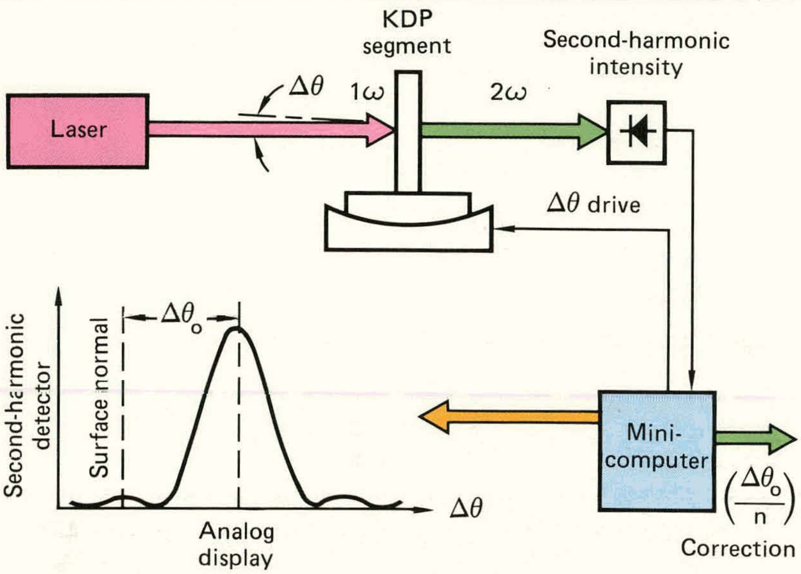

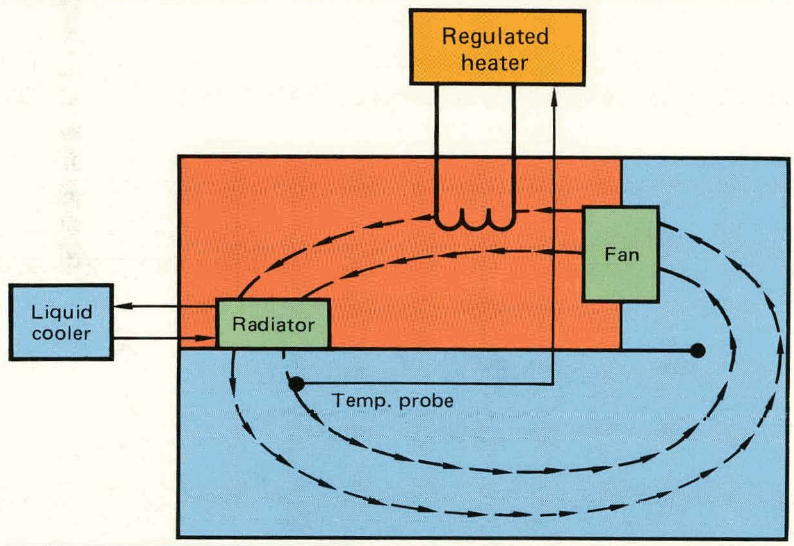

Fig. 2-337. Schematic of▲ the environmental enclosure.

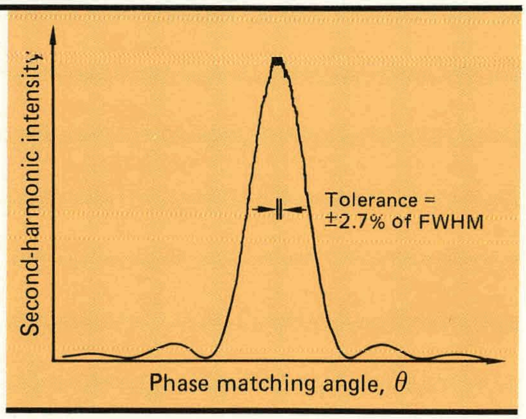

Fig. 2-338. A second-harmonic tuning curve for KDP, showing the large signal-to-noise ratio achieved by using a normalizing signal to eliminate the fluctuation in laser power.

and, thereby, eliminate the fluctuation. This reference could, in principle, be obtained by electronically squaring a detector signal monitoring the laser power. However, the shot-to-shot variation in axial mode structure from a laser of this type creates a fluctuating temporal structure that requires detector and electronic bandwidths of 100 GHz to provide accurate ratios. A simpler technique uses a second fixed-orientation SHG to generate the normalizing signal. The alignment instrument has a reference arm identical to the main signal arm for this purpose.

Figure 2-338 shows the signal-to-noise ratio obtained for KDP tuning data that have been compared to the normalizing signal; the figure also indicates the required measurement tolerance for $\Delta\theta$. Although the peak of the curve is not defined well enough, the signal-to-noise ratio is clearly sufficient for curve fitting to the required accuracy. Note that both the width of the tuning curve and the $\Delta\theta$ tolerance scale inversely with crystal thickness, so that our orientation accuracy does not change with thickness.

We require the $\Delta\theta$ measurement relative to the surface normal of the segment, which requires referencing the surface normal to the laser direction. For this referencing, a TV camera monitors both the reflection from the segment and the incident beam through a lens. With the TV located at the focal length of the lens, the beam positions at the vidicon depend only on the angles of the beams. Therefore, adjusting the orientation of the segment to superimpose the TV images aligns the surface normal to the beam direction. We easily achieve alignments to $\pm 10\ \mu$rad with this technique.

Author: J. E. Murray

Major Contributors: P. C. Baker, R. D. Boyd, S. E. Mayo, R. G. Ozarski, S. Warshaw, and J. Williams

Diamond Turning of KDP. This article will review the reasons for selecting precision machining (diamond turning) for KDP and will describe the LLNL in-house development effort, the outside vendor effort, the LLNL technical exchange, and the Novette fabrication plan.

At the time the frequency-conversion program was begun at LLNL in late 1979, the KDP crystal growers in the USA were the only companies experienced in finishing KDP. Their methods consisted of conventional polishing techniques, similar to glass finishing, adapted to the unique properties of KDP: it is hydroscopic, brittle, thermally sensitive, and requires modified polishing procedures, tooling, and handling, as well as temperature and humidity control. The Argus 2 and 3ω harmonic experiments (see "Argus Frequency Conversion Experiments" earlier in this section) required 100- to 120-mm-diam blanks finished to $\lambda/8$ in transmission. Since these requirements were seriously taxing the capability of the finishers, it became apparent early in 1980 that the requirement for large crystals for Nova (~30 cm square), and the more recent requirements on Novette, were beyond any fabrication capability possessed by the crystal growers. To assess our needs for finishing KDP for Novette and Nova, we evaluated the following parameters:

- Existing vendor capability.
- Upgrading existing capability or facilitizing conventional glass finishes.
- Finishing costs.
- Crystal configuration and tolerances.
- Delivery rate and schedule.

As the program focused on the crystal sizes and configuration (a 3 × 3 array using 27 × 27 -cm-square crystals for Nova and for one arm of Novette and a 15-cm-square 5 × 5 array for the other arm of Novette), it became clear that the KDP growers would not be able to upgrade their facilities in time to handle these sizes using the conventional finishing methods. The alternative of facilitizing existing glass-finishing companies seemed reasonable, as the large flat-lap polishing and testing capability already existed there. However, after we estimated the cost and schedule for finishing the 15-cm-square crystals using a continuous polishing machine (Table 2-68), we found that the schedule was unacceptable and that two additional vendors would have to be facilitized at a cost of approximately $300 000 to bring the schedule within reason. The situation for finishing 27-cm-square crystals was also very unfavorable.

An alternative was necessary, and diamond turning, or, more appropriately, precision machining, presented this alternative. Below, we will describe the effort that has proceeded since March 1980. On the basis of our analyses of costs and schedules (Table 2-68), we decided to use the precision-machining approach.

The precision machining of crystalline material is a technique that is practiced only in a limited way on a few crystalline solids. The work of Decker[155] at the Naval Weapons Center and work sponsored by Los Alamos National Laboratory are probably the major efforts in this area.

Table 2-68. Comparison of finishing costs and schedule for thirty 15-cm² crystals.

	Conventional method	Precision machining method
Manufacturing (h/crystal)	80	20
Unit cost at $40/h	3200	800
Crystal delivery rate	1/2 weeks	4/2 weeks
Total delivery cycle	60 weeks[a]	15 weeks

[a]Upgrading facilities for two vendors plus full operation at LLNL reduces this schedule to 20 weeks. Additional cost = $300 000.

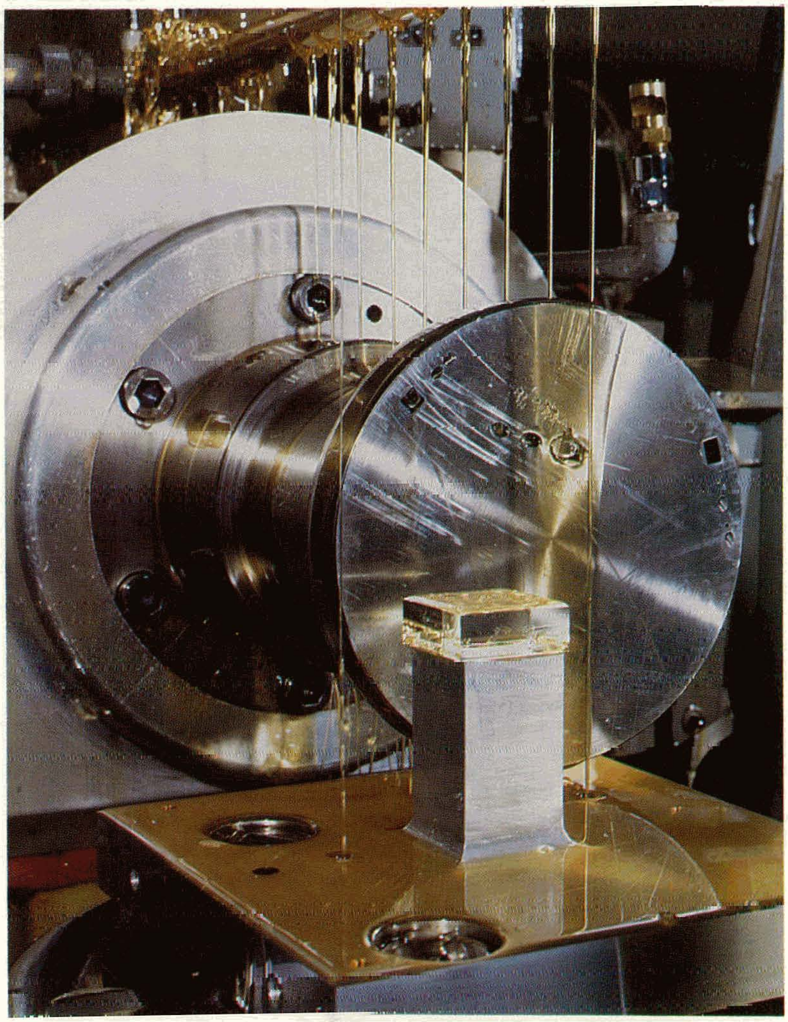

Fig. 2-339. Vacuum chuck holding KDP during diamond machining.▼

A study[156] recently conducted by the LLNL Optics Lab on the machinability of certain glassy materials led us to believe that machining could be used on the KDP material to produce surfaces of acceptable quality. Several KDP samples were prepared and machined on two different precision machines, each having a fly-cutting configuration (described below). The initial machining work was done on a Pneumo machine with a 6-in. capacity. The various tools, configurations, feeds, and spindle speeds were selected on this machine. Test runs were then made on the diamond-turning machine (DTM-1), which also has a fly-cutting configuration, in the LLNL Metrology Group. The latter machine, which is shown in Fig. 2-339 with a 5-cm² crystal being finished, can comfortably handle the size and accuracy of the Novette and Nova crystals and will be used to machine at least the Novette crystals.

The conditions for best machining depend heavily on the quality of the precision diamond cutting tool and on the angle of the tool rake face to the material during machining. This rake angle is a critical parameter in finishing and resultant surface roughness; it has been optimized at an angle of −40°. One other condition that was found to be critical was the relative radial speed change that occurs with lathe machining; this resulted in patterned macrospalling that was concentrated heavily at the center of the sample. This condition was avoided by using successive machine passes at small tool penetrations.

The effect of speed change on the sample was eliminated simply by inverting the role of the tool and sample: the part is held fixed in rotation and the tool is mounted in a wheel on the spindle. This technique is commonly known as fly cutting. The quality of the surfaces produced by this technique are as good as, or, in some cases, even better than traditionally polished KDP. Figure 2-340 illustrates this comparison; typical traces of surface roughness are shown for both polished and diamond-turned surfaces. The rms surface roughness measurements were 58.6 Å for the polished surface and 48.1 Å for the diamond-turned surface. We measured the surface roughness with the noncontact optical heterodyne profilometer at the LLNL Optics Lab. this instrument has been calibrated with Michelson's Lab

Talystep profilometer at the Naval Weapons Center and has a working resolution of 1 Å.

The single-pass wavefront error of a typical diamond-turned KDP sample is shown in Figs. 2-341(a) and 2-341(b). The as-turned error is $\lambda/1.7$; with index oil and cover plates, the error is $\lambda/10$ at 0.6328 μm.

To compare the damage resistance of commercially polished and micromachined KDP, we used 1064-nm, 1-ns laser pulses to irradiate 5- × 5-cm samples that had been prepared from the same parent boule. Both types of surfaces exhibited damage at flux levels of 8 to 12 J/cm^2. These damage thresholds are probably affected by the presence of bulk damage in the KDP samples (see "Bulk Damage in KDP" earlier in this section). We plan additional tests when damage-resistant KDP is available.

We initiated a survey of various precision-machining vendors in an attempt to establish their capabilities and interest and to transfer technology on precision machining of KDP. Four companies directly involved with this technology were contacted:

- Honeywell Electro Optics Center.

Fig. 2-340. Surface roughness of KDP samples. (a) Conventionally polished sample. (b) Diamond-polished sample (precision machined on the DTM-1 at LLNL).

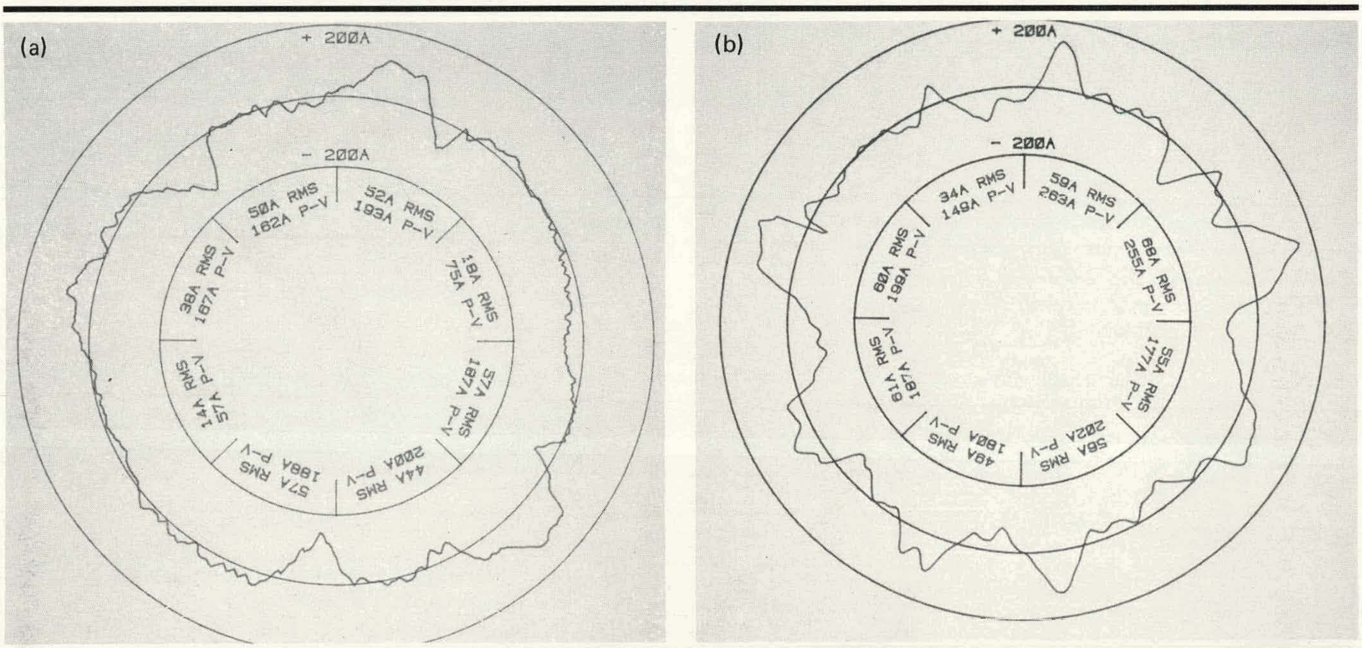

Fig. 2-341. Transmission interferogram of diamond-turned KDP. (a) As turned. (b) Same piece with index-matching oil and cover plates.

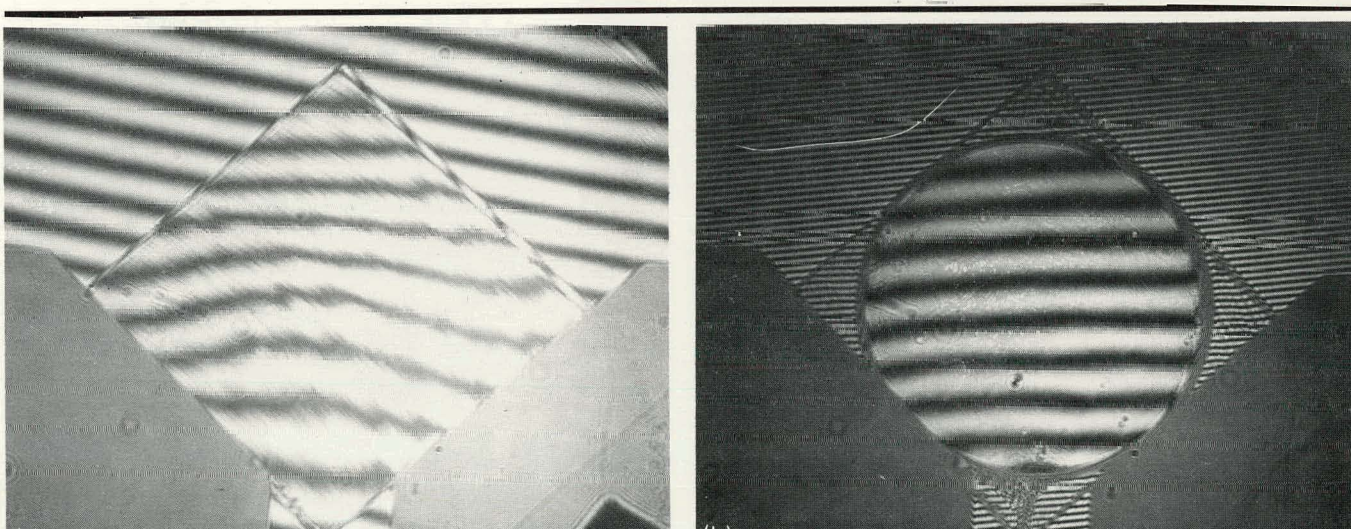

- Pneumo Precision.
- Intop (Division of Kollmorgen).
- Moore Precision Tool Co.

We sent data from the machining tests at LLNL to each vendor, and we followed up with visits to the vendors. The vendors were supplied with sample KDP material for machining and, in some cases, specially designed diamond tooling for their test and evaluation. Personnel from the LLNL Optics Lab and Laser Program were sent on these initial trips to participate in and guide the machining tests.

Two vendors have returned finished samples, which have been evaluated at LLNL[157] for surface finish and flatness. The surface-roughness values of these samples ranged from 30 up to 74 Å, and the flatness ranged from $\lambda/6$ to $\lambda/2$ at 0.6328 μm.

We believe that, with proper test equipment and fixturing, at least two of the vendors would be able to handle the Nova finishing requirements, with LLNL serving as a backup. However, we decided that the KDP crystals for the Novette laser will be precision machined at LLNL because

- Outside vendors could not be facilitized within the time constraints on Novette.
- Integration of the phase-matching instrumentation would be extremely difficult if we were to work with outside vendors.
- Time is needed to develop the type of tooling, tolerances, and finishes that are part of any new technology.
- The best available technical expertise and precision machinery are at LLNL.

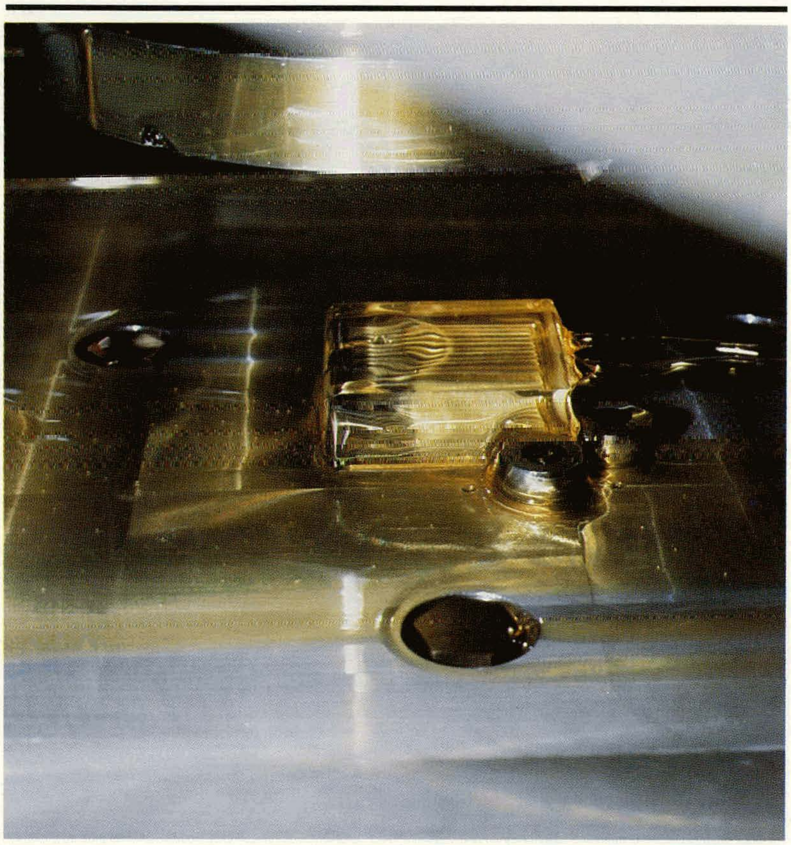

Fig. 2-342. Machining of crystal faces on KDP using the DTM-1.

Since there is a critical requirement for orienting the crystal axes relative to the entrance and exit faces of the finished crystal segment, instrumentation has been designed and is being built to match the fixturing that will be used on the DTM-1. (Refer to the previous article, "Precision Orientation Apparatus," for details of this apparatus.)

Fixturing and tooling on the DTM-1 will use a precision-machined vacuum chuck mounted on a rotary table with five axis adjustments. We anticipate that a minimum of two and a maximum of five iterations will be required between diamond turning and phase-matching measurements before the crystals are finished. Typical tolerances are $\pm 10\ \mu$m on the face dimensions, $\pm 5\ \mu$m on the thickness, and $\pm 60\ \mu$rad on the phase-matching angle. Edges and bevels will also be done on the DTM-1.

A prototype unit using 5-cm-square crystals in a 3 × 3 array will be built first to evaluate all aspects of the machining, tooling, phase matching, and assembly operations. More details on the prototype are available in "10-cm Crystal Array Prototype" earlier in this section. Our schedule requires completion of the prototype in May 1981, with machining to start on the large array by early August 1981.

Figure 2-342 is a view of a 5-cm^2 crystal being machined on the DTM-1. The crystal is mounted on a vacuum chuck and is registered by three precision locating balls. Figure 2-339 shows the same crystal mounted on a horizontal vacuum chuck to allow machining of the edges.

The LLNL Optics Group and the Laser Program have initiated a technical exchange with the KDP crystal growers and the precision-machining vendors. This exchange includes assistance in developing polishing and testing methods, keeping vendors current on diamond-turning technology, and implementing diamond-machining procedures, if feasible.

LLNL has recommended procedures for using diamond tools in conventional milling machines and blanchard generators for finishing KDP blanks. These procedures have already been incorporated by Interactive Radiation, Inc. (Inrad), and we have received nine KDP crystals, 5 × 5 cm square, from Inrad that have been finished to our blank requirements by use of a diamond-finishing technique. These crystals were evaluated interferometrically with oil-on-plates contacted to the diamond-turned surfaces. Conventional finishing of these blanks would have involved lapping and polishing before testing with oil-on-plates and would have taken at least three times longer to complete. Our vendors are already experiencing a reduction in cost with simple adaptations to diamond finishing. Further modifications and upgrading will result in additional cost savings in the near future.

In summary, we believe that diamond turning of KDP crystals will enable us to achieve the specifications for Novette and Nova. This technique is expected to reduce finishing costs and schedules by a factor of 4. The initial Novette crystals will be finished at LLNL, while Nova requirements will be met by outside vendors.

LLNL personnel are working with our KDP growers to upgrade their capabilities in conventional finishing, testing, and precision machining. Results from one vendor already indicate cost savings that can be attributed to this effort.

Authors: F. T. Marchi and P. C. Baker

Major Contributors: J. Bryan, J. Williams, R. Watson, and R. L. Martinek

KDP Crystal Growth. Our desire to produce short-wavelength laser pulses by harmonic generation with our current and future Nd:glass lasers has stimulated development of growth techniques for large KDP crystals. The Nova laser, according to the present design, will use ~300 27-cm-square KDP plates to convert all 20 Nova infrared beams to either green or ultraviolet wavelengths.

Both the number and size of these crystals are much larger than what the KDP manufacturers had produced as of early 1980. We therefore initiated development programs in two areas. The first program is a seed-development program designed to aid the crystal growers in increasing both the KDP crystal size and the growth capacity. The second program is an investigation into growth techniques to speed up the KDP growth rate. Presently, we have 27-cm seeds available, and several large crystallizers are either operating or under construction.

We describe in brief the commercial growth techniques. Potassium dihydrogen phosphate (KH_2PO_4, or KDP for short) is a crystal of tetragonal symmetry (space group, $I\bar{4}2d$). KDP crystal growers use a seeded-growth technique to produce large crystals of high optical quality. In this technique, they place a KDP crystal, called the seed, in a supersaturated solution of the salt. The crystal grows as new crystal material deposits on the {101} surfaces, shown in Fig. 2-343. Normally very little growth occurs on the {100} surfaces; thus, the net crystal growth is along the [001] axis, the crystallographic c-axis. As the crystal boule grows, a temperature controller lowers the solution temperature to maintain the supersaturation; a temperature drop from 65 to 35°C is common. A plastic fixture holds the crystal seeds, and a motor rotates the crystals through the solution, first one way and then the other. Because Holden[158,159] first used this type of crystallizer tank, which is illustrated in Fig. 2-344, the tank is now known as the Holden crystallizer.

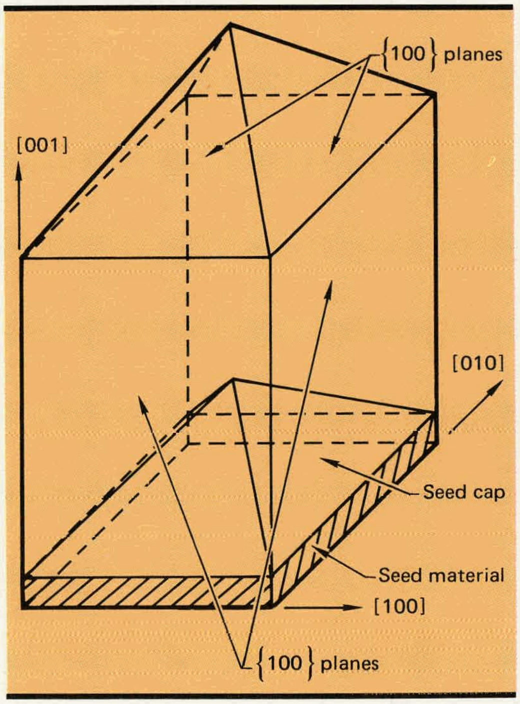

Fig. 2-343. KDP crystal boule, showing the seed material on which growth is initiated, the seed cap, and the crystallographic planes.

Fig. 2-344. Typical solution-growth apparatus for growing water-soluble crystals.

The crystal growers employ pieces cut from previously grown crystals as seed material. Because very little growth occurs on the {100} surfaces, the seed size determines the maximum cross section. If the growers wish to increase the seed size, they change the solution pH and impurity ion levels to promote {100} growth.

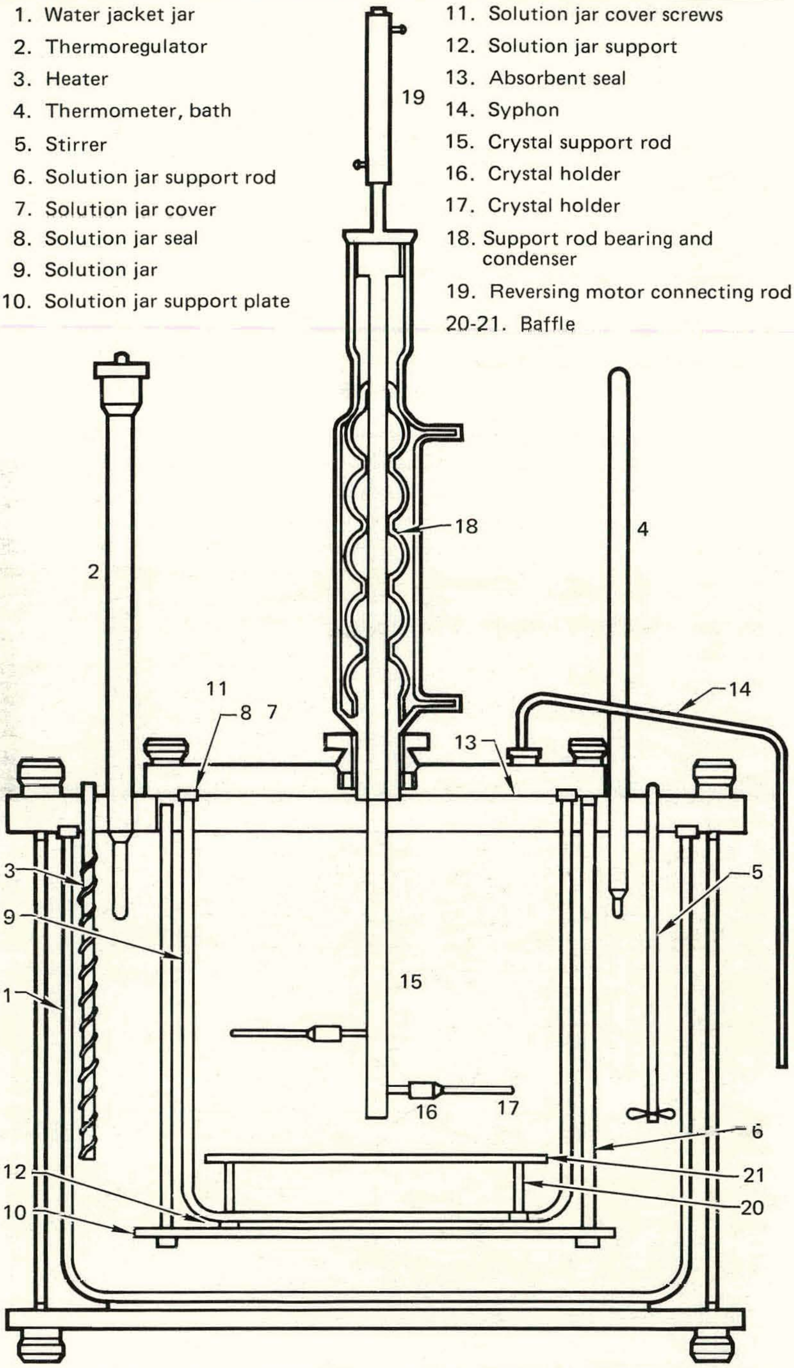

Growth rates along [001] vary from 0.5 to 1.2 mm/d; thus, the elapsed time from the planting of the seed until the boule is removed, or harvested, from the solution is many months. In Fig. 2-345, we plot as a function of boule width the total growth run time that is typical in the industry. This long growth time is one disadvantage of solution-grown crystals.

In 1980, we initiated a program with Dr. G. Loiacono of North American Philips, Inc., to investigate faster growing KDP crystals using a constant-temperature, constant-supersaturation technique. In this technique, the crystal grows in a tank that is kept at constant temperature and, as the crystal grows, the growth solution is replenished from a saturation tank containing KDP solution and salt, which is at a temperature higher than that of the growing tank. Christensen, Walker, and Kohman[160,161] employed this type of system to grow ammonium dihydrogen crystals in the late 1940s. We show a schematic of this multitank system in Fig. 2-346. The third, or stabilizer, tank in the system, which is held at a temperature higher than that of the other two tanks, dissolves any residual micro-crystallites that may have passed through the solution filter.

No commercial KDP crystal grower is using the multitank system, primarily because of its complexity and higher capital cost. However, this system allows better control of the supersaturation than does the Holden crystallizer. We believe that high-optical-quality crystals can be grown faster in multitank systems: several experimenters have obtained KDP growth rates of 2 to 5 mm/d in such systems.[162–165]

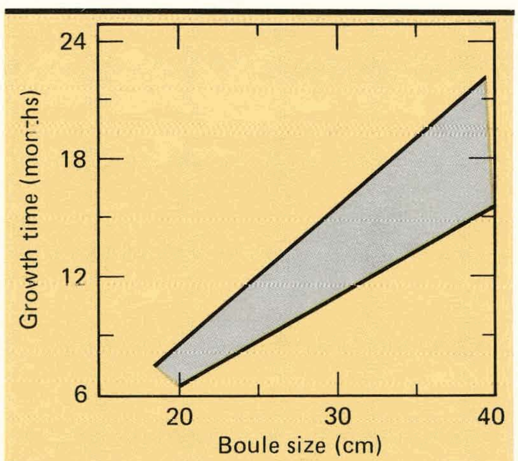

Fig. 2-345. Total growth time for KDP crystal boules vs size.

North American Philips is constructing a multitank system, using a 40-litre growth tank, a 25-litre saturation tank, and a 25-litre stabilizer tank. They plan to start KDP growth in January 1981. We at LLNL will be measuring the optical quality and laser-damage threshold of their crystals.

In our present design for harmonic generation in Nova, we plan to use 3 × 3 arrays of KDP crystal plates to cover the 74-cm aperture. Thus, each plate will be ~27 cm square. At the beginning of 1980, crystals and seeds of this size did not exist; therefore, we supported the crystal-growing companies in a program to develop seed material of this size from the existing 20-cm seed stock. Cleveland Crystals, Inc., Interactive Radiation, Inc. (Inrad), and Lasermetrics, Inc., are participating in this program. To grow the larger seeds, they had to construct larger tanks, such as the one in Fig. 2-347, and to cause crystal growth primarily on the {100} surfaces.

The companies started growth in May and June 1980 and have progressively increased the seed size. So far, the largest seed obtained is 37 cm on a side; this seed is shown in Fig. 2-348. The quality of this particular seed is marginal, and Cleveland Crystals has placed part of it back into solution to grow better-quality material. As a result of our seed program, we presently have ~8 large (>27 cm) crystal boules from which the KDP growers can obtain seed material. They are now growing the additional seed material needed to cover the harmonic conversion of Phase I Nova.

According to our schedule, growth of actual KDP plates for Phase I Nova can start by the summer of 1981. Meanwhile, Inrad and Cleveland Crystals are supplying us with 34 pieces of 15-cm-square, 2-cm-thick KDP to be used on the Novette laser as a 5 × 5

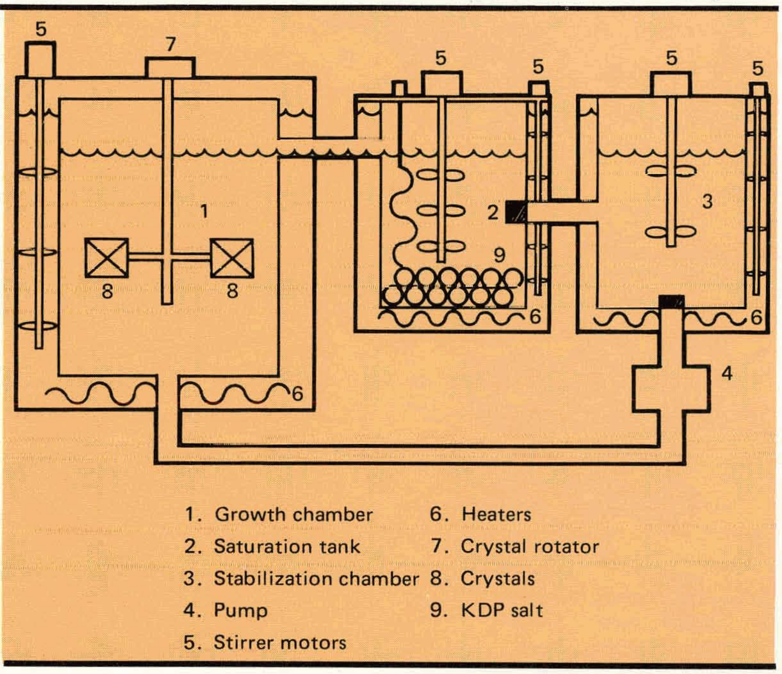

▲ Fig. 2-346. Crystallizer for growth at constant supersaturation and temperature. (Courtesy of Philips Laboratories, Inc.)

Fig. 2-348. A 37-cm KDP seed crystal grown in the KDP seed-development program. (Courtesy of Cleveland Crystals, Inc.)

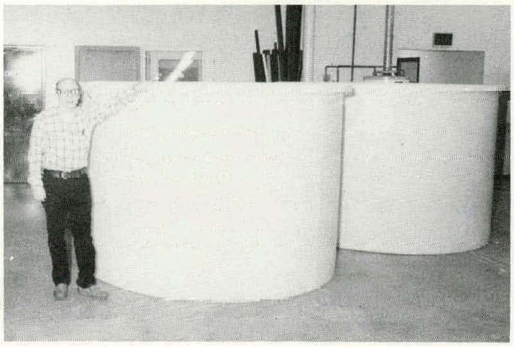

◀ Fig. 2-347. Construction of a 6000-litre growth tank showing inner liner of the tank.

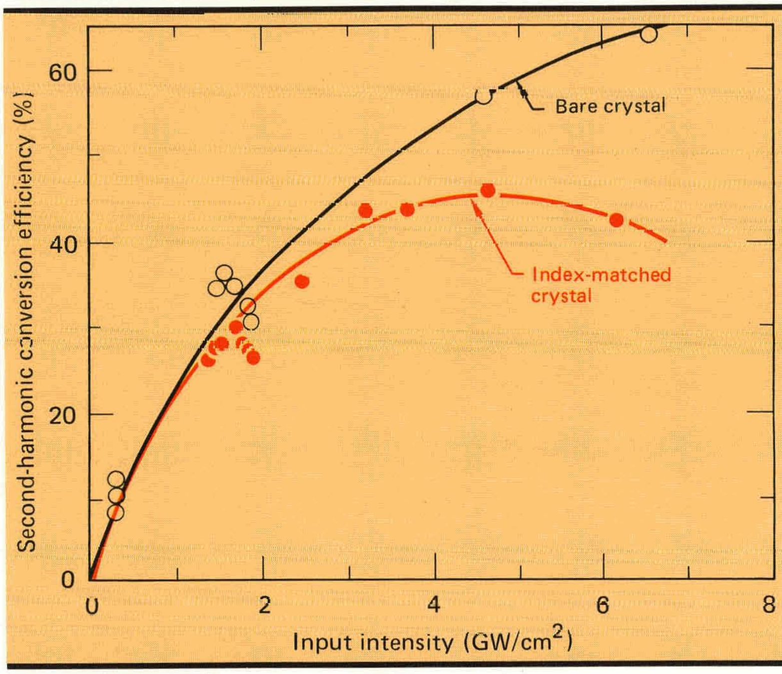

Fig. 2-349. Second-harmonic energy-conversion efficiency vs incident 1064-nm intensity from the Argus laser (8-cm aperture). ▲

array for frequency conversion at the 74-cm aperture. These two vendors now have in growth tanks enough material to supply 12 plates with dimensions of 27 × 27 × 2 cm. These plates will comprise a second array for Novette. Deliveries of the 15-cm crystal plates will be complete in February 1981; final deliveries of the 27-cm plates will be in October 1981.

Author: S. E. Stokowski

Major Contributors: International Radiation, Inc., Cleveland Crystals, Inc., Lasermetrics, Inc., and North American Philips, Inc.

Index-Matching Fluids for Large Apertures. Index-matching fluids (IMF) are transparent liquids used to fill the interstitial regions between individual elements in an optical device. The primary function of these fluids is to minimize the transmission loss and interference effects that would otherwise result from Fresnel reflections at surfaces that cannot be AR coated. In addition, for

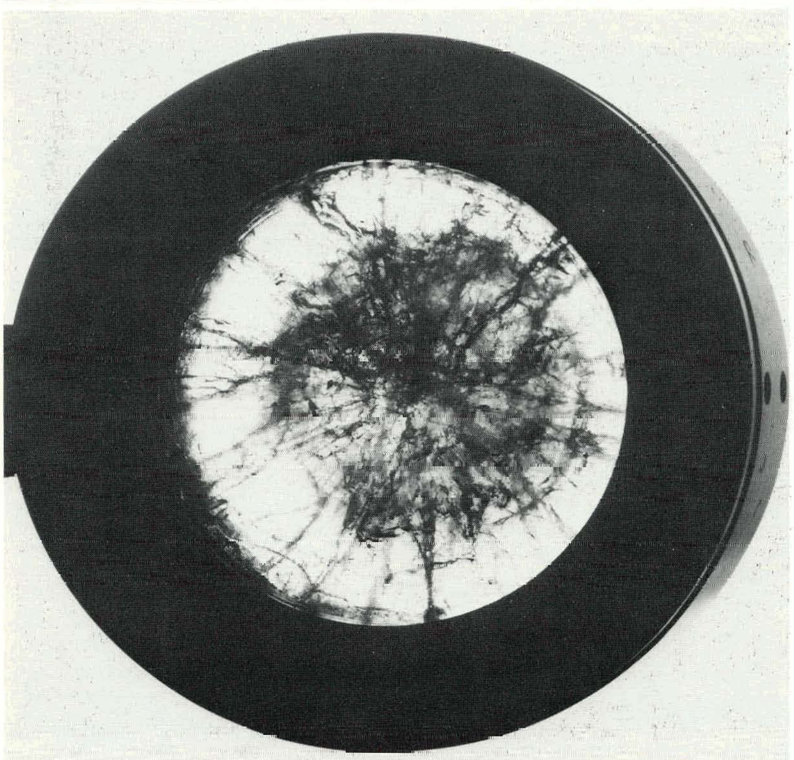

Fig. 2-350. Design of typical fluid-filled harmonic-generation cells used for early 10-cm Argus experiments.

Fig. 2-351. Harmonic-generation cell shattered by a 20 GW/cm², 1064-nm laser pulse. ▶

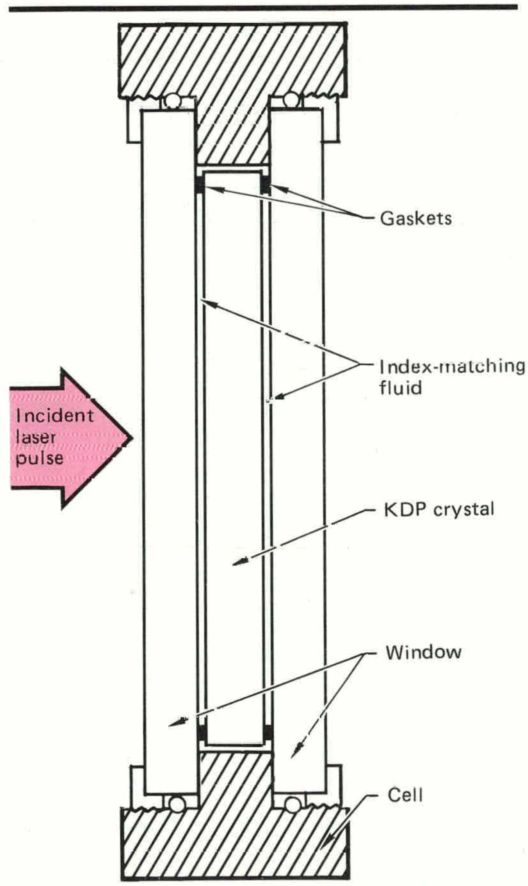

difficult-to-fabricate optical elements that can be immersed in IMF between windows, the IMF relaxes otherwise stringent requirements on the surface finish necessary for wavefront-transmission quality. KDP, used for harmonic generation and in Pockels-cell modulators, is customarily housed in IMF to protect its hygroscopic surfaces, as well as for the above reasons.

In October 1979, we began harmonic-generation studies using spatially flat 8-cm-aperture pulses at 1.06-μm wavelength from the Argus laser (see "Argus Frequency Conversion Experiments," above). Early in 1980, it was determined that the index-matching fluid used in the second-harmonic-generation cell was the source of a significant loss of second-harmonic energy. The data supporting this conclusion are shown in Fig. 2-349 (opposite). A 10-mm Type I KDP doubling crystal was tested in an IMF-filled cell fitted with AR-coated windows. The fluid used was a conventional commercial product, Cargille 5610 oil (Cargille Laboratories, Cedar Grove, N.J.) Afterward, this crystal was removed from the cell, cleaned, and retested with a bare surface. Its conversion efficiency increased substantially for input intensities over about 3 GW/cm^2, as Fig. 2-349 illustrates. Subsequent tests, described below, identified the loss process to be stimulated Raman scattering.

A more dramatic failing of the index-matching fluid occurred in June 1980 in the Argus harmonic experiments. An excessively intense (20 GW/cm^2) pulse was inadvertently fired into a doubler cell (Figs. 2-350 and 2-351). The cell shattered. The IMF in this cell was a commercial fluorocarbon, FC104 (3M Co., St. Paul, Minn.). Figure 2-351 shows the typical design of this cell, and Fig. 2-350 shows its remains, which have been bonded together with epoxy. The manner in which this cell broke is not typical of laser-induced damage; rather, it suggests that pressure, generated by heating the IMF to its relatively low boiling temperature (101°C), burst the cell. As shown in Fig. 2-350, the IMF volume was defined at the edge by a black rubber gasket material. This material would have been heated by the deposition of a significant portion of the transversely-scattered 750-J laser pulse.

Stimulated Raman scattering and stimulated Brillouin scattering (SRS and SBS, respectively) are well-known processes in the field of nonlinear optics.[166] In liquids, SRS arises from the interaction of a light wave with a coherent Raman vibration; with SBS, the material vibration is an acoustic wave. Figure 2-352 illustrates these interactions. In both processes, a laser photon of frequency ν_L is scattered in a material interaction, adding a photon to the scattered wave of frequency $\nu_S = \nu_L - \nu_{vib}$. In Fig. 2-352(a), the interaction involves a molecular vibrational transition, while, in Fig. 2-352(b), an acoustic-frequency wave is the scatterer. Typical frequency shifts shown in Fig. 2-352(a) are 300 to 3000 cm^{-1}, and those shown in Fig. 2-352(b) are ~1 cm^{-1}.

We are concerned here with the intensity, I_S, of the scattered wave, which grows

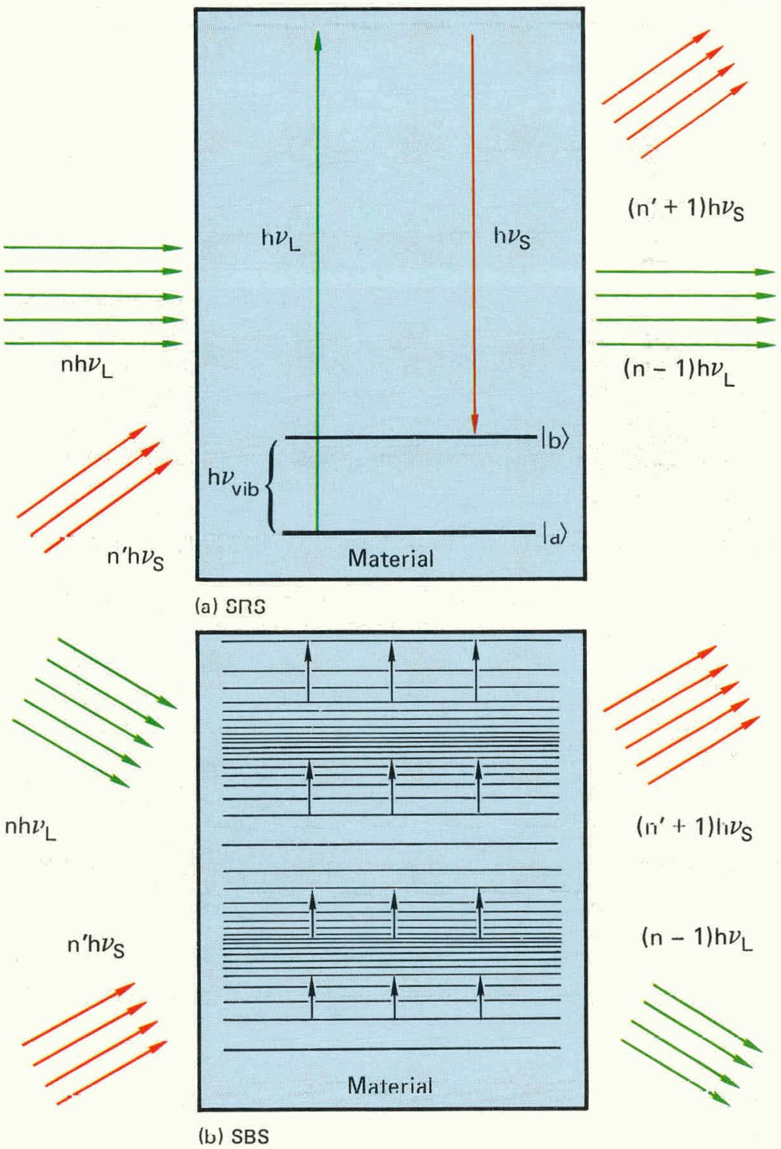

Fig. 2-352. Schematic illustration of (a) stimulated Raman scattering and (b) stimulated Brillouin scattering.

exponentially over a path length, z, at the expense of the laser wave, I_L:

$$I_S(z) = I_{So} \exp(g I_L z) \quad . \qquad (75)$$

Scattered waves of intensity comparable to the incident laser wave can be readily generated.

For SRS, the gain coefficient[166] is

$$g_R = \frac{8\pi^2 (\omega_L - \omega_{vib}) N |\partial\alpha/\partial Q|^2 n_L}{\omega_{vib} \Gamma_R c^2 n_s} \quad , \qquad (76)$$

where N is the number of scattering molecules per unit volume, $\partial\alpha/\partial Q$ is the molecular differential polarizability, Γ_R is the line width of the Raman vibrational transition, c is the speed of light, ω_L and ω_{vib} are the laser and Raman transition frequencies, respectively, and n_L and n_s are the refractive indices at the laser and Stokes wavelengths, respectively. For SBS, the gain coefficient[166] in a transparent material is

$$g_B = \frac{(\omega_L - \omega_{vib})^2 |\gamma^e|^2}{n_L V_{vib} c^3 \rho \Gamma_B} \quad , \qquad (77)$$

where Γ_B is the line width of the acoustic vibration, ω_{vib} is the Brillouin frequency, ρ is the fluid density, γ^e is the electrostrictive coupling coefficient, and V_{vib} is the phonon velocity; the other parameters were defined above for Eq. (76).

Several approaches are available to eliminate transverse-stimulated Raman or Brillouin loss processes. We can select, according to structure and chemical composition, a fluid having low Raman or Brillouin gain. By mixing several fluids whose Raman frequencies do not overlap, the effective Raman gain is reduced. We can add to the fluid an absorber that is chosen so that the optical loss diametrically across the aperture is large, but the optical loss through the thin fluid layer is very small. The fluid region can be made thin, thereby increasing the diffractive loss to the transverse wave; for a thin geometry, waveguiding is circumvented by keeping the fluid refractive index smaller than that of the windows. And we can introduce absorbing beam blocks to divide the aperture into manageable cells.

Effecting the first of the approaches listed above, we measured the threshold for the production of SRS in conventional IMFs and in fluids chosen for low stimulated gain. The experimental layout for this measurement is shown in Fig. 2-353. The collimated 1.06-μm (fundamental) pulses from the ILS laser were frequency doubled in a Type II KDP crystal, yielding linearly polarized 0.53-μm (harmonic) pulses of up to 0.5 J. Most of the diagnostic equipment shown in Fig. 2-353 is needed to measure the intensity of the laser pulse incident on the sample cell and the energy transmitted through the cell. Since the gain for the stimulated scattering processes is higher at the harmonic frequency, we concentrated

Fig. 2-353. Experimental apparatus used to investigate loss mechanisms in index-matching fluids.

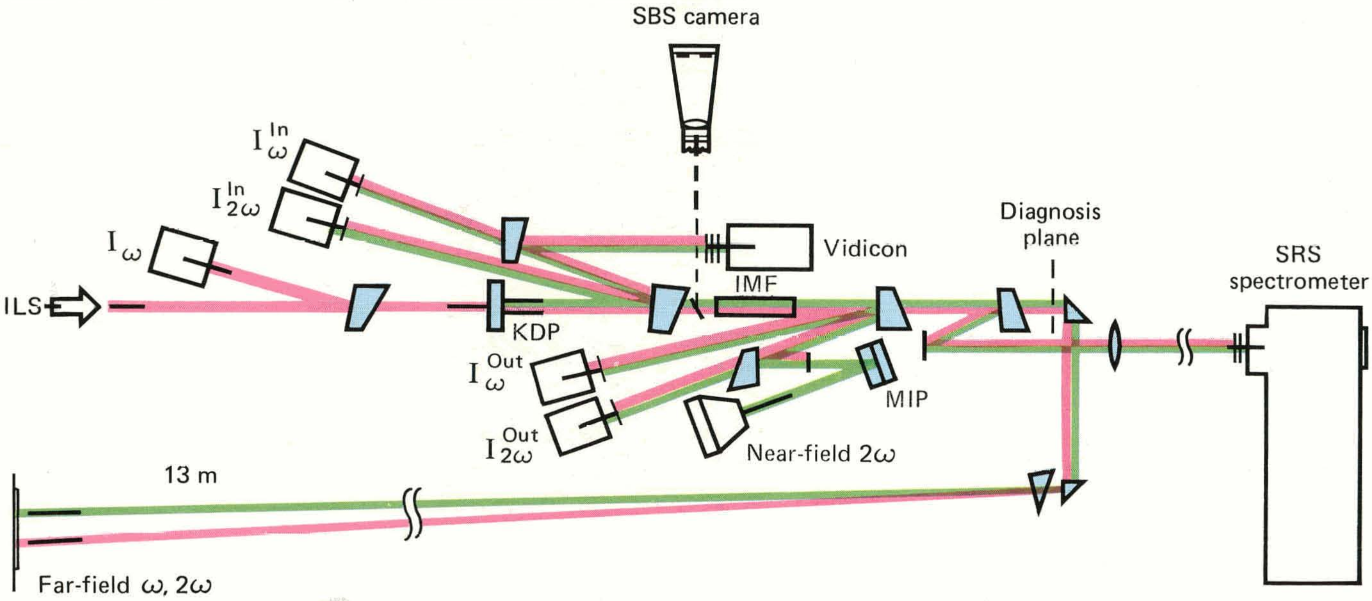

our diagnostics on the harmonic pulses. An LLNL-designed absorbing-glass calorimeter and a calibrated silicon vidicon camera with associated computer equipment were used to measure the energy and spatial profile of the incident harmonic pulse. Another calorimeter measured the incident fundamental energy. The spatial diameter of the harmonic pulse at the sample cell was typically 3 mm. The fluids were contained in silica or glass cells with a standard length of 8 cm.

The laser produced pulses of either 1.0 or 0.1 ns (Gaussian FWHM) for this work. For the harmonic pulses, we used 0.707 times the fundamental duration to convert energy density to power density. The actual duration of the harmonic pulses was slightly longer and the intensity was slightly lower, depending on the degree of saturation in the doubling efficiency at the peak of each pulse. But, for the purpose of these measurements, streak recording of the temporal wave forms was not warranted.

Both the harmonic and fundamental pulse energies were recorded after the sample cell. From these values, the energy transmission through the cell could be plotted vs incident intensity. Beam-splitter angles were carefully measured and, with the sample removed, the input and output calorimeters agreed on the energy content at the sample position to within 2%.

Additional diagnostics were used to indicate the onset of self-focusing effects resulting mainly from the propagation of the laser pulse through the fluid path of up to 16 cm in length. As shown in Fig. 2-353, a multiple-image camera was used to monitor the spatial profile of the harmonic pulse in the near field of the sample cell. The spatial profile at both wavelengths was also recorded at a distance of 13 m from the sample cell. This "far-field" recording indicated that beam breakup occurred routinely when the 16-cm path length was used and, under some conditions, even with shorter fluid-path lengths. However, the multiple-image camera certified that appreciable changes in the spatial profile due to self-focusing did not occur in the near field. One exception, regarding the observation of self-phase modulation in an extreme case, will be mentioned below.

Because of the necessary path length from the sample to a measuring device, we cannot measure the laser pulse shape at the output face of the sample cell. We located the diagnosis plane at a position beyond the sample, as shown in Fig. 2-353, so that both input and output diagnostic equipment sampled the pulse after the same propagation distance. Since the laser was collimated to $\gtrsim 150\ \mu$rad divergence, there was no appreciable error from this procedure.

The final group of diagnostic components in Fig. 2-353 was used to indicate the onset of SRS by spectral signature. The output surface of the sample cell was imaged onto the slit of a McPherson 1.0-m grating spectrometer. A neutral-density filter (OD = 2.0) eliminated stray light, and a Corning 3-67 color filter reduced the harmonic-wavelength energy entering the spectrometer. On each laser firing, a spectrogram was recorded. The series of spectrograms for acetonitrile is shown in Fig. 2-354. The incident intensity ($I_{2\omega}$) increases from bottom to top. The line of varying brightness in the series is the stimulated Raman

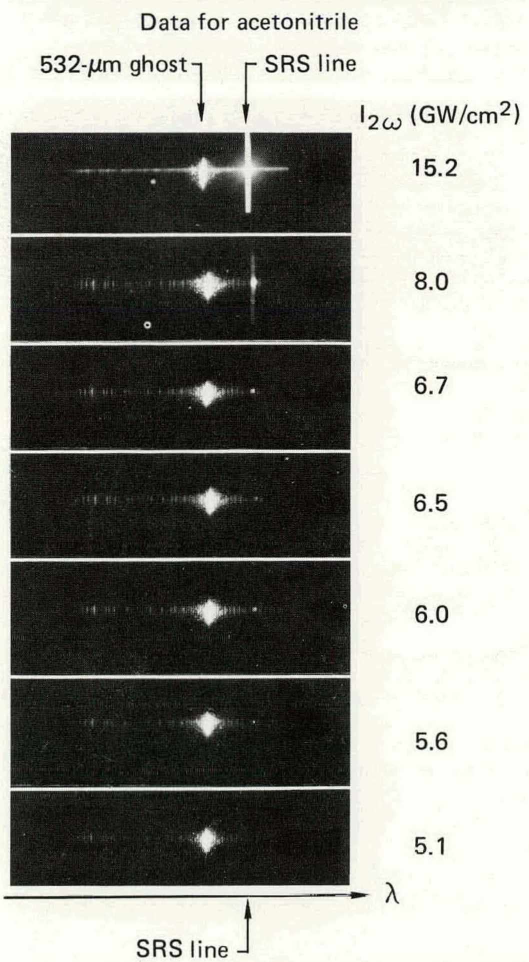

Fig. 2-354. Spectrograms of frequency-shifted light emitted by acetonitrile for seven 532-nm laser shots.

emission at 630.9 nm. The lowest harmonic intensity incident on the sample fluid for which no light was detected at the characteristic Ràman-shifted wavelength was recorded as the SRS threshold for that fluid. The SRS threshold for acetonitrile is 5.6 GW/cm^2. Figure 2-355 shows the harmonic transmission vs incident intensity and the SRS threshold for decahydronaphthalene. The decrease in transmission begins at the stimulated Raman threshold intensity, identified by wavelength signature as shown in Fig. 2-354. The low-intensity transmission of this cell, measured independently, is 80.3% at 532 nm. Although we recorded the fundamental-pulse energy transmission as well, we found that the loss processes were driven by the harmonic pulse in all the fluids.

We tested 10 fluids, two of which, the previously mentioned Cargille 5610 and FC104, have been widely used by the manufacturers of small-aperture Pockels cells and harmonic-generation cells. Cargille 5610 is a mixture of low-index and high-index silicone oils; FC104 is a perfluoroalkane. Five of the other fluids tested were hydrocarbons that, either neat or in mixtures, have refractive indices very close to the desired value; they were acetonitrile, benzonitrile, decahydronaphthalene, tetrachloroethylene, and xylene. We also tested two polymeric fluids that are new to high-power laser applications: polychlorotrifluoroethylene and polybromotrifluoroethylene. These two fluids are marketed under the names Halocarbon 56 and BFC-57, respectively, by Halocarbon Products Corp., Hackensack, N. J. We used benzene in the initial setup work in this experiment because of its known SRS parameters. Except where noted, the sample length was 8 cm.

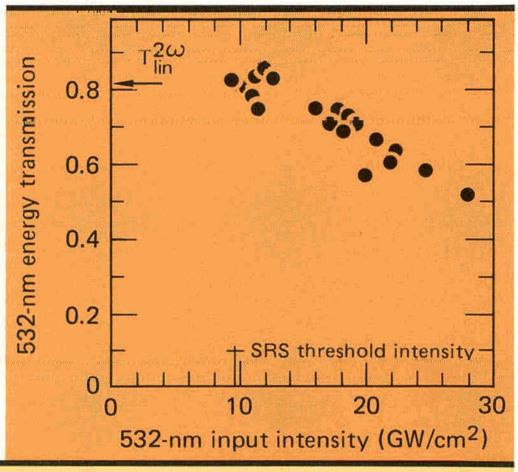

Fig. 2-355. Transmission of 532-nm pulses through 8-cm path of decahydronaphthalene for two pulse durations.

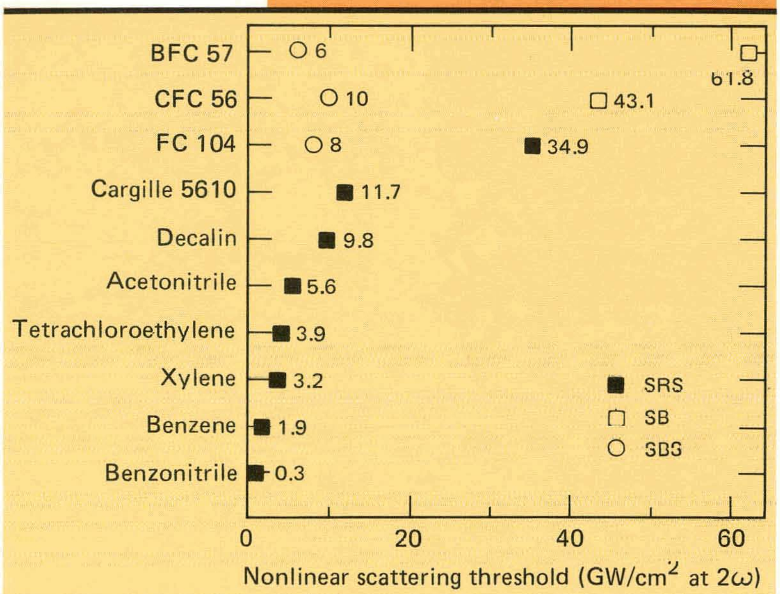

Fig. 2-356. Threshold intensity for stimulated Raman scattering in 10 index matching fluids, measured with the apparatus shown in Fig. 2-353. ▼

Our results are summarized in Fig. 2-356. The straight hydrocarbon fluids were all found to have SRS thresholds lower than Cargille 5610. FC104 showed a high threshold, as expected from the low polarizability of its perfluorinated structure. For the same reason, we expected the polymeric fluids to exhibit high thresholds; encouragingly, they showed no stimulated Raman output, even in the 16-cm path and at incident intensities up to those high enough to cause advanced spectral broadening (superbroadening), which arises from self-focusing. In Fig. 2-356, the thresholds for the observation of superbroadening (SB) in these two fluids are plotted as open squares. We will address in the future the question of whether the polymeric structure itself contributes to this high threshold.

Athough no SRS was detected from the polymer fluids, or from FC104 up to a rather high threshold, harmonic energy loss was detected. The data for BFC 57 in Fig. 2-357 illustrate typical behavior for these three fluids. To identify the cause of the transmission loss evident in Fig. 2-357 for the 0.7-ns pulses, we reduced the harmonic pulse duration to 0.07 ns and fired additional shots of equal and greater intensity—the open circles in Fig. 2-357. No transmission loss was observed for these shots, thereby eliminating two-photon absorption and supporting SBS as the cause. A cursory look for backward-traveling SBS, using the

Fabry–Perot camera shown in Fig. 2-353, indicated the presence of a second wavelength. The thresholds indicated by open circles in Fig. 2-356 show the onset of the transmission loss of the harmonic energy in 8 cm of those three fluids; we tentatively attribute this effect to SBS.

During these tests, we found that polybromotrifluoroethylene became yellow from exposure to bright fluorescent room lighting. This instability terminated our interest in this fluid. However, subsequent UV solarization tests performed at the University of Rochester[167] showed no change in the absorption spectrum of polychlorotrifluoroethylene.

In summary of the tests described above, if geometry or other aspects of a particular application rule out the growth of SBS, then the growth of SRS can be minimized by choosing either FC104 or Halocarbon 56 as the index-matching fluid. Because the refractive index of Halocarbon 56 (1.403 at 1064 nm) is a better match to KDP and to window materials than that of FC104 (1.271 at 1064 nm), Halocarbon 56 is the overall recommended index-matching fluid.

We used the North arm of the Argus laser and the apparatus shown in Fig. 2-358 to test the candidate index-matching fluids in the required transverse geometry. The 28-cm aperture of the Argus beam was reduced to 8 cm, and a 10-cm Type II KDP crystal was used to frequency-double the pulses. Energy transmissions through the IMF cell at the fundamental (ω) and harmonic (2ω) frequencies were measured with calorimeters. Transversely scattered light was directed by fiber-optic cable to grating and Fabry–Perot spectrometers. The fundamental pulse duration was 0.7 ns, and the spatial profile was nominally flat. Pulses of up to 3 GW/cm^2 harmonic intensity were generated. Beam splitters and calorimeters placed before and after the sample cell measured the energy transmission at both the fundamental and harmonic wavelengths.

The sample cells used silica windows to contain a 10-cm-diameter sheet of fluid that was either 1.0 or 0.0125 mm thick. Fiber-optic cables mounted at the edge of the fluid were used to route into spectrometers any light scattered transversely out of the beam.

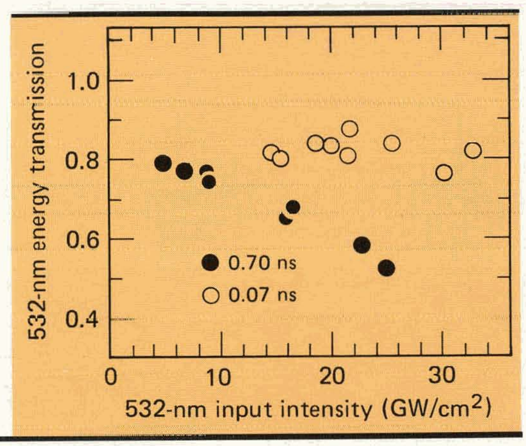

Fig. 2-357. Transmission vs incident 532-nm intensity for 8-cm sample of polybromotrifluoro ethylene (BFC 57) for two pulse durations.

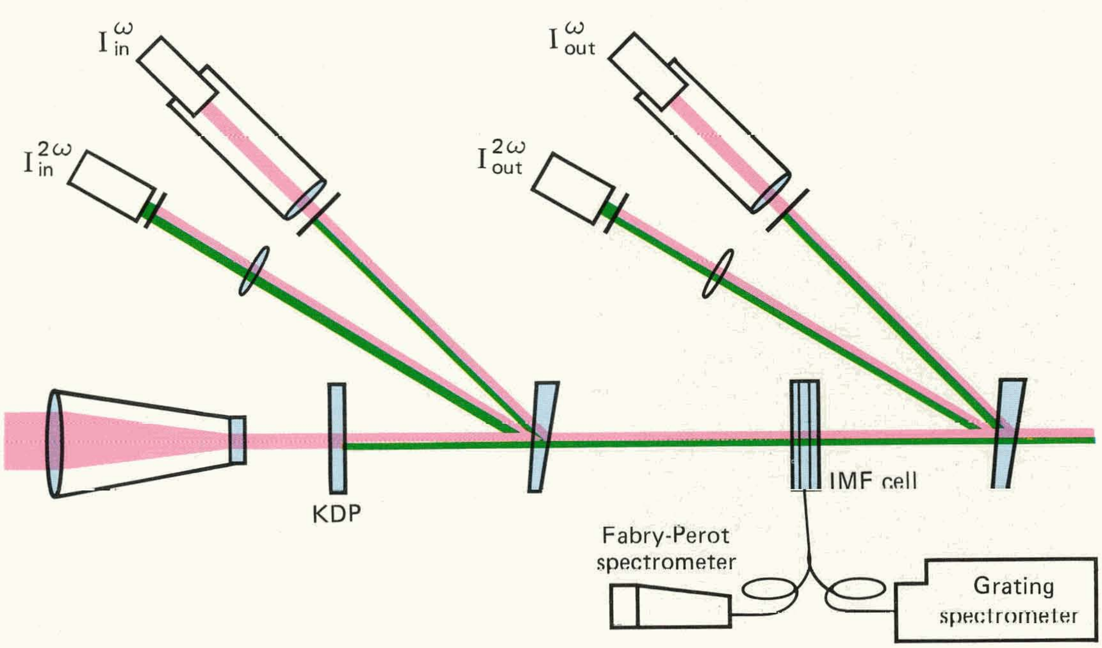

Fig. 2-358. Diagram of the Argus stimulated-loss experiment on index-matching fluids.

The same grating spectrometer and Fabry–Perot camera mentioned above were used for the Argus tests.

The first test employed a 1-mm layer of Cargille 5610 fluid to recreate the original Argus observation. A shot of 2.3 GW/cm^2 incident harmonic intensity induced a transmission loss of 16% of the harmonic energy, in good agreement with the earlier observations. Furthermore, the spectrogram showed the presence of light shifted in frequency by 2933 wave numbers, identifying the loss mechanism in Cargille 5610 to be SRS. A second test of Cargille 5610 in a 0.0125-mm layer at similar intensity showed no measurable transmission loss (<1%), but still gave a Raman-shifted signal on the spectrometer. This result indicates that the thinness of the layer was only marginally capable of preventing stimulated loss in this fluid. We also encountered a damage problem, as Fig. 2-359 indicates. The dense field of bubbles and scattering sites was created as the laser pulse heated foreign matter in the fluid.

Further Argus tests investigated FC104 and Halocarbon 56 fluids in 0.0125-mm layers. We solved the damage problem by filtering the Halocarbon 56 fluid in stages down to a pore size of 0.08 μm to remove the particulate matter and trapped gases. The final test on Argus showed no stimulated loss or damage in the polychlorotrifluoroethylene at a harmonic intensity of 2.3 GW/cm^2.

In summary,

- We ranked 10 index-matching fluids and, from them, selected Halocarbon 56 and FC 104 as promising for use at 1064-nm and 532-nm wavelengths.

Fig. 2-359. Photograph of laser-induced damage sites in a 12.5-μm layer of Cargille 5610 index-matching fluid.

- We demonstrated loss-free performance for these two fluids in 0.0125-mm layers at the 532-nm wavelength and at an intensity-aperture product of up to 18 GW/cm.
- We established a procedure for filtering the fluids to eliminate damage effects.
- The fluids recommended are highly inert, safe for extended human contact, and compatible with KDP.
- A scale-up experiment for testing at the Nova/Novette intensity-aperture product of 225 GW/cm is being planned for the Argus laser in early 1981.
- The results and techniques reported here are valuable for the future selection of an index-matching fluid for use at 355 nm.

Author: W. L. Smith

Major Contributors: D. Eimerl, B. L. Freitas, P. R. Hammond, G. J. Linford, W. H. Lowdermilk, and M. C. Staggs

Wavelength Separation Filters. When we produce visible (2ω) or ultraviolet (3ω) light with a Nd^{3+} glass laser by harmonic generation in a nonlinear optical material, residual light of the lower frequencies is present. This light must be removed before it enters the fusion target chamber because it will detrimentally affect target performance and the target diagnostic instruments. We can use filters that either absorb or reflect the unwanted frequencies to remove the residual light.

For the Nd^{3+} glass laser operating at 1053-nm (or 1064-nm), we need 2ω-filters that have <1% transmission at the laser wavelength and >99% transmission at 527.5 nm (or 532-nm) when coated with an AR film. A 3ω-filter must transmit <1% of the 1053- and 527 nm light and must transmit >99% at 351-nm (or 355-nm). No commercially available filters meet these requirements. Thus, in 1980, we initiated development of both absorptive and thin-film filters to meet these specifications in the 80-cm diameter needed for Nova.

Summarizing our results, we have found excellent candidates for the absorptive 2ω filter, and we are progressing well in developing 3ω filters.

The effectiveness of an absorptive filter for wavelength separation depends on the ratio between absorption coefficients at different wavelengths. We illustrate this dependence in Fig. 2-360, which displays the internal transmission loss at the desired wavelength vs the transmission at the rejected wavelength, with the absorption coefficient ratio as a parameter. To meet the transmission specification, the absorption-coefficient ratio must be above 500.

Absorptive filters are colored in most cases by transition-metal ions, such as Cu^{2+}, Fe^{2+}, Cr^{3+}, Ni^{2+}, Co^{2+}, and V^{3+}. The Cu^{2+} ion is the most useful for a 2ω-filter, as shown by the spectrum in Fig. 2-361. Commercially available filter glasses doped with Cu^{2+} are type BG-38, produced by Schott Optical Glass, and type C-500, produced by the Hoya Corporation. Transmission characteristics of these filters are listed in Table 2-69.

In 1980, Schott and Hoya modified their commercial filter glasses by lowering the Cu^{2+} concentration, and they now have 2ω filter glasses with the improved absorption characteristics listed in Table 2-69. Both companies are now working towards scaling up the melt size to produce 80-cm pieces.

We have more difficulty in obtaining a 3ω filter glass that meets our specifications. The commercial filter glass UG-11, produced by Schott, does not have sufficient rejection of 1053-nm light. To improve these characteristics, we investigated the spectra of Ni^{2+} and Co^{2+} in phosphate and fluorophosphate glasses. D. Blackburn of the National Bureau of Standards melted some of these glasses for us. The measured absorption spectra of these glasses are shown in Figs. 2-362 and 2-363. We see that Co^{2+} is an excellent absorber in the green region. Unfortunately, Ni^{2+}, which we considered as a possible 1053-nm absorber, does not have an absorption band near 1053-nm. In this same period, Hoya and Schott initiated their own filter-development projects and have made progress towards increasing the

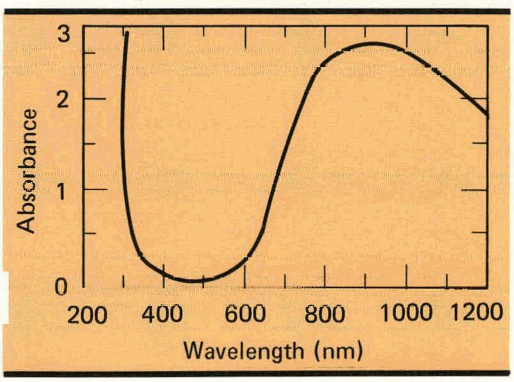

◀ **Fig. 2-361. Optical density of a 1-mm-thick phosphate glass sample doped with 1.5 wt% CuO.**

Fig. 2-360. Calculated characteristics for a wavelength-separation filter (shaded area shows acceptable range).

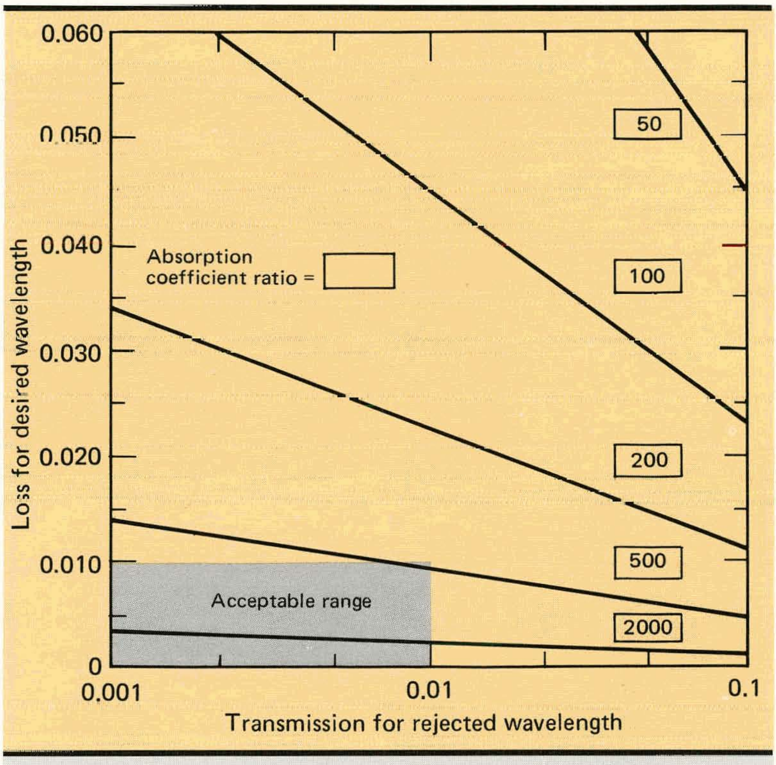

Filter type	Manufac-turer	Absorption coefficient (cm^{-1}) for 1053 nm	527 nm	361 nm	Ratios $\alpha(1053)/\alpha(527)$	$\alpha(1053)/\alpha(351)$	$\alpha(527)/\alpha(351)$
BG-38	Schott	26.6	0.19	2.1	140	12.7	–
C-500	Hoya	42	0.6	–	70	–	–
BG-38 (modified)	Schott	4.7	0.002	0.028	2350	168	–
LC-1	Hoya	9.3	0.04	–	233	–	–
UG-11	Schott	40.2	120	1.09	37	110	–
LC-14	Hoya	5.6	5.8	0.108	52	53	–
LC-1	Schott	–	14.4	0.026	–	–	552
Co-doped phosphate	NBS	–	4.8	0.021	–	–	228

▲ **Table 2-69. Absorption characteristics of wavelength separation filters.**

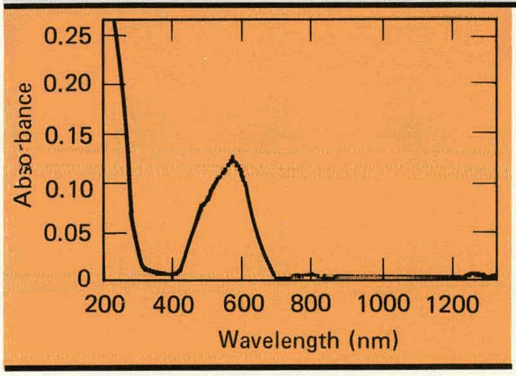

Fig. 2-362. Optical density of a 0.047-cm-thick phosphate glass sample with 0.5 wt% Co_2O_3 added.

$\alpha(1053)/\alpha(351)$ ratio. We plan to continue this effort in 1981.

At high laser fluxes, the filter transmission may decrease due to two-photon absorptive transitions. We examined the two-photon absorption coefficient, β, of the commercial filters BG-18, C-500, and UG-11 by subjecting them to 532-nm, 100-ps laser pulses with intensities of up to 3 GW/cm^2. We saw no change in filter transmission; therefore, β is <0.001 cm/GW and is not a problem in a Nova-type system.

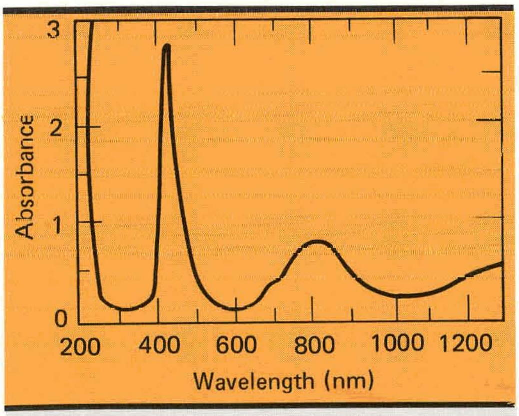

Fig. 2-363. Optical density of a 0.209-cm-thick phosphate glass sample with 3 wt% NiO added.

Thin-film filters separate wavelengths by selective transmission or reflection. In 1980, we funded Optical Coating Laboratory, Inc. (OCLI) and Spectra Physics to deposit thin-film, multilayer coatings for wavelength separation filters. These two vendors investigated the production of four filter designs for 2- and 3-ω filters that would meet the criteria listed in Table 2-70. In addition, we requested that the filters have the highest obtainable laser-damage thresholds.

In Fig. 2-364, we show schematically the spectral characteristics of designs Nos. 1 and 3, in which the desired short-wavelength component is transmitted. The coating manufacturers provided us with several samples of all four designs. The measured reflectivities and transmissivities of the best filters are shown in Table 2-71. In general, the spectral characteristics of the 2-ω filters meet our requirements, but the 3-ω filters need some improvement. We plan to test these filters for their laser-damage resistance early in 1981.

Table 2-70. Design criteria for reflective wavelength separation filters. ▶

Design No.	Wavelength 1064 nm (%)	532 nm (%)	355 nm (%)
1	R = >99	T = >95	N/A
2	T = >95	R = >99	N/A
3	R = >99	R = >99	T = >90
4	T = >95	T = >95	R = >98

Table 2-71. Measured characteristics for the best wavelength-separation filters. ▼

Design No.	1064 nm (%)	532 nm (%)	355 nm (%)	Vendor
1	R = 99.7	T = 98.5	N/A	OCLI
	R = 99.9	T = 97.9	N/A	Spectra
2	T = 99.4	R = 99.8	N/A	OCLI
	T = 99.0	R = 99.8	N/A	Spectra
3	R = 99.2	R = 98.9	T = 94.8	OCLI
	R = 99.3	R = 99.8	T = 82.3	Spectra
4	T = 96.3	T = 98.1	R = 97.7	OCLI
	T = 96.9	T = 95.8	R = 99.9	Spectra

Notes: Measurement at 1064 nm were made using laser photometers.
Measurements at 532 and 355 nm were made using a Cary 14 spectrophotometer.
Values are corrected for back-surface reflectance.

Authors: S. E. Stokowski and G. R. Wirtenson

Major Contributors: J. Lynch and W. L. Smith; D. Blackburn (National Bureau of Standards), Hoya Corporation, OCLI, Schott Optical Glass, and Spectra Physics

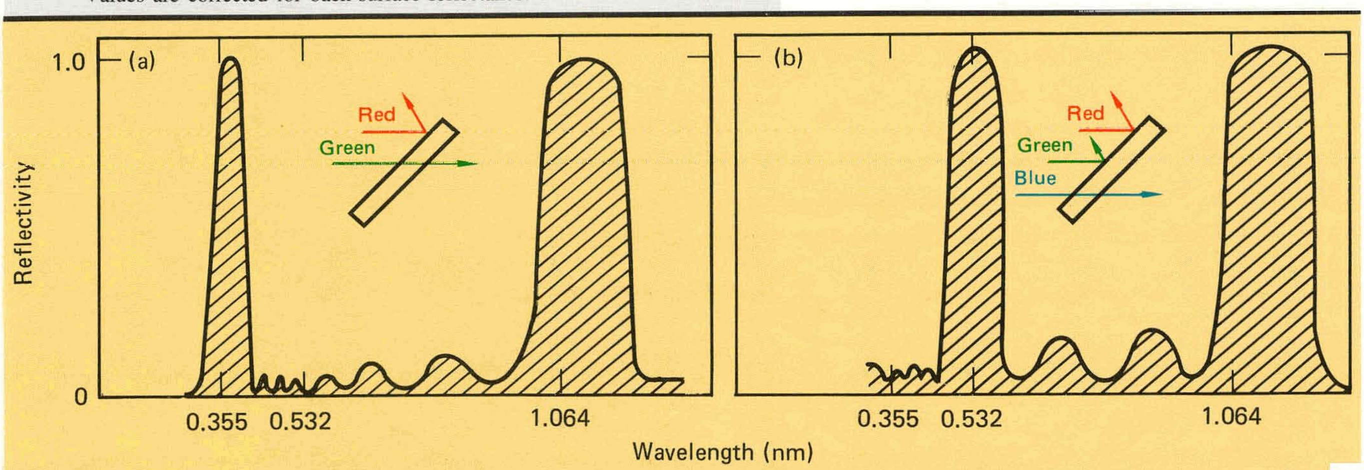

Fig. 2-364. Spectral characteristics for typical thin-film wavelength-separation filters. (a) Two-wavelength filter (design 1); quarter stack reflects 1053 nm and transmits 527 nm wavelengths. (b) Three-wavelength filter (design 3); 2:1 multilayer stack reflects 1053 and 527 nm and transmits 351 nm wavelengths.

Compensated Pulsed Alternator

Current Program. Research has been going on for many years to develop efficient repetitively pulsed power systems that can deliver several megajoules of electrical energy in pulse widths of 1 ms or less. Our interest in such systems stems from a desire to develop cost-effective alternatives to large capacitive energy-storage systems, such as those now being used to drive Shiva and being planned for Nova.

The compensated pulsed alternator "compulsator," first proposed by the University of Texas, Center for Electromechanics (UT-CEM),[168] is a device that stores very high energy density as kinetic energy in a rotor and then releases this energy in short electrical pulses with both high voltage and high current. This device embodies an original operating principle that overcomes self-inductance, the inherent limitation of ac machines as pulse generators. The theory of operation of the compulsator has been described in several previous reports,[169,170] and a prototype compulsator (Fig. 2-365) that was built and tested at the UT-CEM in 1979 has demonstrated these principles by delivering 139 kJ in 1.3 ms to a flashlamp load in a Shiva-type laser disk amplifier.

Summary. During 1980, we made significant progress toward understanding the basic concepts and limitations of the rotary flux compression method for converting stored inertial energy into high-power pulses of electrical energy. Our experimental efforts have been focused on evaluating the performance of the engineering prototype (15-in.-diam rotor) and modifying the prototype to correct the short-circuit fault deficiency that caused the termination of testing in December 1979.

In addition, a small machine (8-in.-diam rotor) was built to quantify inductance variation and to investigate pure flux compression. This machine was assembled with both rotor and stator laminated. Static and dynamic tests on this machine have shown very clearly that laminating the stator minimized eddy current losses and, indeed, makes possible a significant flux compression. An inductance variation of 45:1 has been both predicted and measured for this active rotary flux compressor (ARFC). We obtained a current gain of 10.3:1 with this machine operating at 3000 rpm—about one-third of its maximum speed. This was realized by pulsing flux into the gap from an external capacitor.

We developed computer codes and used them extensively to analyze the performance of the large 15-in.-diam prototype and the 8-in.-diam ARFC. We have obtained a high degree of confidence in our present modeling techniques by comparing computer predictions for prototype inductance variation, flux compression, and pulse width and shape with the measured experimental results. We are presently using these codes to conduct simulation studies of variable-inductance machines to determine their scalability to large ($\approx$10 MJ) machines.

In an effort to communicate the status of this project to the technical community, we have prepared an 18-min documentary film, "The Compensated Pulsed Alternator—A High Power Pulsed Energy Storage Concept," that uses animation and computer modeling to describe the principle of operation of the compulsator and includes sequences showing the construction and testing of the engineering prototype. A companion document, "Compensated Pulsed Alternator—A New Concept for Generating High Powered Pulsed Energy,"[171] was prepared to complement the film. Additionally, a two-day seminar was

Fig. 2-365. Prototype compensated pulsed alternator.

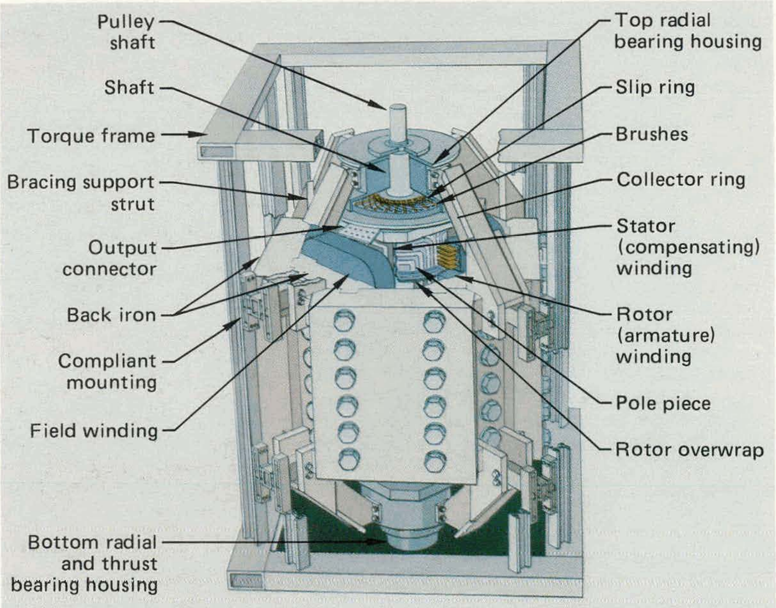

held in Austin, Tex., on November 18 and 19, 1980, to review the progress and achievements thus far and to solicit technical contributions from other scientists and engineers.

Engineering-Prototype Compulsator. The engineering prototype was constructed to obtain the vital data and experience needed to verify the analytical predictions and scaling parameters and to investigate the ability of the conductor insulation system to withstand the stresses (both electric-field and mechanical) caused by electromagnetic forces, rotor reaction forces, and thermal expansion of the conductors.[172]

In December 1979, during a high-speed discharge test on the prototype, an electrical flashover in the rotor windings caused damage that required disassembly of the machine. Subsequent evaluations were conducted to determine the cause of this failure and to define a plan for further analysis and experimentation.[173] We postulate that mechanical abrasion of the solid dielectric in the air gap at the top (high-voltage) end of the rotor contributed to the fault.

An improved end-region design, which increased the radial separation of the high-voltage and low-voltage copper terminals, was studied to correct this fault condition. Tests were conducted on various Litz-wire coil configurations to determine the effect of increasing the basic filament size of the conductor from 30 AWG to 22 to 24 AWG. These tests of the armature conductor were needed to improve the mechanical integrity of the winding during manufacture and assembly and to reduce the probability of hot-spot formation during operation at high current densities.

Analysis of the test results revealed that the prototype experienced large eddy currents that reduced the armature inductance and increased the armature

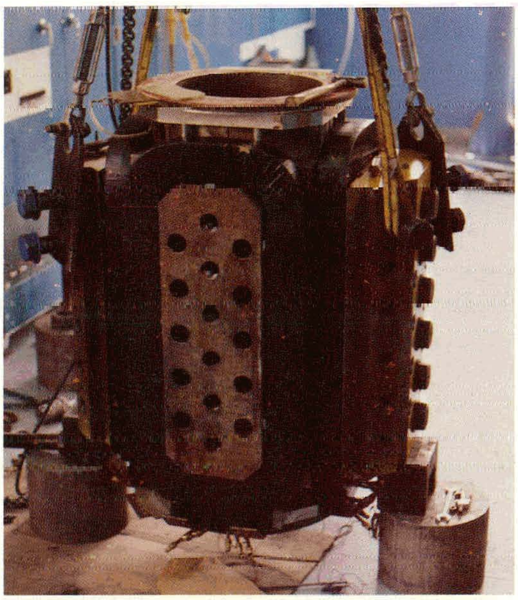

Fig. 2-366. Engineering prototype stator assembly and field coils.

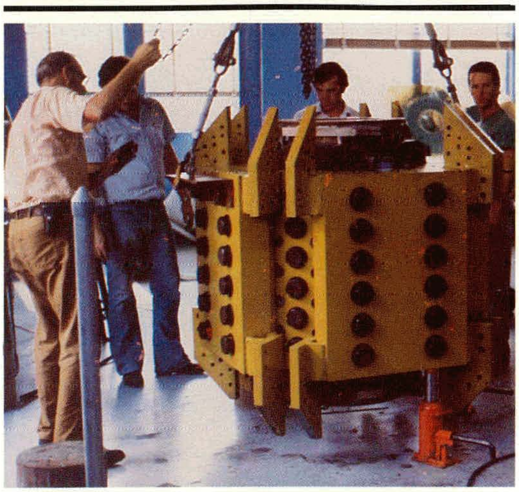

Fig. 2-367. Complete prototype assembly of stator, field coils, and back iron.

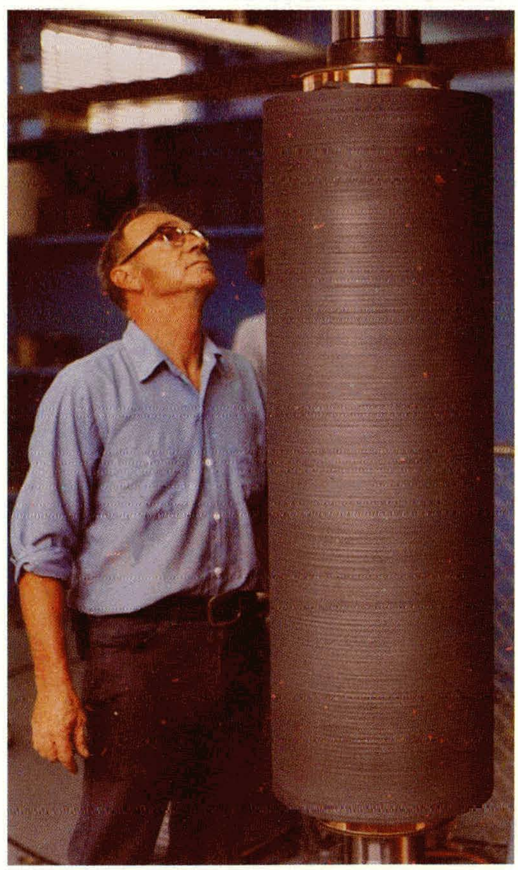

Fig. 2-368. Prototype rotor assembly.▶

resistance when the rotor winding was not in the compensating position. As a result, the flux compression was low, and the peak output power was less than expected. This meant that the current pulse was broader than predicted, and the energy delivered to the flashlamps was somewhat reduced. A separate report[172] describes in detail the apparatus and experimental results.

During 1980, UT-CEM developed a space harmonic, magnetic-field distribution analysis code to investigate inductance variation and losses in these machines. The code was modified and improved by LLNL. These codes, together with static pulse tests on the machine, revealed the solid pole pieces of the stator to be the principal source of the losses.

The compulsator was then redesigned. Since it was not feasible to laminate the pole pieces to eliminate eddy currents, the decision was made to shield the poles with a conducting copper ring or cylinder. While this ring maximizes the eddy currents, it reduces the overall losses because of the relatively high conductivity of copper compared to steel pole faces.

The compulsator has thus become a four-pole alternator with wave-wound armature windings on the rotor and external field windings on the stator. It has a low-inductance current return path provided by the copper ring. This ring is bonded to the inside of the stator and serves both as an eddy-current shield and as the current return path.

The rotor of the machine was rewound as before, with a 47-turn Litz-wire wave winding. The new winding used fewer strands of heavier-gage wire (22 AWG as opposed to 30 AWG). Improved air-gap insulation was also used, i.e., GE 77904/77940 mica-mat tape and sprayed epoxy sealer. The modified prototype was reassembled (Figs. 2-366 through 2-368) and electrically and mechanically examined before the mechanical spin test and electrical-discharge tests were begun.

Computer analysis of the reconstructed machine showed that this prototype should deliver its design goal of 200 kJ to 16 parallel Shiva-type flashlamps at a rotor speed of 5400 rpm; the desired pulse width of 500 to 700 μs will probably be broadened to about 1.2 ms.

Prototype Static Testing. Static impedance measurements were made on the assembled compulsator to verify values calculated by the space harmonic distribution computer code. Measurements were made of inductance and resistance vs frequency; these measurements compared favorably with calculated values (Figs. 2-369 and 2-370).

Prototype Dynamic Testing. Mechanical spin tests were conducted up to 2500 rpm, and open-circuit voltage measurements were made at 550 rpm, 1060 rpm, and 2340 rpm. During the open-circuit discharge test at 2340 rpm, there were indications of electrical breakdown. Further examination revealed that the rotor winding had shorted between winding turns. A review of the rotor-assembly records indicated that a complication with the conductor windings was encountered during the fabrication process: one of the Litz-wire bundles had popped out and had to be pressed back into the winding at the end turn.

The fabrication and insulation difficulties encountered with the rotor windings on this prototype precipitated a study to eliminate the problems. The presence of pinholes in the insulation material creates electrical weak points that allow arcing and the destruction

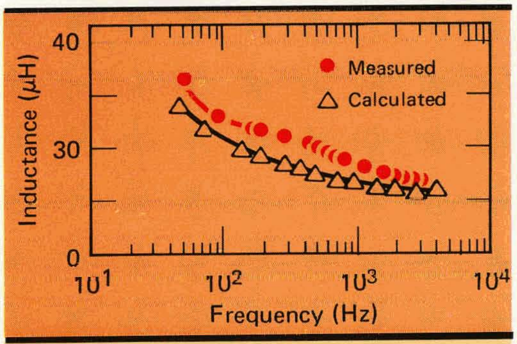

Fig. 2-369. Engineering prototype armature inductance.

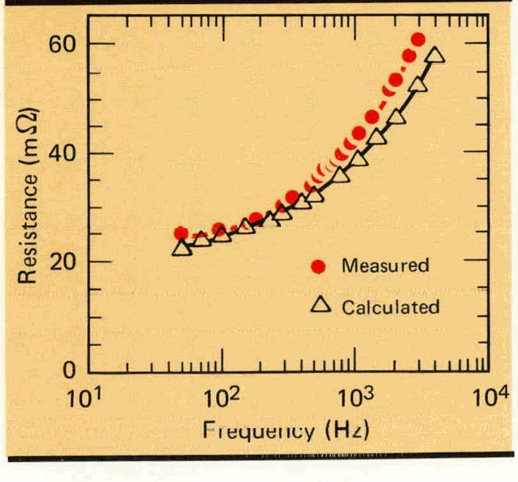

Fig. 2-370. Engineering prototype armature resistance.

of the windings. To improve the prototype, epoxy vacuum-impregnation techniques are being investigated for building the rotor and stator structure; these techniques should improve the electrical and mechanical integrity of the prototype.

Active Rotary Flux Compressor (ARFC). A small-scale rotary flux compressor was constructed with a laminated stator and rotor (8-in. diam), an air-gap armature winding, and an active air-gap compensating winding. This ARFC (Fig. 2-371) was designed to verify the impedance calculations of the space harmonic distribution computer model. The design parameters for this machine are presented in Table 2-72.

The key feature of the ARFC is that it has no field windings and, therefore, cannot generate power until a starting current is driven through the machine. This current provides initial flux that the machine then compresses.

The circuit diagram for the prototype test is given in Fig. 2-372. At the appropriate time on the ARFC's rotation cycle, both the flashlamp and the ignitron switch are fired, and the startup capacitor dumps through the machine and the load. The timing is such that the peak current in this starting circuit is reached when the machine is at or just past its highest inductance value. This current then becomes the initial startup current, i_O, and the diode shorts out the capacitor and switch for the rest of the discharge.

The ARFC takes initial current i_O and compresses it via the diode and load to a high value as the machine reduces its inductance by mechanical rotation. The basic circuit equation is given by

$$\dot{\phi} + \frac{R}{L}\phi = 0 \quad , \tag{78}$$

where the flux ϕ = Li in this inductive/resistive series circuit. Substituting, we obtain

$$i\frac{dL}{dt} = L\frac{di}{dt} + iR = 0 \quad . \tag{79}$$

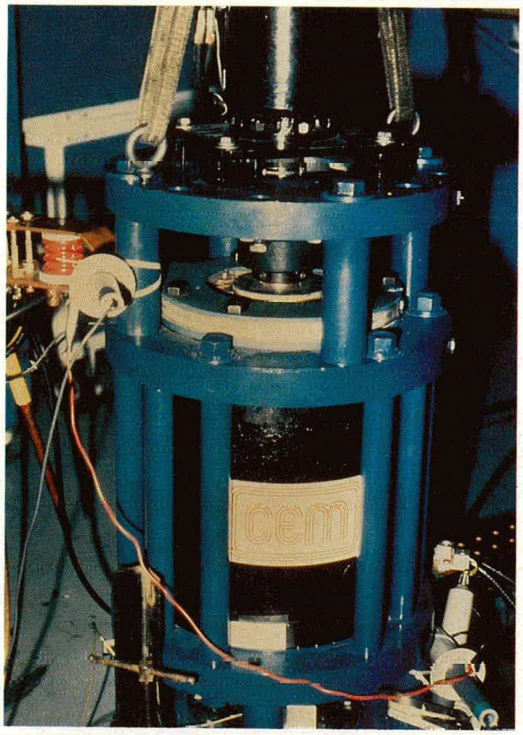

Fig. 2-371. Active rotary flux compressor and flashlamp load.

Table 2-72. Design parameters for active rotary flux compressor (ARFC).

Rotor diameter (cm)	20
Rotor length (cm)	50
Stator diameter (cm)	38
Stator length (cm)	30.5
No. of poles	4
No. of turns/pole	12

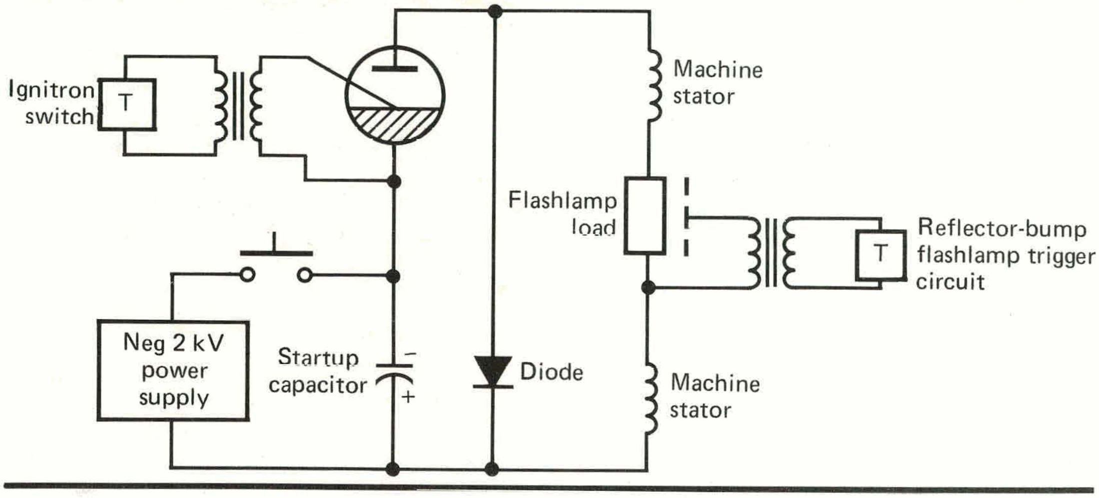

Fig. 2-372. Test circuit for prototype active rotary flux compressor.

The solution of this equation is given by

$$= \left(i_0 \frac{L_0}{L} \right) \exp \left(- \int \frac{R}{L} \, dt \right) \quad , \qquad (80)$$

where i, L, and R are the current, inductance, and resistance of this series circuit, respectively. The subscripts i_O and L_O refer to starting conditions.

When the inductance reaches its minimum value, L_{min}, the current peaks and thereafter shuts off very sharply as the machine increases its inductance. The ratio $S = L_O/L_{min}$ must be high to produce a high energy gain $G = W_L/W_O$, where W_L is the energy delivered to the load and W_O is the initial energy stored in the startup capacitor.

ARFC Test Results. Computer modeling of the small prototype rotary flux compressor was used to predict the impedance values of the machine. In Table 2-73, these values are compared with those measured on the device.

The prototype AFRC was also tested to about 3000 rpm, one-third its design speed. Two test loads have been used: one is a 91.5-cm loop of AWG 2/0 stranded wire; the other is a parallel bank of four flashlamps, each with 7.62-cm arc length and 1-cm bore.

During the testing sequence, a startup current of about 700 A was injected with a 175-μF capacitor charged to 3 kV. When a cable load was used, the current gain was about a factor of 10.3 at 2844 rpm on the ARFC. Peak current reached was 7672 A (Fig. 2-373). When the flashlamp load was used, the current more than doubled, and a peak current of 1430 A was reached at 2956 rpm (Fig. 2-374). Also shown in Fig. 2-374 is an overlay of the startup current decaying through the flashlamp load with the machine turned off.

These preliminary results have substantiated computer predictions, but the machine must yet be tested at full speed and current so that the effects of saturation in the iron laminations can be properly modeled. The computer predicted that this prototype ARFC would not produce a very high compression factor through a resistive flashlamp load. Even so, the machine amply demonstrates the principle of flux compression and current multiplication, even at low speeds. Furthermore, the computer model appears to be accurate, and computational designs of high-gain machines are being produced.

Computer Simulations. The objectives of computer simulation studies of variable-inductance machines are to determine the limitations on their performance due to mechanical and electrical constraints and to determine their scalability to large ($\approx$10 MJ) machines. We developed a computer code that has been used extensively to analyze the prototype performance and to determine the optimum machine parameters for the application of one specific machine to flashlamp power conditioning. The code and some predictions are described here.

The scaling analysis has been divided into three largely independent parts. The first part models the machine and computes the relevant electrical parameters, such as generator voltage, inductance variation, and eddy-current resistance. The second part

Table 2-73. Comparison of predicted and measured values for small prototype rotary flux compressor.

	Predicted	Measured
Minimum inductance (mH)	26.4	23.2
Maximum inductance (mH)	1190	1040
Rotor design speed (rpm)	8900	3000 (to date)
Inductance variation	45:1	47:1
Anticipated energy gain	17	—
Measured energy gain	—	10.3 (at 3000 rpm)

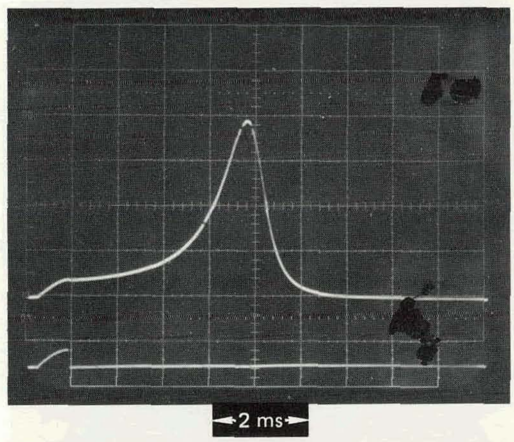

Fig. 2-373. Top trace: current through a 91.5-cm 2/0 cable lead with the prototype ARFC at 2844 rpm. Bottom trace: start-up capacitor current.

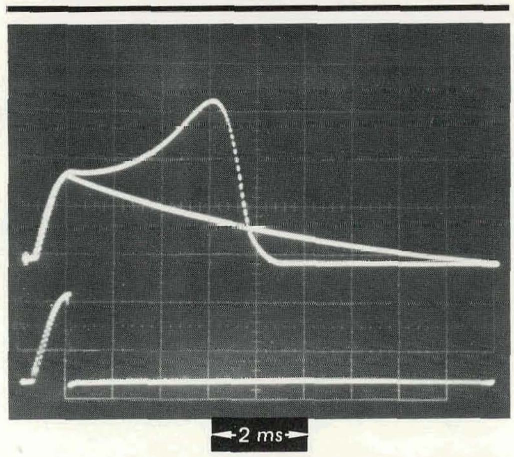

Fig. 2-374. Top trace: current through four parallel flashlamps showing 2.1 to 1 compression. Bottom trace: start-up capacitor current.

uses these electrical parameters to model the behavior of the machine when it is hooked up to a load. A subset of the possible circuits is included in the code, which integrates the circuit equations and computes many diagnostic parameters, such as the stress in the windings, the temperature rise of the windings, internal machine voltages, energy balance, etc. Thus, the first two parts take only the mechanical dimensions of the machine and the external circuit parameters and predict the entire process whereby energy is delivered to a load, including those parameters that are constrained by material limitations. This part of the code was used to model the first sequence of experiments carried out in October through December 1979, and a typical result is shown in Fig. 2-375. The agreement with experiments is excellent, and, in many cases, we have pinpointed possible experimental uncertainties by being unable to reconcile data at one rotational speed with that at another. In particular, the analysis highlighted the need for accurate timing in discharge experiments and the need for accurate information on the back-iron magnetic field.

The third part of the code is an optimization package, based on earlier work by E. Goodwin and J. Trenholme. The code, CREEPER, feeds the mechanical machine parameters and external circuit parameters to the first two parts and adjusts these input values to obtain the maximum value of a given function, subject to the constraints. Although CREEPER is much faster then manual optimization, many iterations are necessary, and a single optimization run can take several days to complete. CREEPER is being used to determine the largest energy machine compatible with the constraints. Present results indicate that the primary constraint on the device is the shear stress on the windings. From this, we concluded that the winding design is a key issue in the scaling of the compulsator to large delivered energies, a result that will be reflected in work during 1981.

Fig. 2-375. Typical computer simulation of compulsator performance.

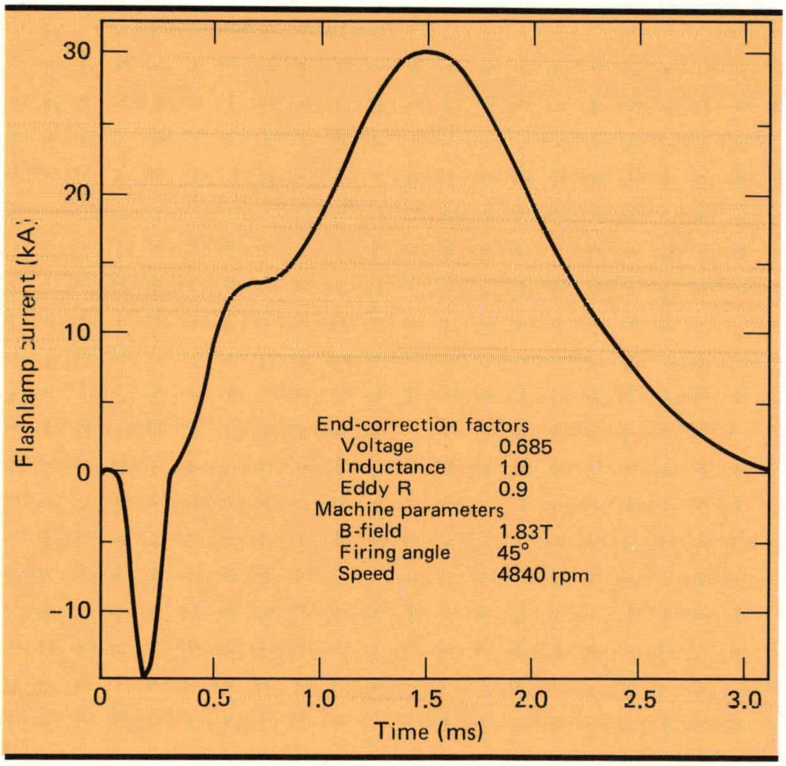

Conclusions. The construction of the engineering prototype compulsator and the ARFC, and the comparison of their performances with computational models, have allowed us to lay the foundation for engineering designs of future machines.

Our current plans are to refine and improve the computer models through verification with experimental data, to improve the engineering systems, and to increase component reliability. In addition, the systems application of these devices remain to be examined, including distribution, switching, and safety problems.

Author: R. J. Foley

Major Contributors: W. L. Gagnon, D. Eimerl, and B. M. Carder; W. Weldon and W. Bird (University of Texas)

The Nova Plasma Shutter

Introduction. When fusion targets are irradiated, a substantial portion of the energy is absorbed, but the remainder is scattered away and reflected back into the laser chains. To protect laser components from the excessively high intensity ($>10^{10}$ W/cm^2 for 1 ns pulses) of reflected laser light, the reflected pulse must be diverted or otherwise prevented from returning to the laser chains. On Shiva and most other large fusion-laser systems, this function is accomplished by isolators comprised of Faraday rotators and polarizers. To replace the largest Faraday isolators, we are currently developing a plasma shutter—a device that rapidly produces a plasma to block the retroreflected pulse. The plasma shutter will cost approximately one-tenth as much as the Faraday rotator that it will replace.

Along with isolators and amplifiers, the laser chain has spatial filters that pass the beam through a pinhole and remove high-spatial-frequency noise on the beam. The plasma shutter is located close to the pinhole of the last spatial filter, where the beam is naturally small in cross section, as shown in Fig. 2-376. The distance from the shutter to the target is 60 m, so the closure time must be less than 400 ns. With the shutter nozzle placed downstream (optically) from the pinhole, where the beam is 6 mm in diameter, the plasma must attain the relatively high velocity of 16 km/s.

The plasma shutter uses the simple circuit shown in Fig. 2-377. After the laser pulse passes the shutter on its way to the target, a capacitor charged to 35 kV is switched to cause a 500-kA current to flow through a 250 μm-diam aluminum wire. By resistive heating, the atoms of the wire are heated to 15 eV (2×10^5 K) and become free atoms. This heating also strips electrons from the atoms, creating a hot plasma that expands out into the optical beam path. Thermal expansion of the plasma is not fast enough to move the plasma into position in the required time; therefore, we have arranged the electrodes attached to the wire as parallel feed rails that extend beyond the wire, orthogonal to the beam path. The magnetic field within the loop formed by the capacitor, feed rails, and wire is much higher on the back side of the plasma; therefore, the magnetic field accelerates the plasma. As the plasma moves down the rails, the current continues to flow through it and the acceleration continues. The combined effect of the plasma kinetic energy and the magnetic propulsion moves the dense plasma into position at 16 km/s. The ionized aluminum plasma has a density of 1.5×10^{21} cm^{-3} (1/60 of solid density), which blocks the laser beam because it is above the critical density of 10^{21} cm^{-3} for the 1.06-μm laser light.

We have finished building two plasma-shutter pulser modules, both of which are undergoing testing and refinement. One module has been configured with extensive plasma diagnostics to verify plasma parameters, to characterize the high-voltage electronics, and to ensure high reliability and long life. The other module is being used to evaluate the control system, to minimize

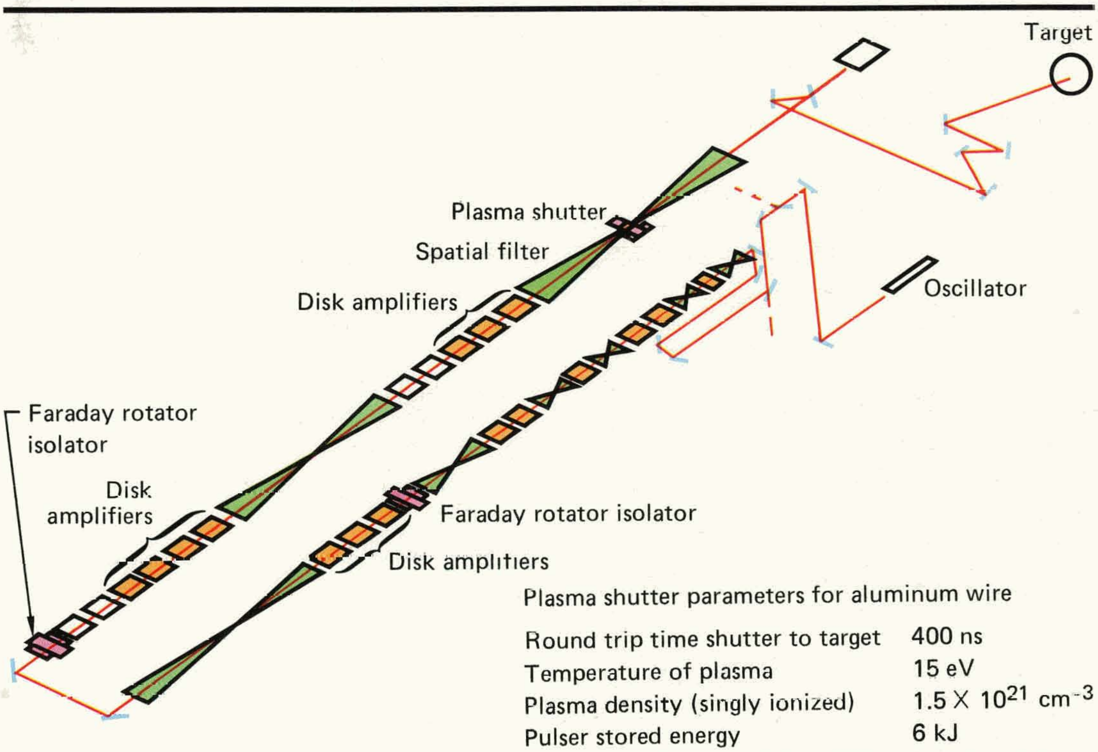

Fig. 2-376. Position of the plasma retropulse shutter in the Nova laser chain.

Plasma shutter parameters for aluminum wire

Round trip time shutter to target	400 ns
Temperature of plasma	15 eV
Plasma density (singly ionized)	1.5×10^{21} cm^{-3}
Pulser stored energy	6 kJ

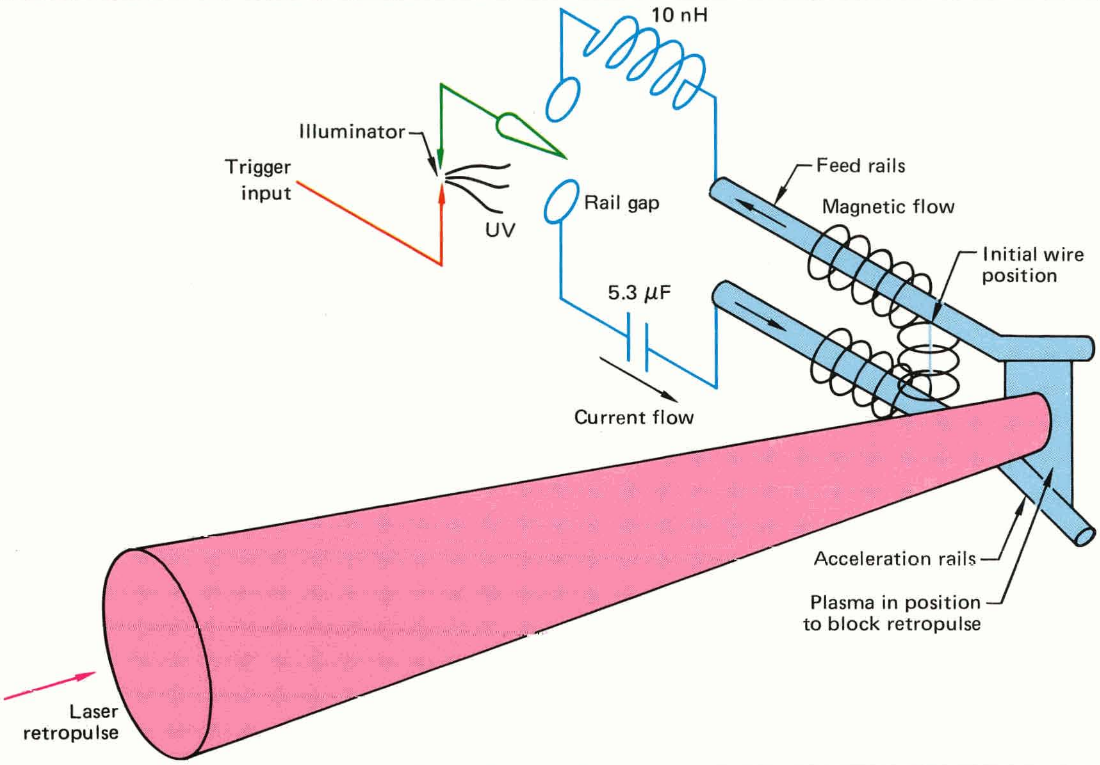

Fig. 2-377. Conceptual geometry of the plasma shutter, showing pulser circuit and asymmetrical magnetic field that accelerates the plasma in the rail-gap geometry.

electromagnetic interference, to test the wire-changing mechanism, and to perform high-power tests on the Shiva laser system.

The basic design requirements of the pulser circuit are dictated by its task. Since resistive heating occurs primarily at burst, we need a high current at burst and, hence, a fast current rise time. This requires a very low inductance circuit. Since magnetic propulsion occurs after burst, the current must continue to flow at an increasing rate after burst; the burst must occur early in the current wave form. The circuitry must be of extremely high reliability, for a single misfire could permit the laser retropulse to significantly damage the laser system and result in expensive repairs. Since the plasma-forming wire is destroyed, it must be replaced after each shot. This wire-changing operation must be accomplished within the evacuated spatial filter, and sufficient wire-holding chips must be available to minimize periodic reloading of the 20 plasma-shutter modules. Little or no plasma can be allowed to reach the inside surface of the spatial filter optics, which are in direct view of the plasma.

The final prototype design contains eight parallel 0.66-μF, 20-nH, 50-kV capacitors connected through four parallel 10-nH rail-gap switches via a coaxial 3-nH vacuum feedthrough to the load. The total pulser inductance is 10-nH. This design is shown in Fig. 2-378.

Plasma-Shutter Pulser Elements. In the simplified equivalent circuit of the pulser shown in Fig. 2-377, a logic signal is sent to a trigger amplifier, which consists of a current-pulse generator and transformer; this signal triggers a coaxial two-stage Marx circuit, which is charged by the main power supply. The Marx circuit then provides an output of 100 kV rising in 8 ns to trigger the rail gaps.

The rail gap has semi-Rogowski electrodes and a longer graded trigger blade. The trigger pulse is fed through a peaking gap on the end, with its spark located on-axis with the rails, thereby preilluminating the rails with UV light. The switching gas is 20% SF_6 and 80% Ar. The function of the UV light (produced primarily in the argon) is to provide free electrons and metastable states in the main gap region. These electrons help in initiating avalanches and streamers. We have extensively tested and characterized the system; it provides nanosecond jitter from logic signal to rail-gap closure.

The electrodes are currently fabricated from low-lead brass. During 1981, we will continue to examine Schwarzkoph K25 tungsten, Poco AXF5QC and ACFIOQ graphites, and other materials to minimize

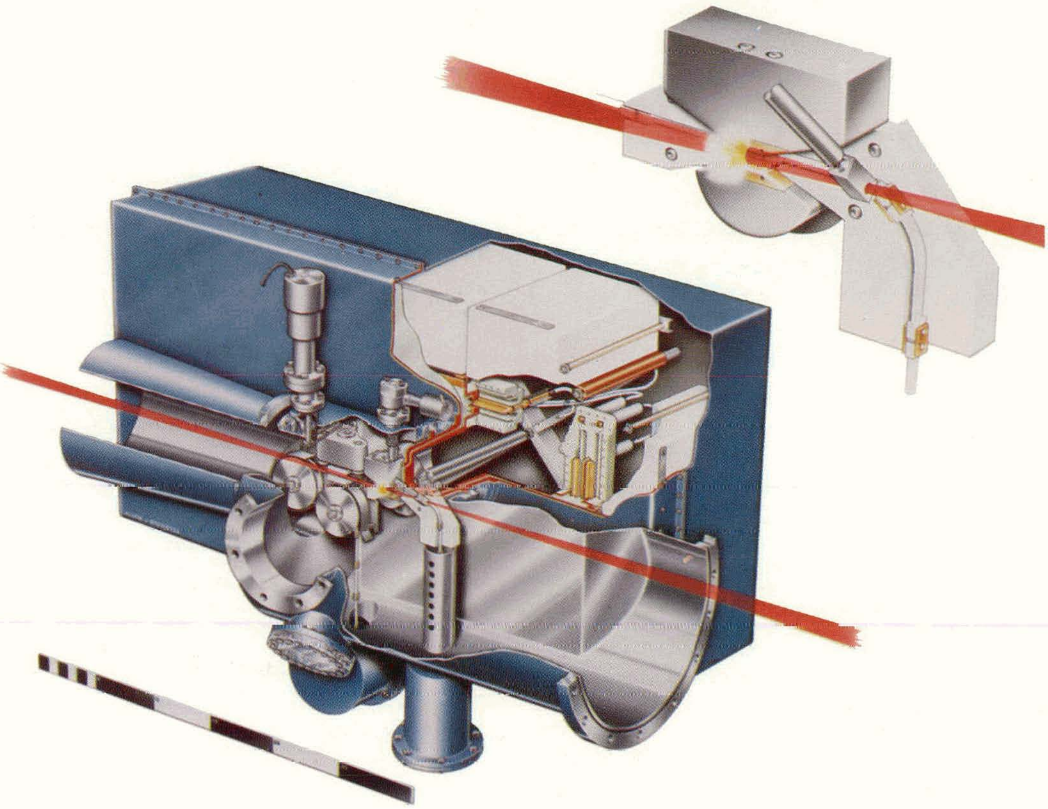

Fig. 2-378. The plasma-shutter module.

erosion and, most importantly, to minimize prefire.

The 0.66-μF, 20-nH, 50-kV capacitor was developed by Maxwell Corp. for this application. It has a plastic case with a parallel rail header, and the expected life is 10^5 shots at 80% reversal. The dielectric, developed for this application by Dielectric Sciences, Inc., is a special silicone elastomer that was molded in the shape required for the coaxial feedthrough, as shown in Fig. 2-379. The coaxial design minimizes the number of exposed high-voltage edges. The silicone is designed to minimize surface tracking under or between capacitors and switches; its elasticity will restore its shape and, in particular, its contact with the conductors after a magnetically induced mechanical impulse. This insulator constitutes one of the major innovative developments of this project.

Plasma-Shutter Mechanical System. The explosion of the wire that forms the plasma generates an extremely high-pressure pulse within the chip that confines the wire. The explosion must be confined for several hundred nanoseconds, during which time the wire melts, vaporizes, and expands through a confining slot. The slot shapes and directs the plasma and prevents stray plasma from being deflected toward the lenses of the spatial filter. Figure 2-378 shows the location of the wire-holding chip in relation to the electronic pulser and the laser beam.

The extremes of temperature and pressure make the selection of a chip material difficult. It was unusual to find a glass-fiber epoxy material with both good tensile and impact strengths. However, an optimum material, E-260H from Fiberite

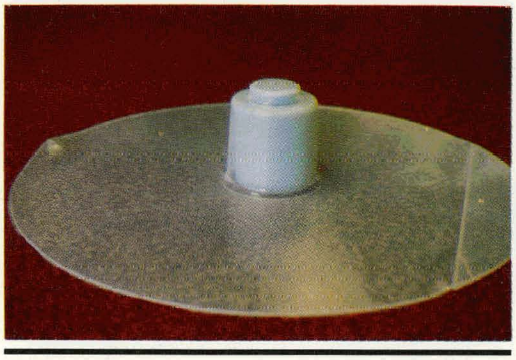

Fig. 2-379. The silicone-rubber insulator molded to fit the contours of the rail-gap switch and the coaxial vacuum feed-through line.

Corporation, was found, as seen from Figs. 2-380(a) and 2-380(b), which show the typical before and after firing shape of the optimum material. For comparison, Figs. 2-380(c) and 2-380(d) show examples of the extreme distortion of two unsatisfactory polycarbonate materials. The distortion of the materials resulted in significantly lower plasma densities, whereas the material of choice shows virtually no change in slot shape.

Plasma-Shutter Electronics. We have spent the past year implementing and testing the electronics reported previously.[174] Although some details remain to be finalized, the system concept has been proven and the system is operational. Not previously reported is a thyratron-based trigger system that replaces the auxiliary trigger gap originally used. The new system has the advantages of compactness, redundancy, compatibility with low-level fiber-optic input triggers, and virtual freedom from periodic maintenance.

A simplified schematic of this trigger system is shown in Fig. 2-381. It is a stand-alone module that is incorporated within the pulser housing, and it requires only ac power and fiber-optic trigger inputs. Triggers are redundant and originate either from the fast timing controller in the master oscillator room or from a local maintenance panel. Either trigger will fire an avalanche silicon-controlled-rectifier (SCR) stack that delivers an 800-V pulse into a step-up and inverting transmission-line transformer. The rise time of this pulse is on the order of 10 ns. The output of the transformer provides a 1600-V positive pulse into the 100-Ω-terminated G2 grid of the tetrode thyratron.

A second, identical, trigger is wired in parallel to the output transformer, the rationale being that all trigger elements beyond that point are few and passive and will, therefore, have an acceptably low failure rate. Firing of either thyratron will deliver a negative going pulse to the output transformer, which is a stacked array of three ferrite torroids with single-turn primaries and a single-turn secondary consisting of a rod passing through the center of the stack. The transformer output impedance is 50 Ω, which drives four parallel 200-Ω, 3-m-long twisted-pair transmission lines. These lines were found necessary to isolate the rails and prevent misfiring.

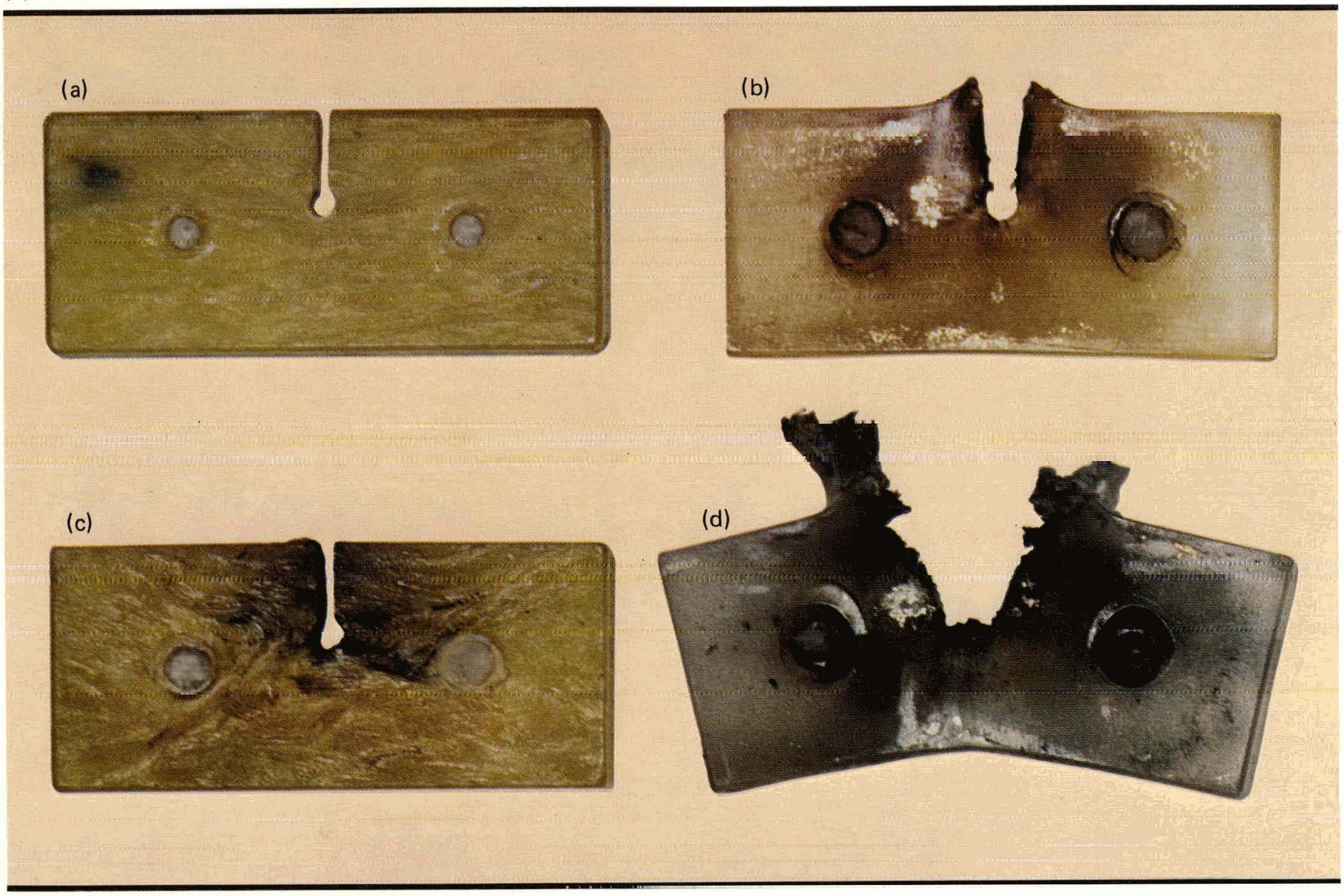

Fig. 2-380. Before firing (a) and after firing (b) conditions of the optimum plasma-shutter chip material, E-260H, showing little damage, as contrasted with the inferior polycarbonate samples shown in (c) and (d).

Voltage doubling at the end of the open line yields a roughly 80-kV, 15-ns-rise, 100-ns-wide pulse at each rail trigger blade. Pulse-to-pulse and rail-to-rail jitter has been demonstrated to be less than 5 ns relative to the optical-trigger input.

Plasma Characteristics and Performance. We have used extensive electrical diagnostics to establish the pulser characteristics, and we have developed a set of plasma diagnostics to characterize the primary features of the plasma. Electrical diagnostics include monitors to record the charge voltage of the capacitors and the current and voltage near the foil. For plasma diagnostics, we used witness plates of glass or metal, or both, placed in front of the plasma to collect the vapor, enabling us to record the angular distribution of the emitted plasma and, thereby, determine density. We directly recorded the plasma-front velocity with a TRW streak camera focused along the laser-beam optical axis with the camera slit oriented parallel to the plasma-expansion axis. A cw YAG probe laser with a 10-nm narrowband filter and a UV-blocking filter has also been used with a photodiode to directly monitor shutter closure.

The foregoing diagnostics are somewhat indirect, but, in conjunction with a computer simulation code,[175] they have provided us with a picture of the plasma characteristics. However, we have needed a more direct diagnostic tool to measure plasma size, uniformity, and density profile, so we recently installed a unique 5-keV x-ray backlighter source that was developed at LLNL.[176] This source has a sensitivity of 0.1 mg/cm^2 and a spatial resolution of at least 25 μm.

The x-ray backlighter has been invaluable for observing details of the plasma. Most importantly, it has directly confirmed the Faraday-cup and streak-camera data and agreed with the computer-code prediction. It revealed several previously unidentified plasma modes, including arcing around the chip, jetting caused by the ends of the wire bursting first, and striating caused by a sausage instability. All these modes led to the bulk of the current flowing through a small portion of the plasma, carrying it off at high speed and subcritical density, leaving the rest of the plasma behind.

We have eliminated these undesirable modes by simple redesigns of the wire-holding chip. We prevented the arcing by making tight electrical-current joints and by using elastomer gaskets around the chip; we eliminated the end jetting by developing improved fabrication techniques; and we eliminated the instability by tamping the plasma with a thin plastic cover. A typical x-ray shadowgraph of the plasma in an

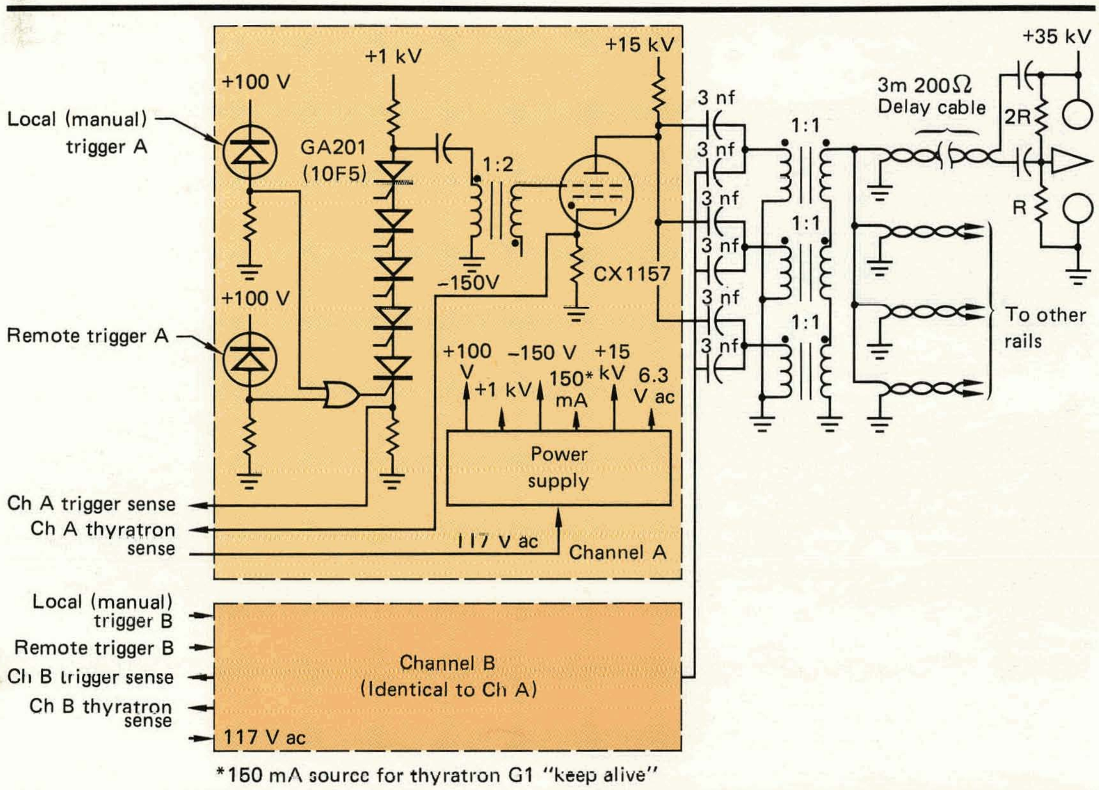

Fig. 2-381. Schematic of plasma-shutter trigger system, showing the optically triggered tetrode thyratron.

experimental chip geometry is shown in Fig. 2-382.

The angular divergence of the plasma from the slot has been recorded with a glass witness plate that was read on a scanning densitometer. We established that the mean divergence of the plasma is only 10°. The plasma density in the interaction region was geometrically determined by using the divergence measurement, the nozzle geometry, the initial wire size, and the arrival time recorded by the Faraday cup. The peak density measured was 1.5×10^{21} cm^{-3}. (The critical density for 1.06-μm light is 10^{21} cm^{-3}.) These data were recently confirmed by the x-ray diagnostic. With the electron stripping and multiple ionization that will result from the intense laser beam interacting with the plasma, the density in the interaction region should be more than adequate to stop the retropulse.

We have examined small-signal beam-blocking action with a cw 1.06-μm YAG probe laser and demonstrated closure. The optical beam was blocked as expected. However, since a full-power Nova beam has more energy than Shiva, we have no facility to fully test the Nova shutter; therefore, we have simulated the Nova conditions using the LASNEX computer code. In these simulations, a full-power beam only burned through 2% of the plasma thickness; however, other simulations have shown that, if the plasma is located too close to the focal region ($>10^{14}$ W/cm^2), burn-through (hole boring) might be possible. Consequently, we have positioned the shutter so as not to exceed this beam intensity. Additionally, for a plasma that was 50% of critical density, no burn-through was observed (in simulation), but, for an even lower-density plasma, some leakage was observed before the plasma was stripped sufficiently to block the remaining beam.

Conclusions. We have developed a plasma shutter to project a critical-density plasma across an optical beam path sufficiently fast to block a reflected laser pulse. The shutter will be used on the Nova laser system instead of the more costly Faraday rotator-isolator packages to prevent scattered light from returning into the laser chain. The cost savings will be $1 million per beam.

To block the full-power Nova beam, the plasma will reach or exceed the critical density necessary to totally reflect 1.06-μm light. Two prototypes have been constructed to evaluate the concept, one being used for plasma diagnostics, the other being used to develop the electronic controls and wire-changing mechanism. They will be installed in the Shiva laser for full-scale testing.

Because of the unique components within the shutter, its development required very close cooperation among experts in pulsed power, plasma physics, electronics and controls, mechanical engineering, and electromechanical packaging design. The development project has required three years to reach the full-scale testing stage, which will take place early in 1981.

Authors: I. F. Stowers, L. P. Bradley, and J. A. Oicles

Major Contributors: W. A. Aceves and staff, R. Anderson, R. D. Behymer, J. R. Braucht, T. Connor, W. H. Cowens, S. Fulkerson, B. M. Gim, R. J. Hampton, M. A. Marcon, E. L. Orham, E. Silva, and G. Wills

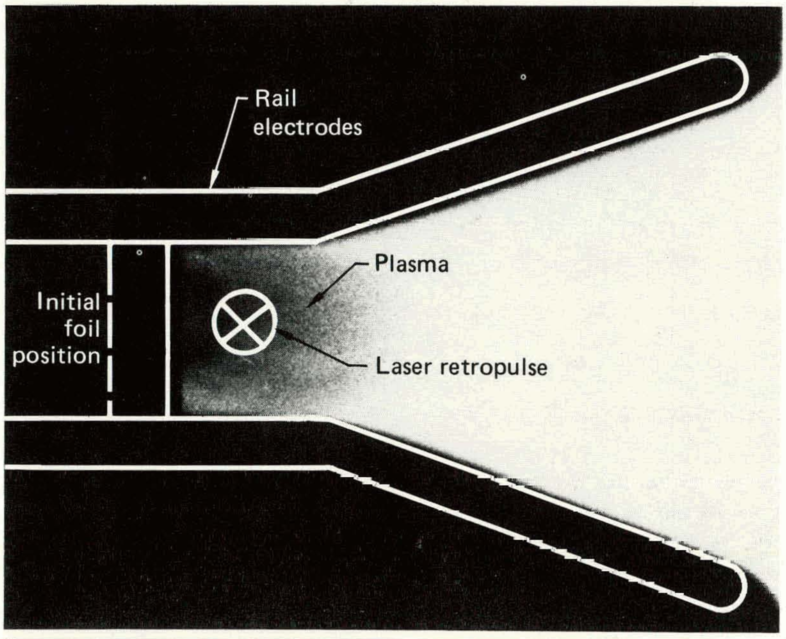

Fig. 2-382. Pulsed soft x-ray shadowgraph, taken with the unique LLNL source, showing the dense expanding plasma.

Fast-Pulse Development

We have developed an eight planar triode Pockels' cell driver, as reported previously.[177] Our efforts in 1980 were to improve the design and to produce five production units for use on Shiva, Argus, and other lasers. A representative output pulse from one of these units is shown in Fig. 2-383. This two-chassis unit has been reserved for use in the laboratory for fast-pulse development. Figure 2-384 shows this unit; the left module contains the avalanche transistor stack (on the rear panel) and the two-tube preamplifier, and the right unit contains the six identical parallel-output stages, which can be ganged for higher output current as desired. Each module contains its own ac power conditioning, including an isolation transformer, so that the only interconnection between the two modules is a pair of 75-Ω coaxial cables.

We have learned from Shiva experience that the preamplifier output was inadequate to drive the output stage properly. After an operational period of approximately a month, the tube aged and lowered the circuit gain. By modifying the cascade connection used between the tubes of the first stage, we have increased the gain sufficiently to provide adequate output to the driver chassis. The modified schematic is shown in simplified form in Fig. 2-385. We have, however, sacrificed speed with this modification because of the difficulty of implementing a transformer that will not degrade rise time when driving the low-impedance cathode of V2. We are now experimenting with a common-cathode stage for V2 that appears to give us both the speed and drive capability we require.

As is evident by the need to employ six parallel-output tubes in our drivers, the maximum current output of existing tubes is

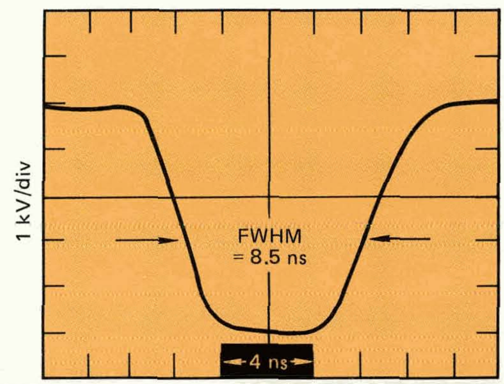

Fig. 2-383. A 5-kV output into 50 Ω using experimental avalanche transistor stack to improve fall time.

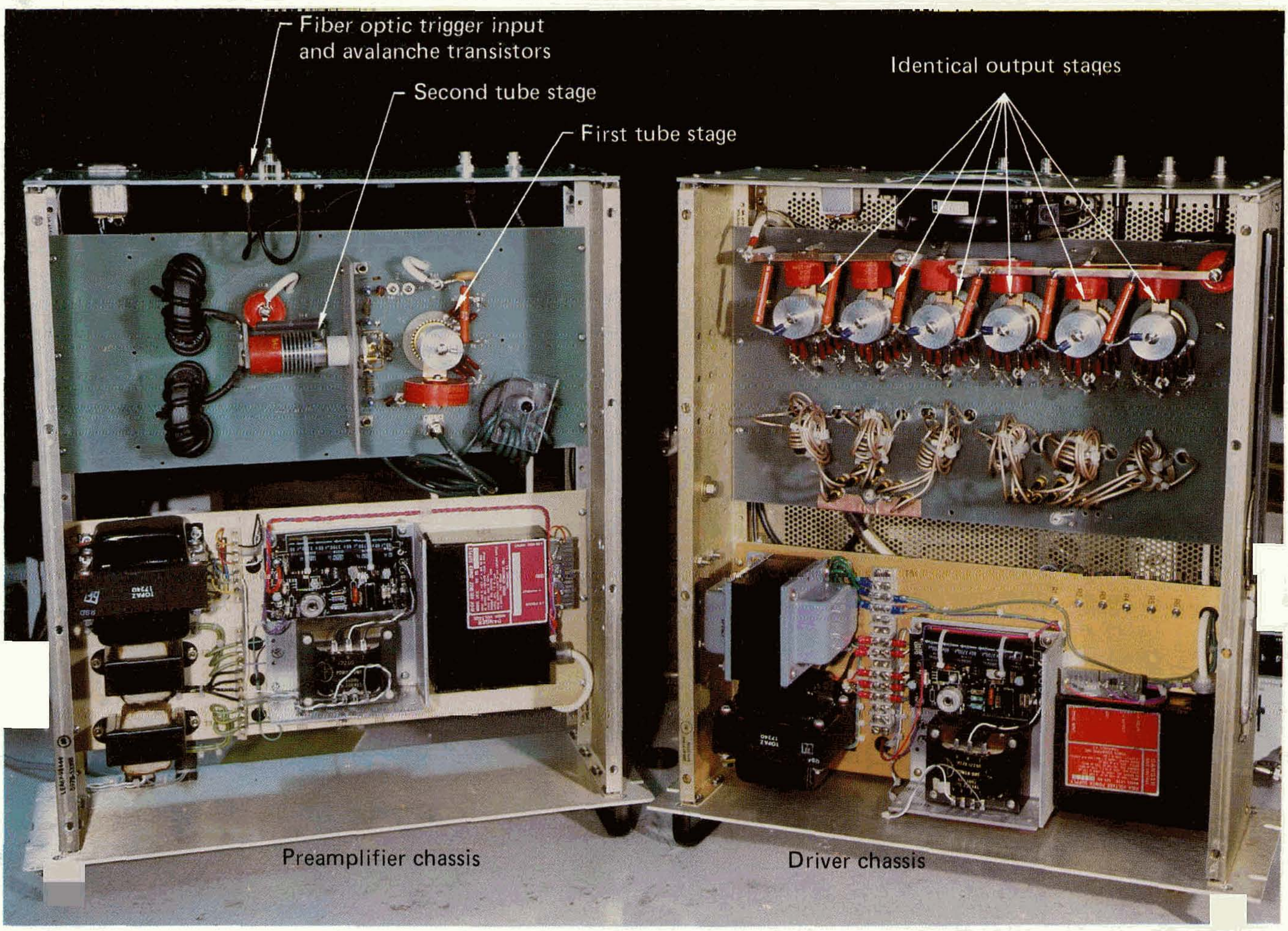

Fig. 2-384 Planar-triode Pockels cell pulser.

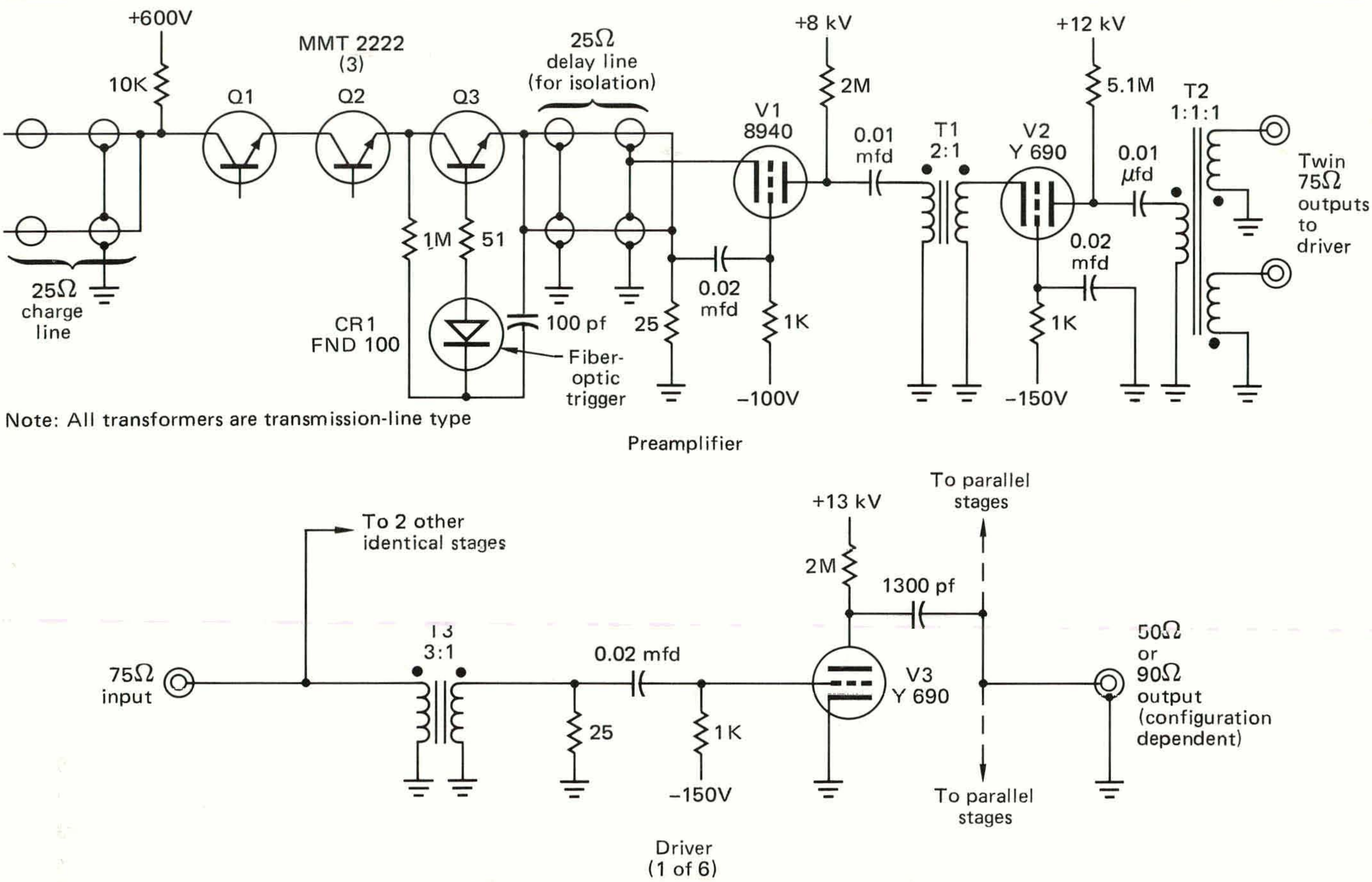

Fig. 2-385. Simplified ▲ schematic diagram of cascade connection.

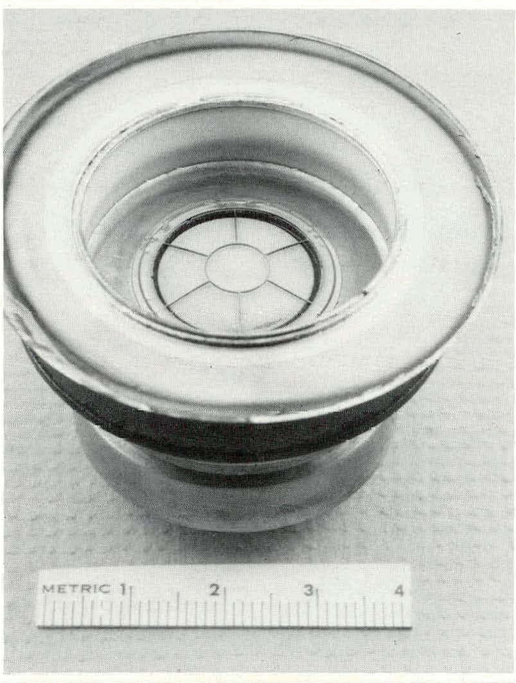

Fig. 2-386. Cutaway experimental tube showing 2-cm^2 domed triode structure.

a limitation, and we are currently funding Varian/Eimac, Inc., Salt Lake City, Utah, to develop larger-area cathode tubes suitable for our use. In the meantime, to overcome this limitation, we resorted to a more complex dome-element geometry; currently, a 2-cm^2 domed triode is operational in the laboratory (Fig. 2-386). The next phase will be to extend the approach to a heretofore unattainable cathode area of 3 cm^2. Ultimately, an area of 4 cm^2 or more may be attainable.

On both Nova and Novette, the laser-bay Pockels cells will be switched by using a single pulser that will be fanned out to each cell. We used this approach on Shiva, and the 20 way triggered spark-gap driver design is being modified to include a thyratron as a switch element. Other evolutionary modifications have been made, and the new design will actually be able to incorporate the thyratron, a triggered gap, or a bulk silicon (Auston) switch, giving the unit great versatility.

Authors: J. A. Oicles and B. M. Carder

Major Contributors: D. C. Downs, D. J. Kuizenga, and B. Mass (ILC, Inc.)

Cyclops Design and Performance

We redesigned the Cyclops laser to extend our capability for measurements requiring 1053-nm pulses with durations greater than 1 ns. Prior to the rebuilding of Cyclops, the VPL facility was the only laser at LLNL capable of long-pulse operation, and we were required to change materials in VPL frequently to operate at either 1053 or 1064 nm. Having Cyclops as a dedicated 1053-nm laser will extend our measurement capability with no time lost to conversions of VPL.

The laser, rebuilt in the former Cyclops facility, is shown in Fig. 2-387 at its present state of development. The oscillator was provided by the Oscillator Development Group. The cavity of a standard mode-locked oscillator was shortened, a 4-plate etalon was installed as the output coupler, and the acoustic mode-locker was removed. The stable flashlamp circuitry and acoustic Q-switch were retained, and the lasing material is Nd:YLF. The laser operates in a single-cavity mode, emitting 1-mJ, 100-ns, 1053-nm pulses at a repetition rate of 10 pps. The laser output varies with time due to the interaction of small cavity-length changes and the complicated output etalon, but this slow drift can easily be compensated for by using a piezoelectric motion of the cavity mirror. Details of long-pulse oscillator design are described in "Long-Pulse Oscillator Development" earlier in this section.

The pulses are amplified by a Nd:YLF preamplifier before arriving at the shutter. The preamplifier uses a 6-mm-diam Nd:YLF rod, 75 mm in length, with bare ends oriented at 6° relative to the rod axis. The gain at 1053 nm is 12.

The duration of the pulse propagated through the remainder of the chain is determined by a shutter consisting of a Pockels cell driven by a laser-triggered spark gap. The shutter time can be adjusted to provide seed pulses with durations ranging from 1 ns to the full 100-ns duration of the Q-switched pulse.

The shaped pulse is amplified by two phosphate-glass preamplifiers (0.95- by 12.7-cm rods, gain = 7), two α-rod amplifiers (2.5- by 40-cm rods, gain = 80), and a β-rod amplifier (5- by 40-cm rod, gain = 15). Laser output is controlled by rotational adjustment of a half-wave plate located ahead of the polarizer at the end of the first α rod.

The beam is diffraction propagated from a single "in-air" spatial filter. The divergence

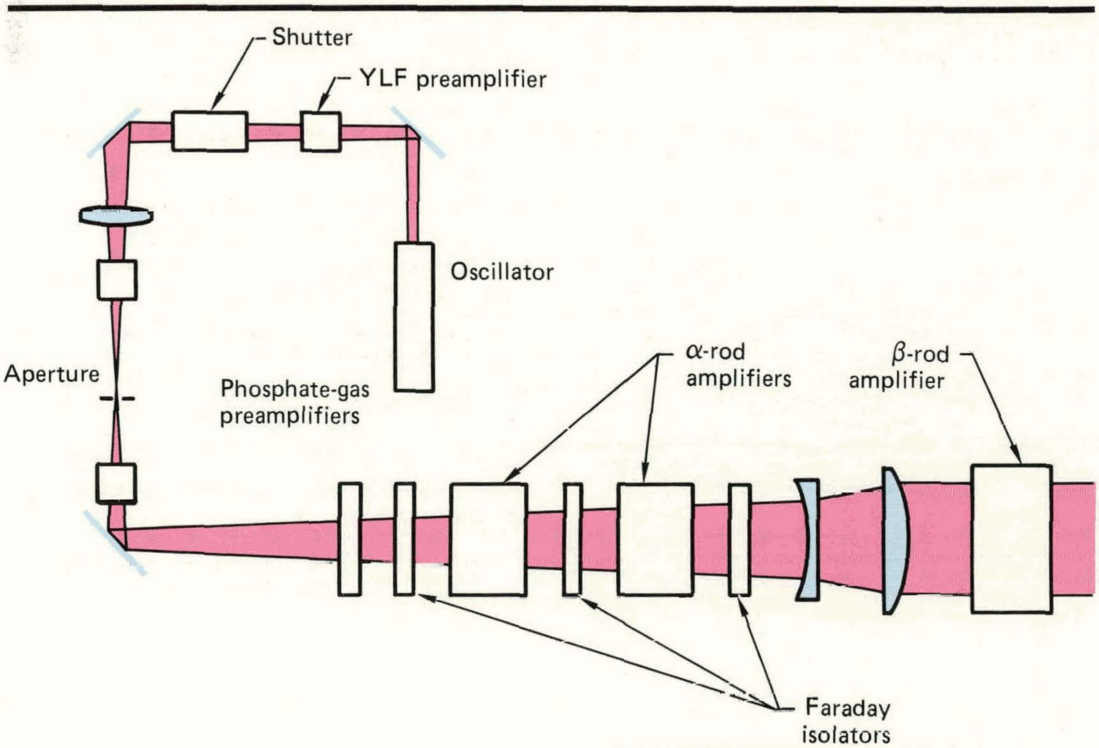

Fig. 2-387. Rebuilt Cyclops laser.

angle was adjusted to give an approximate fill of the output end of the second α amplifier, and an inverted telescope is used to increase the beam size at the β rod. Use of diffraction propagation of an approximately Gaussian beam provides a beam that is easily used in experiments, but at the cost of reducing the fill factor in the amplifiers. The spatial structure caused by diffraction is comparable in amplitude to that present on typical beams formed by image relaying.

Two problems that may have some generality were encountered in assembly of the laser. The 1-cm-diam Nd:YLF rods, slated for use in preamplifiers, were found to be of insufficient optical quality to allow their usage in a system containing only one spatial filter, and the thin-film polarizers, designed for use at 1064 nm, function poorly at 1053 nm. The polarizers can be tipped to peak the transmission of polarized light, but tipping the substrate away from Brewster's angle causes a weak modulation of the beam. Both these problems have potential impact on larger lasers and will be further investigated.

The laser has operated since mid-October 1980. It is currently capable of generating 10 to 20 J in a 1.4-ns pulse. Pulses of this type are being used as input pulses in measurements of gain saturation in phosphate glasses. No major problems have been encountered.

Author: D. Milam

Major Contributors: D. J. Kuizenga, G. J. Linford, G. E. Murphy, S. E. Peluso, and S. M. Yarema

Repetitive Preamplifier Power-Conditioning System

We undertook the task of developing a flashlamp driver for a laser preamplifier to provide 300-J pulses at a 1-Hz repetition rate for the ILS laser (a small laser system used to support research and development on solid-state lasers) and at a 10-Hz repetition rate to drive rod amplifiers for the Nova laser. The power-conditioning system for this driver contains two main elements: a power supply, and a pulse-forming and pulse-switching network.

After reviewing the several techniques normally used to trigger flashlamps, we selected a simmer approach, whereby a low current continuously maintains the flashlamp at a low level of intensity of ionization. Simmering typically increases lamp lifetime by an order of magnitude, greatly increases reproducibility, and enhances reliability.

For the immediate ILS use, we employed available Argus-type 5-kVA and 1-kVA power supplies. For the higher repetition rate required for Nova, we are designing a switching power supply.

The two series flashlamps to be driven by the pulse-forming network contain 0.59 atm of xenon, are 5-mm in diameter, and have a net length of 150 mm. With these values fixed, we used a simple code to select and optimize components of the lamp firing circuit. The nominal parameters selected were 2.5 kV with a 105-μF capacitor and a 250-μH inductor. We designed the circuit shown in Fig. 2-388 to operate to a maximum of 5 kV to provide the experimenter with flexibility. A dc simmer current of 70 mA was empirically selected.

The lamp firing circuit delivers 300-J pulses to the flashlamps. It contains two series SCRs, protective diodes, and a trigger-coupling circuit. Dumping circuits are used to protect the large SCRs and diodes.

The simmer start circuit is directly analogous to the lamp firing circuit, but its output to the lamp is a 1.5-μs, 30-kV pulse. It is protected from the lamp firing circuit and simmer circuit by a blocking diode. Lamp simmer commences with the start circuit and is maintained by the simmer circuit. The simmer maintenance circuit contains a filter capacitor, a current-limiting resistor, and a protective diode. Interlocks, dump, and protective relays are used where required.

We have tested this power-conditioning system extensively with the Argus-type power supplies and have used it for experiments on the Cyclops laser. It operates as desired at up to 10 Hz, where overheating of the Argus-type power supply presently limits the operating time.

The power supply selected for the 10-Hz Nova operation uses a 20-kHz switching circuit. The advantages of a high-frequency switching supply, as contrasted with the Argus-type voltage-doubling supply, are regulation within 1%; greatly reduced physical size; constant current charging, which extends capacitor life; and lower cost.

The main potential disadvantage of a switching supply is the problem of radiated noise. We will take special care to ensure that radiated noise is minimized.

A schematic of the basic supply is given in Fig. 2-389. The input voltage is 208 V, three phase. The output voltage is 0 to 3 kV dc, and the output power rating is 3000 W. The control of this supply is based on a controller chip (Silicon General SG3526). The base drive circuits are transformer isolated from the controller.

The control unit is designed to start the simmer automatically, sequence the flashlamp firing, and control the power supplies. The simmer command, given once on startup, follows a logic sequence. The sequence begins with the opening and closing of appropriate relays in the pulse-forming network and produces a charge command to the 1-kVA power supply; 2 seconds later, a simmer fire command is sent to the simmer circuit; 5 seconds after simmer commences, a charge command is sent to the 5-kVA power supply; and, 15 seconds later, the pulse-forming network is connected to the lamps via a relay.

The command for the simmer start is produced by relays and a 9602 integrated circuit. A laser photodiode circuit monitors the simmer current to verify that the flashlamp is simmering.

Integrated-circuit technology is used for the flashlamp fire-command circuits. Three variable-time-delay circuits are employed to provide commands to the flashlamp driver and to enable the 5-kVA power supply. The variable-delay circuits operate on a constant-current capacitor-charge circuit referenced to a comparator network. These combinations of circuits determine the length of time delay and generate the pulses required for flashlamp drive. The 5-kVA enable is used to keep the power supply from recharging immediately after trigger, thereby protecting the SCR from restrike. To make the flashlamp fire-command circuit compatible with the existing ILS rate generator, an 8820 integrated circuit is used

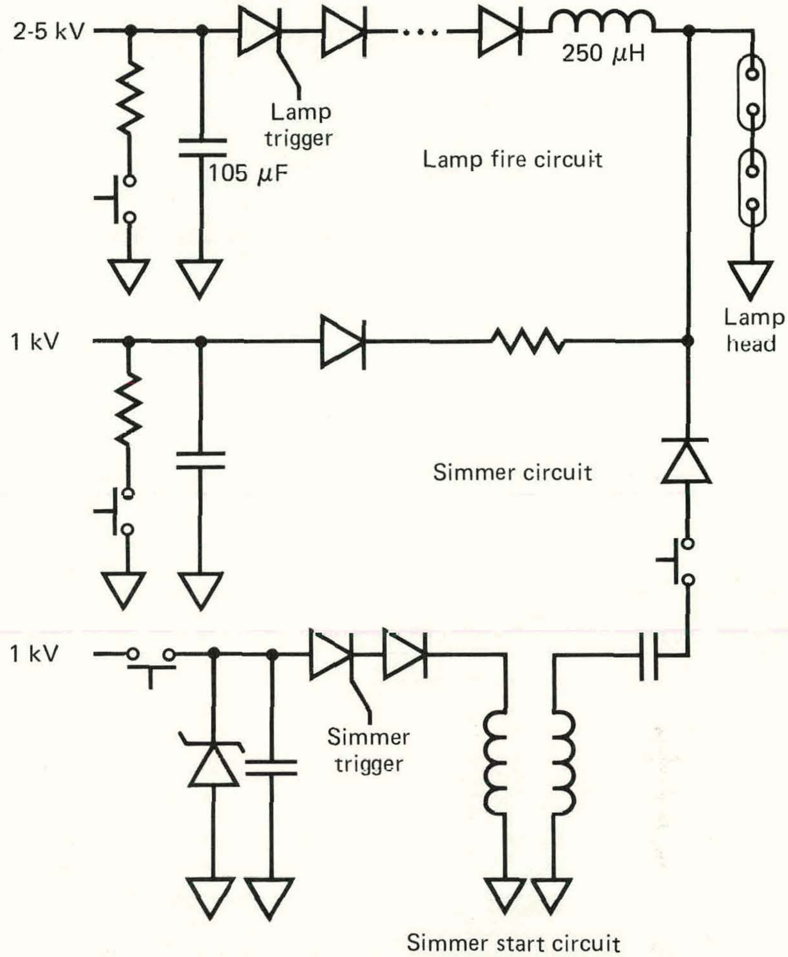

Fig. 2-388. The 10-Hz flashlamp pulse-forming and simmer circuits.

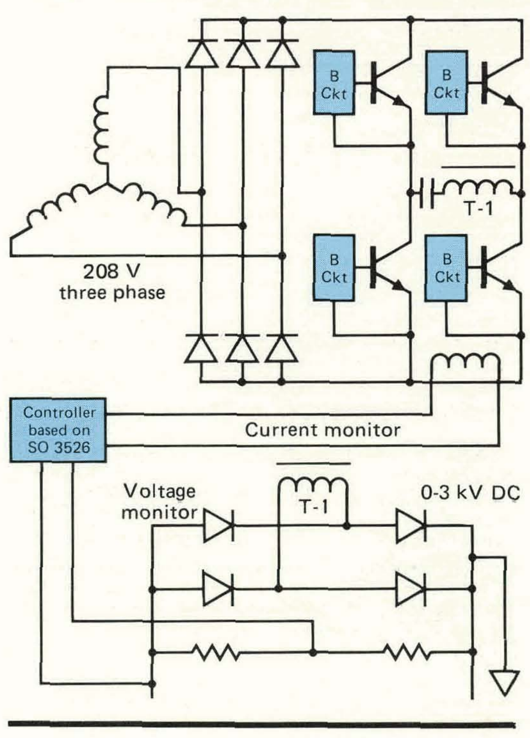

Fig. 2-389. The 20-kHz switching power supply for the Nd:YLF rod amplifier.

as an input. For single-pulse mode, we use a push button and a 9602 integrated circuit as a parallel input. Both inputs are connected through a 4070B OR gate.

Authors: L. P. Bradley, B. T. Merritt, and E. L. Orham

Major Contributors: D. Johnson and R. Birch

Basic Research

Introduction

Three research programs are supported by the Division of Materials Science of the DOE Office of Basic Energy Sciences (BES). These programs, devoted to studying properties and operating characteristics of optical materials for high-power lasers, are conducting research in the following fields:

- Optical materials.
- Laser-excited fluorescence in amorphous solids.
- Surface physics and chemistry of laser-induced damage.

These programs complement those of the Laser Fusion Program by exploring basic phemomena of importance to the development of improved laser materials.

Optical Materials Research. In the past several years, we have investigated many different low-optical-index materials in an effort to find materials with very small nonlinear refractive indices, n_2. Solids having the smallest n_2 values at wavelengths of 1 μm are fluoride crystals and glasses containing low-atomic-number cations.[178] Of these, beryllium–fluoride-based glasses are particularly attractive for high-power-laser applications because of the combination of several favorable optical, spectroscopic, and physical properties.[179]

Beryllium–fluoride glasses have several unique properties[180] and, therefore, have been the subject of many additional studies. During the past year, we prepared a number of special samples for spectroscopic measurements at wavelengths ranging from microwaves to x rays. Experiments included the following (titles in parentheses cite articles found in this section):

- Laser-induced fluorescence-line-narrowing (FLN) spectroscopy of rare-earth ions in unitary and binary fluoroberyllate glasses. The results were compared with the local structure predicted by computer simulations ("Computer Simulations of Glass Structure").
- Fluorescence line-narrowed measurements of the homogeneous line widths of neodymium (Nd^{3+}) in glass, variations of the line widths with glass composition, and the effects of line widths on energy extraction from glass lasers ("Homogeneous Line Widths and Energy Extraction in Laser Glass").
- Electron-spin-resonance investigations of iron-group impurities in beryllium–fluoride glasses ("Beryllium–Fluoride Glasses").
- Studies of the phonon spectrum and ion-phonon coupling in glasses from FLN vibronic spectra ("Vibronic Spectra of Rare Earths in Glass").
- Vacuum-ultraviolet-reflectance measurements of single- and multi-component-BeF_2 glasses ("Beryllium–Fluoride Glasses").
- Extended-x-ray-absorption-fine-structure (EXAFS) studies of rare earths in BeF_2 to obtain information about the average coordination at rare-earth sites ("Beryllium–Fluoride Glasses").
- Preparation of isotopically enriched, rare-earth-doped glasses of zero neutron coherent scattering length to investigate the local environments ("Beryllium–Fluoride Glasses").

For fusion lasers operating at shorter wavelengths, such as rare-gas-halide lasers (e.g., KrF at 248 nm) or the higher harmonics of the neodymium-laser wavelength, wide band gap optical materials are needed to reduce both linear and nonlinear absorption. When the laser-photon energy becomes on the order of, or greater than, one-half the fundamental band gap, two-photon absorption (2PA) is energetically possible. Data on 2PA coefficients of wide band gap optical material are limited.[181] To measure not only values at discrete wavelengths of interest, but also the 2PA spectrum, we first set up an Nd:YAG (yttrium–aluminum–garnet) laser, a tunable dye laser, and harmonics generators as a source to cover a wide spectral range, and, second, developed photoacoustic and photorefraction techniques for detecting the weak 2PA. The development of the instrumentation and techniques is discussed under "Nonlinear Optics" in this section.

At higher photon energies, the nonlinear refractive index of optical materials will also change. (The n_2 and the 2PA coefficient are related to the real and imaginary parts of the third-order susceptibility, respectively.) To investigate the wavelength dispersion of n_2, we set up a time-resolved interferometer, similar to that used previously for n_2 measurements at 1 μm.[178] A major improvement to the system was made by adding a vidicon readout to the streak camera, thus reducing data-analysis time (described in "Nonlinear Optics"). Measurements of n_2 of various optical glasses and crystals, at higher harmonics of the Nd-laser frequency, are planned using this interferometer system.

There is a continued need for crystalline materials for solid-state laser systems, both as lasing media and as nonlinear materials for frequency conversion. We have, therefore, set up a state-of-the-art crystal-growth facility, which uses the Czochralski method for preparing materials from the melt (this facility is discussed in this section under "Crystal Growth Facilities").

Laser-Excited Fluorescence. For solid-state lasing media, such as Nd-doped glass, we are interested in the spectroscopic properties of the Nd^{3+} ions, in addition to the nonlinear-optical properties. The second BES research program uses laser-induced-FLN techniques to explore the site-to-site variations in the spectroscopic properties of activator ions in amorphous materials.[182] While these microscopic inhomogeneities are not evident for lasers operating under small-signal conditions, they become important for lasers operating under large-signal or saturated-gain conditions where hole burning and gain reduction occur.

To investigate the local structure and fields at laser ion sites in glass, and the site-to-site variations that cause inhomogeneous broadening, we are calculating the structure of glass from first principles. Each simulation shows a different ion configuration about the laser-ion; the collection of such configurations reproduces the inhomogeneities in an actual glass. Our computer simulations of the local structure in simple rare-earth-doped BeF_2 glass[183] demonstrated that there is no single rare-earth-site symmetry, or nearest-neighbor distance, or coordination number. Probability distributions for these properties were derived from the computer-predicted structures. We have now extended the computer simulations of glass, using molecular-dynamics (MD) techniques, so that systems of 400 ions of five different species can be treated. This allows us to model the complexities present in commercial multicomponent glasses. Radial distribution functions and coordination numbers at cation sites in beryllium–fluoride glasses, both simple and modified, have been determined. These determinations and their interpretation are found summarized under "Computer Simulations of Glass Structure" in this section.

Knowing the positions of the anions and cations surrounding the rare-earth ion in glass, the next step is to model the interactions and calculate electronic energy levels and transition probabilities. From these results, broadband-excited and laser-excited optical spectra can be simulated. The simulations will be done using molecular orbital self-consistent-field calculations. Programs for these calculations are currently being developed.

Both averaged and dynamic processes can be studied using MD methods. In the course of our simulations of BeF_2 glass we discovered some anomalous low-frequency excitations at defect sites. These may be related to the many anomalous properties of amorphous materials at low temperatures (see "Anomalous Low Frequency Excitations in BeF_2 Glass" in this section).

Laser-excited-fluorescence studies in glass have clearly demonstrated site-dependent differences in energy levels and in transition probabilities.[182] Variations in the ion–phonon coupling strength are evident from studies of homogeneous line-broadening and relaxation by multiphonon emission. More direct evidence can be obtained from vibronic spectra, but good, easily interpretable data are not readily available. We have found, however, that using trivalent gadolinium as the probe-ion and sensitive FLN techniques, excellent vibronic spectra can be obtained. Results for a number of different glasses have provided new information about the ion-phonon interactions for rare earths in glass (see "Vibronic Spectra of Rare Earths in Glass" in this section). These interactions affect both the quantum efficiency and the energy extraction efficiency of glass lasers.

Laser-Induced Damage. As noted throughout our discussions of solid-state-laser technology in this and previous annual reports, thresholds for laser-induced damage continue to be a limiting factor in the design and performance of fusion lasers. The lowest damage thresholds occur at surfaces, in thin-film coatings, and at film-substrate interfaces. The third BES program is a study of the physical and chemical properties of surfaces governing optical damage thresholds.

To address the effects of surface physics and chemistry on damage thresholds, we built an ultra-high-vacuum chamber for in situ sample preparation, damage testing, neutral- and charged-particle emission measurements, and surface diagnostics. This apparatus, and the results obtained thus far, are described in this section under "Surface Physics and Chemistry of Laser-Induced Damage." Carefully controlled surface preparation and characterization, and accurate damage threshold measurements, should yield new insights into the stubborn problem of laser-induced damage.

Other Activities. We have continued our survey of laser host materials in the search for special characteristics and property extremes. Halide glasses were considered because the local fields should be relatively weak, resulting in narrow fluorescence bandwidths; and the phonon frequencies are low, resulting in more fluorescing states with high quantum efficiency. Last year we reported on the investigation of a series of mixed-anion chlorophosphate glasses. These glasses exhibited the largest simulated emission cross section, for the ${}^4F_{3/2} \rightarrow {}^4I_{11/2}$ transition of Nd^{3+}, in any glass measured to date.[184] We have extended those studies to pure chloride and bromide glasses and have found even larger lasing cross sections for glasses based on bismuth chloride as the glass former. These results and a review of the spectroscopic properties of rare-earth-doped glasses and how they can be tailored are presented in this section under "High Cross Section Nd^{3+} Laser Glasses."

The radiative quantum efficiency of the upper laser state of ions in solids affects the overall pumping-efficiency. Accurate measurements of the quantum efficiency are frequently plagued by systematic errors or inadequate sensitivity. We have used photoacoustic techniques to measure the nonradiative contribution to excited-state decays and to determine, therefrom, the quantum efficiency. This method has been applied to rare-earth-doped glasses of both high and low quantum efficiencies, and to Nd:YAG crystals. The results, which differ, in some cases, from earlier values obtained by others, are presented under "Quantum Efficiency Measurements Using Photoacoustic Techniques" in this section.

The observation of FLN is a simple method to prove that a lasing medium is inhomogeneous and, therefore, subject to spectral hole burning.[185] Since FLN is observed in all Nd-doped glasses studied to date, hole burning is a common phenomenon. The degree of spectral hole burning is dependent on the ratio of the homogeneous-to-inhomogeneous line widths; therefore, we have investigated the relative magnitude of these line widths as a function of glass composition.[186] As described under "Homogeneous Line Widths and Energy Extraction in Laser Glass" in this section, an empirical relationship was discovered between the homogeneous line width and the velocity of sound in the glass. This provides guidance in selecting materials that minimize the effects of hole burning and maximize the output energy.

Author: M. J. Weber

Optical Materials Research

Beryllium–Fluoride Glasses. Beryllium–fluoride (BeF_2) glasses possess several attractive features as optical materials for high-power lasers. These include:

- The lowest known refractive-index nonlinearities in solids and, hence, small self-focusing and self-phase-modulation effects.
- A wide range of transparency, particularly in the ultraviolet.
- Laser-gain parameters in the range of interest for fusion lasers.

- Satisfactory thresholds with respect to laser-induced damage.[187,188]

We have investigated beryllium–fluoride glasses extensively in the last few years (described in the preceding four annual reports). These studies have extended beyond the application for lasers. Simple and multicomponent BeF_2 glasses are characterized by a continuous random-network model of glass structure, analogous to silicate glasses. However, the BeF_2 glasses are more ionic, wide-bandgap glasses and, hence, are more appropriate for many fundamental glass studies.

We have maintained a capability for preparing beryllium–fluoride glass at LLNL and have melted several special glasses during the past year. Because of the toxic nature of beryllium, special facilities are required. The melting and casting facilities and general experimental techniques for preparing these glasses are described elsewhere.[187,189]

A large number of rare-earth-doped fluoroberyllate glasses were prepared for optical-spectroscopy measurements. Those included several samples for fluorescence-line-narrowing experiments reported in detail later in this section (see "Computer Simulations of Glass Structure," "Vibronic Spectra of Rare Earths in Glass," and "Homogeneous Line Widths and Energy Extraction in Laser Glass").

Beryllium–fluoride glass is expected to have a very large bandgap. Thus far, however, efforts to determine the intrinsic bandgap from vacuum-ultraviolet (VUV) absorption spectra have been plagued by the presence of trace impurities and scattering centers which mask the true absorption edge.[187,190] In a collaborative effort with R. T. Williams and D. J. Nagel of the Naval Research Laboratory, we have recorded VUV-reflectance data for pure and multicomponent BeF_2 glasses in the 8- to 100-eV range; measurements were also made of optical transmission, photoemission, and angle-dependent VUV light scattering. The VUV source employed for these experiments was the SURF II electron-storage ring at the National Bureau of Standards.

The near-normal reflectance spectrum in Fig. 2-390 provides the first direct indication of the intrinsic bandgap of vitreous BeF_2, as well as the electronic structure above the gap. A prominent peak at 12.8 eV is presumed to be associated with an exciton. A second steep rise beginning at 14 eV may then be associated with the onset of band-to-band transitions. A small peak near 30 eV is probably associated with transitions from the F^- 2s level. For a multicomponent glass of composition (mole %) 49 BeF_2, 27 KF, 14 CaF_2, 10 AlF_3, the dominant low-energy peak shifted from the 12.8 eV of the vitreous BeF_2 to 11.3 eV. (The corresponding increase in the refractive index at 593 nm is from 1.28 to 1.34.) To compare the spectra of crystalline and amorphous phases of BeF_2, several polycrystalline samples were prepared. Measurements are scheduled for 1981.

Electron-spin-resonance investigations of undoped, unirradiated BeF_2 glasses were conducted by D. L. Griscom and M. Stapelbroek of the Naval Research Laboratory. Two relatively intense resonances were observed, one of which was due to Mn^{2+} impurities. The second resonance was shown—by temperature and frequency dependence studies coupled with computer line-shape analysis—to be a ferromagnetic-resonance signal due to precipitated-ferrite phases. The data suggest that these ferrites are somewhat heterogeneous and most likely comprise magnetite-like phases, similar to $NiFe_2O_4$. An optical-extinction curve, rising into the ultraviolet with an approximate fourth-power dependence on wavelength, was tentatively ascribed to light-scattering by ferrite particles 100 nm in diameter.

Knowledge of the rare-earth-ion environment is important for optimizing laser glasses for fusion lasers. The local structure in BeF_2 glasses has been simulated using Monte Carlo and molecular-dynamics methods (for a description of this work see

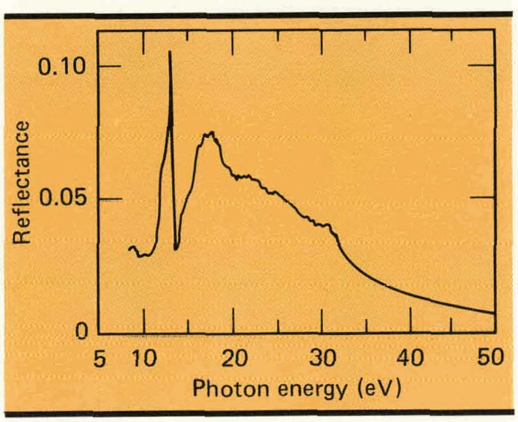

Fig. 2-390. Near-normal reflectance spectrum of pure BeF_2 (from Williams and Nagel).

"Computer Simulations of Glass Structure" in this section). Validity of these computer simulations has been tested, to a limited extent, by comparing the results with optical spectra. A direct probe of the local environment can also be obtained from an analysis of the extended x-ray-absorption fine-structure (EXAFS) of the rare-earth absorption edge. Such spectra for neodymium in glassy BeF_2 were recorded in a collaborative effort by J. Wong of General Electric at the Stanford Synchrotron Radiation Laboratory. Data on crystalline NdF_3 were also recorded to obtain the necessary phase shifts required in analyzing the spectra. Data reduction is presently in progress. The results should yield the average rare-earth nearest-neighbor fluoride distance-and-coordination number for Be^{2+} by F^-.

The rare-earth environment can also be probed using neutron-scattering techniques. The particular system to be studied, in collaboration with A. Wright and R. Sinclair, is $NaF–DyF_3–BeF_2$. Measurements will also be made on pure BeF_2 and a $NaF–BeF_2$ glass having the same $Na:BeF_2$ ratio as the DyF_3-containing glasses. To permit study of the environment of the Dy^{3+} ion, two $NaF–DyF_3–BeF_2$ samples having the identical chemical composition are being prepared; but one of them will contain Dy isotopically enriched to give a zero neutron coherent scattering length (denoted ^0Dy). The neutron-diffraction pattern of the latter will give information on the modification of the $NaF–BeF_2$-glass matrix caused by the introduction of DyF_3, while the difference between the two Dy-containing samples will give the environment of the Dy ion. These results can be compared with the EXAFS data and provide a further test of our computer-simulated glass structure. Preparation of the glasses for this investigation is under way. Beam time for conducting these experiments is scheduled for the second half of 1981.

Author: M. J. Weber

Major Contributor: D. D. Kingman

Nonlinear Optics

Measurements of Nonlinear Refractive Index. As an intense laser pulse propagates through a fusion laser, its phase front, initially planar, accumulates phase alterations. One class of these alterations arises from the intensity-dependent refractive index.[191] An optical component with a large nonlinear index effectively maps the local intensity pattern onto the laser phase-front. For bell-shaped laser pulses, typical in small lasers, this effect increases the axial intensity of the pulse as it propagates, causing "whole-beam self-focusing." For high-fill-factor fusion-laser pulses, the result is slightly different. These pulses have modulation in the form of spikes and ripples superimposed on an otherwise flat profile, and these "hot spots" are intensified as the pulse propagates through the laser chain. This process is "small-scale self-focusing" and, if uncontrolled by spatial-filtering, leads to damage in laser components or to a reduction in the focusable energy for target experiments. For optimum performance in high-power fusion lasers, we desire optical materials with the lowest nonlinear index, which will minimize the effects of small-scale self-focusing.

A major trend in laser fusion research is toward the use of short wavelengths (<1 μm) for improved target performance. In 1980, harmonic generation was used on the Argus laser, and incorporated into the design of the Nova and Novette lasers, to produce fusion pulses at 0.53 and 0.35 μm. We anticipate the need to measure the nonlinear index at these wavelengths, because physical theories[192] indicate that as the wavelength is shortened, the index rises. In particular, we expect some enhancement from near-resonant, two-photon transitions in typical laser glasses. (The extent of this expected enhancement and its potential impact on laser designs is unknown; however, the two-photon question is being investigated, as reported in the second portion of this article.)

In addition, even with a constant nonlinear index, the growth rate of small-scale self-focusing[193] depends inversely on wavelength and is therefore three times larger at the third-harmonic wavelength than at the familiar fundamental wavelength. This fact increases the importance of measuring the nonlinear index.

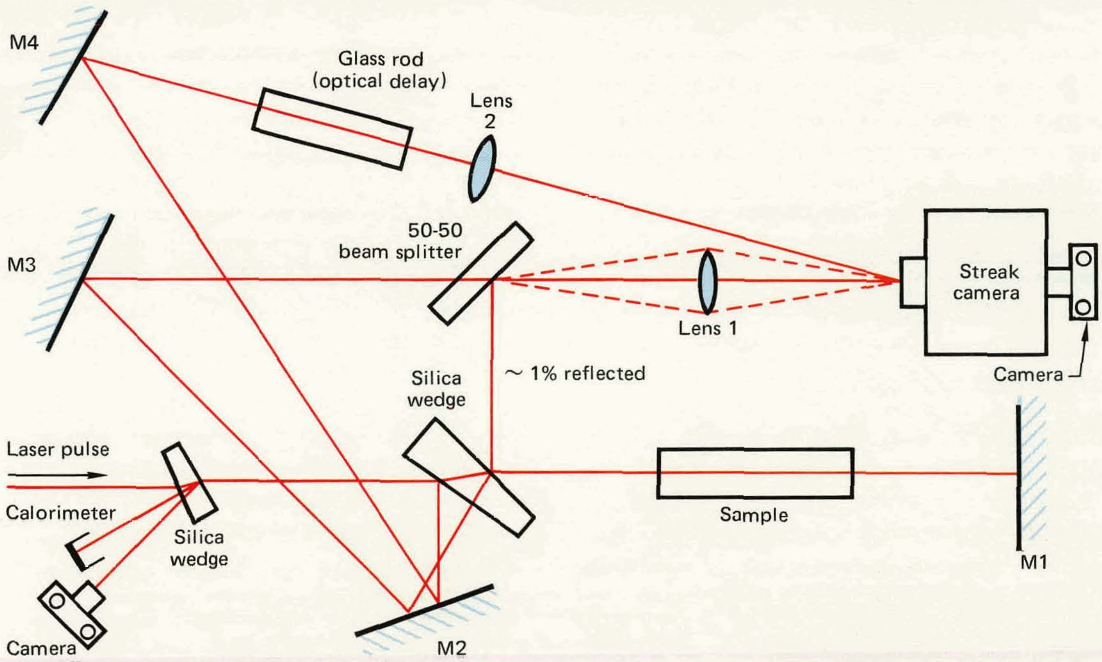

Fig. 2-391. Time-resolved interferometer configuration for measuring the nonlinear refractive index of optical materials.

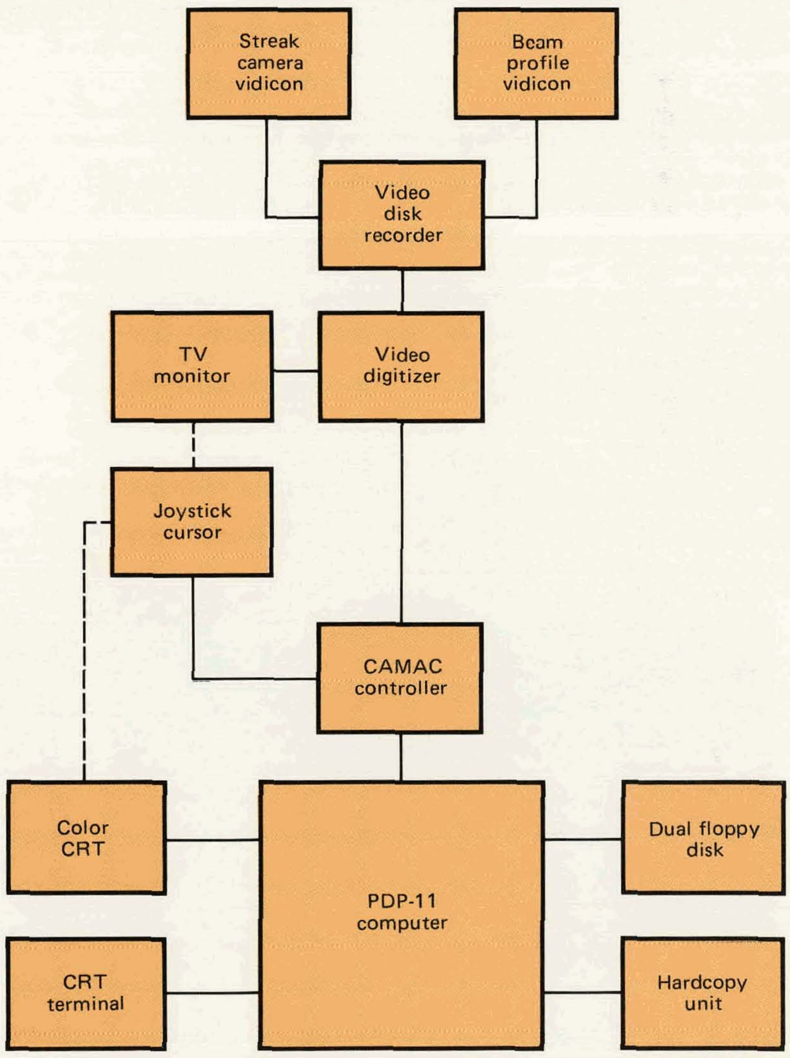

Fig. 2-392. Schematic diagram of the vidicon computer-based data-acquisition and analysis system used for time-resolved interferometry (after Ref. 197).

In 1980, we began a project to measure the nonlinear index in fusion materials at harmonic wavelengths of the Nd:YAG laser. As our first step, we reconstructed the time-resolved interferometer, used previously by Bliss,[194] Milam,[195] and others,[196] for accurate nonlinear-index measurements. Figure 2-391 shows the basic layout of this experiment. A streak camera monitors the real-time fringe-pattern shift that is induced by the passage of the intense laser pulse through the sample. Simultaneously, the temporal and spatial distributions of the laser pulse are recorded. By correlating peak fringe-shift with peak laser-irradiance, the nonlinear refractive index of the sample is determined.

A significant addition to the apparatus was made by using a digital video system,[197] in place of photographic film, to record the streak and laser profiles. Figure 2-392 shows a block diagram of the new recording and analysis equipment. We anticipate a major improvement in the rapidity of data analysis for each sample: several minutes with the video system vs several days with the previous film techniques. Figures 2-393(a) and 2-393(b) illustrate the data output from the vidicon–computer analysis system. Figure 2-393(a) shows the color-encoded spatial-energy distribution at a plane equivalent to the front surface of the sample. Figure 2-393(b) shows the time-dependent fringe pattern recorded with the streak camera.

We are validating the performance of the present apparatus by measuring the well-known nonlinear index in a rod of Nd-doped ED-2 laser glass. These tests will be completed in early 1981. We will then convert the apparatus for measurement of the nonlinear index at 0.53 and 0.35 μm, using harmonic pulses of the ILS laser.

Two-Photon Spectroscopy Studies. As fusion lasers are extended to ever shorter wavelengths, the question of two-photon absorption in wide-bandgap optical materials needs to be addressed. For this reason we are setting up a laser laboratory for two-photon spectroscopy studies. The primary goals of these studies are to obtain accurate absolute values of two-photon absorption coefficients for all presently used optical materials at the operating wavelengths of the projected visible and UV-fusion lasers, and to find a relationship between the two-photon absorption cross section and some more easily measured sample parameter(s). With the above information, we can make informed decisions when selecting optical materials for short-wavelength, high-power fusion lasers.

There are several techniques in use for measuring two-photon absorption cross sections. These include transmission measurements, laser calorimetry, photoacoustic, and photorefractive techniques. Of these methods, only the intensity-dependent transmission method, using well-calibrated high-intensity laser pulses, has been used for wide-bandgap materials.[198] Laser calorimetry studies have been performed on narrow-bandgap semiconductors;[199] while the photoacoustic experiments have been on either gases[200] or liquids[201,202] with relatively large two-photon absorption cross sections. A photorefractive thermal-lens technique has also been used for liquids.[203] In this technique the change of focus of a low-intensity probe beam is measured as it traverses the region of the sample that has been momentarily heated by the linear- and nonlinear-absorption processes that occur when a high-intensity laser pulse traverses the sample. Of the methods described above, the most sensitive appear to be the photoacoustic and photorefractive techniques.

In our laboratory we have set up a Molectron Nd:YAG-pumped dye laser, capable of producing 250-, 125-, and 50-mJ pulses at the harmonic wavelength of 530, 350, and 270 nm, respectively, and, reasonably energetic pulses in the regions between, by pumping a dye laser. These pulses are 15 ns in duration, and thus fairly high intensities can be achieved by beam focusing. In fact, at most wavelengths, with our focused beams, our operating intensity levels are limited by the damage thresholds of the materials.

We have also designed and assembled both a photoacoustic and a photorefractive detection system. The photoacoustic system is similar to the one that we used previously[204] for measuring thin-film linear absorptions as low as one part in 10^{-5}. To achieve similar sensitivities with our new

Fig. 2-393. Vidicon/computer analysis data output. (a) Color-encoded spatial profile of laser energy distribution in sample. (b) Video picture of the time-dependent output of the streak camera.

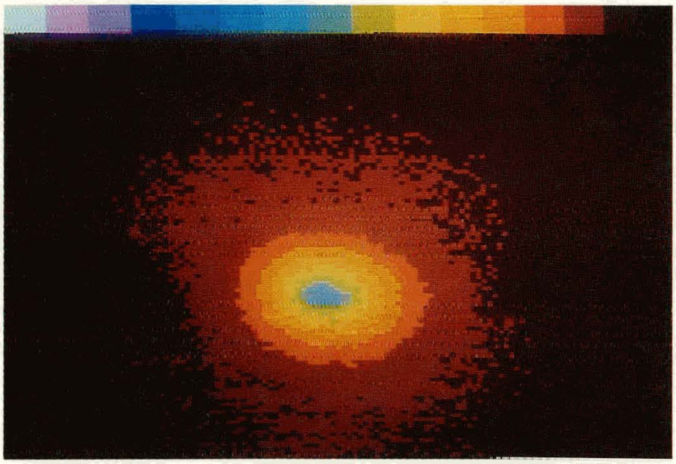

(a) Color encoded laser energy distribution in sample

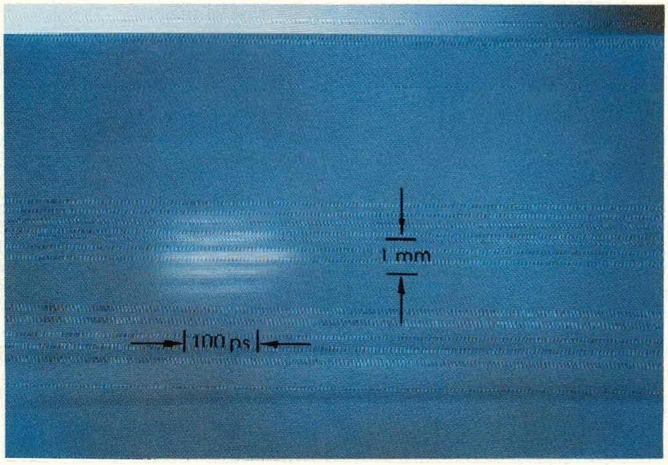

(b) Streak camera output video picture; pulse width (FWHM)=120 ps

15-ns pulse laser, the piezoelectric transducer must have a resonance frequency in the 50-MHz region. The need for these higher frequencies has presented us with some difficulties. The photorefractive system can measure either the thermal blooming[205] or the deflection of a probe He–Ne laser beam that occurs because of the presence of thermally induced refractive index changes. This system appears to be operating nicely.

We have, at this point, performed only a preliminary photorefractive experiment using excitation radiation of 560 nm on a Corning UV filter glass (3-75) with an absorption threshold at 350 nm. Figure 2-394 shows the data from this experiment. We plot the energy-normalized photorefractive signal, q/E, vs the beam energy E. From these data and knowing, from conventional spectrophotometry, that the linear absorption coefficient $\alpha \simeq 0.1\ \mathrm{cm}^{-1}$, we obtain, using beam intensities estimated from energy measurements and from pulse-width and beam-diameter requirements, a value for the two-photon absorption coefficient $\beta \simeq 6 \times 10^{-4}$ cm/MW. This value for β is reasonable for this particular material. We are assembling a beam-diagnostic system which will provide us with a more accurate evaluation of beam intensity in the future. From the signal-to-noise ratio obtained in this experiment, we believe that we will be able to measure βs of the order of 10^{-5} cm/MW with the intensities available, and thus be able to fulfill our stated goals.

Authors: W. T. White, W. L. Smith, and A. Rosencwaig

Major Contributors: D. Milam, M. J. Weber, M. A. Henesian, and T. W. Hindley

Crystal Growth Facilities. To provide for the growth of new optical crystals for laser and nonlinear optics applications, an automated crystal puller facility was put into operation. Figure 2-395 shows the facility and a technician measuring the temperature of a melt contained in an iridium crucible prior to pulling a crystal by the Czochralski technique.

High-frequency power, for induction heating of the melt, is supplied by a 25-kW, 10-kHz solid-state generator. A flow of nitrogen gas is employed to minimize oxidation of the crucible. Other equipment shown in the photograph is the vertical console containing the electronic components for controlling power to the furnace and for programming the crystal-pulling operation. The pulling feature uses a crystal-weighing technique for automatic control of diameter from the point of seed-on to completion of the growth run.[206–208] The electronic balance for continuously weighing the crystal and the apparatus for

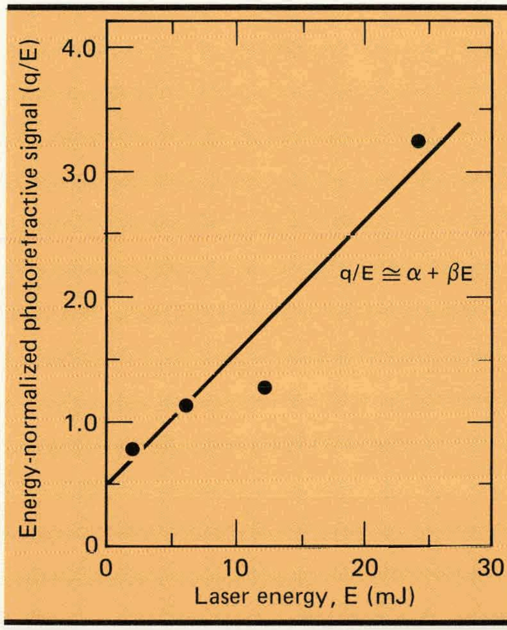

Fig. 2-394. The energy-normalized photorefractive deflection signal q/E vs incident laser beam energy.

Fig. 2-395. Crystal growth station.▼

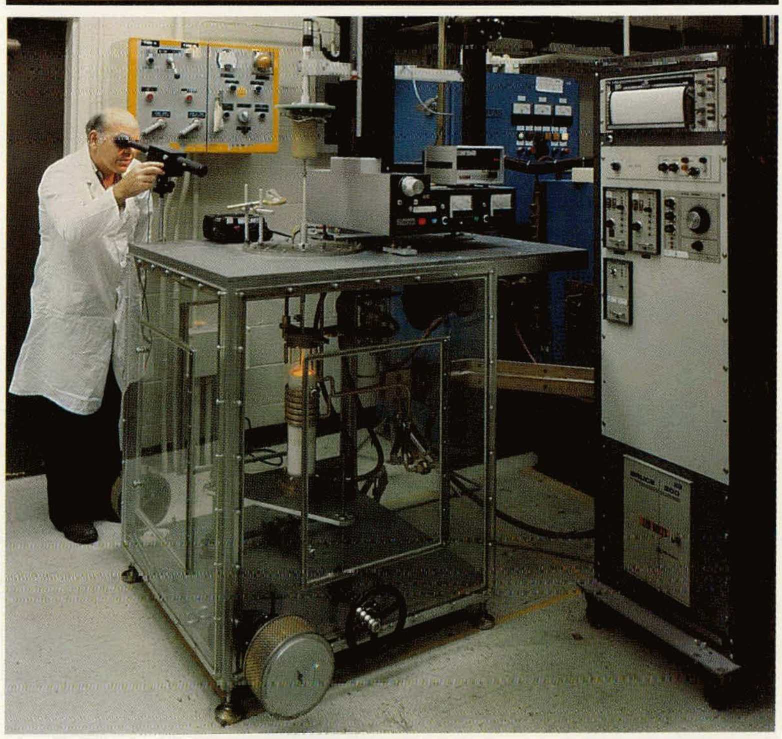

pulling the crystal are on top of the furnace cabinet. The entire system is state-of-the-art and provides growth rates from 0.5 to 250 g/h, with growth diameter controlled over 90% of the crystal length. Maximum capacity is 400 g; maximum temperature is limited by the size and melting point of the crucible material.

Not pictured are the facilities currently being installed for powder feed preparation and for the purification of starting materials. These operations will be important in growing high-optical-quality laser crystals.

This year we successfully synthesized $Na_3Li_3Al_2F_{12}$ (cryolithionate) powder by fluorinating $AlCl_3$, LiCl, and NaCl powders with aqueous HF. Powder-pattern data indicate a cubic garnet lattice[209–211] (a = 12.12 Å) with a melting point at 750°C. This is a potentially interesting low-index laser host-material; techniques for growing large single crystals are under consideration.

A sample of crystalline BeF_2, produced by hot pressing powdered BeF_2 glass and isomorphous with quartz, was cut and polished for optical-reflectivity measurements by personnel from the Naval Research Laboratory at the National Bureau of Standards. Results will be compared to those obtained from the amorphous phase of BeF_2 described earlier in "Beryllium–Fluoride Glasses."

We plan to investigate the growth of several low-index fluoride crystals including both simple compounds such as AlF_3 (cubic AlF_3 crystals have been grown using molten $PbCl_2$ as a solvent[212]) and complex compounds such as the cryolithionate above. Hosts for either transition-metal or rare-earth ions are of interest. Of particular interest are hosts that can be co-doped with both groups of ions, thereby providing the possibility of using sensitized fluorescence to improve optical pumping efficiency. Another material of interest is the fluoro chlorides MFCl (M = Ba, Sr) as a possible host for V^{2+} and divalent rare earths. As described in the section on "Energy-Storage Solid State Lasers V:MgF_2", V^{2+} in MgF_2 is a good energy-storage solid state laser.

Authors: C. F. Cline and H. W. Newkirk

Laser-Excited Fluorescence Studies of Amorphous Solids

Computer Simulations of Glass Structure. We have simulated rare-earth-doped fluoroberyllate glasses by the molecular-dynamics (MD) technique of statistical mechanics.[213] The result of the simulation is similar to the results of Monte Carlo calculations described previously[214]: a collection of glasses, each containing one rare-earth ion, and in which the local environment of each rare earth is different. From these structures, the spectroscopic properties of the simulated glasses can be computed and compared with experiment.[215]

The MD technique, which is widely used to simulate fluids and glasses,[213] involves numerically integrating Newton's equations of motion. A number of ions (our current programs can treat 400 ions of five different species) are contained in a cubic box whose size is determined by the density of the material. The ions i,j interact with the potential

$$V_{ij}(r) = \frac{q_i q_j}{r} + A_{ij} e^{-\sigma r} \tag{81}$$

where r is the distance between the ions, and q_i the charge of ion i. The parameter A_{ij} is positive and is fixed according to the ion size. Periodic boundary conditions[213] eliminate surface effects. The temperature of the material is determined by initially creating a Maxwell–Boltzmann distribution of ion velocities such that for N ions the total kinetic energy = 3N/2kT, T being the absolute temperature. Newton's equations of motion are integrated numerically using an algorithm due to Verlet[216] with a time step of 0.002 ps. (The maximum vibrational frequency of BeF_2 is about 0.033 ps^{-1}.) We made runs on a PDP 11-55 computer with an array processor (Floating Point Systems model 120B). Six hundred time steps were generated per hour.

We began with a fluid started from random initial conditions at 10 000 K and slowly cooled. For temperatures above 1300 K, where all fluids were in thermal equilibrium, considerable topological changes in the fluid structure occurred over times greater than 20 ps (computed using the methodology of Ref. 217. A time of 20 ps is a reasonably long computer run). At temperatures of 1000 K and below, fluids were metastable since relaxation times were so long that topological changes rarely occurred over 20 ps. Thus, on a time scale of 20 ps, the glass transition region is between 1000 and 1300 K. (The glass transition region, for computer glasses, is quite broad, as discussed in Ref. 218.)

We formed glasses by lowering the temperature (in 10 temperature steps) of an initial equilibrated-fluid configuration to temperatures from 33 to 900 K while integrating the equations of motion. Generally, quenches were made over 4 to 6 ps. As discussed in Ref. 218, computer simulated glasses have astronomically higher quench rates than laboratory glasses.

The MD technique provides information about both the static and dynamic properties of systems. Here we describe the structure of the simulated glasses. Work on dynamic properties is presented in the following article.

We have simulated rare-earth (RE)-doped BeF_2 and also RE-doped BeF_2 glass with additional alkali or alkaline-earth modifiers. We give the compositions of the simulated glasses in Table 2-74, along with a brief summary of some structural features of the simulated glasses. Figure 2-396 is a computer graphics display of a binary fluoroberyllate glass containing a rare-earth impurity. (The blue balls represent beryllium, the green balls fluorine, the red balls calcium, and the white ball in the center, a rare-earth ion.) A collection of 100 such structures is used to represent an actual glass.

The most important structural property of fluoroberyllate glasses is the nearly universal tetrahedral coordination of Be ions by F ions. In BeF_2 the F ions are coordinated by 2 Be ions, while, in the modified glasses, a number of F ions have a single Be neighbor. The 2-fold coordinated F are referred to as *bridging*, while the 1-fold coordinated F are *nonbridging*. In general, nonbridging F are the anions nearest the modifier cations and also the RE, while bridging F are located farther from these cations. Although the Be ions have well-defined coordination numbers, the coordination shells of the modifiers are, in general, poorly defined.

In Fig. 2-397 we show the Be-F Radial Distribution Function (RDF) g(r) and the average coordination number (CN) n(r) for pure BeF_2 and for a glass modified by Na. (The RDF is normalized to unit ion density at large r. Also, note the increase in the Be coordination number with increasing

Table 2-74. Compositions of computer-simulated glasses.

Glass	L(Å)	r_1	n_1	r_2	n_2	r_3	n_3
100 BeF_2 1EuF_3	17.24	1.55	4.1	2.35	7.27	—	—
100 BeF_2 3NaF 1EuF_3	15.85	1.55	4.1	2.35	7.46	2.3	4.5
76 BeF_2 74NaF 1EuF_3	16.61	1.55	4.52	2.35	8.36	2.3	6.8
76 BeF_2 74RbF 1EuF_3	18.09	1.55	4.35	2.35	8.51	2.8	10.0
76 BeF_2 37CaF_2 1EuF_3	16.04	1.55	4.47	2.35	8.68	2.3	7.0

Note: L-cell size; r_1 — Be–F distance at first maximum of Be–F RDF; n_1 — average coordination number of Be by F at 2.4 Å; r_2 — Eu–F distance at first maximum of Eu-F RDF; n_2 — average coordination number of Eu by F at 3.2 Å; r_3 — M-F distance at first maximum of M-F RDF, where M = modifier cation; n_3 — average coordination number of M by F at first minimum of M-F RDF.

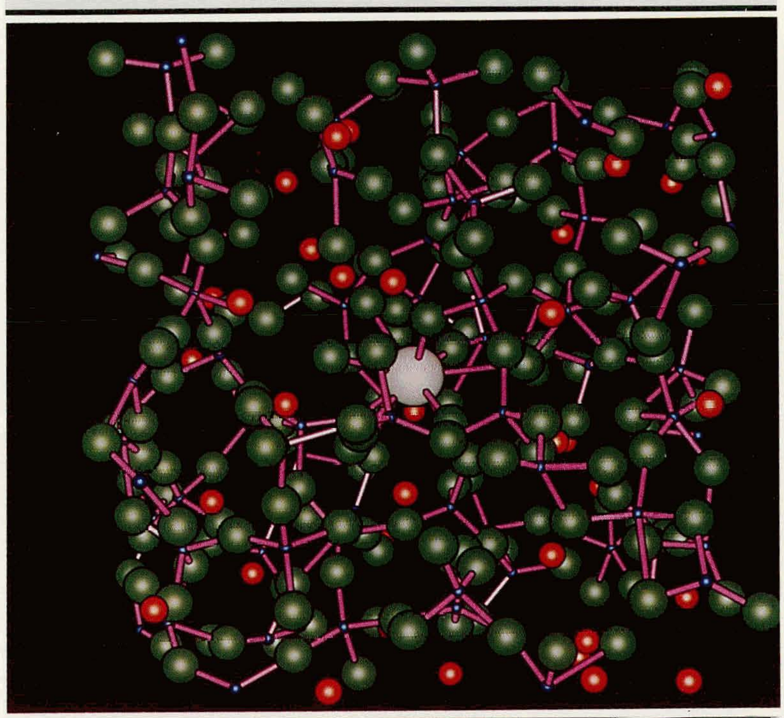

▲ **Fig. 2-396. Computer graphics display of one configuration of a computer-simulated fluoroberyllate glass.**

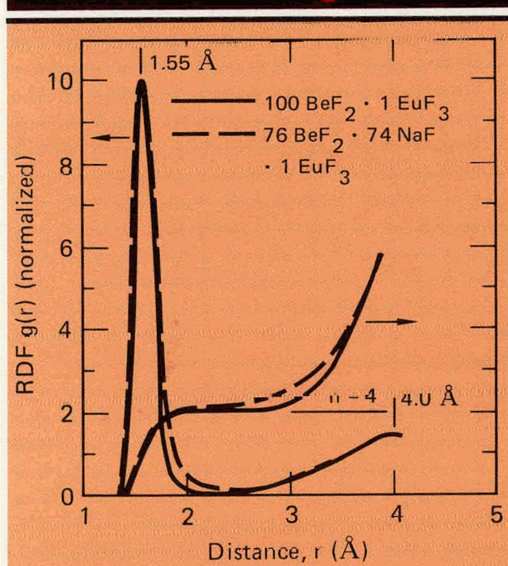

Fig. 2-397. Be-F RDF, g(r), and average coordination number of Be by F, n(r), for BeF_2 and Na modified glass.

modifier content.) The Na curve is typical of all glasses with a high concentration of modifier (glasses 3, 4, 5 of Table 2-74). The Be-F RDF is sharply peaked at 1.55 Å, and n(r) has a broad plateau at about n(r) = 4, due to the well-defined tetrahedral coordination of Be by F. Note that the Be CN by F for the Na-doped glass is larger than for pure BeF_2. This indicates non-bridging F can often lower their potential energies by approaching relatively closely to the BeF_4 tetrahedra.

The Na-F, Rb-F and Ca-F RDFs for various fluoroberyllate glasses are shown in Fig. 2-398. (The labels on the curves refer to the glasses $76BeF_2 \cdot 74NaF \cdot 1EuF_3$, $76BeF_2 \cdot 74RbF \cdot 1EuF_3$, $76BeF_2 \cdot 37CaF_2 \cdot 1EuF_3$. Note that the width of the RDF increases with decreasing field strength of the modifier.) In Fig. 2-399 we show the average CN by F of the modifier cations as well as of the RE and Be (the CN is the average number of F about the cation) (The labels on the curves refer to the average CN of that particular cation in the following glasses: Na–$76BeF_2 \cdot 74NaF \cdot 1EuF_3$; Ca–$76BeF_2 \cdot 37CaF \cdot 1EuF_3$; Rb–$76BeF_2 \cdot 74RbF \cdot 1EuF_3$; Eu–same as Na; Be–same as Na.) We see that the larger the field strength of the cation, the more defined the plateau in n(r) and hence the more well-defined the coordination sphere about the cation. (The field strength of a cation of charge q and radius r is q/r^2. Field strengths decrease in the order Be > Eu > Ca > Na > Rb.) Thus Be ions, with the highest field strengths, have the most well-defined coordination sphere, while the large, monovalent Rb ions, with the smallest field strength, cannot be said to have a coordination sphere at all. As a corollary, the width of the cation-F RDF (Figs. 2-397 and 2-398) increases with decreasing cation field strength, and the first minimum of the RDF is more pronounced

Fig. 2-398. Cation-F RDFs for modified fluoroberyllate glasses.

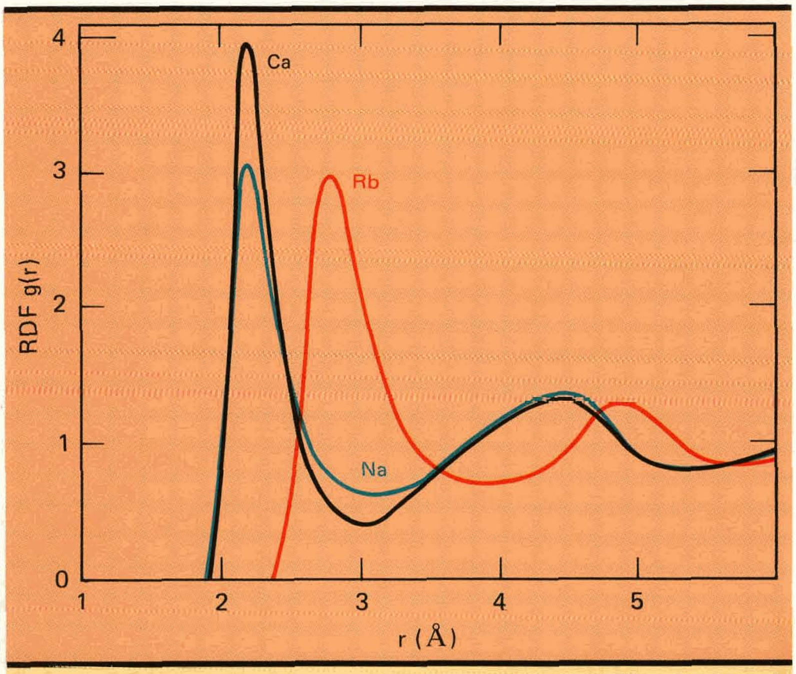

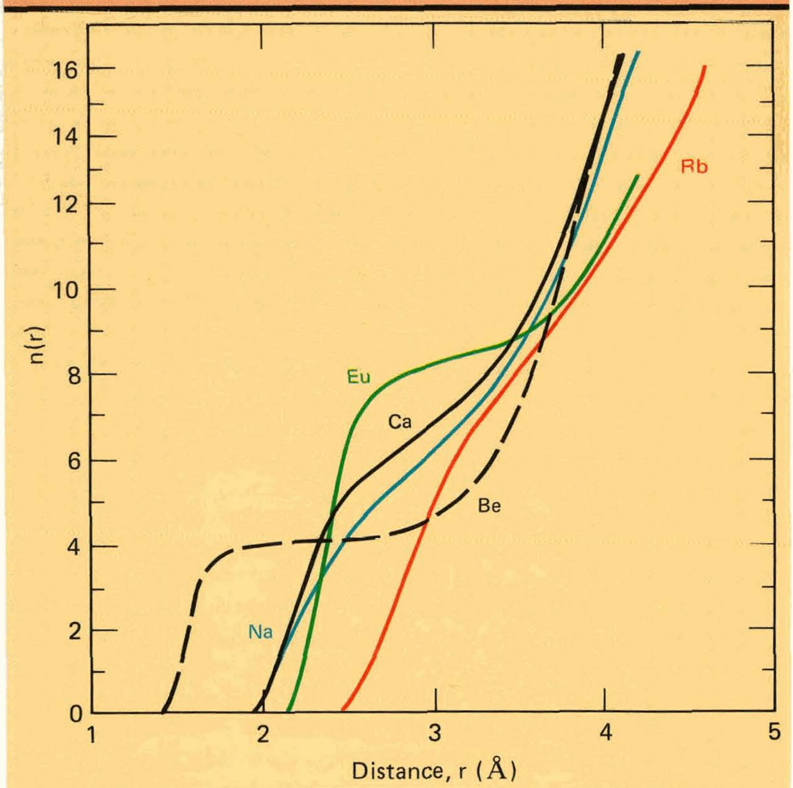

Fig. 2-399. Average coordination number of cations by F, for simulated glasses.

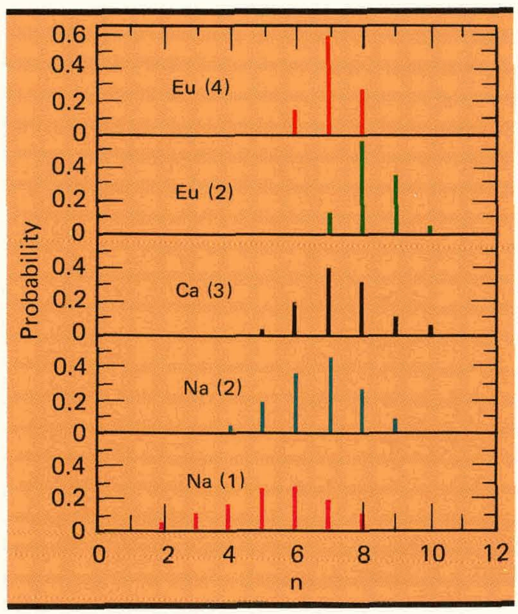

Fig. 2-400. Probability ▶ that a cation has exactly n F neighbors within 3.2 Å.

with increasing field strength of the cation. Comparing the three ions in Fig. 2-399 of the same size (the Eu, Ca, and Na, of charge 3, 2, 1, respectively), we see that the CN by fluorine increases with increasing charge of the cation. All of the properties described above are not surprising and are easily anticipated on physical grounds.

In Fig. 2-400 we show the distribution of F neighbors about the cations for glasses of Table 2-74. (The curves in Fig. 2-400 are labeled by the cation whose coordination distribution is shown. The numbers refer to the glasses: (1) $100BeF_2 \cdot 3NaF \cdot 1EuF_3$ (2) $76BeF_2 \cdot 74NaF \cdot 1EuF_3$ (3) $76BeF_2 \cdot 37CaF \cdot 1EuF_3$ (4) $100BeF_2 \cdot 1EuF_3$.) Specifically, we show the probability that a cation has exactly n F neighbors within 3.2 Å. The fact that these histograms are not delta functions at a single n means that different cations have different numbers of F neighbors within 3.2 Å, and that the same cation will have a different CN in different configurations. Note that the distribution of neighbors is wider the weaker the field strength, in agreement with Fig. 2-399. Note, in addition, that the Na CN for glass 2 (3% Na) is much smaller than for glass 3 (45% Na) and that the RE CN in glass 1 (BeF_2) is less than in the modified glasses (glasses 3, 4, 5).

We deduce from Figs. 2-397 and 2-400 that *the coordination number of all cations increases with increasing modifier concentration.* A similar effect has been observed experimentally by Raman spectroscopy for aluminum coordination of oxygen in silicate glasses.[219]

To explore the structure of the RE site, we show in Fig. 2-401 the RE-F RDFs (the cation label refers to the glasses: Rb–$76BeF_2 \cdot 74RbF \cdot 1EuF_3$; Ca–$76BeF_2 \cdot 37CaF_2 \cdot 1EuF_3$; BeF_2–$100BeF_2 \cdot 1EuF_3$) and in Fig. 2-402 the average RE CNs by F for several glasses (the labels of the curves refer to the glasses: Na–$76BeF_2 \cdot 74NaF \cdot 1EuF_3$; Rb–$76BeF_2 \cdot 74RbF \cdot 1EuF_3$; Ca–$76BeF_2 \cdot 37CaF_2 \cdot 1EuF_3$; BeF_2–$100BeF_2 \cdot 1EuF_3$). Note the increase in CN with increasing modifier concentration, as discussed above. The peak of the RE-F RDF moves to slightly larger distances in the modified glasses. Note also that n(r) has a more well-defined plateau for the Na and Rb glasses than for the Ca glass and for pure BeF_2. The divalent Ca in the second coordination sphere of the RE competes more effectively with the RE for the F ligands than does monovalent Na or Rb and is about as effective as Be in pure BeF_2 in this regard. This disordering effect of modifiers has already been detected, in another context, in silicate glasses by Raman spectroscopy.[220]

In Fig. 2-403 we plot the distribution of F ligands about the RE for the glasses of Table 2-74. (The cation name refers to the glasses: Na–$76BeF_2 \cdot 74NaF \cdot 1EuF_3$; Rb–$76BeF_2 \cdot 74RbF \cdot 1EuF_3$; Ca–$76BeF_2 \cdot 37CaF_2 \cdot 1EuF_3$; BeF_2–$100BeF_2 \cdot 1EuF_3$.) This gives the probability that the RE has exactly n F

Fig. 2-401. The RE-F RDFs.

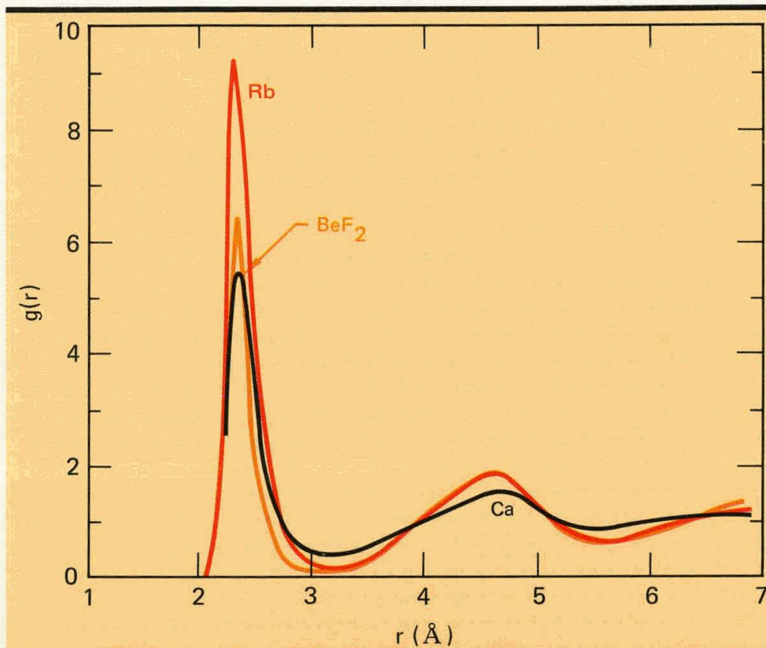

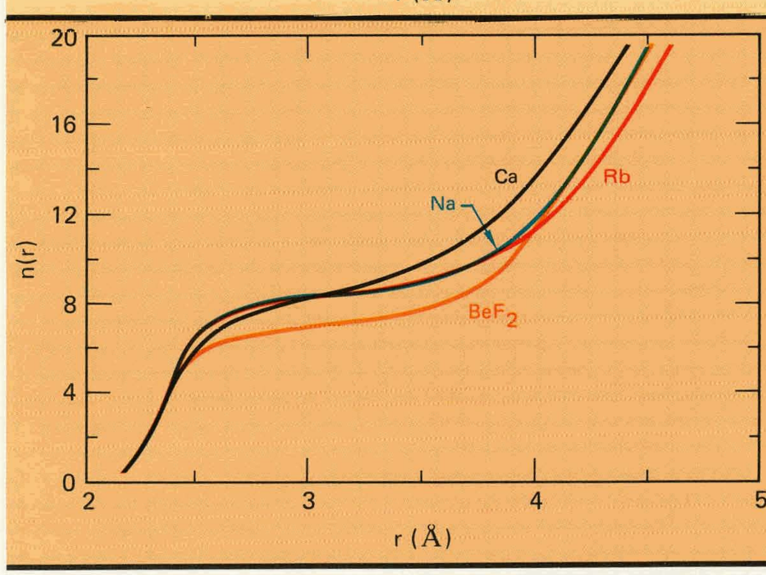

Fig. 2-402. Average coordination number n(r) of the RE by F for various glasses.

neighbors within 3.2 Å. The widths of the distribution are about the same in all glasses. However, the Na distribution is a bit sharper than that for Ca, in agreement with Fig. 2-402 and the discussion above. In addition, all RE-F distributions in modified glasses are somewhat more peaked than that for pure BeF_2 glass. (The distribution of glass 2, with only 3% Na, is about the same as in pure BeF_2.) The differences between the RE site in pure BeF_2 and the sites in modified glasses become greater when we examine distribution functions more carefully. For instance, the F ligands near the RE can have 0, 1, or 2 Be neighbors (within 2.4 Å), and the number of neighbors can depend upon the distance of the ligand from the RE. This distribution of Be neighbors is a type of disorder not given in the RDFs. It can have a profound effect on the F wave function and hence can affect the crystal field and the energy levels of the rare earth.

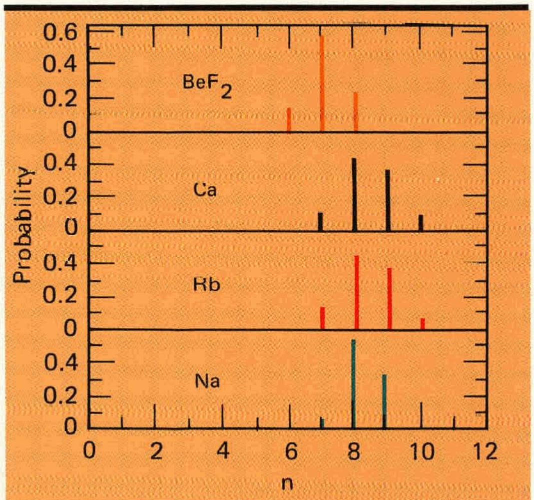

Fig. 2-403. Probability that the RE has exactly n F neighbors within 3.2 Å.

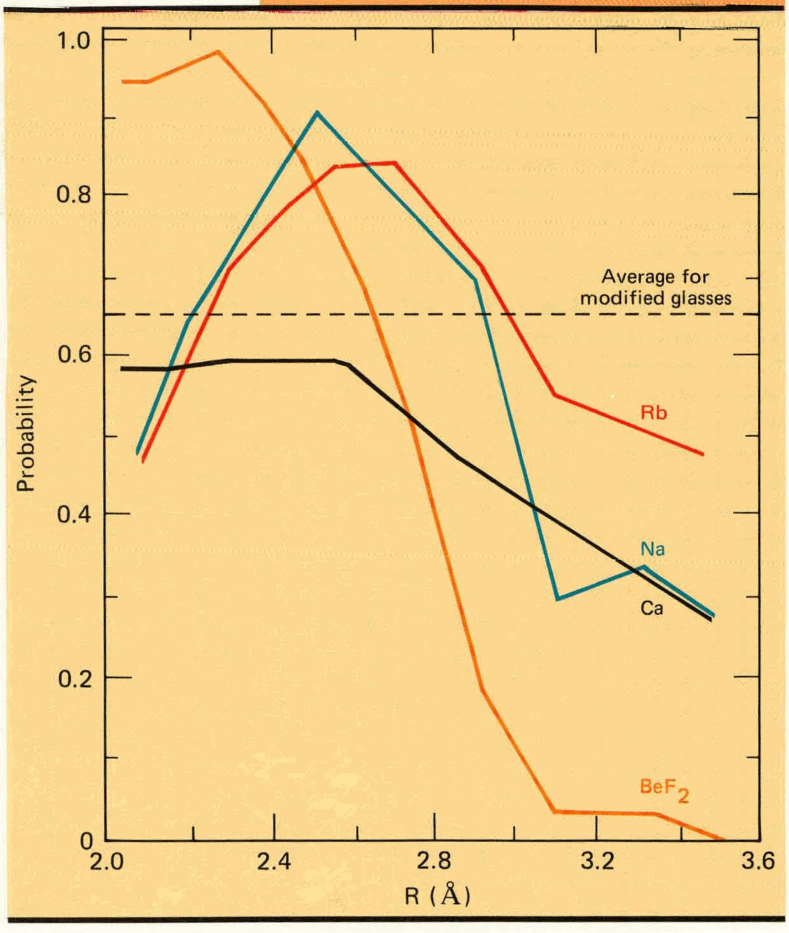

Fig. 2-404. Probability that a F has exactly 1 Be neighbor (within 2.4 Å) as a function of RE-F distance.

In Fig. 2-404 we show the fraction of F ligands with exactly one Be neighbor (within 2.4 Å) as a function of the RE F distance R. This is the probability that the F is nonbridging. (The labels refer to the glasses: Na–$76BeF_2 \cdot 74NaF \cdot 1EuF_3$; Rb–$76BeF_2 \cdot 74RbF \cdot 1EuF_3$, Ca–$76BeF_2 \cdot 37CaF_2 \cdot 1EuF_3$; BeF_2–$100BeF_2 \cdot 1EuF_2$.) A Be-F coordination sphere of 2.4 Å, the first minimum of the RDF in Fig. 2-397, has been shown to be reasonable.[217,221] Note that the behavior of this distribution is quite different in BeF_2 and in the modified glasses. In BeF_2, F ions at distances greater than 2.8 Å from the RE are virtually all 2-fold coordinated by Be and bridging, while in the modified glasses many F are nonbridging throughout the glass and near the RE as well. The maximum in the distribution of Fig. 2-404 for Na and Rb modified glasses is an intriguing result which at present has no simple physical explanation.

In the modified glasses some F near the RE have no Be neighbors within 2.4 Å and are thus "free." In Fig. 2-405 we show the probability that a F has exactly zero Be neighbors (within 2.4 Å) as a function of the RE-F distance R. (The cation labels of the curves refer to the glasses: Na–$76BeF_2 \cdot 74NaF \cdot 1EuF_3$; Rb–$76BeF_2 \cdot 74RbF \cdot 1EuF_3$; and Ca–$76BeF_2 \cdot 37CaF \cdot 1EuF_3$; BeF_2–$100BeF_2 \cdot 1EuF$.) Note that, except at the closest distances, the higher the field strength of the modifying cation, the greater the probability that a F has no Be neighbors. This is intuitively reasonable, since the higher field strength cations have a larger interaction energy with the F and presumably compete more effectively with Be for F neighbors. There are no free ions in any unmodified BeF_2 glass we have simulated.

Figures 2-404 and 2-405 show that there are significant differences in the structures of the RE coordination spheres between BeF_2

glass and glasses with a considerable amount of modifier.

Finally, consider glass 2 (Table 2-74) with its small concentration (3%) of Na modifier. In Fig. 2-406 we show the RE-Na RDF for this glass and, for comparison, that of glass 3 (45% Na). Note that in the glass with a small amount of Na, there is a strong tendency for the alkali to cluster about the RE. This result is consistent with the general observation that RE ions are only sparsely soluble in pure glass-network formers such as BeF_2 but are very soluble in glasses with even a few percent modifier ion.

Additional insight into the geometry of the RE coordination shell results from a treatment similar to the one used for the moments of inertia of irregular bodies and which is described elsewhere.[215,222] We can form the matrix

$$M_{ij} = \sum_L q(L) \frac{r_i(L) r_j(L)}{R(L)^n} \theta[R_m - R(L)] \qquad (82)$$

where L runs over all the ligands, $r_1(L)$ is the x-projection of the vector from the RE to ligand L (and r_2, r_3 are y and z), R(L) $= \Sigma r_i(L)^2$ is the RE-ligand distance, and q(L) is the charge of ligand L. The matrix M can be diagonalized for each site. The three eigenvalues λ_1, λ_2, λ_3 are generally unequal. These eigenvalues are the length of the three principal axes of an ellipsoid which the ligands can be imagined to form about the RE. In Fig. 2-407 we plot λ_i for the Na-doped glass (glass 3 of Table 2-74), for R_m = 3.2 and n = 5 in Eq. (82). The site order is one of decreasing values of the smallest λ_i, and is not the order in which the configurations were generated. In going to the right in Fig. 2-407, the distribution of the R^{-5} weighted *charge distribution* of the ions about the RE becomes flatter (like a pancake), since one of the eigenvalues decreases much more than the other two. (R_m = 3.2 Å, n = 3, for the glass $150BeF_2 \cdot 1EuF_3$. The sites are ordered by decreasing smallest eigenvalue. In general, this order corresponds to increasing $^7F_0$–$^5D_0$ splitting for Eu as the RE.)

The use of the eigenvalues λ_i provides a convenient way of describing the structure about the RE. In fact, they provide a generalization of symmetry to C_1, since, when the site symmetry becomes greater than C_1, some of the eigenvalues λ_i become equal.

The second-order crystal field in a point-charge model [n = 5 in Eq. (82)] can be expressed in terms of the eigenvalues λ_i. For Eu^{3+} the $^5D_0$–$^7D_0$ energy level separation is, to a good approximation,

$$E = -\text{const} \times (\lambda_1 - \lambda_2)^2 + (\lambda_1 - \lambda_3)^2 + (\lambda_2 - \lambda_3)^2 \qquad (83)$$

Fig. 2-405. Probability that a F has exactly 0 Be neighbors (within 2.4 Å) as a function of RE-F distance R. This is the probability of a free fluorine. BeF_2 has no free F for any R.

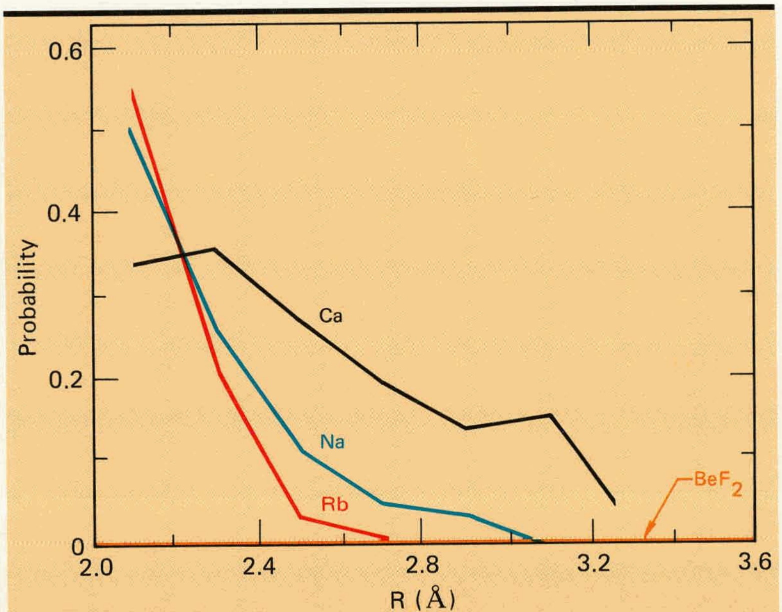

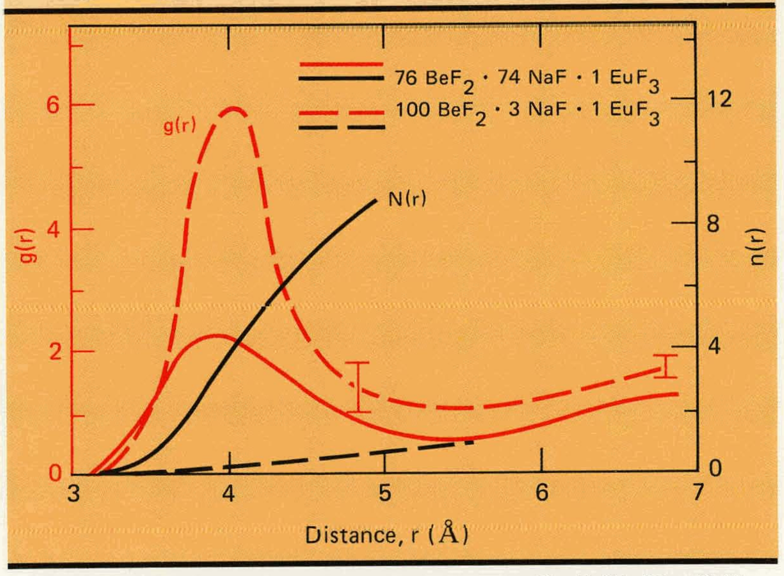

Fig. 2-406. The RE-Na RDF for two fluoroberyllate glasses with different amounts of Na modifiers. (Note that RE-Na clustering tendency in the lightly modified glass.)

In general, E decreases (i.e., becomes more negative) in going to the right in Fig. 2-407.

The distribution p(E) of $^7F_0$ energies derived from Eq. (83) is shown in Fig. 2-408 for several glasses. It is seen that the width for BeF_2 is considerably wider than for the Na- and Rb-modified glasses. The width for the Ca-modified glass is about the same as in pure BeF_2. This trend is observed experimentally, for example in the splitting of $^4F_{3/2}$ level of Nd^{3+} in fluoroberyllate glass. Thus the decrease in width of the spectrum seems due to an increase in regularity of the ligand coordination about the RE.

Fig. 2-407. Eigenvalues λ_i of the matrix M in Eq. (82) of the text as a function of the RE site.

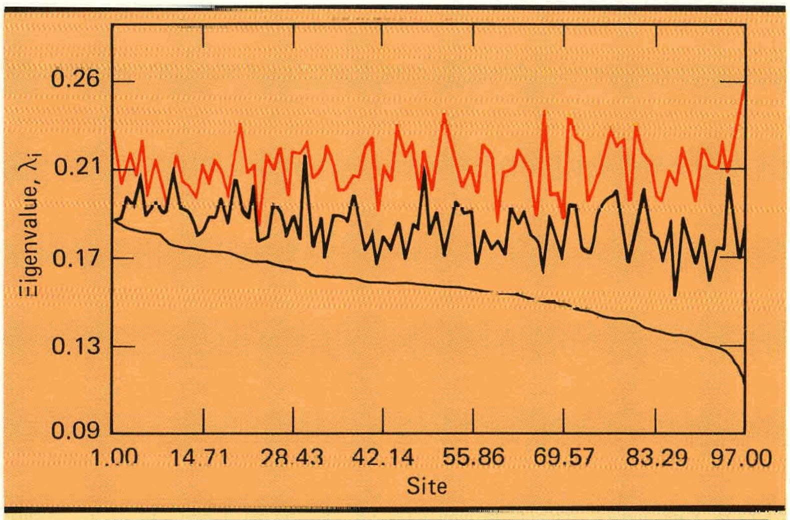

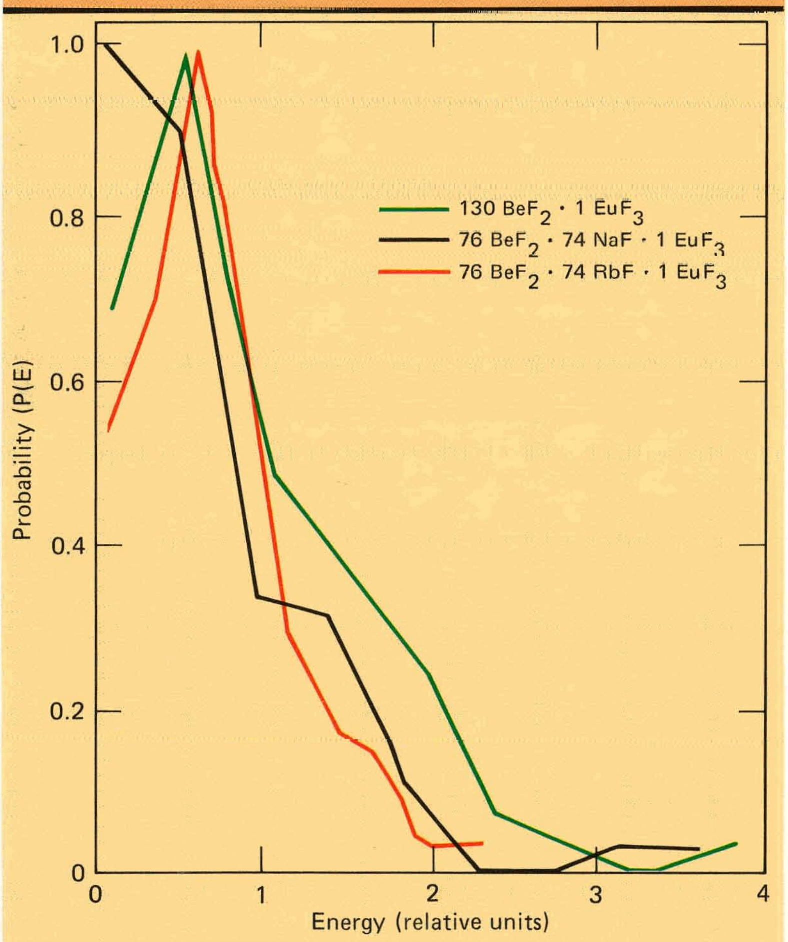

Fig. 2-408. Probability distribution of $^5D_0$–$^7F_0$ energies E from Eq (83) for different simulated glasses calculated for R_m = 3.2 Å and n = 3.

The conclusions reached in our glass simulations to date are

- The average coordination number of all cations increases in going from a unitary to a binary BeF_2 glass.
- The RE does not have a single coordination number, and the distribution of F ions about the RE is approximately equally disordered in all the glasses. There is a small trend in increasing order in the RE coordination sphere in the direction (BeF_2, Ca)–(Na, Rb), where glass compositions (Table 2-74) are denoted by the modifying ion.
- The probability that F ligands of the RE have 0 or 1 Be neighbors (within 2.4 Å) is different in BeF_2 from the modified glasses.
- Modifier cations tend to cluster near RE ions, in agreement with the observed solubility behavior of RE in BeF_2 and modified glasses.
- The principal axis treatment shows that the distribution of F ligands about the RE ranges from near spherically symmetric (on the average) to a pancake-like distribution of nearby ligands.

Authors: S. A. Brawer and M. J. Weber

Anomalous Low-Frequency Excitations in BeF_2 Glass. Many inorganic glasses have anomalous thermal, acoustic, and dielectric properties at temperatures ranging from a few millidegrees to 100 K (see Ref. 223). While these properties have been documented by many workers, they have had no explanation in terms of glass structure. We have formulated a microscopic model, based on molecular-dynamics simulations, of the types of structures causing the anomalies in beryllium fluoride (BeF_2) glass. This technique provides a new way of investigating the low-temperature anomalous properties of glass, and is applicable to a wide variety of amorphous materials.

The measured anomalies are of two types. In a number of glasses (including BeF_2 and silica), when their temperatures are above 10 K, broad, strong, acoustic absorption occurs that is associated with activated-hopping over potential barriers. The barrier heights vary from a few hundred to about a thousand K (Refs. 223 and 224). At temperatures below a few K, the situation is different. There, the specfic heat, thermal resistance, and negative thermal expansion are all unusually large and have anomalous temperature dependencies. There is considerable saturable acoustic absorption at all frequencies below 35 GHz. Phenomenologically, the excitations producing these very low temperature anomalies are two-level systems (TLS) interacting among themselves, and with acoustic and dielectric disturbances.[225–227] The energy separations of the TLS range from 0 to at least 35 GHz.[228]

The experimental results in both temperature ranges indicate that an atom, or group of atoms, is somehow loosely enough bound to move about relatively freely (presumably over distances greater than 0.5 Å) encountering potential barriers small compared to the activation energy for fluorine diffusion ($\approx$1.5 eV).[223,225–227] Thus, for instance, TLS and activated hopping can both result from some ions in double-well potentials with barrier heights ranging from a few hundred to a few thousand K. Such a model has been widely used.[225,226]

As described in the preceding article, we have simulated BeF_2 glass using molecular-dynamics techniques. The result is a glass whose structural properties are those commonly attributed to BeF_2 made in the lab. Most Be ions are 4-fold coordinated by F in approximate tetrahedra, and most F ions are 2-fold coordinated by Be ions with widely varying Be–F–Be angles.

Central to our discussion is the observation of a number of 3- and 5-fold coordinated Be ions and 3-fold coordinated F ions in the simulated glasses. We call these ion defects. Defects are always observed in simulated glasses.[229,230] The exact number of such defects depends on the radius of the Be coordination sphere, which we take as 2.4 Å, the location of the first minimum of the Be–F radial distribution function. It is convenient to use the terminology that a Be–F pair are *bonded* if they are within 2.4 Å of each other. Here, bonded means proximity (see Ref. 229). With this, the definition of a defect as a Be ion with coordination number other than 4 (or an F ion with a coordination number other than 2) is unambiguous.

Defects are present in simulated fluids in thermal equilibrium. The number of defects in the fluid decreases as the temperature is lowered, and increases as the temperature is raised, provided that the temperature is above the glass transition region so the fluid can relax (showing that such defects are not peculiar metastable structures trapped during cooling). In addition, when a fluid at a temperature of 1300 K is quenched to a glass (T = 900 K) over a time scale of 5 ps, the quench is so rapid that the fluid does not remain in thermal equilibrium, and the number of defects does not decrease appreciably during the quench. As a result, the defect structure of the parent fluid is frozen into the glass quenched from that fluid. The fraction of defects in a glass, as a function of the fluid temperature from which the glass was quenched (the *fictive temperature*), is given in Table 2-75. As we expected, the lower the fictive temperature is, the fewer the number of defects.

We found that even below the glass transition region ions are capable of moving distances of 0.5 to 1.0 Å in times of 1 to 10 ps. The presence of defects is important because virtually all such low temperature atomic motion occurs at defect sites.

To show this, we computed the coordination number (CN) of those ions involved in a "bond-breaking" event. Let a Be–F pair break a bond under the following conditions: the pair are initially within 2.4 Å for at least 0.03 ps; later they are separated by a distance larger than some R_m for at least 0.03 ps (R_m is typically 2.4 to 4.0 Å). Now

Table 2-75. Ion coordination numbers vs fictive temperature.

T_f	3334	1668	1501	1334
P_5	0.153	0.108	0.078	0.055
P_3	0.091	0.038	0.012	0.008
F_3	0.050	0.035	0.031	0.023
F_1	0.012	0	0	0

Note: P_c, the probability that a Be ion has coordination number CN, and F_c, the probability that a fluorine ion has coordination number CN, vs T_f, the fictive temperature.

consider the set "A" of all F ions involved in a bond-breaking event during an interval of from 1 to 20 ps). We compute the CN of each F in Set A when it is a distance, r, from the Be ion to which it was originally bonded, and then find the distribution of coordination numbers for all F ions in Set A. In this way, we get $P_f(n,r)$, the probability that an F in Set A (i.e., undergoing bond breaking) has exactly n Be neighbors when it is a distance r from the Be to which it was originally bonded. For a given F, different values of r are different points in the same trajectory. Values of $r < 2.4$ Å describes coordination before bond breaking begins.

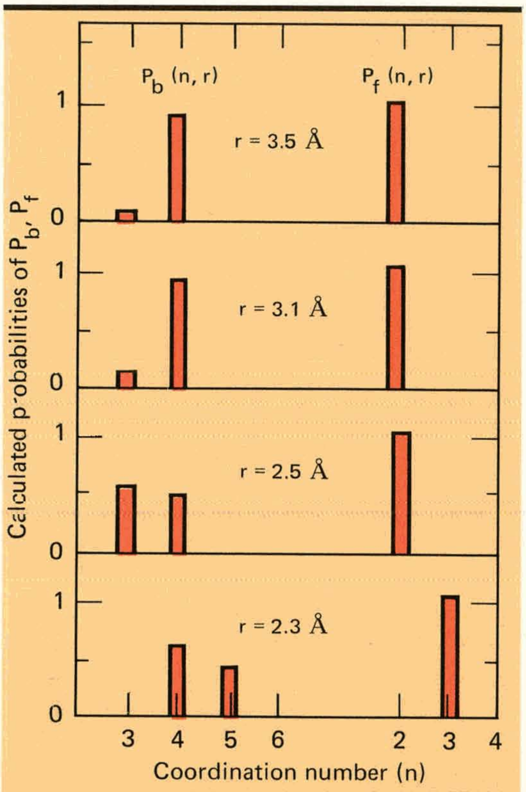

Fig. 2-409. Distribution of coordination numbers for ions involved in bond breaking at 333 K.

The quantity $P_f(n,r)$ is shown in Fig. 2-409 for a run of 1-ps duration, starting from a well-equilibrated initial configuration, and $R_m = 3.5$ Å. ($P_b(n,r)$ is the probability that a Be ion has exactly n F neighbors averaged only over those Be ions involved in bond breaking, P_f is similar for F ions, with Be neighbors, and r is the distance between separating Be–F pairs.) If B is the set of Be ions involved in bond breaking, then $P_b(n,r)$ is the equivalent quantity to $P_f(n,r)$ when averaged over the Set B ($P_b(n,r)$ is also shown in Fig. 2-409).

Figure 2-409 shows that the ions involved in bond breaking at low temperature are defects. The glass, quenched from a fluid at 1660 K, is at a temperature of 300 K. A total of five bonds were broken for this run with $R_m = 3.5$ Å; for $R_m = 3$ Å, about two to three times more bonds are broken. These results are typical of all temperatures below the glass transition region. Thus, at 1000 K, some 90% of the F involved in bond breaking are 3-fold coordinated, and about 90% of Be ions are 5-fold. Even at 33 K, several F ions (typically 1 to 4) are found to move 0.5 to 1.0 Å away from the Be ions to which they were originally "bonded" in 1 ps. While simulation at 33 K is not physically realistic, since quantum effects dominate in real systems, the results still show that small activation energies are involved.

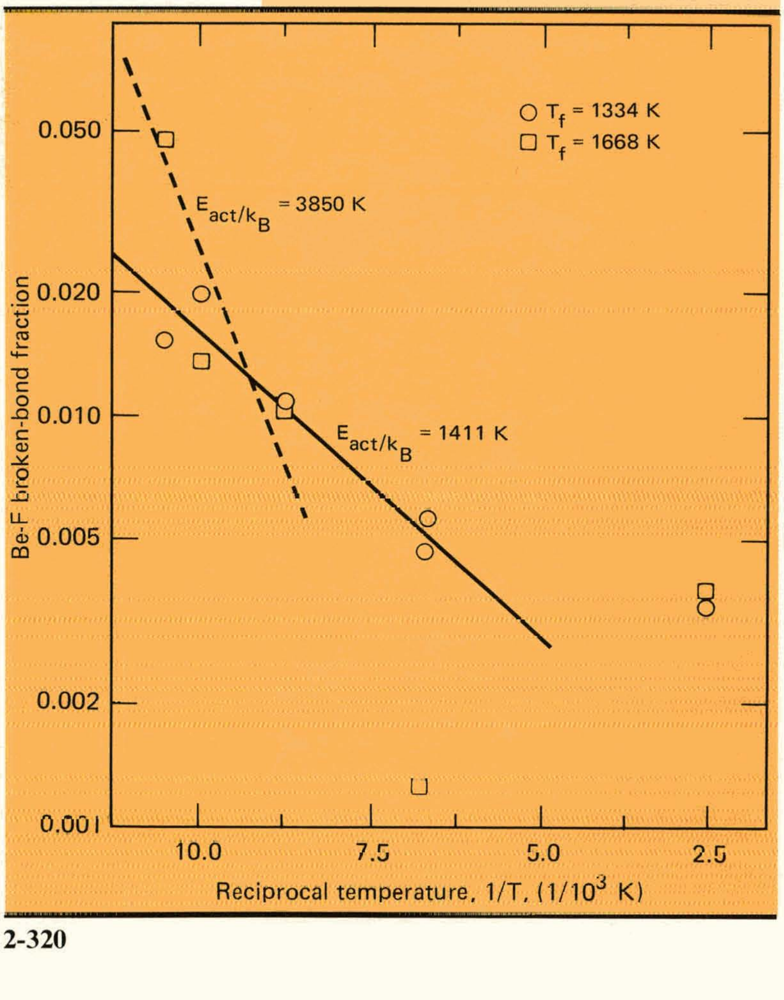

Fig. 2-410. Fraction of Be–F bonds broken after 3 ps vs the inverse temperature, for glasses.

It is clear that for temperatures below 1000 K, and over times of 1 ps or greater, ion motion over a distance of 0.5 to 1.0 Å occurs at defect sites. The activation energy for such motions was estimated by making runs at a series of temperatures. At each temperature, we calculated the fraction of initially bonded Be–F ions that separate by a distance of 3.0 Å or greater after 3 ps. The results are shown in Fig. 2-410 for two glasses with fictive temperatures of 1668 and 1334 K. ($R_m = 3.0$, k_b is Boltzman's constant, and E_{act} is an effective activation energy.) While the data have considerable scatter, an estimate of the activation energy shows that the majority of sites have activation energies between 0.1 and 0.2 eV. A few sites are still active below 300 K and have activation energies less than 0.1 eV. Similar results are obtained for different R_m and other time intervals.

In many cases the motion is quasiperiodic, that is, some (but not all) of the F ions are observed to become rebonded (during 10 ps) to the same Be ion from which they had separated. The separation of several Be–F pairs vs time (at 300 K) is shown in Fig. 2-411 for a glass with fictive temperatures of 1667 K (curve N is the Be–F distance for a "normal" Be–F ion, that is, an ion not at a defect site). This typical result indicates the existence of at least two metastable equilibrium positions, qualitatively consistent with the double-well model of TLS.[225,226] We also have that breaking a bond typically requires 0.1 to 0.5 ps. This is some 8 to 25 vibrational periods. Therefore the separation does not occur in a brief hop and, in this sense, bond breaking is more complex than the usual TLS model might predict.

It is plausible that the defects observed in simulated BeF_2 can give rise to anomalous low-temperature properties. The presence of activated-hopping over potential barriers less than 1000 K is consistent with sound absorption observed in BeF_2 above 10 K. In addition, the existence of activation energies on the order of 0.2 eV and motions that are quasi-periodic (indicating several metastable equilibrium positions) means the defects have the qualitative requirements for giving rise to a TLS.[223,225,226] Finally, Table 2-75 indicates that in laboratory BeF_2, with fictive temperatures around 300 K, the number of defects will be much less than 1%, which, based on results with other glasses, was to be expected.

Author: S. A. Brawer

Vibronic Spectra of Rare Earths in Glass. Our past studies of the properties of RE (rare earth) ions in glass have concentrated on the structure of the host and its perturbation of the energy levels of the optically active RE dopant. The RE ions are enclosed in rigid cages of atoms that vary in geometry from site to site throughout the glass. The glass network, of course, is not fixed but vibrates. These vibrations, describable in terms of quantized normal modes (phonons), give rise to dynamic effects that are very important to laser action in RE-ion glass lasers. Ion–phonon coupling affects the rate of nonradiative decay by multiphonon emission, the homogeneous line width, and quantum efficiency. These, in turn, affect the energy storage and saturation behavior of RE laser glass, as well as influence phenomena such as spectral hole burning.

One manifestation of this ion–phonon interaction is the creation of side bands in fluorescence spectra. Specifically, side bands are attributed to vibrational-electronic or "vibronic" transitions. In a vibronic transition an excited RE ion relaxes to its

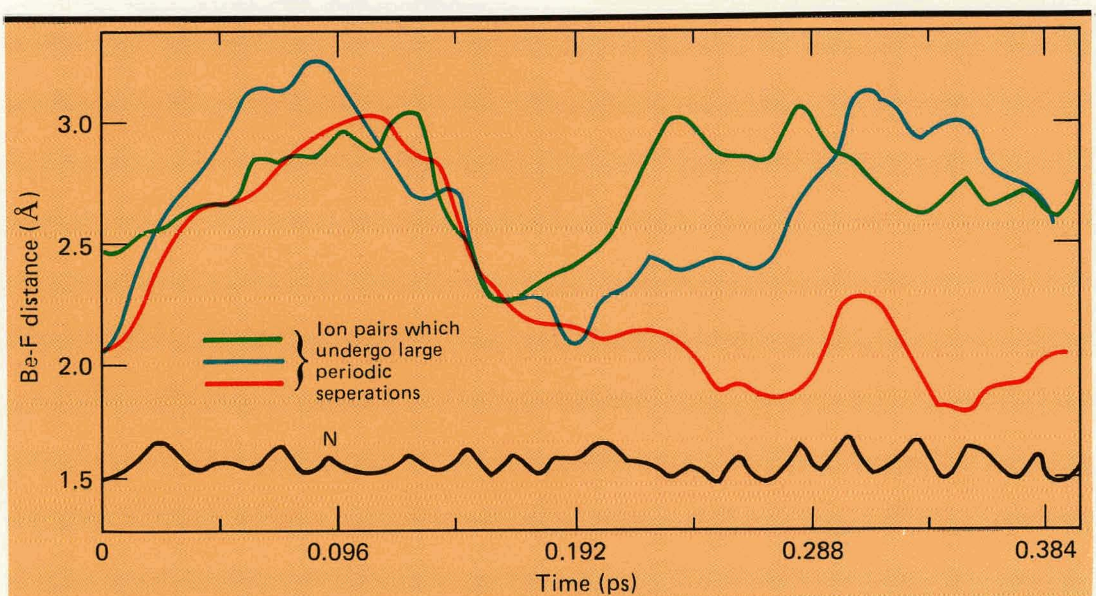

Fig. 2-411. Be–F distance vs time for four Be–F pairs.

ground state by creating a phonon in the host as well as emitting a photon. Since some of the original electronic energy has gone into the vibration, the observed photon is of lower energy (longer wavelength) than the more probable zero-phonon transition. The range of phonon energies in solids cause vibronic transitions to appear as bands shifted from the zero-phonon transition band. By emphasizing the energy difference of shifted photons from the zero-phonon line, we can map out the vibrational density of states around the RE, weighted by a selection rule that accounts for differences in coupling to the electronic transition.

Vibronic side bands associated with REs in crystals are commonly observed and are well understood. In glass, however, RE vibronics are obscured by the large inhomogeneous broadening of zero-phonon transitions. The only previously reported observation of RE–Glass vibronics[231] was obtained from excitation spectra. In this method, the vibronic structure is subject to the same inhomogeneous broadening as the zero-phonon line.

During the past year, we made the first observation of vibronics associated with a RE in glass using the laser-induced FLN (fluorescence line narrowing) technique of Ref. 232, which allows quantitative measurement of spectral structure. We conducted experiments addressing the following questions about the ion–phonon interaction. First, is there a site-to-site variation in vibronic structure? Second, are vibronics characteristic of vibrations of the entire glass network or impurity modes created by the presence of the RE? Third, what are the selection rules that govern vibronic transitions in glass?

Fig. 2-412. Vibronic sidebands associated with Gd^{3+} in three glass hosts.

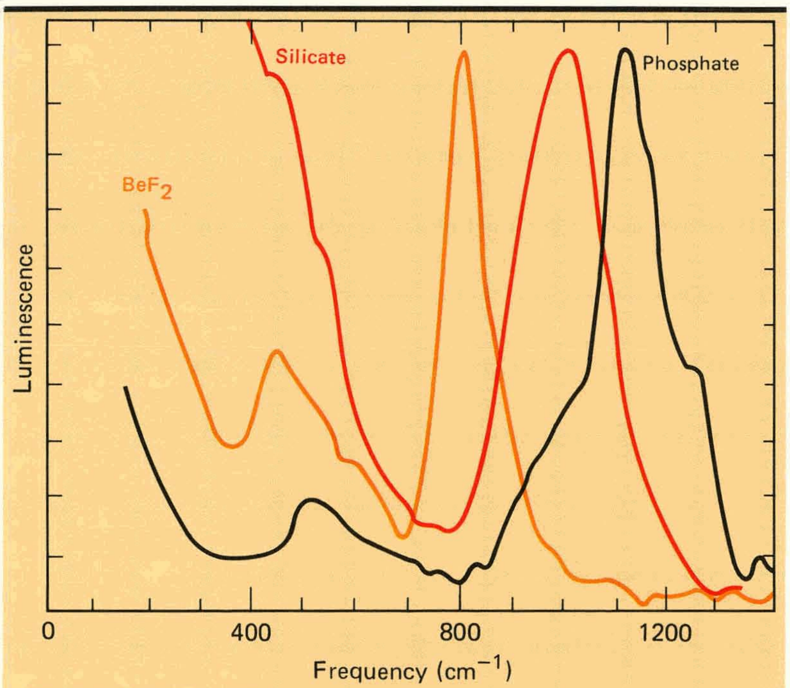

Our experiments use a frequency-doubled Rh6G pulsed dye laser to excite a small resonant subset of ions (ones with similar local environments) from the inhomogeneously broadened absorption band. Samples are held at 20 K in a helium refrigerator to permit maximum line narrowing. The weak, frequency-shifted vibronic spectrum is detected using sensitive photon counting techniques. An LSI-II microcomputer controls the experiment, stores and displays data, and permits noise reduction through averaging of several runs.

Gadolinium was chosen as the RE probe ion in all samples because of its $^8S_{7/2}$ ground level. Since an S state experiences negligible splitting of Stark levels in any perturbing environment, we avoid overlap of vibronic and zero-phonon transitions from different levels. Excitation was into either the $^6P_{7/2}$ or $^6P_{5/2}$ manifolds and fluorescence involved $^6P_{7/2}$–$^8S_{7/2}$ transitions.

Oxide glass samples, containing 1 mole % Gd_2O_3, were melted by the Inorganic Glass Section of the National Bureau of Standards. Beryllium–fluoride glass with 0.5 mole % GdF_3 was melted and prepared at LLNL. Vibronic spectra for three different glass hosts are shown in Fig. 2-412. The locations of high-frequency peaks in each spectrum correspond well with frequencies of the bond-stretching modes of the glass-forming tetrahedra (BeF_4, SiO_4, PO_4) in each material. The large signal at low frequencies does not imply a large density of states but is due instead to the long tail of the zero-phonon line. Modes that include motion of the massive RE ion itself are very low frequency and are obscured by the zero-phonon tail.

To explore the question of site-to-site variation of ion–phonon coupling, we chose the simple glass former BeF_2 as host glass. The structure of BeF_2 glass around RE dopants is known from previous computer simulations.[233-236] By changing the excitation wavelength, we selected a different subset of ions with different local environments. Within the 10 cm^{-1} resolution of our experiment, the answer to the first question posed is that vibronic peak frequencies and relative intensities do not vary from site to site. (However, we know from FLN[2] studies that ion–phonon coupling does vary from site to site; the possibility that the relative intensity of vibronic structure with respect to the zero-phonon line may also exhibit site-to-site variation warrants further investigation.)

Four different metaphosphate glasses were studied with respect to our second question to determine whether vibronics arise from vibrations of the glass network or from modes perturbed by the RE. Metaphosphate glass consists of phosphate tetrahedra joined at two corners to form long chains. Modifier cations sit between nonbridging oxygens, weakly linking the chains. Modifiers in our samples were La, Al, Ba, and Mg. La has the same charge and approximately the same mass as Gd; therefore, doping the glass with La should have little effect on vibrational spectra. Al has the same +3 charge but less mass than Gd, whereas Ba has nearly the same mass but different charge (+2). Mg differs from Gd in both mass and charge.

For reference, we recorded the Raman-scattering spectra of our samples. Raman scattering probes vibrations over a much larger spatial scale (>3.5 nm) than vibronic spectra. Two different polarized spectra exhibit different selection rules and emphasize different modes: the H–H Raman spectrum has the electric field of the scattered light parallel to the electric field of the incident beam and couples strongly to the symmetric modes; the H–V Raman spectrum measures scattered light with the electric field perpendicular to that of the incident beam and tends to couple to antisymmetric modes. (We did not correct the recorded spectra to account for the low-frequency photon population at room temperature.)

Vibronic spectra for all metaphosphates show similar structure below 800 cm^{-1}. The high-frequency spectral structure, associated with phosphate-tetrahedra-stretching modes of the glasses, differs with each modifier. This structure is made up of the superposition of three peaks whose relative sizes vary with each sample. The center of gravity of the structure consistently varies in frequency with variations in Raman structure.

Figure 2-413 compares H–H, H–V, and vibronic spectra for Gd:La$(PO_3)_3$. The similarity between the H–V Raman and vibronic spectra, for high frequencies, is striking. Figure 2-414 shows results of Gd:Mg$(PO_3)_2$, the material with the greatest difference between modifier and dopant. The similar high-frequency peaks in vibronic and H–V Raman spectra indicate that the rare earth does not greatly perturb these vibrations. Thus, in response to the second question, vibronics appear to be characteristic of the vibrations of the glass as a whole.

The experimental results for metaphosphate glasses point to the answer of our third question—vibronic selection rules are very similar to those governing H–V Raman scattering. This is not true without qualification however. Figure 2-415 compares vibronic and Raman spectra for

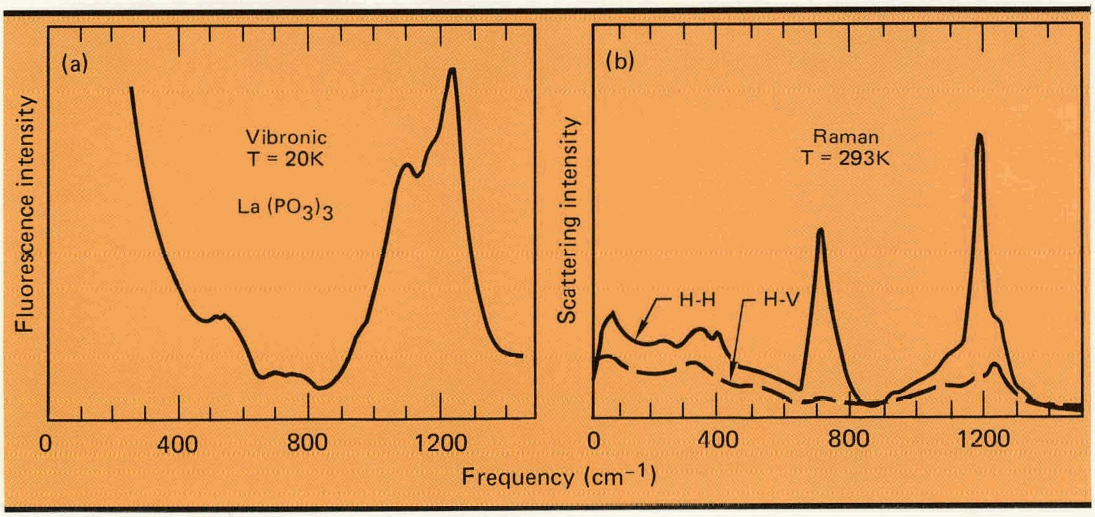

Fig. 2-413. Vibronic and polarized Raman spectra for La$(PO_3)_3$:Gd glass.

Fig. 2-414. Vibronic and polarized Raman spectra for $Mg(PO_3)_2$:Gd glass.

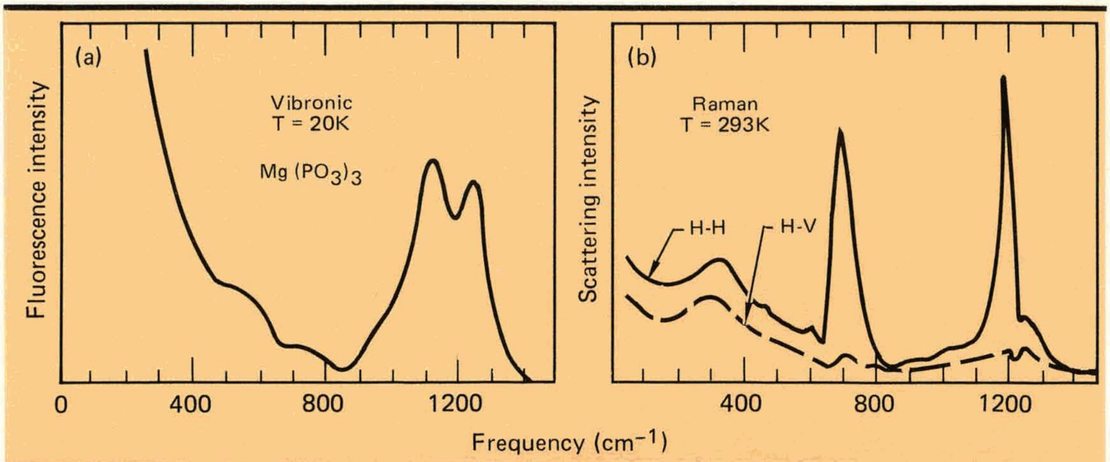

Fig. 2-415. Vibronic and polarized spectra for BeF_2:Gd glass.

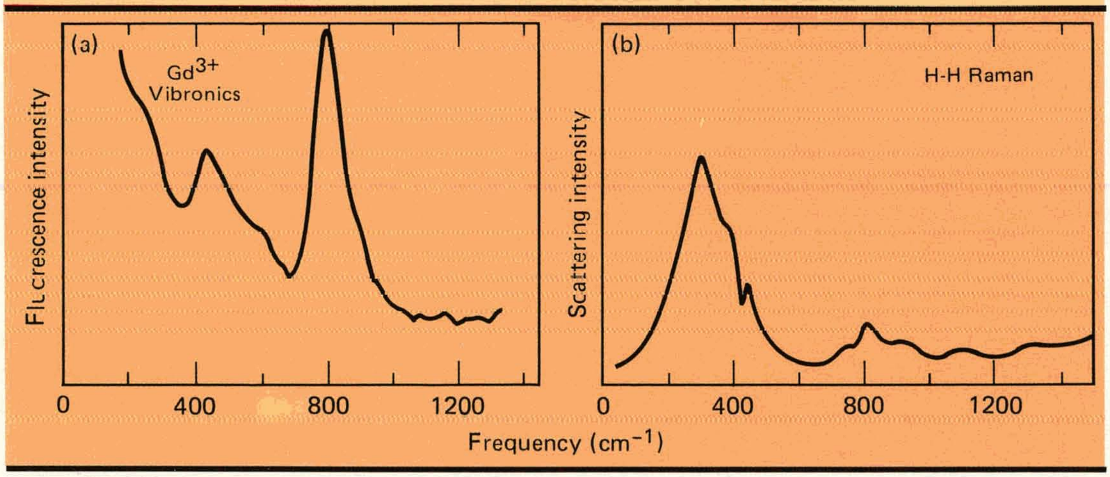

BeF_2. An extremely weak Raman scatterer, BeF_2 exhibits a large high-frequency vibronic peak and there is little correlation beween the two spectroscopies. High-frequency Raman scattering in BeF_2 is attributed to tetrahedral stretching modes just as it is in metaphosphates. The relative weakness of BeF_2 scattering is explained by its closed structure; its tetrahedral building blocks are joined at all four corners. As one tetrahedron expands, neighboring tetrahedra close, making the net change in the volume that the Raman-scattered photon probes nearly zero. This (anti)correlation of vibrations does not influence the more localized vibronic probe.

In summary, we have observed vibronic transitions of RE in glass using line-narrowed techniques and have begun to employ vibronic data to investigate the ion–phonon interaction. We have demonstrated that vibronics generate an independent vibrational spectroscopy that differs from the more conventional spectroscopies (Raman, infrared, neutron) in that it probes network vibrations on a localized scale.

Author: D. W. Hall

Major Contributors: S. A. Brawer, M. J. Weber, and D. D. Kingman

Surface Physics and Chemistry of Laser-Induced Damage

This program complements the directed research and development of damage-resistant materials reviewed earlier in "Damage Studies." The goals of this study are to determine the following:

- Physical mechanisms of surface and bulk material damage.
- Relation between damage thresholds of the bulk and atomically clean surfaces.
- Dependence of the threshold on physical structure of the surface.

- Effect of surface absorption of foreign atoms, deposition of one or more atomic layers of foreign atoms, and of surface chemical reactions such as segregation of constituents or migration of impurities to the surface.

The basic approach taken in these experiments is to prepare and characterize the surface in ultrahigh vacuum (UHV) and to measure the damage threshold and phenomena associated with surface damage in situ.

Our experiments in 1979 showed that surfaces of NaCl, KCl, and fused silica emit charged and neutral particles long before visible damage occurs. This fact has long been known,[237,238] and it is actively studied in the recent Russian literature.[239–242] None of these experiments, however, is performed under carefully controlled surface conditions, even though it is recognized by all experimenters that the emission signal depends strongly on surface conditions, and no experiment is specifically directed towards establishing the relationship between these phenomena and damage threshold. During 1980 we concentrated on measuring photoelectron emission from various dielectrics under UHV conditions. We hope that careful analysis of multiphoton–photoelectron emission processes (dependence on bandgap, dependence on work function, dependence on surface properties, distribution of energy) can be used to differentiate between the two processes—multiphoton ionization and avalanche ionization—postulated to be responsible for laser-induced breakdown of transparent dielectrics.[243–245]

To study laser-induced multiphoton–photoelectron emission, we modified our UHV chamber, a commercially produced (Physical Electronics, ULTEK) stainless steel chamber designed for surface analysis (Auger, Sims, Esca), by attaching a 2-m extension to each of two opposing flanges to reduce the photon flux on the entrance and exit windows, and to discriminate against multiphoton photoelectrons emitted from these windows. We manufactured a doubly electrically insulated target holding chamber. A diagram of the experimental system is shown in Fig. 2-416. The laser wavelength is 1.06 μm, the pulse length is always 1 ns. The laser has a spot size of 3 mm. Laser intensity is given as J/cm^2 per pulse, by integrating the peak spatial intensity over time.

The total charge emitted by the target (front and backface) is collected by a Coulomb meter with a resolution of 10^{-15} C ($\approx$6000 electrons). To test whether electronic noise, generated by the laser firing procedure, or stray charges, produced by laser passage through the vacuum system (10^{-9} Torr), produce spurious signals, we fired the laser through the system without installing a target. For fluxes up to 3.6 J/cm^2 (per nanosecond pulse), we find stray signals to be less than 10^{-14} C. To test whether the target chamber contains the emitted charges without significant leakage, we installed a gold foil as a target. The foil is electrically connected to the inner target chamber. The results are shown in Fig. 2-417, together with the results of the blank shots. It is known that at the photon fluxes investigated, gold foils will emit charges many orders of magnitude above the charge measured; i.e., the leakage of charges from the openings of the target chamber represents a small percentage of the total charges generated. Multiphoton–photoelectric emission from metals, generated by neodymium-laser

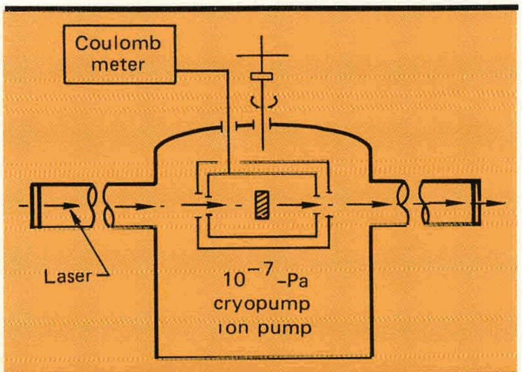

Fig. 2-416. Experimental system.

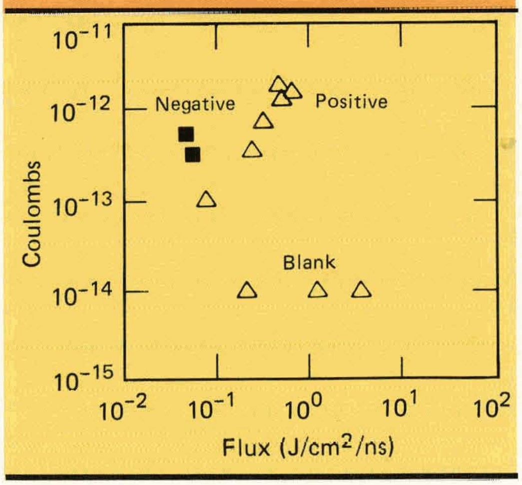

Fig. 2-417. Charge measured for blank shots and for gold foil connected to inner chamber.

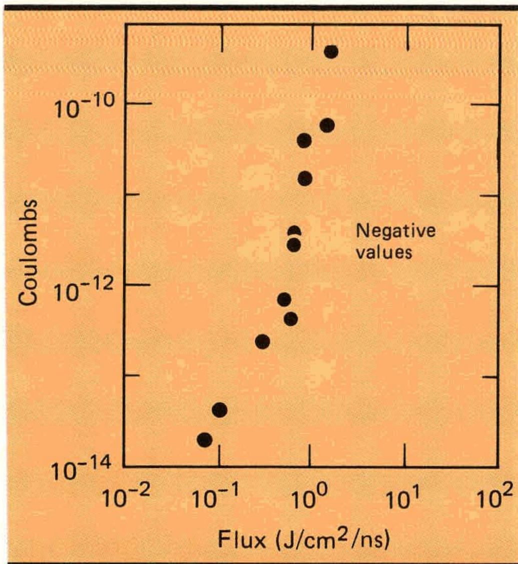

Fig. 2-418. Negative charge emitted from a CdTe surface as a function of photon flux ($J/cm^2/ns$).

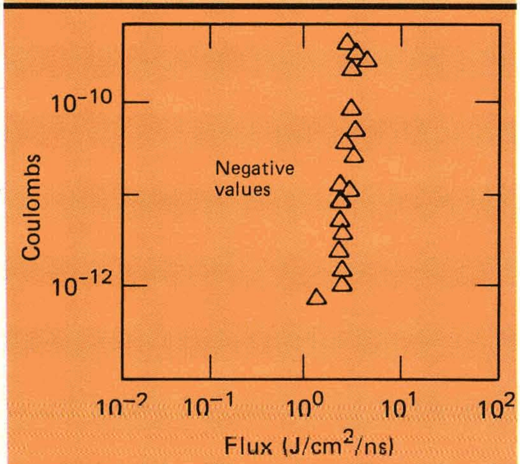

Fig. 2-419. Negative charge emitted by NaCl as a function of photon flux ($J/cm^2/ns$).

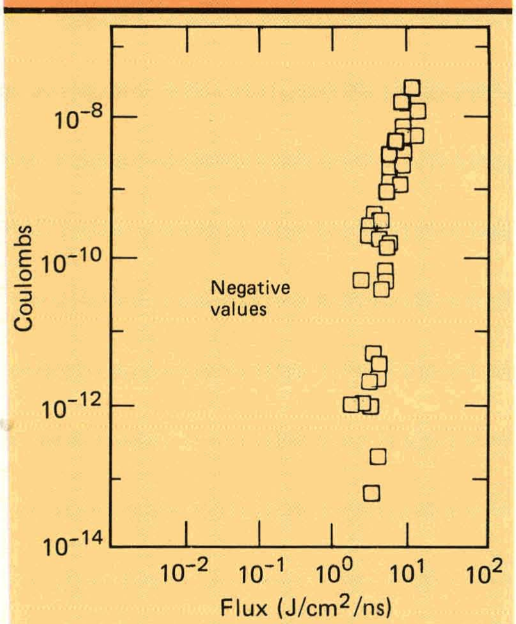

Fig. 2-420. Negative charge emitted by a fused silica surface as a function of photon flux ($J/cm^2/ns$).

pulses of 30-ps duration, has been studied carefully in recent publications.[246] The total emitted charge has been found to be proportional to the photon flux to the power n, where n is equal to integer [(Work function/photon energy) + 1]. To relate our experimental results to these studies, we determined the multiphoton–photoelectron emission from cadmium telluride. Cadmium telluride has a bandgap of 1.5 eV (see Ref. 247) and a work function of 6 eV.[248] The experimental results are shown in Fig. 2-418. The collected charge, c, is dependent on the flux, f, in the expected relationship $c = f^n$, with n defined as above. A value of n = 5 fits the data above 10^{-13} C. This is reasonable since the Fermi level may shift significantly as electrons are promoted into the conduction band. Since the neodymium alignment-laser beam was highly attenuated, it is clear that interband transitions are easily promoted in cadmium telluride.

Next we turned our attention to high-bandgap materials, NaCl and fused silica, with bandgaps of 8.97 eV and 8 to 8.4 eV (Ref. 247) and work functions of 4.2 and 5 eV, respectively.[248] NaCl data are presented in Fig. 2-419. The photon flux was raised above the damage threshold (as determined by emission of visible light), and it appears that, in the predamage region, the photoelectron charge, c, varies with the flux, f, as $c = f^n$, where n = integer (bandgap/photon energy) + 1 = 8 to 10. At the damage threshold of approximately 5 J/cm^2/pulse there is a change in n. Fused silica (Fig.

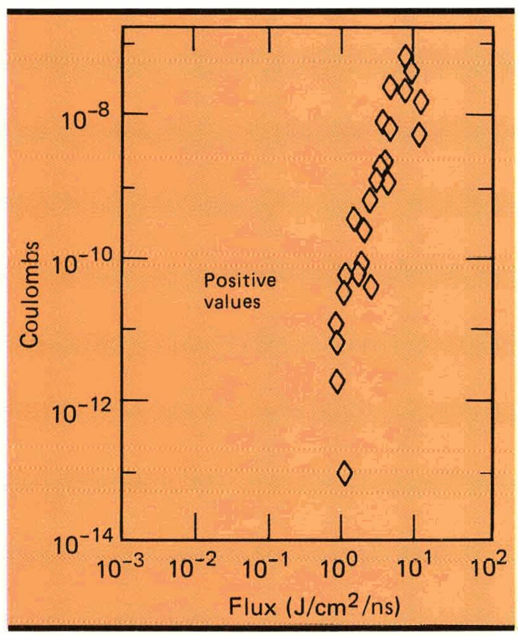

Fig. 2-421. Positive ▶ charge emitted as a function of photon flux ($J/cm^2/ns$) by a fused silica surface contaminated with metal.

2-420) shows a similar phenomenon at a flux of 10 J/cm^2/pulse. The value of n for fused silica is again determined by the bandgap energy. In Figs. 2-421 and 2-422 we show the photoelectric-charge emission from a fused-silica surface which has been contaminated by exposure to a plasma generated by laser light irradiation of stainless steel at approximately 5 J/cm^2/pulse (we irradiated the inside of the inner target-holding chamber). The collected charge is positive, and the functional dependence on flux is changed. The value of n is 4 to 5.

It is apparent from Figs. 2-420 through 2-422 that photoemission from very-high-bandgap insulators leads to large scatter in the data. This is partly due to the fact that the laser flux is accurate only to ±10%. We chose, therefore, zinc sulfide, with a bandgap of 3.88 eV (Ref. 247) and a work function of 5.5 eV[3], as the next material for study. In Figs. 2-423 and 2-424 we see the results of two runs. The best fit of n to both curves is n = 4. This may imply that the rate-limiting process is an interband transition, not transition into the vacuum. The electron affinity of ZnS must be known before a definitive statement can be made. In Fig. 2-424, we see a very clear change at the optically observed damage threshold—the collected charge is independent of flux above 5 J/cm^2.

Conclusion. We have investigated the dependence of photoelectron emission on photon flux for CdTe, ZnS, SiO_2, and NaCl. The electron emission is controlled either by interband transitions (for ZnS, NaCl, SiO_2) or by the work function (for CdTe). These data do not allow us to differentiate between multiphoton and avalanche processes, but they do allow estimates of electron concentrations in the conduction band at the threshold for damage, and provide some insight into the effect of surface contaminations on damage processes.

Authors: W. J. Siekhaus and W. G. Boyle

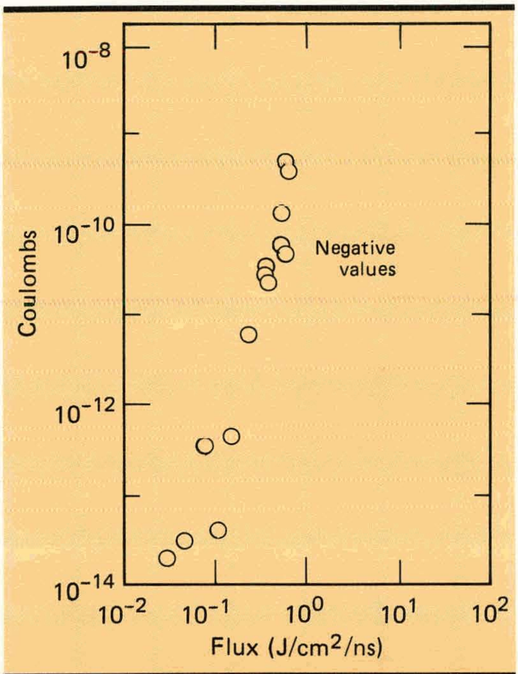

Fig. 2-423. Negative charge emitted by a ZnS surface as a function of photon flux.

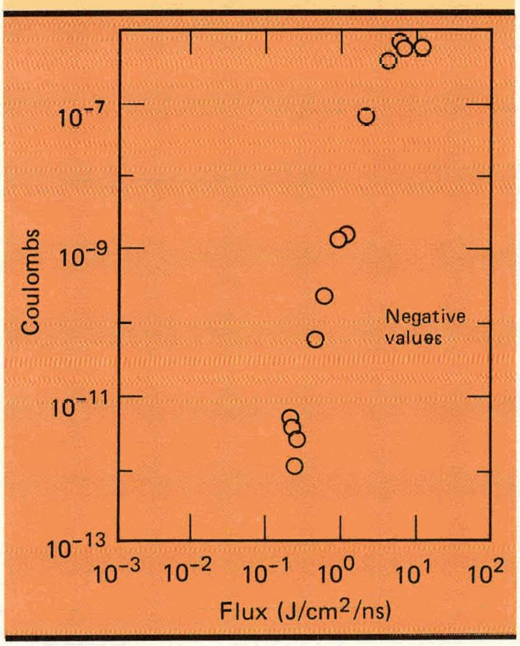

Fig. 2-424. Negative charge emitted by a ZnS surface as a function of photon flux.

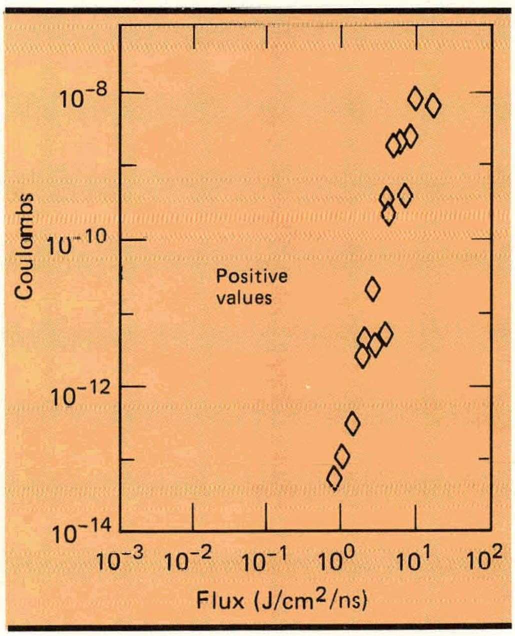

◀ Fig. 2-422. Positive charge emitted as a function of photon flux by a fused silica surface contaminated with metal.

Laser Material Studies

High-Cross-Section Nd^{3+} Laser Glasses. The effective stimulated-emission cross sections of rare-earth ions in glass are about one order of magnitude smaller than in crystals because of inhomogeneous line broadening. For laser applications, the increased line width in glass is favorable for absorption of broadband-pump radiation and large energy storage, but the reduced stimulated-emission cross section is unfavorable for low-threshold, high-gain operation. In addition because of site-to-site variations in the spectroscopic properties of the laser ions in glass, there is a distribution of cross-section values. For a given laser frequency and polarization, this results in hole burning and reduced energy extraction under large-signal or saturated-gain operation.

A number of studies in the past decade have demonstrated that not only is there a large variation in the spectroscopic properties of rare-earth-laser ions in glass, but that these properties can be tailored, within limits, by the choice of the glass network-forming and network-modifying ions.[249] In the case of Nd^{3+}, variations of the stimulated-emission cross section and fluorescence lifetime by more than a factor of 5 have been demonstrated. Below, we summarize those properties which account for these variations and show how the largest stimulated-emission cross section observed to date was achieved in an inorganic chloride glass based on $BiCl_3$ as the glass former.

The stimulated-emission cross section σ for a transition at wavelength λ is given by

$$\sigma = \frac{8\pi^3 e^2 \chi S}{3hc(2J + 1)\lambda\Delta\nu} \quad , \qquad (84)$$

where $\Delta\nu$ is the line width (in cm^{-1}), S is the line strength, J is the angular-momentum quantum number for the upper laser level, and χ is a local-field correction. For a medium of refractive index n, χ is approximated by $n(n^2 + 1)^2/9$ and n^3 for electric-dipole and magnetic-dipole transitions, respectively. Therefore, from Eq. (84), four quantities governing the emission cross section are affected by the host composition: line strength, line width, refractive index, and wavelength.

Line Strength. Optical transitions between states of the $4f^n$ configuration of rare-earth ions in solids are predominantly of electric-dipole nature. Transitions between J states can be treated using the approach of Judd and Ofelt[250] with the line strength described by

$$S(J;J') = \sum_{t=2,4,6} \Omega_t |\langle \dot{S}\dot{L}\dot{J} || U(t) || SLJ \rangle|^2 \quad , \qquad (85)$$

where the doubly reduced matrix element of the tensor operator $U^{(t)}$ is evaluated for intermediate coupling and the Ω_T's are empirical intensity parameters. Electric-dipole transitions become allowed by admixing of 5d states into 4f by odd-parity terms in the expansion of the crystal field interaction. These enter squared in the definition of the parameters and account for their variability with host. The range of variations observed for the intensity parameters of Nd^{3+} in various glasses are summarized in Ref. 251. The line strength is the most host-sensitive quantity in determining σ.

Line Width. Both homogeneous and inhomogeneous line broadening of optical transitions in glass are host dependent.[252] Inhomogeneous broadening dominates the line widths measured at temperatures ≈ 300 K. Stark structure of rare-earth spectra in glasses is usually only partially resolved. For the ${}^4F_{3/2} \rightarrow {}^4I_{11/12}$ lasing transitions of Nd^{3+}, only a broad, asymmetric band is observed at room temperature. Since the line shape changes with composition, an effective emission line width

$$\Delta\nu_{eff} = \frac{\int I(\nu)d\nu}{I_{max}} \qquad (86)$$

is used instead of the FWHM line width.[253] This effective line width is a measure of a combination of the extent of the Stark splitting of the initial and final J manifolds and the inhomogeneous broadening resulting from site-to-site variations in the Stark splitting.

For a given glass network former, the rare-earth line width generally increases with increasing charge and decreasing size of the modifier cations.[254] Changes in the anions have a greater influence on the rare-earth line width since they are the nearest neighbors. Mixed anion glasses introduce an additional degree of disorder. For mixed nearest-neighbor coordination, such as occurs in fluorophosphate glass, broad lines, straddling the two spectral regions for pure fluoride and pure oxide glasses, are observed.

Refractive Index. The effect of the refractive index in the local field correction is significant. As shown in Fig. 4 of Ref. 255, for a refractive-index change from $n = 1.3$ for a fluoroberyllate glass to $n = 2$ for a tellurite glass, the local field correction produces a change of ≈ 1.7 in the cross section of electric-dipole transitions for the same parameters.

Wavelength. The peak wavelength of a fluorescence band in glass depends on the centers of gravity and the relative probabilities of transitions between Stark levels of the initial and final J manifolds. These are both host dependent. Although the wavelength shifts with composition are small, $\approx$2%, the half-widths are only 1 to 2% of the peak wavelength. Therefore, a significant spectral mismatch may occur if different glasses are used in various stages of oscillator–amplifier systems.

We have applied the above compositional variations to tailor the peak cross section for the Nd^{3+} ${}^4F_{3/2} \rightarrow {}^4I_{11/2}$ transition. To narrow the effective line width, halide rather than oxide glass formers and large, monovalent modifier cations such as K, Rb, Cs, or Tl should be used. The line strength is increased by using larger, more polarizable halides such as Cl or Br. This also increases σ due to the larger refractive index of these glasses.

Of the chloride glasses, zinc chloride is a well-known but very hygroscopic glass former. These glasses have been proposed for fiber-optics applications.[256] Our attempts to prepare water-free, Nd-doped $ZnCl_2$ glasses with high-fluorescence quantum efficiency were not successful, however.

Recently, a new class of inorganic chloride glasses based on $BiCl_3$ as the glass former was described.[257] Several of these glasses doped with 1 mole % $NdCl_3$ were prepared by D. C. Ziegler and C. A. Angell of Purdue University. Most studies involved $BiCl_3$–KCl compositions. The glasses were prepared from purified $BiCl_3$ and dry, reagent-grade, second components fused under a chlorine-gas atmosphere to repress the tendency to form reduced-bismuth polynuclear centers, principally Bi_4^{4+}, which gives the glass a pink coloration due to a strong broad absorption band at $\approx$520 nm. Samples for spectroscopic studies were sealed in glass ampoules. The glass transition temperatures were low, 100°C. The refractive index and Abbé number were estimated to be approximately 2.0 and 20. Other properties of the glasses are given in Ref. 257.

The measured fluorescence line widths of Nd^{3+} in $BiCl_3$ glasses are extremely narrow, comparable to the narrowest line widths of fluoroberyllate glasses. In Fig. 2-425 the ${}^4F_{3/2} \rightarrow {}^4I_{11/2}$ fluorescence spectra of Nd^{3+} in some simple fluoride, chloride, and silicate glasses are compared. (Glass compositions (mole %): fluoride–60 BeF_2 40 KF; chloride–60 $BiCl_3$ 40 KCl; silicate–67 SiO_2 33 K_2O.) The figure illustrates the changes in line width and line shape and the shifts in peak wavelength with composition. For halide glasses, this nephelauxetic shift follows the series F^-, Cl^-, Br^-, I^-.

Judd–Ofelt intensity parameters were derived from a least-squares fit of measured and calculated absorption-band strengths. The values are given in Table 2-76 together with corresponding results for other simple oxide and halide glasses. The values vary widely for different glass formers. Using the

Fig. 2-425. Comparison for the ${}^4F_{3/2} \rightarrow {}^4I_{11/2}$ fluorescence spectrum of Nd^{3+} in halide and oxide glasses at 295 K.

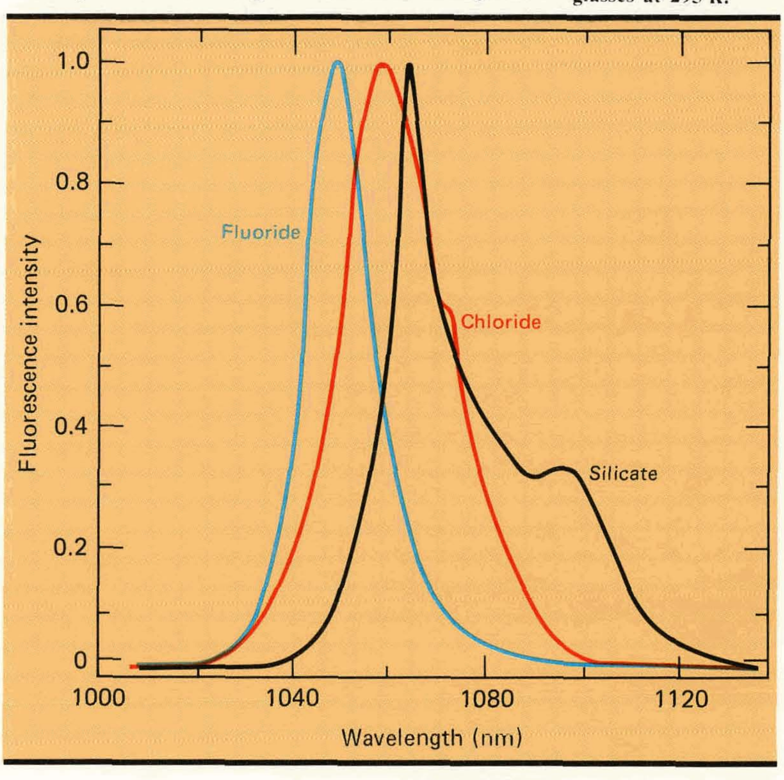

calculated line strength and the measured line width, the stimulated-emission cross section for the $^4F_{3/2} \rightarrow {}^4I_{11/2}$ transition was 5.9×10^{-20} cm^2. This is the highest value determined for any glass we have studied. For comparison, in Table 2-76 we show the range of spectroscopic properties for Nd^{3+} observed in other glass types. The large value of σ for the $BiCl_3$–KCl glass is a result of a combination of large line strength, narrow line width, and high refractive index. The large cross section and narrow line widths obtained for transitions of Nd^{3+} in $BiCl_3$ glasses should also be applicable to other trivalent rare-earth ions.

Several additional $BiCl_3$ glasses were prepared and their properties examined including a 57 $BiCl_3$ 43 TlCl glass. With respect to the $BiCl_3$–KCl glass, there was a slight increase in line width (19.6 nm) and a shift in peak wavelength (1065.5 nm).

Glasses of the heavier halides should be the extremes in terms of narrow optical line widths. The narrowest $^4F_{3/2} \rightarrow {}^4I_{11/2}$ line observed was $\Delta\lambda_{eff}$ = 18.1 nm for a glass having a composition 69.2 $BiCl_3$ 30.1 KBr 0.7 $NdCl_3$ (mole %). The peak wavelength did not change. In this mixed anion glass, the number of chlorine atoms is still much greater than the number of bromine atoms. Thus, the probability of Nd sites having a large number of Br^- ligands, and hence of large nephelauxetic shift, is small. Similar behavior was observed for a chlorophosphate glass.[258]

Pure bromide glasses can also be prepared. A glass containing 69.2 % $BiBr_3$ 30.1 % KBr and 0.7 % $NdCl_3$ (mole %) was melted and sealed under vacuum. The glass-transition temperature for the undoped glass was below 10°C. Unfortunately the signal-to-noise ratio was very small and no useful spectroscopic data were obtained.

The optical pumping efficiency[259] of the Nd-doped 60 $BiCl_3$ 40 KCl glass relative to ED-2 silicate glass was 91% for xenon flashlamp radiation in the 400 to 950 nm spectral region and for an ion-density-pathlength product of 5×10^{20} ions/cm^2. Because of the absorption edge, radiation of wavelength <400 nm is absorbed by the $BiCl_3$ glasses. This is not a big loss in pumping efficiency for Nd^{3+}, but might be for other laser ions. Because of the shorter fluorescence lifetimes in the bismuth chloride glasses, short pump pulses are needed for efficient pumping.

Good optical-pumping efficiency combined with the very large stimulated-emission cross sections make these glasses of interest for low-threshold, high-gain application. The resistance of the $BiCl_3$–KCl glasses to moisture attack is good compared to $ZnCl_2$ glass, but poor by usual optical glass standards. For practical applications, these glasses require protection from the atmosphere (the glass develops a weakly protective, white surface film of BiOCl after a few minutes exposure to air). The addition of other modifier cations, e.g., Ag, Tl, Pb, may lessen the atmospheric attack but will also modify the spectroscopic properties somewhat.

Author: M. J. Weber

Table 2-76. Range of variation of spectroscopic properties for the $^4F_{3/2} \rightarrow {}^4I_{11/2}$ transition of Nd^{3+} in various glasses.

Glass	Cross section (10^{20} cm^2)	Wavelength λ_p (nm)	Line width eff (nm)	Lifetime τR (μs)
Silicates	1.0–3.6	1057–1065	34–43	170–1010
Phosphates	2.0–4.8	1052–1057	22–35	280–530
Tellurites	3.0–5.1	1056–1063	26–31	140–240
Fluorophosphates	2.2–4.3	1050–1056	27–34	310–570
Fluoroberyllates	1.6–4.0	1046–1050	19–28	460–1030
60 $BiCl_3$ 40 KCl	5.9	1064.5	19.2	–

Note: All measurements were made at 295 K.

Quantum Efficiency Measurements. One of the principal parameters of interest for luminescence and quantum electronics applications is the absolute radiative quantum efficiency of the materials of interest. The precise determination of absolute fluorescence quantum yield by conventional luminescence means, where the number of quanta absorbed from a beam of monochromatic light is compared to the number of quanta emitted in the polychromatic fluorescent light, has proven to be very difficult.[260] Another technique involves the measurement of fluorescence lifetime,[261] also a difficult procedure, since a separate measurement of the nonradiative contribution to the lifetime of the fluorescent electronic state must be made, or alternatively the radiative lifetime must be calculated as with Judd–Ofelt calculations for rare-earth fluorescent ions.[262]

There is another method that has been somewhat neglected until recently, which obtains the radiative quantum efficiency by determining the nonradiative part of the absorbed energy through calorimetry. The photoacoustic technique is a sensitive means for performing such calorimetric measurements,[263] and it has been used quite successfully to obtain accurate absolute radiative quantum efficiencies in gases, liquids and highly absorbing solids. Recently, photoacoustic experiments have also been performed on fluorescent laser materials that are only weakly absorbing, such as Nd:YAG and Nd-doped glasses. Unlike the experiments on more highly absorbing solids, these photoacoustic studies have given quantum-efficiency values considerably different from those usually measured or calculated for Nd:YAG and Nd-doped glasses.

We have investigated the problem of photoacoustic measurements of fluorescence quantum efficiencies, and have concluded that the discrepancies encountered in the experiments with the lightly doped samples are primarily due to the neglect of surface absorptions.[264]

For a sample of thickness $d > \mu$ (the thermal diffusion length), which has only one fluorescent level with lifetime τ much shorter than ω^{-1} (the photoacoustic modulation period), we can show that the photoacoustic signal is given by[264]

$$q_k = Sa_kP_k\left\{1 - \eta \frac{\lambda_k}{\lambda_e}\right\} \tag{87}$$

Here a_k is the absorbance of the sample, P_k is the incident power at the excitation wavelength λ_k, and S is the system sensitivity (V/W). The quantum efficiency of the fluorescent level is given by η and the mean emission wavelength by λ_e. In the case of Nd^{3+} where there are several discrete emission wavelengths arising from transitions from the $^4F_{3/2}$ fluorescent state to the various ^4I_j terminal states, the mean emission wavelength is given by

$$1/\lambda_e = \sum_t b_t/\lambda_t \tag{88}$$

where the b_t's are the branching ratios to the various ground levels E_t, and the λ_t's are the corresponding emission wavelengths.

Clearly, in order to obtain an absolute value for η, we need to know the sensitivity factor S, which in turn depends critically on such difficult-to-measure parameters as the volume of gas in the cell, the acoustic reflectivity of the cell walls, etc. A ratiometric approach offers a convenient solution to this problem. If the photoacoustic signal is measured at two absorbing wavelengths λ_i and λ_j, the ratio of the two signals will be given by

$$\frac{q_i}{q_j} = \frac{a_iP_i\left\{1 - \eta \frac{\lambda_i}{\lambda_e}\right\}}{a_jP_j\left\{1 - \eta \frac{\lambda_j}{\lambda_e}\right\}} \tag{89}$$

And if we define a normalized photoacoustic signal $q^* = q/aP$, then the absolute quantum efficiency is determined by

$$\eta = \frac{(q_i^* - q_j^*)\lambda_e}{(q_i^*\lambda_j - q_j^*\lambda_i)} \tag{90}$$

It is important to note that an accurate evaluation of η requires very high accuracy in the determination of the photoacoustic signal, and particularly so for systems with low η since here $q_i^* \simeq q_j^*$.

Quimby and Yen[265] (QY), using a gas-microphone photoacoustic method, obtained a value of η for lightly doped ED-2 Nd:glass of 0.65 ± 0.05. This value is considerably less than the value of 0.9 found by the luminescence-sphere method, and predicted by the exponential-energy-gap law. Quimby and Yen have suggested that the reason for this discrepancy might be site selectivity[266] resulting from their use of a narrow energy laser line for excitation. Powell, Neikirk, and Sardar[267] (PNS) have also used a PAS gas-microphone ratiometric technique to obtain absolute quantum efficiencies for Nd^{3+} in garnet, vanadate, and phosphate host crystals. For the more highly concentrated samples, PNS obtained results in good agreement with previous measurements and calculations. However, for lightly doped Nd:YAG they obtained $\eta = 0.60$, while most previous measurements and Judd–Ofelt calculations indicate that η is in the range of 0.91 to 0.88. In addition to this discrepancy, Powell et al. also observed that their photoacoustic signal varied as ω^{-1} for their lightly doped samples, whereas the Rosencwaig–Gersho theory[268] predicts an $\omega^{-3/2}$ behavior for these samples. Neither the apparently low value of η nor the observed frequency dependence in the PNS experiment are adequately explained.

In both the QY and PNS experiments, a gas-microphone photoacoustic system was used, and, in order to obtain sufficient signal strength, argon ion lasers were employed as the light sources. Both the 476.5 nm and the 514.5 nm argon lines are far from the major absorption bands of the Nd^{3+} ions. Thus, for the typical lightly doped laser materials, containing 1 wt% or less of Nd_2O_3, the absorption coefficient of the Nd^{3+} ions at these two wavelenghts is of the order of 0.1 cm^{-1} or less.

In a gas-microphone photoacoustic experiment, only the light absorbed within a thermal-diffusion length below the surface is relevant.[268] At the modulation frequencies used in the QY and PNS experiments, the thermal-diffusion lengths were generally less than 100 μm. Now the absorption term a in Eq. (90), is given by

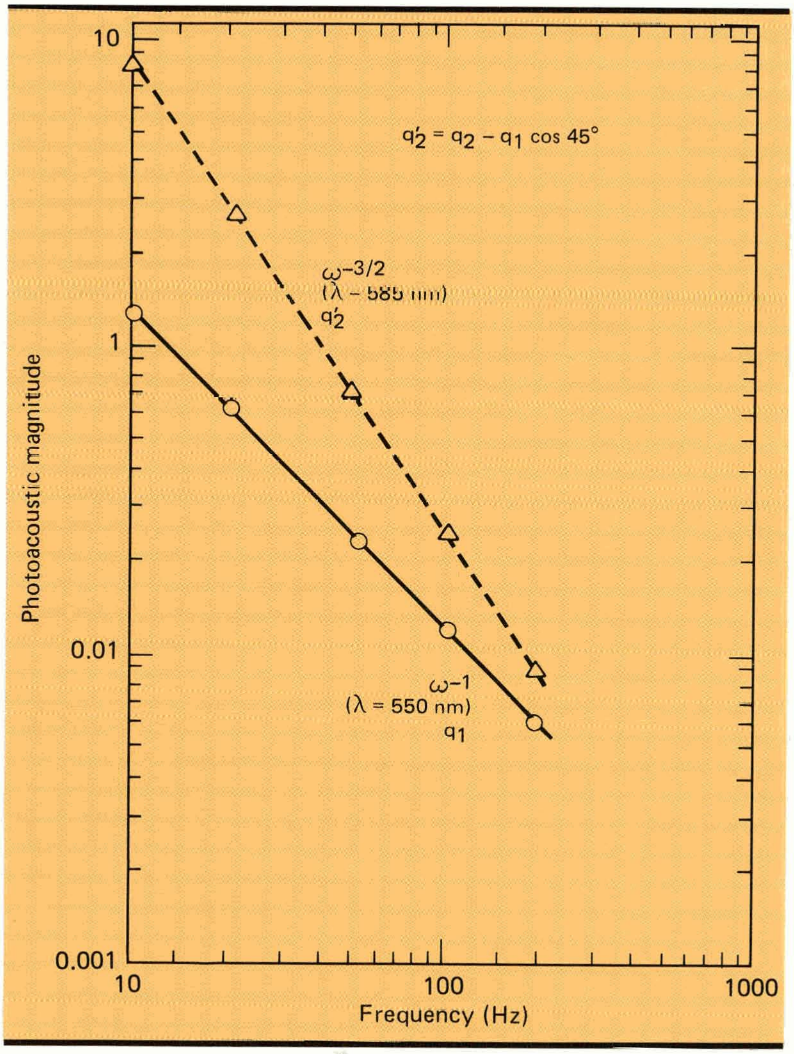

Fig. 2-426. Dependence of photoacoustic signal with frequency in Nd-doped silicate glass.

$$a = (1 - e^{-\alpha\mu}) \simeq \alpha\mu \tag{91}$$

where α is the absorption coefficient. Thus, the total photoacoustic absorption due to the Nd^{3+} ions is less than 0.1% of the incident radiation. With such a low absorption due to the intrinsic bulk ions, it is imperative to consider the influence of any surface absorptions arising from contamination or surface state effects.

The anomalous ω^{-1} frequency dependence observed by PNS is a further indication that surface-absorption terms may be of considerable importance. From the Rosencwaig–Gersho theory,[268] one can readily show that in the presence of both a surface-absorption term of absorbance α_s, and a weak bulk absorption with absorption coefficient α, the photoacoustic signal is given by

$$q = I_o Z \left\{ \frac{(1 - i)\alpha_s}{\omega} - \frac{i\alpha\mu'}{\omega^{3/2}} \right\} \tag{92}$$

where I_o is the incident light intensity, Z is a frequency-independent term containing all the thermal and geometric parameters, and where $\mu' = \mu\omega^{1/2}$ and is itself a frequency-independent term.

We note that the first term, the surface-absorption term, varies as ω^{-1}, while the bulk-absorption term varies as $\omega^{-3/2}$. Furthermore, the two terms are 45° out-of-phase. If the first term is much larger than the second term, then an ω^{-1} dependence will be observed, and conversely, if the second term is larger, an $\omega^{-3/2}$ dependence will be seen.

To test this concept we studied several lightly doped Nd:glass (ED-2 silicate) samples using a gas-microphone photoacoustic system with a Xenon lamp and monochromator optical system. With this optical system we were able to measure the photoacoustic signal both at a wavelength of strong Nd^{3+} absorption (585 nm) and at a wavelength of very low Nd^{3+} absorption (550 nm). We found that the 550 and 585 nm signals were 45° out-of-phase and that these signals have different frequency dependencies [Fig. 2-426; the signal at 585 nm has been corrected for background ($q_2' = q_2 - q_1 \cos \pi/4$)]. We see that, indeed, the 550-nm signal shows an ω^{-1} dependence indicative of surface absorption while the 585-nm signal shows an $\omega^{-3/2}$ dependence indicative of bulk absorption. Our results also show that the surface absorption in our samples is not negligible, and in fact at the argon-laser wavelengths of 476.5 and 514.5 nm, the signal is found to be predominantly due to surface absorption, particularly, at frequencies greater than 50 Hz. We found a significant surface-absorption contribution to the total photoacoustic signal at these two wavelengths, even in ultra-clean samples. Thus, we believe that both the QY and PNS results were considerably disturbed by the surface-absorption term, which was not considered.

In our experiments, we employed a conventional gas-microphone photoacoustic system with a Xenon lamp and monochromator arrangement. We made measurements at 585 and 750 nm, both positions of relatively strong Nd^{3+} absorption, and also at 550 and 700 nm, where there is essentially no Nd^{3+} absorption. These two latter measurements provide us with the needed correction for the background surface-absorption term. Our measured quantum efficiencies for a set of Nd^{3+}-doped ED-2 glasses are plotted in Fig. 2-427 with probable error bars shown. We see that the quantum efficiency at low Nd^{3+} concentration approaches 0.9, in good agreement with both luminescence and lifetime values.

Also in Fig. 2-427, we have plotted the quantum efficiencies that would be determined from relative average fluorescence-lifetime measurements[269] after assuming the PAS value of 0.71 for the 2% sample to be correct. We see that the photoacoustic η's and the relative lifetime η's agree very well with respect to the dependence on Nd^{3+} concentration. This then indicates that when dealing with a set of similar samples that have different concentrations of Nd^{3+}, we would need to obtain an absolute value of η with photoacoustics for only one sample, and then obtain the other η's from the easier-to-measure relative fluorescence lifetimes.

The sizable decrease in quantum efficiency at higher Nd^{3+} concentration is, of course, a result of ion–ion quenching. Using both the PAS-measured quantum efficiency at low concentration and the lifetime measurements, we obtain absolute values for the nonradiative decay rate ω_{nr} for Nd^{3+} in ED-2 glass as a function of Nd^{3+} concentration, c (Fig. 2-428). The nonradiative decay rate is composed of two terms; a concentration-independent term that arises from multiphonon processes, and an ion–ion quenching term that varies as c^2. The multiphonon term dominates until $c > 1\%$, after which the ion–ion term quickly becomes the factor determining the fluorescence quantum efficiency. Layne, Lowdermilk, and Weber[270] have shown that the average multiphonon rate for ED-2 glass is $\sim 200\ s^{-1}$ in good agreement with our result in Fig. 2-428.

Although it is possible to obtain fairly reliable measurements of the absolute radiative quantum efficiency with gas-microphone photoacoustics, the pervasive presence of a sizable surface-absorption term makes this method difficult, particularly for lightly doped samples in which the surface-absorption term may be comparable to the bulk-absorption term.

We have, therefore, developed an alternative procedure which employs a piezoelectric photoacoustic technique. As

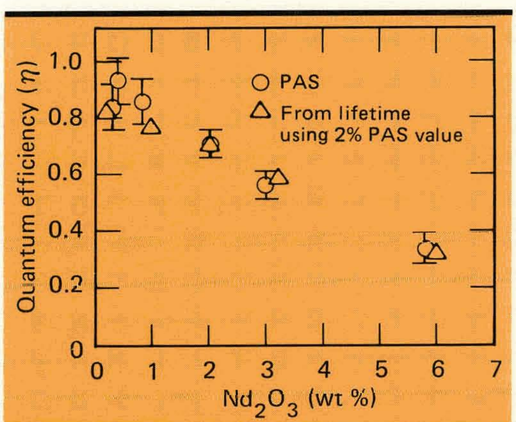

Fig. 2-427. Photoacoustic and relative lifetime-fluorescence quantum efficiencies vs Nd_2O_3 concentration in ED-2 silicate glasses.

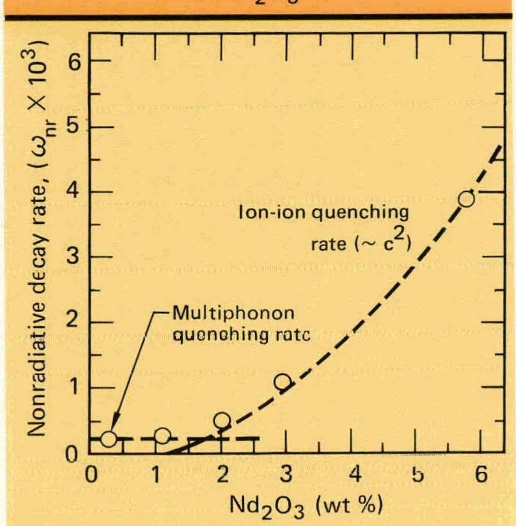

Fig. 2-428. Nonradiative decay rate vs Nd_2O_3 concentration in ED-2 silicate glasses.

shown in Fig. 2-429, a mirror is bonded to a ceramic piezoelectric transducer, and the mirrored transducer is then acoustically bonded with phenylsalicylate to the side of the sample. The mirror serves to minimize background signal due to the absorption of scattered light by the transducer.

In a gas-microphone system, only that light absorbed within a thermal diffusion length beneath the sample surface plays a role in determining the photoacoustic signal. In a piezoelectric system, however, the light absorbed throughout the entire sample contributes to the photoacoustic signal. Since the samples are 0.2 to 1 cm thick, this provides us with a bulk absorption signal considerably greater than the surface absorption signal; thus surface absorptions generally present no problem in a piezoelectric measurement. Nevertheless, we still must take measurements at both 550 and 700 nm to subtract out any other background signals.

In piezoelectric photoacoustic detection, the magnitude and phase of the photoacoustic signal are both complex functions of the thermal spatial profile produced in the sample through the absorption of the optical beam.[271] To minimize this very difficult problem we attempt to have the same thermal spatial profile at both of the absorbing wavelengths. Thus, we do not use the 585 nm wavelength, but rather a wavelength nearby that has the same optical absorption as that measured for 750 nm. In addition, since the absorption bands have quite different line shapes at the two wavelengths we use, we have found it best to work only with lightly doped samples so as to obtain nearly identical thermal profiles at the two wavelengths.

Fig. 2-429. Sample-detector mounting arrangement for piezoelectric photo acoustic experiments.

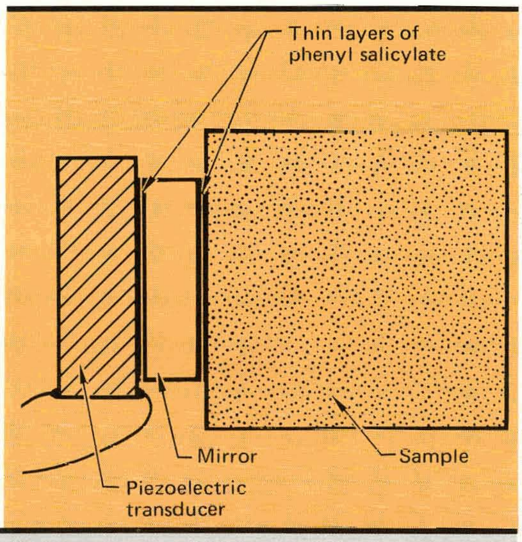

Table 2-77. Quantum efficiencies of Nd laser materials. ▼

Sample	PAS (gas-microphone)	PAS (piezoelectric)	Other methods	References
ED-2 silicate glass ($wt\%\ Nd_2O_3$)				
0.3	0.85 ± 0.08	—	0.90	(269)
0.4	0.93 ± 0.08	0.91 ± 0.05	0.90	(269)
0.8	0.86 ± 0.08	—	0.90	(269)
1.0	—	0.93 ± 0.05	0.87	(269)
2.0	0.71 ± 0.05	—	0.79	(269)
3.0	0.56 ± 0.05	—	0.64	(269)
5.8	0.34 ± 0.05	0.40 ± 0.05	0.37	(269)
Borate glass (0.2 wt% Nd_2O_3)	—	0.16 ± 0.07	0.16	(272)
$Y_3Al_5O_{12}$ (1.2 at.% Nd)	—	0.97 ± 0.02	0.91	(261)
			0.88	(269, 273)
			1.00	(274)
			0.98	(275)
			0.56	(276)
			0.63	(277)
			0.60	(267)

In Table 2-77, we list the fluorescence quantum efficiencies measured for some of the ED-2 silicate glass samples with both the piezoelectric and gas-microphone methods. There is quite good agreement between the two sets of values, and the probable error for the low concentration samples is less in the piezoelectric measurements. The good agreement between the gas-microphone and piezoelectric measurements provides further confidence in the value of 0.9 for η that we obtain for ED-2 silicate glass.

We repeated the silicate piezoelectric photoacoustic experiment with Nd^{3+}-doped borate glass. Borate glass has a high nonradiative multiphonon decay rate at room temperature of $\sim 14\,000\ s^{-1}$, resulting in an average quantum efficiency substantially less than unity.[273] We obtain with the piezoelectric photoacoustic technique a value for η for the borate sample (see Table 2-77) of 0.16 ± 0.07, a value in excellent agreement with the lifetime measurement. The relatively large uncertainty in our value is a result of the increased probable error that occurs when the quantum efficiency is low and the quantity $(q_i^* - q_j^*)$ in Eq. (90) becomes very small.

There has been, for many years, considerable interest in the absolute fluorescence quantum efficiency of Nd:YAG, a widely used laser material. In spite of many different experiments there is still uncertainty about the value of η for this material. Judd–Ofelt and lifetime calculations[274] indicate that a 1 wt% Nd:YAG sample should have an η of ~0.91. However, experimental results over the years have ranged from 0.98 to 0.56. (See Refs. 261, 267, 269, and 274–277.)

We have measured the quantum efficiency of a 1.2 wt% Nd:YAG sample using the piezoelectric photoacoustic technique, and have obtained a value for η of 0.97 ± 0.02. Our result clearly supports the contention that the quantum efficiency for Nd:YAG is close to unity.

In conclusion, the photoacoustic technique provides a reliable means for obtaining absolute values for the radiative quantum efficiency. The gas-microphone technique is quite accurate for highly absorbing solids. We have shown that in lightly doped laser materials with relatively weak bulk absorptions, surface absorptions from contamination or from surface energy states can play a major role in gas-microphone photoacoustic measurements and thus must be taken into account. We believe that it was neglect of this surface absorption that led to anomalous results in previous experiments. We have also shown that a piezoelectric photoacoustic technique is an attractive alternative procedure that is relatively immune to surface absorption effects. However, here too, care must be taken. This technique works best for weakly absorbing samples with measurements made at two wavelengths having equal absorptions. In both the gas-microphone and piezoelectric methods, accurate measurements of η require good signal-to-noise ratios and careful measurements of background signals at wavelengths where there is no absorption by the fluorescent ions.

We recommend the piezoelectric method for a routine-measurement facility, particularly when dealing with Nd^{3+} laser materials. Other techniques should be considered for laser materials, such as Cr^{3+} systems, which have very broad absorption bands that present background-measurement difficulties. We are presently investigating the use of photorefractive techniques, which, when used with pulsed excitation, may provide absolute quantum efficiencies without the need for background measurements.

Author: A. Rosencwaig

Major Contributor: E. A. Hildum

Homogeneous Line Widths and Energy Extraction in Laser Glass. Optical spectra of ions in glasses are inhomogeneously broadened due to site-to-site variations in the local fields. Laser ions in different spectral regions of the inhomogeneous-gain distribution act independently and varying degrees of spectral hole burning result. The energy extractable from an inhomogeneously broadened amplifier compared to that of a homogeneously broadened amplifier is a function of the ratio of the homogeneous to the inhomogeneous line widths. As this ratio increases, the amplifying medium behaves more homogeneously and energy extraction for a given input becomes more efficient. Therefore, the dependence of the homogeneous line width of optical transitions on glass composition is a consideration in the selection of host glass for laser applications.

Homogeneous Line Widths. There has been recent interest in the question of homogeneous line widths of paramagnetic ions in amorphous materials. Efforts thus far have been concerned with temperature dependence of the optical line widths of rare-earth ions which are anomalous when compared to their low-temperature crystalline counterparts.[278,279] To obtain additional information about line broadening mechanisms, we measured the homogeneous line width of the $^4F_{3/2} \rightarrow {}^4I_{9/2}$ fluorescence transition of Nd^{3+} as a function of host glass composition. We found a broad range of homogeneous and inhomogeneous line width values, with minimum and maximum values differing by at least a factor of 3. In addition, these values scale approximately as the inverse 2.5 power of the velocity of sound in the glass.

Samples included 10 oxide glasses: borate, silicate, borosilicate, alkali and alkaline earth phosphates, germanate, tellurite, and 2 fluoride glasses: fluoroberyllate and fluorozirconate. The compositions of these glasses are given in Table 2-78.

As a measure of the inhomogeneous broadening, the line width $\Delta\nu_{IH}$ (FWHM) of the transition between the lowest Stark levels of the $^4I_{9/2}$ and $^4F_{3/2}$ manifolds was determined from the absorption spectrum recorded at 4.2 K. At liquid helium temperatures, the homogeneous line width of this transition is expected to be $\ll 1$ cm^{-1} and hence negligible.

Corresponding homogeneous line widths $\Delta\nu_H$ were measured using laser-induced fluorescence line-narrowing techniques.[280] The excitation source was a pulsed $LiF:F_2^+$ color-center laser which had a tuning range from 0.86 to 1.0 μm. All line width measurements were made by J. M. Pellegrino of the University of Wisconsin.

Sound velocities of the glasses at 295 K were determined from ultrasonic time-delay measurements using the pulse-echo-overlap method.[281] For the glass compositions studied, values of both the longitudinal and transverse velocities exhibited variations by a factor of about 2.

There is a definite correlation between the homogeneous line width and sound velocity in a glass at ambient temperature. In Fig. 2-430, $\Delta\nu_H$ is plotted as a function of the root-mean-square velocity of sound given by

$$v_{rms} = \left[\frac{v_\ell^2 + 2v_t^2}{3} \right]^{1/2} , \tag{93}$$

assuming one longitudinal and two transverse modes of propagation. For the large number of different glasses considered, the data exhibit a general trend given by

$$\Delta\nu_H \propto v_{max}^{-2.6\pm0.2} \tag{94}$$

Similar agreement is found for v_t, but the correlation with v_ℓ is poorer.

Due to the large differences in glass compositions and site-to-site variations in the local fields and interactions at the Nd ion in amorphous hosts, a smooth dependence of $\Delta\nu_H$ with v is not expected. The borosilicate glass, which is a mixture of two glass network formers, shows a large deviation from the general trend in Fig. 2-430. However, for subsets of glasses from a single source and with similar compositions and Nd concentrations, such as the Al, Mg, Ba metaphosphate glasses and the alkali phosphate glasses, the correlation is very good.

The inhomogeneous line width $\Delta\nu_{IH}$ determined from the $^4F_{3/2}(1) \rightarrow {}^4I_{9/2}(1)$ transition at 4 K correlates well with the

Table 2-78. Compositions (in mole %) of glasses used in studies of homogeneous line widths.

Silicate	Phosphate
$67B_2O_3 \cdot 15Na_2O \cdot 18BaO$	$50P_2O_5 \cdot 50MgO$
Borate	$50P_2O_5 \cdot 50BaO$
$67SiO_2 \cdot 15Na_2O \cdot 18BaO$	$75P_2O_5 \cdot 25Al_2O_3$
Borosilicate	$55P_2O_5 \cdot 30Li_2O \cdot 10CaO \cdot 5Al_2O_3$
$75SiO_2 \cdot 9B_2O_3 \cdot 9Na_2O \cdot 6K_2O \cdot 1BaO$	$55P_2O_5 \cdot 30Rb_2O \cdot 10CaO \cdot 5Al_2O_3$
Fluorozirconate	Phosphotellurite
$60ZrF_4 \cdot 34BaF_2 \cdot 6NdF_3$	$89TeO_2 \cdot 11P_2O_5$
Fluoroberyllate	Germanate
$49BeF_2 \cdot 27KF \cdot 14CaF_2 \cdot 10AlF_3$	$67GeO_2 \cdot 15Na_2O \cdot 18BaO$

Note: All samples were doped with $\lessapprox 1$ mole % of Nd_2O_3 or NdF_3.

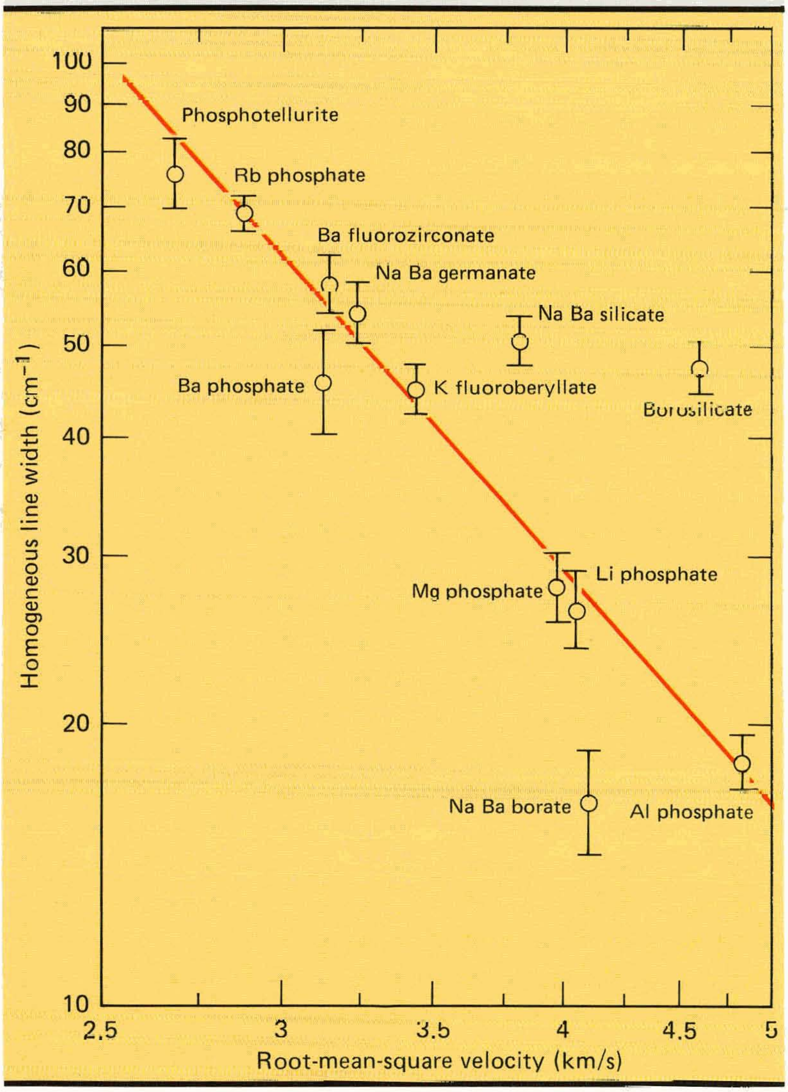

Fig. 2-430. Log—log plot of the homogeneous line width of Nd^{3+} vs rms sound velocity for various glasses; compositions are given in Table 2-78.

effective line width of the $^4F_{3/2} \rightarrow {}^4I_{11/2}$ laser transition at 295 K. This is shown in Fig. 2-431. The latter is obtained by integrating over all Stark transitions and is used to determine effective stimulated-emission cross sections.

There is no obvious correlation between $\Delta\nu_{IH}$ and the homogeneous line width $\Delta\nu_H$ at 300 K. The ratio $\Delta\nu_H/\Delta\nu_{IH}$ does vary considerably for the present selection of glass hosts, from 0.16 for borate glass to 1.86 for rubidium-phosphate glass. Thus the ratio can be tailored, within limits, by changing glass network-forming and network-modifying ions.

In summary, we have determined that $\Delta\nu_H$ for Nd^{3+} varies widely for different glass hosts. The observed widths are strongly correlated with the velocity of sound in the material; however, the dependence of $\Delta\nu_H$ on v does not agree with predictions based on known mechanisms for line broadening in crystals.[282] Also, there are special cases, such as the borosilicate glass, where $\Delta\nu_H$ differs significantly from the trend followed by the majority of the other samples. Nevertheless, the correlation of $\Delta\nu_H$ with v should be helpful in selecting glass hosts to maximize energy extraction from laser ions. Further details of this work are presented in Ref. 282.

Energy Extraction. The reduction in the energy extracted from an inhomogeneously broadened-gain medium compared to that from a homogeneous medium of the same small-signal gain is a function of the ratio of the homogeneous and inhomogeneous line widths $\Delta\nu_H/\Delta\nu_{IH}$. If this ratio is $\gtrsim 1$, ions in different spectral regions of the inhomogeneous distribution act independently and various degrees of spectral hole burning will result. To quantify this effect, we considered the case of a Gaussian frequency distribution of Lorentzian lines, which is a reasonable approximation for many ion-glass combinations. The fraction of the energy extracted from such a system compared to that of a homogeneous system of the same initial small-signal gain is plotted as a function of $\Delta\nu_H/\Delta\nu_{IH}$ in Fig. 2-432. The product of the initial gain coefficient of the medium times the path length was 1.0. The results are shown for two input fluences, where Φ_s is the saturation fluence for the homogeneous two-level system. For the small-signal case, ($\Phi_{in} = 0.01\Phi_s$), the deviation from the output of a homogeneous medium is small even for large inhomogeneities because the depth of the hole is still small. For $\Phi_{in} = \Phi_s$, however, a deep hole is burned and the gain coefficient is severely reduced when $(\Delta\nu_H/\Delta\nu_{IH}) < 1$. If $(\Delta\nu_H/\Delta\nu_{IH}) \ll 1$, the energy extracted under large-signal conditions is greatly reduced. This would occur, for example, for glass at

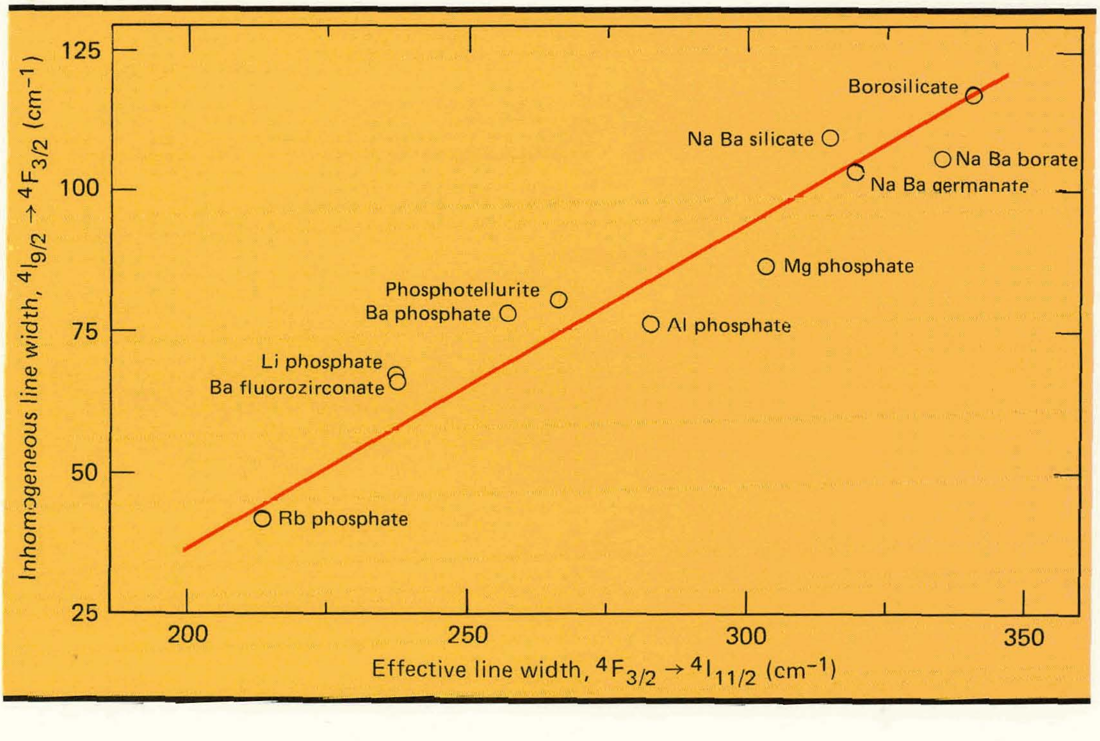

Fig. 2-431. Comparison of effective line width of fluorescence (at 300 K) and inhomogeneous line width of absorption (at 4 K) for Nd^{3+} in various glasses.

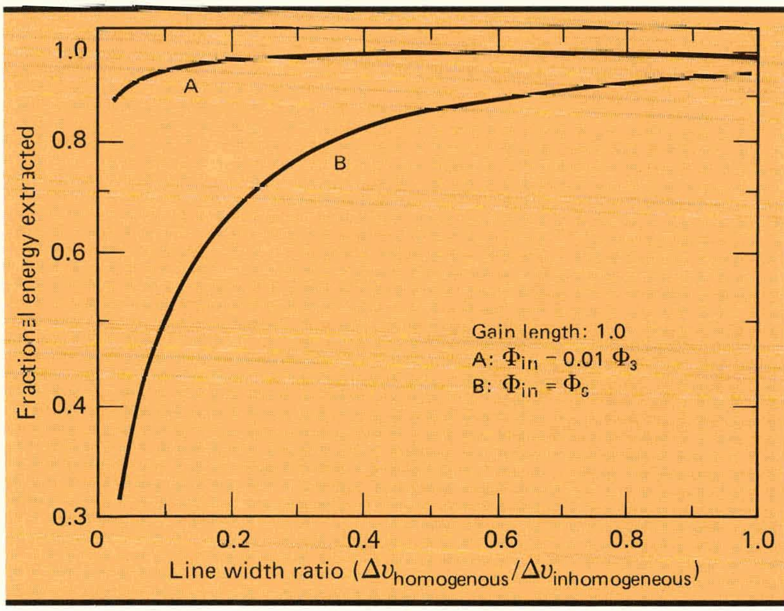

Fig. 2-432. Fraction of the energy extracted from an inhomogeneously broadened glass amplifier relative to that of a homogeneously broadened glass.

low temperatures where the homogeneous line widths become very small. Homogeneous line widths of optical transitions of rare earths in glass are directly proportional to the square of the absolute temperature of the sample in the range from 4 to 400 K.[279,283] Therefore high-temperature laser operation is desirable to reduce spectral hole burning.

At a given operating temperature, the selection of host affects $\Delta\nu_H/\Delta\nu_{IH}$. For example, in the case of phosphate glasses, the use of higher atomic-number alkali- or alkaline-earth modifier cations increases $\Delta\nu_H$ and decreases $\Delta\nu_{IH}$ and thereby improves the capability for energy extraction. As we have shown, the velocity of sound is a good indicator of the relative values of $\Delta\nu_H$.

Reduction in energy extracted occurs whenever the glass has a distribution of stimulated-emission cross sections at the laser wavelength. This can arise not only from site-to-site variations in the center frequency, but also from site-to-site variations in the homogeneous line width or the transition probability for stimulated emission for a specific wavelength and polarization.[284] When the cross sections of a given site geometry are different for different polarizations, then, because of the random orientation of the principal axes in glass, there will be a range of extraction rates if a polarized laser beam is used. Note that, in this case, no *spectral* hole burning will be evident.

Knowledge of the distribution of cross-section values for a given frequency and polarization is essential to modeling the saturation behavior in glass lasers. The use of unpolarized or circularly-polarized beams and multiple or swept frequencies are methods for operationally overcoming the consequences of the inhomogeneities in glass. Finally, it should be noted that hole filling by ion–ion cross relaxation in Nd-doped laser glasses occurs on time scales of $>10\ \mu s$ and hence is not effective on the time scale of pulses used in fusion lasers, 1 to 10 ns.[285]

Author: M. J. Weber

Major Contributors: R. A. Haas and J. M. Pellegrino

Argus Operations 2-6

1. *Laser Program Annual Report—1979*, Lawrence Livermore National Laboratory, Livermore, Calif., UCRL-50021-79 (1980), pp. 2-3 and 6-41.
2. V. D. Volosov, A. G. Kalintsev, and V. N. Krylov, *Sov. J. Quantum Electron.* **6**, 1163 (1976).
3. J. M. Yarborough, J. Falk, and C. B. Hitz, *Appl. Phys. Lett.* **18**, 70 (1971).
4. F. Zernike and J. E. Midwinter, *Applied Nonlinear Optics* (John Wiley and Sons, New York, 1973), p. 61.

Target Diagnostics 2-17

5. *Laser Program Annual Report—1977*, Lawrence Livermore National Laboratory, Livermore, Calif., UCRL-50021-77 (1978), pp. 3-11, 3-22, and 3-90.
6. *Laser Program Annual Report—1978*, Lawrence Livermore National Laboratory, Livermore, Calif., UCRL-50021-78 (1979), p. 2-56.
7. *Laser Program Annual Report—1979*, Lawrence Livermore National Laboratory, Livermore, Calif., UCRL-50021-79 (1980), p. 2-29.
8. *Laser Program Annual Report—1976*, Lawrence Livermore National Laboratory, Livermore, Calif., UCRL-50021-76 (1977), p. 2-139.

Optical Pulse Generation 2-20

9. *Laser Program Annual Report—1978*, Lawrence Livermore National Laboratory, Livermore, Calif., UCRL-50021-78 (1979), p. 2-41.
10. *Laser Program Annual Report—1978*, Lawrence Livermore National Laboratory, Livermore, Calif., UCRL-50021-78 (1979), p. 2-17.
11. *Laser Program Annual Report—1979*, Lawrence Livermore National Laboratory, Livermore, Calif., UCRL-50021-79 (1980), p. 2-52.
12. *Laser Program Annual Report—1979*, Lawrence Livermore National Laboratory, Livermore, Calif., UCRL-50021-79 (1980), p. 2-197.
13. *Laser Program Annual Report—1978*, Lawrence Livermore National Laboratory, Livermore, Calif., UCRL-50021-78 (1979), p. 2-18.
14. *Laser Program Annual Report—1979*, Lawrence Livermore National Laboratory, Livermore, Calif., UCRL-50021-79 (1980), p. 2-232.
15. *Laser Program Annual Report—1979*, Lawrence Livermore National Laboratory, Livermore, Calif., UCRL-50021-79 (1980), p. 2-234.
16. *Laser Program Annual Report—1976*, Lawrence Livermore National Laboratory, Livermore, Calif., UCRL-50021-76 (1977), p. 2-296.

Electronic Systems 2-26

17. *Laser Program Annual Report—1978*, Lawrence Livermore National Laboratory, Livermore, Calif., UCRL-50021-78 (1979), p. 2-37.
18. B. M. Carder, *Driving Pockels Cell Gates in Multi-Arm Lasers*, Lawrence Livermore National Laboratory, Livermore, Calif., UCRL-81241 (1978).
19. *Laser Program Annual Report—1979*, Lawrence Livermore National Laboratory, Livermore, Calif., UCRL-50021-79 (1980), p. 2-52.

Laser Diagnostics 2-30

20. *Laser Program Annual Report—1975*, Lawrence Livermore National Laboratory, Livermore, Calif., UCRL-50021-75 (1976), p. 399.
21. P. R. Rupert et al., "New Isolation and Control Systems for Large Pulse Power Systems," in *Proc. IEEE 7th Symposium on Engineering Problems of Fusion* (Knoxville, Tenn., Oct. 25–28, 1977).

Mechanical Maintenance and Upgrades 2-32

22. *Laser Program Annual Report—1979*, Lawrence Livermore National Laboratory, Livermore, Calif., UCRL-50021-79 (1980), p. 2-46.

Shiva Component Maintenance Summary 2-36

23. H. G. Patton et al., *Techniques for Preventing Damage to High Power Laser Components*, Lawrence Livermore National Laboratory, Livermore, Calif., UCRL-78923 (1977).
24. *Laser Program Annual Report—1978*, Lawrence Livermore National Laboratory, Livermore, Calif., UCRL-50021-78 (1979), p. 7-26.

Novette Design Considerations 2-39

25. *Laser Program Annual Report—1979*, Lawrence Livermore National Laboratory, Livermore, Calif., UCRL-50021-79 (1980), p. 2-63.

Novette Master Oscillator Room 2-48

26. *Laser Program Annual Report—1979*, Lawrence Livermore National Laboratory, Livermore, Calif., UCRL-50021-79 (1980), p. 2-73.
27. *Laser Program Annual Report—1978*, Lawrence Livermore National Laboratory, Livermore, Calif., UCRL-50021-78 (1979), p. 7-9.
28. *Laser Program Annual Report—1978*, Lawrence Livermore National Laboratory, Livermore, Calif., UCRL-50021-78 (1979), p. 7-11.
29. J. E. Murray and D. J. Kuizenga, "Regenerative Compression of Laser Pulses," *Appl. Phys. Lett.* **37**, 27 (1980).

Nova Laser System Design and Performance 2-57

30. *Laser Program Annual Report—1979*, Lawrence Livermore National Laboratory, Livermore, Calif., UCRL-50021-79 (1980).

Nova Laser Chain—Components 2-64

31. *Laser Program Annual Report—1979*, Lawrence Livermore National Laboratory, Livermore, Calif., UCRL-50021-79 (1980), p. 2-82.

References

Spatial Filters
2-67

32. *Laser Program Annual Report—1979,* Lawrence Livermore National Laboratory, Livermore, Calif., UCRL-50021-79 (1980), p. 2-82.
33. K. Bathe, E. L. Wilson, and F. E. Peterson, *SAP IV—A Structural Analysis Program for Static and Dynamic Response of Linear Systems,* College of Engineering, University of California, Berkeley, Calif., Report EERC 73-11 (1973, Rev. 1974).

Faraday Rotator Isolators
2-68

34. *Laser Program Annual Report—1976,* Lawrence Livermore National Laboratory, Livermore, Calif., UCRL-50021-76 (1977), p. 2-85.

Beam Transport: Mirror Assemblies
2-71

35. *Laser Program Annual Report—1976,* Lawrence Livermore National Laboratory, Livermore, Calif., UCRL-50021-76 (1977), p. 2-88.
36. K. Bathe, E. L. Wilson, and F. E. Peterson, *SAP IV—A Structural Analysis Program for Static and Dynamic Response of Linear Systems,* College of Engineering, University of California, Berkeley, Calif., Report EERC 73-11 (1973, Rev. 1974).

Nova Optical Components
2-72

37. *Laser Program Annual Report—1979,* Lawrence Livermore National Laboratory, Livermore, Calif., UCRL-50021-79 (1980), p. 2-153.
38. *Laser Program Annual Report—1979,* Lawrence Livermore National Laboratory, Livermore, Calif., UCRL-50021-79 (1980), p. 2-75.
39. L. Cook, Schott Optical, private communication (September 24, 1980).
40. N. Brown, *Flat Lapping Revisited,* Lawrence Livermore National Laboratory, Livermore, Calif., UCRL-83500 (1979). Presented at OSA/SPIE Optical Fabrication Workshop, Tucson, Ariz. (1979).
41. *Laser Program Annual Report—1979,* Lawrence Livermore National Laboratory, Livermore, Calif., UCRL-50021-79 (1980), p. 2-79.
42. D. Bajuk, "A High Accuracy Surface Contour Measuring Machine," in *Proc. OSA/SPIE Opt. Fab. Wkshp, Tucson, Ariz., 1979* (OSA/SPIE, 1979), Vol. 171.
43. *Laser Damage Thresholds of 1064-nm Coatings as a Function of Vacuum Pumping Systems,* Spectra Physics, Inc., Mountain View, Calif. (1980).
44. *Accuracy and Repeatability of Zapp Using Several Examples,* Zygo Corporation, Middlefield, Conn., Product Bulletin 0050 (1979).

Frequency Conversion
2-90

45. V. D. Volosov et al., *Sov. Tech. Phys. Lett.* **5** (1), 1979.
46. V. D. Volosov et al., *J. Sov. Quantum Electron.* **6** (10), 1976.
47. S. A. Akhmanov et al., "Limiting Efficiency of Optical Multipliers with Birefringent Crystals," *Quantum Electronics,* Rabe and Tang, Eds. (Academic Press, New York, 1975), pp. 532–535.
48. W. Seka et al., "Demonstration of High Efficiency Third Harmonic Conversion of High Power Nd:Glass Laser Radiation," *Opt. Commun.* **34**(3), 1980.

Space Frames
2-97

49. *Laser Program Annual Report—1979,* Lawrence Livermore National Laboratory, Livermore, Calif., UCRL-50021-79 (1980), pp. 2-82 to 2-92.
50. K. Bathe, E. L. Wilson, and F. E. Peterson, *SAP IV—A Structural Analysis Program for Static and Dynamic Response of Linear Systems,* College of Engineering, University of California, Berkeley, Calif., EERC 73-11, Rev. 1 (1974).

Nova Power Supply
2-105

51. *Laser Program Annual Report—1979,* Lawrence Livermore National Laboratory, Livermore, Calif., UCRL-50021-79 (1980), Vol. 1, pp. 2-96 to 2-98.
52. *Power Supply for Nova Capacitor-Bank Charging,* LES 22264 (1979).

Capacitor Development
2-106

53. *Laser Program Annual Report—1979,* Lawrence Livermore National Laboratory, Livermore, Calif., UCRL-50021-79 (1980), p. 2-94.
54. C. A. Moyer et al., "The Weibull Distribution Function for Fatigue Life," *Mat. Res. Stand.* 5, 405 (1962).
55. D. Nyman, *Weibull Analysis for Fatigue Failures When Non-Failed Samples Are Removed from Test,* Maxwell Laboratories Inc., San Diego, Calif. (1969).
56. B. Carder, Lawrence Livermore National Laboratory, Livermore, Calif., private communication (1979).

Flashlamps
2-111

57. K. Yoshida, Osaka University, Institute of Laser Engineering, private communication (1980).

Control System
2-113

58. *Laser Program Annual Report—1978,* Lawrence Livermore National Laboratory, Livermore, Calif., UCRL-50021-78 (1979).

Nova Alignment/ Laser Diagnostics
2-119

59. B. H. Mueller and S. Sheldrake, "Pulse Synchronization System," *IEEE/OSA Conference on Laser Engineering and Applications, Technical Digest,* paper 11.9 (1977).
60. *Laser Program Annual Report—1979,* Lawrence Livermore National Laboratory, Livermore, Calif., UCRL-50021-79 (1980), pp. 2-111 to 2-113.

Nova Alignment Laser Diagnostics (cont.)

61. *Laser Program Annual Report—1979*, Lawrence Livermore National Laboratory, Livermore, Calif., UCRL-50021-79 (1980), pp. 2-25 to 2-29.
62. D. R. Speck et al., "The Shiva Laser Fusion Facility," *J. IEEE Quant. Elec.*, to be published (1981).
63. *Laser Program Annual Report—1979*, Lawrence Livermore National Laboratory, Livermore, Calif., UCRL-50021-79 (1980), pp. 2-110 to 2-111.
64. E. S. Bliss, "Alignment of the Twenty-Beam Shiva Laser," *Energy and Technology Review*, Lawrence Livermore National Laboratory, Livermore, Calif., UCRL-5200-78-12 (1978).
65. *Laser Program Annual Report—1978*, Lawrence Livermore National Laboratory, Livermore, Calif., UCRL-50021-78 (1979), pp. 2-28 to 2-34.
66. *Laser Program Annual Report—1978*, Lawrence Livermore National Laboratory, Livermore, Calif., UCRL-50021-78 (1979), pp. 2-106 to 2-108.
67. *Laser Program Annual Report—1980*, Lawrence Livermore National Laboratory, Livermore, Calif., UCRL-50021-80 (1981), pp. -
68. *Laser Program Annual Report—1979*, Lawrence Livermore National Laboratory, Livermore, Calif., UCRL-50021-79 (1980), pp. 2-114 to 2-119.

Nova Control-System Development 2-131

69. G. J. Suski and F. W. Holloway, "The Evolution of a Large Laser Control System—from Shiva to Nova," *IEEE Circ. Syst.* **1**, 3 (1980).
70. *Laser Program Annual Report—1979*, Lawrence Livermore National Laboratory, Livermore, Calif., UCRL-50021-79 (1980), pp. 2-102 to 2-108.

Novanet 2-133

71. *Laser Program Annual Report—1979*, Lawrence Livermore National Laboratory, Livermore, Calif., UCRL-50021-79 (1980), pp. 2-124 to 2-125.
72. *Laser Program Annual Report—1979*, Lawrence Livermore National Laboratory, Livermore, Calif., UCRL-50021-79 (1980), pp. 2-104 to 2-105.
73. *Electronics Engineering Quarterly Report—1980*, Lawrence Livermore National Laboratory, Livermore, Calif., UCRL-50025-80-2 (1980), pp. 9 to 16.

Nova Image Processing 2-147

74. Gregory I. Suski, *Shiva Automatic Pinhole Alignment*, Lawrence Livermore National Laboratory, Livermore, Calif., UCRL-84903 (1980).

Praxis 2-154

75. J. Walker, J. R. Greenwood, A. Evans, Jr., C. R. Morgan, and M. C. Zarnstorff, *Praxis Language Reference Manual*, Lawrence Livermore National Laboratory, Livermore, Calif., UCID-15331 (1981).
76. J. R. Greenwood, A. Evans, Jr., C. R. Morgan, and M. C. Zarnstorff, *An Introduction to Praxis*, Lawrence Livermore National Laboratory, Livermore, Calif., UCRL-52957 (1980).
77. J. R. Greenwood, W. I. Nowicki, A. Evans, Jr., C. R. Morgan, and M. C. Zarnstorff, *Programming in Praxis*, Lawrence Livermore National Laboratory, Livermore, Calif. (1981).

Target Systems 2-158

78. *Laser Program Annual Report—1979*, Lawrence Livermore National Laboratory, Livermore, Calif., UCRL 50021-79 (1980), pp. 2-119 to 2-122.
79. *Laser Program Annual Report—1977*, Lawrence Livermore National Laboratory, Livermore, Calif., UCRL 50021-77 (1978), p. 2-103.
80. R. J. Calliger, *Nova/Novette Vacuum System Controls*, Lawrence Livermore National Laboratory, Livermore, Calif., Internal Memorandum NCSA-223, Nova File-35 (1980).
81. *Laser Program Annual Report—1979*, Lawrence Livermore National Laboratory, Livermore, Calif., UCRL-50021-79 (1980), pp. 2-102 to 2-106.
82. *Laser Program Annual Report—1979*, Lawrence Livermore National Laboratory, Livermore, Calif., UCRL-50021-79 (1980), p. 2-107.
83. *Laser Program Annual Report—1979*, Lawrence Livermore National Laboratory, Livermore, Calif., UCRL-50021-79 (1980), p. 2-122.
84. *Laser Program Annual Report—1977*, Lawrence Livermore National Laboratory, Livermore, Calif., UCRL-50021-77 (1978), pp. 3-9 to 3-22.
85. *Laser Program Annual Report—1978*, Lawrence Livermore National Laboratory, Livermore, Calif., UCRL-50021-78 (1979), p. 2-56.
86. *Laser Program Annual Report—1979*, Lawrence Livermore National Laboratory, Livermore, Calif., UCRL-50021-79 (1980), pp. 2-29 to 2-34.
87. *Laser Program Annual Report—1979*, Lawrence Livermore National Laboratory, Livermore, Calif., UCRL-50021-79 (1980), pp. 2-104 to 2-125.
88. *Laser Program Annual Report—1977*, Lawrence Livermore National Laboratory, Livermore, Calif., UCRL-50021-77 (1978), pp. 2-101 to 2-118.
89. *Laser Program Annual Report—1978*, Lawrence Livermore National Laboratory, Livermore, Calif., UCRL-50021-78 (1979), pp. 2-109 to 2-118.
90. *Laser Program Annual Report—1979*, Lawrence Livermore National Laboratory, Livermore, Calif., UCRL-50021-79 (1980), pp. 2-118 to 2-127.
91. M. S. Singh and M. A. Summers, *Neutron Irradiation Effects on KDP Crystals Used for Harmonic Generation* (to be published).

Conventional Facilities 2-168

92. *Laser Program Annual Report—1978*, Lawrence Livermore National Laboratory, Livermore, Calif., UCRL-50021-78 (1979), pp. 2-123 to 2-126.
93. *Laser Program Annual Report—1979*, Lawrence Livermore National Laboratory, Livermore, Calif., UCRL-50021-79 (1980), pp. 2-127 to 2-134.

Project Management Systems 2-172

94. *MISTER: Management Information System for Time, Expenses, and Resources, Version 5.1*, Computer Sciences Corporation, Los Angeles, Calif., E00192-01, Rev. 6-CP (1979).
95. "Project Management System," *U.S. Department of Energy Order 5700.4*, U.S. Department of Energy (1981).

MALAPROP Code 2-187

96. A. J. Glass and W. E. Warren, *MALAPROP-Light Propagation in a Nonlinear Medium*, Lawrence Livermore National Laboratory, Livermore, Calif., UCRL-80316 (1977).
97. *Laser Program Annual Report—1979*, Lawrence Livermore National Laboratory, Livermore, Calif., UCRL-50021-79 (1980), p. 2-149.
98. W. W. Simmons and W. E. Warren, Lawrence Livermore National Laboratory, Livermore, Calif., Internal Laser Program Memorandum, Nova 80-137 (December 1980).
99. *Laser Program Annual Report—1978*, Lawrence Livermore National Laboratory, Livermore, Calif., UCRL-50021-78 (1979), p. 7-112.
100. *Laser Program Annual Report—1979*, Lawrence Livermore National Laboratory, Livermore, Calif., UCRL-50021-79 (1980), p. 2-64.
101. G. G. Peterson, Lawrence Livermore National Laboratory, Livermore, Calif., private communication (1980).

Nova Target Illumination Studies 2-189

102. *Laser Program Annual Report—1979*, Lawrence Livermore National Laboratory, Livermore, Calif., UCRL-50021-79 (1980), p. 2-139.
103. *Laser Program Annual Report—1974*, Lawrence Livermore National Laboratory, Livermore, Calif., UCRL-50021-74 (1975), p. 227.
104. *Laser Program Annual Report—1979*, Lawrence Livermore National Laboratory, Livermore, Calif., UCRL-50021-79 (1980), p. 2-139.
105. *Laser Program Annual Report—1979*, Lawrence Livermore National Laboratory, Livermore, Calif., UCRL-50021-79 (1980), p. 6-47.

Nova Pulse Shape Generation 2-194

106. J. D. Lindl, Lawrence Livermore National Laboratory, Livermore, Calif., private communication (1980).

Evaluation of the Iodine Laser 2-197

107. K. J. Witte, *Eine Abschatzung der Ausbleichverluste beim Jod Laser*, Institut fur Plasma Physik, Garching, Federal Republic of Germany, Report No. 4 (1976).
108. G. Brederlow, R. Brodmann, K. Eidmann, H. Krause, M. Nippus, R. Petsch, R. Volk, S. Witkowski, and K. J. Witte, *Asterix III High Power Iodine Laser System Performance Summary*, Projektgruppe fur Laserforschung, Institut fur Plasma Physik, Garching, Federal Republic of Germany, PLF Report No. 5 (1979).
109. *Laser Program Annual Report—1975*, Lawrence Livermore National Laboratory, Livermore, Calif., UCRL-50021-75 (1976), p. 69.
110. *Laser Program Annual Report—1977*, Lawrence Livermore National Laboratory, Livermore, Calif., UCRL-50021-77 (1978), p. 2-66.
111. W. F. Hagen, *Evaluation of the Iodine Laser*, Lawrence Livermore National Laboratory, Livermore, Calif., Foreign Research Leave Report (1979).

Short-Pulse Flashlamp Model 2-203

112. J. B. Trenholme and J. L. Emmett, "Xenon Flashlamp Model for Computer Simulation," in *Proc. 9th Intern. Congress High Speed Photography, Denver, 1970* (SMPIE, New York, 1970) p. 209.
113. G. J. Linford, *Short-Pulse Flashlamp Investigation for the Iodine Laser Research Program*, Lawrence Livermore National Laboratory, Livermore, Calif., Foreign Research Leave Report (1979).
114. G. I. Taylor, "The Formation of a Blast Wave by a Very Intense Explosion," *Proc. R. Soc. A*. **201**, 159 (1950).
115. S. I. Drabkina, *JETP* **21**, 437 (1951).
116. Shao Chi Lin, "Cylindrical Shock Wave Produced by Instantaneous Energy Release," *J. Appl. Phys.* **25**, 54 (1954).
117. H. Morgenroth, H. Heb, K. Kischel, K. Rademacher, and K. Seliger, "Zur Theorie der StoBwellenausbreitung und der Kanalentwicklung bei starken Funkenentladungen," *Ann. Phys. (Leipz.)* **8**, 175 (1961).
118. I. S. Marshak, "Strong Current Pulse (Spark) Discharges in Gas Used in Pulsed Light Sources," *Sov. Phys.-Usp.* **5**, 478 (1962).
119. G. J. Linford and S. C. Roberts *Updating VODEP Flashlamp Model*, Lawrence Livermore National Laboratory, Livermore, Calif., Memo AD-77-61 (1977).
120. J. L. Emmett and A. L. Schawlow, "Direct Measurement of Xenon Flashtube Opacity," *J. Appl. Phys.* **35**, 2601 (1964).
121. W. F. Hagen, *Evaluation of the Iodine Laser*, Lawrence Livermore National Laboratory, Livermore, Calif., Foreign Research Leave Report (1979).

Super Nova 2-206

122. W. E. Martin and D. Milam, *Gain Saturation in Nd:Doped Laser Material*, Lawrence Livermore National Laboratory, Livermore, Calif., UCID-18868 (1980).

Fluorophosphate Glass Development 2-211

123. *Laser Program Annual Report—1979*, Lawrence Livermore National Laboratory, Livermore, Calif., UCRL-50021-79 (1980), p. 2-153.

Phosphate Glasses 2-212

124. *Laser Program Annual Report—1979*, Lawrence Livermore National Laboratory, Livermore, Calif., UCRL-50021-79 (1980), p. 2-155.

Gain-Saturation Properties of Laser Materials 2-219

125. *Laser Program Annual Report—1979*, Lawrence Livermore National Laboratory, Livermore, Calif., UCRL-50021-79 (1980), p. 2-160.
126. W. E. Martin and D. Milam, *Gain Saturation in Nd:Doped Laser Materials*, Lawrence Livermore National Laboratory, Livermore, Calif., UCID-18868 (1980).
127. L. M. Frantz and J. S. Nodvik, *J. Appl. Phys.* **34**, 2346 (1963).

Electron-Beam-Deposited AR Films 2-222

128. *Laser Program Annual Report—1979*, Lawrence Livermore National Laboratory, Livermore, Calif., UCRL-50021-79 (1980), p. 2-170.

Graded-Index Surfaces 2-226

129. *Laser Program Annual Report—1979*, Lawrence Livermore National Laboratory, Livermore, Calif., UCRL-50021-79 (1980), p. 2-172.
130. W. H. Lowdermilk and D. Milam, "Graded-Index Surfaces for High-Power Applications," *Appl. Phys. Lett.* **36**, 891 (1980).

Bulk Damage in KDP 2-226

131. R. M. Wood, "Laser Damage in Optical Materials at 1.06 μm," *General Electric Co. J. Sci. Tech.* **45**, 109 (1979).

Damage Thresholds at 532, 355, and 248 nm 2-229

132. D. Milam, "Measurement and Identification of Laser-Damage Thresholds in Thin-Films," *SPIE* 140, 52 (1978).
133. *Laser Program Annual Report—1979*, Lawrence Livermore National Laboratory, Livermore, Calif., UCRL 50021-79 (1980), p. 2-180.
134. W. L. Smith, A. J. DeGroot, and M. J. Weber, "Silicon Vidicon System for Measuring Laser Intensity Profiles," *Appl. Opt.* **17**, 3938 (1978).
135. W. H. Lowdermilk, D. Milam, and F. Rainer, "Damage to Coatings and Surfaces by 1.06-μm Pulses," in *Laser-Induced Damage in Optical Materials: 1979*, Special Publication of the National Bureau of Standards (1980), p. 568.

Amplifier Development 2-234

136. W. Koechner, *Solid State Laser Engineering*, (Springer-Verlag, New York, 1976), pp. 344, 352.
137. T. M. Pollak, Sanders Associates, Inc., Nashua, N. H., private communication (1979).
138. G. A. Massey, *Appl. Phys. Lett.* **17**, 213 (1970).
139. *Laser Program Annual Report—1979*, Lawrence Livermore National Laboratory, Livermore, Calif., UCRL-50021-79 (1980), p. 2-189.

Oscillator Development 2-244

140. D. J. Kuizenga, "Generation of Short Pulses for Laser Fusion in an Actively Mode-Locked Nd:YAG Laser," *Opt. Commun.* **22**, 156 (1977).
141. *Laser Program Annual Report—1976*, Lawrence Livermore National Laboratory, Livermore, Calif., UCRL-50021-76 (1977), p. 2-289.
142. *Laser Program Annual Report—1977*, Lawrence Livermore National Laboratory, Livermore, Calif., UCRL-50021-77 (1978), pp. 2-17, 2-207, 2-219.
143. *Laser Program Annual Report—1978*, Lawrence Livermore National Laboratory, Livermore, Calif., UCRL-50021-78 (1979), pp. 2-14, 7-9.
144. *Laser Program Annual Report—1979*, Lawrence Livermore National Laboratory, Livermore, Calif., UCRL-50021-79 (1980), p. 2-197.
145. *Laser Program Annual Report—1979*, Lawrence Livermore National Laboratory, Livermore, Calif., UCRL-50021-79 (1980), p. 2-49.
146. *Laser Program Annual Report—1979*, Lawrence Livermore National Laboratory, Livermore, Calif., UCRL-50021-79 (1980), p. 2-232.

Large-Aperture Harmonic Generation—Introduction 2-254

147. W. L. Smith and M. A. Summers, *Harmonic Generation for Fusion Laser Systems*, Lawrence Livermore National Laboratory, Livermore, Calif., Internal Memorandum UVM 80 14 (May 1980).

Argus Frequency-Conversion Experiments 2-259

148. *Laser Program Annual Report—1979*, Lawrence Livermore National Laboratory, Livermore, Calif., UCRL 50021 79 (1980), p. 2 209.

Intensity-Dependent Angular Offset Experiments 2-262

149. *Laser Program Annual Report—1979*, Lawrence Livermore National Laboratory, Livermore, Calif., UCRL-50021-79 (1980), p. 2-209.

10-cm Crystal-Array Prototype 2-265

150. *Laser Program Annual Report—1979*, Lawrence Livermore National Laboratory, Livermore, Calif., UCRL-50021-79 (1980), p. 2-203.
151. D. Milam, *Appl. Opt.* **16**, 1204 (1977).

Precision Orientation Apparatus 2-269

152. F. Zernike and J. E. Midwinter, *Applied Nonlinear Optics* (John Wiley & Sons, New York, 1973), p. 61.
153. W. L. Smith and M. A. Summers, *Harmonic Generation for Fusion Lasers*, Lawrence Livermore National Laboratory, Livermore, Calif., Internal Memorandum UVM 80-14, Appendix II (May 1980), p. 38.
154. R. J. Pressley, Ed., *Handbook of Lasers* (Chemical Rubber Co., Cleveland, 1971), p. 381.

Diamond Turning of KDP 2-271

155. D. L. Decker, D. S. Grandjean, and J. M. Bennett, "Optical and Surface Physical Characteristics of Diamond-Machined Infrared Windows," in *Symposium on the Sciences of Ceramic Machining and Surface Finishing II*, National Bureau of Standards Special Publication 562, p. 293.
156. G. M. Sanger and P. C. Baker, "Feasibility of Glass Processing by Precision Machine Technology," *SPIE* **183**, 139 (1979).
157. P. C. Baker, Lawrence Livermore National Laboratory, Livermore, Calif., Internal Memorandum No. 80-331 (1980).

KDP Crystal Growth 2-275

158. A. N. Holden, *Discuss. Faraday Soc.* **5**, 312 (1949).
159. A. N. Holden, U.S. Patent 2,484,829 (1949).
160. C. J. Christensen and A. C. Walker, U.S. Patent 2,459,869 (1949).
161. A. C. Walker and G. T. Kohman, *AIEE Trans.* **67**, 565 (1948).
162. I. A. Batyreva, V. I. Bespalov, V. I. Bredikhin, G. L. Galushkina, V. P. Ershov, V. I. Katsman, S. P. Kuznetsov, L. A. Lavrov, M. A. Novikov, and N. R. Shvetsova, "Growth and Investigation of Optical Single Crystals for High Power Laser Systems," *ICCG-6 Extended Abstracts* (Moscow, September 1980), p. 79.
163. R. Janssen-van Rosmalen, W. H. van der Linden, E. Dobbinga, and D. Visser, "The Influences of the Hydrodynamic Environment on the Growth and the Formation of Liquid Inclusions in Large Potassium Dihydrogen Phosphate (KDP) Crystals," *Kristall und Technik* **13**, 17 (1978).
164. M. I. Kozlooskii, "Kinetics of Crystallization at Constant Temperature and Supersaturation," *Sov. Phys. Crystallography* **2**, 745 (1957).
165. M. I. Kozlooskii, A. V. Komolobai, I. I. Melentyev, and M. F. Burchakov, "Apparatus and Procedure for Study of the Effects of the Crystallization Conditions on the Growth and Properties of Crystals," in *Growth of Crystals*, Vol. 6A (N. N. Sheftal, Ed.) (Consultants Bureau, New York, 1968), p. 7.

Index-Matching Fluids for Large Apertures 2-278

166. W. Kaiser and M. Maier, "Stimulated Rayleigh, Brillouin and Raman Spectroscopy," in *Laser Handbook*, F. T. Arecchi and E. O. Schulz-DuBois, Eds. (American Elsevier Publishing Co., New York, 1972), p. 1077.
167. S. D. Jacobs, University of Rochester, Rochester, N.Y., private communication (1980).

Compensated Pulsed Alternator 2-287

168. W. F. Weldon et al., *Alternator for Pulsed Power Duty*, U. S. Patent disclosure (January 23, 1978).
169. *Laser Program Annual Report—1978*, Lawrence Livermore National Laboratory, Livermore, Calif., UCRL-50021-78 (1979), p. 7-14.
170. W. F. Weldon et al., *Compensated Pulsed Alternator*, Lawrence Livermore National Laboratory, Livermore, Calif., (1978).
171. R. J. Foley et al., *Compensated Pulsed Alternator—A New Concept for Generating High Powered Pulsed Energy*, Lawrence Livermore National Laboratory, Livermore, Calif., LLL-TB-23 (1980).
172. W. L. Bird and H. H. Woodson, *Detailed Design, Fabrication and Testing of an Engineering Prototype Compensated Alternator*, Center for Electromechanics, University of Texas at Austin (1980).
173. W. L. Bird, *The Continued Testing and Evaluation of the Engineering Prototype Compulsator*, Center for Electromechanics, University of Texas at Austin, Monthly Progress Report (1980).

The Nova Plasma Shutter 2-292

174. *Laser Program Annual Report—1979*, Lawrence Livermore National Laboratory, Livermore, Calif., UCRL-50021-79 (1980), p. 219.
175. L. P. Bradley, E. L. Orham, I. F. Stowers, and P. Koert, *Development of A Plasma Retropulse Shutter for Shiva and Nova*, Lawrence Livermore National Laboratory, Livermore, Calif., UCRL-52830 (1979).
176. Q. Johnson and A. C. Mitchell, "Flash X-ray Tube for Diffraction Studies on a Two-Stage Light Gas Gun," *Rev. Sci. Instrum.* **51**, 741 (1980).

Fast-Pulse Development 2-298

177. *Laser Program Annual Report—1979*, Lawrence Livermore National Laboratory, Livermore, Calif., UCRL-50021-79 (1980), p. 232.

Basic Research—Introduction 2-304

178. M. J. Weber, D. Milam, and W. L. Smith, "Nonlinear Refractive Index of Glasses and Crystals," *Opt. Eng.* **17**, 463 (1978).
179. M. J. Weber, "Properties of Low-Index Laser Materials," *Basic Optical Properties of Materials: Summaries of Papers*, NBS Spec. Publ. 574 (1980).

Basic Research—Introduction (cont.)

180. C. F. Cline and M. J. Weber, "Beryllium Fluoride Optical Glasses: Preparation and Properties," in *Proc. 1st Otto Schott Symposium, Ztschr. Friedrich-Schiller-Univ. Jena; Math-Nat. R.* **28**, Jg. H. 2/3, 351 (1979). Also available at Lawrence Livermore National Laboratory, Livermore, Calif., UCRL-81168 (1979).
181. W. L. Smith, "Laser-Induced Breakdown in Optical Materials," *Opt. Eng.* **17**, 489 (1978).
182. M. J. Weber, "Laser Excited Fluorescence Spectroscopy of Glass," in *Laser Spectroscopy in Solids* (Springer–Verlag, Heidelberg, in press).
183. S. A. Brawer and M. J. Weber, "Monte Carlo Simulation of Eu^{3+}-Doped BeF_2 Glass," *Phys. Rev. Lett.* **45**, 460 (1980).
184. M. J. Weber and R. M. Almeida, "Large Stimulated Emission Cross Sections of Nd^{3+} in Chlorophosphate Glass," *J. Non-Cryst. Solids* (in press).
185. S. A. Brawer and M. J. Weber, "Observation of Fluorescence Line Narrowing, Hole Burning, and Ion-Ion Energy Transfer in Neodymium Laser Glass," *Appl. Phys. Lett.* **35**, 31 (1979).
186. J. M. Pellegrino, W. M. Yen, and M. J. Weber, "Composition Dependence of Nd^{3+} Homogeneous Line Widths in Glass," *J. Appl. Phys.* **51**, 6332 (1980).

Beryllium–Fluoride Glasses 2-306

187. C. F. Cline and M. J. Weber, "Beryllium Fluoride Optical Glasses: Preparation and Properties," in *Proc. 1st Otto Schott Symposium, Ztschr. Friedrich-Schiller-Univ. Jena; Math-Nat. R.* **28**, Jg. H. 2/3, 351 to 364 (1979). Also available at Lawrence Livermore National Laboratory, Livermore, Calif., UCRL-81168 (1979).
188. M. J. Weber, "Properties of Low-Index Laser Materials," *Basic Optical Properties of Materials: Summaries of Papers*, NBS Spec. Publ. 574 (1980), pp. 3–8.
189. *Laser Program Annual Report—1976*, Lawrence Livermore National Laboratory, Livermore, Calif., UCRL-50021-76 (1977), p. 243.
190. D. L. Griscon, M. Stapelbroek, and M. J. Weber, "Electron Spin Resonance Studies of Iron-Group Impurities in Beryllium Fluoride Glasses," *J. Non-Cryst. Solids* **41**, 329 (1980).

Nonlinear Optics 2-308

191. *Laser Program Annual Report—1974*, Lawrence Livermore National Laboratory, Livermore, Calif., UCRL-50021-74 (1975), pp. 178 to 217.
192. See, for example, N. Bloembergen, *Nonlinear Optics* (W. A. Benjamin Inc., Reading, Mass., 1965); P. W. Langhoff, S. T. Epstein, and M. Karplus, "Aspects of Time-Dependent Perturbation Theory," *Rev. Mod. Phys.* **44**, 602 (1972); R. W. Hellwarth, "Third-Order Optical Susceptibilities of Liquids and Solids," *Prog. Quant. Electron.* Vol. 5, Part I (Permagon Press, New York, 1977).
193. M. J. Weber, D. Milam, and W. L. Smith, "Nonlinear Refractive Index of Glasses and Crystals," *Optical Engineering* **17**, 463 (1978).
194. E. S. Bliss, D. R. Speck, and W. W. Simmons, "Direct Interferometric Measurements of the Nonlinear Coefficient n_2 in Laser Materials," *Appl. Phys. Lett.* **25**, 728 (1974).
195. D. Milam and M. J. Weber, "Measurements of Nonlinear Refractive-Index Coefficients Using Time-Resolved Interferometry: Application to Optical Materials for High-Power Neodymium Lasers," *J. Appl. Phys.* **47**, 2497 (1976).
196. M. J. Moran, C. Y. She, and R. L. Carman, "Interferometric Measurements of the Nonlinear Refractive-Index Coefficient Relative to CS_2 in Laser-System Related Materials," *IEEE J. Quant. Electron.* **QE-11**, 259 (1975).
197. W. L. Smith, A. J. DeGroot, and M. J. Weber, "Silicon Vidicon System for Measuring Laser Intensity Profiles," *Appl. Opt.* **17**, 3938 (1978).
198. P. Liu, W. L. Smith, H. Lotem, J. H. Bechtel, and N. Bloembergen, "Absolute Two-Photon Absorption Coefficients at 355 and 266 nm," *Phys. Rev. B* **17**, 4620 (1978).
199. M. Bass, E. W. Van Stryland, and A. F. Stewart, "Laser Calorimetry of Two-Photon Absorption," *NBS Special Publication* **541**, 19 (1978).
200. T. Fukami, "Optoacoustic Study of the Infrared Multiphoton Excitation of Ethylene," *Opt. Commun.* **30**, 351 (1979); and references therein.
201. A. M. Bonch-Bruevich, T. K. Razumova, and I. O. Starobogatov, "Single and Two-Photon Spectroscopy of Liquid Media Using the Pulsed Acuosto-Optical Effect," *Opt. Spectrosc.* **42**, 45 (1977).
202. A. C. Tam and C. K. N. Patel, "Two-Photon Absorption Spectra and Cross-Section Measurements in Liquids," *Nature* **280**, 304 (1979).
203. A. J. Twarowski and D. S. Kliger, "Multiphoton Absorption Spectra Using Thermal Blooming," *Chem. Phys.* **20**, 259 (1977).
204. A. Rosencwaig and T. W. Hindley, "Photoacoustic Measurements of Low-Level Absorptions in Solids," *Appl. Opt.* **20**, 606 (1981).
205. A. C. Boccara, D. Fournier, W. Jackson, and N. M. Amer, "Sensitive Photothermal Deflection Technique for Measuring Absorption in Optically Thin Media," *Opt. Lett.* **5**, 377 (1980).

Crystal Growth Facilities 2-311

206. W. Bar, B. Cockayne, G. W. Green, D. T. J. Joyce, J. M. Roslington, P. J. Tufton, H. C. Webber, and M. Healey, "Development in the Weighing Method of Automated Crystal Pulling," *J. Cryst. Growth* **24/25**, 369 (1974).
207. W. Bardsley, D. T. J. Hurle, G. C. Joyce, and G. J. Wilson, "The Weighing Method of Automatic Czochralski Crystal Growth II. Control Equipment," *J. Cryst. Growth* **40**, 21 (1977).

Crystal Growth Facilities (cont.)

208. T. R. Kyle and N. G. Zydzik, "Automated Crystal Puller," *Mater. Res. Bull.* **8**, 443 (1973).
209. R. DePope, J. Portier, G. Gauthier, and P. Hagenmuller, *Compt. Rend.* **265**, 124 (1967).
210. G. Garton and B. M. Wanklyn, *J. Amer. Ceram. Soc.* **50**, 395 (1967).
211. Y. Takeda, M. Sane, Y. Sweva Inagaki, and S. Naka, *J. Solid State Chem.* **20**, 261 (1977).
212. B. M. Wanklyn, "The Flux Growth of Some Fluorides (AlF_3, CrF_3, NiF_2, $KNiF_3$, CoF_2, $KCoF_3$)," *J. Cryst. Growth* **5**, 279 (1969).

Computer Simulations of Glass Structure 2-312

213. L. V. Woodcock, in *Advances in Molten Salt Chemistry*, J. Braunstein et al., Eds. (Plenum, New York, 1975).
214. *Laser Program Annual Report—1979*, Lawrence Livermore National Laboratory, Livermore, Calif., UCRL-50021-79 (1980).
215. S. A. Brawer and M. J. Weber, *Phys. Rev. Lett.* **45**, 460 (1980).
216. L. Verlet, *Phys. Rev.* **159**, 98 (1967).
217. S. A. Brawer, *J. Chem. Phys.* **72**, 4264 (1980).
218. C. A. Angell, to be published in *Adv. Chem. Phys.*
219. S. A. Brawer and W. B. White, *J. Non-Cryst. Sol.* **23**, 261 (1977).
220. S. A. Brawer and W. B. White, *J. Chem. Phys.* **63**, 2421 (1975).
221. S. A. Brawer, submitted to *Phys. Rev. Lett.*
222. S. A. Brawer and M. J. Weber, *J. Non-Cryst. Solids* **38**, 9 (1980).

Anomalous Low-Frequency Excitations in BeF_2 Glass 2-318

223. S. Hunklinger and W. Arnold, in *Phys. Acoustics*, Vol. 12, W. P. Mason and R. N. Thurston, Eds. (Academic Press., New York, 1976).
224. J. T. Krause and C. R. Kurkjian, *J. Am. Ceram. Soc.* **51**, 226 (1968).
225. P. W. Anderson, B. J. Halperin, and C. M. Varma, *Philos. Mag.* **25**, 1 (1972).
226. J. Jackle, *Z. Phys.* **257**, 212 (1972).
227. B. Fischer and M. W. Klein, *Solid State Commun.* **35**, 37 (1980).
228. R. Vacher, H. Sussnr, and S. Hunklinger, *Phys. Rev.* **B21**, 5850 (1980).
229. S. A. Brawer, *J. Chem. Phys.* **72**, 4264 (1980).
230. S. A. Brawer and N. J. Weber, *Phys. Rev. Lett.* **45**, 460 (1980).

Vibronic Spectra of Rare Earths in Glass 2-321

231. V. K. Zakharov, I. V. Kovaleva, V. P. Kolobkov, and L. F. Nikolsev, *Opt. Spektrosk.* **42**(5), 532 (1977).
232. M. J. Weber, "Laser Excited Fluorescence Spectroscopy of Glass," *Laser Spectroscopy in Solids*, W. M. Yen and P. M. Selzer, Eds. (Springer-Verlag, Berlin, 1981) (in press).
233. *Laser Program Annual Report—1979*, Lawrence Livermore National Laboratory, Livermore, Calif., UCRL 50021-79 (1980), p. 2-240.
234. S. A. Brawer and M. J. Weber, "Studying Glass Structure with Laser-Excited Fluorescence and Computer Simulation," *Energy and Technology Review*, Lawerence Livermore National Laboratory, Livermore, Calif., UCRL-52000-80-4 (1980), pp. 1-12.
235. S. A. Brawer and M. J. Weber, "Theoretical Study of the Structure and Optical Properties of Rare-Earth-Doped BeF_2 Glass," *J. Non-Cryst. Solids* **38/39**, 9-14 (1980).
236. S. A. Brawer and M. J. Weber, "Monte Carlo Simulation of Eu^{3+}-Doped BeF_2 Glass," *Phys. Rev. Lett.* **45**, 460–463 (1980).

Surface Physics and Chemistry of Laser-Induced Damage 2-324

237. D. L. Rousseau, G. E. Leroi, and W. E. Falconer, "Charged Particle Emission Upon Laser Irradiation of Transparent Dielectric Materials," *J. Appl. Phys.* **39**, 3328 (1968).
238. E. M. Logothetis and P. L. Hartmann, "Laser Induced Electron Emission from Solids: Many Photon Photoelectric Effects and Thermionic Emission," *Phys. Rev.* **187**, 460 (1969).
239. M. M. Sobolev and V. S. Myl'nikov, "Emission of Electrons from a Zinc Sulfide Crystal Excited with Neodymium Laser Irradiations," *Sov. Phys. Solid State* **18**, 1046 (1976).
240. V. P. Krutyakova and V. N. Smirnov, "Electron Emission from Alkali Halide Crystals Irradiated by a Pulsed CO_2 Laser," *Sov. Phys. Tech. Phys.* **24**, 1085 (1979).
241. T. Kykova, Yu. P. Efimov, and A. M. Tyutikov, "Some Features of Emission from Transparent Dielectrics Under Laser Irradiation," *Izvestiya Akademii Nauk SSSR, Seriya Fizicheskaya* **43**, 601 (1979).
242. T. T. Kykova, Yu. P. Efimov and A. M. Tyutikov, "Emission Delay in the Laser Irradiation of LiF," *Sov. Phys. Tech. Phys.* **24**, 520 (1979).
243. B. G. Gorshkov, A. S. Epifanov, and A. A. Manenkov, "Avalanche Ionization Produced in Solids by Large Radiation Quanta and Relative Role of Multiphoton Ionization in Laser Induced Breakdown," *Sov. Phys. JETP* **49**, 309 (1979).
244. B. G. Gorshkov, Yu. K. Danileiko, A. S. Epifanov, V. A. Lobachev, A. A. Manenkov, and A. V. Sidorin, "Laser Induced Breakdown of Alkali Halide Crystals." *Sov. Phys. JETP* **45**, 612 (1977).
245. S. Brawer, "Phenomenological Theory of Laser Damage in Insulators," *Phys. Rev.* **20**, 3422 (1979).
246. R. Yen, J. Liu, and N. Bloembergen, *Opt. Commun.* **35**, 277 (1980).
247. W. H. Strehlow and E. L. Cook, "Compilation of Energy Band Gaps in Elemental and Binary Compound Semiconductors and Insulators," *J. Phys. Chem. Ref. Data* **2**, 177 (1973).
248. V. S. Fomenkow, *Handbook of Thermionic Properties* (Plenum Press Data Division, New York, 1966).

High-Cross-Section Nd^{3+} Laser Glasses 2-328

249. See, for example, P. H. Sarkies, J. N. Sandoe, and S. Parke, *Br. J. Appl. Phys. (J. Phys. D)* **4**, 1642 (1971); R. R. Jacobs and M. J. Weber, *IEEE J. Quantum Electron.* **QE-12**, 102 (1976); N. B. Brachkovskaya, A. A. Grubin, S. G. Lunter, A. K. Przhevuskii, E. L. Raaben, and M. N. Tolstoi, *Sov. J. Quantum Electron.* **6**, 534 (1976); and references cited therein.
250. W. F. Krupke, *IEEE J. Quantum Electron.* **QE-10**, 450 (1974).
251. M. J. Weber, *J. Non-Cryst. Solids* **42**, 189 (1980).
252. J. M. Pellegrino, W. N. Yen, and M. J. Weber, *J. Appl. Phys.* **51**, 6332 (1980).
253. O. K. Deutschbein, C. C. Pautrat, and I. M. Suirchevsky, *Rev. Phys. Appl.* **2**, 29 (1967).
254. O. K. Deutschbein and C. C. Pautrat, *IEEE J. Quantum Electron.* **QE-4**, 48 (1968).
255. M. J. Weber, J. D. Myers, and D. H. Blackburn, *J. Appl. Phys.* (in press).
256. L. G. Van Uitert and S. H. Wemple, *Appl. Phys. Lett.* **33**, 57 (1978).
257. C. A. Angell and D. C. Ziegler, "Inorganic Chloride and Mixed Halide Glasses with Low Maximum Phonon Frequencies," *Mat. Res. Bull.* (in press).
258. M. J. Weber and R. M. Almeida, "Large Stimulated Emission Cross Sections of Nd^{3+} in Chlorophosphate Glass," *J. Non-Cryst. Solids* (in press).
259. G. J. Linford, R. A. Saroyan, J. B. Trenholme, and M. J. Weber, *IEEE J. Quantum Electron.* **QE-15**, 510 (1978).

Quantum Efficiency Measurements 2-330

260. J. G. Calvert and J. N. Pitts, Jr., *Photochemistry* (Wiley, New York, 1966).
261. E. M. Dianov, A. Ya. Karasik, V. B. Neustruev, A. M. Prokhorov and I. A. Shcherbakov, *Dokl. Akad. Nauk SSSR (Sov. Phys. Doklady)* **20**, 622 (1976).
262. L. A. Riseberg and M. J. Weber, in *Progress in Optics XV*, E. Wolf, Ed. (North-Holland Publishing Co., New York, 1976).
263. A. Rosencwaig in *Advances in Electronics and Electron Physics* **46**, L. Marton, Ed. (Academic Press, New York, 1978).
264. A. Rosencwaig and E. A. Hildum, "Nd^{3+} Fluorescence Quantum Efficiency Measurements With Photoacoustics," Lawrence Livermore National Laboratory, Livermore, Calif., UCRL-85099 (1980); *Phys. Rev.* **B1**, in press.
265. R. S. Quimby and W. M. Yen, *Opt. Lett.* **3**, 181 (1978).
266. C. Brecher, L. A. Riseberg, and M. J. Weber, *Appl. Phys. Lett.* **30**, 475 (1977).
267. R. C. Powell, D. P. Neikirk and D. Sardar, *J. Opt. Soc. Am.* **70**, 486 (1980).
268. A. Rosencwaig and A. Gersho, *J. Appl. Phys.* **47**, 64 (1976).
269. A. J. DeGroot and M. J. Weber, unpublished.
270. C. B. Layne, W. H. Lowdermilk, and M. J. Weber, *IEEE J. Quantum Electron.* **11**, 798 (1975).
271. A. Hordvik and H. Schlossberg, *Appl. Opt.* **16**, 101 (1977).
272. C. Brecher, L. A. Riseberg, and M. J. Weber, *Phys. Rev. B* **18**, 5799 (1978).
273. W. F. Krupke, *IEEE J. Quantum Electron* **7**, 153 (1971).
274. T. Kushida and J. Geusic, *Phys. Rev. Lett.* **21**, 1172 (1968).
275. P. F. Liao and H. P. Weber, *J. Appl. Phys.* **45**, 2931 (1974).
276. S. Singh, R. G. Smith, and L. G. Van Uitert, *Phys. Rev. B* **10**, 2566 (1974).
277. C. J. Kennedy and J. D. Barry, *Appl. Phys. Lett.* **31**, 91 (1977).

Homogeneous Line Widths and Energy Extraction in Laser Glass 2-335

278. P. M. Selzer, D. L. Huber, D. S. Hamilton, W. M. Yen, and M. J. Weber, *Phys. Rev. Lett.* **36**, 813 (1976).
279. P. Avouris, A. Campion, and M. A. El-Sayed, *J. Chem. Phys.* **67**, 3397 (1977).
280. T. Kushida and E. Takushi, *Phys. Rev. B* **12**, 824 (1975).
281. E. P. Papadakis, *J. Acoust. Soc. Amer.* **42**, 1045 (1967) and references therein.
282. J. M. Pellegrino, W. M. Yen, and M. J. Weber, *J. Appl. Phys.* **51**, 6332 (1980).
283. J. Hegarty and W. M. Yen, *Phys. Rev. Lett.* **43**, 1126 (1979).
284. M. J. Weber, "Laser Excited Fluorescence Spectroscopy in Glass" in *Laser Spectroscopy in Solids*, W. M. Yen and P. M. Selzer, Eds. (Springer-Verlag, Berlin, 1981).
285. S. A. Brawer and M. J. Weber, *Appl. Phys. Lett.* **35**, 31 (1979).

Work performed under the auspices of the U.S. Department of Energy by Lawrence Livermore National Laboratory under Contract W-7405-Eng-48.

U.S. Government Printing Office/1981/11—587/209

Lawrence Livermore National Laboratory